Geological and Metallogenic Evolution of the Palaeoproterozoic Adam Ahmed Mouloude Region of the Reguibat Shield, Western Sahara

by

Joshua Combs



Thesis submitted to the University of Oxford

for the degree of Doctor of Philosophy

Department of Earth Sciences

and

Wolfson College

Trinity Term 2018

Geological and Metallogenic Evolution of the Palaeoproterozoic Adam Ahmed Mouloude Region of the Reguibat Shield, Western Sahara

Joshua Combs

Thesis submitted to the University of Oxford for the degree of Doctor of Philosophy
Department of Earth Sciences and Wolfson College
Trinity Term 2018

Abstract

The Adam Ahmed Mouloude Region of the Liberated Territories of Western Sahara is a previously unstudied region of the Reguibat Shield. Crucially, the region covers a large portion of the 'Contact Zone' between the Archaean and Palaeoproterozoic components of the Reguibat Shield, exposed as only a small wedge in neighbouring Mauritania. Two distinct tectonic terranes were identified in the study area, the Leaareig Terrane (ca. 2.22 to 2.15 Ga) in the west and the Sfariat-Bu Daira Terrane (ca. 2.14 to 2.09 Ga) in the east. The Sfariat-Bu Daira Terrane contains the only known anorthosite complex to contain both megacrystic and massif-type anorthosite, normally formed in different tectonic settings at different periods in the Earth's history.

Strong geological and geophysical correlations between the Leaareig and Sfariat-Bu Daira Terrane formed the basis for the proposal of the first geodynamic model for the formation of the West African Craton. This model includes the formation of two volcanic arc terranes (>2.13 Ga), their collision with each other (~2.13-2.12 Ga), a collisional event between the now fully assembled Palaeoproterozoic Terrane with the Archaean Terrane (~2.10-2.09 Ga) followed by mantle delamination and widespread post-collisional magmatism (2.09-2.02 Ga).

The Leaareig and Sfariat-Bu Daira Terranes are highly prospective for gold with the potential for other types of mineral deposits including magmatic Ni-Cu-(Co-PGE) sulphide, platinum group element-bearing chromitite, orthomagmatic Fe-Ti-V oxide and Superior-type Iron.

Geological and Metallogenic Evolution of the Palaeoproterozoic Adam Ahmed Mouloude Region of the Reguibat Shield, Western Sahara

Joshua Combs

Thesis submitted to the University of Oxford for the degree of Doctor of Philosophy

Department of Earth Sciences and Wolfson College

Trinity Term 2018

Extended Abstract

The West African Craton is one of the largest cratons in Africa extending from Morocco, Algeria and Western Sahara in the north to Liberia, Ivory Coast and Ghana in the south. It is comprised of two outcropping shields of Precambrian basement separated by the Neoproterozoic to Palaeozoic Taoudeni Basin. The basement material is exposed in the south of the craton as the Man-Leo Shield, and, due to prolific gold mineralisation has been relatively well studied over the past 100 years. By contrast, the basement material that outcrops in the north as the Reguibat Shield is relatively understudied, due to remoteness and regional politics. Both the Man-Leo and Reguibat shields are composed of an Archaean terrane in the west and a Palaeoproterozoic terrane in the east.

The Adam Ahmed Mouloude Region of the Liberated Territories of Western Sahara represents a previously unstudied region of the Reguibat Shield. Crucially, the region covers a large portion of the 'Contact Zone' between the Archaean and Palaeoproterozoic components of the Reguibat Shield, exposed as only a small wedge in neighbouring Mauritania.

Geochronological work completed as part of this project involved U-Pb zircon geochronology on nineteen samples from across the Adam Ahmed Mouloude region. The results from the geochronology provided the basis for the differentiation of the study area, previously grouped as the 'Contact Zone', into two separate Palaeoproterozoic terranes. The

Leaareig Terrane in the west contains plutonic and sub-volcanic rocks ranging in age from ca. 2220 to 2150 Ma, while plutonic and volcanic rocks of the Sfariat-Bu Daira Terrane are younger at ca. 2140 to 2090 Ma.

The Leaareig Terrane consists of four domains; the Leaareig Domain, the Taghsoumat-Aghsoumal Belt, the Agarasras Lakhadar Complex and the Sassaiate-Temmimichate–Tsabaya Complex.

- The Leaareig Domain is major component of this terrane, forming a wedge of orthogneiss and metasedimentary rocks with belts of paragneiss and marble to the northeast and southwest. The domain is bound to the northeast by a major northwest-southeast trending shear zone, to the south by the Sassaiate-Temmimichate–Tsabaya Complex, and the Taghsoumat-Aghsoumal Belt to the north.
- The Taghsoumat-Aghsoumal Belt consists of northwest-southeast trending volcanic, volcanosedimentary, metasedimentary and orthogneiss belts intruded by late stage syn- to post tectonic granites.
- Not directly connected with the rest of the Leaareig Terrane within the study area, the Agarasras Lakhadar Domain represents a back-arc basin formed from the same arc as the rest of the Leaareig Terrane. It consists of an ophiolite sequence (ultramafics-gabbro-pillow basalts), with lithologies to the west including units of basalt and chert, paragneiss and marble, and undifferentiated mafic/ultramafic rocks, and is bounded by a sole thrust emplacing the package over the Oum Abana Belt (of the Sfariat-Bu Daira Terrane).
- The Sassaiate-Temmimichate–Tsabaya Complex forms a belt at the south of the terrane consisting of intermediate to mafic orthogneiss, paragneiss, migmatite, amphibolite as well as thick beds of marble (up to 1km) and iron rock. The complex

extends into Mauritania, where it consists of quartzo-feldspathic and mafic gneisses intruded by granodiorite.

The Sfariat-Bu Daira Terrane forms a northwest-southeast trending belt between the Leaareig Terrane in the south and the Palaeoproterozoic granites to the northeast. It comprises four Domains: the Elmalhat Domain, the Oum Abana Belt, the Anajim Guebli Suite and the Riche Anajim Group:

- Outcropping almost exclusively in Western Sahara, the Elmalhat Domain and Oum Abana Belt respectively represent the mid-crustal and extrusive remnants of an Eburnean island arc sequence.
    - The Oum Abana Belt consists of northwest-southeast trending, metamorphosed belts of sedimentary, volcanosedimentary and volcanic sequences interspersed with granite-gneiss belts, all intruded by syn- and post-tectonic granitoid and gabbroic intrusions.
    - To the southeast of the Oum Abana Domain, the Elmalhat Domain represents the mid-crustal plutonic rocks of the volcanic arc sequence. It is composed of granite intrusions, orthogneiss, and gabbro intrusions, as well as the Elmalhat Anorthosite Complex (EAC), which forms a major feature of the Elmalhat Domain.
- In Mauritania the Sfariat-Bu Daira Domain is represented mainly by the Anajim Guebli Suite, consisting of abundant thin units of ferruginous quartzite and marble, BIF, migmatitic gneiss, and amphibolite facies paragneiss, as well as syntectonic granite. These have been interpreted during previous work as representing the deformed remnants of the continental platform sediments, deposited at what was then the edge of the craton.

- The Riche Anajim Group makes up the central zone of the Sfariat Shear Zone, a major NW-SE striking shear zone ranging in width from ~4 to ~6km within the field area. It comprises largely mylonitic, migmatitic paragneiss and quartzofeldspathic schist, aplitic microgranite as well as foliated metagranite. The most prominent feature of the shear zone is ridges of banded iron formation (BIF), with thin beds of locally brecciated impure marble.

The Elmalhat Domain is defined by the presence of the Elmalhat Anorthosite Complex (EAC). It appears to be the only known anorthosite complex on earth to contain both 'megacrystic' and 'massif-type' anorthosite. Field relationships demonstrate that the anorthosite was formed in at least two stages, with the earlier forming megacrystic anorthosite having been intruded by massif-type anorthosite. A combination of relative dating, constrained by U-Pb zircon geochronology, and whole rock Sm-Nd geochronology constrain the age of the massif-type anorthosite to be ca. 2.13 Ga. No maximum age constraints exist for the megacrystic anorthosite, though it is unlikely to be older than the oldest (~2.2Ga) rocks in the Palaeoproterozoic terrane, potentially making it the youngest megacrystic anorthosite in the world.

Megacrystic and massif-type anorthosites are believed to form in different tectonic settings and different crustal levels. Megacrystic anorthosites are attributed to an island arc (or Archaean equivalent) type setting, emplaced in shallow sub-volcanic settings, while massif-type anorthosites are emplaced at mid-crustal levels, requiring the presence of thickened continental crust at continental arc settings. Detailed work completed on each type of anorthosite in the EAC, including petrology, mineral chemistry and trace element geochemistry is consistent with these different tectonic settings. This disparity is resolved when the regional tectonic environment is considered. The process of terrane accretion can result in rapid thickening of the crust and a transition from an island arc setting (e.g. Japan)

to a continental arc setting (e.g. the Andes). This rapid transition in tectonic setting allowed for the formation of the Elmalhat Anorthosite Complex, with the megacrystic anorthosite forming in a pre-accretion island arc setting, while the massif-type anorthosite formed in the post-accretion continental arc setting.

A new tectonic model is proposed for the formation of the Leaareig and Sfariat-Bu Daira Terranes. The region appears to have formed though the accretion of two distinct Palaeoproterozoic (Leaareig and Sfariat-Bu Daira) volcanic arcs, and later collision with the Archaean craton. The geodynamic model involves four stages of terrane growth and assembly:

- 2.24 to 2.15 Ga – Formation of the Leaareig Terrane as an island arc of evolving maturity. During the growth of this arc a back-arc basin was formed and filled with sediments shedding off the arc. At the end of subduction, a piece of the back arc was obducted and is now observed as the ophiolite complex in the Agarasras Lakhadar Domain.
- 2.14 to 2.13 Ga - Formation of the Sfariat-Bu Daira Terrane as an island arc of evolving maturity. The megacrystic anorthosite was formed at a shallow, sub-volcanic level in a relatively immature island arc environment.
- 2.13 to 2.12 Ga – The collision between the Leaareig and Sfariat-Bu Daira Terranes involved the thickening of the crust allowing for the formation of the massif-type anorthosite. In the same event the previously sub-volcanic megacrystic anorthosite is tectonically buried to a mid-crustal level and is intruded by the massif-type anorthosite.
- ~2.10 Ga – Collision of the Palaeoproterozoic Terrane with the Archaean Terrane in a sinistral transpressive event. This results in increased magmatic activity at ~2.10-

2.09 Ga within the study area, with a sample of migmatite close to the contact with the Archaean Terrane revealing an age of anataxis of 2.10 Ga.

The definition of the Oum Abana and Taghsoumat-Aghsoumal Belts allows for the first direct comparison of specific belts in the Reguibat Shield with those in the Man-Leo Shield. Strong similarities in terms of stratigraphy and the timing of magmatic events are observed between these belts and a series of Birimian belts in Burkina Faso and Mali. The presence of a number of rare geological features in these belts on either side of the Taoudeni Basin strengthens this correlation. These geological features include the presence of megacrystic anorthosite in the Boromo and Houndé Belts of Burkina Faso. The Boromo and Houndé Belts also contain sequences of ultramafic rocks, gabbro and pillow basalt, very similar to the sequence that has been interpreted as an ophiolite sequence in the Agarasras Lakhadar Domain. Additionally, geophysical anomalies are observed across the Taoudeni Basin, generally trending from these belts in the Man-Leo Shield toward the centre of the Reguibat Shield where the study area is located.

These direct correlations of volcanosedimentary belts across the Taoudeni Basin allows for the comparison of the geodynamic model proposed for the formation of the Sfariat-Bu Daira and Leaareig Terranes, of the Reguibat Shield, with recently proposed models for the formation and assembly of the Man-Leo Shield during the Palaeoproterozoic. The proposed model for the geodynamic evolution of a combined Reguibat – Baoulé-Mossi Block involves three stages:

- 2.25 to 2.125 Ga – growth and assembly of the Palaeoproterozoic terranes. Like the Reguibat Shield (Leaareig and Sfariat-Bu Daira Terranes), by ~2.15 Ga, the domain comprised two separate tectonic blocks that collided at ~2.13 Ga.
- 2.125 to 2.09 Ga – collision of the Palaeoproterozoic and Archaean Terranes. The collision between the Palaeoproterozoic Baoulé-Mossi and Archaean Kenema-Man

Domains of the Man-Leo Shield is constrained to 2.10 to 2.09 Ga. This timing is similar to the equivalent contact in the Reguibat Shield, on the eastern margin of the Kenema-Man Domain. This collision occurred during a sinistral transgressive event.

- 2.09 to 2.02 Ga – post-collisional magmatism. Following the collision, widespread magmatism occurs in the western block of the Baoulé-Mossi Domain and the eastern and northern margins of the Kenema-Man Domain. This magmatism is not observed in the Archaean of the Reguibat Shield or proximal to the contact, though the eastern portion of the dominated by extensive ~2.09-2.05 Ga post-collisional magmatism.

A metallogenic profile produced during this project revealed numerous styles of mineralisation including orogenic gold and superior-type banded iron formation (BIF), predominantly in the north of the study area, as well as chromitite-hosted platinum group elements (PGE), Fe-Ti-V oxide and Ni-Cu(-Co-PGE) magmatic sulphide mineralisation associated with the EAC. Based on these observed mineral occurrences and correlations with the Birimian of the Man-Leo Shield, a prospectivity assessment was constructed for the study area. In order of significance, the prospectivity of the region is as follows:

- Orogenic gold mineralisation. Strong geochronological and lithological correlations between heavily mineralised Birimian belts, and direct evidence of vein-hosted and disseminated gold mineralisation within the field area make the Sfariat-Bu Daira and Leaareig Terranes highly prospective regions for orogenic gold mineralisation. More specifically, the Oum Abana and Taghsoumat-Aghsoumal Belts have the highest potential orogenic gold mineralisation.
- Magmatic Ni-Cu-(Co-PGE) magmatic sulphide mineralisation. The EAC fulfils several key exploration criteria for Voisey's Bay-style Ni-Cu-(Co-PGE) magmatic sulphide mineralisation including:

- The presence of magmatic sulphides. This indicates that sulphide saturation was reached within the complex.
- Derivation from a primitive, Ni-rich magma. Olivine mineral chemistry suggests that the labradorite massif-type anorthosite, and associated lithologies, were derived from a parent magma that was enriched in Ni. Furthermore, the high forsterite content of the olivine indicates that the magma was more primitive than the world-class Voisey's Bay deposit.
- Furthermore, olivine mineral chemistry indicates that the leucotroctolite is Ni-depleted compared to its ultramafic equivalent, indicating that it may have experienced a sulphur saturation event.
- Palaeoproterozoic to Archaean in age. The EAC is formed at ~2.13 Ga.
- Location proximal to the Archaean-Palaeoproterozoic contact, much like the Voisey's Bay deposit and other Ni-Cu deposits in Canada relating to mafic-ultramafic complexes.

- Chromitite-hosted PGE mineralisation.
  - Assay results and the observation of magmatic sulphides within the chromitite seam indicate the potential for Pt + Pd concentration associated with a sulphur saturation event during the formation of the chromitite seam. Evidence also exists for the preferential removal of mobile Pt and Pd-bearing PGE grains due to hydrothermal fluids.
  - The host rock, size and mineral chemistry of the chromitite seam within the Northern Limb of the EAC are very similar to the Archaean Sittampundi (megacrystic-) Anorthosite Complex in India. Mineralisation at Sittampundi only exists over a strike of 3.6 km in a ~17 km long complex.

    - Therefore, potential exists for significant PGE mineralisation in the Northern Limb of the EAC, with unaltered sections of chromitite being the best targets along the 19 km strike of the chromitite seam.
- Orthomagmatic Fe-Ti-V oxide mineralisation. Magnetite seams within the Southern Bulb of the EAC contain high grades of Fe, Ti and V, although only limited outcrop has been observed. Ground magnetic surveys reveal a magnetic anomaly associated with these seams, striking 6 to 8 km under regions covered by sand and sabkhas, suggesting potentially significant mineralisation within the Southern Bulb.
- Superior-type iron formations. Significant portions of Superior-type iron are observed, tectonically thickened within the Sfariat Shear Zone. Although all samples taken are low-grade, if a zone of enrichment (silica-leaching) can be identified, this belt could contain significant mineralisation.
- Correlations between the Boromo Belt of Burkina Faso and the Leaareig Terrane suggest the potential for volcanic massive sulphide (VMS) and/or porphyry Cu-Au mineralisation, although no evidence has been observed in the field.

Acknowledgements

First and foremost, I would like to thank my supervisors Laurence Robb and Dave Waters. Their combined influence sees me ten times the geologist I was when I started. Laurence's encyclopaedic geological knowledge helped me greatly in my overall interpretation of the region. His feedback on my work was always amazing, forcing me to raise my standards and take my work to a higher level. As someone who is looking at a future career in economic geology, I could not think of a better person to have studied under for the past 4 years. Dave's enthusiasm for petrology and attention to detail is second to none. His skills in petrology are out of this world, I can only hope that a little bit of it rubbed off on me during my time here.

I'm extremely grateful for the support and funding from Hanno Resources Limited that I received over the course of the PhD. A massive thank you to Caedmon Marriott for making it all possible. Without Caed, I would never have ended up in Oxford and none of this would have taken place. His continued support over the duration of the project is also appreciated.

I'd also like to extend my sincere thanks to the entire Hanno Resources field team. Without the team, the field trips would not have been possible. Thanks in particular to Bachir Mehdi for taking care of logistics on the ground and bringing it all together to make the field trips run smoothly.

I'd like to thank Joan Carles Melgarejo Draper and the University of Barcelona for hosting me on two occasions, once at the start of 2014 prior to my commencement at Oxford and again in January this year. From the bottom of my heart I'd like to thank Joan Carles for the time and effort he put in helping me with microprobe analysis and with general petrological work while I was there. Saleh Lehbib was also always very willing to help me with general knowledge about Western Sahara geology and would always go out of his way to provide me with the data that I required. Thanks also to Jingyao Xu for your time and effort on the microprobe analyses.

Thanks to Grant Bybee for our valuable discussions about anorthosite and for the feedback on my model.

A special shout out to Chris Lyche. Talking to Chris every night when I was in the wars kept me sane. He also helped out a lot with proof reading the final drafts.

Completing a PhD is a long and hard road and would not have been possible without the support of my amazing friends. To little Ed, having you as a friend has made this year much easier. For my rowing friends – whilst you may have done the exact opposite of helping me to complete my PhD, you mentally aided me enormously. My friends in the department, for general chit chat and just keeping me sane. A special shout out to the best office in Oxford – 30:17 with Andrzej Wolniewicz, Danielle Kondla, Jenny Weeks and Grace Manley. You've been a blast and helped me to relax when things were stressful. Thanks also to Isobel Talks for reading my thesis and helping me out with grammar and spelling. Special mention to Tom Lamont for always being there for me and making me feel much more at home in the UK and to James King (the good looking one) for all of the romantic lunches. Honourable mention also to Phillip Gopon, for our thought provoking discussions during my PhD and for taking a (quartz) bullet for me in the field, allowing me to finish my thesis.

Thanks a heap to Peter Spitalny. It was his contagious passion for geology that inspired me to become a geologist and set me on this path in the first place.

Last but not least, I'd like to thank my family. Not only for the years of support before coming to Oxford but for your emotional support since I've been here and for all pitching in when I needed help. Especially Mum, Dad, Matthew, Nathan, grandad and grandma. Without your support, I would never have made it through this last year.



Hanno Resources Limited Exploration Team October 2014



Western Sahara geology's answer to the A-team.

Laurence Robb on the left and Caedmon Marriott on the right

Table of contents

Abstract i
Extended Abstract ii
Acknowledgements xi
Table of Contents xiii
List of Figures xxii
List of Tables xxxii

1.0 Introduction and Background Geology 1
1.1 Aims and Objectives 1
1.2 Research Location 3
1.3 Previous Work 4
1.4 Regional Geology 11
1.4.1 West African Craton 11
1.4.2 Man-Leo Shield 11
1.4.2.1 Kéména-Man (Archaean) Domain 12
1.4.2.2 Palaeoproterozoic Baoulé-Mossi Domain 14
1.4.2.2.1 Geology 14
1.4.2.2.2 Geodynamic Evolution 18
1.4.3 Reguibat Shield 22
1.4.3.1 Archaean Domain 24
1.4.3.1.1 Tasiast-Tijirit Terrane 24
1.4.3.1.2 Amsaga Complex 25
1.4.3.1.3 Layuad Domain 27
1.4.3.1.4 Mijek Domain 28
1.4.3.1.5 Ghallaman Domain – Zednes Suite 28
1.4.3.2 Palaeoproterozoic Domain 29
1.4.3.2.1 Leaareig Terrane 31
1.4.3.2.2 Sfariat-Bu Daira Terrane 36
1.4.3.2.3 Adam Esseder Domain 39

1.4.3.2.4 Yetti Terrane 43
1.4.3.2.5 Eglab Terrane 44
1.4.4 Overview of the Metallogeny of the West African Craton 49
1.4.5 Comparison of the Shields 53
1.4.5.1 Tectonic Setting 53
1.4.5.2 Comparison of the Volcanosedimentary Belts 59
2.0 U-Pb Zircon Geochronology of the Leaareig and Sfariat-Bu Daira Terranes 61
2.1 Introduction 61
2.2 Results 63
2.3 Definition of Terranes 72
3.0 Geology of the Leaareig Terrane 75
3.1 Leaareig Domain 77
3.1.1 Introduction 77
3.1.2 Geology and Structure (Mapping/field relations) 78
3.1.2.1 Orthogneiss-granite basement 80
3.1.2.2 Paragneiss and Metasedimentary Rocks 81
3.1.2.3 Contact near the Elmalhat Domain 82
3.1.3 Petrography 82
3.2 Taghsoumat-Aghsoumal Domain 86
3.2.1 Introduction 86
3.2.2 Geology and Structure (Mapping/field relations) 86
3.2.2.1 Orthogneiss 88
3.2.2.2 Volcanosedimentary Belt 89
3.2.2.3 Marble and metabasalt 91
3.2.2.4 Late intrusions 91
3.3 Agarasras Lakhadar Domain 92
3.3.1 Introduction 92
3.3.2 Geology and Structure (Mapping/Field Relations) 93
3.3.2.1 Mafic-Ultramafic Complex 93
3.3.2.1.1 Ultramafics 94
3.3.2.1.2 Gabbro 97
3.3.2.1.3 Dolerite (Sheeted?) 97
3.3.2.1.4 Pillow Basalt 99
3.3.2.1.5 Carbonatite Vein 102
3.3.2.1.6 Structure of the Complex 103

3.3.2.2 Basalt and Chert 106
3.3.2.3 Metasedimentary Rocks 107
3.3.2.4 Mafic-Ultramafic Intrusion 108
3.3.2.5 Structural Features 109
3.3.3 Petrography 110
3.3.3.1 Mafic-Ultramafic Complex 110
3.3.3.1.1 Ultramafics 110
3.3.3.1.2 Gabbro 114
3.3.3.1.3 Basalt 115
3.3.3.1.4 Carbonatite 117
3.3.4 Whole Rock Geochemistry of the Pillow Basalts 117
3.3.4.1 Traditional Diagrams 117
3.3.4.2 Multi-dimensional Tectonic Discrimination Diagrams 122
3.3.5 Discussion and Tectonic Setting 124
3.4 Sassaiate -Temmimichate-Tsabaya Complex 124
3.4.1 Introduction 124
3.4.2 Geology and Structure (Mapping/field relations) 125
3.4.3 Age of the Complex 128
3.5 Geochemistry and tectonic setting 129
3.5.1 Whole Rock Geochemistry 129
3.5.1.1 Introduction to Tectonic Discrimination diagrams 129
3.5.1.2 Traditional tectonic discrimination diagrams 134
3.5.1.2.1 Mafic and intermediate rocks 135
3.5.1.2.2 Felsic rocks 140
3.5.1.3 Multi-dimensional tectonic discrimination diagrams 140
3.5.1.3.1 Mafic rocks 141
3.5.1.3.2 Intermediate rocks 143
3.5.1.3.3 Felsic rocks 146
3.5.2 Tectonic setting 148
4.0 Geology of the Sfariat-Bu Daira Terrane 152
4.1 Elmalhat Domain 154
4.1.1 Introduction 154
4.1.2 Geology and Structure 157
4.1.2.1 Basement 157
4.1.2.1.1 Orthogneiss and Granite 157

4.1.2.1.2 Paragneiss 159
4.1.2.2 Elmalhat Anorthosite complex 161
4.1.2.2.1 Introduction to Anorthosite 161
4.1.2.2.2 Megacrystic anorthosite 167
4.1.2.2.2.1 Northern Limb 167
4.1.2.2.2.2 Anorthosite and related rocks along the contact with the Oum Abana Domain 180
4.1.2.2.2.3 Other Megacrystic Anorthosite 183
4.1.2.2.3 Massif-type anorthosite 185
4.1.2.2.3.1 Main Bulb 185
4.1.2.2.3.2 Southern Bulb 197
4.1.2.2.3.3 Moug El Kaleb 205
4.1.2.2.4 Satellite Intrusions 210
4.1.2.3 Gabbro and Ultramafic Intrusions 210
4.1.2.4 Late Granite Intrusions 215
4.1.2.5 Structure 215
4.1.2.6 Field Relations and Geochronology 216
4.1.3 Petrography 219
4.1.3.1 Basement 219
4.1.3.1.1 Orthogneiss 219
4.1.3.1.2 Paragneiss 220
4.1.3.2 Elmalhat Anorthosite Complex 222
4.1.3.2.1 Northern Limb 222
4.1.3.2.1.1 Megacrystic (Meta-)anorthosite 223
4.1.3.2.1.2 Chromitite 227
4.1.3.2.1.3 Amphibolite 229
4.1.3.2.2 Main Bulb 230
4.1.3.2.2.1 Dark Anorthosite 230
4.1.3.2.2.2 Contact Diorite 235
4.1.3.2.2.3 Ultramafic Intrusions 235
4.1.3.2.2.4 Massif-type Anorthosite with Megacrystic Anorthosite Xenoliths 237
4.1.3.2.2.5 White Anorthosite 238
4.1.3.2.3 Satellite Intrusions 241
4.1.3.3 Gabbro, Ultramafics and Listwanite 245
4.1.3.4 Late Granite Intrusions 249

4.1.4 Mineral Chemistry 252
4.1.4.1 Silicate Mineral Chemistry 253
4.1.4.2 Chromite Mineral Chemistry 259
4.1.4.3 Sulphur isotopes 260
4.1.4.4 Clinopyroxene tectonic discrimination 261
4.1.5 Whole Rock Geochemistry 263
4.1.5.1 Tectonic Discrimination of Non-Cumulate Rocks Related to the Elmalhat Anorthosite Complex 264
4.1.5.2 Trace Element Chemistry 265
4.1.5.3 Th/Yb-Nb/Yb Comparison to Archaean Anorthosite 268
4.1.5.4 Major Element Geochemistry 269
4.1.6 Discussion and Tectonic Setting 272
4.1.6.1 Megacrystic Anorthosite (Northern Limb) 272
4.1.6.2 Main Bulb (Massif-type Anorthosite) 277
4.1.6.3 Tectonic Setting 282
4.2 Oum Abana Belt 283
4.2.1 Introduction 283
4.2.2 Geology and Structure 286
4.2.2.1 Granite-gneiss belts 286
4.2.2.2 Volcanic Belt 287
4.2.2.3 Sedimentary Belts 289
4.2.2.4 Late intrusions 291
4.2.2.4.1 Granitoids 291
4.2.2.4.1.1 Agarasras Labiad 292
4.2.2.4.1.2 Agarasras G52 293
4.2.2.4.2 Red Porphyry 293
4.2.2.4.3 Gabbro-Diorite Intrusion 294
4.2.2.4.4 Ultramafic 295
4.2.2.4.5 Anorthosite 295
4.2.2.4.6 Dolerite dykes 296
4.2.2.5 Field Relations and Geochronological constraints 296
4.3 Anajim Guebli Domain 297
4.3.1 Introduction 297
4.3.2 Geology and Structure (Mapping/field relations) 297
4.4 Riche Anajim Group 300

4.4.1 Introduction 300
4.4.2 Geology and Structure 301
4.4.2.1 Geology 301
4.4.2.2 Structure 308
4.4.3 Petrography 310
4.4.3.1 BIF 310
4.4.3.2 Marble 312
4.4.3.3 Gneiss to Mylonite 313
4.5 Geochemistry and Tectonic Setting 315
4.5.1 Whole Rock Geochemistry 315
4.5.1.1 Traditional Tectonic Discrimination Diagrams 316
4.5.1.1.1 Mafic and Intermediate Rocks 317
4.5.1.1.2 Granitic Rocks 321
4.5.1.2 Multi-Dimensional Tectonic Discrimination Diagrams 322
4.5.1.2.1 Mafic Rocks 322
4.5.1.2.2 Intermediate Rocks 322
4.5.1.2.3 Felsic Rocks 325
4.5.2 Tectonic Setting 327
5.0 Metallogeny of the Leaareig and Sfariat Bu-Daira Terranes 330
5.1 Gold 330
5.1.1 Orogenic Gold 331
5.1.1.1 Introduction to Orogenic Gold 331
5.1.1.2 Mineralisation in the Study Area 333
5.1.1.2.1 Agarasras G52 335
5.1.1.2.2 Agarasras Labiad 338
5.1.1.2.3 Moug El Kaleb (Cu-Au) 339
5.1.1.2.4 Guelb Koujil 341
5.1.1.2.5 Agarasras Lakhadar 342
5.1.1.2.6 Taghsoumat 342
5.1.1.2.7 Elmalhat 343
5.1.2 Near-surface Enrichment 343
5.2 Magmatic Sulphides (Ni, Cu, PGMs) 345
5.2.1 Introduction 345
5.2.2 Model of Formation within Anorthosite Complexes 345
5.2.3 Mineralisation in the Elmalhat Anorthosite Complex 347

5.3 Chromitite-hosted PGE Mineralisation 348
5.3.1 Chromite 348
5.3.2 Platinum Group Elements 350
5.4 Orthomagmatic Fe-Ti-V Oxide Seams 354
5.5 Superior-type Iron Formation of the Riche Anajim Group 358
6.0 Geological Synthesis 361
6.1 Elmalhat Anorthosite Complex (Petrogenetic Model) 362
6.2 Geodynamic Model for the Reguibat Shield 368
6.2.1 Introduction 368
6.2.2 Leaareig (~2.24-2.18 Ga) and Sfariat-Bu Daira (~2.14-2.13 Ga) Volcanic Arcs 370
6.2.3 Leaareig- Sfariat-Bu Daira Collision (~2.13-2.12 Ga) 370
6.2.4 Palaeoproterozoic-Archaean Collision (~2.10 Ga) 371
6.2.5 Pan African overprint (~600-500 Ma) 372
6.3 Archaean-Palaeoproterozoic Boundary 373
6.4 Correlations with the Palaeoproterozoic Baoulé Mossi Domain of the Man-Leo Shield 376
6.4.1 Previous comparisons 377
6.4.2 General trends in the Palaeoproterozoic of the Reguibat Shield compared to the Baoulé-Mossi Domain 380
6.4.3 Direct lithological and geochronological comparisons 386
6.4.3.1 General comparison with the Birimian belts 386
6.4.3.1.1 Stratigraphic 386
6.4.3.1.2 Geochemistry 387
6.4.3.1.2.1 Traditional 387
6.4.3.1.2.2 Multidimensional discrimination 388
6.4.3.2 Comparisons between individual belts 389
6.4.3.2.1 Morila 391
6.4.3.2.2 Banfora belt 393
6.4.3.2.3 Boromo and Houndé belts 395
6.4.4 Geophysics 397
6.4.5 Proposed Geodynamic Setting for a Combined Reguibat – Baoulé-Mossi Block 399
6.4.5.1 2250 to 2125 Ma – Assembly of the Baoulé-Mossi Domain 399
6.4.5.2 2125 to 2090 Ma – Collision of Baoulé-Mossi Domain with the Kéména-Man Domain 402

6.4.5.3 2090 to 2020 Ma – Post-Collisional Process 405
6.4.6 Lithological differences 408
6.4.7 Conclusions 409
7.0 Prospectivity Assessment of the Study Area 411
7.1 Gold 414
7.1.1 Orogenic Gold 414
7.1.2 Intrusion-related Gold 420
7.2 Elmalhat Anorthosite Complex 420
7.2.1 Magmatic Ni-Cu-(Co-PGE) Sulphide Deposits 420
7.2.2 Platinum Group Element-Bearing Stratiform Chromitite 429
7.2.3 Orthomagmatic Fe-Ti-V Oxide Seams 430
7.3 Iron Ore in Riche 431
7.4 Mineralisation in the Boromo Belt of Burkina Faso 433
7.4.1 Volcanic Massive Sulphide Deposits 433
7.4.2 Porphyry Systems 433
7.4.3 Potential for Similar Mineralisation in the Leaareig Terrane 434
8.0 Conclusions and Recommendations 436
8.1 Conclusions 436
8.2 Recommendations 442
9.0 References 444
Appendices 459
Appendix A – Methodology 459
Appendix B – Geochronology 460
Appendix B1 – U-Pb Zircon Data 460
Appendix B2 – U-Pb Zircon Processing 485
Appendix B3 – Whole Rock Sm/Nd Geochronology 513
Appendix C – Whole rock Geochemistry 515
Appendix C1 – Data 515
Appendix D – Microprobe Analyses 525
Appendix E – Assay Results from Hanno Resources Limited 551

List of Figures

Figure 1-1- Simplified tectonic map of the West African Craton 2
Figure 1-2– Map of the United Nations Mission for the Referendum in Western Sahara 4
Figure 1-3 - Simplified metallogenic of the West African Craton 10
Figure 1-4 – Simplified geological map of the Man-Leo Shield. 12
Figure 1-5- Zircon and monazite U-Pb age distribution across the southern West African Craton for the period between 2250 and 2050 Ma 19
Figure 1-6 – Illustration of the crustal blocks of the Baoulé-Mossi Domain. 20
Figure 1-7 - Diagram illustrating the 2.20–2.08 Ga geodynamic evolution of the northern Palaeoproterozoic margin of the Archean Kéména-Man domain 22
Figure 1-8 - Terrane map of the Reguibat Shield. 23
Figure 1-9- Simplified geological map of the Leaareig and Sfariat-Bu Daira Terranes. 33
Figure 1-10 - Geological map of the Leaareig and Sfariat-Bu Daira domains. 34
Figure 1-11- Generalized tectonic map of Mauritania 41
Figure 1-12 - Geological sketch map of the Eglab massif and of the eastern Yetti massif 45
Figure 1-13 - Proposed geodynamic evolution of the Eglab massif from 2.73 to 2.07 Ga. 48
Figure 1-14 – Distribution of mineral deposits in the West African Craton 51
Figure 1-15 - Mid-crustal geophysical features of the West African Craton 54
Figure 1-16 – Overview of the crustal domains of the Man-Leo Shield 57
Figure 1-17 –Palaeoproterozoic geophysics structural map of the WAC 59
Figure 2-1 – Geochronology Sample locations from this study. 63
Figure 2-2 – Tera Wasserburg plots showing the concordant age of samples: a) J204; b) J238; c) J287; d) J273 64
Figure 2-3 – Tera Wasserburg plots with ages calculated using a regression line: a) J231; b) J179; c) J246 (crystallisation age; skinny zircons and rims of blocky zircons); d) J246 (inheritance; cores of blocky zircons); e) J219; f) J213 66
Figure 2-4 – $^{207}Pb/^{206}Pb$ weighted average age calculations for samples a) J240; b) J197; and c) J227 67
Figure 2-5 – Tera Wasserburg plots and age regression age calculation of Andersen (2002) common lead corrected data. a) J234; b) J292; d) J205; and e) J253 68
Figure 2-6 – $^{207}Pb/^{206}Pb$ weighted average age calculations for sample J220, following the Andersen (2002) common lead correction 69
Figure 2-7 - J275 (lead loss event; anchored to a common lead ratio ($^{207}Pb/^{206}Pb$) of 0.83 and projected back to concordia). 69
Figure 2-8 – Simplified geological map of the study area with domains defined according to lithological associations and new geochronology data 73
Figure 3-1 – Position of the Leaareig Terrane relative to the Archaean Terrane and other Palaeoproterozoic Terrane 76
Figure 3-2 – Domain map of the Leaareig and Sfariat-Bu Daira Terranes 77
Figure 3-3 - Detailed geology of the Leaareig Domain 79
Figure 3-4 – Field photograph of a representative outcrop of orthogneiss from the Leaareig Domain 81
Figure 3-5 - Field photograph of metasedimentary rocks within the Leaareig Domain 82
Figure 3-6 – Photomicrograph of J231 – biotite gneiss 84
Figure 3-7 - Photomicrograph of J234 - granodiorite gneiss 86
Figure 3-8 – Detailed geology of the Taghsoumat-Aghsoumal Belt 87

Figure 3-9 – Field photograph of migmatitic orthogneiss in the west of the Taghsoumat-Aghsoumal Domain 89
Figure 3-10 - Field photographs of interbedded volcanic and sedimentary rocks outcropping in Aghsoumal Hill 90
Figure 3-11 - Field photograph of extensive Marble outrcops in the south of the Taghsoumat-Aghsoumal Belt 91
Figure 3-12 - Detailed geology of the Agarasras Lakhadar Domain 92
Figure 3-13 Sketch of the ophiolite sequence in the Agarasras Lakhadar Domain 94
Figure 3-14 -- Field photograph of a hand sample of the ultramafic unit 95
Figure 3-15- Field photograph of the large ultramafic boulders near the boundary between the ultramafics and the gabbro 96
Figure 3-16- Field photographs of asbestos in the ultramafic unit 96
Figure 3-17 - Field photographs of coarse grained, poikilitic metapyroxenite 97
Figure 3-18 – Field photographs of dolerite from the complex 98
Figure 3-19- Field photograph of pillow basalt 100
Figure 3-20- Field photographs of garbenschiefer texture 101
Figure 3-21 - Field photographs of carbonatite dyke cutting the basalt 102
Figure 3-22 – Field photographs of sheared contacts observed within the mafic-ultramafic complex 104
Figure 3-23 - Field photographs of shear zone between the unit of basalt and the eastern exposure of ultramafic rocks 105
Figure 3-24 – Field photographs of a) Subcrop of metabasalt. b) subcrop of metabasalt to the west of the Agarasras Lakhadar hills 106
Figure 3-25 – Field photographs of outcrops of ferruginous chert of varying thickness .. 107
Figure 3-26 - Field photographs of marble from the metasedimentary unit 108
Figure 3-27 – Field photographs of weathered hornblendite within the mafic-ultramafic region 109
Figure 3-28 – Photomicrographs of J026 – altered ultramafics 112
Figure 3-29 – Photomicrographs of J027 – altered peridotite 113
Figure 3-30 – Photomicrographs of J064 – metapyroxenite 114
Figure 3-31 – Photomicrographs of J025– carbonate altered gabbro 115
Figure 3-32 – Photomicrographs of J062 - fine grained amphibolite 116
Figure 3-33 – Photomicrographs of J065 - metabasalt 116
Figure 3-34 - Photomicrographs of J023 - carbonitite 117
Figure 3-35 – Metabasalts from the mafic-ultramafic complex plotted on classification diagrams for all igneous and meta-igneous rocks from the Leaareig Terrane 118
Figure 3-36 – Basalt samples from Agarasras Lakhadar plotted on a) Th/Nb proxy b) Ti/Nb proxy 119
Figure 3-37 – Basalt samples from Agarasras Lakhadar plotted Ternary tectonic discrimination diagrams 120
Figure 3-38– Basalt samples from Agarasras Lakhadar plotted on La-Y-Nb ternary discrimination diagram 121
Figure 3-39 – Basalt samples from Agarasras Lakhadar plotted on Total Alkali-Iron-Magnesium (AFM) plot for pillow basalt 122
Figure 3-40 – Basalt samples from Agarasras Lakhadar plotted on a set of five multi-dimensional discrimination diagrams based on immobile trace elements (Agrawal et al., 2008) 123

Figure 3-41 – Detailed geology of the Sassaiate-Temmimichate-Tsabaya Complex 126
Figure 3-42 –Field photographs of variations in the appearance of marble within the Sassaiate-Temmimichate-Tsabaya Complex 127
Figure 3-43 – Field photographs of amphibolite (metabasalt). 127
Figure 3-44 – Field photographs of migmatitic gneiss within the complex..... 128
Figure 3-45 – Th–Nb and Ti–Yb proxy diagrams proposed by Pearce (2008) 133
Figure 3-46 – Whole rock geochemical classification diagrams for all igneous and meta-igneous rocks from the Leaareig Terrane..... 135
Figure 3-47 – Samples from the Leaareig Terrane ploted on a) Th/Nb proxy to distinguish volcanic arc settings from mid-oceanic ridge/ocean island basalt settings, b) Ti/Nb proxy to fingerprint samples from the MORB-OIB array..... 137
Figure 3-48 – Samples from the Leaareig Terrane ploted on ternary tectonic discrimination diagrams for mafic and intermediate samples a) Th-Hf/3-Ta B) Th-Zr/117-Nb/16 138
Figure 3-49 – Samples from the Leaareig Terrane ploted on La-Y-Nb ternary discrimination diagram..... 139
Figure 3-50 - Samples from the Leaareig Terrane ploted on Total Alkali-Iron-Magnesium (AFM) plot 139
Figure 3-51 – Samples from the Leaareig Terrane ploted on tectonic discrimination diagrams for granitic rocks (Pearce et al., 1984)..... 140
Figure 3-52 - Basalt samples from the Leaareig Terrane (minus the ophiolite samples), plotted on a set of five multi-dimensional discrimination diagrams based on immobile trace elements (Agrawal et al., 2008). 142
Figure 3-53 – Intermediate igneous rocks from the Leaareig Terrane plotted on a series of five multi-dimensional discriminant function diagrams based on log-ratios of immobile trace elements (Verma and Verma, 2013)..... 144
Figure 3-54 – Felsic igneous rocks from the Leaareig Terrane plotted on a series of five multi-dimensional discriminant function diagrams based on log-ratios of immobile trace elements (Verma et al., 2013). 147
Figure 3-55 – Proposed tectonic setting of the Leaareig Domain..... 151
Figure 4-1 – Domain map of the study area..... 153
Figure 4-2 – Geology of the Elmalhat Domain with key locations labelled..... 155
Figure 4-3 – Field photographs of orthogneiss in the east of the Elmalhat Domain..... 158
Figure 4-4 – Field photographs of metasedimentary basement 160
Figure 4-5 – Field photographs of the typical appearance of megacrystic anorthosite.... 164
Figure 4-6 – Field photographs of the typical appearance of massif-type anorthosite 166
Figure 4-7 – Field photographs of the typical pegmatitic pods in a massif-type anorthosite complex 167
Figure 4-8 – Geological map of the Northern Limb 168
Figure 4-9 – Field photographs showing the typical appearance of the megacrystic textures in in leucogabbro/anorthosite within the Northern Limb..... 172
Figure 4-10 - Field photographs of megacrystic anorthosite with blebs of more mafic material..... 173
Figure 4-11 - Field photographs of Anorthosite from the Northern Limb containing sulphides..... 173
Figure 4-12 – Field photograph of magma mixing/liquid immiscibility textures of the Northern Limb of the EAC 174

Figure 4-13 – Field photographs of convoluted compositional banding in the anorthosite proximal to the chromitite seam 175
Figure 4-14 – Field photographs of outcrops of megacrystic-type anorthosite to the south of the Main Bulb of the EAC 176
Figure 4-15 - Field photograph of massive Chromitite from the Northern Limb 177
Figure 4-16 – Field photographs of outcropping chromitite 178
Figure 4-17 - Field photograph of amphibolite layer ~30 m to the west of the chromitite 180
Figure 4-18 - Field photograph of quartzite 181
Figure 4-19 – Field photographs of deformed megacrystic anorthosite..... 182
Figure 4-20 – Field photograph of poikilitic metapyroxenite close to the contact with the Oum Abana Domain 182
Figure 4-21 – Field photograph the interleaved contact of the anorthosite intrusion. Rocks to the right of them on the photograph are the host orthogneiss while rocks to the left are anorthosite 183
Figure 4-22 – Field photograph of interleaved anorthosite-orthogneiss contact, with anorthosite emplaced along en-echelon tearing in the orthogneiss 184
Figure 4-23 – Field photograph of interleaved contact between anorthosite and host orthogneiss..... 184
Figure 4-24 - Field photograph of pink orbicals found in anorthosite 185
Figure 4-25 – Field photograph of outcrop of fresh anorthosite from the Main Bulb 186
Figure 4-26 - Photograph of hand sample of leucogabbro from the Main Bulb 187
Figure 4-27 – Field photograph of compositional layering in the in the bulb of the EAC defined by differences in plagioclase content..... 188
Figure 4-28 - Field photograph of altered pale anorthosite from the bulb of the EAC 188
Figure 4-29 - Field photograph of magma-mixing textures 189
Figure 4-30 – Field photograph of xenoliths of megacrystic-type anorthosite within the Main Bulb. 190
Figure 4-31 - Field photographs of pods of white anorthosite and spinel in massive purple anorthosite 191
Figure 4-32 - Field photographs of ultramafic intrusions within the bulb of EAC. 192
Figure 4-33 - Field photographs of ridge of gabbro defining the southern contact of the bulb anorthosites with the host orthogneiss..... 193
Figure 4-34 – Field photographs of south of the sabkha representing the contact between massif-type and megacrystic anorthosite..... 194
Figure 4-35 Geological map of and ground magnetics from the Main Bulb 195
Figure 4-36 – Field photographs of sheared gabbro representing the northern contact of the Main Bulb of the EAC 197
Figure 4-37 Geological map of and ground magnetics from the Southern Bulb 199
Figure 4-38 – Field photograph of typical view of the sand covered Southern Bulb 200
Figure 4-39 – Field photograph of anorthosite with a green tinge from malachite present from the oxidation of primary chalcopyrite..... 201
Figure 4-40 – Field photograph of outcrop of coarse grained anorthosite containing plagioclase oikocrysts up to ~3 cm..... 201
Figure 4-41 - Field photograph of mortar texture observed in the Southern Bulb..... 202
Figure 4-42 - Field photographs of pegmatitic textures observed in leucogabbro within the Southern Bulb. 202

Figure 4-43 – Field and hand sample photographs of Hornblendite (meta-pyroxenite) from the Southern Bulb of the EAC 204
Figure 4-44 – Field photograph of typical subcrop of magnetite seams 204
Figure 4-45 – Geological map of Moug El Kaleb 205
Figure 4-46 – Field photograph of orbicular texture at Moug el Kaleb 207
Figure 4-47 – Field photograph of magma mixing/immiscibility textures in leucogabbro at Moug El Kaleb 207
Figure 4-48 - Field photograph of sheared ultramafic rocks on the western margin of the Moug El Kaleb intrusion 208
Figure 4-49 – Field photographs of the pyrite and chalcopyrite-bearing magnetite layer within the Moug El Kaleb intrusion. 209
Figure 4-50 - Geological map of the centre of the Elmalhat Domain 211
Figure 4-51 - Field photograph of the gabbroic and ultramafic unit is largely obscured by large areas of sand, mostly appearing as small areas of subcrop 212
Figure 4-52 - Field photographs of listwanite and fresh ultramafic rocks 214
Figure 4-53 – Field photographs of massif-type anorthosite cross-cutting the fabric of the orthogneiss basement dated at 2140 ± 19 Ma 217
Figure 4-54 – Sm-Nd isochron for samples from the EAC, including two samples of white anorthosite and one of an ultramafic dyke in the Main Bulb, a sample of gabbro proximal to the Main Bulb, and olivine gabbro from a satellite intrusion. 218
Figure 4-55 - Photomicrographs of sample J179 – migmatitic orthogneiss 219
Figure 4-56 - Photomicrographs of sample J117 – orthogneiss. 220
Figure 4-57 – Photomicrographs of J240 – paragneiss 221
Figure 4-58 – Photomicrographs of J114 - Carbonate BIF 222
Figure 4-59 – Photomicrographs of J111 – megacrystic anorthosite with a megacrystic plagioclase grain 224
Figure 4-60 - Photomicrographs of J108 - metamorphosed megacrystic anorthosite 224
Figure 4-61 - Photomicrographs of J103 metagabbro 225
Figure 4-62 - Photomicrographs of sample J107 – metagabbro 225
Figure 4-63 - Photomicrographs of J264 - adcumulate anorthosite 226
Figure 4-64 – Photomicrographs of J270 megacrystic anorthosite 226
Figure 4-65 - Photomicrographs of J103 - megacrystic anorthosite 227
Figure 4-66 - Photomicrographs of J103 - Clinozoisite at margin of amphibole cluster .. 227
Figure 4-67 - Photomicrographs of J105 massive chromitite 228
Figure 4-68 - Photomicrographs of J106 - chromite bearing anorthosite 228
Figure 4-69 - Photomicrographs of J104 - metagabbroic amphibolite 229
Figure 4-70 - Photomicrographs of J104 - primary magmatic sulphides within the amphibolite layer. 230
Figure 4-71 – Photomicrographs of J414 - Banded Anorthosite in the Main Bulb. 231
Figure 4-72 – Photomicrographs of J122 banded anorthosite 232
Figure 4-73 – Photomicrographs of J404 - banded leucodiorite in the Main Bulb 232
Figure 4-74 - Photomicrographs of sample J263 leucogabbronorite cumulate 233
Figure 4-75 - Photomicrographs of J259 - leocoabbronorite cumulate 234
Figure 4-76 – Photomicrographs of J413 - massive leucogabbro of the Main Bulb 234
Figure 4-77 – Photomicrographs of J418 - olivine-quartz gabbro 235
Figure 4-78 - Photomicrographs of J262 - cumulate peridotite with intercumulus plagioclase. 236

Figure 4-79 – Photomicrographs of J124 - metapyroxenite cross-cutting anorthosite in the bulb 237
Figure 4-80 - Photomicrographs of J310 – xenoliths of megacrstic anorthosite in the main bulb 238
Figure 4-81 – Photomicrographs of J257 - meta-anorthosite 240
Figure 4-82 – Photomicrographs of J258 - meta-anorthosite 241
Figure 4-83 - Photomicrographs of J258 - meta-anorthosite 241
Figure 4-84 - Photomicrographs of J118 - olivine basalt/dolerite in satellite bodies 242
Figure 4-85 - Photomicrographs of J255 - porphyritic olivine, biotite gabbro 243
Figure 4-86 – Photomicrographs of J126 - hornblende gabbroperidotite 244
Figure 4-87 - Photomicrographs of J256 - metagabbro 246
Figure 4-88 – Photomicrographs of J116 - metapyroxenite 248
Figure 4-89 - Photomicrographs of J115 - listwanite, microcrystalline and columnar silica with some carbonate, filling void 248
Figure 4-90 - Photomicrographs of J113 - listwanite, agate-like silica filling void 249
Figure 4-91 – Photomicrographs of sample J247 – weakly deformed granite 251
Figure 4-92 - Photomicrographs of J246 - general view of granitoid 252
Figure 4-93 - Magnesium number of mafic minerals versus anorthite content of plagioclase of samples from the EAC, compared to other anorthosite complexes and layered mafic intrusions 254
Figure 4-94 -Temporal distribution of different types of anorthosite complexes, displayed as An content vs age 255
Figure 4-95 – Andesine anorthosite samples plotted stratigraphically taking 0 m as the centre of the intrusion 256
Figure 4-96 - Mineral composition of plagioclase and amphibole in samples from the Northern Limb 258
Figure 4-97 – Mineral chemistry of chromitite from the EAC compared to Archaean anorthosite-hosted Chromitites and Stratiform Chromites 259
Figure 4-98 – Mineral chemistry of chromitite within the EAC compared to chromite in Archaean megacrystic anorthosite complexes 260
Figure 4-99 - Tectonic discrimination diagrams based on clinopyroxene chemistry from samples of leucogabbro from the Main Bulb, olivine gabbro from the satellite bodies (green) and gabbro proximal to the Main Bulb 263
Figure 4-100 - Tectonic discrimination diagrams for non-cumulate rocks associated with the EAC 265
Figure 4-101 - Legend for plots of EAC anorthosite/leucogabbro from Figure 4-102 267
Figure 4-102 – Chondrite normalised spider plots of anorthosite and leucogabbro samples from the EAC 268
Figure 4-103 – Anorthosite/leucogabbro samples plotted on the modified Th/Nb proxy with oceanic arc and continental arc fields defined by Pearce (2014) 269
Figure 4-104 - Harker variation diagrams for anorthosite/leucogabbro from the EAC. Mineral compositions are shown for clinopyroxene (Cpx), enstatite (En), anorthite (An), albite (Ab) and olivine (Ol) 271
Figure 4-105 - Schematic illustration showing the principal processes involved in the formation of Archaean anorthosites 275
Figure 4-106 – Illustration of as Andean-type continental arc 278
Figure 4-107 – Model for the formation if massif-type anorthosites 279

Figure 4-108 – Detailed geology of the Oum Abana Belt 284
Figure 4-109 - Field photograph of mafic lens in granite-gneiss in the Oum Abana Belt 287
Figure 4-110 – Field photographs of lithologies from the volcanic belts of the Oum Abana Belt 288
Figure 4-111 – Field photograph of interbedded metamorphosed quartzite and hornblende schist 290
Figure 4-112 - Field photograph of a metasomatised sedimentary package 291
Figure 4-113 – Field photograph of Adam Anajim granodiorite intrusion 292
Figure 4-114 – Field photograph of strongly foliated Agarastas Labiad Intrusion, outcropping as a series of hills parallel to the foliation 293
Figure 4-115 – Field photograph of a small outcrop of the red porphyry unit 294
Figure 4-116 – Field photographs of poikilitic metapyroxenite with pyroxene oikocryst, observed intruding metasediments in the north of the Oum Abana Belt 295
Figure 4-117 a – Detailed geology of the Anajim Guebli Domain 299
Figure 4-118 – Domain map showing the location of the Riche Anajim Group 301
Figure 4-119 - Field photograph of the Riche Belt, showing the black BIF ridges 303
Figure 4-120- Field photograph of the gneissic unit in the Riche Belt 304
Figure 4-121 - Field photograph of boudinage of hematite within gneiss in the Riche Belt, with the boudins shown by the black ovals 304
Figure 4-122 - Field photograph of migmatitic gneiss within the Riche Bel 305
Figure 4-123- Field photograph of mylonite in the Riche Belt 306
Figure 4-124- Field photographs of marble in the Riche Belt, showing banding 307
Figure 4-125- Field photograph of folded inclusions within the marble unit in the Riche Belt 307
Figure 4-126- Field photographs of the BIF unit within the Riche Belt 308
Figure 4-127- A series of field photographs that illustrate that kinematic indicators within the Riche Belt 310
Figure 4-128 - Photomicrographs of J046 - BIF 311
Figure 4-129 - Photomicrographs of J049 - BIF with high-strain microstructure 311
Figure 4-130 - Photomicrographs of J055 - BIF 312
Figure 4-131 – Photomicrographs of J047 marble with chlorite and tremolite 312
Figure 4-132 - Photomicrographs of J052 - forsterite marble 313
Figure 4-133 - Photomicrographs of J053 marble with forsterite, diopside and some fine tremolitic amphibole 313
Figure 4-134 - Photomicrographs of J054 - granitic biotite gneiss 314
Figure 4-135 - Photomicrographs of J045 - mylonitic granite 315
Figure 4-136 – Photomicrographs of J048 - granite mylonite 315
Figure 4-137 – Whole rock geochemistry classification diagrams for all igneous and meta-igneous rocks from the Sfariat-Bu Daira Terrane 316
Figure 4-138 - Discrimination diagrams for fingerprinting tectonic setting (Th/Nb and Ti/Nb proxy diagrams 318
Figure 4-139 – Ternary tectonic discrimination diagrams for mafic and intermediate samples (Th-Hf/3-Ta and Th-Zr/117-Nb/16). 319
Figure 4-140 – All mafic and intermediate igneous samples from the Sfariat-Bu Daira Terrane, plotted on a La-Y-Nb ternary discrimination diagram 320
Figure 4-141 – Total Alkali-Iron-Magnesium (AFM) plot of all samples within the Sfariat-Bu Daira Terrane 320

Figure 4-142 – Tectonic discrimination diagrams for granitic rocks a) Nb vs Y b) Rb vs (Y + Nb) c) Rb vs (Yb + Ta) d) Ta vs Yb 321
Figure 4-143 – Intermediate igneous rocks from the Sfariat-Bu Daira Terrane plotted on a series of five multi-dimensional discriminant function diagrams based on log-ratios of immobile trace elements (Verma and Verma, 2013)..... 323
Figure 4-144 – Felsic igneous rocks from the Sfariat-Bu Daira Terrane plotted on a series of five multi-dimensional discriminant function diagrams based on log-ratios of immobile trace elements (Verma et al., 2013)..... 326
Figure 4-145 – Illustration of the Japanese type island arc for comparison of a modern day analogue 328
Figure 5-1 - Tectonic settings of orogenic and other of gold deposits 333
Figure 5-2 – Gold and Copper rock chip assay results from across the study area..... 334
Figure 5-3 – Geological map of the G52 region with disseminated sulphides across the granite-rhyolite contact..... 336
Figure 5-4 – Field photograph of an outcrop of mineralised ferruginous chert and an outcrop of mineralised (visible gold bearing) quartz vein near the contact with the Agarasras Labiad intrusion..... 337
Figure 5-5 – Au and Cu soil results and Au rock chips results for Agarasras G52..... 338
Figure 5-6 – Field photograph of mineralised quartz vein in sheared granite at Agarasras Labiad..... 339
Figure 5-7 – Field photograph of an outcrop and close up photographs silicified, gold and copper-bearing magnetite at Moug El Kaleb Labiad..... 340
Figure 5-8 – Map of the Moug El Kaleb region with rock chip sample assay results 341
Figure 5-9 – Photographs of a chalcopyrite-bearing quartz vein cross-cutting the dolerite unit at Agarasras Lakhadar..... 342
Figure 5-10 – Field photograph of tourmaline-bearing quartz vein in the south of the Taghsoumat-Aghsoumal volcanosedimentary belt 343
Figure 5-11 – Field photograph of artisanal pits in the study area..... 344
Figure 5-12 – Photograph of Gold nugget from artisanal pits in between Agarasras Labiad and Agarasras Lakhadar 345
Figure 5-13 – Simplified geological sections through the Voisey's Bay deposit 346
Figure 5-14 – Photograph of patchy sulphides within anorthosite of the EAC. O..... 347
Figure 5-15 - Rock chip samples showing Ni and Cu anomalies in the EAC associated with magmatic sulphides 348
Figure 5-16 - Field photographs of the chromitite seam in the EAC 349
Figure 5-17 – Rock chip analyses showing Cr_2O_3 of the chromitite seam. 350
Figure 5-18 – Rock chip sample analysis, showing distribution of PGE mineralisation of the Northern Limb within the chromitite seam 351
Figure 5-19 - SEM image and spectra of a primary grain of Laurite hosted in chromite . 352
Figure 5-20 – SEM image of sample J105 showing secondary PGM grain crystallized in chlorite..... 352
Figure 5-21 - Ternary diagram with the composition PGM grains from the chromitite... 354
Figure 5-22 - Images of the magnetite seams within the southern bulb and the anomaly produced on the ground magnetics..... 356
Figure 5-23 – SEM images of magnetite with ilmenite exsolutions, ilmenite and spinel from orthomagmatic Fe-Ti-V deposit of the Southern Bulb Elmalhat..... 357

Figure 5-24 – Rock chip samples from the orthomagmatic Fe-Ti-V mineralisation in the Southern Bulb of the EAC. 357
Figure 5-25 – Schematic diagram showing the depositional settings for Superior, Algoma and Rapitan type iron formations 359
Figure 5-26 – Field photograph showing the view of the dark beds of BIF forming ridges along the Riche Anajim Group..... 360
Figure 6-1 – Schematic diagram illustrating the formation of megacrystic anorthosite of the EAC 364
Figure 6-2 – Schematic diagrams illustrating terrane accretion at a convergent continental margin..... 366
Figure 6-3 – Model for the formation of massif-type anorthosites 367
Figure 6-4 – Histogram showing the distribution of ages in the Leaareig and Sfariat-Bu Daira Terranes. 368
Figure 6-5 - Model of formation for the Leaareig and Sfariat-Bu Daira Terranes 369
Figure 6-6 - Schematic illustration of partitioned sinistrally transpressive structures preserved in the Sfariat Belt 372
Figure 6-7 – Simplified geological map of the region showing geochronological data either side of the Archaean- Palaeoproterozoic contact 374
Figure 6-8 - Terrane map of the Reguibat Shield..... 376
Figure 6-9 – Previous links that have been made between the Reguibat and Man Leo Shield..... 377
Figure 6-10 – Simplified geological map of the Archaean-Palaeoproterozoic contact of the Man-Leo Shield..... 379
Figure 6-11 – Longitudinal variations in magmatic activity across the Baoulé-Mossi Domain 381
Figure 6-12 – Schematic cartoon showing the proposed boundaries and crustal blocks.. 382
Figure 6-13 – Longitudinal variations in magmatic activity across the Palaeoproterozoic domain of the Reguibat Shield 383
Figure 6-14 – Histogram showing the distribution of ages in various belts in the Baoulé-Mossi Domain compared to individual domains within the study area. 385
Figure 6-15 - Simplified geological map of the West African craton..... 386
Figure 6-16 - Tectonic discrimination diagrams for Birimian intrusive and volcanic rocks of the Baoulé-Mossi Domain compared to that of the study area 388
Figure 6-17 – Simplified stratigraphic sequences for the Sfrariat-Bu Daira terrane, Leaareig Terrane, and Agarasras Lakhadar Domain of the Regquibat Shield compared with similar belts of the Baoulé-Mossi Domain..... 390
Figure 6-18 – Simplified geological map of the south of Mali 392
Figure 6-19 - Geological map of the western Burkina Faso 394
Figure 6-20 – Comparison of whole rock geochemistry of pillow basalts associated with ultramafic intrusions in the Boromo-Houndé belts with those of the Agarasras Lakhadar ophiolite sequence 397
Figure 6-21 –Palaeoproterozoic structural map for the West African Craton 398
Figure 6-22 – Early stages of formation of the Man-Leo Shield (>2125-2115 Ma)..... 401
Figure 6-23 – Evolution of the Man-Leo Shield from ~2125-2090 Ma 404
Figure 6-24 – Late stages in the formation of the Man-Leo Shield (2090-2115 Ma)..... 407
Figure 6-25 – Palaeomagnetic reconstruction of continents at 2.00 Ga 409

Figure 7-1 – Simplified map showing the distribution of crust of a given age and the distribution of significant orogenic gold occurrences within Africa and Europe..... 412
Figure 7-2 – Metallogenic map of the study area 413
Figure 7-3 - Location of the major gold mines in the Man-Leo Shield..... 415
Figure 7-4 – Correlation between ages of gold deposits obtained by Re-Os dating and the geodynamic evolution of the West African craton in Burkina Faso and Ghana 416
Figure 7-5 – Most prospective regions for orogenic gold mineralisation within the study area..... 420
Figure 7-6 – Simplified North-South sections through the Voisey's Bay deposit 421
Figure 7-7- Geological map of the Namibian portion of the Kunene Anorthosite complex 422
Figure 7-8 – The Canadian Shield showing the distribution major magmatic Ni-Cu sulphide deposits relative to Archaean and Palaeoproterozoic terranes..... 423
Figure 7-9 -Nickel vs. forsterite contents of olivine from selected troctolitic intrusions compared to compilation of basaltic and komatiitic lavas 426
Figure 7-10 – Most prospective sites for magmatic sulphide deposits within the EAC overlaid on Ni and Cu results for rock chip samples..... 428
Figure 7-11 - Magnetic anomaly highlighting the extend of the Fe-Ti-V oxide mineralisation in the Southern Bulb 431
Figure 7-12 – Tectonic interpretation of the Kediat inlier with respect to the location of the Sfariat Belt..... 432
Figure 7-13 – Diagram summarising major mineralisation events of the Gaoua region, Burkina Faso..... 435

List of Tables

Table 1-1 - Frequency distribution of West African mineral deposits, highlighting major deposit types for various commodities in consideration of their spatial distribution..... 52
Table 2-1 – Summary of geochronology samples analysed in this study. 70
Table 3-1 - Application of multidimensional diagrams to ~2240-2180Ma intermediate rocks of the Leaareig. 145
Table 3-2 - Application of multidimensional diagrams to ~2240-2180Ma acid rocks of the Leaarieg. 148
Table 4-1 – Whole rock Sm-Nd isotopic data for samples across the Elmalhat Anorthosite Complex 218
Table 4-2 - Sulphur isotope chemistry pyrite taken from samples around in the EAC. ... 261
Table 4-3 - Application of multidimensional diagrams to ~2140-2090 Ma intermediate rocks of the Sfariat-Bu Daira Terrane. 324
Table 4-4 - Application of multidimensional diagrams to ~2140-2090 Ma acid rocks of the Sfariat-Bu Daira Terrane. 327

1.0 Introduction and Background Geology

The West African Craton is one of the largest in Africa, comprising two outcropping shields of Precambrian basement covered in its central portion by the Neoproterozoic to Palaeozoic Taoudeni Basin (Figure 1-1). The basement material is composed of Archaean and Palaeoproterozoic rocks outcropping as the Reguibat Shield in the north and the Man-Leo Shield in the south.

Known as the Adam Ahmed Mouloude Region to the locals, the study area is located in the Liberated Territories of Western Sahara, between a belt of hills known as Riche, and the settlement of Mijek (Figure 1-2). The political situation in Western Sahara following Spain's relinquishment of the colony in 1975 has made it extremely difficult to access, and as such the geology of the region has never been studied in any detail. Prior to the commencement of this project, the only geological maps of the region were 1:1,000,000 scale maps of the Reguibat Shield, based entirely on remote sensing and historical mapping. Recent work undertaken by Schofield et al. (2006) in Mauritania, directly adjacent to the study area, indicated that the region is Palaeoproterozoic, representing the 'Contact Zone' between Archaean and Palaeoproterozoic components of the Reguibat Shield. The present study is aimed at filling in the gap of geological knowledge on the Contact Zone and providing constraints on the likely nature and distribution of natural mineral resources in the region.

1.1 Aims and Objectives

The main objective of this study is to improve the understanding of the geological and metallogenic history of the Contact Zone in the Reguibat Shield through undertaking detailed work in Western Sahara. This is to be achieved through a combination of regional

and detailed geological mapping, with the aid of satellite imagery and geophysics, and a series of geochemical, petrological and geochronological studies on samples collected from the field (Appendix A). This enhanced understanding of the geological and metallogenic history of this important Contact Zone will feed back into the knowledge of the evolution of the Reguibat Shield and West African Craton during the Palaeoproterozoic Era.

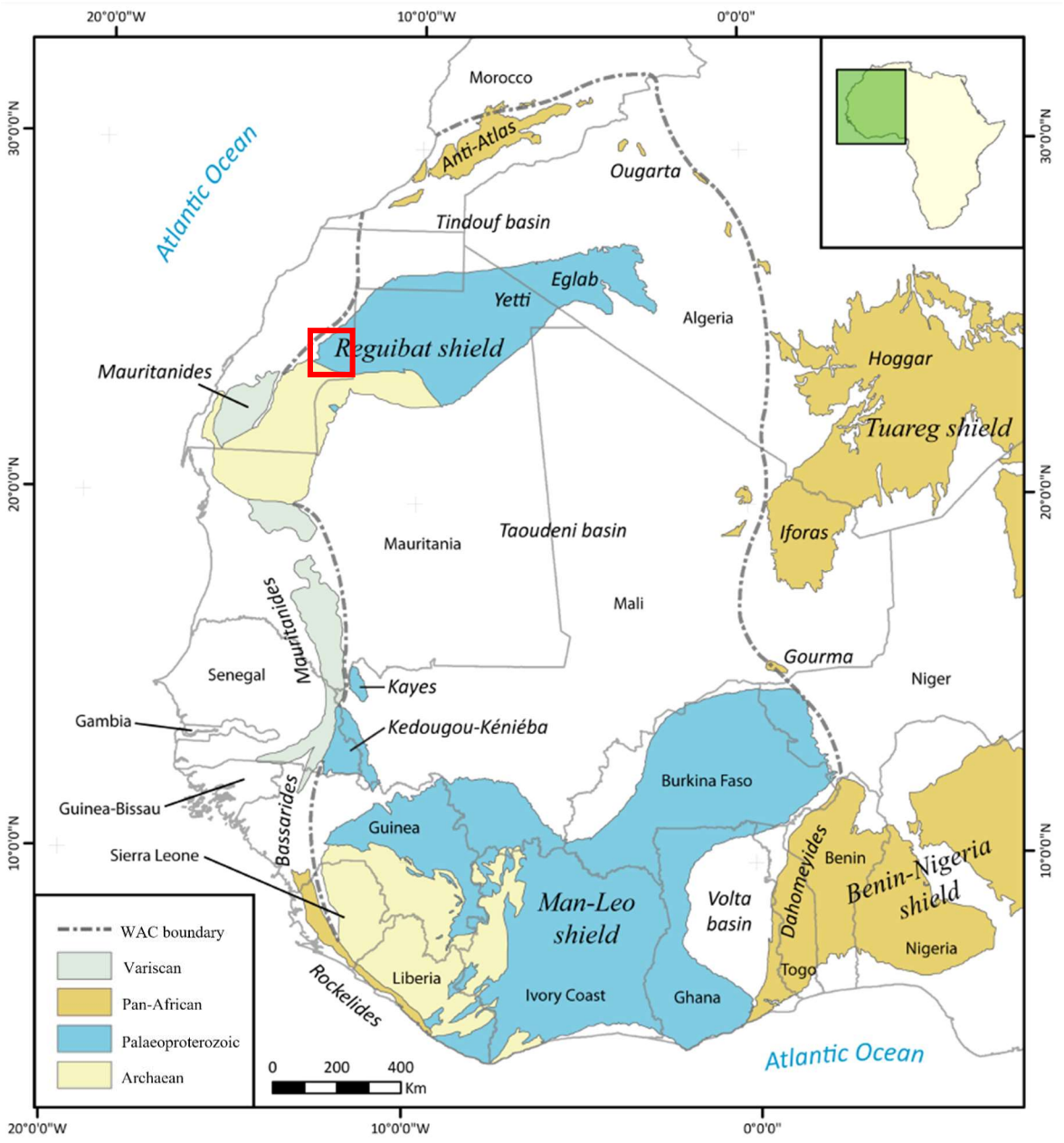

Figure 1-1- Simplified tectonic map of the West African Craton and adjacent Pan-African-Hercynian fold and thrust belts with the approximate location of the field area highlighted in red. Modified from Grenholm (2014). Mesoproterozoic to Recent sedimentary rocks are not depicted. The map has been compiled from the following sources; Man-Leo shield, Kedougou-Kéniéba, Kayes (Baratoux et al., 2011, Egal et al., 2002a), Reguibat Shield (Peucat et al., 2005, Schofield et al., 2012), Pan-African belts (Persits et al. 2002; Baratoux et al. 2011) and Variscan belt (Abouchami et al. 1990; Schofield et al. 2012). WAC boundaries after Ennih & Liégeois (2008)

1.2 **Research Location**

Western Sahara is a disputed territory in the Maghreb region of northwest Africa. The 266,000km^2 territory borders Morocco in the north, Algeria (to a very little extent) to the northeast, Mauritania to the east and the Atlantic Ocean to the west (Figure 1-2). It is one of the most sparsely populated regions of the world, administered by one of the longest running United Nations peacekeeping missions. A Spanish colony (the Spanish Sahara) until 1975, the region underwent a period of war immediately after the Spanish withdrew when armies from Morocco and Mauritania invaded. They fought the Saharawi population as the self-proclaimed Saharawi Arab Democratic Republic (SADR), fighting for an independent Sahara. The war continued until the UN mediated a cease-fire in 1991 and the country was divided into two parts. The western two thirds of the country are illegally occupied by Morocco and referred to as the "Occupied Territories", while the eastern third is governed by the SADR and referred to as the "Liberated Territories". The two regions are separated by a sand berm, 2700km in length, built by the Moroccan army during the conflict along which landmines were placed. The field area (Figure 1-2) covers the Adam Ahmed Mouloude region to the north of Mijek and spans the width of the Liberated Territories.

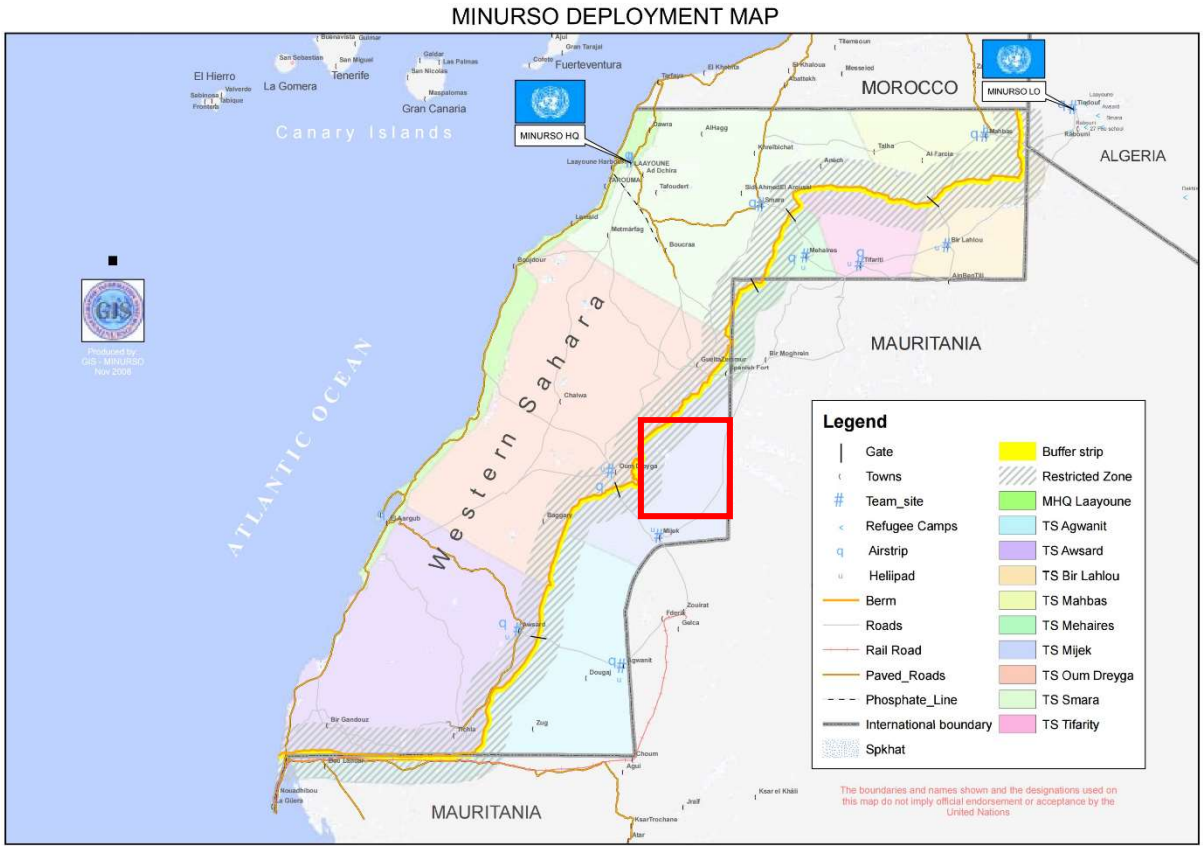

Figure 1-2– Map of the United Nations Mission for the Referendum in Western Sahara (MINURSO) operational area including the refugee camps. The location of the field area is indicated by the red square. Map from MINURSO

1.3 Previous Work

Extending through Western Sahara, Algeria and Mauritania, the Reguibat Shield is composed of Archaean and Palaeoproterozoic basement material with a wedge-shaped Contact Zone between the two. The study area covers a major portion of the Contact Zone and lies in the largely unstudied Liberated Territories of Western Sahara.

As part of his PhD on the geology of Western Sahara, Lehbib (2016) compiled a detailed history of the geological work undertaken in Western Sahara to date. Geological work started in the region at the same time as colonial settlement. Quiroga (1885) was the first to commence work on the geology of Western Sahara, establishing the major geological and geomorphological units including the Precambrian basement, Palaeozoic series and the Cenozoic cover (Quiroga, 1886a, Quiroga, 1886c, Quiroga, 1886b, Quiroga, 1886d,

Quiroga, 1886e, Quiroga, 1887a, Quiroga, 1887b, Quiroga, 1889). Work at the beginning of the 20th century largely consisted of expeditions focusing on the stratigraphy and palaeontology of the coastal areas (Lehbib, 2016 and references therein). The fossiliferous deposits of the Palaeozoic syncline of the Tindouf basin were first described by Spanish geologists in the mid-1930s and later studied in the 1960s by a mix of American and Spanish geologists (Lehbib, 2016 and references therein). It was not until the 1940s that the first syntheses of the geology of the entire territory were published by Flores (1946) and Hernández-Pacheco et al. (1949). By 1950 the arrival of trucks in the Sahara allowed for the transport of large amounts of water facilitating systematic exploration of the innermost zones of the Spanish colony. It was from the work done in this period of time that the first synthesis of the Spanish Saharan geology was created. However, as in previous years, much of the focus was on the cover with only cursory mapping of the basement (Alvarado et al., 1958).

At the same time as the advances of the geological survey, mineral resources began to be valued. As phosphate deposits were already known in Morocco it was hypothesised that the Spanish Sahara could contain similar phosphate mineralisation, the first signs of which were discovered by Alía Medina in 1947 (Alía Medina, 1950, Alía Medina, 1951, Alía Medina, 1971). It wasn't until the 1960's that a detailed study was completed by the National Mining Company of the Sahara (INI), directed by Dr. M. Rios, in which the deposits were estimated at about 500 Mt at 45 to 50% of phosphate (Lehbib, 2016 and references therein). Further strategic exploration campaigns, including airborne magnetic and aeroradiometric exploration, as well as detailed fieldwork, opened up the possibility of industrial exploitation of the world-class deposits (Lehbib, 2016). These resources turned the Spanish Sahara into a coveted territory and were one of the factors that encouraged Morocco (which already had major phosphate reserves) and Mauritania to invade in 1975.

Studies of the Precambrian basement only began in the late 1940's with exploration for mineral deposits becoming more common in the 1950's, when a mining service was created (Lehbib, 2016 and references therein). During the 1950's a team of Spanish geologists, including Antonio Arribas, working in mineral resources in the Spanish Sahara went on several expeditions to the territory. The results of the expeditions went largely unpublished at the time, though the data and samples from these expeditions were incorporated into the thesis of Lehbib (2016) (see below). Mingarro and Arribas (1956) were the first to apply geochronological techniques in the Spanish Sahara, using K/Ar isotopes to date fuchsite in a mineralised shear zone, and finding an age of 1750 ± 50Ma.

Gavala (1952) and Alía Medina (1953) described banded iron formation (BIF) in the Precambrian, while Comba (1965) initially evaluated the aeromagnetic surveys that resulted in a resource of 70 Mt of Fe ore with 57% Fe, 13% TiO2 and 0.6 to 0.8% V being declared in the Agracha gabbros. By the 1960's geological studies for exploration of new mineral resources had focused on the Precambrian (Alía Medina, 1960, Arribas, 1960, Arribas, 1968, Sougy, 1962, Sougy, 1969). This improved knowledge and the diffusion of the data meant that by the 1970's the BIF deposits of the central part of the Precambrian outcrops were attracting attention (eg. Theurkauf and Grover, 1974). There were some initial studies carried out to try to locate on-shore petroleum deposits on the Saharan coastal shelf but these ultimately proved unsuccessful (Lehbib, 2016).

In the 1970's more detailed geological maps began to be made at larger scale. However, as they were funded by oil companies, they focused on the cover areas and the basement materials were ignored and even erased on these maps (Lehbib, 2016). With the Moroccan occupation of much of Western Sahara from 1975, the geological works were carried out by the Geological Service of Morroco, supported by French teams, the BRGM and universities

(Lehbib, 2016). As such, geological maps of Morocco erroneously include the Western Sahara as part of Morocco, although the level of detail (1:5,000,000) was low since much of the information had to be obtained from satellite photos (Lehbib, 2016). Supported by geologists from the BRGM and French universities, the Service Géologique du Maroc completed studies of the country's mineral resources and synthesized the works published by them as a metallogenic map of the country at a scale of 1:1,000,000 (Service géologique du Maroc, 1999).

Due to limited access to the Liberated Territories of Western Sahara between 1975 and 1991, no direct work could be carried out there (Lehbib, 2016). Sources of information on the geology of the Liberated Territories was limited to bibliographical studies, and work carried out by various universities, geological services and mining companies in neighbouring countries (namely Algeria and Mauritania). Many of whose geological units are shared with the Sahara and therefore are easily correlated or comparable (Lehbib, 2016).

Systematic studies of the Reguibat Shield, including the Mauritanides, began toward the end of the 20th century (Lehbib, 2016). In the Occupied Territories, where the Mauritanides are present, there was collaboration between the Moroccan geological service and the French and Spanish research centres where large-scale geological maps were produced (Fabre et al., 1978, Marchand et al., 1984, Piqué, 2001). Several groups worked in more detail to define the structure of the Mauritanides**,** including Western Sahara (Sougy, 1969, Bronner et al., 1983, Dallmeyer et al., 1987, Lécorché et al., 1991, Villeneuve and Cornée, 1994, Villeneuve, 2005, Villeneuve et al., 2006), while Villeneuve et al. (2006), Gasquet et al. (2008) and Gärtner et al. (2013) all worked on dating the Precambrian of the zone of Adrar Souttouf in the Mauritanides using U/Pb dating.

In terms of the Reguibat Shield there are relatively few recent studies in Western Sahara, although the region is relatively well studied in parts of Mauritania and Algeria (Lehbib, 2016 and references therein). Most relevant to the Adam Ahmed Mouloude Region was work done by Schofield et al. (2006) who investigated the Contact Zone between the Archaean and Palaeoproterozoic components of the shield in Mauritania, directly adjacent to the field area. They investigated the timing and kinematics of the Contact Zone in the Reguibat Shield and found that they were similar to those of the Man-Leo Shield and proposed that this indicated structural continuity beneath the Taoudeni Basin between the two regions of the West African Craton at around 2100 Ma.

In terms of mineral resources in the Western Sahara, the Liberated Territories are underexplored. Work done in the neighbouring countries is not abundant, though important work has been undertaken in Mauritania (Lehbib, 2016) including on the BIF of the Ijil Group (Bronner and Chauvel, 1979) and exploration for gold mineralisation in the northwest of Mauritania, close to the border with the Western Sahara (e.g. Conchita (Markwitz et al., 2016b)). Additionally, in the west of Mauritania, to the south of Western Sahara, the world class Tasiast gold deposit has been exploited since 2006 (Heron et al., 2016, Lehbib, 2016) and the presence of chromite deposits has been described in the Guelb el Azib layered complex of the Amzaga complex (Berger et al., 2013). At the northeast end of the Reguibat Shield, kimberlites have been reported (Kahoui et al., 2008) and in the junction between the Eglab and Yetti terranes molybdenum-copper porphyry mineralisation has been described (Lagraa et al., 2017). On a more regional scale, Markwitz et al. (2016a) completed a metallogenic portfolio of the craton, compiling a database of all known mineral deposits in the West African Craton (Figure 1.2; Markwitz et al., 2016b). It is notable that the largely unexplored region of the Reguibat Shield in Western Sahara has no recorded occurrences of mineral deposits.

As seen from the historical work detailed previously, much of the prior geological work done in Western Sahara was based on colonial expeditions between 1900 and 1975, with little or no interpretation in terms of current tectonic or petrogenetic models for the region, and with a lack of metallogenic interpretations. The state of war and difficult political situation in the period post-1975 have complicated or completely prevented geological studies of the region since this time. Accordingly, Western Sahara is one of the least studied regions in the world in terms of geology and metallogenesis. As such, a systematic synthesis of the geology and metallogeny was required (Lehbib, 2016).

Ismail Ahamed (1994) attempted a synthesis of Western Sahara geology, basing his work purely on bibliographical and photogeological sources. The second, and more systematic study, was started by Australian mineral exploration company Hanno Resources Limited in 2007. After signing a Technical Cooperation Agreement with the Saharawi government, the work was initially based on interpretation of satellite imagery, though unprecedented post-war access to the Liberated Territories meant that their studies progressed further than those in the intervening years. They initially produced a geological map of the entire Liberated Territories based entirely on satellite imagery and mapping in the neighbouring countries. Access to the Liberated Territories allowed for ground truthing of the mapping work and samples to be taken out of the field for further analysis.

Combs (2012) and Lyche (2012) were the first post-war authors with access to the field to complete mapping the Liberated Territories of Western Sahara, working in the Palaeoproterozoic close to the contact with the Archaean. Lyche (2012) completed a detailed mapping project over a gneissified tonalitic intrusion related to copper and gold mineralisation. Combs (2012) completed a more regional investigation mapping a 50 x 50 km area to a scale of 1:100,000 covering the ‘Oum Abana Greenstone belt’. These studies

were largely limited to field observations and a few thin sections that had already been prepared for Hanno Resources from the area.

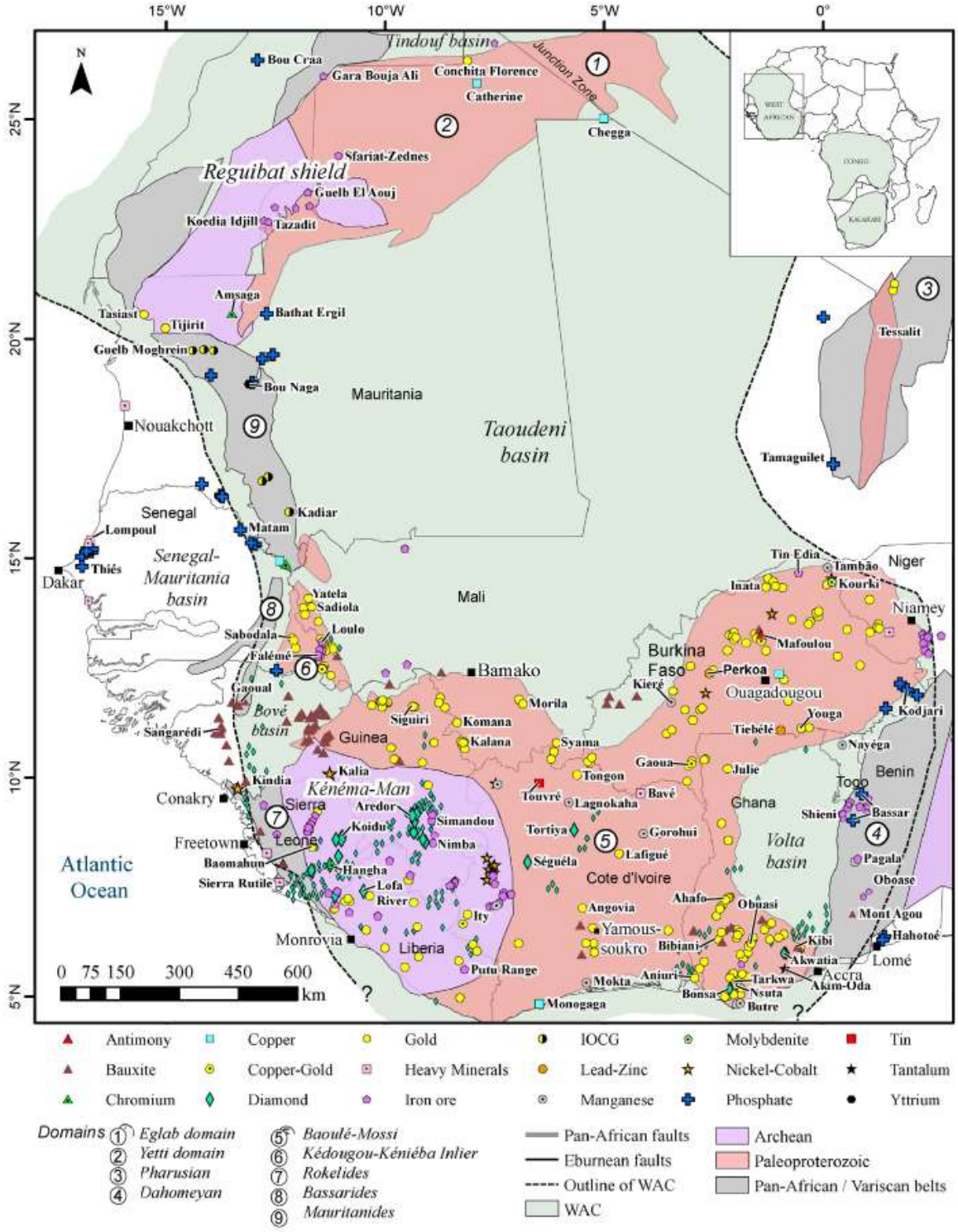

Figure 1-3 - Simplified map of the West African Craton highlighting the distribution of known mineral deposits. (Markwitz et al., 2016b)

Lehbib (2016) completed a PhD at the University of Barcelona focusing on the geology and metallogeny of the Precambrian Basement in Western Sahara. The work incorporated samples collected by Prof. Antonio Arribas in the 1950's, as well as a number of trips to the field. The work largely focussed on the Archaean component of the Reguibat Shield. With a large portion of the Archaean located in the Western Sahara, Lehbib (2016) was able to define new domains that were not previously recognised due to limited outcrop in Mauritania.

1.4 **Regional Geology**

1.4.1 West African Craton

The West African Craton, one of the largest in Africa, covers a major portion of the north-western quadrant of the continent (Youbi et al., 2013). It comprises two outcropping shields of basement rock, covered in its central part by the Neoproterozoic to Palaeozoic Taoudeni Basin (Rocci et al., 1991, Schofield et al., 2006). The basement, composed of Archaean and Palaeoproterozoic rocks, outcrops in the north as the Reguibat Shield, and in the south as the Man-Leo Shield (Figure 1-1; Key et al., 2008, Rocci et al., 1991). Due to an abundance of mineral resources, the Man-Leo Shield has been studied extensivally over the past 100 years (Jessell and Liégeois, 2015) and hence is the most well understood region of the West African Craton. When investigating the geology of the relatively unstudied Reguibat Shield it is therefore important to consider the studies on the Man-Leo Shield. This will allow the study to be placed in the more regional context of the West African Craton.

1.4.2 Man-Leo Shield

The southern part of the West African Craton, known as the Man-Leo shield (Figure 1.4) is composed of the Archaean Kéména-Man Domain in the west and the Palaeoproterozoic

Baoulé-Mossi Domain in the east and north (Sylvester and Attoh, 1992, Lompo, 2010). The Kéména-Man Domain is largely composed of greenstone belts intruded by tonalite-trondhjemite-granodiorite (TTG) rocks. The Baoulé-Mossi Domain consists of three lithological groups: volcanic belts, sedimentary basins and granite-gneiss domains. The granite-gneiss domains are the main unit in the Baoulé-Mossi Domain, comprising 50-60% of the region. The volcanic belts and sedimentary basins form linear north-northeast to south-southwest trending structurally controlled belts (Grenholm, 2014).

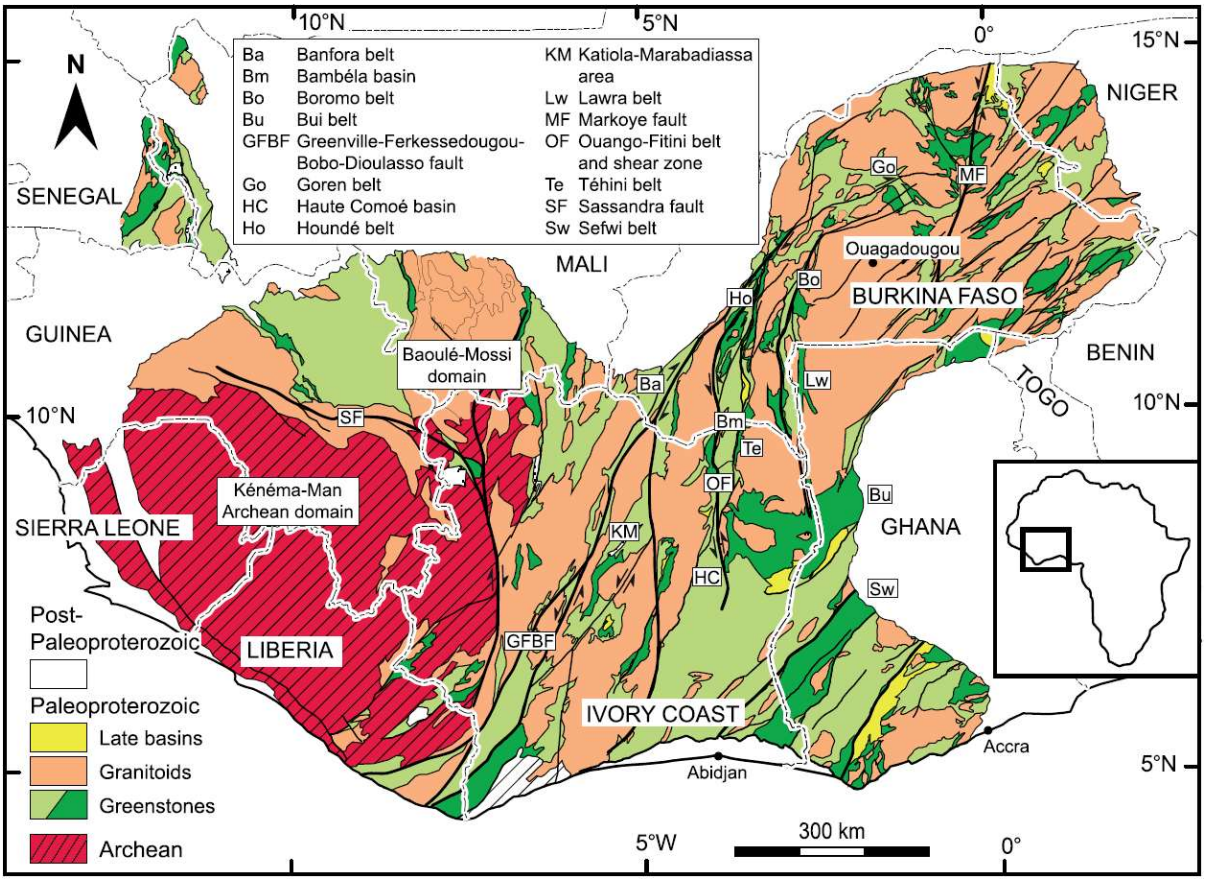

Figure 1-4 – Simplified geological map of the Man-Leo Shield modified after Amponsah et al. (2015) and Block et al. (2015). The dark green areas are mafic to felsic lavas and the light green areas are volcaniclastic and sediments.

1.4.2.1 Kéména-Man (Archaean) Domain

The Kéména-Man Domain broadly consists of belts of greenstone successions interleaved with granitic rocks (Rollinson, 2016, Grenholm, 2014). A typical Archaean greenstone succession in the Man-Leo Shield was described by Williams (1988) as comprising 'isolated

elongate outcrops of basaltic amphibolites, minor ultramafics, overlain by a sedimentary succession of greywackes, pelites and banded iron formation', 'engulfed by and infolded into a heterogeneous granitic migmatite complex'. Granulite facies assemblages are observed in some of these greenstone belts, while amphibolite facies assemblages are observed in others (Grenholm, 2014).

It is one of the least known Archaean terranes in the world with few recent detailed geological or petrological studies in this region (Rollinson, 2016). To better understand the Archaean crustal evolution in the region Rollinson (2016) compiled a synthesis of the geology and geochronology of the Archaean rocks in Sierra Leone, Liberia, Guinea and Ivory Coast in light of the improvements in understanding of Archaean crustal process over recent decades. Rollinson (2016) found that the cratonic nucleus is composed of four main geological units.

- Only outcropping in the east of the craton in Guinea, the oldest crust is composed of 3.5-3.6 Ga TTG (tonalite–trondhjemite–granodiorite) gneisses. Their presence is also noted as zircon xenocryst cores in younger rocks.
- The most common rock type found in the craton is 3.26-2.85Ga old TTG gneisses. They formed in two magmatic episodes, the first between 3.05-3.26 Ga and the other 2.85-2.96 Ga. Eclogite xenoliths (3.4 Ga) in kimberlite derived from sub-continental lithospheric melting are believed to be restite after partial melting of the basaltic protolith in the production of the TTG magmas, with the presence of inherited zircons in the younger suite indicating that the event represents the partial reworking of the older gneisses.
- Infolded into the TTG gneisses are linear belts of supracrustal rocks, metamorphosed to amphibolite and granulite facies, containing a variety of lithological sequences that vary in size and age. An important resource for gold, iron-ore, chromite and

columbite-tantalite, the larger supracrustal belts in Sierra Leone contain thick basalt-komatiite sequences derived from the partial melting of two distinct mantle sources, unconformably overlain by a sedimentary formation.

- A structural and thermal event at 2800 ± 20 Ma resulted in a suite of late Archaean granitoids formed from the partial melting of the TTG gneisses. This event is believed to be responsible for the stabilisation of the craton.
- As with most Archaean granite-greenstone terranes world-wide, the Kéména-Man Domain is characterised by a distinctive metallogenic style predominantly made up of orogenic gold and Algoma style BIF (Iron formations (typically >2.5 Ga) hosted in meta-volcanic settings and linked to exhalative processes on the sea-floor (Gross, 1980)) (Markwitz et al., 2016a, Markwitz et al., 2016b).

1.4.2.2 Palaeoproterozoic Baoulé-Mossi Domain

1.4.2.2.1 Geology

The Palaeoproterozoic Baoulé Mossi Domain (Figure 1-4) consists of volcanic, volcano-sedimentary and sedimentary sequences (the Birimian Supergroup) separated by extensive TTG and granitoid provinces, or by younger sedimentary basins (Baratoux et al., 2015, Baratoux et al., 2011, Feybesse et al., 2006, Leube et al., 1990b, Milési et al., 1992). It consists of juvenile crust largely independent from the influence of Archaean crust (Abouchami et al., 1990, Boher et al., 1992). The geodynamic evolution of the Baoulé Mossi Domain can be broadly characterized by an initial accretionary phase of short-lived oceanic island arcs, followed by collision as the Birimian crust is juxtaposed with the Archean crust of the Man Domain (Abouchami et al., 1990, Feybesse and Milési, 1994, Hirdes and Davis, 2002, Baratoux et al., 2011, de Kock et al., 2011, Grenholm, 2014). Although blueschist facies metamorphism has been reported in eastern Burkina Faso, the majority of the volcanic

and volcano-sedimentary rocks underwent lower to upper greenschist facies metamorphism (Baratoux et al., 2015), though locally amphibolite to upper amphibolite facies conditions have been observed related to granitoid intrusions, or on a regional scale associated with the major collisional phase of the Birimian orogeny (Baratoux et al., 2015; and references therein).

The volcanic/volcano-sedimentary sequences comprise basaltic flows, andesitic to dacitic pyroclastic rocks and lavas, volcanogenic turbidites, and manganiferous cherts. The belts form synclinal structures cored by late-orogenic, alluvial, molasse-type sedimentary rocks and have been metamorphosed to greenschist facies (Lompo, 2010, Sylvester and Attoh, 1992). The stratigraphic sequence comprises a basal mafic tholeiitic volcanic succession, overlain by calc-alkaline extrusives (Baratoux et al., 2011, Baratoux et al., 2015, Hirdes and Davis, 1998, Hirdes et al., 1996, Oberthür et al., 1998), interpreted to have formed as oceanic plateaus (Abouchami et al., 1990, Baratoux et al., 2015, Boher et al., 1992) and/or volcanic island arcs (Baratoux et al., 2011, Baratoux et al., 2015, Dampare et al., 2008, de Kock et al., 2011). The Birimian metasedimentary belts are composed of fragmented felsic rocks, flysch-type turbidites and large, concordant, peraluminous granitic plutons, metamorphosed to amphibolite facies and are generally deformed into regional scale antiformal structures (Sylvester and Attoh, 1992). Radiometric dating puts the main peak of Birimian volcanism at around 2190-2160 Ma, while detrital zircons from the Birimian sedimentary basins yield dates as young as 2130 Ma to 2107 Ma putting constrains on the maximum age of deposition (Baratoux et al., 2015; and references therein).

Granitoid-gneiss domains are the dominant unit in the Baoulé Mossi Domain, comprising 50-60% of its total area (Grenholm, 2014). Several generations of granitoid, exhibiting a wide range in compositions from Na-rich tonalite-trondhjemite-granodiorite (TTG) to K-rich granites that were emplaced during a series of discrete magmatic pulses from about 2250

Ma to 2060 Ma (Baratoux et al., 2015; and references therein). Generally, the older intrusive rocks (>2.15 Ga) belonging to the TTG suite, commonly contain mafic enclaves, while the younger rocks are more K-rich with more abundant sedimentary xenoliths (Baratoux et al., 2011, Boher et al., 1992, Doumbia et al., 1998, Grenholm, 2014, Lompo, 2010). Granites and monzogranites are also present among the older intrusive TTGs, though they are temporally restricted to 2200-2190 Ma and 2160-2150 Ma respectively in eastern Baoulé Mossi Domain (de Kock et al., 2011, Feybesse et al., 2006, Grenholm, 2014). Common minerals found in these intrusive rocks include quartz, feldspar, biotite, muscovite, amphibole and clinopyroxene (Grenholm, 2014). Intrusive magmatism was ongoing throughout the Birimian event and magmatic ages overlap with magmatic activity can be seen in the volcanic rocks of the volcanic belts and the sedimentary basins (Baratoux et al., 2011, Doumbia et al., 1998, Feybesse et al., 2006, Grenholm, 2014). These similarities in age and composition suggest that the granitoid-gneiss domains may be the middle crustal equivalents of the volcanic rocks of the volcanic and volcano-sedimentary belts (Grenholm, 2014).

The Birimian granitoids can be classified as Basin and Belt types according to their geologic association (Leube et al., 1990b, Yao et al., 2001, Yao and Robb, 2000). Belt granitoids are dioritic to granodioritic in composition, with hornblende and biotite as the dominant mafic minerals. Basin granitoids are granodioritic to granitic in composition, with biotite as the major mafic mineral (Yao and Robb, 2000). Based on their geological occurrences, geochemical characteristics and whole-rock isotopes, it is thought that the Belt granitoids are I-type granites (Leube et al., 1990b, Yao and Robb, 2000) formed from the partial melting of basaltic rocks. Basin granitoids on the other hand are typically S-type formed from the melting of crustal materials with a minor mantle component (Yao et al., 2001). U-Pb zircon and monazite ages show that the Belt (2179 ± 2–2136 ± 10 Ma) and Basin (2125

± 2–2088 ± 1 Ma) granitoids were emplaced during two discrete periods (Hirdes et al., 1992, Oberthür et al., 1998), potentially reflecting the progressive accretion of magmatic areas from the southeast to the northwest of Ghana (Hirdes et al., 1992, Yao et al., 2001).

From an economic standpoint, Basin and Belt types of granitoids can be further subdivided into nonmineralised and mineralised plutons, with more than 20 Belt and Basin granitoids known to contain gold mineralization in the Birimian of Ghana (Yao et al., 2001, Yao and Robb, 2000). Mineralised Belt and Basin granitoids occur as small steeply dipping stocks, concordant with regional northeast-southwest trending faults and shear zones (Yao et al., 2001, Yao and Robb, 2000). Gold mineralisation is similar in both Belt and Basin granitoids and is not associated with any specific type of granitoid within the Birimian terrane (Yao and Robb, 1999). The granitoids range from granodiorite to granite in composition, and are comparable in terms of geological, mineralogical, geochemical, and petrogenetic characteristics with their non-mineralised counterparts, though the mineralised granitoids typically occur as smaller intrusions (Oberthür et al., 1998, Yao et al., 2001, Yao and Robb, 2000). This suggests that both mineralized Belt and Basin granitoids are genetically similar to their non-mineralized equivalents (Yao and Robb, 2000). It is thought that they provide preferential conduits for fluid flow due to their brittle character during regional deformation making them favourable sites for mineralization (Yao et al., 2001, Yao and Robb, 1999).

The mineralisation is characterized by quartz veins and/or stockworks and pervasive alteration zones within granitoids with crosscutting relationships, indicating that gold mineralisation took place in multiple phases, postdating granitoid emplacement (Yao et al., 2001). The ore mineral assemblage within the granitoid-hosted mineralisation is dominated by early stage pyrite and arsenopyrite, with minor late stage chalcopyrite, sphalerite, galena, native gold, and rutile. U-Pb dating of hydrothermal rutile has been used to constrain the

ages of mineralisation in both Belt and Basin granitoids, showing that mineralisation generally postdates the corresponding granitoid emplacement by about 5 to 30 Ma (Yao et al., 2001). Mineralisation of Belt-type granodiorite from the Sakpa mine of the Bole-Navrongo Belt was constrained to have occured at 2133 ± 21 to 2110 ± 32 Ma (Yao and Robb, 1999), corresponding with peak metamorphism in Northwest Ghana (Block et al., 2015) and peak metamorphism in the eastern block of the Baoulé-Mossi Domain (Parra-Avila et al., 2017). Basin-type granitoids of the Obuasi and Ayanfuri mines of the Kumasi basin were emplaced at 2098 ± 7 to 2086 ± 4 Ma respectively. The age range of mineralisation in both cases coincides with the second of the major magmatic pulses (e.g. Basin-type granitoid intrusion) of the Birimian orogeny (see 1.4.2.2.2 for detail).

1.4.2.2.2 Geodynamic Evolution

In order to study the geochronological evolution of the Baoulé-Mossi Parra-Avila et al. (2017) compiled a database including eighty-four new felsic intrusions and existing age data. The data revealed that the entire domain experienced continuous magmatic activity for at least 150 million years, demonstrating a craton-scale diachronous geochronological pattern characterized by a westward migration of magmatic activity. An apparent offset of approximately 50 million years was noted between the commencement and termination of the magmatic activity between the east and west (Figure 1.5). Parra-Avila et al. (2017) also noted that there is a higher incidence of inherited ages in the westernmost portion when compared to the easternmost region. The distribution of the inherited ages and the offset in magmatism suggests that the Baoulé-Mossi Domain formed from the accretion of at least two major crustal blocks, with the boundary likely located between the Banfora and Bagoe Belts (Parra-Avila et al., 2017).

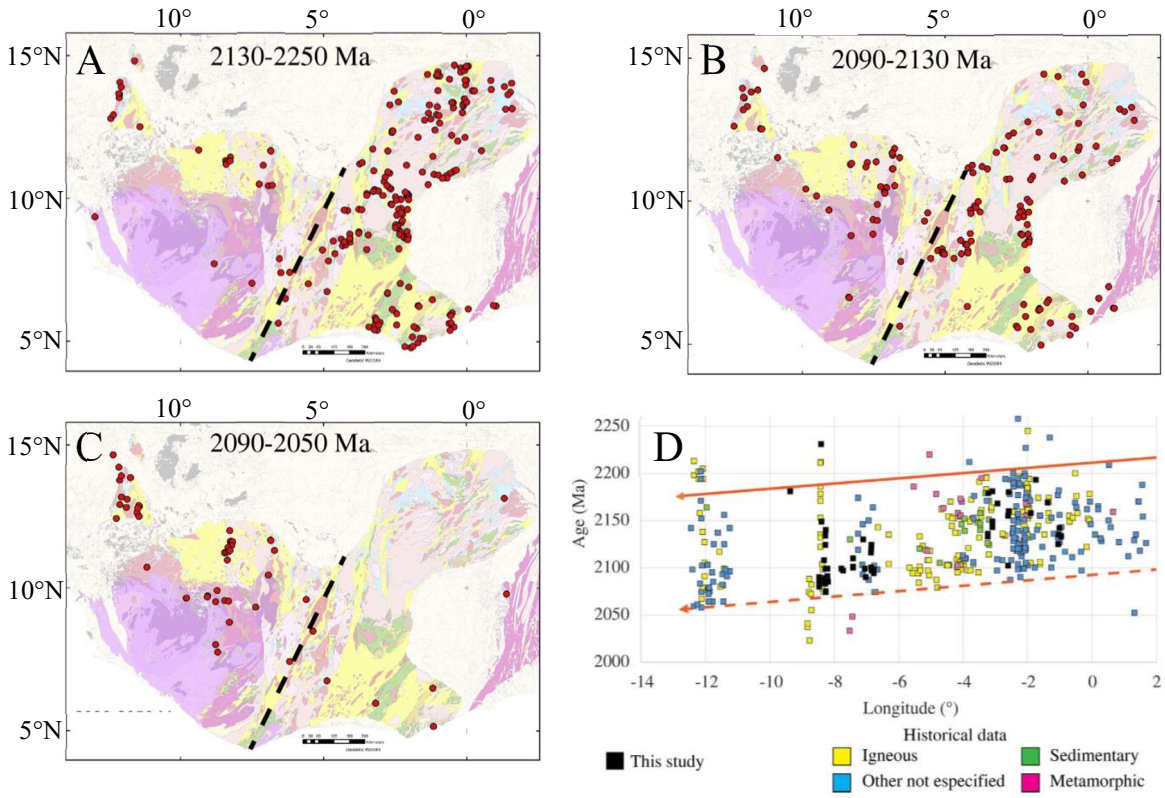

Figure 1-5 – Zircon and monazite U-Pb age distribution across the southern West African Craton for the period between 2250 and 2050 Ma (from Parra-Avila et al., 2017). A) Ages between 2300 and 2130 Ma, showing a marked concentration of ages in the eastern craton, and no recorded ages within the Archaean host rocks; B) Ages between 2130 and 2090 Ma, showing a uniform coverage of ages across craton for this age bracket, and several ages recorded within the Archaean host rocks; and C) Ages for the period 2090–2050 Ma, clearly showing that most ages are concentrated west of the Banfora-Bagoe belts in the westernmost portion of the study area. D) Longitudinal variations in magmatic activity illustrating a westward migration of the magmatic activity.

Peak magmatism in the eastern portion is coincident with peak metamorphism at ca. 2130 Ma (Block et al., 2015) providing an indication of the timing at which the two blocks were docked (Figure 1.6; Parra-Avila et al., 2017). Inherited grains with ages up to 2250 Ma were generally noted in intrusions younger than ca. 2130 Ma, indicating that the crust was thicker after that time, allowing for incorporation of older components (Parra-Avila et al., 2017). This is consistent with an accretionary model whereby magmas younger than ca. 2130 Ma interacted directly with intrusions emplaced between ca. 2250 and 2150 Ma, or sampled sediments derived from them.

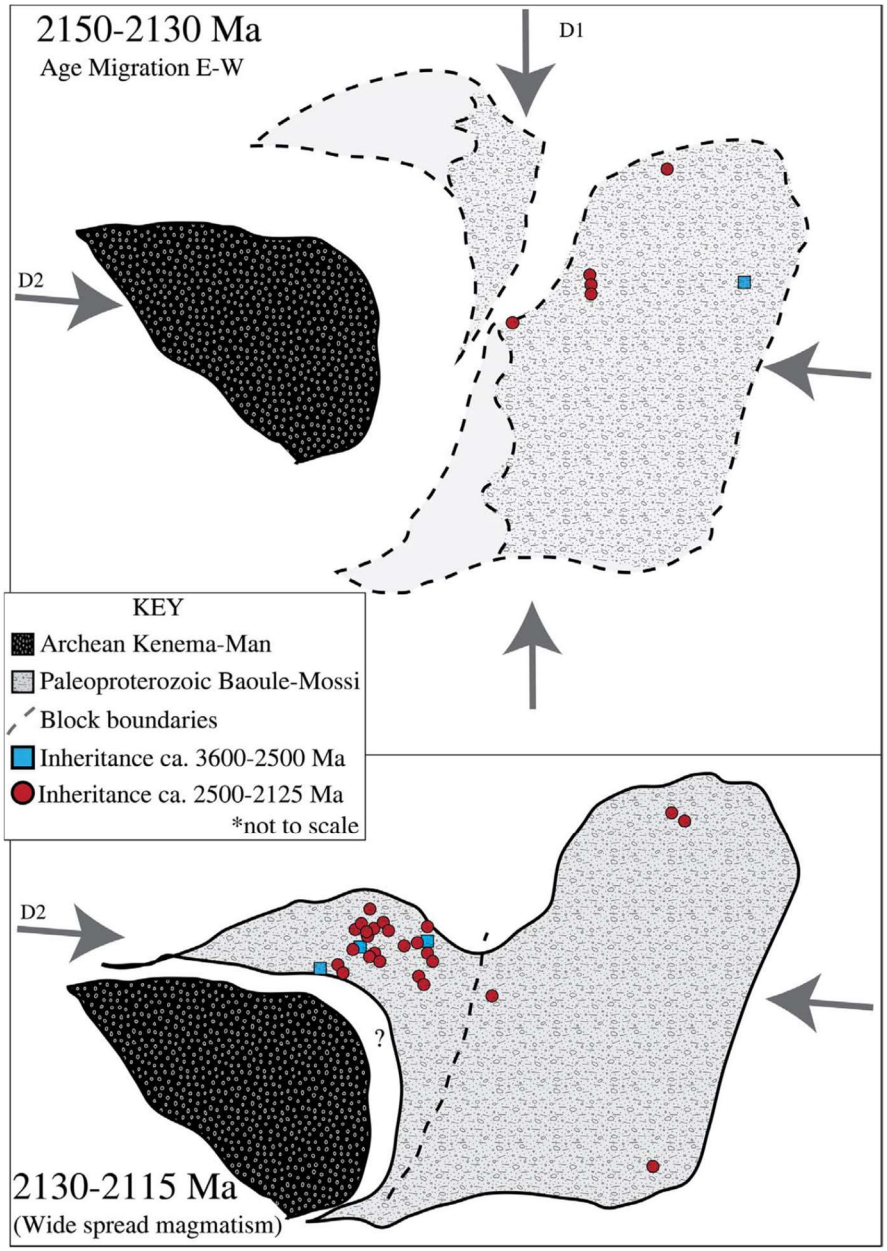

Figure 1-6 – Schematic cartoon showing the proposed boundaries and crustal blocks by (Parra-Avila et al., 2017). Top, shows the Archean Kénéma-Man and the Baoulé-Mossi Domain. The Baoulé-Mossi Domain is divided into two major crustal blocks during the period 2160–2130 Ma. During this period the assemblage blocks are affected by compressional forces, first N-S (D1) followed by a E-W compression (D2) (Parra-Avila et al., 2017; and references therein). Density of the dot pattern indicates distribution of magmatic activity with higher density corresponding to a greater degree of magmatism. Bottom shows the amalgamation of the Palaeoproterozoic blocks under a D2 compressions for the period 2130–2110 Ma. Note the occurrence of inherited grains. Inheritance is largely concentrated in the eastern portion of the Baoulé-Mossi, predominately represented by ages between ca. 2500 and 2125 Ma which are common crystallization ages across the eastern block, indicating that the western block is contaminated by crustal material derived from the eastern block.

Eglinger et al. (2017) presented a geochronological study on the Palaeoproterozoic margin of the Archaean Kéména-Man Domain in Guinea. The study involved U–Pb dating of magmatic zircon grains from quartz-monzodiorites and biotite-granites from the margin. The

results demonstrate that a period of potassic magmatic activity was continuous between ca. 2.10 and 2.08 Ga along the northern margin of the Kéména-Man Domain, similar to U–Pb ages ranging from ca. 2.09 to 2.07 Ga obtained from plutonic rocks along the eastern margin of the Kéména-Man Domain (Egal et al., 2002b). With the collision between the Kéména-Man and Baoulé- Mossi Domains constrained to a period between ca. 2.10 and 2.09 Ga (Feybesse et al., 2000, Parra-Avila, 2015), lithospheric delamination is expected to have taken place between ~2.09 and 2.07. Eglinger et al. (2017) concluded that heat from the resultant asthenosphere upwelling resulted in the melting of the different crust and mantle domains within a relatively short period of time of <20 Ma (Figure 1.7). Granites proximal to the Archaean nucleus showed evidence of interaction with, and reworking of, Archaean material while those forming further away were formed by a mixture of crustal melts and juvenile sanukitoids (Mg-rich felsic to intermediate granitoid characterised by the presence of orthopyroxene as the mafic mineral) (Eglinger et al., 2017). Heat from the asthenospheric upwelling also caused melting of Au-rich metasomatized mantle source, enriched by pre-Eburnean subduction-accretion events, and was the driving force for large-scale fluid migration within the crust (Eglinger et al., 2017). As such, Eglinger et al. (2017) proposed that it was the driving force behind late orogenic gold mineralisation known in the western part of the Baoulé-Mossi Domain.

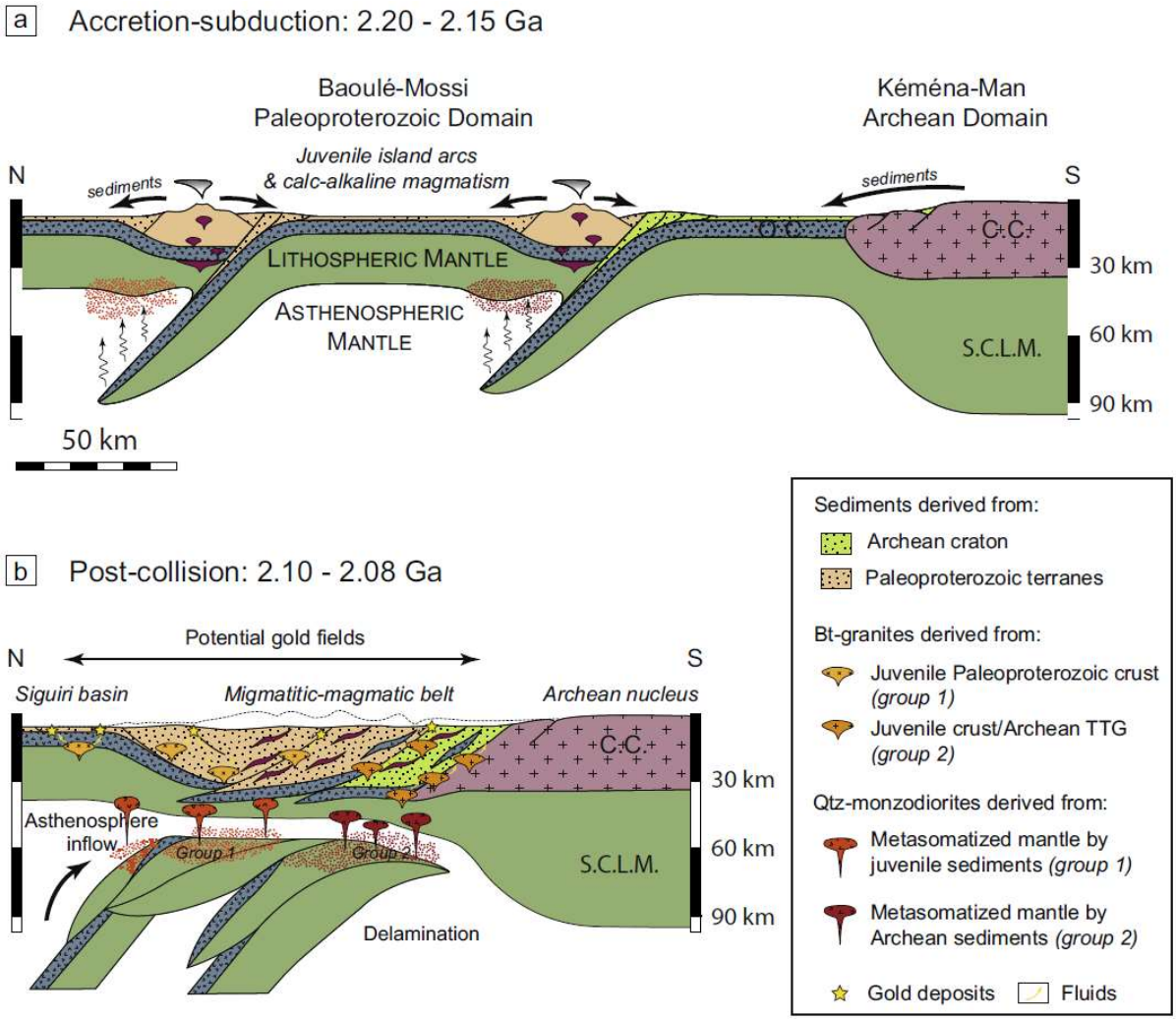

Figure 1-7 - Schematic diagram illustrating the 2.20–2.08 Ga geodynamic evolution of the northern Palaeoproterozoic margin of the Archean Kéména-Man domain. C.C. = continental crust; O.C. = oceanic crust; SCLM = subcontinental lithospheric mantle.

1.4.3 Reguibat Shield

The Reguibat Shield, the name given to the northern exposure of the West African Craton, extends approximately 1,500 km in a southwest-northeast direction and ranges in width from around 250 to 400 km. It covers most of northern Mauritania and extends west into the southern and eastern parts of Western Sahara and east into Algeria (Figure 1.8). Like the Man-Leo Shield, the Reguibat Shield can be divided into Archaean and Palaeoproterozoic domains. The western Archaean terrane is dominated by gneisses and granitic rocks, while the eastern Eburnean terrane is mainly composed of Palaeoproterozoic granitic and

metasedimentary rocks. These crustal domains are believed to have been juxtaposed during the Eburnean Orogeny (2.10-2.00 Ga) (Schofield and Gillespie, 2007, Schofield et al., 2006).

The Reguibat Shield is bounded on its western side by the Mauritanides orogenic belt. This Pan African to Hercynian age fold-thrust belt outcrops in southern Western Sahara and western Mauritania and is thought to be an African continuation of the Appalachian Orogenic Belt (Dallmeyer et al., 1987). To the south the Reguibat Shield is covered by the Proterozoic to Palaeozoic age Taoudeni Basin. This inland basin is the largest Proterozoic-Paleozoic basin in Africa and covers the central part of the West African Craton dividing the Reguibat and Leo-Man Shields. The Reguibat Shield is overlain to the north by the Mesozoic Tindouf Basin, outcropping in northern Western Sahara and southern Algeria.

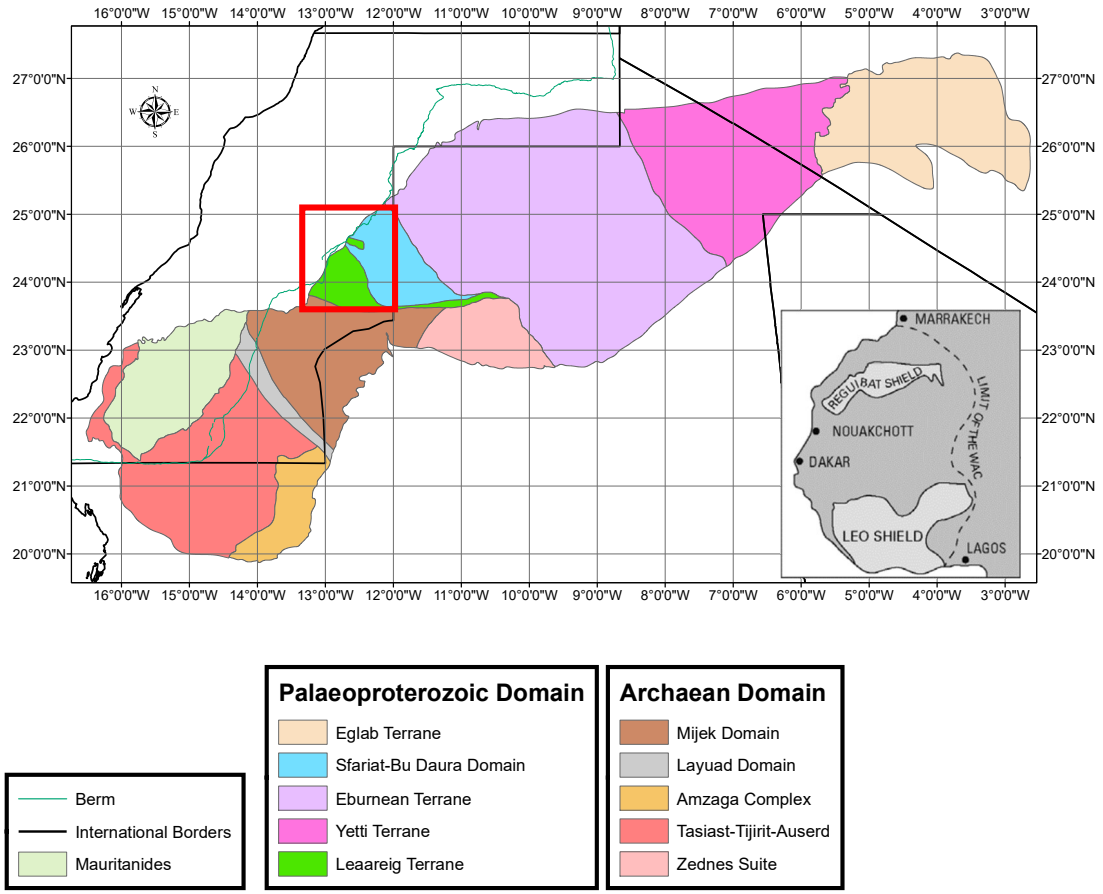

Figure 1-8 - Terrane map of the Reguibat Shield. The newly defined Leaareig and Sfariat-Bu Daira Terranes were defined in Western Sahara as part of this project, and extrapolated into Mauritania based on Schofield et al. (2006) and Schofield et al. (2012). The other terranes in Mauritanian are based on Bradley et al. (2015a), the portion of Eglab and Yetti terranes in Algeria was based on Peucat et al. (2005) and the Archaean portion of the within Western Sahara based on Lehbib (2016)

The study area covers 12,000km^2 in Western Sahara to the north of the Archaean-Palaeoproterozoic contact (Figure 1.8). Previous work in the region had relied on literature from mapping in Mauritania and using satellite imagery to extrapolate units over the border. As a major portion of the wedge-shaped Contact Zone between the Archaean and Palaeoproterozoic crust falls in this understudied region of Western Sahara, valuable information about the nature of the contact was previously unknown.

1.4.3.1 Archaean Domain

The Archaean part of the Reguibat Shield was divided by Rocci et al. (1991) into three lithostratigraphic domains, including the Tasiast-Lebzenia Domain in the southwest, the Amasaga-Tiris-Ouassat Domain in the centre and the Ghallaman Domain in the northeast (Schofield et al., 2012). The Tasiast-Lebzenia Domain was renamed Tasiast-Tijirit Terrane following work by Pitfield et al. (2005). Schofield et al. (2012) divided the Amasaga-Tiris-Oussat Domain into separate lithostratigraphic entities, including the Tiris and Amsaga Complexes, whilst the Oussat Complex was renamed the 'Contact Zone', shown by Schofield et al. (2006) to comprise accreted parts of the eastern Palaeoproterozoic Domain (Figure 1.8). Lehbib (2016) completed the first study of the Archaean of the Reguibat Shield in Western Sahara and subdivided the Tiris terrane into two domains including the Layuad and Mijek Domains.

1.4.3.1.1 Tasiast-Tijirit Terrane

The Tasiast-Tijirit Terrane is characterised by major greenstone belts and tonalitic and granitic migmatitic gneisses surrounded by younger, tonalitic-granodioritic plutons (Key et al., 2008, Schofield et al., 2012). North to northeast-oriented gneissic/greenstone belts and shear zones dominate the overall architecture of the terrane (Schofield et al., 2012), with cross cutting plutons of biotite-tonalite and metaluminous granitoids which commonly core

in dome-like structures (Key et al., 2008). The Tasiast-Tijirit Terrane can be divided into three major lithological groups including migmatitic (tonalitic) gneisses, greenstone belt lithologies (interlayered mafic and ultramafic metavolcanic rocks with minor felsic metavolcanics) and post-greenstone belt granitoid intrusions (primarily large biotite-tonalite/granodiorites granitoids and small pegmatitic muscovite-granites) (Key et al., 2008). Most of the rocks dated in the terrane are gneiss, TTG and granite samples, yielding ages between 2.97 Ga and 2.91 Ga (Schofield et al., 2012, Heron et al., 2016). Syntectonic augen granite from the Tâcarât-Inemmaûdene Shear Zone (between Tasiast-Tijirit Terrane and the Amsaga Complex) was dated at 2954 ± 11 Ma (Key et al., 2008, Schofield et al., 2012). Recent work in Western Sahara (in which a large portion of the terrane lies) by Lehbib (2016) also produced a comparable age of 2942 ± 11 Ma. In addition, dates of 2494 ± 15 Ma and 2494 ± 20 Ma were produced from U-Pb zircon dating for samples of kalsilite syenite and nepheline syenite respectively. These are comparable to work completed within this terrane in the Occupied Territories of Western Sahara where syenite was dated at 2460 ± 0.1 Ma using SIMS (Bea et al., 2014).

The Tasiast-Tijirit Terrane is also of economic importance, hosting the world class (>10 Moz) Tasiast gold deposit within one of three major greenstone belts within the terrane (Heron et al., 2016). The mine consists of two deposits hosted in metasedimentary (metaturbidites and banded iron formation where the main mineral association consists of magnetite-quartz-pyrrhotite ± actinolite ± garnet ± biotite) and stratigraphically lower meta-igneous rocks (mainly diorites and quartz diorites) (Heron et al., 2016).

1.4.3.1.2 Amsaga Complex

The Amsaga Complex forms the meta-igneous and metasedimentary basement below the Taoudeni Basin in the southwest of the Reguibat Shield (Bradley et al., 2015b). Mapping of

the Amsaga Complex by O'Connor et al. (2005b) and Pitfield et al. (2005) established that a large part of the complex includes a varied association of quartzo-feldspathic granoblastic and migmatitic gneisses with tonalitic, trondhjemitic and granodioritic (TTG) composition in addition to hypersthene-bearing charnockitic gneisses (with minor units of garnet–cordierite–sillimanite gneiss and basic to ultrabasic rocks) (Schofield et al., 2012). These units are interleaved along a network of curved NNE- to N-trending ductile shear zones (Schofield et al., 2012). The formation of the orthogneisses in the Amsaga Complex was constrained by Potrel et al. (1996), who dated the two oldest samples of orthogneiss in the region at 3515 and 3422 Ma (Potrel et al., 1996, Schofield et al., 2012), while the youngest thermal/magmatic events preserved in the complex was shown to be at 2.71 Ga on the basis of a granulitic gabbro dated by Auvrey et al. (1992). The dating of the youngest event is supported by dating of discrete, post-tectonic granite bodies (2715 ± 11 Ma and 2726 ± 7 Ma (Auvray et al., 1992, Potrel et al., 1998)) which cross-cut the gneisses of both the Amsaga Complex and Tasiast-Tijirit Terrane, also providing a minimum age for their amalgamation (Schofield et al., 2012).

Important to note in the Amsaga Complex is the presence of concordant sheets of anorthosite found throughout the complex (Bradley et al., 2015b). When analysed by the SIMS method, zircons from one anorthosite sample hosted within charnockitic gneiss yielded a poorly resolved age of 2930 ± 33 Ma (MSWD 38) with points near concordia not grouping very well and Phanerozoic lead-loss resulting in most of the zircons being discordant (Bradley et al., 2015b). Bradley et al. (2015b) proposes that although the age of the sample is poorly constrained, it still appears to be the oldest 'massif-type' anorthosite in the world – commonly referred to as 'Proterozoic massif-type anorthosites' due to their temporal distribution (Ashwal, 2010). Two separate samples of quartzofeldspathic gneiss-hosted anorthosite from the complex were also dated by Bradley et al. (2015b) using LA-ICPMS.

Coarse-grained and fine-grained samples of anorthosite were dated separately yielding dates of 2718 ± 7 Ma and 2743 ± 4 Ma respectively. A crosscutting granite phase yielded a U-Pb zircon age 2726 ± 7 Ma (Potrel et al., 1998).

1.4.3.1.3 Layuad Domain

Defined by Lehbib (2016), the Layuad domain is a Saharawi unit, outcropping almost exclusively in Western Sahara making it one of the least studied units of the entire craton. Lehbib (2016) suggests that tentative correlations can be made to the Choum and Rag-El-Abiod of the Amsaga Complex in Mauritania, but with no previous descriptions of this domain in Western Sahara the correlations are not strong.

Like the Tasiast-Tijirit Terrane, orthogneiss is the dominant lithology with occurrences of alkali granite, peraluminous paragneisses, amphibolites and BIF. The north to northeast-oriented gneissic/greenstone, typical of the Tasiast-Tijirit Domain, is absent in the Layuad Domain. Instead, the main alignments trend roughly northwest-southeast, parallel to the fault that puts this unit in contact with the one of Tasiast-Tijirit Terrane. The rocks were metamorphosed to high grade up to granulite facies, differentiating it from the rocks from the Mijek Domain dominated by amphibolite facies metamorphism (Lehbib, 2016).

The orthogneiss tend to be coarse-grained, of variable composition ranging from leucotonalitic to tonalitic and even granodioritic (TTG). In the most felsic members, it is not uncommon for them to present megacrystals of potassium feldspar. Paragneiss are recognised by well defined banding, finer grain size and they are finely interspersed with other sedimentary materials. Associated with the paragneiss, and sometimes amphibolites, BIF layers are present, up to 50 m thick (possibly structurally exaggerated by the repetition

through thrusting and folding). This has led to significant accumulation of iron ore in the domain (e.g. Guelb Admar (Lehbib, 2016)).

Lehbib (2016) dated 5 samples from the domain using LA-ICPMS. Of the metamorphic samples, a granulite was dated at 2530 Ma, with the orthogneiss dated at 2473.5 ± 15.3 Ma. A sample of granite was dated at 2493.2 ± 17.3 Ma, while two alkali granites returned dates of 2490 ± 15.3 Ma and 2478 ± 23 Ma. These are comparable to the ages of the syenite intrusion in the Tasiast-Tijirit Terrane.

1.4.3.1.4 Mijek Domain

The Miyec-Ijil Domain, defined by Lehbib (2016), is a northwest-southeast trending domain, being limited by a series of thrusts on the unit of Layuad to the southeast and El M'dena Fault to north (Figure 1.8). Extensive mapping, including some geochronology, has been carried out in the domain in Mauritania due to the presence of large iron ore deposits. Due to differences in how lithologies were grouped in the mapping in Mauritania, difficulties arose in correlating units established in Mauritania with those defined by Lehbib (2016) in Western Sahara.

The domain essentially represents a basin, consisting of two major units. The crystalline basement is emerging as metamorphic domes of orthogneiss, and the discordantly overlying metasedimentary rocks include schists, greywacke, quartzite, marbles and BIF (Lehbib, 2016). Schofield et al. (2012) dated two samples of foliated biotite granite and one sample of granite from the basement at 2482 ± 7 and 2487 ± 8 and 2948 ± 11 Ma respectively.

1.4.3.1.5 Ghallaman Domain – Zednes Suite

Lahondère et al. (2003) defined the Ghallaman Domain as consisting of two lithostratigraphic associations recognised within the Mesoarchaean basement including the

Zednes Suite and Temmimichate-Tsabaya Complex. The Zednes Suite consists of an association of tonalitic plutonic and gneissose rocks dated at around 3044 ± 5 Ma, intruded by a suite of unfoliated granite and granodiorite dated at 2915 ± 18 and 2832 ± 4 Ma (Lahondère et al., 2003).

The undated Temmimichate-Tsabya Complex, interpreted by Rocci et al. (1991) as being Archaean, and was grouped by Lahondère et al. (2003) in with the Zednes Suite as part of the Ghallaman Domain. However, recent geochronology produced by Lehbib (2016) and as a part of this project have demonstrated that this unit is Palaeoproterozoic and as such will be discussed in section 1.4.3.2.1 with the Sfariat-Bu Daira and Leaareig Terranes.

1.4.3.2 Palaeoproterozoic Domain

The Palaeoproterozoic component of the Reguibat Shield is referred to as the Eglab Shield by authors studying this domain in Algeria (Barbey, 1975, Allek and Hamoudi, 2008, Kahoui et al., 2012, Kahoui and Mahdjoub, 2004, Markwitz et al., 2016b, Merabet et al., 2014, Merabet et al., 2016, Mohammed et al., Peucat et al., 2005, Tokarski, 1991), or as the Eburnean terrane by authors working in Mauritania (Rocci et al., 1991, Schofield and Gillespie, 2007, Schofield et al., 2006, Schofield et al., 2012).

It has been subdivided into five terranes including the newly defined, in this study, Leaareig Terrane, and the redefined Sfariat-Bu Daira Domains (collectively referred to as the Sfariat-Bu Daira Domain by Lehbib (2016) 'The Contact Zone' by (Schofield and Gillespie, 2007)) and Adam Esseder, Yetti and Eglab Domains to the east (Figure 1.8; Kahoui and Mahdjoub, 2004, Peucat et al., 2005). The Leaareig Terrane, directly north of the Archaean terrane, consisting largely of orthogneiss representing the mid crustal remnants of an Eoeburnean island arc as well as metasediments, only extends into Mauritania as a sheared belt mapped over the border as the Temmimichate-Tsabaya Complex (Figure 1.9). The Sfariat-Bu Daira

Domain in Mauritania is observed as ferruginous quartzite and marble, BIF, migmatitic gneiss, amphibolite facies paragneiss, interpreted as continental platform sediments (Lahondère et al., 2003, Schofield et al., 2006, Bradley et al., 2015b). In Western Sahara the Sfariat-Bu Daira Domain presents itself largely as fault-bound northwest-southeast belts of volcanic, volcano-sedimentary, and sedimentary belts interleaved with granite gneiss. The Yetti Domain is primarily composed of folded volcano-sedimentary sequences intruded by granites, while the Eglab Domain consists of large undeformed and unmetamorphosed granitoids and felsic volcanic rocks of the Eglab Series (Kahoui and Mahdjoub, 2004, Peucat et al., 2005, Merabet et al., 2014, Markwitz et al., 2016b).

The Palaeoproterozoic arc complex to the northeast of the Sfariat Bu-Daira Domain comprises mostly of plutons belonging to ten intrusive suites, interrupted by northwest-southeast trending belts of deformed supracrustal rocks (Figure 1.11; Bradley et al., 2015b). Piggybacking on terminology used to describe 2.2 to 2.0 Ga orogenic events in Ghana, Lahondère et al. (2003) assigned the Palaeoproterozoic rocks in the Reguibat Shield to a subdivision defined as Eobirimian, Mesobirimian, Tardibirimian, Neobirimien, and post-Neobirimien tectono-magmatic phases. As 'Birimian' is a regionally specific term applying to tectonic events in Ghana, the broader term 'Eburnean' is preferred here. As such, Eoeburnean (>2150 Ma), Mesoeburnean (~2150 to 2078 Ma), Tardieburnean (2073 to 2067 Ma), Neoeburnean (2040 to 1995 Ma) and post-Neoeburnean (undated) (Bradley et al., 2015b) will be used.

The study area for this project covers essentially the entire exposure of the Sfariat-Bu Daira and Leaareig Terranes in Western Sahara, stretching from the border with Mauritania to where they disappear under the Aaiun Basin to the west (Figure 1.8.)

1.4.3.2.1 Leaareig Terrane

Perhaps largely due to a high degree of sand cover, the newly defined Leaareig Terrane had never been described in the literature, though recent work as part of this project has differentiated this unit as a separate terrane (Chapter 3). The major component of this terrane is a wedge (the Leaareig Domain) of predominantly orthogneiss with belts of northwest-southeast trending paragneiss and marble and mafic intrusions near the southeast contact with the Sfariat-Bu Daira Terrane (Figure 1.9). Only the southern belt (the Sassaiat Shear Zone) of the terrane extends into Mauritania, where it has been mapped as the southern Temmimichate-Tsabaya Complex.

The previously undated Temmimichate-Tsabaya Complex has always been thought of as being Archaean (eg. Rocci et al., 1991, Lahondère et al., 2003, O'Connor et al., 2005b, Schofield et al., 2006, Schofield et al., 2012). The unit comprises mafic and ultramafic gneisses and calcsilicate rocks forming an arcuate band around the margin of the Archaean terrane. It was interpreted as part of the Mesoarchaean Ghallaman Domain with ages inferred from the Zednes Suite (Rocci et al., 1991, Schofield and Gillespie, 2007). Mapping by O'Connor et al. (2005b) demonstrated that the Temmimichate-Tsabya Complex was structurally contiguous with granitic gneisses and ferruginous quartzites of the Tiris Complex, persuading Schofield et al. (2012) that it was likely a Mesoarchaean basement, an interpretation shared by Taylor et al. (2016). Rocks from the complex were reported to have a geochemical signature similar to modern boninitic and tholeiitic lavas, leading Lahondère et al. (2003) to conclude that it formed in an oceanic island arc setting, though it was still unclear as to if it represented part of the Archaean foreland or whether it was part of the accretionary margin of the adjacent Eburnean terrane (Schofield and Gillespie, 2007).

In Western Sahara, the Temmimichate-Tsabaya Complex is present as intermediate to mafic orthogneisses, paragneiss and, amphibolite as well as thick units of marble (up to 1km) and

iron-formation (with the proportion of marble and iron rock increasing to the west). Lehbib (2016) maps it as a series of BIF, schists, greywackes, amphibolites, quartzites and marbles with two very thick units of marble in the west of the complex that are possibly Neoarchaean in age (Figure 1.10). U-Pb zircon dating of a tonalite at 2099.3 ± 15 Ma (Lehbib, 2016) and migmatite at and 2100 ± 19 Ma (Chapter 2, Table 2-1), with no indication of inheritance, demonstrate that the complex is Palaeoproterozoic in age and represents an accretionary margin of the adjacent Eburnean terrane. The whole rock geochemistry of the 2099.3 ± 15 Ma tonalite reveals it to be a calc-alkaline intrusion from a volcanic arc setting.

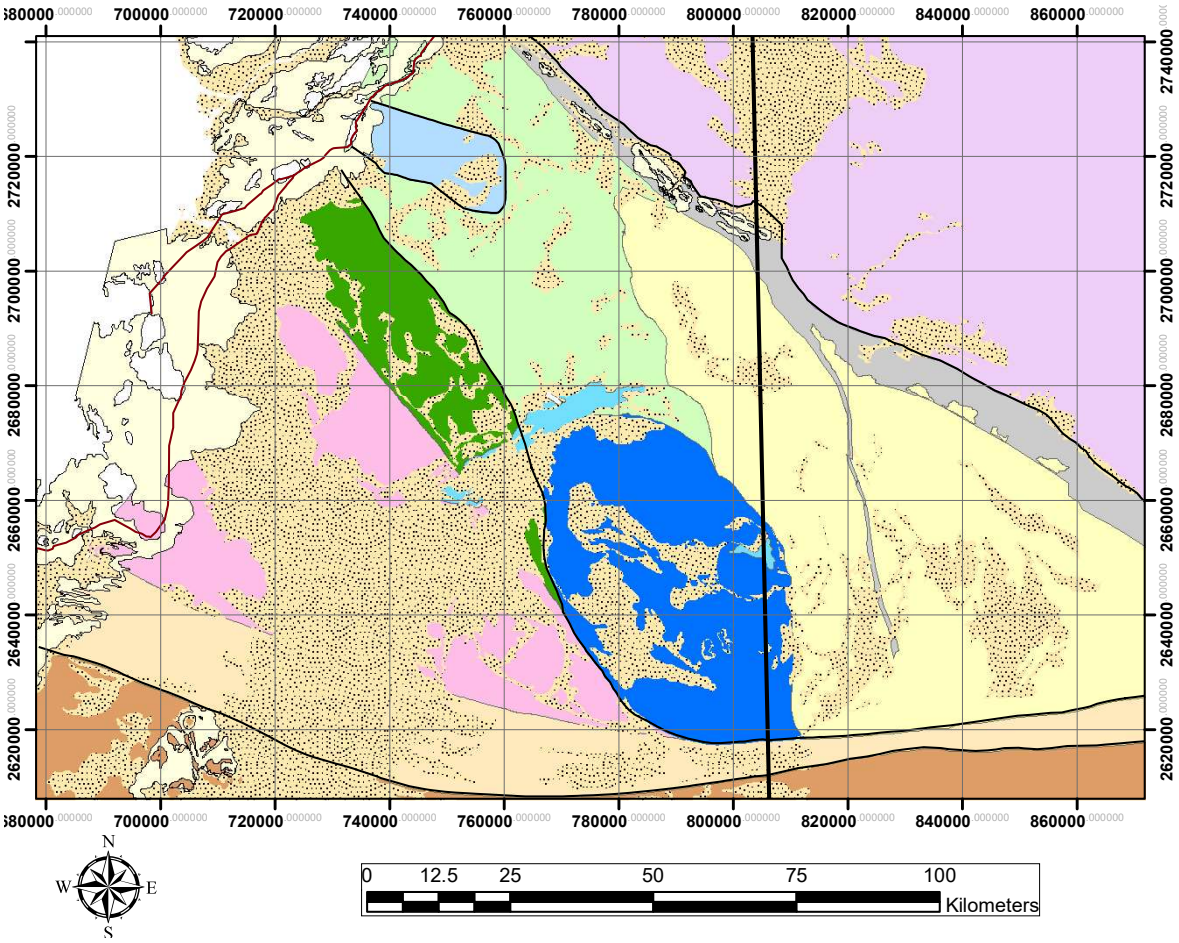

Figure 1-9- Simplified geological map of the Leaareig and Sfariat-Bu Daira Terranes.

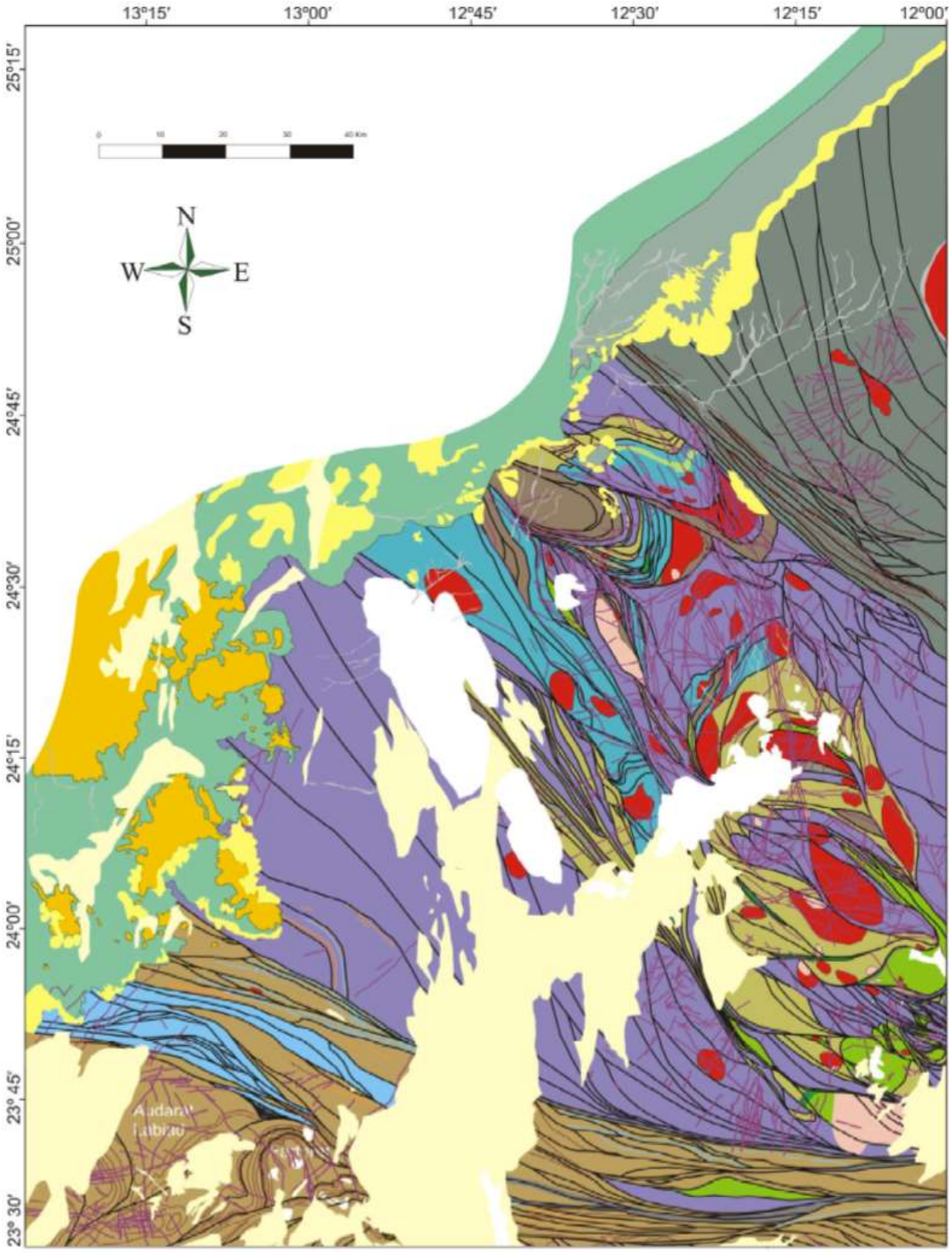

Figure 1-10 a - Geological map of the Leaareig and Sfariat-Bu Daira domains by Lehbib (2016), mapped by the author to represent a single terrane, the 'Sfariat Bu Daira Domain'. See the legend on the following page.

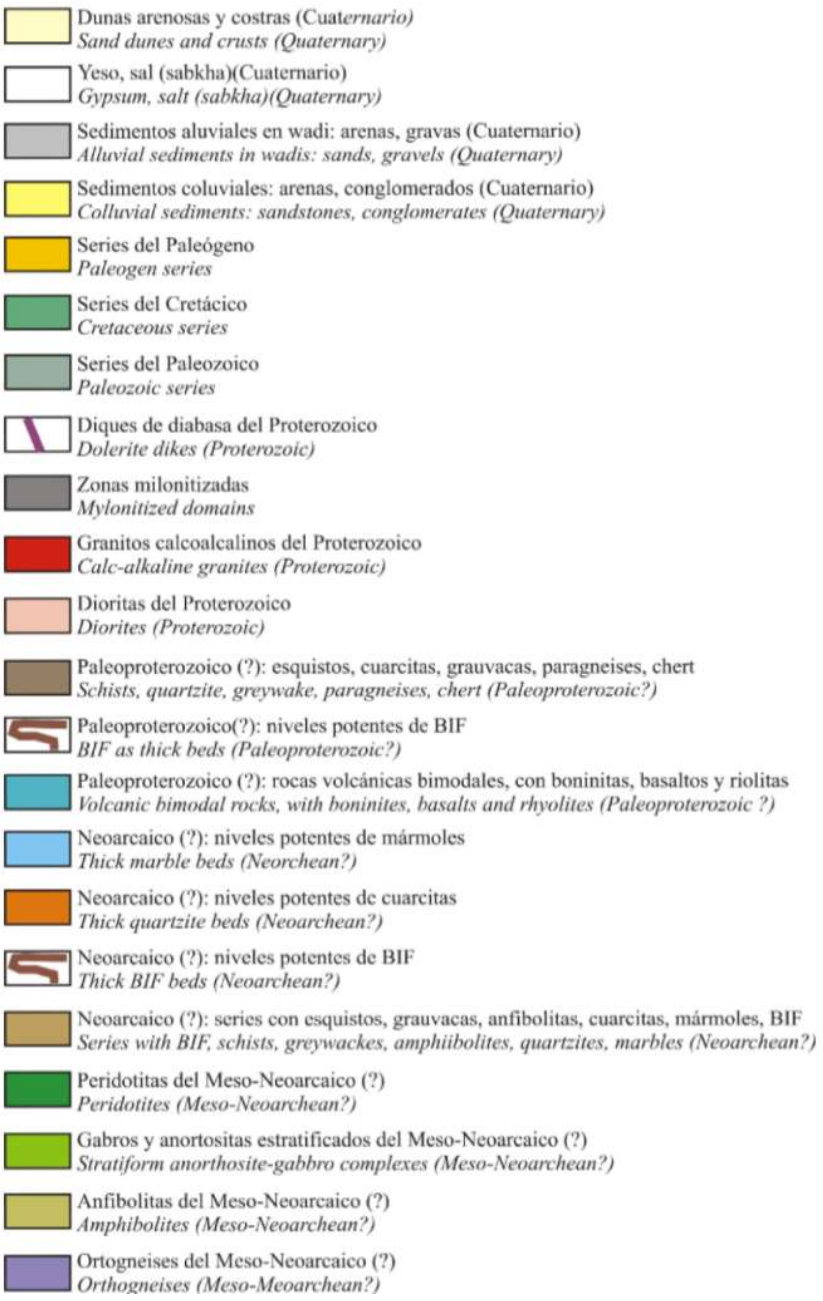

Figure 1.10 b - Legend

Very little work had been completed on the orthogneissic wedge due to sand dunes obscuring much of the geology (Section 3.1). Lehbib (2016) mapped the undated region as entirely orthogneiss with minor bands of marble, hypothesizing its age to be Mesoarchean, representing the northern edge of the 'Mijek-Ijil basin'. As part of this current project U-Pb zircon dating of the granodiorite gneiss from the wedge revealed ages of 2240 ± 65 Ma and 2207 ± 57 Ma (Chapter 2). It is suggested that this wedge represents the mid to lower crustal

remnants of an Eoeburnean island/mature arc system formed at 2.25 to 2.18 Ga, similar to the basement of the Eglab Terrane (Section 1.4.3.2.5).

A sole thrust is mapped within the Sfariat-Bu Daira Domain (Section 1.4.3.2.2) containing a mafic-ultramafic complex moving to the west into units of basalt and chert, paragneiss and marble, and undifferentiated mafic/ultramafic rocks. The region bounded by the thrust was interpreted as containing an attenuated back-arc basin ophiolite sequence with overlying marine sediments, with the paragneiss and marble interpreted as a mixture of accumulation of carbonates in a shallow marine environment and the influx of clastic sediments from a more continental type setting. A sample of low grade paragneiss dated at 2176 ± 32 Ma leads to an interpretation that it represented detrital zircons from the Eoeburnean proto-continent represented by the orthogneiss wedge depositing in the back-arc basin. The sequence was interpreted as having thrust over Sfariat-Bu Daira Terrane as the two terranes collided (Section 3.3.5).

A large portion of the Contact Zone between the Archaean and Palaeoproterozoic terranes is defined by the west-trending El Mdena Fault Zone at the south of this domain (Schofield et al., 2006). Late movement along the structure destroyed field evidence of Eburnean displacement, though the fault zone granitoids of the Sfariat Igneous Complex (~2090 Ma) were observed intruding into the Temmimchate–Tsabya Complex. These granitoids are coeval with anatexis and suggests that the Sfariat Igneous Complex effectively sutures the terrane boundary meaning that docking of the Palaeoproterozoic arc terranes (Lahondère et al., 2003) with the Archaean terrane must have occurred by this time (Schofield et al., 2006).

1.4.3.2.2 Sfariat-Bu Daira Terrane

Lehbib (2016) initially defined the Sfariat-Bu Daira Domain as a very similar region to the ‘Contact Zone’ coined by Schofield and Gillespie (2007) (based on work by Schofield et al.,

2006) though Lehbib (2016) included the Temmimichate-Tsabaya Complex in the domain. It was re-defined in this project to exclude the Leaareig Terrane. Commonly mentioned in literature and on maps as being part of the Ouassat Complex (Bronner et al., 1990, Rocci et al., 1991, Bronner et al., 1992) it was previously thought to be Archaean in age, but U–Pb zircon ages by Schofield et al. (2006) for anatectic migmatites and syn-tectonic granites (at 2.11 - 2.06 Ga) demonstrated it to be part of the Palaeoproterozoic domain.

The Sfariat-Bu Daira Domain forms a northwest-southeast trending belt between the Leaareig Terrane in the south and the Palaeoproterozoic granites to the northeast. In Mauritania it comprises the Anajim Guebli Suite (Figure 1.9), consisting of abundant thin units of ferruginous quartzite and marble, BIF, migmatitic gneiss, amphibolite facies paragneiss, as well as syntectonic granite (Schofield et al., 2006). These are interpreted to be the deformed remnants of continental platform sediments, deposited at what was then the edge of the craton (Schofield et al., 2006). Schofield et al. (2006) inferred that it represented a passive margin within the Leaareig Terrane (Temmimichate-Tsabaya Complex) as opposed to a convergent one based on the nature of the protolith assemblage and the notable lack of Palaeoproterozoic magmatism in the Archean domain (Bradley et al., 2015b).

The Sfariat Shear Zone is a major northwest-southwest striking shear zone running through the Sfariat-Bu Daira Domain (Bronner et al., 1992). Outcropping over ~200 km amd ranging in width from 3 to 7 km, the Sfariat Belt disappears under Neoproterozoic cover in Western Sahara at its northwestern extremity, and tapers out toward the SE in Mauritania where it disappears at the junctions of several major faults (Bronner et al., 1992). Studies from the Mauritanian part of the Sfariat Belt have established that the belt consists of three to four parallel and straight secondary ranges, which gradually decrease in altitude toward their extremities (Bronner et al., 1992). The central part of the belt comprises mylonitic, migmatitic gneiss and quartzofeldspathic schist, aplitic microgranite and foliated

metagranite with ridges of ferruginous quartzite and thin impersistent units of locally brecciated impure marble (Bronner et al., 1992, Schofield et al., 2006). The southern part of the shear zone contains migmatitic gneiss, quartzofeldspathic schist and gneiss with abundant amphibolite and chert lenses interpreted as metavolcanic rocks (Bronner et al., 1992, Schofield et al., 2006).

Schofield et al. (2006) carried out a study on the timing and kinematics of Eburnean tectonics in the Archaean-Palaeoproterozoic contact zone of the Reguibat Shield. Investigating the Sfariat region in Mauritania, they found that it consisted of a Palaeoproterozoic continental margin succession that had been intruded by, and intercalated with, synorogenic granitoids. They found that the region had been transported southwest onto the Archaean foreland during sinistral oblique collision preserved as strongly partitioned D1 shortening followed by D2 strike-slip-dominated transpression within the Sfariat Belt. The timing of the sinistral transpression was constrained to between ~2117 and 2064 Ma.

Lehbib (2016) mapped the region as being dominated by orthogneiss basement (of possible Mesoarchaean age), with north-northwest trending belts of probable Palaeoproterozoic volcanics (bimodal rocks with boninites, basalts and rhyolites) dominant in the northwest of the region, with the southwest dominated by belts of amphibolite and the presence of a stratiform anorthosite-gabbro complex (Figure 1.10).

Combs (2012) mapped a portion of the Oum Abana Belt demonstrating that the region consists of northwest-southeast trending faults separating metamorphosed belts of sedimentary, volcanosedimentary and volcanic sequences interspersed with granite-gniess belts that are all intruded by syn- and post-tectonic granitoid and gabbroic intrusions. With no additional geochronological, data Combs (2012) interpreted the region to be Palaeoproterozoic, after the Schofield et al.'s (2006) interpretation. Lyche (2012) studied the Agarasras Labiad granitoid intrusion located within the Oum Abana Belt where gold and

copper anomalies had been detected. Based on a combination of field mapping and petrological analysis, Lyche (2012) concluded that it was a syntectonic granitoid ranging in composition from tonalite to granodiorite.

The Elmalhat intrusives (Figure 1.9) represent the mid crustal plutonic rocks of the volcanic arc sequence (Section 4.5.2). It is composed of granite intrusions, orthogneiss, gabbro intrusions as well as the Elmalhat Anorthosite Complex (referred to by Lehbib Nayem et al. (2016b) as the 'Bir Malhat stratiform complex'), the only anorthosite complex on earth to apparently contain both 'megacrystic' anorthosite and 'massif-type' components, as defined by Ashwal (1993). It represents syn- and post-tectonic mid-crustal plutonic rocks formed during and after terrane accretion and collision of the Sfariat-Bu Daira Terrane with the Leaareig Terrane. The unique nature of the anorthosite reflects a rapidly changing tectonic environment during the Eburnean Orogeny (Section 6.1).

Whole rock geochemical analyses of samples from the late stage Agarasras Labiad granitoid intrusion indicated that it formed in a volcanic arc setting leading to the interpretation that it formed as an syntectonic intrusion in an island arc system (Lyche, 2012). Whole rock geochemical analysis in the domain was undertaken by Lehbib (2016) on a sample of a late diorite intrusion in the northwest and a sample of leucogabbro from the 'massif-type' portion of the Elmalhat Anorthosite Complex. He found that both samples belonged to the calc-alkaline series, exhibiting geochemical signatures of having formed in a volcanic arc setting. Additionally, leucogabbro had a positive europium anomaly (Lehbib, 2016) caused by the preferential fractionation of europium into plagioclase.

1.4.3.2.3 Adam Esseder Domain

To the northeast of the Sfariat Bu-Daira Domain, the newly defined Adam Esseder Domain largely comprises Palaeoproterozoic granites with northwest-southeast trending belts of

supracrustal rocks, interpreted by Lahondère et al. (2003) to be the mid-crustal remnants of island arcs accreted during the Eburnean Orogeny (Figure 1.11). These Palaeoproterozoic arc complexes comprise mostly plutons belonging to ten intrusive suites, interrupted by northwest-southeast trending belts of deformed supracrustal rocks (Bradley et al., 2015b, Bradley et al., 2015a). The complex consists of components from five orogenic events including Eoeburnean (>2150 Ma), Mesoeburnean (~2150 to 2078 Ma), Tardieburnean (2073 to 2067 Ma), Neoeburnean (2040 to 1995 Ma) and post-Neoeburnean (undated) (Bradley et al., 2015b).

Eoeburnean rocks (>2150 Ma) of the Adam Esseder domain are mainly supracrustal (Bradley et al., 2015b). Three of these supracrustal belts are present in the domain. From west to east they are as follows. The Complexe d'Aguelt abd el Maï comprises a mixed supracrustal and intrusive assemblage that includes metamorphosed mafic rocks, quartzite, and marble (Bradley et al., 2015b). The Complexe de Tsalabia El Khadra comprises mafic, intermediate, and felsic metavolcanic rocks, marble, quartzite, and meta-arkose (Bradley et al., 2015b, Lahondère et al., 2003). The Complexe du Ghallamane is composed of aluminous and calcareous schist and gneiss, quartzite, meta-arkose, and amphibolite (Bradley et al., 2015b, Lahondère et al., 2003). At least part of the Complexe du Ghallamane appears to be Mesoeburnean in age with detrital zircon data from a metasandstone indicating a depositional age of 2135 Ma or younger (Bradley et al., 2015b).

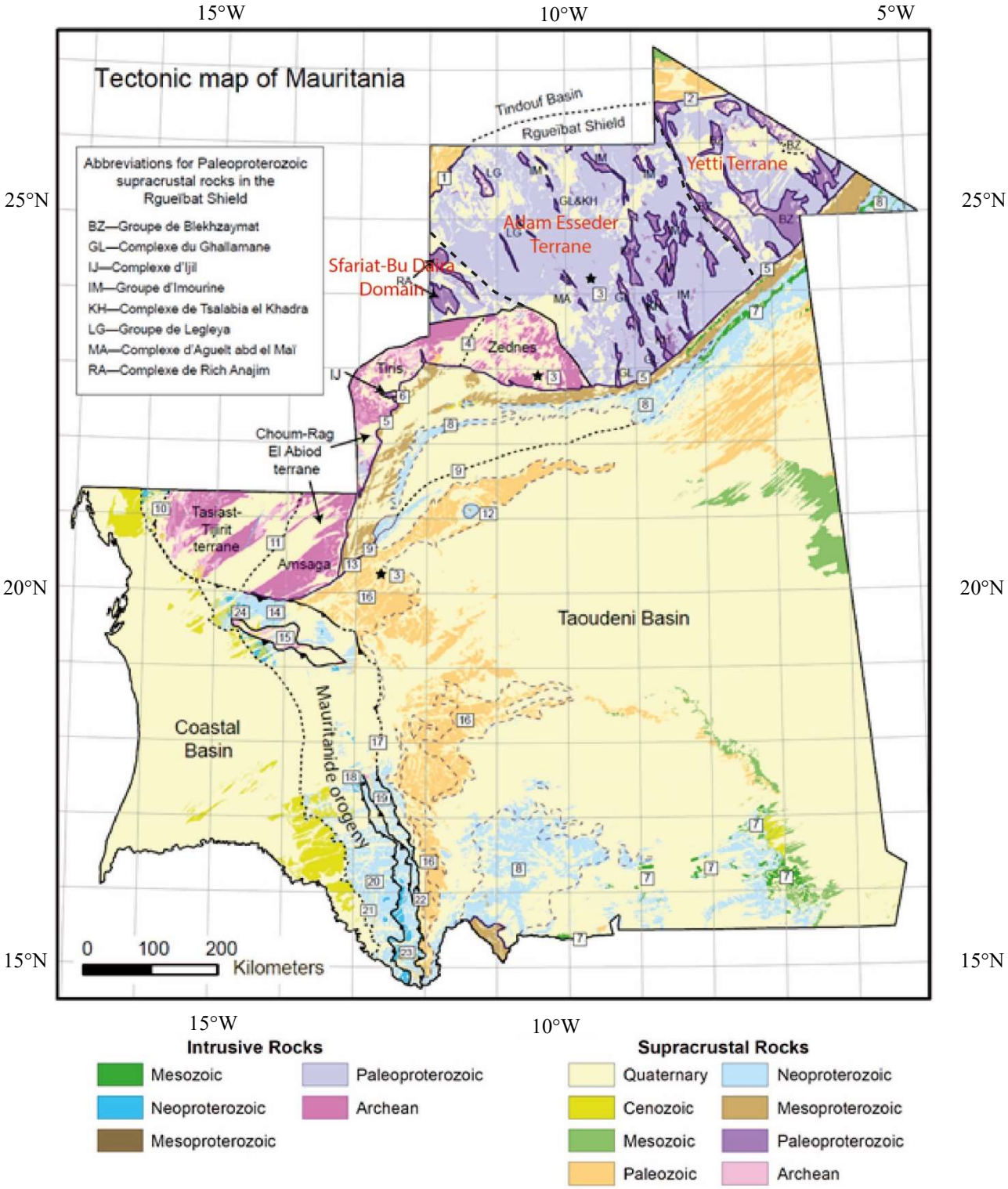

Figure 1-11 – Generalized tectonic map of Mauritania, modified from Bradley et al. (2015b) and references therein. Grid in Latitude and Longitude.

The first stage of the Mesoeburnean (~2150 to 2078 Ma) was characterized in the Adam Esseder Domain by the emplacement of an extensive calc-alkaline suite of mainly diorite,

tonalite, and granodiorite of the Complexe de Tin Bessais (Lahondère et al., 2003, Bradley et al., 2015b). These have yielded U-Pb zircon ages of 2146 ± 5 Ma, 2141 ± 4 Ma, and 2122 ± 5 Ma (Lahondère et al., 2003, Bradley et al., 2015b). Note that quartz diorite (2146 ± 5 Ma) and granodiorite-tonalite was also mapped in the Yetti Terrane (Bradley et al., 2015a). A later phase of the Mesoeburnean is observed as the Complexe de Tmeïmichatt Ghallamane, a vast intrusive complex of evolved, peraluminous granites emplaced west of the Complexe de Tin Bessais (Bradley et al., 2015b). These rocks have yielded U-Pb zircon ages of 2118 ± 14 Ma, 2103 ± 13 Ma, and 2078 ± 5 Ma (Bradley et al., 2015b, Lahondère et al., 2003).

The Tardieburnean consists of supracrustal and intrusive rocks falling in a narrow age range of 2073 to 2067 Ma (Bradley et al., 2015b, Lahondère et al., 2003). In the west, the Groupe de Legleya consists of felsic volcanic rocks, tuff, granophyre (2072 ± 6 Ma, U-Pb zircon), microgranite, microgabbro, and basalt (Bradley et al., 2015b, Lahondère et al., 2003). In the central part of the Adam Esseder Domain, the Groupe d'Imourène, comprises intermediate and felsic volcanics (2067 ± 9 Ma) and shallow intrusives plus sandstone and conglomerate (Bradley et al., 2015b, Lahondère et al., 2003).

The Neoeburnean is represented in the Adam Esseder Domain by a single late granitic complex spanning the entire width of the domain, referred to as the Complexe d'Adam Esseder (Bradley et al., 2015a). The complex largely comprises granite, granodiorite, and monzogranite (2059 ± 4 Ma) (Bradley et al., 2015a) with minor monzodiorite (commonly porphyritic) gabbro, hypersthene gabbro, leucogabbro, quartz diorite, ultramafic rocks and pegmatite (Bradley et al., 2015a). Age control on the granitoids is based on microprobe monazite ages and is only approximate, in the range 2060 to 1995 Ma (Bradley et al., 2015a, Bradley et al., 2015b, Lahondère et al., 2003).

Lehbib (2016) investigated outcrops of the Adam Esseder Terrane in Western Sahara, referring to it as the 'Tifariti-Bir Lehlu-Ain Ben Tili' Domain. He maps it as being largely dominated by late Palaeoproterozoic intrusions of 'calc-alkaline granites', and 'alkali feldspar granites and Rapakivi granites' (corresponding to 'granite and granodiorite' and 2059 ± 4 Ma 'monzogranite' units mapped in the Adam Esseder Complex) intruding a unit of bimodal volcanic rocks with boninites, basalts and rhyolites (corresponding to the 2067 ± 9 Ma igneous components of the Imourène Group consisting of microgranite, microgranodiorite; porphyritic andesitic to dacitic tuff; rhyolite, rhyolitic ignimbrite). Whole rock geochemistry results from a sample of an alkaline granophyric granite from the region showed that it is an A-type 'within plate' granite. LA-ICPMS U-Pb geochronology results reveal a crystallization age for the sample at 2064.9 ± 12.9 Ma.

1.4.3.2.4 Yetti Terrane

East of the Adam Esseder Terrane, the Yetti Terrane consists of a higher portion of supracrustal material (northwest-southeast trending belts of the Groupe de Blekhzaymat), though it is still dominated by the extensive granititc rocks from the Neoeburnean Yetti Suite (Bradley et al., 2015a, Bradley et al., 2015b, Lahondère et al., 2003). The Yetti Suite largely consists of granite (2002 ± 12 Ma, 1995 ± 20 Ma) with minor amounts of cordierite granite and biotite-muscovite ganite (Bradley et al., 2015a).

The Groupe de Blekhzaymat, consists mostly of sandstone and conglomerate and minor felsic to intermediate volcanic rocks. Ages of the group have been constrained by U-Pb zircon ages of 2069 ± 10 Ma from andesite (Lahondère et al., 2003) and 2104 ± 13 Ma from a rhyolitic tuff (Bradley et al., 2015b). Minimum depositional ages of 2141 and 2094 Ma were indicated by detrital zircons from two samples in the group (Bradley et al., 2015a, Bradley et al., 2015b).

Workers in Algeria define the small portion of the Yetti Domain that outcrops in Algeria as an independent tectonic terrane from the Eglab Terrane (Lefort et al., 2004). Lefort et al. (2004) and Peucat et al. (2005) refer to the Groupe de Blekhzaymat as a strongly folded volcanosedimentary series (the Yetti volcanic, volcano-sedimentary and sedimentary series) of the Lower Reguibat Complex (LRC). They describe the LRC as having been crosscut by granites of the Upper Reguibat Complex (URC), referring to the Yetti Suite granites.

In Algeria, the Yetti Terrane is described as a northwest-southeast trending basin composed primarily of the Yetti volcanic (rhyolite, rhyodacite), volcano-sedimentary (tuffs) and sedimentary (quartzite, pelite, arkose, conglomerate) series of the LRC (Kahoui and Mahdjoub, 2004, Peucat et al., 2005, Merabet et al., 2014, Allek and Hamoudi, 2008) intruded by granites (Markwitz et al., 2016b). Lefort et al. (2004) interprets the Yetti Terrane as having existed as an independent terrane (from the Eblab Terrane) before being involved in the collision with the Eglab Domain that resulted in a 'mega-shear-zone' known as 'the Junction Zone' (Allek and Hamoudi, 2008).

1.4.3.2.5 Eglab Terrane

The Eglab Terrane differs from the Yetti Terrane in terms of its structural, lithological, stratigraphic and metamorphic characteristics (Figure 1.12; Lefort et al., 2004, Peucat et al., 2005). It formed during two distinct orogenic phases (Barbey, 1975) reflected in the Lower Reguibat Complex (LRC) and the Upper Reguibat Complex (URC) (Peucat et al., 2005). The terrane is largely composed of undeformed and unmetamorphosed post-tectonic granites (Aftout granitoids) and late-stage felsic volcanics (Eglab Series), cross-cutting or overlying folded volcanosedimentary formations (Oued Souss Series), and older metamorphic rocks (Peucat et al., 2005). Rocks of the Aftout, Eglab and Oued Souss Series are all assigned to

the URC, though the vertically foliated plutono-metamorphic units (of the LRC) appear as windows or enclaves within the URC units.

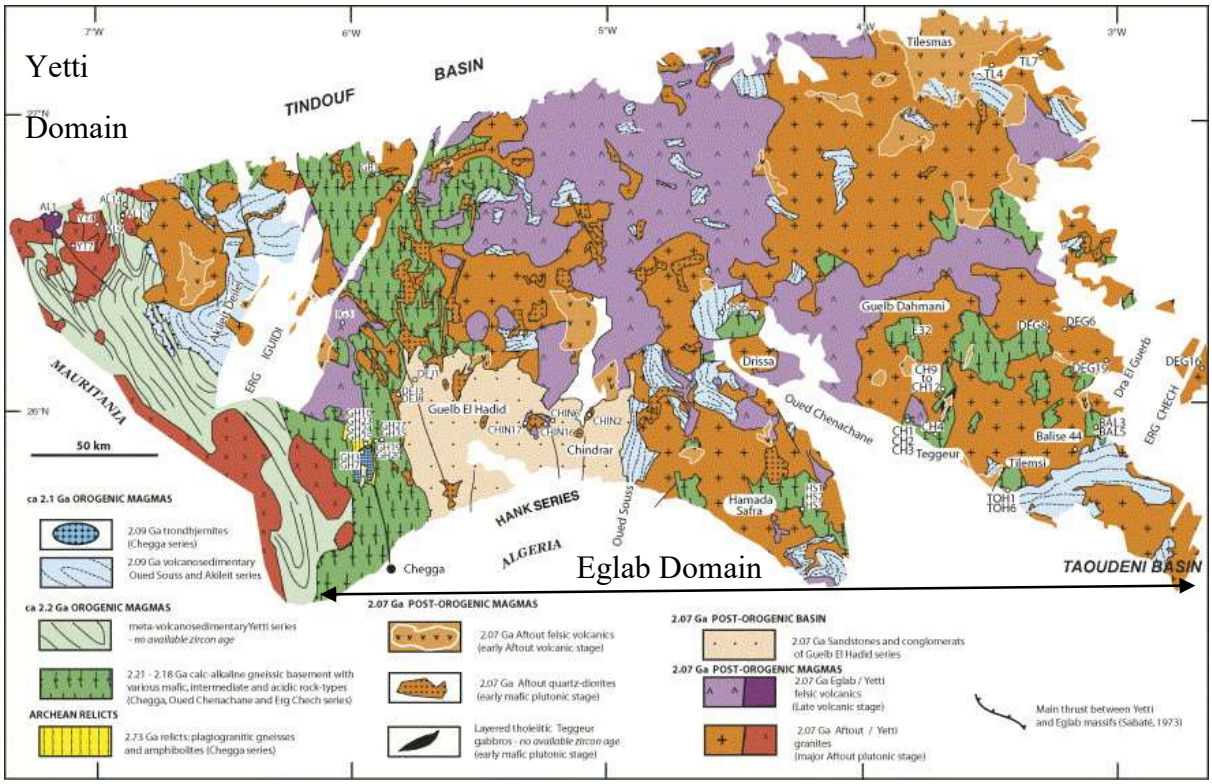

Figure 1-12 – Geological sketch map of the Eglab massif and of the eastern Yetti massif (from Peucat et al., 2005).

The Eglab massif is largely composed of post-tectonic granites (Aftout granitoids with amphibole granite, pink to red granite (most extensive), undifferentiated microgranite and Tilesmas granite) and late-stage felsic volcanics (Eglab series - rhyodacitic to rhyolitic lavas generally of ignimbritic textures), both of which are undeformed and unmetamorphised (Kahoui and Mahdjoub, 2004, Peucat et al., 2005). These rocks cross-cut or overlie the folded volcano-sedimentary formations (Oued Souss Series composed of calc-alkaline volcanic and volcano-sedimentary rocks) and older metamorphic rocks (granito-gneiss, migmatite, amphibolite) (Kahoui and Mahdjoub, 2004, Peucat et al., 2005). Kahoui and Mahdjoub (2004) recognised three major lithological complexes in the Eglab domain that are all intruded by late doleritic sills and dykes:

- The Eoeburnean Lower Reguibat Complex (LRC) is represented to the west by the granite-gneissic, migmatitic and Chegga amphibolites units and to the east by the Chenachane-Erg Chech units. Dated at around 2.21-2.18 Ga (Peucat et al., 2005), these metamorphosed plutonic rocks constituted various juvenile calc-alkaline orogenic suites related to active subduction processes within a margin of a mature island arc setting (Peucat et al., 2005). Forming part of the calc-alkaline magmatic suite (Teggeur Group), Peucat et al. (2005) noted the presence of coarse to medium-grained anorthosites, mainly composed of bytownite with intercumulus augite (altered to hornblende) and Fe–Ti oxides. These two samples of anorthosites returned TIMS evaporation zircon $^{207}Pb/^{206}Pb$ ages of 2200 ± 2 Ma and 2199 ± 3 Ma.
- The Upper Reguibat Complex (URC) is represented by N–S-striking volcano-sedimentary basins containing siliciclastic (sandstone, arkose, conglomerate), calc-alkaline volcanic and volcano-sedimentary rocks of the Oued Souss Series and the Akilet Deleil Series. Along the northwest-southeast-striking, sub-vertical 'Junction Zone', the Chegga (LRC) and the Oued Souss (URC) Series are affected by ductile deformation, characterized by a north-south striking vertical foliation associated with a very strong flattening. The syntectonic Chegga trondhjemitic pluton puts a date of 2.09 Ga on both the tectonic event and on the second stage of calcalkaline magmatism. It is believed that this event is related to oblique convergence between the Yetti and the Eglab newly accreted blocks (Kahoui et al., 2008).
- The continental Guelb El Hadid series, including arkose, sandstone, pink quartzite, arkosic sandstone, conglomerate with some interbedded felsic volcanic rocks, is contemporaneous with the post-collisional Aftout magmatic suite consisting of felsic (Aftout/Eglab) volcanic rocks, mafic intrusions and large Aftout plutons (Kahoui et al., 2008). The high-K to peralkaline post-orogenic (Aftout and Eglab) magmas,

dated at 2.07 Ga, are interpreted to be the result of asthenospheric upwelling (Peucat et al., 2005).

Peucat et al. (2005) defined a comprehensive five-stage model for the geodynamic evolution of the Eglab Terrane from 2.73-2.07 Ga (Figure 1.13). The first stage occurred in the Archean, corresponding to the occurrence of metamorphic relics of a 2.73 Ga oceanic crust in an ophiolite sequence. This is potentially thought to have obducted over an Archean island arc to form an arc/ophiolite composite crust (Figure 1.13a). This was followed by a phase of orogenic activity between 2.21–2.18 Ga involving the emplacement of a batholith interpreted as formed in a mature island arc setting with uplift and metamorphism and uplift of this batholith thought to be related to this ~2.2 Ga orogeny (Figure 1.13b). A younger orogenic phase (~2.1 Ga) is indicated by the presence of syn-tectonic trondhjemites and the Oued Souss volcano-sedimentary series forming in an active-margin setting (Figure 1.13c). The Yetti and Eglab tectonic units collided at ~2.09 Ga deforming the Oued Souss Series (Figure 1.13d). This collision would have resulted in uplift, leading to crust-mantle delamination and slab rollback. The heat produced from the resultant asthenospheric upwelling resulted in the partial melting of fertile sources in the Yetti and Eglab Terranes, producing large amounts of post-orogenic magmas (the Aftout and Eglab units in the Eglab Terrane and the Yetti granites and rhyolites of the Yetti Terrane) during a wide-spread rifting stage at ~2.07 Ga (Figure 1.13e).

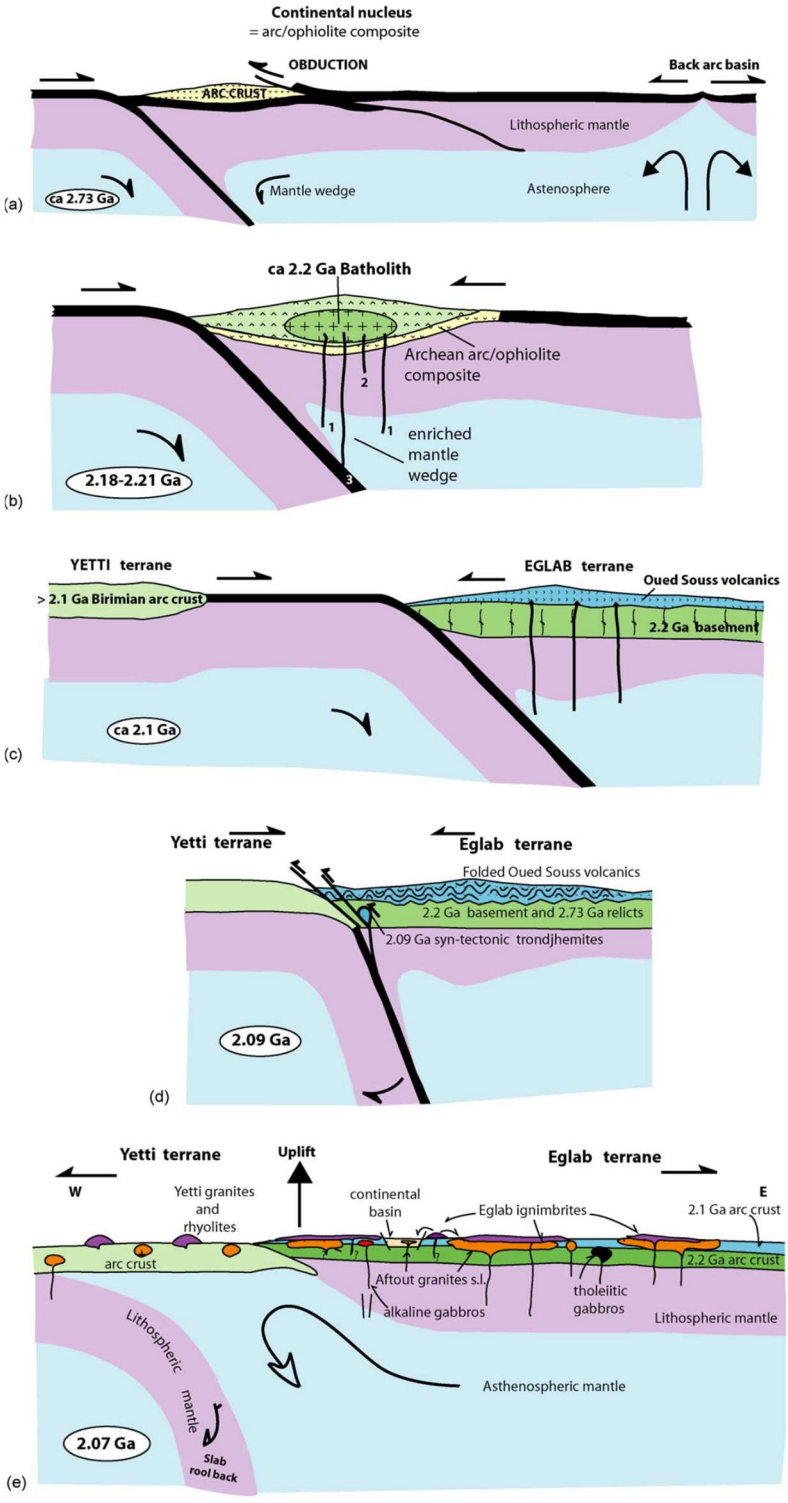

Figure 1-13 – Proposed geodynamic evolution of the Eglab massif from 2.73 to 2.07 Ga from Peucat et al. (2005). "(a) Obduction of the 2.73 Ga ophiolite on an arc–crust and formation of an Archean nucleus. (b) A first orogenic setting ca. 2.2 Ga: a mature-arc involving Archean nucleus and forming a batholith. 1: Calc-alkaline gabbros formed from an enriched mantle wedge, 2: quartz diorite formed from a less enriched mantle, 3: TTG magmas formed from melting of oceanic crust. Metamorphism, shearing, uplift and erosion are considered as related to this cycle. (c) A second orogenic cycle ca. 2.1 Ga: an active margin developed on the margin of the 2.2 Ga basement. The Oued Souss felsic volcanics were erupted on the 2.2 Ga basement. (d) Collage of Yetti and Eglab terranes at 2.09 Ga. Oued Souss series are folded and syn-tectonic trondhjemites are emplaced. (e) Delamination, uplift and mantle uprising. Emplacement of the 2.07 Ga Aftout and Yetti plutons, Eglab ignimbrites and Guelb el Adid continental basin in an extensional setting."

1.4.4 Overview of the Metallogeny of the West African Craton

Over the past forty years the West African Craton has been a major focus of mineral exploration and exploitation (Markwitz et al., 2016a, Markwitz et al., 2016b); however most of the exploration has been focused in the Man-Leo Shield. As a result, the vast majority of the literature has been written on this region, and because of its remoteness, very few studies have been conducted in the Reguibat Shield, with the exception of Mauritania where a number of gold and iron deposits have been found (Markwitz et al., 2016b). Markwitz et al. (2016b) compiled the West African Mineral Deposit Database (WAMDD) documenting available geological and resource data for 441 mineral deposits from across (and adjacent to) the West African Craton. This was used to analyse the spatial (Figure 1.14) and temporal distribution of economically significant West African mineral deposits (Markwitz et al., 2016a). Due to the lack of recent research having been carried out in the Liberated Territories of Western Sahara no data was presented for the large portion of the Reguibat Shield in Western Sahara (Figure 1.14). This gap was bridged by Lehbib Nayem et al. (2016a) investigating the geology and metallogeny of the Precambrian of Western Sahara.

Seven main commodities are found in West African (Table 1-1; Markwitz et al., 2016b, Markwitz et al., 2016a). These include:

- gold (as orogenic, intrusion related, skarn-hosted, porphyry-hosted, palaeoplacer and within Iron-Oxide-Copper-Gold (IOCG) style);
- iron ore (as BIF, skarn-hosted, oolitic ironstones, lateritic duricrust, and intrusion related);
- aluminium (as bauxite);
- diamonds (as kimberlite pipes or placers)
- base metals and REE (as intrusion-related, laterite, unconformity-related, orogenic and sedimentary)

- phosphate (as sedimentary deposits); and
- manganese (as sedimentary deposits).

Of these seven, gold is commercially the most important accounting for 198 of the 441 deposits recorded in the WAMDD, with the vast majority hosted in the Birimian Supergroup (Table 1-1; Markwitz et al., 2016b). Within the Birimian, gold mineralisation is orogenic or intrusion-related; occurring either as quartz vein-hosted gold in shear zones or associated with disseminated sulphide deposits (Béziat et al., 2008, Leube et al., 1990b). Orogenic gold mineralisation (accounting for 153 of the 198 gold deposits in the craton; Table 1-1) largely occurred in the late stages of the Eburnean Orogeny (2.1-2.02 Ga) (Eglinger et al., 2017). Intrusion related deposits are constrained to the early stages of the orogeny between 2.2 and 2.1 Ga, with palaeoplacer deposits forming in late- to post-Eburnean times at ca. 2.06 and 1.8 Ga (Markwitz et al., 2016b).

Within the Precambrian basement of Western Sahara, Lehbib Nayem et al. (2016b) noted evidence for three separate styles of orogenic gold deposits including:

a) carbonate or siliceous replacement of ultrabasic rocks (listwänites or birbirites respectivally), with Au-PGE and rare sulphides (as occurs near the Palaeoproterozoic Elmalhat Anorthosite Complex and in the Archaean Zug ultramafic complex);

b) gold-bearing quartz, commonly associated with scarce sulphides, tourmaline and/or fuchsite; and as is sometimes associated with sericitisation of host granitoids/siliceous sedimentary rocks;

c) IOCG-type replacement of carbonates along shear zones, as in some places close to Mijec and probably others in the Mauritanides domain.

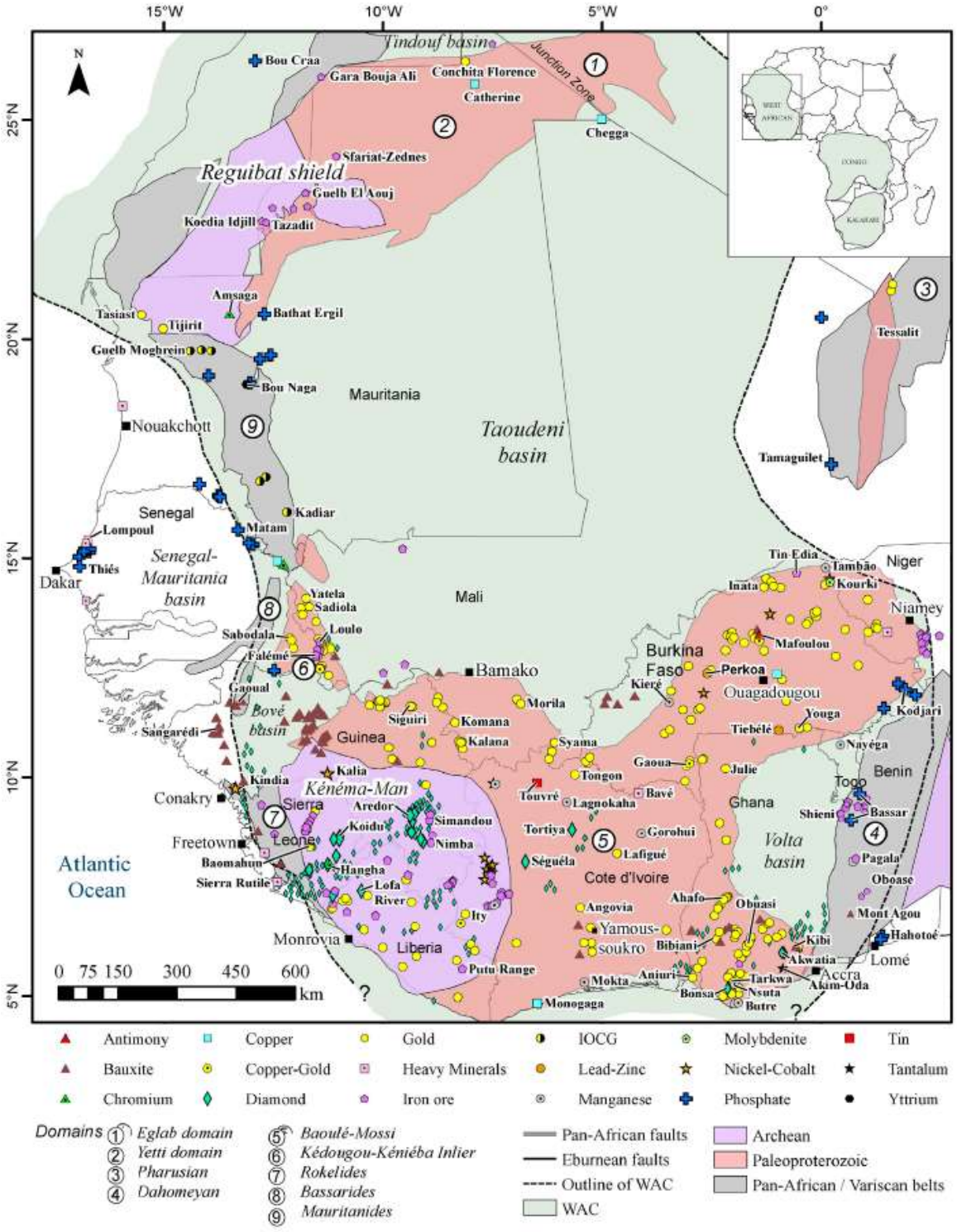

Figure 1-14 - Simplified map of the West African Craton highlighting the distribution of all known mineral deposits. (Markwitz et al., 2016b)

Table 1-1 – Frequency distribution of West African mineral deposits, highlighting major deposit types for various commodities in consideration of their spatial distribution (from Markwitz et al., 2016b based on the WAMDD)

	Deposit types	Frequency	Archean	Paleoproterozoic	Pan-African	Intracratonic and coastal basins
Gold/copper-gold	Orogenic	153	16	133	3	
	Alluvial/Paleo-placer	27	9	18		
	Intrusion-related (+ skarn)	5	1	4		
	Porphyry Au-Cu	10	1	6	3	
	IOCG	3			3	
		198				
Iron ore	BIF/Sedimentary	42	37	5		
	Skarn	7		7		
	Oolitic ironstone	7				7
	Laterite	18		1	10	7
	Intrusion-related	2		1	1	
		76				
Bauxite	Laterite	57		14	2	41
		57				
Diamond	Alluvial placer	11	9	2		
	Paleoplacer	3		3		
	Kimberlite	6	6			
		20				
Phosphate	Sedimentary	**32**				32
Manganese	Sedimentary	18		7	1	10
	BIF	12	3	7	2	
	Laterite	2		1	1	
		32				
Base metals + REE						
Lead–zinc		4		2	2	
Copper		5		3	1	1
Nickel–cobalt		12	10	2		
TantalumTinYttriumChromiumAntimony		7	1	4	2	
		28				
Heavy minerals		**10**		1		9
			93	**221**	**31**	**109**

1.4.5 Comparison of the Shields

The Reguibat and Man-Leo Shields are in the northern and southern Precambrian exposures of the West African Craton, sharing considerable characteristics and history, covered in its central part by the Neoproterozoic to Palaeozoic Taoudeni Basin (Rocci et al., 1991). They both contain Archaean domains in the West and Palaeoproterozoic domains to the east, though there is debate as to the extent of their connection.

1.4.5.1 Tectonic Setting

Due to the presence of the Kedougou-Kéniéba and Kayes inliers between them, some authors propose that the Archaean domains of the Reguibat and Man-Leo Shields represent separate blocks (eg. Abouchami et al., 1990, Grenholm, 2014). Rollinson (2016) completed a study on the Archaean evolution in the Kéména-Man Domain. In comparing the results with work by Schofield et al. (2012) on the Archaean domain of the Reguibat Shield, Rollinson (2016) noted major geological and geochronological similarities between the two Archaean domains, suggesting that the two regions were once more closely related and may have once been a single craton. Furthermore, Jessell et al. (2016) suggested the possible continuity of Archean basement of the Reguibat Shield beneath the northern Taoudeni basin based on intermediate-wavelength gravity and magnetic anomalies (Figure 1-15).

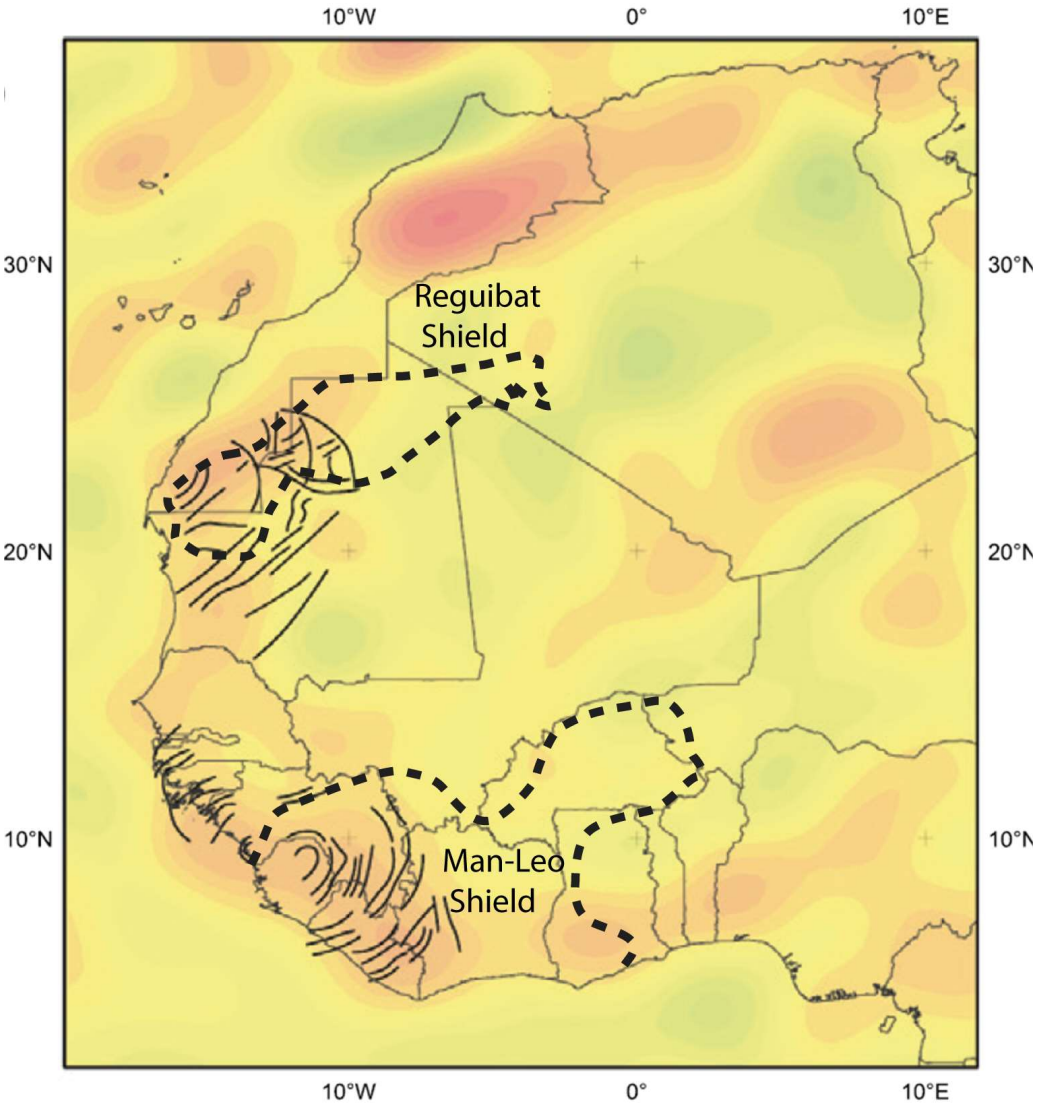

Figure 1-15 - Mid-crustal features assigned by Jessell et al. (2016) to Archaean age overlaid on >500 km gravity anomalies with approximate limits of the shields (from Jessell et al., 2016). Archaean domains of each shield coincidence with gravity highs along the continental margin.

On a broad scale, there are significant differences between the Palaeoproterozoic domains of the Reguibat and Man-Leo Shields. Large portions of the Reguibat Shield (Adam Esseder and Yetti Domains) are dominated by late stage granite intrusions (Figure 1.11), with what appears to be a smaller proportion of the supracrustal sedimentary, volcanosedimentary and volcanic belts. The Baoulé-Mossi Domain, on the other hand, is dominated by parallel volcanosedimentary belts which make up 50% of the terrane (Figure 1.4). However, similarities exist in terms of the tectonic setting and ages from the two shields. The Palaeoproterozoic of the Reguibat and Man Leo Shields both consist of juvenile accreted

rocks with volcanic arc signatures, with very little interaction with Archaean crust (Abouchami et al., 1990, Boher et al., 1992, Lahondère et al., 2003). Additionally, domains are interpreted as having formed during the Eburnean orogenic event (~2.2-2.0 Ga) in volcanic arc setting, forming through a combination of cycles of sedimentary basin development accompanied by subduction-related magmatism and collisional tectonics (Abouchami et al., 1990, Boher et al., 1992, Lahondère et al., 2003, Schofield et al., 2006). The lack of supracrustal belts within the Reguibat Shield could potentially be an artefact of preservation, with uplift and erosion removing the more surficial geology exposing mid-crustal rocks. Although the timing and tectonic settings are broadly similar for the two shields, there have been questions raised and debate over the evolution and crustal growth processes of the Palaeoproterozoic domains of the respective shields and how they are related (Grenholm, 2014, Peucat et al., 2005).

Peucat et al. (2005) conducted a study of the Eglab Terrane in Algeria looking at the petrology, geochemistry and geochronology of the terrane. They recognised that several features are unique to the Eglab Terrane, notably the lack of parallel volcanic, sedimentary and plutonic belts extensively described in the Baoulé-Mossi Domain. Peucat et al. (2005) interpret the Eglab Terrane as having formed from two major orogenic stages. The first orogenic event corresponds to a 2.21–2.18 Ga magmatic event forming a metamorphosed batholith composed of various juvenile calc-alkaline orogenic suites. The composition of these intrusions is compatible with a deep part of a mature island arc setting. The final stages of this orogenic event involved uplift and erosion, largely removing volcanic rocks from the arc, although it is still locally visible in out crop. The following orogenic stage occurred at 2.09 Ga, resulting in the intrusion of syn-tectonic trondhjemites and the formation of the Oued Souss volcano-sedimentary series. These units were deformed by the subsequent collision of the Yetti and Eglab tectonic units. The resulting crust-mantle delamination and

slab rollback resulted in partial melting of fertile sources in both terranes and the production of large volumes of post-orogenic magmas in a widespread rifting stage at 2.07 Ga. This lies in stark to with the accepted geodynamic evolution of the Birimian in the Baoulé Mossi Domain with accretion of short-lived oceanic island arcs.

Grenholm (2014) suggests a potential link between the Eglab and Yetti Terranes of the Reguibat Shield and the Baoulé Mossi Domain. The predominantly calc-alkaline magmatism and mafic-ultramafic volcanics within the 2.10-2.07 Ga Eburnean 'IIA' domain (Figure 1-16) are interpreted as having formed within an extensional environment with crustal thinning and mantle upwelling (Grenholm, 2014). The 2.10-2.07 Ga ('EIIA') magmatism is contemporaneous with widespread shearing along the Sassandra (Egal et al., 2002b) and Banifin shear zones (Liégeois et al., 1991) as well as with the peak collision between Archaean and Birimian crust (2.10-2.09 Ga). Eoeburnean rocks dated in Upper Guinea at 2212 ± 6 Ma (Lahondère et al., 2002) form the basement for the magmatism. Grenholm (2014) argues this is analogous to the Yetti and Eglab tectonic units described by Peucat et al. (2005) as consisting of ~2.2 Ga basement cut by extensive 2.10-2.07 Ga intrusive and extrusive magmatism resulting from an extensional regime. He suggests that geochemical differences in magmas produced between 2.10-2.07 Ga can be explained by drier and hotter magmatism in the Yetti-Eglab Domain compared with the EIIA, perhaps relating to a more proximal position to an active subduction zone of the latter -providing more water to the system. He suggests that these domains could be connected along a northeast-southwest trending belt potentially corresponding to what would be the oldest siliceous large igneous province in the world.

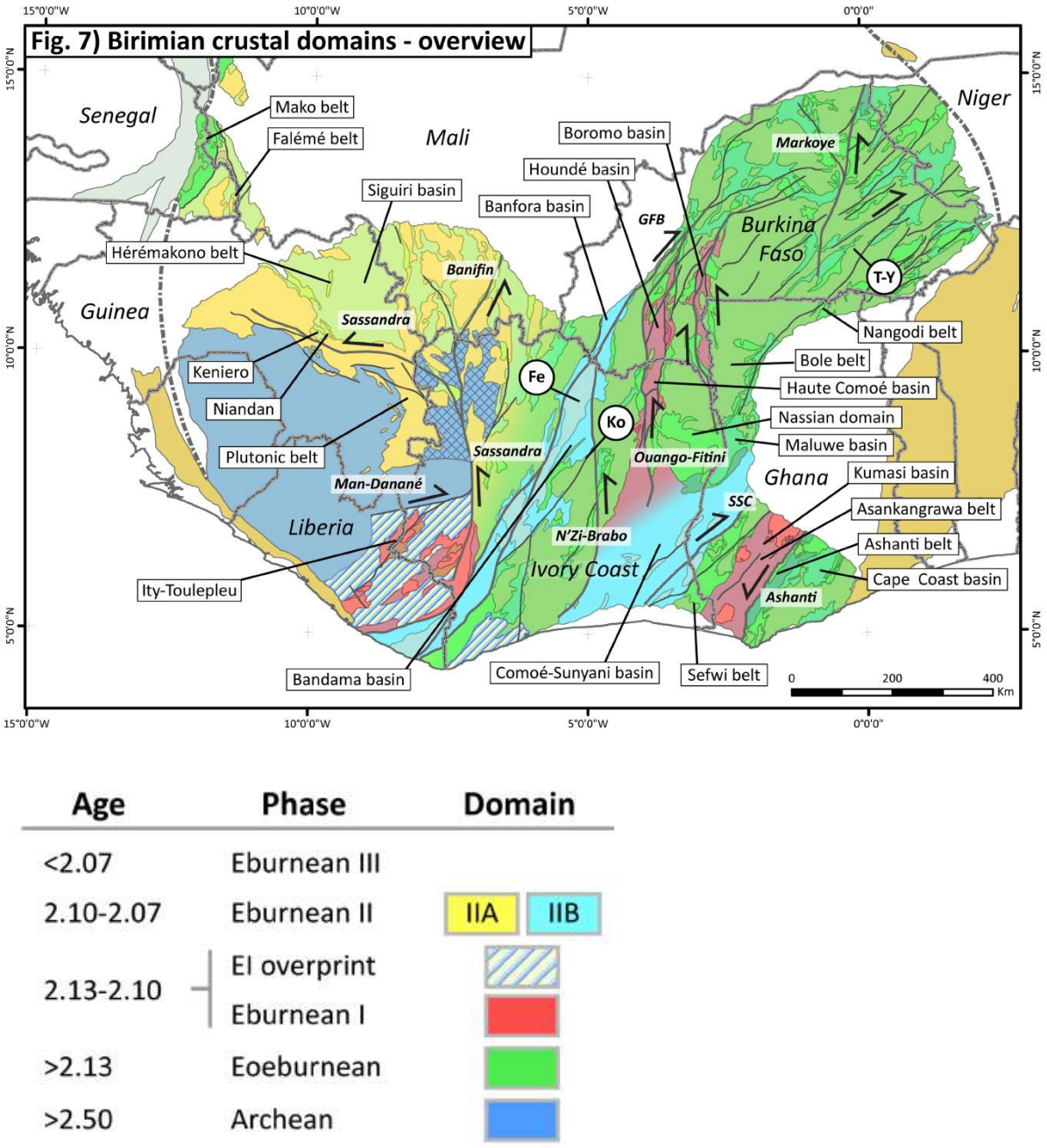

Figure 1-16 – Overview of the crustal domains associated with phases of the geodynamic model for the Man-Leo Shield (from Grenholm, 2014).

Schofield et al. (2006) carried out a study on the timing and kinematics of Eburnean tectonics in the Archaean-Palaeoproterozoic Contact Zone of the Reguibat Shield. Investigating the Sfariat region in Mauritania, they found that it consisted of a Palaeoproterozoic continental margin succession that had been intruded by, and intercalated with, synorogenic granitoids. They concluded that the region had been transported southwest onto an Archaean foreland

during sinistral oblique collision preserved as strongly partitioned D1 shortening followed by D2 strike-slip-dominated transpression within the Sfariat Belt. The timing of the sinistral transpression was constrained to between ~2117 and 2064 Ma (Schofield et al., 2006). Schofield et al. (2006) noted that the timing and kinematics of the Contact Zone in the Reguibat Shield were similar to those observed in the Eburnean of the Man-Leo Shield, which also underwent southwest sinistral transpression at the time (Feybesse and Milési, 1994). On this basis Schofield et al. (2006) proposed structural continuity between these two regions of the West African Craton at ~2100 Ma.

Jessell et al. (2016) created a structural map of West Africa based on gravity and magnetic data, attributing structures to their age group according to geophysical attributes (Figure 1-17). The Eburnean structures can be observed continuing under the Taudeni Basin from the Baoulé Mossi Domain in a north-south to northwest-southeast orientation. The trends of the Eburnean structures in the Reguibat Shield are also observed continuing under the Taoudeni Basin in a north-south to northwest-southeast trend.

Eglinger et al. (2017) presented a geochronological study on the Palaeoproterozoic contact with the Archaean Kéména-Man Domain in Guinea. They proposed a model involving the frontal collision of the Archaean and Palaeoproterozoic domains at 2.10-2.09 Ga in a convergent tectonic setting followed by a period of magmatism at 2.10-2.08 Ga (~2.09-2.07 Ga in the eastern part of the contact) resulting from asthenospheric upwelling following delamination. Magmas proximal to the Archaean craton showed evidence for an interaction with the Archaean crust and Archaean-derived sediments. Schofield et al. (2006) interpreted the passive nature of the Archaean-Palaeoproterozoic contact of the Reguibat Shield based on the geology of the Contact Zone and the lack of subduction-related Palaeoproterozoic intrusions in the Archaean domain.

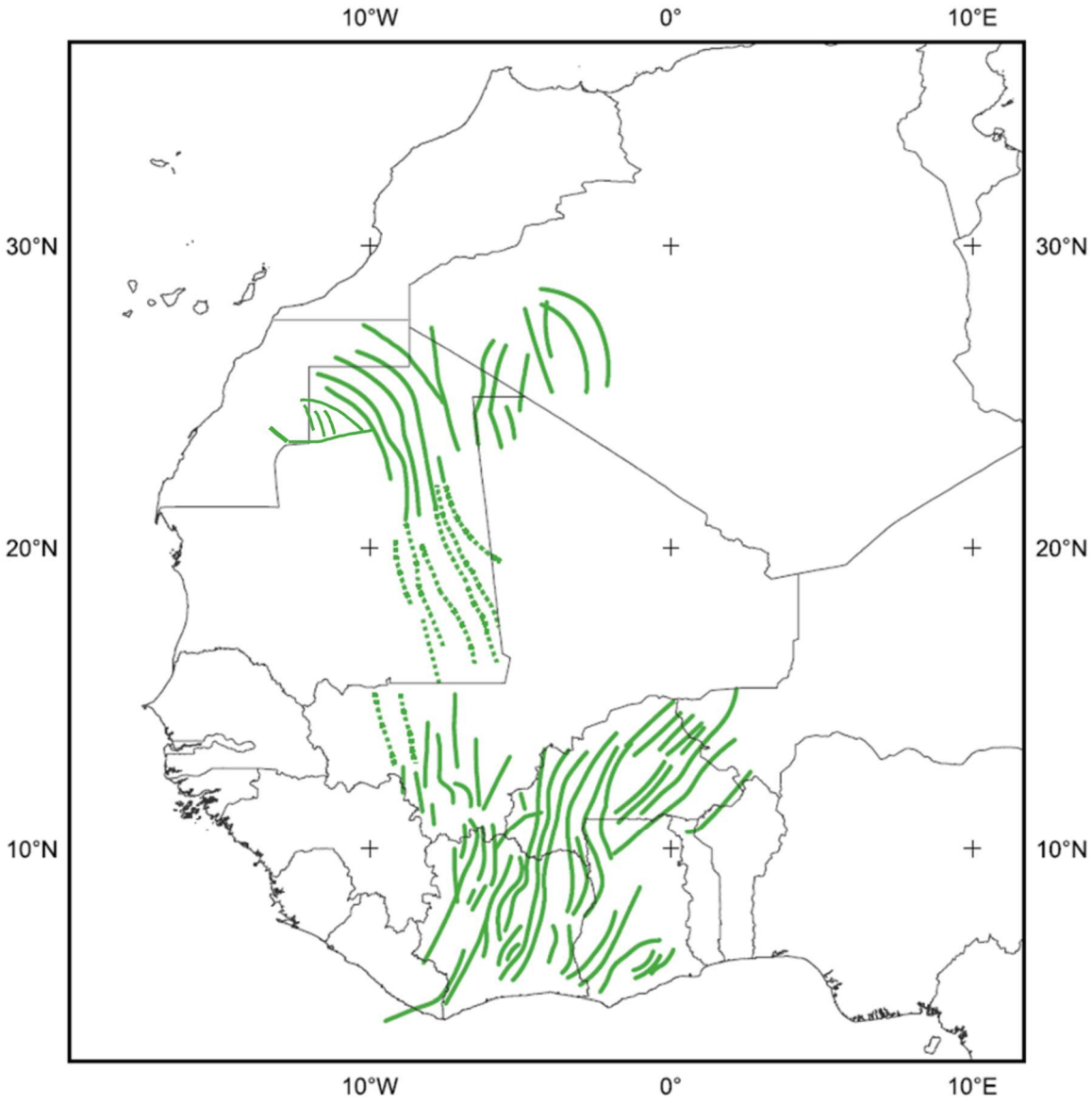

Figure 1-17 –Palaeoproterozoic structural map for West Africa based interpreted from of medium-wavelength gravity and magnetic data with less-certain structures dashed (modified from Jessell et al. (2016)).

1.4.5.2 Comparison of the Volcanosedimentary Belts

As mentioned previously, there are fewer sedimentary, volcanosedimentary and volcanic belts present within the Palaeoroterozoic of the Reguibat Shield than the Baoulé Mossi Domain. The Sfariat-Bu Daira Domain is an exception, containing the largest supracrustal belt (Oum Abana Belt) preserved in the Reguibat Shield. Therefore, the Oum Abana (Section 4.2) and Taghsoumat-Aghsoumal Belts (Section 3.3) provide an excellent type-region to compare the belts of the Reguibat Shield with those in the Man-Leo Shield (Section 6.4).

The architecture of the belt is almost identical to those in the Baoulé Mossi Domain, consisting of alternating, fault-bounded metamorphosed belts of volcanic, volcanosedimentary and sedimentary sequences interleaved with granite-gneiss units, all of which are cut by late stage intrusions ranging in composition from I-type granitoids and gabbro. However, two major differences exist: the absence of Basin granites in the Oum Abana Belt; and the presence of thick beds of marble not observed anywhere in the Baoulé Mossi Domain.

Although I-type belt granites are abundant within the Oum Abana Belt, S-type basin granitoids are absent. Widespread throughout the Baoulé Mossi Domain, these S-type Basin granitoids are observed within sedimentary belts representing the melting of crustal material during a magmatic event a 2125 ± 2 to 2088 ± 1 Ma. By contrast, I-type Belt granitoid intrusions are observed within volcanic and volcanosedimentary belts, forming from the partial melting of basaltic rocks during a magmatic event 2179 ± 2 to 2136 ± 10 Ma.

The presence of thick (>1km) beds of marble present in the Oum Abana Belt are also unique to the Reguibat Shield. They represent a generally higher portion of chemical sediments (marble, BIF and chert) within the metasedimentary belts of the Oum Abana Belt compared to the more clastic dominated sedimentary belts of the Baoulé Mossi Domain. The presence of the thick marble is thought to represent a higher carbonate production in the shallow marine environments offshore of the Palaeoproterozoic arcs of the Reguibat Sheild compared to that of the Man-Leo Shield, potentially representing a more equatorial setting (Chapter 6.4.6).

2.0 U-Pb Zircon Geochronology of the Leaareig and Sfariat-Bu Daira Terranes

2.1 Introduction

Nineteen samples were selected from across the field area for the geochronological study. The samples were selected based on the likelihood of yielding zircon grains (petrology and geochemistry), location, field relations and the importance of dating the formation. Figure 2-1 details the location of the samples, illustrating their geographical and geological relation to existing geochronological data in the region provided by Lahondère et al. (2003), Schofield et al. (2006) and Lehbib (2016).

For all but one of the samples (J213), zircon grains were separated using standard heavy liquid and frantz magnetic separation techniques. Zircon grains were mounted in epoxy resin mounts and polished to expose a section. Zircon grains were imaged by cathodoluminescence (CL) using the Scanning Electron Microscope (SEM) facilities at the University of Oxford. With sample J213, a precipitate formed during the heavy liquid separation stage making it impossible to retrieve any zircon grains. For this sample, two polished thin sections were made with zircon grains imaged and analysed in-situ.

Samples were analysed for zircon U-Pb through laser ablation inductively-coupled plasma mass spectrometry (LA-ICP-MS) at the John de Laeter Centre, at Curtin University, Western Australia. Zircon grains were ablated using a Resonetics RESOlution M-50A-LR sampling system (incorporating a Compex 102 excimer laser) coupled to an Agilent 7700 ICP-MS. Following 15-20 seconds of background analysis, samples were ablated for 30 seconds at a 7 Hz repetition rate using a 33 μm beam spot, and laser energy of 1.5 J/cm^2. The sample cell was flushed by ultrahigh purity He (0.68 L min^{-1}) and N2 (2.8 mL min^{-1}). Isotopic intensities were

measured using an Agilent 7700s quadrupole ICP-MS, with high purity Ar as the plasma gas. In each scan of the mass spectrum, the dwell time for most elements was 0.01 s, with the exception of ^{88}Sr (0.02 s), ^{139}La (0.04 s), ^{141}Pr (0.04 s), ^{204}Pb, ^{206}Pb, ^{207}Pb, ^{208}Pb (0.03 s), ^{232}Th (0.0125 s), and ^{238}U (0.0125 s). Standards OCG, Temora 2 and M257 were used. Standard blocks were typically run after 20 unknown analyses. During the time-resolved analysis, contamination resulting from inclusions and compositional zoning was monitored, and only the relevant part of the signal was integrated.

The zircon U-Pb analyses in many of the samples were affected by lead loss and/or the presence of common lead, leading to discordant data. Most of the samples were only affected by relatively recent lead loss, and in this case, the age of the sample was calculated from the intersect of a regression line through the data on a Tera-Wasserburg plot, or by taking a weighted average of the $^{207}Pb/^{206}Pb$ ages for all the analyses. For data comprising significant common lead, and where a statistically valid number of concordant analyses were present, a subset of concordant data points was used to calculate an age of the sample. In samples with insufficient concordant data, common lead was evaluated and corrected for using the numerical solution described by Andersen (2002). In cases where the Andersen (2002) common lead correction is applied, a subset of the most concordant points are used to calculate the age either from the intersect of a regression line through the data on a Tera-Wasserburg plot, or by taking a weighted average of the $^{207}Pb/^{206}Pb$ ages.

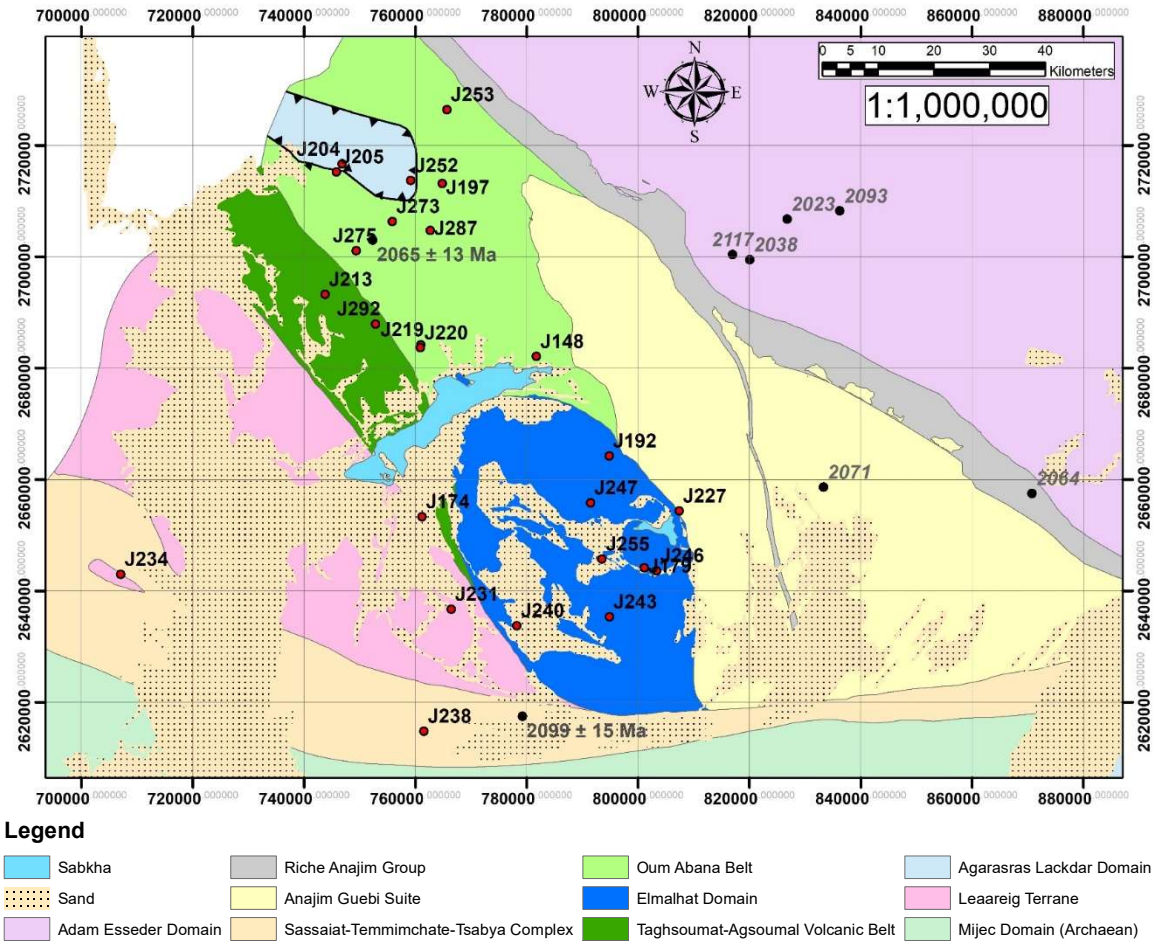

Figure 2-1 – Sample locations from this study are shown in red with black text. Existing age data from Lahondère et al. (2003), Schofield et al. (2006) and Lehbib (2016) are presented as black dots with grey text.

This chapter presents a summary of the geochronology results from across the region. This provides the basis for the differentiation of the region into two terranes. The context and relevance of each sample are presented in the following chapters. Brief descriptions for each of the geochronology samples are provided in Appendix B1, with details of the age interpretation and techniques used provided in Appendix B2. Note that the uncertainty given for the age data is 2 sigma.

2.2 **Results**

A concordant subset of data from samples J204, J238, J287 and J273 were used to calculate concordant ages for the samples (Figure 2-2). The age of 2176 ± 32 Ma (MSWD = 1.3) for sample **J204** (paragneiss) represents a detrital zircon age. The age of 2100 ± 19 Ma (MSWD

= 1.05) for sample **J238** (migmatitic gneiss) represents the age of anataxis for the sample. Ages of 2122 ± 18 Ma (MSWD = 1.2) for sample **J287** (rhyolite), and 2093 ± 17 Ma (MSWD = 1.13) for sample **J273** (granodiorite gneiss) represent ages of crystallisation.

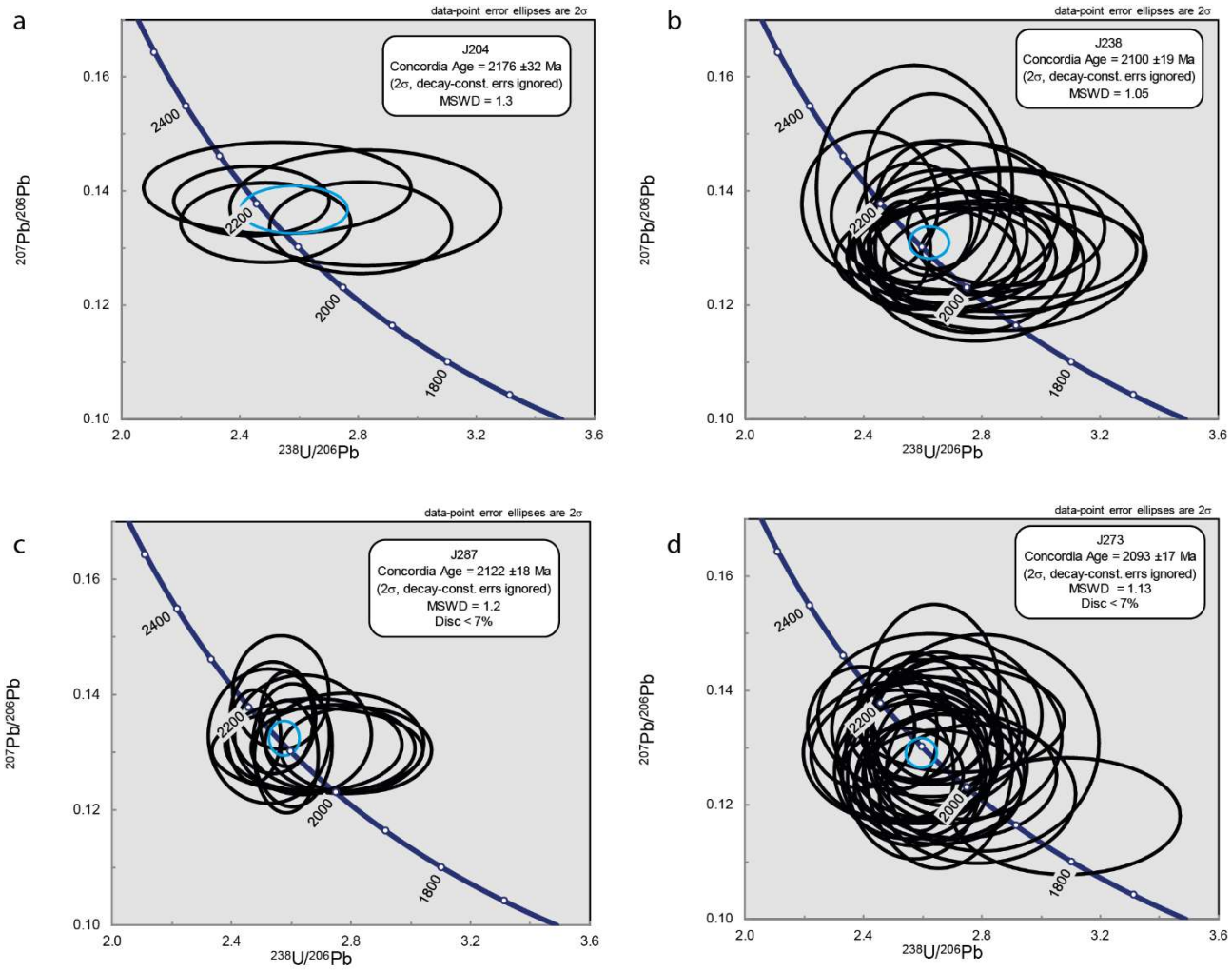

Figure 2-2 – Tera Wasserburg plots showing the concordant age of samples: a) J204; b) J238; c) J287; d) J273.

Samples J231, J179, J246, 219 and J213 experienced recent lead loss, so ages were calculated by the upper intercept of a regression line through the data (Figure 2-3). Ages of 2216 ± 60 Ma (MSWD = 2.0) for sample **J231** (granite orthogneiss)**,** 2140 ± 19 Ma (MSWD = 1.01) for sample **J179** (gneiss), 2103 ± 24 Ma (MSWD = 1.16) for sample **219** (quartz monzonite gneiss), and 2149 ± 21 Ma (MSWD = 0.53) for sample **J213** (foliated granite) represent ages of crystallisation. Two ages were calculated for sample **J246** (granite porphyry). Cores of blocky zircon grains give the age of inherited zircons as 2282 ± 54 Ma (MSWD = 1.02), while

more acicular grains (and rims of blocky grains) give the crystallisation age for the granite as 2123 ± 69 Ma (MSWD = 0.57).

Weighted average $^{207}Pb/^{206}Pb$ ages were used to calculate the age of samples J240, J197 and J227 (Figure 2-4). Ages of 2127 ± 20 Ma (MSWD = 0.98) for sample **J240** (muscovite-rich leucogranite) and 2097 ± 21 Ma (MSWD = 0.98) for sample **J197** (tonalite) represent the age of crystallisation. The age of 2099 ± 45 Ma (MSWD = 1.4) for sample **J227** (biotite-muscovite paragneiss) represents the age of detrital zircons in the metasedimentary rock.

Samples J234, J292, J247, J205, J253, and J220 contained significant amounts of common lead such that the ages could not be interpreted. Therefore, the Andersen (2002) common lead correction was applied, and a subset of the most concordant data was used to calculate a meaningful age for each sample. Ages for samples J234, J292, J247, J205, and J253 were calculated from the upper intercept of the regression line (Figure 2-5), while the age of sample J220 was calculated by taking the weighted average $^{207}Pb/^{206}Pb$ ages of the corrected data (Figure 2-6). Calculated ages of 2174 ± 69 Ma (MSWD = 0.78) for sample **J234** (granite orthogneiss), 2159 ± 140 Ma (MSWD = 1.03) for sample **J292** (porphyry), 2123 ± 50 Ma (MSWD = 1.08) for sample **J247** (monzogranite), 2109 ± 43 Ma (MSWD = 0.94) for sample **J253** (granite), and 2130 ± 25 Ma (MSWD = 0.96) for sample **J220** (orthogneiss) represent crystallisation ages for the samples. The age of 2110 ± 25 Ma (MSWD = 1.3) calculated for sample **J205** (biotite-muscovite paragneiss) represents the age of detrital zircons.

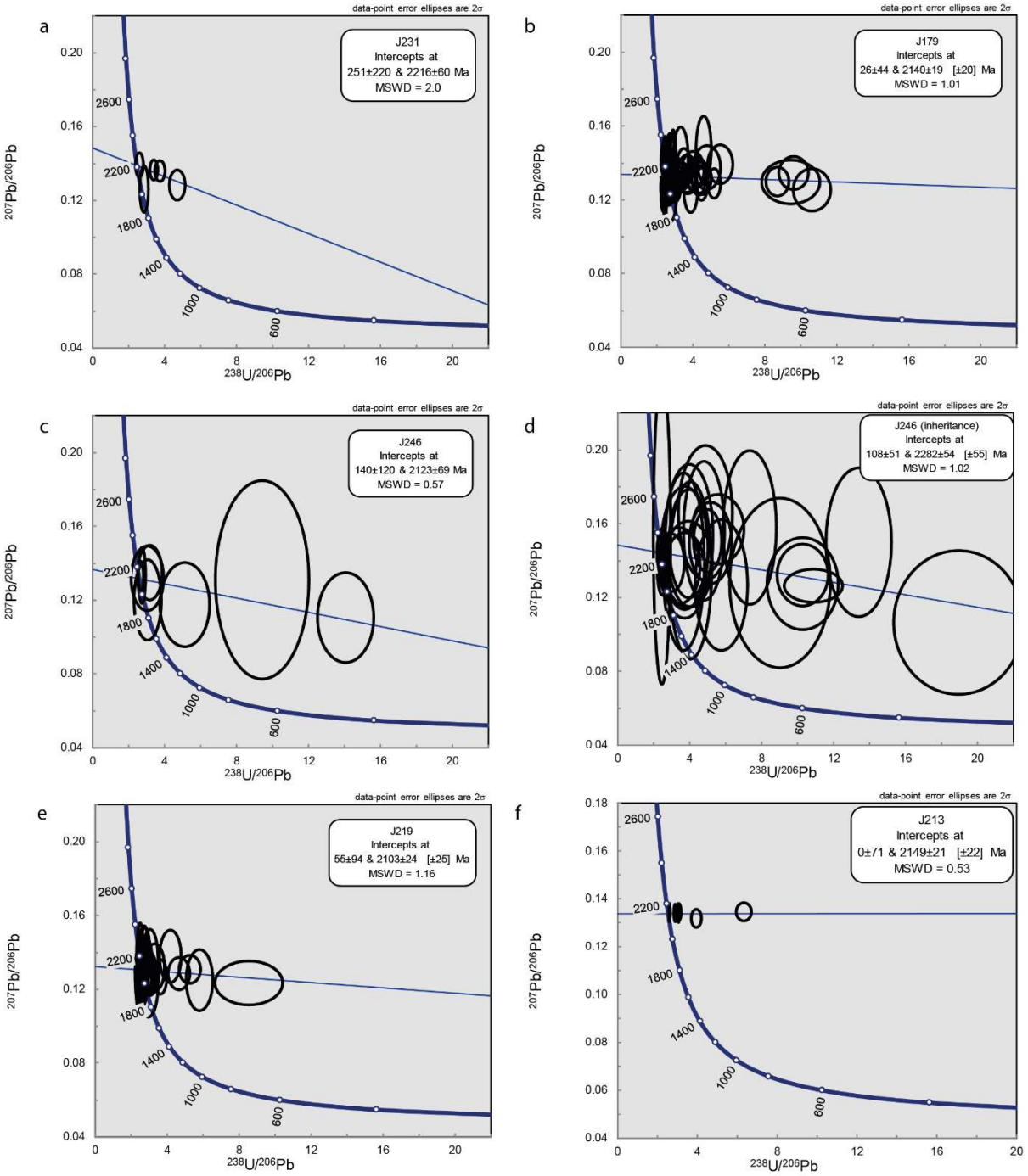

Figure 2-3 – Tera Wasserburg plots with ages calculated using a regression line: a) J231; b) J179; c) J246 (crystallisation age; skinny zircons and rims of blocky zircons); d) J246 (inheritance; cores of blocky zircons); e) J219; f) J213

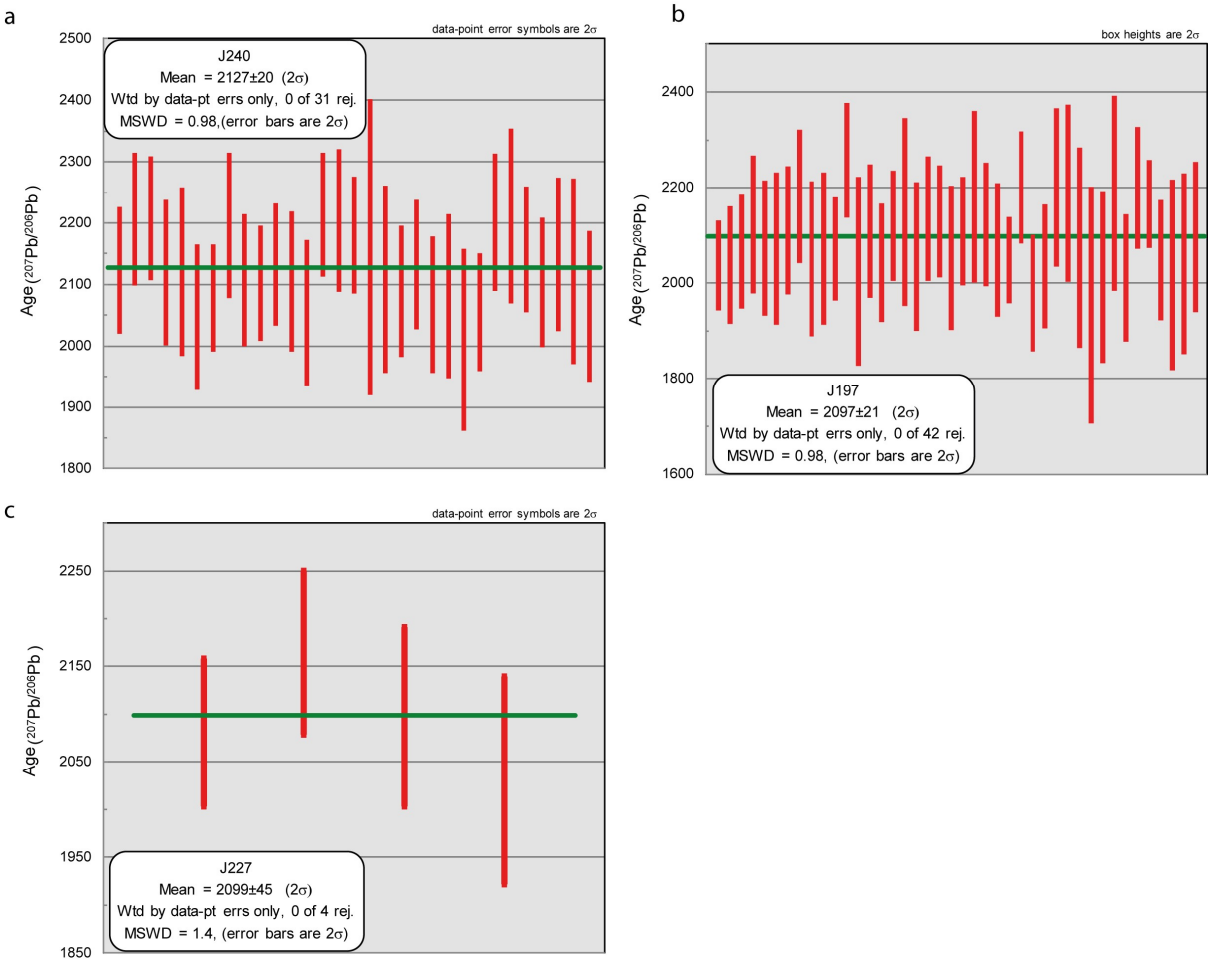

Figure 2-4 – $^{207}Pb/^{206}Pb$ weighted average age calculations for samples a) J240; b) J197; and c) J227

Sample **J275** (granodiorite) was affected strongly by lead loss and the presence of common lead. A cluster of three points from the only non-metamict zircon was used to interpret an age for the sample. To remove the effect of common lead, a regression line anchored to a common lead to a ratio ($^{207}Pb/^{206}Pb$) of 0.83 was plotted through the data (Figure 2-7). This revealed an age of 513 ± 17 Ma (MSWD = 0.84), interpreted as a lead loss event.

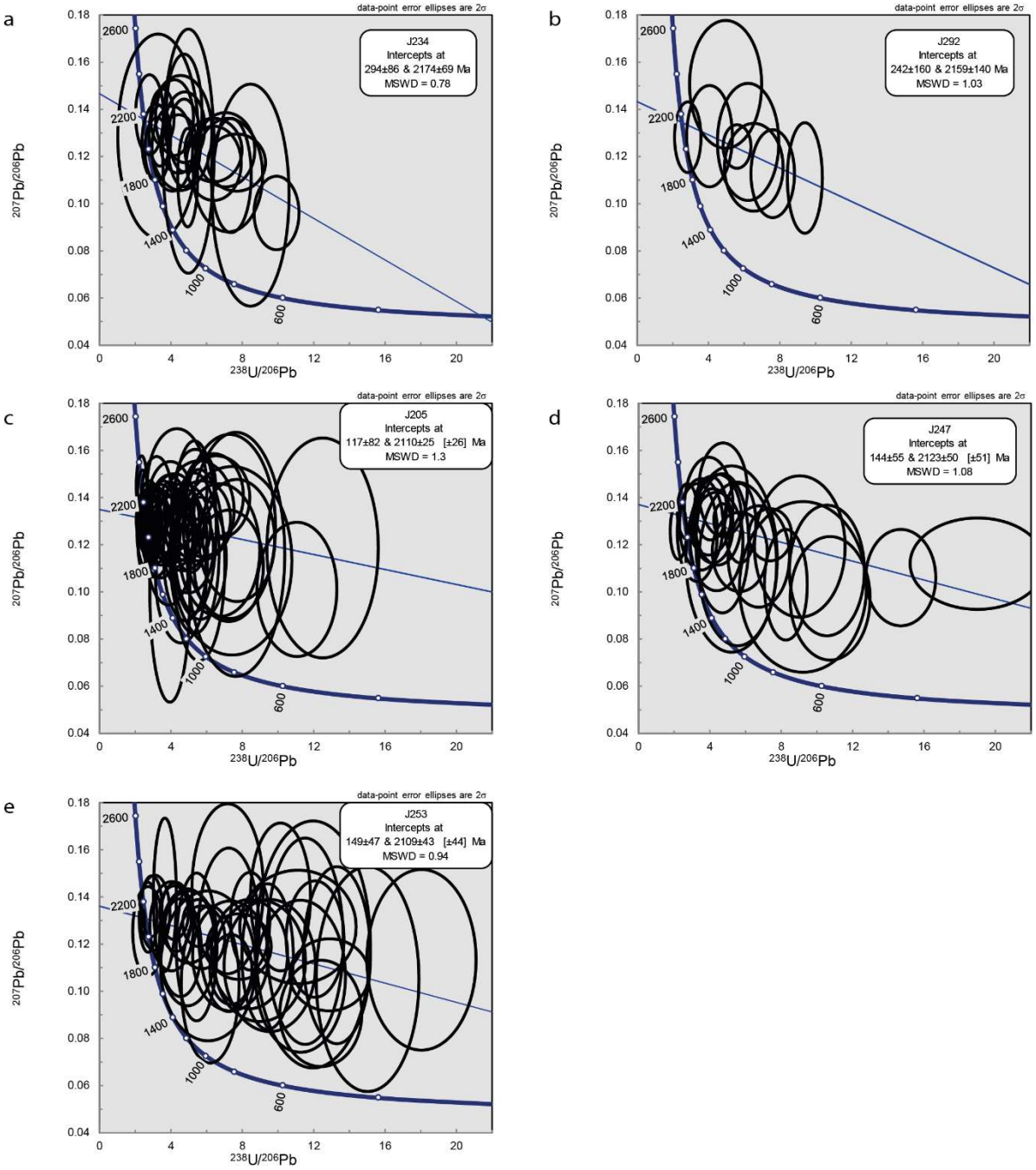

Figure 2-5 – Tera Wasserburg plots and age regression age calculation of Andersen (2002) common lead corrected data. a) J234 (excluding data with a discordance > 70%, and metamict points with U^{238}>1300 ppm); b) J292 (excluding data with a discordance > 65%); c) J247(excluding data with a discordance > 65%); d) J205; and e) J253

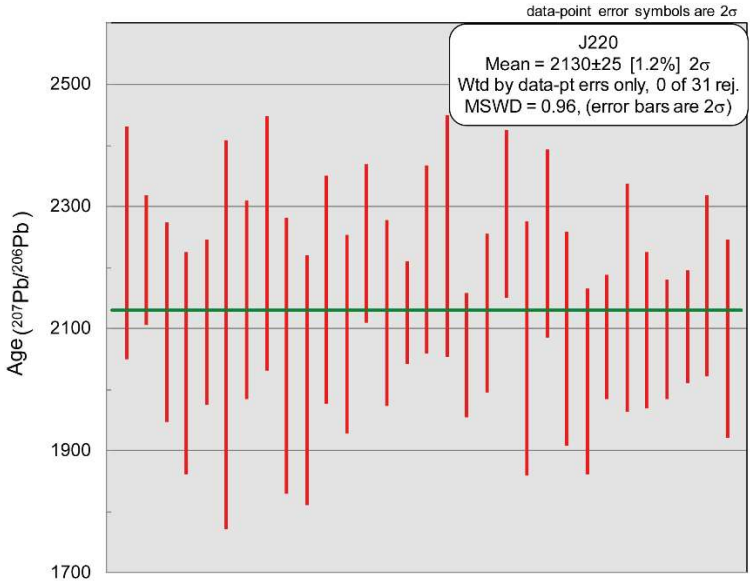

Figure 2-6 – $^{207}Pb/^{206}Pb$ weighted average age calculations for sample J220, following the Andersen (2002) common lead correction (excluding metamict points with ^{238}U>400 ppm).

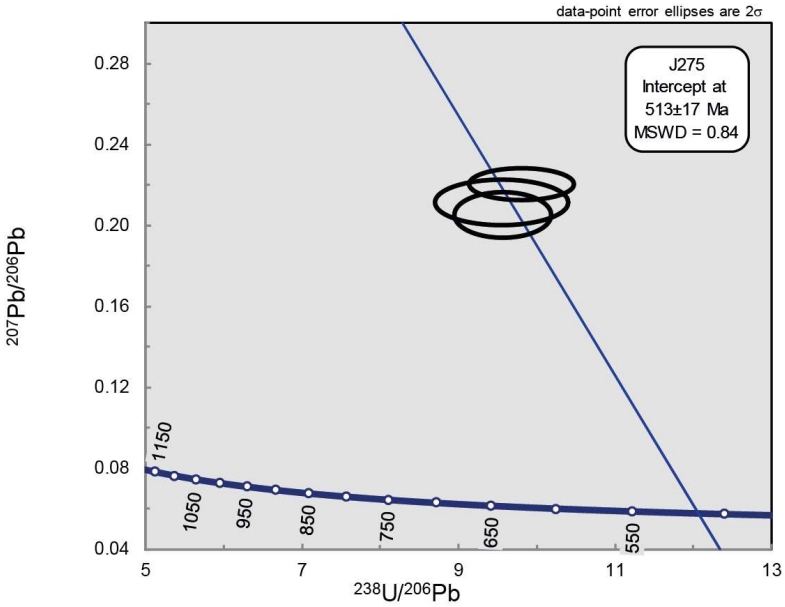

Figure 2-7 - J275 (lead loss event; anchored to a common lead ratio ($^{207}Pb/^{206}Pb$) of 0.83 and projected back to concordia).

A summary of the geochronological results is presented in Table 2-1 along with lithology, domain, tectonic setting, and the method for the age calculation. The tectonic setting is interpreted from the whole rock chemistry of each sample using multidimensional tectonic discrimination diagrams for felsic and intermediate rocks as defined by Verma et al. (2012) and Verma and Verma (2013) respectively (see Section 3.5 for a more detailed explanation).

Table 2-1 – Summary of geochronology samples analysed in this study. Unless stated otherwise in the lithology column, ages represent the age of crystallisation. Tectonic setting is interpreted from the whole rock chemistry of each sample using multidimensional tectonic discrimination diagrams for felsic and intermediate rocks as defined by Verma et al. (2012) and Verma and Verma (2013) respectively (see Section 3.5 for a more detailed explanation).

Sample ID	Lithology	Domain (Terrane: Leaareig/ Sfariat-Bu Daira)	Tectonic setting from Geochemistry	Method of interpretation	Age
J231	Granite Orthogneiss	Leaareig Domain	Collisional	Regression (4 points)	2216 ± 60 Ma
J234	Granite Orthogneiss	Leaareig Domain	Continental arc	Regression after Andersen (2002) common lead correction.	2174 ± 69 Ma
J204	Paragneiss (Detrital)	Agarasras Lakhadar	Metasedimentary	Concordant age (subset of 5 points)	2176 ± 32 Ma
J292	Porphyry	Taghsoumat-Aghsoumal	Continental arc	Regression after Andersen (2002) common lead correction.	2159 ± 140 Ma
J213	Granite, weakly foliated	Taghsoumat-Aghsoumal	Continental arc	Regression	2149 ± 21 Ma
J238	Migmatitic Gneiss (Age of anataxis)	Sassaiat - Temmimchate-Tsabya Complex	Collisional	Concordant age (subset of 21 points)	2100 ± 19 Ma
J179	Gneiss	Elmalhat Domain	Continental arc	Regression	2140 ± 19 Ma
J240	Weakly foliated muscovite-rich leucogranite	Elmalhat Domain	Collisional	$^{207}Pb/^{206}Pb$ Weighted Average	2127 ± 20 Ma
J247	Monzogranite intrusion	Elmalhat Domain	Continental arc	Regression after Andersen (2002) common lead correction.	2123 ± 50 Ma

J246a	Porphyry (crystallisation age)	Elmalhat Domain	Continental arc	Regression (acicular grains and rims of blocky zircon grains)	2123 ± 69 Ma
J246b	Porphyry (inheritance)	Elmalhat Domain	Inherited	Regression (cores of blocky zircon grains)	2282 ± 54 Ma
J220	Orthogneiss	Oum Abana Belt	Continental arc	$^{207}Pb/^{206}Pb$ Weighted Average after Andersen (2002) common lead correction.	2130 ± 25 Ma
J287	Rhyolite	Oum Abana Belt	Collisional	Concordant age (subset of 13 points)	2122 ± 18 Ma
J205	Biotite-Muscovite-Paragneiss (Detrital)	Oum Abana Belt	Metasedimentary	Regression after Andersen (2002) common lead correction.	2110 ± 25 Ma
J253	Granite	Oum Abana Belt	Continental arc	Regression after Andersen (2002) common lead correction.	2109 ± 43 Ma
J219	Quartz Monzodiorite gneiss	Oum Abana Belt	Continental arc	Regression	2103 ± 24 Ma
J197	Foliated Tonalite intrusion	Oum Abana Belt	Continental arc	$^{207}Pb/^{206}Pb$ Weighted Average	2097 ± 21 Ma
J273	Granodiorite Orthogneiss	Oum Abana Belt	Continental arc	Concordant age (subset of 23 points)	2093 ± 17 Ma
J275	Granodiorite (Lead loss event)	Oum Abana Belt	Collisional	Projecting back to concordia from a common lead ratio of 0.83 (subset of 3 points)	513±17 Ma*
J227	Biotite-Muscovite-Paragneiss (Detrital)	Anajim Guebli Suite	Metasedimentary	$^{207}Pb/^{206}Pb$ Weighted Average (4 points from 2 zircon grains)	2099 ± 45 Ma

2.3 **Definition of Terranes**

The results from the geochronological work provide the basis for the differentiation of the study area into two separate Palaeoproterozoic terranes. The Leaareig Terrane in the west contains plutonic and sub-volcanic rocks ranging in age from ca. 2220 and 2150 Ma, while plutonic and volcanic rocks of the Sfariat-Bu Daira Terrane are younger at ca. 2140 to 2090 Ma (Table 2-1, Figure 2-8Table 2-1). Work presented in Chapters 3 and 4 demonstrate that in addition to the age difference, the terranes are distinct in terms of lithologies present, stratigraphy, mineral chemistry and tectonic setting. Each terrane is further broken down into domains (Figure 2-8) based on lithological associations (Chapters 3 and 4).

The suture between the Leaareig and Archaean terranes is defined by the southern margin of the Sasassaiat-Temmimichate-Tsabaya Complex, while the suture between the Sfariat-Bu Daira and the Palaeoproterozoic Adam Esseder Terrane to the north is defined by the northern margin of the Riche Anajim Group (Figure 2-8). The suture between the Sfariat-Bu Daira and Leaareig Terranes forms two parts, defined by a suture between the Elmalhat Doman/Oum Abana belt and the Taghsoumat-Aghsoumal Belt/Leaareig Domain, and a sole thrust that emplaces the Agarasras Lakhadar Domain (including an ophiolite sequence) on top of the Oum Abana belt (Section 3.3.5). A detailed geological description of the newly defined Leaareig and Sfariat-Bu Daira Terranes will be provided in Chapters 3 and 4.

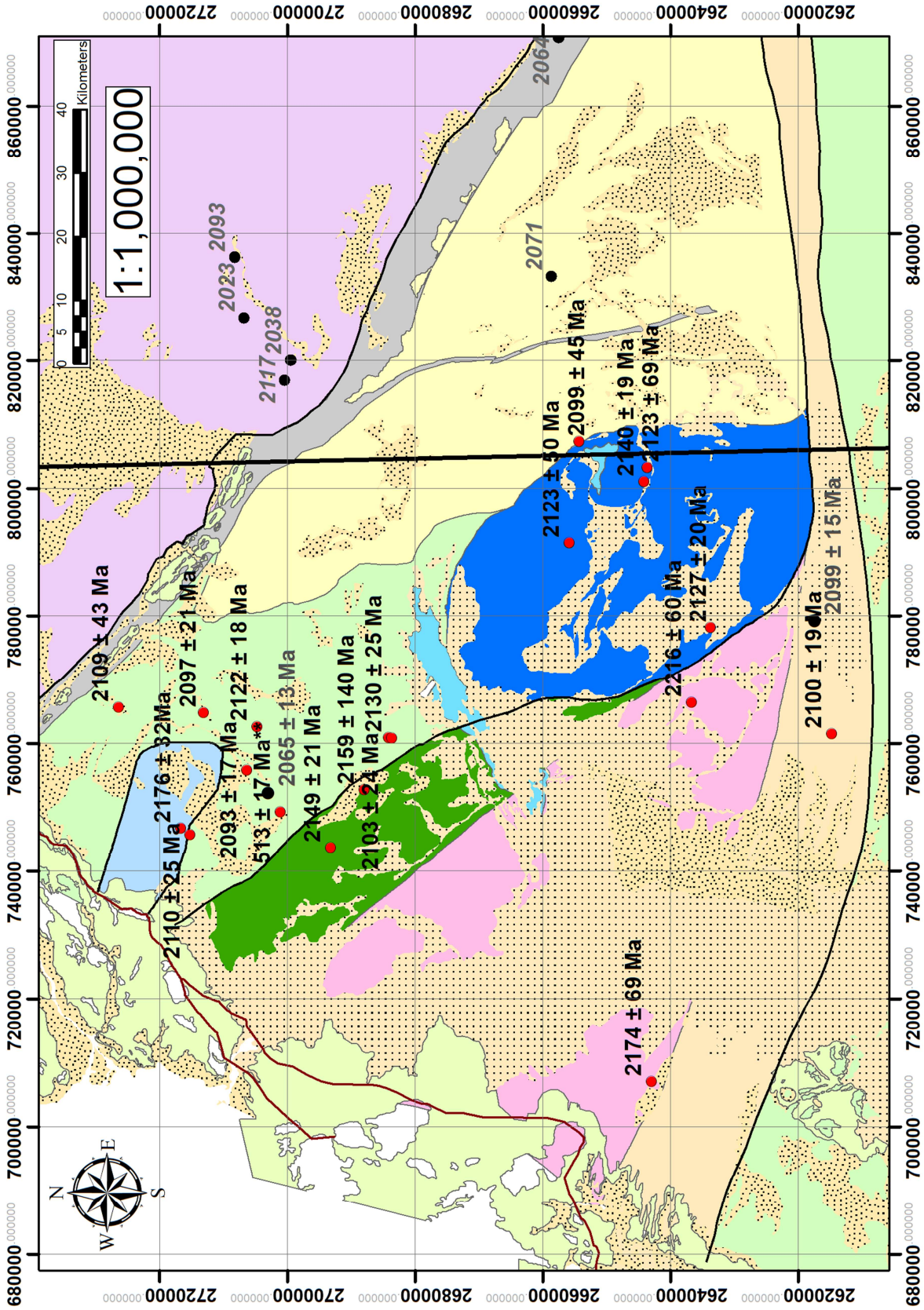

Figure 2-8 a – Simplified geological map of the study area with domains defined according to lithological associations and new geochronology data. Geochronology results from this study are shown in as red dots and black text; with existing age data from Lahondère et al. (2003), Schofield et al. (2006) and Lehbib (2016) is shown as black dots with grey text.

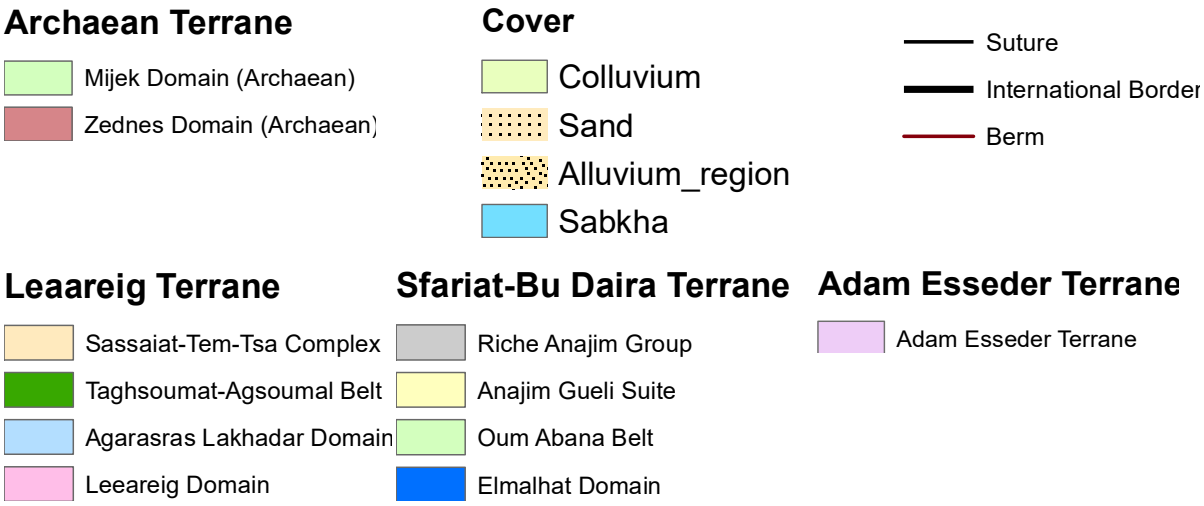

Figure 2-8 b – Legend

3.0 Geology of the Leaareig Terrane

Perhaps largely due to a high degree of sand cover, the newly defined Leaareig Terrane has never been described in the literature, though recent work as part of this project has differentiated it as a separate terrane (Figure 3-1). The Leaareig Terrane consists of four domains; the Leaareig Domain, the Taghsoumat-Aghsoumal Belt, the Agarasras Lakhadar complex and the Sassaiate-Temmimichate–Tsabaya Complex.

The Leaareig Domain is major component of this terrane, forming a wedge of orthogneiss and metasedimentary rocks. A major northwest-southeast trending shear zone defines the north-eastern boundary of the Leaareig Domain, making contact with the Elmalhat domain (of the Sfariat-Bu Daira Terrane) in the south and the Taghsoumat-Aghsoumal Belt to the north (Figure 3-2).

The Taghsoumat-Aghsoumal Belt consists of northwest-southeast trending fault-bounded, alternating volcanic, volcanosedimentary, metasedimentary and orthogneiss belts intruded by late stage syn- to post tectonic granites.

Not directly connected with the rest of the Leaareig Terrane within the study area, the Agarasras Lakhadar Domain is bounded by a sole thrust emplacing the package over the Oum Abana Belt (of the Sfariat-Bu Daira Terrane). The Agarasras Lakhadar Domain consists of an ophiolite sequence (ultramafics-gabbro-pillow basalts), with lithologies to the west including units of basalt and chert, paragneiss and marble, and undifferentiated mafic/ultramafic rocks.

The Sassaiate-Temmimichate–Tsabaya Complex forms a belt at the south of the terrane consisting of intermediate to mafic orthogneiss, paragneiss, migmatite, amphibolite as well as thick beds of marble (up to 1km) and iron rock. The complex extends into Mauritania, where

it consists of quartzofeldspathic and mafic gneisses intruded by granodiorite (Schofield et al., 2006).

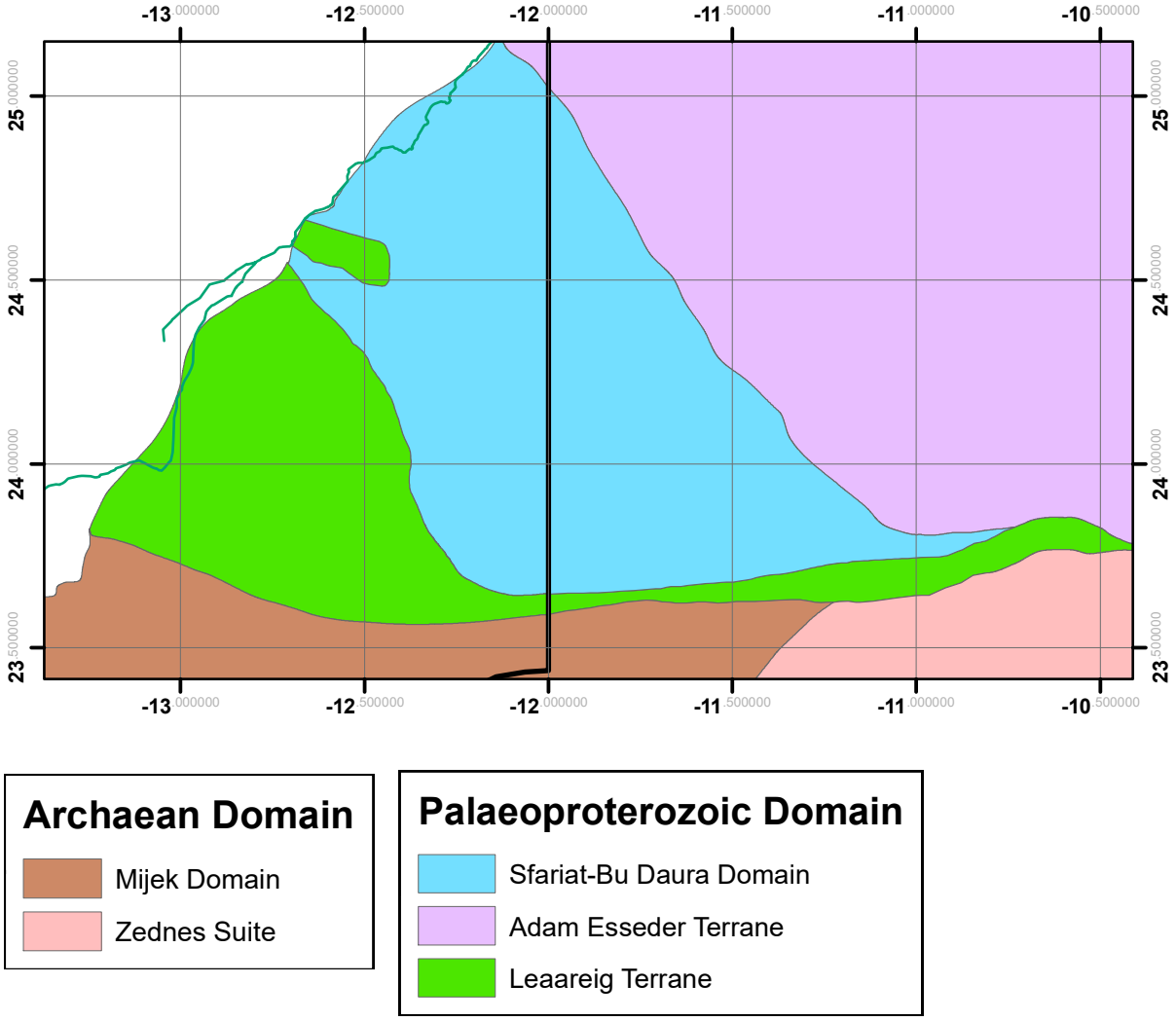

Figure 3-1 – Position of the Leaareig Terrane relative to the Archaean Terrane and other Palaeoproterozoic Terrane

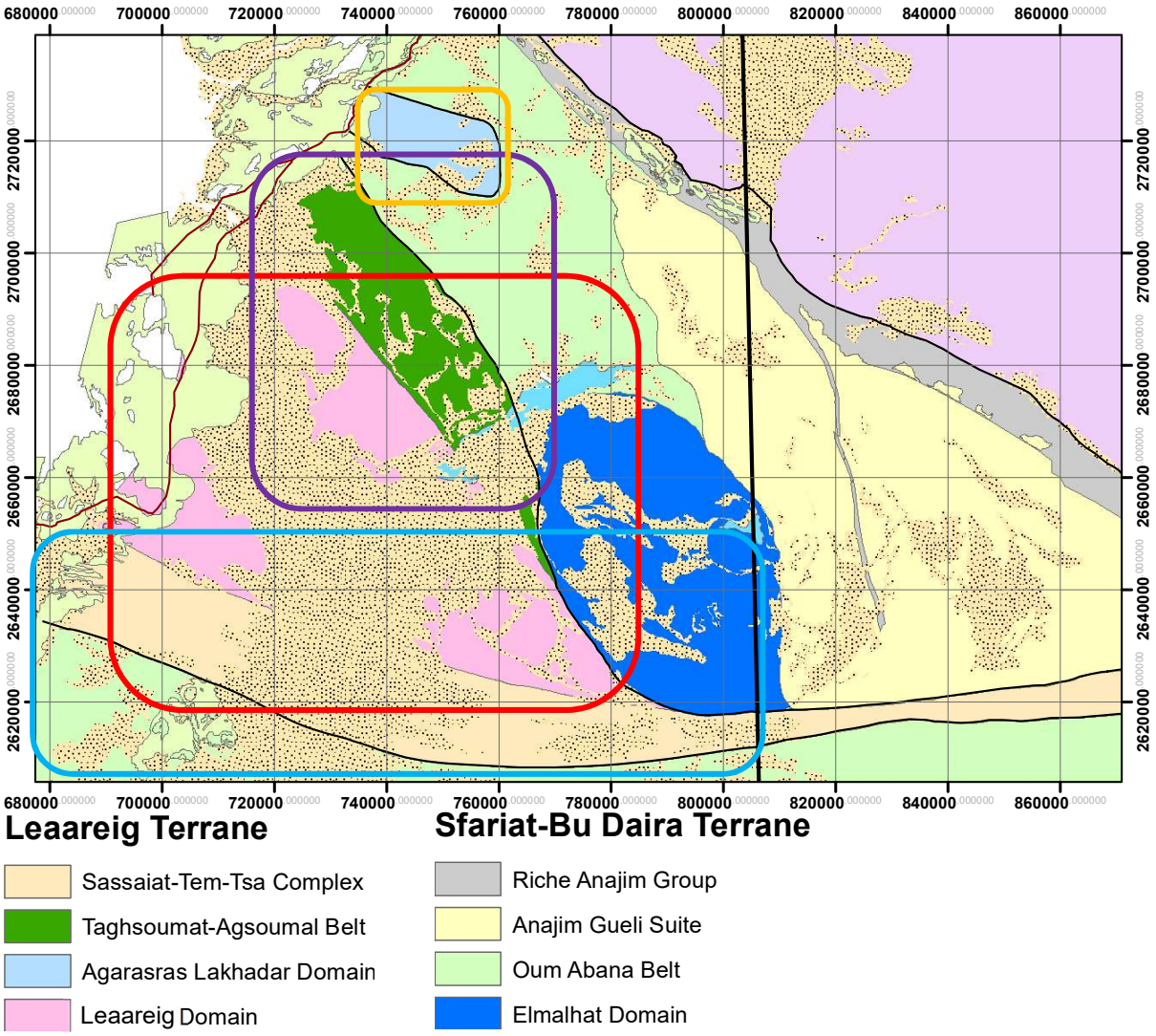

Figure 3-2 – Domain map of the Leaareig and Sfariat-Bu Daira Terranes (UTM Zone 28N). For detailed geology of the Leaareig Domain (red) - see Figure 3-3. For detailed geology of the Taghsoumat-Agsoumal Belt (purple) – see Figure 3-8. For detailed geology of the Agarasras Lakhadar Domain (orange) – see Figure 3-12. For detailed geology of the Sassaiate-Temmimichate-Tsabaya Complex (blue) – see Figure 3-41.

3.1 **Leaareig Domain**

3.1.1 Introduction

The Leaareig Domain contains the oldest rocks in the study area, with two samples of granodioritic orthogneiss dated at 2216 ± 60 Ma and 2174 ± 69 Ma (Table 2.1; Section 2.1.1). The domain largely comprises orthogneiss with minor belts of paragneiss and marble and outcrops of gabbro along its eastern contact.

3.1.2 Geology and Structure (Mapping/field relations)

Due to the inhospitable terrain, extensive sand cover, and remoteness from field camps or civilisation, the Leaareig Domain is relatively understudied compared to other domains. Only one traverse was completed across the entire unit, largely hindered by sand cover (Figure 3-3). Therefore, much of the mapping in the region involved extensive use of satellite imagery for interpretation and extension of observed units.

The Leaareig Domain is dominated by metasedimentary rocks and paragneiss in the northeast and southwest, with the traverse across the belt revealing subcrops of orthogneiss, paragneiss and marble. The orthogneiss, dated at 2216 ± 60 Ma and 2174 ± 69 Ma is thought to form the basement onto which the sedimentary rocks were deposited. The domain is bounded by the Taghsoumat shear zone to the northeast and the El Medna fault zone to the south, disappearing under El Aaiun basin sediments to the west.

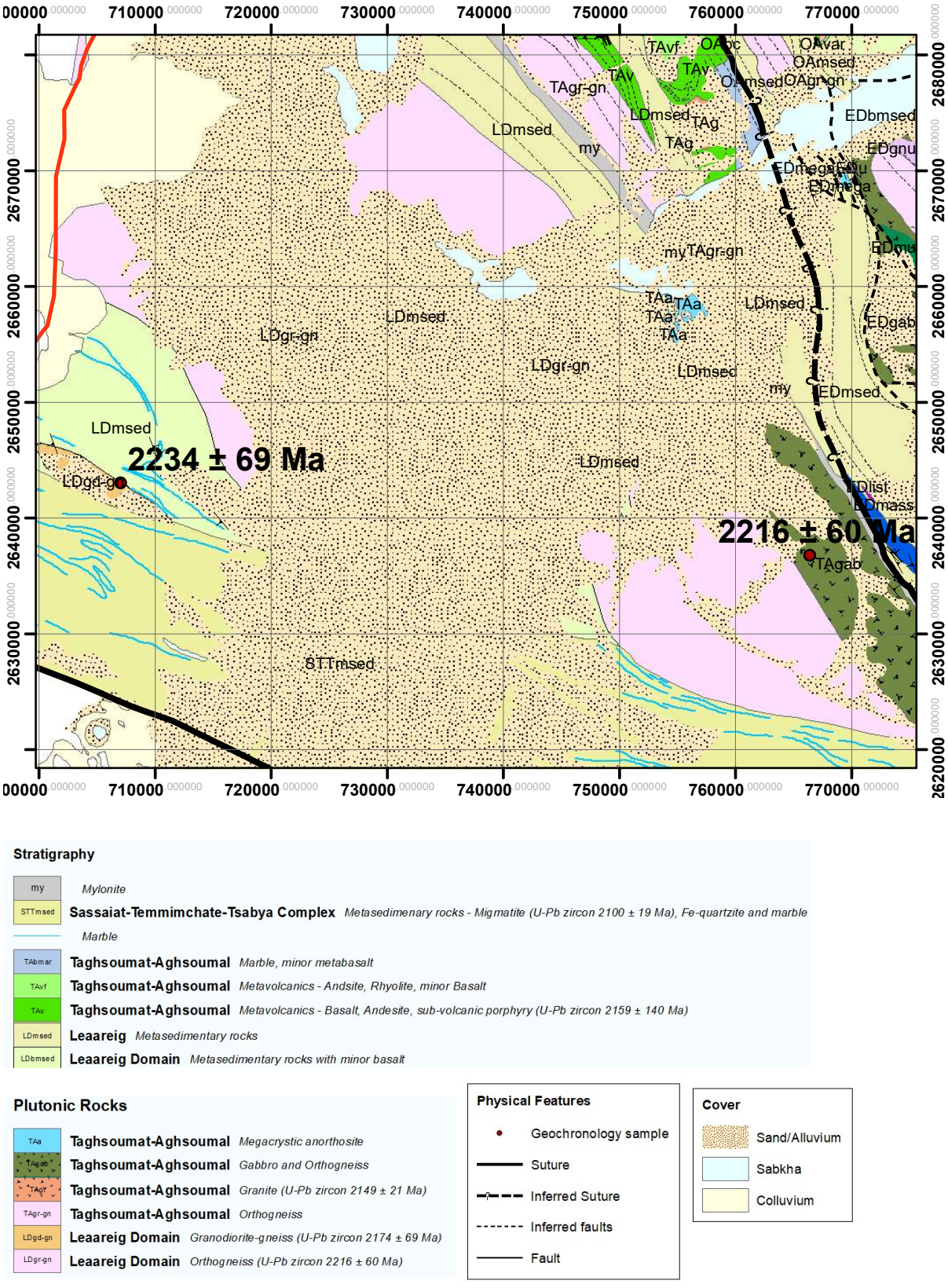

Figure 3-3 - Detailed geology of the Leaareig Domain (UTM Zone 28N). For location map, see the red square in Figure 3-2.

3.1.2.1 Orthogneiss-granite basement

The orthogneiss within the Leaareig Domain forms the basement for the metasedimentary material. The traverse across the domain revealed alternating subcrops of orthogneiss and metasedimentary rocks in the form of paragneiss and marble though it is hard to know what the extent of each lithology is under the sand cover.

The orthogneiss is leucocratic-mesocratic, grey to white, medium to coarse grained (1.5-2.5mm), and has a well-defined gneissose foliation (Figure 3-4), and is locally migmatitic. It ranges in composition from granodiorite through tonalite to quartz diorite; comprising plagioclase (~35-40%), hornblende (~5-50%), quartz (~10-20%), alkali feldspar (~0-10%) biotite (~0-5%), and muscovite (~0-3%).

Locally within the sand region, unfoliated granite intrusions are observed. These intrusions are leucocratic, grey, medium to coarse grained (~1.5-2mm), and weather to form round boulders. They consist of plagioclase (~20-40%), quartz (~25-30%), alkali feldspar (~20-30%), biotite (~10%) and muscovite (~0-5%).



Figure 3-4 – Field photograph of a representative outcrop of orthogneiss in the southwest of the Leaareig Domain cut by small lens of metadolerite. This is also the location of geochronology sample J234 (photo from Laurence Robb). (UTM 28 707061 mE, 2642989 mN)

3.1.2.2 Paragneiss and Metasedimentary Rocks

To the northeast of the domain, a belt of metasedimentary material consists of interbedded biotite schist (Figure 3-5a, b) and white and pink marble. In the southwest of the domain, the metasedimentary unit consists of interbedded quartz rich and garnetiferous paragneiss, ferruginous quartzite, marble and minor volcanic rocks (andesite and basalt) (Figure 3-5c, d).

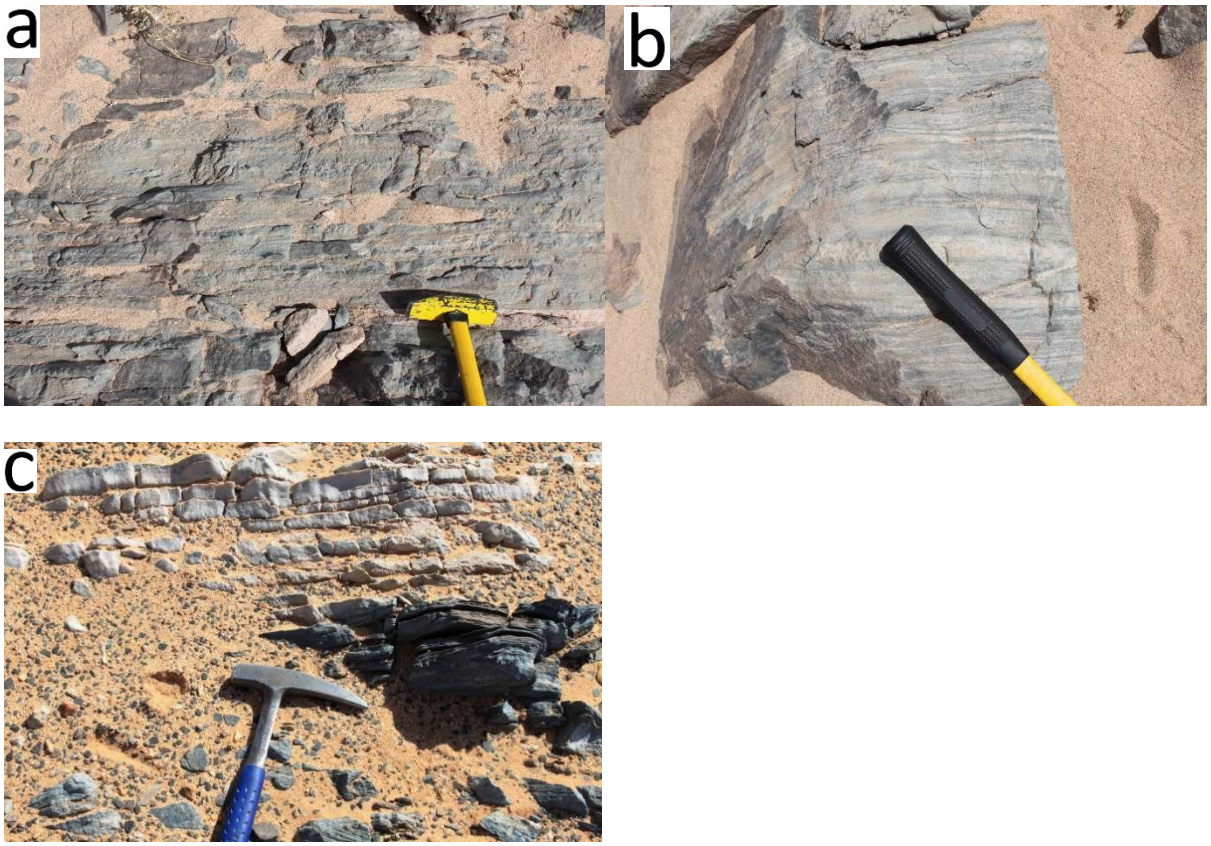

Figure 3-5 - Field photograph of metasedimentary rocks within the Leaareig Domain (photos from Laurence Robb). a, b) metasedimentary rocks from the northeast of the domain (UTM 28 747521 mE, 2664142 mN). c) interbedded marble and metabasalt in the southwest of the Leaareig Domain (UTM 28 757711 mE, 2678026 mN).

3.1.2.3 Contact near the Elmalhat Domain

Proximal to the contact with the Elmalhat domain, the geology is dominated by altered mafic and ultramafic rocks. Lithologies include sheared amphibolite, talc-chlorite schist, serpentinite and altered pyroxenite. Metasedimentary rocks (metamorphosed pyritic shales and quartzite) are locally present, as well as epidote altered orthogneiss.

3.1.3 Petrography

Samples J231 and J234 are representative samples of orthogneiss from the Leaareig that were dated using U-Pb zircon geochronology (Chapter 2.1)

Sample J231 comprises biotite gneiss with a granitic composition. It consists of plagioclase, quartz and feldspar with, minor biotite, some chlorite (replacing biotite) (Figure 3-6a, b). Some

muscovite/sericite occurs in foliation zones wrapping around feldspar porphyroclasts (Figure 3-6c, d). The strain in quartz is mostly at the low-temperature end of grain boundary migration regime. This represents relatively high strain at temperatures in the low 500s °C, below the temperature where significant feldspar plasticity or recrystallization occurs.

Sample J234 comprises a relatively coarse-grained, granodiorite gneiss with a granoblastic texture containing k-feldspar (microcline), plagioclase, quartz, hornblende, biotite, chlorite and sericite (Figure 3-7 a, b). The chlorite is iron-rich (blue birefringence), and replaces biotite and hornblende (Figure 3-7 c, d). Feldspars are locally sericitized but mostly fresh, with myrmekitic microstructures well preserved (Figure 3-7 e, f). A hornblende-biotite aggregate can be seen replacing what might have been a previous igneous hornblende.

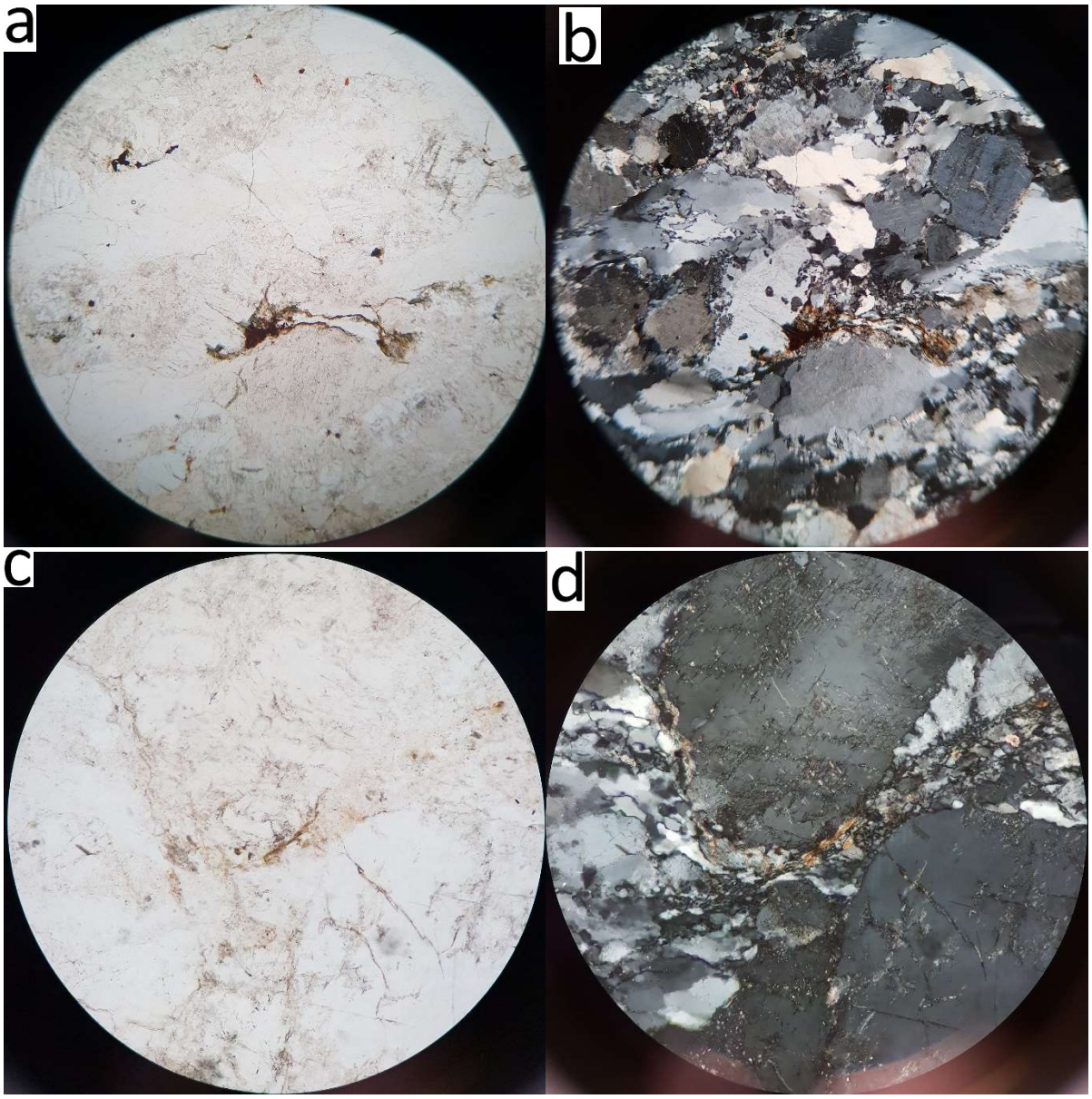

Figure 3-6 – Photomicrograph of J231 – biotite gneiss (UTM 28 766445 mE, 2636718 mN). a, b) Granitic composition: Plagioclase, quartz alkali feldspar, with minor mica mostly biotite, and some chlorite (probably replacing biotite). Field of view (FOV) 5mm, [a) PPL, b) XPL]. c, d) Some muscovite/sericite is present in foliation zones, wrapping around feldspar porphyroclasts. Strain in quartz is mostly at low-temperature end of grain boundary migration regime. Strain is relatively high at temperatures in low 500s °C, below T of significant feldspar plasticity or recrystallization. FOV 1.25mm [c) PPL, d) XPL]

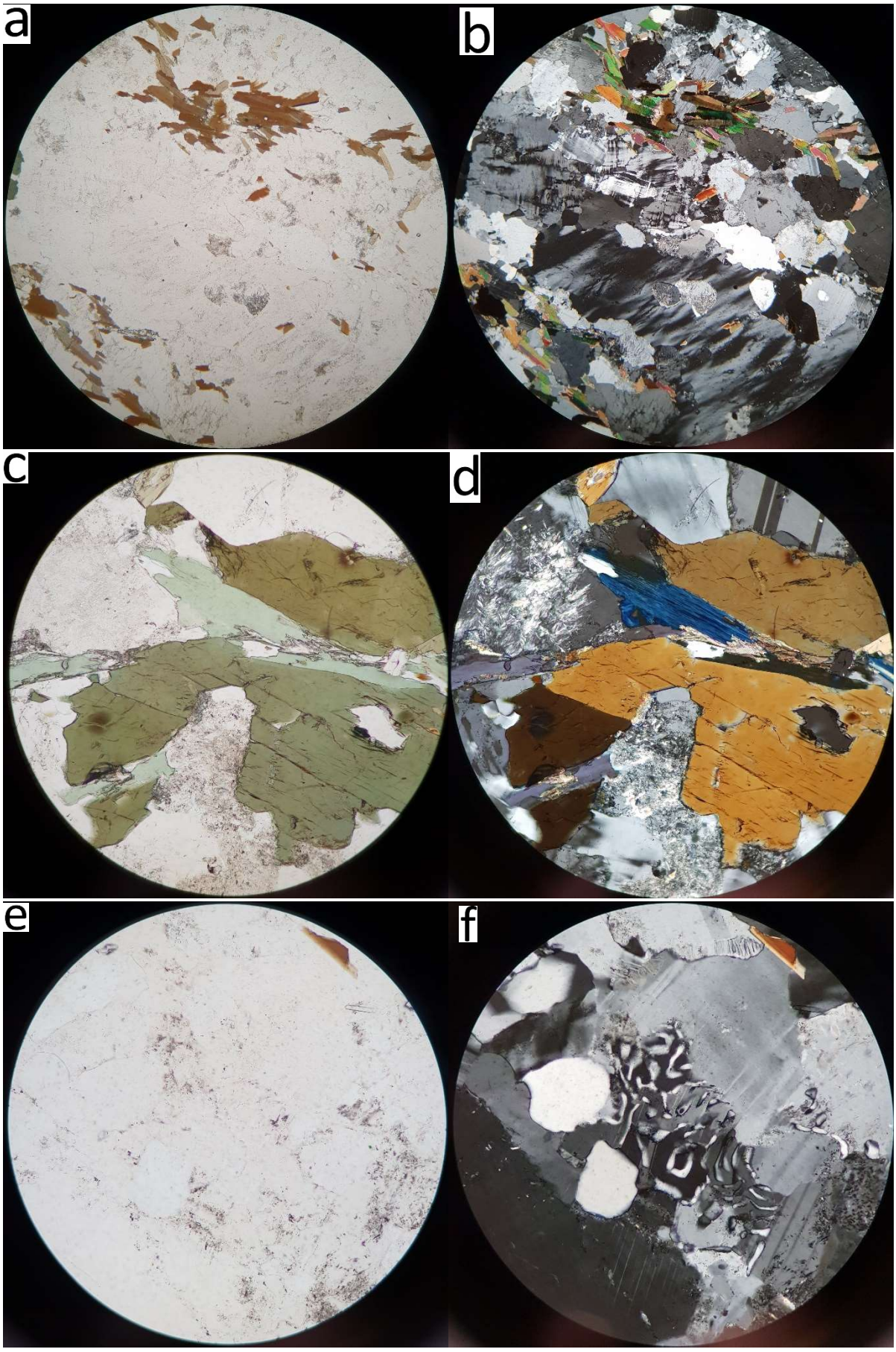
a
b
c
d
e
f

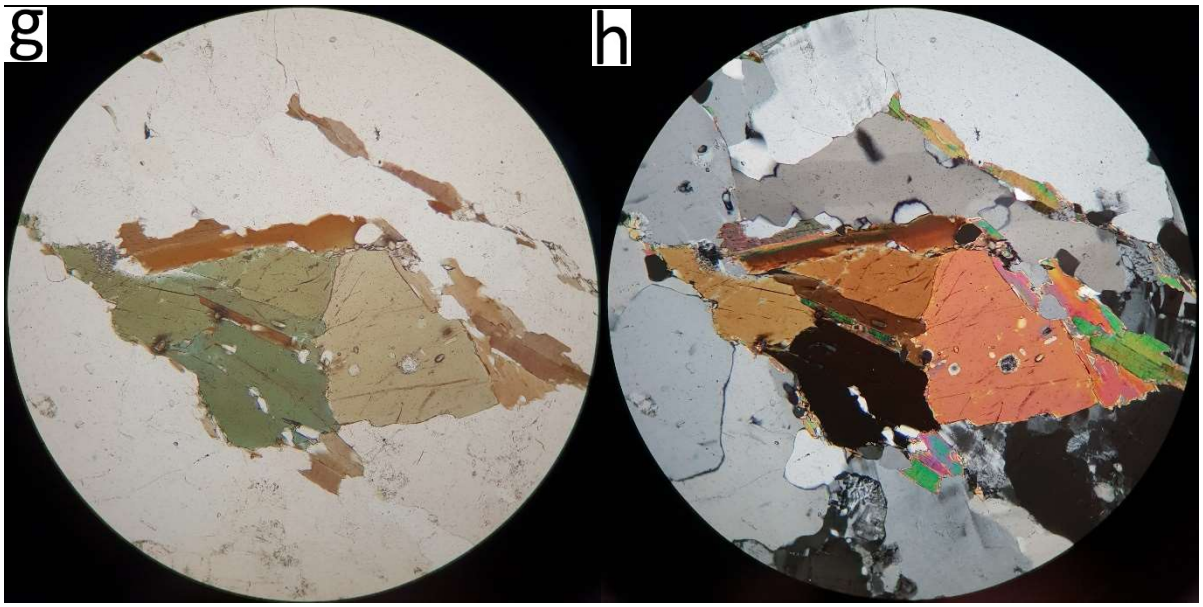

Figure 3-7 - Photomicrograph of J234 - granodiorite gneiss (UTM 28 707061 mE, 2642989 mN). a, b) General view of granodiorite gneiss. Biotite-rich layers present with k-feldspar (microcline), plagioclase, quartz in-between. FOV 5mm. [a) PPL, b) XPL]. c, d) Chlorite is Fe-rich (blue birefringence), replacing hornblende Field of view 2.5mm [c) PPL, d) XPL]. e, f) myrmekitic microstructures well preserved FOV 1.25mm. e) ppl, f) xpl. g, h) relict igneous hornblende now forming an aggregate of hornblende and biotite. FOV 2.5mm. [e) PPL, f) XPL].

3.2 **Taghsoumat-Aghsoumal Domain**

3.2.1 Introduction

The Taghsoumat-Aghsoumal Belt consists of alternating belts of orthogneiss, metasedimentary and volcanosedimentary belts intruded by late stage granites. A sub-volcanic porphyry from a volcanic belt was dated at 2159 ± 140 Ma while the age of a late stage granite intrusion was dated at 2149 ± 21 Ma (Section 2.1; Table 2.1).

3.2.2 Geology and Structure (Mapping/field relations)

The Taghsoumat-Aghsoumal belt consists of northwest-southeast trending fault-bounded, alternating volcanic, volcanosedimentary, metasedimentary and orthogneiss belts intruded by late stage syn- to post tectonic granites (Figure 3-8).

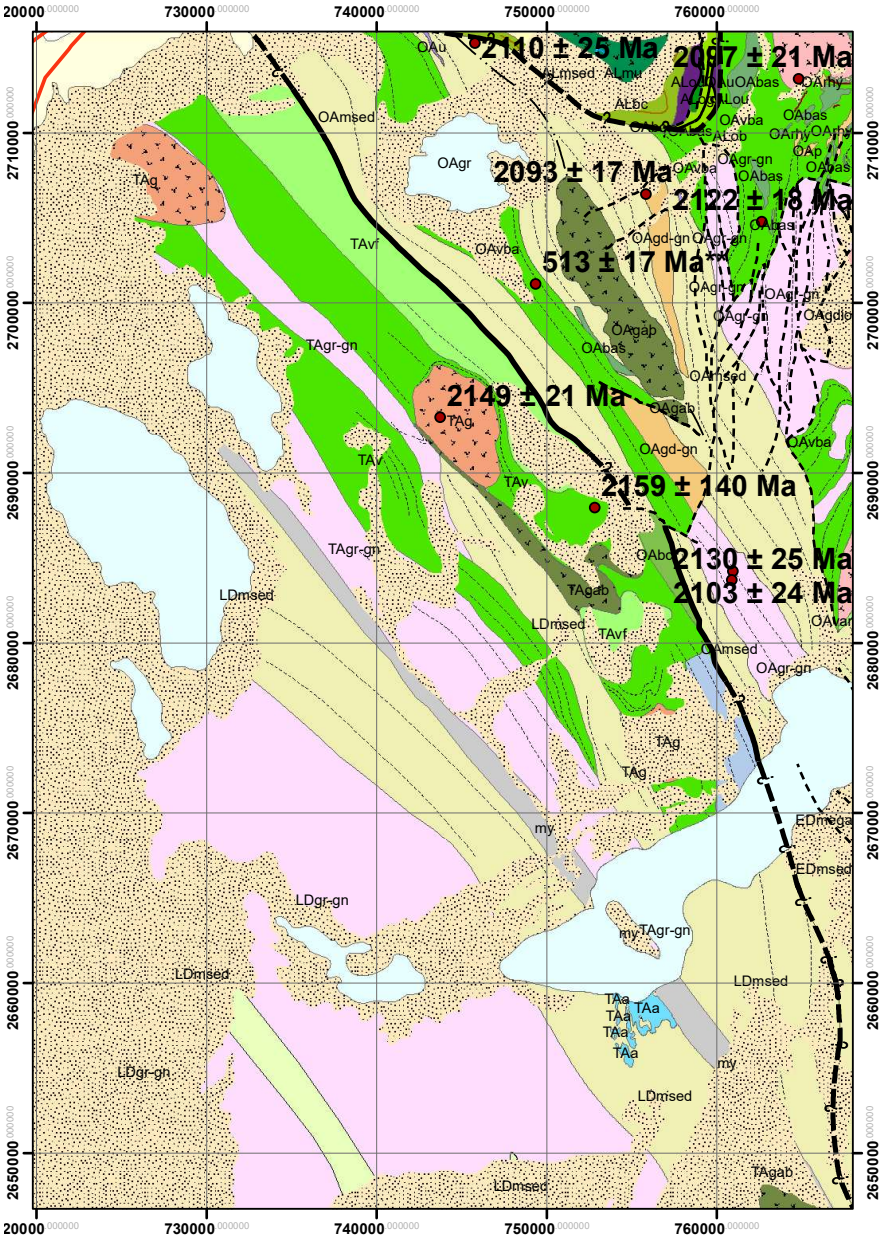

Figure 3-8 a – Detailed geology of the Taghsoumat-Aghsoumal Belt (UTM Zone 28N). For location map, see the purple square in Figure 3-2.

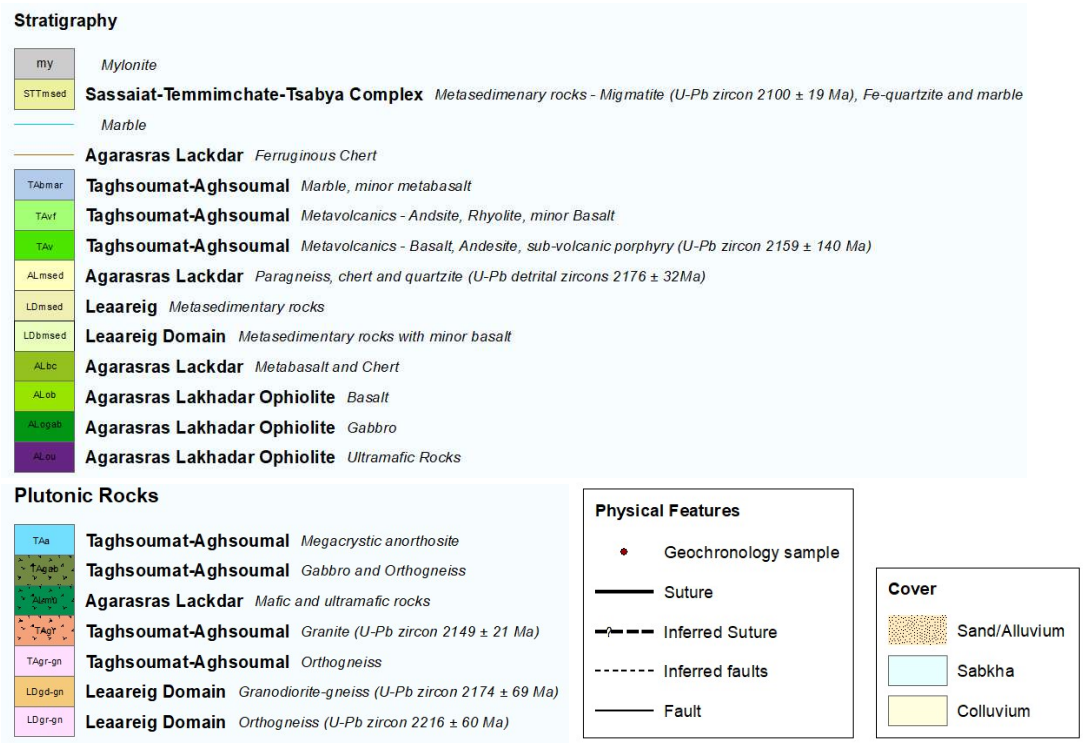

Figure 3-8 b - Legend

3.2.2.1 Orthogneiss

Orthogneiss is the prominent lithology in the west of the domain, consisting of granite-granodiorite porphyry. The orthogneiss contains a well-developed gneissose fabric and is locally migmatitic (Figure 3-9)



Figure 3-9 – Field photograph of migmatitic orthogneiss in the west of the Taghsoumat-Aghsoumal Domain (UTM 28 744710 mE, 2679660 mN).

3.2.2.2 Volcanosedimentary Belt

The belts within the Taghsoumat-Aghsoumal Domain comprise largely of volcanic rocks, locally interbedded with clastic sedimentary material (Figure 3-10 a, c, e). The volcanic rocks range in composition from basalt (Figure 3-10c), through andesite and dacite to rhyolite (Figure 3-10b). A trend is observed across the belt with predominantly andesite (locally porphyritic), dacite and rhyolite (Figure 3-10b) in the east, with increasing portions of basalt and andesite to the west.

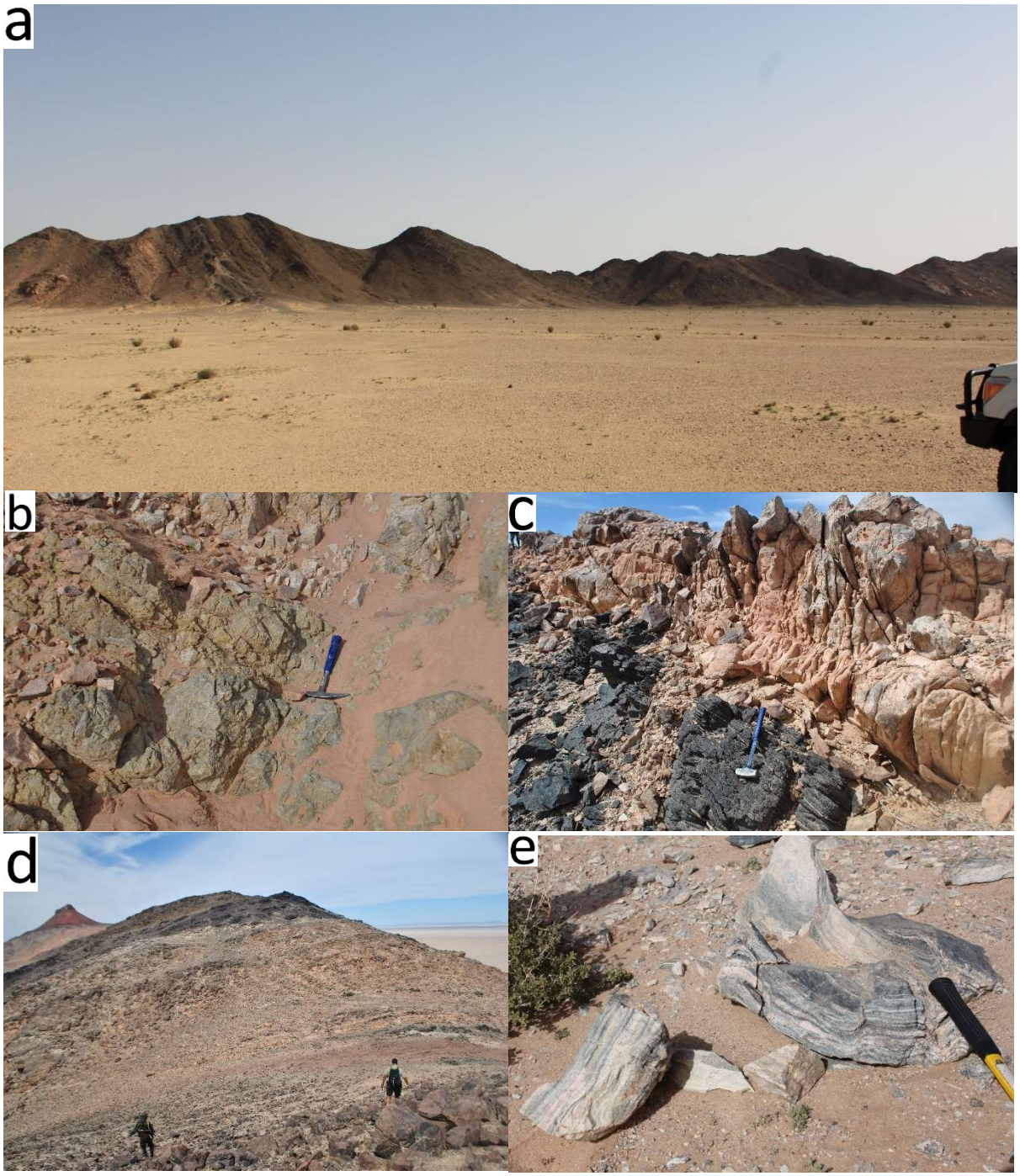

Figure 3-10 - Field photographs of interbedded volcanic and sedimentary rocks outcropping in Aghsoumal Hill. a) bedding between volcanic and sedimentary units on a large scale (UTM 28 747942 mE, 2682252 mN). b) Rhyolite in the east of the belt (UTM 28 748362 mE, 2682090 mN). c) interbeded metabasalt and clastic sediments (UTM 28 748099 mE, 2682052 mN). d) wider view of interbedded metabasalt and clastic sediments. Black ridges are metabasalt, in between is clastic sedimentary material (UTM 28 748177 mE, 2682067 mN); e) outcrop of metasedimentary material (UTM 28 748889 mE, 749123 mN).

3.2.2.3 Marble and metabasalt

In the southeast of the belt, a unit exists composed primarily of thick units of marble (up to ~500m thick), with interbedded layers of basalt (Figure 3.4). The marble is white to orange in colour.



Figure 3-11 - Field photograph of extensive Marble outrcops in the south of the Taghsoumat-Aghsoumal Belt (UTM 28 758689 mE, 2678434 mN).

3.2.2.4 Late intrusions

Several late intrusions cross-cut the volcanosedimentary and orthogneiss units. These are relatively undeformed and range in composition from diorite, through tonalite to granite.

3.3 **Agarasras Lakhadar Domain**

3.3.1 Introduction

The Agarasras Lakhadar Domain represents a section of rocks from the Leaareig Terrane, interpreted as structurally overlying the Oum Abana Belt (Figure 3-12). In the east, the domain consists of a mafic-ultramafic complex. To the west a series of basalt and chert belts, and metasedimentary belts are intruded by a mafic/ultramafic intrusion.

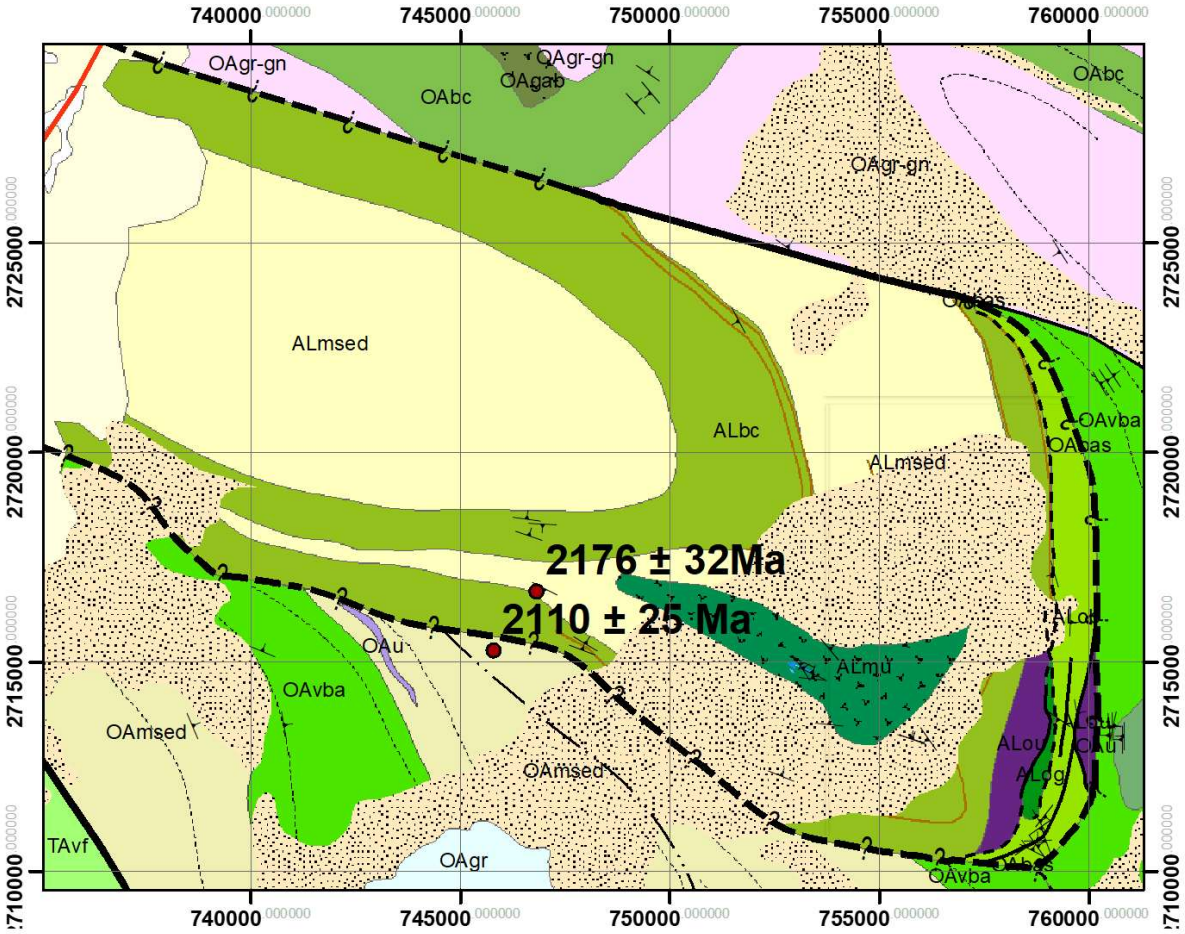

Figure 3-12 a– Detailed geology of the Agarasras Lakhadar Domain (UTM Zone 28N). For location map, see the orange square in Figure 3-2.

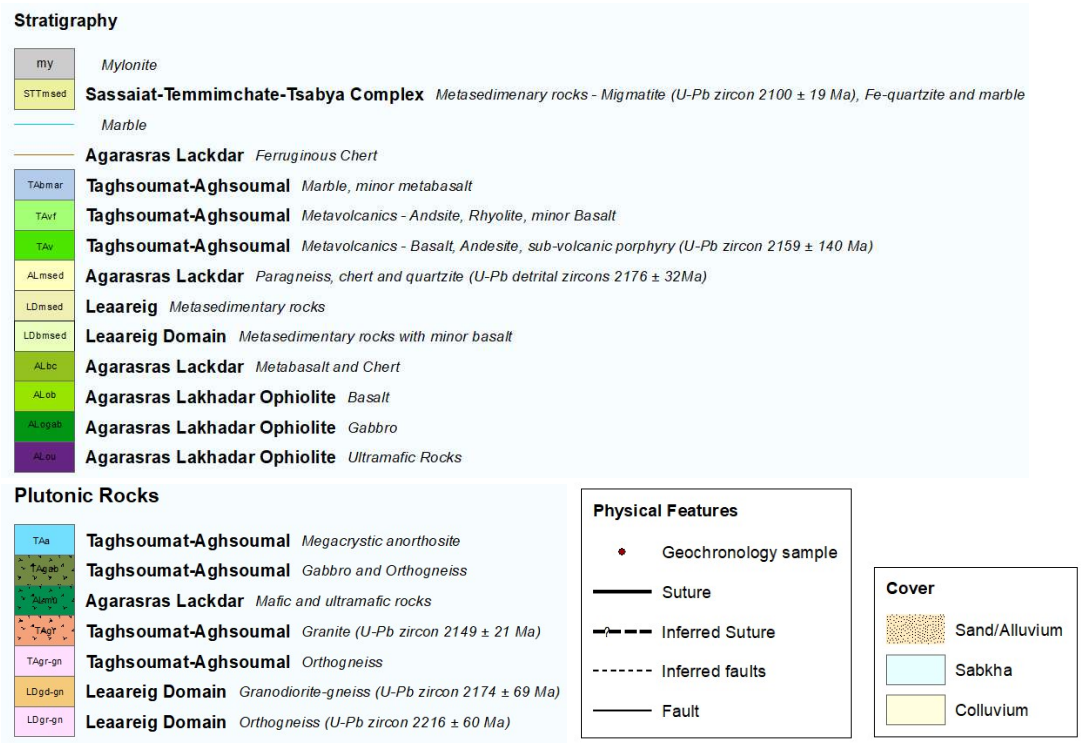

Figure 3-12 b Legend

3.3.2 Geology and Structure (Mapping/Field Relations)

3.3.2.1 Mafic-Ultramafic Complex

Work on the field geology and structure is largely based on the work by Combs (2012) who recognised a north-south trending sequence consisting, from west to east, of coarse ultramafic rocks, gabbro, dolerite and eastward-younging pillow basalt (Figure 3-13). This lead Combs (2012) to interpret the sequence as representing an attenuated ophiolite sequence cut by multiple faults and shear zones, a conclusion Lehbib (2016) concurred with. The lithological observations presented here are largely taken from Combs (2012). Updated mapping, field diagrams, petrological and geochemical work on the complex is original work.

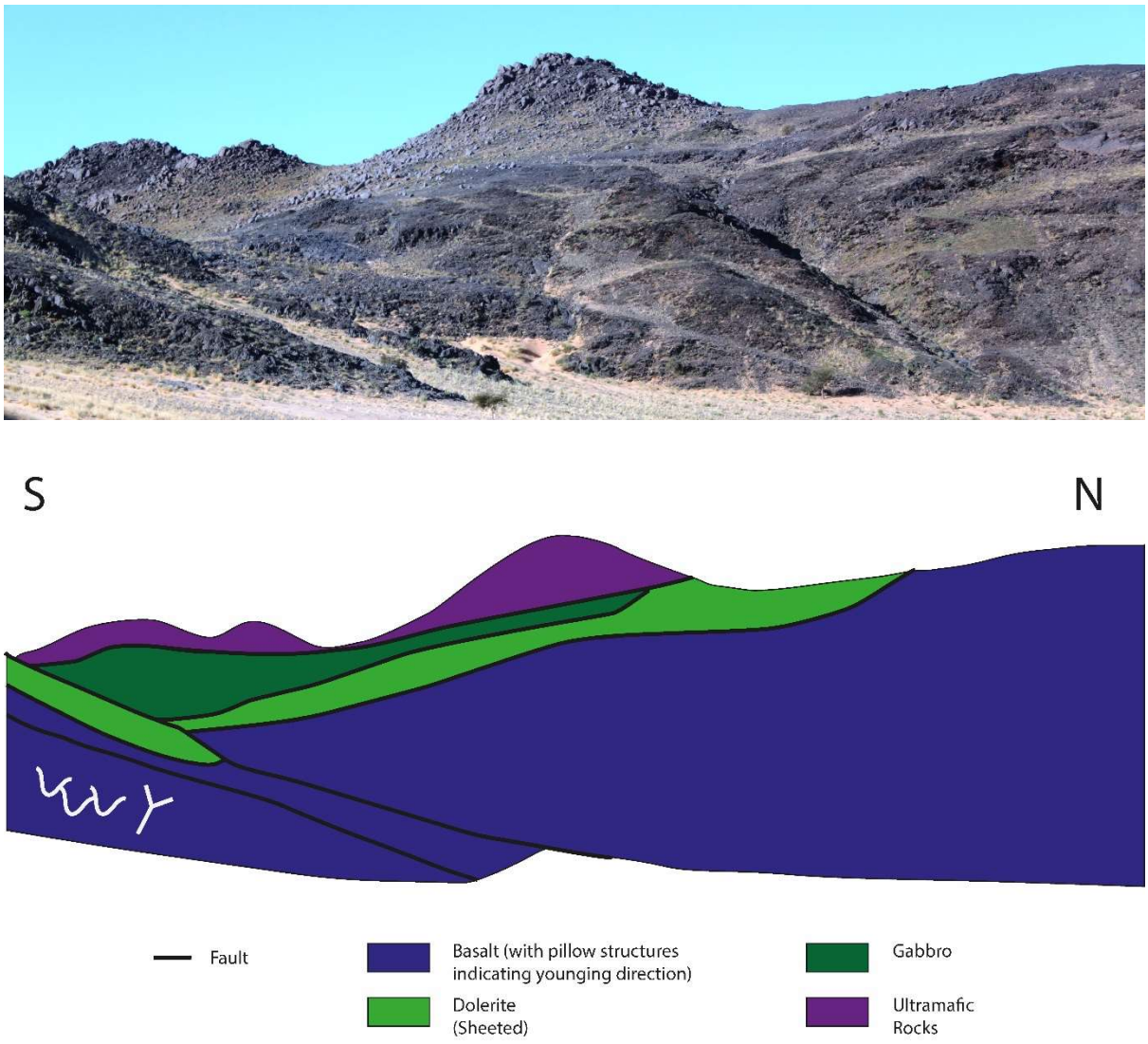

Figure 3-13 – Field photograph and sketch of the mafic-ultramafic complex. The sequence consists of ultramafic rocks, gabbro, dolerite and basalt, locally pillowed indicating an eastward younging direction. Photo from Laurence Robb (UTM 28 759523 mE, 2713928 mN).

3.3.2.1.1 Ultramafics

The ultramafic unit is a melanocratic, dark green, coarse-grained (~2-3mm), equigranular, rock (Figure 3-14). It weathers to form very hard, dark boulders on the surface (Figure 3-15) up to 4m in diameter. The surfaces of these boulders gave a metallic sound when struck by a geological hammer. It is primarily composed of chlorite (~60-85%), talc (20-30%), hornblende (0-15%), and an opaque, highly magnetic brown mineral, possibly pyrrhotite (0-30%). Compositional layering was present on approximately a metre scale, with variations in the

amount of the brown mineral in the rock. Locally the unit displays a very coarse poikilitic texture, with pyroxene oikiocrysts up to 3cm in size (Figure 3-17).

Asbestos veining was present throughout the ultramafic unit (Figure 3-16). The orientations of these veins are highly variable and they ranged in thickness from approximately 1 to 6cm. The veins are brown, consisting of crystals of highly fibrous brown asbestos, amosite (100%), an amphibole belonging to the cummingtonite-grunerite series.

The ultramafic unit is also present to the east of the basalt, separated by a ~30m wide, north-south trending shear zone consisting of talc-chlorite schist. The ultramafic rocks to the east of the basalt are highly magnetic.



Figure 3-14 -- Field photograph of a hand sample of the ultramafic unit (28 758915mE, UTM 2713904mN).



Figure 3-15- Field photograph of the large ultramafic boulders near the boundary between the ultramafics and the gabbro. The man in the image is ~1.93 cm tall. (28 759101mE, UTM 2713693mN).



Figure 3-16- Field photographs of asbestos in the ultramafic unit. a) Asbestos vein in ultramafic rock. b) Asbestos from the vein, showing fibrous habit. Geological hammer for scale (28 759033mE, UTM 2713644mN).



Figure 3-17 - Field photographs of coarse grained, poikilitic metapyroxenite (UTM 28 759127 mE, 2713729 mN).

3.3.2.1.2 Gabbro

The north-south trending gabbro is located to the east of the ultramafic unit across a north-south trending shear zone (167/71º W). The gabbro is a melanocratic, dark grey to black (brown on weathered surfaces) coloured rock that is coarse-grained (3-4mm), equigranular and magnetic, with no foliation. The gabbro is composed of amphibole (~70-80%), plagioclase (~10-20%), magnetite (~5-10%), olivine (~0-5%) and biotite (~0-5%).

3.3.2.1.3 Dolerite (Sheeted?)

The dolerite is a relatively small unit to the east of the gabbro. It is melanocratic, dark blue, medium-grained (~1mm) and magnetic. It is composed of amphibole (~65-80%), plagioclase (~15-35%) and magnetite (~5%). The dolerite forms a series of sheeted dykes, on a scale of ~20-50cm (Figure 3-18a) grading from medium grained (~1mm) in the centre of each dyke to aphanitic in the chilled margin (Figure 3-18b).



Figure 3-18 – Field photographs of dolerite from the complex. a) an example of a ~0.5m sheeted dyke. b) Detailed field photograph showing the chilled margin of one of the sheeted dolerite dykes (360/60°E – UTM 28 759336 mE, 2713658 mN)

3.3.2.1.4 Pillow Basalt

To the east of the dolerite is a basaltic unit. The basalt is melanocratic, dark blue, aphanitic and magnetic. Olivine is present locally. Locally within the basalt, pillow basalts are present indicating an eastward younging direction (Figure 3-19). Garbenschiefer texture (a post-kinematic metamorphic structure) is observed locally, in which amphibole crystals up to 5cm long are observed forming in random orientations (Figure 3-20). It indicates a structural event generating a foliation, with movement stopping before the heat is lost, resulting in preferential, feather-like amphibole growth along the foliation plain.

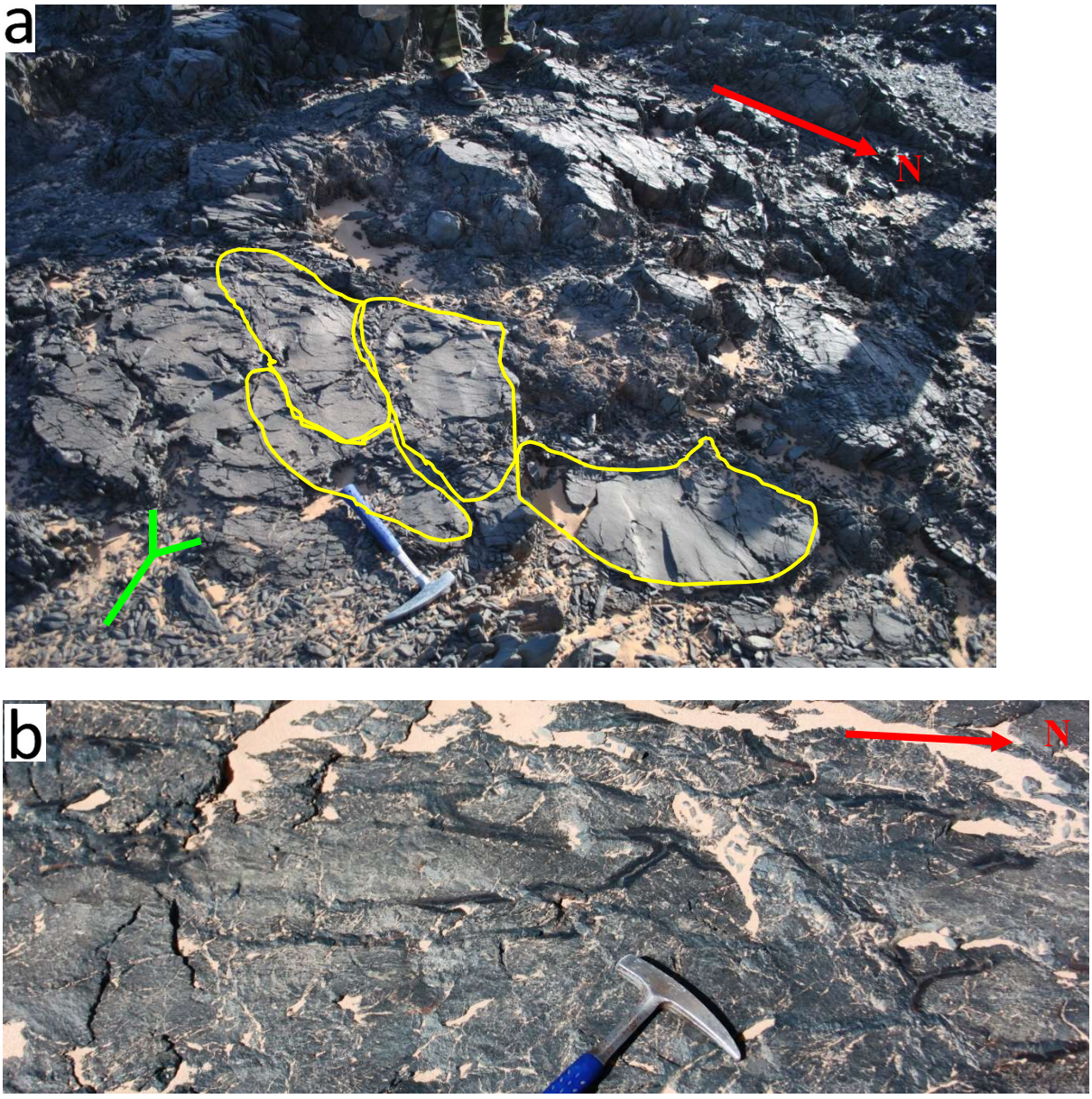

Figure 3-19- Field photograph of pillow basalt (yellow outlines), indicating an eastward younging direction (green younging symbol). North is indicated by the red arrow. Geological hammer for scale (UTM 28 759251mE, 2713618mN) (Combs, 2012). b) other examples of pillow basalt from the unit (UTM 28 759126 mE, 2714883 mN) (Photo from Laurence Robb).

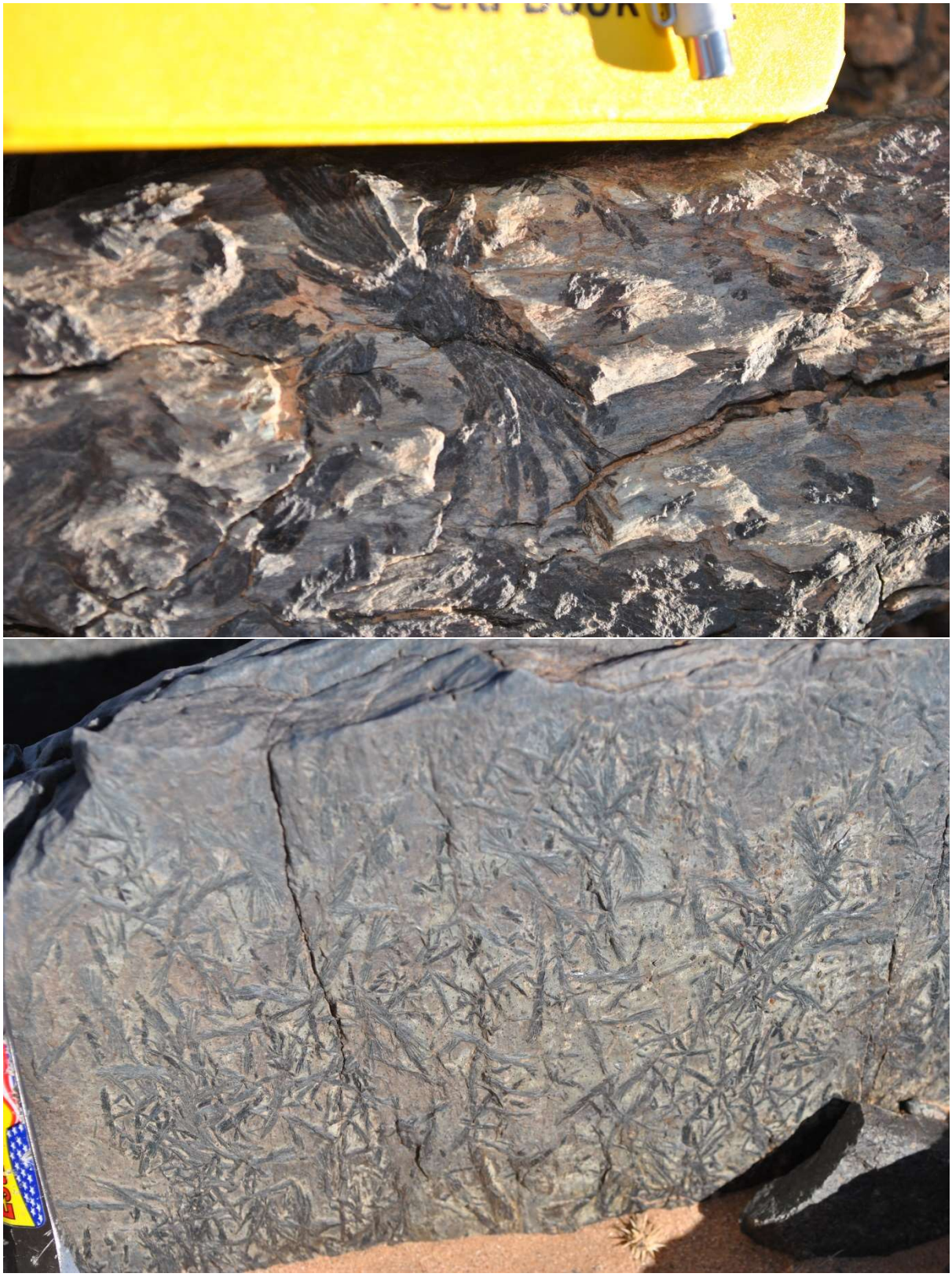

Figure 3-20- Field photographs of garbenschiefer texture exhibited in the dolerite unit (UTM 28 760634mE, 2713324mN).

3.3.2.1.5 Carbonatite Vein

A brown carbonatite dyke is observed cutting the basalt within the sequence (Figure 3-21). The dyke is ~30cm to 2m wide trending ~038º. The carbonatite is fine grained and consists mainly of carbonate with intermittent quartz veins cross-cutting it. Small xenoliths (up to ~2cm) of the host metabasalt are present in the dyke.

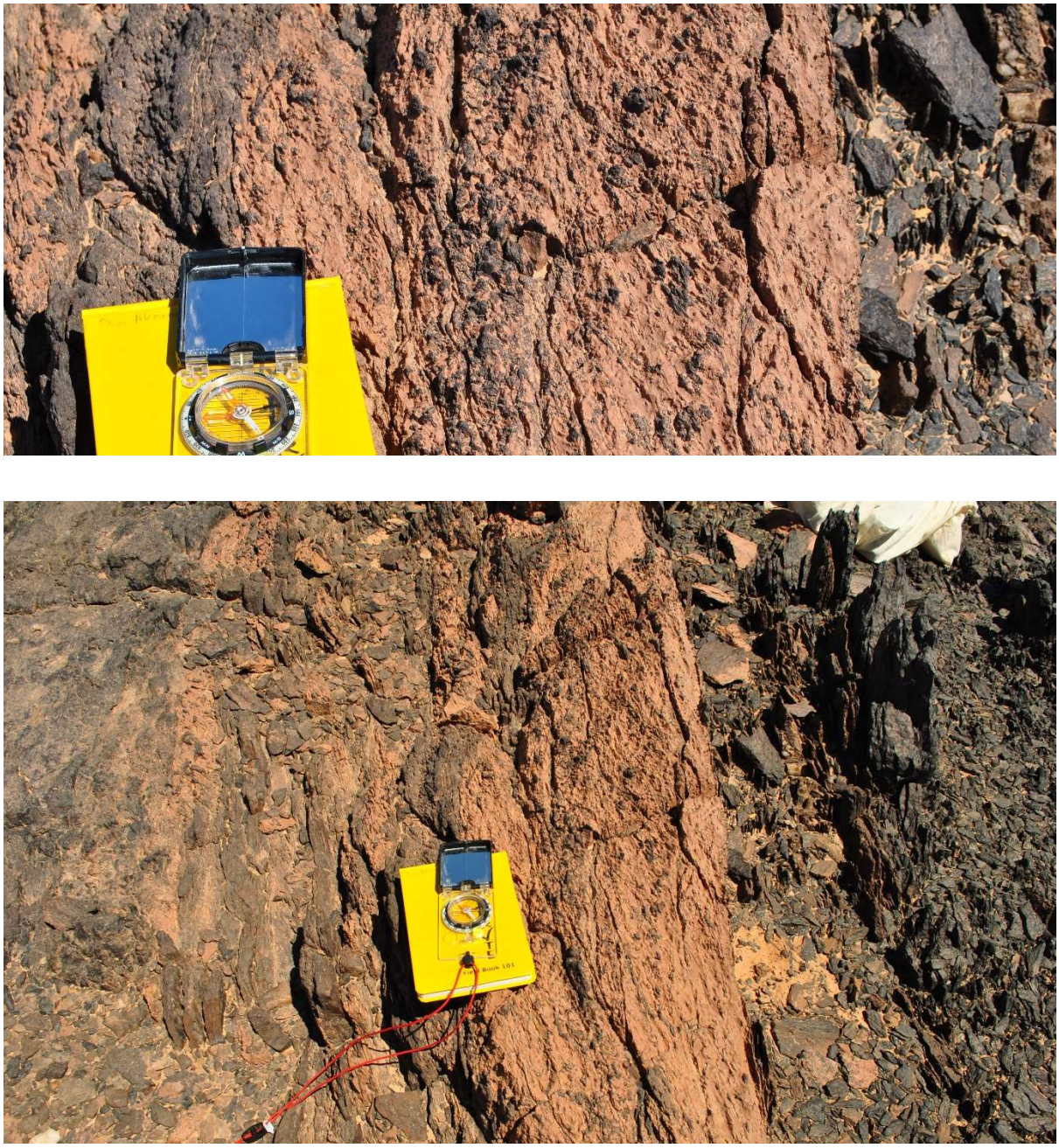

Figure 3-21 - Field photographs of carbonatite dyke cutting the basalt (UTM 28 758954 mE, 2711107 mN)

3.3.2.1.6 Structure of the Complex

The mafic-ultramafic sequence is cut by several structures with many of the observed lithological contacts defined by faults and shear zones. These structural contacts act to pinch out units, such as gabbro and dolerite, and causes the repetition of the ultramafic unit. Detailed mapping has not been undertaken, so the structures are not well defined.

A shear contact is observed between the basalt and pyroxenite in the north of the complex where the gabbro and dolerite had been structurally pinched out (Figure 3-22a,b). A strong sheared fabric (167/71º W) is observed in the pyroxenite, with only minimal shearing observed in the basalt. Further south a sheared contact is observed between the gabbro and dolerite (Figure 3-22c). To the east of the pillow basalt a north-south trending shear zone is observed with a repetition of the ultramafic unit to the east of the shear zone (Figure 3-23). It appears that the thickness and distribution of the units are structurally controlled, locally resulting in the units being out of sequence.

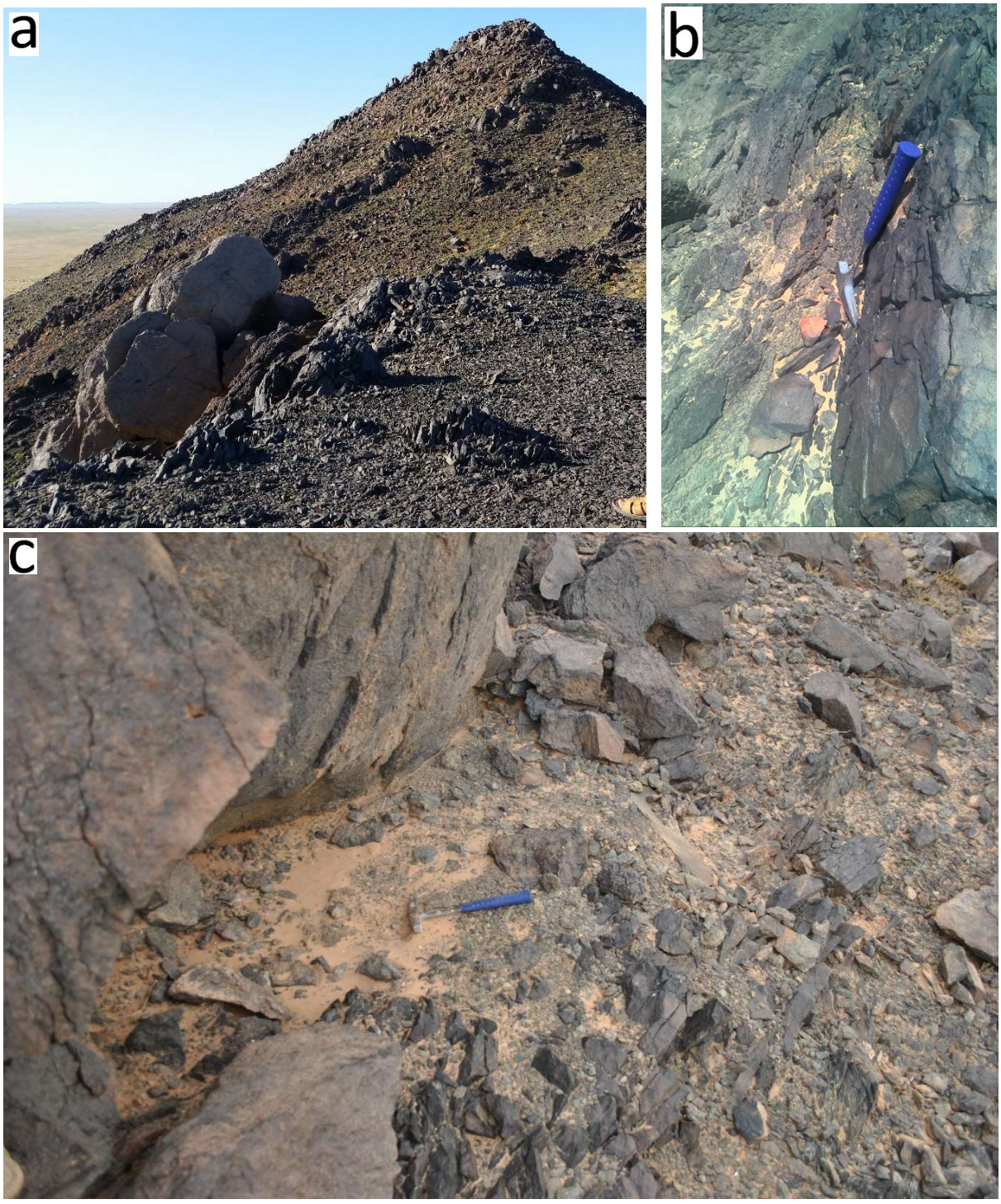

Figure 3-22 – Field photographs of sheared contacts observed within the mafic-ultramafic complex. a, b) contact between basalt and ultramafic rocks to the north of the complex where the gabbro and dolerite units have been pinched out (UTM 28 759127 mE, 2713729 mN). c) contact between dolerite and gabbro in the middle of the complex (UTM 28 759159mE, 2713710mN).

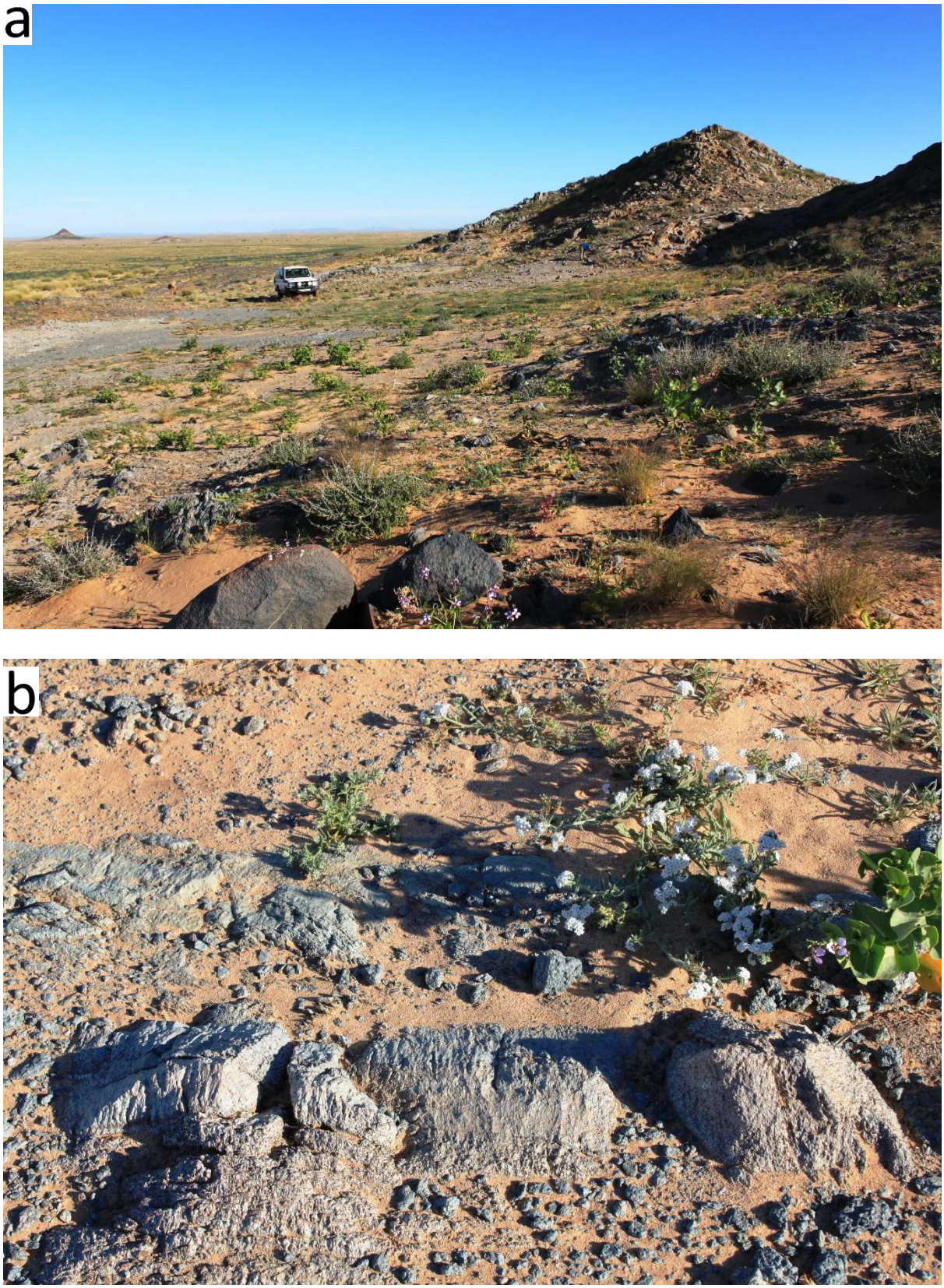

Figure 3-23 - Field photographs of shear zone between the unit of basalt and the eastern exposure of ultramafic rocks (UTM 28 759692 mE, 2713371 mN). a) general view with the hill of ultramafic rocks on the right and the light coloured sheared ultramafic rocks to the left. b) close up of sheared ultramafic rocks.

3.3.2.2 Basalt and Chert

This unit consists of metabasalt with thin continuous beds of ferruginous chert. The metabasalt is melanocratic, dark blue, aphanitic and contains a weak, sub-vertical foliation parallel to the chert beds (Figure 3-24). The ferruginous chert is a dark grey, weakly magnetic unit forming continuous layers (~0.3-3m thick). Locally the chert appears to have been recrystallised to a fine grained (~0.2mm) quartzite (Figure 3-25).

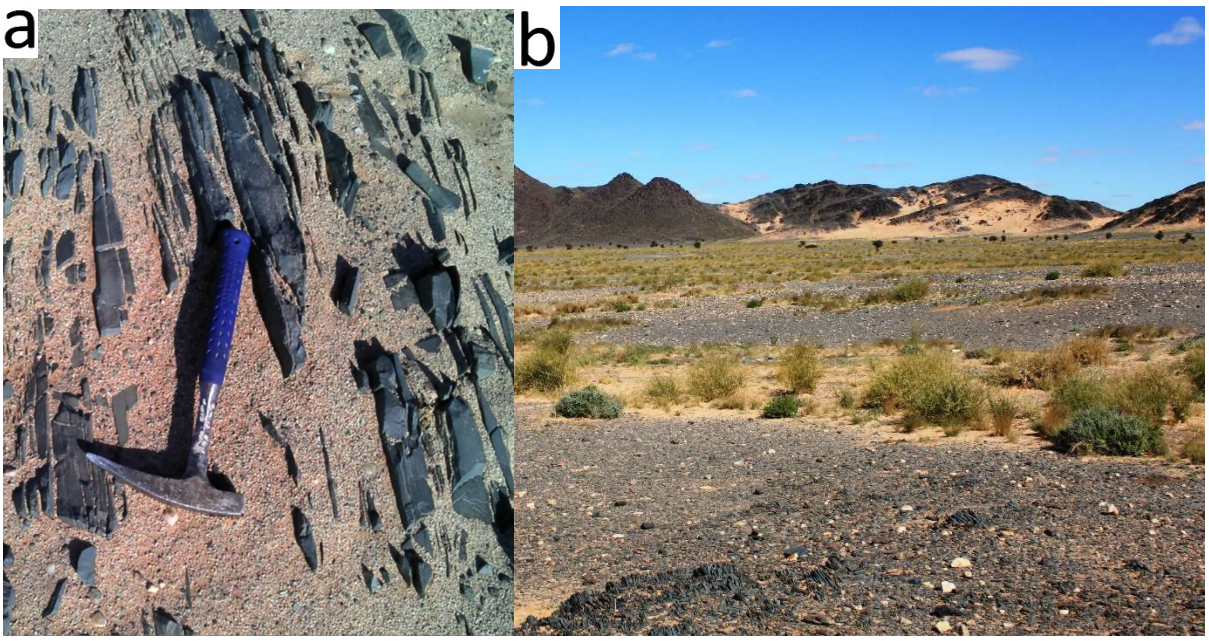

Figure 3-24 – Field photographs of a) an outcrop of metabasalt. b) subcropping metabasalt to the west of the Agarasras Lakhadar hills. (UTM 28 755943 mE, 2713237 mN)



Figure 3-25 – Field photographs of outcrops of ferruginous chert of varying thickness (UTM 28 753955 mE, 2713625 mN).

3.3.2.3 Metasedimentary Rocks

The unit of metasedimentary rocks largely consist of a series of meta-arkose/greywacke schists and gneisses, with layers of metachert and marble present.

Biotite schist within the unit is leucocratic, light brown, soft and weathered, equigranular, fine grained (~0.2mm) with a schistose foliation, with quartz (~80%) and mica, (mainly biotite) (~20%).

Gneiss within the unit is fine grained (~0.25mm), with a well-developed gneissose foliation. It is generally very quartz and mica rich consisting of quartz (~50%), feldspar (~25%), muscovite (~5-20%), biotite (~5-20%), and garnet (0-5%).

Blue marble beds, 0.2-1m thick (Figure 3-26), and grey to dark beds of quartzite, sometimes ferruginous, are present throughout the schists and gneisses of the unit.

The quartz and mica rich nature of the gneiss, combined with its association with other metasedimentary rocks (marble and quartzite) leads to the inference of a sedimentary origin. This unit as a whole is interpreted as representing a metamorphosed sedimentary accumulation

consisting clastic sediments (greywackes/arkoses) and chemical sediments (carbonate and chert).



Figure 3-26 - Field photographs of marble from the metasedimentary unit (UTM 28 755024mE, 2716601mN).

3.3.2.4 Mafic-Ultramafic Intrusion

Within the metasedimentary unit lies a unit of mafic and ultramafic rocks with some small outcrops of metasedimentary rock. The unit has variable grainsize, from medium- to very coarse, and appears to be retrogressed with amphiboles and chlorite representing the main mafic phases (Figure 3-27). The entire unit consists of >70% mafic minerals. It has been weathered and only subcrops as saprock. It likely represents a metamorphosed intrusion of gabbro and pyroxenite/peridotite containing xenoliths of metasedimentary rocks.

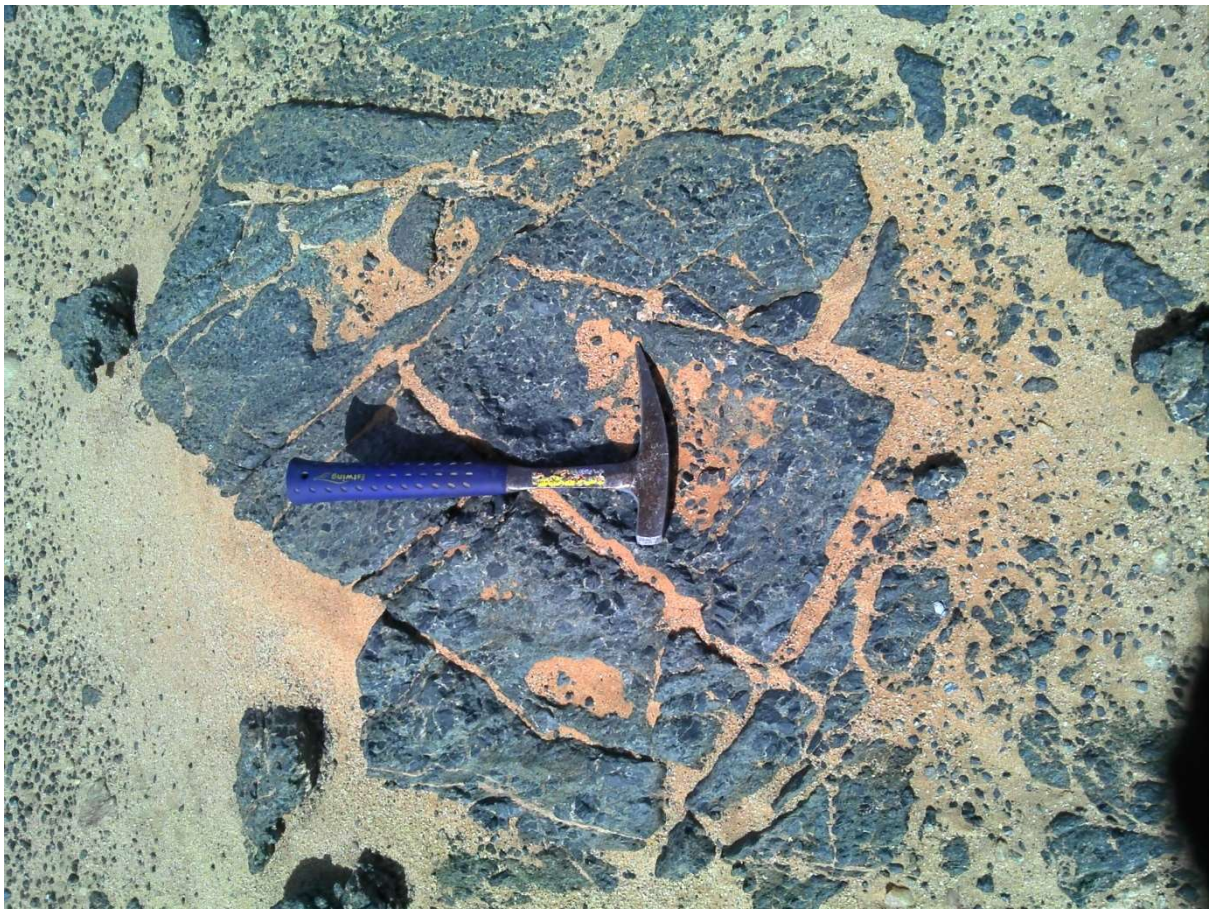

Figure 3-27 – Field photographs of weathered hornblendite within the mafic-ultramafic region. This likely represents meta-peridotite/pyroxenite (UTM 28 753567 mE, 2714837 mN).

3.3.2.5 Structural Features

The entire Agarasras Lakhadar Domain has been interpreted as being structurally bounded, although the expression of the bounding shear zone on the surface is limited due to poor exposure. Several lines of evidence were used in this interpretation and to constrain its location and orientation.

In the southeastern corner of the Agarasras Lakhadar Domain, the metapyroxenite is strongly sheared with the shear fabric trending 325°. To the south of the metapyroxenite lie large volumes of quartz, to the south of which is a change in lithology to volcanic rocks of the Oum Abana Domain. Moving eastwards, the orientation of this foliation progressively curves toward a more north-south orientation. A highly silicified listwanite is observed on the bottom edge of

the shear zone with an orientation of 285/65º N. A little to the northeast, serpentinite is observed with a foliation of 170/47ºW. Although none of these are a direct indication of a major shear zone, it would be consistent with a thrust with an orientation curving around to the north (as mapped).

A major shear zone is observed between the pillow basalt unit and a repetition of the ultramafic rocks in the east (Figure 3-23). This is observed as a ~15m thick section of intensely sheared ultramafic rocks (018/85º W) with talc-chlorite schist in the centre, grading to highly magnetic ultramafic rocks in the east. This would be consistent with a second shear zone, sub-parallel to a major structure to the east. This is too steep to represent a thrust, although it could have been steepened by multiple subsequent deformation events (discussed in Section 6.2).

Other observations consistent with the presence of a thrust as mapped include:

- Lithological changes from Oum Abana volcanics (basalt, andesite, and rhyolite) and metasedimentary rocks to Agarasras Lakhadar basalt and chert and ultramafic-mafic complex
- Change in foliation from the northwest-southeast trending Oum Abana belt to the north-south trending Agarasras Lakhadar lithologies (in the east of the domain)
- Age difference observed in metasedimentary rocks either side of the inferred thrust

3.3.3 Petrography

3.3.3.1 Mafic-Ultramafic Complex

3.3.3.1.1 Ultramafics

The ultramafic rocks within the complex (samples J026, J027 and J064) are retrogressed, with several samples also carbonated during alteration.

Sample J026 consists of lizardite with magnesite and various oxide and sulphide minerals (Figure 3-28 a-d). Chromite is altered to magnetite along its edges (Figure 3-28 f). Sulphide minerals present include pentlandite and pyrrhotite (Figure 3-28 e) while magnetite is also present as alteration on the edge of chromite grains (Figure 3-28 f). The protolith is likely peridotite.

Samples J027 also represents altered peridotite now composed of mostly chlorite, carbonate, goethite, and oxides (ilmenite, magnetite) (Figure 3-29).

Sample J064 consists of a very amphibole-rich rock containing coarse amphibole crystals with distinct cores and rims, potentially representing amphibole replacing earlier pyroxene and then overgrowing other parts of rock matrix (Figure 3-30). The matrix consists of smaller diamond-cross-section amphiboles and chlorite. This sample likely represents a metamorphosed pyroxenite.

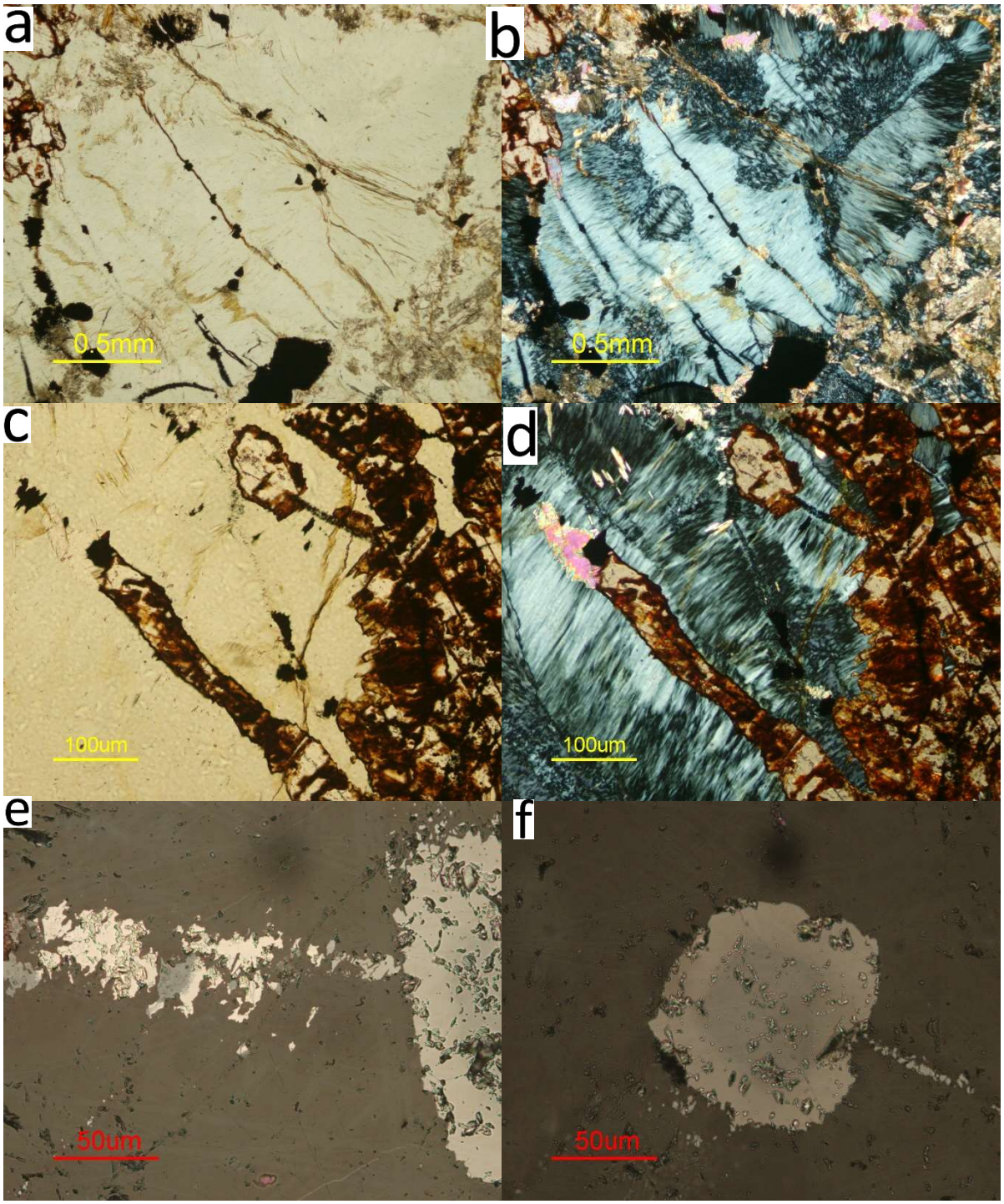

Figure 3-28 – Photomicrographs of J026 (UTM 28 759101 mE, 2713693 mN) – altered ultramafic rock. a-d) Lizardite (Serpentine) with magnesite (carbonate) and minor cummingtonite [a, c) PPL, b, d) XPL]. e, f) reflected light photomicrograph showing pentlandite, pyrrhotite, chromite and magnetite. f) reflected light photomicrograph of chromite grains are altered to magnetite on the edges.

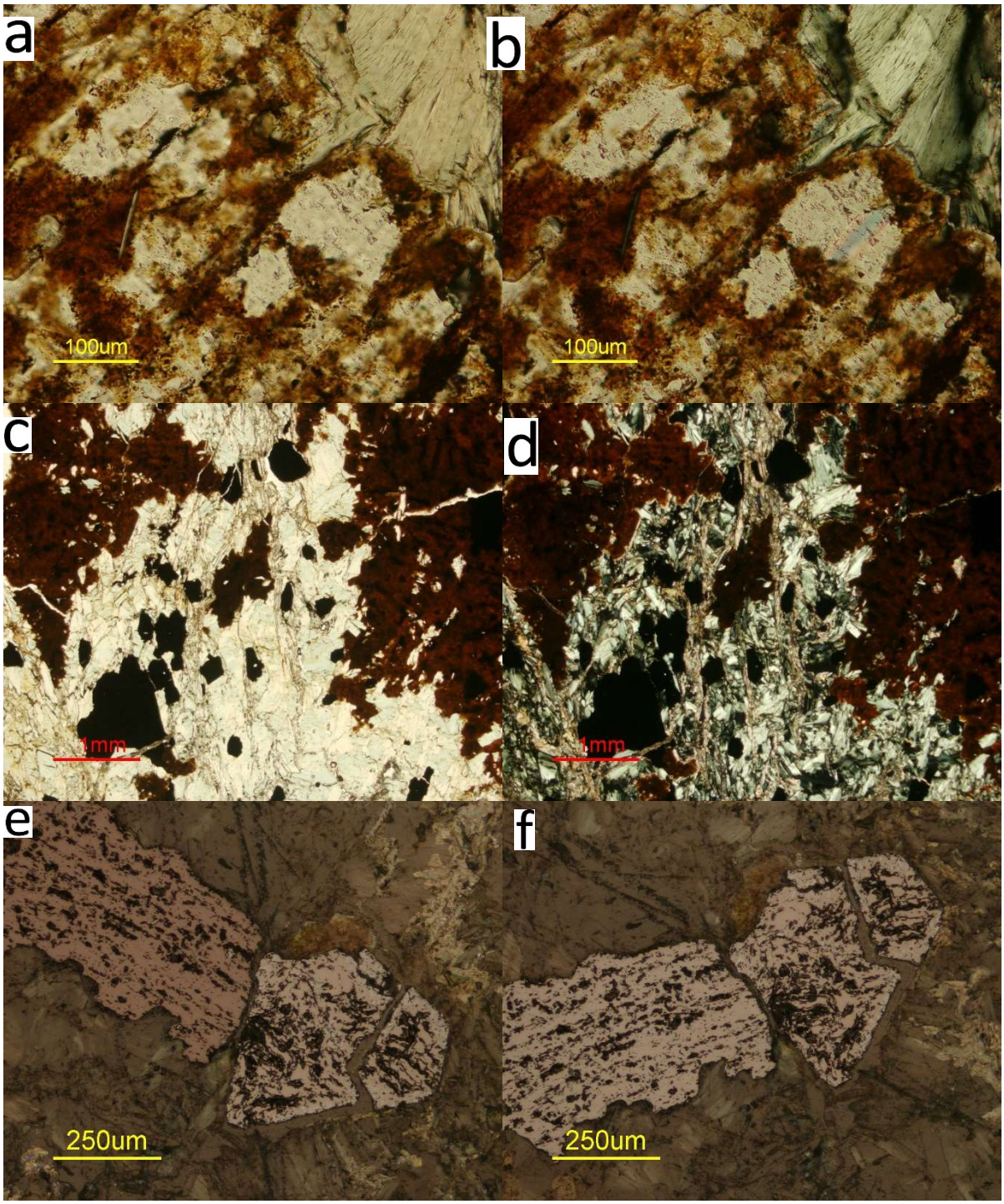

Figure 3-29 – Photomicrographs of J027 (UTM 28 758915 mE, 2713904 mN) – altered peridotite, mostly chlorite, carbonate, goethite, with oxides [a, c) PPL, b, d) XPL]. e, f) Reflected light showing ilmenite (pleochroic) and magnetite.

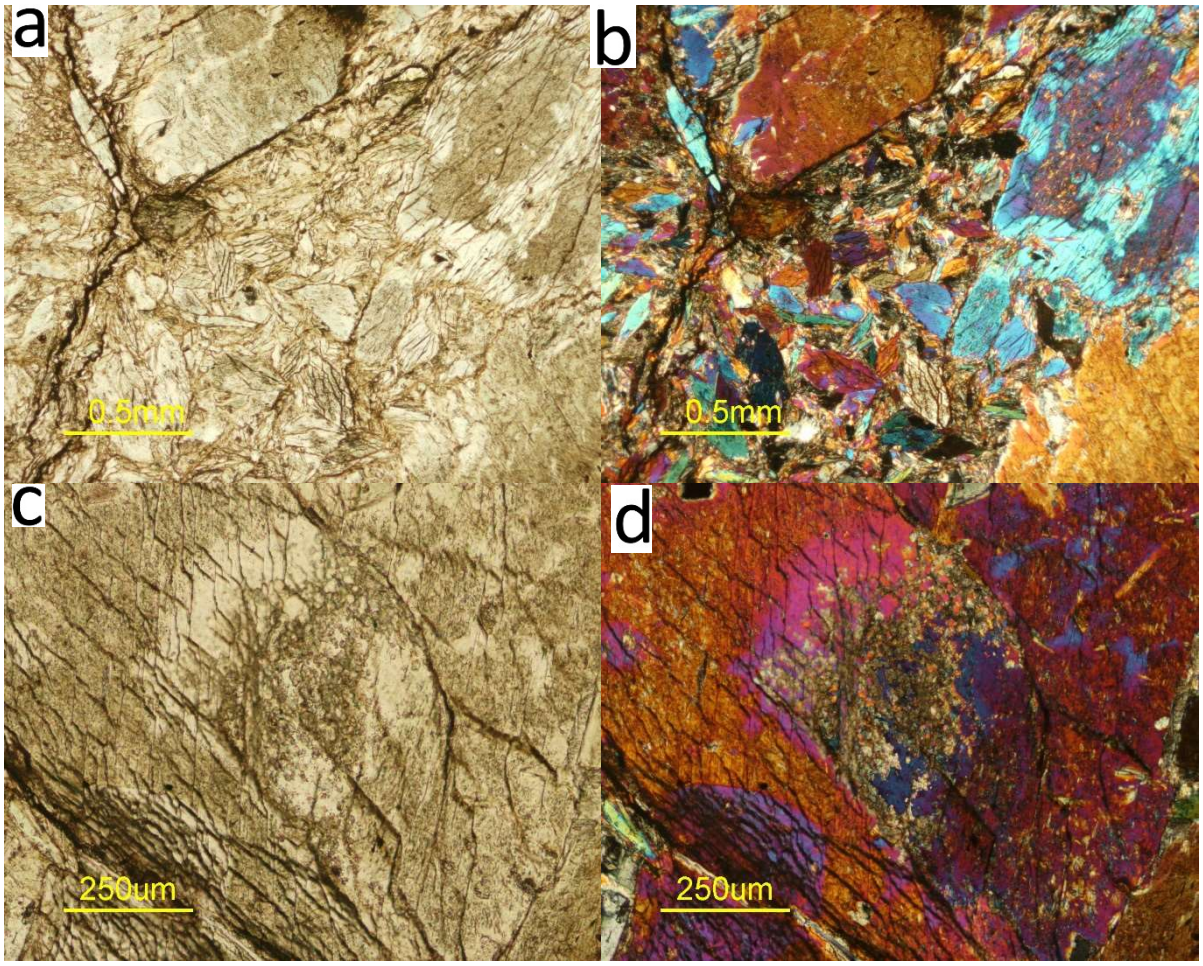

Figure 3-30 – Photomicrographs of J064 (UTM 28 758983 mE, 2711691 mN) metapyroxenite – a, b) General view of coarse amphibole with distinct core and rim, and smaller diamond-cross-section amphiboles and chlorite forming the groundmass [a) PPL, b) XPL]. c, d) Detail of coarse amphibole with distinct rim and core [c) PPL, d) XPL].

3.3.3.1.2 Gabbro

Gabbro has also been strongly affected by carbonate alteration. Sample J025 represents an altered, carbonated gabbro (Figure 3-31). Relics of clinopyroxene are cut and surrounded by very fine carbonate (Figure 3-31 a, b). Rounded grains of what may have been olivine are defined by magnetite rims surrounding replacement talc and chlorite. Large ragged platy pseudomorphs of anomalous-blue chlorite (Fe- or Si-rich) are present. Other chlorite pseudomorphs in the rock are more Mg-rich.

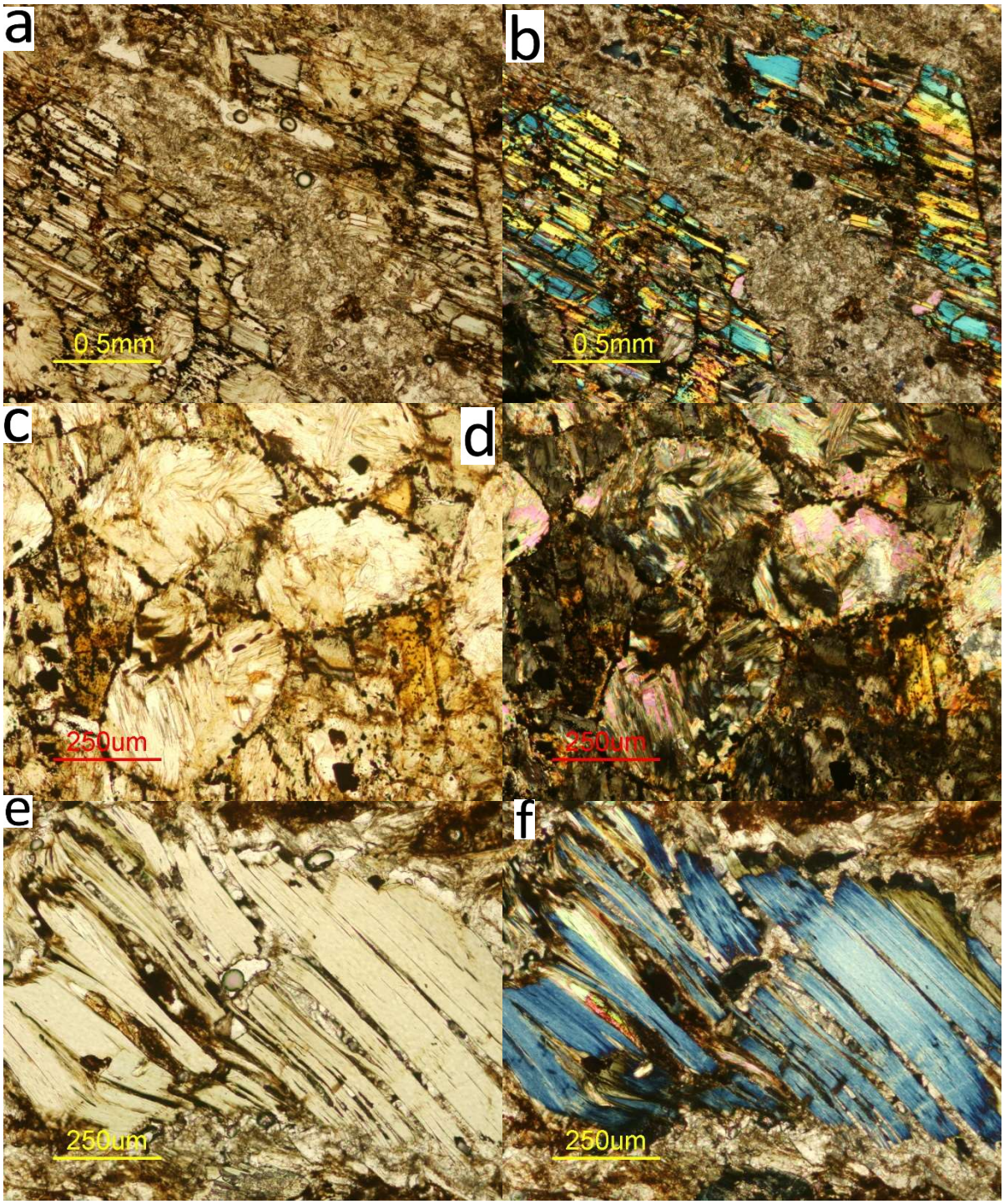

Figure 3-31 – Photomicrographs of J025 (UTM 28 759869 mE, 2713652 mN) – Carbonate altered gabbro. a, b) Relics of clinopyroxene cut and surrounded by very fine carbonate [a) PPL, b) XPL]. c, d) Rounded grains of what may have been olivine are defined by magnetite rims surrounding replacement talc and chlorite [c) PPL, d) XPL]. e, f) Large ragged plate pseudomorph of anomalous-blue chlorite (Fe- or Si-rich) is present [e) PPL, f) XPL].

3.3.3.1.3 Basalt

Samples from the basalt (J062 and J065) are composed mainly of amphibole and plagioclase, with minor, scattered poikilitic opaque oxides (Figure 3-32), and titanite (Figure 3-33).

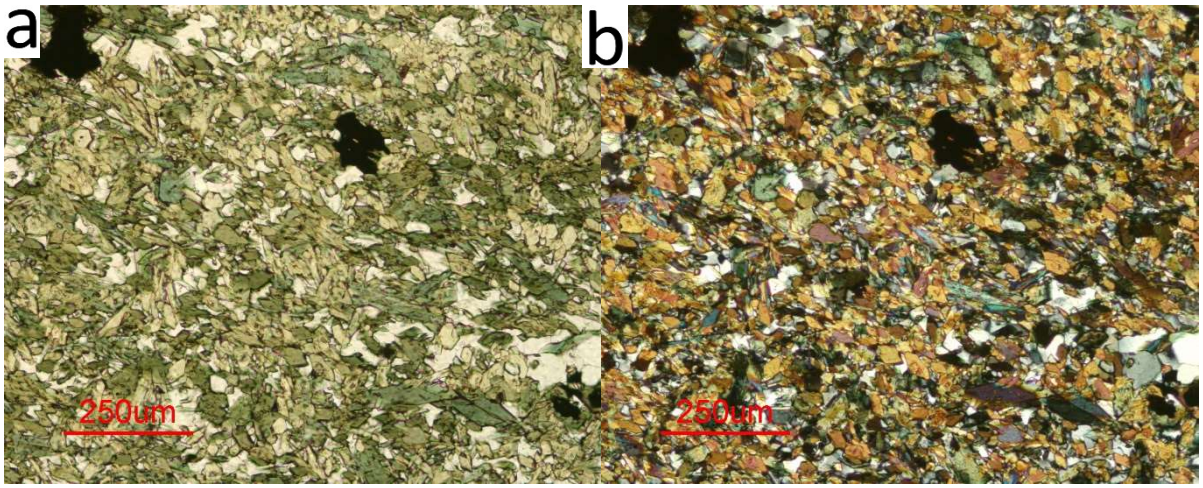

Figure 3-32 – Photomicrographs of J062 (UTM 28 758878 mE, 2710687 mN) - fine grained amphibolite, green hornblende/actinolite, probably albite, scattered somewhat poikilitic opaque oxide. No obvious epidote [a) PPL, b) XPL].

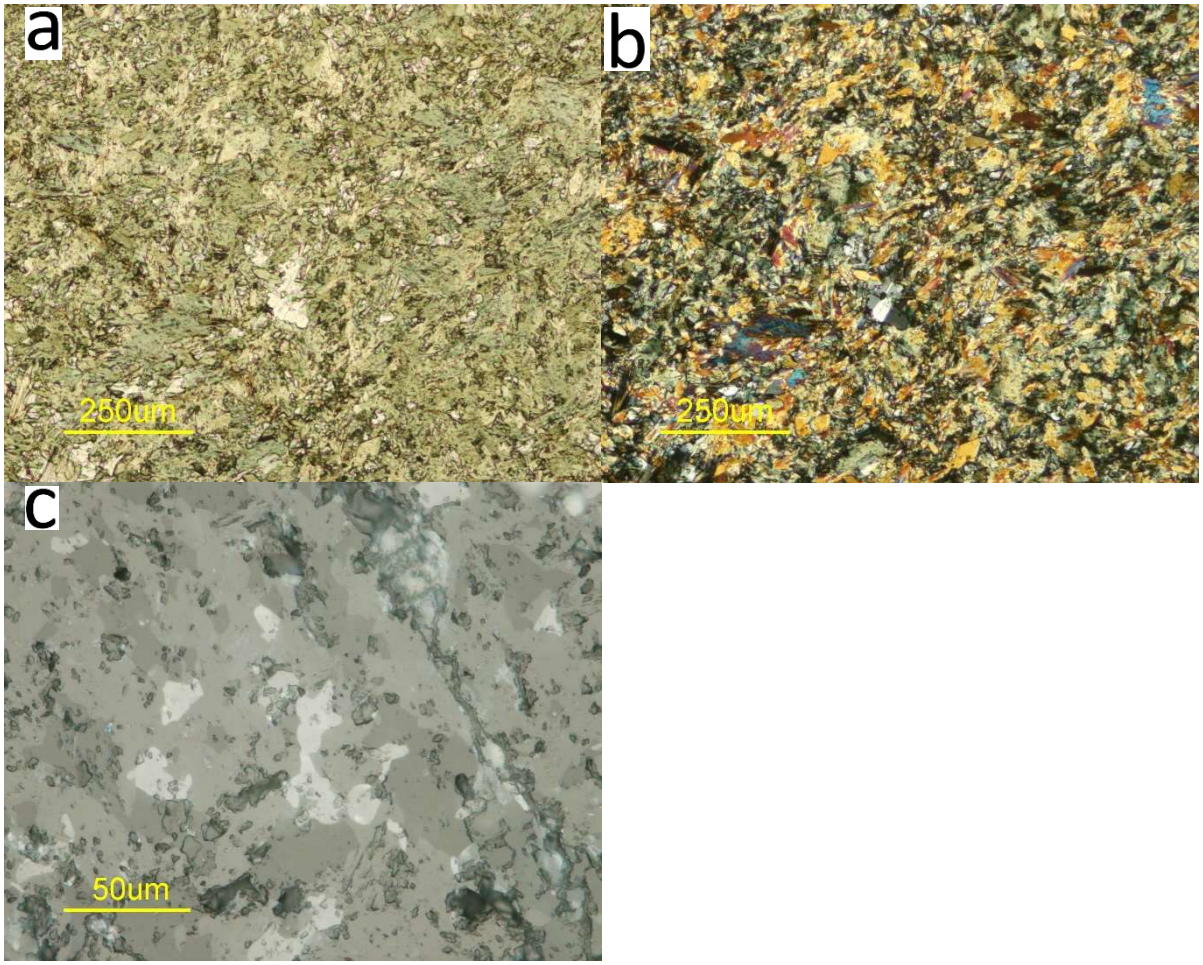

Figure 3-33 – Photomicrographs of J065 (UTM 28 759175 mE, 2712626 mN) - fine-grained amphibole-rich mafic rock, no fabric. Granular reflective appears to be titanite. Metabasalt. [a) PPL, b) XPL, c) reflected light]

3.3.3.1.4 Carbonatite

The carbonatite shows a fine, granoblastic texture (Figure 3-34). It consists of dolomite, olive coloured chlorite and alteration products. Figure 3-34 c, and d show detail of the fine granoblastic dolomite, with partly chloritised phlogopite/biotite.

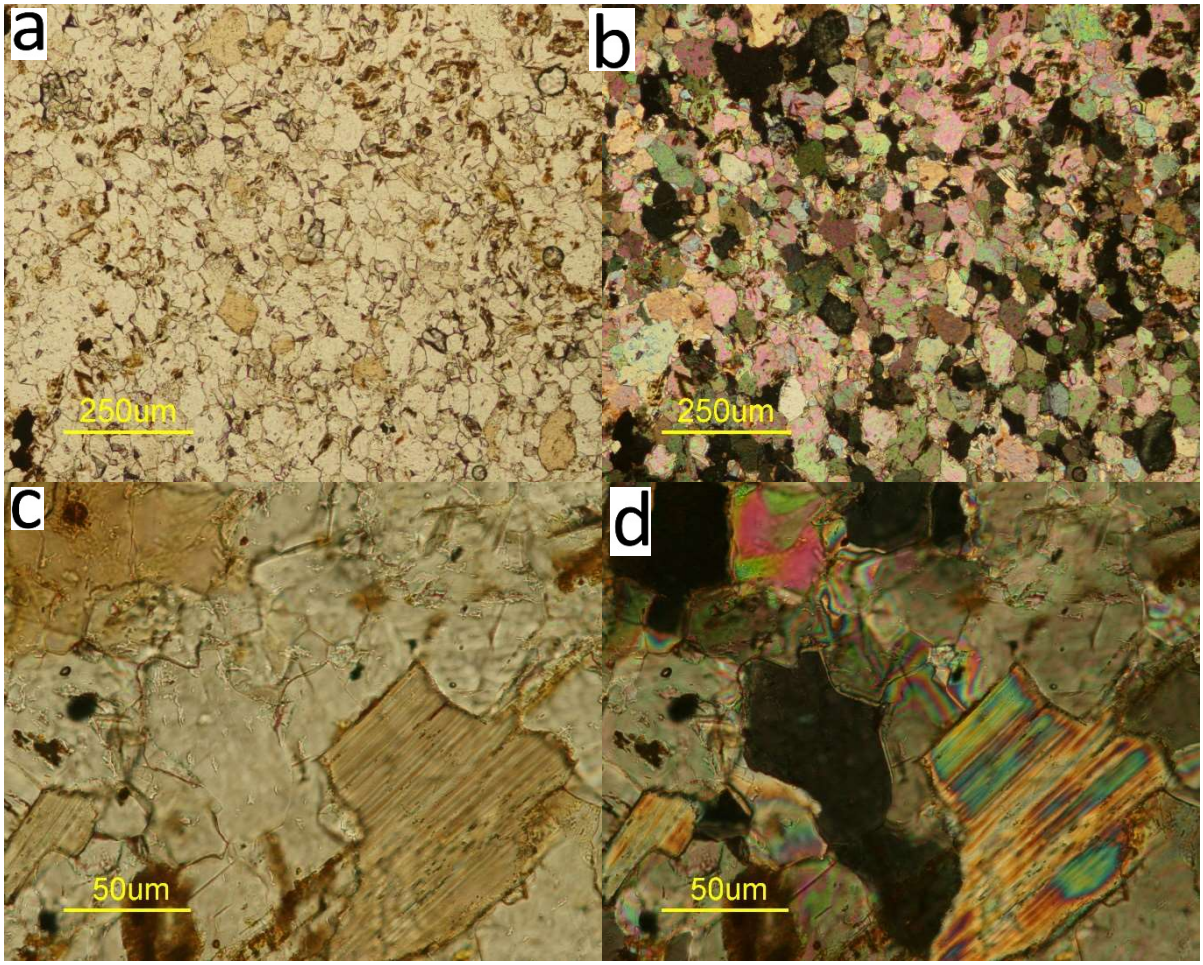

Figure 3-34 - Photomicrographs of J023 (UTM 28 758954 mE, 2711107 mN) - Carbonitite, a, b) general view showing hranoblastic texture of the dolomite [a) PPL, b) XPL]. c, d) Fine granoblastic dolomite with partially chloritized phlogopite [c) PPL, d) XPL].

3.3.4 Whole Rock Geochemistry of the Pillow Basalts

For a detailed explanation for the methodology of the whole rock chemistry, see Section 3.5.1.1

3.3.4.1 Traditional Diagrams

Classification diagrams demonstrate variable siliceous alteration of the metabasalts, with Pearce (1996) immobile element proxies plotting the samples with a very similar basaltic

composition (Figure 3-35 a) and the TAS diagram plotting a spread of compositions from basaltic to basaltic andesite (Figure 3-35 b). The samples cluster in the edge of the MORB-OIB array Th-Nb proxy (Figure 3-36a; Pearce (2014)). Pearce (2008) notes that this is a common feature in old (Archaean) terranes, as for a variety of reasons older samples pick up a continental signature (Th) more readily than modern analogues. As recommended by Pearce (2008), a filter was applied (Th/Nb<0.2) to remove any samples that may have experienced crustal contamination before plotting them on the Ti-Nb proxy. The Ti-Nb proxy revealed an N-MORB signature for the basalt (Figure 3-36 b). The samples plot broadly with MORB signatures on the Wood (1980) Th-Hf-Ta, and Th-Zr-Nb plots (Figure 3-37). The Cabanis and Lecolle (1989) La-Y-Nb plot shows the samples as clustering with a back-arc basin signature (Figure 3-38). The AFM plot shows a tholeiitic signature for the basalt (Figure 3-39).

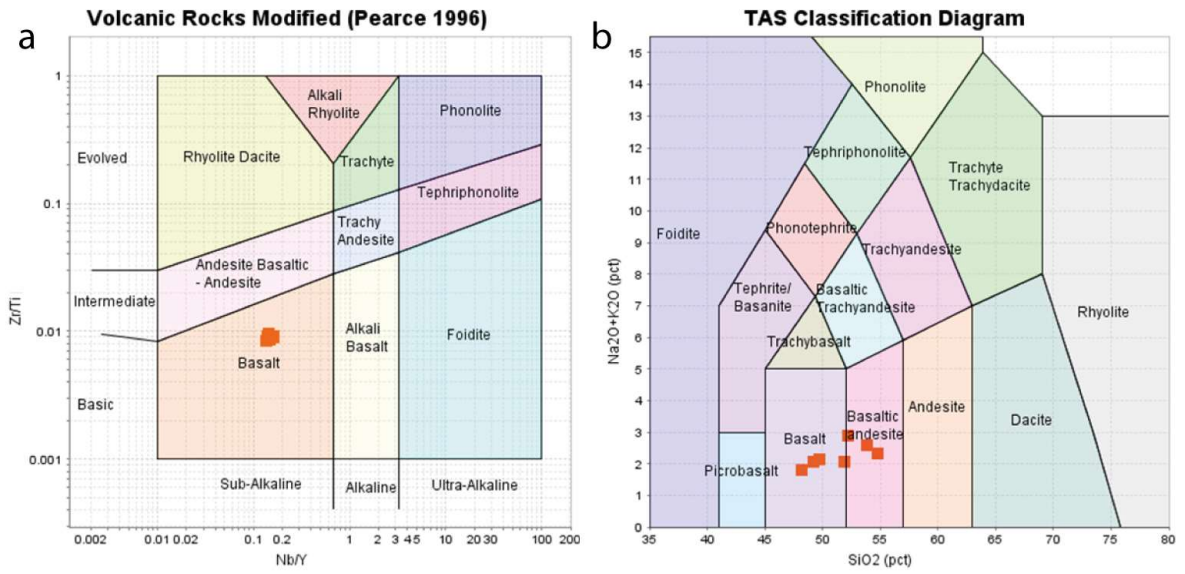

Figure 3-35 – Metabasalts from the mafic-ultramafic complex plotted on classification diagrams for all igneous and meta-igneous rocks from the Leaareig Terrane. a) immobile element based TAS proxy diagram from Pearce (1996) after Floyd and Winchester (1977). b) IUGS-recommended TAS diagram from Le Bas and Streckeisen (1991).

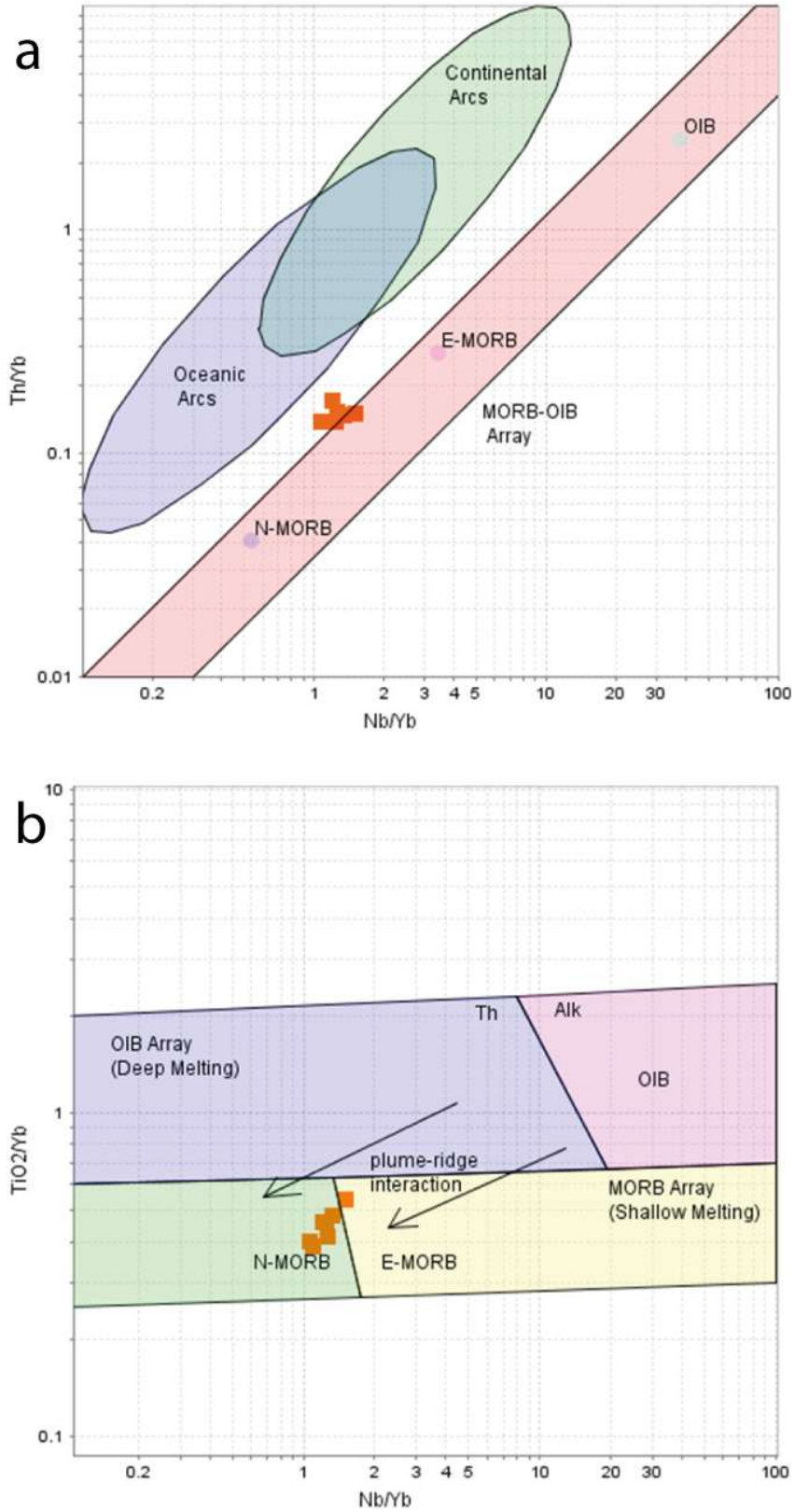

Figure 3-36– Discrimination diagrams for fingerprinting tectonic setting a) Th/Nb proxy to distinguish volcanic arc settings from mid-oceanic ridge/ocean island basalt settings Pearce (2014) adapted from Pearce (2008) b) Ti/Nb proxy to fingerprint samples from the MORB-OIB array (Pearce, 2008). As these are Precambrian samples, an extra filter was applied (Th/Nb < 0.2) to remove samples that may have experienced significant crustal contamination - as recommended by Pearce (2008).

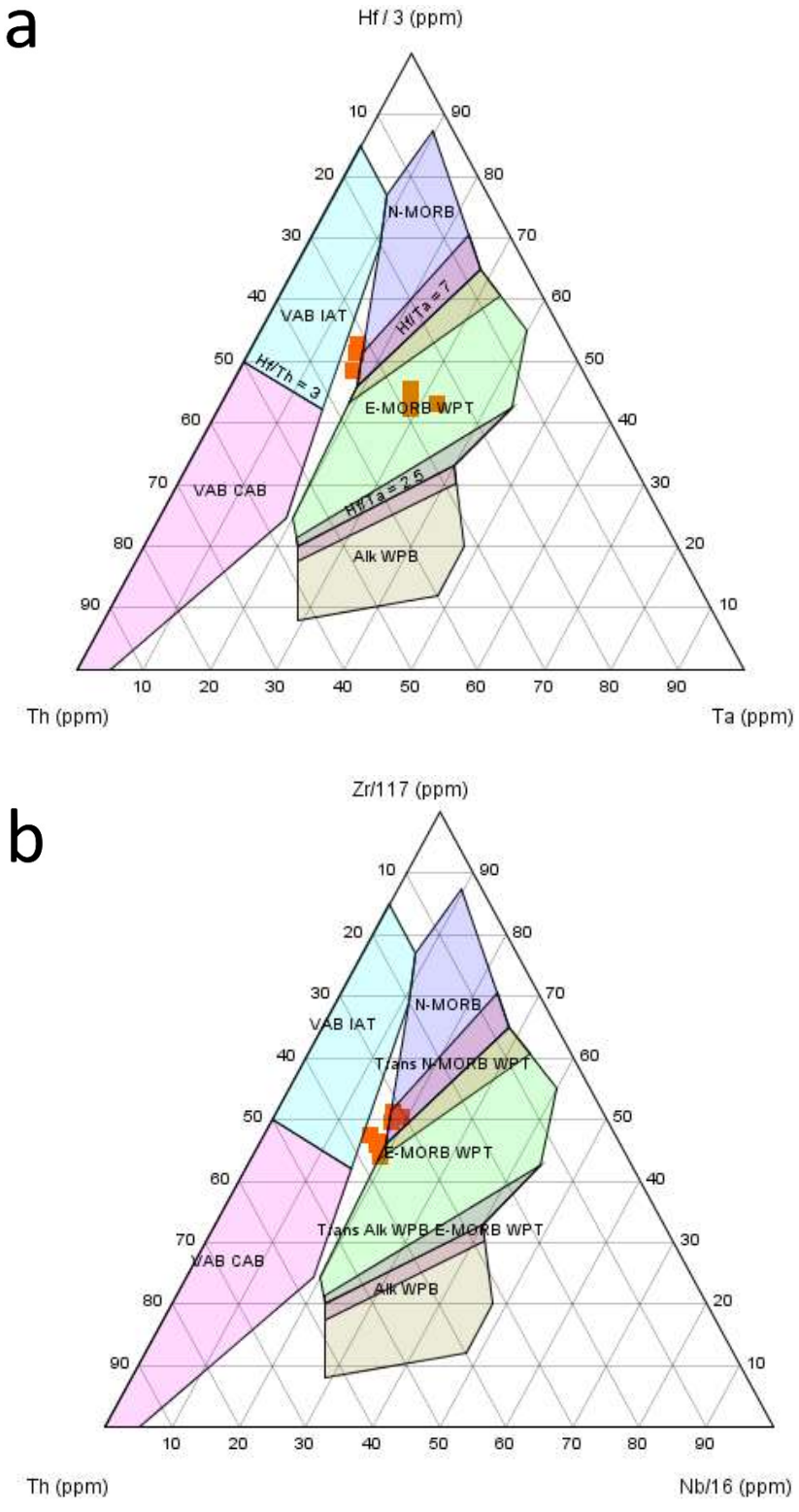

Figure 3-37 – Ternary tectonic discrimination diagrams for mafic and intermediate samples (Wood, 1980) a) Th-Hf/3-Ta discrimination diagram. b) Th-Zr/117-Nb/16 discrimination diagram.

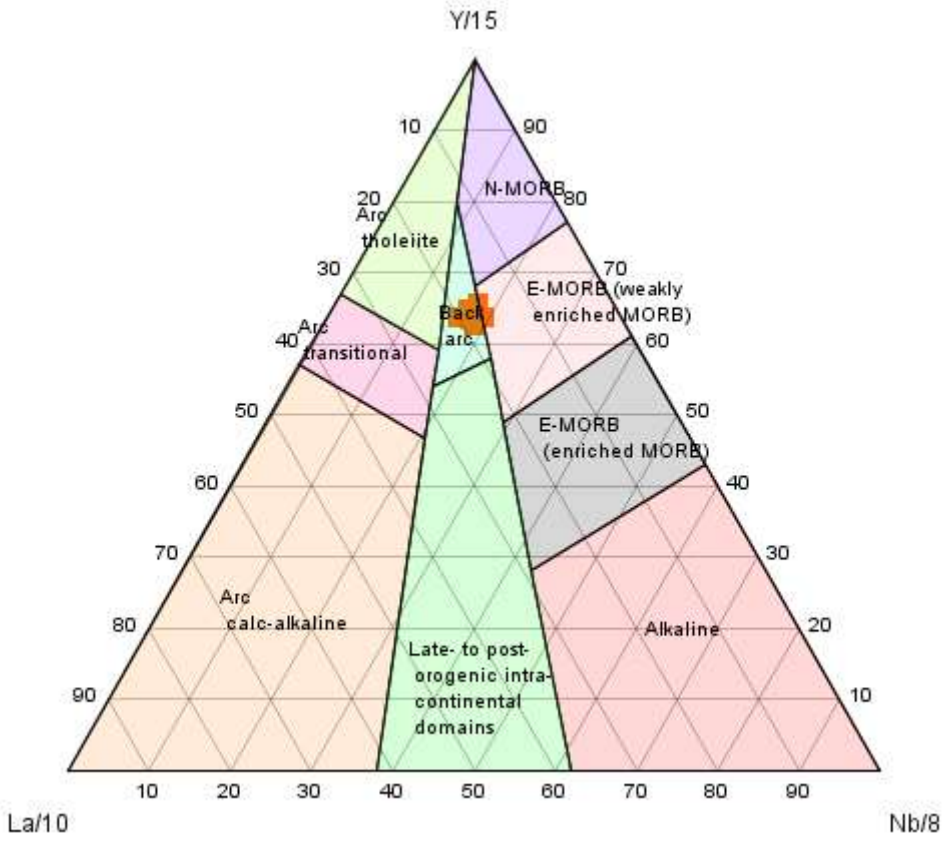

Figure 3-38– La-Y-Nb ternary discrimination diagram (Cabanis and Lecolle, 1989) samples of basalt from the ophiolite sequence at Agarasras Lakhadar

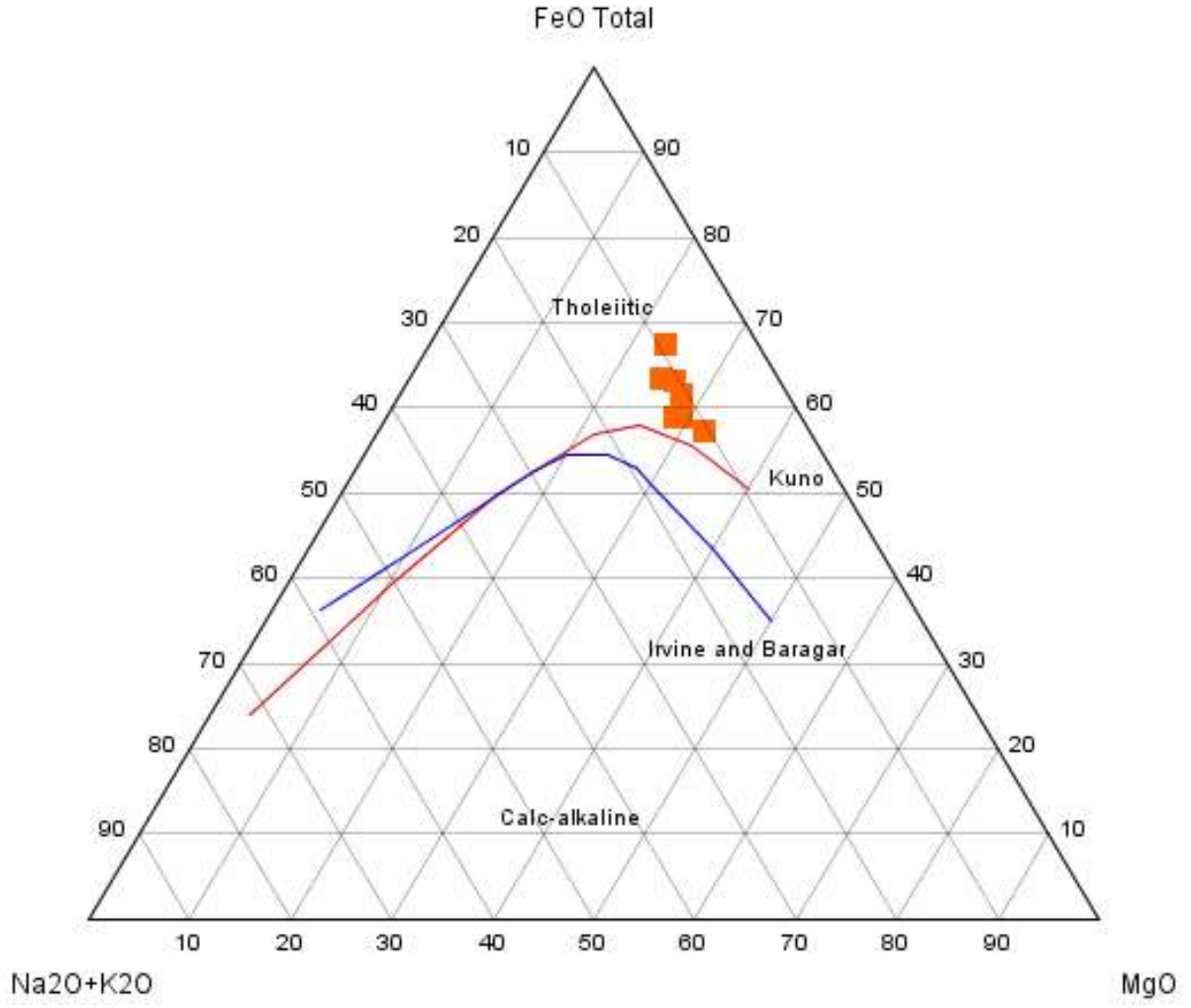

Figure 3-39 – Total Alkali-Iron-Magnesium (AFM) plot (Rollinson, 1993) of all samples within the Leaareig Terrane with Tholeiitic and Calc-alkaline fractionation trends defined by (Kuno, 1968) and (Irvine and Baragar, 1971).

3.3.4.2 Multi-dimensional Tectonic Discrimination Diagrams

Due to alteration, only immobile elements were used for fingerprinting the mafic rocks from the Leaareig Terrane, using the set of five diagrams described by Agrawal et al. (2008). The series of diagrams identifies four tectonic settings for basaltic samples including IAB, MORB, CRB and OIB. In interpreting the results, it must be remembered that only four of the diagrams relate to each tectonic setting. All seven samples of basalt from the ophiolitic sequence at Agarasras Lakhadar plot in the MORB field (Figure 3-40) on the Agrawal et al. (2008) discrimination diagrams.

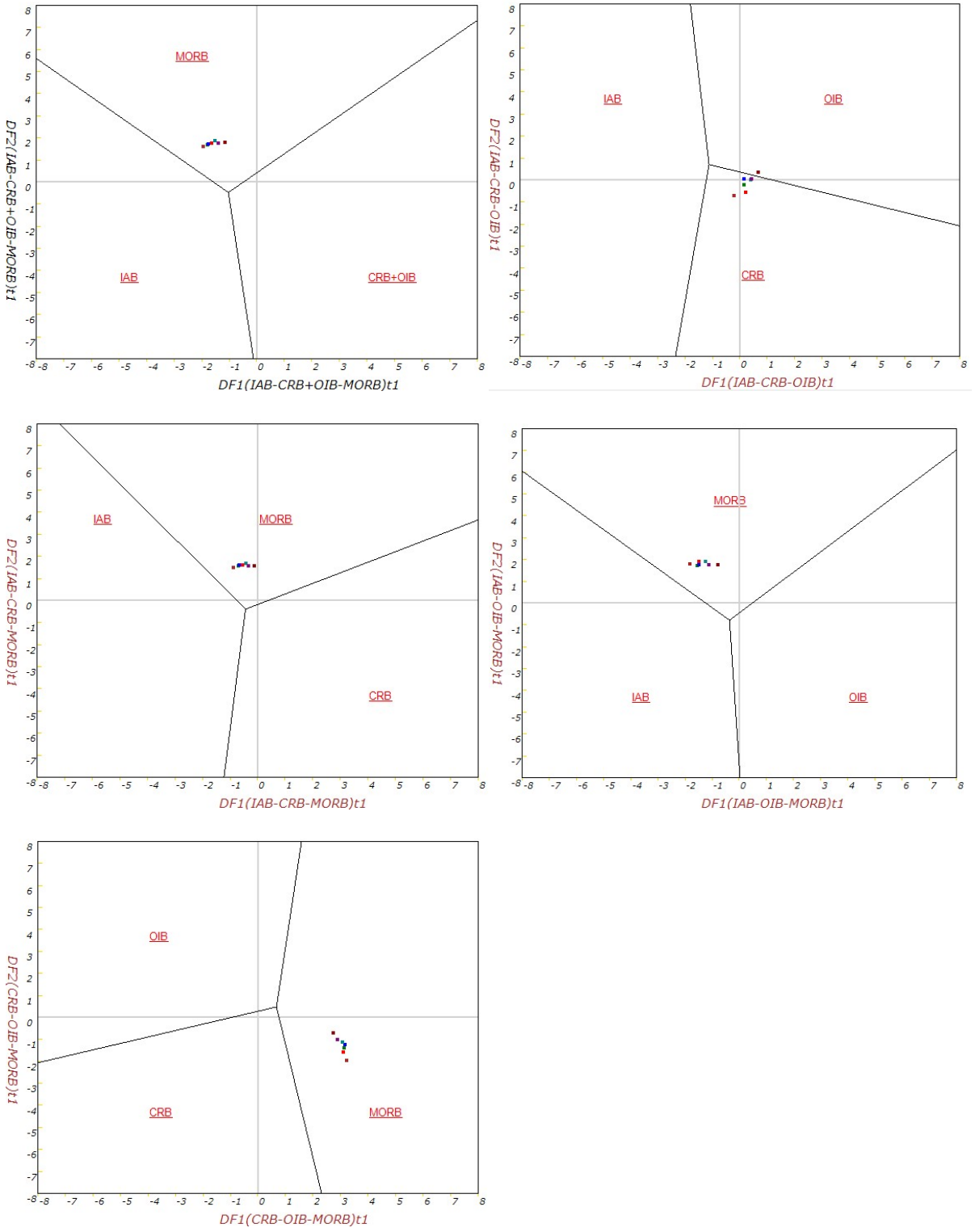

Figure 3-40 – Basalt samples from Agarasras Lakhadar plotted on a set of five multi-dimensional discrimination diagrams based on immobile trace elements (Agrawal et al., 2008).

3.3.5 Discussion and Tectonic Setting

Several geochemical discrimination diagrams indicate a MORB tectonic setting for the basalt at the top of the mafic-ultramafic complex (Section 3.3.4). The Cabanis and Lecolle (1989) La-Y-Nb plot, however, shows the samples as clustering with a back-arc basin signature (Figure 3-38). This is consistent with the interpretation by Combs (2012) that Agarasras Lakhadar represents an ophiolite sequence. Although not directly observed, several lines of evidence (including the presence of an ophiolite sequence) seem to indicate the presence of a thrust fault around the edges of the domain (Section 3.3.2.5), structurally placing the domain on top of the Oum Abana belt. Detrital zircons in the metasedimentary rocks were dated at 2176 ± 32 Ma (Chapter 2) which is similar to other ages from the Leaareig Terrane. Therefore, the Lakhadar Domain is interpreted as the back-arc basin from the arc that was forming the Leaareig Terrane. When subduction ceased in the domain, a section of the back-arc basin was obducted forming the ophiolite. The metabasalt and chert unit represents the sea floor environment, while the metasedimentary rocks represent the accumulation of a mix of terrestrial sediments shed from the Leaareig Terrane (including detrital zircons), and marine carbonates (marble).

3.4 Sassaiate -Temmimichate-Tsabaya Complex

3.4.1 Introduction

The Sassaiate-Temmimichate-Tsabaya Complex is the southernmost Palaeoproterozoic Domain of the Reguibat Shield, with its southern contact defining the Archaean-Palaeoproterozoic contact. The complex outcrops in Mauritania, where it was mapped as the Temmimichate-Tsabaya Complex, consisting of mafic and ultramafic gneisses and calcsilicate rocks (Schofield et al., 2006). With no previous geochronological constraints, the unit was thought to be part of the Archaean Terrane.

3.4.2 Geology and Structure (Mapping/field relations)

The complex comprises intermediate to mafic orthogneisses, paragneiss and, amphibolite, as well as thick beds of marble and iron-formation (Figure 3-41).

Beds of marble are very thick in the west (up to 1km; Figure 3-42 a, b and c), with a lower proportion of marble and thinner beds in the east. The marble is cross-cut by an iron rich rock with botryoidal textures (Figure 3-42 d). Amphibolite (metabasalt) up to ~20m wide are interbedded with the marble (Figure 3-43). The contains a well-developed fabric and is mylonitic in places (Figure 3-44).

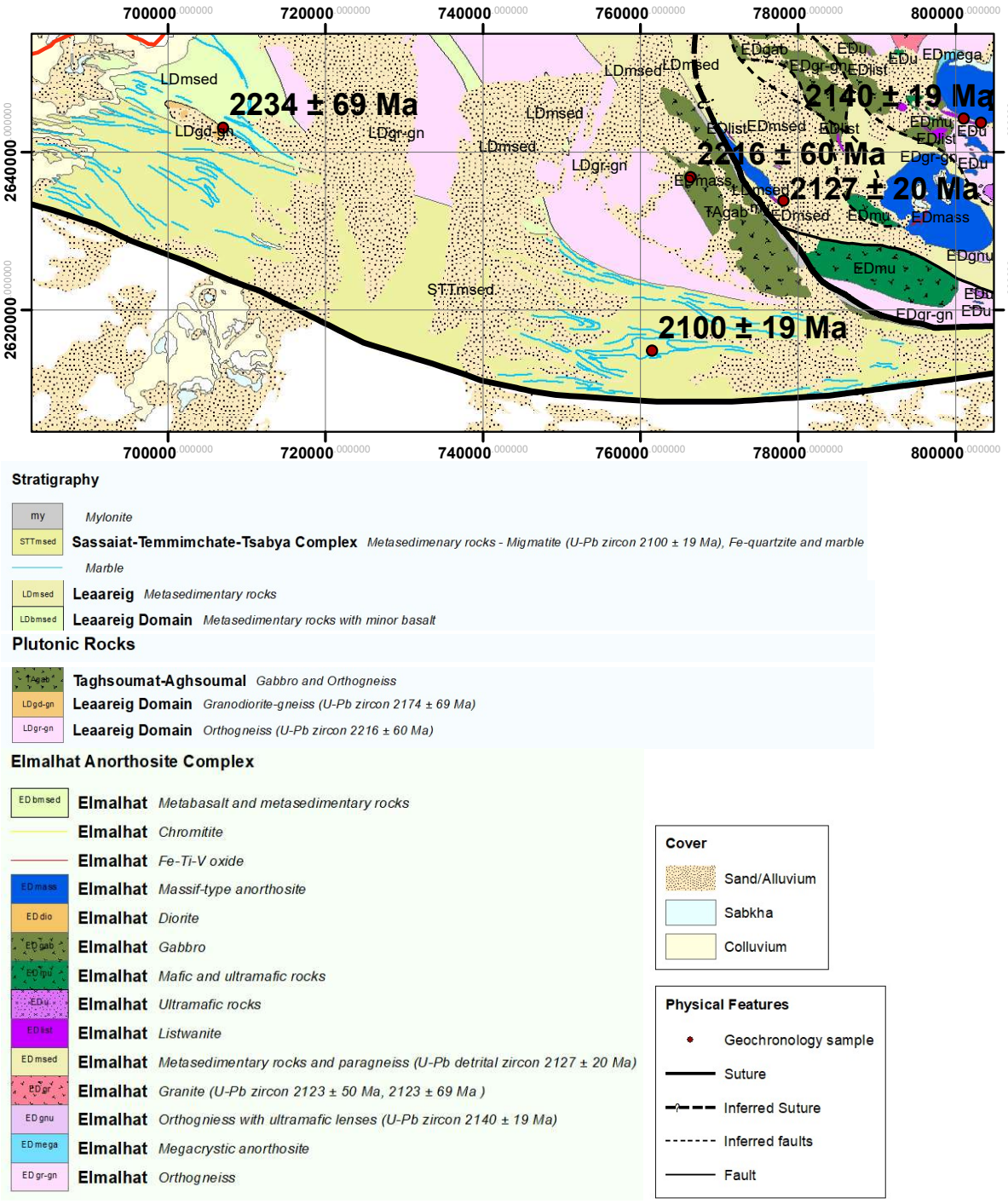

Figure 3-41 – Detailed geology of the Sassaiate-Temmimichate-Tsabaya Complex (UTM Zone 28N). For location map, see the blue square in Figure 3-2.

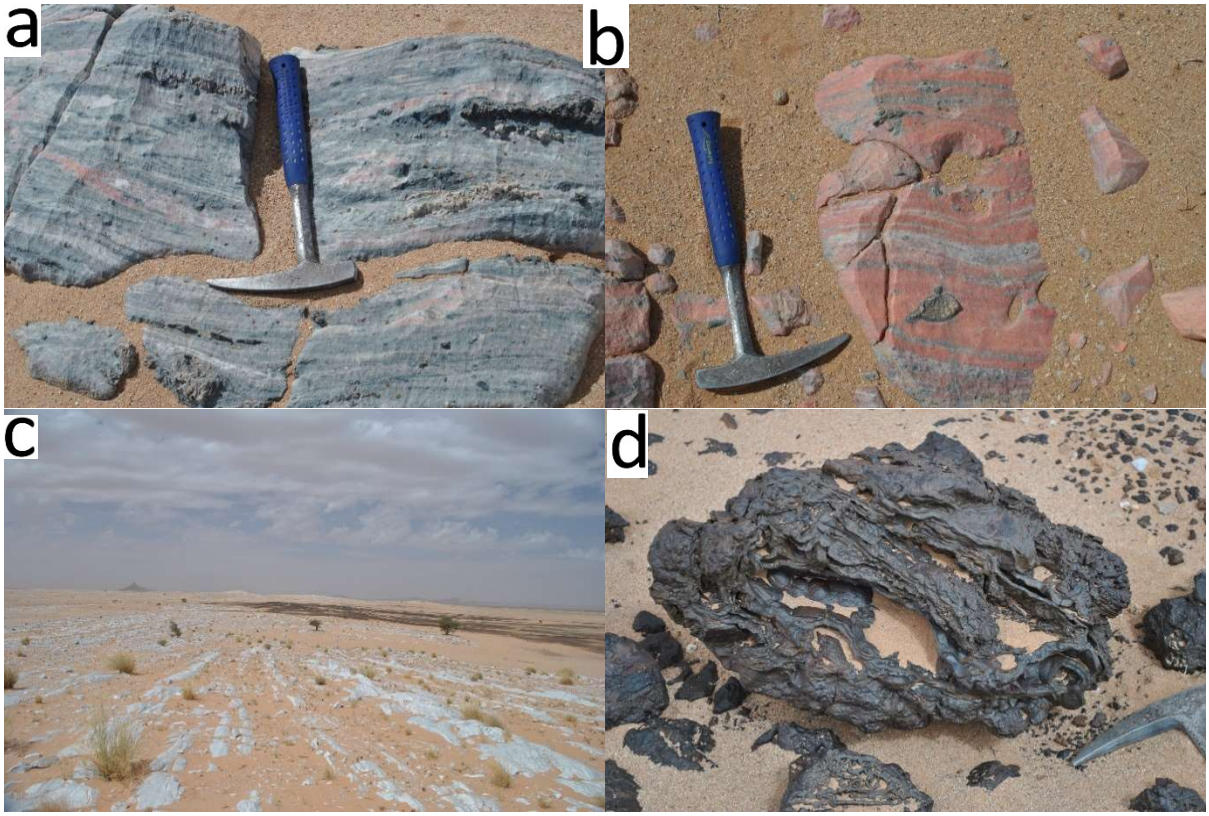

Figure 3-42 – a, b) Field photographs of variations in the appearance of marble within the complex (UTM 28 696005 mE, 2639570 mN). c) extensive outcrops of marble, cross-cut by the discordant iron formation (UTM 28 696322 mE, 2639099 mN). d) Iron formation cross-cutting the marble (UTM 28 696142 mE, 2639105 mN).



Figure 3-43 – Field photographs of amphibolite (metabasalt). Photo by Laurence Robb (UTM 28 696142 mE, 2639105 mN).



Figure 3-44 – Field photographs of migmatitic gneiss within the complex. Location of geochronology sample J238 (UTM 28 696142 mE, 2639105 mN - photo by Laurence Robb)

3.4.3 Age of the Complex

With no previous geochronological constraints, the unit was thought to be part of the Archaean Terrane (Rocci et al., 1991, Schofield and Gillespie, 2007). U-Pb zircon geochronology by Lehbib (2016) on a sample of tonalite (2099.3 ± 15 Ma) and as a part of this study (Table 2.1; Chapter 2) on a sample of migmatite (2100 ± 19 Ma) demonstrated that the complex is Palaeoproterozoic in age, and hence the Archaean-Palaeoproterozoic boundary is placed to the south of the complex.

3.5 **Geochemistry and tectonic setting**

3.5.1 Whole Rock Geochemistry

3.5.1.1 Introduction to Tectonic Discrimination diagrams

Tectonic discrimination diagrams can be a very useful tool in identifying tectonic environments, although they must be applied critically, incorporating all available information including field relationships, petrology and mineralogy (Rollinson, 1993; and references therein). Although a number of discrimination diagrams have been proposed for mafic igneous rocks (Rollinson, 1993, Verma, 2010), relatively few diagrams have been designed for the tectonic discrimination of felsic magmas and granitic rocks (eg. Pearce et al., 1984) or for intermediate magmas (Verma et al., 2013). Nevertheless, lavas of andesitic composition are often plotted on discrimination diagrams designed for mafic rocks (Rollinson, 1993).

In evaluating the effectiveness of traditional bivariate or ternary tectonomagmatic diagrams, Verma (2010) concluded that most of them provided low success rates and/or only allowed discrimination of a limited number of plate tectonic settings. Major flaws prevalent in all of them included the use of limited databases, the problem of closed or constant sum compositional variables, and tectonic field boundaries fitted by eye (Agrawal and Verma, 2007).

The most commonly used discrimination diagram for granitic rocks is that proposed by Pearce et al. (1984), who loosely defined the term ‘granite’ to apply to apply to any plutonic rock containing more than 5% modal quartz (Rollinson, 1993). The Pearce et al. (1984) diagrams proved no exception to the problems highlighted by Verma et al. (2012), who noted that many of the fields overlap and that mobile elements such as Rb are used in the axis. As a result, Verma et al. (2012) concludes that the Pearce et al. (1984) diagrams perform poorly in identifying collisional settings and have only limited success in discriminating between

volcanic-arc and within-plate settings. Verma et al. (2012), therefore argued that new multi-dimensional diagrams could be a better option for better tectonic discrimination, especially with felsic and intermediate rocks. These authors proposed nine sets of multi-dimensional diagrams based on either all major elements [(SiO_2), (TiO_2), (Al_2O_3), (FeO), (Fe_2O_3), (MnO), (MgO), (CaO), (Na_2O_3), (K_2O), and (P_2O_5) in wt%]; a combination of selected relatively immobile major and trace elements [(TiO_2), (MgO), and (P_2O_5) in wt% and Nb, Ni, V, Y, and Zr in ppm]; or selected relatively immobile trace elements [La, Ce, Sm, Yb, Nb, Th, Y, and Zr in ppm] (Verma, 2017).

Due to the fact that all of the major elements add up to 100%, statistical correlations can be induced between sets of major oxides that have the potential to mask important geological correlations (Rollinson, 1993; and references therein). For instance, if a rock contains 65% SiO_2, the sum total of the rest of the major oxides is restricted to a wt% of 35%. This introduces a negative bias in the correlation of SiO_2 with other major oxides – known as the 'closure problem' (Rollinson, 1993). To address this problem Aitchison (1986) proposes the use of ratios of major elements to compare the relative magnitudes of the ingredients rather than raw percentages. These ratios are best presented in (natural) logarithm form, to allow for a wider range of data to be explained (Aitchison, 1986). For this reason, the multi-dimensional, multivariant tectonic discrimination diagrams proposed by Verma et al. (2006), Verma and Agrawal (2011), Verma and Verma (2013), Verma et al. (2012) and Verma et al. (2013) are based on log-ratios of major elements and/or trace elements (listed above). Each diagram presented (as part of the multi-dimensional analysis) involves plotting set of discrimination functions (DF1-DF2) specifically designed to discriminate three or four tectonic settings (see Appendix C2 for the discrimination functions for each diagram). For each diagram, probability values are calculated for each sample (using methods outlined in Agrawal, 1999, Verma and Agrawal, 2011) in order to assign it to a tectonic field. A set of five discrimination function

diagrams are presented for each tectonic interpretation in order to produce a robust interpretation of the tectonic setting.

Two sets of diagrams were developed for use on mafic ((SiO_2) < 52%) magmas (major and immobile trace elements; Verma et al., 2006, Verma and Agrawal, 2011), three sets of the five diagrams for intermediate ((SiO_2) = 52%–63%) magma (major elements, major-trace elements and immobile trace elements; Verma and Verma, 2013) and four sets of the five diagrams for felsic ((SiO_2) > 63%) magma (two sets of major elements, one major-trace elements and one immobile trace elements; Verma et al., 2012, Verma et al., 2013). The discrimination diagrams for mafic magmas identifies four different tectonic settings including island arc basalt (IAB), continental rift basalt (CRB), ocean-island basalt (OIB), and mid-oceanic ridge basalt (MORB). The discrimination diagrams for felsic and intermediate magmas distinguish four tectonic settings (island arc (IA), continental arc (CA), within-plate (WP), and continental collision (COL)). This was the first time that a geochemical diagram has been able to differentiate the very similar tectonic settings of island and continental arcs (Verma et al., 2012, Verma and Verma, 2013). Subsequently Pearce (2014) presented separate fields for these settings for mafic magmas in a refined version of the Pearce (2008) Th/Yb-Nb/Yb or 'Th-Nb proxy' diagram.

Verma et al. (2013) applied their newly developed set of discrimination diagrams for felsic rocks on nine Precambrian case studies. The results obtained were consistent with previous interpretations in the literature, although they found that island and continental-arc settings can sometimes be difficult to discriminate. Verma (2017) applied these multi-dimensional discrimination diagrams on thirteen existing geochemical datasets of Precambrian rocks from across Africa, including the Birimian (from southern Ghana). In this study all sets of diagrams were applied respectively to mafic, intermediate and felsic rocks. It was found that in most cases the results obtained were consistent with the tectonic setting already interpreted. These

diagrams therefore represent a good tool for identification of tectonic settings in Precambrian rocks.

In order to identify the tectonic setting of oceanic basalts Pearce (2008) proposed two tectonic discrimination diagrams with a Th-Nb proxy for differentiation of volcanic arc basalts from oceanic basalts (MORB and OIB), with a Ti-Yb proxy to differentiate MORB from OIB (Figure 3-45). Both Th and Nb are both highly incompatible elements during mantle melting, though have significantly different properties in subduction settings where Nb is still immobile, but Th is mobile (Pearce, 2008, Pearce, 2014). This results in a high higher Th/Nb ratio in subduction settings compared to oceanic settings (Pearce, 2008, Pearce, 2014). As continental crust is, at least partially, derived from volcanic arc magmatism, it too has a high Th/Nb ratio (Pearce, 2008, Pearce, 2014). Based on this relationship, Pearce (2008) proposed a discrimination diagram, normalising Th and Nb against Yb, in order to differentiate oceanic basalts from those produced in a volcanic arc setting with continental input (Figure 3-45a). This proxy was further refined by Pearce (2014) to differentiate oceanic arc settings from continental arc settings based on the degree of crustal input. The Ti-Yb proxy is based on the behaviour of Ti and Yb at different depths of melting (Pearce, 2008, Pearce, 2014). During shallow melting (from spinel peridotites), Ti and Yb are partitioned similarly into the melt, though during deep melting (from garnet peridotites), the Yb is partitioned strongly into garnet and therefore is retained in residual grains of garnet. Therefore, deeper melting is reflected in a higher Ti/Yb ratio (Pearce, 2008, Pearce, 2014). Pearce (2008) proposed a tectonic discrimination diagram to reflect the chemistry of deep melting in a OIB setting compared to the shallow melting at a MORB setting.

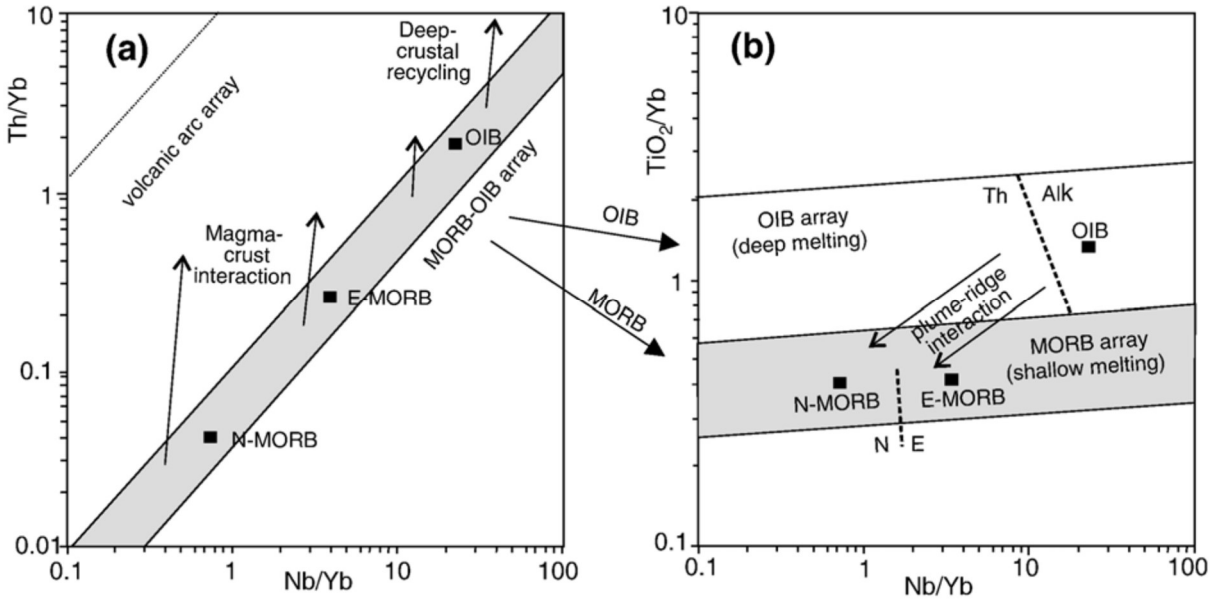

Figure 3-45 – Two discrimination diagrams proposed by Pearce (2008). (a) the Th–Nb proxy for crustal input highlighted in where oceanic basalts plot within the MORB–OIB array (shaded) and volcanic arc basalts plot above the array. Vectors show the effects of crustal input and deep-crustal recycling. (b) utilizes the Ti−Yb proxy for deep melting where OIB have higher Ti/Yb ratios than MORB reflecting deeper melting, resulting from a combination of a thicker lithospheric cap and hotter mantle temperatures. Within the OIB field, alkalic basalts have the higher Nb/Yb and Ti/Yb ratios. Within the MORB field, N-MORB lie to the left of the array and E-MORB to the right of the array. Plume-distal ridges tend to produce N-MORB in the upper part of the MORB field, whereas plume-proximal ridges plot in the lower part of the MORB field. In regions of plume−ridge interaction, basalts follow a diagonal trend from the tholeiitic OIB to the MORB array. Data from oceanic plateaus typically cluster in the centre of the MORB array.

Care must be taken when applying traditional discrimination diagrams to very old rocks (Rollinson, 1993, Pearce, 2008). The trace element composition of mantle source regions have likely changed through time and the mantle may have been less fractionated in early Earth history meaning that the boundaries will be in different places (Rollinson, 1993). Additionally with higher temperatures in the Archaean, higher degrees of mantle melting and a greater likelihood of crustal melting must be taken into account (Pearce et al., 1984).

Pearce (2008) notes that very few Archaean suites plot within the 'OIB-MORB' array on the Th-Nb proxy. Pearce (2008) explains this by arguing that in the Archaean, the magmas were hotter and the Th content of felsic rocks was higher than modern analogues, and therefore Archaean magmas were more sensitive to magma-crust interaction. Therefore, caution is warranted when applying the Th–Nb proxy to define old oceanic basalts, with Pearce (2008)

recommending that a filter be applied (Th/Nb < 0.2) to remove the effect of crustal contamination.

For this review, a combination of traditional bivariate and ternary discrimination diagrams will be presented alongside the newly developed multi-dimensional diagrams to produce a robust tectonic interpretation for the terrane. Traditional bivariate and ternary discrimination diagrams largely focus on fingerprinting mafic magmas, thus will be useful to apply to mafic rocks from the region – though caution is required in applying these to these old rocks (~2.24-2.09Ga). The multi-dimensional diagrams fill the gap for the tectonic interpretation of intermediate and felsic rocks and will therefore provide a more robust interpretation for their setting.

3.5.1.2 Traditional tectonic discrimination diagrams

Twenty-five samples from the Leaareig Terrane were analysed for whole rock major and trace element geochemistry using ICP-MS facilities at ALS geochemistry laboratories in Dublin, Ireland (Appendix C). Samples from the Agarasras Lakhadar Terrane were presented in Section 3.3.4 as part of the interpretation for the ophiolite sequence and have therefore been excluded from the analyses presented below unless otherwise stated.

Data plotted on immobile element-based discrimination diagrams must first be filtered according to rock type (Pearce, 2014). Pearce (2014) highlights the importance of the correct classification of rocks, with some discrimination diagrams only applicable to specific rock types. For fresh rocks, they could be classified using a IUGS total alkali-silica (TAS) diagram (Figure 3-46a; Le Bas and Streckeisen (1991)), although these elements (K, Na and Si) are mobile. Therefore, Pearce (2014) recommends classifying them according to immobile element proxies for use in tectonic discrimination diagrams. Pearce (1996) adapted a diagram devised by Floyd and Winchester (1977) using Nb/Y as a proxy for total alkalis and Zr/Ti as a proxy for SiO_2 (Figure 3-46b). Therefore for use in traditional tectonic discrimination diagrams, these classifications will be used.

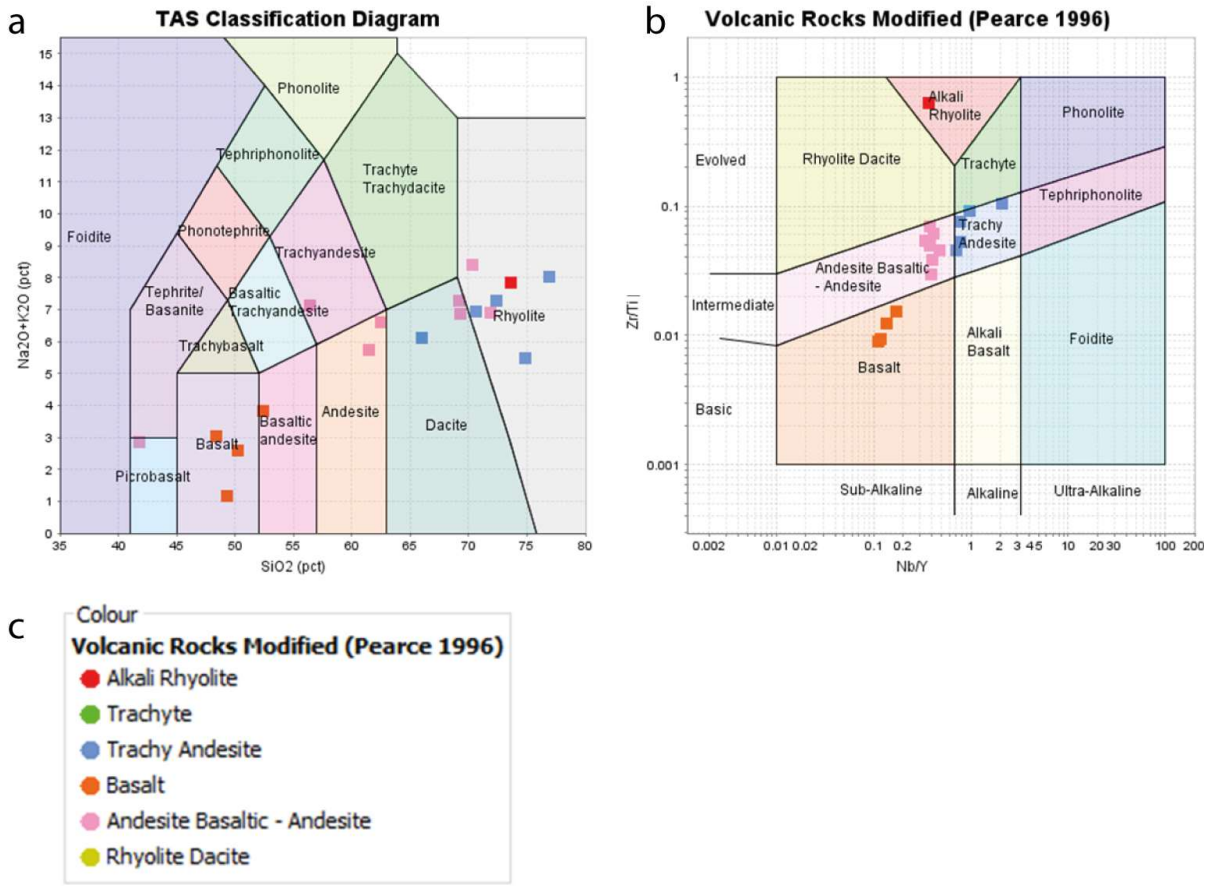

Figure 3-46 – Classification diagrams for all igneous and meta-igneous rocks from the Leaareig Terrane. a) IUGS-recommended TAS diagram from Le Bas and Streckeisen (1991). b) immobile element based TAS proxy diagram from Pearce (1996) after Floyd and Winchester (1977). c) legend for rock-type for the rest of Chapter 3.5.1 – based on Pearce (1996) classification

3.5.1.2.1 Mafic and intermediate rocks

The Th-Nb proxy (Figure 3-46; Pearce (2014)) illustrates that that mafic rocks within the Leaareig Terrane have a MORB signature with variable crustal input with one sample showing a mixed oceanic arc-continental arc signature. The samples display more of a continental arc signature with increasing SiO_2, with andesitic-basalt and trachy-andesite displaying continental arc signatures. Pearce (2008) notes that old samples pick up crustal signatures very easily, so that mafic suites may be difficult to interpret. Therefore, as recommended by Pearce (2008), a filter was applied to the cluster of samples on the edge of the MORB-OIB array (Figure 3-49 a) to remove samples with significant crustal contamination before the application of the Ti-

Yb proxy. The Ti-Yb proxy (Figure 3-47b) indicates that the basaltic samples in that cluster have an N-MORB affinity.

When plotted on the Th-Hf/3-Ta and Th-Zr/117-Nb/16 ternary discrimination diagrams (Figure 3-48) from Wood (1980), the basalts also show MORB characteristics, with more intermediate samples showing a calc-alkaline, volcanic arc affinity (consistent with the Pearce (2014) Th-Nb plot). The La-Y-Nb plot (Cabanis and Lecolle, 1989) shows that basalts in the terrane largely plot in the back-arc/NMORB section of the plot with intermediate samples reflecting a calc-alkaline, volcanic arc signature (Figure 3-49a). Basalt samples from Agarasras Lakhadar, interpreted to form part of an ophiolite sequence, display a back-arc basin signature (Figure 3-49b). The AFM plot (Irvine and Baragar, 1971, Kuno, 1968, Rollinson, 1993) shows a cluster of basaltic compositions of tholeiitic affinity as well as a calc-alkaline fractionation trend from one point of basalt, through intermediate compositions, to felsic (Figure 3-50).

Notably, the samples of tholeiitic MORB/back arc basin affinity are located in the Taghsoumat-Aghsoumal Belt, proximal to the proposed suture between the Leaareig and Sfariat-Bu Daira Terranes.

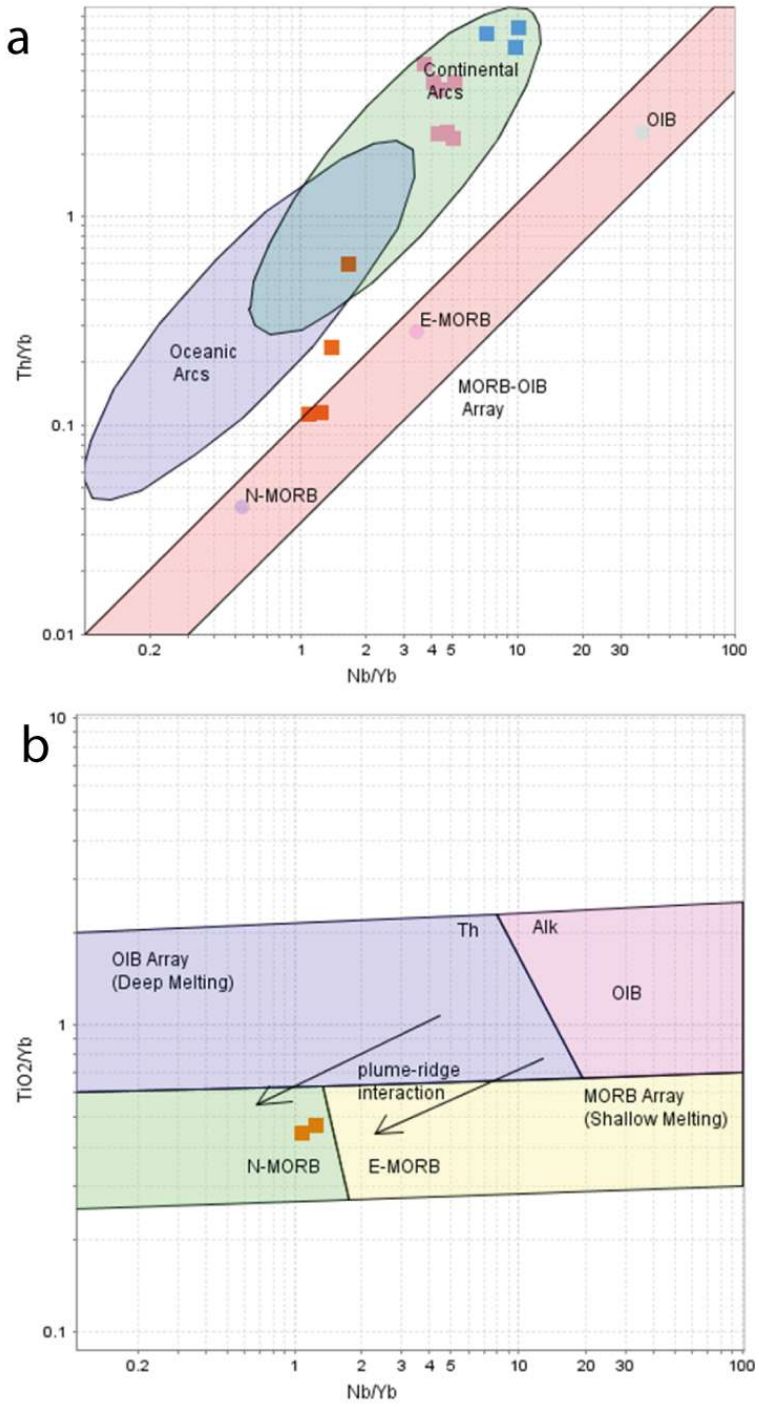

Figure 3-47 – Discrimination diagrams for fingerprinting tectonic setting a) Th/Nb proxy to distinguish volcanic arc settings from mid-oceanic ridge/ocean island basalt settings Pearce (2014) adapted from Pearce (2008) b) Ti/Nb proxy to fingerprint samples from the MORB-OIB array (Pearce, 2008). As these are Precambrian samples, an extra filter was applied (Th/Nb<0.2) to remove samples that have experienced significant crustal contamination - as recommended by Pearce (2008).

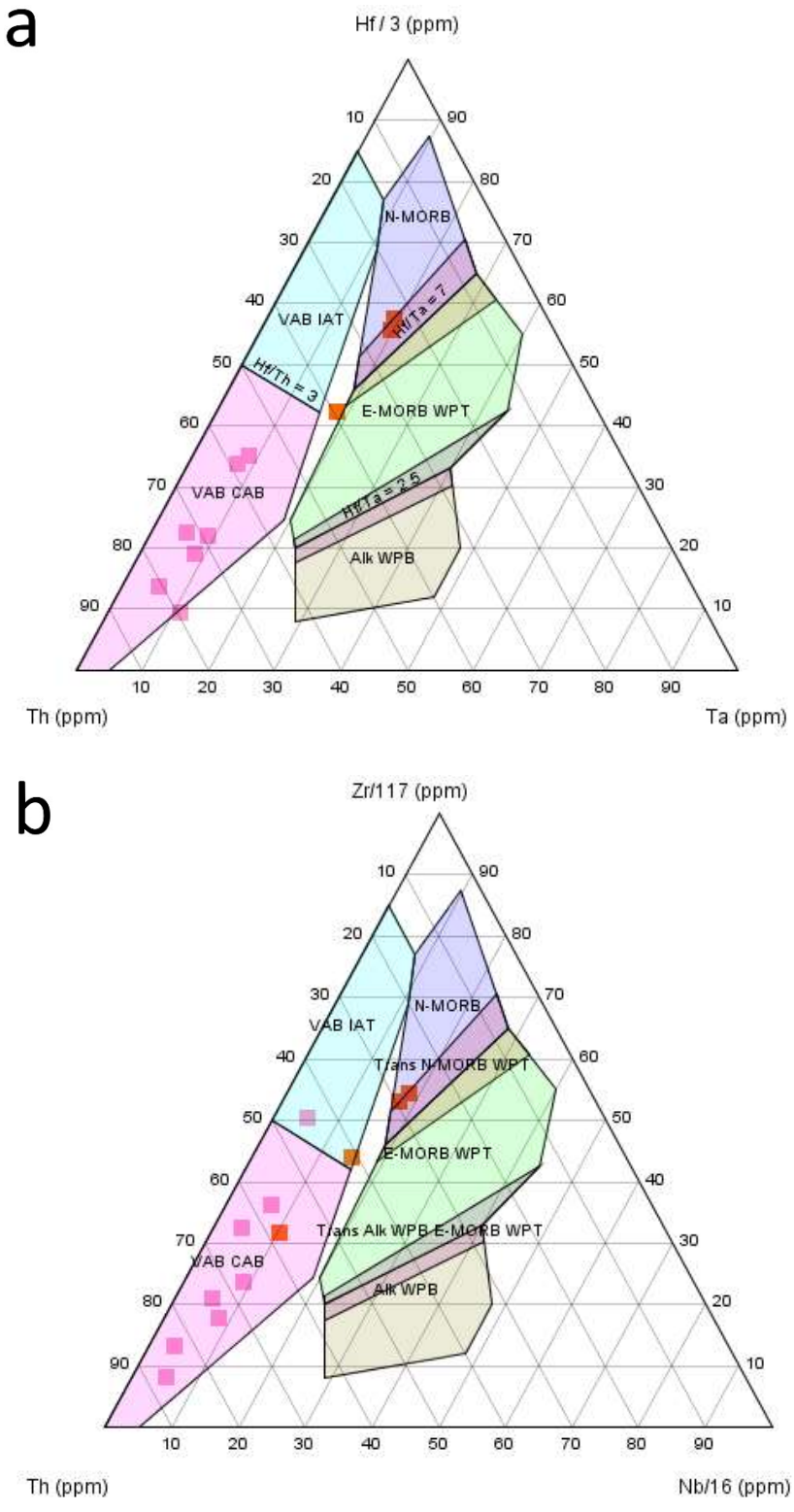

Figure 3-48 – Ternary tectonic discrimination diagrams for mafic and intermediate samples (Wood, 1980) a) Th-Hf/3-Ta discrimination diagram. B) Th-Zr/117-Nb/16 discrimination diagram.

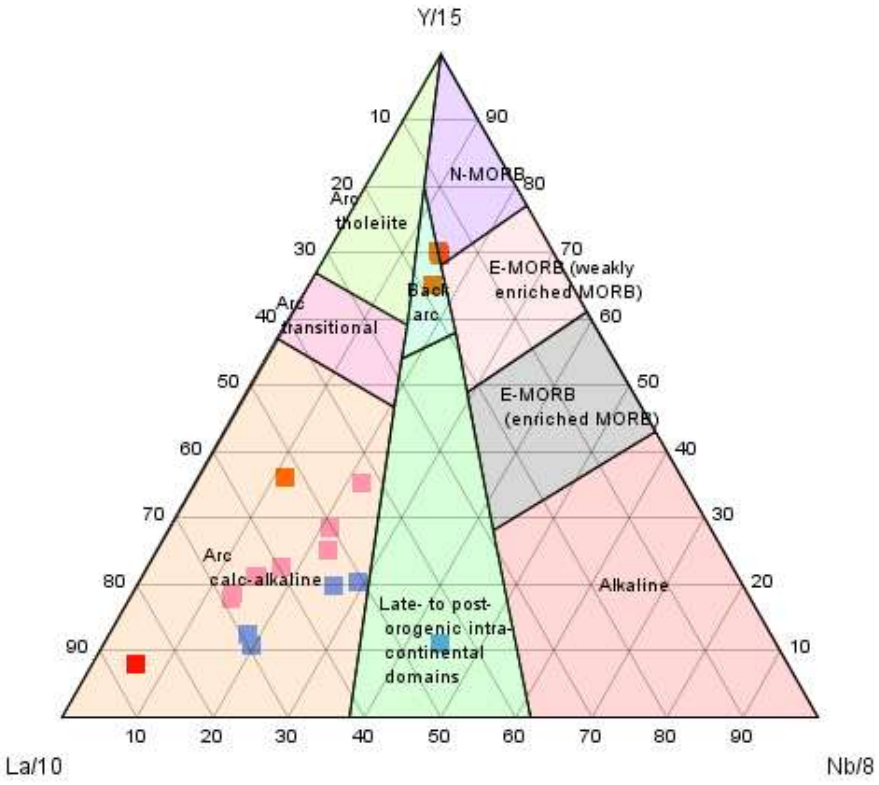

Figure 3-49 – La-Y-Nb ternary discrimination diagram (Cabanis and Lecolle, 1989).

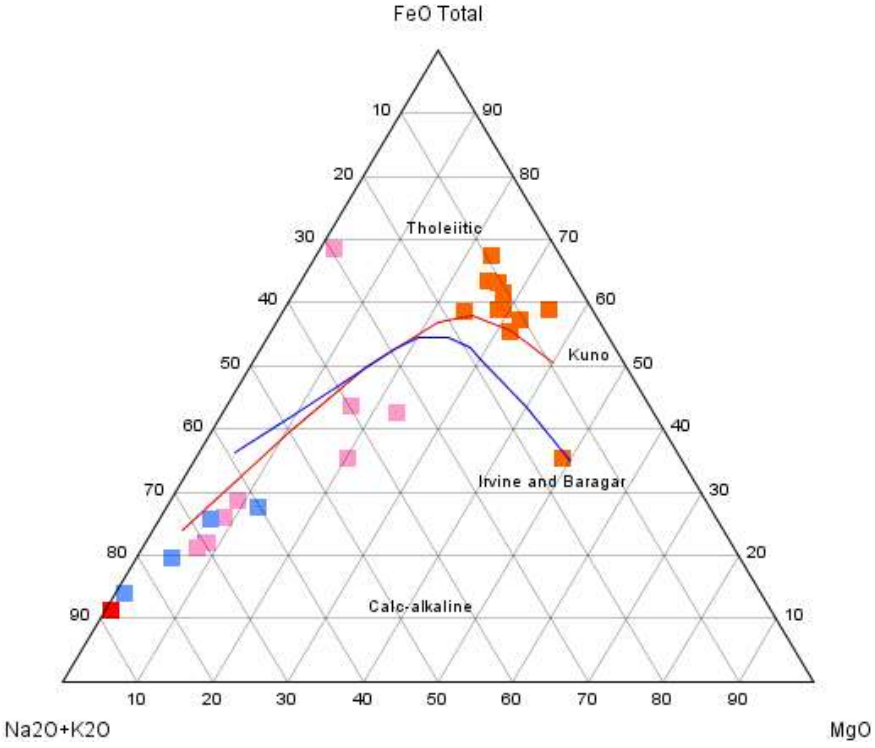

Figure 3-50 - Total Alkali-Iron-Magnesium (AFM) plot (Rollinson, 1993) of all samples within the Leaareig Terrane (including Agarasras Lakhadar) with Tholeiitic and Calc-alkaline fractionation trends defined by (Kuno, 1968) and (Irvine and Baragar, 1971).

3.5.1.2.2 Felsic rocks

A series of diagrams presented in Pearce et al. (1984) are the most commonly used discrimination diagram for felsic rocks. Granitic rocks within the Leaareig Terrane display volcanic arc characteristics according to these diagrams (Figure 3-51).

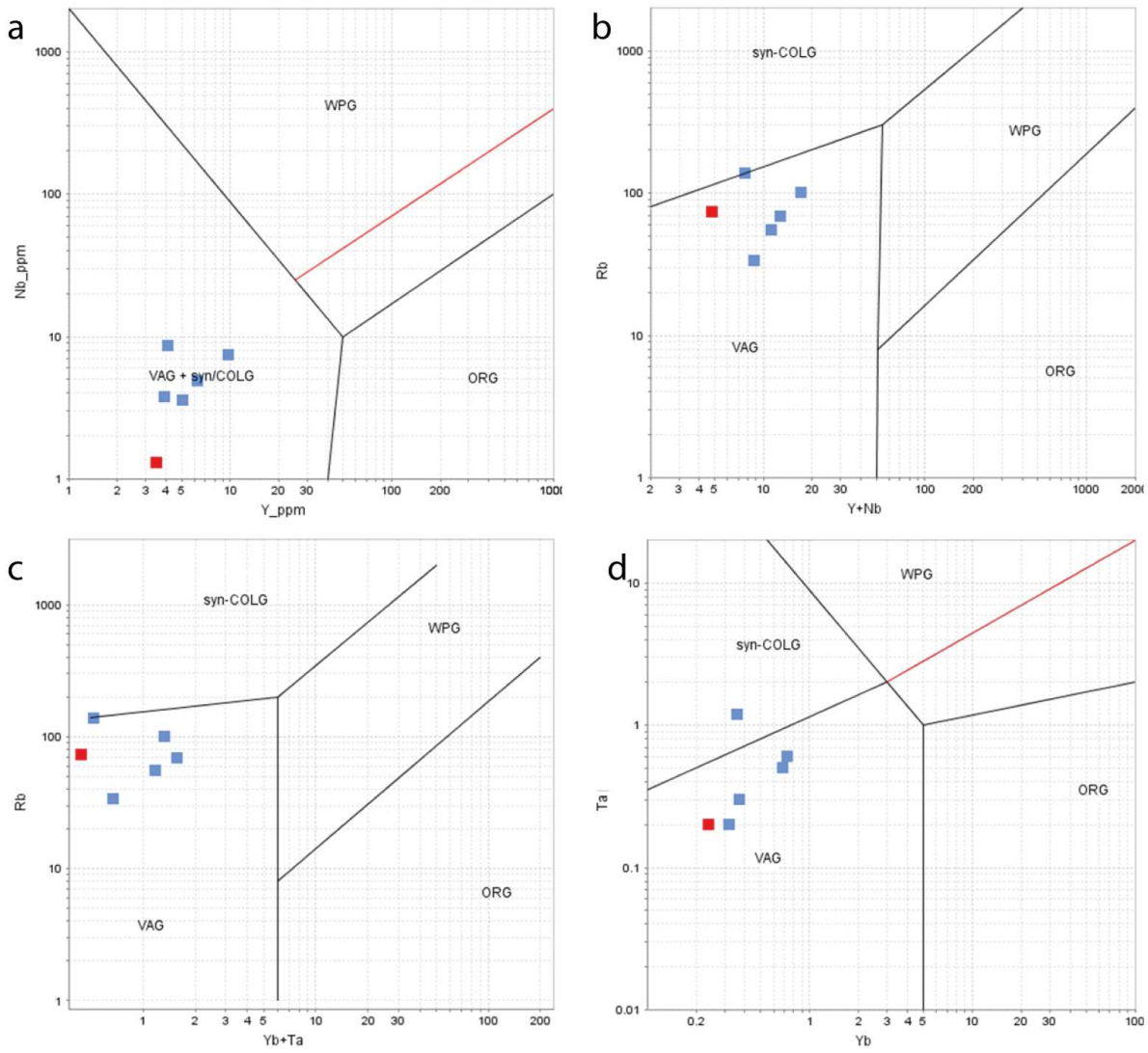

Figure 3-51 – Tectonic discrimination diagrams for granitic rocks (Pearce et al., 1984). VAG – volcanic arc granite, syn-COLG – syn-collisional granite, WPG – within plate granite, ORG – ocean ridge granite. a) Nb vs Y b) Rb vs (Y + Nb) c) Rb vs (Yb + Ta) d) Ta vs Yb.

3.5.1.3 Multi-dimensional tectonic discrimination diagrams

Evaluation of the tectonic setting using these discriminant-function-based multi-dimensional discrimination diagrams was completed using a series of programs downloadable from the

website of the Institute of Renewable Energy at the National Autonomous University of Mexico (http://tlaloc.ier.unam.mx/index.html). The first stage of analysis uses the IgRoCS (Verma and Rivera-Gómez, 2013a) program to calculate the adjusted values for major elements to 100%, on an anhydrous basis, using the method of Middlemost (1989) after Fe-oxidation ratio adjustment as described by Verma et al. (2002). The rocks are then classified using the IUGS TAS diagram (Figure 3-46 Le Bas and Streckeisen (1991)), splitting the rocks up into mafic, intermediate and felsic categories. For mafic samples ($(SiO_2)_{adj} < 52\%$), the 'TecD' program (Verma and Rivera-Gómez, 2013b) was used for production of the sets of discrimination diagrams. For intermediate ($(SiO_2)_{adj} = 52\%–63\%$) and felsic ($(SiO_2)_{adj} > 63\%$) samples the 'TecDIA' program (Verma et al., 2015) was used for the production and statistical analysis of each set of discrimination diagrams.

3.5.1.3.1 Mafic rocks

Owing to alteration, only immobile elements were used for fingerprinting the mafic rocks from the Leaareig Terrane, using the set of five diagrams described by Agrawal et al. (2008). The series of diagrams identifies four tectonic settings for basaltic samples including IAB, MORB, CRB and OIB. In interpreting the results, it must be remembered that only four of the diagrams relate to each tectonic setting.

Excluding the seven samples of basalt from the ophiolite, the six remaining samples of basalt from the Leaareig Terrane were plotted on the Agrawal et al. (2008) discrimination diagrams (Figure 3-52). Two samples have an island arc signature with four samples from the Taghsoumat-Aghsoumal domain close to the contact with the Oum Abana domain yielding a MORB signature.

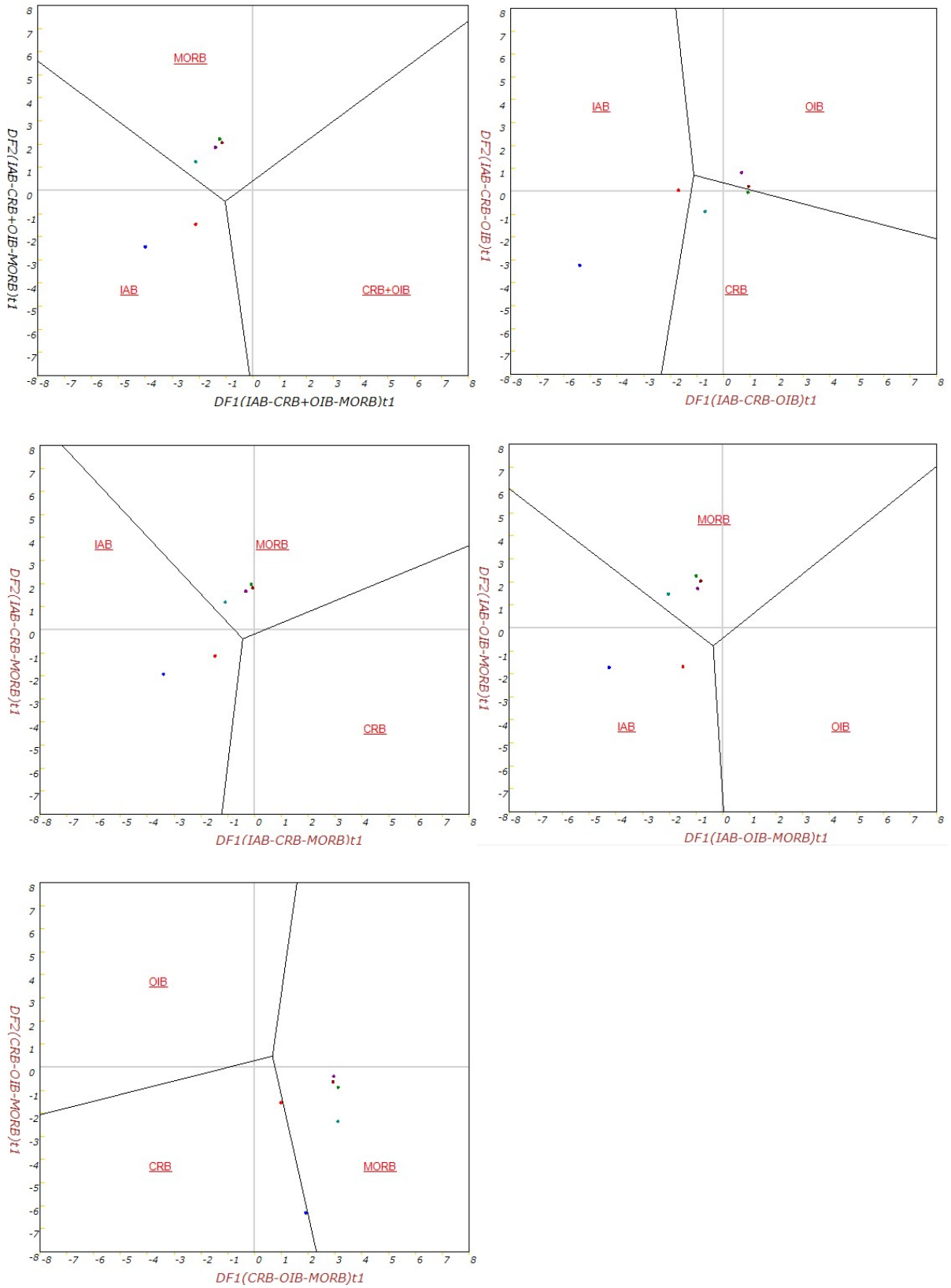

Figure 3-52 - Basalt samples from the Leaareig Terrane (minus the ophiolite samples), plotted on a set of five multi-dimensional discrimination diagrams based on immobile trace elements (Agrawal et al., 2008). IAB – Island Arc Basalt, MORB – Mid Oceanic Ridge Basalt, CRP – Continental Rift Basalt, OIB – Oceanic Island Basalt.

3.5.1.3.2 Intermediate rocks

The intermediate igneous rocks of the Leaareig Terrane largely display island arc characteristics with some samples displaying collisional characteristics (Figure 3-53, Table 1). Both major and trace elements (Table 3-1) reflect this characteristic when plotted on the respective sets of discrimination diagrams defined in Verma and Verma (2013). As this is an old, altered terrane more weighting has been placed on the immobile trace elements for the interpretation (though in this case the major element chemistry is consistent). Of the seven intermediate samples from the domain, five display island arc characteristics while two indicate a collisional environment (Figure 3-53, Table 3-1).

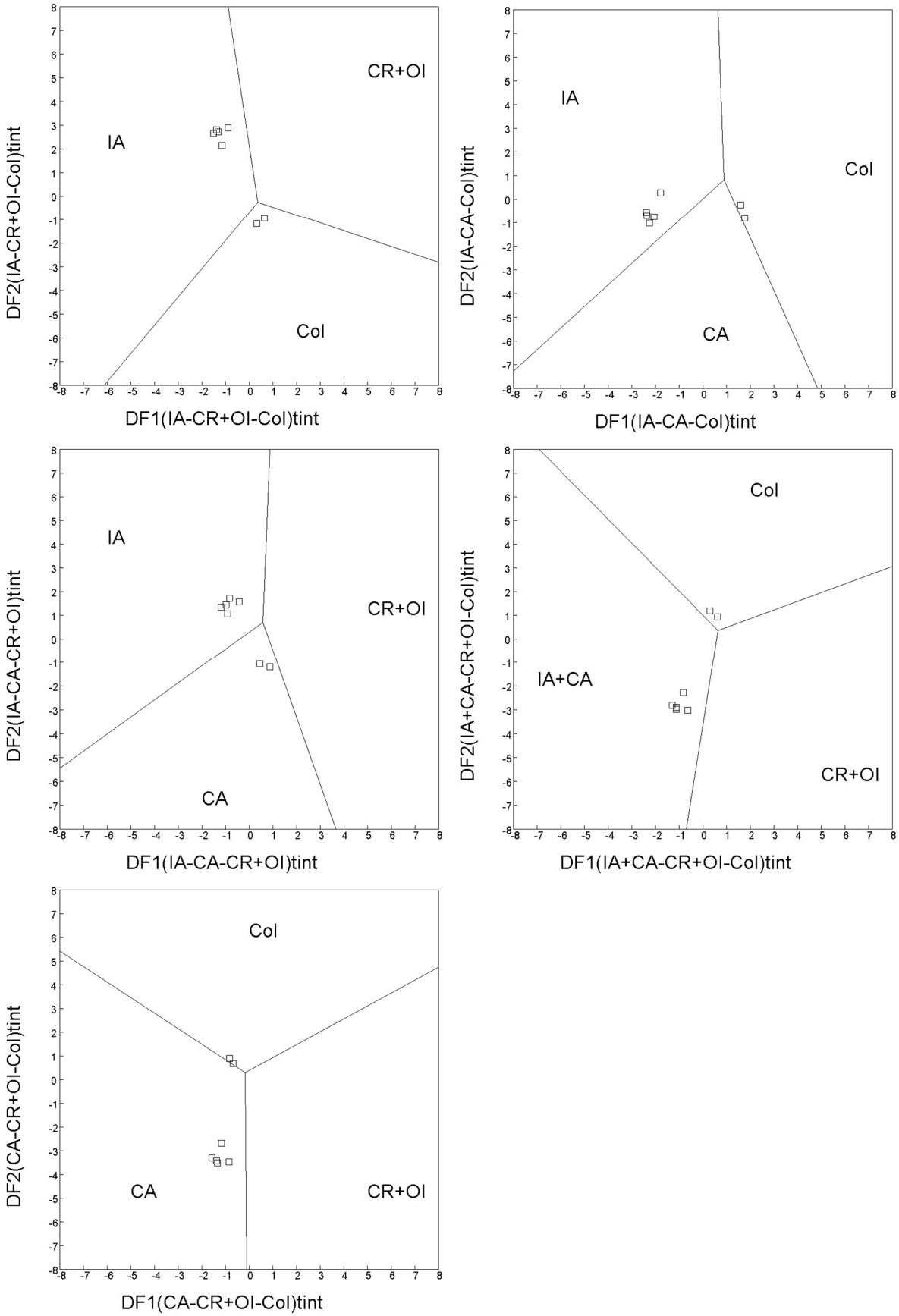

Figure 3-53 – Intermediate igneous rocks from the Leaareig Terrane plotted on a series of five multi-dimensional discriminant function diagrams based on log-ratios of immobile trace elements (Verma and Verma, 2013). IA – Island Arc, CA – Continental Arc, Col – Collisional, CR+OI – Combined Continental Rift and Ocean Island.

Table 3-1 - Application of multidimensional diagrams to ~2240-2180Ma intermediate rocks of the Leaareig.

Magma type, Figure name	Figure type	Total number of samples	Number of discriminated samples				
			Arc			CR+Ol [x ± s]	Col [x ± s]
			IA+CA [x ± s] [p_IA+CA] Θ	IA [x ± s] [p_IA] Θ	CA [x ± s] [p_CA] Θ	[p_CR+Ol] Θ	[p_Col] Θ
Intermediate; Verma and Verma (2013); log-ratios of all major elements	(IA+CA-CR+Ol-Col)	7	5 [0.830±0.086] (0.7029-0.9283)	---	---	1(0.7913)	1(0.8489)
	(IA-CA-CR+Ol)	7	---	5 [0.743±0.124] (0.5669-0.8883)	0 (0)	2 [0.797±0.182] (0.6688, 0.9259)	---
	(IA-CA-Col)	7	---	5 [0.890±0.075] (0.8012-0.9778)	1(0.7603)	---	1(0.7646)
	(IA-CR+Ol-Col)	7	---	5 [0.858±0.105] (0.7209-0.9491)	---	1(0.7472)	1(0.8473)
	(CA-CR+Ol-Col)	7	---	---	6 [0.657±0.168] (0.3733-0.8953)	0 (0)	1(0.8007)
Diagrams based on log-ratios of major elements	***{Σn} {Σprob} [%prob]***	**35**	**{5} {4.1522} [---]**	**{15} {12.4503} [56%]**	**{7} {4.7006} [21%]**	**{4} {3.1332} [11%]**	**{4} {3.2614} [12%]**
Intermediate; Verma and Verma (2013); log-ratios of immobile trace elements	(IA+CA-CR+Ol-Col)	7	5 [0.9590±0.0361] (0.8974-0.9869)	---	---	0 (0)	2 [0.6719±0.0268] (0.6529, 0.6908)
	(IA-CA-CR+Ol)	7	---	5 [0.8567±0.0335] (0.8176-0.8890)	2 [0.718±0.065] (0.6717, 0.7637)	0 (0)	---
	(IA-CA-Col)	7	---	5 [0.787±0.056] (0.7206-0.8567)	0 (0)	---	2 [0.5732±0.0168] (0.5613, 0.5851)
	(IA-CR+Ol-Col)	7	---	5 [0.9689±0.0276] (0.9204-0.9887)	---	0 (0)	2 [0.7521±0.0325] (0.7291, 0.7751)
	(CA-CR+Ol-Col)	7	---	---	5 [0.9473±0.0411] (0.8780-0.9811)	0 (0)	2 [0.508±0.065] (0.4621, 0.5542)
Diagrams based on log-ratios of immobile trace elements	***{Σn} {Σprob} [%prob]***	**35**	**{5} {4.7952} [---]**	**{15} {13.0615} [56%]**	**{7} {6.1719} [27%]**	**(Piqué) (Piqué) [0%]**	**{8} {5.0106} [17%]**

IA−island arc; CA−continental arc; IA+CA–combined island and continental arcs, i.e., arc setting; CR−continental rift; OI−ocean island; CR+OI –combined continental rift and ocean island, i.e., within-plate (WP) setting; Col−collision; Θ the probability values for samples from a given locality are represented by (pIA+CA) – probability for the combined island and continental arc setting in the first diagram; [pIA] – probability for the island arc setting in the diagrams; [pCA] – probability for the continental arc setting in the diagrams; [pCR+OI] – probability for the combined continental rift and ocean island setting in all diagrams; [pCol] – probability for the collision setting in the diagrams; − mean ± 1SD (standard deviation) of the probability estimates for all samples discriminated in a given tectonic setting; these are reported in [], the values are rounded mostly following the indications put forth by Verma (2005); the final rows give a synthesis of results as {Σn} {Σprob} [%prob], where {Σn} is the total number of samples or data points plotting in all five diagrams is reported in the column of total number of samples, whereas the sum of samples plotting in a given tectonic field is reported in the respective tectonic field column; {Σprob} is the sum of probability values for all samples plotting in a given tectonic field is reported in the respective tectonic field column; and [%prob] is the total probability of a given tectonic setting expressed in percent after assigning the probability of IA + CA to IA and CA (using weighing factors explained in Verma and Verma, 2013).

3.5.1.3.3 Felsic rocks

Verma et al. (2013) noted problems in applying these diagrams to Neoarchaean rocks in the Eastern Dharwar craton, India. All three diagrams Verma et al. (2013) indicated a subduction-related setting although major element discrimination plots weakly indicated island arc setting while the less mobile elements strongly favoured a continental arc setting – an interpretation that Verma et al. (2013) used. As these rocks in this region are old and altered, only trace element geochemistry has been used for tectonic discrimination of the felsic rocks (Verma et al., 2013). They display continental arc to collisional characteristics with eight samples indicating a continental arc setting and three representing a collisional setting (Figure 10, Table 3-2).

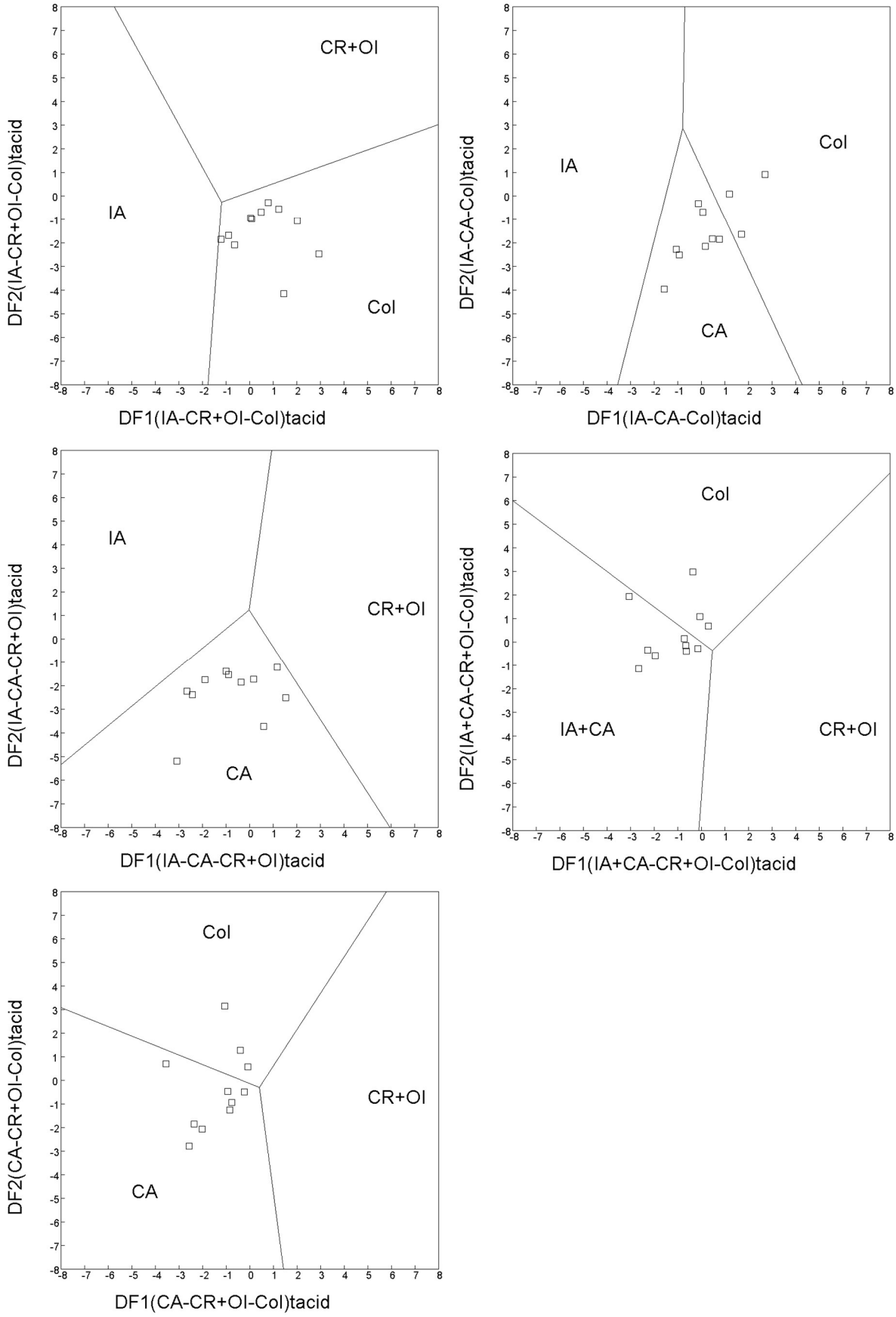

Figure 3-54 – Felsic igneous rocks from the Leaareig Terrane plotted on a series of five multi-dimensional discriminant function diagrams based on log-ratios of immobile trace elements (Verma et al., 2013). IA – Island Arc, CA – Continental Arc, Col – Collisional, CR+OI – Combined Continental Rift and Ocean Island.

Table 3-2 - Application of multidimensional diagrams to ~2240-2180Ma acid rocks of the Leaarieg.

Magma type, Figure name	Figure type	Total number of samples	Number of discriminated samples				
			Arc			CR+OI [x ± s]	Col [x ± s]
			IA+CA [x ± s] [p_IA+CA] Θ	IA [x ± s] [p_IA] Θ	CA [x ± s] [p_CA] Θ	[p_CR+OI] Θ	[p_Col] Θ
Acid; Verma et al. (2013); log-ratios of immobile trace elements	(IA+CA-CR+OI-Col)	11	8 [0.776±0.168] (0.5811-0.9911)	---	---	0 (0)	3 [0.840±0.130] (0.7290-0.9832)
	(IA-CA-CR+OI)	11	---	0 (0)	11 [0.953±0.077] (0.7358-0.9999)	0 (0)	---
	(IA-CA-Col)	11	---	0 (0)	8 [0.837±0.094] (0.7168-0.9469)	---	3 [0.776±0.178] (0.6303-0.9741)
	(IA-CR+OI-Col)	11	---	0 (0)	---	0 (0)	11 [0.919±0.109] (0.6194-1.0000)
	(CA-CR+OI-Col)	11	---	---	8 [0.853±0.143] (0.6131-0.9979)	0 (0)	3 [0.854±0.149] (0.6963-0.9914)
Diagrams based on log-ratios of immobile trace elements	***{Σn} {Σprob} [%prob]***	**55**	**{8} {6.2073} [---]**	**(Piqué) (Piqué) [0%]**	**{27} {24.0064} [63%]**	**(Piqué) (Piqué) [0%]**	**{20} {17.5230} [37%]**

IA−island arc; CA−continental arc; IA+CA–combined island and continental arcs, i.e., arc setting; CR−continental rift; OI−ocean island; CR+OI –combined continental rift and ocean island, i.e., within-plate (WP) setting; Col−collision; Θ the probability values for samples from a given locality are represented by (pIA+CA) – probability for the combined island and continental arc setting in the first diagram; [pIA] – probability for the island arc setting in the diagrams; [pCA] – probability for the continental arc setting in the diagrams; [pCR+OI] – probability for the combined continental rift and ocean island setting in all diagrams; [pCol] – probability for the collision setting in the diagrams; − mean ± 1SD (standard deviation) of the probability estimates for all samples discriminated in a given tectonic setting; these are reported in [], the values are rounded mostly following the indications put forth by Verma (2005); the final rows give a synthesis of results as {Σn} {Σprob} [%prob], where {Σn} is the total number of samples or data points plotting in all five diagrams is reported in the column of total number of samples, whereas the sum of samples plotting in a given tectonic field is reported in the respective tectonic field column; {Σprob} is the sum of probability values for all samples plotting in a given tectonic field is reported in the respective tectonic field column; and [%prob] is the total probability of a given tectonic setting expressed in percent after assigning the probability of IA + CA to IA and CA (using weighing factors explained in Verma and Verma, 2013).

3.5.2 Tectonic setting

All tectonic discrimination diagrams presented, both traditional and multi-dimensional, indicate strongly that the Leaareig Terrane represents a calc-alkaline series of rocks formed in a volcanic arc. The chemistry of arc magmas exhibits broad temporal and spatial trends during arc evolution (Murphy, 2007). Tholeiitic magmas are the dominant suite during the early stages of oceanic island arc formation, whereas the calc-alkaline suite is the predominant suite in mature oceanic arcs and is especially common in continental arcs (Murphy, 2007). Tholeiitic

magmas are more prevalent closer to the trench whereas calc-alkaline magmas generally occur farther from the subducting plate than arc tholeiites (Kuno, 1966, Murphy, 2007). Additionally, there is a trend toward more silicic compositions with increasing arc maturity and crustal thickness in both suites (Murphy, 2007).

The Pearce (2014) Th-Nb proxy diagram illustrates a progression in the characteristics of the calc-alkaline volcanic arc samples (Figure 3-47a), with mafic samples plotting in the ocean arc-continental arc transition area with progressively more intermediate rocks containing stronger continental arc characteristics. This progression is also observed in the multidimensional diagrams with mafic rocks displaying island arc characteristics (Figure 3-53), intermediate rocks displaying island arc (with minor collisional) characteristics (Figure 3-54, Table 3-1) and felsic rocks displaying continental arc (with minor collisional) characteristics (Figure 3-54, Table 3-2).

Although the progression towards more continental arc characteristics with progressively more felsic magmas is the same, there is a slight offset between the Th-Nb proxy diagram and the multi-dimensional analysis where the former interprets intermediate rocks to already have continental arc characteristics while the multi-dimensional diagrams plot them as island arc. Pearce (2008) notes that within older terranes, the hotter magmas assimilate high Th crustal material more readily, and hence would display more continental characteristics on the Th-Nb plot. As this proxy is effectively controlled by two elements, it may be more sensitive to crustal input than the multidimensional equivalent. This may explain the discrepancy, with the Pearce (2014) diagram potentially over-representing the continental nature of the samples. Therefore, for this interpretation the multidimensional diagrams will be used as they are specifically designed for intermediate and felsic rocks and appear to be more durable for slight amounts of alteration. Additionally, they have been widely applied to Archaean terranes (Verma and Rivera-Gómez, 2013b), particularly in Africa and the WAC (Verma, 2017).

One notable exception to these calc-alkaline, volcanic arc magmas, is a number of samples of tholeiitic series basalt from the ophiolite sequence in the Agarasras Lakhadar Domain (Section 3.3.4; Figure 3-50) and from the Taghsoumat-Aghsoumal Belt (Figure 3-50) close to the suture with the Sfariat-Bu Daira Terrane. These samples reflect MORB/BABB (Back Arc Basin Basalt) characteristics on both traditional binary (Figure 3-36, Figure 3-47) and ternary (Figure 3-38, Figure 3-49) diagrams as well as multi-dimensional analysis (Figure 3-40, Figure 3-52). These samples from the Taghsoumat-Aghsoumal Belt represent pieces of oceanic crust forming along the suture between the two terranes emplaced during their collision. For the samples from the Agarasras Lakhadar Domain, these samples add further weight to the interpretation that that the sequence of mafic to ultramafic rocks represents an ophiolite obducted over the Oum Abana domain (Section 3.3.5).

In summary, the progression seen in the data from the Leaareig Terrane, represents the evolution of the volcanic arc over time (as discussed by Murphy, 2007). With increasing arc maturity and increasing crustal thickness, the characteristics of the magmas within the Leaareig Terrane transition from island arc-like to continental arc-like and this is reflected in the increasingly felsic nature of the magmas produced (Figure 3-55 - red). Samples displaying collisional characteristics will be discussed in more detail in Section 6.2. Tholeiitic MORB samples observed in the Taghsoumat-Aghsoumal along the contact with the Oum Abana Domain, representing the suture with collisional intermediate and felsic rocks also produced due to this collision (and later with the Archaean craton). The Agarasras Lakhadar (Figure 3-55 - yellow) represents a back-arc basin formed from the same arc as the rest of the Leaareig Terrane which was obducted at a later stage.

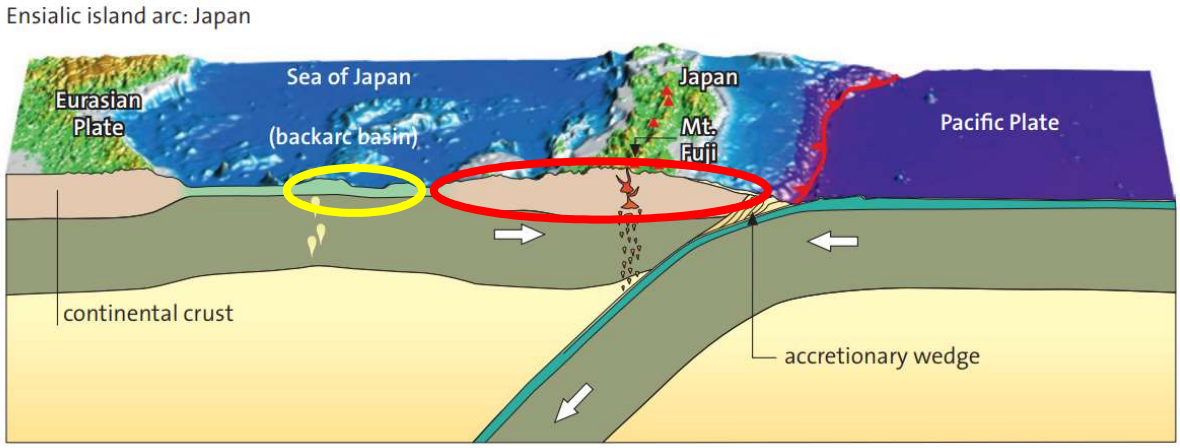

Figure 3-55 - Illustration of the Japanese island arc, where the oceanic lithosphere is subducted beneath continental lithosphere and the island arc is underlain by continental crust. The island arc of this system is separated from the continent by a marine basin underlain by oceanic crust. (modified from Frisch et al., 2011). Yellow circle represents the tectonic environment of the Agarasras Lakhadar Domain, while the red circle represents the setting of the rest of the Leaareig Terrane.

4.0 Geology of the Sfariat-Bu Daira Terrane

The Sfariat-Bu Daira Terrane forms a northwest-southeast trending belt between the Leaareig Terrane in the south and the Palaeoproterozoic granites to the northeast (Figure 4-1). It comprises four Domains: the Elmalhat Domain, the Oum Abana belt, the Anajim Guebli Suite and the Riche Anajim Group

Outcropping almost exclusively in Western Sahara, the Elmalhat Domain and Oum Abana belt (Figure 4-1) represent the mid-crustal and extrusive remnants of an Eburnean island arc sequence respectively. Combs (2012) mapped a portion of the Oum Abana belt demonstrating that the region consists of northwest-southeast trending fault bounded metamorphosed belts of sedimentary, volcanosedimentary and volcanic sequences interspersed with granite-gneiss belts, all intruded by syn- and post-tectonic granitoid and gabbroic intrusions. Lyche (2012) studied the Agarasras Labiad granitoid intrusion located within the Oum Abana Belt where gold and copper anomalies had been detected. Based on a combination of field mapping and petrological analysis Lyche (2012) concluded that it is a syntectonic intrusion ranging in composition from tonalite to granodiorite.

To the southeast of the Oum Abana Domain, the Elmalhat Domain (Figure 4-1) represents the mid-crustal plutonic rocks of the volcanic arc sequence. It is composed of granite intrusions, orthogneiss, gabbro intrusions as well as the Elmalhat Anorthosite Complex (EAC), referred to by Lehbib Nayem et al. (2016b) as the 'Bir Malhat stratiform complex', which forms a major feature of the Elmalhat Domain. It consists of anorthosite, leuco-gabbro(-norites), troctolites with minor ultramafic rocks as well as seams of PGE-bearing chromitite and orthomagmatic Fe-Ti-V deposits/horizons.

In Mauritania the Sfariat-Bu Daira Domain is represented mainly by the Anajim Guebli Suite (Figure 4-1), consisting of abundant thin units of ferruginous quartzite and marble, BIF,

migmatitic gneiss, amphibolite facies paragneiss as well as syntectonic granite (Schofield et al., 2006). These are interpreted to be the deformed remnants of continental platform sediments, deposited at the then edge of the craton (Schofield et al., 2006). Schofield et al. (2006) inferred that the Anajim Guebli Suite represented a passive margin to the Leaareig Terrane (Temmimichate-Tsabaya Complex) (Bradley et al., 2015b) forming during sinistral oblique collision. This is preserved as strongly partitioned D1 shortening followed by D2 strike-slip-dominated transpression within the Sfariat Belt during the Eburnean orogeny (~2117 to 2064 Ma).

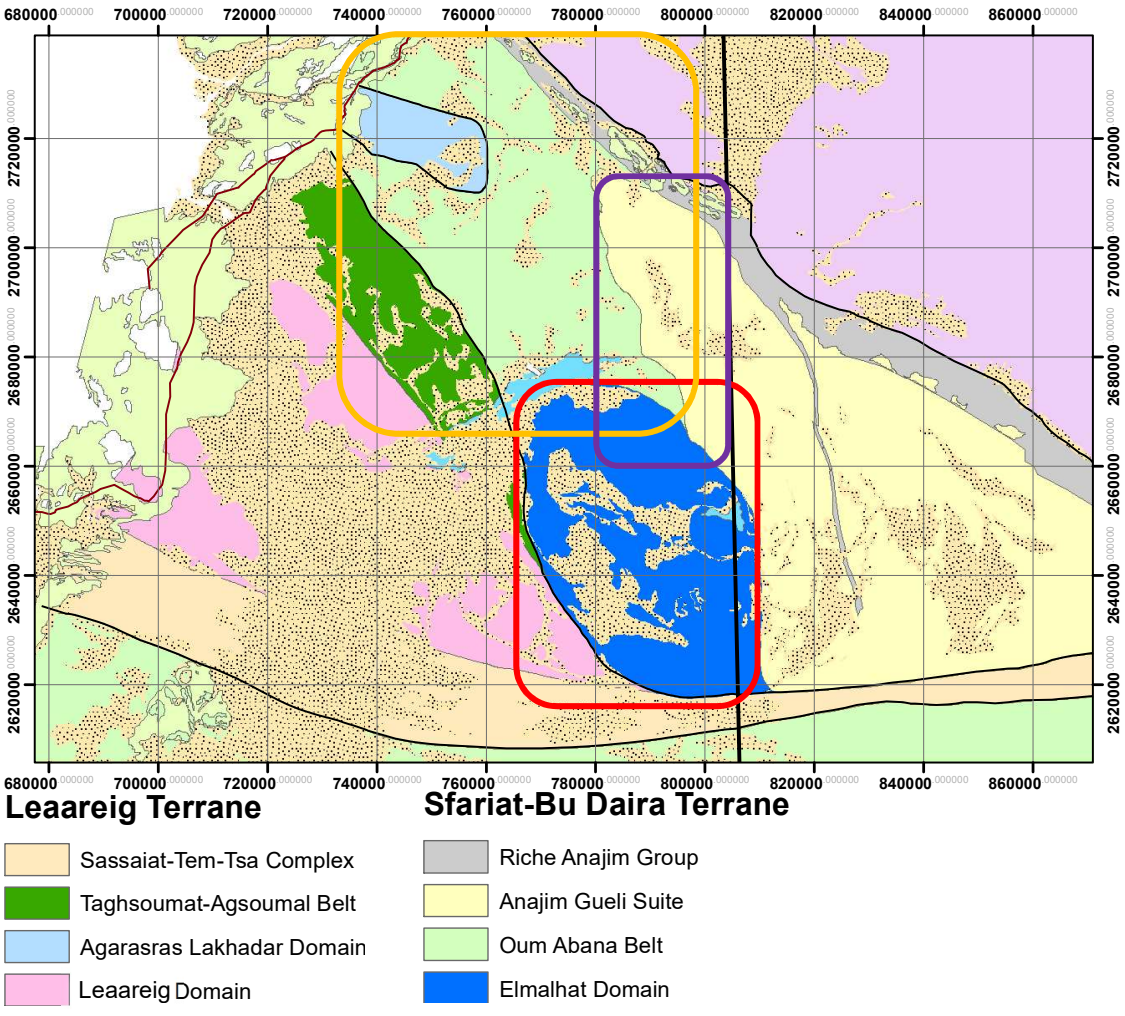

Figure 4-1 – Domain map of the study area with the location of the Elmalhat Domain shown in red (UTM Zone 28N). For detailed geology of the Elmalhat Domain (red) – see Figure 4-2. For detailed geology of the Oum Abana Belt (orange) – see Figure 4-108. For detailed geology of the Anajim Guebli Domain (purple) – see Figure 4-117.

4.1 **Elmalhat Domain**

4.1.1 Introduction

The Elmalhat Domain occupies the southeastern portion of the study area (Figure 4-1). It is separated from the Leaareig Domain, Sassaiat-T-T and Anajim Guebli Suite by faults. To the northeast, it grades into the Oum Abana belt with the gradual increase in the proportion of volcanosedimentary material and the loss of distinctive Elmalhat lithologies (Figure 4-2).

The basement of the Elmalhat Domain is composed of orthogneiss (intruded at 2142 ± 20 Ma) in the east and paragneiss (2127 ± 20 Ma) in the west, both of which contain lenses of sheared mafic to ultramafic rocks in the south of the Domain (Figure 4-2). These units are intruded by extensive mafic and ultramafic intrusions forming a sheared northwest-southeast trending belt through the centre of the Domain as well as in the south.

The most notable feature of the Elmalhat Domain, is the presence of the Elmalhat Anorthosite Complex (EAC). It appears to be the only known anorthosite complex on earth to contain both ‘megacrystic’ anorthosite and ‘massif-type’ anorthosite as defined by Ashwal (1993). With strict temporal distributions, the occurrence of megacrystic anorthosite is otherwise restricted to the Archaean while the occurrence of massif-type anorthosite is largely confined to the Proterozoic with peak production between ~1.8 – 1 Ga (Ashwal, 1993, Ashwal, 2010, Ashwal and Bybee, 2017). Furthermore, each type of anorthosite is believed to form in different tectonic settings and different crustal levels (Ashwal and Bybee, 2017) making the formation of the EAC an enigma. Most of the megacrystic anorthosite is exposed on the Northern Limb of the complex, hosting a seam of PGM-bearing chromitite, while other smaller bodies are present in the north of the Elmalhat Domain (Figure 4-2). The massif-type anorthosite crops out as three separate bodies, comprising the Main Bulb, the Southern Bulb and Moug El Kaleb

body (Figure 4-2). The bulk of the work on the Elmalhat Domain is focussed on the EAC in order to produce a petrogenetic model.

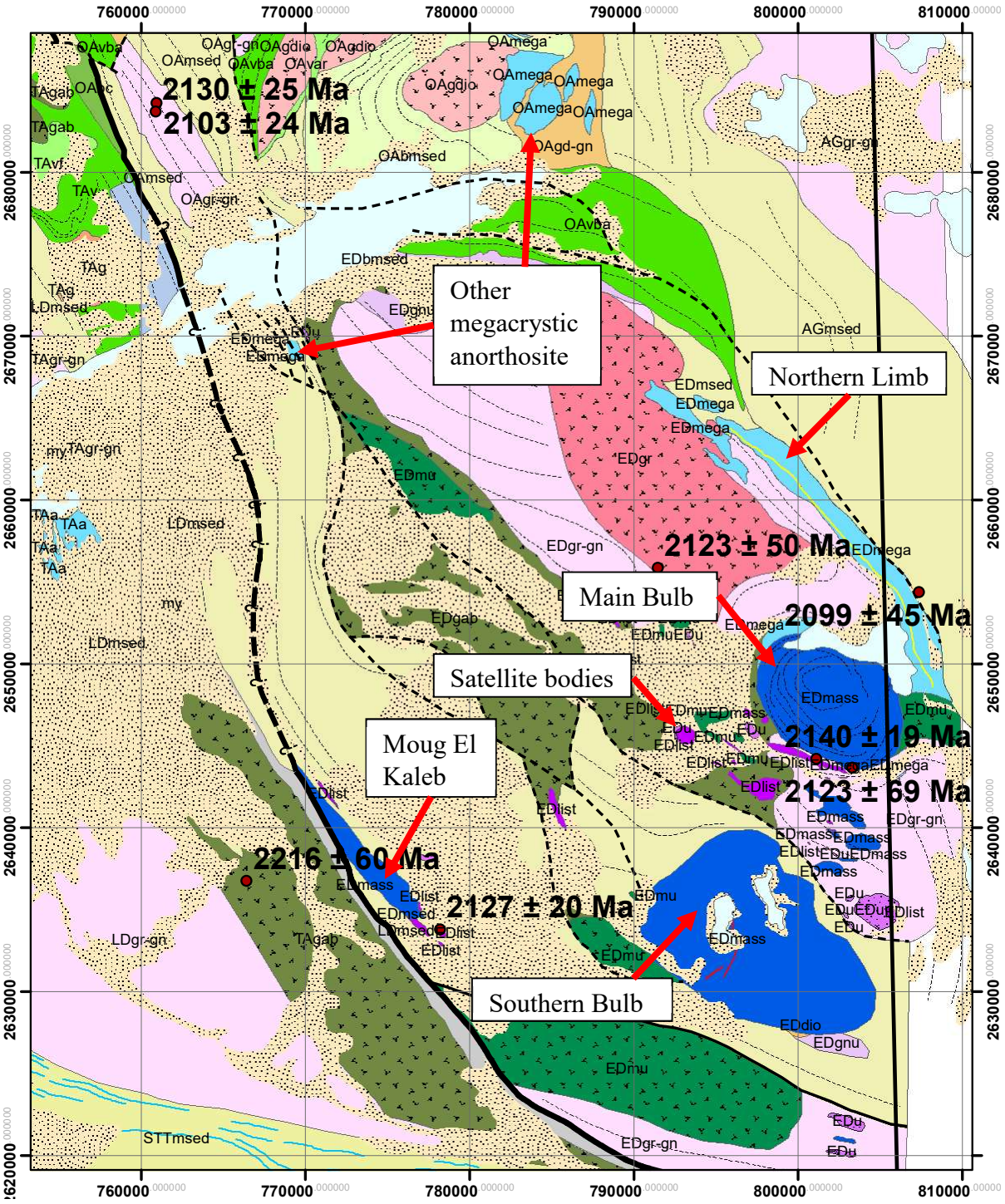

Figure 4-2 a – Geology of the Elmalhat Domain with key locations labelled (UTM Zone 28N). See attached map for legend. For location map, see the red square in Figure 4-1.

Elmalhat Anorthosite Complex:

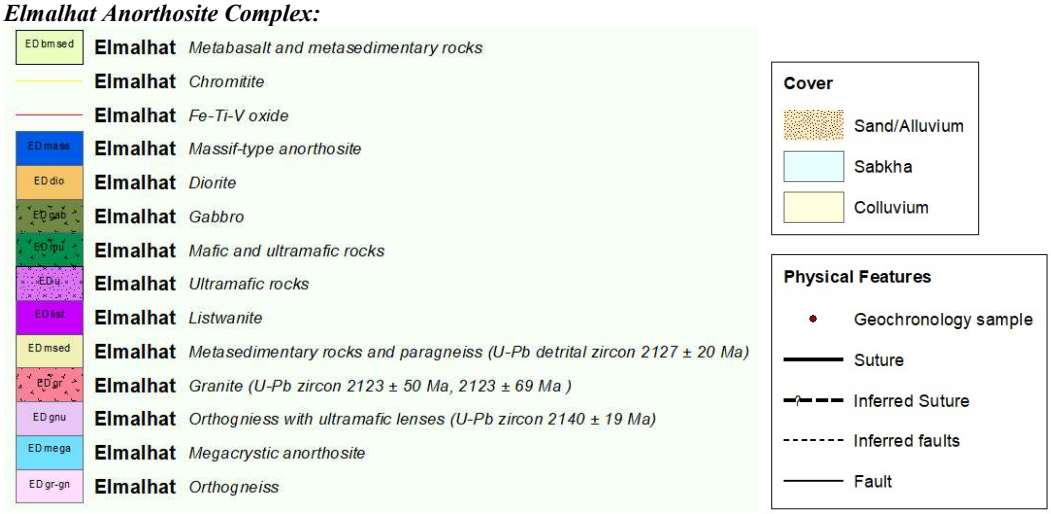

Sfariat-Bu Daira Terrane:

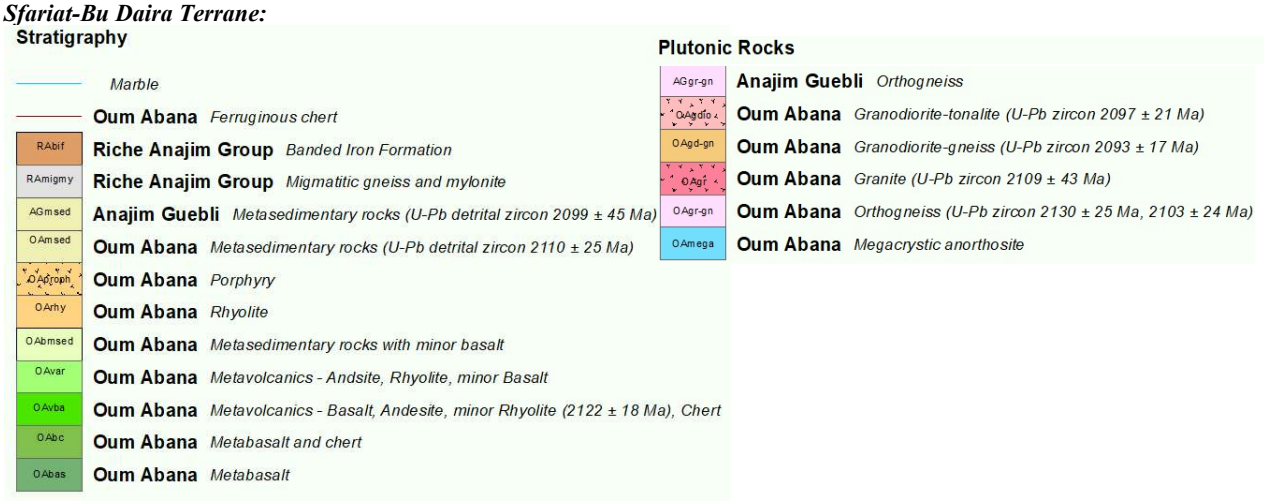

Leaareig Terrane:

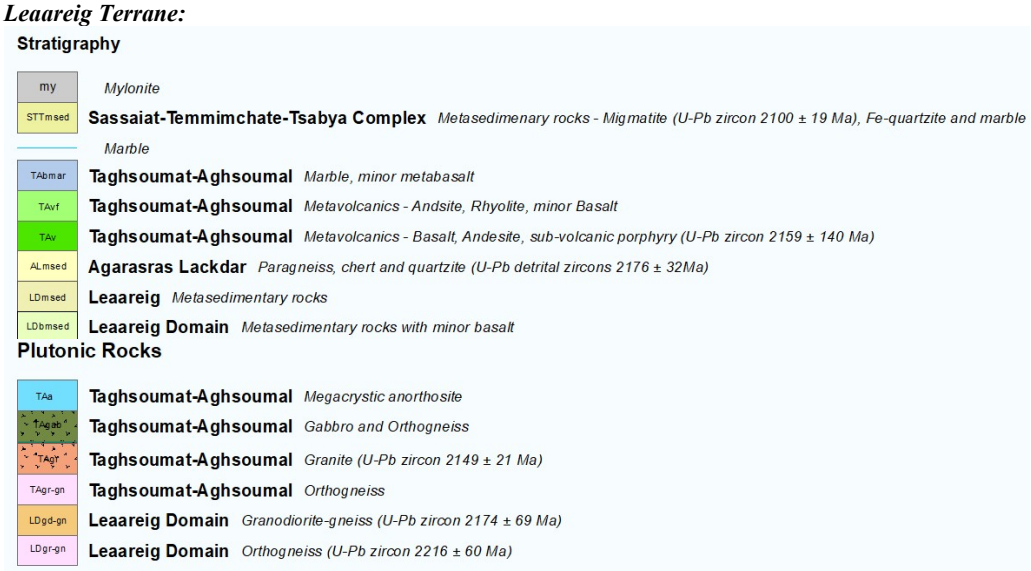

Figure 4-2 b – Legend.

The entire region is cross-cut by late stage granite (2129 ± 46 Ma, 2123 ± 69 Ma), pegmatite, and dolerite intrusions.

4.1.2 Geology and Structure

4.1.2.1 Basement

4.1.2.1.1 Orthogneiss and Granite

Orthogneiss is the dominant basement material in the eastern part of the Elmalhat Domain. The orthogneiss is variable in appearance and compositional though it consistently contains a well-developed gneissose fabric (Figure 4-3). The orthogneiss formed from I-type granites containing magnetite as the opaque fraction. It is leucocratic-mesocratic, pink-grey, medium-coarse grained (~1.5-2mm) rocks with a sub-vertical foliation striking ~300°. It consists of quartz (~35-50%), alkali-feldspar (10-45%), plagioclase (10-30%), biotite (~10-15%), and muscovite (~0-5%). Igneous zircons from a representative sample of migmatitic orthogneiss was dated using U-Pb geochronology at 2142 ± 20 Ma.

The orthogneiss is cross cut by late, foliated, granitoid intrusions (Chapter 4.1.1.4) and near the contact with the Northern Limb is cut by late metadolerite dykes. In the north, proximal to the Northern Limb, the orthogneiss hosts ultramafic lenses, altered in shear zones to malachite and sulphide-bearing listwanite.

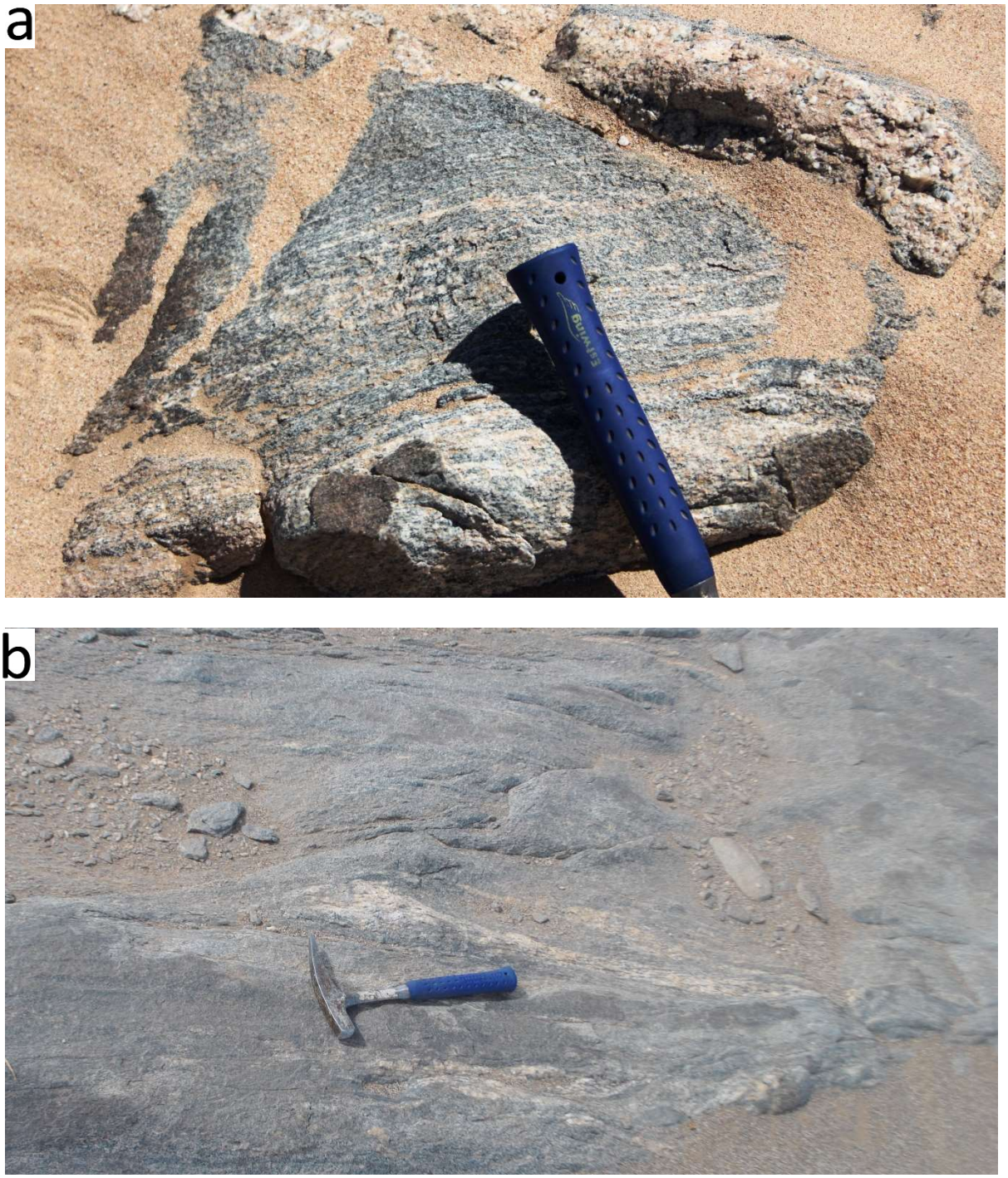

Figure 4-3 – Field photographs of basement rocks of in the east of the Elmalhat Domain. a) Orthogneiss cut by a granitic dyke (UTM 28 805092 mE, 2644383 mN) b) migmatitic orthogneiss to the south of the Main Bulb of EAC (UTM 28 801922 mE, 2644342 mN).

4.1.2.1.2 Paragneiss

The basement material of the western part of the Elmalhat Domain is dominated by paragneiss interlayered with minor layers of quartzite, BIF, carbonate-BIF, marble and amphibolite (Figure 4-4). The unit consists of quartzite, schist, amphibolite and altered granite in the north.

The BIF is mesocratic, grey, and is banded on a 1-2 cm scale with alternating layers of hematite, chert, and sometimes calcite (Figure 4-4c). Proximal to the Taghsoumat shear zone, the BIF is strongly epidote altered.

The amphibolite is porphyroblastic, melanocratic, dark blue, fine-medium grained (~0.25 mm) with ~0.5-1mm porphyroblasts of amphibole, and a sub-vertical schistose foliation. It consists of amphibole (~50-60%), and plagioclase (~40-50%).

The main rock in southern part of the unit is leucocratic, fine-coarse grained with a sub-vertical (northwest-southeast striking) gneissic foliation (locally strongly lineated) (Figure 4-4a, b). Generally very quartz-rich, it consists of quartz (~30-70%) feldspars (~15-65%), muscovite (~5-15%) and garnet (~0-5%) (Figure 4). Based on its composition and association with metasedimentary rocks such as quartzite, BIF and marble the unit has been interpreted as being of a metasedimentary origin and is hence a paragneiss. The paragneiss is the unit that hosts both the Southern Bulb and the Moug El Kaleb anorthosites.

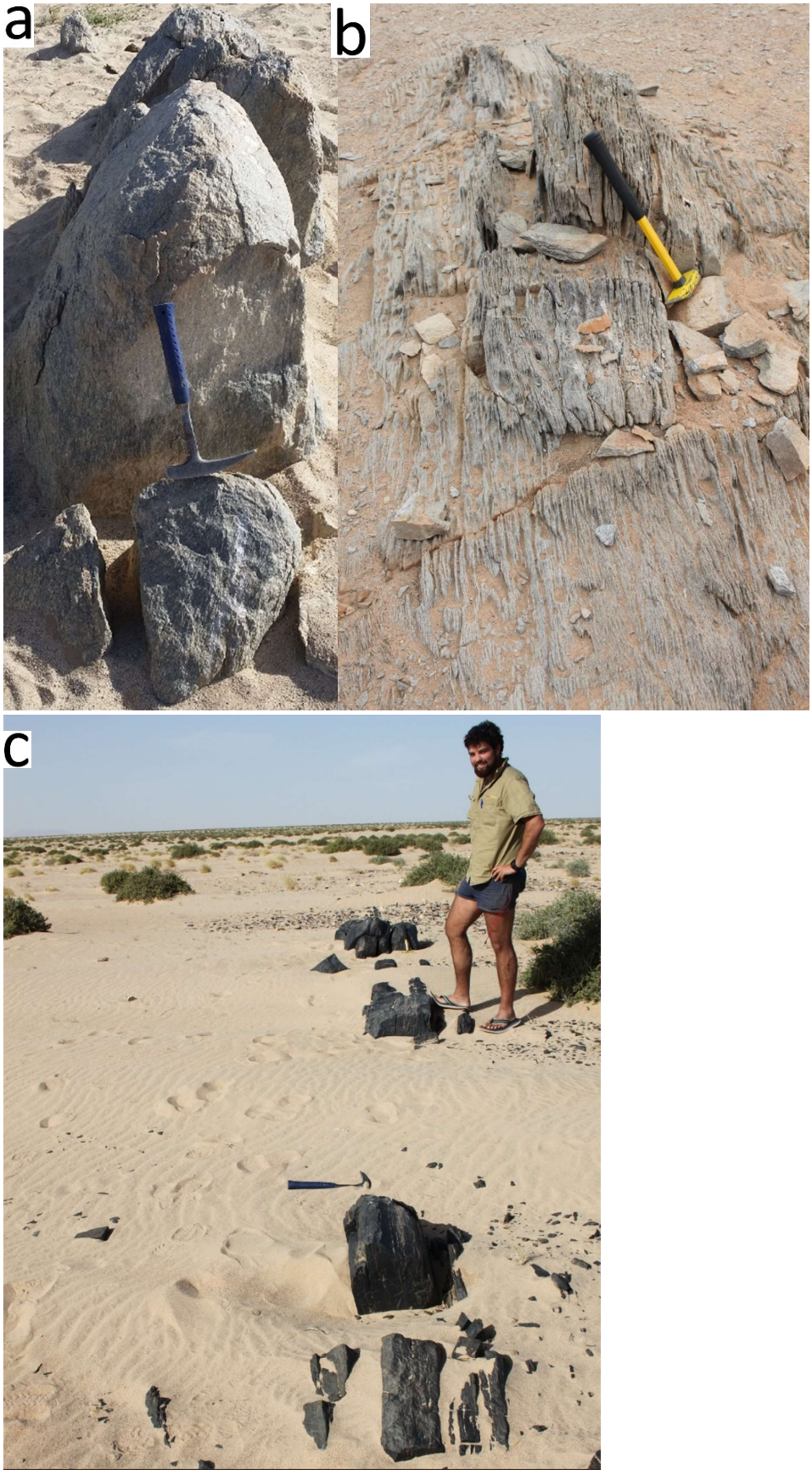

Figure 4-4 – Field photographs of metasedimentary basement. a) photograph of a paragneiss outcrop (UTM 28 776938mE, 2633751 mN). b) photograph of paragneiss subcrop (from Laurence Robb - UTM 28 778231 mE, 2634909 mN). c) layer of BIF in the paragneiss (UTM 28 769529 mE, 2659858 mN).

4.1.2.2 Elmalhat Anorthosite complex

4.1.2.2.1 Introduction to Anorthosite

A relatively rare rock type on Earth, anorthosites are strictly defined as an igneous rock consisting of or more than 90% plagioclase (Streckeisen, 1976). However within anorthosite complexes, the definition is stretched to include rocks containing more than 65% plagioclase with minor amounts of mafic minerals such as orthopyroxene, clinopyroxene and olivine (leuco- norite, gabbro and troctolite respectively) all of which are considered part of the anorthosite series (Ashwal, 2010). Ashwal (1993) characterised anorthosites into six basic categories based on their distinctive features and associations. These include Archaean megacrystic anorthosites, Proterozoic (massif-type) anorthosites, anorthosites of layered mafic intrusions, anorthosites of oceanic settings, anorthosite inclusions in other rock types and extra-terrestrial anorthosites.

A noteworthy feature of anorthosites is that they are one of only a few rock types that appear to be temporally restricted, or to show peaks in the timing of their production (Ashwal and Bybee, 2017, Ashwal, 2010). Temporally restricted anorthosites on earth include Archaean and Proterozoic anorthosites which have distinctive characteristics, whereas other types of terrestrial anorthosites such as those in layered mafic intrusions occur throughout geological time (Ashwal, 1993).

Archaean Megacrystic-type Anorthosites

Anorthosites are often, but not always, found as a minor component of Archaean greenstone belts, associated with mafic intrusive and extrusive rocks (Ashwal, 1993, Ashwal, 2010). Temporally restricted to the Archaean (2.73-3.73 Ga), their primary textures, when preserved, are characterised by equidimensional megacrysts (from ~0.5 cm to >30 cm in diameter) of calcic plagioclase (An_{70-94}, average $An_{\sim 82}$) in a finer groundmass of gabbroic composition

(Figure 4.6; Ashwal and Bybee, 2017, Ashwal, 2010). In Archaean megacrystic anorthosite complexes leucogabbro (75-90% plagioclase) is much more abundant than true anorthosite (>90% plagioclase). Metamorphic grades vary from sub-greenschist to granulite facies, with magmatic textures, structures and mineralogy best preserved in lower grade occurrences (Ashwal and Bybee, 2017). In high grade examples the anorthositic and related rocks sometimes have been deformed and smeared out into mylonites or finely banded gneisses (Myers, 1978). However, distinctive megacrystic textures are well preserved at amphibolite/granulite facies in the Fiskenæsset Complex of West Greenland (Rollinson et al., 2010). Archaean anorthosites typically form much smaller thin, but laterally extensive sequences smaller than 500 km^2, ranging in size from small bodies ~10 km^2 to ~560 km^2 (Shawmere anorthosite complex Ontario) and ~500 km^2 for the remarkably well preserved Fiskenæsset Complex (Rollinson et al., 2010).

In terms of their petrogenesis, Archaean anorthosites have a genetic connection to the mafic volcanic rocks of the greenstone belts. This is implied by occurrence of basaltic flows, sills and dykes containing similar megacrystic calcic plagioclase, as well as chemical similarities between the basalts and the mafic groundmass surrounding the megacrysts in some anorthosites (Ashwal, 1993, Ashwal, 2010, Ashwal and Bybee, 2017). Archaean anorthosite complexes seem to represent accumulations of calcic plagioclase megacrysts in sub-volcanic magma chambers that feed mafic lavas to the surface during crystallisation (Ashwal and Bybee, 2017). The high An content of the plagioclase megacrysts has never been fully explained. Elevated H_2O content in the parent magma may have been a factor, with Sisson and Grove (1993) demonstrating on arc basalts that high water contents had the effect of increasing Ca content as well as suppressing plagioclase production. Broadly speaking, crystallisation of calcic placioclase from a broadly basaltic melt is favoured by low pressure, high H_2O contents

and/or high Ca/Na and Al/Si ratios of parental melts (Ashwal and Bybee, 2017 and references therein).

It seems likely that Archaean anorthosites are formed in oceanic rather than continental crust (Ashwal and Bybee, 2017). This is indicated by the large volume of pillow basalts and other mafic magmatic rocks within the greenstone belts, as well as petrological, geochemical and isotopic data supporting a genetic connection (Ashwal and Bybee, 2017, Ashwal, 2010). The exact oceanic environment for the greenstone belts in general is still a topic of debate with whether mid-ocean ridge, back-arc basin, island arc, oceanic plateau, or even if modern analogues are even applicable at all (de Wit and Ashwal, 1997 and references therein). Ashwal and Bybee (2017) tentatively concluded a consensus is being approached that Archaean anorthosite complexes are best interpreted in terms of their derivation from hydrous basaltic magmas in ancient oceanic arc environments. This interpretation is made on the back of multiple geochemical studies all indicating/being consistent with an island arc setting (Ashwal and Bybee, 2017and references therein).

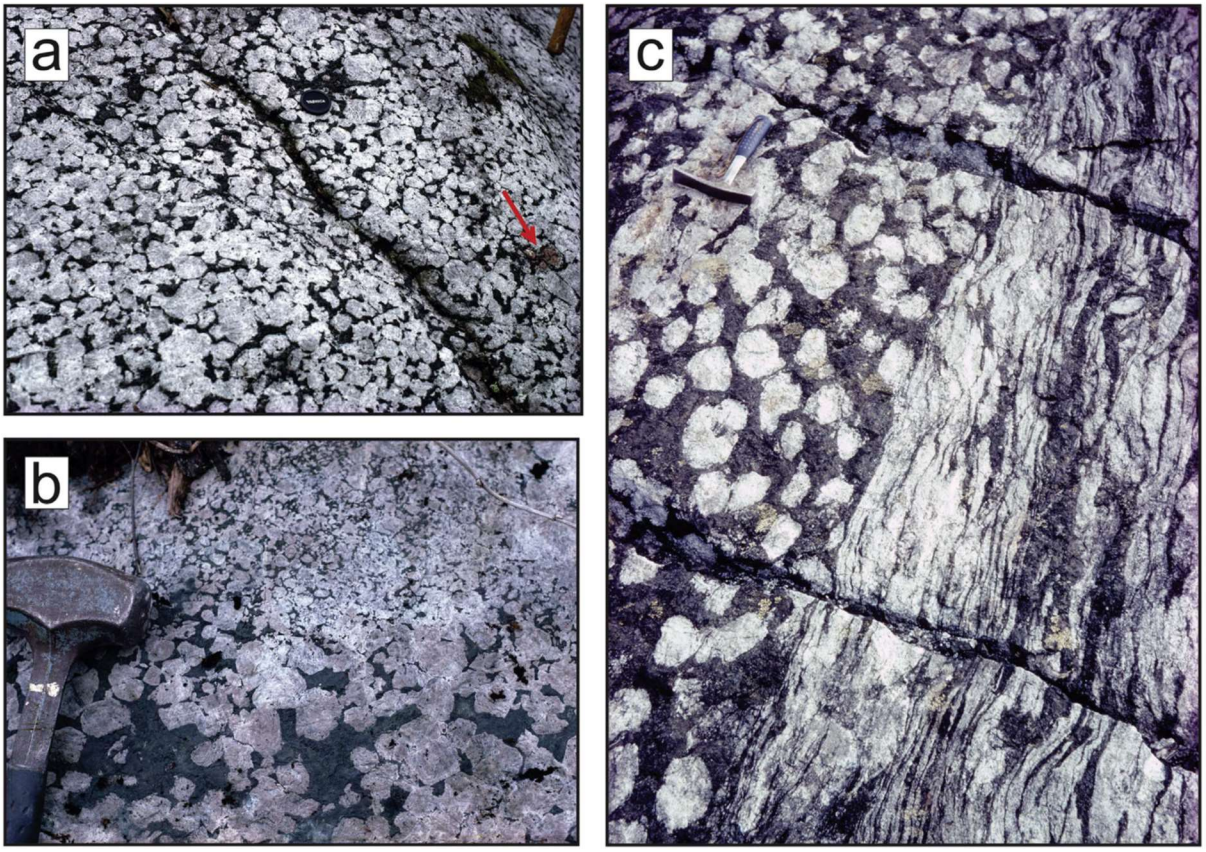

Figure 4-5 – Field photographs of Archaean anorthosite highlighting their general appearance (from Ashwal and Bybee, 2017; and references therein) a)- Outcrop appearance typical of Archean anorthosites (the 2.76 Ga Shawmere anorthosite complex in the Superior Province of Ontario), showing equant megacrysts of calcic plagioclase in a matrix of finer-grained mafic minerals. The primary magmatic texture has been preserved, despite metamorphism to granulite facies. b) Small-scale variations in grain size of plagioclase megacrysts and abundance of mafic matrix in anorthositic rocks of the 2.74 Ga Bird River sill, southeastern Manitoba. c) Undeformed megacrystic leucogabbro (left) has been transformed in a shear zone into highly strained gneiss (right). Upper leucogabbro unit of the 2.97 Ga Fiskenæsset anorthosite complex, southwestern Greenland (Myers, 1978).

Proterozoic Massif-type Anorthosites

By far the most abundant type of terrestrial anorthosite, massif-type anorthosites appear to be restricted to the Proterozoic (2.7-0.55 Ga), with the majority having been emplaced between 1.8 Ga and 0.9 Ga (Ashwal, 2010). They occur as small plutons ~1-10 km^2 (eg. Lofoten, Norway) to batholith-sized composite intrusive complexes up to ~18000 km^2 (eg. Kunene Complex, Namibia/Angola) (Ashwal and Twist, 1994). They are characterised by plagioclase of intermediate composition (typically An_{45-70}; average An_{53}) and a variety of mafic minerals including ortho- and clinopyroxene, olivine and magnetite/ilmenite (Ashwal, 2010, Ashwal and Bybee, 2017). Generally, the complexes show very narrow ranges of plagioclase compositions (e.g. Rogaland Anorthosite Province – $An_{45\pm3}$), though some massifs such as the

Nain Plutonic Suite show a wide range of anorthite contents (An_{34-90} with peaks at An_{45} and An_{52}) (Duchesne and Demaiffe, 1978). Pristine plagioclase crystals display a wide variety of colours in Proterozoic anorthosites (black-grey-blue-red-pink-purple) due to the presence of fine (< 1 μm), dust-like needles of Fe-Ti oxides, thought to be exsolution products (Anderson, 1966).

Aside from anorthosite, dominant rock types observed in these complexes include leucogabbro, leuconorite, leucotroctolite, and minor gabbroic rocks; with ultramafic components being extremely rare or absent (Ashwal, 2010). Although they are characterised by a relatively simple mineral assemblage, at outcrop scale they display heterogeneous textures and complex macro- and microscopic textural variation and features (Figure 4.7; Ashwal and Bybee, 2017) including layering and pegmatitic textures in which plagioclase crystals reach 1m across (Figure 4.8; Ashwal, 2010). The cumulus plagioclase is frequently euhedral and lath-shaped, though polygonal/annealed grain boundaries are also common (Figure 4.7; Ashwal and Bybee, 2017). Recrystallisation and grain size reduction on the grain boundaries is also commonly observed (Ashwal and Bybee, 2017). Termed mortar (or 'core and mantle') texture *(Morse, 1968)*, this recrystallisation has been attributed to protoclastic deformation and may occur during the mush movement or subsequent subsolidus tectonic movements (Ashwal and Bybee, 2017).

The model of formation for massif-type anorthosites involves ponding of basaltic magmas at the Moho, crystallization and sinking of mafic silicates, and eventual flotation of buoyant plagioclase diapirs, emplaced at a mid-crustal level (Figure 4.7; Ashwal, 1993, Ashwal and Bybee, 2017). The aluminous, broadly basaltic, parent magmas responsible for the formation of massif-type anorthosites are thought to be mantle-derived with petrological, geochemical and isotopic data suggesting that they have undergone a variable degree of contamination with continental crust (Ashwal and Bybee, 2017; and references therein). Based on many lines of

evidence, Ashwal and Bybee (2017) suggest the most likely setting for massif-type anorthosites to be an Andean-type continental arc setting.

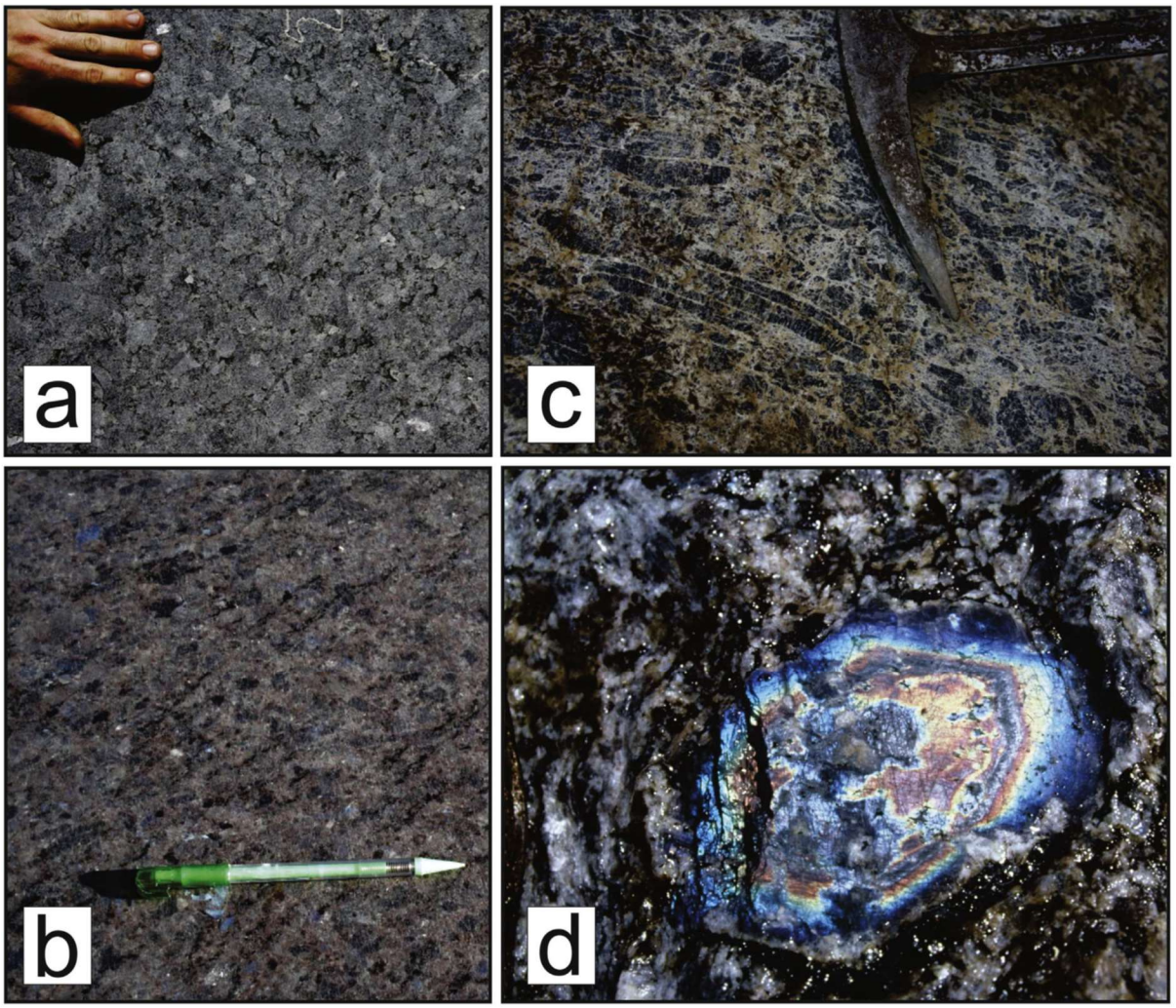

Figure 4-6 – Photographs of Proterozoic massif-type anorthosite highlighting their general appearance (from Ashwal and Bybee, 2017 and referrences therein) . a) Typical texturally-homogeneous leucotroctolite from the ~1.4 Ga Kunene Anorthosite Complex, Angola (Ashwal and Twist, 1994), dominated by intermediate plagioclase (~85 modal %), with intercumulus olivine and minor Fe-Ti oxides. b) Leuconorite from the 0.93 Ga Rogaland Anorthosite Province with a weak magmatic foliation defined by tabular, iridescent plagioclase crystals and interstitial orthopyroxene. c) A well-developed example of typical "mortar" texture in the ~1.4 Ga Kunene Anorthosite Complex, Angola. The white material surrounding well-aligned, grey plagioclase crystals mark areas of intense recrystallization and grain size reduction. d) Megacryst (~6 cm across) of zoned iridescent plagioclase hosted by leuconorite at Paul Island, in the ~1.3 Ga Nain Anorthosite Complex, Labrador (Ashwal, 1993). An irregular core of grey plagioclase is surrounded by oscillatory compositional zoning cycles, visible in iridescent shades of red, blue and yellow.

As the EAC is Palaeoproterozoic in age (Section 4.1.2.4), common terminology in the literature of 'Archaean-type anorthosite' and 'Proterozoic massif-type anorthosite' are not as applicable as descriptive classifications. Therefore, anorthosites with Archaean-type characteristics will be referred to as 'megacrystic anorthosite', while those with Proterozoic-type characteristics

will be referred to as ‘massif-type anorthosite’. Additionally, the complex consists largely of anorthosite and leucogabbro. The term ‘anorthosite’ may also include leucogabbro as they both form the anorthosite series.



Figure 4-7 –Local development of leuconoritic pegmatitic zone, approximately 1 m across, within finer grained (~2 cm) leuconorite from the 1.63 Ga Mealy Mountains Intrusive Suite, Labrador (Bybee et al., 2015)

4.1.2.2.2 Megacrystic anorthosite

4.1.2.2.2.1 Northern Limb

The Northern Limb represents the largest body of megacrystic anorthosite in the EAC (Figure 4-8a). It is a northwest-southeast striking, sub-vertical body of anorthosite and leucogabbro concordant with the host orthogneiss. The anorthosite unit displays a wide variety of textures and compositions across the intrusion. A seam of orthomagmatic chromitite is present within the anorthosite, running parallel to and ~30-50 m to the east of a distinctive amphibolite layer. A ground magnetic survey of the Northern Limb reveals a strong magnetic anomaly at the contact with metasedimentary rocks to the north, and weak magnetic anomaly corresponding with the chromitite seam (Figure 4-8b).

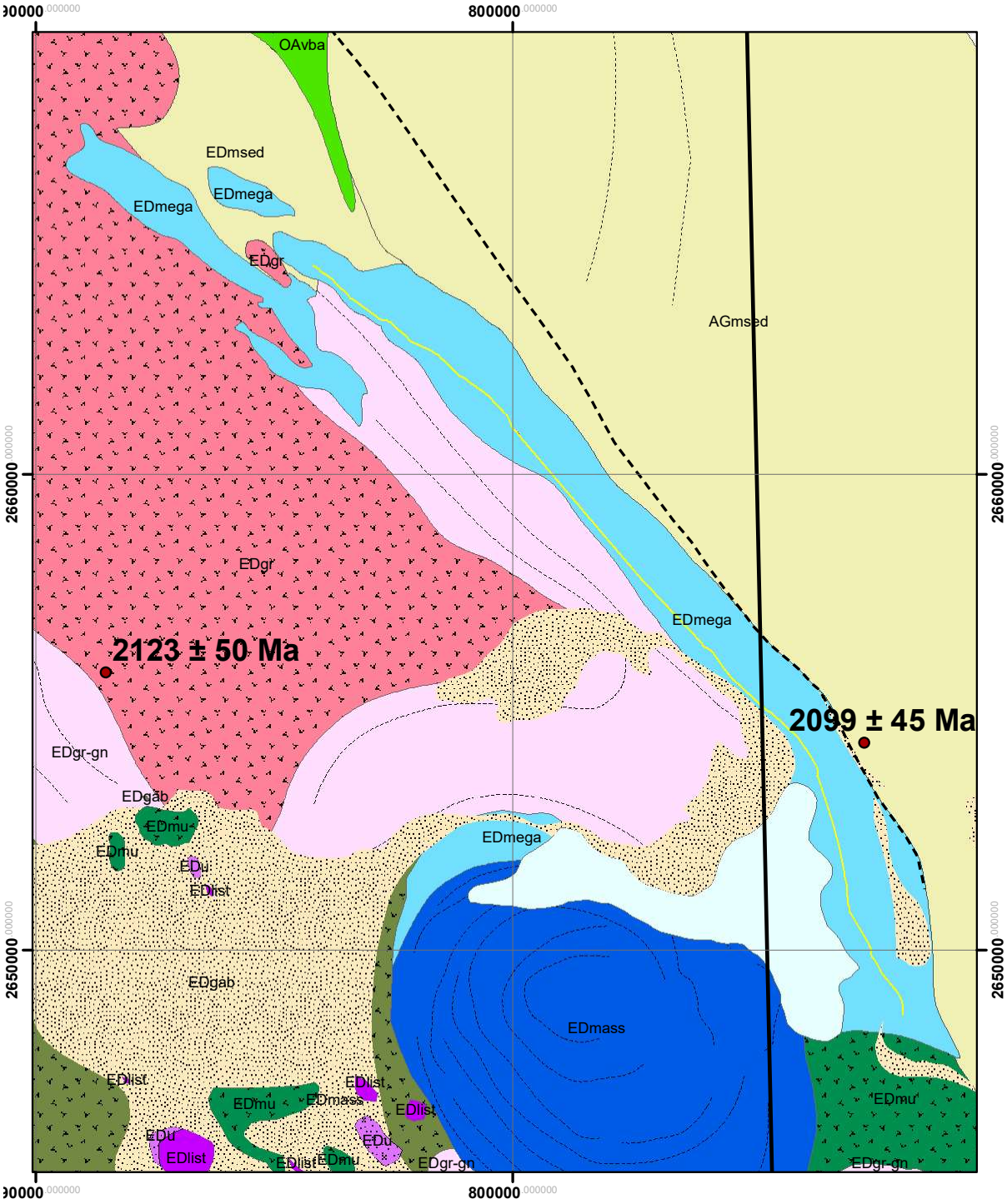

Figure 4-8 a – Geological map of the Northern Limb (UTM Zone 28N).

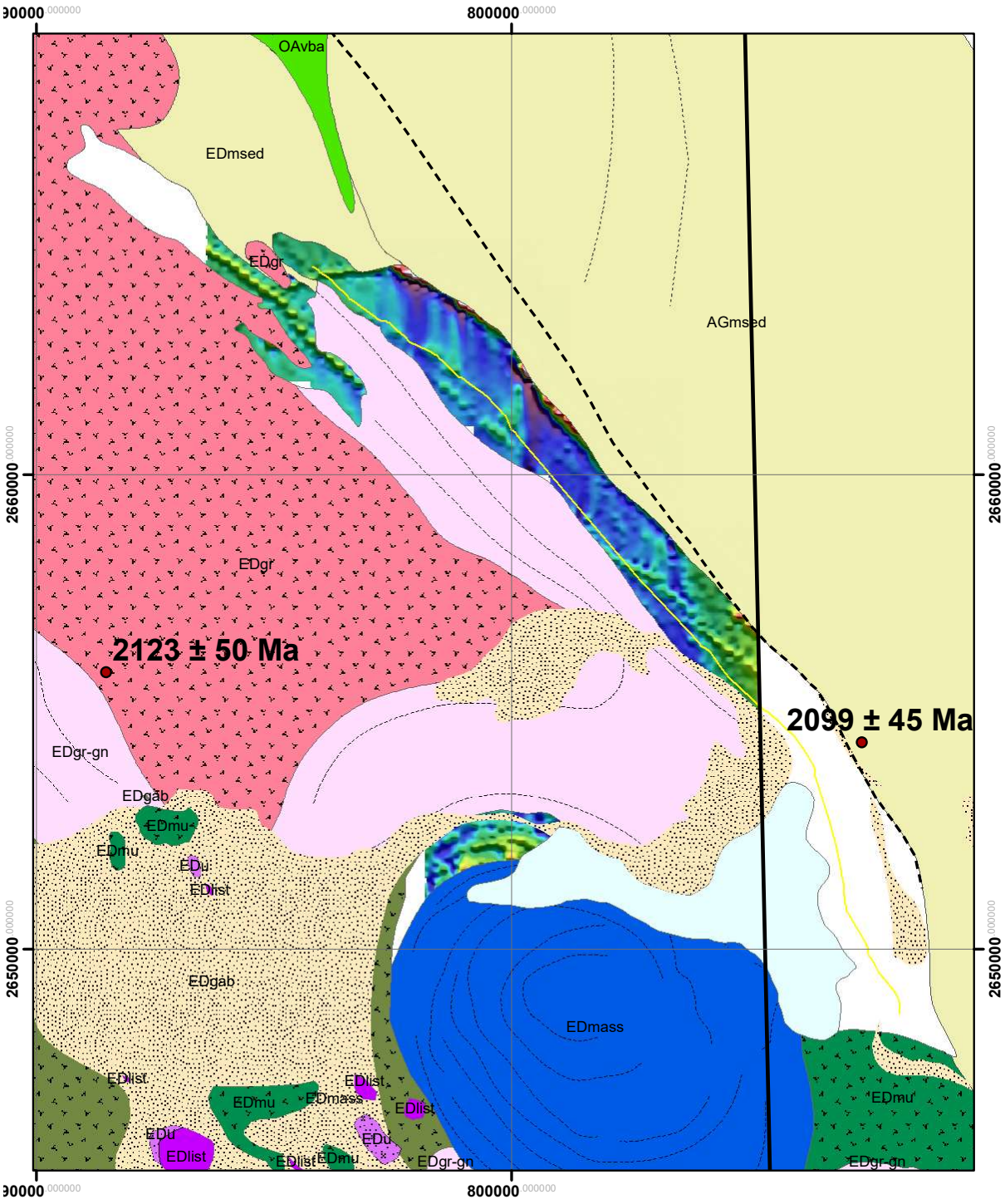

Figure 4-8 b – Ground magnetic data from the Northern Limb. The one of layers running parallel to the chromitite seam shows a weak magnetic anomaly, with a strong magnetic anomaly along the northern margin of the limb.

Elmalhat Anorthosite Complex:

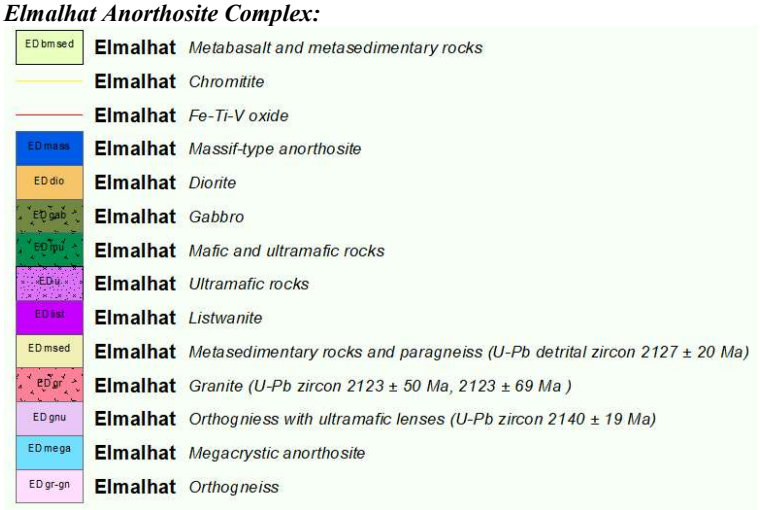

Sfariat-Bu Daira:

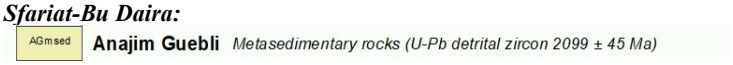

Figure 4-8 c - Legend

4.1.2.2.2.1.1 Anorthosite

The anorthosite is generally leucocratic to melanocratic and is dark green through green-grey, to white in colour depending on the proportion of the mafic component and degree of alteration. The intrusion is defined by the distinct megacrystic textures of the anorthosite (Figure 4-9). Rounded, equidimensional megacrysts of plagioclase ranging in size from ~0.2-15 cm (mostly ~0.5-2 cm) are supported by a fine grained mafic groundmass. The plagioclase megacrysts are white (sometimes with a tinge of green) and make up ~50-100% of the rocks in the Northern Limb, averaging 85-95%. Primary igneous mineralogy is not preserved in the Northern Limb with mafic minerals having been metamorphosed to hornblende, clinozoisite and chlorite; and the plagioclase having undergone minor sericite and epidote alteration. The fine-grained groundmass consists of varying portions of hornblende (50-100%), plagioclase (0-50%) and chlorite (0-50%). Disseminated or patchy magmatic sulphides (up to ~5%), mainly chalcopyrite and pyrite, are commonly observed throughout the anorthosite in the Northern Limb. There is a variation in grainsize of the sulphides, ranging from fine grained (<~1mm) in more plagioclase-rich areas (Figure 4-11a) to coarse grained (~2mm) where more patchy textures are observed (Figure 12b).

Several unusual textures are observed throughout the Northern Limb. The distribution of the interstitial mafic groundmass is commonly uneven within the anorthosite, concentrating in more mafic blebs (Figure 4-10, Figure 4-12a). This is quite often observed as an orbicular texture within the anorthosite with orbicules containing a more mafic core of gabbroic composition, with plagioclase-rich rims (Figure 4-12b). At several localities textures resembling magma mixing and immiscibility are observed. A graphic example of this can be seen in Figure 4-12c; A compositionally layered leucogabbro is observed interacting with a more mafic magma containing large (up to ~15 cm) plagioclase megacrysts. The layers in the leucogabbro can be seen bending around the plagioclase megacrysts indicating that the leucogabbro was not yet completely solid when this interaction occurred, and thus there were two magmas interacting.

Compositional layering is sometimes observed, defined by varying proportions of mafic minerals (Figure 4-12c, Figure 4-13). This generally consists of alternating layers of melanocratic mafic material and pure plagioclase. Directly adjacent to the seam of chromitite in the south of the Northern Limb, this compositional variation is observed as convoluted bedding (Figure 4-13). The compositional layering is generally sub-vertical, trending northwest-southeast. Cross-bedding is also observed in anorthosite close to the chromitite and convoluted layers in the south of the Northern Limb.



Figure 4-9 – Field photographs showing the typical appearance of the megacrystic textures in in leucogabbro/anorthosite within the Northern Limb. Equant plagioclase megacrysts (0.2-15 cm) with a mafic groundmass (UTM 28 804094 mE, 2656378 mN).



Figure 4-10 - Field photographs of megacrystic anorthosite with blebs of more mafic material (Photo from Laurence Robb - UTM 28 795943 mE, 2662614 mN)

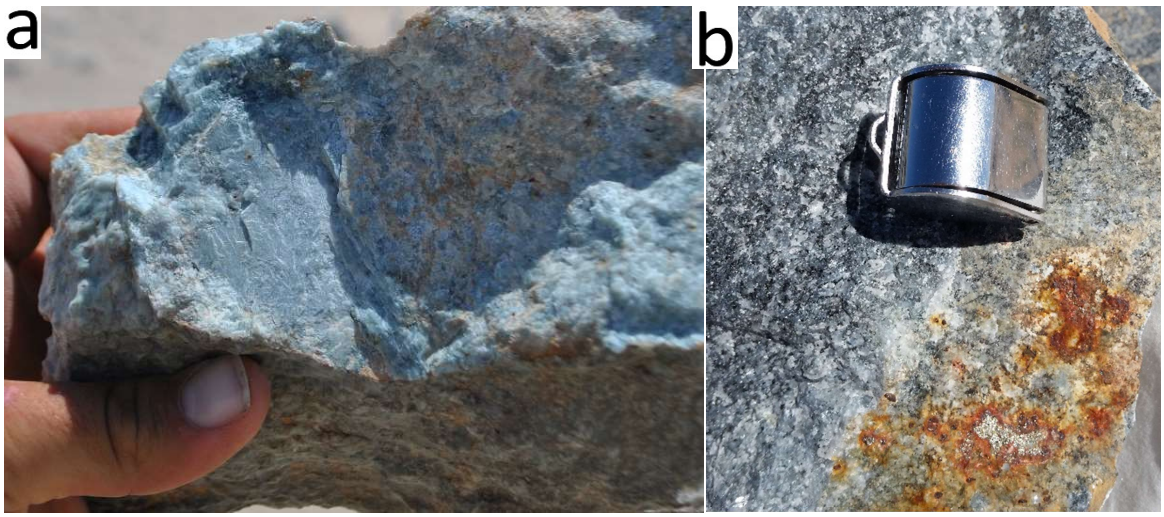

Figure 4-11 - Field photographs of Anorthosite from the Northern Limb containing a) fine disseminate pyrite (UTM 28 804599 mE, 2655712 mN); and b) patchy pyrite (UTM 28 804546 mE, 2655795 mN).

In the south, the Northern Limb is truncated by medium-coarse grained mafic/ultramafic intrusive rocks consisting of amphibole (70-100%) and plagioclase (0-30%). While not directly connected to the rest of the Northern Limb, there are some outcrops of anorthosite (~10-100 m in size) within the orthogneiss to the south of the ultramafic intrusion and Main Bulb. They show very similar characteristics to the Northern Limb including megacrystic texture (Figure 4-14a) and compositional banding on a scale of ~1-3 cm (Figure 4-14b).

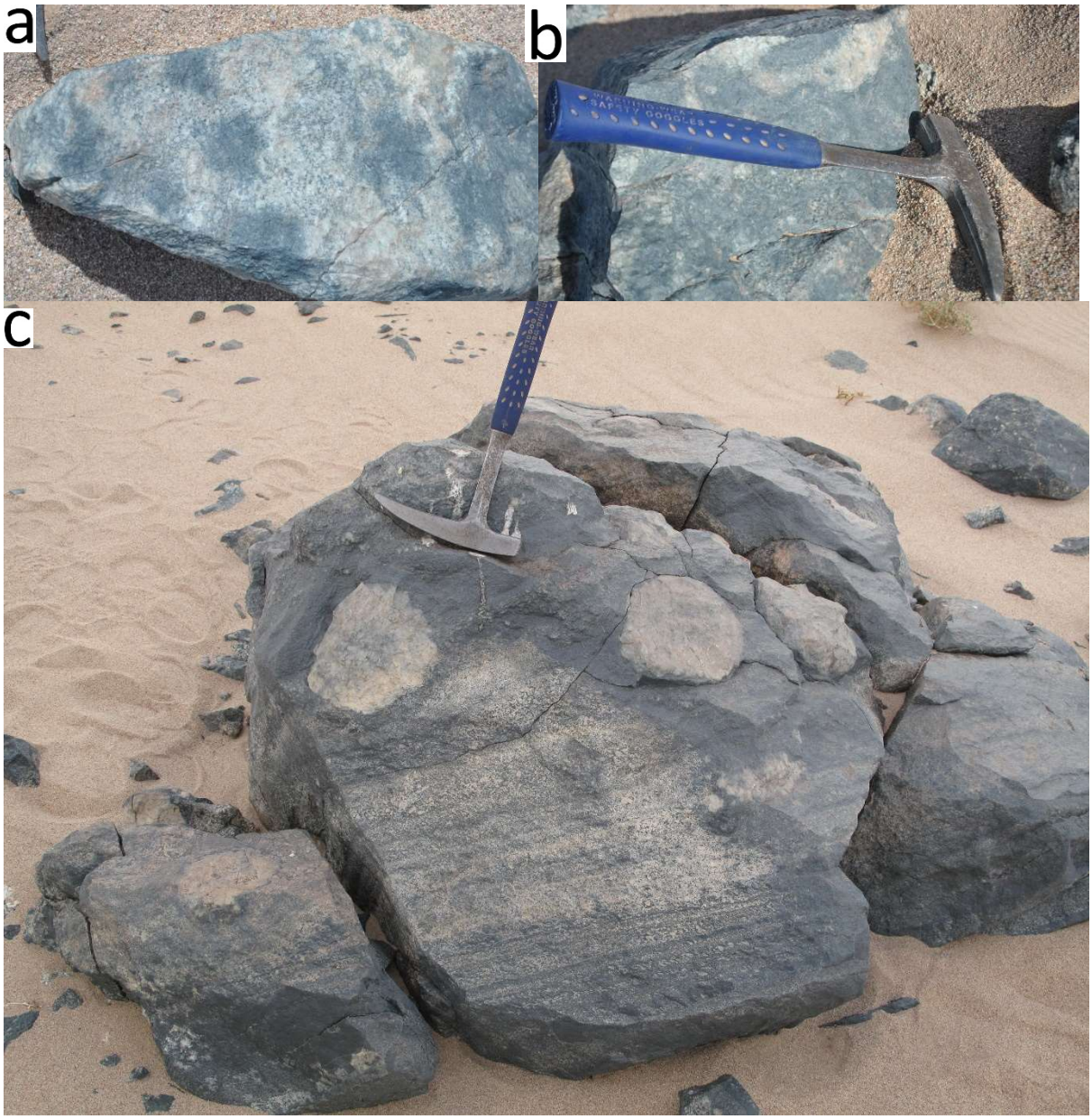

Figure 4-12 – Field photograph of magma mixing/liquid immiscibility textures of the Northern Limb of the EAC. a) mafic blebs in a more plagioclase-rich melt (UTM 28Q 803969mE, 2655967mN). b) orbicular texture showing a typical orbicule of the Northern Limb consisting of a more mafic centre and a more plagioclase-rich rim (UTM 28Q 794873 mE, 2635335 mN). c) Three separate phases present, interacting with each other. Coarse-grained leucogabbro displating compositional layering, cut by a basaltic material containing large rounded plagioclase megacrysts up to ~15 cm in diameter.



Figure 4-13 – Field photographs of convoluted compositional banding in the anorthosite proximal to the chromitite seam (UTM 29 196244 mE, 2651495 mN).



Figure 4-14 – Field photographs of outcrops of megacrystic-type anorthosite to the south of the Main Bulb of the EAC. Displaying a) megacrystic texture (UTM 29 194976 mE, 2643147 mN); and b) compositional banding (UTM 29 195515 mE, 2641932 mN)

4.1.2.2.2.1.2 Chromitite

The seam of massive chromitite (Figure 4-15) strikes northwest-southeast, parallel to the layering in the anorthosite (Figure 4-8). It is a concordant, sub-vertical seam averaging ~30-80 cm (Figure 4-16a) in thicknessal, though in places it narrows to stringers, a few mm in thickness (Figure 4-16b, c) or thickens up to ~2.5 m (Figure 4-16 d, e). Where the seam thickens, layering is observed with distinct grainsize variations within the beds (Figure 4-16e). It has been mapped over a total strike of ~19km, though is largely obscured by sand cover with chromitite lag marking its occurrence.

The chromitite seam is black, very dense and has a cumulate texture. Generally medium grained, it ranges in grainsize from ~0.1-10 mm. The seam is composed of a chromite (~65-90%) cumulate phase with interstitial chlorite and minor amphibole. Some parts of the chromitite appear to be sheared resulting in a reduction in grainsize of the chromite grains. The anorthosite adjacent to the chromitite often contains up to ~15% chromite with chromite sometimes comprising the only intercumulus phase of the anorthosite (Figure 4-16b)



Figure 4-15 - Field photograph of massive Chromitite from the Northern Limb (UTM 28 804575 mE, 2655735 mN).



Figure 4-16 – Field photographs of outcropping chromitite. a) ~1m wide outcrop of massive chromitite (UTM 29 197244 mE, 2648999 mN). b) Chromitite is present as stringers within anorthosite, with chromite forming the intercumulus mineral in the anorthosite (UTM 29 195773 mE, 2653622 mN). c) chromitite pinching out seam hosted in convoluted bedded anorthosite (from Laurence Robb - UTM 29 196244 mE, 2651495 mN).

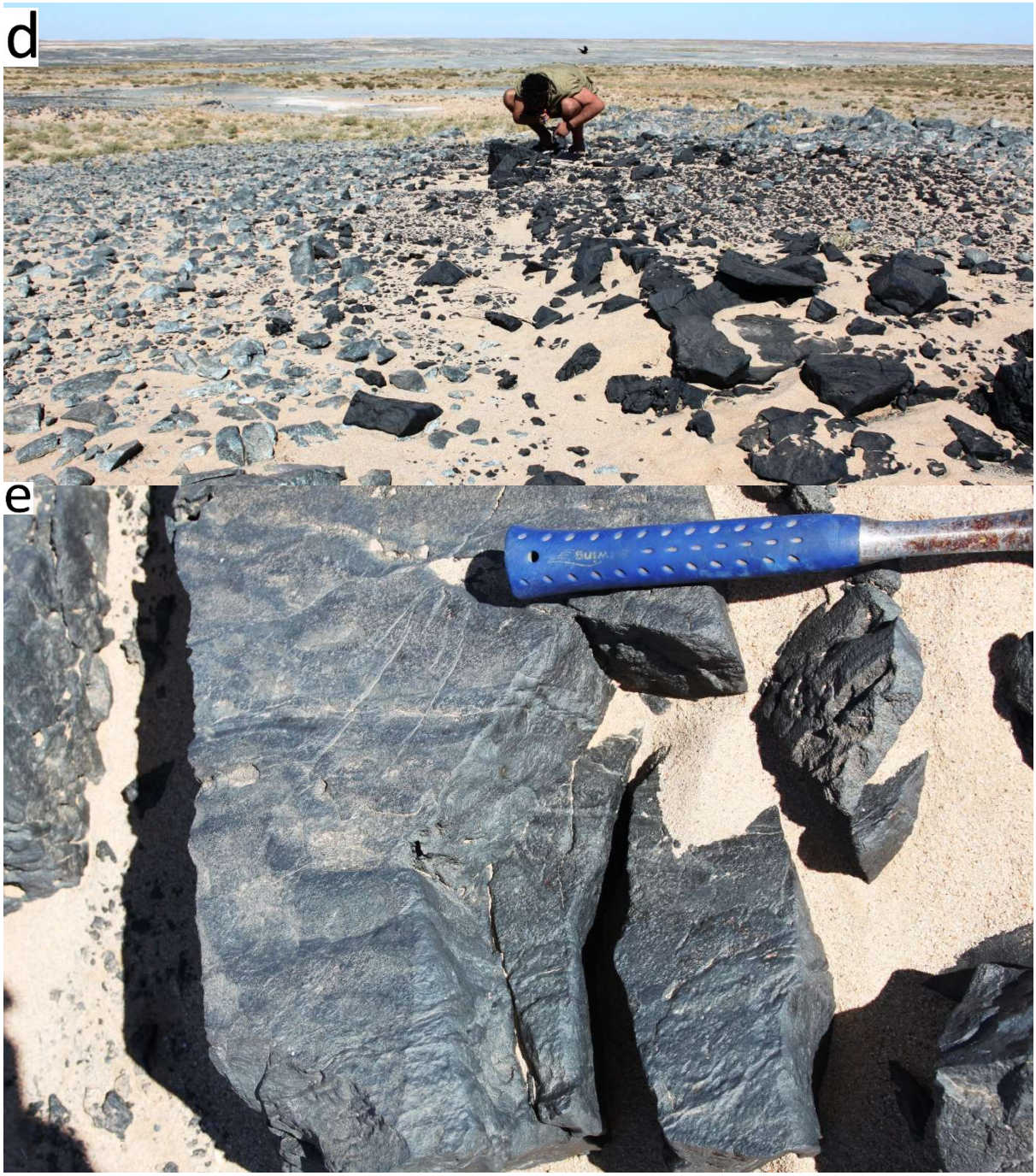

Figure 4-16 – Continued. d) ~2.5 m thick outcrop of massive chromitite. Graded bedding is observed in the chromite at this outcrop (UTM 29 197244 mE, 2648999 mN). e) graded bedding within the chromitite seam (UTM 29 197244 mE, 2648999 mN).

4.1.2.2.2.1.3 Amphibolite

The amphibolite forms a ~10-30 m wide layer (though it thickens to ~250 m in the south of the Northern Limb) ~30-50 m to the west of the chromitite seam. It forms a melanocratic, dark green, medium grained (~1.5 mm) layer that is strongly foliated and appears to be locally

sheared (Figure 4-17). It contains a significantly higher portion of mafic minerals than the anorthosite/leucogabbro comprising amphibole (~40-70%), plagioclase (~30-60%).



Figure 4-17 - Field photograph of Amphibolite layer ~30 m to the west of the chromitite (UTM 29 197206 mE, 2649024 mN).

4.1.2.2.2.2 Anorthosite and related rocks along the contact with the Oum Abana Domain

The contact zone between the Oum Abana and Elmalhat Domains contains a mix of rocks from both Domains including metasediments (Figure 4-18) and metavolcanics from the Oum Abana Domain and intrusive rocks from the Elmalhat Domain including megacrystic anorthosite (Figure 4-19) and poikilitic metapyroxenite (Figure 4-20). Proximal to an east-west trending shear zone at the southern edge of the contact zone, megacrystic anorthosite with originally equidimensional plagioclase megacrysts define the strong foliation and lineation of the rock, effectively acting as strain ellipsoids (Figure 4-19). The poikilitic metapyroxenite consists of large amphibole oikocrysts (~up to 2-3 cm) in a fine mafic matrix. The metapyroxenite froms lenses ~40 m long and 5-10 m wide.

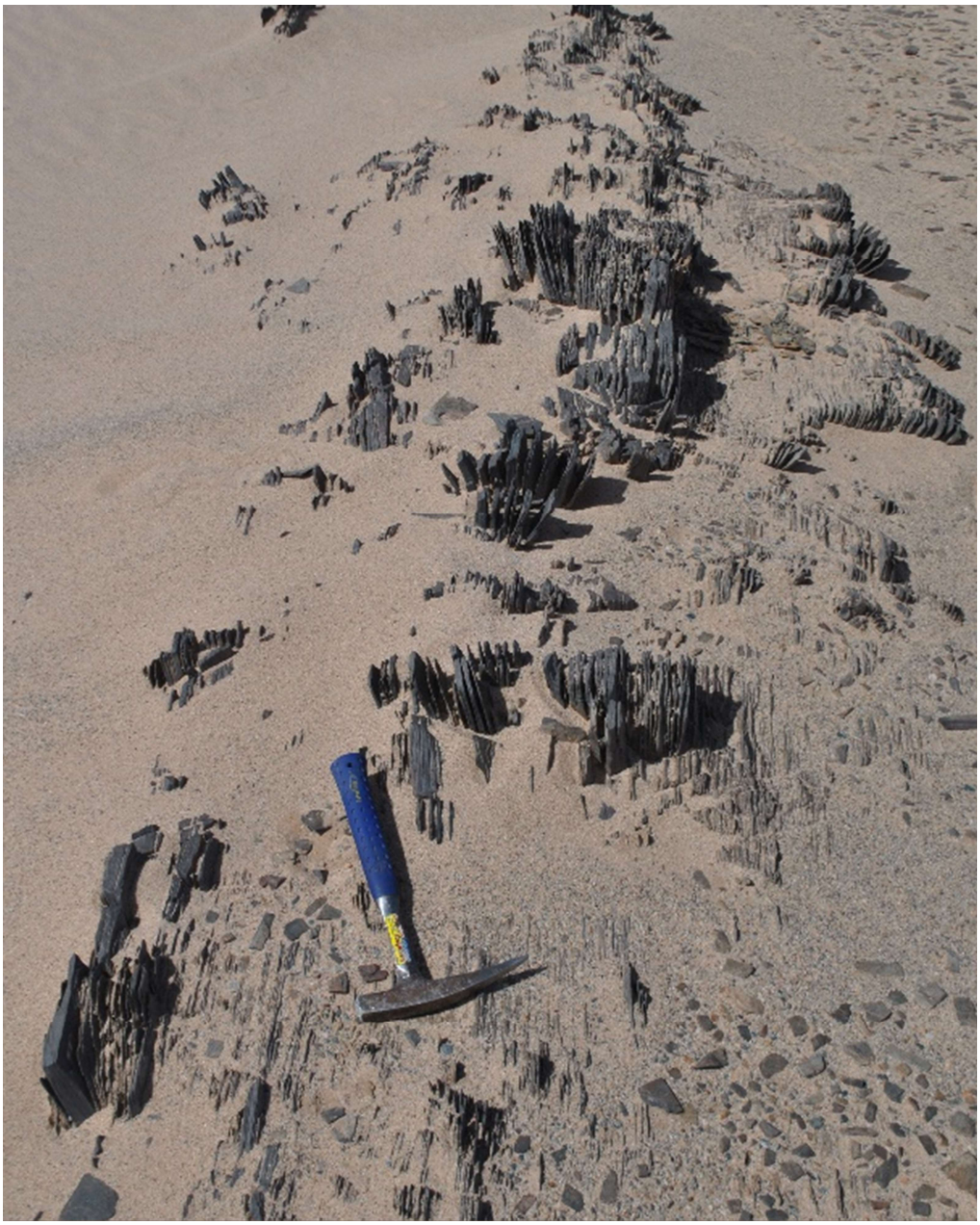

Figure 4-18 - Field photograph of quartzite in the E-W trending shear zone defining the contact between the Elmalhat and Oum Abana Domains (UTM 28 784241 mE, 2675326 mN).

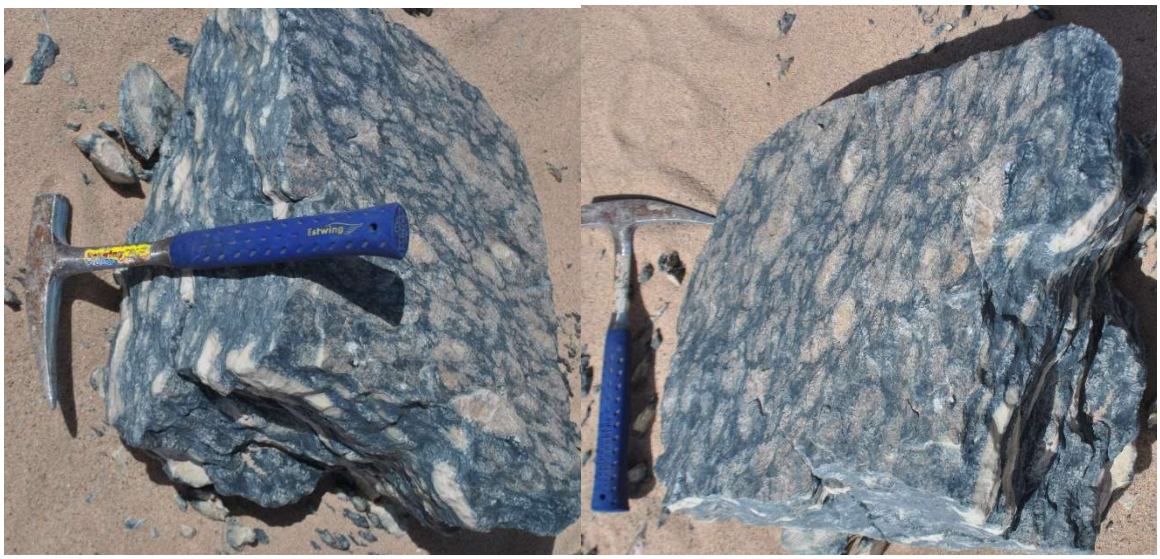

Figure 4-19 – Field photographs of megacrystic anorthosite with originally equidimensional plagioclase megacrystic define the strong foliation and lineation of the rock effectively acting as strain ellipsoids (UTM 28 784238 mE, 2675307 mN).



Figure 4-20 – Field photograph of poikilitic metapyroxenite close to the contact with the Oum Abana Domain (photo from Laurence Robb - UTM 28 784224 mE, 2674211 mN)

4.1.2.2.2.3 Other Megacrystic Anorthosite

In the northern part of the Elmalhat Domain, there are several, smaller, megacrystic-type anorthosite intrusions hosted in orthogneiss. In one such intrusion, the interleaved contact of the host granodiorite gneiss with anorthosite is well-exposed (Figure 4-21). Anorthosite is emplaced along en-echelon tearing in the orthogneiss (Figure 4-22) with clear alteration and resorption of the gneiss in the anorthosite (Figure 4-23). Orbicular textures present within the intrusion differed from those elsewhere in the EAC, containing white plagioclase cores with a pink rim (Figure 4-24; the opposite of the those observed in Moug El Kaleb Chapter 4.1.2.2.3.3). Xenoliths of host gneiss within the anorthosite appear to be more felsic and appear to be partially absorbed by the hot anorthosite magma.



Figure 4-21 – Field photograph of the interleaved contact of the anorthosite intrusion. Two good looking geologists (V. Robb, pers. comm.) for scale. To the right of them on the photograph are the host orthogneiss while rocks to the left are anorthosite (UTM 28 787233 mE, 2683296 mN).

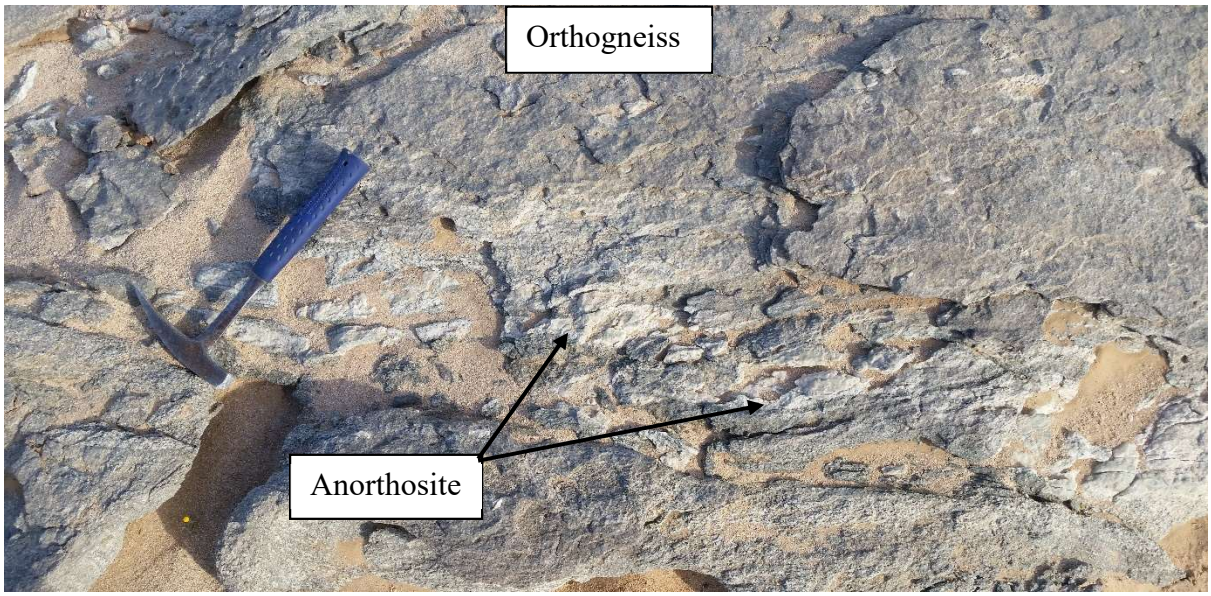

Figure 4-22 – Field photograph of interleaved anorthosite-orthogneiss contact, with anorthosite emplaced along en-echelon tearing in the orthogneiss (UTM 28 787233 mE, 2683296 mN).

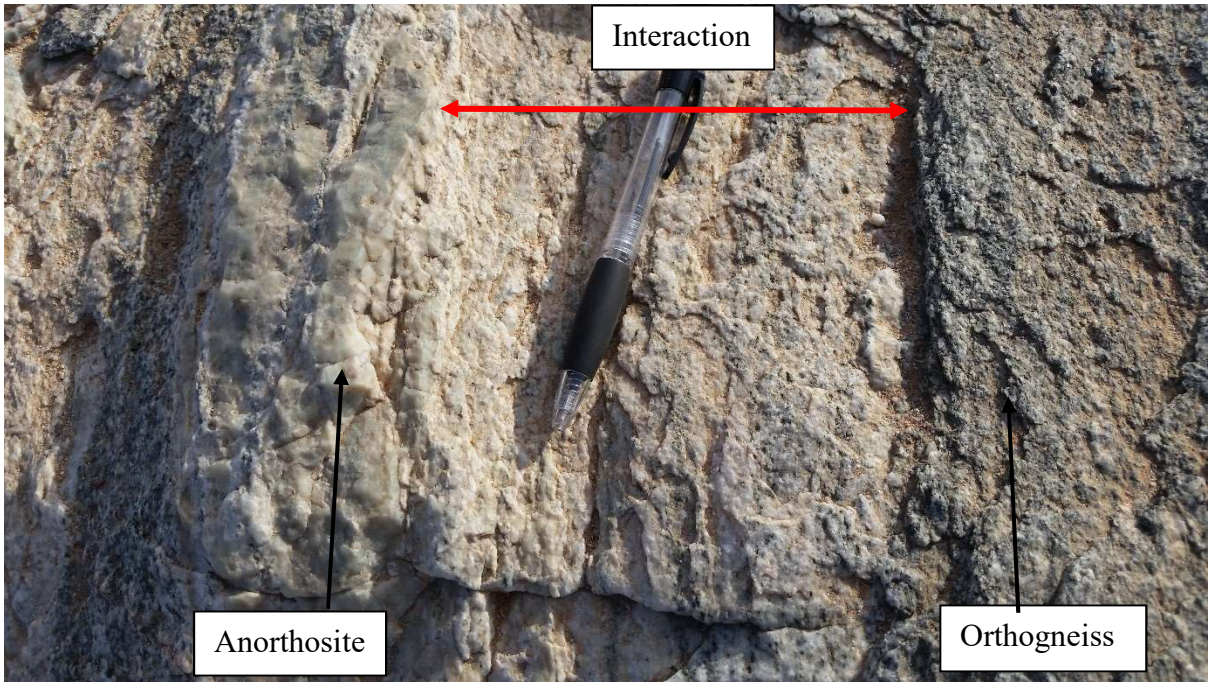

Figure 4-23 – Field photograph of interleaved contact between anorthosite and host orthogneiss showing the interaction between the gneiss and the anorthosite melt. It appears that the gneiss is progressively adsorbed within the anorthositic melt, becoming more leucocratic towards the intrusion (UTM 28 787233 mE, 2683296 mN).



Figure 4-24 - Field photograph of pink orbicals found in anorthosite in the Oum Abana belt representing a large plagioclase crystal (from Laurence Robb – UTM 28 787238 mE, 2683293 mN).

4.1.2.2.3 Massif-type anorthosite

4.1.2.2.3.1 Main Bulb

The Main Bulb is the most well exposed and best-preserved exposure of massif-type anorthosite in the EAC. The bulb forms an oval-shaped depression elongate along its northwest-southeast axis. It broadly consists of banded leucogabbro and anorthosite, cross cut by ultramafic, gabbroic, and granitic dykes. Xenoliths of megacrystic anorthosite are also observed within the massif-type anorthosite and leucogabbro of the bulb and around the edges of the intrusion.

The main lithology in the bulb is dark, banded anorthosite (Figure 4-25). In fresh samples where primary igneous mineralogy is preserved, the anorthosite consists of plagioclase (65-100%), pyroxenes (0-35%), biotite (0-5%), amphibole (0-5%), magnetite (0-2%) and various sulphide minerals (0-2%). Fresh samples are a dark brown-purple colour (Figure 4-25), coloured by the purple plagioclase and dark mafic minerals (Figure 4-26). Within fresh samples, exsolution lamellae of orthopyroxene in clinopyroxene are observed in hand sample.

The anorthosite is generally coarse grained, ranging from 2-6mm. The magmatic banding observed in the anorthosite is defined by the alignment of lath-shaped plagioclase crystals and elongate clusters of pyroxene. Compositional banding parallel to the grain orientation is also observed within the bulb defined by differences in the proportion of mafic minerals (Figure 4-27).



Figure 4-25 – Field photograph of outcrop of fresh anorthosite from the Main Bulb (UTM 28 799676 mE, 2650555 mN).

Within the bulb, most of the rocks preserve their primary igneous mineralogy. Adjacent to structures and quartz veins, the anorthosite can be affected by metasomatism. These altered samples have a massive texture, are mesocratic and grey in colour with the plagioclase having been altered to a white colour, similar to what Ashwal and Twist (1994) observe in the Kunene Complex where the plagioclase is sericite and chlorite-altered (Figure 4-28). The pyroxene in these samples have been metamorphosed to amphibole and chlorite.



Figure 4-26 - Photograph of hand sample of leucogabbro from the main bulb of the EAC (UTM 28 799676 mE, 2650555 mN).



Figure 4-27 – Field photograph of compositional layering in the bulb of the EAC defined by differences in plagioclase content. Layering is parallel to the banding defined by the orientations of the plagioclase laths and mafic minerals (UTM 28 805366mE, 2648182mN).



Figure 4-28 - Field photograph of altered pale anorthosite from the bulb of the EAC (UTM 28 800097 mE, 2648289 mN).

Magma-mixing textures are also observed in the east of the bulb illustrating the interaction and immiscibility of two separate magmas (Figure 4-29).



Figure 4-29 - Field photograph of magma-mixing textures observed within the eastern magnetic anomaly (UTM 28 805363mE, 2648252mN).

Xenoliths observed within the bulb include the host orthogneiss and megacrystic-type anorthosite. Xenoliths of orthogneiss are largely present toward the edges of the intrusion. The only observed gneissic xenoliths are ~30 cm in size and are very similar in appearance to the host orthogneiss.

Megacrystic anorthosite xenoliths are observed in the centre of the bulb (Figure 4-30) and close to the eastern edge (Figure 4-31). Megacrystic-type anorthosite xenoliths are generally coarse grained (3-4mm) and have a massive texture contrasting with the distinct lath-shaped plagioclase texture observed in the massif-type anorthosite. The anorthosite xenoliths are distinctly more plagioclase-rich (optically determined at >90%), and are grey in colour. In terms of mafic mineralogy, pyroxene is not observed in these xenoliths, instead amphibole and chlorite are observed.

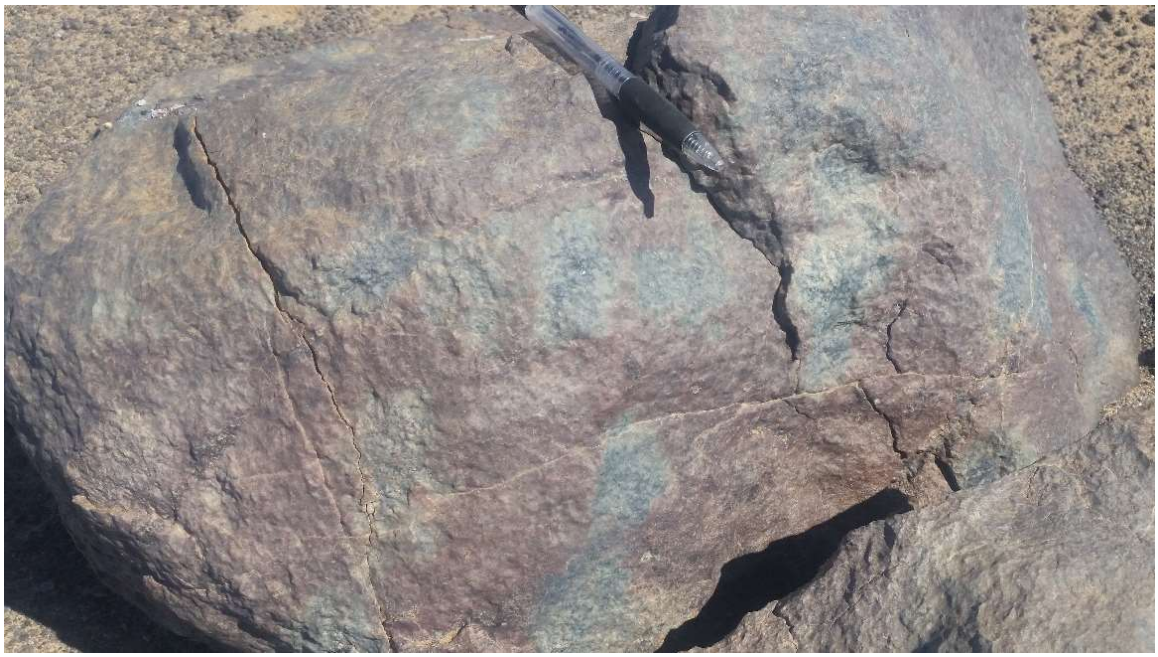

Figure 4-30 – Field photograph of xenoliths of megacrystic-type anorthosite within the bulb. Contains purple plagioclase, not observed in megacrystic anorthosite elsewhere in EAC with altered patches of grey anorthosite. The grey anorthosite contains a higher portion of mafic minerals potentially representing magma-mixing textures (UTM 28 801561 mE, 2648244 mN).

The megacrystic anorthosite xenoliths near the eastern edge of the intrusion exist in a layer of medium (0.5-2mm) grained, massive purple anorthosite with pods and stringers of white anorthosite and spinel (Figure 4-31). The elongated pods are ~0.5-10 cm in size and consist of a rim enriched in spinel with a centre of massive white anorthosite. The zone containing the pods is ~3m wide, striking roughly north-south.

Late sub-vertical ultramafic and gabbroic intrusions are present throughout the bulb. They range in size from ~2 cm to ~10 m wide (Figure 4-32) and are often observed intruding, white altered anorthosite. These intrusions are melanocratic, dark green-blue, medium-coarse grained (1-4mm) dykes containing less than 20% plagioclase. The mafic mineralogy of fresh, unaltered dykes is mostly pyroxene (up to 9%) and olivine (~5-20%) with minor biotite and magnetite. In metamorphosed samples the mafic phases are represented by amphibole and chlorite. One outcrop of pyroxenite displayed a poikilitic texture containing pyroxene oikiocrysts ~2 cm in size.

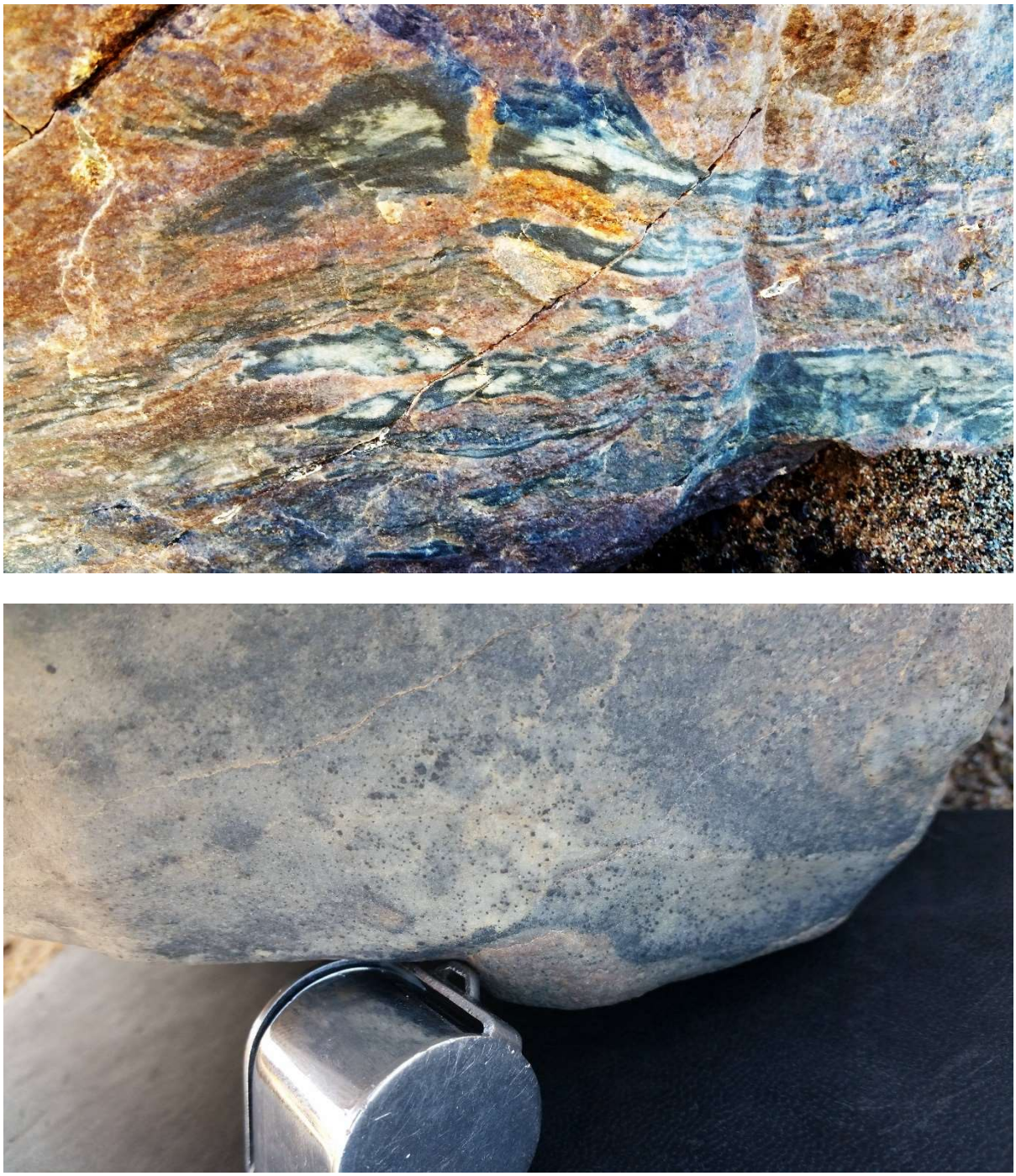

Figure 4-31 - Field photographs of pods of white anorthosite and spinel in massive purple anorthosite (UTM 28 805306 mE, 2648959 mN).

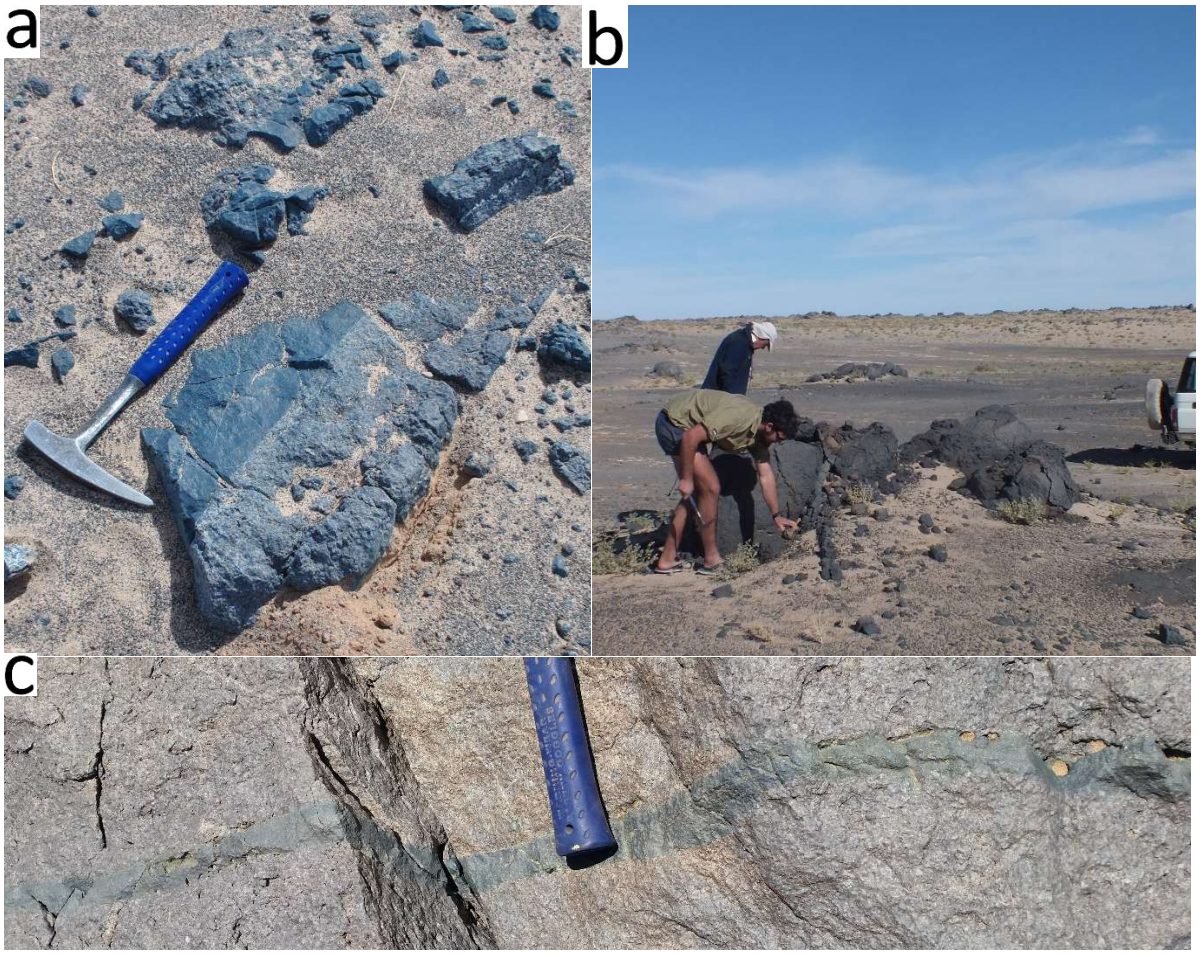

Figure 4-32 - Field photographs of late stage ultramafic intrusions within the bulb of EAC. a) ~15 cm sub-vertical ultramafic dyke cross-cutting leucogabbro. B) ~5 m wide ultramafic dyke cross-cutting the anorthosite within the eastern magnetic area. c) ~2 cm vein of ultramafic material intruding anorthosite (UTM 28 805285 mE, 2648869 mN).

To the west of the bulb the anorthosite and host gneiss contact appears to be interleaved with the proportion of gneiss gradually increasing away from the bulb until there are only a small (~5 m) lenses of anorthosite in the gneiss.

The southern contact of the bulb with the host orthogneiss is associated with a rise in topography to a distinct massive gabbroic unit. Forming a ridge on the southern contact, the weathering pattern of the unit is a granite-like exfoliation pattern (Figure 4-33). The unit is mesocratic, brown, medium grained and slightly magnetic. It consists largely of plagioclase (~50%), and pyroxene (~50%) with minor magnetite.



Figure 4-33 - Field photographs of ridge of gabbro defining the southern contact of the bulb anorthosites with the host orthogneiss. The gabbroic unit demonstrates distinctive granite-like exfoliation weathering patterns (UTM 29 194987 mE, 2644695 mN).

To the east, the contact between the massif-type anorthosite and megacrystic-type anorthosite is largely obscured by a sabkha and sand (Figure 4-34). Strongly altered massif type anorthosite and minor ultramafic dykes are present directly to the west of the sabkha and on the other side the southern continuation of the Northern Limb is present. To the south of the sabkha, two main lithologies are observed including a friable, brown, slightly magnetic, gabbro very similar in appearance to the gabbro on the southern contact, though with a different weathering style (Figure 4-34). The gabbro strikes to the north under the sabkha. The friable nature of the gabbro results in preferential weathering meaning that it probably represents the major lithology under the sabkha. The gabbro is cross-cut by late stage hard mafic dykes (2-50 cm wide) also north-south striking. Thus, this rock likely represents the contact between the two types of anorthosite.



Figure 4-34 – Field photographs of south of the sabkha representing the contact between massif-type and megacrystic anorthosite (UTM 29 195243 mE, 2648116 mN). A friable, brown, slightly magnetic gabbro is the major lithology present. The gabbro is cut by thin (2-50 cm) dykes, both striking north under the sabkha. The friable nature of the gabbo results in preferential weathering meaning that it potentially represents the major lithology under the sabkha.

Field observations show that the igneous banding of the anorthosite and leucogabbro dips towards the centre of the intrusion with dips increasing away from the centre, revealing a basin architecture (Figure 4-35a). A ground magnetic survey over the intrusion defines concentric magnetic anomalies around the centre of the intrusion (Figure 4-35b). These anomalies are parallel to the igneous banding and as such probably reflect slightly more magnetic layers. The cause of the strong magnetic highs in the south of the bulb are unknown. Thin seams (~1-2 cm) of magnetite are observed at two localities in the south of the bulb, though are not persistent. The soil contains very small pieces of magnetite. With its significant sand cover following the peak of the magnetic anomalies it is possible that the cover is obscuring a magnetic layer.

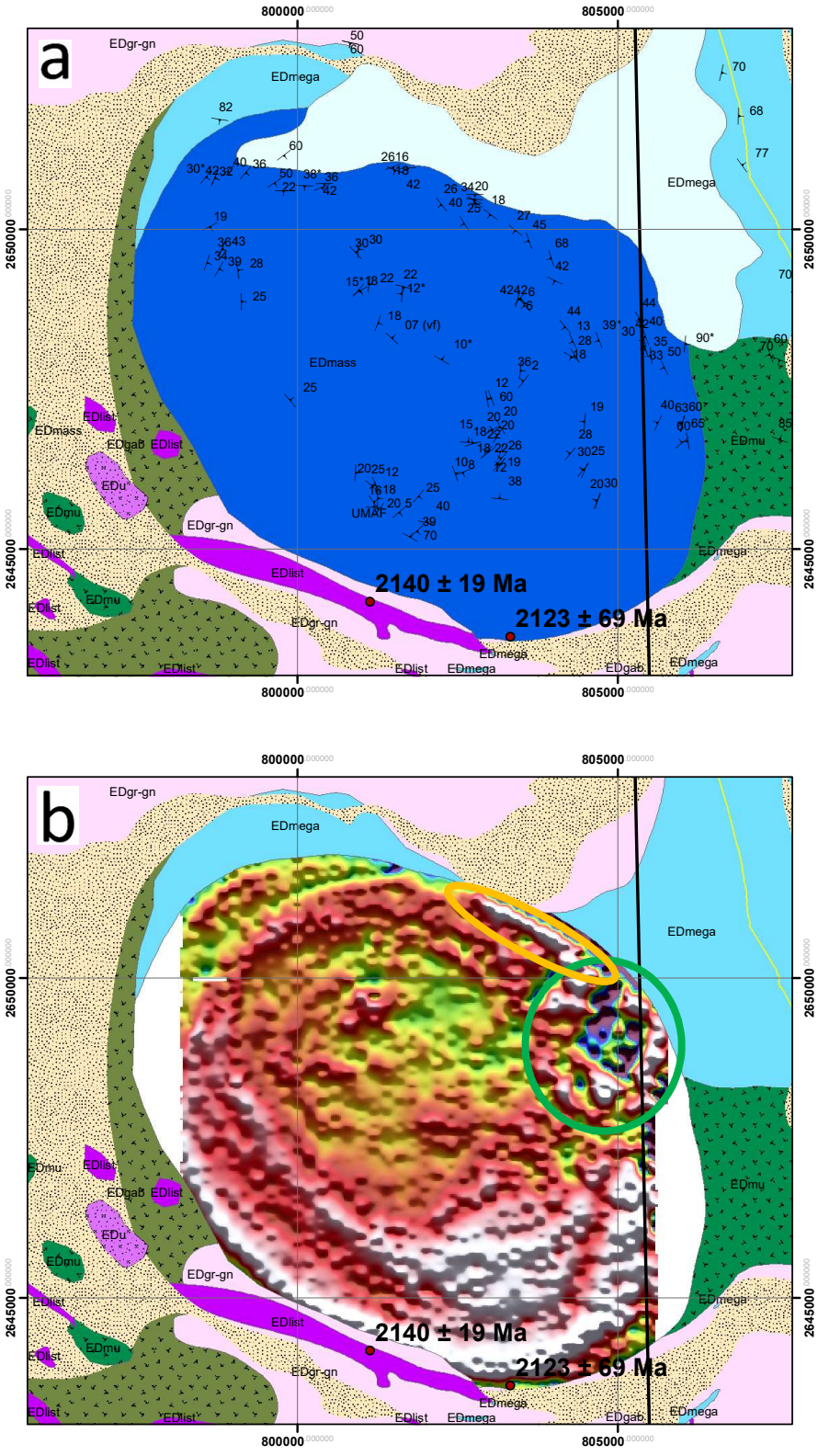

Figure 4-35 a) Orientation of the primary igneous banding in the bulb of the EAC showing a basin-like architecture. b) Concentric magnetic anomalies in the bulb of the EAC from ground magnetic data provided by Hanno Resources. A magnetic anomaly in the northern part of the bulb is shown by the orange circle, while a magnetic anomaly in the east is indicated by the green circle.

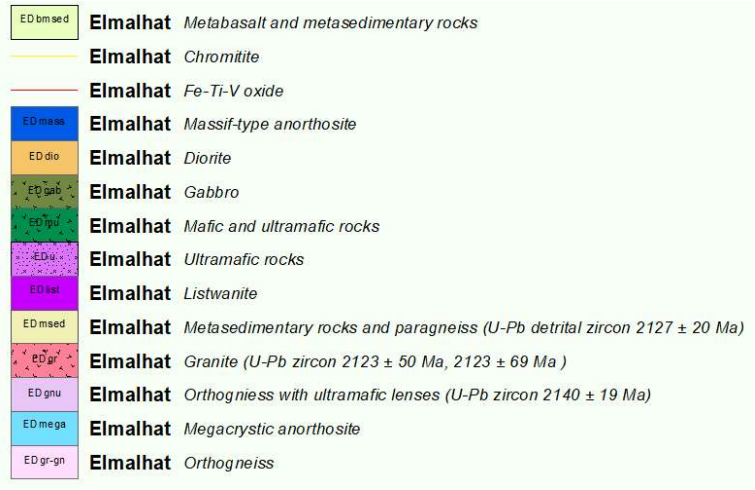

Figure 4-35 c - Legend

The northern contact of the bulb is also obscured by a sabkha, though in the rocks directly to the south, gabbro is observed, cut by roughly a east-west trending shear zone (Figure 4-36). The gabbro in the north appears to be different to the gabbro along the southern and eastern contacts. The magnetic anomaly in the north (Figure 4-35 b) is caused by a sheared layer of magnetic gabbro. The magnetite gabbro is mesocratic, brown, coarse grained (~2.5 mm) and dense. It consists of plagioclase (~50-60%), pyroxene (~30%) and magnetite (~10-20%). It is present in subcrops across the northern contact sabkha.

A magnetic anomaly in the east, apparently disrupts the concentric nature of the other magnetic anomalies of the bulb (Figure 4-35 b). The region lies between the sabkha representing the eastern contact and a smaller north-south trending sabkha ~200 m to the west. Like the rest of the bulb, the anorthosite in this region consists of dark, banded anorthosite, dipping toward the centre of the bulb. This region does however have a few features not observed commonly throughout the bulb. The previously described magma mingling textures (Figure 4-29) are only observed in this portion of the main bulb. The magnetic anomaly is the only place in the bulb to contain magmatic sulphides with chalcopyrite, pyrrhotite and pyrite observed disseminated in the anorthosite. Notably, the patchy sulphides are ~20 m away from the megacrystic anorthosite xenoliths (Figure 4-31).



Figure 4-36 – Field photographs of sheared gabbro representing the northern contact of the Main Bulb of the EAC (UTM 28 800514 mE, 2652072 mN).

4.1.2.2.3.2 Southern Bulb

The Southern Bulb of the EAC is located to the south of the Main Bulb (Figure 4-2). It is separated from the Main Bulb by a major shear zone of orthogneiss with lenses of massif-type anorthosite, ultramafic rocks and listwanites (Figure 4-37 a). Like the Main Bulb, the Southern Bulb is a massif-type anorthosite intrusion that has undergone metamorphism such that primary

igneous mineral assemblages have not been preserved although typical massif-type anorthosite textures are preserved. Ground magnetic data reveals arcuate anomalies in the Southern Bulb (Figure 4-37 b), roughly corresponding to the presence of magnetite (Fe-Ti-V) seams and patchy sulphides present in the anorthosite, though a large portion of the anomaly is over a sabkha. Due to extensive sand cover (Figure 4-38) and the presence of sabkhas, the Southern Bulb is not as well characterised as the Main Bulb.

Like the Main Bulb, the Southern Bulb is largely composed of anorthosite and leucogabbro, which will be collectively referred to as anorthosite for this section. The rocks in the Southern Bulb are much more leucocratic than in the Main Bulb, ranging in colour from white to mesocratic dark grey depending on the portion of mafic minerals and the amount of alteration of the plagioclase (Figures 4.42-46). Anorthosites in the Southern Bulb are composed of plagioclase (70-100%), amphibole (0-30%) with minor chlorite and variable sericite alteration. Disseminated to patchy sulphides (up to ~5%) are locally present in the anorthosite (Figure 4-39) close to the western contact with the mafic/ultramafic unit and close to the magnetite layers. Sulphide minerals observed include pyrite, chalcopyrite and minor pyrrhotite-pentlandite.

Massive textures dominate the Southern Bulb (Figure 4-39), although two other common textures of massif-type anorthosites are present. Mortar texture is prevalent (Figure 4-41) in the Southern Bulb representing the recrystallisation and grain size reduction of the plagioclase, also resulting in the whitening at the grain boundaries, possibly produced during movement of crystal-rich magmas (Ashwal and Bybee, 2017). Localised pods of anorthosite/leucogabbro are also observed (Figure 4.46) within the massive anorthosite. These range in size from ~20 cm to ~10 m with plagioclase crystals up to ~60 cm long. Locally, compositional banding is observed with alternating leucocratic and more mafic melanocratic layers on a cm scale.

Orbicular textures are also locally present within the Southern Bulb though with mafic orbicules rather than plagioclase orbicules observed in other parts of the EAC.

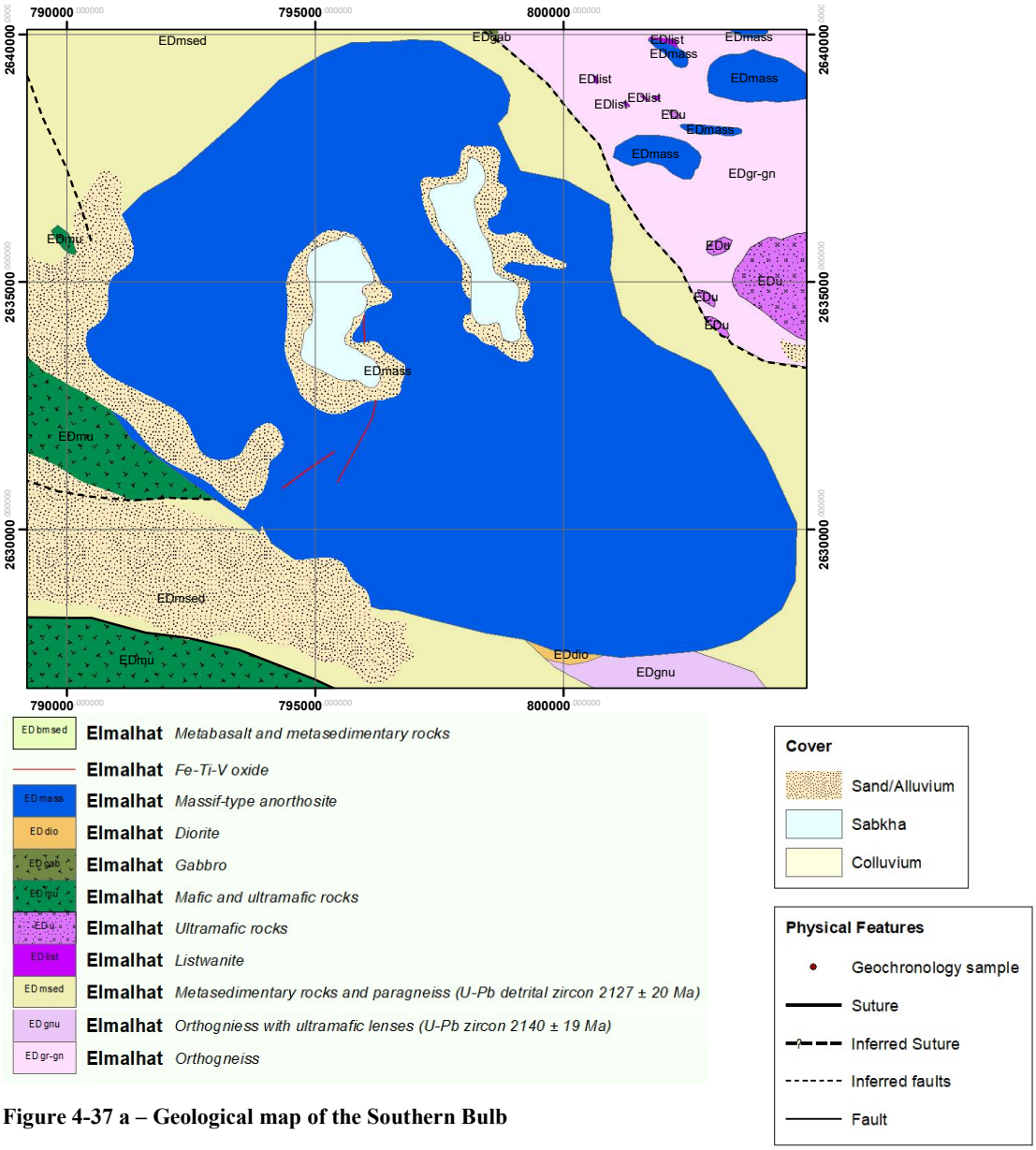

Figure 4-37 a – Geological map of the Southern Bulb

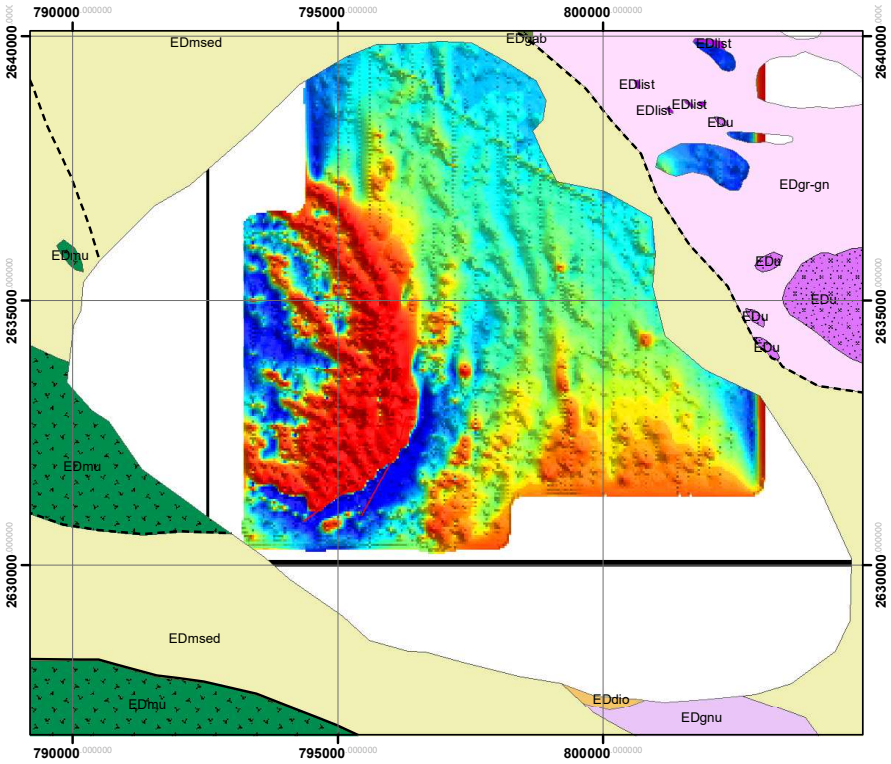

Figure 4-37 b - Ground magnetic data from the Southern Bulb of the EAC, showing arcuate anomalies; roughly matching the position of magnetite seams and the presence of patchy sulphides. The magnetic data was provided by Hanno Resources.



Figure 4-38 – Field photograph of typical view of the sand covered Southern Bulb. The anorthosite and leucogabbro boulders observed were dug out from the well 'Bir Elmalhat' after which the complex and domain were named (UTM 28 789260 mE, 2632029 mN).



Figure 4-39 – Field photograph of anorthosite with a green tinge from malachite present from the oxidation of primary chalcopyrite (UTM 28 795486 mE, 2631945 mN).



Figure 4-40 – Field photograph of outcrop of coarse grained anorthosite containing plagioclase oikocrysts up to ~3 cm (UTM 28 791627 mE, 2632532 mN).



Figure 4-41 - Field photograph of mortar texture observed in the Southern Bulb. A typical igneous feature of massif-type anorthosite complexes caused by the dynamic recrystallisation of plagioclase crystals in a plagioclase rich mush (UTM 28 791627 mE, 2632532 mN).



Figure 4-42a - Field photographs of pegmatitic textures observed in leucogabbro within the Southern Bulb. a) ~20 cm wide pod of pegmatitic leucogabbro within homogeneous coarse grained (2mm) leucogabbro (UTM 28 791708 mE, 2632437 mN).

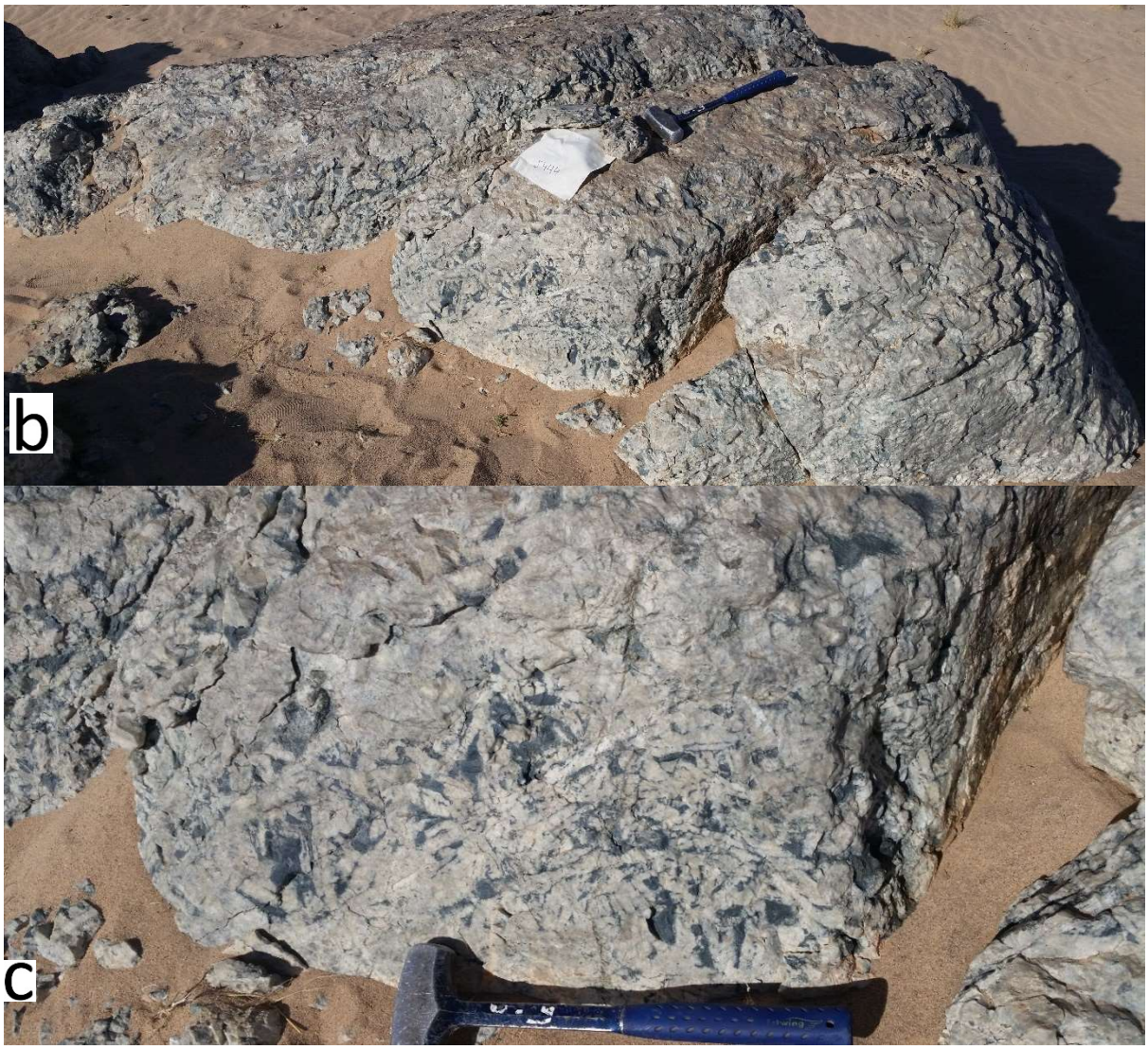

Figure 4-42 – Continued b, c) ~5 m outcrop of pegmatitic leucogabbro with plagioclase crystals up to ~60 cm in length (UTM 28 793348 mE, 2632649 mN).

The west of the Southern Bulb is composed of ultramafic and mafic rocks with low plagioclase content, cross-cut by pegmatitic granite veins (Figure 4-43). These rocks are composed of amphibole (85-100%), and plagioclase (0-15%). The contact between the anorthosite and ultramafic rocks consists of alternating patches of ultramafic/mafic rocks and leucogabbro. Moving from west to east in the contact zone, the gabbroic and ultramafic rocks give way to globules of leucogabbro and anorthosite. The first occurrence of leucogabbro moving from the ultramafic unit is marked by the appearance of (now partially weathered-out) sulphides. Green staining is observed around the brown oxidised sulphide blebs and is caused by malachite around chalcopyrite (Figure 4-39).

A number series of magnetite seams of magnetite are observed within the Southern Bulb ranging from ~70 cm to ~1.5 m in wide (Figure 4-44). Along the eastern margin of the magnetic anomaly, multiple, parallel magnetite layers ~1m thick are observed subcropping. The shallow dip of the seams results in the subcrop covering a region tens of meters wide and a few hundred meters long.

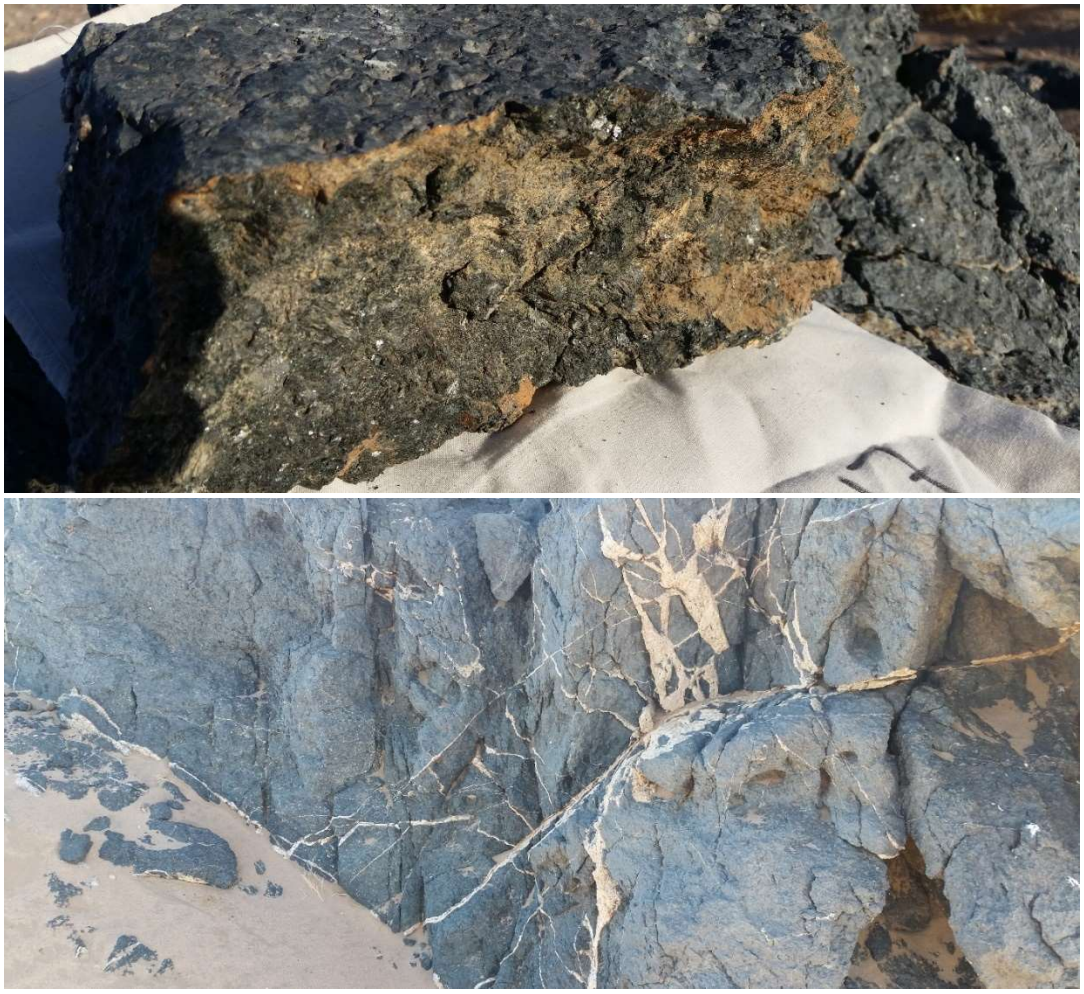

Figure 4-43 – Field and hand sample photographs of ultramafic amphibolite (meta-pyroxenite) from the Southern Bulb of the EAC, graphically cross-cut by late pegmatitic granite veins (UTM 28 800322 mE, 2631751 mN).



Figure 4-44 – Field photograph of typical subcrop of magnetite seams (the black rocks subcropping across the photo) on the edge of a sabkha in the Southern Bulb (UTM 28 795966 mE, 2632077 mN).

4.1.2.2.3.3 Moug El Kaleb

The Moug El Kaleb intrusion is an elongated body of massif-type anorthosite and leucogabbro approximately 30 km to the south west of the Main Bulb forming along the contact between the Elmalhat and Leaareig Domains (Figure 4-45). It strikes ~12km in the northwest-southeast orientation with a maximum width of ~1km. The anorthosite is hosted in paragneiss and is associated with several lenses of mafic and ultramafic intrusive rocks.

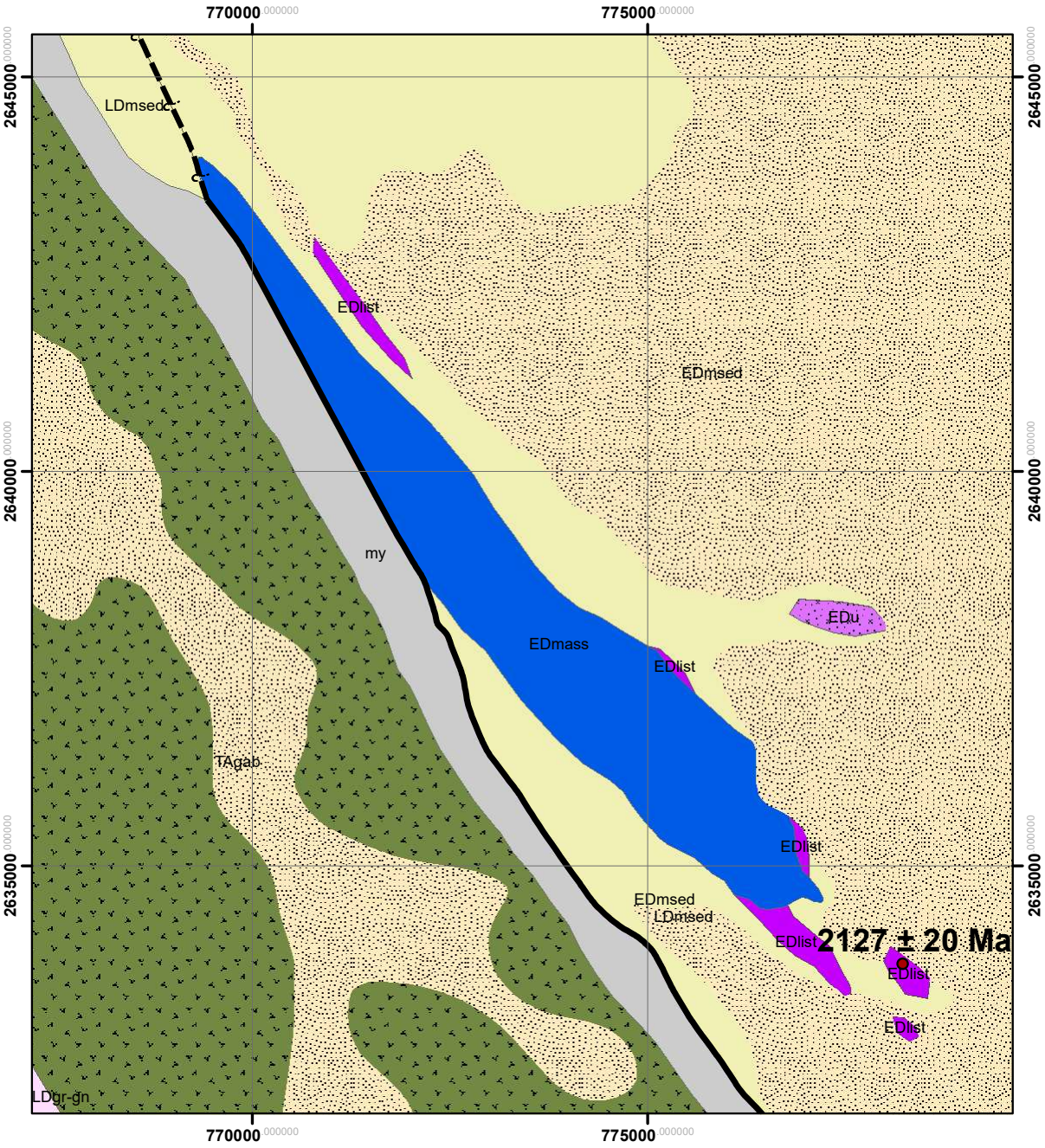

Figure 4-45 a – Geological map of Moug El Kaleb

Elmalhat Anorthosite Complex:

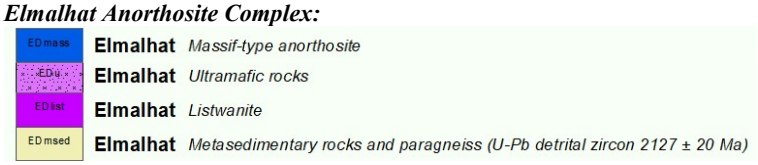

Leaareig Terrane:

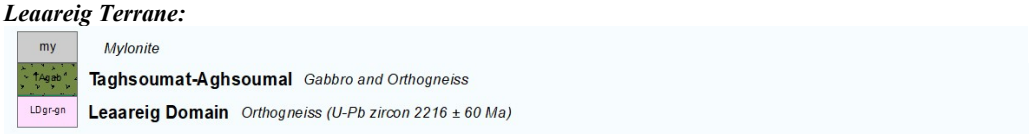

Figure 4-45 b - Legend

Located close to a major regional shear zone, the Moug El Kaleb anorthosites are more altered than the Main Bulb and Southern Bulb consisting of white plagioclase, with all of the mafic minerals having been altered to amphibole and chlorite (Figure 4-46, and Figure 4-47). It is highly variable in composition ranging in plagioclase content from ~50% to 100%. Patchy sulphides are present within 1-2m lenses where up to ~5-10% chalcopyrite and pyrite has been observed.

A large variety of textures are observed within the anorthosite including massive anorthosite, a distinctive orbicular texture anorthosite (Figure 4-46), and graphic magma mixing/liquid immiscibility textures (Figure 4-47). The orbicular anorthosite contains orbicules ~5-20 cm in size consisting of pink cores, white plagioclase rims and then more mafic-rich rim.



Figure 4-46 – Field photograph of orbicular texture at Moug el Kaleb (photo from Laurence Robb - UTM 28 774521 mE, 2636916 mN).



Figure 4-47 – Field photograph of magma mixing/immiscibility textures in leucogabbro at Moug El Kaleb (UTM 28 774671 mE, 2636824 mN).

The western edge of the Moug El Kaleb body consists of metamorphosed ultramafic rocks. These ultramafic are sheared and deformed to talc-chlorite schist on the western margin where the intrusion meets the Taghsoumat shear zone (Figure 4-48).

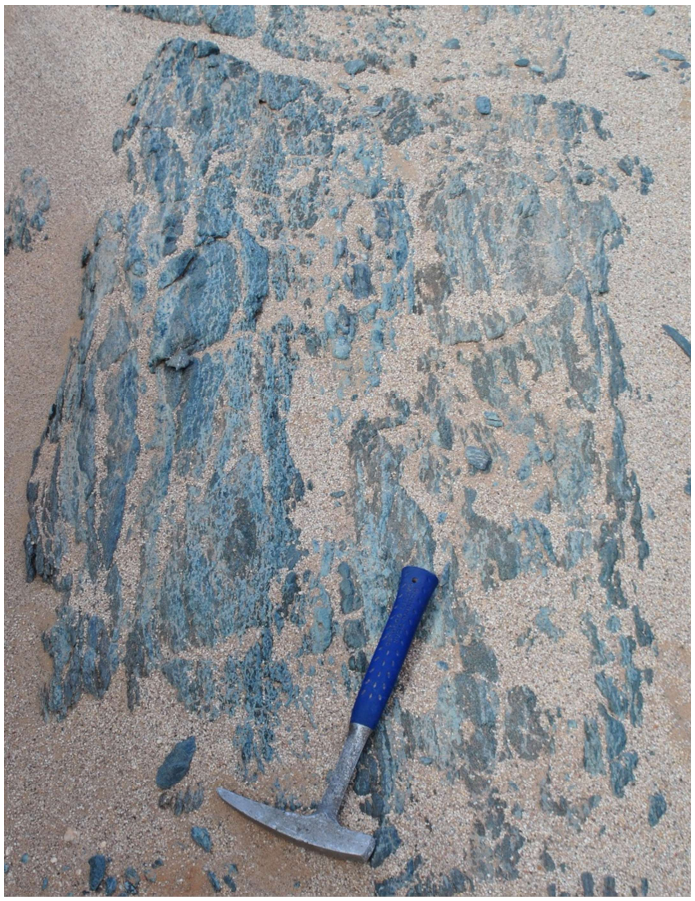

Figure 4-48 - Field photograph of sheared ultramafic rocks on the western margin of the Moug El Kaleb intrusion (UTM 28 775415 mE, 2635542 mN).

A chalcopyrite and pyrite-bearing magnetite layer is present near the western contact of the intrusion (Figure 4-49). The magnetite layer is ~2m wide and outcrops over ~40 m of strike. It appears to have been strongly altered by siliceous-carbonate fluids.

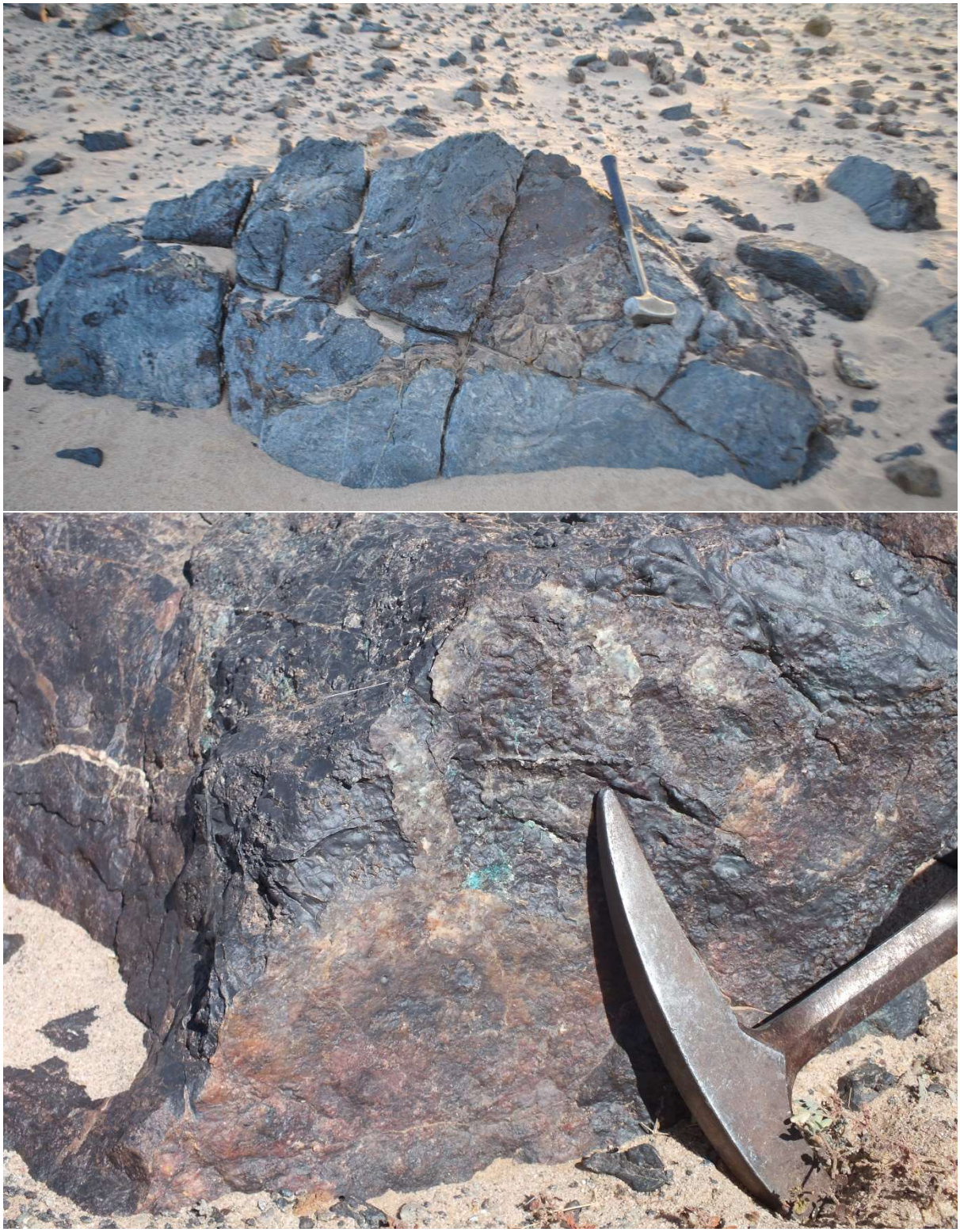

Figure 4-49 – Field photographs of the pyrite and chalcopyrite-bearing magnetite layer within the Moug El Kaleb intrusion (UTM 28 774137 mE, 2636653 mN).

4.1.2.2.4 Satellite Intrusions

Although not physically connected to the massif-type anorthosite intrusions at the surface, several related satellite bodies are present relating to the Main Bulb and Southern Bulb, similar to what is observed in other massif-type anorthosite complexes (such as Kunene; Maier et al., 2013).

These satellite bodies relating to the Main Bulb are hosted in gabbro. More resistant to weathering than their host gabbro, they form rounded outcrops down to ~2m in size and hills up to ~200 m wide. They consist of melanocratic, medium-coarse grained (~1-3mm), magnetic, black rocks outcropping as rounded boulders. They consist of a plagioclase (~50%), pyroxene (~10-30%) and magnetite (0-5%) groundmass with phenocrysts of olivine (~10-20%) and biotite (0-10%). These olivine gabbro(-dolerite) intrusions are much fresher than the host gabbro, having retained an original igneous mineralogy.

Satellite bodies relating to the Southern Bulb consist of coarse grained, gabbros comprising plagioclase (~50%) and igneous pyroxene (~50%), cut by fine grained leucotroctolite dykes comprising plagioclase (~80%), olivine (~10%), and pyroxene (~10%).

4.1.2.3 Gabbro and Ultramafic Intrusions

The gabbroic and ultramafic intrusive rocks are the dominant lithologies between the orthogneiss basement in the east and paragneiss basement in the west (Figure 4-50). Largely obscured by sand (Figure 4-51) and duricrust, outcrops are relatively scarce leading to this unit being not as well defined as other units in the Elmalhat Domain. The unit consists largely of gabbro with lenses comprising a mix of gabbro and ultramafic intrusive rocks as well as lenses of ultramafic rocks.

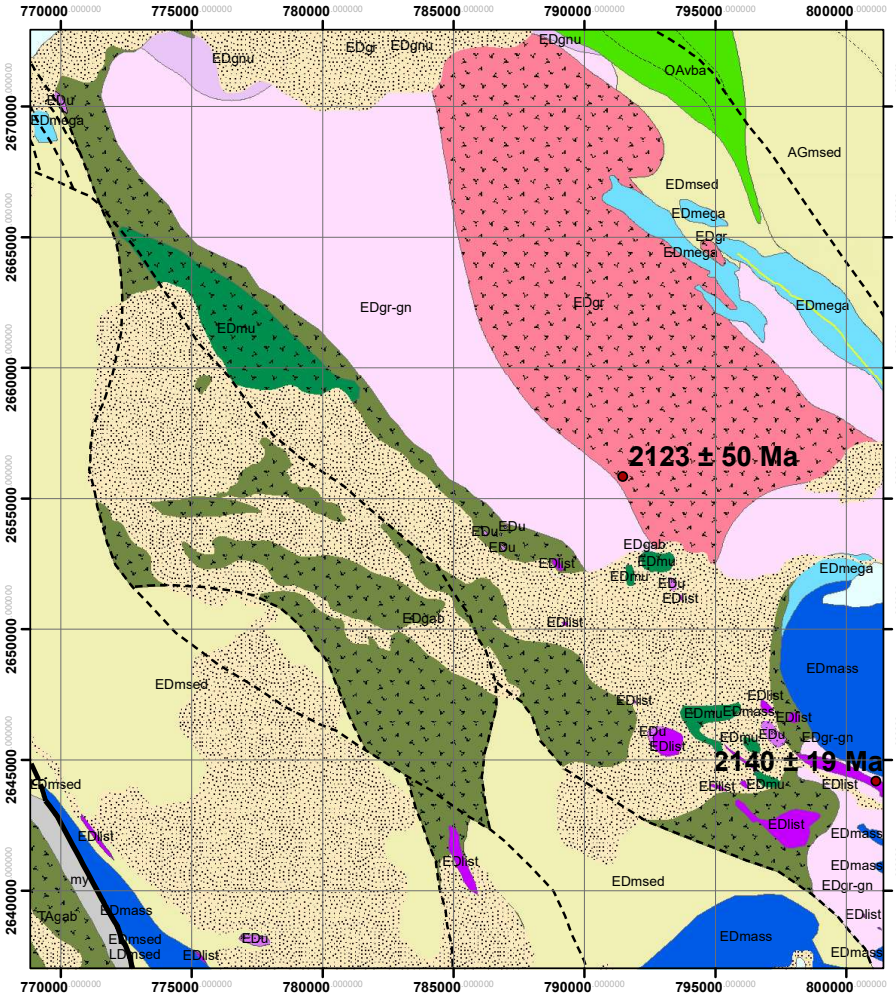

Elmalhat Anorthosite Complex:

EDbmsed	**Elmalhat**	*Metabasalt and metasedimentary rocks*
	Elmalhat	*Chromitite*
	Elmalhat	*Fe-Ti-V oxide*
EDmass	**Elmalhat**	*Massif-type anorthosite*
EDdio	**Elmalhat**	*Diorite*
EDgab	**Elmalhat**	*Gabbro*
EDmu	**Elmalhat**	*Mafic and ultramafic rocks*
EDu	**Elmalhat**	*Ultramafic rocks*
EDlist	**Elmalhat**	*Listwanite*
EDmsed	**Elmalhat**	*Metasedimentary rocks and paragneiss (U-Pb detrital zircon 2127 ± 20 Ma)*
EDgr	**Elmalhat**	*Granite (U-Pb zircon 2123 ± 50 Ma, 2123 ± 69 Ma)*
EDgnu	**Elmalhat**	*Orthogniess with ultramafic lenses (U-Pb zircon 2140 ± 19 Ma)*
EDmega	**Elmalhat**	*Megacrystic anorthosite*
EDgr-gn	**Elmalhat**	*Orthogneiss*

Cover

- Sand/Alluvium
- Sabkha
- Colluvium

Physical Features

- Geochronology sample
- Suture
- Inferred Suture
- Inferred faults
- Fault

Sfariat-Bu Daira Terrane:

OAvba	**Oum Abana**	*Metavolcanics - Basalt, Andesite, minor Rhyolite (2122 ± 18 Ma), Chert*

Leaareig Terrane:

Stratigraphy

my		*Mylonite*
TAgab	**Taghsoumat-Aghsoumal**	*Gabbro and Orthogneiss*

Figure 4-50 - Geological map of the centre of the Elmalhat Domain showing the northwest-southeast trending mafic and ultramafic units dominating the region between the orthogneissic and paragneissic basement.



Figure 4-51 - Field photograph of the gabbroic and ultramafic unit is largely obscured by large areas of sand, mostly appearing as small areas of subcrop. The hill in the background is composed of listwanite (UTM 28 777348 mE, 2659454 mN).

The gabbroic rocks of the unit are mesocratic to melanocratic, ranging from salt and pepper colour to dark blue or green. In most areas, the original mafic minerals have been replaced by hornblende. They range from fine-coarse grained (~0.5-2.5 mm, usually ~1.5 mm) and are generally massive but can be locally foliated. They broadly consist of hornblende (~40-60%), plagioclase (~40-60%), though in a few places they are much more mafic, ranging up to ~60-90% hornblende. Locally present is mesocratic, blue, medium grained (~1mm), equigranular, quartz diorite, consisting of plagioclase (~40%), amphibole (~30%), quartz (~15%) and muscovite (~15%).

Xenoliths of paragneiss (muscovite-garnet gneiss) are common within the mafic unit, especially in the north of the Elmalhat Domain. Minor xenoliths of orthogneiss are also in the south. Slivers of paragneiss within the mafic unit generally strike northwest-southeast parallel with the regional trend. The paragneiss xenoliths are fine-medium grained (~0.75-1mm), strongly foliated, comprising mostly garnet-muscovite gneiss or garnet gneiss. They consist of feldspars (~55-70%), quartz (~30%), muscovite (~0-10%) and garnet (~2-3%). Orthogneissic xenoliths in the south of the unit are medium grained (1.5 mm), migmatitic and contain feldspar (~55%), quartz (~25%) and hornblende (~20%).

Lenses of ultramafic rocks within the unit are mixed with gabbroic rocks as well as in discrete lenses of ultramafic rocks. Within the mixed mafic and ultramafic units, the ultramafic rocks occur as lenses from ~1m to ~50 m in size. The composition of the gabbro surrounding the ultramafic lenses displays a gradually increasing proportion of hornblende towards the ultramafic lenses. The metamorphosed ultramafic rocks have had their mafic minerals completely converted to amphibole consisting of amphibole (90-100%) and plagioclase (0-10%) with minor magnetite in places.

Within the largely flat, sand covered, region making up the mafic unit, small hills are present with outcrops ~10-100 m in size comprised of listwanite (Figure 4-52a). The listwanite (a rock that forms from alteration of ultramafic rocks with CO_2 and SiO_2-rich fluids) appears as a mesocratic, brown rock with extensive stockwork quartz-carbonate veining (Figure 4-52b), often containing veinlets of magnetite likely formed during serpentinisation. Locally present within the listwanite are ~0.3-2m sized lenses of dark green, mesocratic, coarse grained, very crumbly and soft rocks, comprised of chlorite (~85-95%) and talc (~5-15%) (Figure 4-52c). These talc chlorite schists also represent altered ultramafic rocks. The distribution of the listwanite appears to be structurally controlled, forming in belts parallel to regional shear zones with adjacent ultramafic rocks displaying a strongly sheared foliated fabric.

Several flat-topped mesas are present within the mafic unit, proximal to the Main Bulb. The top of these mesas are white to light grey in colour and are composed entirely of silcrete. There is a strong correlation between the location of these mesas and lithology, with ultramafic or very mafic (<20% plagioclase) rocks always present at the base of the mesas. In places silcrete and calcrete are observed infilling cracks in ultramafic rocks.

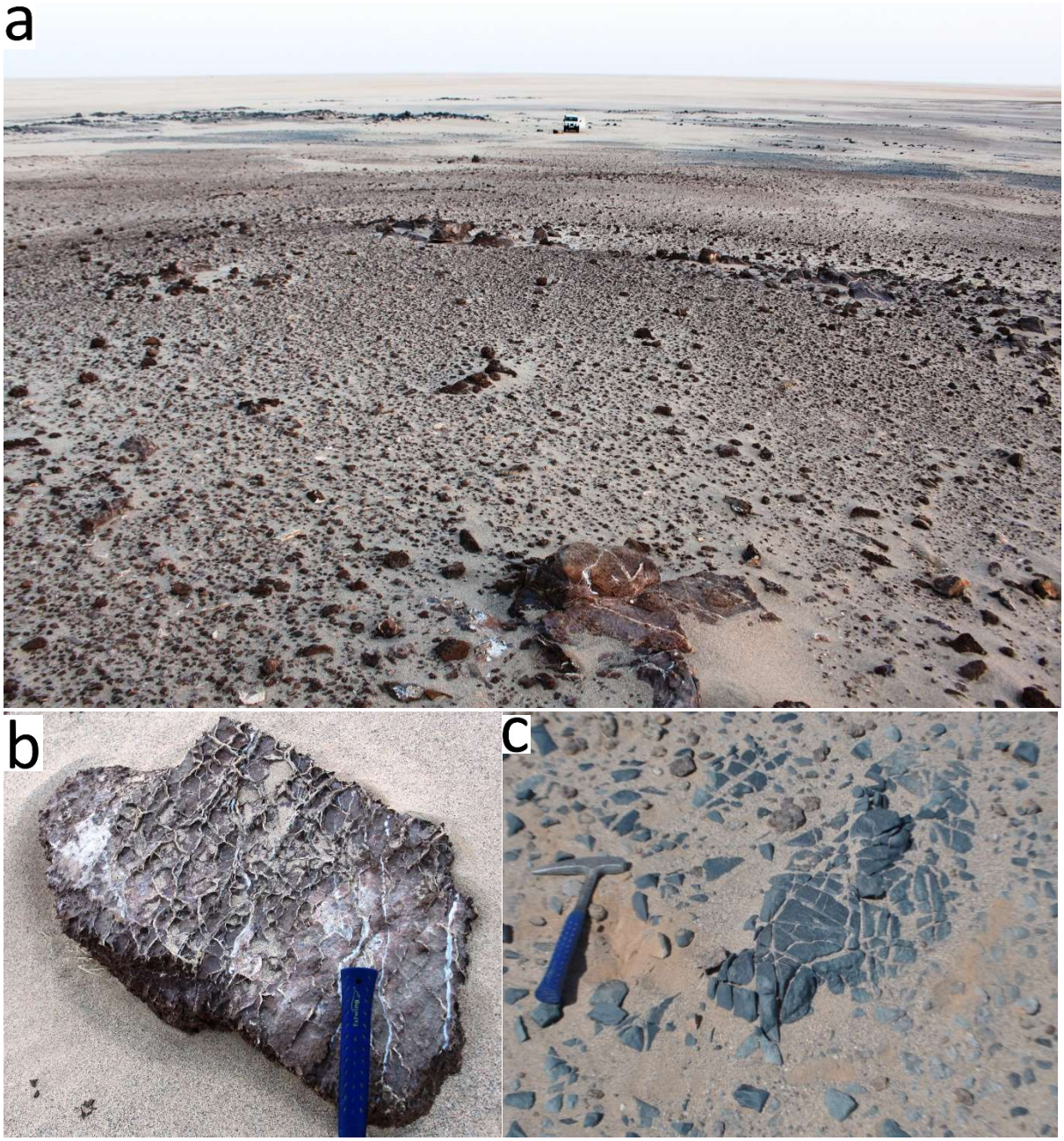

Figure 4-52 - Field photographs of a) Listwanite forming elevated topography (from Laurence Robb UTM 28 793519 mE, 2645704 mN) b) Close up of listwanite. (from Laurence Robb - UTM 28 793519 mE, 2645704 mN) c) lens of fresh ultramafic in the listwanite (UTM 28 793519 mE, 2645704 mN).

Metadolerite dykes (~1-10 m in width) cross-cut the orthogneiss and granitoid intrusions in the east of the Elmalhat Domain. The dykes are melanocratic, dark blue, weakly foliated and weakly magnetic. Many of the dykes are aphanitic though some are medium to coarse grained (~1-3mm). They consist of plagioclase (~50%) and amphibole (~50%) with minor magnetite.

4.1.2.4 Late Granite Intrusions

Granite intrusions are observed intruding the orthogneiss and locally cross-cutting the Main Bulb of the EAC. These intrusions are typically meso- to leucocratic, grey-white to pink, medium-coarse grained (~1-3mm) generally tonalitic I-type granitoids composed of plagioclase (30-60%), quartz (~20-30%), alkali feldspar (0-20%) biotite (~0-10%), hornblende (~0-20%), muscovite (~0-15%) and magnetite (up to ~2%). These granites and associated pegmatites cross-cut the anorthosite of the Northern Limb of the EAC. A representative sample of biotite granite was dated using U-Pb zircon geochronology at 2129 ± 46 Ma.

4.1.2.5 Structure

The Elmalhat Domain is bound on its western, southern and eastern boundaries by the Taghsoumat, El Medna and CSM faults. To the north, it grades into the Oum Abana belt with the gradual increase in the proportion of volcanosedimentary material and the loss of distinctive Elmalhat lithologies such as anorthosite. Although the change to the north is somewhat gradational, a notable change occurs across an east-west trending sabkha where Elmalhat lithologies are dominant to the south and Oum Abana lithologies to the north. This change indicates that potentially the sabkha covers a major structure raising the Elmalhat Domain closer to the surface.

The other major structure in the Domain is a shear zone between the main and Southern Bulbs of the EAC. The region between the bulbs consist of orthogneiss with contains several lenses of anorthosite (from ~2m to 500 m wide), amphibolite (tens of meters in size) and ultramafic material (generally tens of meters but ranging from ~1m-1km in size). The ultramafic lenses are medium to coarse grained (~1-2mm), foliated, and composed completely of amphibole, representing metapyroxenite. The ultramafic lenses are mostly altered to listwanite where they

more intensely sheared, and the orthogneiss is protomylonitic in places strongly affected by epidote alteration.

4.1.2.6 Field Relations and Geochronology

Samples associated with the EAC failed to yield zircons so U-Pb geochronology could not be applied to the complex. Therefore, the timing of formation of the complex must be constrained through a combination of field relations, relative dating (compared to dated granite and gneiss), and whole rock Sm-Nd dating.

On a regional scale, the massif type anorthosite forms a symmetrical bowl-shaped intrusion, discordant to the regional trend with little evidence for significant internal deformation. The massif-type anorthosite is observed in outcrop scale directly cross-cutting the host orthogneiss (Figure 4-53). This orthogneiss (sample J179) was dated at 2140 ± 19 Ma (Table 2-1; Chapter 1), providing a maximum age for the intrusion. The minimum age was constrained by a granitoid dyke cross-cutting the anorthosite (J267) dated using U-Pb zircon geochronology at 2123 ± 69 Ma. These dates overlap within uncertainty indicating that the massif-type anorthosite was essentially coeval with plutonism that formed the granite and gneiss within the domain.

The megacrystic anorthosite appears to be concordant with the orthogneiss, forming a sub-vertical northwest-southeast trending body. This indicates that it is pre-tectonic and therefore was emplaced prior to the (discordant) massif-type intrusions. The presence of megacrystic anorthosite xenoliths in massif-type anorthosite of the Main Bulb (Figure 4-30, Figure 4-31) confirms that the megacrystic anorthosite is the older of the two. Not enough field data is available to apply a robust interpretation for the maximum age of the megacrystic anorthosite, though it is unlikely to be much older than the oldest dated sample Palaeoproterozoic terrane of the Reguibat Shield (sample J231) at 2216 ± 60 Ma. That sample was from the older

Leaareig Terrane. Therefore, uncertainty exists as to the age of the megacrystic anorthosite though it is almost certainly Palaeoproterozoic in age.

Six whole-rock samples from the EAC were analysed (Table 4-1) to obtain a Sm-Nd isochron date for the complex (see Appendix B3 for specifications analysis completed). As the megacrystic anorthosite is older than the other lithologies, sample J270 was excluded from the plot. The isochron gives the crystallisation age for samples associated with the Main Bulb as 2175 ± 160 Ma (MSWD 4.3).

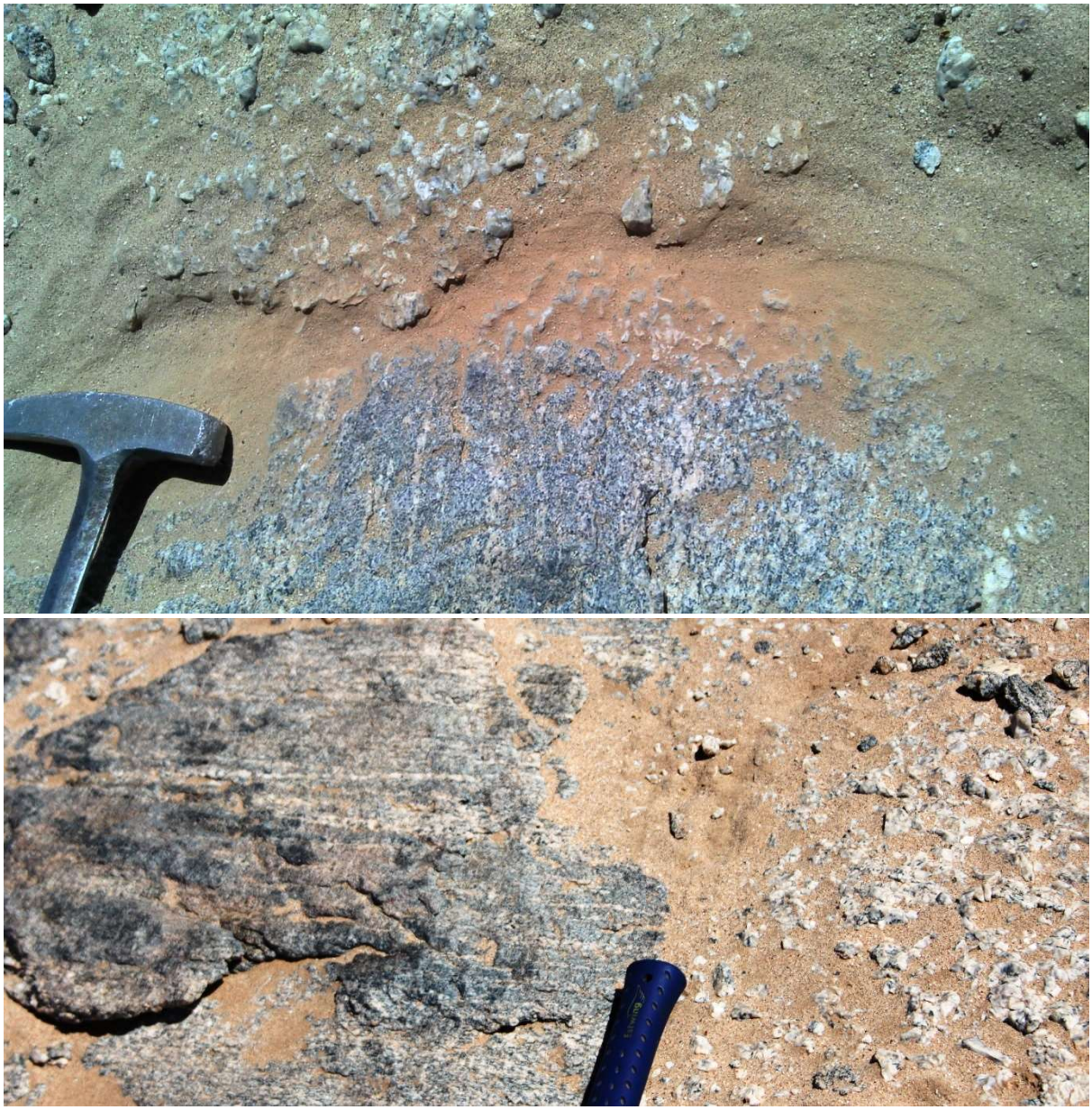

Figure 4-53 – Field photographs of massif-type anorthosite cross-cutting the fabric of the orthogneiss dated at 2140 ± 19 Ma (UTM 28 801757 mE, 2640565 mN).

Table 4-1 – Whole rock Sm-Nd isotopic data for samples across the Elmalhat Anorthosite Complex. T(DM2) – Sm-Nd model age using the TCHUR depleted-mantle model, T(DM) de Paolo – Sm-Nd model age using the depleted-mantle model of de Paolo (1981).

Sample ID	Lithology	Location	Sm (ppm)	Nd (ppm)	$^{147}Sm/^{144}Nd$ (± 0.4%)	$^{143}Nd/^{144}Nd$ (±0.000005)	T(DM2)	T(DM) de Paolo
J255	Olivine Gabbro	Satellite intrusion	2.0	8.2	0.146076	0.00058	2142	2016
J256	Gabbro	East of Main Bulb	1.3	6.1	0.132402	0.00053	2181	2080
J259	White Massif-type Anorthosite	Main Bulb	2.6	11.8	0.133066	0.00053	2153	2050
J262	White Massif-type Anorthosite	Main Bulb	3.1	12.4	0.150487	0.00060	2185	2051
J263	Ultramafic dyke	Main Bulb	5.8	31.1	0.112704	0.00045	2169	2090
J270	Megacrystic anorthosite	Northern Limb	0.5	1.9	0.158337	0.512338	2094	1935

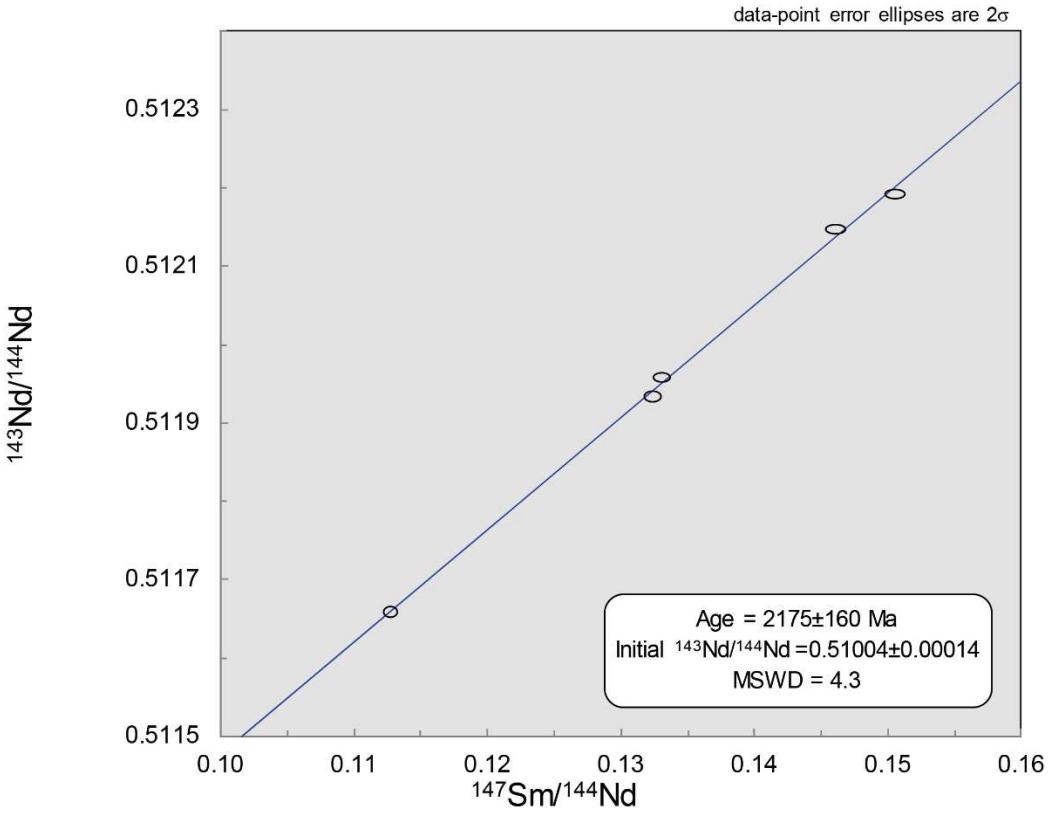

Figure 4-54 – Sm-Nd isochron for samples from the EAC, including two samples of white anorthosite and one of an ultramafic dyke in the Main Bulb, a sample of gabbro proximal to the Main Bulb, and olivine gabbro from a satellite intrusion.

4.1.3 Petrography

4.1.3.1 Basement

4.1.3.1.1 Orthogneiss

The orthogneiss (Figure 4-55, Figure 4-56,) is medium-coarse grained (0.2-2mm), consisting of sericitized plagioclase, quartz, pale bluish-green amphibole, biotite, epidote (some after allanite; Figure 4-56a, b), and Mg-rich chlorite, ± alkali-feldspar. Gneissic banding is present, defined by hornblende- (±biotite-) bearing and hornblende- (±biotite-) poor layers, with epidote throughout but more prominent in plagioclase-rich domains. Larger feldspars may represent igneous relics (Figure 4-56a, b). It has a broadly tonalitic(-granodioritic) composition.



Figure 4-55 - Photomicrographs of sample J179 (UTM 28 801140 mE, 2644170 mN) – migmatitic orthogneiss. Equigranular, medium grained (0.1-1.5 mm, average ~1mm). Moderately defined fabric with alternating quartz(±feldspar)-rich and biotite-amphibole-(±feldspar)-rich layers. XPL, field of view (FOV)1x1.5 cm.

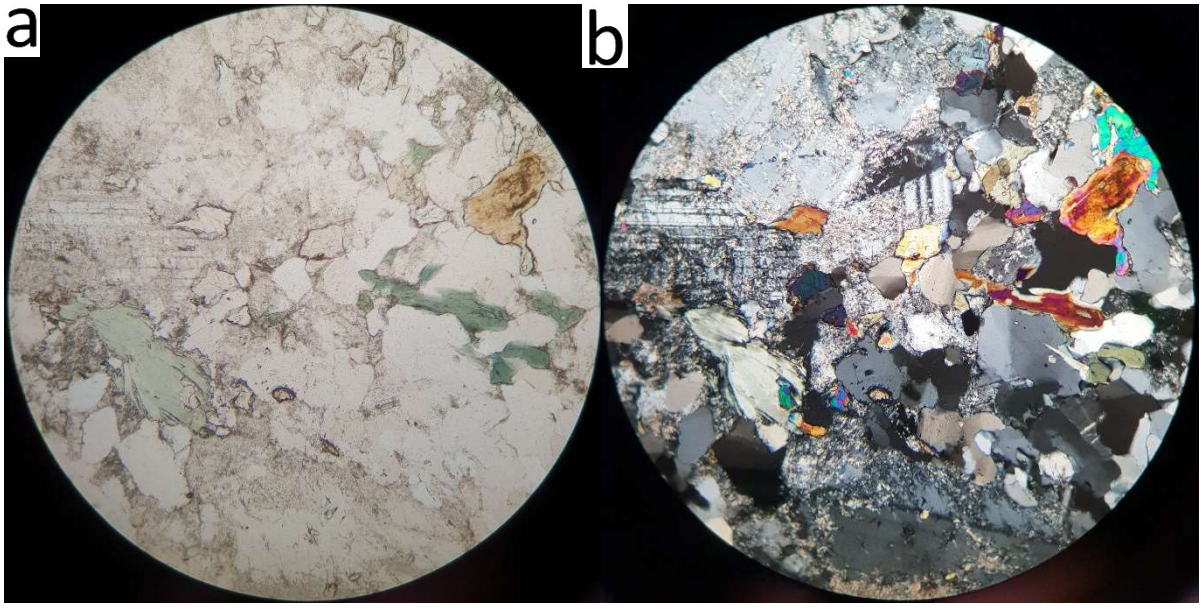

Figure 4-56 - Photomicrographs of sample J117 (UTM 28 779445 mE, 2649005 mN) – orthogneiss. a, b) general view showing chlorite, sericite, epidote and chlorite; FOV 2.5 mm [a) PPL, b) – XPL].

4.1.3.1.2 Paragneiss

The paragneiss (Figure 4-57) consists of muscovite defining a weak fabric, abundant K-feldspar (intermediate microcline) and abundant myrmekitic microstructures. Quartz is coarse, only partly recrystallized, with GRAIN BOUNDARY MIGRATION grain-boundary modification (coarsely lobate).

The carbonate BIF associated with the paragneiss consists of calcite, quartz, and Fe-oxide ± traces of biotite (Figure 4-58). The calcite occurs as larger elongate twinned grains and a finer, more granoblastic generation. The quartz shows quite well-organized ground boundary migration adjusted granoblastic texture, the contacts broadly lobate or subangular, with some late undulose extinction and prism-parallel subgrain boundaries. Oxides are not stretched or deformed.

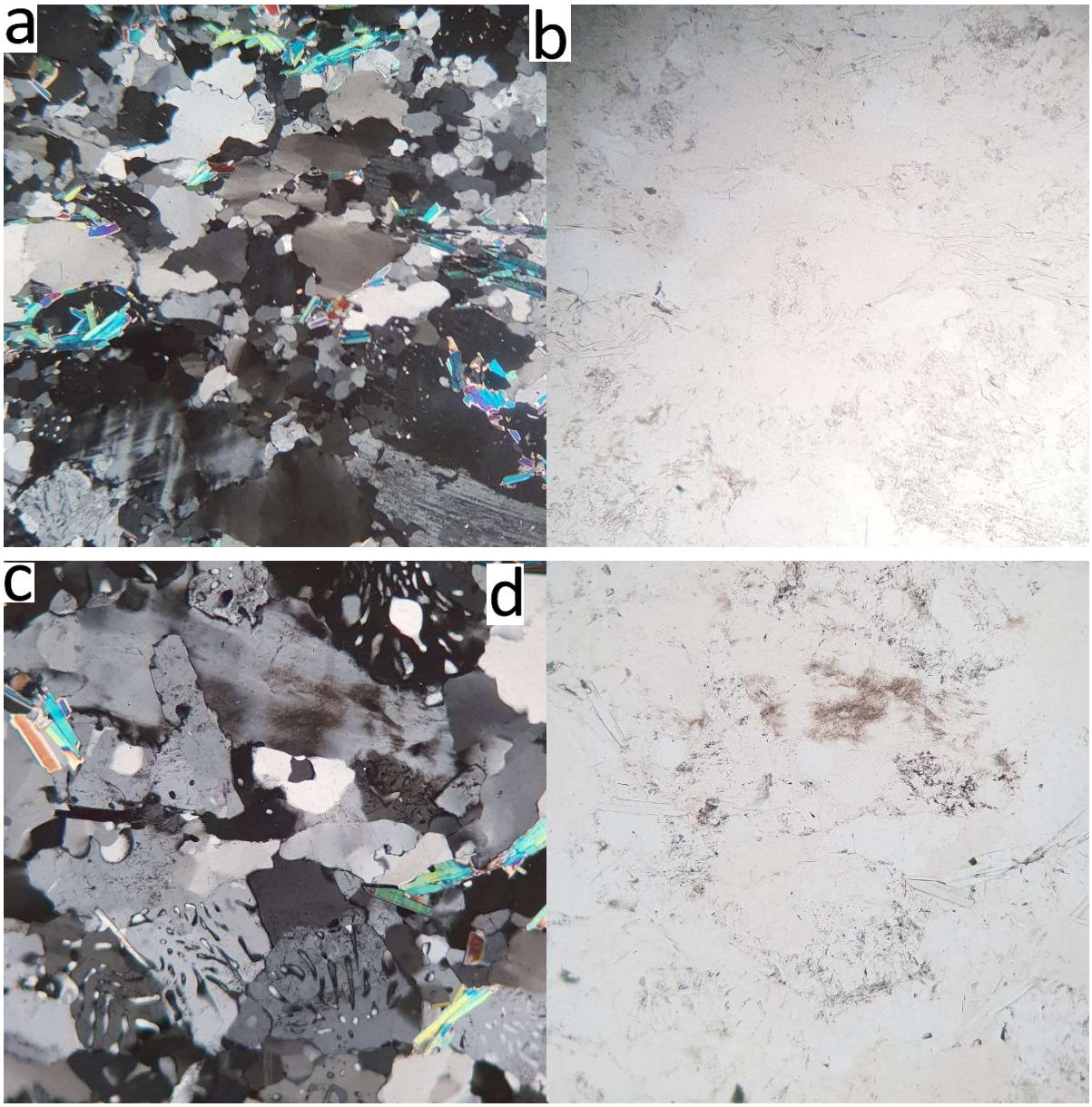

Figure 4-57 – Photomicrographs of J240 (UTM 28 778231 mE, 2633751 mN) – paragneiss. a, b) Represetnative view of paragniess. FOV – 4mm [a) XPL, b) – PPL]. c, d) myrmekitic microstructures FOV 2mm [c) XPL, d) – PPL].

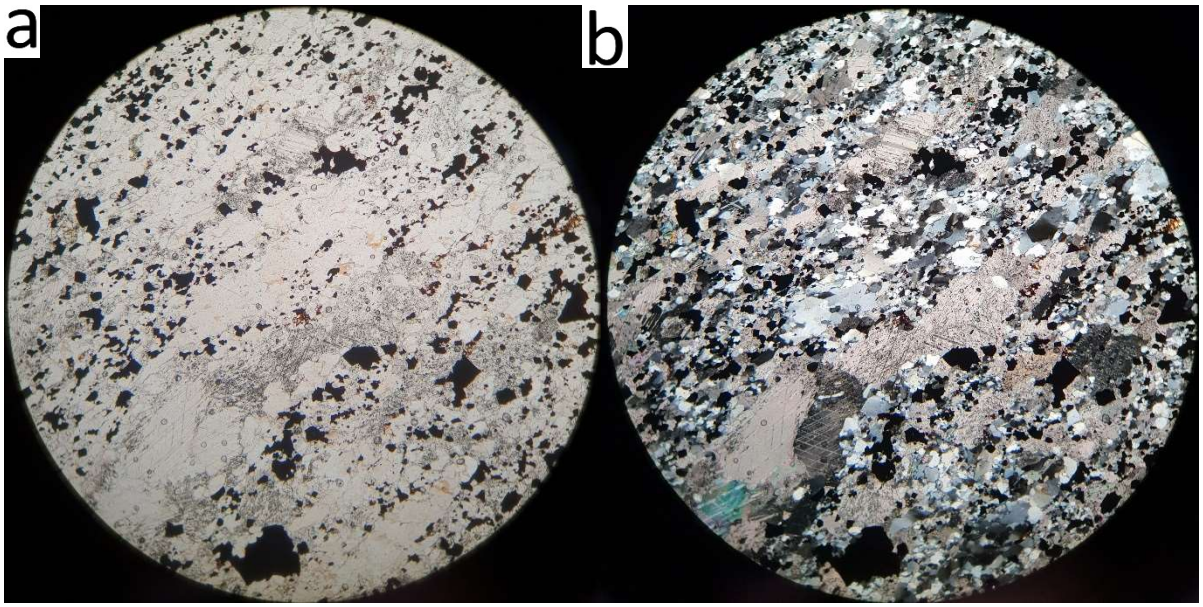

Figure 4-58 – Photomicrographs of J114 (UTM 28 769529 mE, 2659858 mN) - Carbonate BIF containing calcite, quartz, Fe-oxide. FOV – 5 mm [a) PPL, b) – XPL]

4.1.3.2 Elmalhat Anorthosite Complex

4.1.3.2.1 Northern Limb

The Northern Limb has largely undergone amphibolite facies metamorphism, with the primary mineralogy having been replaced by retrograde mineral phases. Proximal to shear zones where hydrothermal fluid flow is facilitated, the mineral assemblage is further retrograded to greenschist facies assemblages. The Northern Limb is largely composed of metamorphosed megacrystic anorthosite displaying a variety of relict igneous textures as well as a metamorphic overprint. The compositions of the plagioclase in the Northern Limb anorthosite are highly calcic with optical analysis revealing plagioclase contents between An_{80} and An_{95} in the megacrysts and groundmass. The amphibolite layer in the Northern Limb is a foliated finer grained unit reflecting amphibolite facies metamorphism. The interstitial mineralogy in the chromitite seam reflects a greenschist facies metamorphic assemblage.

4.1.3.2.1.1 Megacrystic (Meta-)anorthosite

The megacrystic anorthosite is largely composed of plagioclase megacrysts (~0.5-2 cm wide, $An_{\sim 80\text{-}95}$ [based on optical microscopy]) comprising 50-100% of the rock (Figure 4-59 and Figure 4-60a). The finer grained (~0.05-2mm averaging ~0.5 mm) interstitial material is of a broadly basaltic composition containing roughly equal portions of plagioclase and hornblende though they can vary from 0-100% of each. The hornblende mostly forms as clusters replacing what was likely clinopyroxene (cpx) (Figure 4-61) with two generations observed (Figure 4-62a, b). In places the anorthosite displays an adcumulate texture composed entirely of plagioclase (Figure 4-63). A very rare occurrence, only observed in one thin section, was the presence of lithic plagioclase in an adcumulate sample (Figure 4-64). In general, plagioclase grains contain inclusions and are weakly sericite altered (Figure 4-60c) and are locally recrystallised (Figure 4-60b, Figure 4-62c). A feature noted in some samples of anorthosite is the presence of trails of amphibole microlites within plagioclase grains with distinct pathways defined by the lack of fine dusty inclusions (Figure 4-65). The anorthosite has also undergone a moderate degree of epidote alteration with clinozoisite often forming along grain boundaries (Figure 4-66). Opaque mineralogy within the anorthosites comprises chromitite and sulphides. The main sulphide species present are pyrite and chalcopyrite forming as an intercumulus phase.



Figure 4-59 – Photomicrographs of J111 (UTM 29 195234 mE, 2655299 mN) – megacrystic anorthosite with a megacrystic plagioclase grain (~2 cm wide, $An_{\sim 88}$) surrounded by a groundmass of basaltic composition. FOV is 1x1.5 cm [XPL]

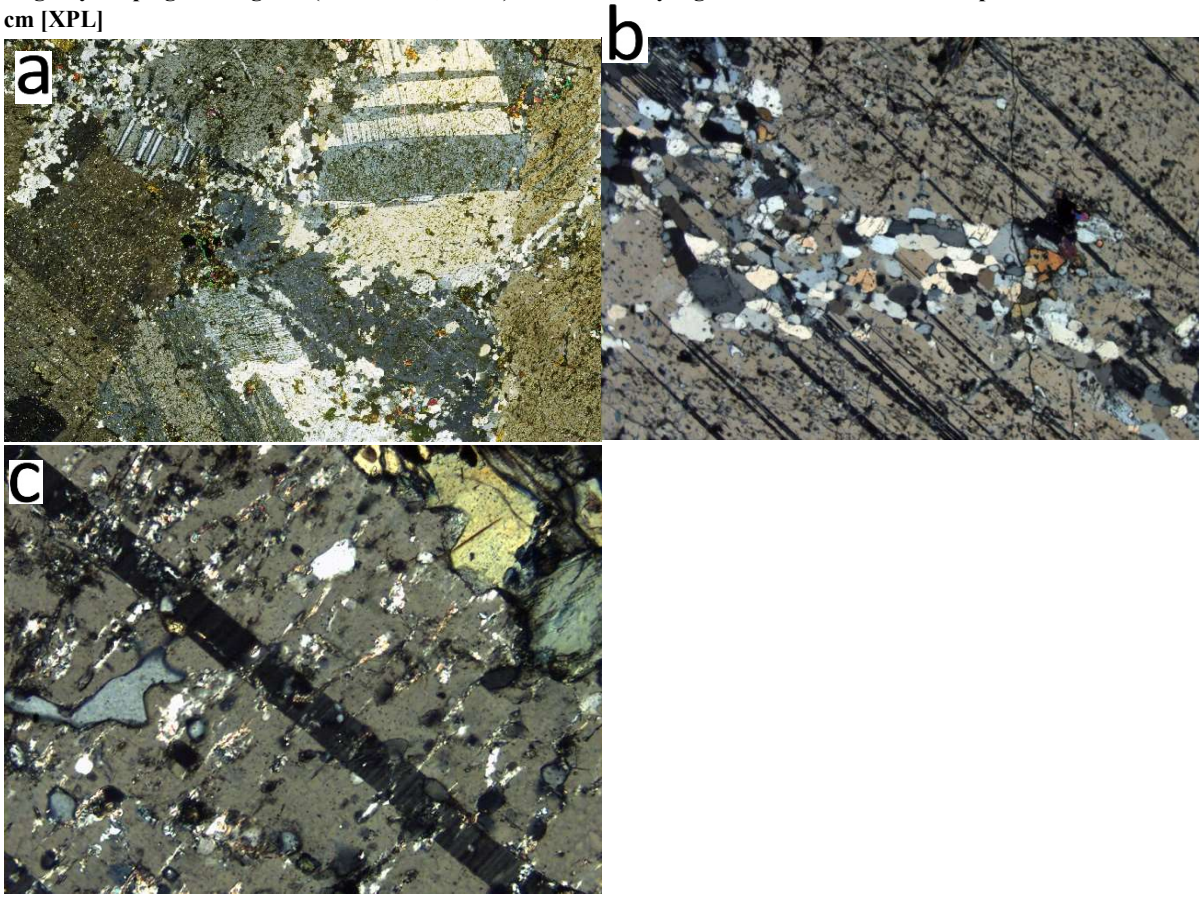

Figure 4-60 - Photomicrographs of J108 (UTM 29 194777 mE, 2655132 mN) - metamorphosed megacrystic anorthosite. a) general field of view showing plagioclase megacrysts. FOV 1x1.5 cm [XPL] b) local recrystallisation of plagioclase. FOV 4 mm [XPL]. c) inclusions and alteration of a plagioclase grain. FOV 0.8 mm [XPL]

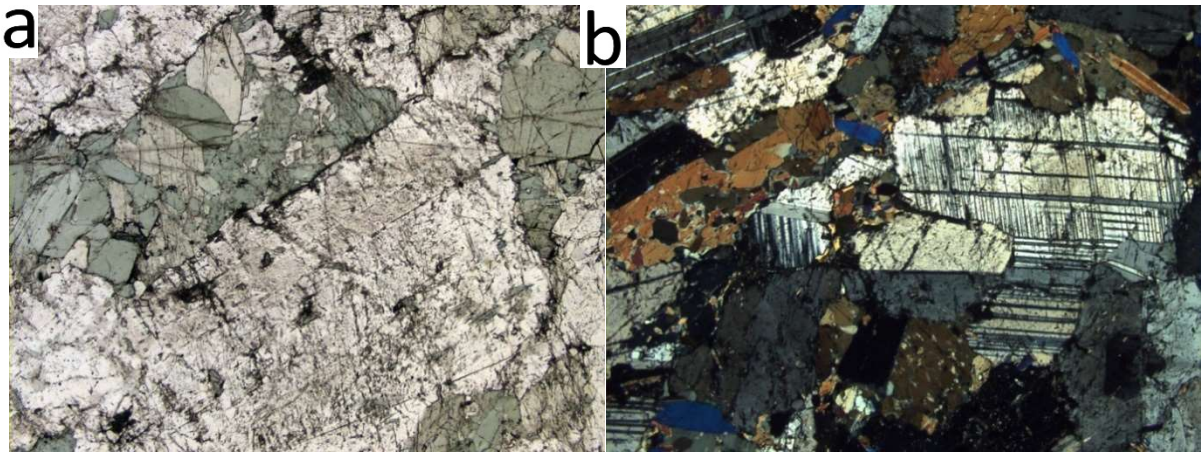

Figure 4-61 - Photomicrographs of J103 (UTM 28 805201 mE, 2655049 mN) Metagabbro, amphibole cluster replacing probable Cpx. FOV 4 mm. [a) PPL, b) XPL]

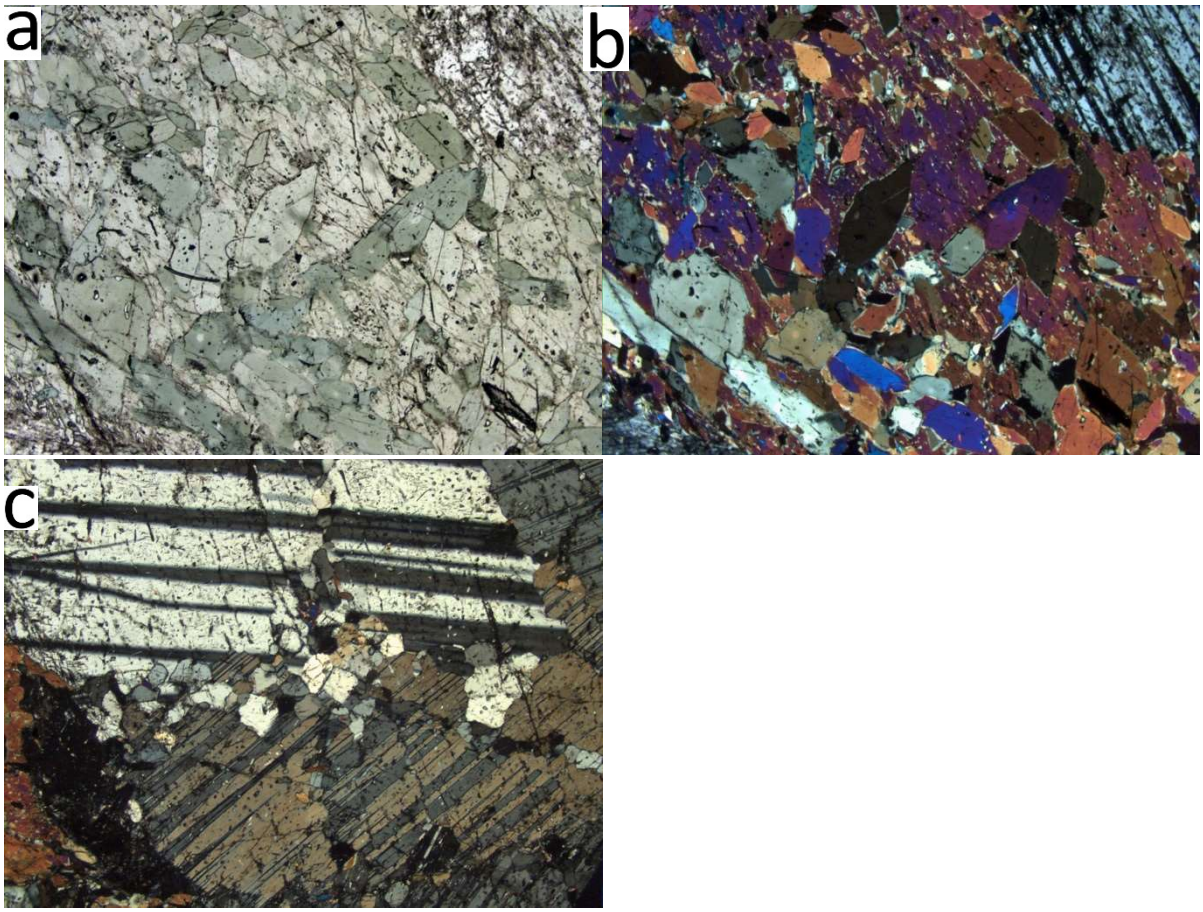

Figure 4-62 - Photomicrographs of sample J107 (UTM 29 194739 mE, 2655071 mN) – metagabbro. a, b) Metagabbro, two generations of amphibole replacing probable Cpx. The first generation of coarse amphibole retains the form of the Cpx and has subsequently been recrystallised by fine amphibole. FOV 4 mm. [a-PPL, b-XPL] c) local recrystallisation of plagioclase. FOV 4 mm [XPL].



Figure 4-63 - Photomicrographs of J264 (UTM 28 803892 mE, 2656222 mN) - adcumulate anorthosite from the Northern Limb. FOV 1x1.5 mm [XPL].

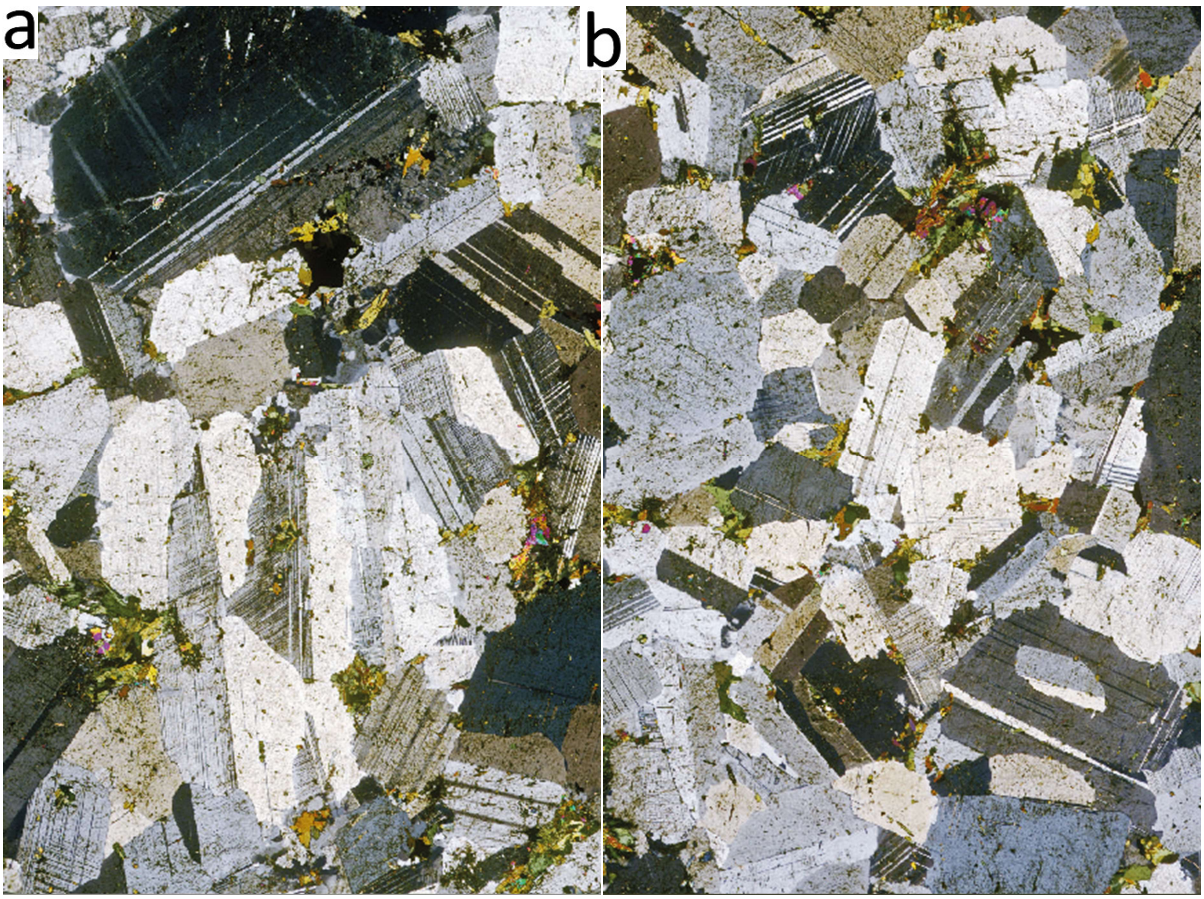

Figure 4-64 – Photomicrographs of J270 (UTM 28 804467 mE, 2656911 mN) – megacrystic anorthosite, showing textural variation within a single thin section. FOV 1x1.5 cm area [XPL]. a) lath-shaped plagioclase. b) massive adcumulate texture.

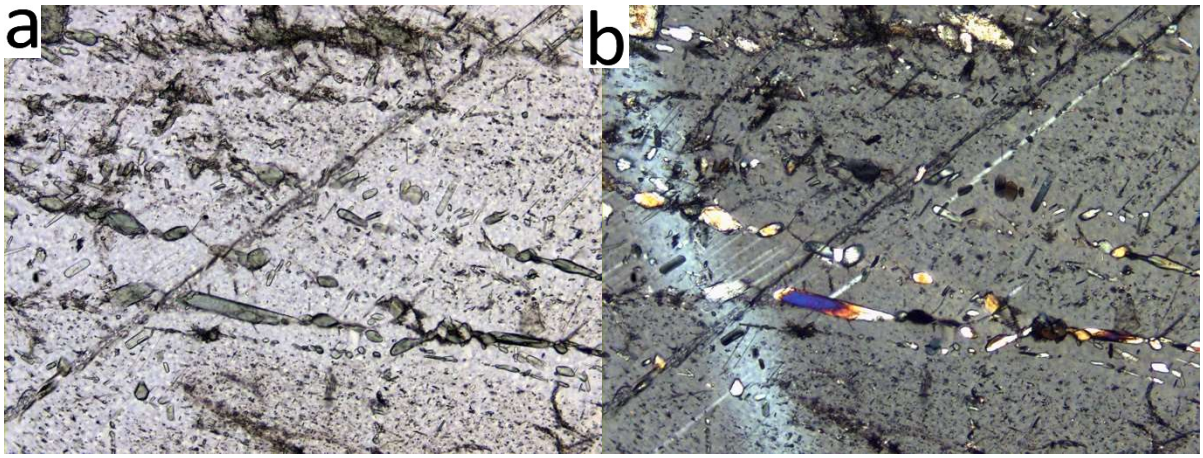

Figure 4-65 - Photomicrographs of J103 (UTM 28 805201 mE, 2655049 mN) - Megacrystic anorthosite. Trails of amphibole microlites in plagioclase, pathways cleared of fine dusty inclusions. FOV 0.8 mm [XPL].

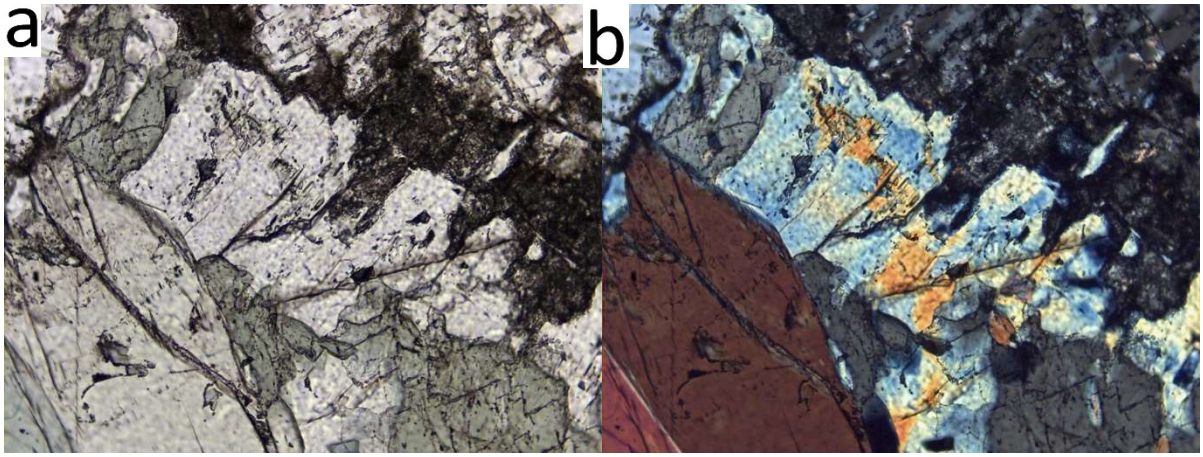

Figure 4-66 - Photomicrographs of J103 (UTM 28 805201 mE, 2655049 mN) - Clinozoisite at margin of amphibole cluster. FOV 0.8 mm [a) PPL b) XPL].

4.1.3.2.1.2 Chromitite

The massive chromitite is composed of a chromite (~65-80%) cumulate phase with interstitial Mg-rich chlorite and minor amphibole, rutile, and an unidentified yellow twinned mineral (pyroxenoid?) (Figure 4-67). Chromite is also hosted in anorthosite and amphibole-rich layers directly adjacent to the massive chromitite seam. Within the chromite-bearing anorthosite, chromite grains are concentrated along the plagioclase grain boundaries (Figure 4-68). The chromite ranges in grainsize from ~0.1-10 mm. Individual chromite grains show alteration to magnetite around the edges of the grains and along internal cracks. Some parts of the chromitite

are sheared resulting in a reduction in the grainsize of the chromite grains and a more complete alteration of the grains to magnetite.

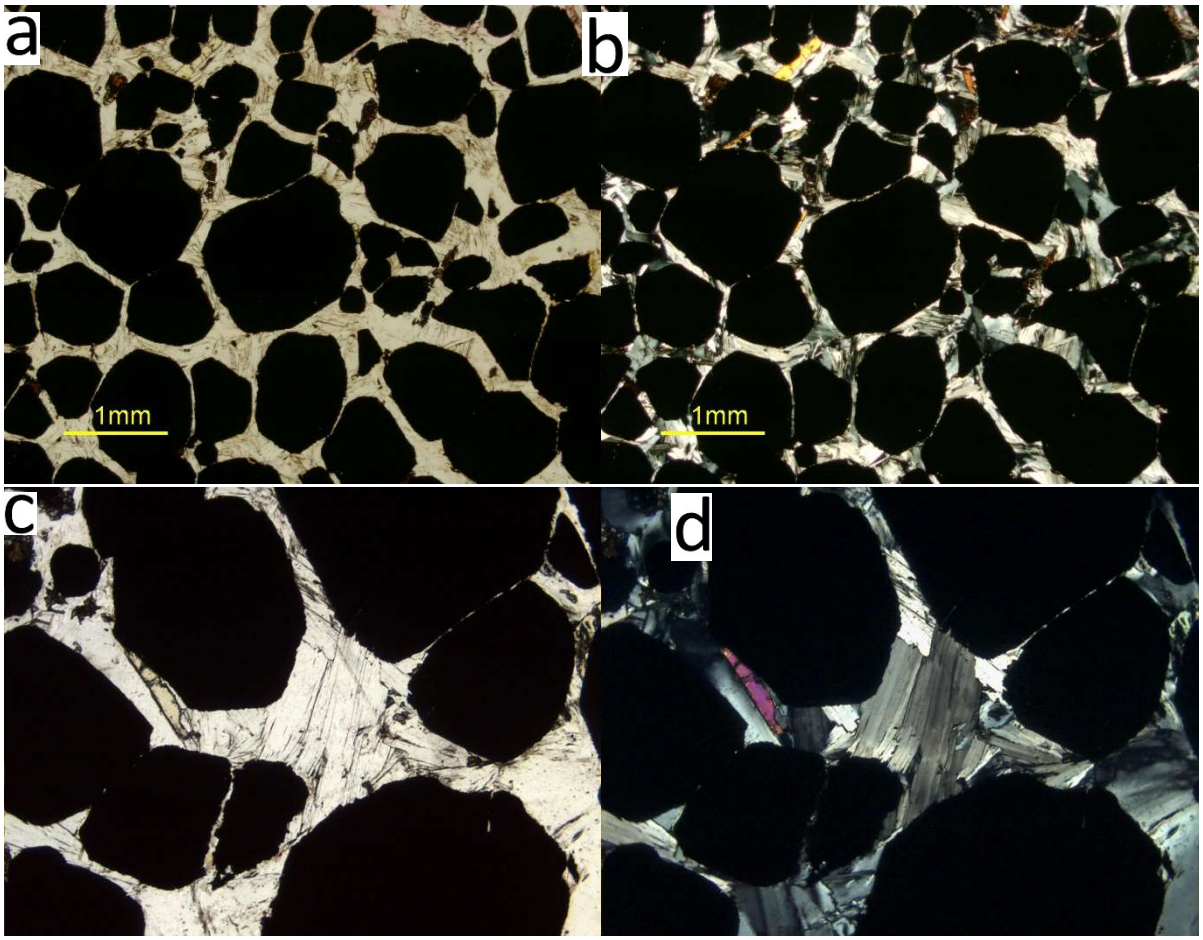

Figure 4-67 - Photomicrographs of J105 (UTM 29 194744 mE, 2655070 mN). a, b) General views of massive chromtitie [a) PPL b) XPL]. c, d) view of chromitite with interstitial Mg-chlorite and a yellow prismatic mineral. FOV 2 mm [c) PPL d) XPL].

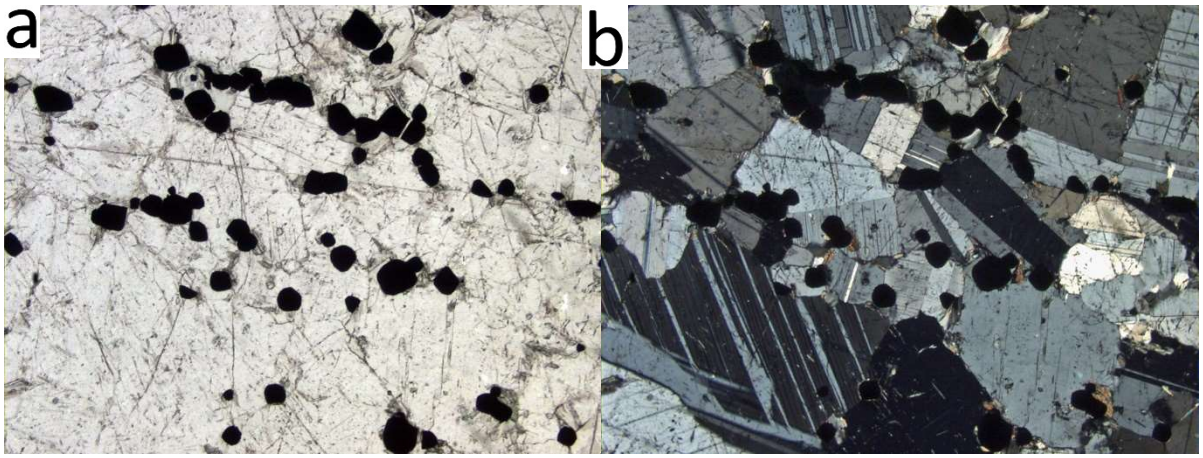

Figure 4-68 - Photomicrographs of J106 (UTM 29 194744 mE, 2655070 mN) - Chromite bearing anorthosite with chromite concentrated along edges of plagioclase grains and excluded from the cores of megacrysts. FOV 4 mm [PPL].

4.1.3.2.1.3 Amphibolite

The amphibolite body is remarkably consistent in terms of petrology. More mafic than the anorthositic rocks either side of the seam, it consists of roughly equal portions of hornblende and plagioclase. It contains a strong fabric defined by recrystallised hornblende and plagioclase (Figure 4-69a, b). Although now medium grained (~0.25-1mm) it contains possible relicts of a coarse texture (Figure 4-69c, d). Locally it contains small amounts of magmatic pyrite and chalcopyrite (Figure 4-70).

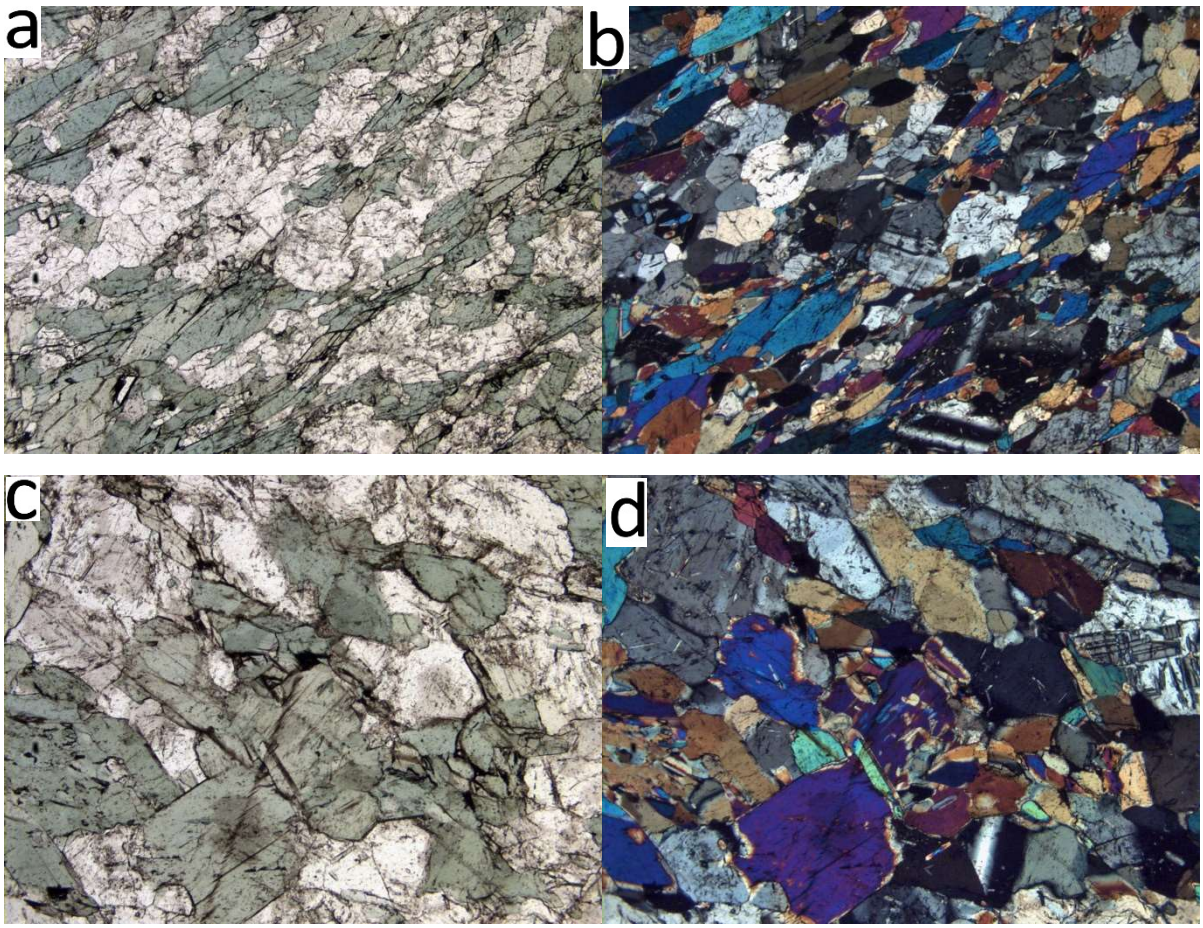

Figure 4-69 - Photomicrographs of J104 (UTM 28 805201 mE, 2655049 mN) - metagabbroic amphibolite layer running parallel to the chromitite seam. a, b) Metagabbroic amphibolite, recrystallised and foliated. FOV 4 mm [a) PPL b) XPL]. c, d) possible relics of coarse texture. FOV 2mm [c) PPL d) XPL].

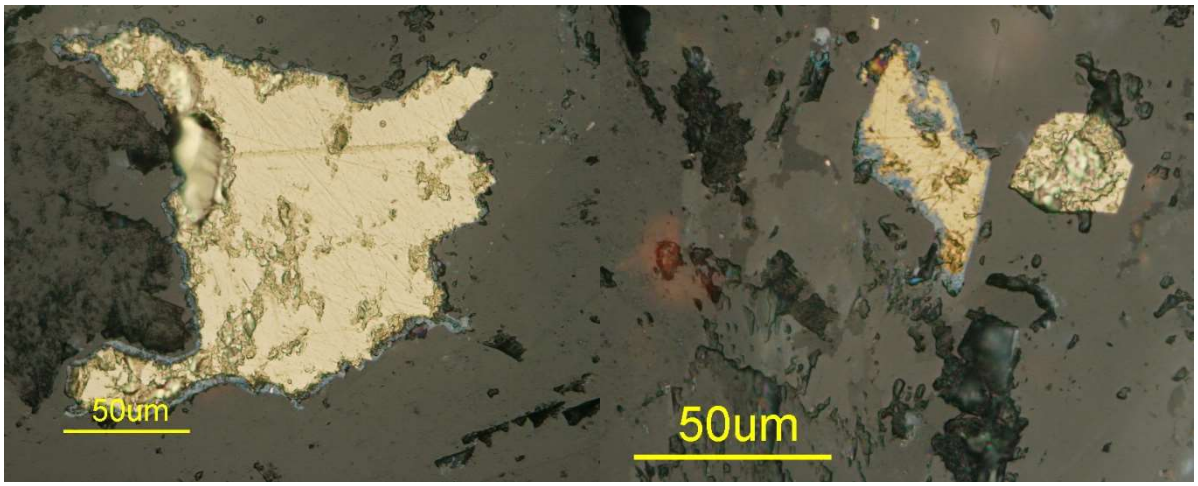

Figure 4-70 – Reflected light photomicrographs of J104 (UTM 28 805201 mE, 2655049 mN) - primary magmatic sulphides within the amphibolite layer. Pyrite and chalcopyrite rimmed by a blue alteration mineral (azurite).

4.1.3.2.2 Main Bulb

4.1.3.2.2.1 Dark Anorthosite

In samples of dark anorthosite from the Main Bulb, optically determined plagioclase compositions revealed two distinct populations of anorthosite. Samples containing andesine have been classified as 'leucodiorite' or 'andesine anorthosite', while samples containing labradorite have been classified as 'leucogabbro' or 'labradorite anorthosite'

4.1.3.2.2.1.1 Banded Leucodiorite/Andesine Anorthosite

The banded leucodiorite is a fresh unit showing good preservation of igneous mineralogy and textures (Figures 4.75 – 4.79). Plagioclase (andesine) is the dominant mineral (~70-97%), while clinopyroxene is the major mafic mineral present, with orthopyroxene, opaque minerals, biotite, apatite and trace amounts of amphibole replacing pyroxene. The opaque phase is mainly hematite with ilmenite exsolutions (Figure 4-72c).

The plagioclase is cloudy in PPL (Figure 4-74) caused by microscopic acicular inclusions (Figure 4-74 e), likely responsible for the purple colour in hand specimens. The plagioclase grains are largely lath-shaped, defining the igneous banding (Figures 4.75-4.78), more equant grains displaying mortar texture (Figure 4-71b, Figure 4-72b). Both textures are igneous with

the mortar texture representing grain-size reduction and dynamic recrystallisation along grain boundaries, potentially formed during movement of the crystal-rich magma (Ashwal and Bybee, 2017). The relatively high aspect ratio of the more lath-shaped crystals potentially representing a faster crystallising phase (Holness, 2014). The lath-shaped plagioclase appears to be the second phase, growing around the equant grains (Figure 4-72b).

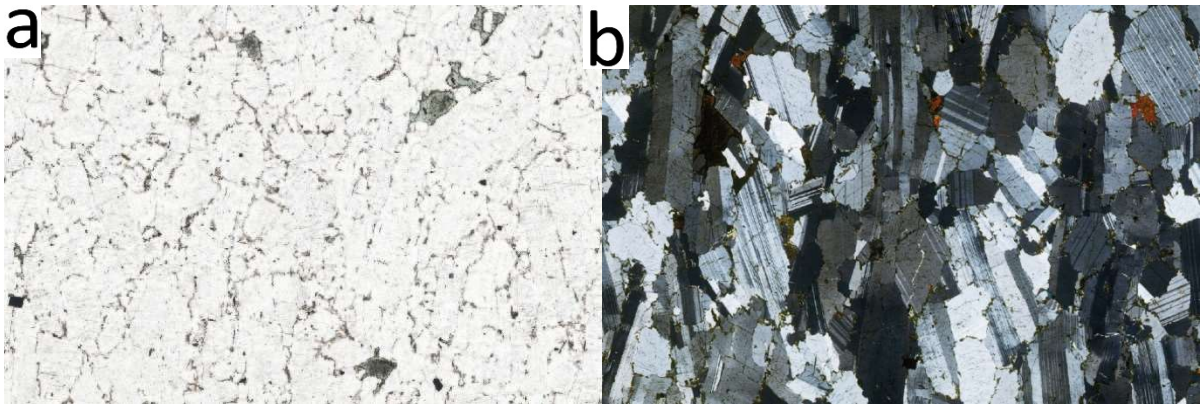

Figure 4-71 – Photomicrographs of J414 (UTM 28 803508 mE, 2645620 mN) - Banded Anorthosite in the Main Bulb. FOV – 1x1.5 cm. [a) PPL b) XPL]

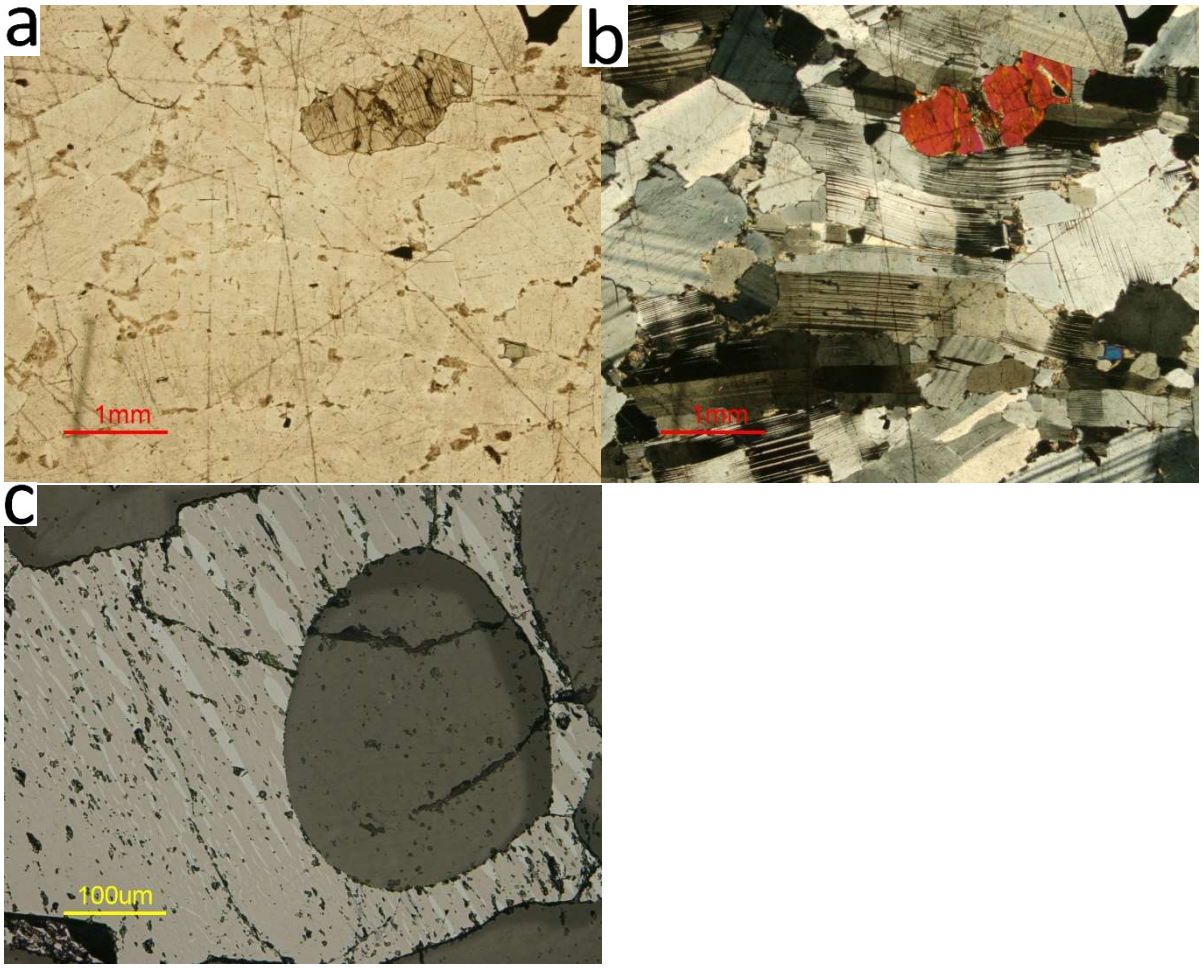

Figure 4-72 – Photomicrographs of sample J122 (UTM 28 802814 mE, 2650059 mN) – banded anorthosite a, b) general view anorthosite with a strong fabric defined by the alignment of lath shaped plagioclase crystals [a) PPL, b) XPL]. c) hematite with ilmenite exsolution laminae [reflected light].

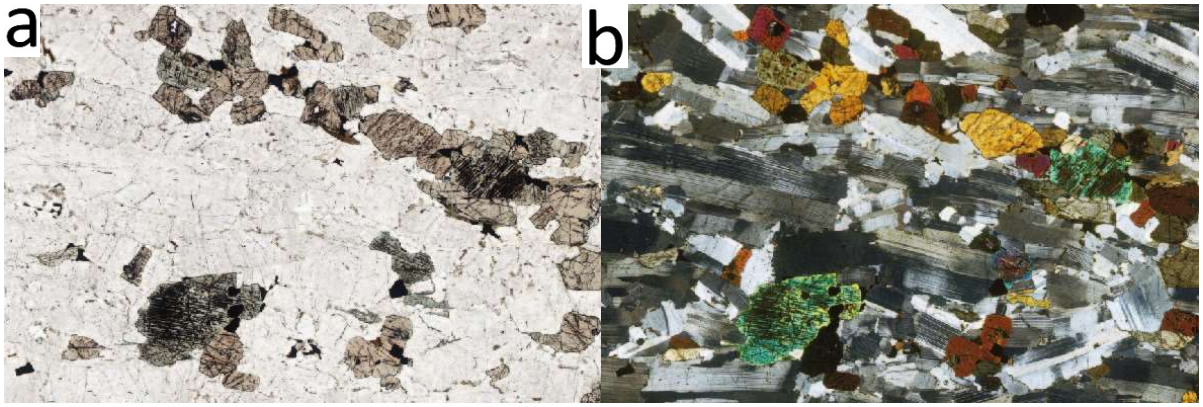

Figure 4-73 – Photomicrographs of J404 (UTM 28 799676 mE, 2650555 mN) - banded leucodiorite in the Main Bulb. FOV – 1x1.5 cm [a) PPL b) XPL]

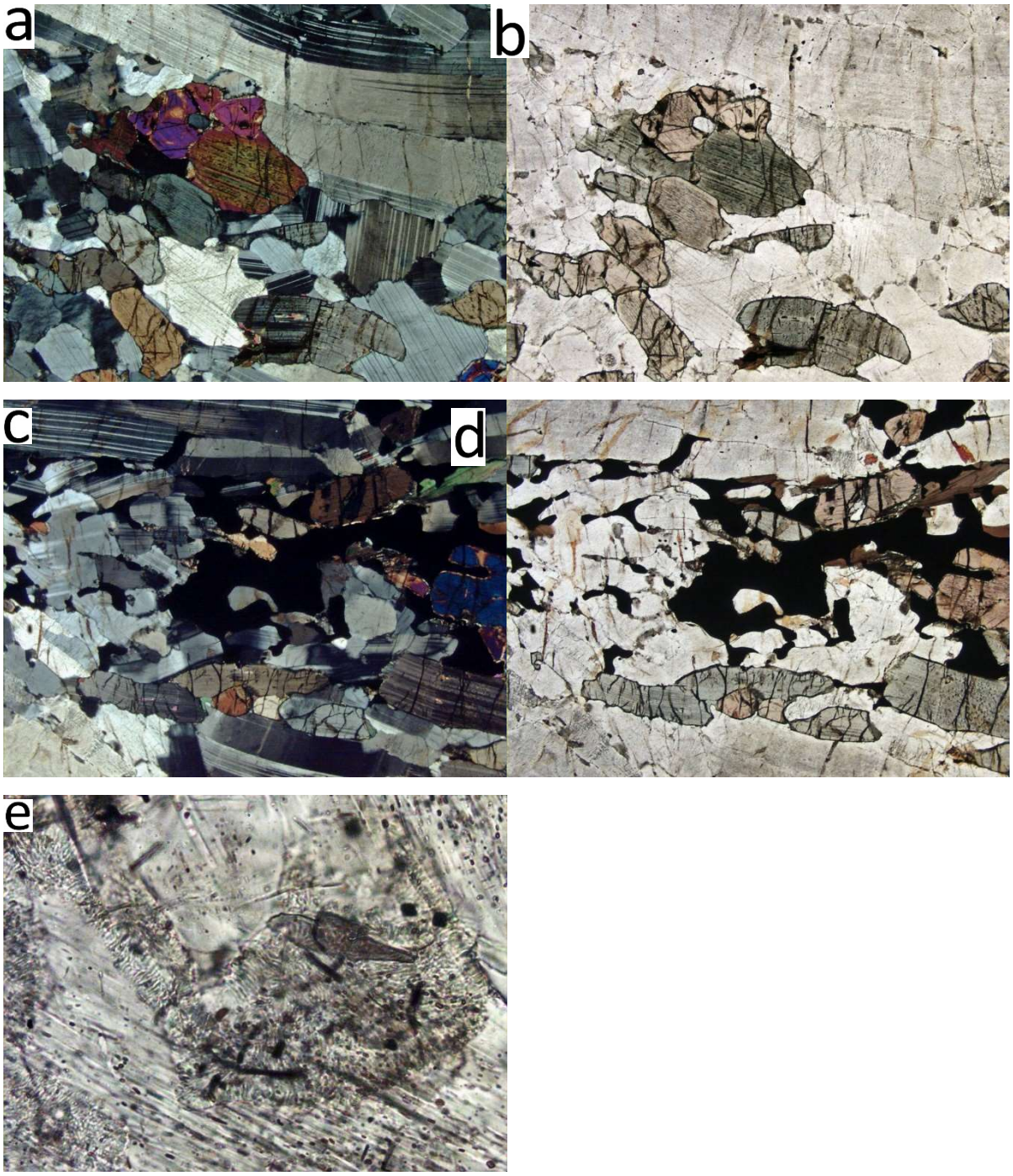

Figure 4-74 - Photomicrographs of sample J263 (UTM 28 804338 mE, 2648432 mN) – a, b) Leucogabbronorite cumulate with strong igneous fabric. Field of view 4 mm [a) XPL b) PPL]. c, d) Leucogabbronorite cumulate with interstitial magnetite. FOV 4 mm [c) XPL d) PPL]. e) Detail of fine intergrowths forming at plagioclase grain boundaries. FOV 0.2 mm [PPL].

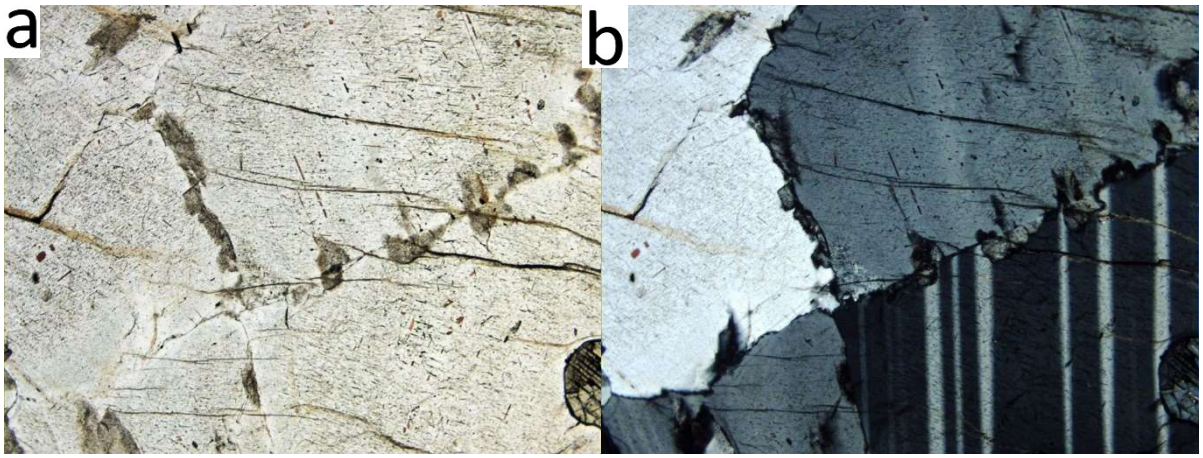

Figure 4-75 - Photomicrographs of J259 (UTM 28 800362 mE, 2648339 mN) - leucogabbronorite cumulate. Turbid growths at grain boundaries of clouded igneous plagioclase. FOV 2mm [a) PPL b) XPL].

4.1.3.2.2.1.2 Massive Leucogabbro/ Labradorite Anorthosite

The massive leucogabbro largely comprises plagioclase (labradorite), with clinopyroxene representing the dominant mafic phase with minor phases of orthopyroxene, amphibole, and opaque minerals (Figure 4-76). Although representing relatively minor quantities olivine is present in all samples of this kind. Mortar texture is observed with clear grain boundaries on otherwise clouded plagioclase representing dynamic recrystallisation in the magma chamber. The low aspect ratio of the plagioclase reflects a relatively slow cooling rate for this magma (Holness, 2014).

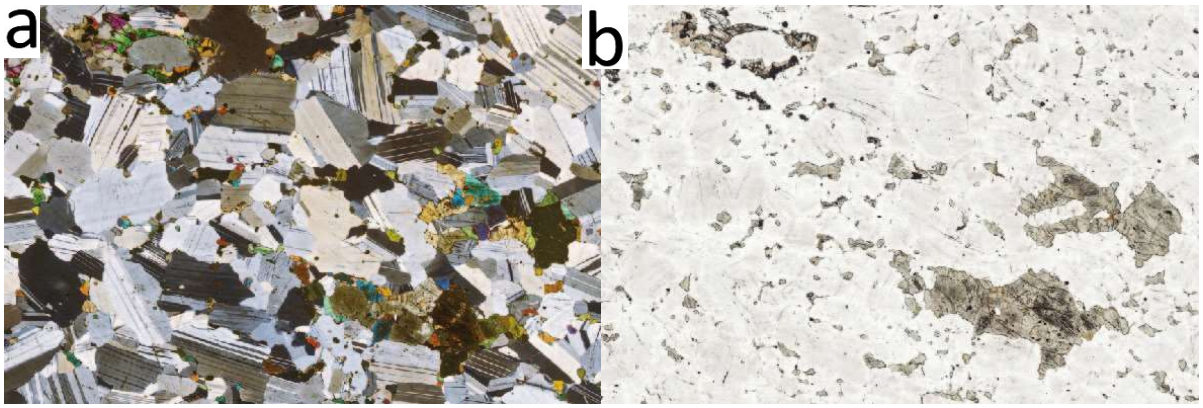

Figure 4-76 – Photomicrographs of J413 (UTM 28 802624 mE, 2645729 mN) – general view of massive leucogabbro of the Main Bulb. Plagioclase displays mortar texture with clear rims from dynamic recrystallisation in the magma chamber. Mafic minerals include orthopyroxene, amphibole, and opaque minerals. FOV – 1x1.5 cm [a) XPL, b) PPL]

4.1.3.2.2.2 Contact Diorite

A sample from the southern contact (Figure 34) between the Main Bulb and host gneiss is a quartz-, olivine-bearing diorite. The sample consists of plagioclase, clinopyroxene, amphibole, biotite, magnetite, olivine, apatite and quartz. The plagioclase is zoned, potentially representing a change in composition of the magma as it was crystallising. Olivine is only present enclosed in clinopyroxene and magnetite, with quartz only present as a very minor intercumulus phase (Figure 4-77). These observations might be consistent with a shift to a more siliceous magma composition after some crystallisation had already taken place. This would be consistent with the plagioclase zoning, the resorption of any olivine not protected from the magma and a minor amount of late-stage interstitial quartz forming.

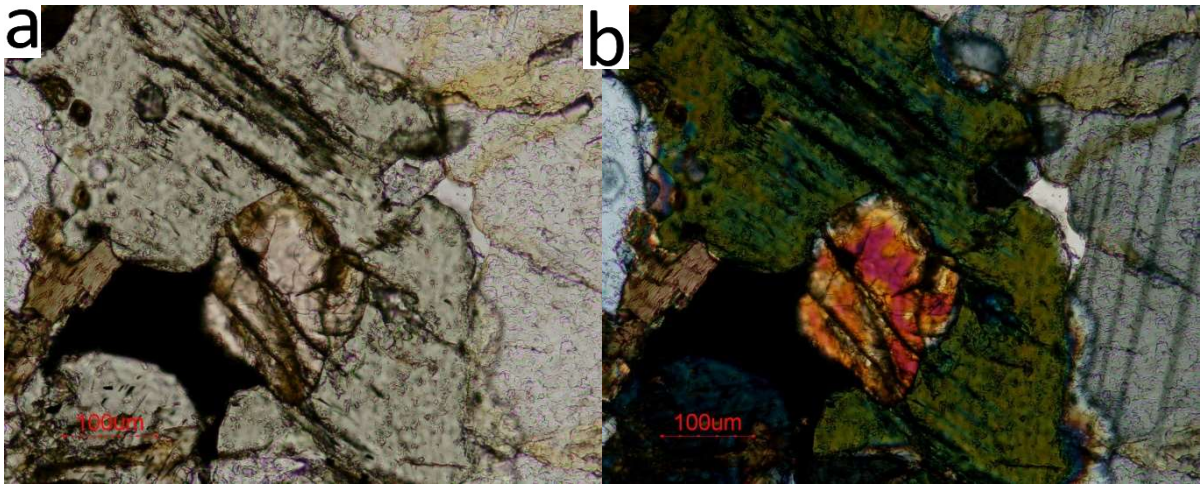

Figure 4-77 – Photomicrographs of J418 (UTM 29 194987 mE, 2644695 mN) - olivine-quartz gabbro. Olivine encased in clinopyroxene and magnetite. Interstitial quartz forming on the grain boundary between clinopyroxene and plagioclase.

4.1.3.2.2.3 Ultramafic Intrusions

The ultramafic intrusions consist of clinopyroxene, olivine, biotite, orthopyroxene and plagioclase with minor opaque minerals (Figure 4-78). The mafic minerals form the cumulus phase with poikilitic texture observed locally with plagioclase oikocrysts enclosing pyroxene, olivine and biotite. Orthopyroxene rims are present around the olivine crystals enclosed in plagioclase oikocrysts (Figure 4-78 b, c).

The ultramafics can be seen cross-cutting white anorthosite in on a microscopic scale (Figure 4-79), as well as in the field (Figure 4-32). The epidote-alteration can be observed in anorthosite that makes contact with the cross-cutting ultramafic rock (Figure 4-79).

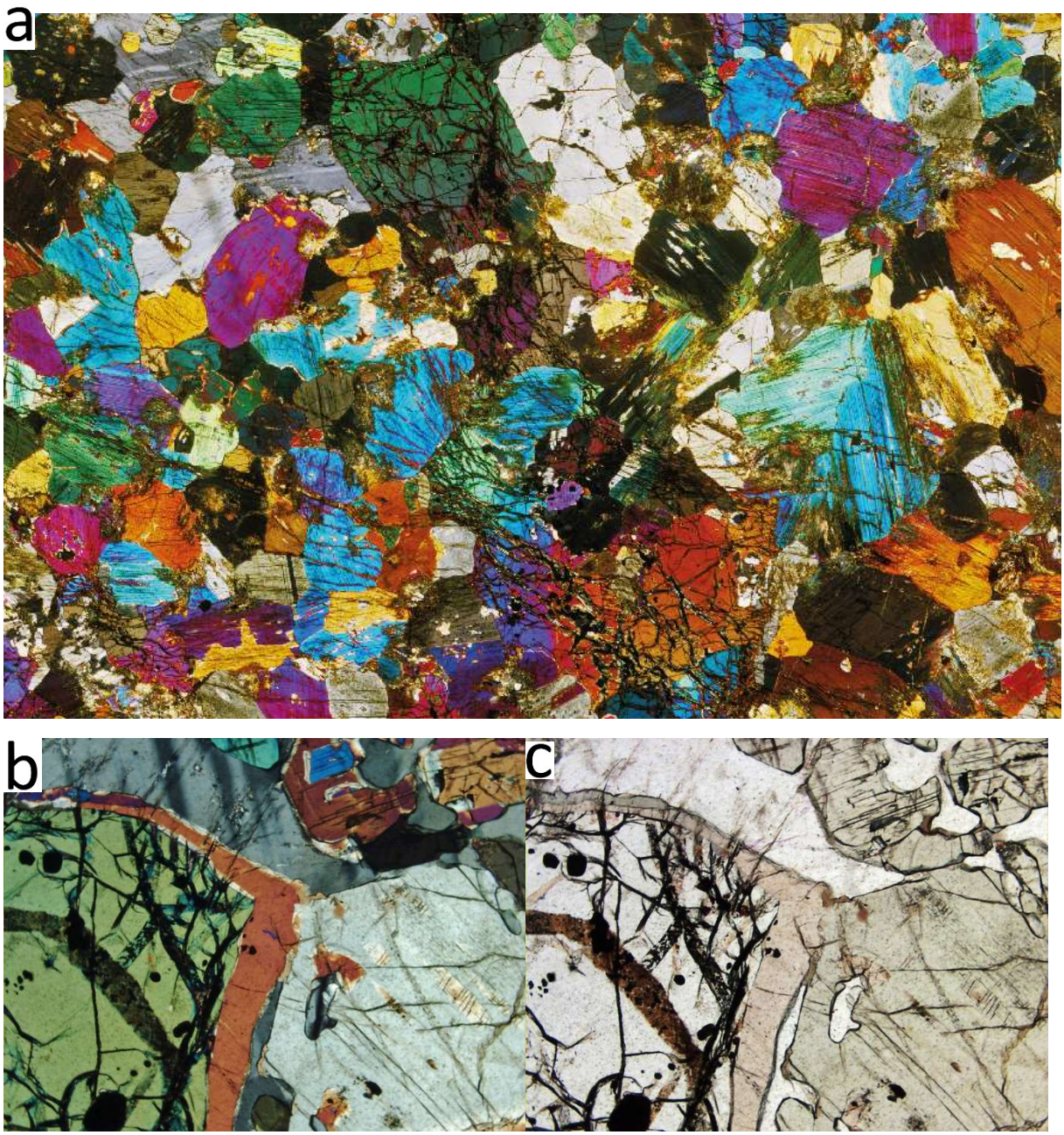

Figure 4-78 - Photomicrographs of J262 (UTM 28 803065 mE, 2648258 mN) - cumulate peridotite with intercumulus plagioclase. a) general view. FOV 1x1,5 cm [XPL]. b, c) Opx rim on olivine. FOV 2 mm [b) XPL, c) PPL].



Figure 4-79 – Photomicrographs of J124 (UTM 28 803004 mE, 2647505 mN) - metapyroxenite cross-cutting anorthosite in the bulb. Epidote alteration can be seen in the white anorthosite in contact with the ultramafic rock. FOV – 1x1.5 cm [XPL].

4.1.3.2.2.4 Massif-type Anorthosite with Megacrystic Anorthosite Xenoliths

Within the eastern magnetic anomaly (close to the eastern edge of the Main Bulb) we find white pods of anorthosite rimmed by spinel, hosted within purple anorthosite (Figure 4-31). The purple plagioclase in hand sample corresponds to the coarser plagioclase (0.5-1mm) with minor clinopyroxene (Figure 4-80). The white plagioclase is much finer grained (0.1-0.3mm) and is associated with green (Mg) spinel and very fine-grained chains of corundum – parallel to the spinel-defined fabric. The sample has a very well-developed granoblastic texture, and a strong fabric in the spinel layers.

The texture and mineral assemblage suggest that it has been annealed at high temperature. Additionally, the presence of spinel and corundum requires a source rich in aluminium – especially within the white plagioclase. A lack of regional granulite-facies conditions, means that it is likely that the assemblage and fabric developed in the Complex during the high-

temperature emplacement. A possible hypothesis for the formation of these aluminium-rich pod-like features is the presence of highly anorthitic (and hence aluminous) xenoliths of megacrystic anorthosite getting metamorphosed by the hot emplacement of the massif-type anorthosite. This would account for the presence of aluminium for the formation of corundum and spinel as well as the local granulite-facies conditions responsible for the metamorphic minerals and textures.

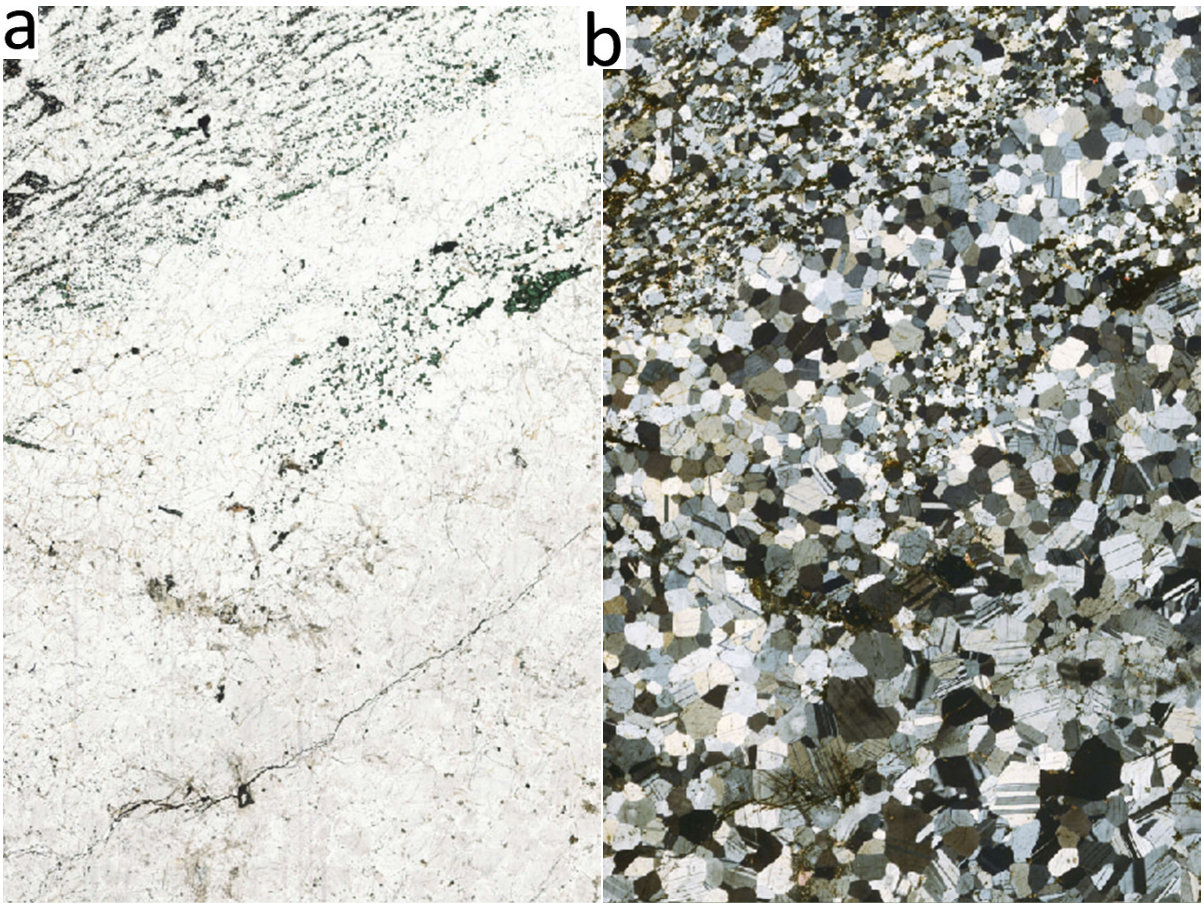

Figure 4-80 - Photomicrographs of J310 (UTM 28 805306 mE, 2648959 mN) - strange pods of spinel and white plagioclase in purple plagioclase anorthosite. Field of view 1.5 cm x 1 cm. [a) PPL, b) XPL].

4.1.3.2.2.5 White Anorthosite

The white anorthosite is completely altered with no primary igneous mafic minerals preserved. The mineralogy of the white anorthosite includes plagioclase (andesine-bytownite) amphibole, biotite, epidote, with minor components of titanite and rutile. All samples of white anorthosite would be strictly classified as anorthosite, containing upwards of 90% plagioclase with none

of the samples containing more than 4% mafic minerals. Both the lath-shaped and equant phases of plagioclase are present (Figure 4-81a). Biotite is observed locally, potentially pseudomorphing primary amphibole (Figure 4-82). Spongy amphibole and epidote are present in association with wormy intergrowths of quartz (Figure 4-81c,d, Figure 4-83). Spongy epidote and white mica is also observed, locally enclosing rutile rimmed by titanite (Figure 4-83). Trails of mineral alteration and fractures are present throughout, often leading to clusters of altered mafic minerals (biotite, amphibole and epidote) (Figure 4-81a) giving the appearance that fluids have moved through the rock

The pervasive epidote alteration, and alteration of amphibole to biotite (Figure 4-81) in a region that otherwise reflects amphibolite-facies conditions leads to the conclusion that the rock has been altered by hyrothermal fluids. The spongy texture observed in the amphibole and epidote indicates that there was a limit to the rate of input of these fluids, affecting the growth of these secondary minerals. The broad similarity of the plagioclase form and chemistry (though slightly more albitic based on optical microscopy) suggests that the leucodiorite may represent the parent rock. Potentially the more anorthositic (plagioclase > 90%) end members of this unit are preferentially fractured and hence locally metasomatised forming the white anorthosite. These could represent regional hydrothermal fluids or fluids coming off later anorthosite intrusions.

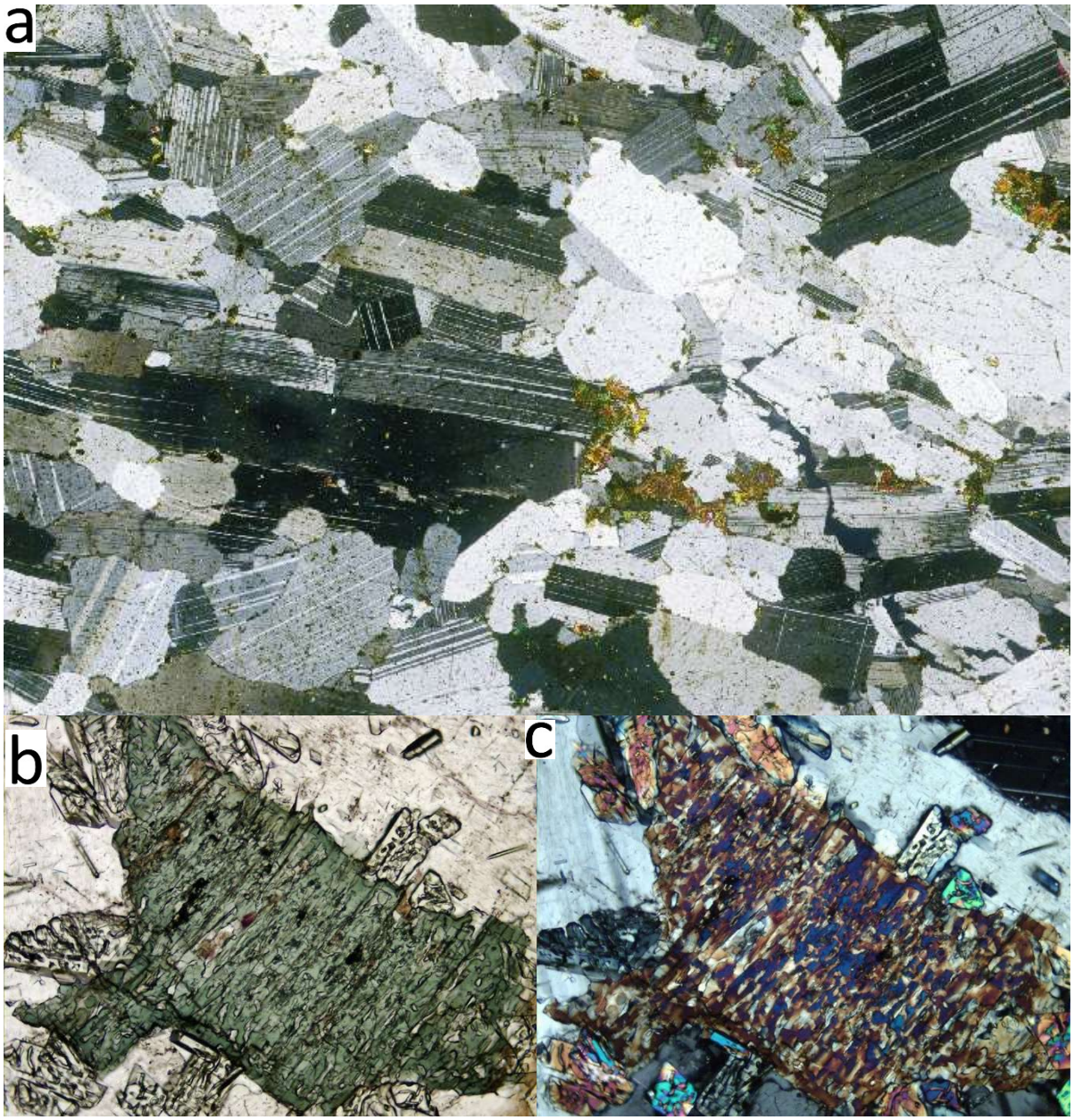

Figure 4-81 – Photomicrographs of J257 (UTM 28 799394 mE, 2647638 mN) - meta-anorthosite. a) general view of lath-shaped and equant plagioclase grains. FOV 1x1.5 cm [XPL]. b, c) Detail of spongy amphibole-epidote association with wormy intergrowths of quartz. FOV 0.8 mm [a) PPL b) XPL].

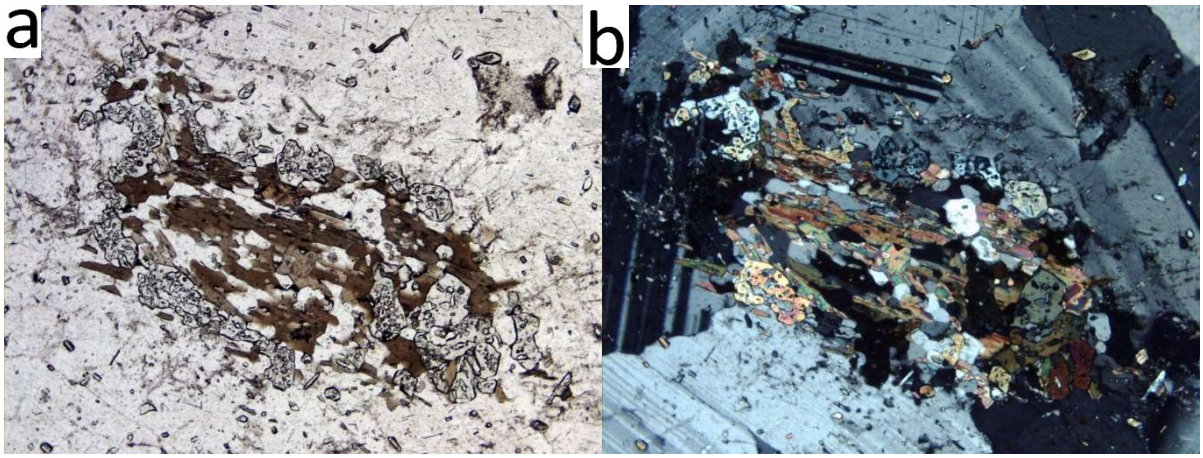

Figure 4-82 – Photomicrographs of J258 (UTM 28 800097 mE, 2648289 mN) - meta-anorthosite. Interstitial cluster of biotite and epidote, possibly pseudomorphing amphibole. FOV 2 mm [a) PPL b) XPL].

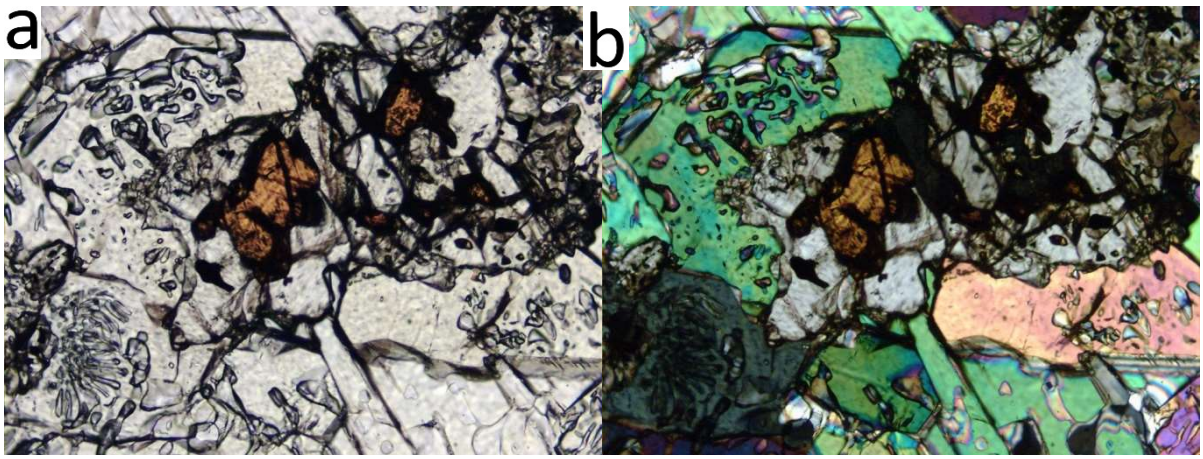

Figure 4-83 - Photomicrographs of J258 (UTM 28 800097 mE, 2648289 mN) - meta-anorthosite. Detail of interstitial cluster- rutile rimmed by titanite, enclosed in spongy epidote and white mica. FOV 0.8 mm [a) PPL b) XPL].

4.1.3.2.3 Satellite Intrusions

Broadly consisting of olivine gabbro/basalt, the satellite intrusions display large textural variations. Samples J118 (Figure 4-84) and J255 (Figure 4-85) represent samples from the same intrusion, both showing slow cooling features despite J118 having a relatively fine groundmass (Figure 4-84). J118 comprises an olivine diorite with olivine phenocrysts and a groundmass of plagioclase, clinopyroxene, biotite, magnetite and orthopyroxene. The olivine phenocrysts appear to have been partially resorbed before the crystallisation of the groundmass. J255 is a porphyritic olivine gabbro with phenocrysts of olivine, biotite and augite and a groundmass of plagioclase, clinopyroxene and orthopyroxene (Figure 4-85b). Some olivine

phenocrysts are surrounded by a rim of symplectic intergrowth between orthopyroxene and magnetite (Figure 4-85 b, c). This type of texture has been observed in the Skaergaard intrusion of Greenland described by the reaction $6(Fe,Mg)_2SiO_4 + O_2 = 2Fe_2O_4 + 3(Fe, Mg)_2Si_2O_6$, or more generally olivine ± anorthite ± $CaO + O_2$ = magnetite + pyroxene ± Al_2O_3 (Holness et al., 2011). The orthopyroxene in the rims display triple junctions (Figure 4-85 d,e) consistent with a late-stage in equilibrium reaction rim. This is consistent with slow cooling.

Some of the satellite intrusions are ultramafic in composition and display a distinctive poikilitic meta-hornblende-clinopyroxenite (Figure 4-86). The cumulus consists of clinopyroxene and hornblende with hornblende oikocryst enclosing clinopyroxene grains. These bodies are associated with anorthosite everywhere from the Main Bulb, Moug el Kaleb and even on the border between the Elmalhat and Oum Abana regions

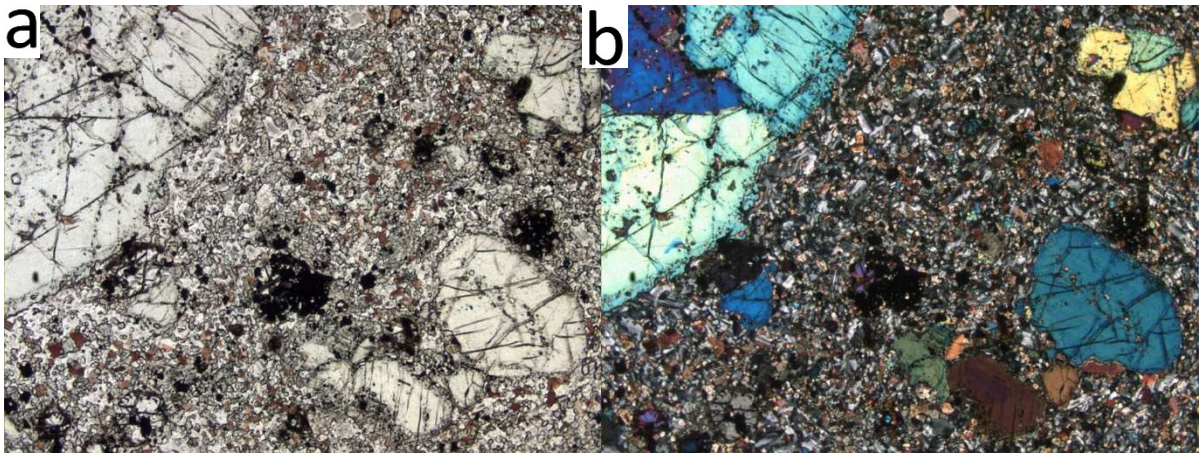

Figure 4-84 - Photomicrographs of J118 (UTM 28 792756 mE, 2645436 mN) - olivine basalt/dolerite in satellite bodies. Porphyritic olivine basalt of hornfelsic aspect. Note the zoned distribution of inclusions and resorbed margins of phenocrysts. FOV 4 mm [a) PPL, b) XPL].

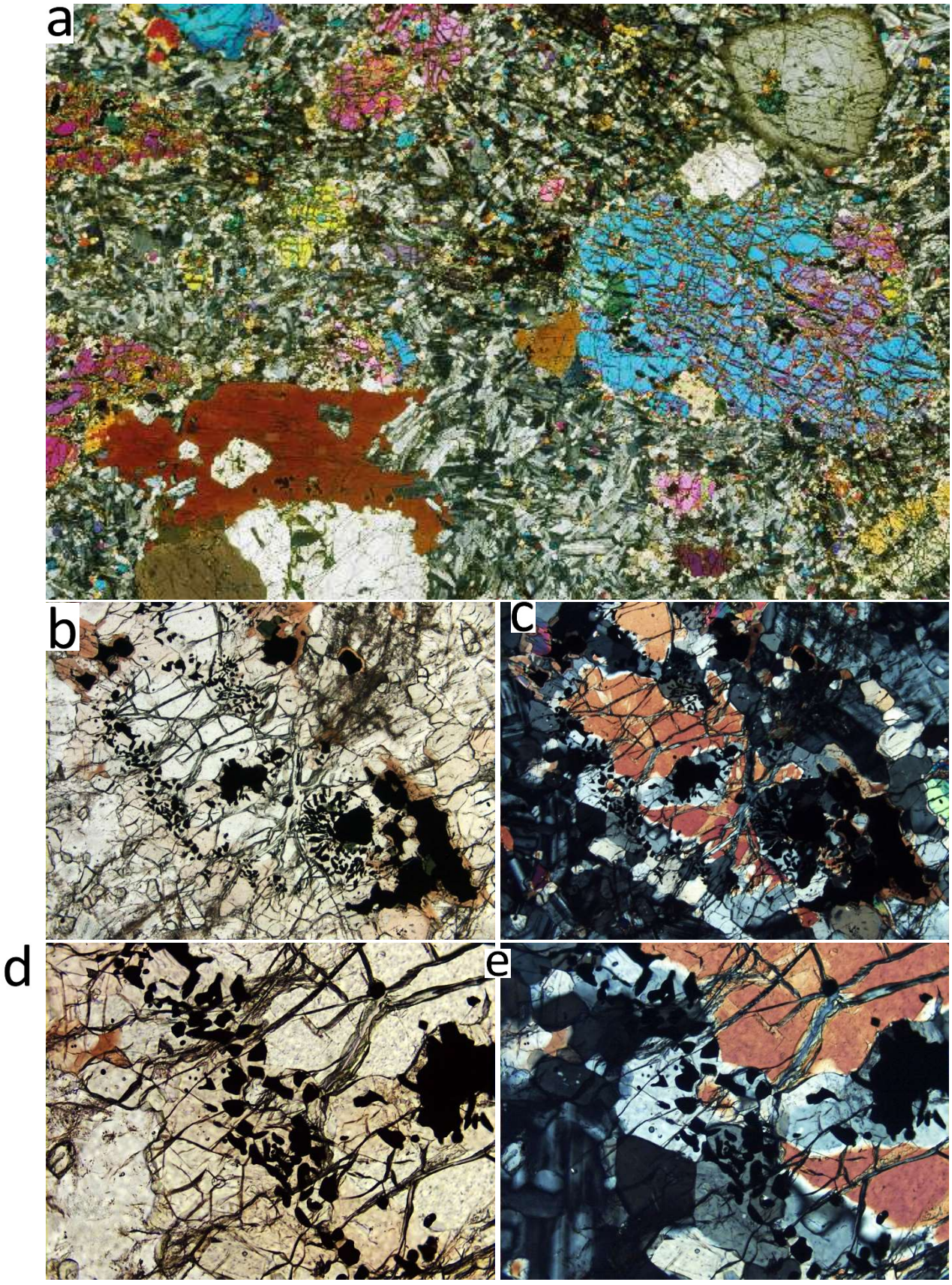

Figure 4-85 - Photomicrographs of J255 (UTM 28 793519 mE, 2645704 mN) - porphyritic olivine, biotite gabbro. a) General view showing olivine, biotite and (zoned) augite phenocrysts in a gabbroic groundmass. FOV 1x1.5 cm [XPL]. b, c) coronas of Opx and fingerprint opaque on olivine. FOV 2 mm [b) PPL, c) XPL]. d, e) Detail of Opx-Opq corona on olivine. FOV 0.8 mm [d) PPL, e) XPL].

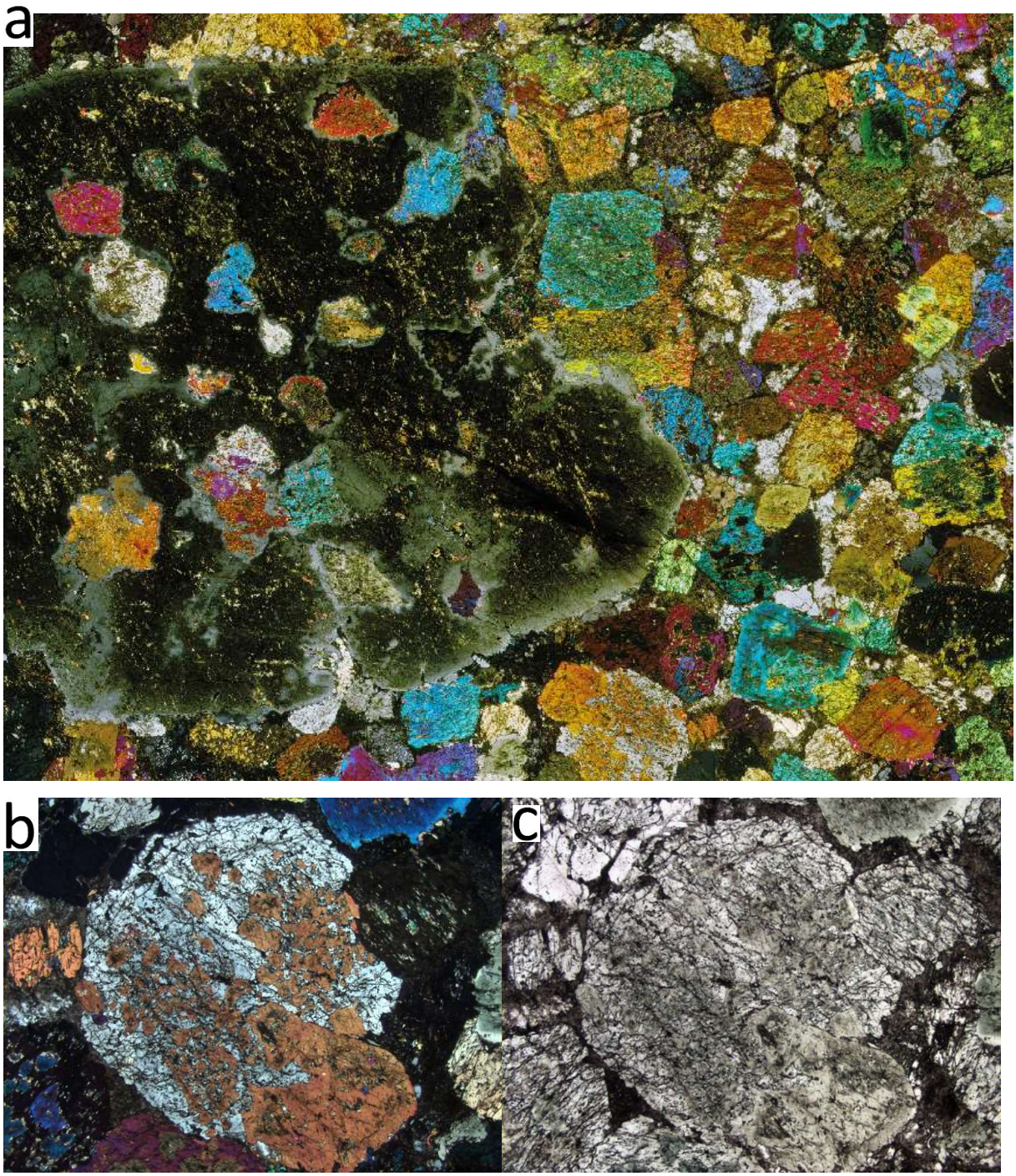

Figure 4-86 – Photomicrographs of J126 (UTM 28 776835 mE, 2638308 mN) - hornblende gabbroperidotite. A) poikilitic texture. FOV 1.5x2 cm [XPL]. b, c) Composite Cpx-hornblende cumulus crystals. FOV 4mm [b) XPL, c) PPL].

4.1.3.3 Gabbro, Ultramafics and Listwanite

The gabbroic unit in the Elmalhat Domain has been metamorphosed and has not retained a complete igneous mineralogy. Zoned grains of hornblende are observed with relict clinopyroxene cores (Figure 4-87). A second generation of hornblende is also observed recrystalising the zoned hornblende (Figure 4-87b,c).

Ultramafic rocks within the unit have been metamorphosed, now comprising almost entirely hornblende (Figure 4-88). Some larger, zoned hornblende crystals likely represent replaced pyroxene (Figure 4-88a, b) while the smaller, well-formed crystals of amphibole are newly grown in the metamorphic overprint (Figure 4-88c, d). The distribution of magnetite potentially represents the outline of former magmatic minerals, likely olivine (Figure 4-88e, f). The sample likely represents a metapyroxenite/peridotite.

Listwanite forms from an extreme degree of silica and carbonate alteration of ultramafic rocks within the area. Spatially associated with ultramafic rocks, especially near shear zones, the listwanite rocks associated with Elmalhat show a completely altered rock with a brown groundmass (Figure 4-90) and multiple cross-cutting silica-carbonate veins with open space textures (Figure 4-89, Figure 4-90).

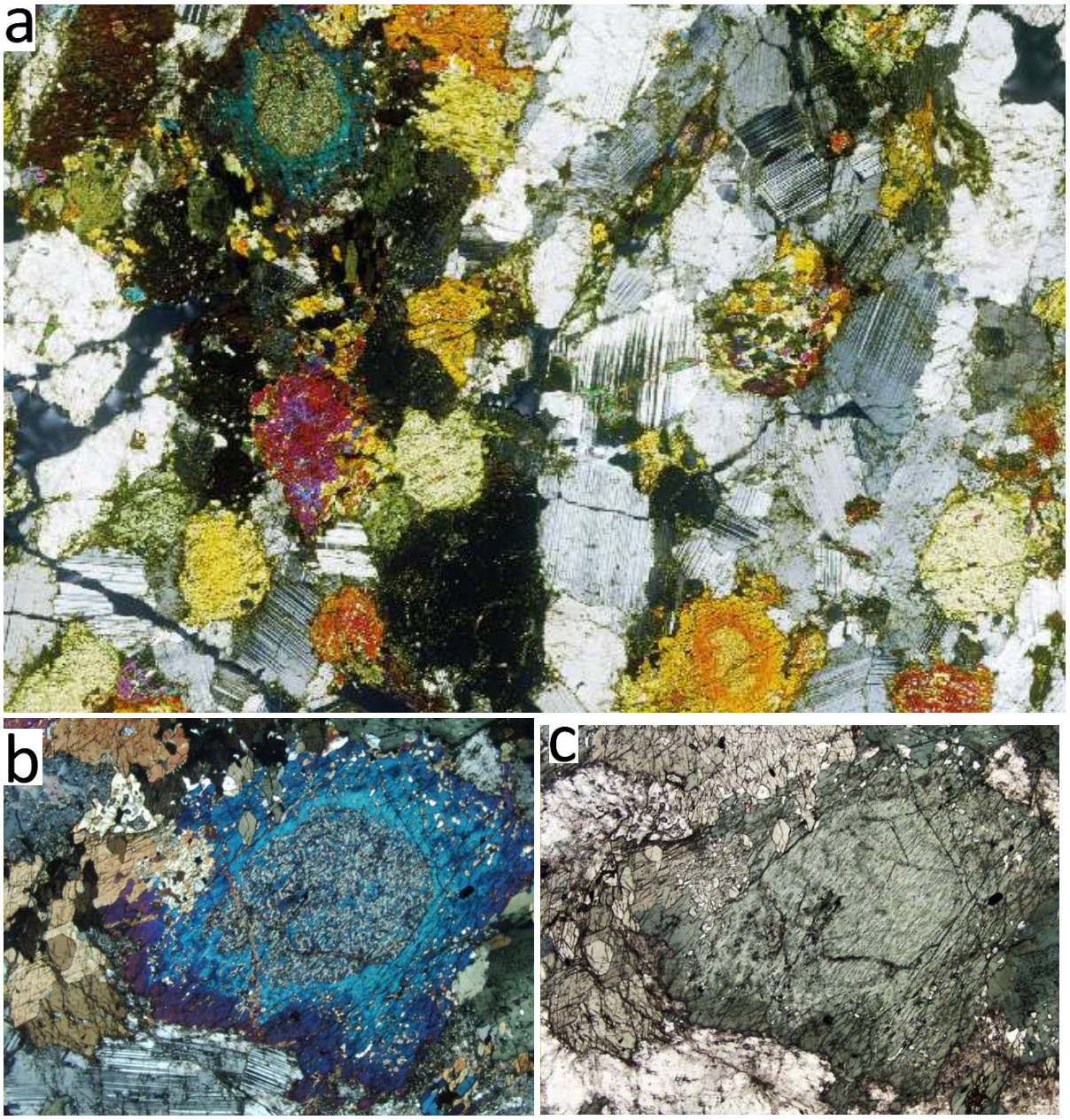

Figure 4-87 - Photomicrographs of J256 (UTM 28 794898 mE, 2647843 mN) - metagabbro. a) general view of the metagabbro, composed of plagioclase and zoned hornblende with clinopyroxene cores. FOV 1x1.5 cm [XPL]. b, c) Large zoned hornblende with darker rim, relict Cpx in core, surrounded by recrystallised Hbl. FOV 4 mm. [b) XPL c) PPL].

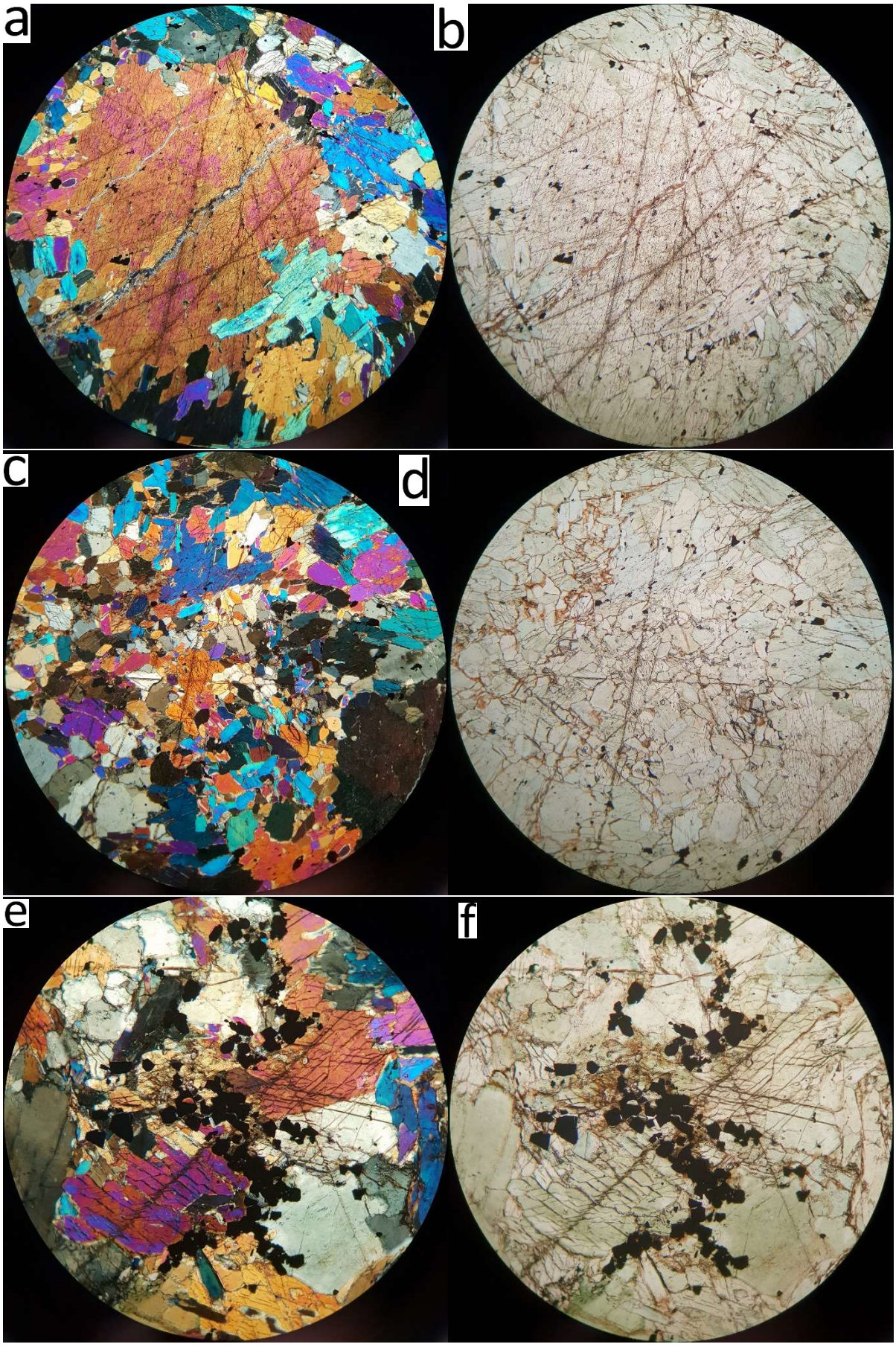
a
b
c
d
e
f

Figure 4-88 – Photomicrographs of J116 (UTM 28 779633 mE, 2649705 mN) - metapyroxenite – a, b) Large, zoned hornblende grain – likely replacing pyroxene. FOV 2.5 mm [b) XPL c) PPL]. c, d) Finer grained recrystallised metamorphic hornblende. FOV 5 mm [c) XPL d) PPL]. e, f) Magnetite outlining previous magmatic mineral – likely olivine. FOV 2.5 mm [e) XPL f) PPL].



Figure 4-89 - Photomicrographs of J115 (UTM 28 779629 mE, 2649670 mN) - listwanite, microcrystalline and columnar silica with some carbonate, filling void. FOV 0.8 mm [XPL].

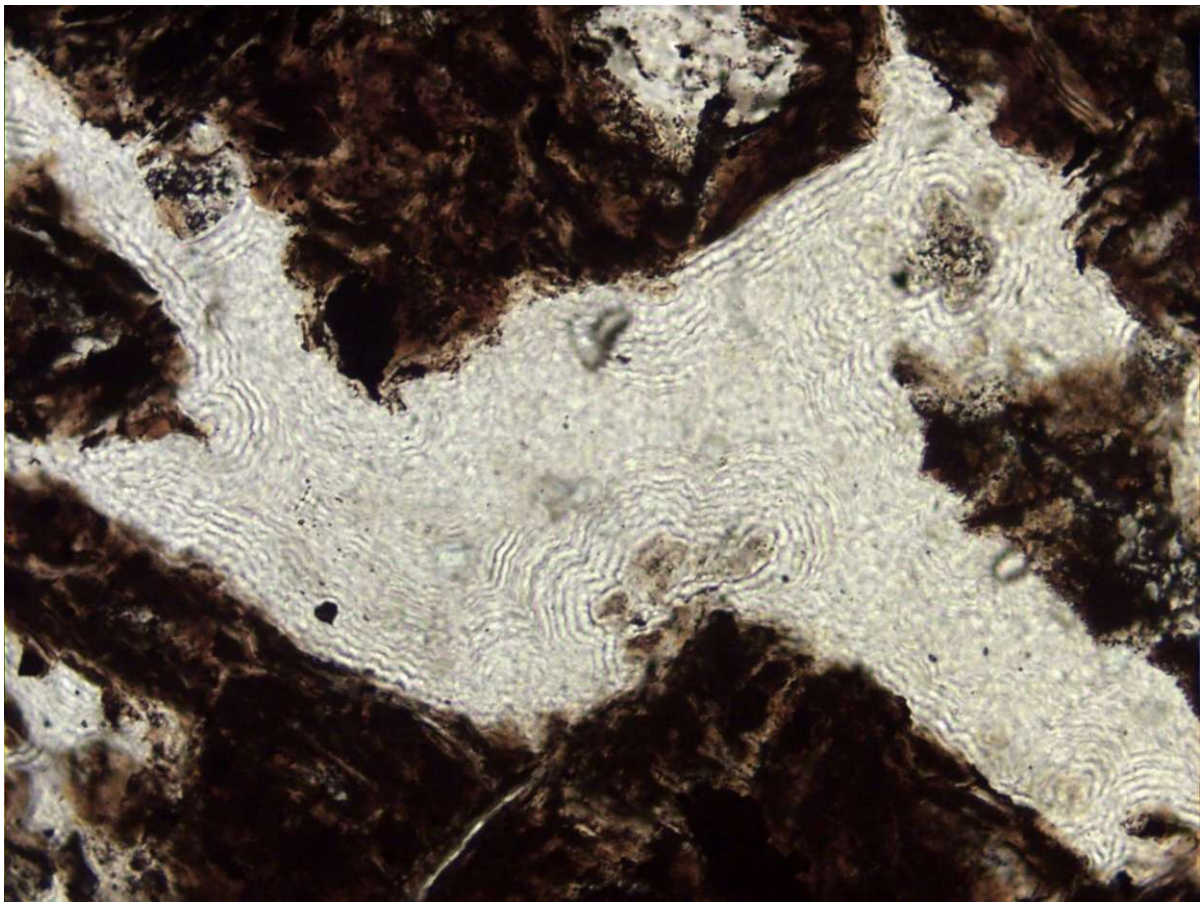

Figure 4-90 - Photomicrographs of J113 (UTM 28 776065 mE, 2660782 mN) - listwanite, agate-like silica filling void. FOV 0.8 mm [PPL].

4.1.3.4 Late Granite Intrusions

The intrusion between the Main Bulb and Northern Limb (J247) is a weakly deformed granitoid, comprising plagioclase, alkali-feldspar, quartz, biotite with minor magnetite and allanite (Figure 4-91). The biotite is randomly orientated and, in places, grades into chloritised biotite (Figure 4-91 a, b). The epidote is observed to form rims on allanite (Figure 4-91b, c). Quartz has relatively low strain, prismatic subgrains (Figure 4-91 d, e). The plagioclase preserves igneous zoning (Figure 4-91 g, h). It is a weakly deformed biotite granite with I-type characteristics (allanite, magnetite).

The late stage porphyry cross-cutting the Main Bulb (J246) is a weakly gneissic plagioclase, quartz, and biotite-bearing granitoid rock (Figure 4-92). The plagioclase is much coarser than

the other constituents and is unevenly altered by fine sericite. The matrix texture is granoblastic. The overall composition of the rock is tonalite-trondhjemite.

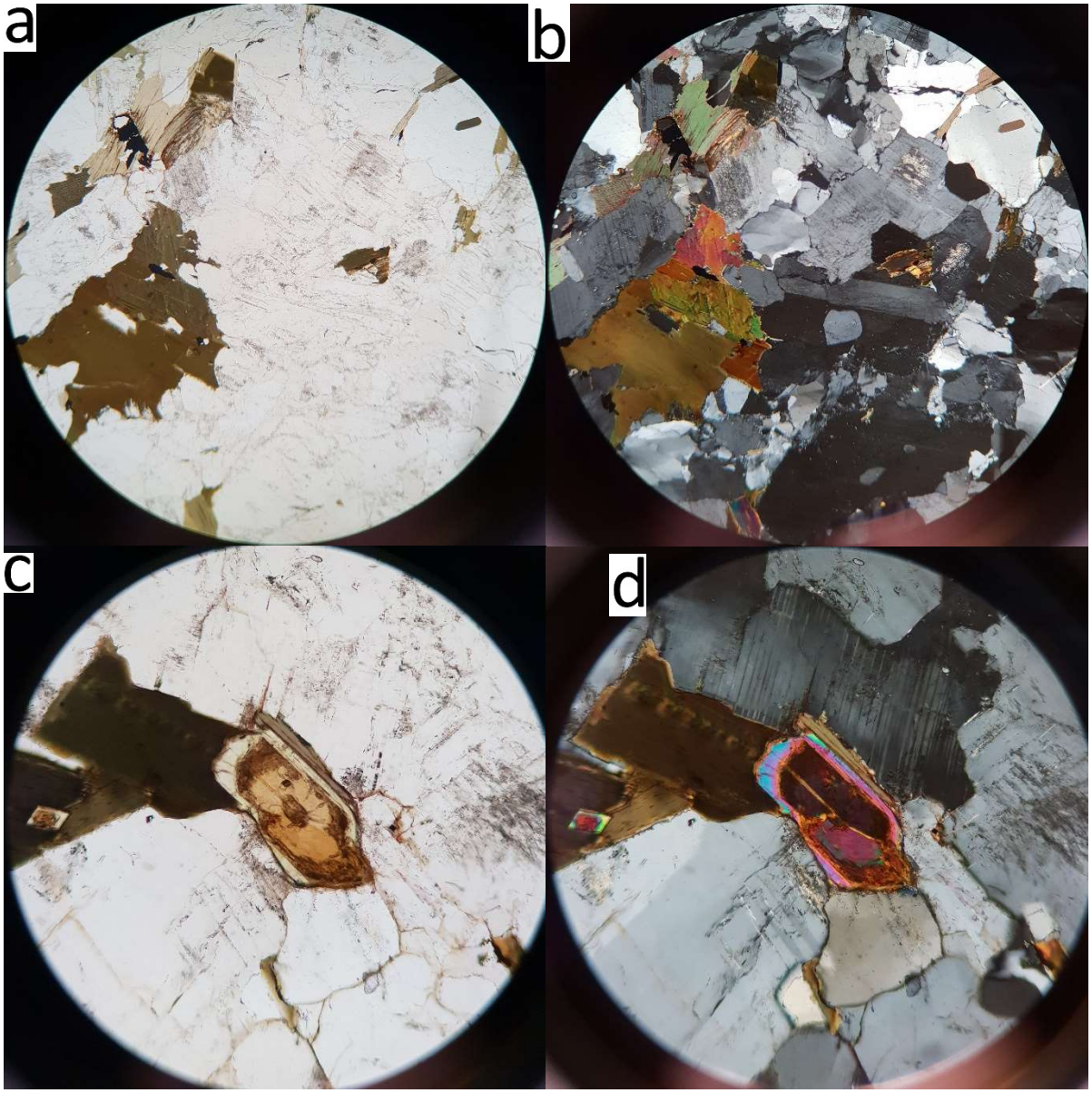

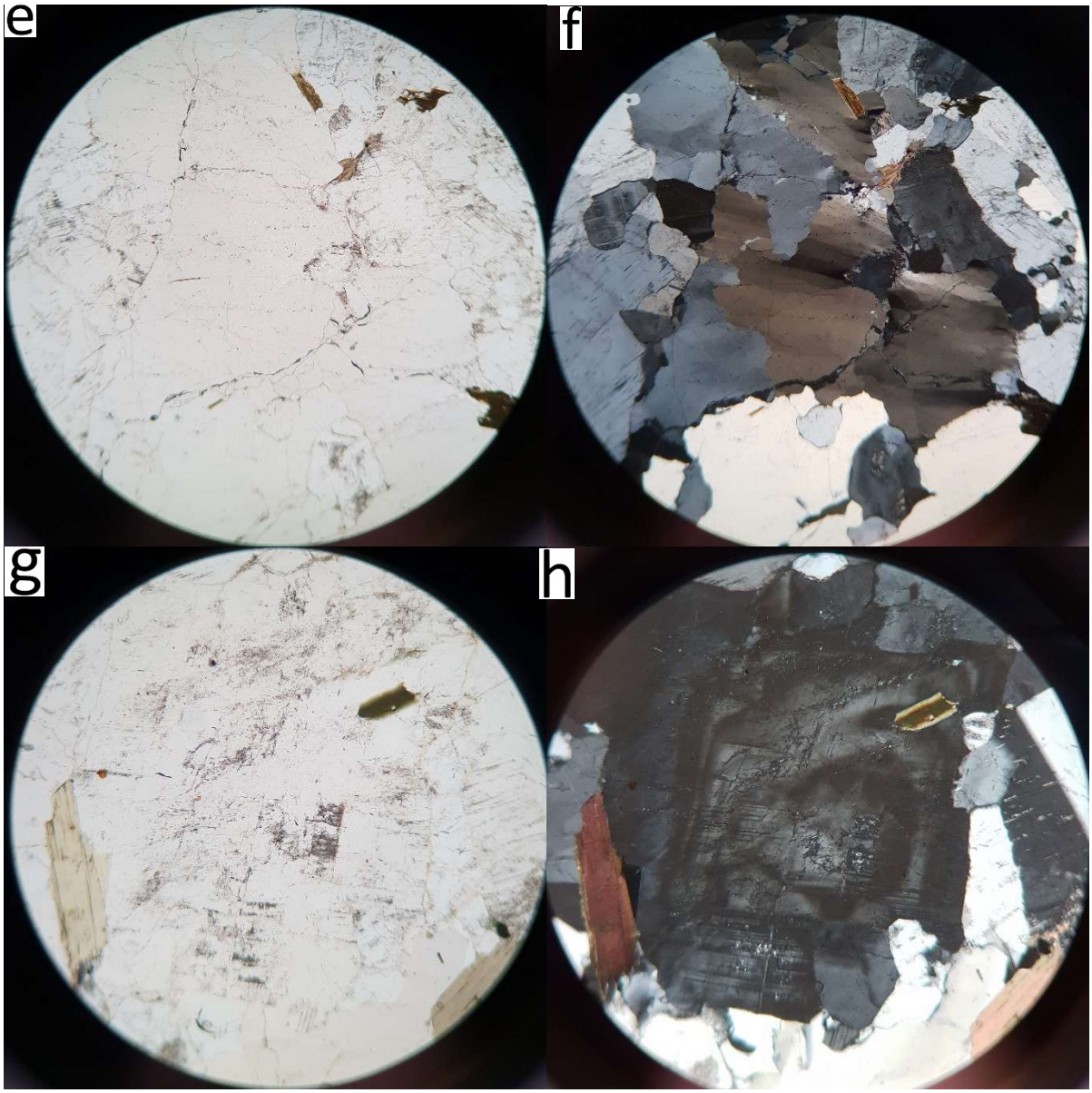

Figure 4-91 – Photomicrographs of sample J247 (UTM 28 791479 mE, 2655830 mN) – weakly deformed granite. a, b) biotite is randomly orientated and in places grades into chloritised biotite. FOV 2.5mm [a) PPL, b) XPL]. c, d) epidote is observed forming rims on allanite. FOV 1.25 mm [c) PPL, d) XPL]. e, f) low strain, prismatic subgrains on quartz. FOV 2.5mm [e) PPL, f) XPL]. g, h). The plagioclase preserves igneous zoning. FOV 2.5mm [g) PPL, h) XPL].

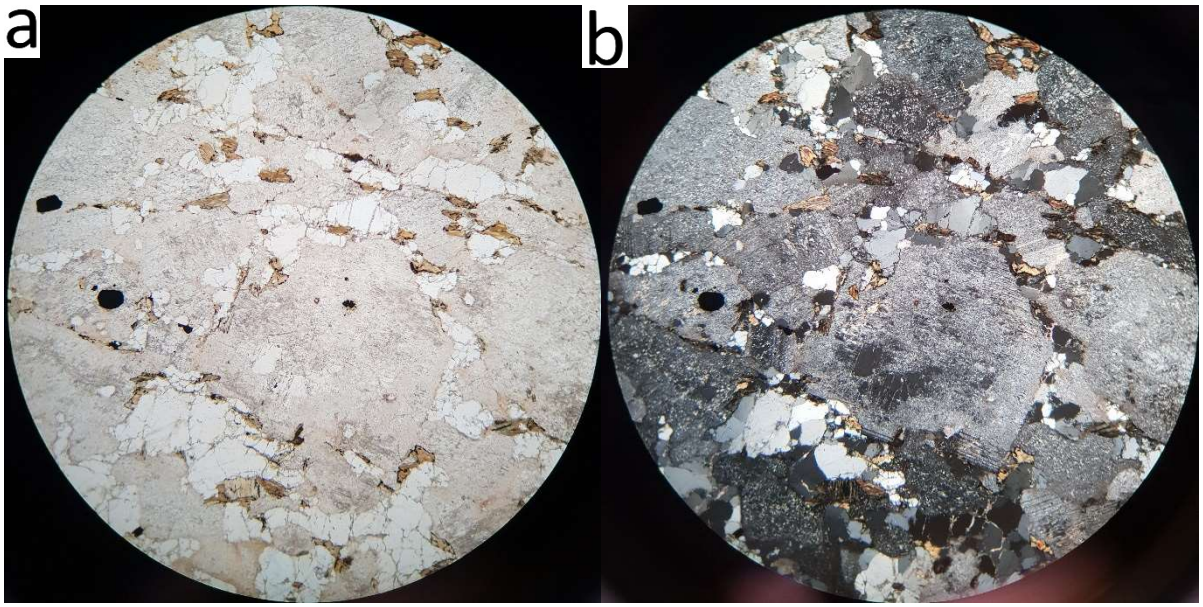

Figure 4-92 - Photomicrographs of J246 (UTM 28 803330 mE, 2643628 mN) - general view of granitoid. FOV 5 mm [a) PPL, b) XPL].

4.1.4 Mineral Chemistry

The mineral chemistry was analysed on the electron microprobe facilities at the University of Barcelona, Department of Materials. We used the JEOL JXA-8230 microprobe, with 5 wavelength dispersal spectrometers (WDS) and energy dispersal spectrometers (EDS-SDD) to analyse the silicate minerals under the following conditions: an electron beam acceleration voltage of 20 kV and a current of 15 nA. Counting times 10s on peak and 5s on each background position. We used the matrix correction effect with the method XPP (type phi-rho-z). Si and Al were analysed using the TAP crystal, Cr and Ti were analysed using the PETJ crystal, Mg and Na were analysed using the TAPH crystal, Fe, Mn and Ni were analysed using the LIFH crystal, and Ca, K and Sr were analysed using the PETL crystal.

The following standards were used for silicates. Albite was used as the Na standard, periclase was used as the Mg standard, corundum was used for the Al standard, wollastonite was used for the Ca and Si standard, orthoclase was used for the K standard, rutile was used for the Ti standard, Cr_2O_3 was used for the Cr standard, rhodonite was used for the Mn standard, Fe_2O_3

was used for the Fe standard, Ni metal was used for the Ni standard, and celestite was used for the Sr standard.

The same conditions were used in the analysis of oxides although a higher current (20 nA) and V metal was used as the V standard. An interference correction for Ti Kβ--> V Kα was applied.

See Appendix D for details of the acquisition and the data.

4.1.4.1 Silicate Mineral Chemistry

When the magnesium number (Mg# - Mg/(Fe + Mg)) of mafic minerals is plotted against anorthite content (An%) of plagioclase, two clusters are observed in the dark (massif-type) anorthosite from the Main Bulb ($An_{\sim 40}$ and $An_{\sim 60}$) and a single fractionation trend (corresponding decrease in Mg# with decreasing An content) is observed from samples from the megacrystic anorthosite in the Northern Limb (Figure 4-93). Notably, both clusters from the Main Bulb have a higher Mg# for the corresponding An content, compared to other massif-type anorthosite complexes. This possibly reflects a higher Al content in the parent magma resulting in the early crystallisation of plagioclase from a more primitive magma. The $An_{\sim 40}$ and $An_{\sim 60}$ clusters within the Main Bulb corresponds to the banded anorthosite/leucodiorite and labradorite anorthosite/leucogabbro samples described previously. Two of the three samples analysed from satellite intrusions (B85 and B87) plot with the labradorite anorthosite, while one (B83) plots in the andesine anorthosite (though has a relatively high Mg# compared to samples from the Main Bulb). The two samples of ultramafic rocks (observed cross-cutting the banded andesine anorthosite) plot with the labradorite anorthosite

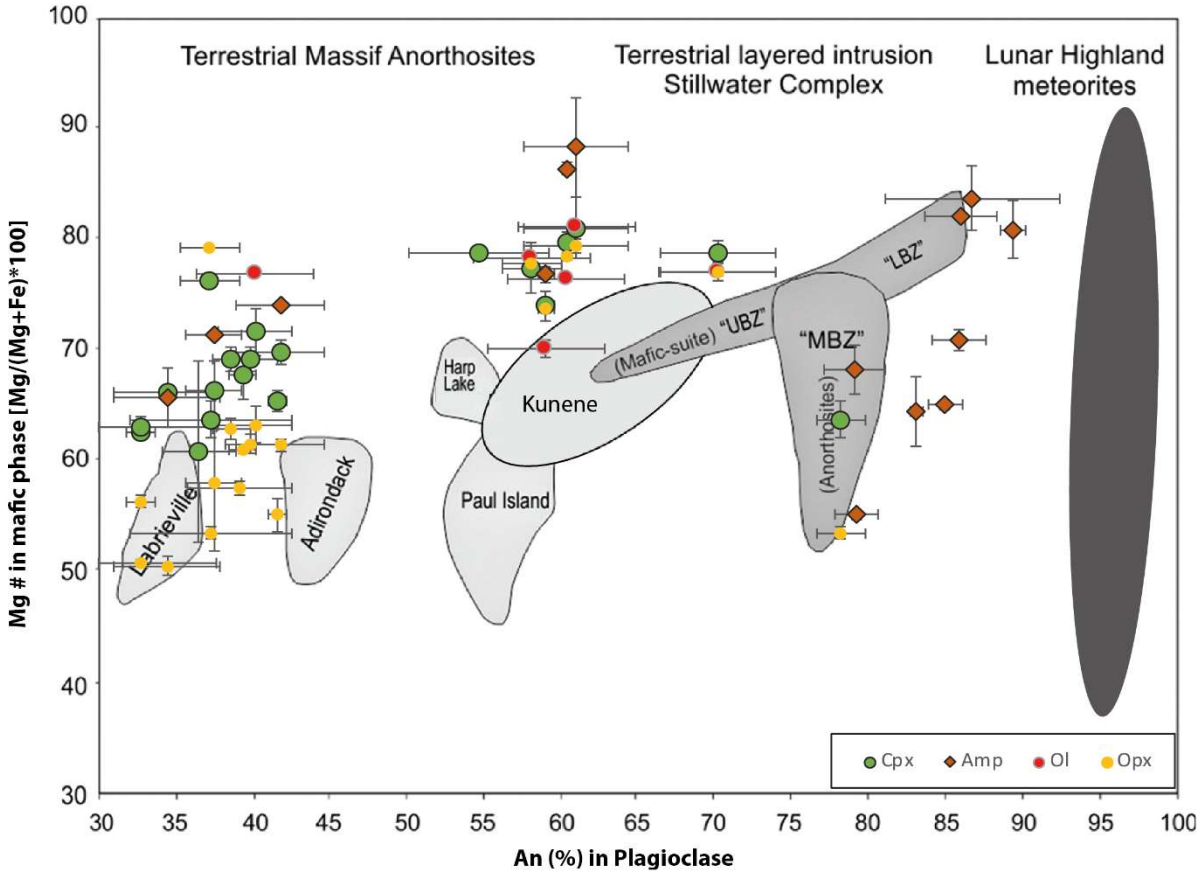

Figure 4-93 - Magnesium number of mafic minerals versus anorthite content of plagioclase of samples from the EAC, compared to other anorthosite complexes and layered mafic intrusions. Anorthosite and layered mafic intrusion fields modified from Gross et al. (2014), with the Kunene field from Ashwal (1993).

Based on relative dating, this mineral chemistry data has been used to compare the EAC with other anorthosite complexes from around the world (Figure 4-94). Notably, this is the only complex in the world to contain both megacrystic and massif-type anorthosite. Additionally, it is located in a break in major anorthosite production between the Archaean (megacrystic anorthosite) and the main production of massif-type anorthosite starting at ~1800 ma. The megacrystic anorthosite is ~600 ma younger than the next youngest anorthosite of its kind.

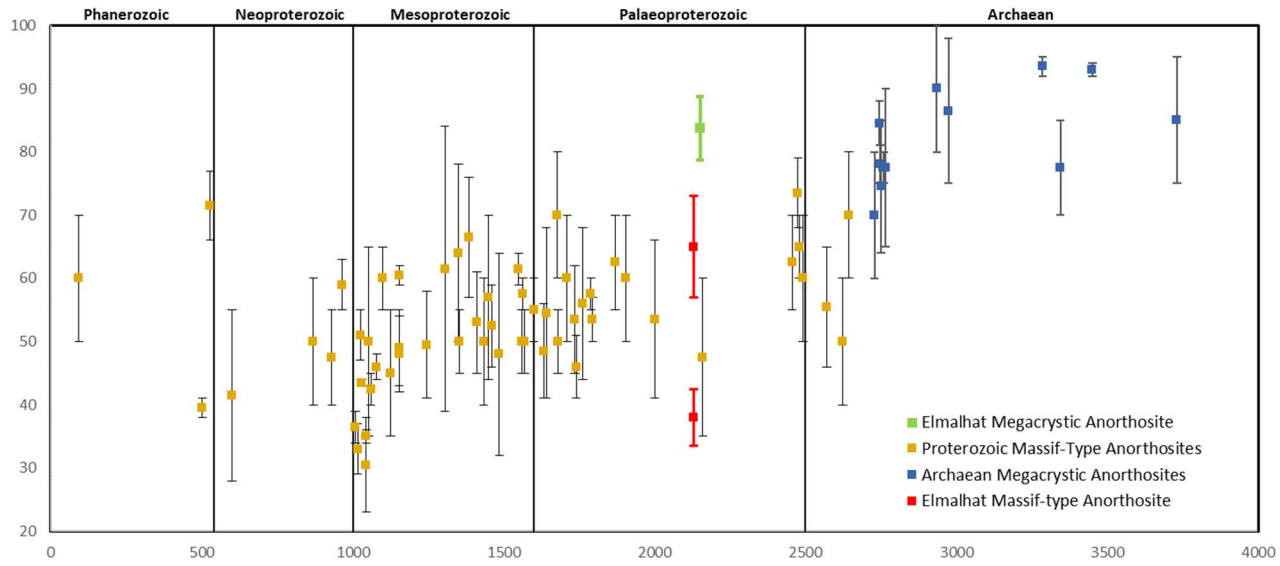

Figure 4-94 -Temporal distribution of different types of anorthosite complexes, displayed as An content vs age. Data for other anorthosite complexes from (Ashwal, 2010). Anorthosite ages are based on relative dating and whole rock Sm-Nd geochronology.

The samples of andesine anorthosite contain primary igneous banding. Using strike and dip data from the field and measurements from the centre of the bulb, it was possible to use trigonometry to calculate the stratigraphic position of each of these samples relative to the centre of the bulb. This data was constrained using ground magnetic data (Figure 4-35 b) under the assumption that each of the concentric magnetic anomalies represented stratigraphic layers. The stratigraphic thickness was calculated from the centre of the Main Bulb to the magnetic anomalies in each direction (northwest, southeast, east and west). The thickness between the magnetic anomalies were consistent in all directions (within ~70 m over ~2000 m of stratigraphic thickness). The stratagraphic location of each of the samples was then calculated relative to the anomalies.

When ordered stratigraphically relative to the centre of the Main Bulb, the mineral chemistry data from the andesine anorthosite shows a relatively consistent An content of the plagioclase with height (Figure 4-95). This likely represents the emplacement of a plagioclase crystal mush with a similar An content. There is a consistent separation in the Mg# of the mafic phases increasing from orthopyroxene to clinopyroxene and then to amphibole (and olivine in one

sample). A weak trend of decreasing Mg# may be present in orthopyroxene from ~-580 m down (a higher frequency of sampling is required to confirm this). A possible explanation for this trend is presented in Section 4.1.6.2. Mineral content varies with stratigraphic height, though no distinct trend is present (Figure 4-95b).

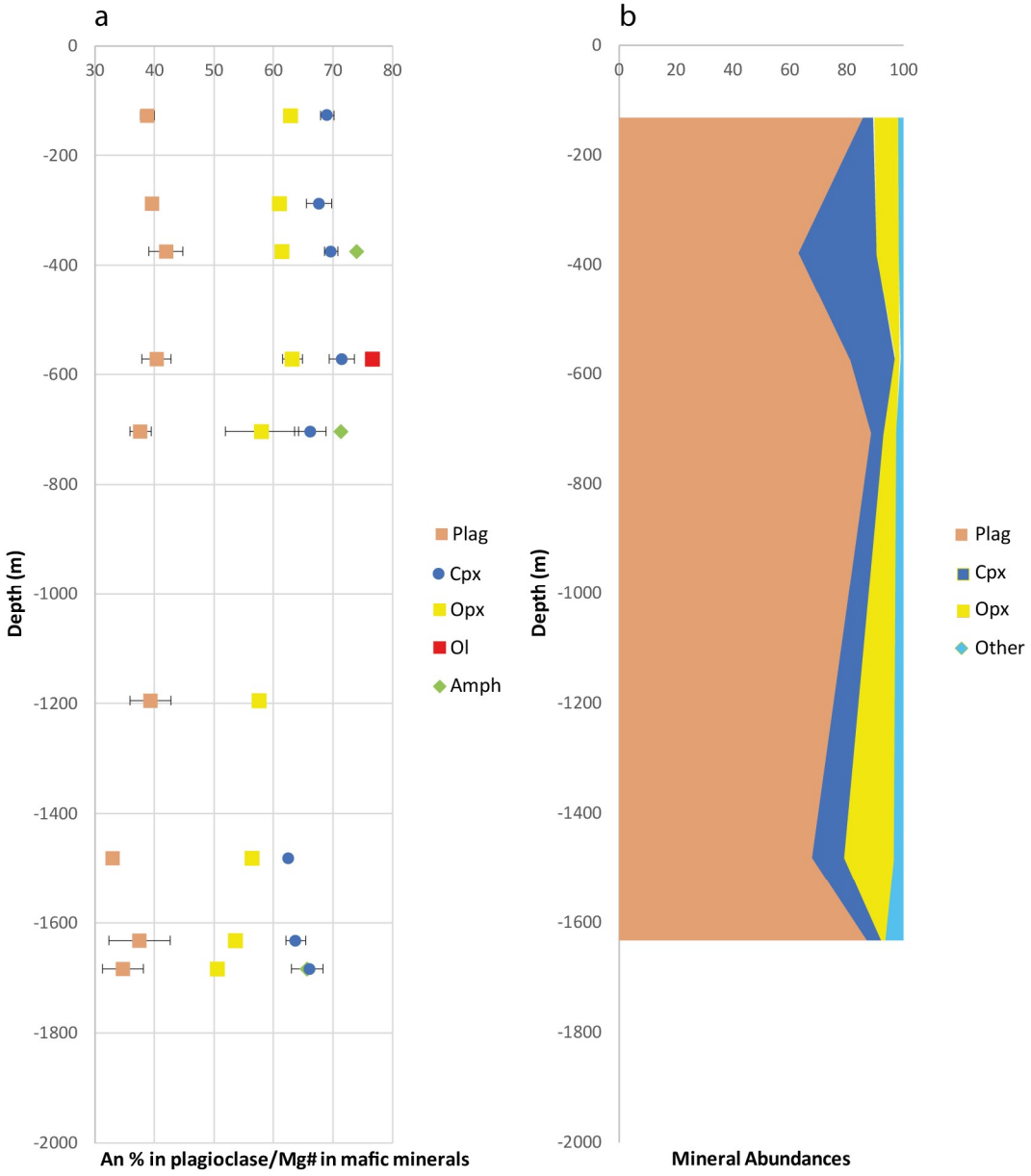

Figure 4-95 – Andesine anorthosite samples plotted stratigraphically taking 0 m as the centre of the intrusion. a) anorthite content of plagioclase and magnesium number of clinopyroxene, orthopyroxene, amphibole and olivine. b) mineral abundances.

The labradorite anorthosite is massive, and due to a lack of igneous banding cannot be placed stratigraphically. Notably in samples from the labradorite anorthosite, the Mg# of the different mafic phases are very similar to each other for a given sample (Figure 4-93). The similarity in

mineral composition of this cluster to that of samples from the satellite bodies, and ultramafic intrusions that cross-cut the andesine anorthosite, suggests that these magmas are related to a later pulse of anorthositic magma.

Samples of megacrystic anorthosite from the Northern Limb plot along a broad fractionation trend with corresponding decrease in Mg# with decreasing An content (Figure 4-95). The strike and dip of igneous banding and the chromitite seam were used to place the samples in stratigraphic order relative to the chromitite seam, assuming that the base of the sequence is in the southwest (the reasons for plotting it this way are presented in Section 4.1.6). A distinct trend is observed in the mineral chemistry (Figure 4-96). The magma becomes more fractionated (decreasing An content and Mg#) up to the chromitite seam when An content and Mg# represents a sudden change to a more primitive magma. From the chromitite seam to the north east the mineral chemistry becomes more fractionated. An interpretation for this trend along with whole rock geochemical data is presented in Section 4.1.6.

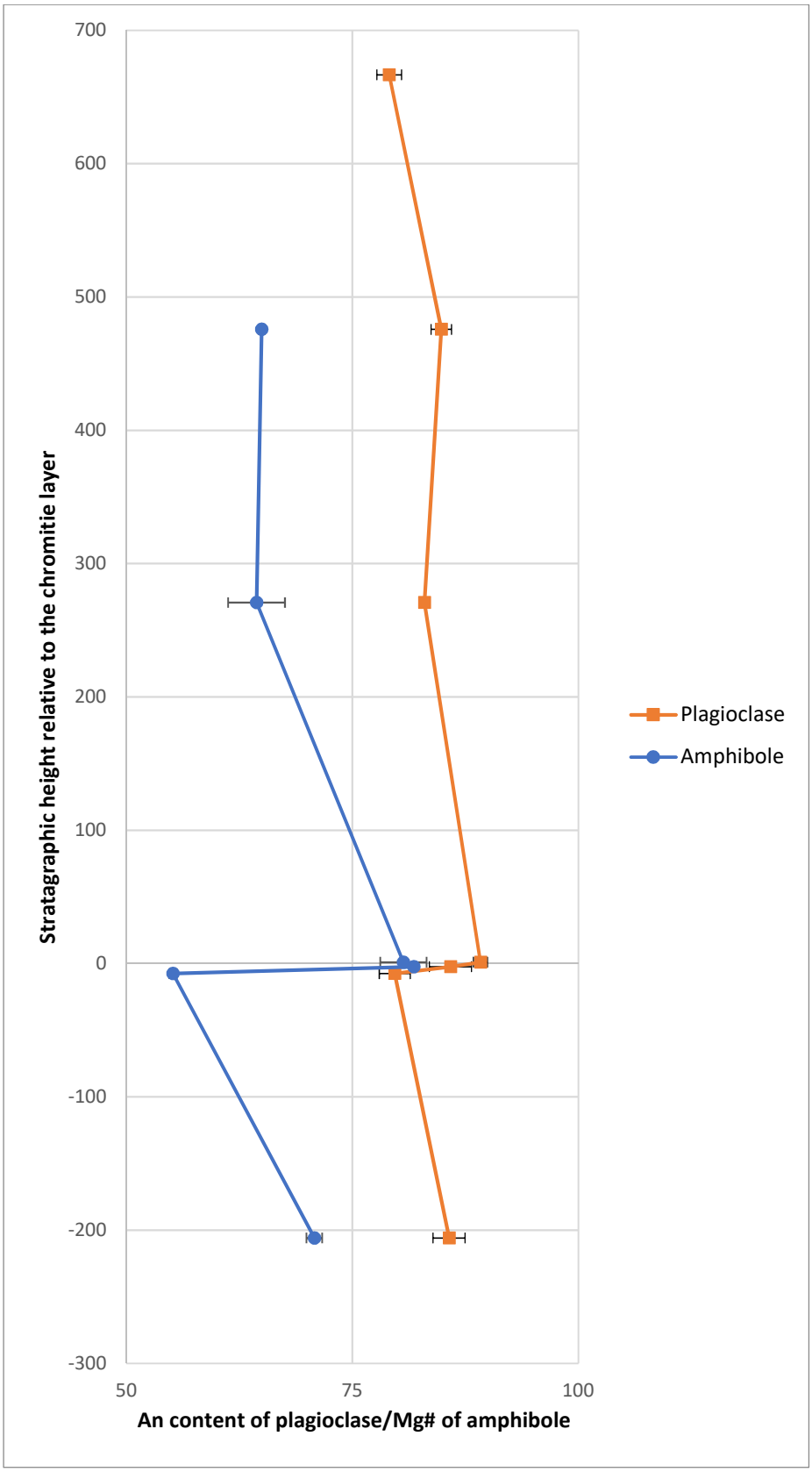

Figure 4-96 - Mineral composition of plagioclase and amphibole in samples from the Northern Limb, placed stratigraphically relative to the chromitite seam, assuming the southwest represents the base of the sequence.

4.1.4.2 Chromite Mineral Chemistry

Analysis of the chromite from the chromitite seam reveals that it is high in Al and Fe. In a plot of Cr# vs Mg# of the chromite has a very similar composition to that of Archaean-type megacrystic anorthosite hosted chromitite seams, especially that of Fiskenæsset (Greenland) and Sittampundi (India) (Figure 4-97). Similarly, when plotted on a ternary diagram with Cr^{3+}, Fe^{3+} and Al^{3+} they plot in the same region as Archaean anorthositic chromitites rather than stratiform or podiform chromitites which contain higher Cr content (Figure 4-98).

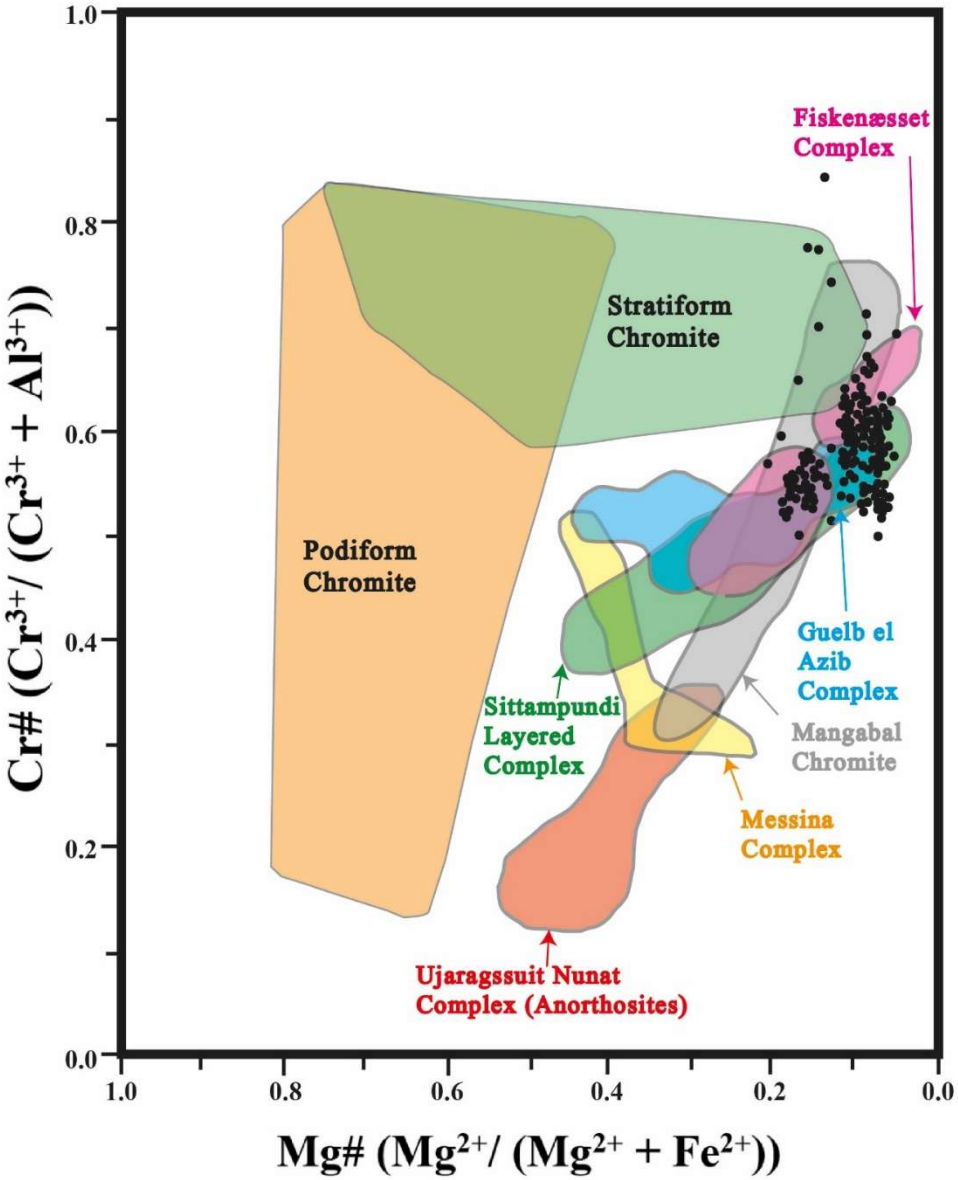

Figure 4-97 – Black dots show analyses from EAC chromitite. Fields for Archaean anorthosite-hosted Chromitites and Stratiform Chromites modified from Talukdar et al. (2017 and references therein), the podifom field was modified from Lehbib et al. (2008)

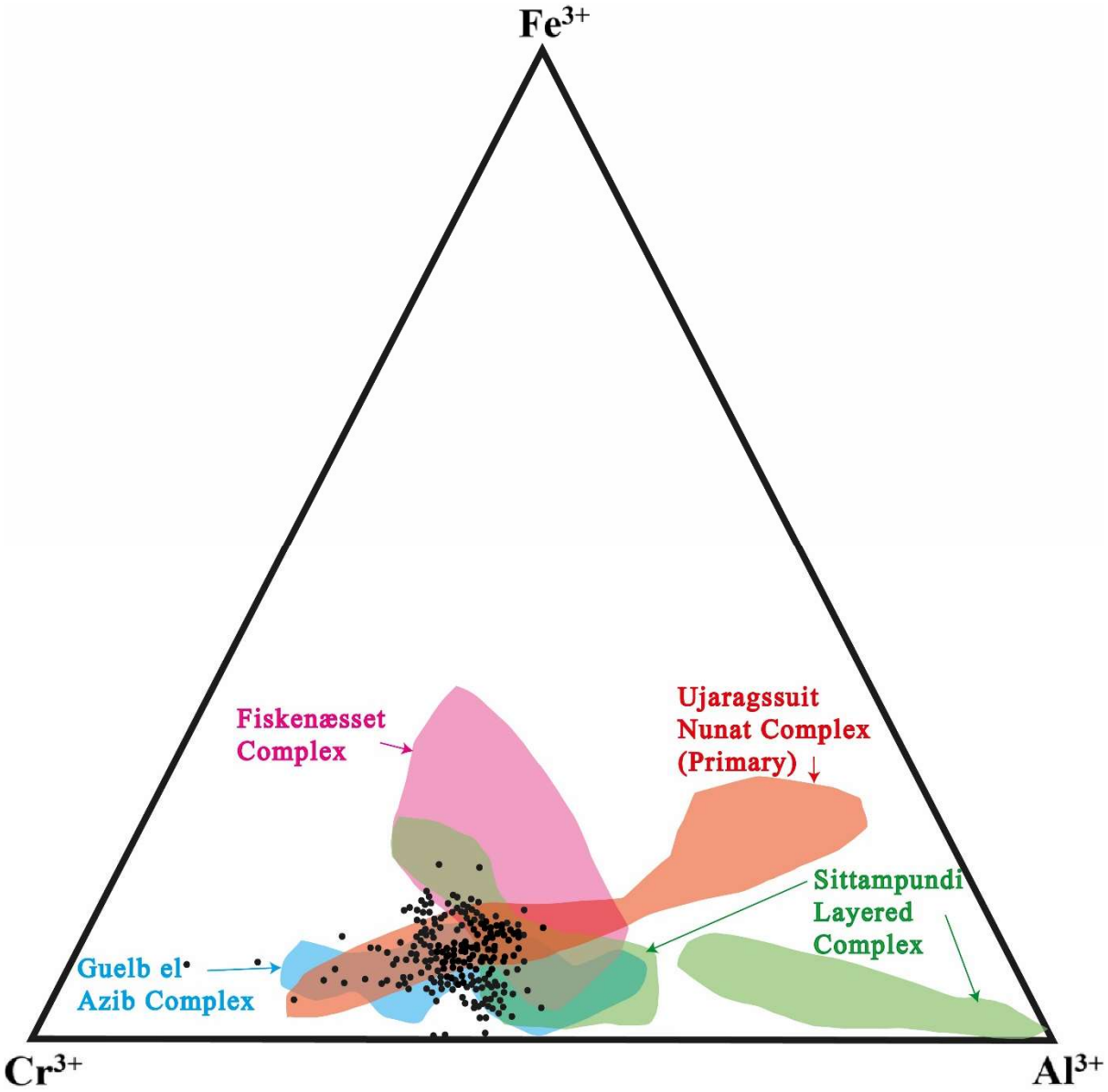

Figure 4-98 – Mineral chemistry of chromitite within the EAC (black dots) compared to chromite in Archaean megacrystic anorthosite complexes. (Modified from Talukdar et al., 2017)

4.1.4.3 Sulphur isotopes

The isotopic composition of sulphur from sulphides in samples from the anorthosite complex were analysed to help determine their provenance. The results samples of pyrite extracted from samples throughout the EAC (Table 4-2). Pyrite in samples from anorthosite in the Northern Limb (J108 – $\delta^{34}S$ 0.4 – 1.2) and the magnetite seam at Moug el Kaleb (B117 – $\delta^{34}S$ 0.6 – 0.9) are indicative of primary magmatic sulphides. The results are used in Section 5.2.3 in evaluating the potential for magmatic sulphide (Ni, Cu, PGM) mineralisation in the Complex.

Table 4-2 - Sulphur isotope chemistry of pyrite taken from samples around in the EAC.

Sample	Location	$\delta^{34}S$ (CDT)	σ ($\delta^{34}S$)	Weight (mg)	% S	Signal (mV)	Int.64	Mineral
B116-1	Moug el Kaleb Carbonate	**2.7**	0.1	0.090	48.2	1151		Pyrite
B116-2	Moug el Kaleb Carbonate	**2.6**	0.1	0.092	51.2	1261		Pyrite
B117-1	Moug el Kaleb Magnetite	**0.9**	0.1	0.085	50.1	1170		Pyrite
B117-2	Moug el Kaleb Magnetite	**0.6**	0.1	0.103	53.1	1418		Pyrite
BJ81	Elmalhat gneiss	**-0.5**	0.1	0.100	51.7	1395		Pyrite
BJ84-1	Elmalhat satellite intrusion	**-1.3**	0.1	0.138	53.0	1999		Pyrite
BJ84-2	Elmalhat satellite intrusion	**-0.7**	0.1	0.123	54.3	1791		Pyrite
J108A-1	Northern Limb anorthosite	**0.7**	0.1	0.092	52.2	1197		Pyrite
J108A-2	Northern Limb anorthosite	**1.2**	0.1	0.099	52.4	1413		Pyrite
J108B	Northern Limb anorthosite	**1.2**	0.1	0.113	53.3	1601		Pyrite
J108C	Northern Limb anorthosite	**0.4**	0.1	0.112	53.2	1626		Pyrite

4.1.4.4 Clinopyroxene tectonic discrimination

As previously mentioned, whole rock geochemical discrimination diagrams cannot be applied to cumulate rocks. However, the composition of clinopyroxene in basalts is a function of the composition of the lava/magma it crystallises from (Rollinson, 1993). Due to crystallisation from a more primitive magma, clinopyroxene phenocryst composition reflects more closely the chemical composition of the basaltic magma type compared to those in the ground mass (Rollinson, 1993). As such, the chemical composition of clinopyroxene phenocrysts can be used to discriminate basalts from different tectonic settings, leading to the development of a number of tectonic discrimination diagrams (eg. Le Bas (1962), Nisbet and Pearce (1977), Leterrier et al. (1982) and for ophiolitic basalt, Beccaluva et al. (1989). These are of particular

interest in altered basalts where cores of clinopyroxene phenocrysts are chemically preserved (Rollinson, 1993). The use of clinopyroxene to fingerprint the parent magmas is not widespread for intrusive rocks and has never been used on anorthosite intrusions. However, it has previously been applied to cumulate mafic rocks (eg. Driouch et al., 2010), and it seems reasonable to apply it to the EAC as an aid to interpreting its tectonic setting.

Clinopyroxene mineral chemistry from samples containing fresh clinopyroxene within the Main Bulb and satellite intrusions were plotted on discrimination diagrams from Nisbet and Pearce (1977) and Leterrier et al. (1982) (Figure 4-99). There seems to be a general fractionation trend between more primitive samples from the satellite bodies, through samples from the labradorite anorthosite, to the more fractionated andesine anorthosite. The Nisbet and Pearce (1977) diagram identifies the magma as having formed in a volcanic arc environment (Figure 4-99a). The Leterrier et al. (1982) plots (Figure 4-99b-d) also identifies the magma as having formed in a volcanic arc setting (Figure 4-99c) with a tholeiitic composition (Figure 4-99d). Therefore, based on this series of diagrams, the massif-type anorthosite of the EAC can be interpreted as having formed from an island arc tholeiite melt (also known as ‘low K basalt’ (Murphy, 2007)).

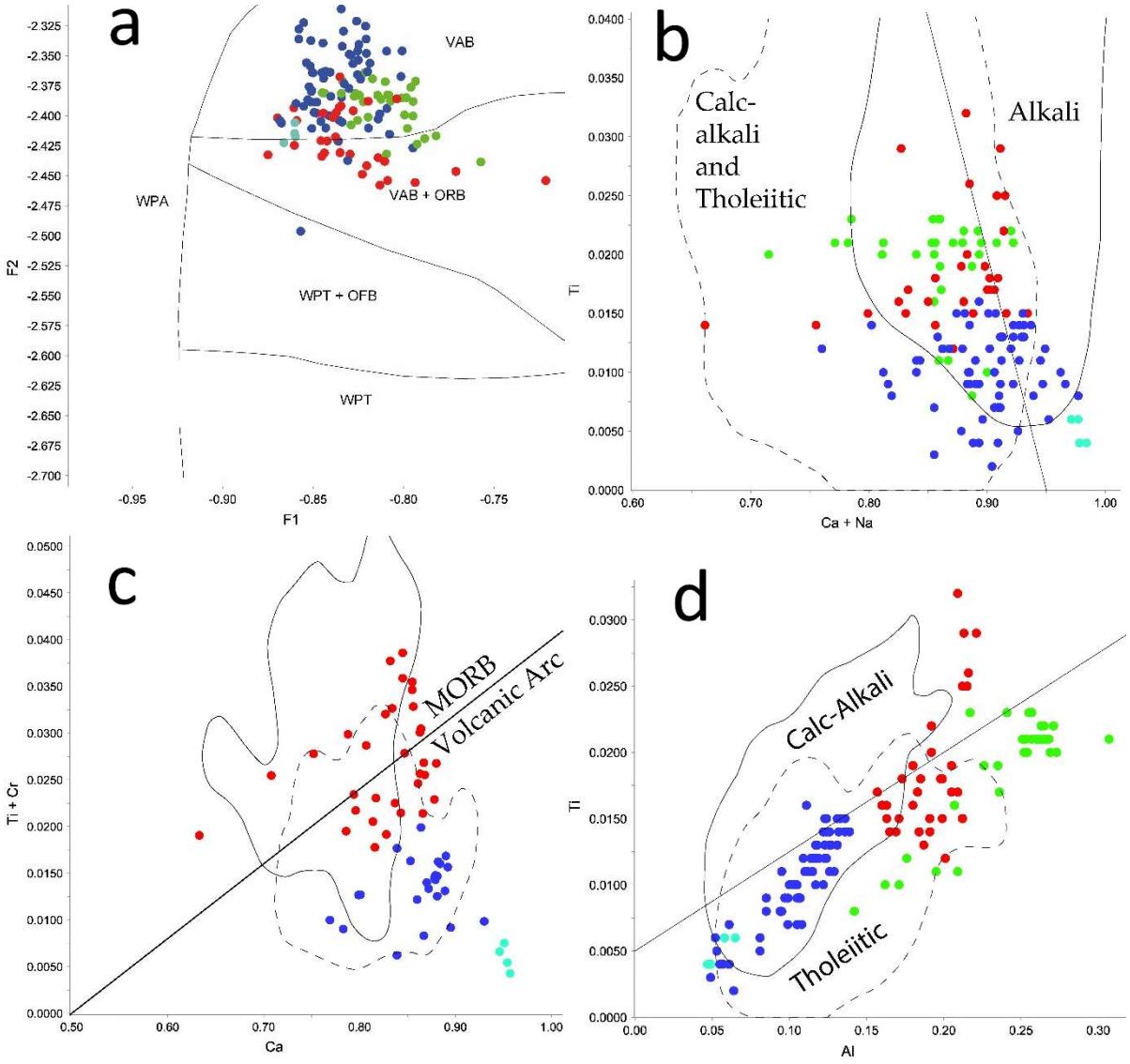

Figure 4-99 - Tectonic discrimination diagrams based on clinopyroxene chemistry from samples of leucogabbro from the Main Bulb (red and blue), olivine gabbro from the satellite bodies (green) and gabbro proximal to the Main Bulb (cyan). Blue points represent samples from the andesine anorthosite group within the Main Bulb, while red samples are from the labradorite anorthosite. a) Discriminant function (F1 vs F2) plot from Nisbet and Pearce (1977) with samples plotting as volcanic arc basalts. b-d) Progressive discrimination diagrams from Leterrier et al. (1982). b) Ti vs Ca + Na plot showing fields for alkali basalts as well as tholeiite and calc-alkaline basalts. c) Ti + Cr vs Ca discrimination diagram for non-alkali basalts, showing fields of non-orogenic tholeiites from mid oceanic ridges and other spreading centres and volcanic arc basalts. d) Ti vs Al discrimination diagram for volcanic arc basalts showing fields of calc-alkaline basalts and island arc tholeiitic.

4.1.5 Whole Rock Geochemistry

Caution needs to be used in interpreting whole-rock geochemical data from cumulate rocks as their composition does not reflect that of the magma that they crystallised from. However, a great deal of information can still be extracted from trends in major and trace element geochemistry in the cumulate rocks of the complex.

4.1.5.1 Tectonic Discrimination of Non-Cumulate Rocks Related to the Elmalhat Anorthosite Complex

Two mafic, intrusive samples associated with the EAC were analysed including the amphibolite (J266) layer from the Northern Limb and a sample of altered gabbro (J256) proximal to the Main Bulb (also analysed using mineral chemistry; Figure 4-100). These samples have undergone amphibolite facies metamorphism (Section 4.1.3.2.1). Since Pearce (2008) warned that the Th-Nb diagram is susceptible for misinterpretation in high metamorphic grade terranes, only tentative interpretations can be made.

The two samples of basaltic composition (Figure 4-100a) display an oceanic arc signature on the Th-Nb diagram (Figure 4-100b) with the Shervais (1982) V/Ti subduction melting proxy revealing a island arc tholeiite/boninitic signature. This is consistent with the results found via analysis of clinopyroxene mineral chemistry (Chapter 4.1.3.4, Figure 4-99).

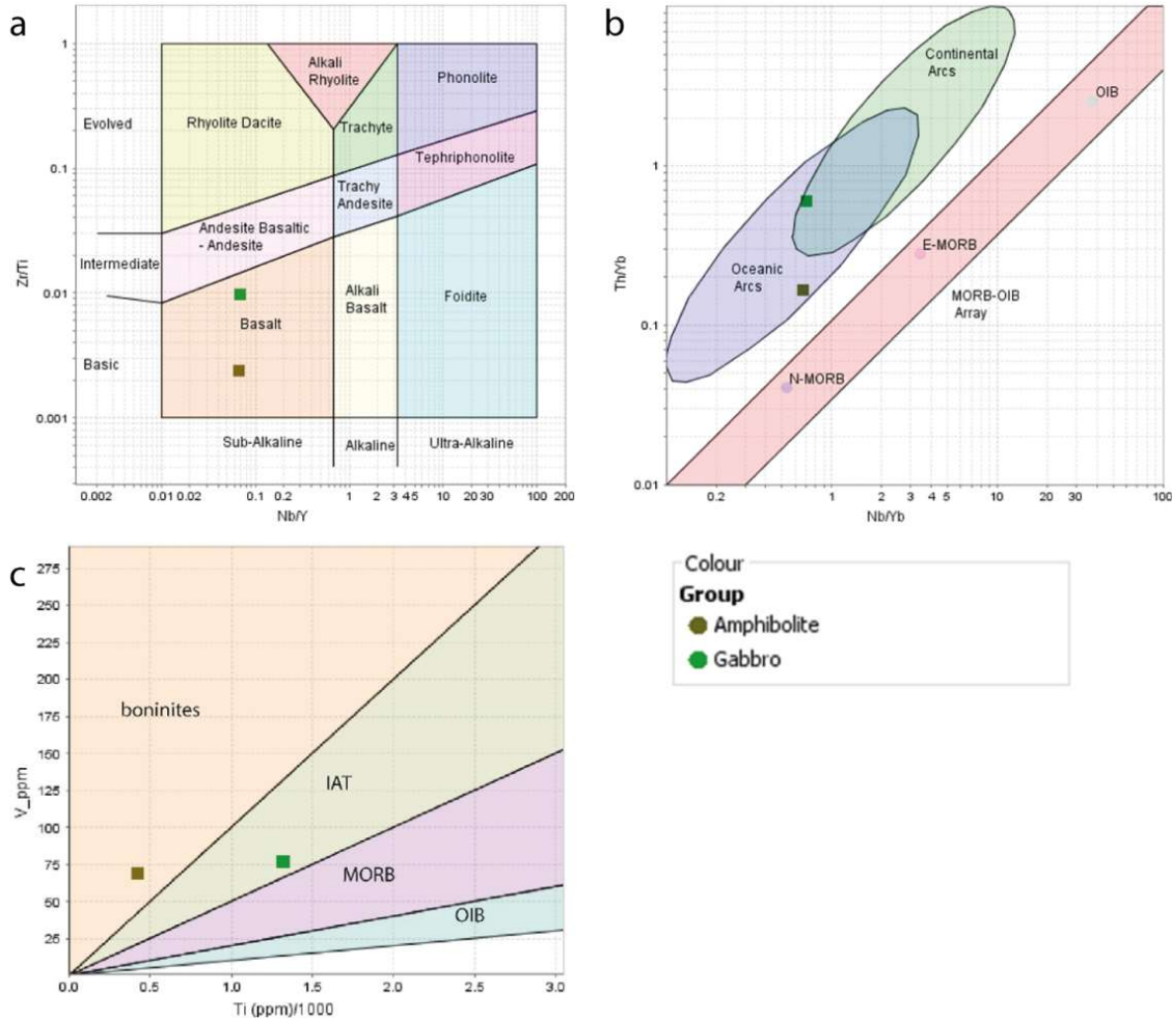

Figure 4-100 - Tectonic discrimination diagrams for non-cumulate rocks associated with the EAC. a) classification of the samples using immobile element based TAS proxy diagram from Pearce (1996) after Floyd and Winchester (1977). b) Th/Nb proxy to distinguish volcanic arc settings from mid-oceanic ridge/ocean island basalt settings Pearce (2014) adapted from Pearce (2008) c) V/Ti subduction-melting proxy is useful to distinguish MORB, island arc tholeiite (IAT) and boninite magma types (Shervais, 1982). D) legend. 'Amphibolite' is a sample from the amphibolite layer in the Northern Limb. 'Gabbro' is altered gabbro to the west of the Main Bulb.

4.1.5.2 Trace Element Chemistry

Although tectonic discrimination diagrams may not be applicable, a great deal of information about geological processes can still be gained from the analysis of trace element geochemistry and the use of normalised spider diagrams. Unfortunately, many samples from the EAC, particularly the Northern Limb, are extremely depleted in several rare earth elements (REE), especially heavy rare earth elements (HREE). Therefore, all samples on, or below, detection

limit have been removed from the database. As a result, certain trace element data are missing from the plots.

One notable feature of the anorthosite rocks from the EAC is a similar feature observed by Ashwal and Bybee (2017) in megacrystic anorthosite complexes from around the world. That is the depletion of Nb relative to Th and HREE (Figure 4-102a), which is a characteristic feature of subduction-related arc magmas (Hawkesworth et al., 1993). This characteristic was used by Ashwal and Bybee (2017) as one of a number of lines of evidence to suggesting a sub-volcanic oceanic arc setting for megacrystic anorthosites.

The other notable feature with the samples of anorthosite is the presence of strong positive Eu anomalies (Eu/Eu*, calculated as per Taylor and McLennan, 1985) in many of the samples (Figure 4-102b). The samples of white anorthosite from the Main Bulb have strong Eu anomalies (6.6-10), whereas samples of fresh leucogabbro from the Main Bulb have very small positive to weakly negative Eu anomalies (0.92 in a sample from the interleaved contact, 1.2-1.5 in fresh samples). Within the Northern Limb, samples of the megacrystic anorthosite to the southwest of the chromitite layer have relatively strong Eu anomalies (2-2.5), similar to those to the northeast (1.8-3.5). Leucogabbro samples from the Southern Bulb have relatively small Eu anomalies (0.8-2). Positive Eu anomalies are a common feature in anorthositic rocks caused by the fractionation of Eu from the parent magma into crystallising plagioclase. As the anorthositic rocks are much more plagioclase rich than their parent magmas, the rocks generally contain a strong positive Eu anomaly.

The degree of REE fractionation for each sample was calculated using the formula (La/0.367)/(Yb/0.248) (Figure 4.106; Taylor and McLennan, 1985) (note that this could not be calculated for a number of samples due to La and/or Yb concentrations at or below detection limit). The most fractionated samples were of the white anorthosite from the Main Bulb (90-125); in contrast, samples of fresh leucogabbro from the Main Bulb have undergone a much

smaller degree of fractionation (5.2-12.5). Within the Northern Limb, the megacrystic anorthosite samples to the southwest of the chromitite layer are more fractionated (7.2-21.5) than those to the northeast (2.3-3.4). Leucogabbro samples from the Southern Bulb have undergone a relatively small degree of fractionation (3-5.9).



Figure 4-101 - Legend for plots of EAC anorthosite/leucogabbro from Figure 4-102 to Figure 4-104. The colour indicate where the sample came from, with the size of the points indicating the degree of REE fractionation calculated using the formula from Taylor and McLennan (1985).

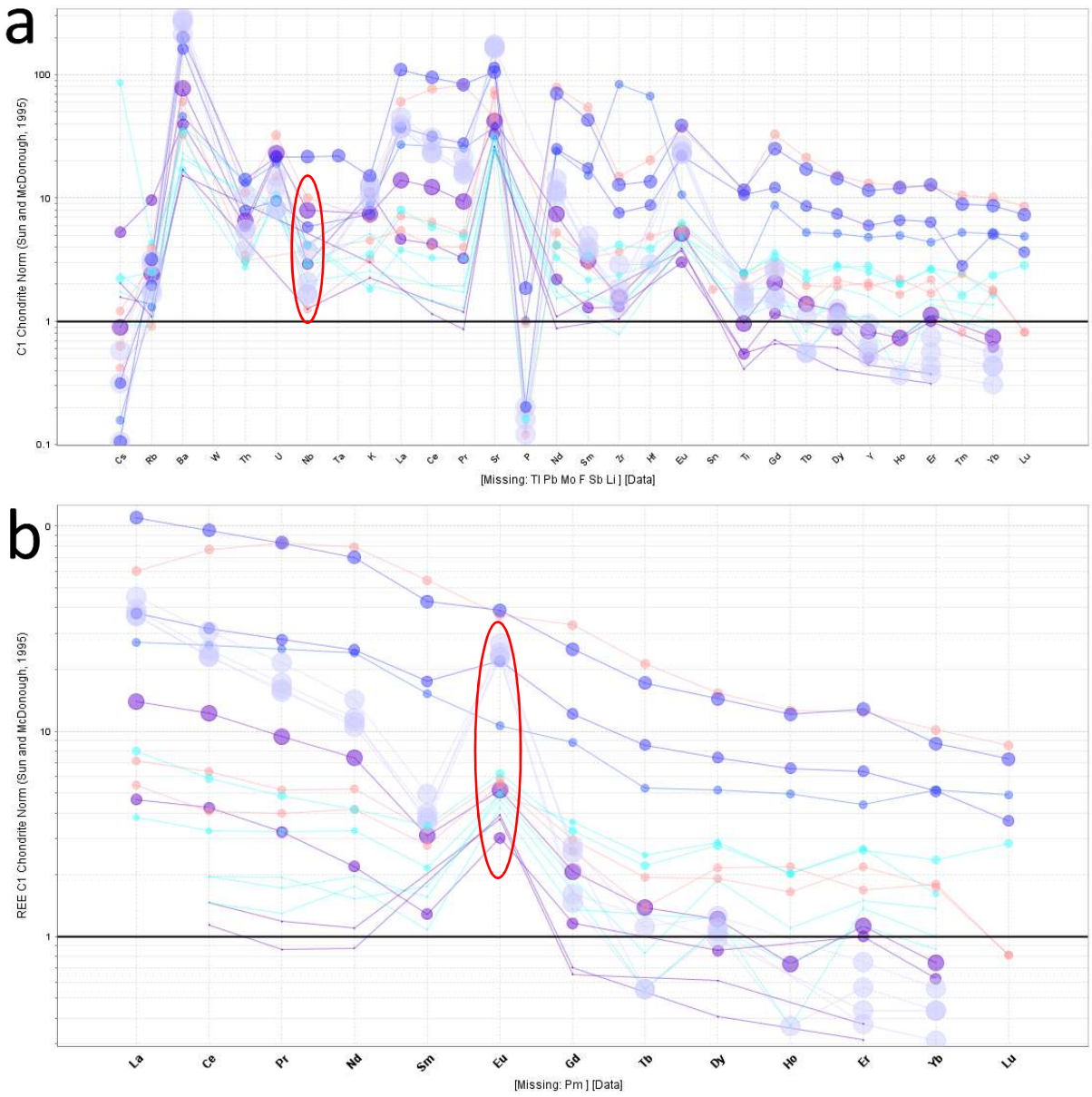

Figure 4-102 – Chondrite normalised (McDonough and Sun, 1995) spider plots of anorthosite and leucogabbro samples from the EAC. a) spider plot of all available trace element data with Nb depletion highlighted in red. b) REE plot with Europium anomaly highlighted.

4.1.5.3 Th/Yb-Nb/Yb Comparison to Archaean Anorthosite

Although tectonic interpretations cannot be confidently made from the Pearce (2014) Th-Nb proxy, it can be used as comparison between samples within the EAC and Archaean (megacrystic) anorthosite complexes from around the world. The less REE fractionated samples of leucogabbro and anorthosite (from the Southern Bulb, Main Bulb and to the northeast of the chromitite in the Northern Limb) all plot within the field for Archaean anorthosites (Figure 4.108; Santosh and Li, 2018; and references therein). However, the more

fractionated samples (white anorthosite from the Main Bulb and samples from the Northern Limb to the southwest of the chromitite layer) have higher Th/Yb and Nb/Yb ratios and lie closer to the OIB and continental arc regions of the diagram as defined by Pearce (2014).

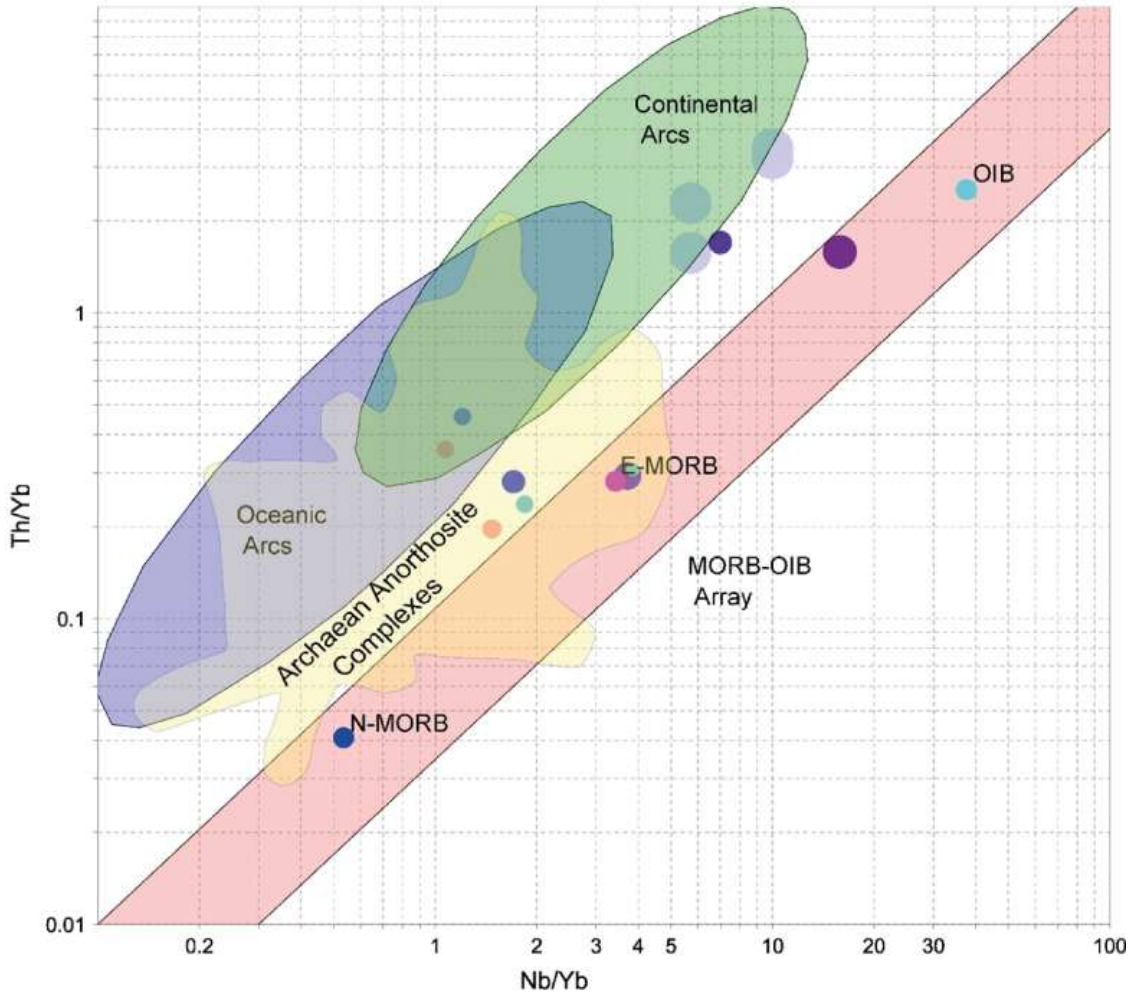

Figure 4-103 – Anorthosite/leucogabbro samples plotted on the modified Th/Nb proxy with oceanic arc and continental arc fields defined by Pearce (2014) (adapted from Pearce (2008)) with the field of Archaean Anorthosite Complex field added from Santosh and Li (2018; and references therein). The size of the points reflects the degree of REE fraction as calculated using the formula defined in Taylor and McLennan (1985).

4.1.5.4 Major Element Geochemistry

The major element whole rock compositions of the megacrystic anorthosite from the Northern Limb form the most silica-poor cluster on a series of Harker variation diagrams (with little difference from either side of the chromitite seam), with anorthosite from the Southern Bulb, Main Bulb (fresh leucogabbro) and xenoliths within the Main Bulb forming clusters with

increasing silica (Figure 4-104). A general trend of increasing silica exists between the clusters with increasing Fe, Mg, Na and K, and decreasing Al and Ca (in three of the diagrams the white anorthosite does not lie on the trend, containing lower percentages of Fe and Mg, and elevated levels of Al). The trends in Na, K, Al and Ca likely represent variable feldspar compositions, with the Fe and Mg reflecting modal portions of mafic minerals in the samples (Chapter 4.1.3.2).

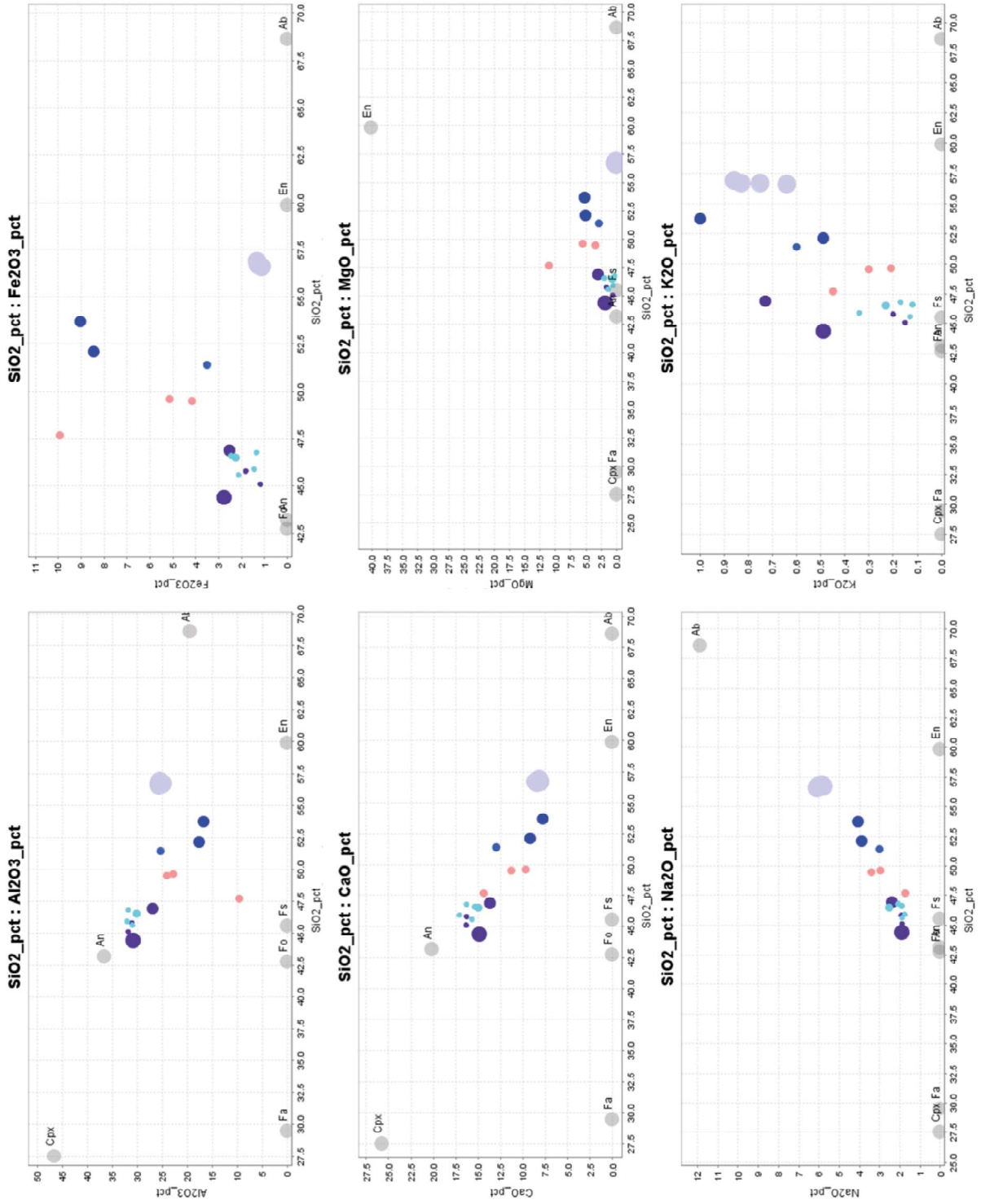

Figure 4-104 - Harker variation diagrams for anorthosite/leucogabbro from the EAC. Mineral compositions are shown for clinopyroxene (Cpx), enstatite (En), anorthite (An), albite (Ab) and olivine (Ol). Diagrams are SiO_2 vs Al_2O_3; SiO_2 vs Fe_2O_3; SiO_2 vs CaO; SiO_2 vs MgO; SiO_2 vs Na_2O; and SiO_2 vs K_2O

4.1.6 Discussion and Tectonic Setting

Based on field observations, as well as whole rock and mineral chemistry, it seems likely that the megacrystic anorthosite of the Northern Limb was the first component to form, followed by the massif-type intrusions. The Northern Limb is concordant with the regional fabric (NW-SE trending and sub-vertical) indicating that it was pre- to syntectonic. The massif-type anorthosite is observed directly cross-cutting the regional gneissic fabric (Figure 4-53). The bowl-shaped Main Bulb itself appears to be relatively undeformed, indicating that it was emplaced at a relatively late stage in the orogenic event, with strain partitioned around it. The better preservation of primary igneous textures and minerals in the Main Bulb also suggests late emplacement. Additionally, mineral and whole rock chemistry suggests that the Northern Limb formed from a much more primitive magma than the massif-type anorthosite.

4.1.6.1 Megacrystic Anorthosite (Northern Limb)

The current orientation of the northern-limb is sub-vertical, although the gravity-settled chromitite layer would have originally been deposited as a sub-horizonal layer. The original way-up of the body is not constrained by current field observations. In this section, all available lines of evidence are examined, resulting in a model of formation for the Northern Limb.

The Northern Limb displays typical features of megacrystic anorthosites including outcrop dimensions (small elongate bodies), textures (both microscopic and macroscopic), and mineral chemistry (calcic anorthite megacrysts and Al-, Fe-rich chromitite; Chapter 4.1.4). Based on field relations and the isotopic and geochemical data the megacrystic anorthosite complexes crystallised from are Fe-rich, aluminous, calcic and hydrous tholeiitic basaltic magmas (Ashwal and Bybee, 2017, Rollinson et al., 2010). A lack of evidence for silicic crustal contamination in these tholeiitic melts leads Ashwal and Bybee (2017) to interpret the tectonic setting of these complexes to be mantle-derived melts related to subduction in oceanic arcs,

with the crystallisation of anorthosite at a sub-volcanic level (Ashwal and Bybee, 2017; and references therein). An arc setting is consistent with the petrology and geochemistry of the Northern Limb, since a magma of similar composition would have been required to produce the calcic plagioclase megacrysts and the Nb depletion in the anorthositic rocks (Figure 106a). The oceanic arc signature indicated by the trace element chemistry of the amphibolite layer is constant with this proposed setting (Figure 4-100).

Rollinson et al. (2010), and Ashwal and Bybee (2017) highlight the importance of the presence of H_2O in the magma to promote the crystallisation of the highly calcic plagioclase in megacrystic anorthosite. The Sisson and Grove (1993) experiments that demonstrate the effect of H_2O in increasing Ca content show that it also suppresses plagioclase production. This may also be a factor in controlling plagioclase grain form in the megacrystic anorthosite in the EAC, and other megacrystic complexes. The equant nature of the plagioclase megacrysts indicates a slow (possibly suppressed) crystallisation rate (Holness, 2014) potentially caused, or enhanced, by the presence of water.

Concentrations of chromite are not common in anorthosite complexes (Ashwal, 1993) with just a few known examples including Fiskenæsset (Rollinson et al., 2010), Sittampundi (Dharma Rao et al., 2013, Talukdar et al., 2017), and Messina (Hor et al., 1975). These are all examples of chromite accumulation in megacrystic Archaean-type anorthosites formed at 2973±28 Ma, 2935±60 Ma and 3344±3.6 Ma respectively (Ashwal, 2010; and references therein). The highly calcic plagioclase, ($An_{86.5\pm11.5}$, $An_{90\pm10}$, and $An_{77.5\pm7.5}$ respectively (Ashwal, 2010; and references therein)) and Fe, Al-rich chromite are diagnostic of these complexes (Dharma Rao et al., 2013) and are attributed to their hydrous and aluminous parental melt compositions (Ashwal and Bybee, 2017, Dharma Rao et al., 2013, Rollinson et al., 2010). The PGE mineralisation at Sittampundi is also largely confined to the chromitite seam, with the rest concentrated in adjacent sulphide-bearing anorthosite (Dhanendran et al., 2014)

Although Palaeoproterozoic in age, the chromitite from EAC is also hosted in the highly calcic ($An_{\sim 84\pm 6}$) Northern Limb. The similarity in the composition of the chromitite at Elmalhat to Archaean anorthosite chromitites including Fiskenæsset and Sittampundi (Figure 4-97, Figure 4-98) indicates they were produced from the melting of a very similar aluminous mantle source and that similar petrogenetic processes were in action.

Based on a study on the Fiskenæsset anorthosite complex, Rollinson et al. (2010) proposed a petrogenetic model for the formation of calcic anorthosites and associated chromitites at an arc setting (Figure 4-105). The migration of hydrous fluids from dehydrating subducting oceanic crust causes partial melting of unusually aluminous mantle harzburgite in the mantle wedge resulting in the production of hydrous, aluminous basalt. The hydrous, aluminous basalt is fractionated in magma chambers in the lower crust to producing a variety of high-alumina basalt compositions. The anorthosite complex then forms as a cumulate within the continental crust. The crystallisation of chromite was triggered by the removal of Al from the basaltic melt through plagioclase crystallization with increasing Cr saturation (Moses et al., 1999, Ghosh and Konar, 2011). This explains the increase in Cr# of the chromitite, with the corresponding decrease in Mg# explained by the preferential removal of Mg during amphibole crystallisation (Figure 4.102; Rollinson et al., 2010). This provides an explanation for the distinct chromite chemistry in megacrystic anorthosites compared to stratiform and podiform deposits.

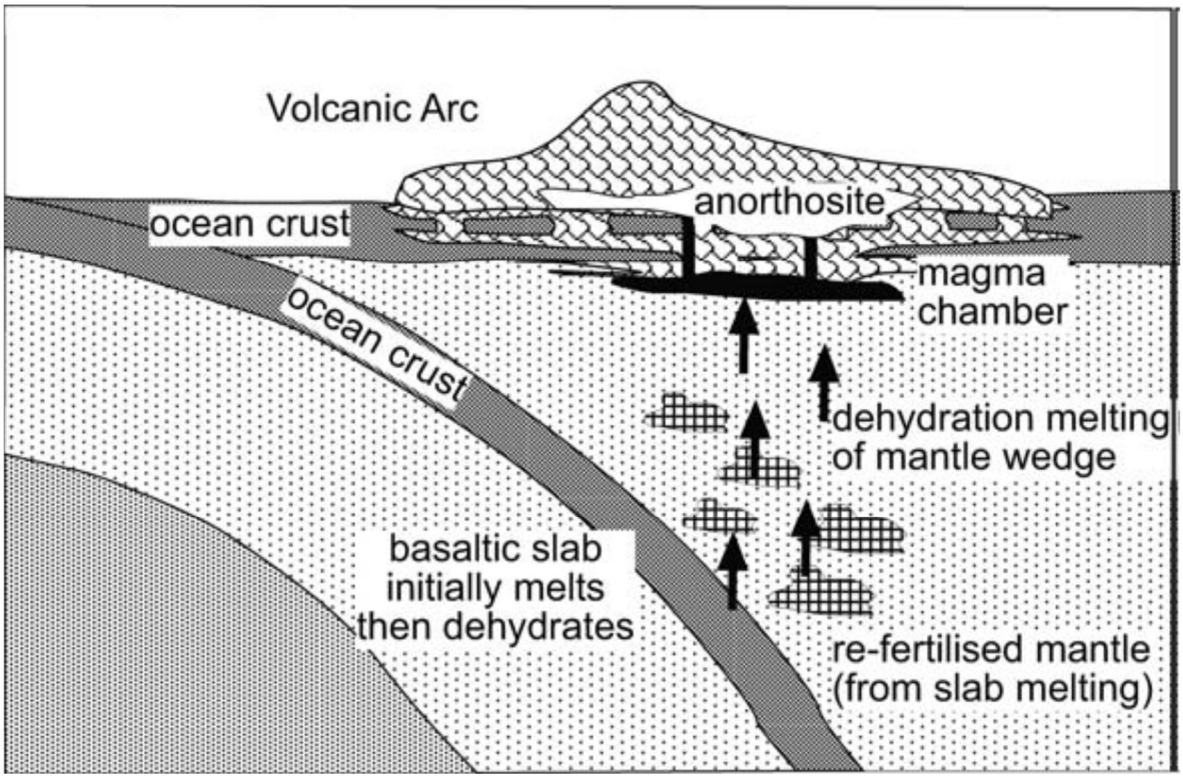

Figure 4-105 - Schematic illustration showing the principal processes involved in the formation of Archaean anorthosites (from Rollinson et al., 2010).

Ternary phase diagrams produced by Irvine (1977) for layered mafic intrusions demonstrate that under equilibrium conditions only very small amounts of chromitite are instantaneously crystallised. In order to form a near-monomineralic chromitite layer there needs to be a disruption to the system, such as magma mixing or siliceous crustal contamination, to force a period in which just chromite is crystallised (Irvine, 1977). In the Northern Limb there is a distinct change in whole rock trace element chemistry either side of the chromitite seam, although the whole rock major element chemistry is very similar (Chapter 4.1.5). To the southwest of the chromitite seam, the samples are much more (REE) fractionated (Figure 4-102) and plot with much higher Th/Yb and Nb/Yb ratios (Figure 4-103) than those from the northeast. According to the Irvine (1977) model, this difference could potentially represent crustal contamination or magma mixing, promoting chromitite crystallisation. These options are explored more here.

- Crustal contamination. This would involve a system where the base is to the northeast and it is crystallising towards the southwest. The earlier crystallising magma (in the northeast) had not undergone a significant degree of fractionation, though following the chromite crystallisation event due to crustal contamination, the resultant magma picks up a more continental signature (Th/Yb and Nb/Yb ratios, and increased REE fractionation) reflected in the samples to the southwest of the chromitite seam. However, following such a contamination, it might be expected that there would be a significant shift in major element chemistry too, and this is not observed (Figure 108)
- Magma mixing. This scenario would begin with an already well fractionated system with the southwest representing the base. An input of fresh, unfractionated magma mixes with the existing well-fractionated magma, promoting chromite crystallisation and giving the resultant magma a less fractionated REE signature and reduces the crustal signature (the Th-Nb proxy) of the magma to the northeast. This works in terms of major element geochemistry as the input of a fresh magma would not necessarily cause a significant shift in the overall composition of the magma. Additionally, this model is consistent with observed mineral chemistry trends observed in the Northern Limb. If the southwest is considered the base, when plotted stratigraphically relative to the chromitite seam distinct trends can be seen (Figure 4-96). The observation of decreasing An content and magnesium numbers of the plagioclase and amphibole with a sudden spike in chromite-bearing anorthosite is consistent with an upwards fractionating system with the influx of hotter, less fractionated magma relating to the chromitite seam. This model would also be consistent with observations in the Fiskenæsset anorthosite with Rollinson et al. (2010) relating the chromitite seam to a late-stage in the crystallisation sequence.

Therefore, an island arc setting is proposed for the Northern Limb, largely based on the presence of megacrystic anorthosite. The magma mixing model is proposed for the formation of the chromitite seam, with the southwest representing the base of the sequence.

4.1.6.2 Main Bulb (Massif-type Anorthosite)

The clinopyroxene mineral chemistry (Figure 4-99), tectonic discrimination diagrams of related non-cumulate rocks (Figure 4-100) and Nb depletion of the anorthosite (Figure 4-102b) are all indicative of a volcanic arc setting. Additionally, clinopyroxene mineral chemistry (Figure 4-99d) indicates that the parent magma had an island arc tholeiitic composition. In arc settings, tholeiitic magmas are more prevalent closer to the trench whereas calc-alkaline magmas generally occur farther from the subducting plate (Kuno, 1966, Murphy, 2007). Tholeiitic magmas are also more dominant during the early stages of oceanic island arc formation, with calc-alkali basalts becoming the principal suite in mature oceanic arcs, and is especially common in continental arcs (Murphy, 2007). Thus, based on mineral and whole rock chemistry, the EAC formed in an immature arc setting, and/or was proximal to the subducting plate. This is consistent with the tectonic setting proposed by Ashwal and Bybee (2017) massif-type anorthosite complexes.

Based on many lines of evidence, Ashwal and Bybee (2017) suggest the most likely setting for massif-type anorthosites to be an Andean-type continental arc setting (Figure 4-106). The aluminous, broadly basaltic parent magmas responsible for the formation of massif-type anorthosites are thought to be mantle-derived with petrological, geochemical and isotopic data suggesting that they are have undergone a variable degree of contamination with continental crust (Ashwal and Bybee, 2017; and references therein). The model of formation for massif-type anorthosites involves ponding of basaltic magmas at the Moho, crystallization and sinking

of mafic silicates, and eventual flotation of buoyant plagioclase diapirs, emplaced at a mid-crustal level (Figure 4.112; Ashwal, 1993, Ashwal and Bybee, 2017).

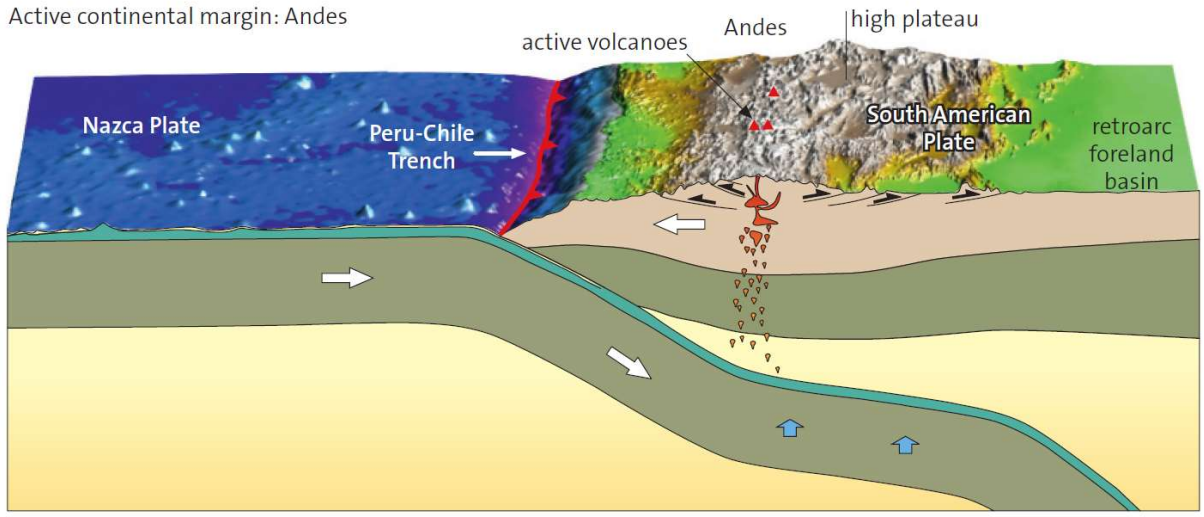

Figure 4-106 – Illustration of as Andean-type continental arc (from Frisch et al., 2011). A modern example of an active continental margins where oceanic lithosphere is subducted beneath continental lithosphere without a marine basin behind the volcanic arc; rather, the arc is built directly on the adjacent continent

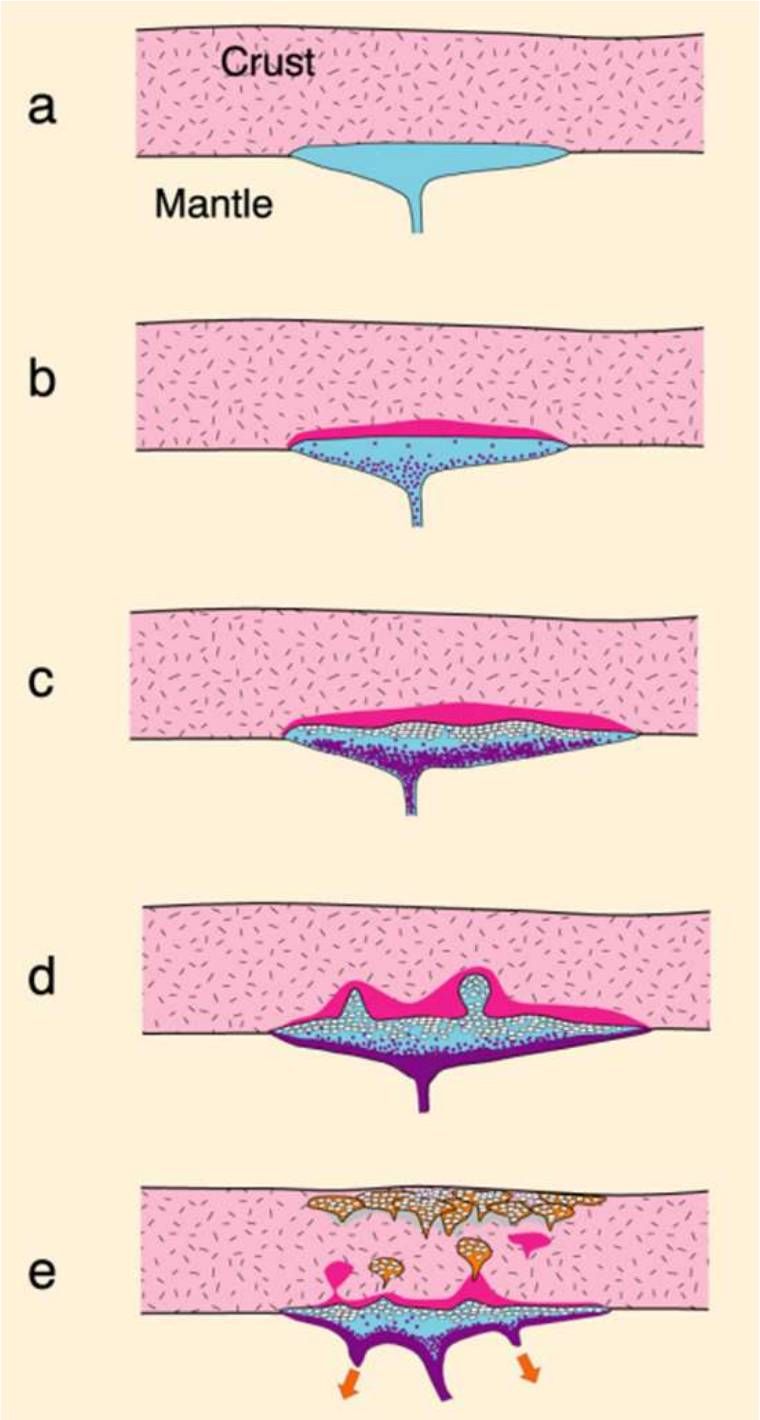

Figure 4-107 – Model for the formation of massif-type anorthosites (from Ashwal, 1993) a) Mantle-derived magma underplates the crust as it becomes density equilibrated. b) Crystallization of mafic phases (which sink), and partial melting of the crust above the ponded magma. The melt becomes enriched in Al and Fe/Mg. c) Plagioclase forms when the melt is sufficiently enriched. Plagioclase rises to the top of the chamber whereas mafic minerals sink. d) Plagioclase accumulations become less dense than the crust above and rise as crystal mush plutons. e) Plagioclase plutons coalesce to form massif anorthosite (orange and white), whereas granitoid crustal melts (pink) rise to shallow levels as well. Mafic cumulates remain at depth or detach and sink into the mantle.

In terms of mineral chemistry, dark anorthosite within the Main Bulb has two clusters of mineral compositions at andesine anorthosite and labradorite anorthosite (Chapter 4.1.4; Figure

4-95), with white anorthosite not having been analysed. This is interpreted as representing two separate pulses of magma forming the complex, with multiple magma pulses being a common feature of massif-type anorthosites (eg. Nain; Xue and Morse, 1993). Compared to other massif-type anorthosite complexes around the world they have higher Mg content in mafic minerals for a given An content in both clusters (Figure 4-95). This indicates a more primitive anorthosite system with a higher Al content in the initial magma resulting in the early crystallisation of plagioclase such that the mafic phases had not removed significant amounts of Mg from the system. This is consistent is consistent with the relatively small degree of fractionation observed in the REE profile for the $An_{\sim 40}$ population (Figure 4-102).

The most abundant dark anorthosite in the field is the $An_{\sim 40}$ group. The dominant mafic phase in these rocks is clinopyroxene with minor orthopyroxene. The high aspect ratios of the plagioclase crystals suggest relatively rapid crystallisation (Holness, 2014), with the lack of variation in An content and Mg# (Figure 4-95) indicating that it was emplaced as a crystal mush (without fractionating as per the Ashwal (1993) model). A trend is observed from ~580 m down with the end of decreasing magnesium content in clinopyroxene and orthopyroxene (i.e. decreasing primitiveness) with depth (olivine only observed in the top sample in that trend). A similar trend is observed in anorthosites in the Main Zone of the Bushveld Complex, which was explained by Hayes et al. (2017) as the downward filtration of a fresh, more primitive noritic magma filtering down through a previously emplaced plagioclase mush. However, it is likely that the Main Bulb formed through multiple pulses of magma, and more data, with a higher sampling rate, is required to see if this is a real trend or just an artefact of sampling. The downward migration of this magma within the chamber could have also contributed to the alignment of tabular plagioclase forming the concentric igneous layering observed in the field. Igneous layering in the Poe Mountain Anorthosite Complex is interpreted by Scoates et al. (2010) as related to the downward migration of dense, residual magma. The

lack of a significant positive Eu anomaly (Figure 4-102b) in the andesine anorthosite suggest that there has been no concentration of plagioclase in the magma since it separated from its source, assuming the source had a level REE profile.

The quartz-olivine-bearing gabbro on the southern (and possibly eastern) contact(/s) of the Main Bulb have been interpreted as being related to the leucodiorite/andesine anorthosite pluton. An important feature of the rock is that it contains two populations of plagioclase at $An_{\sim 23}$, and $An_{\sim 33}$. It also contains clinopyroxene, biotite, magnetite, alkali-feldspar, olivine (enclosed in clinopyroxene), a small amount of interstitial quartz, and trace apatite. This has been interpreted as contamination of a partially crystallised gabbroic magma. The presence of olivine suggests that the original composition of the magma was silica undersaturated. The olivine, clinopyroxene, and $An_{\sim 33}$ would have already crystallised when the magma, along the contact, was locally contaminated with siliceous crustal material. Olivine grains protected by clinopyroxene were preserved, while olivine in contact with the magma would have been changed to other minerals. The continual crystallisation of the magma resulted in a more albitic composition of plagioclase ($An_{\sim 23}$), biotite and with a small amount of interstitial quartz crystallising as the last phase.

The $An_{\sim 60}$ phase has not been mapped out but only makes up a small portion of the Main Bulb. Two samples of ultramafic dykes cross-cutting the andesine anorthosite, plot in this group along with two samples from satellite intrusions. The similarity in mineral chemistry between the ultramafic samples and anorthosite of the $An_{\sim 60}$ group suggest that, although cross-cutting relationships are not observed in the field, the $An_{\sim 60}$ anorthosite is the later phase. With a more primitive composition (higher An contents and Mg# in mafic minerals), the samples in the $An_{\sim 60}$ group are all olivine-bearing, also containing clinopyroxene, with minor orthopyroxene. The lower aspect ratio of the plagioclase indicates a slower cooling rate (Holness, 2014).

The pervasively altered white anorthosite within the Main Bulb is interpreted as having been formed from local metasomatism of the andesine anorthosite (or potentially an earlier phase). In the field the white anorthosite is spatially associated with quartz veins with pervasive silica veinlets observed throughout. Plagioclase compositions from optical determinations are 30-36 %An, consistent with whole-rock chemistry, and more sodic than the dark andesine anorthosite. This would be consistent with metasomatism of the andesine anorthosite resulting in a more sodic plagioclase. These samples display enrichment in light REE and depletion in heavy REE compared to the andesine anorthosite. This, alongside the strong crustal signature displayed on the Th-Nb proxy (Figure 4-103) and in whole rock major element chemistry (Figure 4-104), indicates a significant degree of crustal contamination and/or metasomatic alteration. Similar patterns are observed in the Kunene (particularly in Namibia) where an earlier phase of 'white anorthosite' had been metasomatised by fluids relating to the intrusion of a later phase of 'dark anorthosite' (Ashwal and Twist, 1994, Drüppel et al., 2007). Therefore, the white anorthosite has been interpreted as the metasomatism of the andesine anorthosite (or potentially an earlier phase) by fluids relating to the later emplacement of the labradorite anorthosite (or potentially another source of hydrothermal fluid).

4.1.6.3 Tectonic Setting

The tectonic setting interpreted for the megacrystic and massif-type anorthosite bodies of the EAC is consistent with that of other anorthosite complexes throughout the world. Both magmas are interpreted as aluminium-rich, mantle-derived, broadly basaltic melts relating to arc settings (Ashwal and Bybee, 2017, Rollinson et al., 2010). A lack of evidence for silicic crustal contamination in megacrystic anorthosites led Ashwal and Bybee (2017) to infer that the melts related to an oceanic arc setting, with the anorthosite crystallised at a sub-volcanic level (Ashwal and Bybee, 2017; and references therein). Data from the Northern Limb of the EAC

suggests that this is also the likely setting for the megacrystic anorthosites of the EAC. Variable contamination with continental crust and the necessity to pool and fractionate the plagioclase at the base of a thick Moho, leads to the interpretation that these melts are related to a continental arc setting with anorthosites emplaced at a mid-crustal level (Ashwal and Bybee, 2017; and references therein). This interpretation is also consistent with data from the massif-type anorthosite of the Main Bulb. Therein lies a contradiction; the emplacement of two distinct types of anorthosite, relating to different crustal levels and slightly different tectonic settings. A full petrogenetic model is presented in Chapter 6.1, explaining the formation of the EAC within the broader regional context.

4.2 **Oum Abana Belt**

4.2.1 Introduction

The Oum Abana belt is a northwest-southeast trending belt truncated in the southwest and northeast by the Taghsoumat-Aghsoumal fault and Sfariat shear zone respectively. To the southeast it transitions into the Elmalhat domain and disappears under Ordovician sediments to the northwest. The belt is also overlain by the Agarasras Lakhadar ophiolite sequence in the NW.

Scarce references exist in the literature, though Bronner et al (1990) very briefly described the Oum Abana 'Greenstone Belt' as a mantled gneiss dome structure that was 'probably Archaean in age'. It was recorded as being over 3km thick, containing BIF (~100-200m thick), and with a stratigraphy from east (top) to west (bottom) consisting of leptynites-migmatites, ferruginous quartzite, quartzite, amphibolite and migmatites-migmatitic granite.

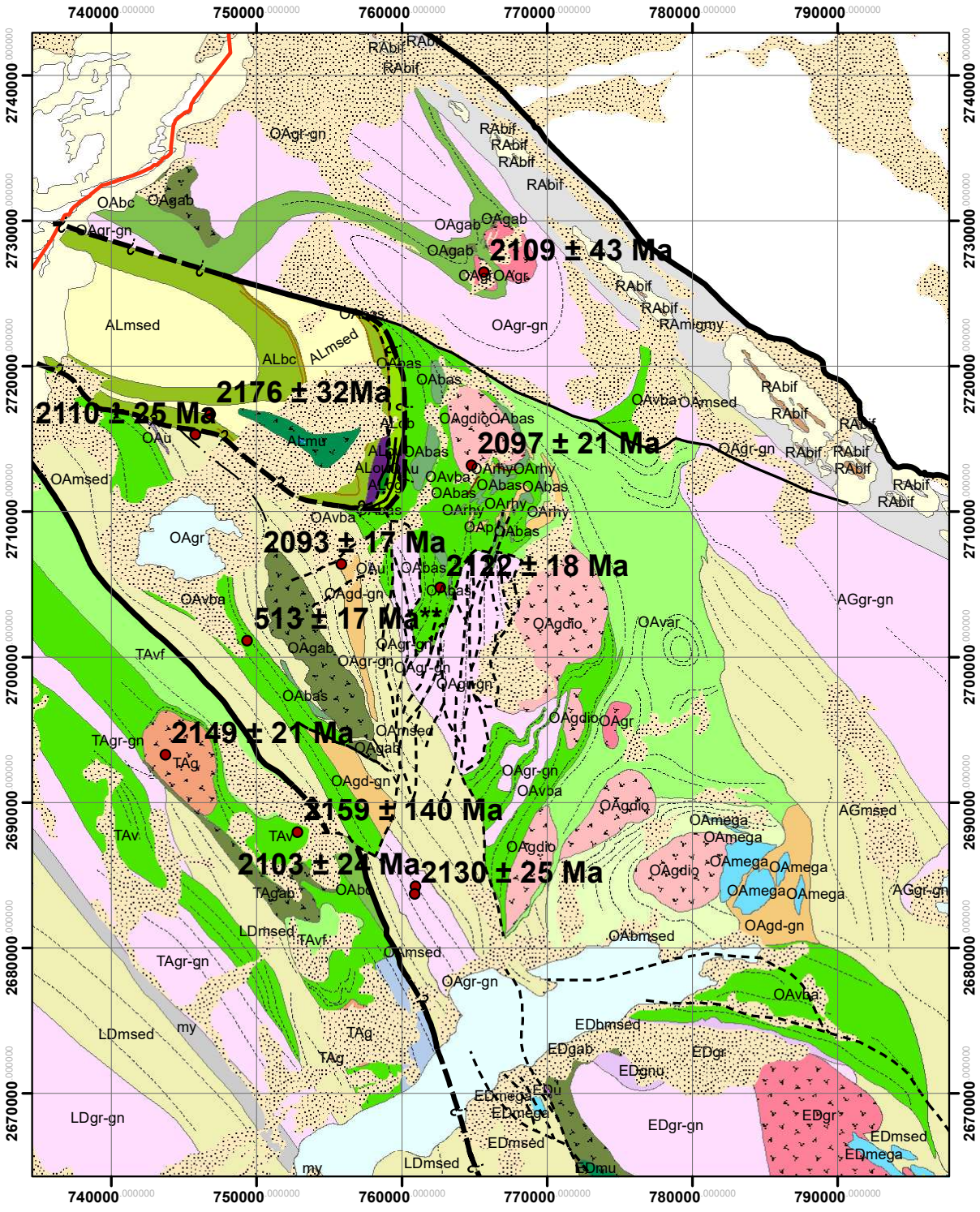

Figure 4-108 a – Detailed geology of the Oum Abana Belt. For location map, see the orange square in Figure 4-1.

Sfariat-Bu Daira Domain



Leaareig Domain

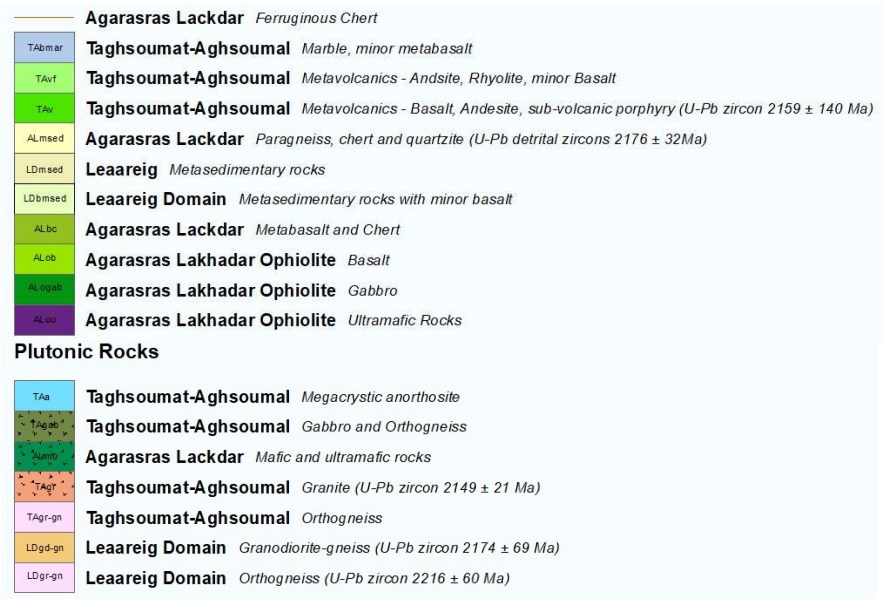

Figure 4-108 b – Legend

Combs (2012) completed an honours project on a 250km^2 section of the region, though with just 10 days of field mapping, and a lack of samples for further work it was somewhat limited. The conclusions from this work was that belt was part of a Palaeoproterozoic terrane (based on geochronology work by Schofield et al. (2006)), consisting of alternating belts of volcano-sedimentary, sedimentary, and granite-gneiss formed as a result of terrane accretion during the Eburnean orogeny. These belts are cross-cut by several late gabbroic and granitoid intrusions. Lyche (2012) presented detailed field and petrological work on one such late granitoid intrusion (Agarasras Labiad), focussing on alteration within the body. Work presented in this chapter is mostly new, as part of this project. Any inclusion of observations or data from these authors is referenced accordingly.

4.2.2 Geology and Structure

4.2.2.1 Granite-gneiss belts

The granite-gneiss belts comprise coarse grained orthogneiss with a well-developed gneissose fabric, cross-cut by foliated granitoid intrusions. The orthogneiss is coarse-grained (1.5-4mm), alternating in composition between granodiorite to tonalite. It is highly variable in composition, from grey granodiorite (quartz ~30%, plagioclase ~50%, alkali-feldspar ~10%, biotite ~5%, chlorite ~5%) to green tonalite (plagioclase ~55%, quartz ~20-40%, hornblende ~5-25%). Epidote and sericite alteration is pervasive throughout the unit, with stronger alteration close to shear zones. More mafic lenses are observed within the unit, concordant with the gneissose fabric, potentially representing remnants of dolerite intrusions (Figure 4-109). Samples of gneiss have been dated at 2130 ± 25 Ma and 2103 ± 24 Ma (Chapter 2).



Figure 4-109 - Field photograph of mafic lens in granite-gneiss in the Oum Abana Belt. Field of view ~1m. (UTM 28 760909 mE, 2683666 mN).

4.2.2.2 Volcanic Belt

The northwest-southeast trending volcanic belt is the dominant unit within the Oum Abana Belt. It comprises basalt, andesite, and rhyolite with minor layers of metasedimentary material, including cherts and rare beds of marble. Small lenses of marble are also observed but do not constitute a major lithology of the belt. A strong lithological trend is observed across the belt with predominantly basalt and andesite in the west, grading into more felsic lithologies toward the east. The eastern margin of the belt is dominantly andesite and rhyolite. All of the units within the volcanic belt have undergone a degree of metamorphism, though for simplicity 'meta' will not be used as a prefix for these lithologies.

Basalt is the dominant lithology in the west of the belt (Figure 4-110a, b). Black and aphanitic, it locally exhibits a moderate to strong northwest-southeast, sub-vertical foliation (Figure 4-110a). Locally, the basalt displays vesicular and amygdaloidal textures (with ~3-5mm round quartz amygdales; Figure 4-110b).

Andesite is present throughout the belt, though is more dominant in the east. It is blue, mesocratic and largely banded, locally containing plagioclase phenocrysts (Figure 4-110c, d).

Rhyolite is absent in the west of the belt with the proportion of rhyolite increasing from the middle towards the east. The rhyolite is white to green, leucocratic, banded, and very plagioclase- (locally altered to epidote) and quartz-rich (Figure 4-110e).

Chert makes up a minor component of the sequence, forming ~0.5-1m layers uniformly distributed across the belt. The chert ranges in appearance from grey chert to black ferruginous chert (Figure 4-110f). Locally the chert is carbonate altered.

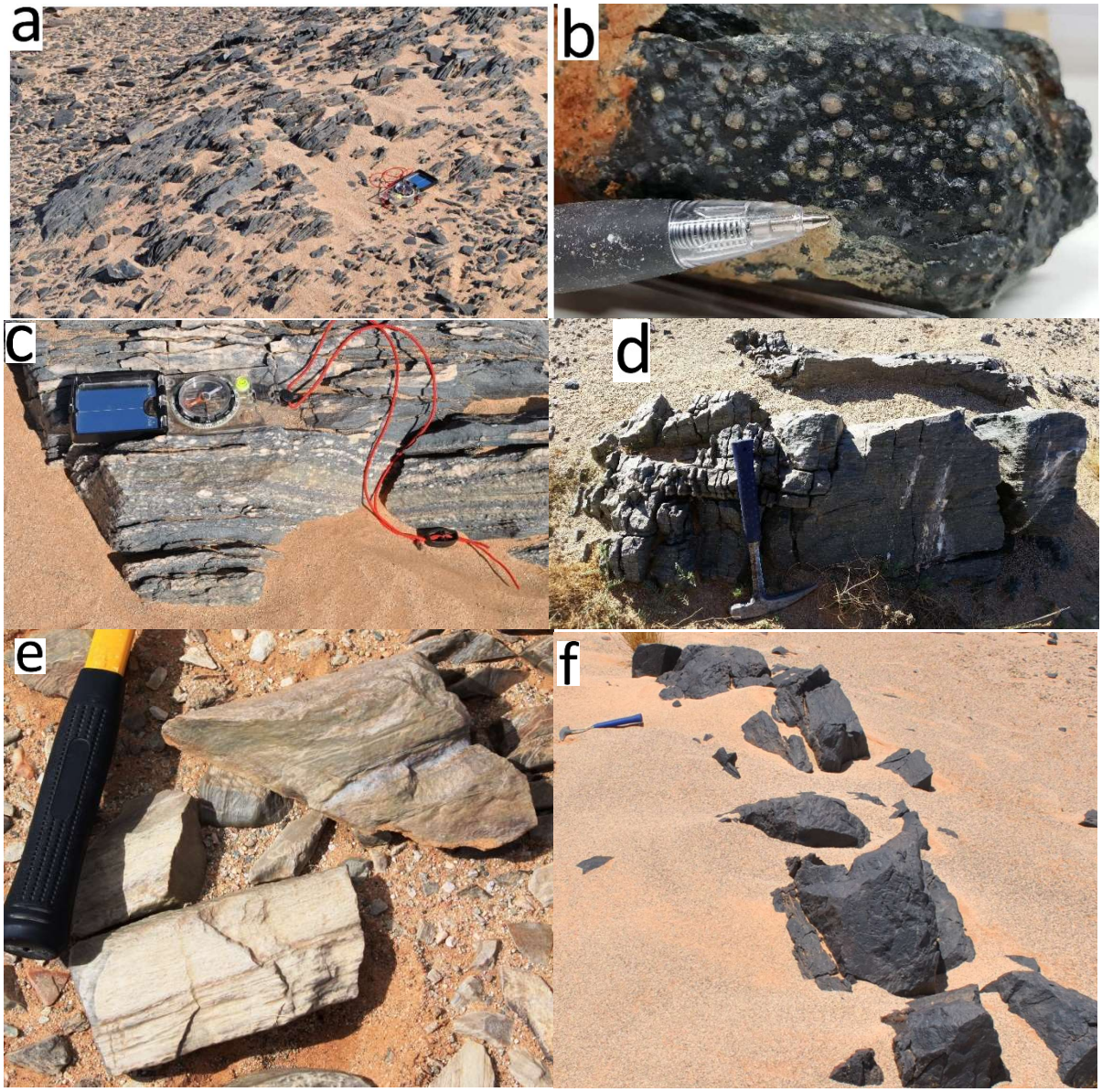

Figure 4-110 – Field photographs of lithologies from the volcanic belts of the Oum Abana Belt. a) Foliated basalt (UTM 28 768075 mE, 2689167 mN). b) Amygdaloidal basalt, with quartz amygdales (UTM 28 762050mE, 2715182mN). c) Banded andesite with plagioclase phenocrysts (UTM 28 769230 mE, 2693794 mN). d) Andesite (UTM 28 776905 mE, 2711278 mN). e) Rhyolite (UTM 28 761330 mE, 2714919 mN). f) Ferruginous chert (UTM 28 768756 mE, 2712636 mN).

Orogenic gold mineralisation is present within the volcanic belt, commonly associated with contacts with late granitoid intrusions. Gold mineralisation within the belt has been observed in quartz tourmaline/sulphide-bearing quartz veins, pyrite-bearing ferruginous chert and altered granite (Section 5.1.1.1).

4.2.2.3 Sedimentary Belts

The sedimentary belt comprises metamorphosed siliciclastic sedimentary rocks including greywacke, sandstone, and minor pelites and conglomerate, as well as very minor basalt and chemical sediments including marble and chert. Shearing through the main sedimentary belt is variable, with strain focused along a major shear zone in the centre of the belt (Figure 4-108). As with the volcanic belt, 'meta' will not be used as a prefix for these lithologies even though they have been metamorphosed.

Biotite-(±hornblende-), muscovite- and/or chlorite- schists/gneiss are common within the sedimentary belt, interlayered with quartzite (Figure 4-111). The schistose layers are light to dark grey/brown in colour, medium-grained (~0.5-2mm), and locally porphyroblastic. They contain quartz (~30-60%), biotite (~20-60%), muscovite (10-20%) and hornblende (~0-30%). The quartzite is foliated and locally lineated, ranges in colour from grey to pink or green (where hematite or epidote staining/alteration has taken place). It is coarse-grained (~2-3mm), and comprises quartz (~95-100%), muscovite (~0-5%) and garnet (~0-5%). This is interpreted as having been an interlayered sequence of arenite and greywacke (± shale). Detrital zircons from a sample of biotite gneiss (J205) were dated at 2110 ± 25 Ma.

Chemical sediments within the belt include dirty marble beds, typically cream to brown in colour, and grey to brown chert with minor iron staining.



Figure 4-111 – Field photograph of interbedded metamorphosed quartzite and hornblende schist, representing the metamorphism of interbedded sandstone and shale (UTM 28 760634 mE, 2713324mN).

Locally within the sedimentary belt, a sedimentary package of sandstone and conglomerate has primary sedimentary bedding preserved (Figure 4-112). At the eastern edge of the gabbro intrusion (Figure 4-108), the steeply dipping package comprises polymict conglomerate and planar bedded sandstone. The matrix-supported conglomerate consists of rounded clasts of marble, quartzite and granite with a sandstone matrix. These sedimentary rocks have experienced a high degree of epidote metasomatism in places from fluids released from a mafic intrusion.

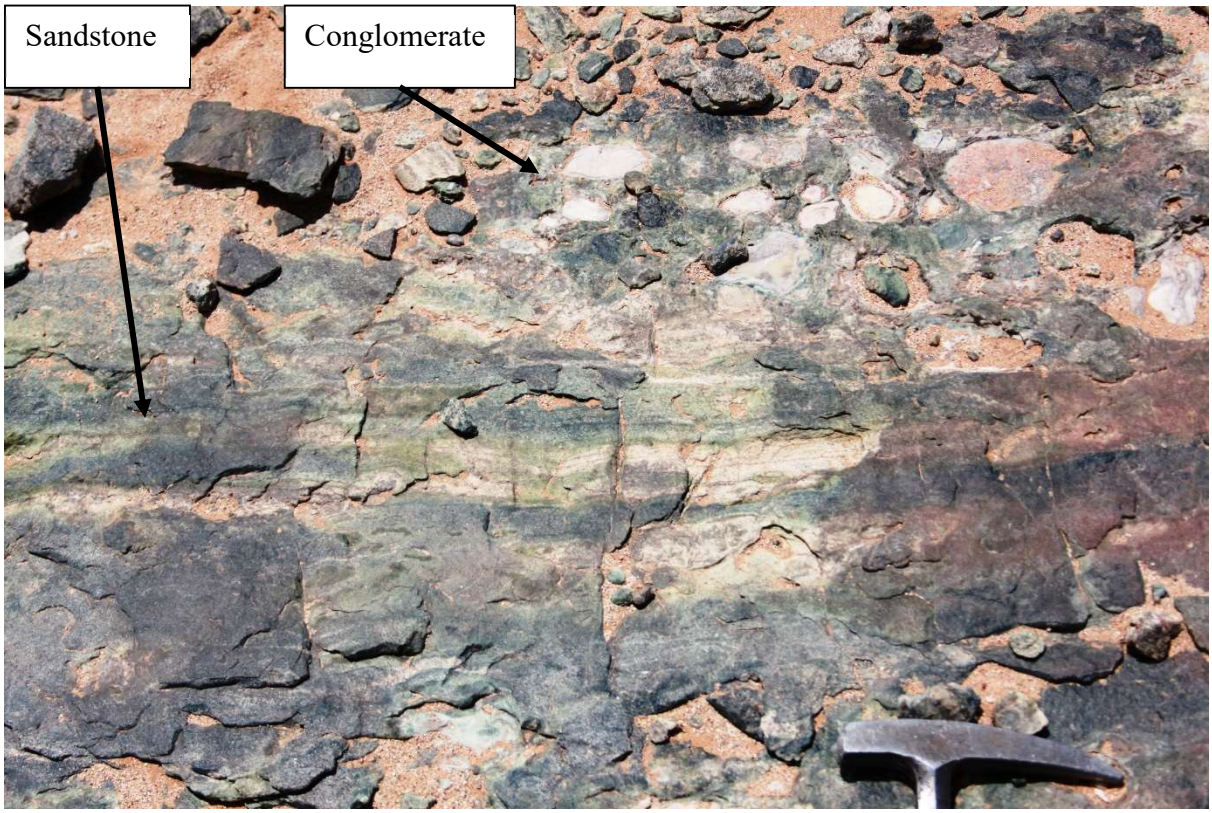

Figure 4-112 - Field photograph of a metasomatised sedimentary package, consisting of conglomerate and planar bedded sandstone (UTM 28 753579 mE, 2704096 mN).

4.2.2.4 Late intrusions

4.2.2.4.1 Granitoids

The Oum Abana Belt is cut by multiple late granitoid intrusions of broadly granodiorite to tonalite composition. (Figure 4-113). Generally, they are cream-grey to green medium to coarse grained (~1-4mm), and are equigranular. Some intrusions are weakly to moderately foliated, but not gneissic. Within the volcanic belt, the contact of granitoid intrusions with the country rock sometimes hosts gold mineralisation (Chapter 5.1.1). The following sections describe some of the more well studied intrusions in the belt. U-Pb dating of magmatic zircons from granitoid intrusions across the belt reveals crystallisation ages of 2109 ± 43 Ma 2097 ± 21 Ma, 2093 ± 17 Ma (J253, J197, and J273; Chapter 2).



Figure 4-113 – Field photograph of Adam Anajim granodiorite intrusion (UTM 28 770099 mE, 2700646 mN).

4.2.2.4.1.1 Agarasras Labiad

Distinct from other flat-lying granitoid intrusions in the belt (eg. Figure 4-113), the Agarasras Labiad intrusion forms a series of prominent hills (Figure 4-114). Lyche (2012) described the Agarasras Labiad intrusion as a strongly foliated, altered granodiorite-tonalitic intrusion comprising quartz, plagioclase, alkali feldspar, chlorite, amphibole, epidote and magnetite. Proximal to shear zones the fabric is mylonised (Lyche, 2012). The intrusion has undergone multiple generations of pervasive epidote, sericite, chlorite and carbonate alteration, attributed to hydrothermal fluids (Lyche, 2012). U-Pb zircon geochronology gives the age of the intrusion as 2097 ± 21 Ma (J197; Chapter 2). Tourmaline-bearing quartz-carbonate veins within, and on the edge of, the intrusion host gold mineralisation, though mineralisation has not been observed in the granite itself (Chapter 5).



Figure 4-114 – Field photograph of strongly foliated Agarastas Labiad Intrusion, outcropping as a series of hills parallel to the foliation (UTM 28 765803 mE, 2716771 mN).

4.2.2.4.1.2 Agarasras G52

Located ~2-3km to the south of the Agarasras Labiad intrusion, the G52 granitoid intrusion is flat lying and very altered. Consisting largely of plagioclase (~50%), quartz (~20-25%), alkali-feldspar (10-20%), amphibole (0-5%) and muscovite (~0-2%), the granitoid has a granodioritic composition, though has locally been severely altered to sericite, chlorite, epidote, ± fuchsite, and ±carbonate. The southern edge of the intrusion is more intensely altered and contains disseminated pyrite and locally gold mineralisation (Chapter 5). The intrusion is cross-cut by leucogranite dykes (~1m wide) trending 043/89º W.

4.2.2.4.2 Red Porphyry

Several red porphyry dykes are present within the eastern portion of the volcanic belt (Figure 4-115). The dykes are ~1-5m wide and occur exclusively within the volcanic belt, potentially representing sub-volcanic porphyries associated with the volcanic rocks.

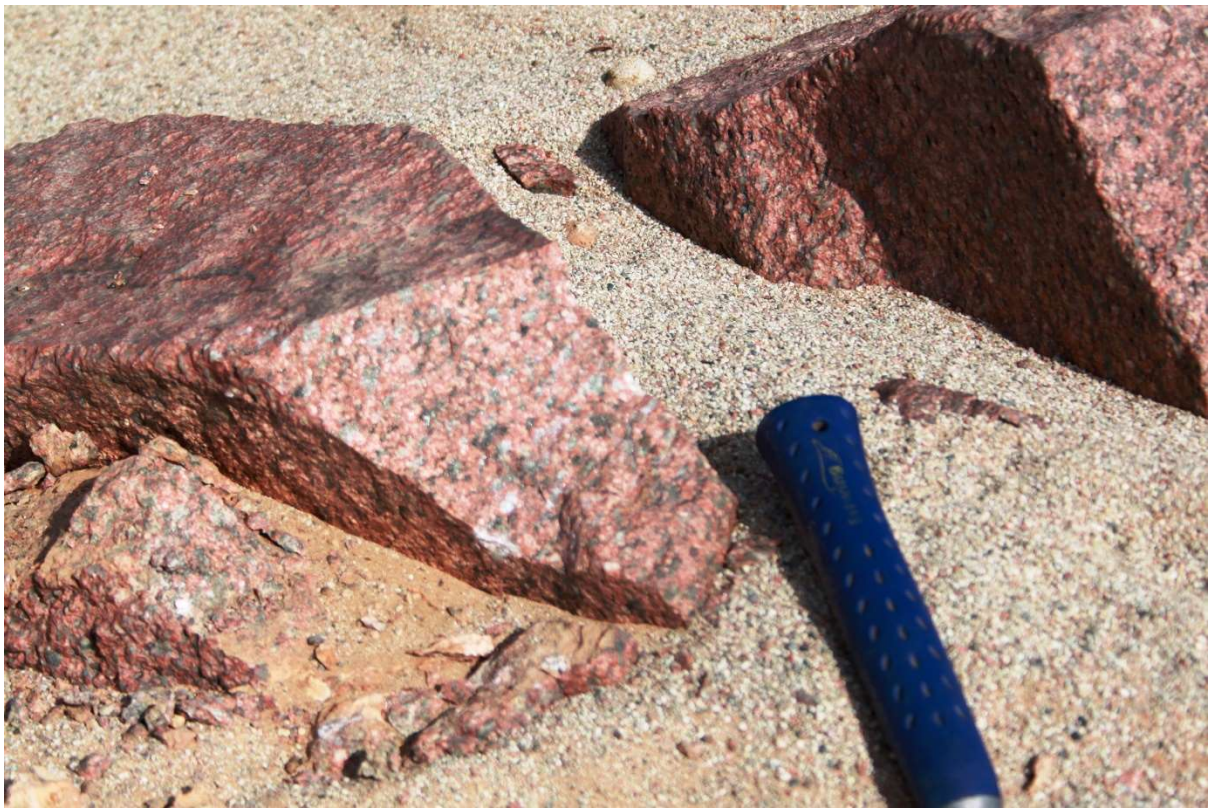

Figure 4-115 – Field photograph of a small outcrop of the red porphyry unit (UTM 28 801742 mE, 2673612 mN).

4.2.2.4.3 Gabbro-Diorite Intrusion

An intrusion ranging in composition from diorite to gabbro is emplaced in the main metasedimentary belt along the La Hida shear zone (Figure 4-108). The intrusion is dark green, coarse grained (~2-4mm) and has been chlorite and epidote altered. It consists of plagioclase (~45%), amphibole (~30-55%), chlorite (~5-15%), epidote (~0-10%), and quartz (0-5%). Lehbib (2016) dated some diorite from the intrusion at 2065 ± 13 Ma using U-Pb zircon geochronology using ICP-MS facilities.

In the north of the belt, relatively undeformed and unaltered intrusions of gabbro are present, hosted in basalt and chert.

4.2.2.4.4 Ultramafic

Small intrusions (~20m wide) of poikilitic ultramafic intrusions are observed in the north of the sedimentary belt (Figure 4-116), as well as proximal to the gabbro-diorite intrusion (Section 4.2.2.4.3). The intrusions are locally altered and foliated and are composed of 100% amphibole, and likely represent metamorphosed pyroxenite.

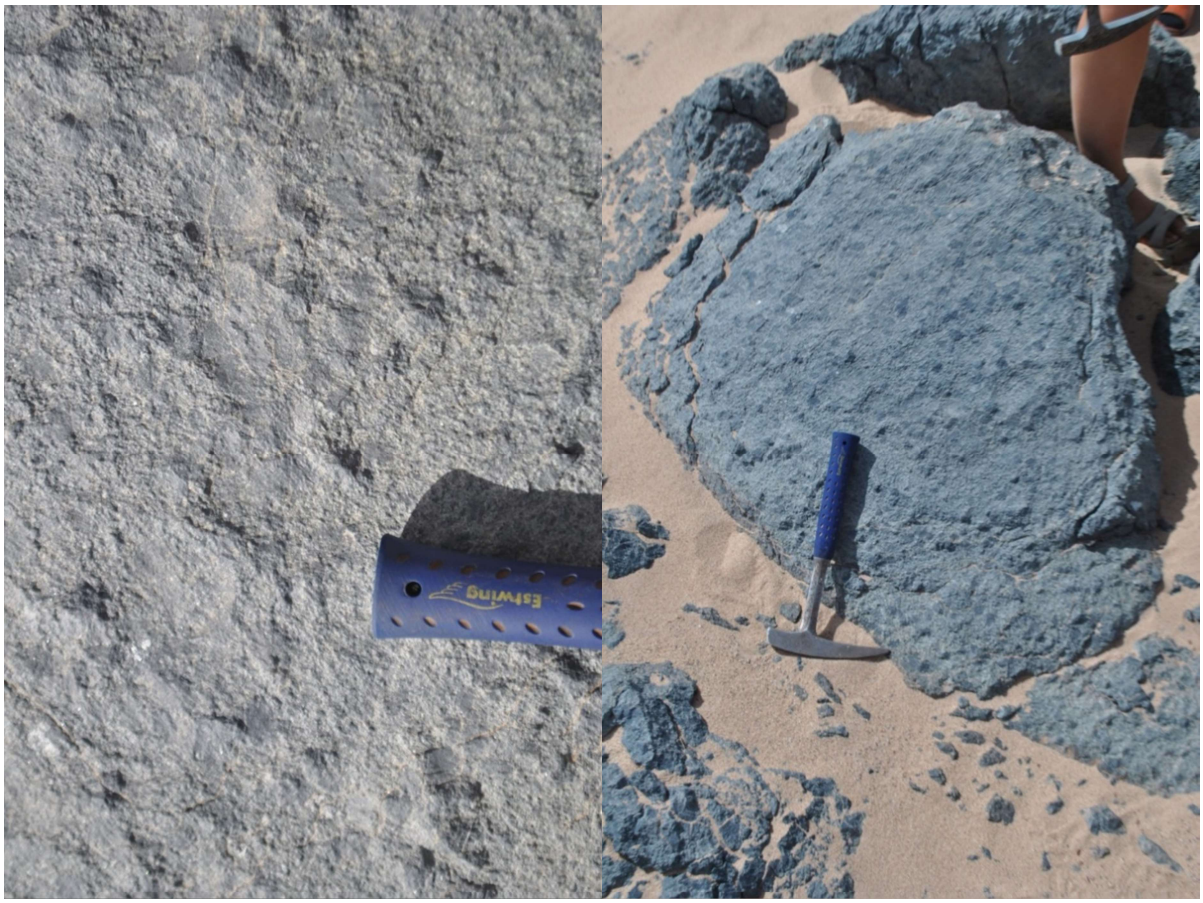

Figure 4-116 – Field photographs of poikilitic metapyroxenite with pyroxene oikocryst, observed intruding metasediments in the north of the Oum Abana Belt (UTM 28 744379 mE, 2714336 mN).

4.2.2.4.5 Anorthosite

Some small units of megacrystic anorthosite are observed hosted in granodiorite-tonalite gneiss in the south of the Oum Abana belt. These are described as part of the Elmalhat Anorthosite Complex (Section 4.1.2.2.2.2).

4.2.2.4.6 Dolerite dykes

Dolerite dykes are observed cross-cutting every unit within the belt. They are dark blue to black, fine to medium-grained (~0.5-1mm), equigranular and foliated. The composition is fairly constant at amphibole 50-60%, plagioclase 30-40%, hornblende 0-20%.

4.2.2.5 Field Relations and Geochronological constraints

A combination of U-Pb geochronology presented in Chapter 2, and relative dating using field observations, enables a stratigraphic sequence to be defined for the Oum Abana Belt. Based on field observations, the oldest unit within the Oum Abana Belt is the (base of the) volcanic belt, although no direct geochronological constraints exist for the base of the unit. A sample of rhyolite forming part of a volcano-sedimentary belt was dated at 2122 ± 18 Ma (J287) and provides a constraint for magmatism higher up in the sequence. Samples from the orthogneiss unit returned magmatic ages of 2130 ± 25 Ma, and 2103 ± 24 Ma (J220, and J219). Three late intrusions of tonalite to granodiorite composition returned ages of 2109 ± 43 Ma, 2097 ± 21 Ma, and 2093 ± 17 Ma respectively (Table 2-1; Section 2.1). A detrital zircon age of 2110 ± 25 Ma from a sample of paragneiss from a metasedimentary belt provides a maximum age constrain for the sedimentary rocks, and indicates that the source of sediments was likely related to the (~2100 Ma) magmatic event responsible for the tonalite and granodiorite intrusions. Diorite (from the gabbro-diorite intrusion) was dated at 2065 ± 13 Ma by Lehbib (2016), providing a minimum age constraint for the sedimentary belt and La Hida shear zone. The late diorite dykes likely post-date the Palaeoproterozoic.

4.3 **Anajim Guebli Domain**

4.3.1 Introduction

The Tmeimichat Group and Anajim Guebli Suite were well defined in Mauritania by Schofield et al. (2006). The Anajim Guebli Domain as defined here, represents a continuation of the Tmeimichat Group and Anajim Guebli Suite into Western Sahara. Only a small portion of the Domain outcrops in Western Sahara. The limited work completed as a part of this project seems to confirm that the northeast of the study area represents the continuation of the Tmeimichat Group and Anajim Guebli Suite (Figure 4-1).

The Anajim Guebli Suite was defined by Schofield et al. (2006) as comprising migmatitic tonalite and granodiorite with abundant enclaves of amphibolite and migmatitic granitic gneiss. This unit corresponds to the orthogneiss unit in Western Sahara

The Tmeimichat Group consists of amphibolite (locally strongly foliated or gneissic), quartz diorite, granodiorite and granitic rock (Schofield et al., 2006). These are intercalated with amphibolitic schist, chert, marble and locally serpentinised pyroxenite. Schofield et al. (2006) interprets the migmatitic paragneisses to have clastic sediment protoliths indicating that they formed in a basin. Locally developed calcareous nodules and limestone units, preserved as lenses of calcsilicate rock and marble, is indicative of a shallow marine environment (Schofield et al., 2006). The Tmeimichat Group corresponds to the metasedimentary unit mapped in Western Sahara

4.3.2 Geology and Structure (Mapping/field relations)

In Western Sahara, the Anajim Guebli Domain consists of metasedimentary rocks to the north of the Northern Limb of the EAC, and granodiorite and granite gneisses in the north.

Due to the significant sand cover, the metasedimentary unit is not well exposed at the contact with the Northern Limb, though is marked by a significant magnetic anomaly in a unit that is otherwise a magnetic low.

The metasedimentary lithologies include brown-cream, medium grained (~1.5mm) marble, quartzite, ferruginous quartzite, quartz diorite, amphibolite and quartz-rich micaceous (±garnet - bearing) paragneiss.

The granite-gneiss to the north is leucocratic and white, pink or green coloured. It is generally coarse-grained (~2-5mm) and equigranular, but may have local alkali-feldspar phenocrysts. It varies between pink alkali-feldspar rich and green epidote-altered plagioclase-rich areas. The composition ranges from monzogranite (quartz (~30-50%), plagioclase (epidote altered) (~30-35%), alkali-feldspar (~20-30%), biotite (~0-8%) and muscovite (~0-4%)) to syenogranite (alkali-feldspar (~50%), quartz (~30%), plagioclase (~15%), muscovite (~5%)). It ranges from not foliated, to a well-developed gneissic foliation. The gneissic foliation is defined by 90% light coloured bands ~2-3cm thick (quartz, plagioclase and alkali-feldspar bearing) and 10% dark bands ~2-4mm thick (mostly biotite, with some hornblende and muscovite). The terrane is cross-cut by a number of granodioritic intrusions.

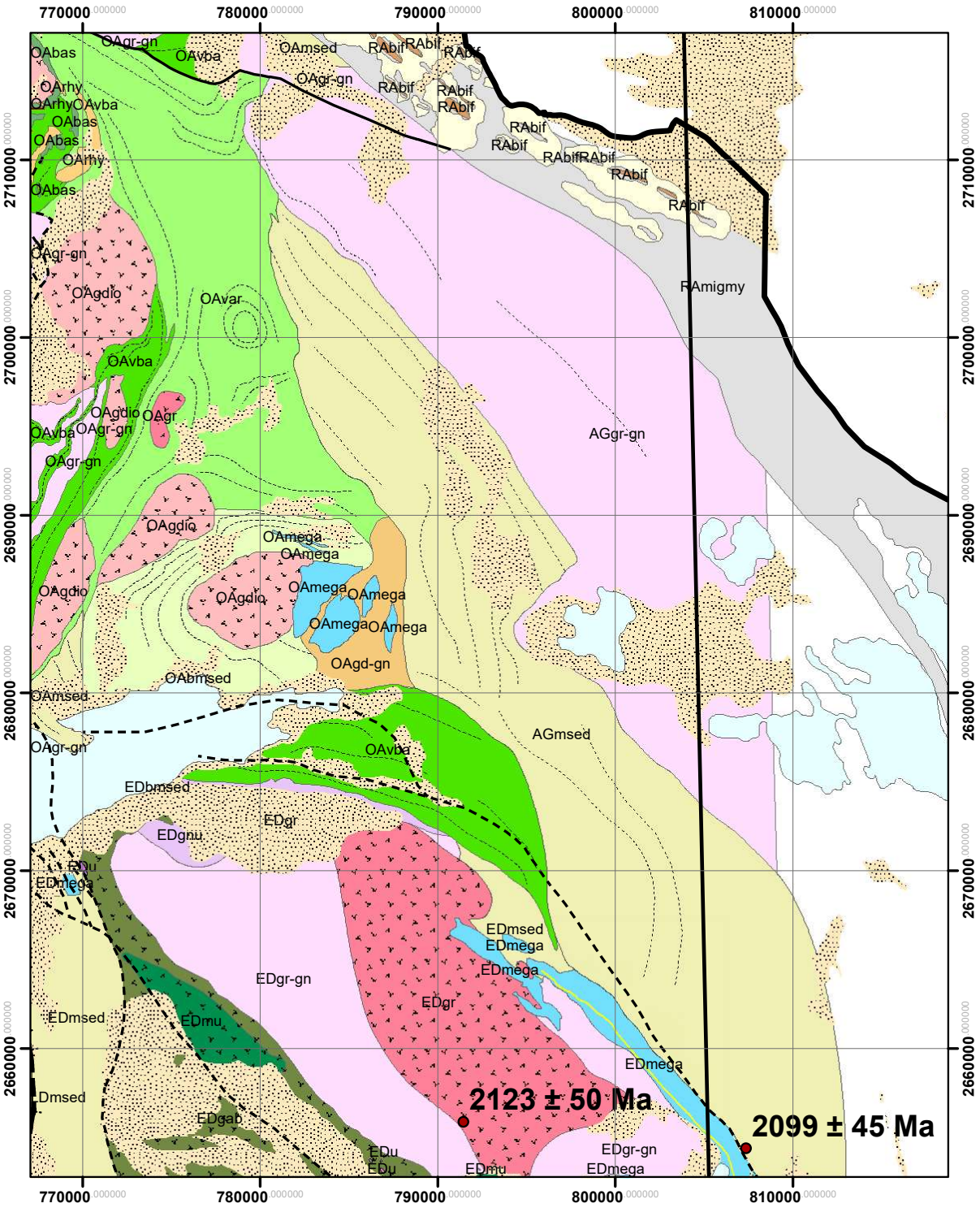

Figure 4-117 a – Detailed geology of the Anajim Guebli Domain. For location map, see the purple square in Figure 4-1.

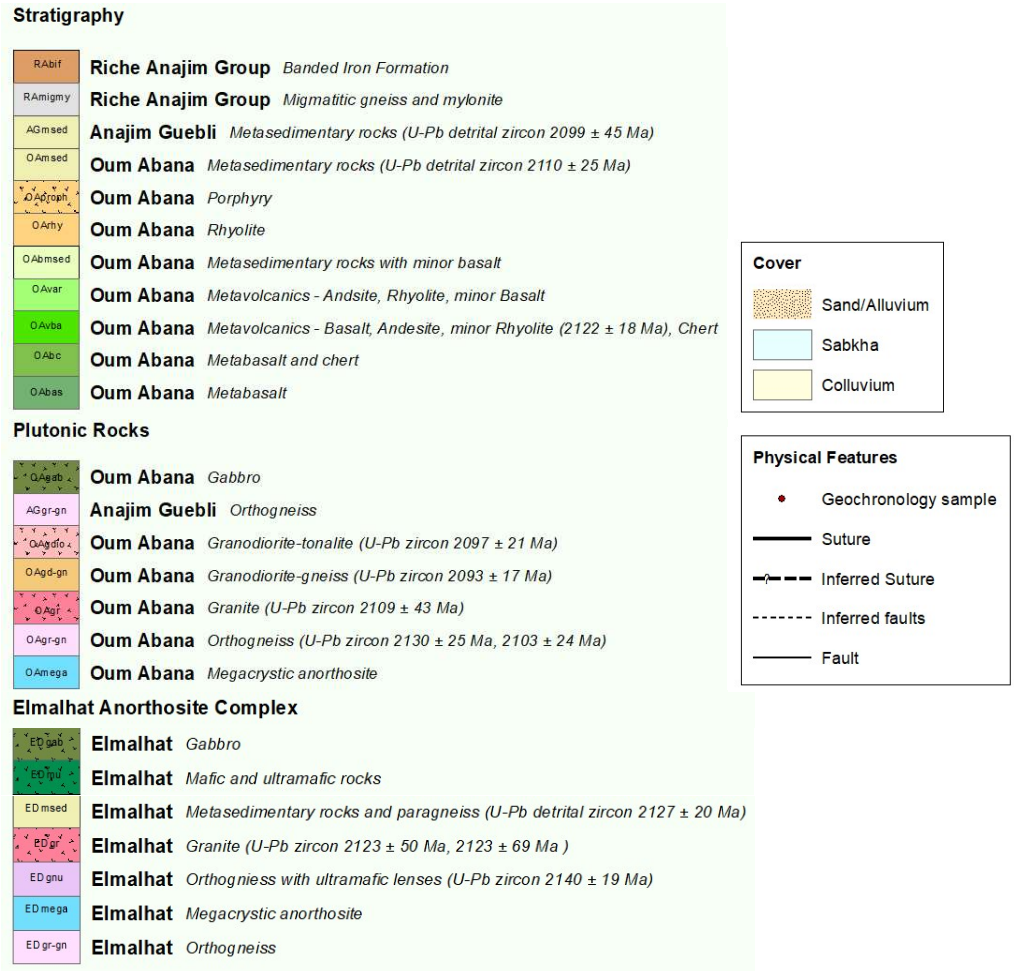

Figure 4-117 b – Legend.

4.4 **Riche Anajim Group**

4.4.1 Introduction

The Riche Anajim Group, makes up the central zone of the Sfariat Belt (Schofield et al., 2006), a major NW-SE striking shear zone ranging in width from ~4 to ~6km within the field area (Figure 4-118). In Mauritania, it comprises largely mylonitic, migmatitic paragneiss and quartzofeldspathic schist, aplitic microgranite as well as foliated metagranite (Schofield et al., 2006). The most prominent feature of the shear zone are ridges of banded iron formation (BIF) with thin beds of locally brecciated impure marble (Schofield et al., 2006, Combs, 2012). The belt contains up to three major parallel ridges of BIF, forming lens-shaped units trending NW-

SE, parallel to the major shear zone. Note that the BIF, is referred to as ferruginous quartzite in all previous literature on the Sfariat Belt (Bronner et al., 1992, Schofield et al., 2006).

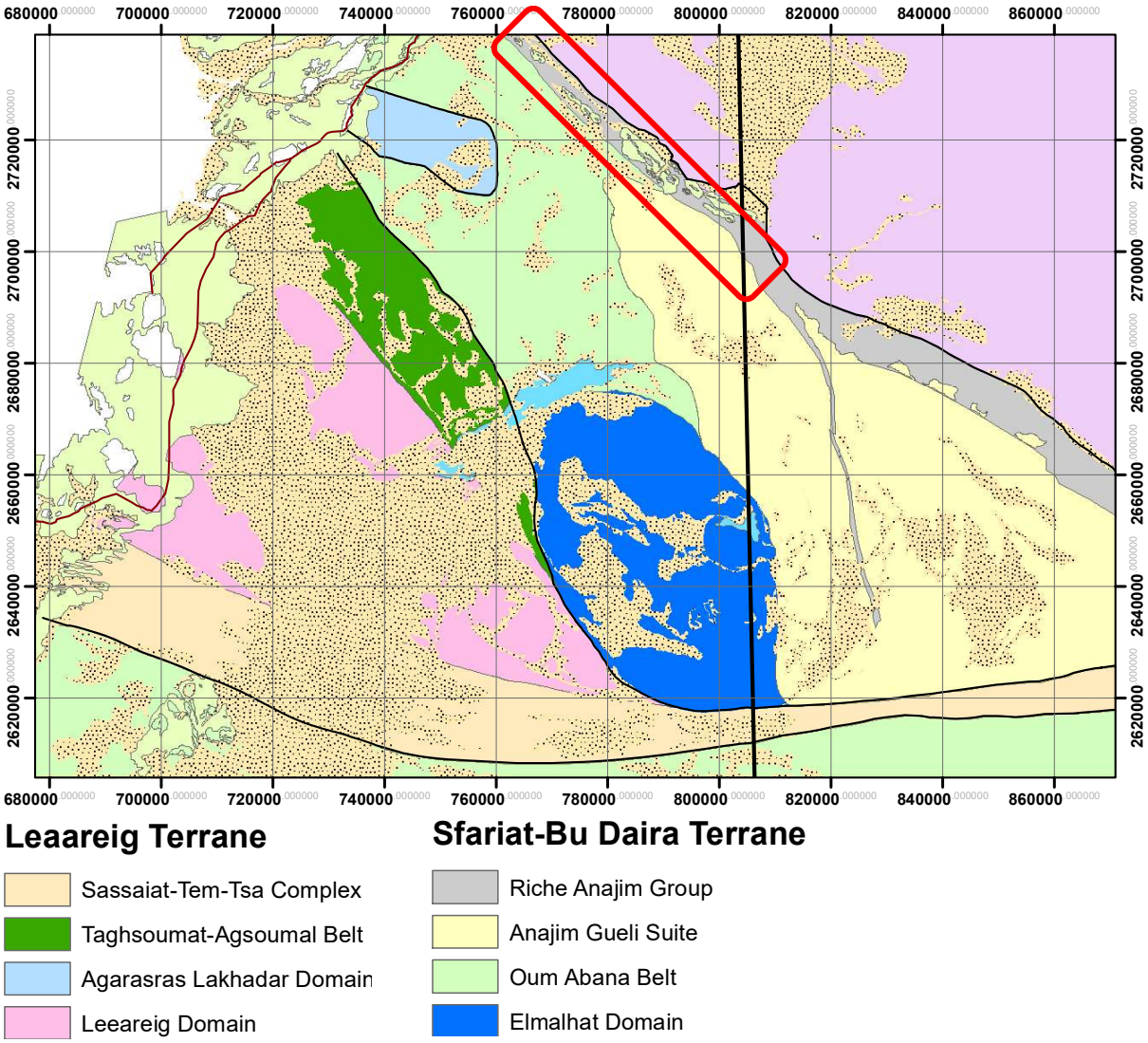

Figure 4-118 – Domain map of the study area with the location of the Riche Anajim Group shown in red.

4.4.2 Geology and Structure

4.4.2.1 Geology

Detailed work on the Riche Anajim Group was completed by Schofield et al. (2006) in Mauritania, with some field work completed in Western Sahara by Combs (2012). The focus of this thesis is on other aspects of the geology of the overall region, with no additional field

work having been undertaken on the Riche Zone. The following field descriptions have been extracted from Combs (2012), with supplementary petrology having been completed as part of this project.

A high degree of sand cover makes it hard to observe the geology in between the ridges (Figure 4-119). Thus, in mapping the Riche Belt, a number of NE-SW traverses were made where the ridges were relatively close together. The geology was carefully documented on the slopes of the ridges to unravel the geology of the Riche Belt. The lithologies observed on the traverses included gneiss (including migmatitic gneiss), mylonite, a blue unit of marble and granite.

The gneissic unit is highly variable in composition, fabric and structure across the shear zone. For the most part, the gneiss consists of alternating light (pink and white), dark (grey) and iron-rich bands on a scale of 0.5cm-1m (Figure 4-120).

Locally, the gneissic banding is on a decimeter scale, with granitic layers (tonalite and syenogranite) and gabbroic layers. The tonalitic granite forms grey, mesocratic, medium-grained (~2mm), equigranular layers, consisting of plagioclase (~45%), hornblende (~40%) and quartz (~15%). The syenogranite forms pink, leucocratic, coarse-grained (~2mm), equigranular bands consisting of alkali-feldspar 58%, quartz 30%, plagioclase 10% and biotite 2%. The layers of gabbro have a dark blue peppered appearance, are coarse-grained (~3mm), equigranular, and are composed of hornblende (~50%) and plagioclase (epidote altered) (~50%).



Figure 4-119 - Field photograph of the Riche Belt, showing the black BIF ridges. Photo taken from UTM 28 783704 mE, 2720813 mN, facing SE.

A pavement of the gneiss within the Riche Anajim Group (UTM 28 791594 mE, 2713263 mN) outcropping on the side of a ridge, provides an ideal area for observation to evaluate the structural regime and history for the Riche Belt. Analysis of the kinematic indicators within the pavement gives an overall sinistral sense of movement. Also present within the pavement

is a considerable amount of boudinage within the hematite layers (Figure 4-121). The boudins range in size from 10cm to 5m long, with thicknesses between 3cm and 50cm. The boudins are all drawn, tapered boudins with interboudin gaps ranging from 5cm to 1.5m. The boudinage of the iron-rich bands present in the gneissic pavement may be representative of boudinage on a larger scale within the Riche Belt. At the map scale, the BIF ridges appear to be boudinaged along strike within the shear zone (Map A, Figure 4.24). The lens-shaped ridges cropping out within the Riche Belt therefore represent individual boudins of 2 or 3 individual BIF layers.



Figure 4-120- Field photograph of the gneissic unit in the Riche Belt. Compass clinometer for scale (~9cm long) (UTM 28 791594 mE, 2713263 mN).



Figure 4-121 -- Field photograph of boudinage of hematite within gneiss in the Riche Belt, with the boudins shown by the black ovals. (UTM 28 791594 mE, 2713263 mN).

Locally within the gneiss, partial melting is observed, resulting in migmatitic gneiss (Figure 4-122). It is mesocratic with a green/grey and cream/pink colour with epidote alteration present. The overall composition of the rock is quartz (~40%), hornblende (~20%), alkali-feldspar (~20%) and plagioclase (~20%). Cream/pink blobs of recrystallised partial melt are present throughout the rock.



Figure 4-122 - Field photograph of migmatitic gneiss within the Riche Belt. Man and geological hammer for scale. (UTM 28 782068 mE, 2720005 mN).

The mylonite in the Riche Belt is a mesocratic, green-grey coloured, intensely foliated quartzofeldspathic mylonite (Figure 4-123). It is primarily composed of layers of quartz and feldspar, with small layers of muscovite and biotite between them. Grain size appears to have been reduced through shearing. The overall composition is quartz 60%, feldspar 28%, muscovite 10% and biotite 2%. Locally, where large alkali-feldspar porphyroclasts are present, the mylonitic unit takes on the appearance of augen gneiss.

The marble within the Riche Belt forms a distinctive blue marker unit for the length of the shear zone (Figure 4-124). It is a mesocratic, blue coloured, fine-grained with rock fragments present ranging in size from 1cm to 30cm. Although it is evident that the unit has been sheared,

some primary sedimentary features can still be made out. In the field this unit was not properly identified, with samples taken for thin section analysis. As the samples were unable to be used, the identification of the rock as marble was achieved through a combination of field observations and a description of the Riche Belt by Bronner et al. (1992) who described the marble in the Riche Belt as forming a light blue coloured marker horizon. The deformation of the rock fragments within the marble are indicative of sinistral movement along the shear zone (Figure 4-125).



Figure 4-123- Field photograph of mylonite in the Riche Belt (UTM 28 784298 mE, 2719901 mN).

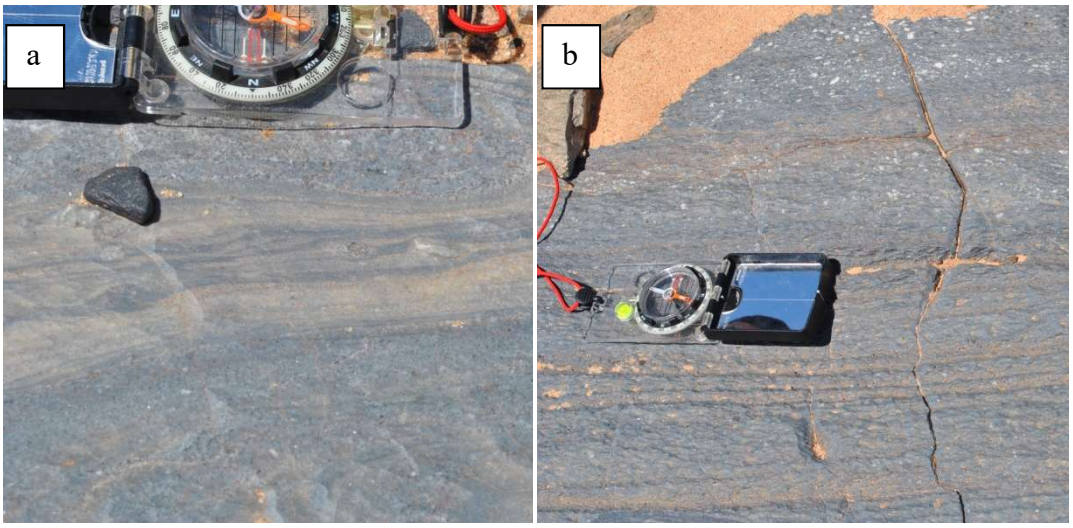

Figure 4-124- Field photographs of marble in the Riche Belt, showing banding. a) also shows inclusions typical of the marble unit (UTM 28 786620 mE, 2717086 mN). b) sedimentary bedding within the marble (UTM 28 786613 mE, 2717054 mN). Compass clinometer (~9cm long) for scale.



Figure 4-125- Field photograph of folded inclusions within the marble unit in the Riche Belt, indicating sinistral shear sense, as indicated by the black arrows. Compass clinometer (~9cm long) for scale. (UTM 28 786620 mE, 2717086 mN).

Two types of iron-rich lithologies are present within the Riche Belt including pure hematite, and BIF. The hematite was relatively uncommon, consisting of a grey, dense lithology with a massive texture. It was non-magnetic and had a red streak. It was hematite that formed the iron-rich boudins observed in the gneiss.

The BIF is composed of alternating bands of chert and bands of iron (Figure 4-126). The BIF layers are strongly magnetic and have a red streak, indicating that it contains both hematite and magnetite. It is melanocratic, black/silver in colour, has a metallic lustre and sounds like ceramic when smashed. Locally the chert has been leached out, leaving the unit enriched in iron. A large amount of parasitic folding is present in the BIF, indicating deformation in the area, and giving some indication of the presence of larger scale folds in the area.

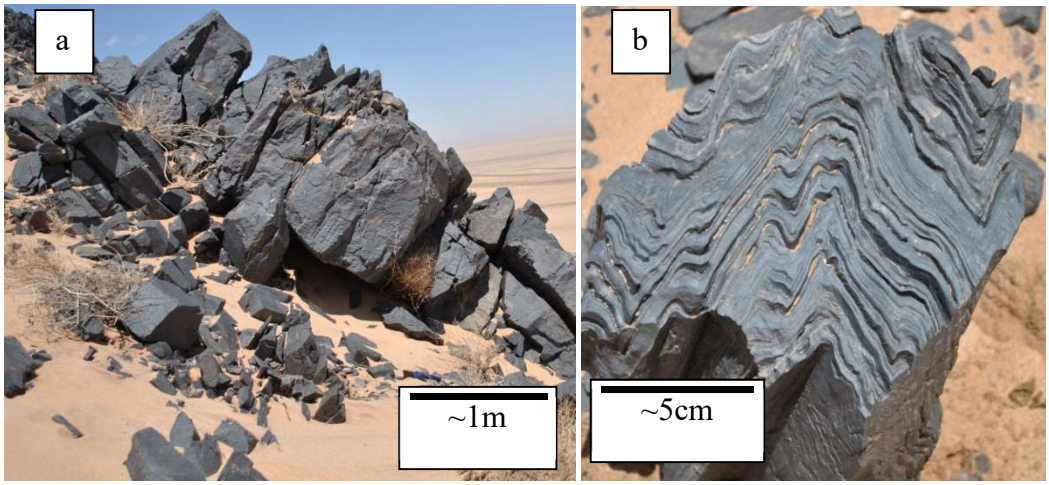

Figure 4-126- Field photographs of the BIF unit within the Riche Belt. a) outcrop with massive BIF (UTM 28 784380 mE, 2719991 mN). b) a loose piece of Banded Iron Formation (BIF), showing alternating bands of chert and hematite/magnetite. It also shows small scale parasitic m-folds (UTM 28 783615 mE, 2720815 mN).

4.4.2.2 Structure

Folding is observed within the BIF lenses within the Riche Belt at various scales. The symmetry and the orientation of the lithological units observed on a traverse across the belt, along with other evidence from the field observations, i.e. parasitic folds (Figure 4-126 b) and changes of dips of the units, all indicate that these units have been folded, producing tight, overturned folds with both limbs and the fold axial plane dipping toward the NE.

Within the Sfariat Shear Zone observations of kinematic indicators were made from the mylonitic gneiss as well as the marble unit, including asymmetrical folding (NW-SE trending sub-vertical hinge lines), the anticlockwise rotation of parts of layers within the gneiss as well as folding of inclusions within the marble. These all indicate sinistral movement along the NW-

SE trending shear zone (Figure 4-127a-e). The cross-sectional view (kinematic X-Y plane) of the migmatitic gneiss does not appear to contain any definitive kinematic indicators, indicating that there might not be much of a dip-slip component to the shearing (Figure 4-127 f).

Hematite layers within the gneiss in the Riche Belt displayed boudinage (Figure 4-121) on a small scale (10cm-5m long with interboudin gaps ranging from 5cm to 1.5m), forming symmetrical, drawn, tapered boudins. The boudinage of these hematite layers present in the gneissic pavement may be representative of boudinage on a larger scale within the Riche Belt. On the map scale, the BIF ridges are boudinaged along-strike within the shear zone (Figure 4-119). The lens-shaped ridges outcropping within the Riche Belt therefore represent individual boudins of 2 or 3 individual boudin trains.

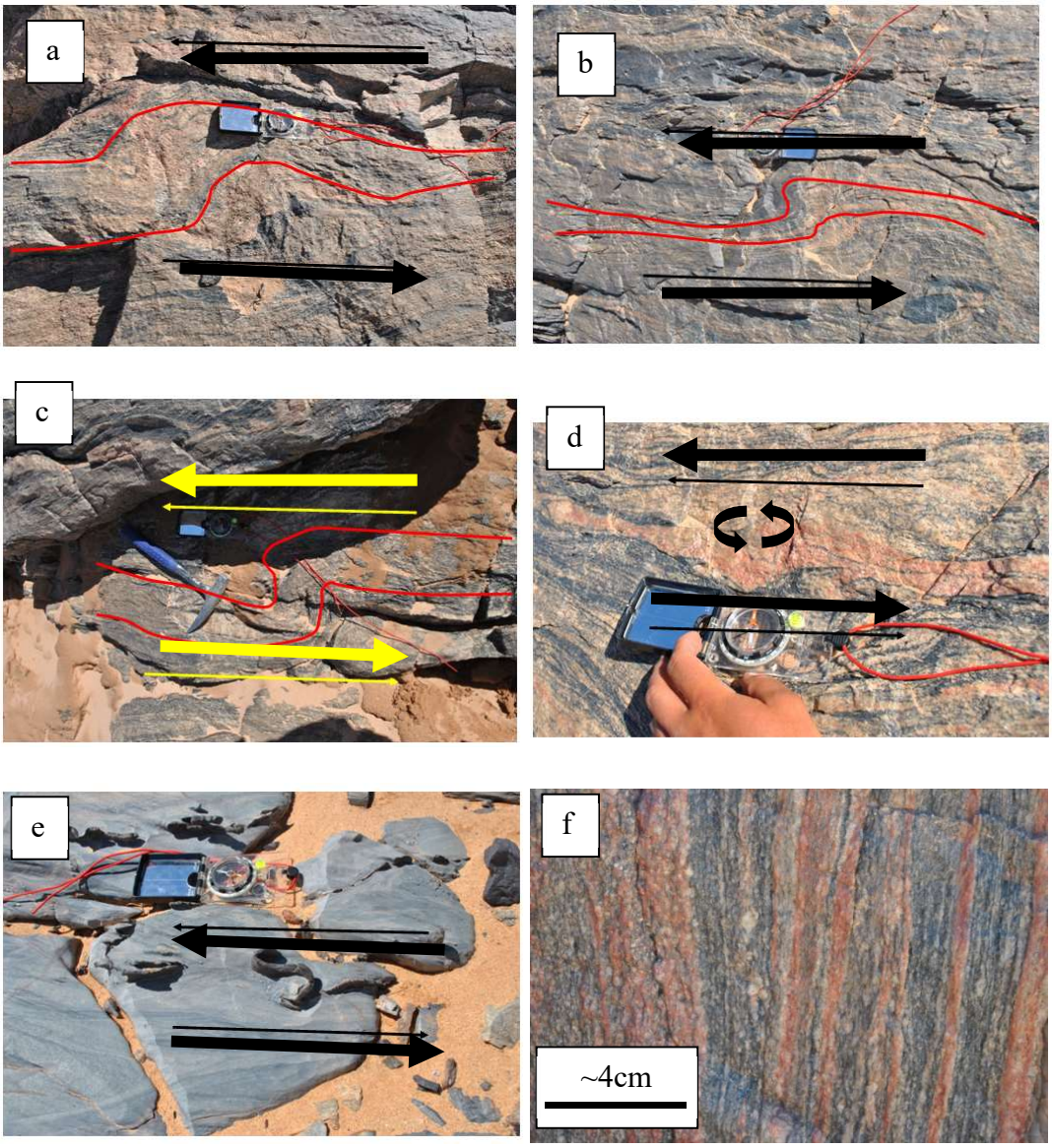

Figure 4-127- A series of field photographs that illustrate kinematic indicators within the Riche Belt, indicating overall sinistral movement along the shear zone (a-e show map view, f shows a cross sectional view, facing SE.) a-c) asymmetrical folding with a sub-vertical hinge within the migmatitic gneiss, indicating sinistral movement in the shear zone (UTM 28 791594 mE, 2713263 mN). d) δ-type kinematic indicator, where part of the pink layer has undergone anticlockwise rotation, indicating sinistral movement (UTM 28 791594 mE, 2713263 mN). e) folding of inclusions within the marble unit in the Riche Belt, indicating sinistral movement (UTM 28 783661 mE, 2720857 mN). f) cross-sectional view (kinematic X-Y plane) facing SE. Shows sub-vertical foliation, with no kinematic indicators to suggest a dip-slip component to the shearing (UTM 28 791594 mE, 2713263 mN).

4.4.3 Petrography

4.4.3.1 BIF

The BIF is largely composed of alternating bands of quartz and hematite (Figure 4-128 a,b). It has been locally sheared, with high strain microstructures are present in sample J049 (Figure

4-129). Subgrain rotation recrystallization is observed in samples J046, and J055 (Figure 4-128 and Figure 4-130) indicating dynamic recrystallisation.

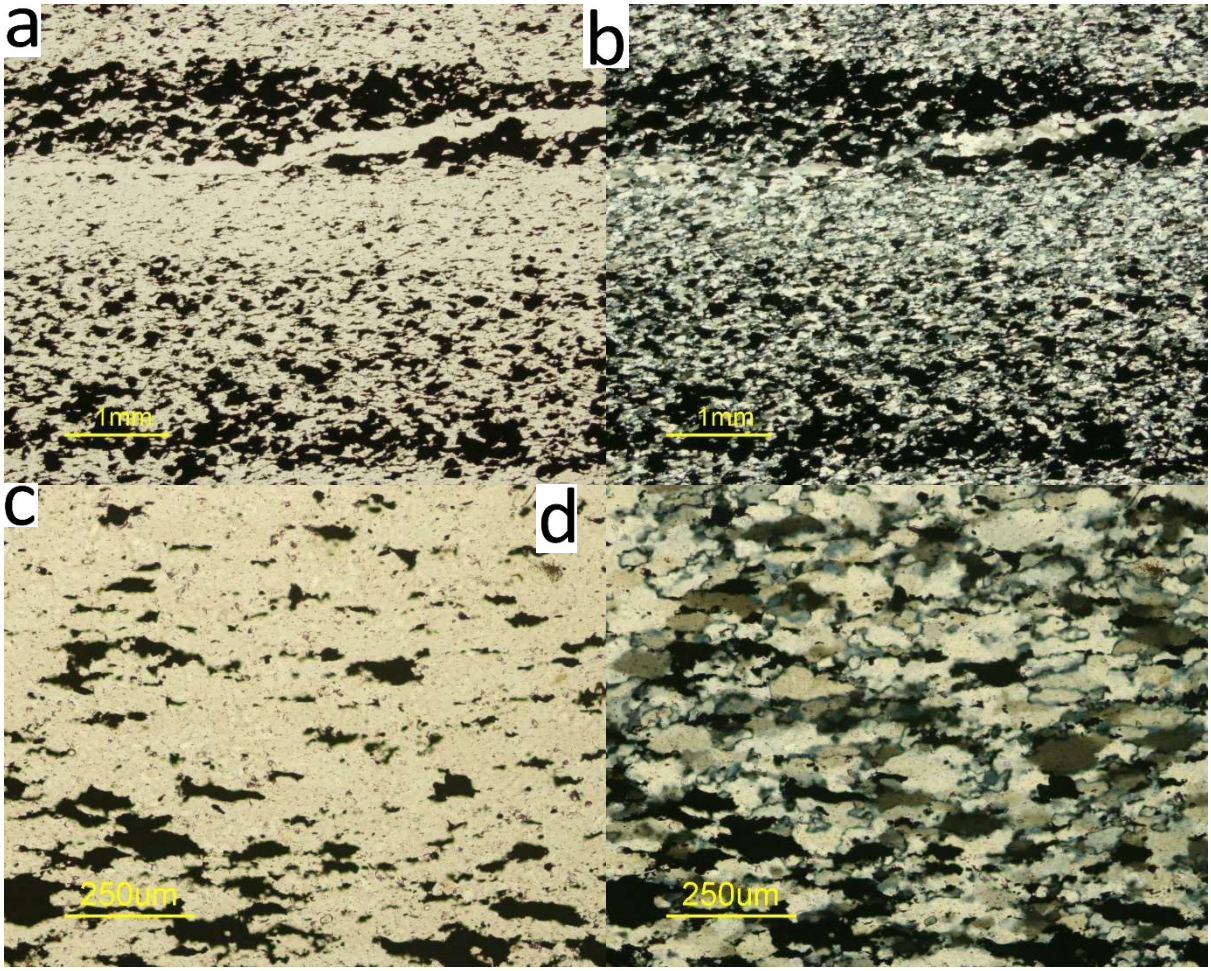

Figure 4-128 - Photomicrographs of J046 (UTM 28 791504 mE, 2713254 mN) - BIF a, b) General view of BIF with alternating bands of quartz and hematite. [a) PPL, b) XPL]. c, d) Fine-grained recrystallized quartz, partly pinned by Fe oxide, transitional subgrain rotation crystallization / grain boundary migration with larger (~200 µm) relict grains [c) PPL, d) XPL].

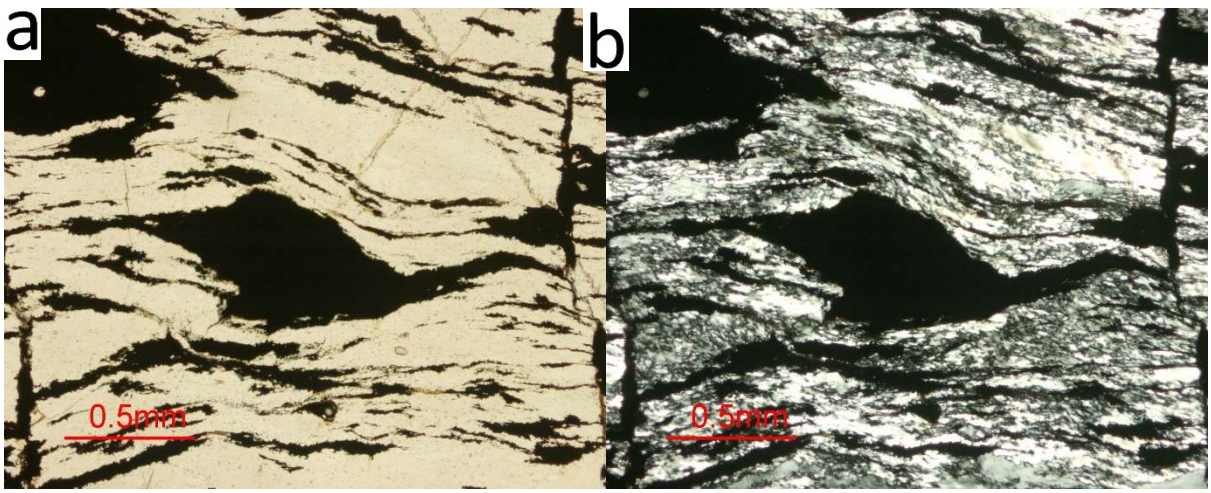

Figure 4-129 - Photomicrographs of J049 (UTM 28 786596 mE, 2717040 mN) - BIF with high-strain microstructure. Lenticular oxides with narrow tails. Quartz ribbons finely recrystallized with elongate grains, locally showing oblique shape fabric. Sinistral shear sense indicators. [a) PPL, b) XPL].

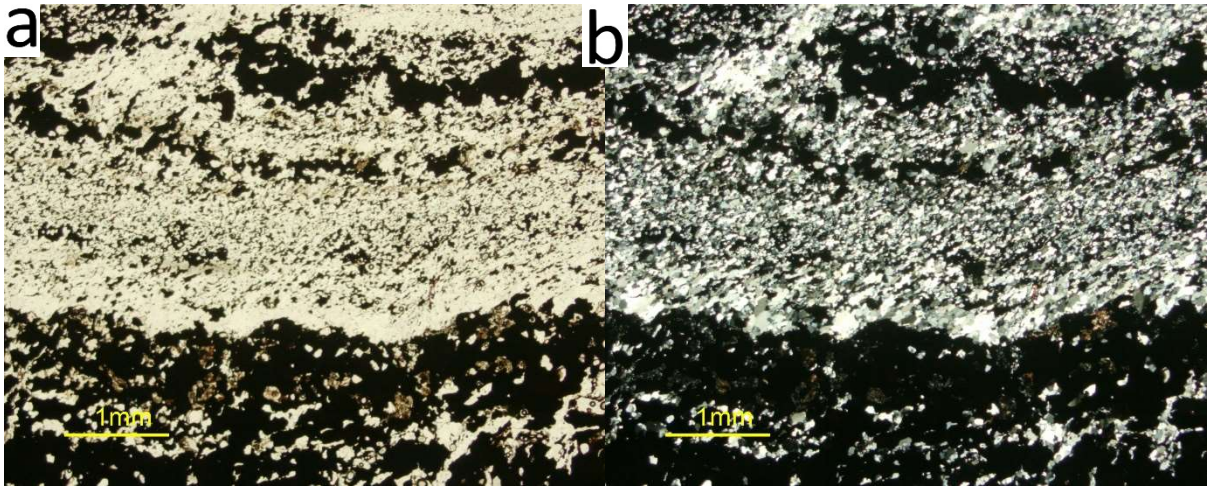

Figure 4-130 - Photomicrographs of J055 (UTM 28 783704 mE, 2720813 mN) - BIF. Quartz fabric oblique to banding, subgrain rotation crystallization transitional to elongate grains. Also sprays of needles, look like low biref, high relief, colourless but rusty, cross-fractures. [a) PPL, b) XPL].

4.4.3.2 Marble

The marble consists largely of calcite with porphyroblasts of what is possibly dolomite (Figure 4-131 and Figure 4-133). The marble is locally forsterite-bearing (Figure 4-132 and Figure 4-133), diopside-bearing (Figure 4-133), with minor tremolite in some samples.

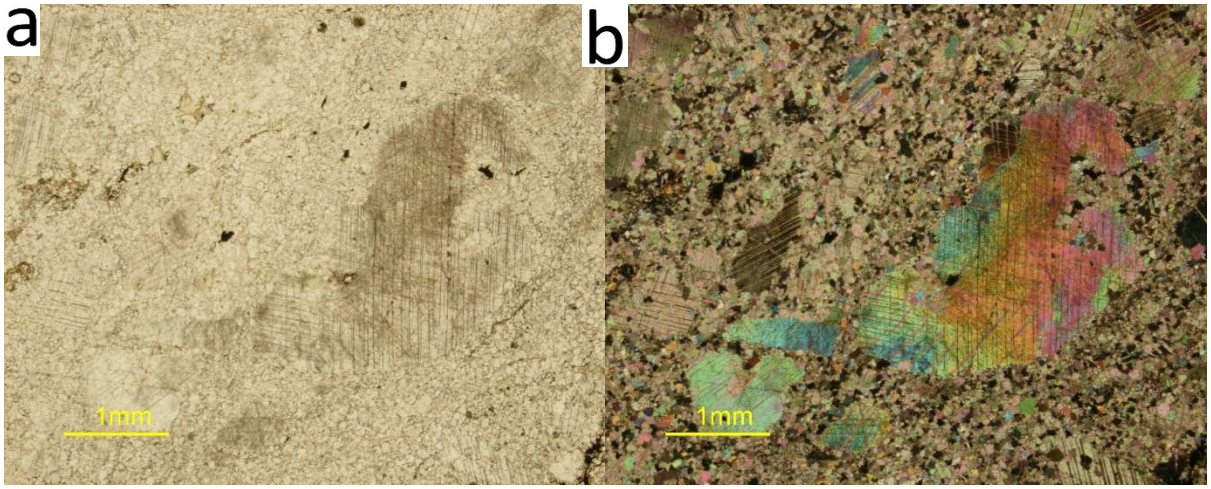

Figure 4-131 – Photomicrographs of J047 (UTM 28 786613 mE, 2717054 mN) PPL, and XPL images of marble with chlorite and tremolite. Finely recrystallized carbonate is likely calcite with large porphyroclasts of dolomite? [a) PPL, b) XPL].

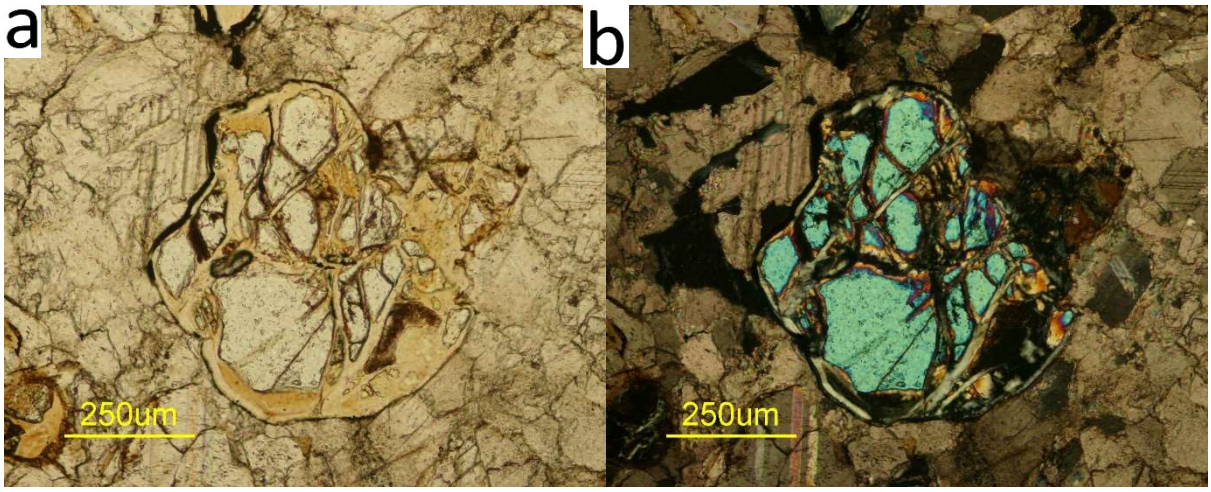

Figure 4-132 - Photomicrographs of J052 (UTM 28 784286 mE, 2719885 mN) - PPL, and XPL images of forsterite marble. Sheaves of Mg-chlorite (white interference colour) locally between serpentinized Fo. [a) PPL, b) XPL].

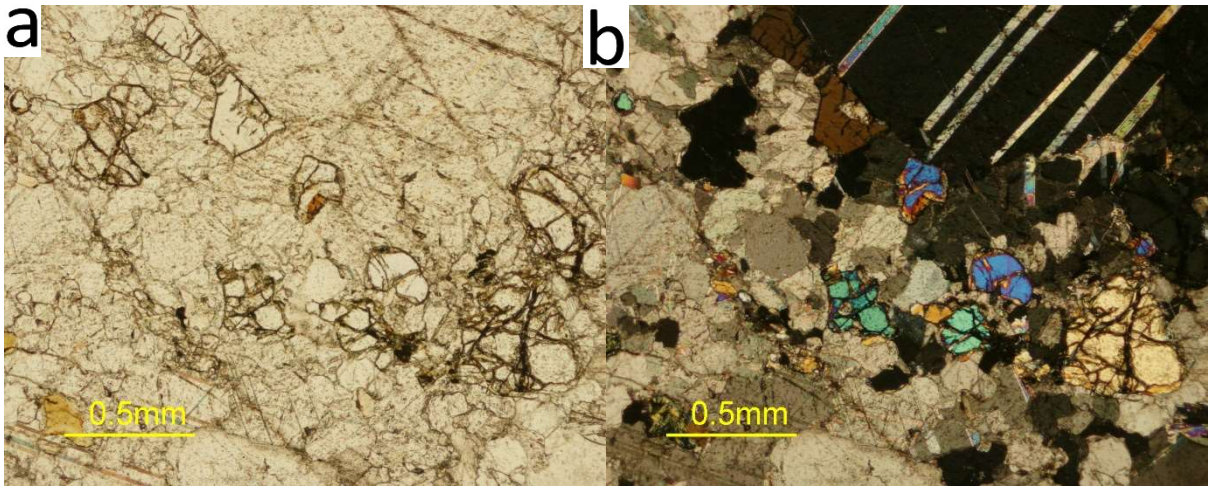

Figure 4-133 - Photomicrographs of J053 (UTM 28 784297 mE, 2719898 mN) - PPL, and XPL images of Marble with forsterite, diopside and some fine tremolitic amphibole. Large porphyroclasts with broad twin lamellae may be dolomite. [a) PPL, b) XPL].

4.4.3.3 Gneiss to Mylonite

Gneiss and granite mylonite form a large portion of the Riche Anajim Group. It appears from petrological evidence that both the gneiss and granite mylonite may have experienced a common high temperature deformation event, followed by further deformation in samples of mylonite.

Sample J054 consists of granitic biotite gneiss. It contains a strong banded fabric, but not mylonitic (Figure 10). It consists of clear twinned microcline (low T), plagioclase ribbons are quite extensively recrystallized, quartz, and biotite. The quartz has seriate grain size

distribution, with finer grains indicating grain boundary migration recrystallization. Some higher-strain slip surfaces are mainly defined by mica trains, rather than quartz ribbons. Main banding fabric is a high-temperature feature, with some later modification.

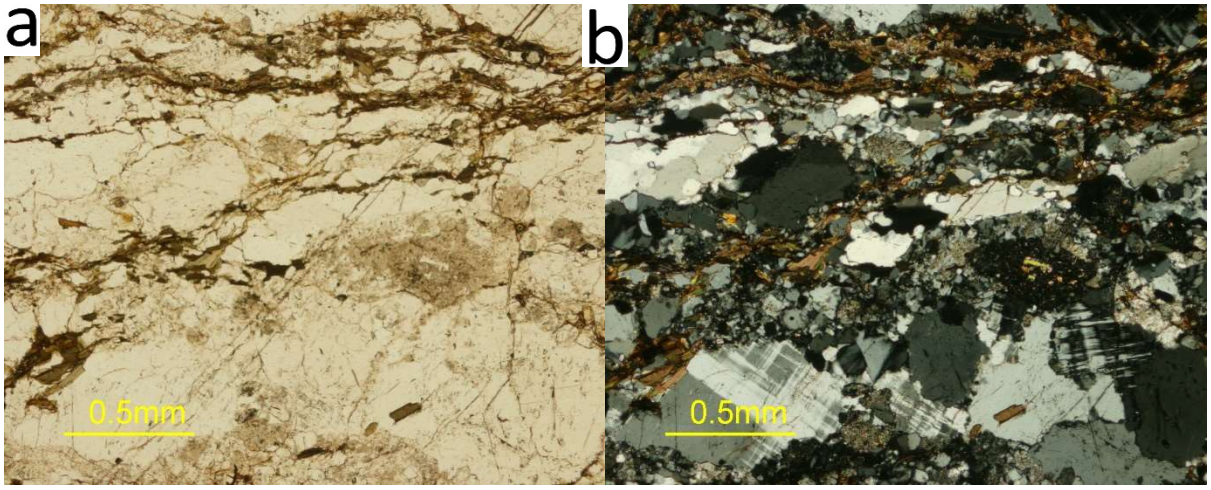

Figure 4-134 -- Photomicrographs of J054 (UTM 28 784319 mE, 2719908 mN) - granitic biotite gneiss. Strong banded fabric, but not mylonitic. Clear twinned microcline (low T); plagioclase ribbons are quite extensively recrystallized; quartz has seriate grain size distribution, finer grains indicate grain boundary migration recrystallization. Some higher-strain slip surfaces are mainly defined by mica trains, not by quartz ribbons. [a) PPL, b) XPL].

Samples J045 and J048 consists of mylonitic granite. Sample J045 consists of slightly rounded feldspar (k-feldspar and plagioclase) porphyroclasts in grain boundary migration-recrystallized quartz, with minor mica (Figure 4-135). Myrmekites are preserved. Locally ribbons with fine mica and quartz down to 50 μm, resemble subgrain rotation crystallization texture. Sample J048 consists of granite mylonite displays a high degree of strain, containing finely recrystallised quartz wrapping around large fractured feldspars (Figure 4-136).

It appears that both the gneiss (J054) and granite mylonite (samples J045 and J048) may have experienced a common high temperature deformation event that defines the gneissic fabric, prior to reactivation of shearing to produce a localised mylonitic fabric.

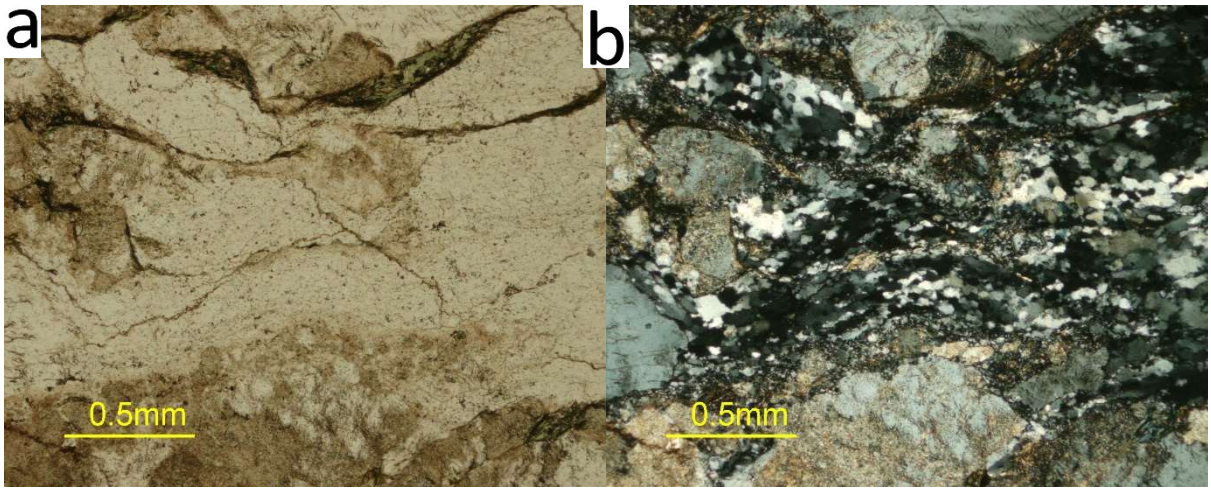

Figure 4-135 - Photomicrographs of J045 (UTM 28 791594 mE, 2713263 mN) - mylonitic granite. Feldspar (k-feldspar and plagioclase) somewhat rounded porphyroclasts in grain boundary migration-recrystallized quartz, minor mica. Maybe some fine recrystallization of feldspar rims in these domains too. [a) PPL, b) XPL].

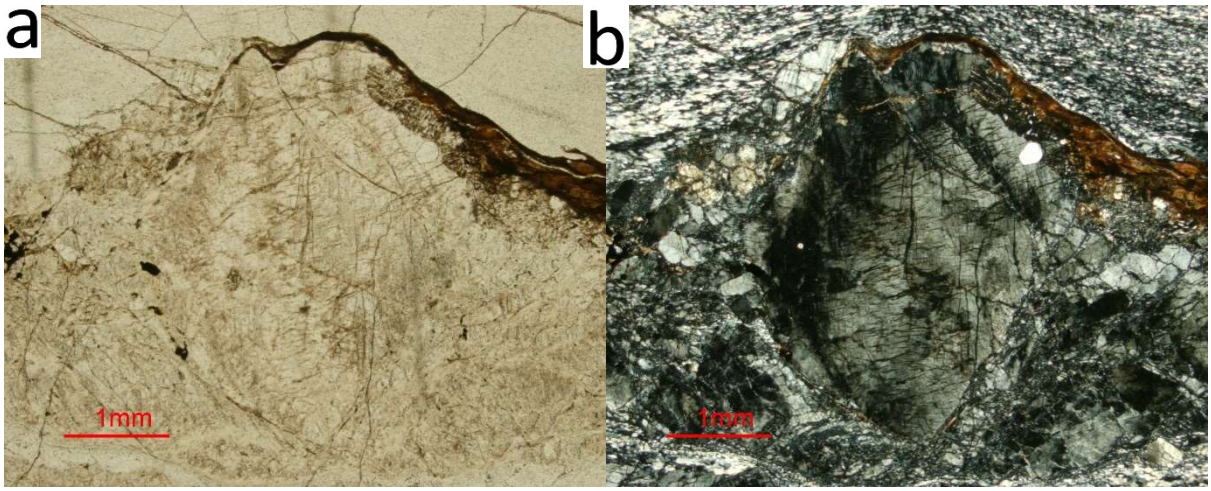

Figure 4-136 – Photomicrographs of J048 (UTM 28 786613 mE, 2717054 mN) - granite mylonite. Large grain of fractured feldspars, wrapped by finely recrystallized quatz indicating high strain. [a) PPL, b) XPL].

4.5 **Geochemistry and Tectonic Setting**

4.5.1 Whole Rock Geochemistry

Sixty-three samples from the Oum Abana, Elmalhat and Anajim Guebli Domains were analysed for whole rock major and trace element geochemistry using ICP-MS facilities at ALS geochemistry laboratories in Dublin, Ireland (Appendix C). Many samples associated with the EAC are cumulate rocks, so are not suitable for plotting on tectonic discrimination diagrams. Therefore, samples from the EAC have been excluded from all whole-rock chemical discrimination diagrams and the geochemistry of the EAC is described separately in Section

4.5.1.3. The same process was followed for analysing the geochemical data from the Sfariat-Bu Daira Terrane as the Leaareig Terrane, described in Section 3.5.

4.5.1.1 Traditional Tectonic Discrimination Diagrams

It is necessary to classify rocks before the application of tectonic discrimination diagrams (as discussed in Chapter 3.5.1.1). As some of the samples have been altered and/or metamorphosed, the classification of the igneous rocks for use in traditional tectonic discrimination diagrams will be done using immobile trace element proxies (Figure 4-137a; Pearce (1996)) as opposed to IUGS-recommended TAS diagram for fresh rocks (Figure 4-137b; Le Bas and Streckeisen (1991)).

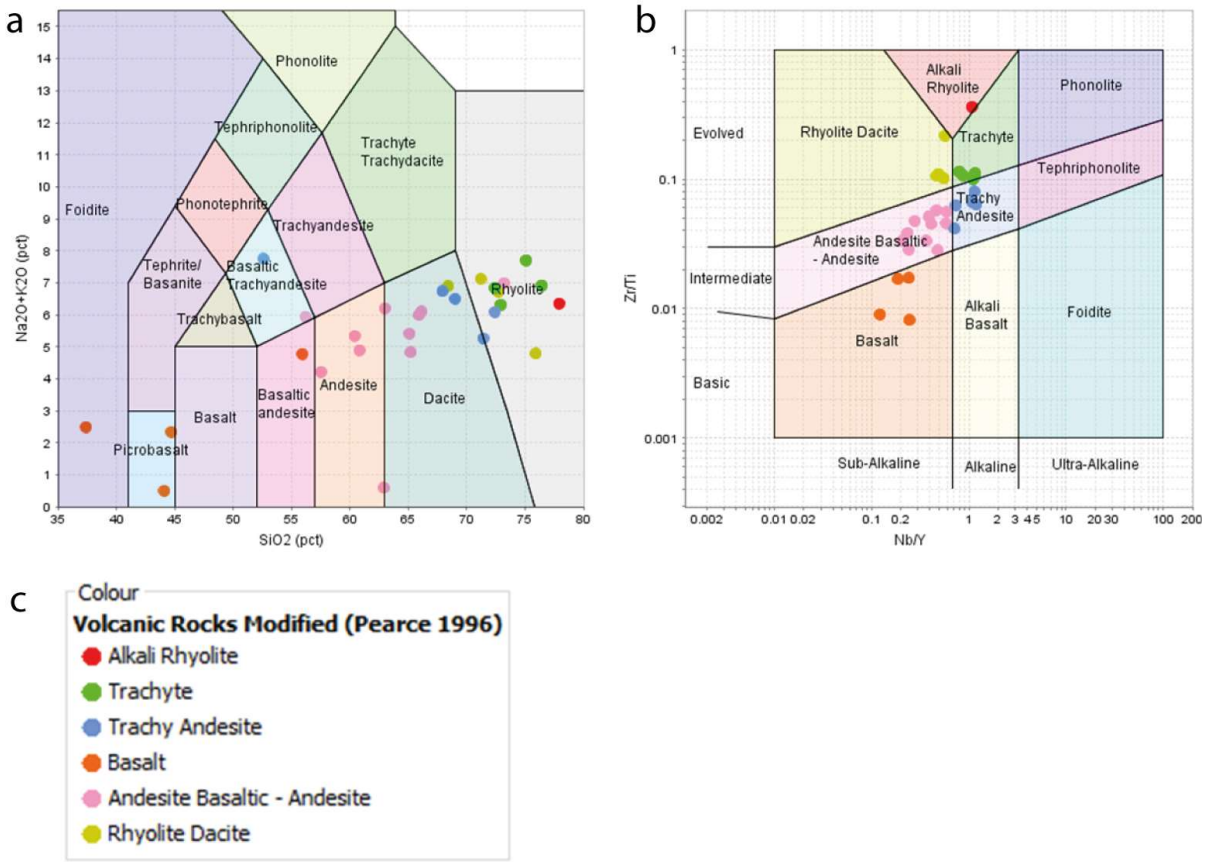

Figure 4-137 – Classification diagrams for all igneous and meta-igneous rocks from the Sfariat-Bu Daira Terrane. A) IUGS-recommended TAS diagram from Le Bas and Streckeisen (1991). b) immobile element based TAS proxy diagram from Pearce (1996) after Floyd and Winchester (1977). C) legend for rock-type for the rest of Chapter 4.5.1 – based on Pearce (1996) classification

4.5.1.1.1 Mafic and Intermediate Rocks

The Th-Nb proxy shows that the majority of the igneous rocks within the Sfariat-Bu Daira Terrane have a continental arc signature with some samples of basaltic/andesitic basalt composition displaying MORB characteristics or a mixed oceanic arc-continental arc signature (Figure 4-138; Pearce (2014)). A distinct trend of increasing continental-arc character with the increasing felsic nature of the sample is observed. The cluster of samples on the edge of the MORB-OIB array, when plotted on the Ti-Nb proxy (Figure 4-138b) samples (both basaltic and andesitic basalt) demonstrate an Enriched MORB (EMORB) signature. (As with the Leaareig Terrane, a filter to remove any samples with significant crustal contamination has been applied (as recommended by Pearce (2008)) before the application of the Ti-Nb proxy.)

When plotted on the Th-Hf/3-Ta and Th-Zr/117-Nb/16 ternary discrimination diagrams (Figure 4-139) from Wood (1980), the basalts also show MORB characteristics, with more intermediate samples showing a calc-alkaline, volcanic arc affinity (consistent with the Pearce (2014) Th-Nb plot). The La-Y-Nb plot (Cabanis and Lecolle, 1989) shows most of the mafic and intermediate samples reflecting a calc-alkaline, volcanic arc signature (Figure 4-140). The AFM plot (Irvine and Baragar, 1971, Kuno, 1968, Rollinson, 1993) shows a calc-alkaline fractionation trend from basalt, through intermediate to felsic compositions (Figure 4-141).

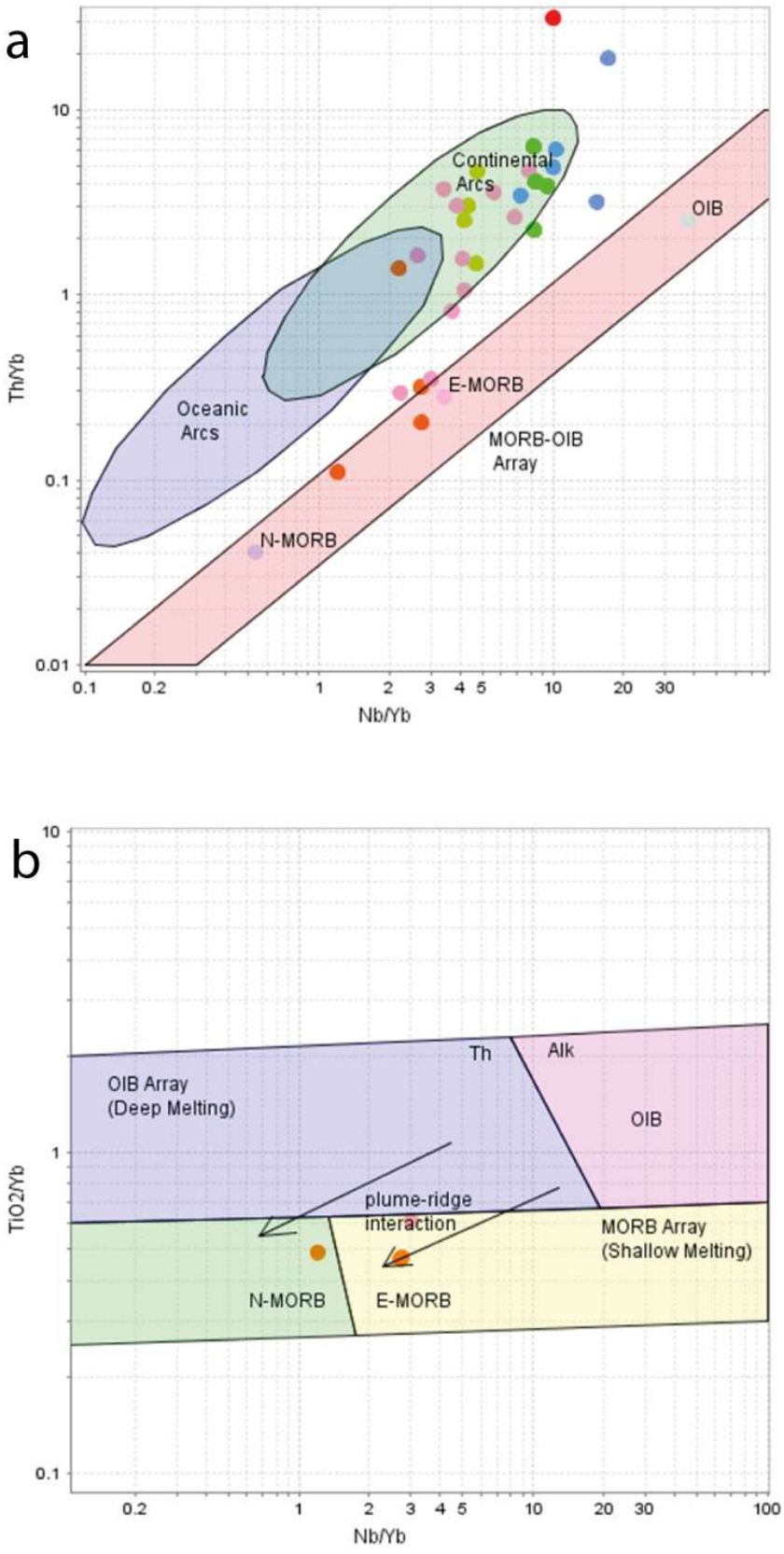

Figure 4-138 - Discrimination diagrams for fingerprinting tectonic setting a) Th/Nb proxy to distinguish volcanic arc settings from mid-oceanic ridge/ocean island basalt settings Pearce (2014) adapted from Pearce (2008). Note that this diagram is robust and works for most rock types, but works best for mafic rocks. b) Ti/Nb proxy to fingerprint samples from the MORB-OIB array (Pearce, 2008). As these are Precambrian samples, an extra filter was applied (Th/Nb<0.2) to remove samples that have experienced significant crustal contamination - as recommended by Pearce (2008).

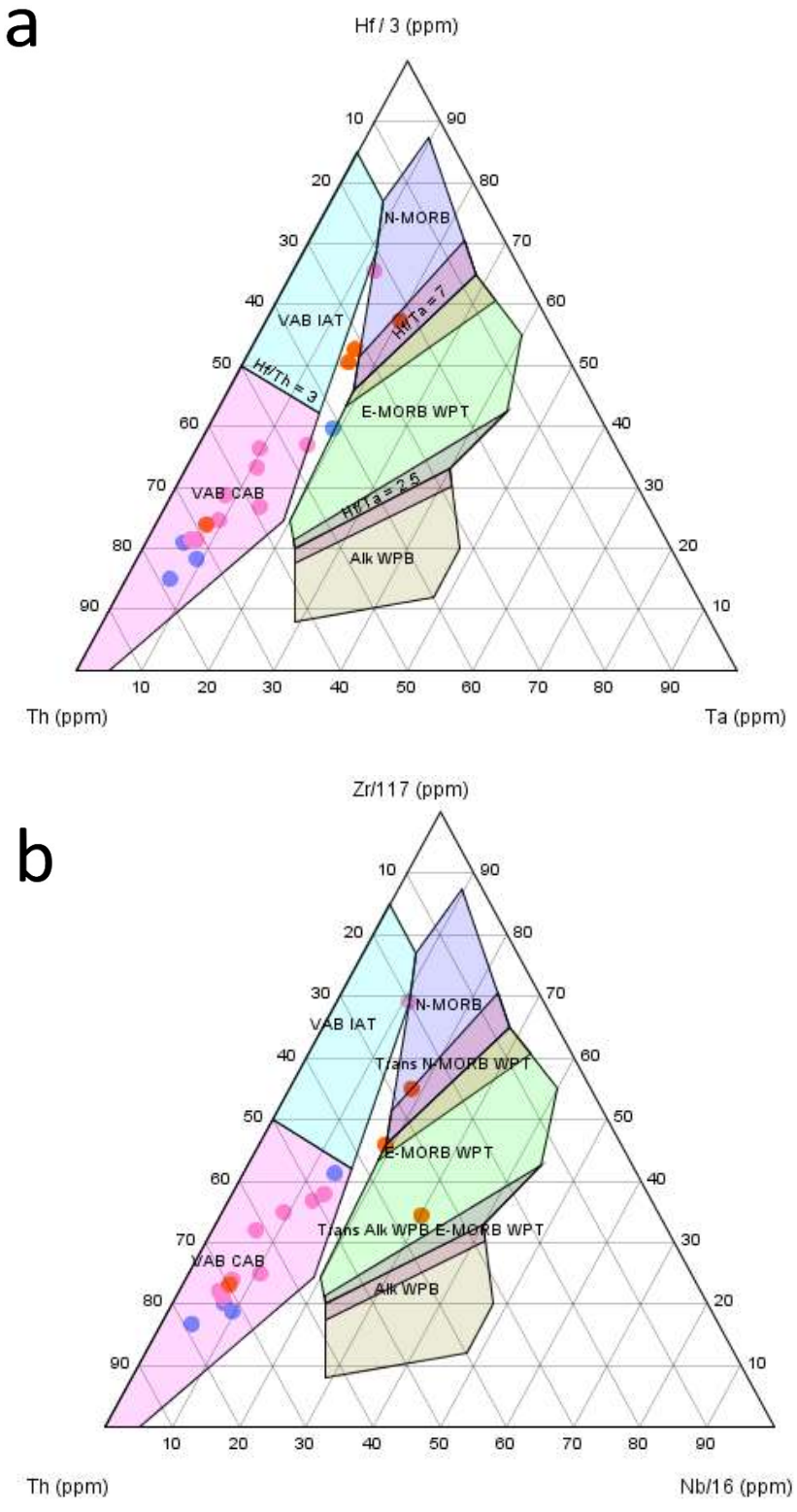

Figure 4-139 – Ternary tectonic discrimination diagrams for mafic and intermediate samples (Wood, 1980) a) Th-Hf/3-Ta discrimination diagram. b) Th-Zr/117-Nb/16 discrimination diagram.

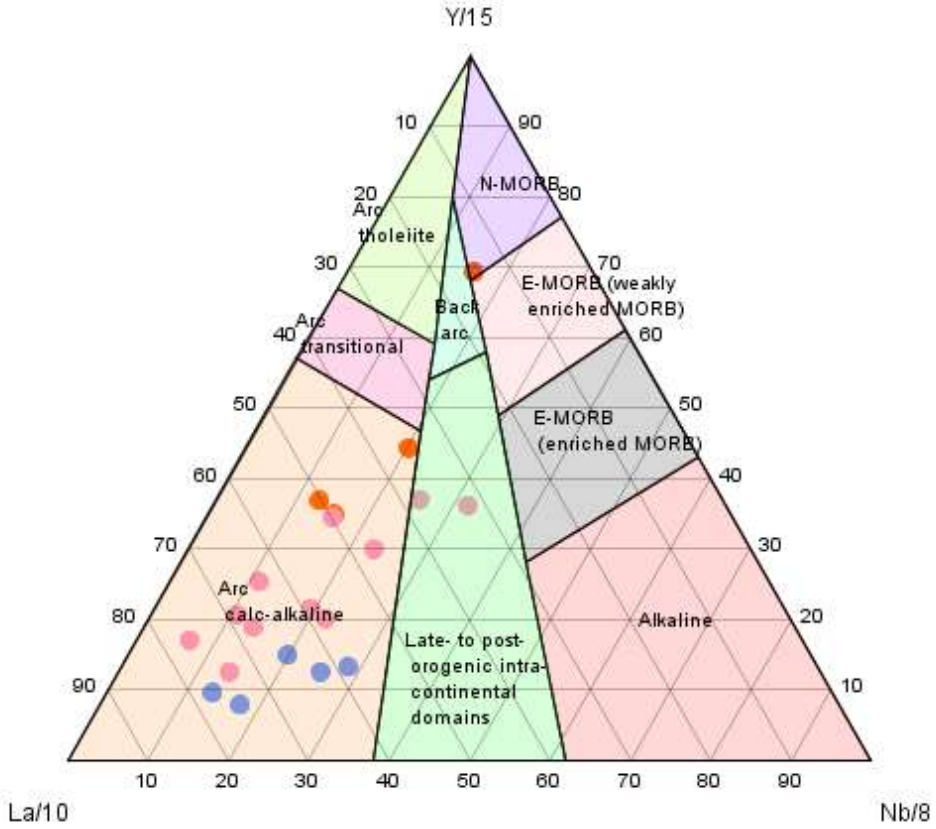

Figure 4-140 – All mafic and intermediate igneous samples from the Sfariat-Bu Daira Terrane, plotted on a La-Y-Nb ternary discrimination diagram (Cabanis and Lecolle, 1989).

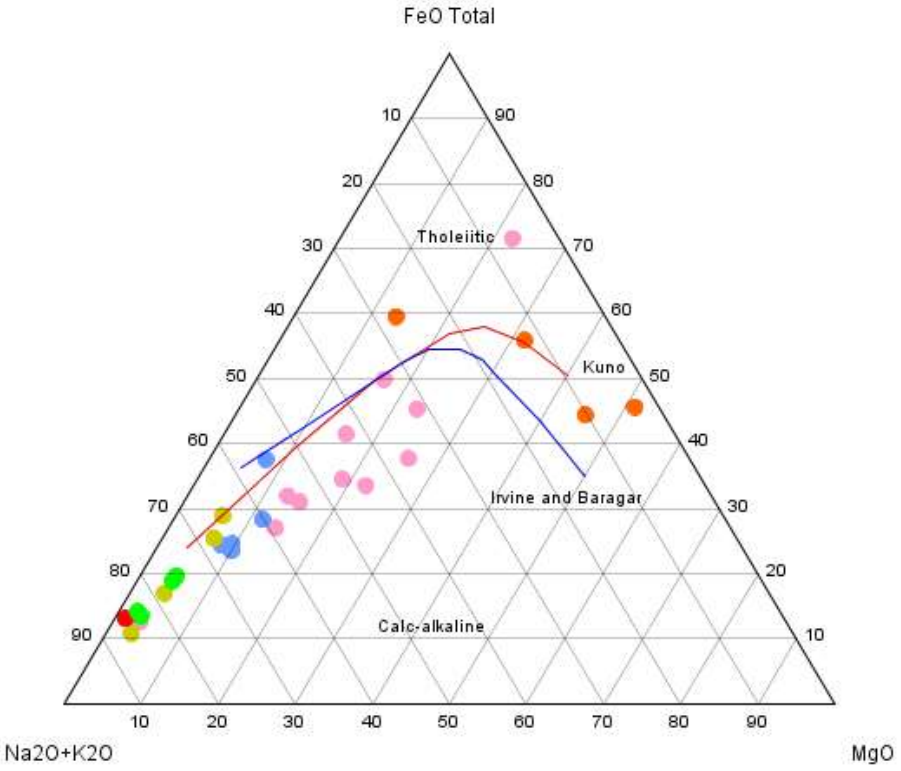

Figure 4-141 – Total Alkali-Iron-Magnesium (AFM) plot (Rollinson, 1993) of all samples within the Sfariat-Bu Daira Terrane with Tholeiitic and Calc-alkaline fractionation trends defined by (Kuno, 1968) and (Irvine and Baragar, 1971).

4.5.1.1.2 Granitic Rocks

A series of diagrams presented in Pearce et al. (1984) are the most commonly used discrimination diagram for felsic rocks. According to these diagrams, granitic rocks within the Sfariat-Bu Daira Terrane display volcanic arc characteristics (Figure 4-142).

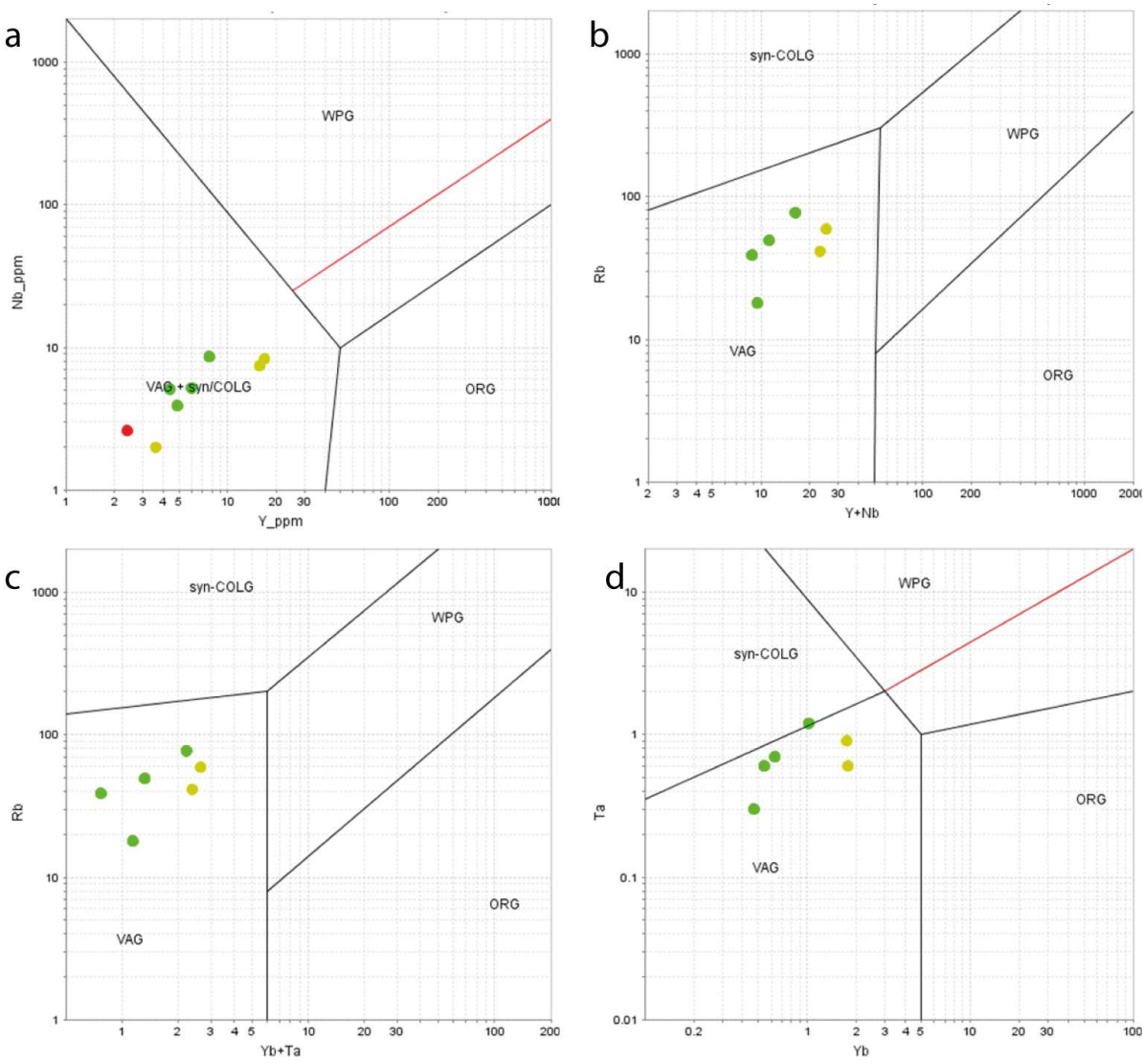

Figure 4-142 – Tectonic discrimination diagrams for granitic rocks (Pearce et al., 1984). VAG – volcanic arc granite, syn-COLG – syn-collisional granite, WPG – within plate granite, ORG – ocean ridge granite. a) Nb vs Y b) Rb vs (Y + Nb) c) Rb vs (Yb + Ta) d) Ta vs Yb.

4.5.1.2 Multi-Dimensional Tectonic Discrimination Diagrams

The steps for the application of the multi-discrimination tectonic discrimination diagrams and the settings used are described in Chapter 3.5.1.2. The same settings/plots are used for the Sfariat-Bu Daira Terrane.

4.5.1.2.1 Mafic Rocks

Excluding cumulate samples from the EAC, there were only four mafic samples in Sfariat-Bu Daira Terrane. This was not enough to get a statistically meaningful result from the multi-dimensional tectonic description diagrams.

4.5.1.2.2 Intermediate Rocks

Intermediate igneous rocks of the Sfariat-Bu Daira Terrane largely display continental arc characteristics with some samples displaying collisional characteristics (Figure 4-143, Table 4-3). Both major and trace elements (Table 4-3) reflect this characteristic when plotted on respective sets of discrimination diagrams defined in Verma and Verma (2013). As this is an old, altered terrane more weighting has been placed on the immobile trace elements for the interpretation (though in this case major element chemistry is consistent). Of the ten intermediate samples from the domain, eight display continental arc characteristics while two indicate a collisional environment (Figure 4-143, Table 4-3).

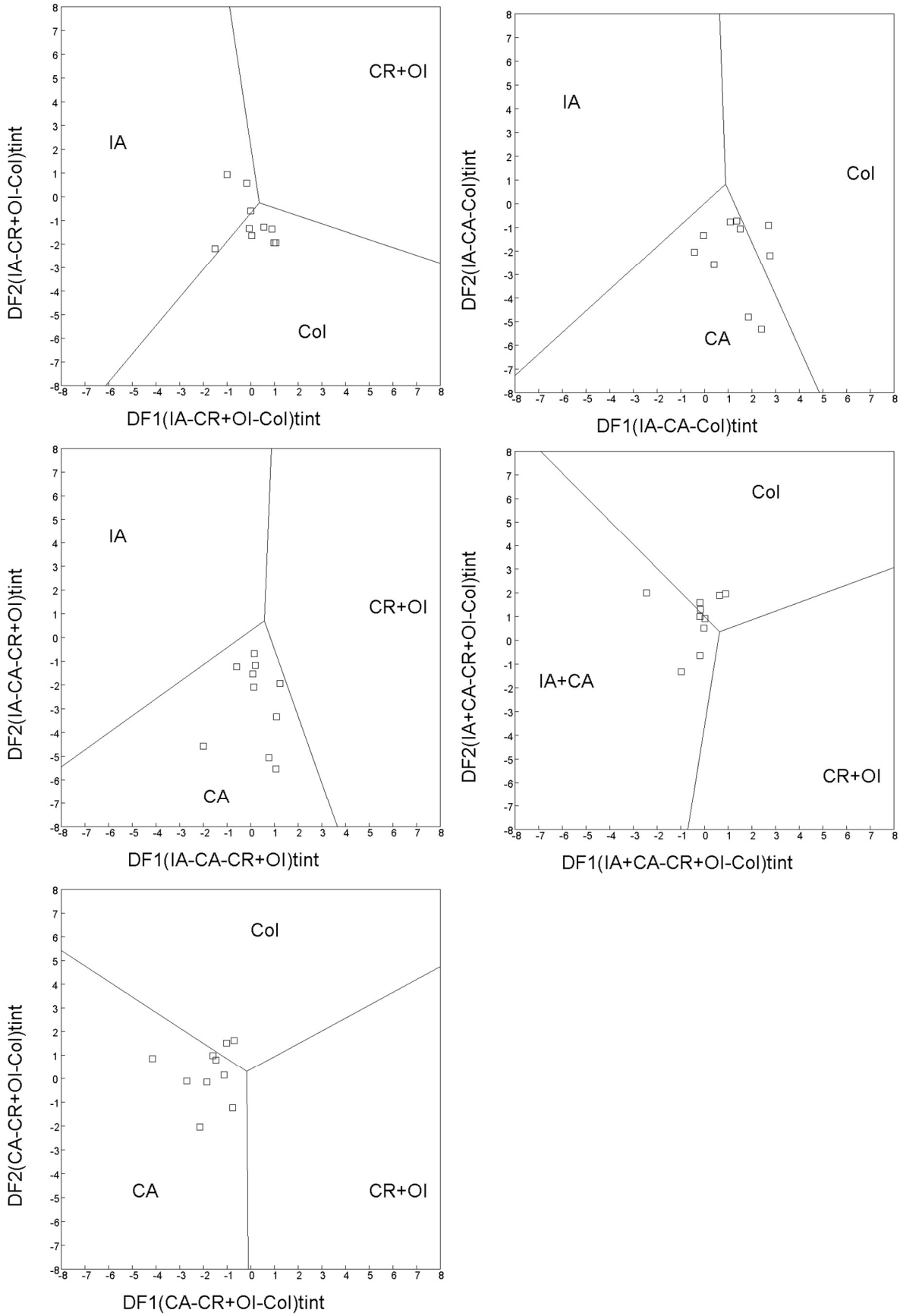

Figure 4-143 – Intermediate igneous rocks from the Sfariat-Bu Daira Terrane plotted on a series of five multi-dimensional discriminant function diagrams based on log-ratios of immobile trace elements (Verma and Verma, 2013). IA – Island Arc, CA – Continental Arc, Col – Collisional, CR+OI – Combined Continental Rift and Ocean Island.

Table 4-3 - Application of multidimensional diagrams to ~2140-2090 Ma intermediate rocks of the Sfariat-Bu Daira Terrane.

Magma type, Figure name	Figure type	Total number of samples	Number of discriminated samples				
			Arc			CR+Ol [x ± s] [p_CR+Ol] Θ	Col [x ± s] [p_Col] Θ
			IA+CA [x ± s] [p_IA+CA] Θ	IA [x ± s] [p_IA] Θ	CA [x ± s] [p_CA] Θ		
Intermediate; Verma and Verma (2013); log-ratios of all major elements	(IA+CA-CR+Ol-Col)	10	5 [0.888±0.151] (0.6249-0.9981)	---	---	0 (0)	5 [0.722±0.234] (0.4538-0.9995)
	(IA-CA-CR+Ol)	10	---	3 [0.99984±0.00017] (0.9996-1.0000)	7 [0.860±0.148] (0.5680-0.9918)	0 (0)	---
	(IA-CA-Col)	10	---	2 [0.99984±0.00006] (0.9998, 0.9999)	5 [0.832±0.102] (0.7285-0.9772)	---	3 [0.731±0.235] (0.4774-0.9406)
	(IA-CR+Ol-Col)	10	---	4 [0.968±0.046] (0.8991-0.9963)	---	0 (0)	6 [0.764±0.145] (0.5554-0.9684)
	(CA-CR+Ol-Col)	10	---	---	6 [0.705±0.215] (0.4552-0.9977)	0 (0)	4 [0.818±0.186] (0.6554-0.9997)
Diagrams based on log-ratios of major elements	***{Σn} {Σprob} [%prob]***	**50**	**{5} {4.4379} [---]**	**{9} {8.8715} [26%]**	**{18} {14.4108} [41%]**	**(Piqué) (Piqué) [0%]**	**{18} {13.6597} [33%]**
Intermediate; Verma and Verma (2013); log-ratios of immobile trace elements	(IA+CA-CR+Ol-Col)	10	6 [0.757±0.204] (0.4979-0.9823)	---	---	0 (0)	4 [0.788±0.194] (0.5600-0.9583)
	(IA-CA-CR+Ol)	10	---	0 (0)	10 [0.854±0.120] (0.6583-0.9900)	0 (0)	---
	(IA-CA-Col)	10	---	0 (0)	8 [0.789±0.159] (0.5792-0.9744)	---	2 [0.843±0.101] (0.7714, 0.9149)
	(IA-CR+Ol-Col)	10	---	4 [0.710±0.208] (0.4741-0.9718)	---	0 (0)	6 [0.872±0.089] (0.7255-0.9649)
	(CA-CR+Ol-Col)	10	---	---	8 [0.864±0.145] (0.6323-0.9957)	0 (0)	2 [0.845±0.058] (0.8039, 0.8856)
Diagrams based on log-ratios of immobile trace elements	***{Σn} {Σprob} [%prob]***	**50**	**{6} {4.5443} [---]**	**{4} {2.8392} [8%]**	**{26} {21.7712} [63%]**	**(Piqué) (Piqué) [0%]**	**{14} {11.7615} [29%]**

IA−island arc; CA−continental arc; IA+CA–combined island and continental arcs, i.e., arc setting; CR−continental rift; OI−ocean island; CR+OI –combined continental rift and ocean island, i.e., within-plate (WP) setting; Col−collision; Θ the probability values for samples from a given locality are represented by (pIA+CA) – probability for the combined island and continental arc setting in the first diagram; [pIA] – probability for the island arc setting in the diagrams; [pCA] – probability for the continental arc setting in the diagrams; [pCR+OI] – probability for the combined continental rift and ocean island setting in all diagrams; [pCol] – probability for the collision setting in the diagrams; − mean ± 1SD (standard deviation) of the probability estimates for all samples discriminated in a given tectonic setting; these are reported in [], the values are rounded mostly following the indications put forth by Verma (2005); the final rows give a synthesis of results as {Σn} {Σprob} [%prob], where {Σn} is the total number of samples or data points plotting in all five diagrams is reported in the column of total number of samples, whereas the sum of samples plotting in a given tectonic field is reported in the respective tectonic field column; {Σprob} is the sum of probability values for all samples plotting in a given tectonic field is reported in the respective tectonic field column; and [%prob] is the total probability of a given tectonic setting expressed in percent after assigning the probability of IA + CA to IA and CA (using weighing factors explained in Verma and Verma, 2013).

4.5.1.2.3 Felsic Rocks

As was the case with the felsic rocks in the Leaareig Terrane (Chapter 3.5.1.2.3), the discrimination diagrams using more mobile major elements showed a bias towards island arc settings compared to continental arc setting (although they consistently identifies them as volcanic arc). As these rocks in this region are old and altered, only immobile trace element geochemistry (Verma et al., 2013) has been used for tectonic discrimination of the felsic rock as was the solution for the Leaareig Terrane when encountering similar problems in Archaean rocks). The felsic samples display continental arc characteristics (61.5%) with potentially a collisional component (20.6%) (Figure 4-144, Table 4-4).

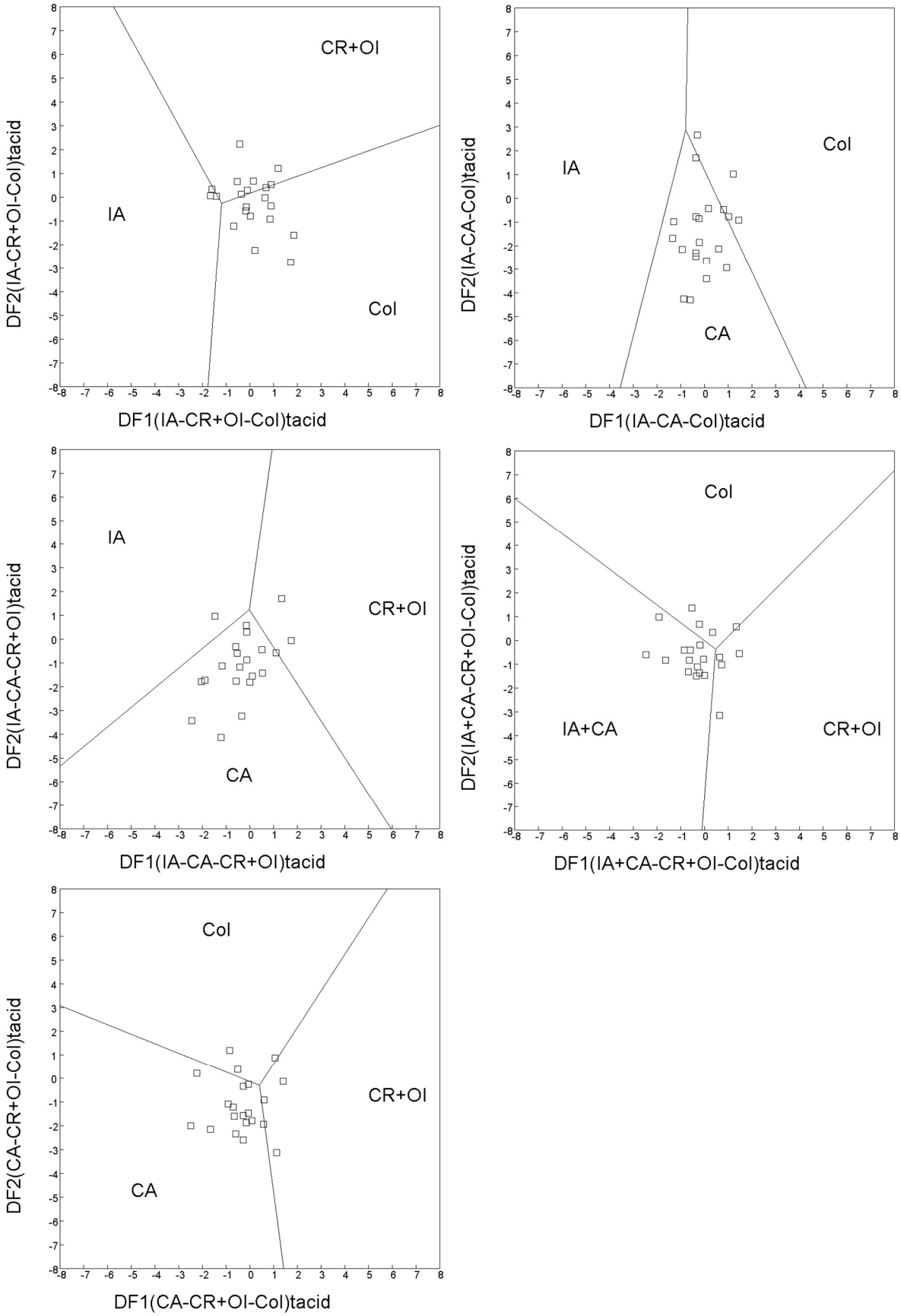

Figure 4-144 – Felsic igneous rocks from the Sfariat-Bu Daira Terrane plotted on a series of five multi-dimensional discriminant function diagrams based on log-ratios of immobile trace elements (Verma et al., 2013). IA – Island Arc, CA – Continental Arc, Col – Collisional, CR+OI – Combined Continental Rift and Ocean Island.

Table 4-4 - Application of multidimensional diagrams to ~2140-2090 Ma acid rocks of the Sfariat-Bu Daira Terrane.

Magma type, Figure name	Figure type	Total number of samples	Number of discriminated samples				
			Arc			CR+OI [x ± s]	Col [x ± s]
			IA+CA [x ± s] [p_IA+CA] Θ	IA [x ± s] [p_IA] Θ	CA [x ± s] [p_CA] Θ	[p_CR+OI] Θ	[p_Col] Θ
Acid; Verma et al. (2013); log-ratios of immobile trace elements	(IA+CA-CR+OI-Col)	21	13 [0.787±0.121] (0.5669-0.9756)	---	---	4 [0.676±0.148] (0.5017-0.8414)	4 [0.649±0.125] (0.5056-0.8060)
	(IA-CA-CR+OI)	21	---	1(0.8875)	18 [0.910±0.134] (0.5287-0.9999)	2 [0.949±0.049] (0.9140, 0.9831)	---
	(IA-CA-Col)	21	---	0 (0)	16 [0.851±0.124] (0.5076-0.9852)	---	5 [0.627±0.126] (0.5163-0.8319)
	(IA-CR+OI-Col)	21	---	3 [0.592±0.128] (0.4881-0.7347)	---	7 [0.735±0.176] (0.5286-0.9970)	11 [0.875±0.147] (0.5060-0.9999)
	(CA-CR+OI-Col)	21	---	---	15 [0.807±0.164] (0.4897-0.9918)	3 [0.673±0.169] (0.4880-0.8198)	3 [0.654±0.159] (0.5248-0.8313)
Diagrams based on log-ratios of immobile trace elements	***{Σn} {Σprob} [%prob]***	**105**	**{13} {10.2265} [---]**	**{4} {2.6643} [3.9%]**	**{49} {42.0808} [61.5%]**	**{16} {11.7608} [14.0%]**	**{23} {17.3227} [20.6%]**

IA−island arc; CA−continental arc; IA+CA–combined island and continental arcs, i.e., arc setting; CR−continental rift; OI−ocean island; CR+OI –combined continental rift and ocean island, i.e., within-plate (WP) setting; Col−collision; Θ the probability values for samples from a given locality are represented by (pIA+CA) – probability for the combined island and continental arc setting in the first diagram; [pIA] – probability for the island arc setting in the diagrams; [pCA] – probability for the continental arc setting in the diagrams; [pCR+OI] – probability for the combined continental rift and ocean island setting in all diagrams; [pCol] – probability for the collision setting in the diagrams; − mean ± 1SD (standard deviation) of the probability estimates for all samples discriminated in a given tectonic setting; these are reported in [], the values are rounded mostly following the indications put forth by Verma (2005); the final rows give a synthesis of results as {Σn} {Σprob} [%prob], where {Σn} is the total number of samples or data points plotting in all five diagrams is reported in the column of total number of samples, whereas the sum of samples plotting in a given tectonic field is reported in the respective tectonic field column; {Σprob} is the sum of probability values for all samples plotting in a given tectonic field is reported in the respective tectonic field column; and [%prob] is the total probability of a given tectonic setting expressed in percent after assigning the probability of IA + CA to IA and CA (using weighing factors explained in Verma and Verma, 2013).

4.5.2 Tectonic Setting

All tectonic discrimination diagrams presented, both traditional and multi-dimensional, indicate strongly that the Sfariat-Bu Daira Terrane represents a calc-alkaline series of rocks (Figure 4-141) formed in a continental arc setting of evolving maturity, with some rocks displaying collisional characteristics. As with the Leaareig Terrane, this is consistent with a

Japanese-type island arc (Figure 4-145), though the Sfariat-Bu Daira Terrane appears to be more evolved.

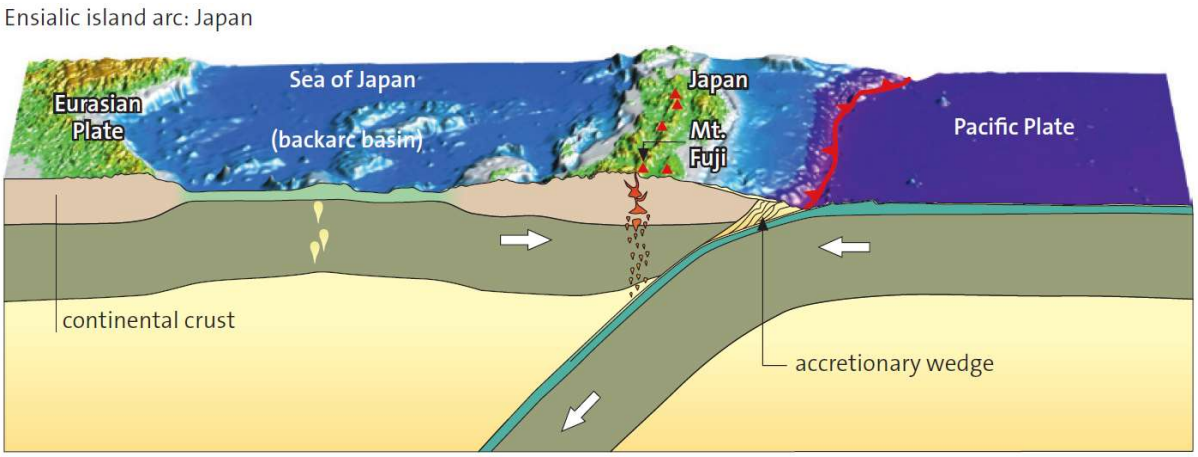

Figure 4-145 – Illustration of the Japanese "ensialic island arc", where the oceanic lithosphere is subducted beneath continental lithosphere and the island arc is underlain by continental crust. The island arc of this system is separated from the continent by a marine basin underlain by oceanic crust. (Frisch et al., 2011)

The Pearce (2014) Th-Nb proxy diagram shows that most of the samples contain continental arc signatures, the increasing acidity of the magmas corresponding to a increasing continental arc signature (Figure 4-138a). Some basaltic and andesitic basalt samples plot in the ocean arc-continental arc transition region with increasingly continental arc signatures seen in rhyolite/dacite, trachyte, trachy-andesite, and alkali rhyolite. These results are consistent with the intermediate and felsic rocks as observed on the immobile trace element multidimensional diagrams (Verma and Verma, 2013, Verma et al. 2013) revealing a continental arc setting with some samples displaying collisional characteristics (Figure 4-143 and Figure 4-144, Table 4-3 and Table 4-4). Samples displaying collisional characteristics (discussed in more detail in Section 6.2.3), represent the collision of the Leaareig and Sfariat-Bu Daira Terranes, and later the collision between the Archaean and Palaeoproterozoic terranes.

As outlined in Section 4.1.6, island arc and continental arc settings are proposed for the formation of different components of the EAC. The presence of megacrystic anorthosite is indicative of an island arc setting (possibly similar to Japan; Figure 4-145, Figure 4-105;

Section 4.1.6.1), while the presence of massif-type anorthosite indicates a thickened continental arc setting (like that of the Andes; Figure 4-106; Section 4.1.6.2). Furthermore clinopyroxene discrimination diagrams from the massif-type anorthosite (Section 4.1.4.4) demonstrate a parental island arc tholeiitic magmas (Figure 4-99) possibly indicating proximity to the subducting slab (Murphy, 2007).

Looking at the terrane as a whole; the Elmalhat, Oum Abana, Anajim Guebli and Riche Anajim Domains each represent different components of the same system. The Elmalhat Domain represents the subduction zone-proximal mid-crustal remnants of the continental arc system with the contemporaneous Oum Abana domain representing the extrusive (and shallow intrusive) equivalents. Igneous rocks from the terrane display an evolution to a stronger continental arc setting over time (i.e. Japanese- to Andean-arc settings). The Anajim Guebli, and Riche domains represent the deformed remnants of the continental platform sediments, deposited at what was then the edge of the Palaeoproterozoic craton (Schofield et al., 2006).

5.0 Metallogeny of the Leaareig and Sfariat Bu-Daira Terranes

Due to a lack of exploration in the region, the metallogeny of the Precambrian of Western Sahara had never been described in a holistic manner. Lehbib Nayem et al. (2016a, b), was the first to described the mineral deposits of Western Sahara noting the presence of orogenic gold, orthomagmatic chromitite, Fe-Ti mineralisation and Banded Iron Formation (BIF). Lehbib Nayem et al. (2016b) additionally noted the presence of orogenic gold (±PGM) mineralisation in association with listwanites in the Elmalhat Domain. As part of this project a metallogenic synthesis has been constructed for the Leaareig and Sfariat-Bu Daira Terranes. Styles of mineralisation noted within the study area include orogenic gold, PGE-bearing chromitite, orthomagmatic Fe-Ti(-V), magmatic sulphides within the EAC, and Superior-type iron formations.

Assay results presented in this chapter are from an internal Hanno Resources Limited report by Fall (2017). Anomalous rock chip geochemisty results from the study area are presented in Appendix E.

5.1 **Gold**

Evidence for hypogene orogenic gold mineralisation is observed across the study area, largely focused in the Oum Abana volcanosedimentary rocks, and/or associated with granitoid intrusions. The gold is mostly hosted within quartz veins, although in some sites mineralisation has been observed in host rocks including magnetite, ferruginous chert, and hydrothermally altered granite. Evidence of near surface enrichment is also observed in the region with extensive artisanal pitting, from which gold nuggets have been extracted.

5.1.1 Orogenic Gold

5.1.1.1 Introduction to Orogenic Gold

In a review of gold deposits within collisional orogenic belts, Groves et al. (1998) noted that a wide variety of gold deposits shared characteristics such as tectonic setting, structural controls, geochemistry of alteration, fluid and isotopic composition, and ore-element association. Hence, Groves et al. (1998) suggested the now widely accepted term 'orogenic gold deposit' to classify a variety of gold deposits that had previously been referred to as 'mesothermal' or 'lode-gold', and had been classified according to ore associations, host sequences, form, or location. Orogenic gold deposits share many characteristics including:

1) timing (very late to post-peak metamorphic);
2) location (consistently in metamorphosed fore-arc, back-arc and terrane accretion settings (Figure 5-1));
3) hydrothermal addition of K, S, CO_2, H_2O, Si, and Au, ± As, B, Bi, Na, Sb, Te, and W; and
4) ore forming fluids (aqueous-carbonic fluids (H_2O–CO_2–CH_4–N_2–H_2S), with low-to-moderate salinity) (Gebre-Mariam et al., 1995, Goldfarb et al., 2005, Goldfarb et al., 2001, Groves et al., 1998, Goldfarb and Groves, 2015).

The source of the gold-bearing hydrothermal fluids is the subject of much debate. Possible sources of the fluids include metamorphic fluids from 1) greenschist and amphibolite facies metamorphism relating to orogenesis; (2) devolatilization of accreted oceanic rocks along an active continental margin caused by crustal thickening and radiogenic heating, slab roll-back and extension, subduction of spreading ridges, and integration with mantle plumes; and 3) from the mantle, enriched by fluids expelled from the subducting slab (Goldfarb and Groves, 2015). The auriferous aqueous-carbonic fluids are transported through structures in the crust, and form

gold deposits if the gold is efficiently precipitated. Efficient gold precipitation requires the destabilisation of gold by changing one or more critical characteristics of the fluid including 1) a reduction in confining pressure causing H_2O–CO_2 phase separation; 2) a change to the total amount of CO_2 in the fluid; 3) a reduction in total amount of sulphur in the fluid; 4) a change in oxygen fugacity (fO_2); and/or 5) a change in pH (Mernagh and Bierlein, 2008). These can be structurally controlled (i.e. change in confining pressure), or can be caused by wall rock interaction (or fluid mixing) (Mernagh and Bierlein, 2008).

General characteristics of orogenic gold deposits pertinent to exploration include that:

1) they are generally related to major fault systems cutting through volcanosedimentary crust;
2) they have relatively consistent chemistry resulting in broadly similar mineralogy and alteration assemblages;
3) igneous intrusions represent rheologically favourable rock for the location of ore-bearing structures;
4) certain rock types (such as the Golden Mile Dolerite, Kalgoorlie (Phillips, 1986)) represent chemically favourable hosts; and
5) they are generally located in greenschist-facies domains (though some Achaean deposits are associated with amphibolite facies conditions) (Goldfarb and Groves, 2015).

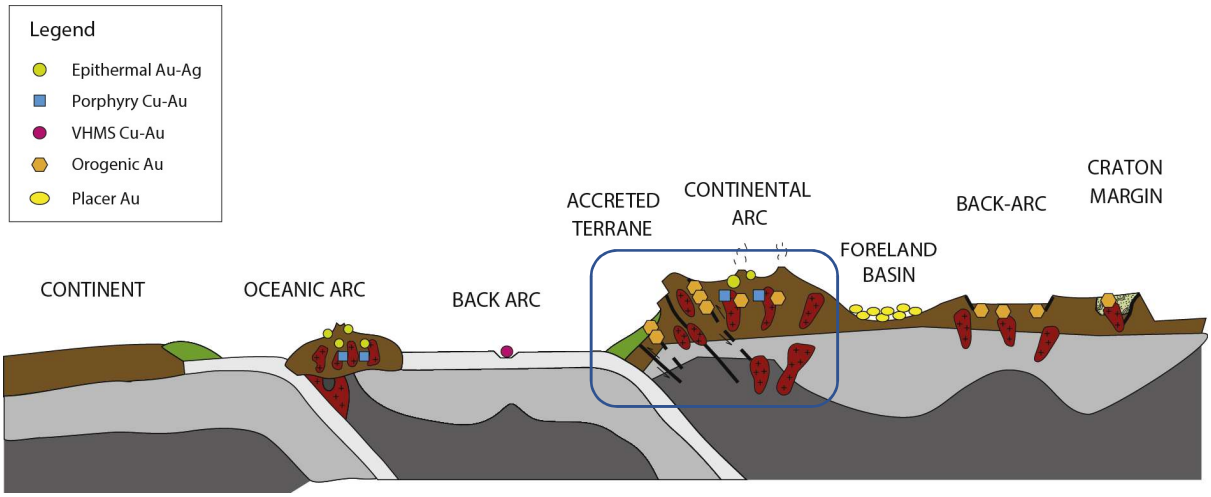

Figure 5-1 - Tectonic settings of orogenic and other of gold deposits, modified from Goldfarb and Groves (2015) after Groves et al. (1998). The Sfariat-Bu Daira and Leaareig Terranes are characterised by the tectonic environment illustrated by the blue rectangle.

5.1.1.2 Mineralisation in the Study Area

Several sites of orogenic gold mineralisation have been identified by Hanno Resources Limited mainly in the north of the study area (Figure 5-2a). Agarasras Labiad and G52 (Oum Abana belt) represent the two most significant occurrences of orogenic gold within the region, with anomalous concentrations of gold in rock chip samples also having been observed at Moug El Kaleb (Elmalhat Domain), Guelb Koujil, Agarasras Lakhadar (Agarasras Lakhadar Domain), Taghsoumat (Taghsoumat-Aghsoumal Domain) and Elmalhat (Elmalhat Domain) (Fall, 2017). Elevated copper contents of rock chip samples broadly correlate with values of gold (Fall (2017); Figure 5-2b), except in the Elmalhat Anorthosite Complex (EAC) where copper is associated with magmatic sulphides (Section 5.2). Disseminated chalcopyrite is observed in gold-bearing quartz veins across the study area suggesting that both copper and gold were likely introduced during hydrothermal event(/s).

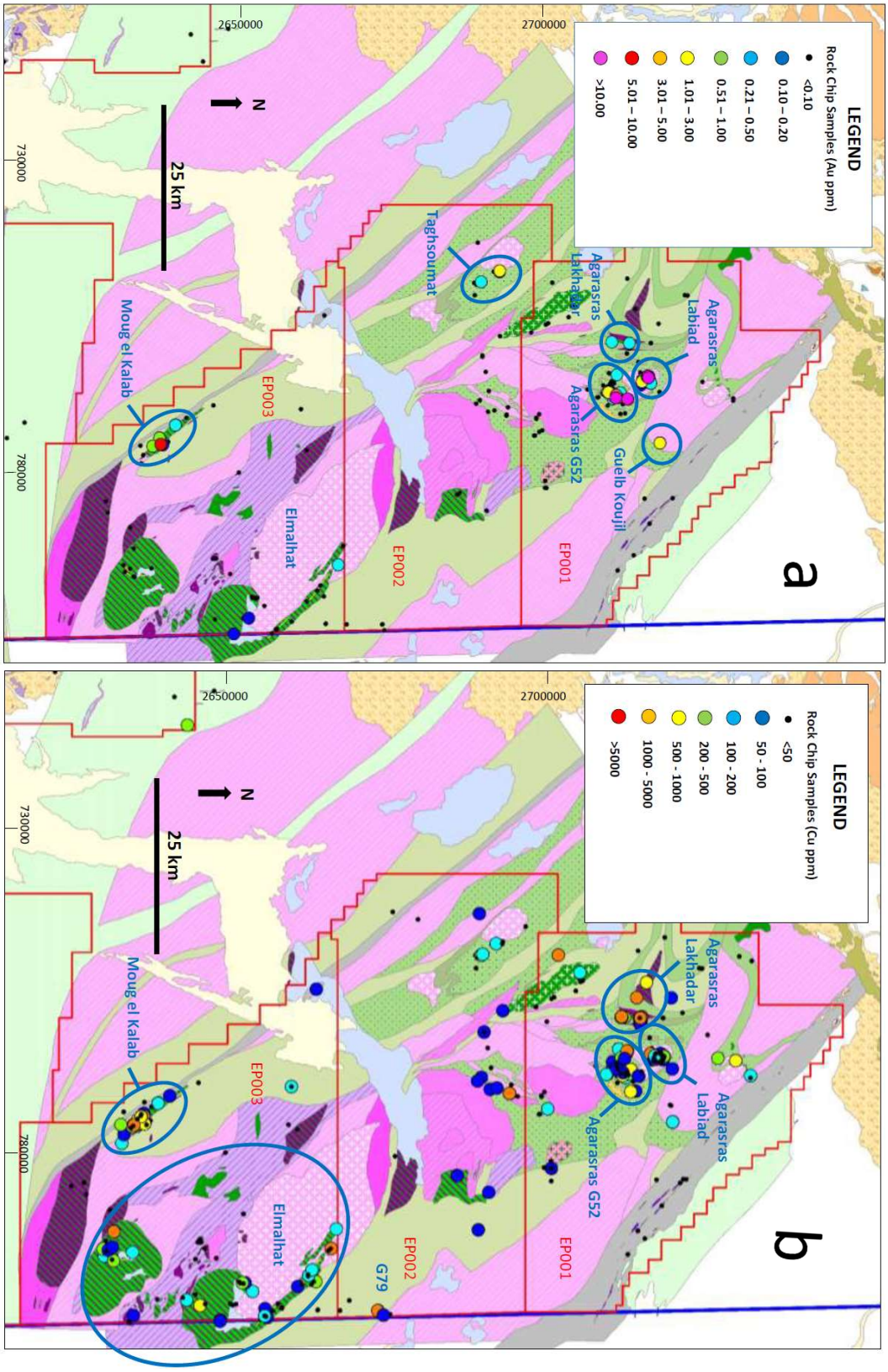

Figure 5-2 – a) Gold and b) Copper rock chip assay results from across the study area (from Fall, 2017)

5.1.1.2.1 Agarasras G52

The Agarasras G52 mineralisation is defined by a soil sample anomaly and assay results from rock chip samples (Figure 5-3). The soil sample anomaly (>100 ppb Au, up to 930 ppb Au) extends over a strike of 1.5 km, and broadly corresponds with disseminated sulphides on the sheared contact between the granitoid intrusion and rhyolite (Figure 5-3a).

Rock chip sampling reveals mineralisation of carbonate-altered, pyrite-bearing granite (up to 1.3 ppm Au), and pyrite-bearing ferruginous chert (up to 12.8 ppm Au; Figure 5-4a). The gold in these samples is probably associated with the sulphide grains. Gold is also found within quartz veins. Tourmaline- and sulphide-bearing quartz veins in the north of the G52 region near the contact with the Agarasras Labiad intrusion, have visible gold (Figure 5-3 b, c) and grades of up to 13,439 ppm Au.

The gold soil anomaly corresponds with the sulphide-related ferruginous chert and altered granite mineralisation, with no soil anomaly present close to the visible gold-bearing quartz vein (Figure 5-3). Conversely, a soil anomaly is observed in the copper close to the visible gold, with no evidence for enrichment associated with mineralisation hosted in ferruginous chert and altered granite (Figure 5-5).

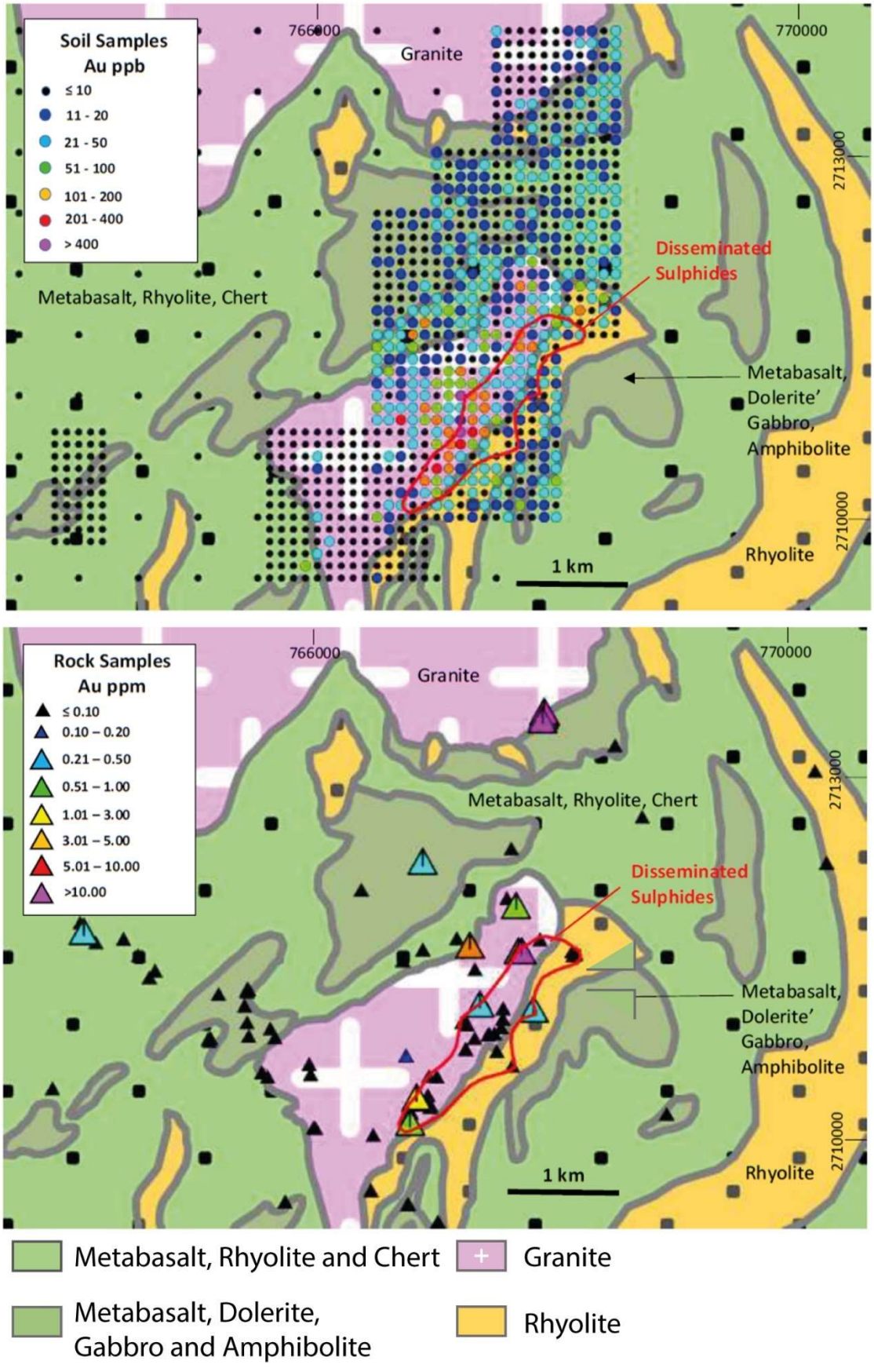

Figure 5-3 – Geological map of the G52 region with disseminated sulphides across the granite-rhyolite contact (from Fall, 2017). Overlay of gold anomalies in a) in soil samples, and b) rock chip samples corresponding to disseminated sulphides.

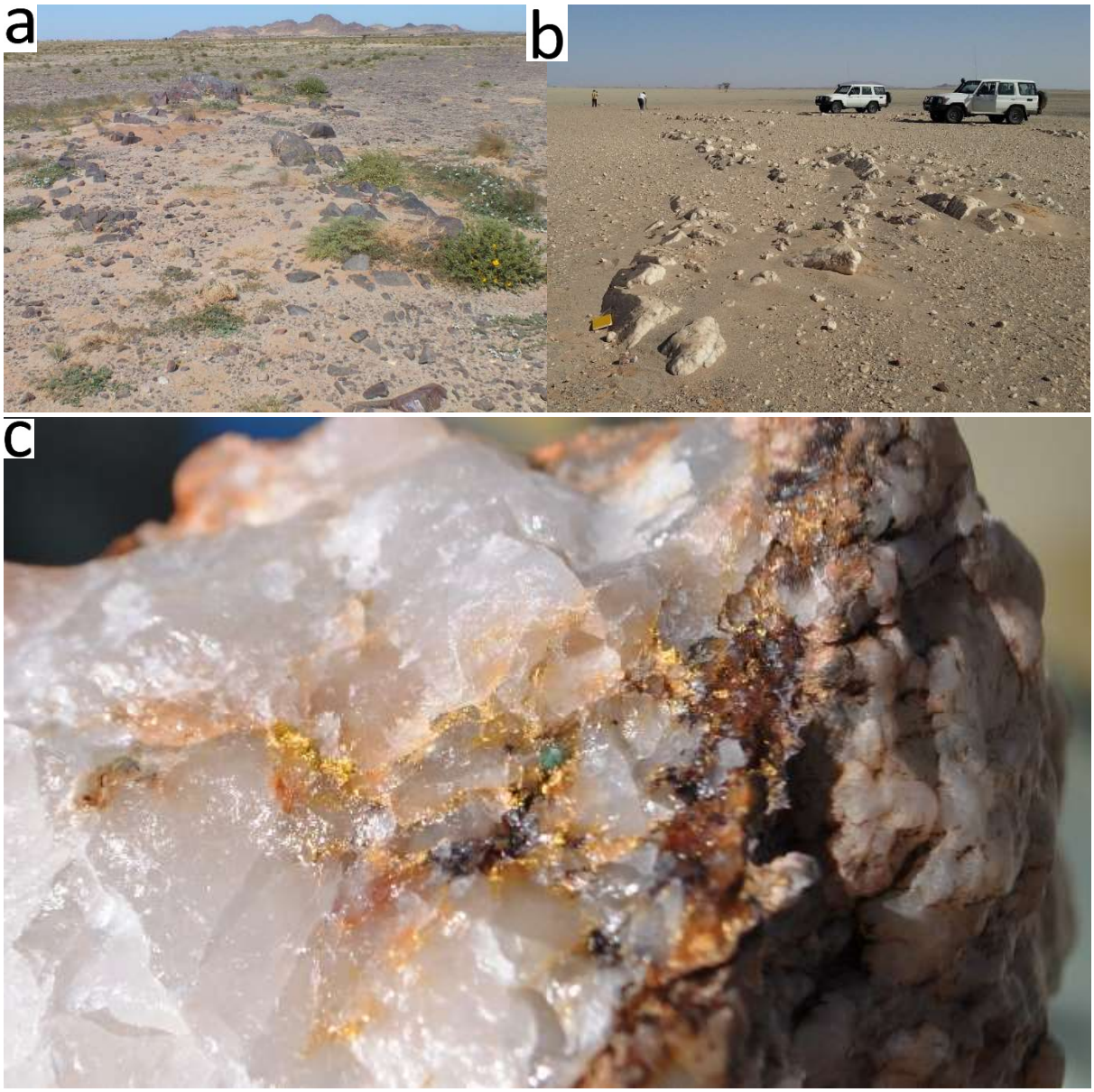

Figure 5-4 – Field photograph of a) an outcrop of mineralised ferruginous chert (UTM 28 767745 mE, 2711509 mN). b) an outcrop of mineralised (visible gold bearing) quartz vein near the contact with the Agarasras Labiad intrusion (UTM 28 767918 mE, 2713426 mN). c) visible gold in quartz vein (UTM 28 767918 mE, 2713426 mN).

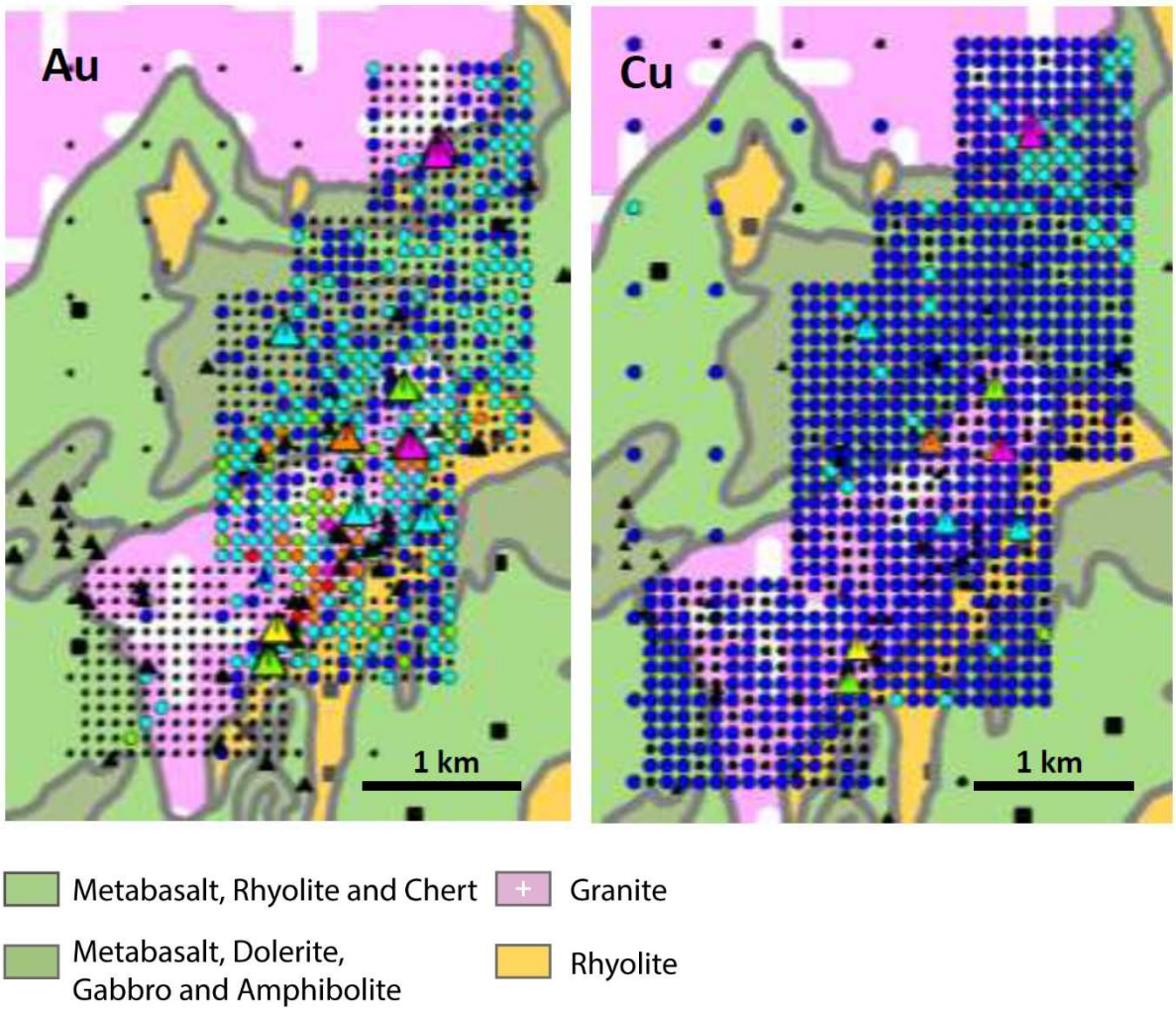

Figure 5-5 – Au and Cu soil results overlain on Au rock chips results for Agarasras G52 (modified from Fall, 2017). (See legend in for Au data). For Cu soils: black = <20 ppm, dark blue = 20 – 50 ppm and light blue = 50 – 100 ppm).

5.1.1.2.2 Agarasras Labiad

Gold mineralisation in the Agarasras Labiad intrusion is largely hosted in tourmaline-bearing quartz-carbonate veins (± pyrite) where rock chip samples have returned grades of up to 20.8 ppm Au (Figure 5-6). The zone of mineralisation strikes over 1500m on a northwest-southeast trend (Lyche, 2012). No significant mineralisation of the host rock has been observed, though grades of up to 2.48 ppm Au are present on the immediate contact with mineralised veins.

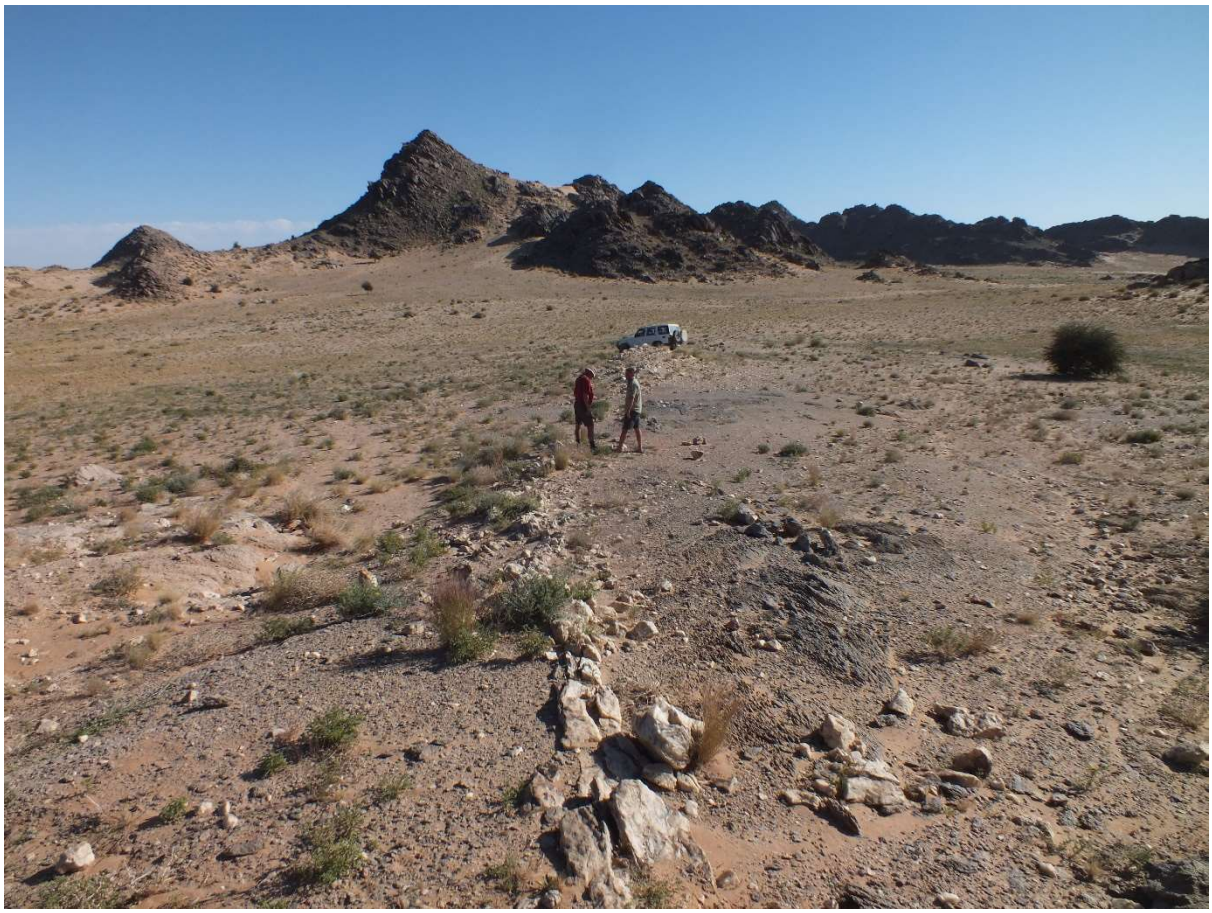

Figure 5-6 – Field photograph of mineralised quartz vein in sheared granite at Agarasras Labiad (UTM 28 764299mE, 2716679 mN).

5.1.1.2.3 Moug El Kaleb (Cu-Au)

Mineralisation at Moug El Kaleb is hosted within hydrothermally altered magnetite (Figure 5-7) in association with gabbro, anorthosite and ultramafic rocks, and in pyrite/arsenopyrite-bearing quartz-carbonate veins immediately east, hosted in metasedimentary rocks. Values of up to 0.58 ppm Au and 1.32% Cu are observed in rock chip samples from the altered magnetite and up to 9.97 ppm Au within the quartz carbonate vein (Figure 5-8 a, b).

The magnetite layer forms part of the anorthosite at Moug El Kaleb and is proximal to the Taghsoumat shear zone (Figure 5-8). The magnetite is interpreted as an orthomagmatic magnetite layer relating to the anorthosite complex (Section 4.1.2.2.3.3). The gold mineralisation is interpreted as orogenic, formed from auriferous fluids from the Taghsoumat shear zone with the pre-existing magnetite layer forming a chemical trap for deposition.

Copper mineralisation is known to occur elsewhere within the EAC associated with magmatic sulphides (more detail in Section 5.2). Copper and nickel enrichment within sulphide-bearing samples in the south of the anorthosite intrusion (Figure 5-8 b, c) indicate that this style of mineralisation is also present within the Moug El Kaleb anorthosite. Therefore, the provenance of the copper enrichment in the magnetite seam likely relates to remobilisation and reprecipitation of copper from magmatic sulphides by the auriferous hydrothermal fluids.

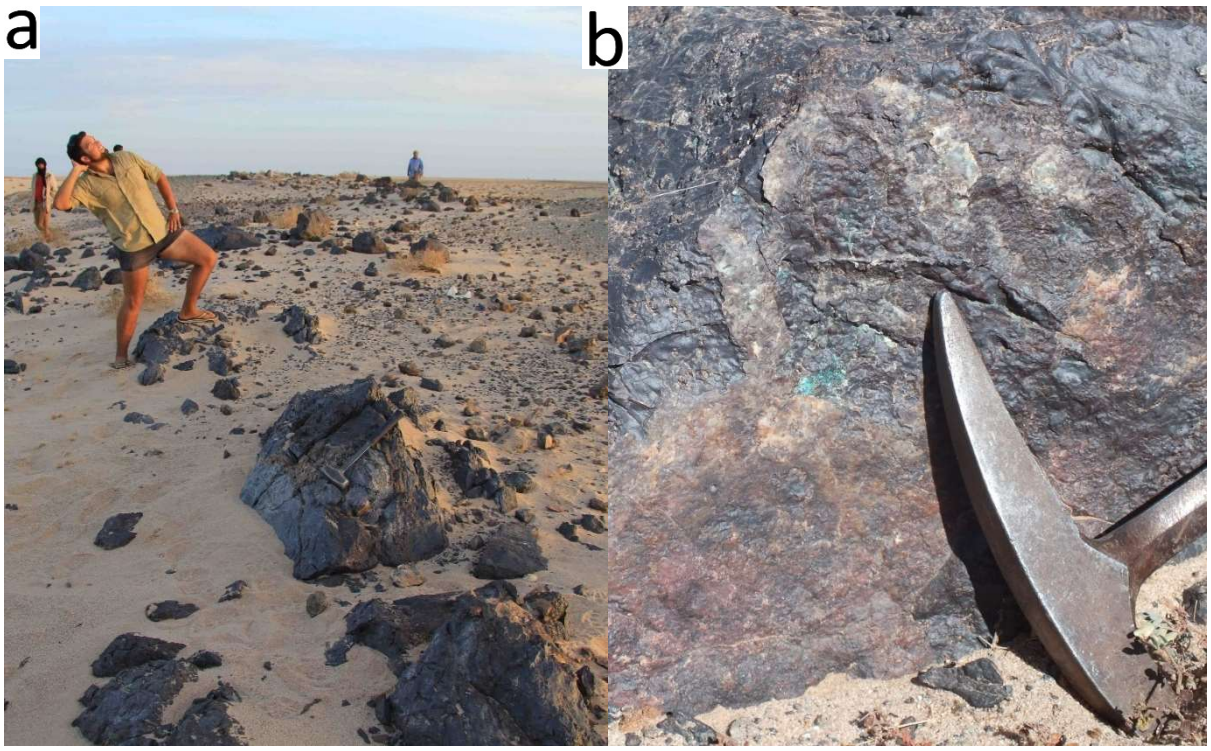

Figure 5-7 – Field photograph of a) an outcrop (UTM 28 774116 mE, 2636679 mN), and b) close up photographs silicified, gold and copper-bearing magnetite at Moug El Kaleb Labiad (UTM 28 774135 mE, 2636651 mN).

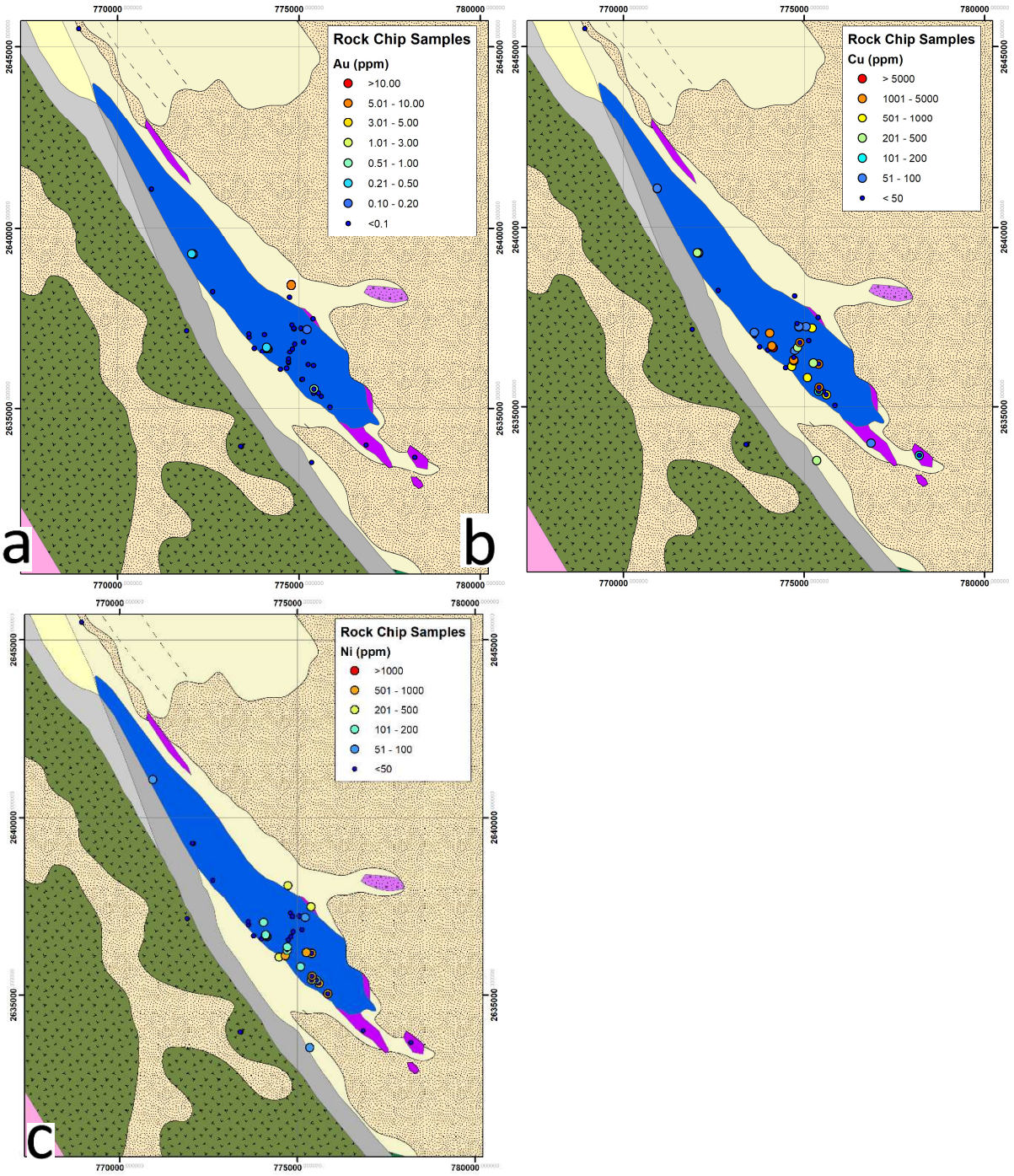

Figure 5-8 – Map of the Moug El Kaleb region with rock chip sample assay results overlaid. a) Au (ppm); b) Cu (ppm); c) Ni (ppm)

5.1.1.2.4 Guelb Koujil

Grades of up to 2.47 ppm Au are observed in disseminated pyrite-bearing quartz veins at Guelb Koujil in the east of the study area (Figure 5-2a).

5.1.1.2.5 Agarasras Lakhadar

A series of ~1-2m wide E-W trending chalcopyrite-, and malachite-bearing quartz veins are present to the south of the Agarasras Lakhadar hills (Figure 5-9). Low grade values of 0.37 ppm Au are present in these for chalcopyrite-bearing quartz, and 0.22 ppm Au in altered pyroxenite, at the base of the Agarasras Lakhadar ophiolite suite.



Figure 5-9 – Photographs of a chalcopyrite-bearing quartz vein cross-cutting the dolerite unit at Agarasras Lakhadar (Combs, 2012) (UTM 28 758843 mE, 2710849 mN).

5.1.1.2.6 Taghsoumat

A value of 1.70 ppm Au was observed in a sample from a pyrite-bearing quartz vein in the Taghsoumat-Aghsoumal volcanosedimentary belt. Soil sampling reveals an anomaly up to 53 ppb proximal to the 1.70 ppm Au rock chip sample.

Although not sampled, a region of hydrothermal alteration in the south of the belt consists of extensive quartz veining, ranging from sheeted veins up to 10cm wide, to massive quartz veins 100m in width, striking 600m. Massive tourmaline is present in these veins (Fall (2017); Figure 5-10).



Figure 5-10 – Field photograph of tourmaline-bearing quartz vein in the south of the Taghsoumat-Aghsoumal volcanosedimentary belt (UTM 28 747530 mE, 2692452 mN).

5.1.1.2.7 Elmalhat

Minor gold mineralisation is observed just to the south of the northern limb. A series of sulphide-bearing quartz veins hosted in orthogneiss in the southern portion of the northern limb contained up to 1.02 ppm Au. A sample from sulphide-bearing listwanite near the northern limb of the EAC returned a grade of 0.23 ppm Au.

5.1.2 Near-surface Enrichment

Evidence for near-surface enrichment of gold mineralisation exists in the form of extensive artisanal pitting across the region (Figure 5-11), from which gold nuggets have been extracted (Figure 5-12). The initial discovery of gold in the region in 2013 has led to a recent artisanal influx. Artisanal pits have been found to the west of Agarasras Labiad, southeast of Taghsoumat, and to the north of the northern limb of Elmalhat (Figure 5-11). These workings consist of shallow diggings, targeting gold nuggets through the use of metal detectors. The nuggets (Figure 5-12) have been found at or near the base of the overburden with a calcrete layer below (Figure 5-11e). The artisanal pits to the north of the northern limb of the EAC go deeper to ~3.5m (Figure 5-11a), apparently targeting a laminated quartz vein hosted in metavolcanics (not yet sampled).

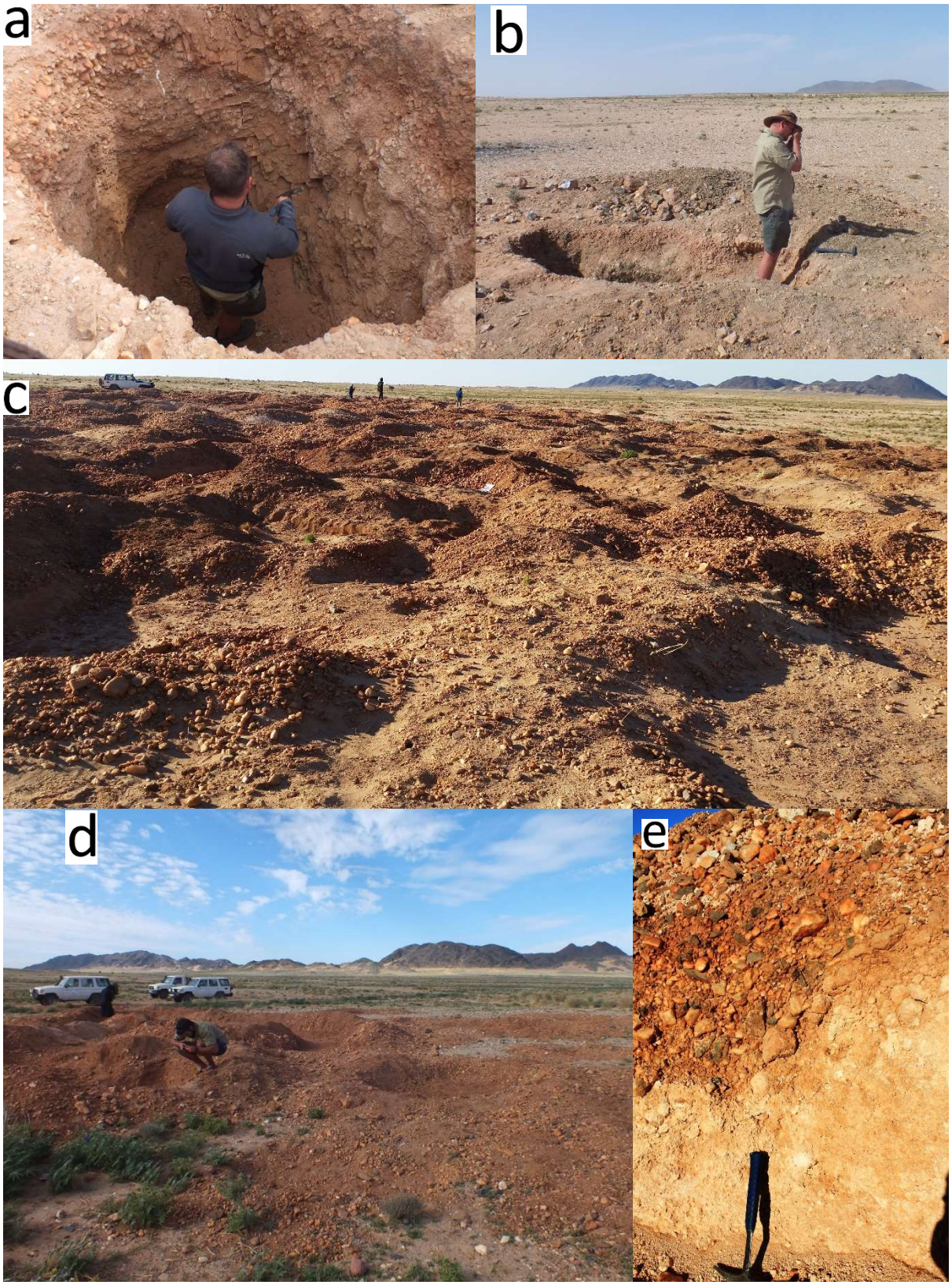

Figure 5-11 – Field photograph of a) a ~3m deep artisanal pit north of the northern limb of the EAC (UTM 28 795326mE, 2669405mN). b) an artisanal pit in the Taghsoumat-Aghsoumal Belt. c, d) extensive, shallow artisanal pits in between Agarasras Labiad and Agarasras Lakhadar (hills in the background (d) are part of the Agarasras Lakhadar ophiolite sequence) (UTM 28 760722 mE, 2714107 mN). e) profile of the pits shown in d. Loose pebbles, with pits dug to the caliche layer (UTM 28 761940 mE, 2717138 mN).



Figure 5-12 – Photograph of Gold nugget from artisanal pits in between Agarasras Labiad and Agarasras Lakhadar. Weight of nugget is ~600g

5.2 **Magmatic Sulphides (Ni, Cu, PGMs)**

5.2.1 Introduction

Magmatic sulphide deposits in mafic and ultramafic magmas result from the formation of an immiscible sulphide phase, into which chalcophile elements strongly partition (Naldrett, 2010). The main cause of sulphur saturation in these types of deposits is the addition of external sulphur, though sulphur saturation can also be achieved by crustal contamination (resulting in a decrease of sulphide solubility) or magma mixing (Naldrett, 2010). The world class Voisey's Bay Anorthosite Complex hosts Ni-Cu mineralisation and is the type example for magmatic sulphide mineralisation in anorthosite complexes (Naldrett, 2010).

5.2.2 Model of Formation within Anorthosite Complexes

Mineralisation at Voisey's Bay occurs in the magma conduits feeding the Voisey's Bay Intrusion (Reid Brook deposit and Ovoid; Figure 5-13a), as well as at the base of the intrusion where troctolite dykes fed the intrusion (Eastern Deeps; Figure 5-13b) (Hiebert et al., 2013). Sulphide immiscibility occurred as a result of contamination of host sediments consisting of

graphite, and sulphide-bearing psammite to pelite (Hiebert et al., 2013, Naldrett, 2010). The magma and sulphide phase intruded through a vertical dyke to form an upper intrusion, with sulphides settling out within thickened zones in the dykes and at the entrance of the dyke with the upper intrusion (Naldrett, 2010). Later surges of magma following the same channels, allows for enrichment of early sulphides (Naldrett, 2010).

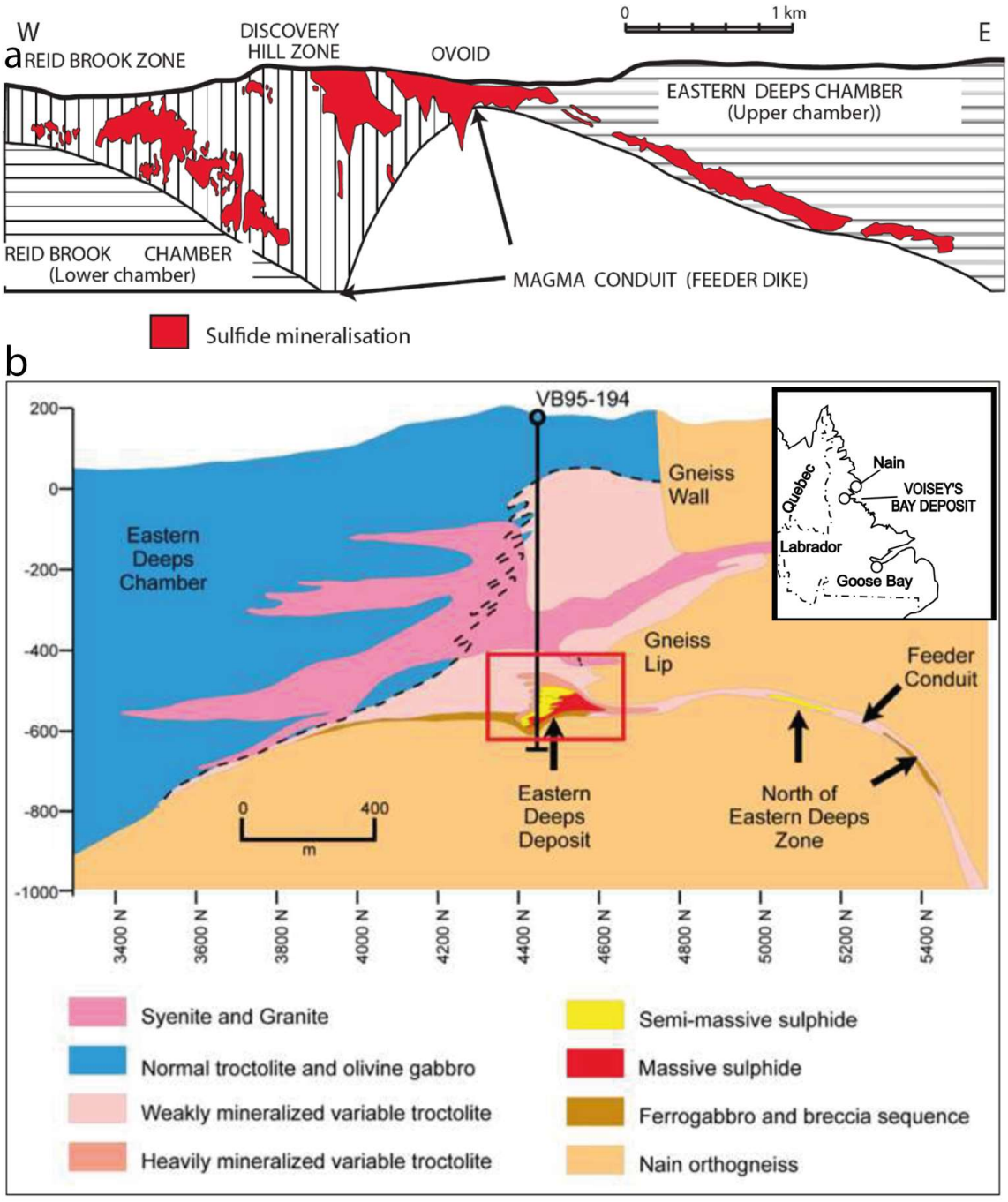

Figure 5-13 – a) E-W (from Naldrett, 2010) and b) N-S sections through the Voisey's Bay deposit showing key features (Fall, 2017).

5.2.3 Mineralisation in the Elmalhat Anorthosite Complex

Disseminated sulphides are present throughout the EAC (Figure 5-14; Sections 4.1.2.2.2.1, 4.1.2.2.3.1, and 4.1.2.2.3.2). Sulphur isotopes indicate that the sulphides are magmatic (Section 4.1.4.3). Anomalous values of Cu (up to 0.79%), Ni (up to 0.13%), ±Co and/or ±PGE (up to 0.3 ppm Pt + Pd) values are observed in sulphide-bearing anorthosite/leucogabbro within the complex (Figure 5-15, Figure 5-8 b, c).

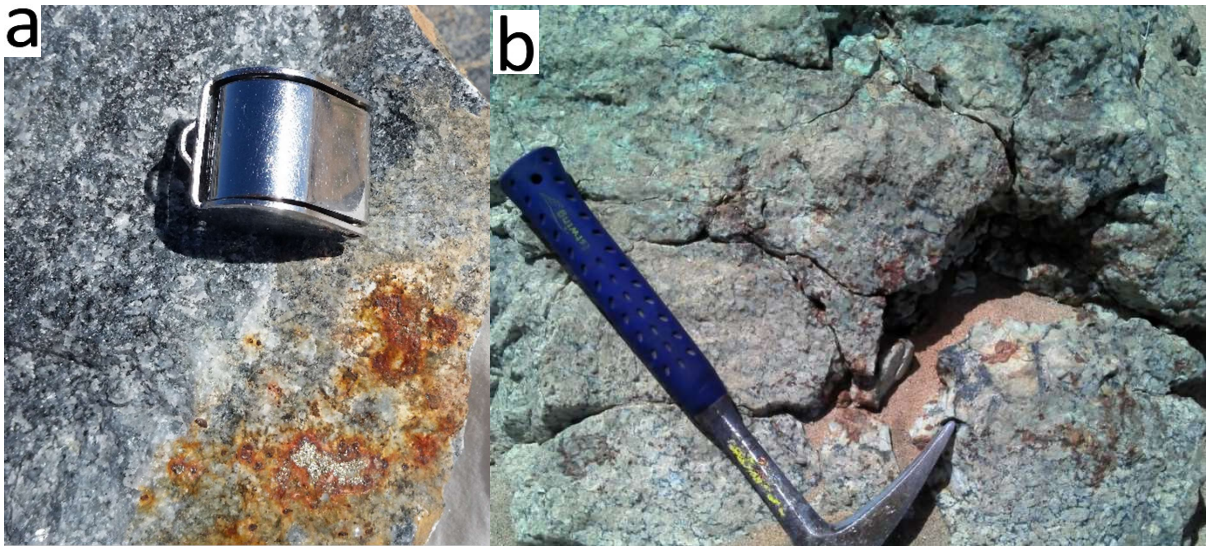

Figure 5-14 – Photograph of patchy sulphides within anorthosite of the EAC. Oxidized brown patches formed from weathering of sulphides (a - UTM 29 194743 mE, 2655065 mN, b - UTM 28 778192 mE, 2633667 mN)

Possible causes of sulphur saturation include the addition of external sulphur, the assimilation of crustal material, or magma mixing (Naldrett, 2010). Within the Northern Limb, the chromite seam formed as the result of magma mixing (Section 4.1.6.1) – a mechanism that likely resulted in the formation of the magmatic sulphides observed in anorthosite. Magma mixing may also be a mechanism for sulphur saturation within the main bulb, as the formation of the massif-type anorthosite required multiple pulses of magma (Section 4.1.6.2). Additionally, the evidence for the assimilation of crustal material observed on the southern margin (Sections 4.1.3.2.2.4.1, and 4.1.6.2) and the presence of megacrystic anorthosite xenoliths (Section 4.1.3.2.2.4.2), known to contain magmatic sulphides, provide two additional mechanisms by which sulphur saturation may have been reached (external sulphur and crustal contamination).

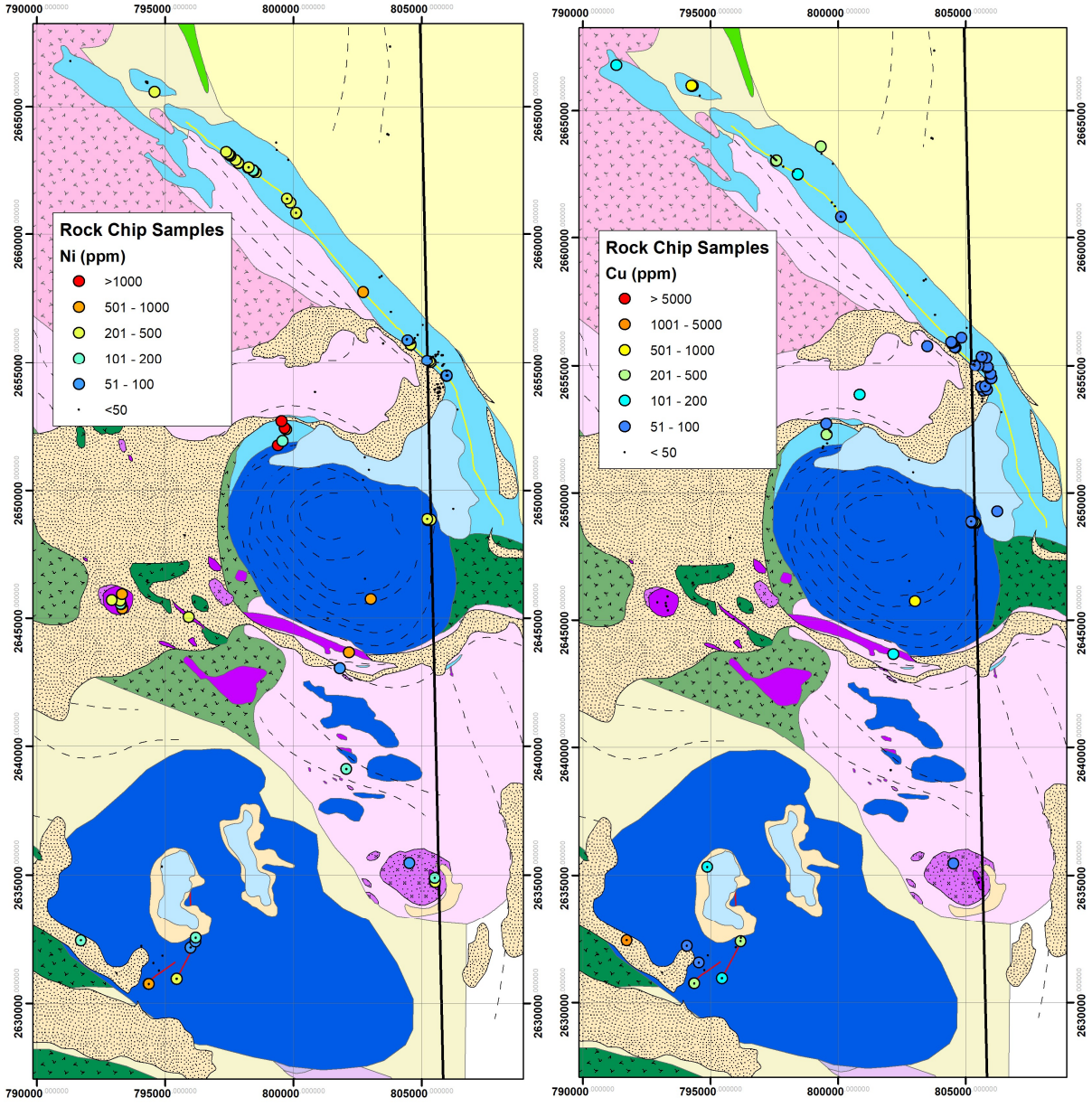

Figure 5-15 - Rock chip samples showing Ni and Cu anomalies in the EAC associated with magmatic sulphides.

5.3 **Chromitite-hosted PGE Mineralisation**

5.3.1 Chromite

A seam of chromitite is hosted in the megacrystic anorthosite/leucogabbro in the northern limb of the EAC. It is a concordant, sub-vertical seam averaging ~30-50cm in thickness, though in places it narrows to stringers, a few mm in thickness or thickens up to ~2.5m (Figure 5-16).

Where the seam thickens, bedding is observed with distinct grainsize variations within the beds. It has been mapped over a total strike of ~19km, although the seam is not observed continuously over this strike as sand cover often fills in the topographic lows that form along the chromitite seam. Cromitite lag is often observed in these lows marking the occurrence of the unit.

The mineral chemistry of the chromitite is very similar to other chromitites associated with megacrystic anorthosite such as Fiskenæsset and Sittampundi (Sections 4.1.4.2). Fractionation trends observed in anorthite content of plagioclase and Mg# of amphibole as well as the degree of REE fractionation either side of the chromite seam indicate suggest magma mixing caused the formation of the chromitite seam (discussed in Section 4.1.6.1).

The seam contains up to 37.2% Cr_2O_3 grade, averaging ~30% Cr_2O_3. (Figure 5-17)

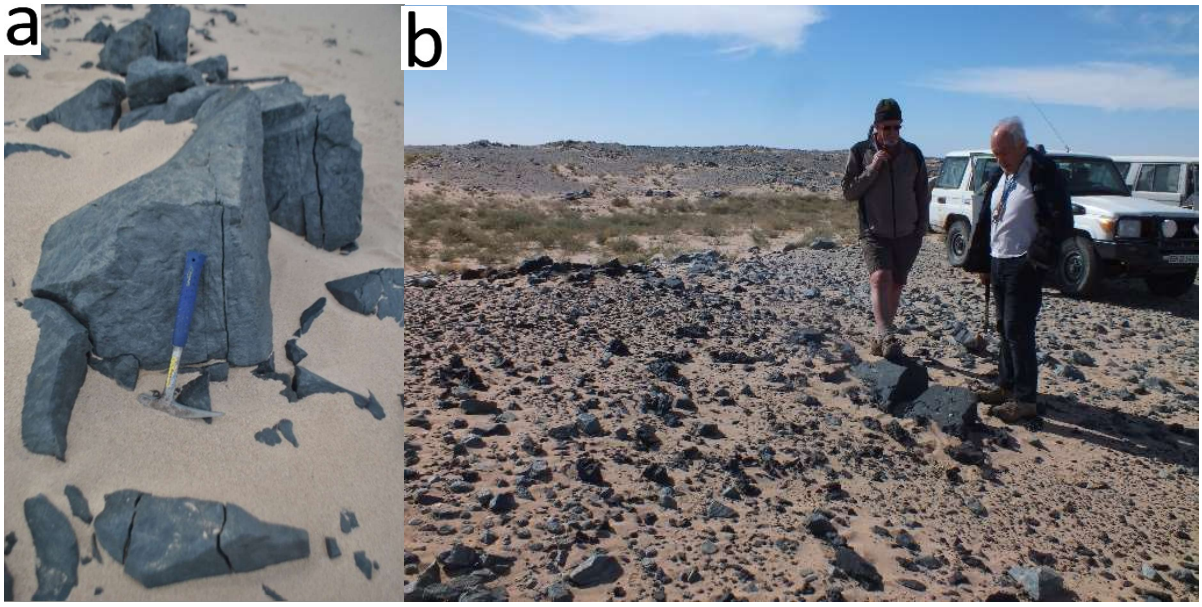

Figure 5-16 - Field photographs of the chromitite seam; a) of average thickness ~0.8m (UTM 29 196309 mE, 2650809 mN), and b) where it thickens to ~2.5m (UTM 28 782450 mE, 2685359 mN).

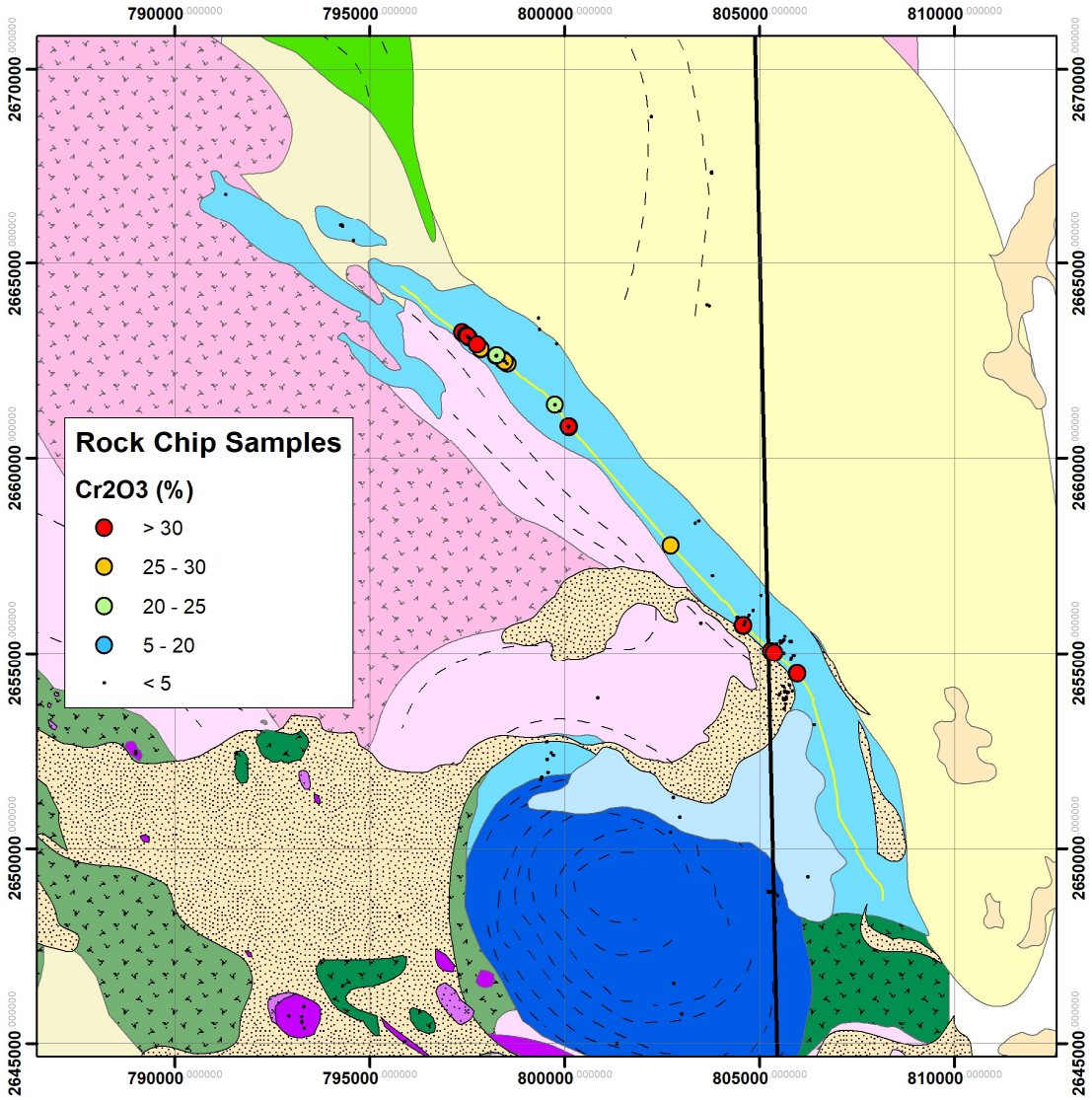

Figure 5-17 – Rock chip analyses showing Cr_2O_3 of the chromitite seam.

5.3.2 Platinum Group Elements

Assay results of chromitite samples reveal anomalous values of up to 238 ppb Pt + Pd (Figure 5-18). Scanning electron microscope (SEM) imaging reveals the widespread presence of small PGM grains (Figure 5-19-Figure 5-20). PGMs within the chromitite are primarily composed of laurite (RuS_2)-erlichmanite (OsS_2) (Figure 5-19). Minor amounts of Ir (Figure 5-20), Pt, Pd, and Rh are present alloyed with Fe, Mn, or Te.

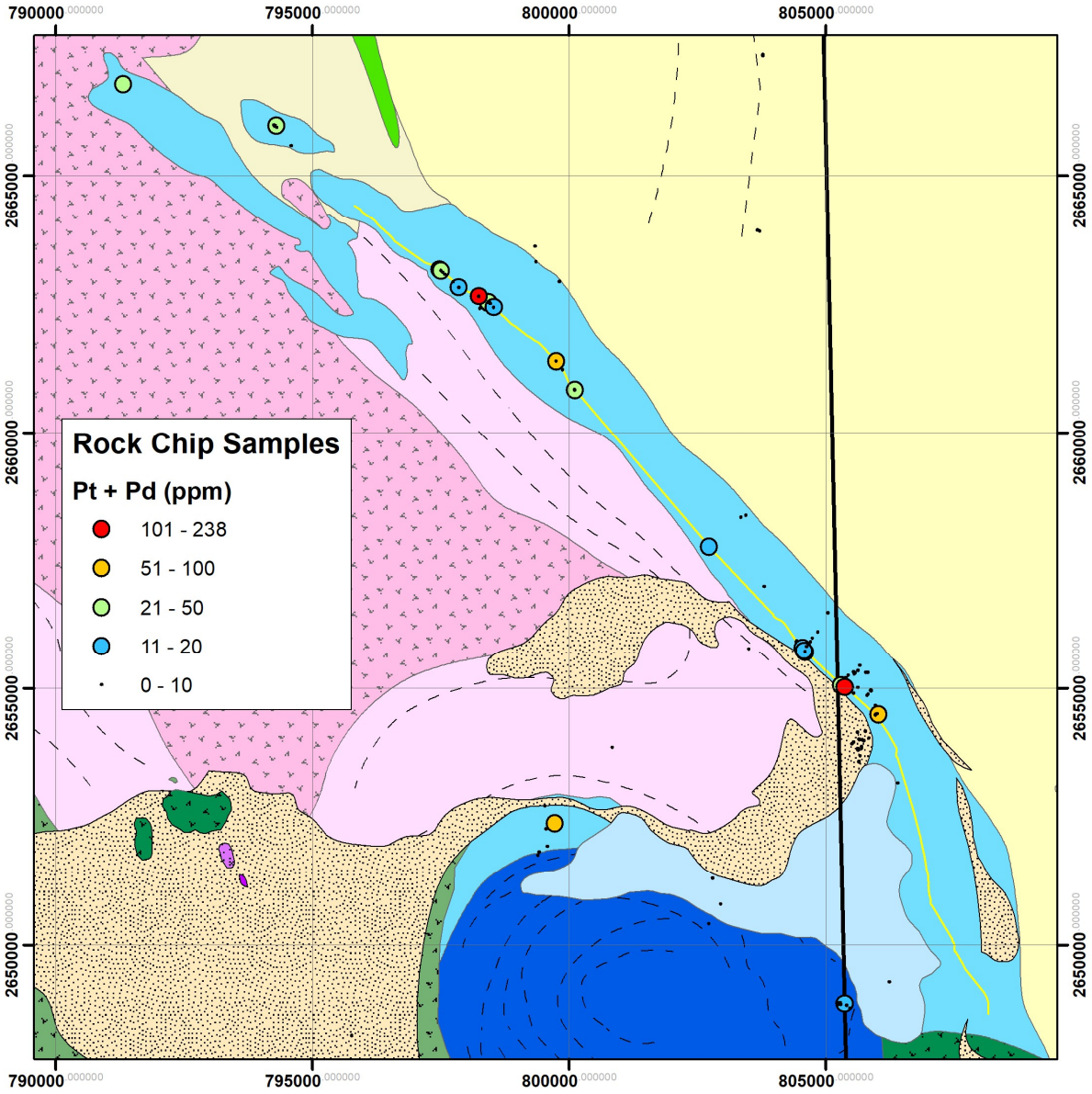

Figure 5-18 – Rock chip sample analysis, showing distribution of PGE mineralisation of the Northern Limb within the chromitite seam.

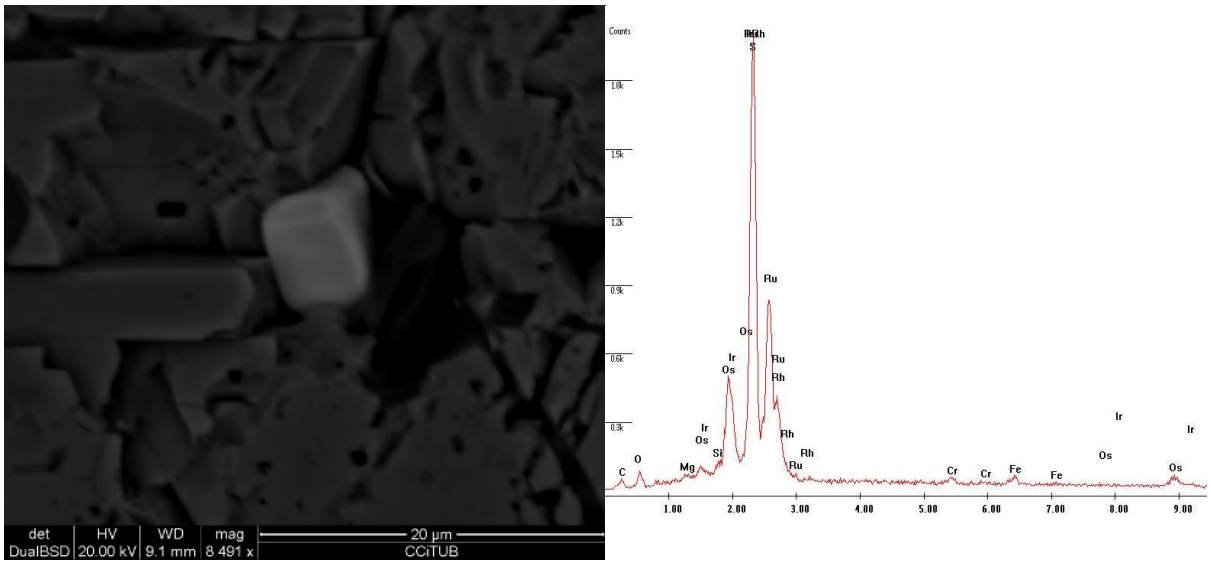

Figure 5-19 - SEM image and spectra of a primary grain of Laurite hosted in chromite sample B34 (UTM 28 799574 mE, 2651942 mN).

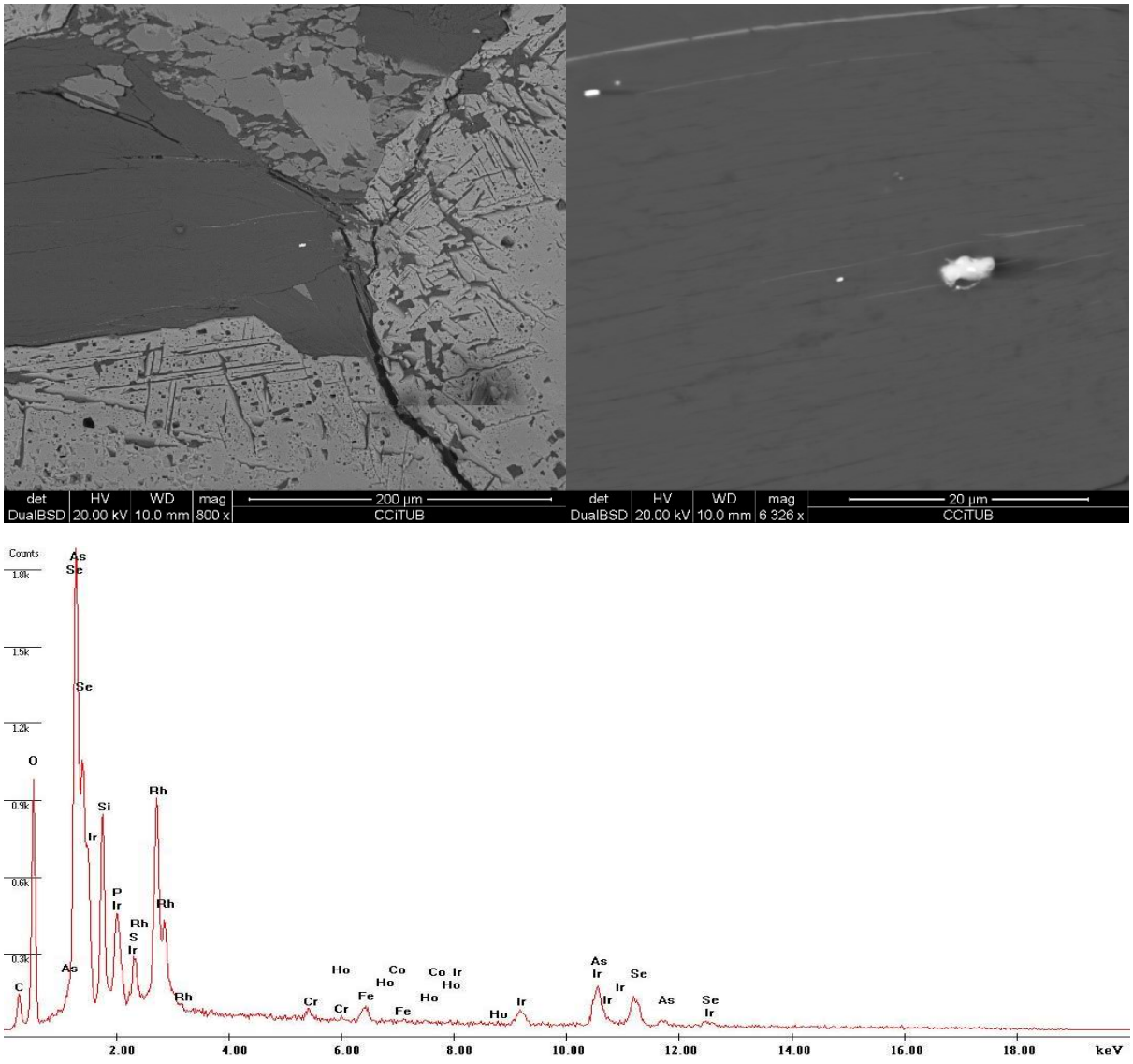

Figure 5-20 – SEM image of sample J105 (UTM 29 194744 mE, 2655070 mN) showing secondary PGM grain crystallized in chlorite. The PGM is a sulphide mineral containing Ru, Os, Ir, and Se.

The distribution and mineralogy of PGM within the chromitite of the northern limb provides some information about their provenance. Naldrett et al. (2009) proposed two models for the origin of PGE concentration associated with chromitites, based on the distribution of PGEs (Pt, Pd vs Ru, Ir, Os). If sulphur saturation occurs during the formation of the chromitite seam, platinum and palladium are strongly partitioned into the sulphide phase resulting in a higher total PGE content, preferentially enriched in platinum and palladium (Naldrett et al., 2009). If sulphur saturation does not occur in the magma, Laurite can still crystallise (Naldrett et al., 2009; and references therein), with Maier et al. (1999) noting a strong association between Laurite and chromitite in the Lower and Critical Zones of the western Bushveld Complex of South Africa. It is thought that the chromite grains attract laurite, possibly acting as a catalyst for laurite crystallisation (Naldrett et al., 2012). Therefore, in the absence of sulphur saturation results in a lower total PGE content preferentially enriched in Ru, Ir and Os (laurite-erlichmanite) (Naldrett et al., 2009).

The chromitite seam in the Northern Limb has evidently undergone hydrothermal alteration. Evidence of hydrothermal fluid flow was noted in many samples with the presence of REE phosphates and Pb-Sb salts present within fluid inclusions in the chromite as well as native gold, silver and abundant As-bearing minerals (both in PGE minerals and as arsenopyrite). Hydrothermal alteration also explains the alteration at the edge of chromite grains to magnetite (Section 4.1.3.2.1.2) as well as the greenschist-facies interstitial mineral assemblage (Section 4.1.3.2.1.2) in an otherwise amphibolite facies region (Sections 4.1.3.2.1.1 and 4.1.3.2.1.3). Additionally, PGM grains appear to have been dissolved and re-precipitated within interstitial minerals, such as along chlorite cleavage plains.

Therefore, PGM grains can be divided into two types: primary grains hosted in chromite and secondary grains mostly contained within interstitial chlorite or on the edge of chromite grains (Figure 5-20). It appears that the interaction with hydrothermal fluids has altered the mineral

chemistry of the primary PGM grains (Figure 5-21). Notably, Pt and Pd-bearing grains are absent from more heavily sheared and altered grains. Additionally, massive, coarser grained samples of chromite were found to contain a higher total of PGM grains, with a higher portion of Pt and Pd than samples with finer chromite and fractured grains. Presumably in the case of the latter the hydrothermal fluids could liberate PGM grains more readily with less protection from grains of chromite, preferentially removing the more mobile Pt and Pd-bearing grains.

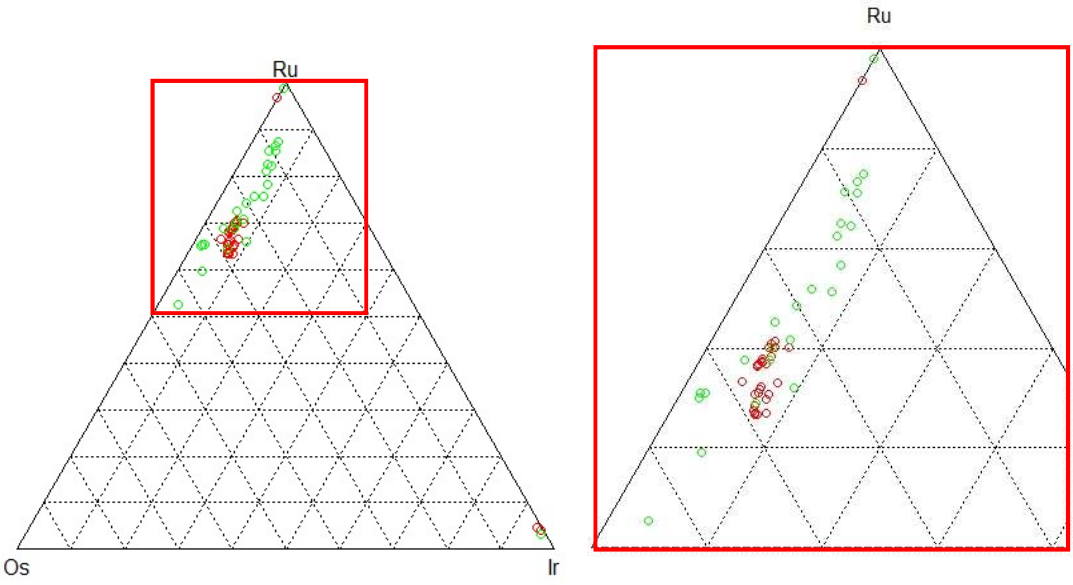

Figure 5-21 - Ternary diagram showing the composition of primary (red) and secondary (green) PGM grains from the chromitite.

Therefore, two possibilities exist for the provenance of the PGE concentrations within the EAC. The relative enrichment of Ru, Ir and Os could relate to primary concentration associated with growth of chromitite grains in the absence of sulphide saturation, and/or the accumulation of a Pt and Pd – rich PGM profile due to sulphur saturation followed by the preferential removal of more mobile Pt, and Pd by hydrothermal fluids.

5.4 **Orthomagmatic Fe-Ti-V Oxide Seams**

Orthomagmatic Fe-Ti(-V) oxide deposits are commonly associated with Proterozoic massif-type anorthosite complexes such as the Allard Lake ilmenite deposit in the Havre-Saint-Pierre

Anorthosite Complex. Their genesis is explained through a number of processes including fractional crystallisation and gravity sorting, silicate-oxide immiscibility, magma mixing, stress-driven melt segregation, solid state remobilisation and hydrothermal remobilisation (Villanova-de-Benavent et al., 2017; and references therein). Anorthosite parental magmas are TiO_2 enriched (>4 wt % TiO_2) which promotes early crystallisation of dense ilmenite which sinks to the bottom of the magma chamber forming concordant bodies (Villanova-de-Benavent et al., 2017). However, this does not explain the occurrence of discordant Fe-Ti(-V) oxides, such as in Damiao in China, Tellnes in Norway, Lac Tio in Canada, and Kunene in Angola and Namibia (Villanova-de-Benavent et al., 2017). Villanova-de-Benavent et al. (2017) interprets the discordant bodies of Fe-Ti(-V) oxide at Kunene as having formed from a later phase of anorthosite intruding the massif-type anorthosite as sills, cross-cutting and altering the original anorthosite and causing doming of the complex. As the complex began to dome, liquid drained from the younger, not yet solidified phase of anorthosite, accumulating oxides and sulphides at the base, discordant from the layering in the complex (Villanova-de-Benavent et al., 2017).

Mappable magnetite(-ilmenite) seams have been discovered in the southern bulb (Figure 5-22a, b, d) and at Moug El Kalab (host to gold and copper mineralisation; Section 5.1.1.3). A land based magnetic survey (Figure 5-22c) highlights the extent of the magnetite seams within the southern bulb; the magnetite seams are ~1-1.5m thick and appear from ground mapping and ground magnetics to be shallowly dipping to the west, with a strike curving around parallel with the eastern margin of the intrusion. Multiple seams are observed within this region, though the size of the geophysics anomaly suggests that there may be more magnetite present than has currently been mapped. The seams consist of massive magnetite with ilmenite exsolutions, ilmenite and spinel (Figure 5-23).

The magnetite seams in the southern bulb contain consistently high grades of iron, titanium, and vanadium (Figure 5-24), up to 58.5% Fe, 8.9% Ti, and 0.74% V.

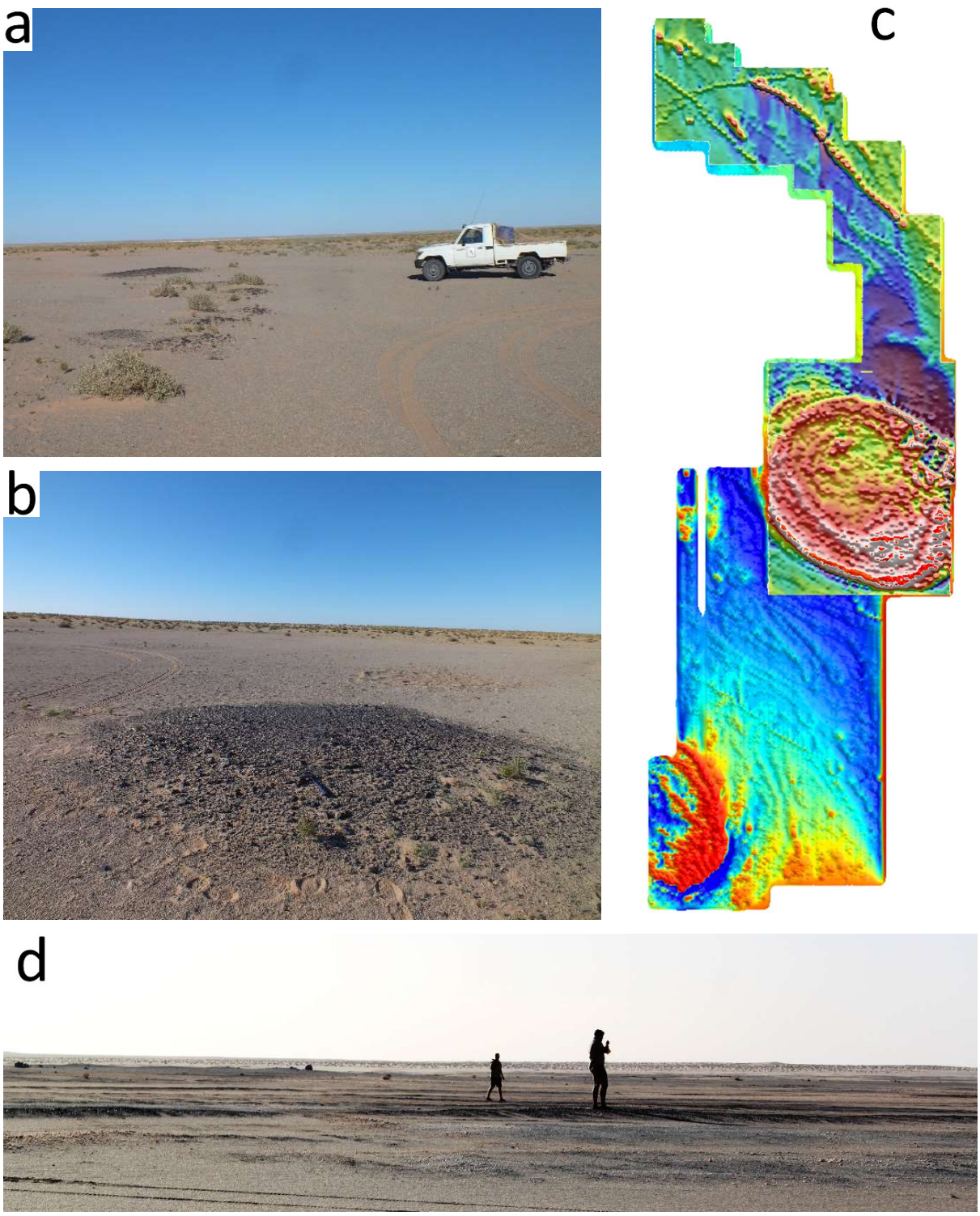

Figure 5-22 - Images of the magnetite seams within the southern bulb and the anomaly produced on the ground magnetics. a) magnetite subcropping intermittently along the strike of the seam. b) magnetite subcrop from a sub-horizontal seam (UTM 28 799755 mE, 2661393 mN). c) ground magnetic survey indicating a magnetic anomaly in the southern bulb corresponding with the magnetite seams (UTM 28 799617 mE, 2661523 mN). d) three parallel, shallowly dipping magnetite seams corresponding with the magnetic anomaly (photo by Laurence Robb) (UTM 28 795966 mE, 2632077 mN).

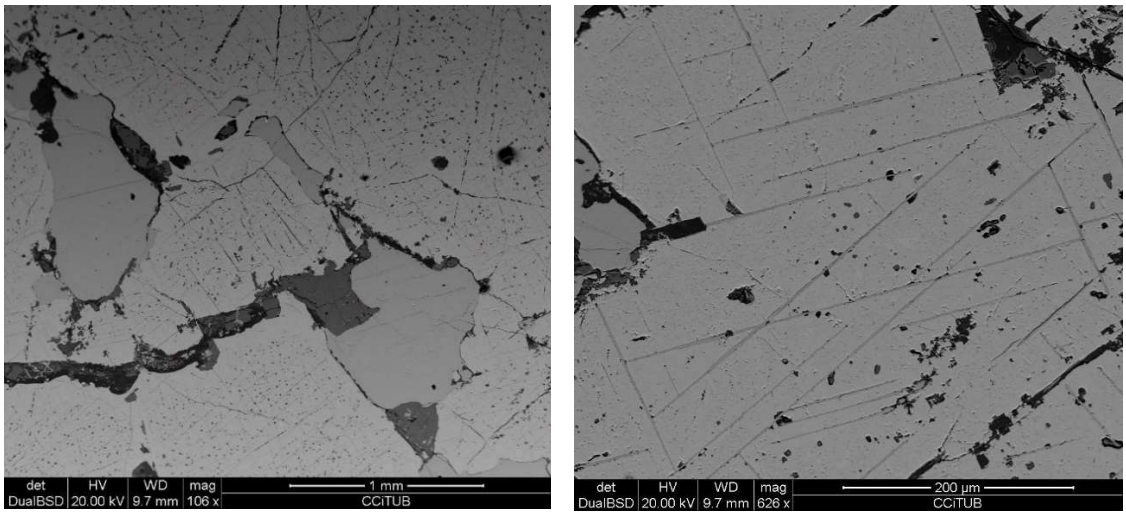

Figure 5-23 – SEM images of magnetite with ilmenite exsolutions, ilmenite and spinel from orthomagmatic Fe-Ti-V deposit of the southern bulb Elmalhat (images from Joan Carles Melgarejo Draper).

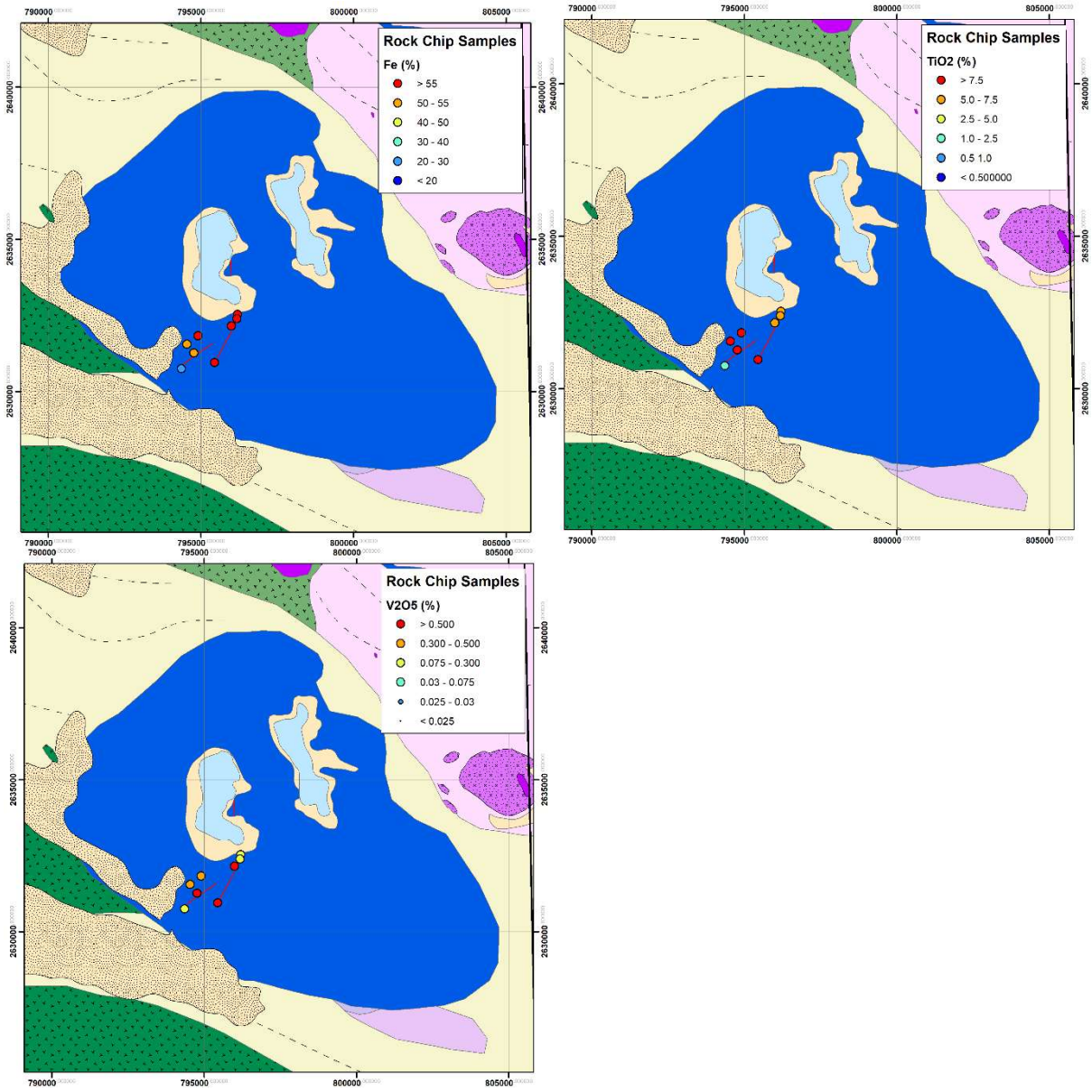

Figure 5-24 – Rock chip samples from the orthomagmatic Fe-Ti-V mineralisation in the Southern Bulb of the EAC.

5.5 **Superior-type Iron Formation of the Riche Anajim Group**

Precambrian iron formations are classified as either Algoma-type or Superior-type based on depositional environment and tectonic setting (Gross, 1980, Bekker et al., 2014). Algoma-type iron formations are typically proximal to volcanic centres and are associated with submarine volcanics, proximal to sea-floor exhalative activity (Figure 5-25; Bekker et al. (2014)). Superior-type iron formations are typically much larger, and form in passive-margin settings and are not associated with volcanic rocks (Figure 5-25; Bekker et al. (2014)).

The Riche Anajim Group contains a series of boudinaged ridges of Banded Iron Formation (BIF) extending the entire strike of the Sfariat Shear Zone (Figure 5-26; Combs (2012), Bronner et al. (1990)). BIF within the group are Superior-type iron formations (Taylor et al., 2016, Bronner et al., 1990). The grade of the BIF within Western Sahara is relatively low (averaging ~36.6% Fe and 47.27% SiO_2; Combs (2012)) though it has not been extensively studied in Western Sahara to identify possible zones of enrichment.

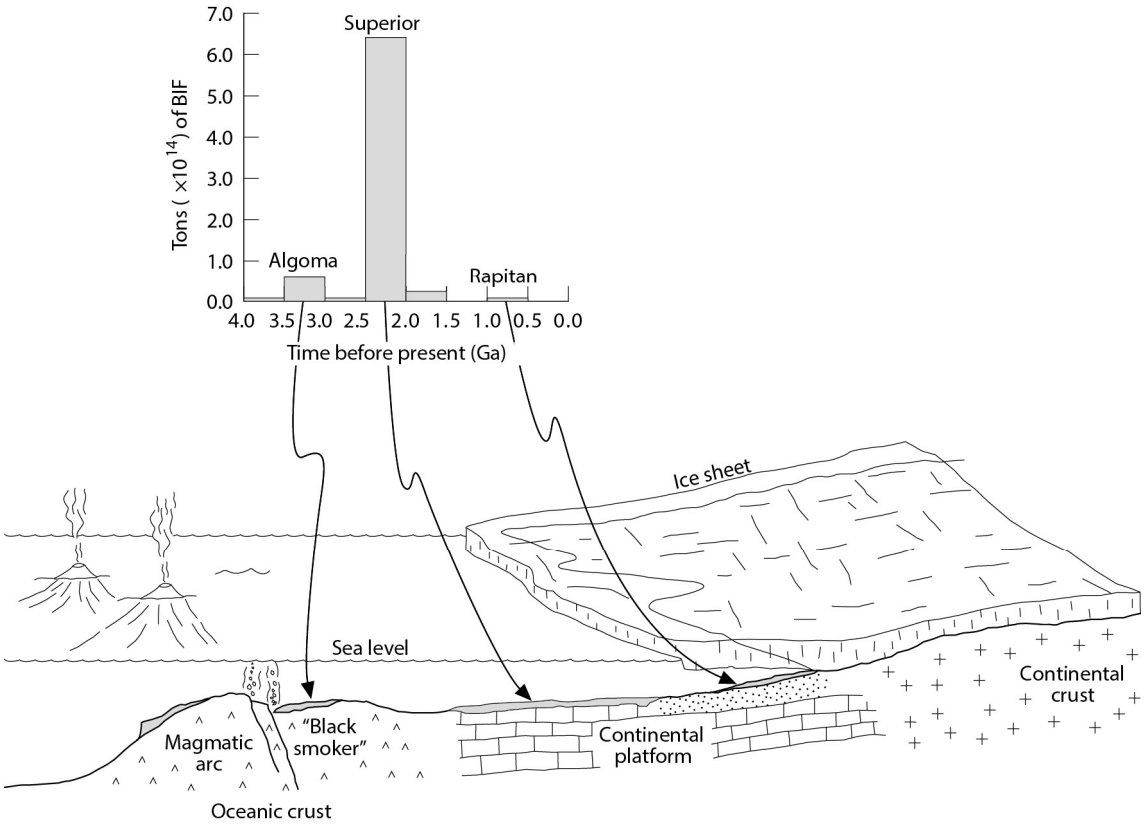

Figure 5-25 – Schematic diagram showing the depositional settings for Superior, Algoma and Rapitan type iron formations (from Robb, 2005). Superior-type formations form in shallow, continental margin marine settings. Algoma-type formations are hosted within meta-volcanic rocks and are linked to volcanic exhalative activity on the sea floor. The histogram shows approximate BIF resource of for each type of iron formation over time (after Holland et al., 1986).



Figure 5-26 – Field photograph showing the view of the dark beds of BIF forming ridges along the Riche Anajim Group (UTM 28 783704 mE, 2720813 mN)

6.0 Geological Synthesis

This project characterizes the geology of a previously understudied region proximal to the Archaean-Palaeoproterozoic boundary of the Reguibat Shield. The region appears to have formed though the accretion of two distinct Palaeoproterozoic volcanic arcs, and later collision with the Archaean craton. These volcanic arcs are expressed in the field as a series of volcanic, volcanosedimentary, and sedimentary belts.

The process of terrane accretion resulted in rapid thickening of the crust and a transition from an island arc setting (eg. Japan) to a continental arc setting (eg the Andes). This rapid transition in tectonic setting allowed for the formation of the Elmalhat Anorthosite Complex, the only know Anorthosite complex in the world to contain both megacrystic and massif-type anorthosite. The megacrystic anorthosite formed in a pre-accretion island arc setting, while the massif-type anorthosite formed in the post-accretion continental arc setting.

The geochronological work as a part of the project has also resulted in an enhanced definition of the Archaean-Palaeoproterozoic contact in the Reguibat Shield.

The definition of the Oum Abana and Taghsoumat-Aghsoumal Belts allows, for the first time, a direct comparison of specific belts in the Reguibat Shield with those in the Man-Leo Shield. Strong similarities in terms of stratigraphy and the timing of magmatic events are observed between these belts and a series of Birimian Belts in Burkina Faso and Mali. Striking similarities between belts from either shield include the presence of rare geological features including megacrystic anorthosite and strong correlations with what has been interpreted in the Agarasras Lakhadar Domain as an ophiolite sequence. Additionally, geophysical anomalies are observed across the Taoudeni Basin generally trending from these belts in the Man-Leo Shield toward the centre of the Reguibat Shield where the study area is located.

These direct correlations of volcanosedimentary belts across the Taoudeni basin allows for the comparison of the geodynamic model proposed for the formation of the Sfariat-Bu Daira and Leaareig Terranes, of the Reguibat Shield, with recently proposed models for the formation and assembly of the Man-Leo Shield during the Palaeoproterozoic. The proposed geodynamic evolution of a combined Reguibat – Baoulé-Mossi Block is presented below as a three stage model.

6.1 **Elmalhat Anorthosite Complex (Petrogenetic Model)**

In a recent synthesis of megacrystic and massif-type anorthosite, Ashwal and Bybee (2017) proposed that both types of anorthosites form in subduction-related settings with parental magmas forming from mantle melting. Ashwal and Bybee (2017) proposed that megacrystic anorthosites formed at relatively shallow crustal levels in oceanic arc-like settings in the Archaean. Massif-type anorthosites formed in the Proterozoic in thickened continental arc settings and were emplaced at a mid-crustal level with the model of formation involving ponding of basaltic magmas at a depth of 35-45km (10–15 kbar), crystallization and sinking of mafic silicates, and eventual flotation of buoyant plagioclase. Detailed geochronology involving cumulate high-alumina orthopyroxene megacrysts suggest these systems are long lived, with magmatism in individual massifs lasting for up to 100 Ma (Bybee et al., 2014). Ashwal and Bybee (2017) also proposed that the change from megacrystic to massif-type anorthosite at the Archaean to Proterozoic transition was driven by crustal evolution during this period. The temporal restrictions of megacrystic anorthosite might be explained either in terms of a hotter or wetter Archaean mantle, or favourable conditions produced by higher heat flow in the Archaean influencing oceanic crustal thickness, subduction rate, sites of magma generation and/or melt composition. Ashwal and Bybee (2017) proposed that global secular cooling of the Earth resulted in increased lithospheric strength and crustal thickness, which in

turn promoted ponding and slow crystallization of basaltic magmas at the Moho in continental arc environments and the formation of massif-type anorthosite.

Characteristics of the megacrystic and massif-type anorthosites of the EAC are consistent with the tectonic settings proposed by Ashwal and Bybee (2017) (Chapter 4.1.6). However, in forming in the Palaeoproterozoic, the megacrystic anorthosite of the EAC is ~500Ma younger than the next youngest of its kind (Chapter 4.1.4.1; Figure 4.98). Therefore, any model explaining the occurrence of the EAC must explain how shallow anorthosites relating to an island arc setting can be emplaced in the same location as mid-crustal anorthosites relating to a continental arc setting.

Multiple lines of evidence suggest that the megacrystic anorthosite was emplaced first, followed by the massif-type anorthosite intrusions (Chapter 4.1.6). This sequence suggests that the initial stages of the EAC involved the formation of megacrystic anorthosite in a shallow, island arc setting (Figure 6.1). The megacrystic anorthosite formed from multiple pulses of magma, with magma mixing between fractionated magma and a pulse of more primitive magma resulting in the formation of the chromitite seam and PGM accumulations. As megacrystic anorthosite is commonly associated with mafic rocks, it follows that significant portions of gabbroic rocks in the Elmalhat domain relate to this phase of formation of the EAC.

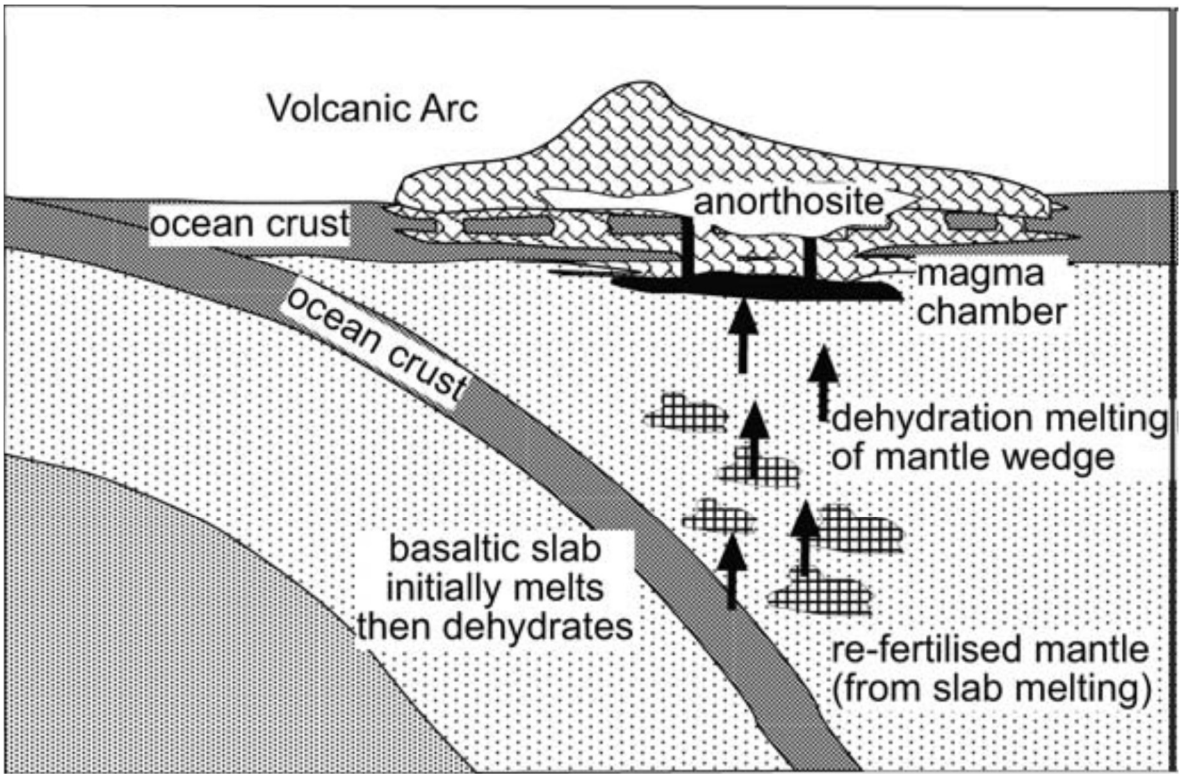

Figure 6-1 – Schematic diagram illustrating the formation of megacrystic anorthosite of the EAC

The second phase of the formation of the EAC requires regional context. It is generally accepted that Palaeoproterozoic domains of the Man-Leo and Reguibat Shields of the WAC formed through a process of terrane accretion (Abouchami et al., 1990, Lahondère et al., 2003), with Schofield et al. (2006) adding that the 'Contact zone' was no exception. Geochemical data indicates an evolution of the Sfariat-Bu Daira Terrane from an island arc setting to a more continental arc setting (Chapter 4.5.2). During the process of terrane accretion, the crust becomes thickened (Figure 6.2; Murphy, 2007). Work by Dewey (2005) on the early Ordovician Grampian Orogeny demonstrates that orogenic events relating to arc-continental collisions can occur in a relatively short timeframe. In the case of the Grampian Orogeny, the collisional shortening, and prograde-metamorphic phases lasted 8 Ma, with a total length of ~18 Ma from initial subduction of continental margin sediments to the end of shortening (Dewey, 2005). Therefore, within a relatively narrow timeframe a terrane can evolve from a relatively thin island arc setting, to an Andean-type continental arc setting with a thickened

lithosphere. Additionally, geological units that were emplaced at relatively shallow crustal level may become structurally emplaced at a deeper (mid-crustal) level. The burial of the pre-orogenic megacrystic anorthosite to mid-crustal levels would explain the amphibolite-facies mineral assemblages present, as well as the concordant nature of the megacrystic anorthosite with the host gneiss. The thickened lithosphere (deepened Moho) would facilitate the ponding of the mantle-derived, high Al basaltic magma at lower crustal depths (~30–40 km). This scenario is consistent with fractionation of the magma at pressures of 10-15kbar, which are necessary conditions for the formation of massif-type anorthosite (Figure 6.3). Multiple (at least two) pulses of plagioclase-rich magma from this fractionation are interpreted to have resulted in the formation of the massif-type anorthosite of the EAC. The emplacement of the andesine anorthosite was emplaced first, followed by the emplacement of labradorite anorthite, and associated ultramafic intrusions (of similar mineral chemistry), observed cross-cutting the andesine anorthosite. The local metasomatism of fresh andesine anorthosite producing the white anorthosite possibly relates to the emplacement of the labradorite anorthosite. The difference in mineral chemistry between andesine and labradorite anorthosite may relate to differences in the compositions of the parent magma and/or different levels of crystallisation.

It appears the two different types of anorthosite in the EAC result from relatively rapid change in tectonic setting from island arc to continental arc due to terrane accretion – possibly over a period of some 10-20 Ma (Dewey, 2005). Bybee et al. (2014) suggested that magmatic systems relating to massif-type anorthosite formation are relatively long-lived (~80–100 Ma), and in this light it is plausible that the broadly aluminous tholeiitic basalt responsible for the formation of both types of anorthosite (Section 4.1.6.2) could have been produced over the duration of anorthosite formation of the EAC. Although the chemistry of the melt evolved over time, many of the distinct features observed in each type of anorthosite can be largely explained by

different processes relating to the each tectonic setting (ie. shallow-emplacement in an island arc vs. ponding and fractionation beneath thickened crust)

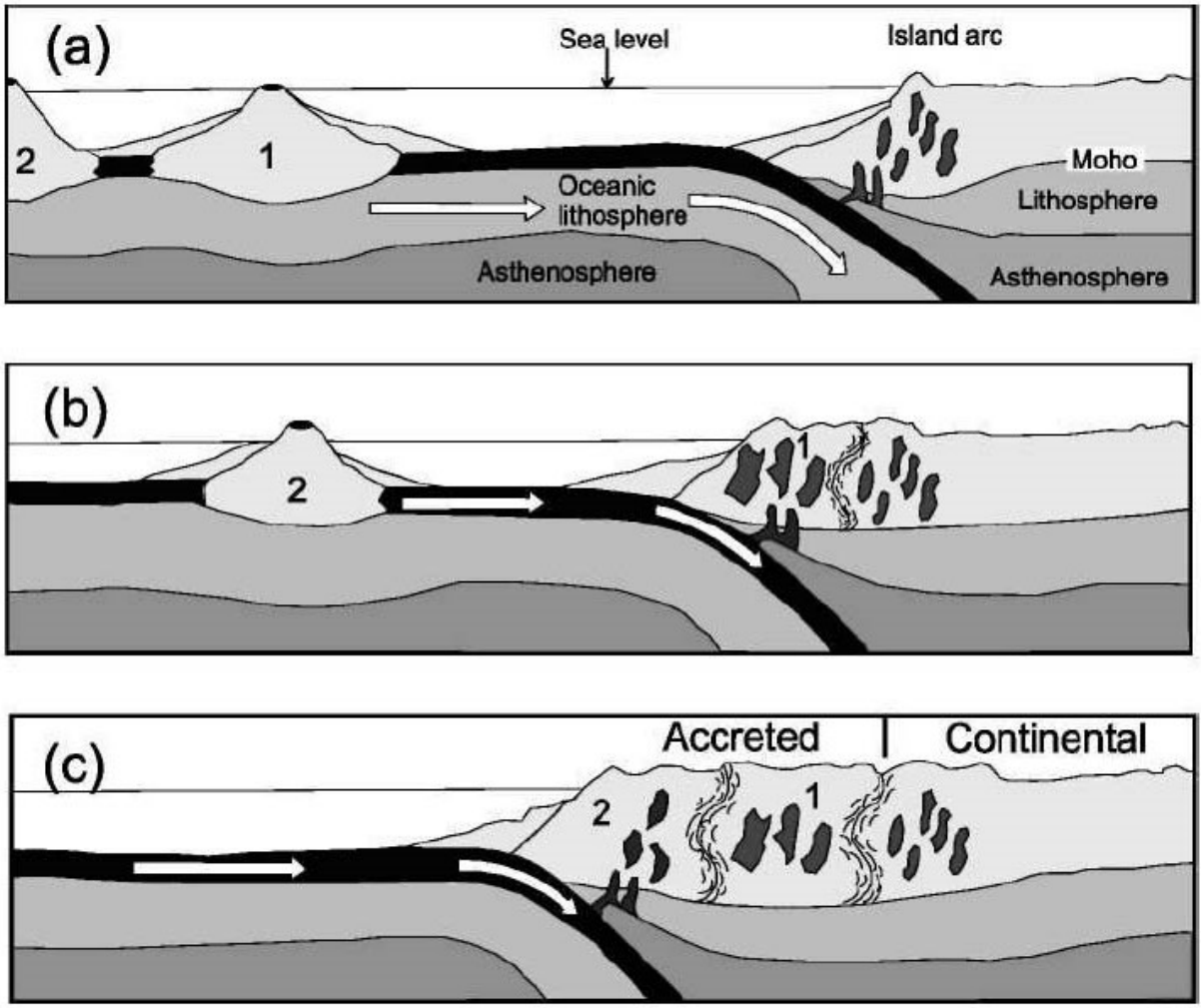

Figure 6-2 – Schematic diagrams illustrating terrane accretion at a convergent continental margin from Murphy (2007). (a) Subduction under the continental margin results in the development of a continental (Andean-style) arc; (b and c) Outboard oceanic terranes are swept into the subduction zone and accreted to the continental margin. After each collision, a new subduction zone forms outboard from the collision zone. The basement and mantle lithospheres become recycled, and are isotopically distinct from the continental arc crust. The line in (c) shows the boundary between magmatism sourced from recycled ancient continental lithosphere (right) and magmatism sourced from recycled juvenile accreted lithosphere. Dark blobs represent melts produced as a result of the subducting slab.

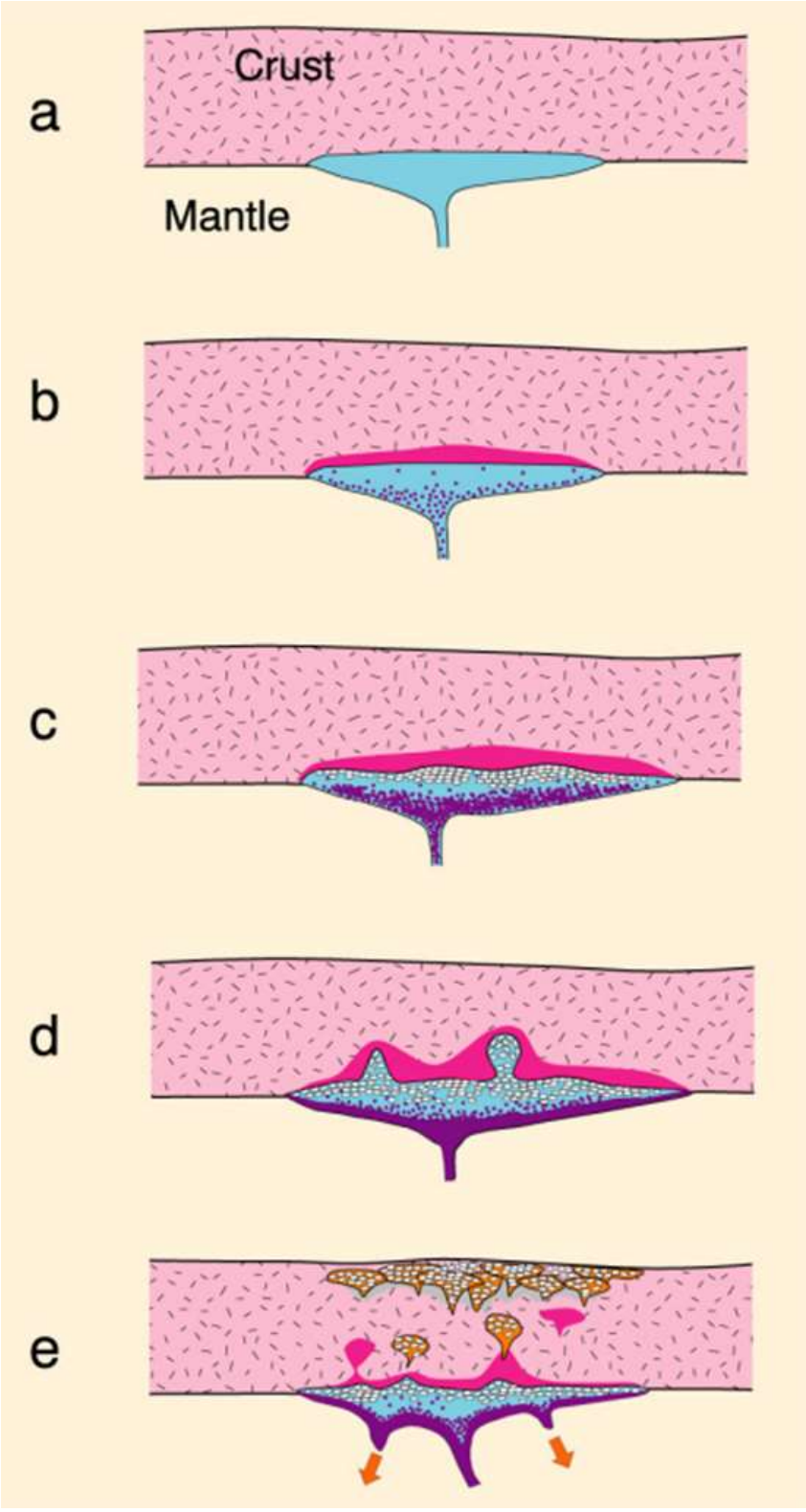

Figure 6-3 – Model for the formation of massif-type anorthosites a) Mantle-derived magma underplates the crust as it becomes density equilibrated. b) Crystallization of mafic phases (which sink), and partial melting of the crust above the ponded magma. The melt becomes enriched in Al and Fe/Mg. c) Plagioclase forms when the melt is sufficiently enriched. Plagioclase rises to the top of the chamber whereas mafic minerals sink. d) Plagioclase accumulations become less dense than the crust above and rise as crystal mush plutons. e) Plagioclase plutons coalesce to form massif anorthosite, whereas granitoid crustal melts rise to shallow levels as well. Mafic cumulates remain at depth or detach and sink into the mantle. From Ashwal (1993)

6.2 **Geodynamic Model for the Reguibat Shield**

6.2.1 Introduction

This work has identified what appear to be two distinct magmatic arcs, the Leaareig and Sfariat-Bu Daira Terranes. These arcs are distinct in terms of lithological, and geochemical characteristics with geochronological data revealing differences timing of magmatic activity (Figure 6.4). A model has been constructed for the formation of the Leaareig and Sfariat-Bu Daira Terranes based on a combination of the lithological, structural, geochronological, geochemical, and petrological data presented (Figure 6.5). It involves the formation, and evolution of two separate Palaeoproterozoic Japan-like island arcs, followed by their collision at ~2130-2120 Ma and ultimate accretion onto the Archaean terrane at ~2100 Ma.

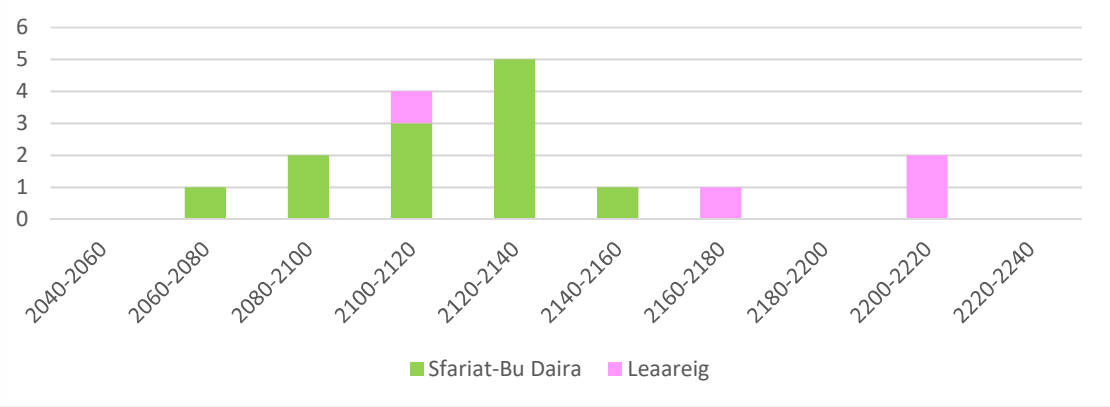

Figure 6-4 – Histogram showing the distribution of ages in the Leaareig and Sfariat-Bu Daira Terranes.

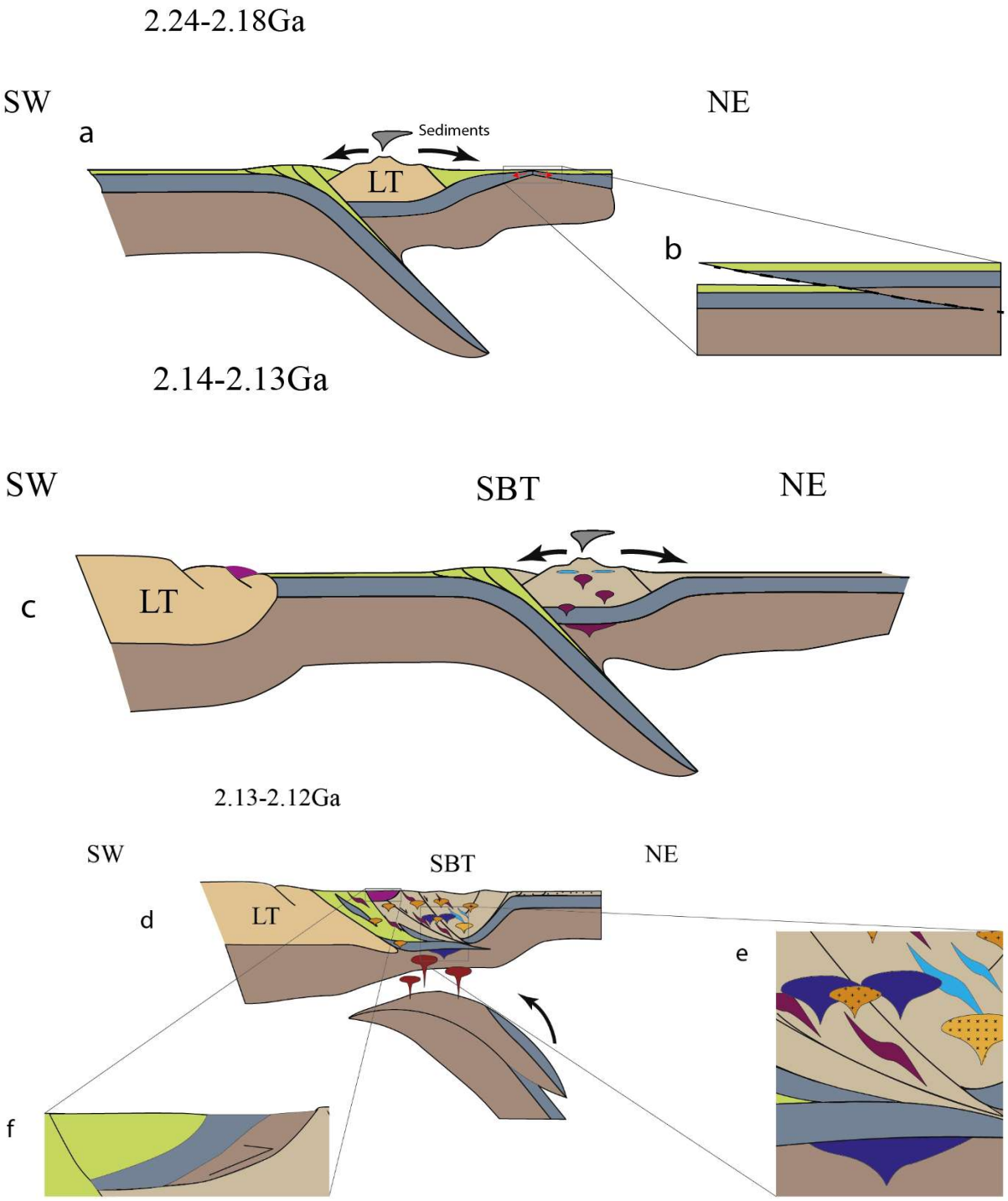

Figure 6-5 - Model of formation for the Leaareig and Sfariat-Bu Daira Terranes. a) ~2.24-2.18 Ga The formation of the Leaareig Terrane as an island arc. Sediments shedding off the island arc fill the back-arc basin, including detrital zircons. b) when subduction stops, the compressive regime results in a short-lived subduction zone in the back-arc basin, resulting in the obduction of an ophiolite sequence (observed in the Agarasras Lakhadar terrane). b) 2.14-2.13 Ga with the Leaareig Terrane now representing a proto-continent, a new island arc sequence develops resulting in the formation of the Sfariat-Bu Daira Terrane. It is during this phase that the megacrystic-type anorthosite is emplaced. d) ~2.13-2.12 Ga collision between the Leaareig and Sfariat-Bu Daira Terranes results in crustal thickening and formation of collisional granites. e) at this stage, high-Al, tholeiitic, mantle-derived melts close to the subducting slab pond at the base of the now thickened Moho. Fractionation at the Moho results in the initial sinking of dense mafic material while relatively early forming plagioclase (due to the high Al nature of the melt) rises to the top of the melt. Plagioclase-rich magmas rise diapirically, emplacing the massif-type anorthosite at a mid-crustal level, cross-cutting the earlier forming, concordant megacrystic anorthosite. f) The Agarasras Lakhadar ophiolite sequence and sediments are thrust over the Oum Abana Belt.

6.2.2 Leaareig (~2.24-2.18 Ga) and Sfariat-Bu Daira (~2.14-2.13 Ga) Volcanic Arcs

The Leaareig Terrane was the first to form as an island arc at ~2.24-2.18 Ga (Figure 6.5a). Whole rock geochemistry of basic and intermediate rocks reflects an island arc signature, while acidic rocks show continental arc characteristics – consistent with an evolving island arc sequence, analogous to the Japanese island arc (Chapter 3.5.2). A back-arc basin associated with this island arc, was filled with sediments shed from the volcanic arc. When subduction ceased, the convergent setting initiated a small, short-lived subduction zone in the back-arc basin, resulting in the obduction of a section of ocean sediments, oceanic crust and mantle now observed as the ophiolite sequence at Agarasras Lakhadar (Figure 6-5b). The ophiolite sequence is obducted onto the Leaareig Terrane at this stage (Figure 6-5c). The sample of paragneiss from the Agarasras Lakhadar Domain contains detrital zircons that were shed from the Leaareig volcanic arc.

The earliest evidence for the formation of the Sfariat-Bu Daira volcanic arc is the crystallisation of early tonalitic granitoids at ~2.14-2.13 (J178, J240; Chapter 2), which now form the gneiss basement in the Elmalhat domain (Figure 6-5c). This stage involved the formation of the megacrystic anorthosite at a shallow crustal level in a relatively primitive oceanic arc setting (Chapter 4.1.6).

6.2.3 Leaareig- Sfariat-Bu Daira Collision (~2.13-2.12 Ga)

The timing of the collision between the Leaareig and Sfariat-Bu Daira Terranes (Figure 6-5d) is constrained partly by the age of sample J246 (Chapter 2). Zircon cores, dated at 2282 ± 54 Ma, are interpreted as zircon xenocrysts, sourced from the Leaareig Terrane, with acicular grains and the rims of blocky zircons revealing an emplacement age of 2123 ± 69 Ma. This suggests that the two terranes must have collided by then and that the crust was thicker after that time, allowing for incorporation of older components from the Leaareig Terrane.

Additionally, tectonic interpretation of the geochronology samples using a series of multidimensional discriminant function diagrams (by Verma et al., 2012) reveals that samples J240, and J287 (2127 ± 20 Ma and 2122 ± 18 Ma respectively), display collisional characteristics. This is consistent with a ~2130-2120 collisional event between the terranes.

With a thickened post-collisional crust, high aluminium, tholeiitic island arc basalt could pool and fractionate at the Moho. This fractionation allowed for the formation of plagioclase-rich diapirs, emplaced at a mid-crustal level forming the massif-type anorthosite of the EAC (Figure 6-5e). The discordant diapirs cross-cut the regionally concordant megacrystic anorthosite intrusions (indicated by the presence of high Ca megacrystic xenoliths within the Main Bulb (Chapters 4.1.2.2.3.1, 4.1.3.2.2.4)).

The ophiolite sequence and metasedimentary rocks of the Agarasras Lakhadar Domain are structurally emplaced over the metavolcanics of the Oum Abana domain in this stage (Figure 6-5f). The tholeiitic basalt present in the Taghsoumat-Aghsoumal Belt (proximal to the Taghsoumat shear) represent remnants of oceanic crust in the suture.

6.2.4 Palaeoproterozoic-Archaean Collision (~2.10 Ga)

Whole rock geochemistry from a sample of migmatite (J238) within the Sassaiate-Temmimichate–Tsabaya Complex reveals a collisional signature. U-Pb zircon geochronology revealed an age of 2100 ± 19 Ma (interpreted as the age of anataxis), similar to an intrusion of pyroxene tonalite from the complex dated at 2099 ± 19 Ma by Lehbib (2016). These ages are interpreted as the timing of the collision between the Palaeoproterozoic and Archaean domains, which is consistent with Schofield et al. (2006) who recorded the contact as a sinistral-oblique collision, with regional anataxis at ‘around 2100 Ma’ (Figure 6-6).

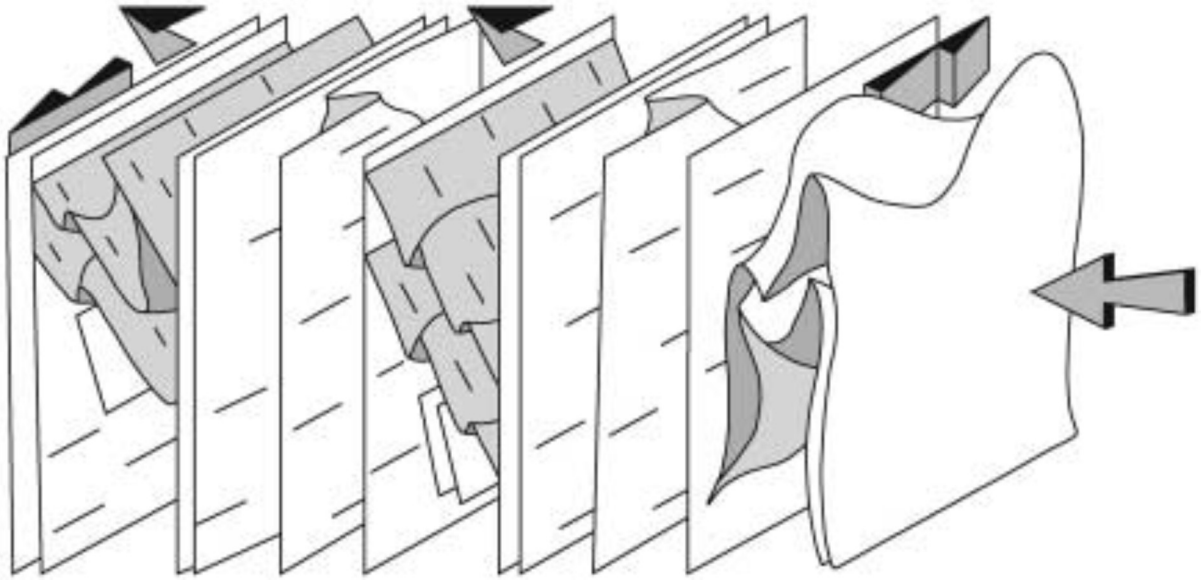

Figure 6-6 - Schematic illustration of partitioned sinistrally transpressive structures preserved in the Sfariat Belt, interpreted by Schofield et al. (2006) as representing the collision between Archaean and Palaeoproterozoic domains at ~2100 Ma.

The age of 2074 ± 51 Ma for the paragneiss in the Anajim Guebli Suite (to the north of the Elmalhat Domain) is comparable to the date of 2070 ± 11 Ma from the metasedimentary 'Tmeimichat group' sampled by Schofield et al. (2006) in Mauritania. With very similar lithologies and ages of the rocks, this belt is interpreted as the continuation of the Anajim Guebli Suite and Tmeimichat group (as described by Schofield et al. (2006)) into Western Sahara.

6.2.5 Pan African overprint (~600-500 Ma)

The lead loss events at c. 500-600 Ma - observed in samples near the terrane boundaries (J275, J292, and J234) - reflect Pan African granite intrusions that intrude meta-volcanosedimentary belts of the Tuareg shield of eastern Algeria (~530 Ma) (Caby, 2003) and the Minna area of Western Nigeria (~590 Ma) (Goodenough et al., 2014). The timing of these lead loss events is also similar to emplacement of the Derraman granites within the Mauritanides in southern Western Sahara (~525 Ma), formed in an intraplate rift setting (Bea et al., 2016). Although the Leaareig and Sfariat-Bu Daira Terranes lack direct evidence for emplacement of Pan African granite intrusions, the lead loss event clearly points to the influence of the Pan African event.

As carbonatite dykes generally relate to continental rifting, the presence of a carbonatite dyke cutting the ophiolite sequence in the Agarasras Lakhadar Domain may be associated with the Pan African rifting event.

6.3 **Archaean-Palaeoproterozoic Boundary**

The Leaareig and Sfariat-Bu Daira Terranes were previously thought to be Archaean in age (Bronner et al., 1990, Rocci et al., 1991, Bronner et al., 1992) until the age determinations by Lahondère et al. (2003), O'Connor et al. (2005a), and Schofield et al. (2006) established them as part of the Palaeoproterozoic domain. However, with a lack of geochronological data for the Sassaiate-Temmimichate–Tsabaya Complex, it was still thought to likely that the latter might represent part of an Archaean foreland (Schofield et al., 2006). Dating of an I-type migmatite in this project, and a pyroxene tonalite dated by Lehbib (2016), at 2100 ± 19 Ma, and 2099 ± 19 Ma respectively now confirm that the complex is part of the Palaeoproterozoic terrane (Figure 6-7). With no evidence of Archaean crust to the north, it suggests that the Archaean-Palaeoproterozoic boundary be defined by the southern edge of the El Medna fault zone (Sassaiate-Temmimichate–Tsabaya Complex) (Figure 6-8). This is more than 100km south of the boundary commonly used, even in recent papers (eg. Lagraa et al., 2017, Launay et al., 2018).

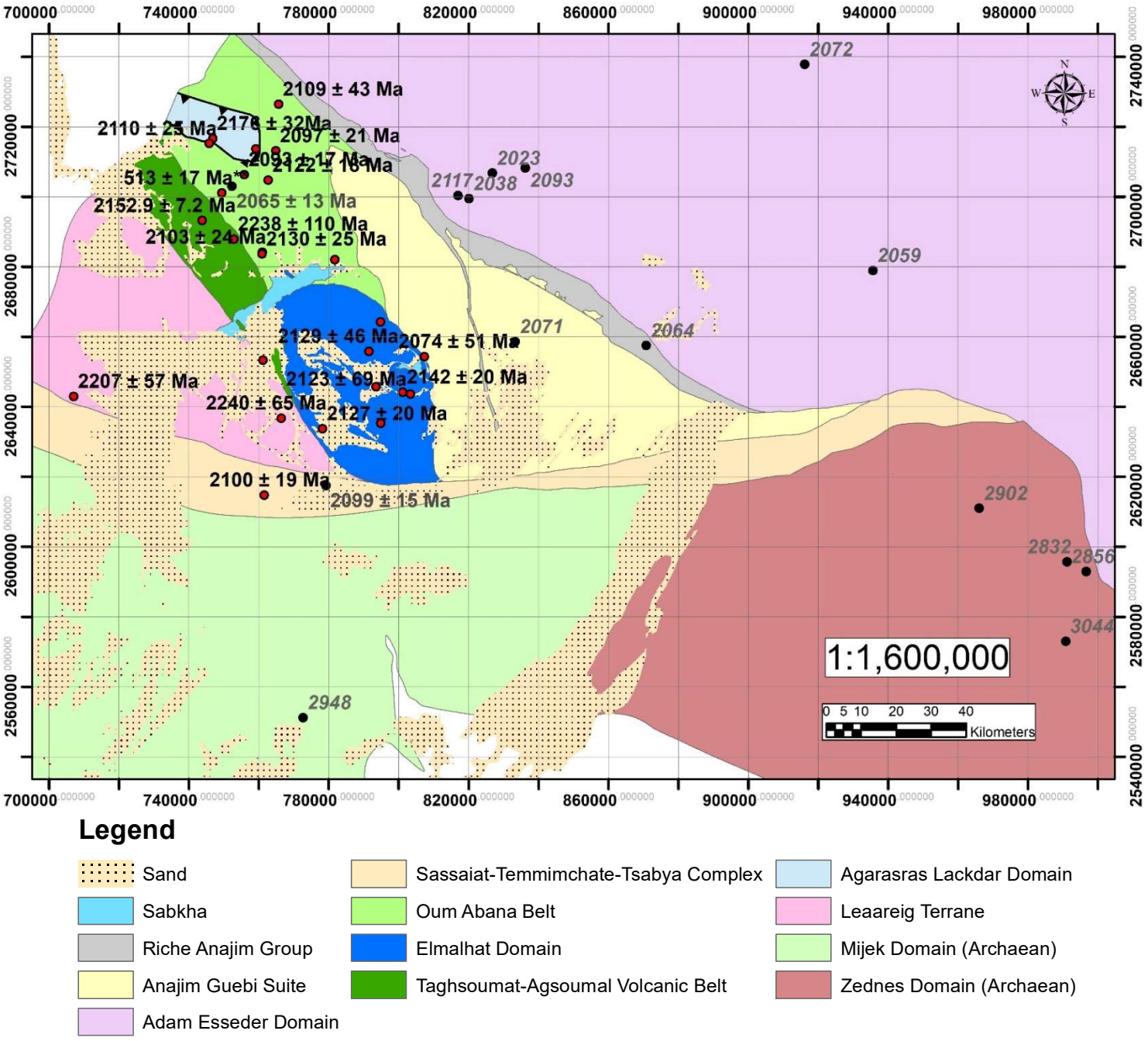

Legend

- Sand
- Sabkha
- Riche Anajim Group
- Anajim Guebi Suite
- Adam Esseder Domain
- Sassaiat-Temmimchate-Tsabya Complex
- Oum Abana Belt
- Elmalhat Domain
- Taghsoumat-Agsoumal Volcanic Belt
- Agarasras Lackdar Domain
- Leaareig Terrane
- Mijek Domain (Archaean)
- Zednes Domain (Archaean)

Figure 6-7 – Simplified geological map of the region showing geochronological data either side of the Archaean- Palaeoproterozoic contact. Geochronology results from this study are shown in as red dots and black text; with existing age data from Lahondère et al. (2003), O'Connor et al. (2005), Schofield et al. (2006) and Lehbib (2016) is shown as black dots with grey text

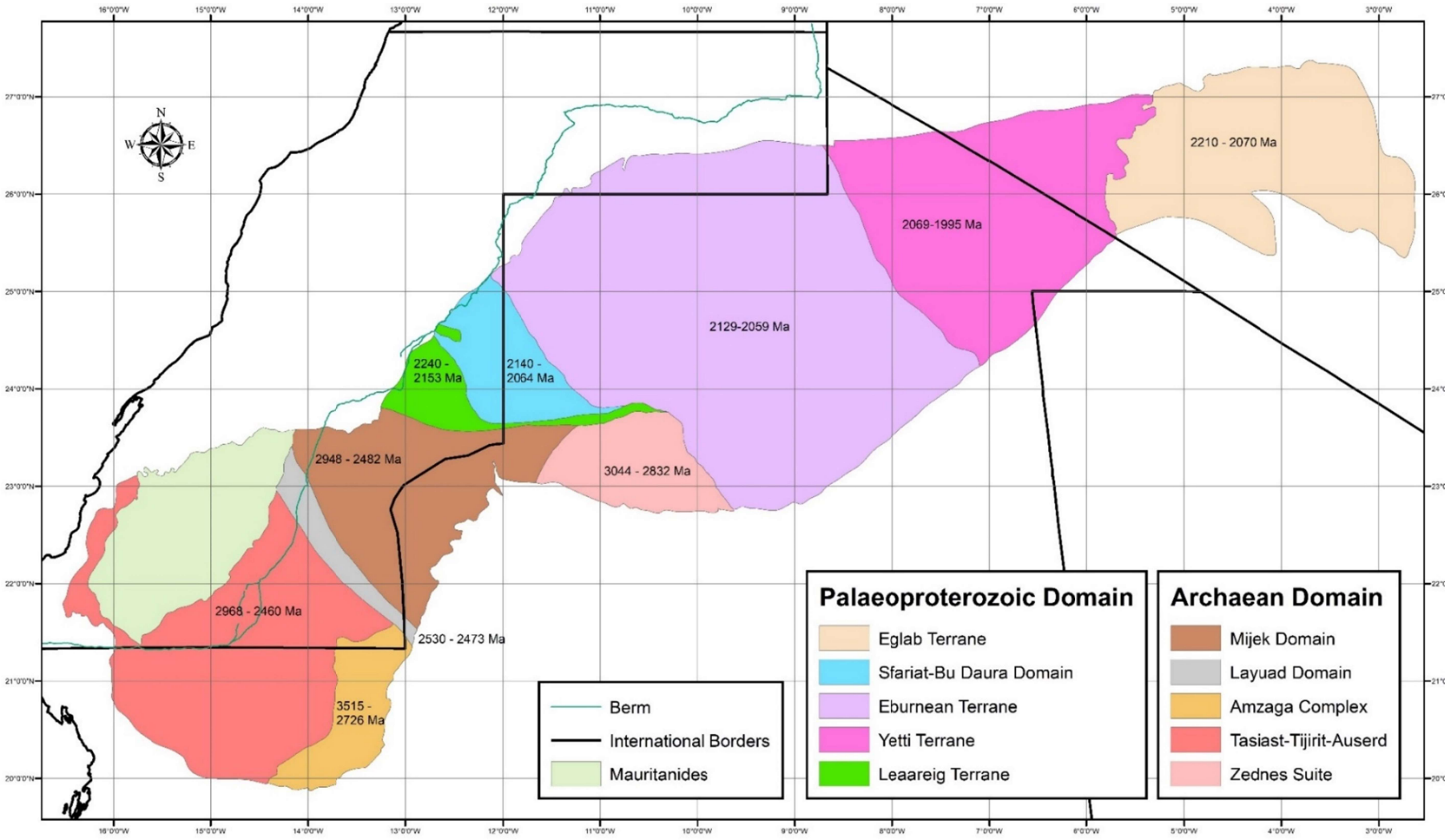

Simplified Geological Map of the Reguibat Shield

Figure 6-8 - Terrane map of the Reguibat Shield. The newly defined Leaareig and Sfariat-Bu Daira Terranes were defined un Western Sahara as part of this project, and extrapolated into Mauritania based on Schofield et al. (2006) and Schofield et al. (2012). The rest of the was Mauritanian was based Bradley et al. (2015a), the portion of Eglab and Yetti terranes in Algeria was based off Peucat et al. (2005) and the Archaean portion of the within Western Sahara (based on Lehbib, 2016; and references within). Age data from Auvray et al. (1992), Potrel et al. (1998), Lahondère et al. (2003), O'Connor et al. (2005a), Peucat et al. (2005), Schofield et al. (2006), Key et al. (2008), Tait et al. (2013), and Lehbib (2016).Correlations with the Baoulé-Mossi Domain of the Man-Leo Shield

6.4 Correlations with the Palaeoproterozoic Baoulé Mossi Domain of the Man-Leo Shield

One of the major outcomes of this research is the definition and characterisation of what is the largest exposed Palaeoproterozoic volcanic arc complex in the Reguibat Shield. Large portions of the Reguibat Shield (Adam Esseder and Yetti domains) are dominated by late-stage granite intrusions (Figure 1.11; Bradley et al., 2015a, Bradley et al., 2015b), with a smaller proportion of the supracrustal sedimentary, volcanosedimentary and volcanic belts that dominate the Baoulé-Mossi Domain of the Man-Leo Shield (Figure 1.4; Grenholm, 2014). Additionally, in a study of the Eglab terrane in Algeria, Peucat et al. (2005) noted a lack of parallel volcanic, sedimentary and plutonic belts as extensively described in the Baoulé-Mossi Domain. As these are the only previously studied regions, the few comparisons previously made between the two shields have been limited to tectonic setting and timing of events (Chapter 1.4.5.1; Figure 6-9). Consequently, work undertaken in this study on the Leaareig and Sfariat-Bu Daira Terranes allows the first direct comparison to be made of portions of the Baoulé Mossi Domain, with those in the Palaeoproterozoic domain of the Reguibat Shield.

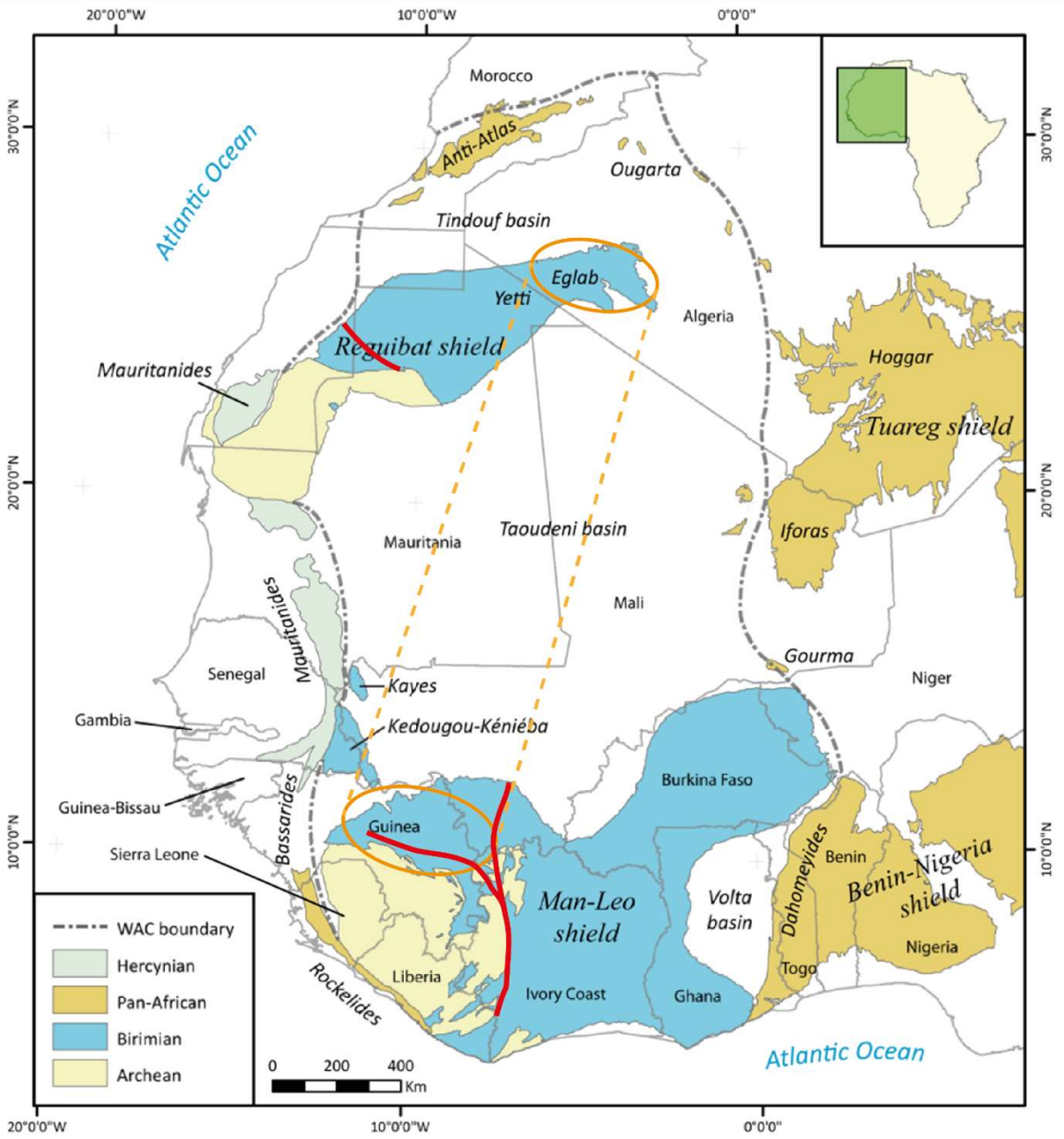

Figure 6-9 – Previous links that have been made between the Reguibat and Man Leo Shield. The structures with similar timing and kinematics are in red, with Schofield et al. (2006) proposing continuity between the regions. The regions circled in orange have similarities in basement age and later magmatism, leading Grenholm (2014) to propose that they might be related.

6.4.1 Previous comparisons

The Palaeoproterozoic terranes of the Reguibat and Man-Leo Shields both comprise juvenile accreted rocks with volcanic arc signatures, and little or no evidence of pre-existing Archaean crust (Abouchami et al., 1990, Boher et al., 1992, Lahondère et al., 2003, Schofield et al., 2006). Schofield et al. (2006) carried out a study on the Sfariat shear zone, investigating the

timing and kinematics of Eburnean tectonics in the Archaean-Palaeoproterozoic contact zone of the Reguibat Shield. It was apparent that similarities exist with the Sassandra shear zone of the Man-Leo shield (Figure 6-10), which also underwent southwest sinistral transpression at that time (Feybesse and Milési, 1994). On this basis Schofield et al. (2006) proposed structural continuity between these two regions of the West African Craton at ~2100 Ma (Figure 6-9). The Banifing shear zone (Man-Leo shield) have since been shown by Wane et al. (2018) to have also undergone sinistral transpression at this time (Figure 6-10).

In comparing a study by Peucat et al. (2005) on the Eblab and Yetti terranes, with extensive research done in the Baoulé Mossi Domain, Grenholm (2014) attempted to draw links between the two regions (Figure 6-9). The area west of the Baoulé Mossi Domain is dominated by 2.10-2.07 Ga calc-alkaline magmatism and mafic-ultramafic volcanics (Grenholm, 2014). This assemblage is interpreted as having formed within an extensional environment with crustal thinning and mantle upwelling (Grenholm, 2014). Eoeburnean rocks dated in Upper Guinea at 2212 ± 6 Ma (Lahondère et al., 2002) form the basement for the 2.10-2.07 Ga magmatism. Grenholm (2014) suggested that this is analogous to the Yetti and Eglab tectonic units. The Yetti and Eglab terranes consist of ~2.2 Ga basement cut by extensive 2.10-2.07 Ga intrusive and extrusive magmatism resulting from an extensional regime (Peucat et al., 2005). This led Grenholm (2014) to propose that the Yetti-Eglab domain of the Reguibat Shield and the EIIA of the Baoulé Mossi Domain could be connected beneath the Taoudeni Basin along a northeast-southwest trending belt, as shown in Figure 6-9.

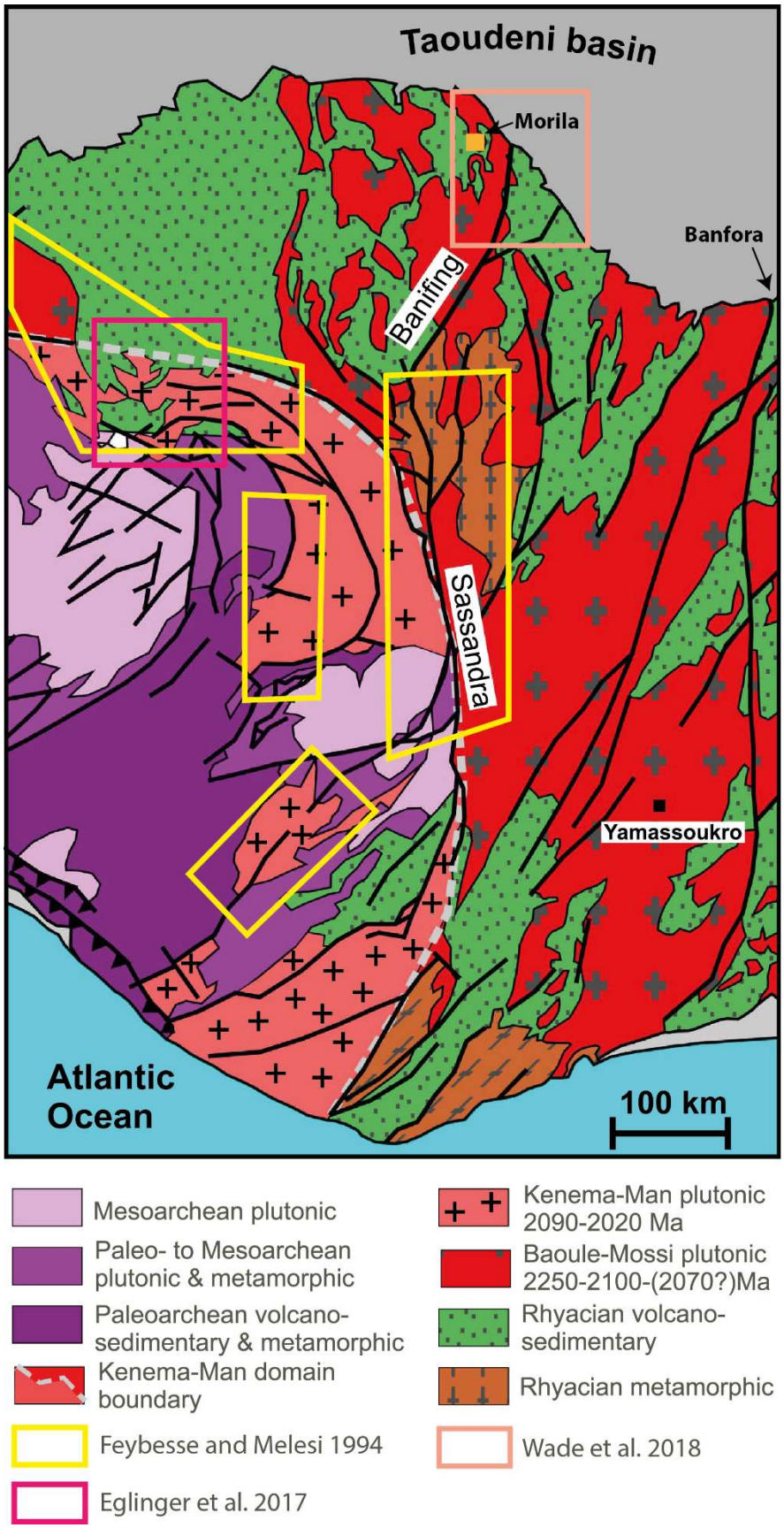

Figure 6-10 – Simplified geological map of the Archaean-Palaeoproterozoic contact of the Man-Leo Shield. Studies by Feybesse and Milési (1994), and Wane et al. (2018) were used to define the timing and kinematics of the Sassandra, and Banifing shear zones respectively.

6.4.2 General trends in the Palaeoproterozoic of the Reguibat Shield compared to the Baoulé-Mossi Domain

The geochronological data compiled by Parra-Avila et al. (2017) reveal a distinct westward younging trend in the Birimian (Figure 6-11). The entire domain experienced continuous magmatic activity for at least 150 million years, with a craton-scale diachronous geochronological pattern characterized by a westward migration of magmatic activity, and a migration rate of ~35km/Ma (Parra-Avila et al., 2017). An apparent 50 million year offset was noted between the commencement and termination of the magmatic activity between the east and west of the Baoulé-Mossi Domain (Parra-Avila et al., 2017).

Fewer data exist for the Palaeoproterozoic of the Reguibat Shield though distinct trends can be seen in available ages. In contrast to the Man-Leo Shield, the Reguibat Shield (Figure 6-8, and Figure 6-13) reveals a younging direction to the east. The Leaareig and Sfariat-Bu Daira Terranes are the oldest Palaeoproterozoic terranes in the Reguibat Shield with rocks dated at 2240 – 2153 Ma, and 2140 – 2071 Ma respectively. The terranes to the east are younger, dominated by ~2090-2050 magmatic activity (Figure 6-13).

Parra-Avila et al. (2017) proposed a model of formation of the Baoulé-Mossi Domain which involve the accretion of at least two crustal blocks, with an older block in the east and a younger block in the west (Chapter 1.4.2.2.2; Figure 6-12). With peak magmatism occurring at ~2130 Ma, and a lack of evidence for intrusions younger than ~2090 Ma, the ages from the Leaareig and Sfariat-Bu Daira Terrane are broadly similar to those of the eastern block of the Baoulé-Mossi Domain (Chapter 1.4.2.2.2; Figure 1.5). In contrast, the Adam Esseder, Yetti, and Eglab domains of the Reguibat Shield contain extensive granitoid plutonism at 2090-2050 Ma (Figure 6-8, and Figure 6-13), similar to the western block of the Baoulé-Mossi Domain (Chapter 1.4.2.2.2; Figure 1.5c). Comparisons made by Grenholm (2014) liken the easternmost terrane (Eglab) with the western block of the Baoulé-Mossi Domain.

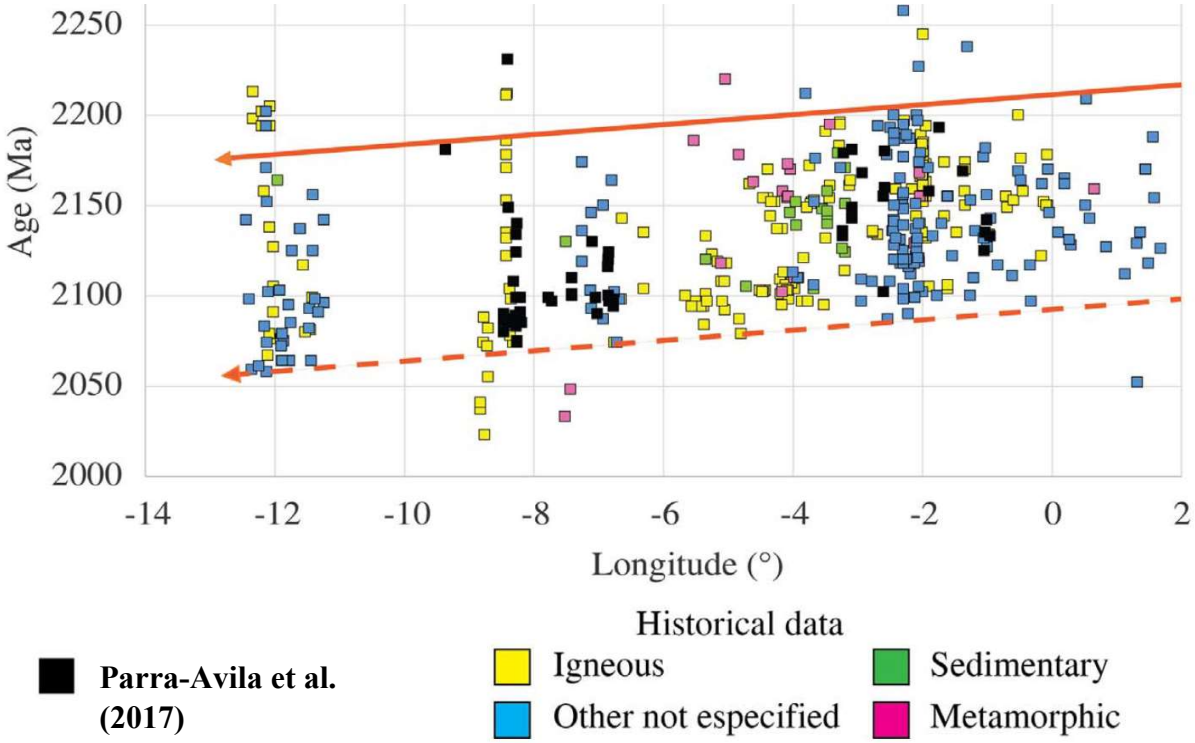

Figure 6-11 – Longitudinal variations in magmatic activity across the Baoulé-Mossi Domain from Parra-Avila et al. (2017). Zircon and monazite U-Pb age distribution as a function of longitude for the age bracket 2260–2000 Ma (455 ages). The progressive cessation of the magmatic activity from east to west during this period in the southern West African Craton equates to a migration of approximately 35 km/Myr. Over 95% of all ages plot above the offset of magmatism line "magmatic front" (dashed bottom arrow).

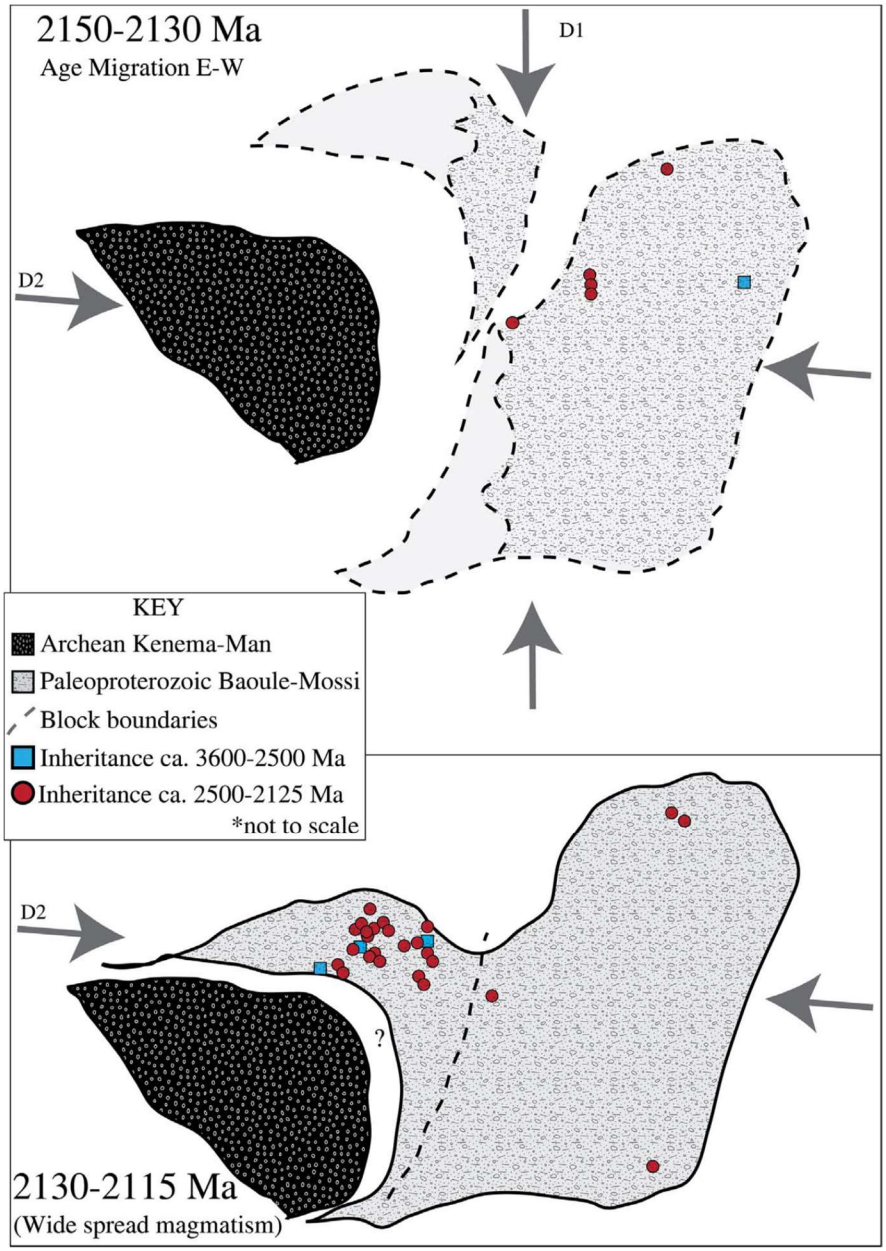

Figure 6-12 – Schematic cartoon showing the proposed boundaries and crustal blocks from Parra-Avila et al. (2017). Top, shows the Archean Kénéma-Man and the Baoulé-Mossi Domain. The Baoulé-Mossi Domain is divided into two major crustal blocks during the period 2160–2130 Ma. During this period the assembled blocks are affected by compressional forces, first N-S (D1) followed by a E-W compression (D2) (Parra-Avila et al., 2017; and references therein). Density of the dot pattern indicates distribution of magmatic activity with higher density corresponding to a greater degree of magmatism. Bottom shows the amalgamation of the Palaeoproterozoic blocks under a D2 compressions for the period 2130–2110 Ma. Note the occurrence of inherited grains. Inheritance is largely concentrated in the eastern portion of the Baoulé-Mossi, predominately represented by ages between ca. 2500 and 2125 Ma which are common crystallization ages across the eastern block, indicating that the western block is contaminated by crustal material derived from the eastern block.

In addition to a reversed younging direction, the transition in the Reguibat Shield (Figure 6-13), appears to be more abrupt than the gradational migration observed in the Baoulé-Mossi Domain (Figure 6-11). This is especially noticeable in the Leaareig and Sfariat-Bu Daira Terranes. There appears to be a sudden transition from 2240 – 2150 Ma to 2140 – 2070 Ma

across the Taghsoumat fault in terranes with a maximum combined width of ~140km (Figure 6-13b). This by far exceeds ~35km/Ma average across the Baoulé-Mossi Domain. There is another transition from the Sfariat-Bu Daira Terranes to predominantly 2117 – 2038 Ma rocks directly across the Sfariat shear zone (Figure 6-13b). Magmatism further east is limited to 2129 – 1995 Ma, with the exception of the 2210 Ma basement of the Eglab.

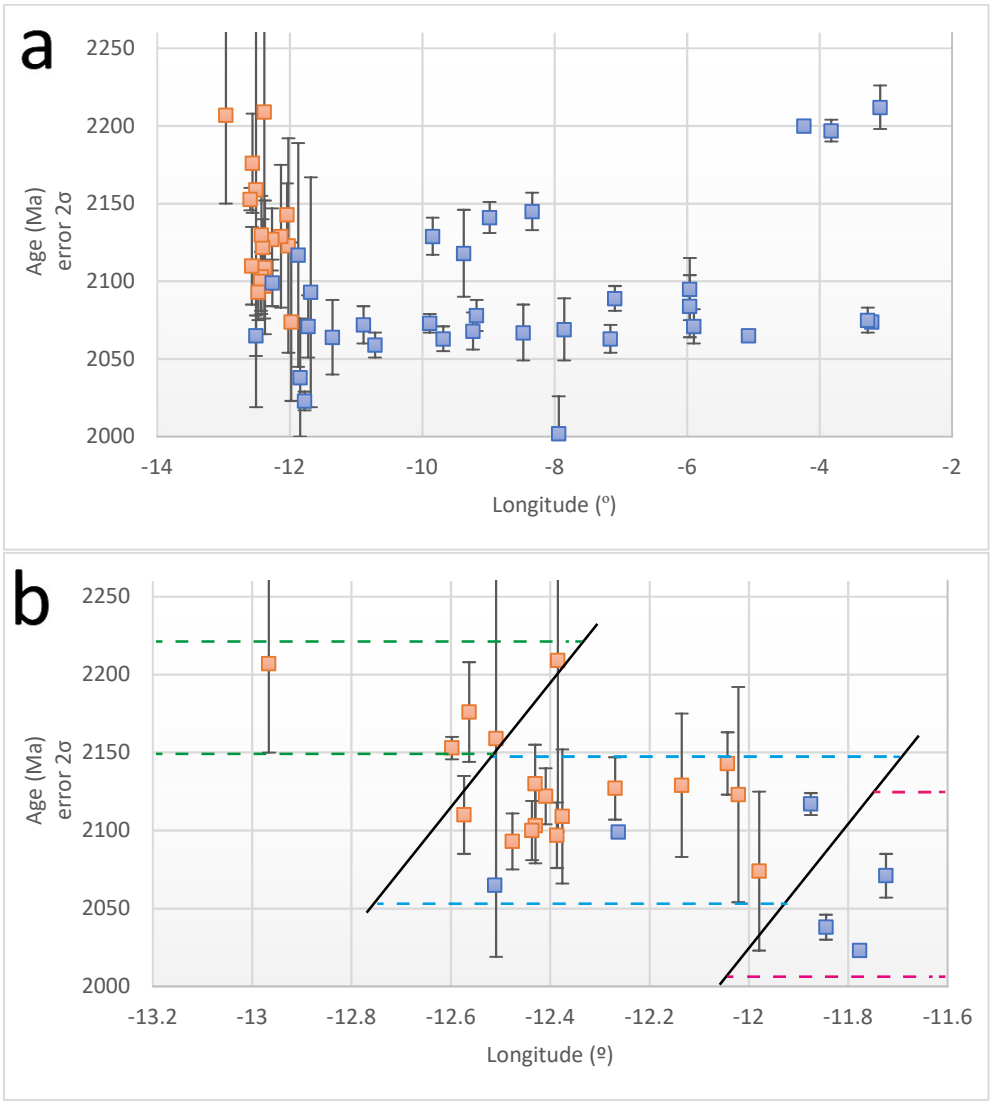

Figure 6-13 – Longitudinal variations in magmatic activity across the Palaeoproterozoic domain of the Reguibat Shield from Parra-Avila et al. (2017). Zircon and monazite U-Pb age distribution as a function of longitude for the age bracket 2260–2000 Ma (51 ages). Orange data was produced as a part of this project. Blue data are a compilation from Lahondère et al. (2003), Peucat et al. (2005), Schofield et al. (2006), and Lehbib (2016). a) all data from the Palaeoproterozoic of the Reguibat Shield. b) detailed view of the study area showing sharp transitions from the Leaareig Terrane (green) to the Sfariat-Bu Daira Terrane (blue), to the Adam Esseder terrane (pink) across the Taghsoumat and Sfariat shear zones respectively.

By directly comparing geochronological data from individual belts within the Baoulé-Mossi Domain (Parra-Avila et al., 2017) with new data from the Leaareig and Sfariat-Bu Daria

terranes, similarities can be seen (Figure 6-14). Age data from the Morila, and Bagoe belts in Mali, and the Banfora belt in Burkina Faso are similar to those from the Sfariat-Bu Daira Terrane (Figure 6-14). Similarities can also be observed in data from other belts in Burkina Faso, including the Belahouro belt, the Po-Tenkodogo-Yamba region and the Goren belt. Peak magmatism in the Boromo-Houndé is earlier than the Sfariat-Bu Daria domain, though there is overlap and it could be similar to the poorly constrained Leaareig Terrane. Other belts to the west of Morila post-date the Sfariat-Bu Daira and Leaareig Domains, experiencing peak magmatism at ca. 2090 Ma. Felsic intrusions in Ghana are largely older than ~2.13 Ga (Grenholm, 2014, Yao et al., 2001, Yao and Robb, 2000), with peak activity at ~2.17 Ga possibly similar to the Leaareig Terrane (Parra-Avila et al., 2017).

The three belts most similar in age to the Sfariat-Bu Daira domain are close to the boundary between the two crustal blocks that make up the Baoulé-Mossi Domain (Parra-Avila et al., 2017). The Morila belt is the closest Birimian belt to the west of the contact defined as being 'to the west of the Banfora-Bagoe belts'. The ~2130 Ma collision between the major crustal units in the Baoulé-Mossi Domain was partially constrained by the presence of inherited ca. 2250 and 2150 Ma zircons in intrusions younger than ~2130 Ma. This collision has similar timing to the ~2130-2120 Ma collision between the Sfariat-Bu Daira and Leaareig Terranes, also constrained by the presence of inherited zircons, as well as whole rock geochemistry (Chapter 6.3). Schofield et al. (2006) noted strong similarities in timing and kinematics of the Sfariat shear zone in the Reguibat Shield and Banifin shear zone (~20km to the west of the Morila belt) at around ~2100 Ma.

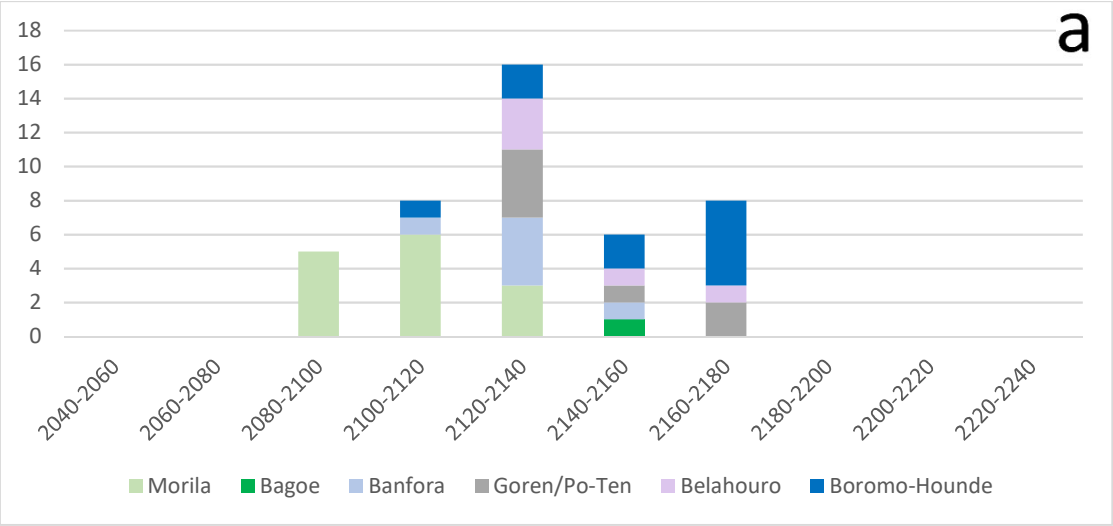

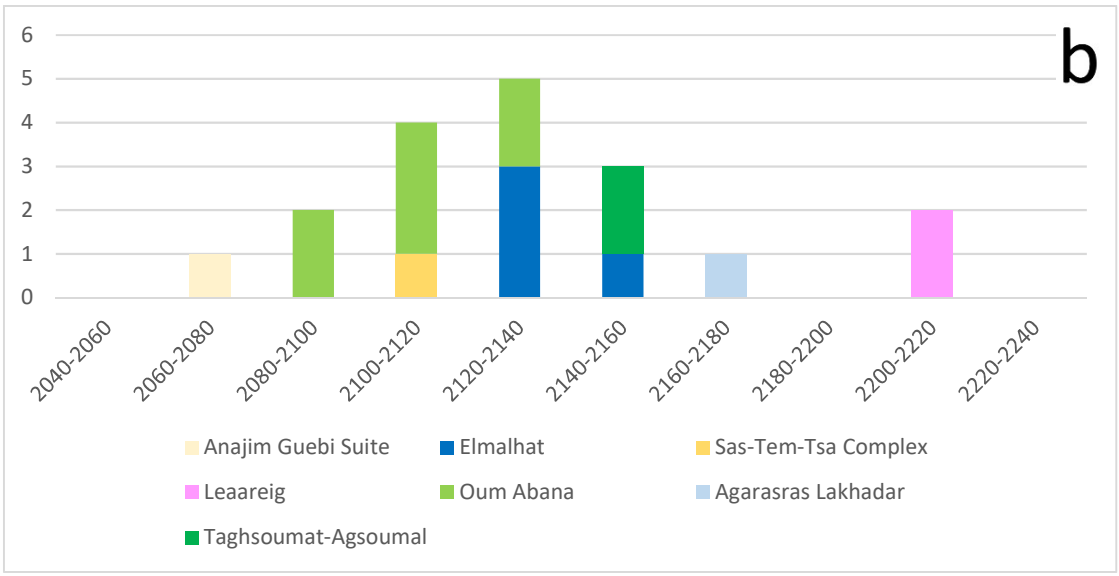

Figure 6-14 – Histogram showing the distribution of ages in a) the Banfora, Po-Tenkodogo-Yamba region (and the Goren Belt), and Belahouro belts of Burkina Faso, as well as the Morila and Bagoe belts in Mali. (data from Parra-Avila et al., 2017) b) the Leaareig and Sfariat-Bu Daira Terranes c) individual domains within the study area.

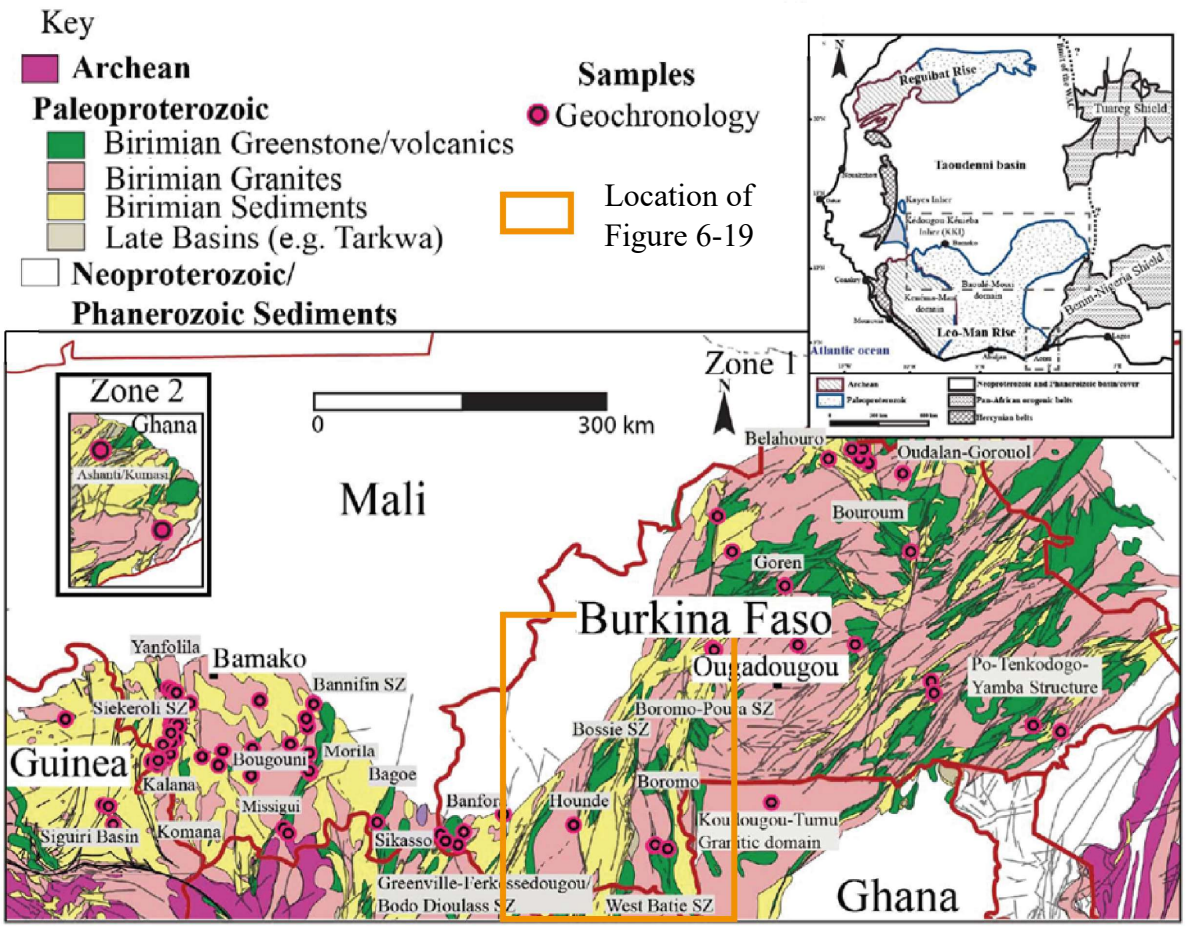

Figure 6-15 - Simplified geological map of the West African craton after Boher et al. (1992). The map shows the extension of the Leo-Man rise in the southern portion of the craton, defined by the Archean Kénéma-Man and Palaeoproterozoic Baoulé-Mossi Domain. Boxed area shown in detail in insert B; B) Simplified geological map, after Lebrun et al. (2016) of the study areas delineated in insert A. Zone 1 covers Burkina Faso, Mali northern Ghana and eastern Guinea, zone 2 covers a portion of the Ashanti belt in southern Ghana. Map includes major structures and samples collected for geochronological work.

6.4.3 Direct lithological and geochronological comparisons

6.4.3.1 General comparison with the Birimian belts

6.4.3.1.1 Stratigraphic

The Birimian stratigraphy broadly consists, from bottom to top, of:

1) a thick sequence of locally pillowed tholeiitic basalts and gabbros (Hirdes et al., 1996, Leube et al., 1990b), interlayered with immature sedimentary rocks and carbonates;

2) a volcano-sedimentary sequence dominated by turbidites, mudstones and carbonates, interbedded with calc-alkaline volcanic and volcaniclastic rocks (Baratoux et al., 2011, Baratoux et al., 2015, Hirdes and Davis, 1998, Hirdes et al., 1996, Oberthür et al., 1998); and

3) metasedimentary belts composed of fragmental felsic rocks, flysch-type turbidites and large concordant peraluminous granitic plutons, metamorphosed to amphibolite facies and generally deformed into regional scale antiformal structures (Sylvester and Attoh, 1992).

The Birimian belts are largely affected by lower to upper greenschist facies metamorphism (Baratoux et al., 2015), though locally amphibolite and granulite facies metamorphism is observed (Parra-Avila et al., 2017). This is broadly comparable to observations in the Leaareig and Sfariat-Bu Daira Terranes.

6.4.3.1.2 Geochemistry

6.4.3.1.2.1 Traditional

Grenholm (2014) compiled a geochemical database for Birimian rocks, (also including some data from the related São Luís Craton) and plotted intrusive and volcanic rocks on traditional discrimination diagrams by Pearce (2008), and Pearce et al. (1984) (Figure 6-16). The samples have not been classified by lithology, although comparisons can be made with samples from the Leaareig and Sfariat-Bu Daira Terranes when plotted on the same plots. The Th/Nb proxy diagrams (Figure 6-16a,c) show very similar trends with the majority of samples from both shields revealing volcanic arc trends, with plutonic rocks exhibiting more of a continental arc signature than the volcanic rocks. The Rb/Y+Nb plots (Figure 6-16b,d) also show very similar spreads with the majority of samples displaying a volcanic arc signature.

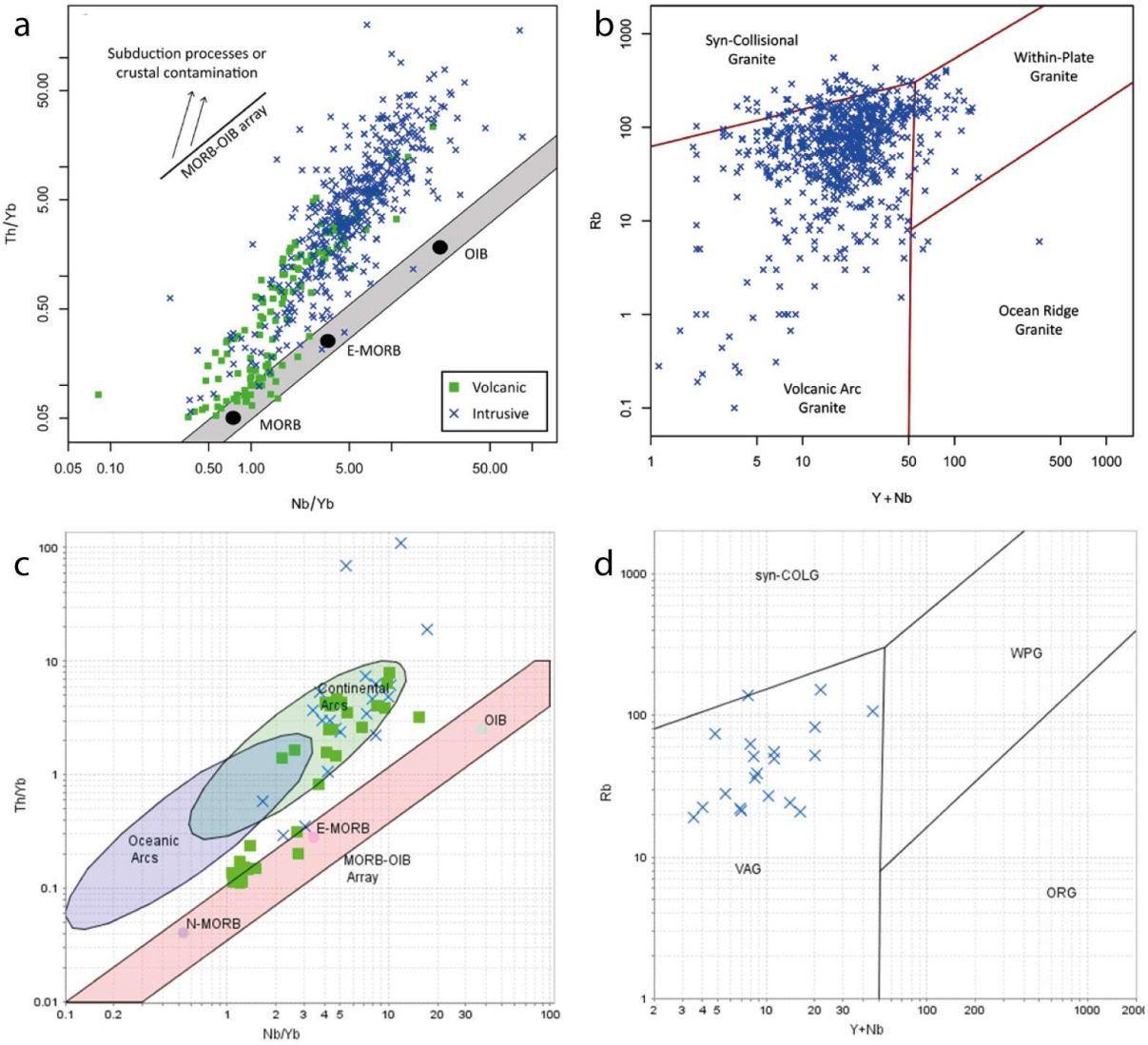

Figure 6-16 - a,b) Tectonic discrimination diagrams for Birimian intrusive and volcanic rocks from Grenholm (2014). ; a) Th/Yb vs. Nb/Yb diagram after Pearce (2008). b) Rb vs. Y+Nb diagram after Pearce et al. (1984) . c,d) Tectonic discrimination diagrams for Eburnean intrusive and volcanic rocks from the Leaareig and Sfariat-Bu Daira Terranes. c) Th/Yb vs. Nb/Yb diagram after Pearce (2014). d) Rb vs. Y+Nb diagram after Pearce et al. (1984), VAG – volcanic arc granite, syn-COLG – syn-collisional granite, WPG – within plate granite, ORG – ocean ridge granite.

6.4.3.1.2.2 Multidimensional discrimination

Verma (2017) applied a series of multidimensional discrimination diagrams to Birimian rocks in southern Ghana as well as to the Katiola-Marabadiassa belt in the Ivory Coast (equivalent of the Banfora belt in Burkina Faso). The results from mafic samples of the Birimian in Ghana revealed an island arc signature (Verma et al., 2006), while both intermediate (Verma and Verma, 2013) and felsic (Verma et al., 2012, Verma et al., 2013) rocks revealed a continental

arc signature. As such Verma (2017) interpreted the region as having formed in a continental arc setting, consistent with the volcanic arc setting suggested by the Pearce et al. (1984) plots.

The Kaliola-Marabadiassa granitoids in the Ivory Coast consist of two generations; the first (2123-2108 Ma) intrudes the greenstone formations (Timb and Tafolo, Kanangono, Fronan and N'Guessankro), while the second intrudes the Bandama sedimentary basin formations and the earlier granitoid intrusions. Verma (2017) only applied the multidiscrimination diagrams to the first generation of felsic granitoids that were already considered to represent a collision setting (Feybesse and Milési, 1994, Ledru et al., 1994). The multidimensional diagrams applied to felsic rocks from the belt suggested continental arc and collisional affinities.

Overall, the geochemical characteristics of the Ghanaian Birimian granitoids and those of the Kaliola Marabadiassa belt in Ivory Coast, are similar to what was observed in the Leaareig and Sfariat-Bu Daira Terranes (Sections 3.5.1.2 and 4.5.1.2).

6.4.3.2 Comparisons between individual belts

The Morila, Banfora, and Boromo-Houndé belts are three well studied belts within in the Baoulé Mossi Domain with comparable ages to the Sfariat-Bu Daira and Leaareig Terranes (Figure 6-14). The following sections directly compare individual volcanic-volcanosedimentary belts from the Reguibat and Man Leo Shields (Figure 6-17).

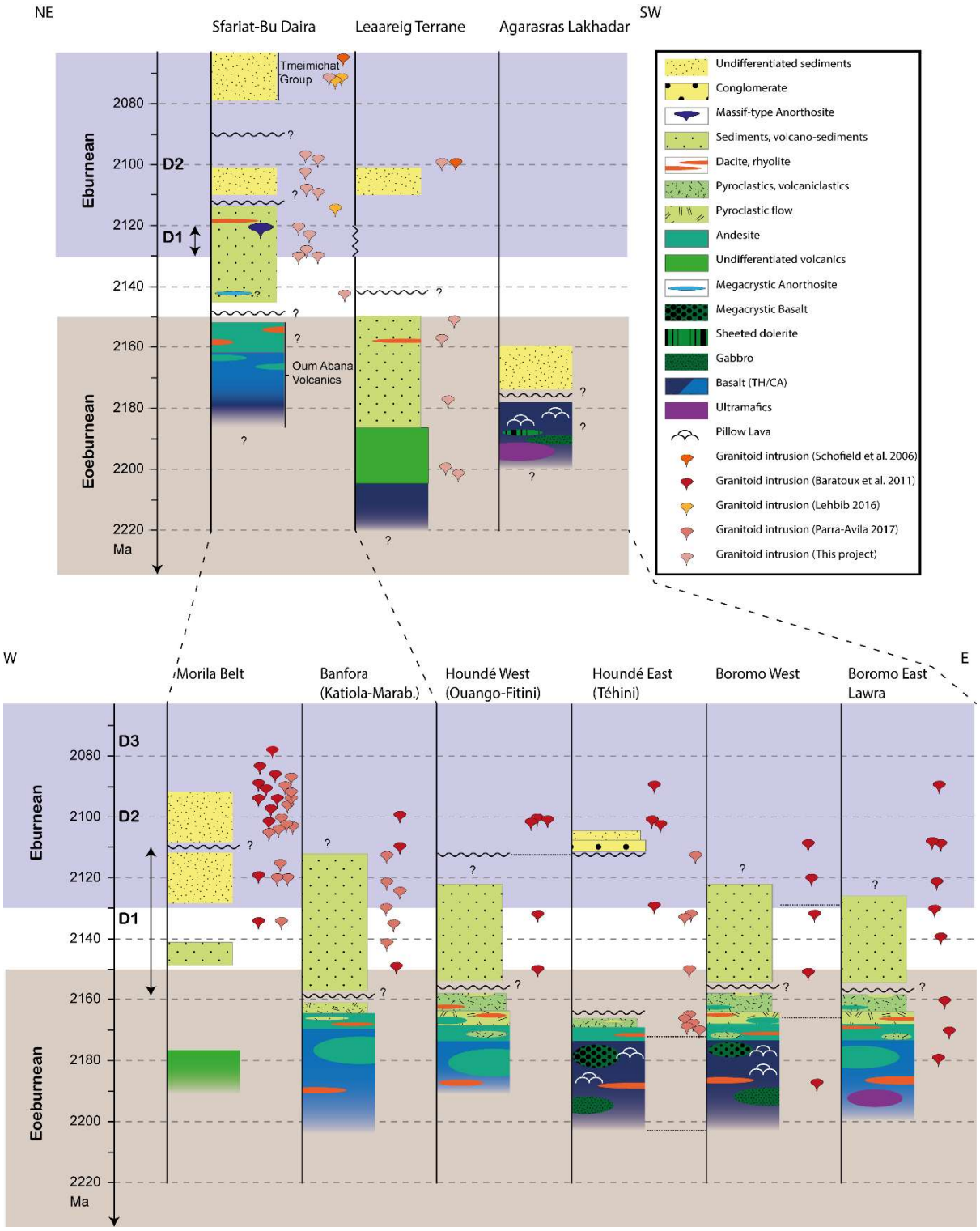

Figure 6-17 – Simplified stratigraphic sequences for the Sfrariat-Bu Daira terrane, Leaareig Terrane, and Agarasras Lakhadar Domain of the Regquibat Shield compared with similar belts of the Baoulé-Mossi Domain. The stratigraphic sequences for the Sfrariat-Bu Daira and, Leaareig Terrane were compiled from data and geochronological constraints presented in sections 4.5 and 3,5 respectively. The stratigraphic sequences for Agarasras Lakhadar Domain is from Section 3.5. Stratigraphy of the Morila belt, Mali is from Parra-Avila et al. (2017) and references therein. The Banfora, Houndé and Boromo belts from Burkina Faso (and corresponding belts in Ivory Coast and Ghana) is from Baratoux et al. (2011). Katiola-Marab. – Katiola-Marabadiassa belt. TH – tholeiitic mafic units, CA – calc-alkaline volcanic sequences.

6.4.3.2.1 Morila

The Morila belt, located between the Kalana– Yanfolila and Syama volcano-sedimentary belts in the Massigui region of Mali (Hammond et al., 2011), is the easternmost belt of Parra-Avila et al's (2017) 'western block'. The belt is dominated by a composite TTG style granitic intrusive complex, with Birimian metavolcanics and a meta-sedimentary sequence comprising locally pillowed basalt to basaltic-andesite lavas, and inter-bedded with a variety of volcano-sedimentary rocks (Figure 6-18; Parra-Avila et al. (2016)).

Near the Morila gold mine, the Birimian volcano-sedimentary rocks are subdivided into two formations, separated by the Massigui granite (with which significant gold mineralization is associated; Hammond et al., 2011). The Kekoro–Bougouni Formation (west of the Massigui granite), comprises pelites and quartzites with minor andesitic to basaltic volcanic rocks (Hammond et al., 2011). The Bagoë volcano-sedimentary formation (east of the Massigui granite) consists of three lithological units with transitional boundaries including pelites in the east, centrally located greywackes, and metavolcanics (rhyodacites and andesites) to the west (Hammond et al., 2011).

The Morila Belt is dominated more by granitoid intrusions than the Oum Abana Belt. However, the pelites, quartzites and andesitic to basaltic volcanic rocks of the Kekoro–Bougouni Formation, and pelites, greywackes and rhyodacites and andesites of the Bagoë volcano-sedimentary formation are very similar to volcanic and sedimentary belts of the Oum Abana Belt, described in Sections 4.2.2.2, and 4.2.2.3. The TTG suite composition (Sections 4.2.2.4.1, and 4.2.3.4), and age distribution (Figure 6-14) of the intrusive granitoids within the Oum Abana Belt are also similar to the composite TTG style granitic intrusive complex of the Morila Belt.

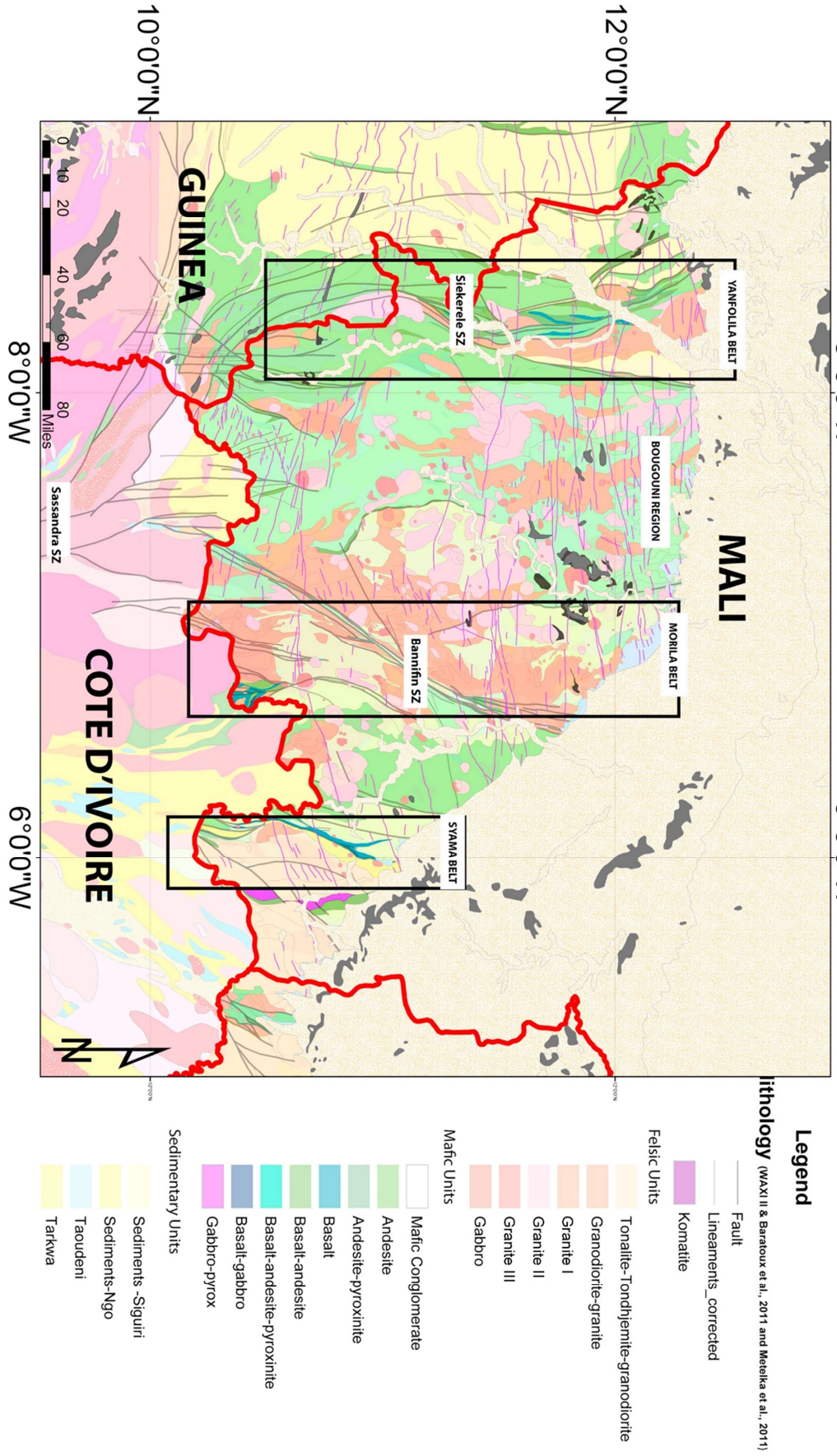

Figure 6-18 – Simplified geological map of the south of Mali, showing the location of the Morila Belt (from Parra-Avila et al., 2016)

6.4.3.2.2 Banfora belt

The Banfora belt consists of basalt, andesite, volcano-sedimentary and rhyolite units (2–4 km thick) in the east, and volcano-sedimentary units in the west (Figure 6.17; Baratoux et al., 2011). The base of the stratigraphic sequence consists of basalts and andesites, with increasing volumes of strongly folded volcano-sediments as you move up the sequence (Figure 6-17). The Banfora belt extends into the Ivory Coast in the form of the Katiola-Marabadiassa greenstone belt and Bandama volcano-sedimentary basin (Baratoux et al., 2011; and referrences therein).

The only geochronological data from the Banfora belt are from granitoid samples dated at 2143 ± 10 Ma and 2108 ± 16 Ma (Parra-Avila et al., 2017). Felsic intrusions in the Katiola-Marabadiassa belt were dated between 2123 ± 3 and 2097 ± 3 Ma (zircon Pb–Pb; Doumbia et al., 1998). Detrital zircons from the sediments of the Bandama basin were dated (Pb–Pb) at ~2133 and 2107 ± 7 Ma (Doumbia et al., 1998) with the deposition age estimated by pre- and post-basin granitoid at 2108 ± 12 to 2097 ± 3 Ma based on the zircon Pb–Pb ages of intrusions (Baratoux et al., 2011).

The volcanic rocks within the Oum Abana belt comprises basalts and andesites at the base (in the west), grading into more felsic lithologies toward the top of the sequence (to the east) where only andesite and rhyolite are present (Section 4.2.2.2). Although no geochronological constraints exist for the volcanic sequence in either belt, the stratigraphy of the volcanic belt of Oum Abana belt similar to that of the Banfora belt (Figure 6-17). The age distributions of granitoid intrusions in the Oum Abana belt and Elmalhat domain are very similar to those of the Banfora belt (Figure 6-14).

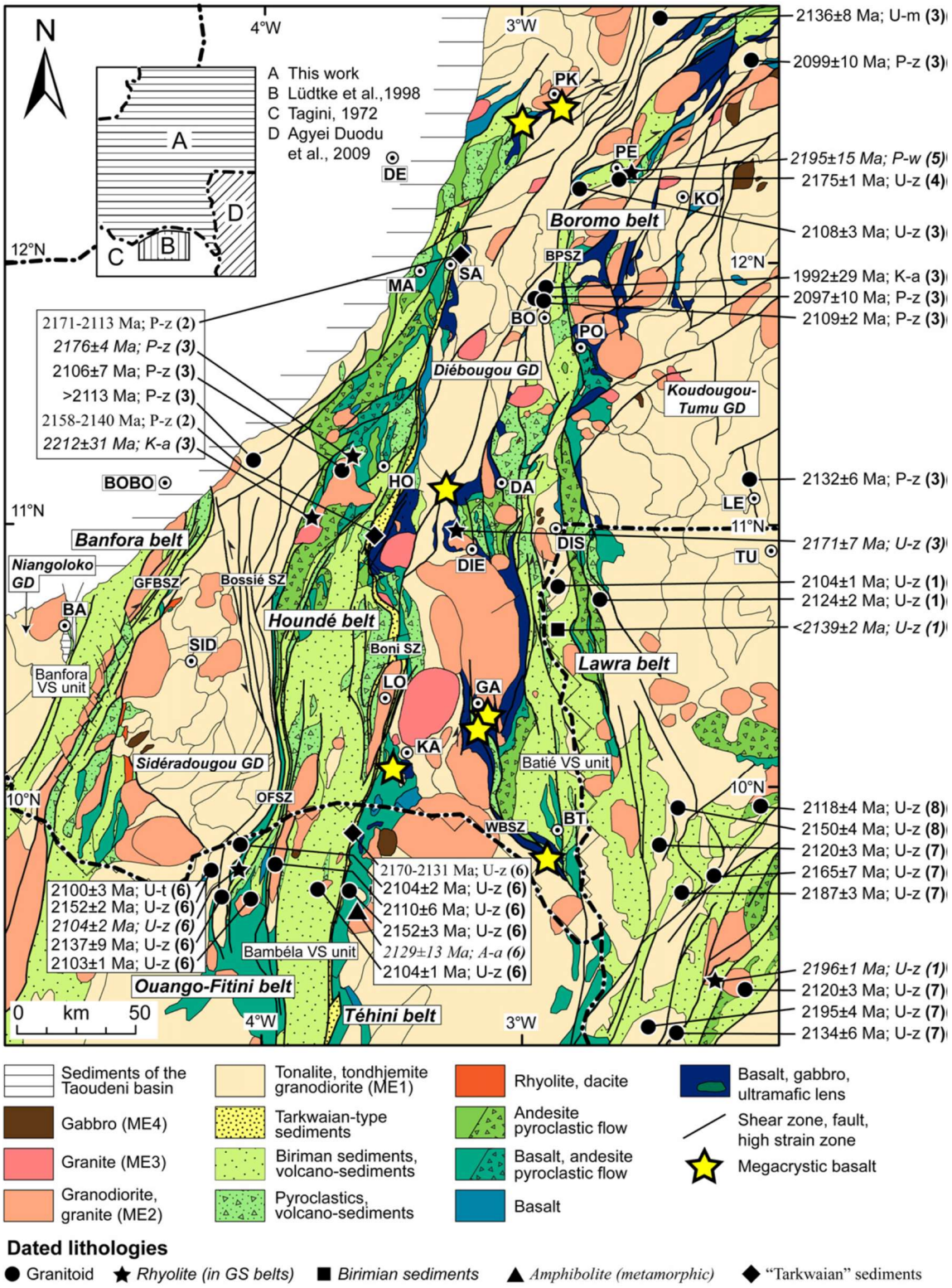

Figure 6-19 - Geological map of the western Burkina Faso (Baratoux et al., 2011; and references therein). The names of the greenstone belts, granitoid domains (GD) and major Birimian (volcano-)sedimentary units referred to in the text are indicated. Dating methods U–Pb (U), Pb–Pb (P), K–Ar (K), and Ar–Ar (A) were applied on zircon (z), monazite (m), t – titanite (t), and amphibole (a). BA – Banfora, BO – Boromo, BOBO – Bobo-Dioulasso, BT – Batié, DA – Dano, DE – Dédougou, DIE – Diébougou, DIS – Dissin, GA – Gaoua, HO – Houndé, MA – Mana, KA – Kampti, KO – Koudougou, LE – Léo, LO – Loropéni, PE – Perkoa, PK – Ponkélé, PO – Poura, SA – Safané, SID – Sidéradougou, TU – Tumu. GFBSZ – Greenville-Ferkessedougou-Bobo-Dioulasso shear zone (SZ), OFSZ – Ouango-Fitini SZ, BPSZ – Boromo-Poura shear corridor, WBSZ – West Batié SZ. See Figure 6-15 for location.

6.4.3.2.3 Boromo and Houndé belts

The Boromo belt (referred to as the "Lawra" belt in its Ghanaian continuation (Leube et al., 1990a)) has many geological features in common with both the Leaareig Terrane, and the Elmalhat domain. It is defined on its east and west by a thick sequence of locally pillowed basalts, intercalated with gabbros, and orthoamphibolites/pyroxenites (Figures 6.16, and 6.17; Baratoux et al., 2011), similar to the Agarasras Lakhadar sequence. Like the Taghsoumat-Aghsoumal Belt, mafic and intermediate volcanism in the east of the Boromo belt varies from tholeiitic to calc-alkaline in composition (Baratoux et al., 2011) with field relationships suggesting that the tholeiitic basalts are older than the calc-alkaline series (Béziat et al., 2000). The volcanic rocks are mostly tholeiitic in the western margin of the belt, where the tholeiitic basalts contain large (up to 10 cm), locally corroded plagioclase megacrysts, and occasional pillow structures (yellow star in Figure 6-17; Baratoux et al., 2011). These units locally contain 90% plagioclase and are comparable to the megacrystic anorthosites described by Ashwal (1993) (Baratoux et al., 2011). This distinctive unit is very similar to the megacrystic anorthosite in the Elmalhat domain, and southernmost Oum Abana belt (Section 4.1.2.2). Moving up in the stratigraphy, the sequence transitions into andesitic lavas of transitional and calc-alkaline composition, interlayered with thick sequences of pyroclastic flows and tuffs and occasional layers of ferruginous cherts (Baratoux et al., 2011), similar to the Taghsoumat-Aghsoumal Belt (Baratoux et al., 2011). The central part of the Boromo belt consists of volcano-sedimentary unit (metasediments, tuffs and epiclastic volcano-sediments and rare andesites) (Baratoux et al., 2011).

The stratigraphy of the Houndé belt is similar to that of the Boromo belt (Figure 6-17). The megacrystic tholeiitic basalt/anorthosite is present in both belts and was used by Baratoux et al. (2011) to demonstrate structural and litho-stratigraphic continuity between the two. Detrital zircons from the Bambéla volcano-sedimentary unit (southern continuation of the Houndé

belt), reveal three clusters of ages (U-Pb) at ca. 2180, 2150, and 2126 Ma (Lüdtke et al., 1999). Few radiometric ages are available for the volcanic rocks of the Boromo belt, with rhyolites and andesites yielding dates of, 2171 ± 7 Ma (from zircon U-Pb) and 2195 ± 15 Ma (from whole rock Pb–Pb) (Baratoux et al., 2011; and referrences therein).

Strong similarities exist between the Leaareig Terrane and the Boromo and Houndé belts (Figure 6-17). No direct age data exists for the volcanic rocks of the Taghsoumat-Aghsoumal Belt, though a porphyry interpreted as sub-volcanic (J292) was dated at 2159 ± 140Ma and the volcanic rocks are cross-cut by an undeformed granite dated at 2152.9 ± 7.2 Ma. Therefore, the Taghsoumat-Aghsoumal Belt is possibly of a similar age to the Boromo and Houndé belt, although further geochronological work is required. The detrital zircon age of 2176 ± 32 Ma from paragneiss from the Agarasras Lakhadar Domain (J204) could potentially be related to the ~2180 cluster observed in the detrital zircons from the Bambéla volcano-sedimentary unit.

Ophiolite sequences have never been interpreted in the Boromo and Houndé belts, however locally pillowed tholeiitic basalts are observed intercalated with gabbros, and pyroxenites. The whole rock geochemistry of these pillow basalts within the Boromo and Houndé belts are very similar to those observed within the ophiolite sequence at the eastern edge of the Agarasras Lakhadar Domain (Figure 6-20). Like the pillow basalts from the Agarasras Lakhadar ophiolite sequence, pillow basalts from the Boromo and Houndé belts are tholeiitic (Figure 6-20d), with normal MORB characteristics (Pearce (2008), (2014); Figure 6-20a, b). Furthermore, pillow basalts from Agarasras Lakhadar and Boromo-Houndé plot with back arc basin characteristics on the Cabanis and Lecolle (1989) La-Y-Nb discrimination diagram (one of the few diagrams to differentiate back arc basins) (Figure 6-20c). Therefore, pillow basalts, gabbros, and pyroxenites within the Boromo and Houndé belts can be correlated with Agarasras Lakhadar ophiolite sequence. Ophiolite sequences are relatively rare in the geological record. The

presence of ophiolite sequences within Agarasras Lakhadar and the Boromo-Houndé belt is a strong correlation between the Reguibat and Man-Leo shields.

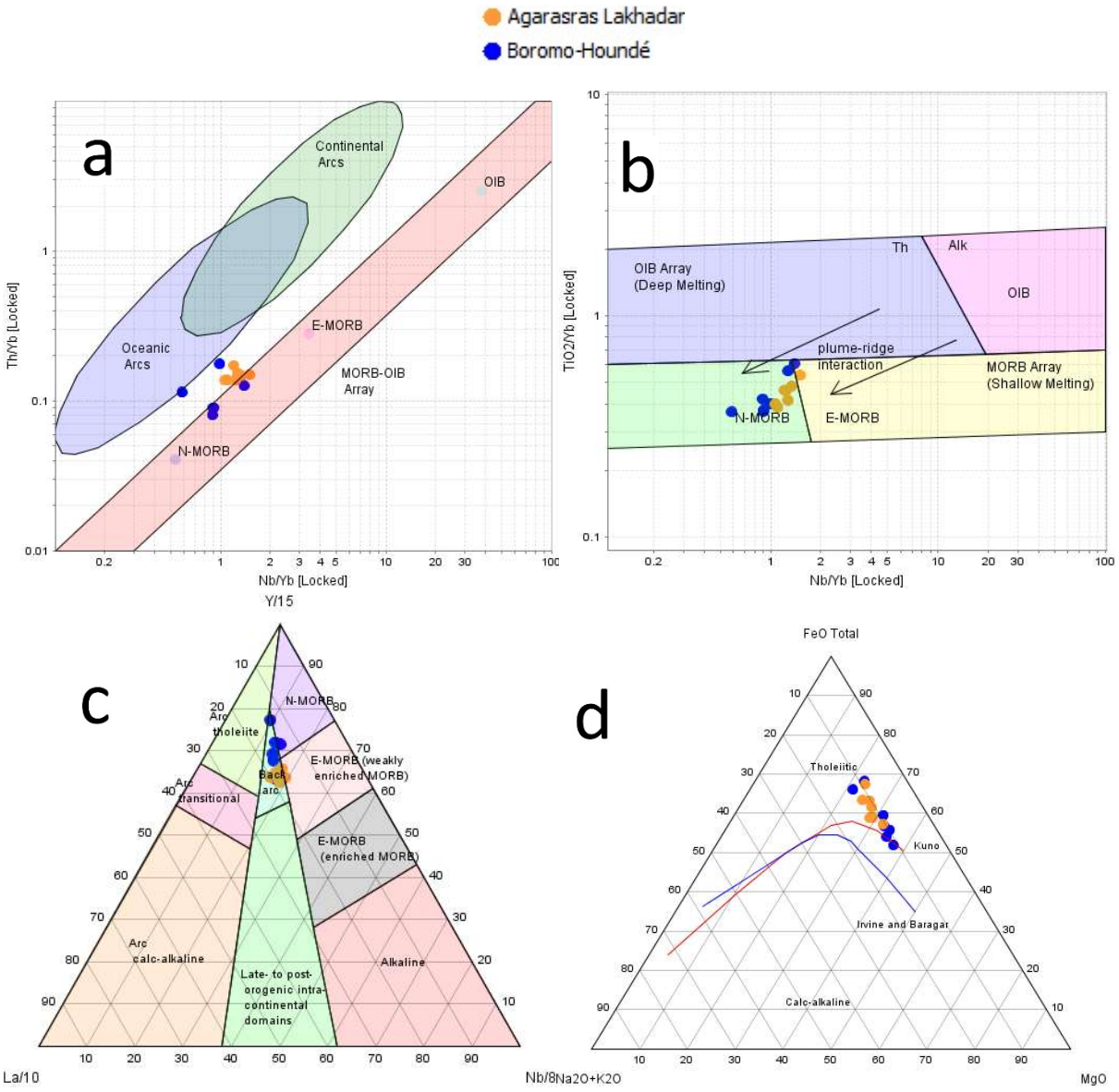

Figure 6-20 – Comparison of whole rock geochemistry of pillow basalts associated with ultramafic intrusions in the Boromo-Houndé belts with those of the Agarasras Lakhadar ophiolite sequence. a) Pearce (2014) Th-Nb proxy, b) (2008) Ti-Nb proxy, c) Cabanis and Lecolle (1989) La-Y-Nd tectonic discrimination diagram, d) AFM plot. Whole rock geochemistry of the Boromo-Houndé belts from Baratoux et al. (2011)

6.4.4 Geophysics

Jessell et al. (2016) created a structural map of West Africa based on gravity and magnetic data, grouping structures to their age according to geophysical attributes (Figure 6-21). The Eburnean structures can be observed continuing under the Taoudeni basin from both the Man-Leo and Reguibat shields in a north-south to northwest-southeast trend. Structures from the

central Reguibat shield (where the Leaareig and Sfariat-Bu Daira Terranes are present) continue under the Taoudeni basin, trending broadly toward the contact between the western and eastern blocks of the Baoulé-Mossi Domain (as inferred by Parra-Avila et al., 2017), and toward comparable belts; the Morila, Banfora, Houndé, and Boromo belts.

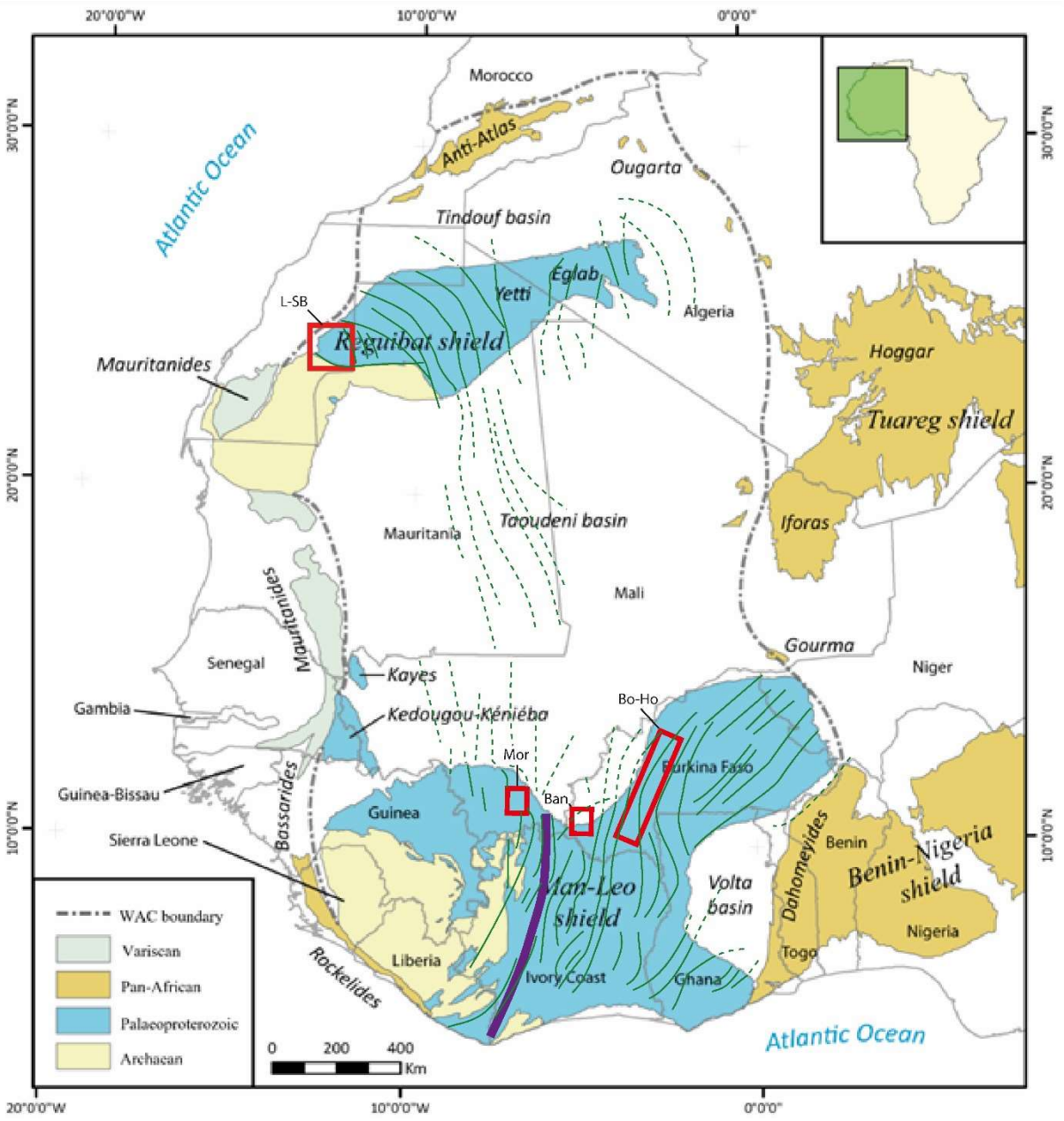

Figure 6-21 –Palaeoproterozoic structural map for the West African Craton. Base map from (Grenholm, 2014). Geophysical structural interpretation based interpreted from of medium-wavelength gravity and magnetic data, with extensions of the structures shown by dashed lines (modified from Jessell et al. (2016)). The purple line represents the boundary between the western and eastern blocks of the Baoulé-Mossi Domain, as inferred by Parra-Avila et al. (2017). L-SB – Leaareig and Sfariat-Bu Daira Terranes, Mor – Morila belt, Ban – Banfora belt, Bo-Ho – Boromo and Houndé belts

6.4.5 Proposed Geodynamic Setting for a Combined Reguibat – Baoulé-Mossi Block

The work undertaken in the present study allows correlations to be made between Palaeoproterozoic volcanosedimentary belts of the Reguibat and Man Leo Shields. Notably, in addition to similar geochronology, the Sfariat-Bu Daira and Leaareig Terranes of the Reguibat Shield, and the Morila, Banfora, Boromo and Houndé belts of the Man-Leo Shield share very similar stratigraphic sequences, including distinct geological units such as megacrystic anorthosite/basalt, and the presence of ultramafic rocks and pillowed tholeiitic basalt representing possible ophiolite sequences (Figure 6-17). Additionally, Palaeoproterozoic structures observed under the Taoudeni basin broadly trend from the Sfariat-Bu Daira and Leaareig Terranes in the centre of the Reguibat Shield toward the Man-Leo Shield (Figure 6-21). With these correlations in mind, the geodynamic model proposed for the formation of the Sfariat-Bu Daira and Leaareig Terranes of the Reguibat Shield (Chapter 6.2; Figure 6-5) can be compared with recently proposed models for the assembly of the Man-Leo Shield during the Palaeoproterozoic. These models cover the formation of the Palaeoproterozoic Baoulé-Mossi Domain (Eglinger et al., 2017, Parra-Avila et al., 2017, Wane et al., 2018), the assembly of its two major crustal blocks (Parra-Avila et al., 2017), the collision of the Baoulé-Mossi Domain with the Archaean Kéména-Man Domain in the north (Eglinger et al., 2017) and northeast (Wane et al., 2018), and subsequent magmatism (Parra-Avila et al., 2017, Wane et al., 2018).

6.4.5.1 2250 to 2125 Ma – Assembly of the Baoulé-Mossi Domain

The first phase (~2250-2125 Ma; Figure 6-22) saw the existence of large portions of the Baoulé-Mossi Domain separated by an ocean from the Archaean Kenema-Man craton (Eglinger et al., 2017, Parra-Avila et al., 2017, Wane et al., 2018). The Baoulé-Mossi Domain formed as a series of island arcs (Figure 6-22a, b), accreted together with a younging towards

the west (Parra-Avila et al., 2017). The oceanic crust was dipping away from the Kenema-Man craton as suggested by studies on the northern (Figure 6.20a; Eglinger et al., 2017) and northeastern margins (Figure 6.20b; Wane et al., 2018). By ~2150 Ma the domain comprised two blocks, which collided at ~2130 Ma; (Figure 6-22c), corresponding with peak magmatism (Parra-Avila et al., 2017) and peak metamorphic grades (Block et al., 2015) in the eastern block.

This collision event accords with the suggestion derived from the present study for a ~2130 – 2120 Ma collision between the Leaareig and Sfariat-Bu Daira Terranes in the Reguibat Shield (Figure 6-5). Notably, it is during this collisional event that the Banfora, Boromo and Houndé belts of the eastern block, are juxtaposed against the Morila belt in the western block (Figure 6-22c).

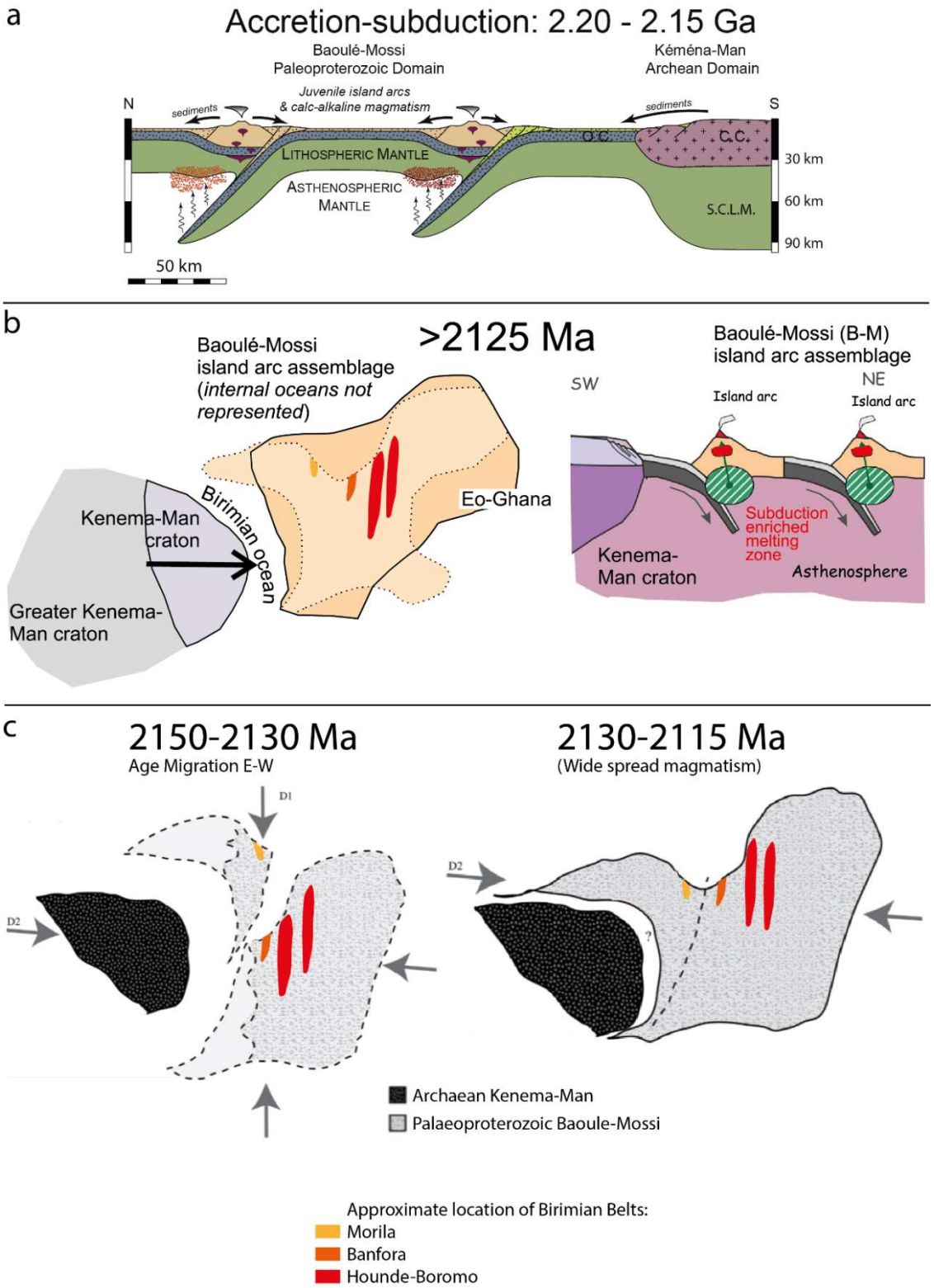

Figure 6-22 – Early stages of formation of the Man-Leo Shield (>2125-2115 Ma). a) geodynamic evolution of the northern Palaeoproterozoic margin of the Archean Kéména-Man domain from 2.20-2.15 Ga (modified from Eglinger et al., 2017). C.C. = continental crust; O.C. = oceanic crust; SCLM = subcontinental lithospheric mantle. b) ~2250-2125 Ma: large portions of the of the Baoulé-Mossi Domain are generated from volcanic arc-related magmatism, with the region still separated by an ocean from the Archean Kenema-Man craton (modified from Wane et al., 2018). c) During the period 2150-2130 Ma, the Baoulé-Mossi Domain formed (at least) two separate blocks, that collided at ~2130 Ma (modified from Parra-Avila et al., 2017). For correlation with the Sfariat-Bu Daira and Leaareig Terranes, locations of similar Birimian belts have been plotted.

6.4.5.2 2125 to 2090 Ma – Collision of Baoulé-Mossi Domain with the Kéména-Man Domain

The second phase of formation of the Man-Leo Shield is represented by the collision of the Baoulé-Mossi and Kéména-Man Domains (Figure 6-23). To the north of the Kéména-Man Domain, a frontal collision between the domains is thought to have occurred between ca. 2.10 and 2.09 Ga (Figure 6-23b).

Although the exact timing of the initiation of the collision is not adequately defined to the northeast of the Kenema-Man craton, it is apparent that the period between ~2125 and 2090 Ma involved an oblique collision between the Baoulé-Mossi and Kéména-Man Domains (Figure 6-23a). Structural studies to the northeast of the region indicate that the Banifing Shear Zone underwent sinistral transpression between ~2125 and 2090 Ma (Wane et al., 2018). The start of the transpression is not dated, but is thought to have begun before ~2115 Ma (the start of transpression-related magmatism), with evidence of earlier compression at ~2125 Ma (Wane et al., 2018). Wane et al. (2018) interprets this as marking the beginning of the transgressive collision between the Baoulé-Mossi and Kéména-Man Domain. However, with no evidence of collision along the northern margin before ~2100 Ma, this present study suggests that this initial deformation could relate to the E-W compressive event (relating to the collision between the two blocks of the Baoulé-Mossi Domain) at ~2130 – 2110 Ma as defined by Parra-Avila et al. (2017) (Figure 6-22c). It is suggested that the major magmatic event recorded by Wane et al. (2018) at around 2100 Ma (2112 ± 5 Ma, 2103 ± 5 Ma, 2095 ± 9 Ma, 2102 ± 10 M, and 2106 ± 11 Ma) more likely corresponds to the oblique collision between the Baoulé-Mossi and the eastern margin of the Kéména-Man Domains. This would be more in line with the timing of the frontal collision of the northern margin (Eglinger et al., 2017).

In the Reguibat Shield, late movement along the El Mdena Shear Zone destroyed Palaeoproterozoic kinematic indicators. This lead Schofield et al. (2006) to interpret the

kinematics of the Archaean-Palaeoproterozoic collision from the Sfariat Shear Zone, as involving sinistral transpression at ~2100 Ma (Figure 6-6). Geochronology work in El Mdena Shear Zone (Sassaiate-Temmimichate–Tsabaya Complex; Chapter 2, (Lehbib, 2016)) confirms the timing of the Archaean-Palaeoproterozoic collision to be ~2100 Ma.

Therefore, the Archaean-Palaeoproterozoic collisional events in the Reguibat and Man-Leo Shields are now considered to be contemporaneous with associated sinistral transpression observed in the Sfariat Shear zone of the Reguibat Shield and the Sassandra and Banifing Shear Zones of the Man-Leo Shield.

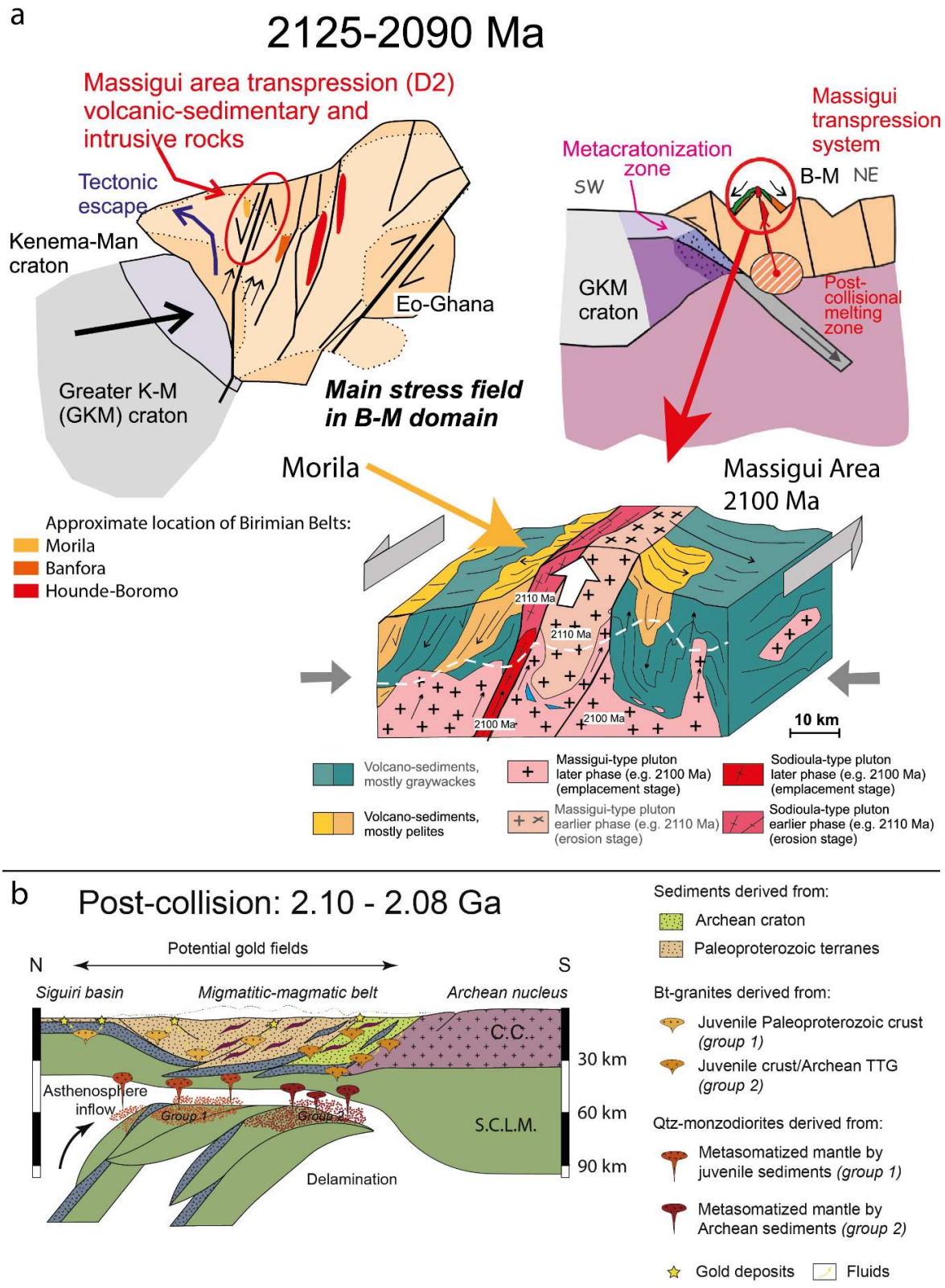

Figure 6-23 – Evolution of the Man-Leo Shield from ~2125-2090 Ma, modified from Wane et al. (2018). a) Collision of the Baoulé-Mossi Domain with the Kenema-Man craton. This induced a continental subduction and the initiation of a metacratonization of the Kenema-Man craton and large transpressive movements in the Baoulé-Mossi Domain; b) especially to the west along the Banifing Shear Zone in the Massigui region. The dashed white line represents current exposed surface. c) collisional and post-collisional evolution of the northern Palaeoproterozoic margin of the Archean Kéména-Man domain at 2.10-2.08 Ga (modified from Eglinger et al., 2017). C.C. = continental crust; O.C. = oceanic crust; SCLM = subcontinental lithospheric mantle. For correlation with the Sfariat-Bu Daira and Leaareig Terranes, locations of similar Birimian belts have been added.

6.4.5.3 2090 to 2020 Ma – Post-Collisional Process

In the Man-Leo Shield, post-collisional lithospheric delamination and metacratonisation of the Kéména-Man Domain resulted in widespread magmatism of the western block of the Baoulé-Mossi Domain, and in the east of the Kéména-Man Domain from ~2090-2020 Ma.

To the north of the Kenema-Man craton, lithospheric delamination resulted in asthenospheric upwelling (Figure 6-23b). The asthenospheric upwelling resulted in ~2.09 to 2.07 Ga magmatic activity observed to the north of the Kéména-Man Domain (Eglinger et al., 2017). This event resulted in the melting of Archaean sediments proximal to the Kéména-Man Domain and Palaeoproterozoic sediments further north of the contact (Figure 6-23b). This event is also responsible for the granulite facies metamorphism along the northern Kéména-Man margin dated by Feybesse et al. (2000) at ca. 2.07 Ga (Feybesse et al., 2000, Eglinger et al., 2017).

The period between ~2090–2020 Ma also saw the metacratonisation of the eastern margin of the Kéména-Man Domain, and a reduction in the sinistral transpression in the Baoulé-Mossi Domain (Wane et al., 2018). The oblique continental collision between Baoulé-Mossi and Kéména-Man Domains resulted in the tectonic tearing of the latter, allowing magmas to be emplaced (Figure 6.24a; Liégeois et al., 2013, Wane et al., 2018). This resulted in the generation of the ~2090–2020 Ma granitoids to the west of the Sassandra fault, (Wane et al., 2018). Additionally, the tearing acted to reduce the stress induced in the Baoulé-Mossi Domain as observed in the kinematics of the Banifing Shear Zone. This reduction in stress drastically reduced the extent of transpression, magmatism, uplift and sedimentation within the eastern block of the Baoulé-Mossi Domain (Wane et al. (2018); Figure 6-24b).

This event is also believed to relate to a craton-scale gold mineralisation event (Eglinger et al., 2017, Le Mignot et al., 2017a, Wane et al., 2018).

Grenholm (2014) proposed links between this event in the Man-Leo shield, and the extensional magmatism (~2.09-2.07 Ga) observed in Algeria within the Eglab and Yetti domains of the Reguibat Shield. A compilation of age data from across the Palaeoproterozoic domain of the Reguibat Shield (Figure 6-13) reveals extensive magmatism at ~2100 to 2050 Ma, extending from the Sfariat Shear Zone to the Eglab Domain. Little evidence for this magmatic event exists within the project area, with a diorite intrusion within the Oum Abana belt dated at 2065 ± 13 Ma (Lehbib, 2016), and two samples dated at within the Abajim Guebli Suite at 2070 ± 11 Ma (Schofield et al., 2006). There is no evidence for this event having affected the Palaeoproterozoic Leaareig and Archaean terranes of the Reguibat Shield. Therefore, the post-collisional magmatism in the Man-Leo Shield (limited to the western block of the Baoulé-Mossi Domain and eastern margin of the Kéména-Man domain) could potentially relate to widespread magmatism to east of the Sfariat Shear Zone in the Reguibat Shield.

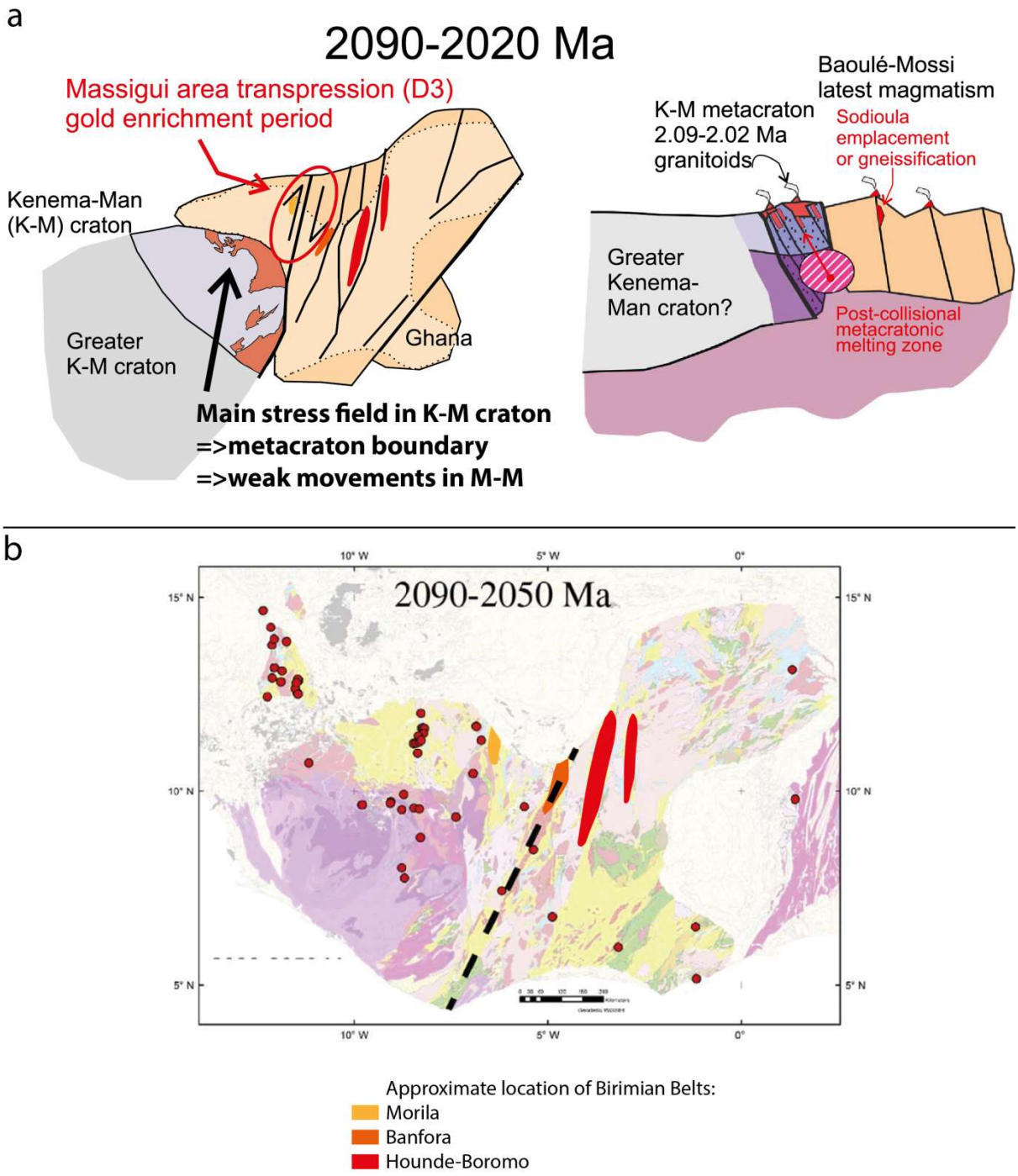

Figure 6-24 – Late stages in the formation of the Man-Leo Shield (2090-2115 Ma). a) Peak metacratonization of the Kenema-Man craton with the contemporaneous intrusion of granitoids (with Archaean protoliths), with a strong decrease of the stress in the Baoulé-Mossi Domain modified from Wane et al., 2018). b) Geochronology samples show a concentration of magmatic activity the western block from 2090 to 2050 Ma modified from Parra-Avila et al. (2017). For correlation with the Sfariat-Bu Daira and Leaareig Terranes, locations of similar Birimian belts have been added.

6.4.6 Lithological differences

Although I-type belt granitoids are abundant within the Sfariat-Bu Daira and Leaareig Terranes, S-type basin granitoids are not observed. S-type Basin granitoids are widespread throughout the Baoulé Mossi Domain, observed within sedimentary belts representing the melting of crustal material during a magmatic event from 2125 ± 2 to 2088 ± 1 Ma (Yao et al., 2001, Yao and Robb, 1999). In contrast, I-type Belt granitoid intrusions are observed within volcanic and volcanosedimentary belts, forming from the partial melting of basaltic rocks during a magmatic event from 2179 ± 2 to 2136 ± 10 Ma (Yao et al., 2001, Yao and Robb, 1999). A potential explanation for the absence of these granitoids in Sfariat-Bu Daira and Leaareig Terranes is a lack of exposure. A large portion of the Leaareig domain is extensively covered by sand, alluvium, colluvium and sabkha. Additionally, due to difficult terrain, limited field work has been completed in the region. Subcrops of marble indicate a potential sedimentary basin setting, where S-type Basin granitoids may exist. Therefore, the lack of observed S-type Basin granitoids in the Sfariat-Bu Daira and Leaareig Terranes is potentially an artefact of a lack of exposure and low degree of work in certain regions.

The presence of thick (>1km) beds of marble in the Oum Abana belt are unique to the Reguibat Shield. They represent a generally higher portion of chemical sediments (marble, BIF and chert) within the metasedimentary belts of the Oum Abana belt (and Sassaiate-Temmimichate-Tsabaya Complex) compared to the more clastic dominated sedimentary belts of the Baoulé Mossi Domain. The presence of the thick marble is interpreted as the product of higher carbonate production in the shallow marine environments offshore of the Palaeoproterozoic arcs of the Reguibat Shield, possibly relating to the effects of palaeolatitude. If the Reguibat Shield was situated more equatorially during this time it might have had higher carbonate production resulting in the deposition of thicker carbonate sequences. Palaeomagnetic reconstructions by Pesonen et al. (2003) broadly places the West African Craton close to the

equator at 2.00 Ga (Figure 6-25). Onstott and Dorbor (1987) puts the Man-Leo shield (Nimba and Harper formation, Liberia) at a latitude of 18ºN at 2050 ± 6 Ma whereas samples of dolerite put the Eglab of the Reguibat Shield as sitting at 5-6 ºN at 2020 ± 54 to 1998 ± 80 Ma. This supports the hypothesis that marble units in the Reguibat Shield reflect a more equatorial setting than other portions of this Eburnean continent.

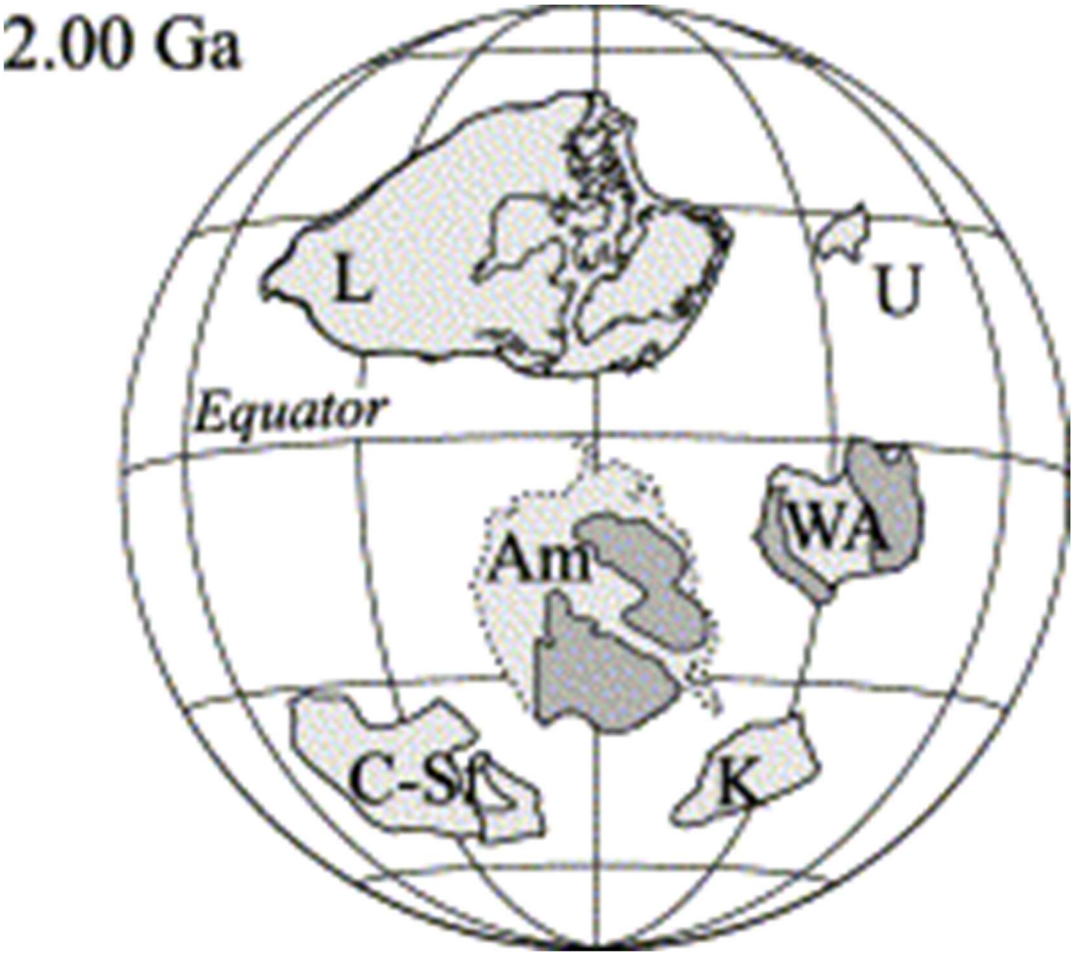

Figure 6-25 – Palaeomagnetic reconstruction of continents at 2.00 Ga by Pesonen et al. (2003). Data available from Laurentia, Congo/Sao Francisco, Amazonia, West Africa, Kalahari and Ukraine. The shaded areas in the West Africa craton represent mainly Eburnean cratonised areas (the Man block to the right and the Reguibat block to the left, Trompette (1994))

6.4.7 Conclusions

Strong similarities are present between Birimian belts of the Baoulé-Mossi Domain and the Leaareig and Sfariat-Bu Daira Terranes of the Reguibat Shield. The regions are very similar in stratigraphy, geochemistry, geochronology, and structural data. The age distribution of

granitoid intrusions within the Oum Abana, and Morila belts is also contemporaneous. The Sfariat-Bu Daira Terrane has very similar lithological, geochemical and geochronological characteristics to the Banfora belt, and its southern continuation in the Katiola-Marabadiassa belt. The Taghsoumat-Aghsoumal Belt and Agarasras Lakhadar Domain (Leaarieg terrane) share many lithological similarities with the Boromo and Houndé belts with broadly similar age constraints (though more sampling is required in the Leaareig Terrane). Additionally, the presence of megacrystic basalt/anorthosite in the Boromo and Houndé belts, comparable megacrystic anorthosite in the Elmalhat domain indicate that very similar processes were happening in these regions during the Eburnean. Additionally, geophysical interpretations reveal Palaeoproterozoic structural features broadly linking the Morila, Banfora, Boromo, and Houndé belts with the central Reguibat Shield. This combined synthesis, supports a strong correlation between the volcanic, volcanosedimentary and sedimentary belts of the Sfariat and Leaareig Terranes and the Birimian belts of the Baoulé-Mossi Domain. A comparison between the geodynamic model created for the Leaareig and Sfariat-Bu Daira Terranes, and a synthesis of the latest models in the formation for the Man-Leo Shield reveals that the timing and characteristics of each major stage of formation and assembly are the same in both shields.

7.0 Prospectivity Assessment of the Study Area

Metallogenic processes have not been well characterised in the Reguibat Shield, although the region is an extension of the highly endowed, and relatively well studied Birimian belts of the Baoulé Mossi Domain to its South (Chapter 6.4). Therefore, it is probable that similar ore forming processes that occurred in the Birimian belts (Chapter 1.4.4) also occurred in the Leaareig and Sfariat-Bu Daira Terranes.

The Man-Leo Shield contains extensive orogenic gold mineralisation, especially associated with Birimian volcanosedimentary belts (Figure 7-1). Models of orogenic-style gold mineralisation events have been well established for these deposits on a craton-scale. Strong geochronological and lithological correlations between these mineralised Birimian belts, and direct evidence of gold mineralisation within the field area (Figure 7-2) suggest that these craton-scale mineralisation events likely occurred within the Leaareig and Sfariat-Bu Daira Terranes of the Reguibat Shield. The study area is therefore highly prospective for orogenic gold mineralisation.

Multiple styles of mineralisation have also been observed within the Elmalhat Anorthosite Complex including the presence of magmatic sulphides (potential for Voisey's Bay-style Ni-Cu-(Co-PGE) mineralisation), PGE-bearing stratiform chromitite, and orthomagmatic Fe-Ti-V mineralisation (Figure 7-2).

Low grade Superior-type banded iron formations are observed in the Sfariat Shear Zone, as part of the Riche Anajim Group (Figure 7-2).

Although little evidence exists for their presence within the field area, Cu-Au, and Mo-Cu porphyry and VMS mineralisation have also been observed in the Man-Leo shield within comparable belts.

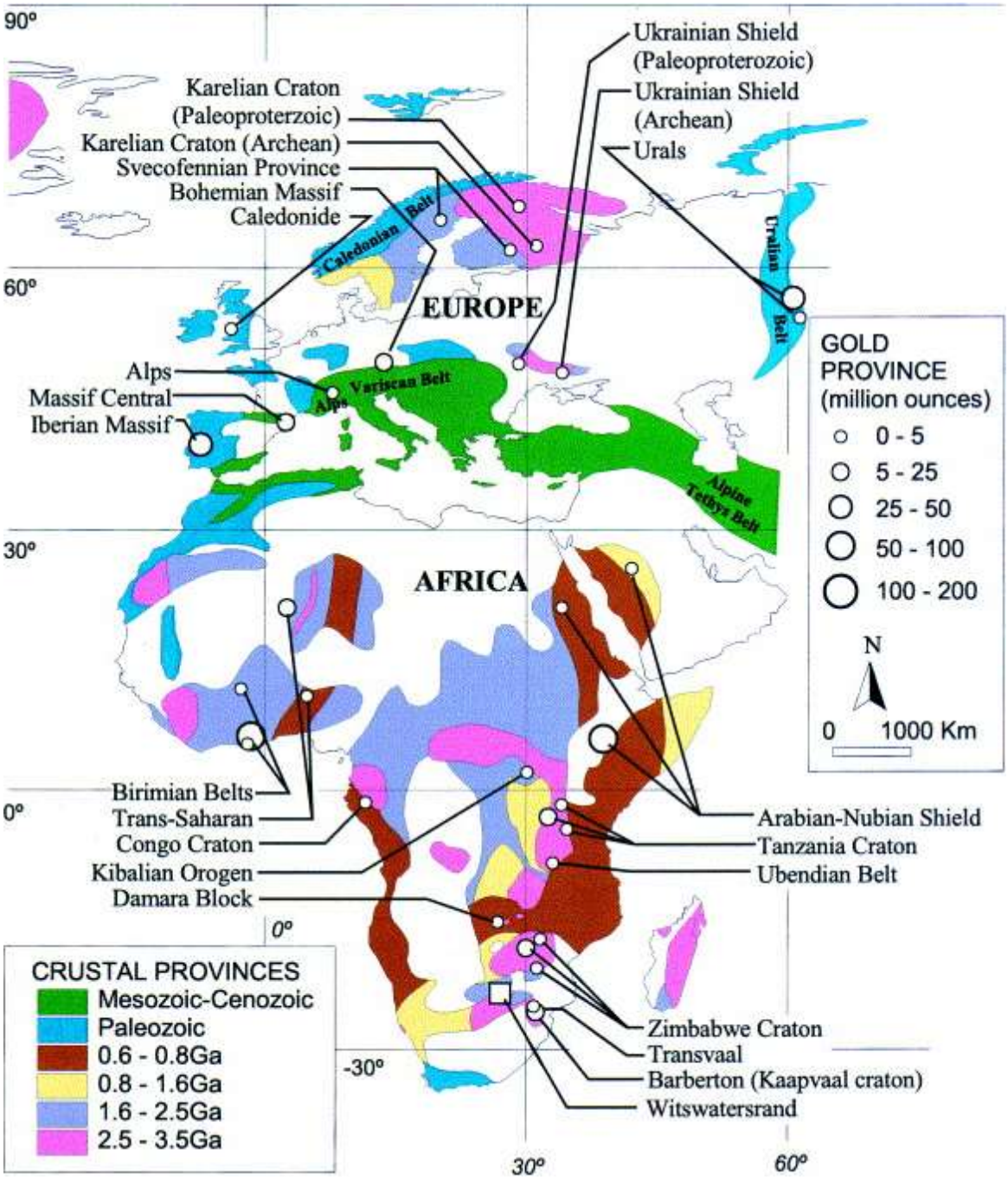

Figure 7-1 – Simplified map showing the distribution of crust of a given age and the distribution of significant orogenic gold occurrences within Africa and Europe (Goldfarb et al., 2001)

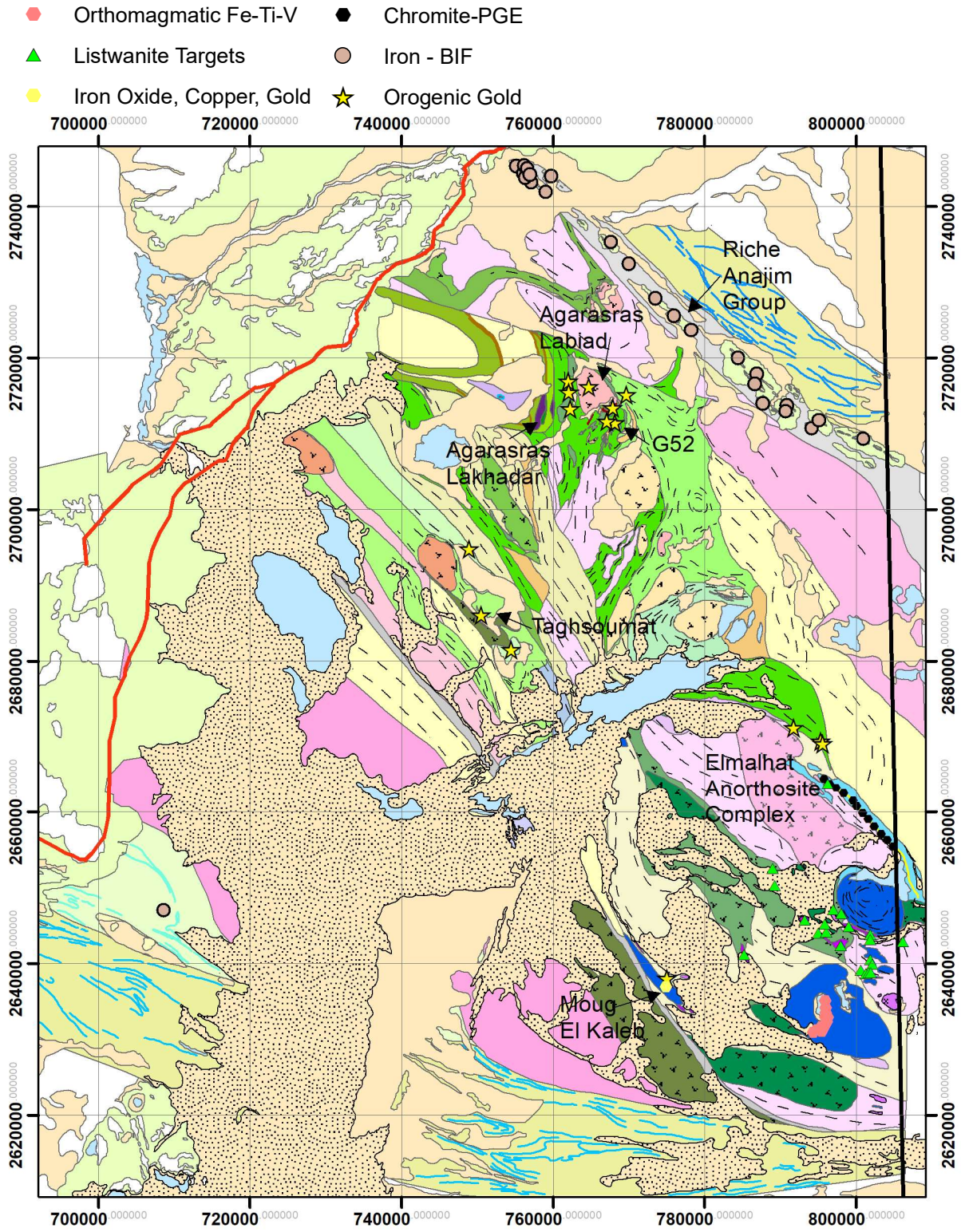

Figure 7-2 – Metallogenic map of the study area, showing locations where evidence of various styles of mineralisation exists.

7.1 **Gold**

7.1.1 Orogenic Gold

The Man-Leo shield hosts extensive gold mineralisation, much of which is situated within the Birimian belts of the Baoulé Mossi Domain (Markwitz et al., 2016b). Gold within the Birimian is the most important economically mineable commodity in West Africa (Markwitz et al., 2016b) and represents one of the most significant occurrences of orogenic gold in Africa (Figure 7-1; Goldfarb et al. (2001)).

Gold mineralisation within the domain is largely hosted by sedimentary and volcanosedimentary belts with many deposits located on the edges of these belts or within granites that intrude them (Figure 7-3). The two main styles of mineralisation observed in the Birimian include quartz vein hosted and disseminated deposits (Béziat et al., 2008). Quartz vein hosted deposits (eg. Fété Kole, Burkina Faso) occur in all lithologies, with gold principally concentrated within the deformed veins, associated with either sulphides or tourmaline (Béziat et al., 2008). The disseminated deposits (eg. Souma, and Inata, Burkina Faso) occur almost exclusively in albitites (± listwanites) with gold largely concentrated within alteration halos of generally undeformed, unmineralized, quartz-albite-carbonate veins (Béziat et al., 2008). Quartz vein hosted gold deposits typically contain higher grades than disseminated deposits, though disseminated mineralisation generally contain higher tonnages (Béziat et al., 2008). The two styles of mineralisation are not mutually exclusive, sometimes occurring within the same belt or deposit (eg. both disseminated (Loraboue´ and Larafella) and quartz-vein hosted (Poura mine) mineralisation is observed within the Poura district, Burkina Faso) (Béziat et al., 2008).

The orogenic gold mineralisation within the Birimian belts occurred during two craton-scale Palaeoproterozoic events (Figure 7-4; Le Mignot et al. (2017a)). The first orogenic gold

mineralisation event occurred between ~2190 and 2125 Ma during the Eoeburnean orogeny and has been responsible for the concentration of large quantities of gold (Le Mignot et al., 2017a). The second phase of mineralisation during the late stages of the Eburnean orogeny (between 2120 and 2000 Ma) represents a prolific period for the formation of high-grade gold mineralization (Le Mignot et al., 2017a). Strong geochronological and lithological correlations between these mineralised Birimian belts (Section 6.4), and direct evidence of gold mineralisation within the field area (Figure 7-2, Chapter 5.1), suggest that these extensive mineralisation events also occurred Leaareig and Sfariat-Bu Daira Terranes. It would therefore appear that there is the potential for significant gold mineralisation in the area.

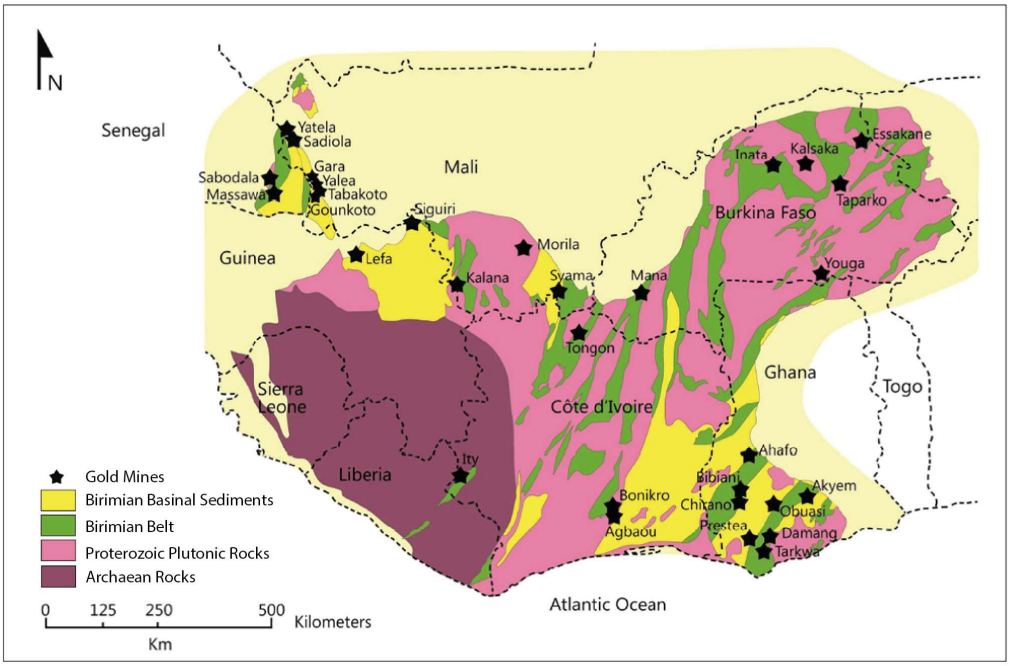

Figure 7-3 - Location of the major gold mines in the Man-Leo Shield in relation to the simplified geology (from Robertson and Peters, 2016)

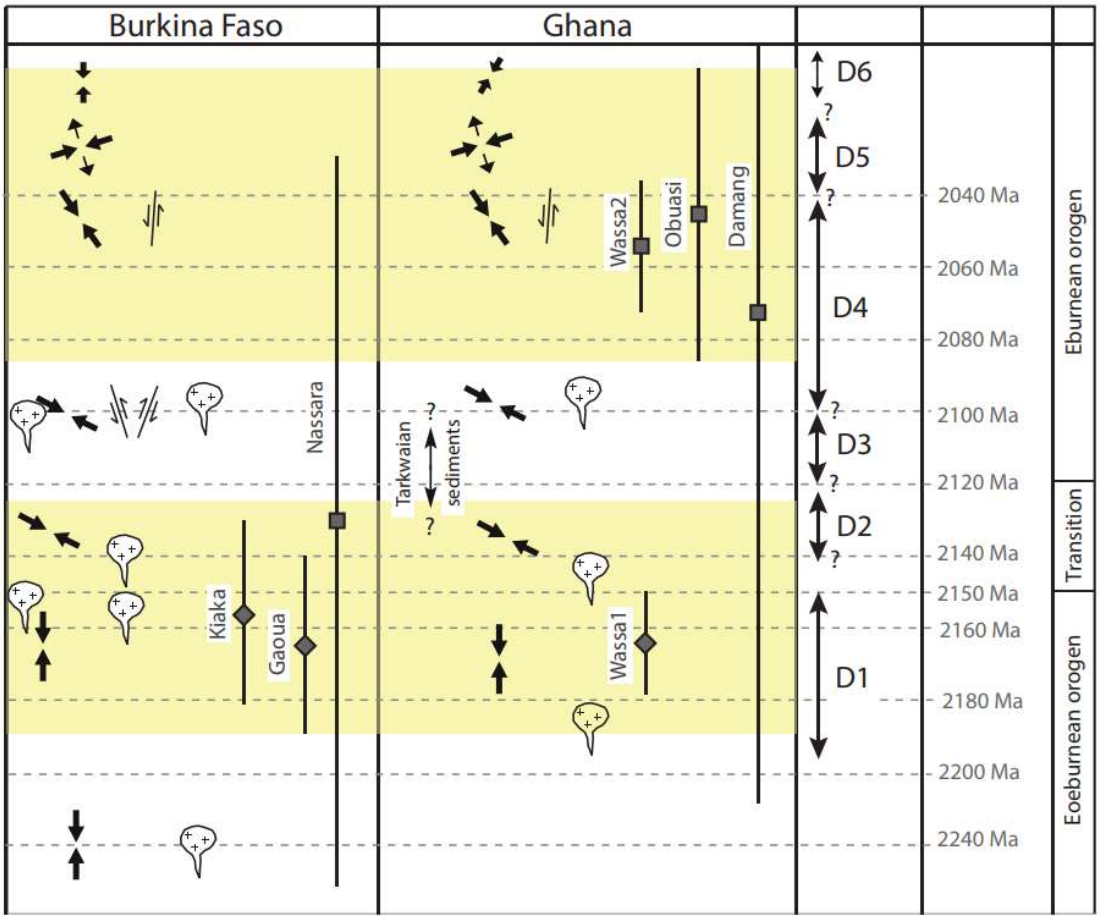

Figure 7-4 – Correlation between ages of gold deposits obtained by Re-Os dating and the geodynamic evolution of the West African craton in Burkina Faso and Ghana. (Le Mignot et al., 2017a)

The distribution of known gold mineralisation in the region is largely concentrated in the volcanic and volcanosedimentary belts of the Oum Abana and Taghsoumat-Aghsoumal belts, with minor occurrences in the Elmalhat Domain (Figure 7-2). The most significant occurrence of gold mineralisation in the region is at Agarasras G52, where mineralisation is hosted in disseminated pyrite-bearing ferruginous chert and altered granite, as well as visible gold-bearing quartz veins on the contact with the Agarasras Labiad intrusion (Section 5.1.1.1). Mineralisation at Moug El Kaleb is hosted within magnetite, proximal to a major regional suture where the orthomagmatic magnetite likely acted as a chemical trap for gold-bearing hydrothermal fluids (Section 5.1.1.3). All other mineralisation within the region is found within pyrite and/or tourmaline-bearing quartz veins. Exploration criteria must therefore include consideration of both structural and chemical traps. As outlined in Section 5.1.1.1, exploration

criteria for orogenic gold must include a structural framework, receptive host rocks (strong competency/rheological contrasts and/or favourable chemistry) evidence of polyphase intrusive formations, deformation and alteration events. Based on these criteria, and mineralisation observed in the study area during this work (Section 5.1.1.2) in the area the most prospective regions for gold mineralisation within the Sfariat-Bu Daira and Leaareig Terranes, in order of importance, are as follows:

- Sites where mineralisation has already been observed warrant further work in defining lithological units, structure, and geological characteristics of mineralisation.
    - Agarasras G2 is of particular interest with mineralisation observed associated with disseminated sulphides (Figure 7-5 – red circle).
    - Mineralisation observed in Agarasras Labiad, Tahgsoumat and Moug El Kaleb warrant further work (Figure 7-5 – orange circles).
- Unsampled regions, where potential for gold mineralisation has been identified by the presence of artisanal mining and/or hydrothermal alteration or veining.
    - This is particularly applicable to the region between Agarasras Labiad and Agarasras Lakhadar (Figure 7-5 – yellow circle) where multiple sites of extensive artisanal pitting have been identified.
    - Extensive hydrothermal veining and artisanal activity has also been observed in the southern part of the Taghsoumat-Aghsoumal belt (Figure 7-5 – purple circle).
    - Little work has been completed near the artisanal mining north of the Northern Limb of the EAC, though the presence of artisanal pits in a (favourable) volcanosedimentary belt warrants further investigation (Figure 7-5 – blue circle)

- Other potential targets identified on the basis of lithological and structural setting. The Oum Abana, and Taghsoumat-Aghsoumal belts are both prospective belts. The most prospective lithologies within these belts for mineralisation include within granitoid intrusions and/or their contacts with host lithologies (structural traps); or iron-rich lithologies such as ferruginous chert and mafic igneous rocks (chemical trap). Disseminated sulphides and/or hydrothermal alteration of these lithologies and/or extensive quartz/carbonate hydrothermal veining may also indicate mineralisation. These will have to be identified during future field work.

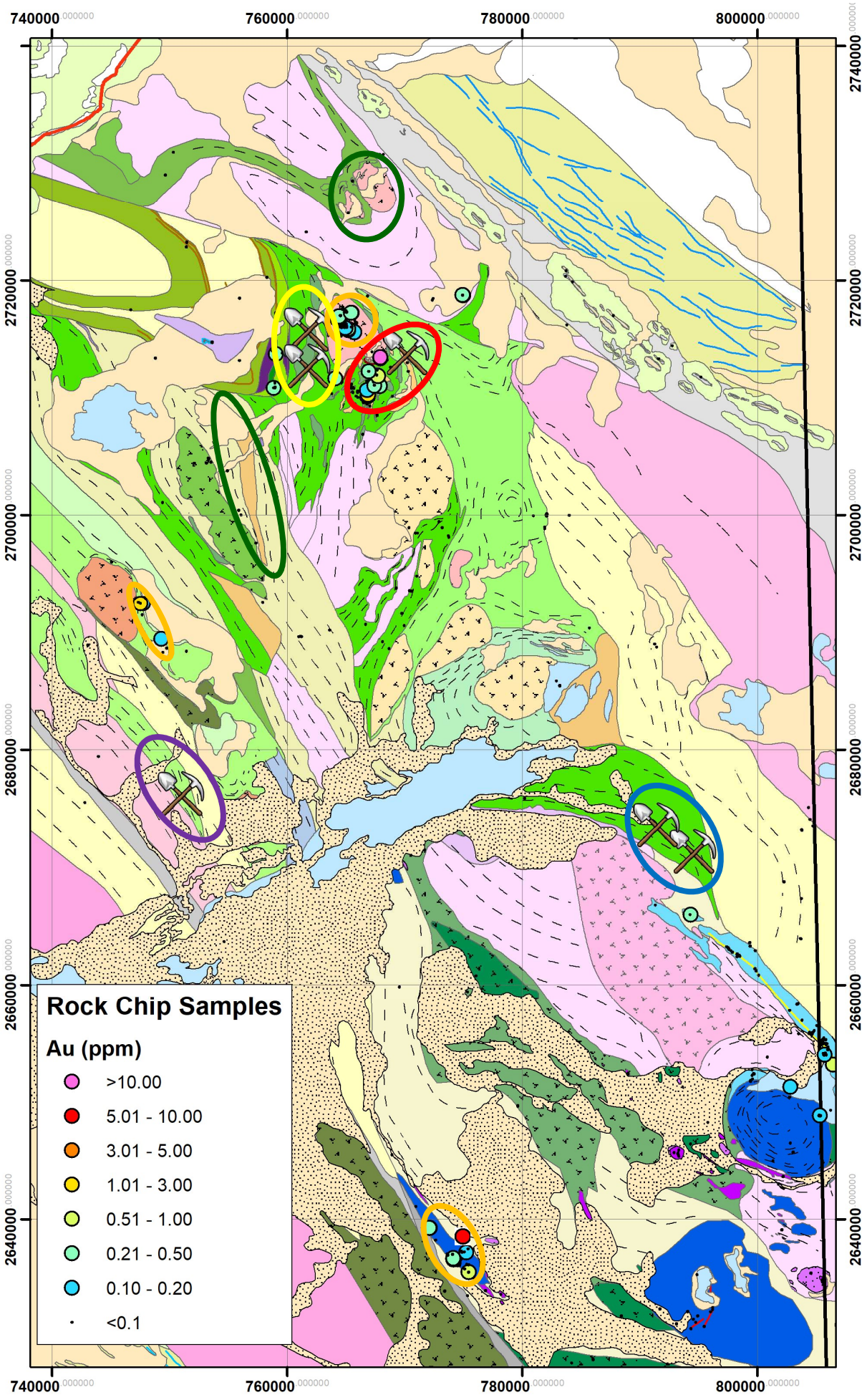
740000
760000
780000
800000
2740000
2720000
2700000
2680000
2660000
2640000
Rock Chip Samples
Au (ppm)
>10.00
5.01 - 10.00
3.01 - 5.00
1.01 - 3.00
0.51 - 1.00
0.21 - 0.50
0.10 - 0.20
<0.1

Figure 7-5 – Most prospective regions for orogenic gold mineralisation within the study area. The base map shows the geology of the region, gold assay results from rock chip samples and sites where artisanal mining has been observed (). Prospective regions include; Red – Agarasras G52; Orange – Agarasras Labiad (to the north), Taghsoumat (in the west) and Moug el Kaleb (to the south); Yellow – Artisanal pitting between Agarasras Labiad and Agarasras Lakhadar; Purple - artisanal pitting and hydrothermal veining near Aghsoumal; and Blue – artisanal pitting to the north of the Northern Limb of the EAC; Dark green – ~2100-2090 Ma intrusions that may relate to intrusion related gold

7.1.2 Intrusion-related Gold

Mineralisation in the ~8 Moz Morila gold mine is hosted in flat-lying metagreywacke (biotite schist) and minor meta-volcanic (metabasalt) and is spatially and temporally associated with arc magmatism Eburnean orogeny (Hammond et al., 2011, McFarlane et al., 2011). Mineralisation at Morila occurred over three major periods of deformation, involving coeval plutonism, deformation and regional metamorphism associated with active orogenesis (Hammond et al., 2011). Fluid inclusion studies by Hammond et al. (2011) revealed that the mineralising fluids were of magmatic origin. The timing of the mineralisation was constrained by McFarlane et al. (2011) event to an interval between 2098 ± 4 and 2074 ± 14 Ma.

Due to striking similarities in the timing of intrusions in the Oum Abana Belt and the Morila Belt (Section 6.4.3.2.1), it is worth noting the potential for intrusion-related gold mineralisation within the belt. Granodiorite and tonalite intrusions within the Oum Abana Belt were intruded contemporaneously with the Morila mineralisation event (2103 ± 24 Ma, 2097 ± 21 Ma, and 2093 ± 17 Ma; Table 2-1; Section 2.1). These intrusions and the regions surrounding them are potential sites for mineralisation of this kind (Figure 7-5 - Green).

7.2 **Elmalhat Anorthosite Complex**

7.2.1 Magmatic Ni-Cu-(Co-PGE) Sulphide Deposits

The Voisey's Bay deposit in Labrador, Canada, is a world class Ni-Cu sulphide deposit, hosted within a massif-type anorthosite complex. Although mineralisation at Voisey's Bay represents the only known significant magmatic sulphide mineralisation in anorthosite complexes (Naldrett, 2010), Maier et al. (2013) notes the occurrence of several small Ni-Cu deposits

within satellite bodies associated with the Kunene Anorthosite Complex (Figure 7-7), suggesting that other anorthosite complexes may also host this style of mineralisation.

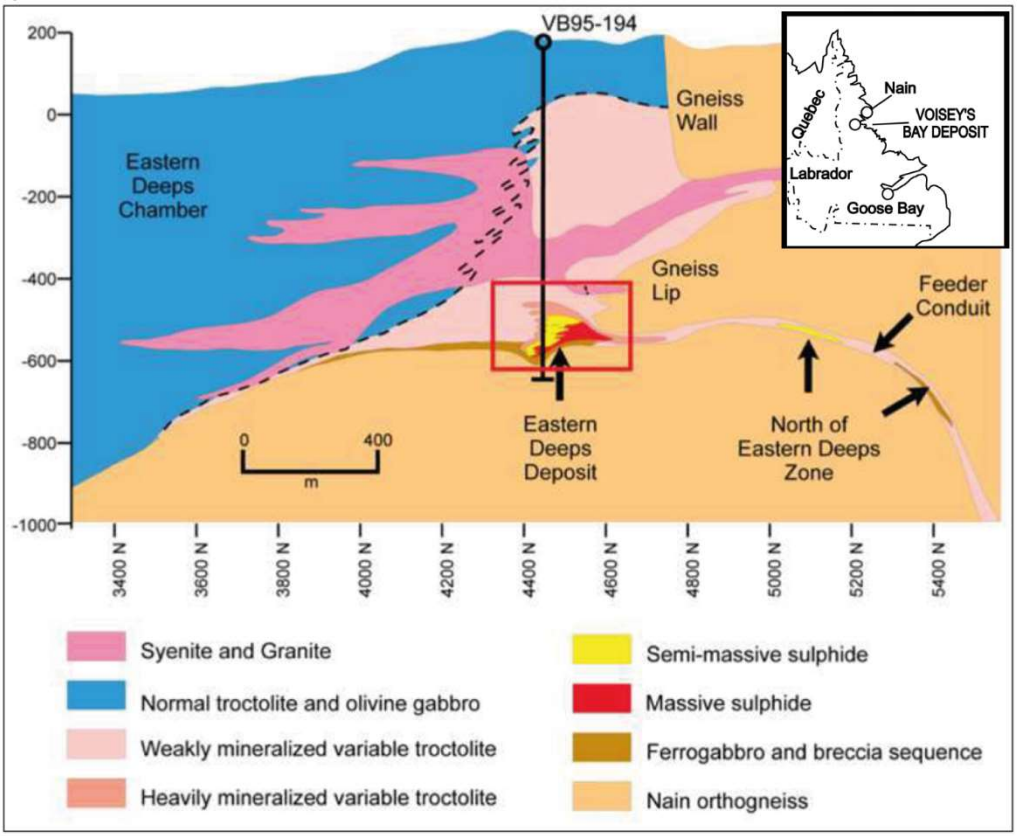

Figure 7-6 – Simplified North-South sections through the Voisey's Bay deposit showing key features (Fall, 2017).

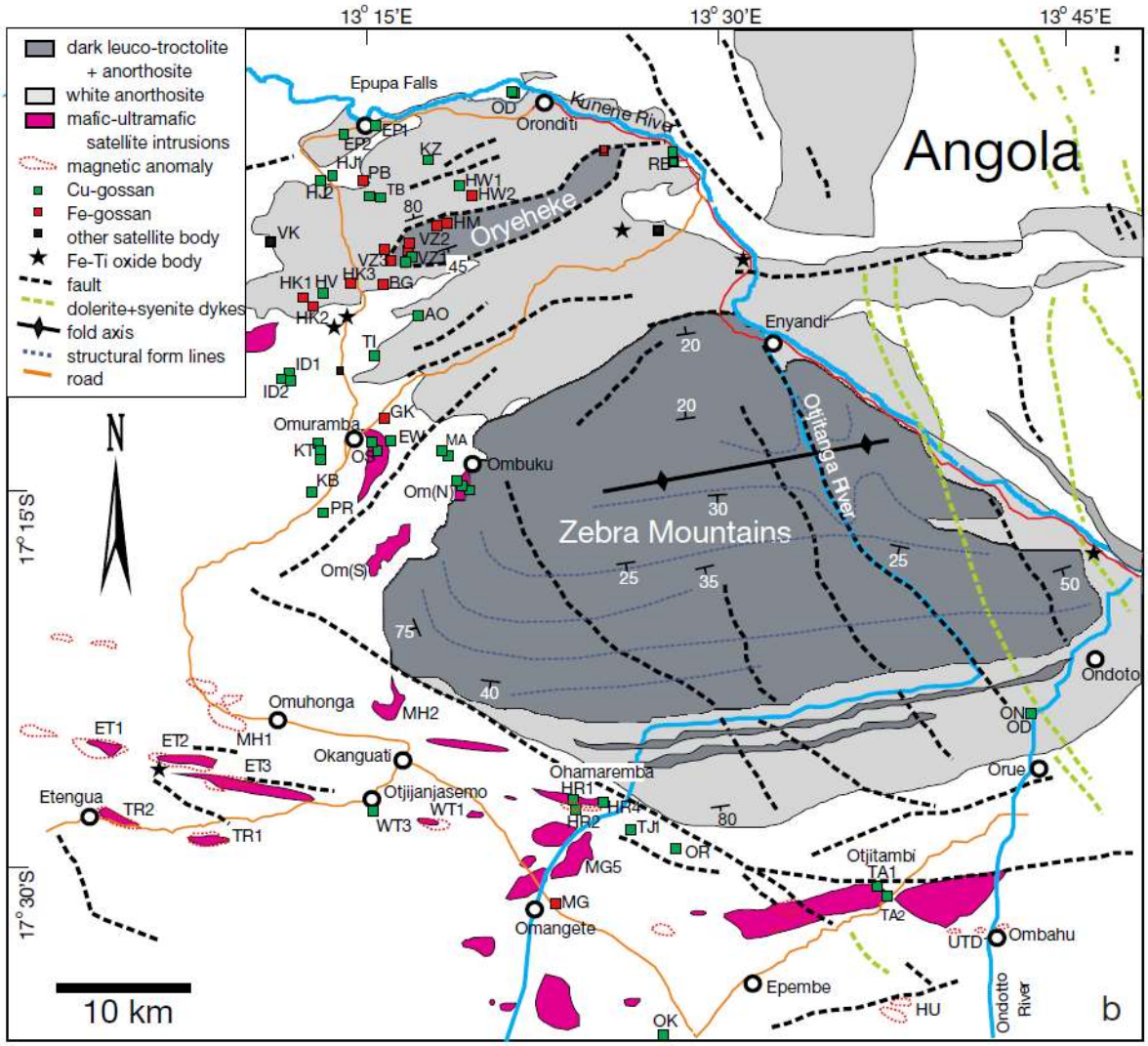

Figure 7-7- Geological map of the Namibian portion of the Kunene Anorthosite complex, showing the distribution of Cu-gossans relating to satellite intrusions (from Maier et al., 2013).

Within the EAC, disseminated magmatic sulphides are observed in anorthosite throughout the complex. The concentration of the sulphides into a focused physical trap site such as a magma chamber floor or conduit would provide the process whereby important mineralisation might have formed in anorthosite bodies in general, and specifically at Elmalhat

A number of factors suggest potential for Voisey's Bay-style magmatic Ni-Cu sulphide mineralisation within the EAC:

1. The presence of magmatic sulphides within the Northern Limb, Main Bulb, and the Southern Bulb, indicate that sulphide saturation has been reached in the complex. These sulphides may have separated out and been concentrated at the base of the intrusion.
2. The Palaeoproterozoic age of the EAC. Most primary magmatic sulphide deposits, including Voisey's Bay, are hosted in Late Archean or Early Proterozoic intrusions (Maier, 2005, Naldrett, 2010).
3. Voisey's Bay and the EAC are located close to contacts between Archaean and Proterozoic terranes (Figure 7-8). Other styles of magmatic Ni-Cu deposit in the Canadian Shield are also proximal to Archaean-Palaeoproterozoic contacts.

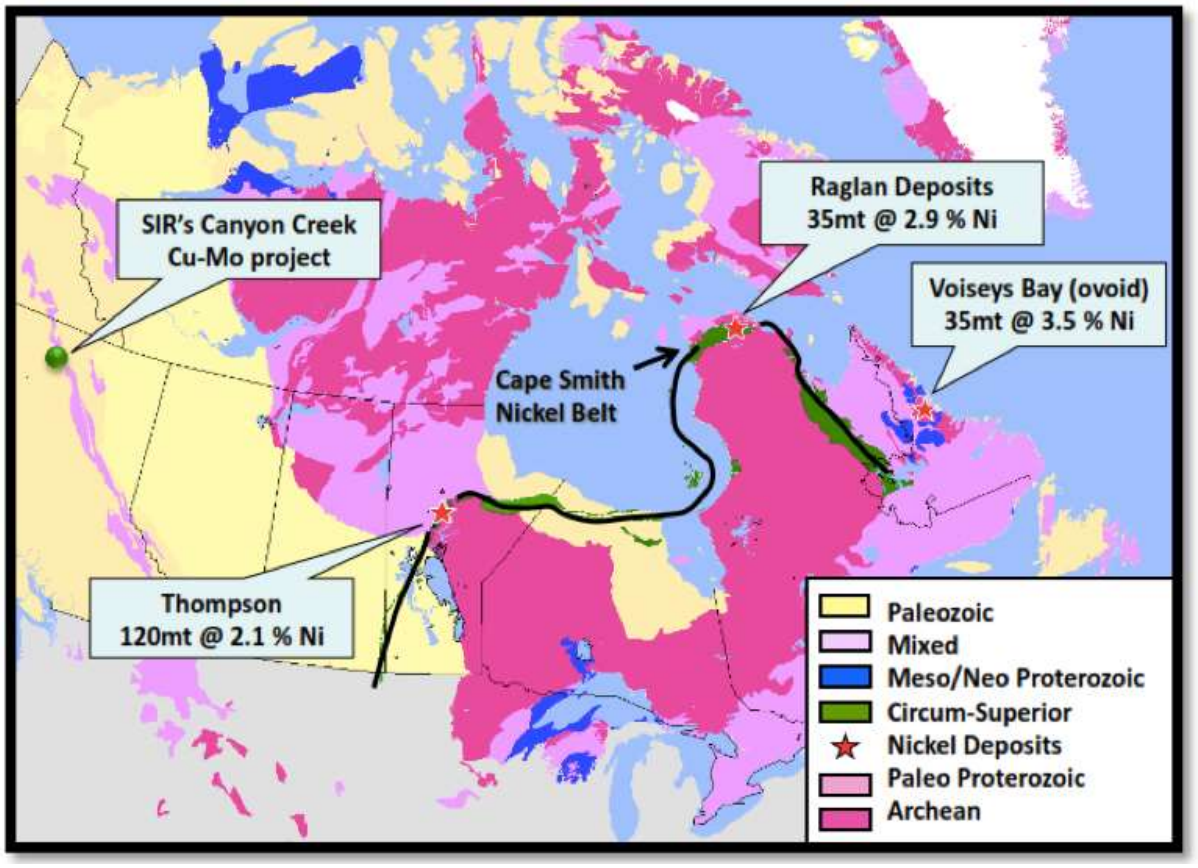

Figure 7-8 – The Canadian Shield showing the distribution major magmatic Ni-Cu sulphide deposits relative to Archaean and Palaeoproterozoic terranes (modified from 'Canada's big nickel discoveries', 2014).

Mineralisation at Voisey's Bay is largely hosted in the magma conduits feeding the intrusion and at the base of the intrusion where the magma is fed. Maier et al. (2013) examined the

economic potential of the Kunene anorthosite complex noting that several small Ni-Cu sulphide deposits are present within relatively small satellite intrusions rather than the main anorthosite complex. Maier et al. (2013) additionally proposed exploration criteria for Ni-Cu sulphide deposits in Kunene and anorthosite complexes in general. The key criteria is primitive magmas crystallised from relatively Ni-rich (~100−150 ppm), high Al basaltic magmas formed as the residual product of high pressure crystallisation of olivine and pyroxene. Any sulphides that form in such a magma would likely have high metal tenors (the ability of a sulphide phase scavange metals), due to elevated Ni contents (Maier et al., 2013). Therefore, if a significant portion of sulphides form in the magma, it has high potential to form an economic deposit. Other criteria relate to mechanisms of reaching sulphur saturation, which in the case of Kunene and Voisey's Bay requires the addition of external sulphur (Maier et al., 2013, Naldrett, 2010).

Within the EAC, olivine composition in ultramafic rocks, and leucogabbro from the Main Bulb (the cluster at $An_{\sim 60}$ cluster on Figure 4.98; Section 4.1.3.1) indicate their crystallisation from a primitive magma (Fo_{69-83}). Additionally, the composition of the olivine indicates that the magma had a high Ni content (up to 2300 ppm in olivine), similar to that of Voisey's Bay and Kunene (Figure 7-9). Note that although the Ni content is similar to that of Voisey's Bay and Kunene, the Elmalhat magma appears to be more primitive (higher Fo) than both – one of the key exploration criteria defined by Maier et al. (2013). As iron content is proportional to sulphide solubility (Naldrett, 1989), the primitive nature of the EAC (i.e. lower iron content) suggests that sulphide solubility of the magma might have been lower than either Voisey's Bay or Kunene. Sulphide saturation might, therefore, have been more achieved more readily and at lower sulphur contents in the EAC than in other less primitive examples. Whereas Voisey's Bay and Kunene required the addition of external sulphur to achieve sulphur saturation (Maier et al., 2013, Naldrett, 2010), this process may have been achieved within the EAC via other mechanisms such as contamination (wall rock assimilation) or magma mixing (Naldrett, 2010).

Furthermore, trends in olivine composition within the Main Bulb of the EAC indicate the removal of Ni by a sulphide phase. During the crystallisation of a magma in the absence of a sulphide phase, Ni partitions into olivine and therefore depletes the residual magma (Hart and Davis, 1978). This results in a fractionation trend of decreasing Ni with decreasing forsterite as can be seen in mafic, ultramafic and anorthosite complexes around the world (Figure 7-9). Due to an extremely high sulphide melt–silicate melt partition coefficient of Ni (776 ± 98 (Patten et al., 2013)), when sulphur saturation is reached, Ni that interacts with the sulphide droplets will partition into the sulphur phase (Duke and Naldrett, 1978). This results in a decrease in the Ni content of the magma with no change in forsterite content. Olivines analysed from the EAC reveal a fractionation trend where Ni content decreases with decreasing Fo in olivine composition (Figure 7-9). However, an additional trend can be seen with a decrease in Ni content for a given Fo content. This trend is best seen in the analyses that plot at $Fo_{76\text{-}78}$ where analyses of ultramafic rocks reveal elevated Ni contents (up to ~1810ppm Ni, and averaging 1630ppm Ni in olivine) but the leucogabbro is Ni depleted (averaging 1070ppm Ni in olivine). It would therefore appear that the samples of leucogabbro (with labradorite plagioclase compositions) are depleted in Ni and may therefore have experienced a sulphur saturation event (Duke and Naldrett, 1978, Naldrett, 1999). Note that, the ultramafic rocks presented on Figure 7-9 are believed to be associated with the satellite intrusions (Section 4.1.4.1; Figure 4.98), suggesting that they too formed from this primitive, Ni-rich magmas, however the Ni content of the satellite bodies in unknown.

Note that depletion of chalcophile element (Ni, Cu, Co, and PGEs) is a common near-deposit feature in rocks around magmatic sulphide deposits (Duke and Naldrett, 1978, Naldrett, 1999). The identification of this chalcophile depletion halo (including reduced Ni content in olivine) is therefore a common lithogeochemical exploration tool on a prospect to camp scale (Le Vaillant et al., 2016).

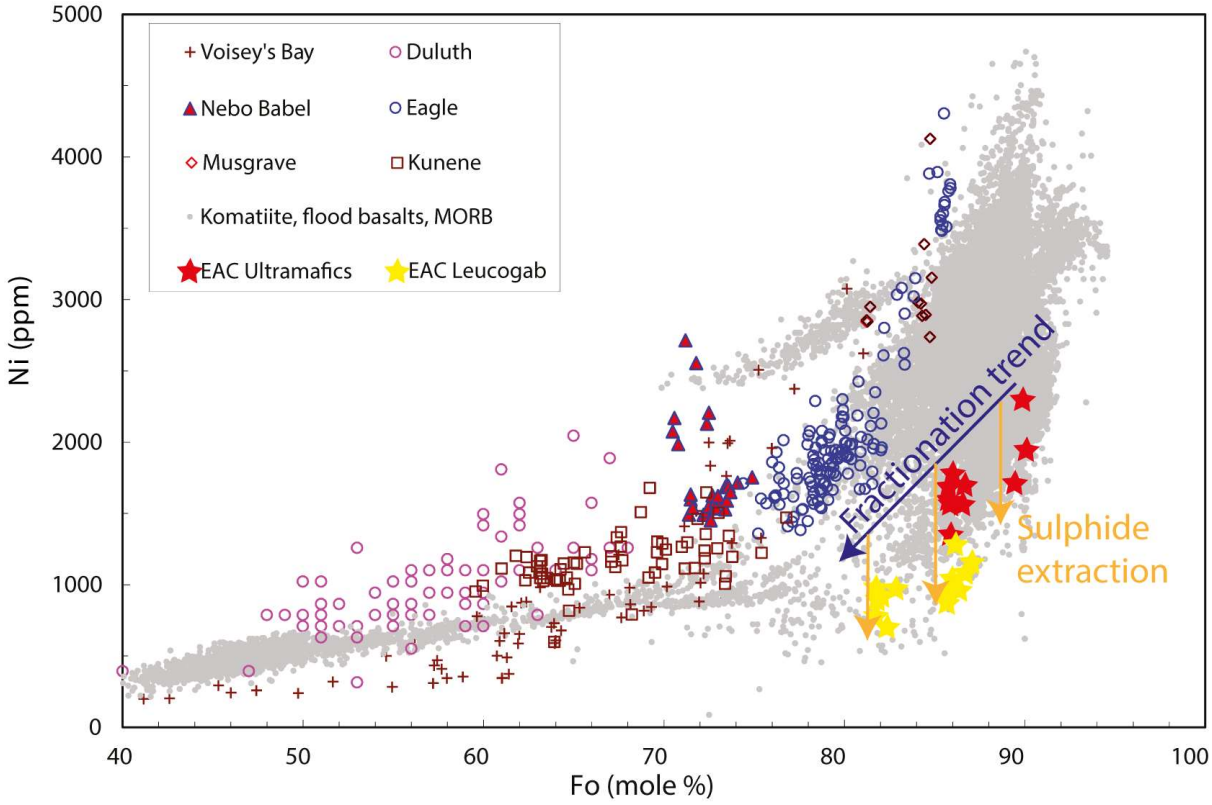

Figure 7-9 -Nickel vs. forsterite contents of olivine from selected troctolitic intrusions compared to compilation of basaltic and komatiitic lavas (adapted from Maier et al., 2013; data from sources cited therein). The general fractionation trend and trends resulting sulphide extraction are plotted in blue and orange respectively.

Based on evidence presented above, the following exploration criteria should be applied for the EAC:

- More primitive rocks in the intrusion (with labradorite plagioclase content - Figure 4.98; Section 4.1.3.1) were derived from a Ni-rich melt.
- Samples of leucogabbro derived from the Ni-rich melt, appear to have experienced a sulphur saturation event (i.e. have had the Ni removed), and therefore are prime targets proximal to samples with low Ni content.
- The presence of magmatic sulphides in the complex and/or rock chip and/or soils sampling anomalies.
- Satellite bodies also formed from the Ni-rich melt and are analogous to the sites of mineralisation at Voisey's Bay (within conduits) and Kunene.

- The base of the intrusion. As the sulphide fraction is dense, it would settle at the base of the intrusion or in hydrological traps.

Based on these criteria, the following regions represent the highest potential to host mineralisation within the EAC:

1. Anorthosite in east of the Main Bulb (Figure 7-10 – Red). The anorthosite in this area contains plagioclase with a labradorite composition, contains patchy sulphides and xenoliths of megacrystic anorthosite (Figure 4.33; Section 4.1.1.2.3.1) indicating contamination and potential addition of external sulphur. Anomalies of up to 689 ppm Cu and 298ppm Ni have been identified in rock chips in this region (Figure 5.15; Section 5.2).
2. The satellite bodies (Figure 7-10 - Orange). These bodies consist of olivine gabbro derived from the Ni-rich melt are in a similar setting to mineralisation at Voisey's Bay and Kunene.
3. Proximal to labradorite anorthosite within the Main Bulb (Figure 7-10 - Yellow). Nearby rock samples have returned anomalous values of 882ppm Cu, 593ppm Ni, 229ppm Co and 38.3% Fe. It also corresponds to a soil sample anomaly up to 293ppm Cu and 131ppm Ni.
4. The Southern Bulb where patchy sulphides have been observed, in particular proximal to the sabkhas (Figure 7-10 - Green). Patchy sulphides have been observed in magnetic leucogabbro close to the edge of the sabkhas under which a magnetic anomaly is present. No microprobe data exists for the Southern Bulb but an optically determined plagioclase composition of one sample from the Southern Bulb indicates a labradorite composition of plagioclase (possibly relating to the primitive, Ni-rich magma source)
5. The Northern Limb where patchy sulphides are observed, magma mixing is believed to have occurred (forming the chromitite layer ± PGE mineralisation; Section 5.2.2.2) and

soil sampling anomalies up to 709 ppm Cu (but only 26 ppm Ni) have been observed (Figure 7-10 – Purple).

6. Moug El Kaleb where anomalous rock chip results have recorded up to 0.42% Cu and 789ppm Ni, ~2km southeast of the gold mineralisation.
7. Geophysical methods such as electromagnetics, resistivity and induced polarisation techniques would help identify and delineate sulphide mineralisation within the EAC.

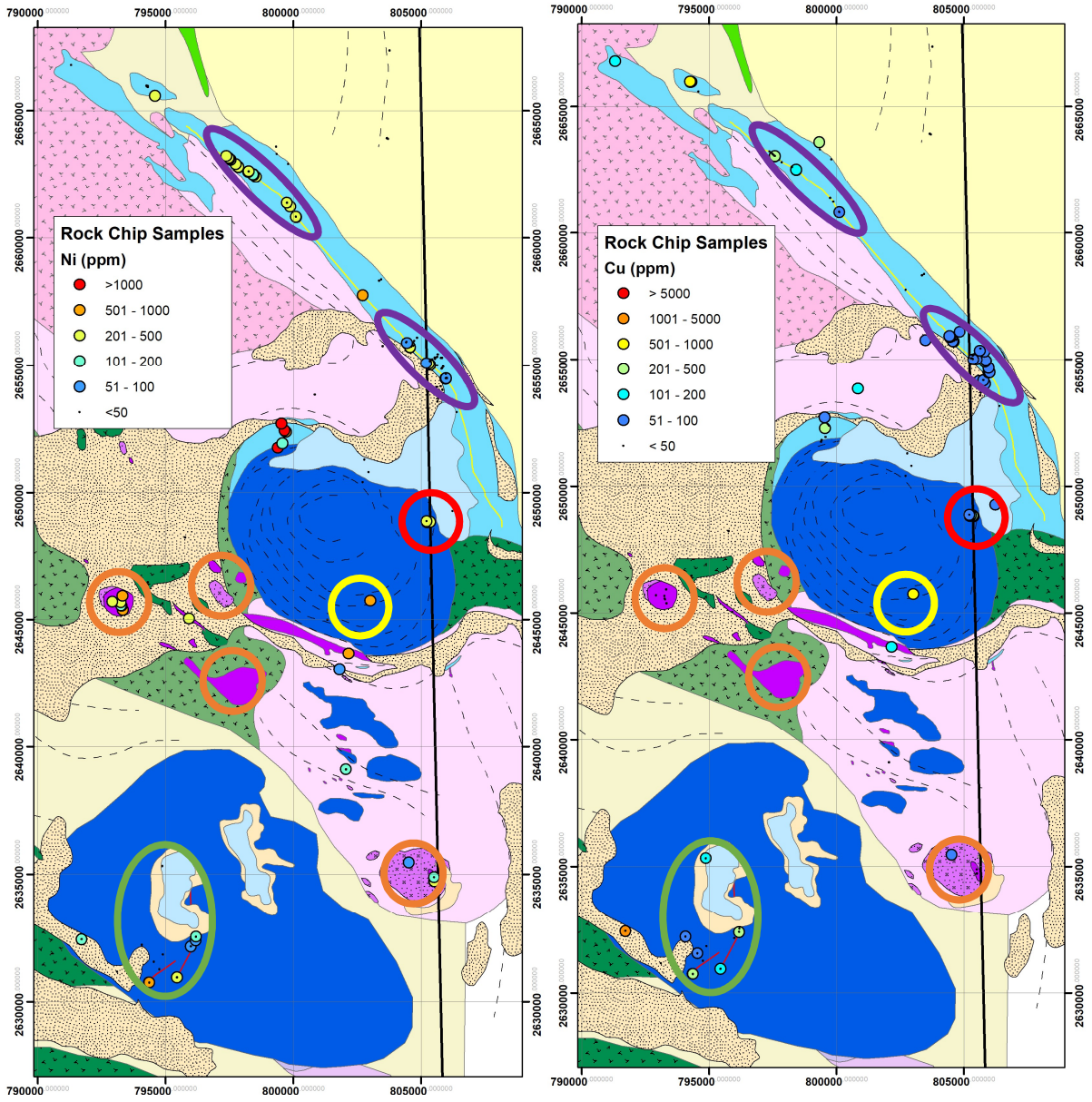

Figure 7-10 – Most prospective sites for magmatic sulphide deposits within the EAC overlaid on Ni and Cu results for rock chip samples.

7.2.2 Platinum Group Element-Bearing Stratiform Chromitite

Chromitite seams are usually associated with layered mafic intrusions, though they have been observed in Archaean megacrystic anorthosite complexes such as Fiskenæsset in West Greenland (Rollinson et al., 2010) and the Sittampundi Complex in India (Dhanendran et al., 2014). Possibly due to similar trigger mechanisms (magma mixing and crustal contamination), the occurrence of PGE enrichment is strongly correlated with the occurrence of magmatic sulphides, as well as, less commonly of chromitite (Maier, 2005). The Archaean Sittampundi chromite seams hosts PGE mineralisation over a strike of 3.6 km, containing Pt + Pd grades of 0.5 to 2.0 ppm (locally up to 25 ppm; Dhanendran et al. (2014)).

Although Palaeoproterozoic in age, the Northern Limb of the EAC (megacrystic anorthosite ~1km wide over a strike of ~19 km) is similar to the Sittampundi Anorthosite Complex (megacrystic anorthosite ~125 to 990 m wide over a strike ~17 km) in terms of size and characteristics. The chromitite seam of the EAC (averaging ~30-80 cm in width, locally up to ~2.5m) is also similar to the Sittampundi in terms of dimensions (a few centimetres to 5m) and mineral chemistry (Figures 4.102, and 4.103; Section 4.1.3.2).

As discussed in Section 5.3.2, PGE enrichment may relate to sulphide saturation (and initial enrichment in Pt and Pd), followed by its preferential removal by hydrothermal fluids, and/or primary crystallisation of laurite-erlichmanite associated with growth the of chromitite grains in the absence of sulphide saturation. The presence magmatic sulphides in nearby anorthosite (Section 4.1.4.3), and Pt and Pd enrichment observed within the chromite (up to 238 ppb Pt + Pd) suggests that, at least locally, the presence of sulphides may have been a dominant factor in PGE concentration. The magma mixing event responsible for the formation of the chromite layer (Section 4.1.6.1) provides a mechanism through which sulphur saturation could have been reached during the formation of the chromitite seam.

Within the Sittampundi complex, mineralisation only occurs over a strike of 3.6 km in a ~17km intrusion. Therefore, further work is warranted within the northern limb of the EAC, with relatively undeformed and unaltered portions of the chromitite, making good targets for PGE mineralisation.

7.2.3 Orthomagmatic Fe-Ti-V Oxide Seams

Proterozoic massif-type anorthosite complexes are known to contain significant Fe-Ti(±V±P) mineralisation, the most notable of which is the Allard Lake deposit, hosted within the Havre-Saint-Pierre Anorthosite Complex. The Allard Lake ilmenite deposit represents the world's largest Fe-Ti oxide deposit containing more than 200 Mt at over 60 wt.% hemo-ilmenite (Charlier et al., 2010). The main ore body is 1.03×1.10 km and 100–300 m thick, forming a is a funnel-shaped intrusion (Charlier et al., 2010).

High grades of Fe, Ti and V are observed within the Fe-Ti-V oxide deposits in the Southern Bulb of the EAC (Figure 5.25; Section 5.4), though the area is largely covered by sand and sabkhas making it difficult to map the extent in the field. Ground magnetic surveys reveal that magnetic anomaly associated with the magnetite seams extend under the sabkha and sand cover over a strike of 6-8 km, covering an area of ~12 km^2. This suggests potentially significant mineralisation within the Southern Bulb.

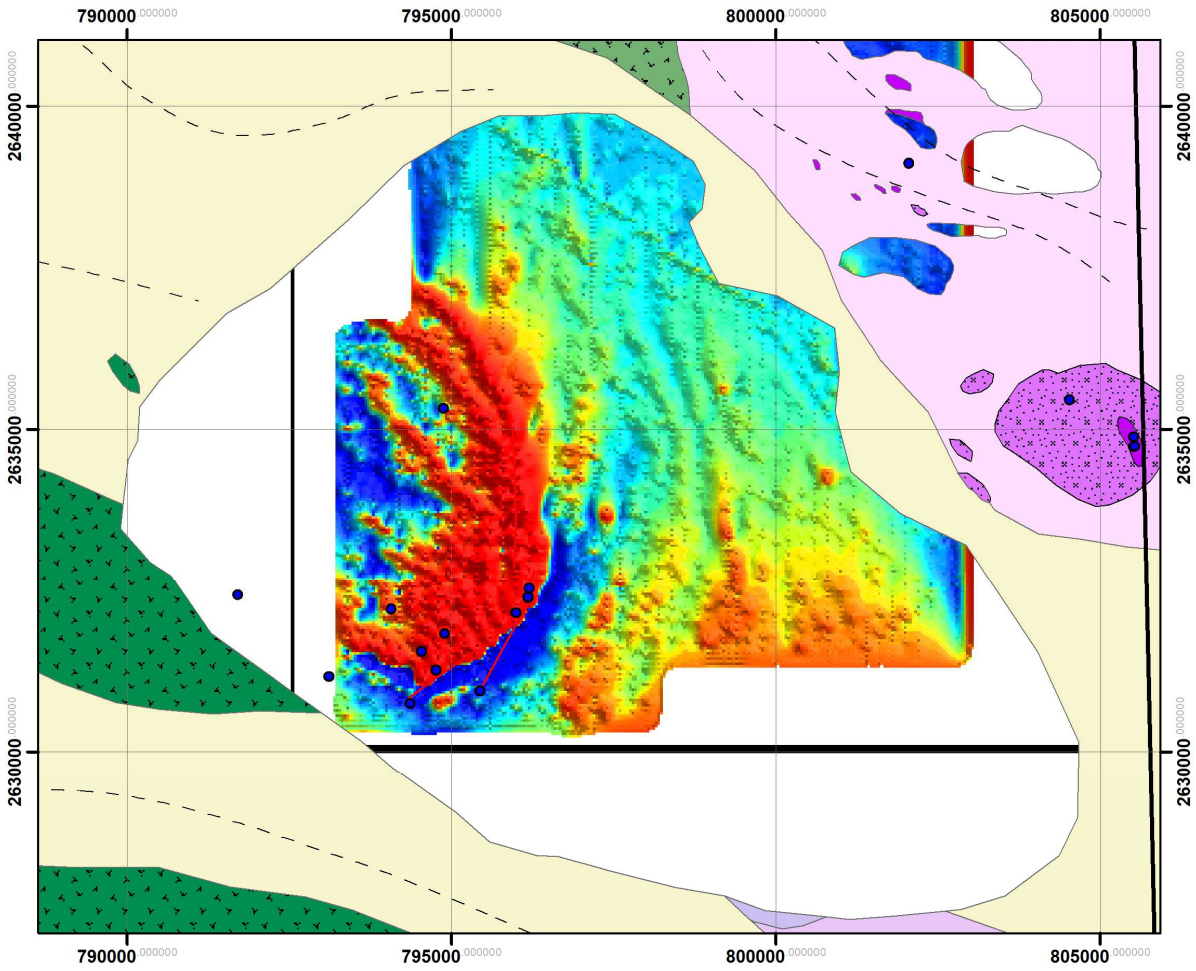

Figure 7-11 - Magnetic anomaly highlighting the extend of the Fe-Ti-V oxide mineralisation in the Southern Bulb

7.3 **Iron Ore in Riche**

Folded and boudinaged ridges of banded iron formation (BIF) outcrops within the Sfariat Shear Zone in the north of the region represent a potential site for Superior-type iron mineralisation (Figure 7-2).

In the F'derik-Zouérate district of Mauritania, high-grade hematitic iron ores (60–65 wt% Fe) have been mined from Superior-type iron deposits since 1952 (Taylor et al., 2016). These Superior-type deposits are located in allochthonous Palaeoproterozoic sequences including the Kediat Ijil massif (Taylor et al., 2016). Schofield and Gillespie (2007) suggested that the Palaeoproterozoic Kediat Ijil massif comprises continental margin sediments that were emplacement over the Archaean foreland by an extensive thin-skinned decollement structure

(Figure 7-12). Superior-type iron formations within the Sfariat Shear Zone could therefore be related to the high-grade hematitic iron ores of the Kediat Ijil massif.

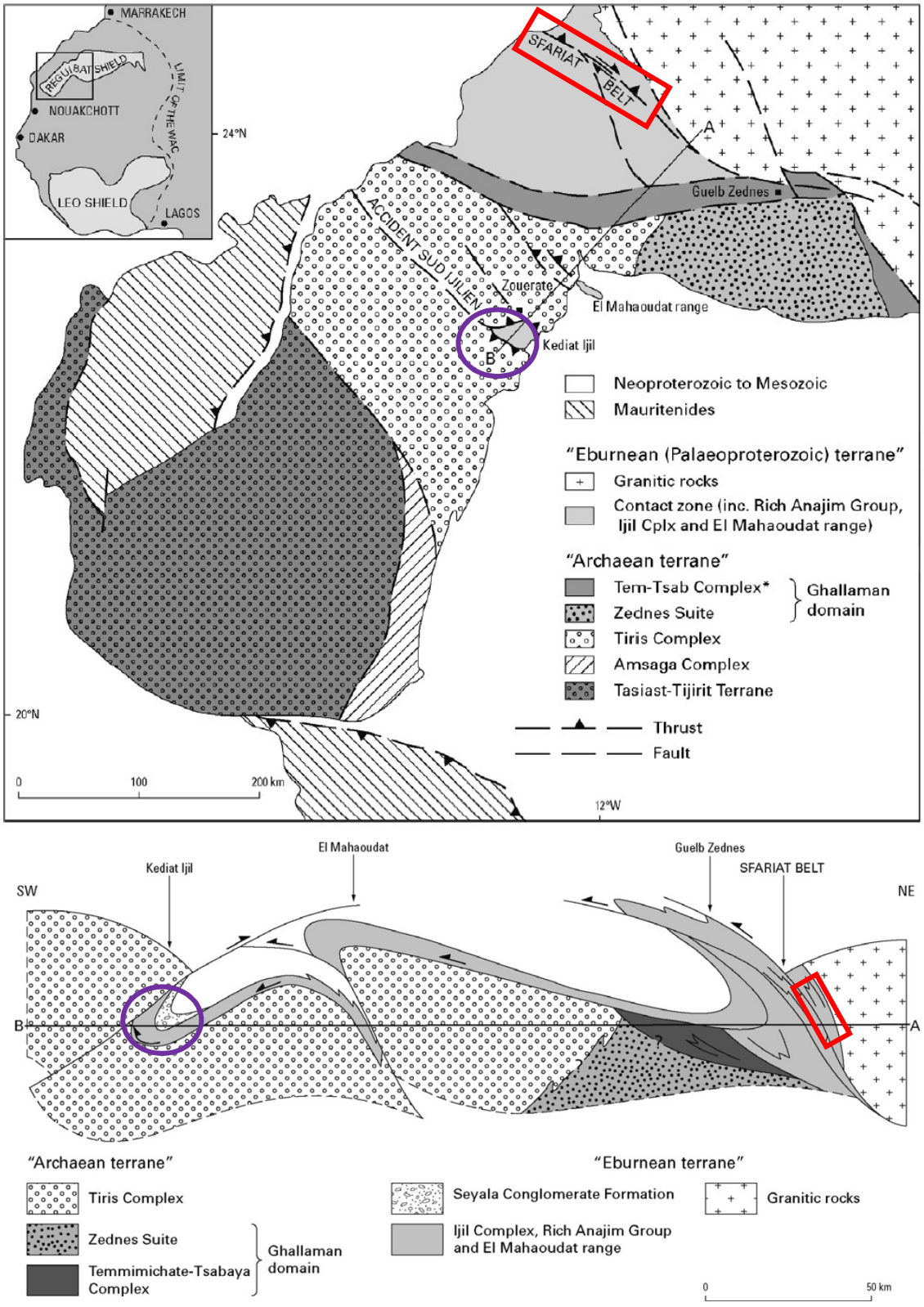

Figure 7-12 – Tectonic interpretation of the Kediat inlier (purple circles) with respect to the location of the Sfariat Belt (red rectangles) (modified from Schofield and Gillespie, 2007).

Superior-type iron formations are much larger deposits than Algoma-type (Bekker et al., 2014). The BIF layers within the shear zone are tightly folded (Figure 4.10; Section 4.4.2.2) effectively thickening the iron formation meaning significant tonnages would be present (Figure 5.27; Section 5.5). In order to make be economically viable, the iron must be enriched through the leaching of silica. This enrichment, if present, would be related to deformation, magma intrusions and/or weathering. With significant tonnages are present, the key to finding an economic deposit, is identification of zones of enrichment.

7.4 **Mineralisation in the Boromo Belt of Burkina Faso**

7.4.1 Volcanic Massive Sulphide Deposits

Volcanogenic massive sulphide (VMS) deposits are rare in the West African Craton. The only known occurrence is the Zn–Ag Perkoa deposit, in the Boromo belt of Burkina Faso (Schwartz and Melcher, 2003). Estimated ore reserves for the Perkoa deposit are 5.7 Mt at 18.2% Zn, 10% $BaSO_4$, 0.06% Pb, 26 ppm Ag, and 50 ppm Cu. The deposit is hosted by tuffs and dioritic to granitic dykes, and structurally overlain by andesite, cumulate-rich basic rocks, and carbonaceous schist. Baratoux et al. (2011) interpreted the deposit to have formed in an early volcanic island arc setting.

7.4.2 Porphyry Systems

The Boromo Belt hosts one of only two porphyry style deposits have been recorded in the West African Craton, the other being molybdenum-copper mineralisation of the Bled M'Dena complex in the Eglab terrane of the Reguibat Shield in Algeria (Lagraa et al., 2017). The Palaeoproterozoic porphyry copper-gold deposits in the Boromo Belt occurs in the Gaoua region (Baratoux et al., 2015, Le Mignot et al., 2017b). The mineralisation in the Gaoua region involved an early phase of copper porphyry mineralisation, followed by orogenic gold

enrichment (Figure 7-13) (Baratoux et al., 2015, Le Mignot et al., 2017b). Re-Os dating of the early pyrite indicates that early porphyry copper (± gold) mineralisation took place at 2165 ± 24 Ma with gold enrichment largely relating to regional orogenic gold mineralisation events (Section 7.1; Figure 7-4).

7.4.3 Potential for Similar Mineralisation in the Leaareig Terrane

No evidence for either VMS or porphyry-style mineralisation currently exists within the study area. However, strong stratigraphic correlations between the Leaareig Terrane and the Boromo belt (Section 6.4.3.2.3), raises the possibility of these styles of mineralisation within the Leaareig Domain.

In terms of the VMS mineralisation, the Taghsoumat-Aghsoumal volcanosedimentary belt presents the most prospective area with the same volcanic arc setting responsible as the mineralisation at Perkoa. Additionally, the back arc setting of the ophiolite sequence of the Agarasras Lakhadar Domain is the environment in which Cyprus-type VMS deposits form.

Given a favourable volcanic arc setting, the plutonic and volcanic activity (2159 ± 140 Ma, and 2149 ± 21 Ma; Table 2-1, Section 2.2) coincident with the porphyry mineralisation (Figure 7-13), the Taghsoumat-Aghsoumal Domain is the most likely region to host porphyry-style mineralisation within the study area.

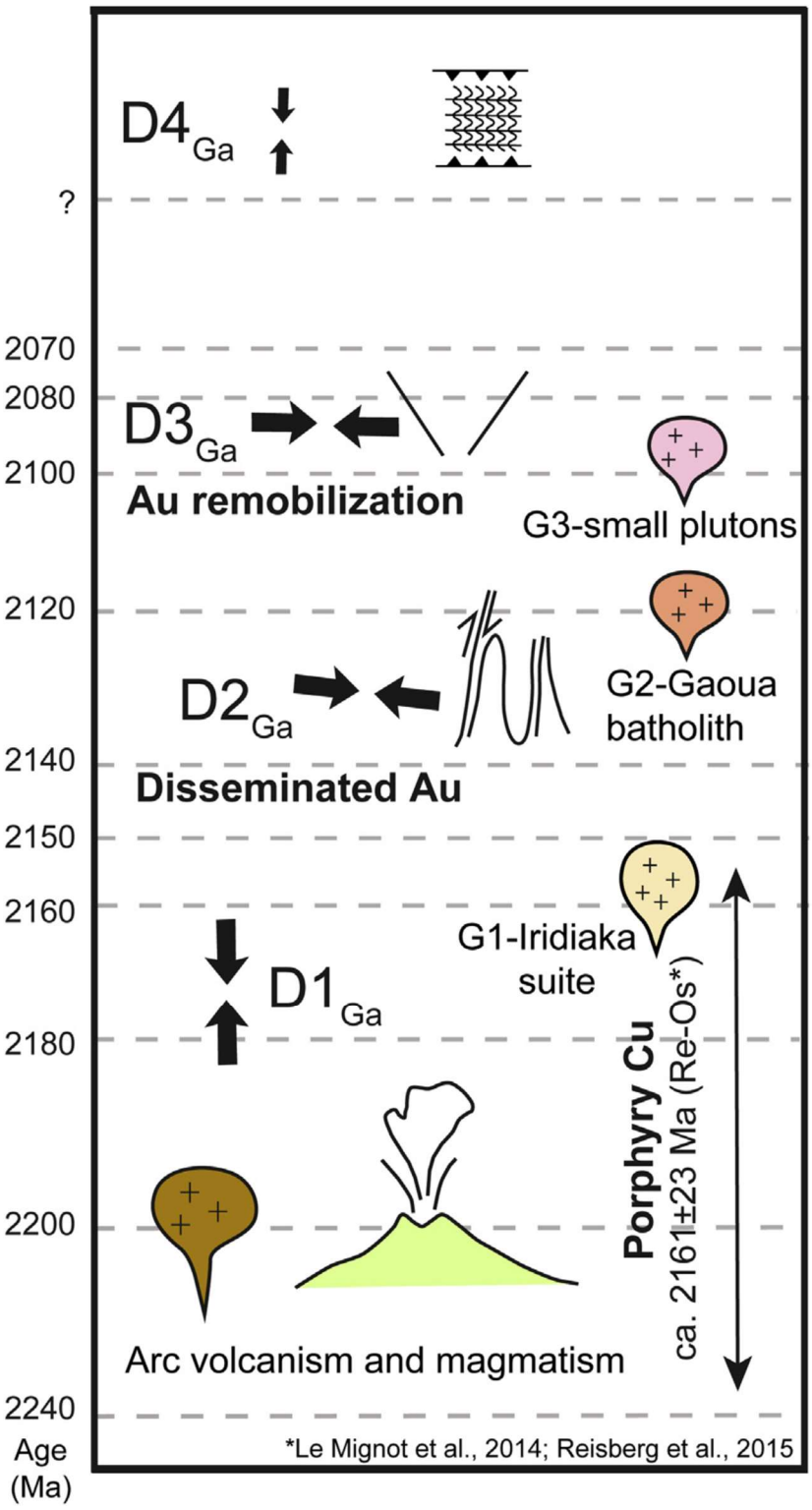

Figure 7-13 – Diagram summarising major mineralisation events of the Gaoua region, Burkina Faso (from Baratoux et al., 2015)

8.0 Conclusions and Recommendations

8.1 **Conclusions**

The Adam Ahmed Mouloude Region of the liberated territories of Western Sahara has proved to be a key region in understanding the Palaeoproterozoic evolution of the Reguibat Shield and the West African Craton as a whole.

A combination of U-Pb zircon geochronology, whole rock geochemistry and field relations have allowed two distinct Palaeoproterozoic terranes to be identified. Both terranes comprise a series of volcanic, volcanosedimentary, sedimentary and gneissic belts interpreted to have formed in evolving volcanic arc settings, analogous to the Japanese island arc setting. The Leaareig Terrane in the west (ca. 2220 and 2150 Ma), is older than the more geochemically evolved Sfariat-Bu Daira Terrane (ca. 2140 to 2090 Ma).

A distinctive feature of the Leaareig Terrane is the presence of an ophiolite complex overlying the Oum Abana Belt of the Sfariat-Bu Daira Terrane emplaced during the collision between the terranes. Geochemistry of the pillow basalts at the top of the sequence indicate a back-arc basin/mid ocean ridge basalt (MORB) setting. Detrital zircons in the sediments overlying the complex were dated at 2176 ± 32 Ma, coeval with magmatism in the Leaareig Domain leading to the interpretation that it represents the back arc setting to the relating to the Leaareig Terrane volcanic arc.

One of the most important features of the Sfariat-Bu Daira Terrane, is defined by the presence of the Elmalhat Anorthosite Complex (EAC) in the Elmalhat Domain. It appears to be the only known anorthosite complex on earth to contain both ‘megacrystic’ and ‘massif-type’ anorthosite. Field relationships demonstrate that megacrystic anorthosite formed first and was intruded by the massif-type anorthosite. A combination of relative dating constrained by U-Pb

zircon geochronology, and whole rock Sm-Nd geochronology constrain the age of the massif-type anorthosite at ~ 2.13 Ga. No maximum age constraints exist for the megacrystic anorthosite, though it is unlikely to be older than the oldest (~2.2 Ga) rocks in the Palaeoproterozoic Terrane, potentially making it the youngest megacrystic anorthosite in the world.

Megacrystic and massif-type anorthosites are believed to from in different tectonic settings and different crustal levels. Megacrystic anorthosites are attributed to an island arc (or Archaean equivalent) type setting, emplaced in shallow sub-volcanic settings, while massif-type anorthosites are emplaced at mid-crustal levels, requiring the presence of thickened continental crust at continental arc settings. Detailed work completed on each type of anorthosite in the EAC in terms of petrology, mineral chemistry and trace element geochemistry are consistent with these different tectonic settings.

The disparity in tectonic setting can be explained when the regional tectonic evolution is accounted for. The process of terrane accretion, can result in rapid thickening of the crust and a transition from an island arc setting (eg. Japan) to a continental arc setting (eg the Andes). This rapid transition in tectonic setting allowed for the formation of the Elmalhat Anorthosite Complex, with the megacrystic anorthosite forming in a pre-accretion island arc setting, while the massif-type anorthosite formed in the post-accretion continental arc setting.

A new tectonic model is proposed for the formation of the Leaareig and Sfariat-Bu Daira Terranes based on work completed in this project. The region appears to have formed though the accretion of two distinct Palaeoproterozoic (Leaareig and Sfariat-Bu Daira) volcanic arcs, and later collision with the Archaean craton. The geodynamic model involves a four stages of terrane growth and assembly:

- 2.24 to 2.15 Ga – Formation of the Leaareig Terrane as an island arc of evolving maturity. During the growth of this arc a back-arc basin was formed and filled with sediments shedding off the arc. At the end of subduction, a piece of the back arc was obducted and is now observed as the ophiolite complex in the Agarasras Lakhadar Domain
- 2.14 to 2.13 Ga - Formation of the Sfariat-Bu Daira Terrane as an island arc of evolving maturity. The megacrystic anorthosite was formed at a shallow, sub-volcanic level in a relatively immature island arc environment.
- 2.13 to 2.12 Ga – The collision between the Leaareig and Sfariat-Bu Daira Terranes involved the thickening of the crust allowing for the formation of the massif-type anorthosite. In the same event the previously sub-volcanic megacrystic anorthosite is tectonically buried to a mid-crustal level and is intruded by the massif-type anorthosite.
- ~2.10 Ma – Collision of the Palaeoproterozoic Terrane with the Archaean Terrane in a sinistral transpressive event. This results in increased magmatic activity at ~2.10-2.09 Ma within the study area, with a sample of migmatite close to the contact with the Archaean Terrane revealing an age of anataxis of 2.10 Ma

The definition of the Oum Abana and Taghsoumat-Aghsoumal Belts allows for the first direct comparison of specific belts in the Reguibat Shield with those in the Man-Leo Shield. Strong similarities in terms of stratigraphy and the timing of magmatic events are observed between these belts and a series of Birimian Belts in Burkina Faso and Mali. The presence of rare geological features in belts either side of the Taoudeni Basin strengthen this correlation. These geological features include the presence of megacrystic anorthosite in the Boromo and Houndé Belts of Burkina Faso. The Boromo and Houndé Belts also contain sequences of ultramafic rocks, gabbro and pillow basalt, very similar to the sequence that has been interpreted as an ophiolite sequence in the Agarasras Lakhadar Domain. Additionally, geophysical anomalies

are observed across the Taoudeni Basin generally trending from these belts in the Man-Leo Shield toward the centre of the Reguibat Shield where the study area is located.

These direct correlations of volcanosedimentary belts across the Taoudeni basin allows for the comparison of the geodynamic model proposed for the formation of the Sfariat-Bu Daira and Leaareig Terranes, of the Reguibat Shield, with recently proposed models for the formation and assembly of the Man-Leo Shield during the Palaeoproterozoic. The proposed model for the geodynamic evolution of a combined Reguibat – Baoulé-Mossi Block involves three stages:

- 2.25 to 2.13 Ga – growth and assembly of the of the Palaeoproterozoic terranes. Like the Reguibat Shield (Leaareig and Sfariat-Bu Daira Terranes), by ~2.15 Ga, the domain comprised two separate tectonic blocks that collided at ~2.13 Ga.
- 2.13 to 2.09 Ga – collision of the Palaeoproterozoic and Archaean Terranes. The collision between Palaeoproterozoic Baoulé-Mossi and Archaean Kenema-Man Domains of the Man-Leo Shield is constrained to 2.10 to 2.09 Ga. This timing is similar to the equivalent contact in the Reguibat Shield, on the eastern margin of the Kenema-Man Domain, this collision occurred during a sinistral transgressive event.
- 2.09 to 2.02 Ga – post-collisional magmatism. Following the collision, widespread magmatism occurs in the in the western block of the Baoulé-Mossi Domain and the eastern and northern margins of the Kenema-Man Domain. Although this magmatism is not observed in the Archaean of the Reguibat Shield or proximal to the contact, the eastern portion of the dominated by extensive ~2.09-2.05 Ga post-collisional magmatism.

The metallogenic profile produced during this project revealed numerous styles of mineralisation including orogenic gold, superior-type banded iron formation (BIF)

predominantly in the north of the study area, as well as chromitite-hosted platinum group elements (PGE), Fe-Ti-V oxide and Ni-Cu(-Co-PGE) magmatic sulphide mineralisation associated with the EAC. Based on these observed mineral occurrences and correlations with the Birimian of the Man-Leo Shield, a prospectivity assessment was constructed for the study area. In order of significance, the prospectivity of the region is as follows:

- Orogenic gold mineralisation. Strong geochronological and lithological correlations between heavily mineralised Birimian belts, and direct evidence of vein-hosted and disseminated gold mineralisation within the field make the Sfariat-Bu Daira and Leaareig Terranes highly prospective regions for orogenic gold mineralisation. More specifically, the Oum Abana and Taghsoumat-Aghsoumal Belts have the highest potential orogenic gold mineralisation.
- Magmatic Ni-Cu-(Co-PGE) magmatic sulphide mineralisation. The EAC fulfils several key exploration criteria for Voisey's Bay-style Ni-Cu-(Co-PGE) magmatic sulphide mineralisation including:
    - The presence of magmatic sulphides. This indicates that sulphide saturation was reached within the complex.
    - Derivation from a primitive, Ni-rich magma. Olivine mineral chemistry suggests that the labradorite massif-type anorthite, and associated lithologies were derived from a parent magma that was enriched in Ni. Furthermore, the high forsterite content of the olivine indicates that the magma was more primitive than the world-class Voisey's Bay deposit.
    - Furthermore, olivine mineral chemistry indicates that the Leucotroctolite is Ni-depleted competed to its ultramafic equivalent indicating that it may have experienced a sulphur saturation event
    - Palaeoproterozoic to Archaean in age. The EAC is formed at ~2.13 Ga.

    - Location proximal to the Archaean-Palaeoproterozoic contact, much like the Voisey's Bay deposit and other Ni-Cu deposits in Canada relating to mafic-ultramafic complexes.
- Chromitite-hosted PGE mineralisation.
    - Assay results and the observation of magmatic sulphides within the chromitite seam indicated the potential for Pt + Pd concentration associated with a sulphur saturation event during the formation of the chromitite seam. Evidence also exists for the preferential removal of mobile Pt and Pd-bearing PGE grains due to hydrothermal fluids.
    - The host rock, size and mineral chemistry of the chromitite seam within the northern limb of the EAC are very similar to the Archaean Sittampundi (megacrystic-) Anorthosite Complex in India. Mineralisation at Sittampundi only exists over a strike of 3.6 km in a ~17 km long complex.
    - Therefore, potential exists for significant PGE mineralisation the Northern Limb of the EAC, with unaltered sections of chromitite being the best targets in the 19 km long chromitite seam.
- Orthomagmatic Fe-Ti-V oxide mineralisation. Magnetite seams within the Southern Bulb of the EAC contain high grades of Fe, Ti and V although only limited outcrop has been observed. Ground magnetic surveys reveal a magnetic anomaly associated with these seams, striking 6-8km under regions covered by sand and sabkhas suggesting potentially significant mineralisation within the Southern Bulb
- Superior-type iron formations. Significant portions of Superior-type are observed, tectonically thickened within the Sfariat Shear Zone. Although all samples taken are low-grade, if a zone of enrichment (silica-leaching) can be identified, this belt contain significant mineralisation.

- Correlations between the Boromo Belt of Burkina Faso and the Leaareig Terrane suggest the potential for volcanic massive sulphide (VMS) and/or porphyry Cu-Au mineralisation although no evidence has been observed in the field.

8.2 **Recommendations**

Many of this project should be expanded on in future work as well as studies that were beyond the scope of this work. This study provides a geological, geochronological and tectonic framework for future work in the region can build upon. Some areas of study that can expand on this project include:

- Further mapping and petrological work in the Leaareig and Taghsoumat-Aghsoumal Domains. These regions were relatively understudied in this project with further mapping required to properly characterise the regions.
- Geophysical methods, in particular magnetic surveys (aerial or ground) would help delineate geological features and improve geological mapping in regions obscured by sand and sabkhas.
- Further Lu-Hf isotope work on the zircons used in the U-Pb geochronology would help to further constrain the tectonic evolution of the region.
- Thermodynamic modelling on samples already collected would aid to constrain the proposed geodynamic model for the region. Currently the model is largely based on magmatic and deformation events, with little in terms of constraining the metamorphic evolution of samples from the region.
- For the EAC much of the work in this study focussed on the Main Bulb and Northern Limb. Further work should include characterisation of other bodies (such as the Southern Bulb and Moug El Kaleb) and direct geochronological constrains on the

different types of anorthosite (possibly through U-Pb apatite and/or zircon geochronology).

- For mineral potential, reccomentations further work and exploration criteria are defined in Chapter 7

9.0 References

ABOUCHAMI, W., BOHER, M., MICHARD, A. & ALBAREDE, F. 1990. A major 2.1 Ga event of mafic magmatism in west Africa: An Early stage of crustal accretion. *Journal of Geophysical Research: Solid Earth,* 95**,** 17605-17629.

AGRAWAL, S. 1999. Geochemical discrimination diagrams: A simple way of replacing eye-fitted field boundaries with probability based classifier surfaces. *Journal of the Geological Society of India,* 54**,** 335-346.

AGRAWAL, S., GUEVARA, M. & VERMA, S. P. 2008. Tectonic Discrimination of Basic and Ultrabasic Volcanic Rocks through Log-Transformed Ratios of Immobile Trace Elements. *International Geology Review,* 50**,** 1057-1079.

AGRAWAL, S. & VERMA, S. P. 2007. Comment on "Tectonic classification of basalts with classification trees" by Pieter Vermeesch (2006). *Geochimica et Cosmochimica Acta,* 71**,** 3388-3390.

AITCHISON, J. 1986. *The statistical analysis of compositional data*, Chapman \& Hall, Ltd.

ALÍA MEDINA, M. 1950. El descubrimiento de los fosfatos del Sáhara Español. *Revista Africa,* 97**,** 8-10.

ALÍA MEDINA, M. 1951. Los yacimientos de fosfatos sedimentarios del Sáhara Español. . *II Congreso Nac. Ingeniería.*: Instituto de Ingenieros Civiles de España tomo V, grupo. IV.

ALÍA MEDINA, M. 1953. Formaciones ferruginosas en el Sáhara meridional Español. Fascículo X, XIX Sesión Congr. Geol. Int. Argel. 10, 39-45. *Fascículo X, XIX Sesión Congr. Geol. Int.* Algiers.

ALÍA MEDINA, M. 1960. La tectónica del Sáhara Español. . *XXI Int. Geol. Congr.,* 18**,** 193-202.

ALÍA MEDINA, M. 1971. Geología básica y aplicada: los fosfatos del Sáhara español. . *Las Ciencias,* 36**,** 1-18.

ALLEK, K. & HAMOUDI, M. 2008. Regional-scale aeromagnetic survey of the south-west of Algeria: A tool for area selection for diamond exploration. *Journal of African Earth Sciences,* 50**,** 67-78.

ALVARADO, A. D., VIÑA, J. D. L. & MUÑOZ CABEZÓN, C. 1958. *Mapa geológico del Sáhara Español y zonas limítrofes.*, 1:500.000. Madrid: Instituto Geológico y Minero de España, Ministerio de Industria.

AMPONSAH, P. O., SALVI, S., BÉZIAT, D., SIEBENALLER, L., BARATOUX, L. & JESSELL, M. W. 2015. Geology and geochemistry of the shear-hosted Julie gold deposit, NW Ghana. *Journal of African Earth Sciences,* 112, Part B**,** 505-523.

ANDERSEN, T. 2002. Correction of common lead in U–Pb analyses that do not report 204Pb. *Chemical Geology,* 192**,** 59-79.

ANDERSON, A. T. 1966. Mineralogy of the Labrieville anorthosite, Quebec. *Am. Mineral.,* 51**,** 1671-1711.

ARRIBAS, A. 1960. Las formaciones metamórficas del Sáhara Español y sus relaciones con el Precámbrico de otras regiones africanas. *Rep. 21st International Geological Congress, Norden 1960.* Copenhagen, Denmark.

ARRIBAS, A. 1968. El Precámbrico del Sáhara español y sus relaciones con el Precámbrico de otros países africanos. *Est. Geol. ,* 16**,** 199.

ASHWAL, L. D. 1993. *Anorthosites*, Springer-Verlag.

ASHWAL, L. D. 2010. The Temprality of Anorthosites. *The Canadian Mineralogist,* 48**,** 711-728.

ASHWAL, L. D. & BYBEE, G. M. 2017. Crustal Evolution and the Temporality of Anorthosites. *Earth-Science Reviews,* 173**,** 307-330.

ASHWAL, L. D. & TWIST, D. 1994. The Kunene complex, Angola/Namibia: a composite massif-type anorthosite complex. *Geological Magazine,* 131**,** 579-591.

AUVRAY, B., BURG, J. P., CARUBA, C., DARS, R. & LO, K. 1992. L'Amsaga (Mauritanie), fragment Archéen du Craton Ouest-Africain: observations et hypothèses nouvelles. *Journal of African Earth Sciences (and the Middle East),* 14**,** 183-190.

AUVREY, B., PEUCAT, J. J., POTREL, A., BURD, J. P., CARUBA, C., DARS, R. & LO, K. 1992. Données géochronologiques nouvelles sur l'Archéen de l'Amsaga (Dorsale Réguibat, Mauritanie). *Comptes Rendus des Séances de L'Académie des Sciences, Paris,* 315**,** 63-70.

BARATOUX, L., METELKA, V., NABA, S., JESSELL, M. W., GRÉGOIRE, M. & GANNE, J. 2011. Juvenile Palaeoproterozoic crust evolution during the Eburnean orogeny (~2.2–2.0Ga), western Burkina Faso. *Precambrian Research,* 191**,** 18-45.

BARATOUX, L., METELKA, V., NABA, S., OUIYA, P., SIEBENALLER, L., JESSELL, M. W., NARÉ, A., SALVI, S., BÉZIAT, D. & FRANCESCHI, G. 2015. Tectonic evolution of the Gaoua region, Burkina Faso: Implications for mineralization. *Journal of African Earth Sciences,* 112, Part B**,** 419-439.

BARBEY, P. 1975. The Adam Talha epizonal sequence (North Mauritania) and a general scheme for the Eburnean orogenic belt of West Africa. *Precambrian Research,* 2**,** 255-262.

BEA, F., MONTERO, P., HAISSEN, F., MOLINA, J. F., MICHARD, A., LAZARO, C., MOUTTAQI, A., ERRAMI, A. & SADKI, O. 2016. First evidence for Cambrian rift-related magmatism in the West African Craton margin: The Derraman Peralkaline Felsic Complex. *Gondwana Research,* 36**,** 423-438.

BEA, F., MONTERO, P., HAISSEN, F., RJIMATI, E., MOLINA, J. F. & SCARROW, J. H. 2014. Kalsilite-bearing plutonic rocks: The deep-seated Archean Awsard massif of the Reguibat Rise, South Morocco, West African Craton. *Earth-Science Reviews,* 138**,** 1-24.

BECCALUVA, L., MACCIOTTA, G., PICCARDO, G. B. & ZEDA, O. 1989. Clinopyroxene composition of ophiolite basalts as petrogenetic indicator. *Chemical Geology,* 77**,** 165-182.

BEKKER, A., PLANAVSKY, N. J., KRAPEŽ, B., RASMUSSEN, B., HOFMANN, A., SLACK, J. F., ROUXEL, O. J. & KONHAUSER, K. O. 2014. 9.18 - Iron Formations: Their Origins and Implications for Ancient Seawater Chemistry. *In:* HOLLAND, H. D. & TUREKIAN, K. K. (eds.) *Treatise on Geochemistry (Second Edition).* Oxford: Elsevier.

BERGER, J., DIOT, H., LO, K., OHNENSTETTER, D., FÉMÉNIAS, O., PIVIN, M., DEMAIFFE, D., BERNARD, A. & CHARLIER, B. 2013. Petrogenesis of Archean PGM-bearing chromitites and associated ultramafic–mafic–anorthositic rocks from the Guelb el Azib layered complex (West African craton, Mauritania). *Precambrian Research,* 224**,** 612-628.

BÉZIAT, D., BOURGES, F., DEBAT, P., LOMPO, M., MARTIN, F. & TOLLON, F. 2000. A Palaeoproterozoic ultramafic-mafic assemblage and associated volcanic rocks of the Boromo greenstone belt: fractionates originating from island-arc volcanic activity in the West African craton. *Precambrian Research,* 101**,** 25-47.

BÉZIAT, D., DUBOIS, M., DEBAT, P., NIKIÉMA, S., SALVI, S. & TOLLON, F. 2008. Gold metallogeny in the Birimian craton of Burkina Faso (West Africa). *Journal of African Earth Sciences,* 50**,** 215-233.

BLOCK, S., GANNE, J., BARATOUX, L., ZEH, A., PARRA-AVILA, L. A., JESSELL, M., AILLERES, L. & SIEBENALLER, L. 2015. Petrological and geochronological constraints on lower crust exhumation during Palaeoproterozoic (Eburnean) orogeny, NW Ghana, West African Craton. *Journal of Metamorphic Geology,* 33**,** 463-494.

BOHER, M., ABOUCHAMI, W., MICHARD, A., ALBAREDE, F. & ARNDT, N. T. 1992. Crustal growth in West Africa at 2.1 Ga. *Journal of Geophysical Research: Solid Earth,* 97**,** 345-369.

BRADLEY, D. C., MOTTS, H., HORTON, J. D., GILES, S. & TAYLOR, C. D. 2015a. *Geological Map of Mauritania*. Reston, VA: U.S. Geological Survey.

BRADLEY, D. C., O'SULLIVAN, P., COSCA, M. A., MOTTS, H. A., HORTON, J. D., TAYLOR, C. D., BEAUDOIN, G., LEE, G. K., RAMEZANI, J., BRADLEY, D. B., JONES, J. V. & BOWRING, S. 2015b. Second Projet de Renforcement Institutionnel du Secteur Minier de la République Islamique de Mauritanie (PRISM-II) Synthesis of Geological, Structural, and Geochronologic Data: Phase V, Deliverable 53. *In:* TAYLOR, C. D. (ed.) *Second Projet de Renforcement Institutionnel du Secteur Minier de la République Islamique de Mauritanie (PRISM-II) Phase V.* Reston, VA: USGS.

BRONNER, G., CHAUVEL, J.-J. & TRIBOULET, C. 1990. Geochemistry and knowledge of banded iron formations: The Western African Shield, an example. *Ancient banded iron formations (Regional presentations).* Athens, Greece: Theophrastus Publ.

BRONNER, G. & CHAUVEL, J. J. 1979. Precambrian banded iron-formations of the Ijil Group (Kediat Ijil, Reguibat Shield, Mauritania). *Economic Geology,* 74**,** 77-94.

BRONNER, G., CHAUVEL, J. J. & TRIBOULET, C. 1992. Structure, mineralogy and P-T-t paths of the Archean Sfariat iron formation (Mauritania). An intracratonic suture in the Reguibat shield. *In:* BRONNER, G. (ed.) *Structure et évolution d'un craton Archéen: la dorsale réguibat occidentale (Mauritanie) tectonique et métallogénie des formations ferrifères.* Orléans, France.

BRONNER, G., MARCHAND, J. & SOUGY, J. 1983. Structure en synclinal de nappes des Mauritanides septentrionales (Adrar Souttouf, Sahara occidental). *Colloque de géologie africaine.* Bruxelles.

BYBEE, G. M., ASHWAL, L. D., GOWER, C. F. & HAMILTON, M. A. 2015. Pegmatitic Pods in the Mealy Mountains Intrusive Suite, Canada: Clues to the Origin of the Olivine–Orthopyroxene Dichotomy in Proterozoic Anorthosites. *Journal of Petrology*.

BYBEE, G. M., ASHWAL, L. D., SHIREY, S. B., HORAN, M., MOCK, T. & ANDERSEN, T. B. 2014. Pyroxene megacrysts in Proterozoic anorthosites: Implications for tectonic setting, magma source and magmatic processes at the Moho. *Earth and Planetary Science Letters,* 389**,** 74-85.

CABANIS, B. & LECOLLE, M. 1989. Le diagramme La/10-Y/15-Nb/8: Un outil pour la discrimination des series volcaniques et lamise en evidence des processus demelange et/ou de contamination crustale. *Compte Rendus de I'Académie des Sciences Series II,* 309**,** 2023-2029.

CABY, R. 2003. Terrane assembly and geodynamic evolution of central–western Hoggar: a synthesis. *Journal of African Earth Sciences,* 37**,** 133-159.

'Canada's big nickel discoveries', 2014. So You Think Sirius Is Big? $5M ASX Explorer Drilling in Weeks. *Next Small Cap,* 25 September 2014. https://www.nextsmallcap.com/so-you-think-sirius-is-big-5m-asx-explorer-drilling-in-weeks/

CHARLIER, B., NAMUR, O., MALPAS, S., DE MARNEFFE, C., DUCHESNE, J.-C., AUWERA, J. V. & BOLLE, O. 2010. Origin of the giant Allard Lake ilmenite ore deposit (Canada) by fractional crystallization, multiple magma pulses and mixing. *Lithos,* 117**,** 119-134.

COMBA, J. A. 1965. XXV años de investigación geológica y minera de las provincias africanas. *Archivos del Instituto de Estudios Africanos.,* 19**,** 7-20.

COMBS, J. 2012. *Geology and Economic Potential of the Oum Abana Region, Western Sahara using Remote Sensing and Field Mapping.* Bachelor of Science (Applied Geology) (Honours) Honours Thesis, Curtin University.

DALLMEYER, R. D., LÉCORCHÉ, J. P. & DIA, O. 1987. Geotraverse excursion across the central Mauritanide orogen. *Terranes in the Circum-Atlantic Paleozoic Orogens.*: IUGS-UNESCO IGCP.

DAMPARE, S. B., SHIBATA, T., ASIEDU, D. K., OSAE, S. & BANOENG-YAKUBO, B. 2008. Geochemistry of Palaeoproterozoic metavolcanic rocks from the southern Ashanti volcanic belt, Ghana: Petrogenetic and tectonic setting implications. *Precambrian Research,* 162**,** 403-423.

DE KOCK, G. S., ARMSTRONG, R. A., SIEGFRIED, H. P. & THOMAS, E. 2011. Geochronology of the Birim Supergroup of the West African craton in the Wa-Bolé region of west-central Ghana: Implications for the stratigraphic framework. *Journal of African Earth Sciences,* 59**,** 1-40.

DE WIT, M. J. & ASHWAL, L. D. 1997. Convergence towards divergent models of greenstone belts. *In:* DE WIT, M. J. & ASHWAL, L. D. (eds.) *Greenstone Belts.* Oxford, U.K.: Oxford University Press.

DEWEY, J. F. 2005. Orogeny can be very short. *Proceedings of the National Academy of Sciences of the United States of America,* 102**,** 15286-15293.

DHANENDRAN, S., NATHAN, N., KUMAR, R. V., PILLAI, L. M. & BALUKKARASU, A. Chromite and Sulphide Hosted PGE Mineralisation in Sittampundi Layered Anorthosite Complex, Tamil Nadu. Conference GSI, 2014. 1-8.

DHARMA RAO, C. V., SANTOSH, M., SAJEEV, K. & WINDLEY, B. F. 2013. Chromite–silicate chemistry of the Neoarchean Sittampundi Complex, southern India: Implications for subduction-related arc magmatism. *Precambrian Research,* 227**,** 259-275.

DOUMBIA, S., POUCLET, A., KOUAMELAN, A., PEUCAT, J. J., VIDAL, M. & DELOR, C. 1998. Petrogenesis of juvenile-type Birimian (Palaeoproterozoic) granitoids in Central Côte-d'Ivoire, West Africa: geochemistry and geochronology. *Precambrian Research,* 87**,** 33-63.

DRIOUCH, Y., BÉZIAT, D., GRÉGOIRE, M., LAGUENINI, F., ABBOU, M. B., NTARMOUCHANT, A., RODDAZ, M., DAHIRE, M., BENNOUNA, A., BELKASMI, M., BRUSSET, S. & DEBAT, P. 2010. Clinopyroxene trace element compositions of cumulate mafic rocks and basalts from the Hercynian Moroccan Central Meseta: Petrogenetic implications. *Journal of African Earth Sciences,* 56**,** 97-106.

DRÜPPEL, K., LITTMANN, S., ROMER, R. L. & OKRUSCH, M. 2007. Petrology and isotope geochemistry of the Mesoproterozoic anorthosite and related rocks of the Kunene Intrusive Complex, NW Namibia. *Precambrian Research,* 156**,** 1-31.

DUCHESNE, J.-C. & DEMAIFFE, D. 1978. Trace elements and anorthosite genesis. *Earth and Planetary Science Letters,* 38**,** 249-272.

DUKE, J. M. & NALDRETT, A. J. 1978. A numerical model of the fractionation of olivine and molten sulfide from komatiite magma. *Earth and Planetary Science Letters,* 39**,** 255-266.

EGAL, E., THIÉBLEMONT, D., LAHONDÈRE, D., GUERROT, C., COSTEA, C. A., ILIESCU, D., DELOR, C., GOUJOU, J.-C., LAFON, J. M., TEGYEY, M., DIABY, S. & KOLIÉ, P. 2002a. Late Eburnean granitization and tectonics along the western and northwestern margin of the Archean Kénéma–Man domain (Guinea, West African Craton). *Precambrian Research,* 117**,** 57-84.

EGAL, E., THIÉBLEMONT, D., LAHONDÈRE, D., GUERROT, C., COSTEA, C. A., ILIESCU, D., DELOR, C., GOUJOU, J.-C., LAFON, J. M., TEGYEY, M., DIABY, S. & KOLIÉ, P. 2002b. Late Eburnean granitization and tectonics along the western and northwestern margin of the Archean Kénéma–Man domain (Guinea, West African Craton). *Precambrian Research,* 117**,** 57-84.

EGLINGER, A., THÉBAUD, N., ZEH, A., DAVIS, J., MILLER, J., PARRA-AVILA, L. A., LOUCKS, R., MCCUAIG, C. & BELOUSOVA, E. 2017. New insights into the crustal growth of the Palaeoproterozoic margin of the Archean Kéména-Man domain, West African craton (Guinea): Implications for gold mineral system. *Precambrian Research,* 292**,** 258-289.

FABRE, J., JONQUET, B. & BRONNER, G. 1978. *Carte géologique du Nord-ouest de l'Afrique*, 1:500.000. Algiers: SNED.

FALL, H. 2017. Independent Technical Report on Exploration Permits in Western Sahara held by Hanno Resources Limited.

FEYBESSE, J.-L., BILLA, M., GUERROT, C., DUGUEY, E., LESCUYER, J.-L., MILESI, J.-P. & BOUCHOT, V. 2006. The palaeoproterozoic Ghanaian province: Geodynamic model and ore controls, including regional stress modeling. *Precambrian Research,* 149**,** 149-196.

FEYBESSE, J.-L., BILLA, M., MILÉSI, J.-P., LEROUGE, C. & LE GOFF, E. 2000. Relationships between metamorphism-deformation-plutonism in the Archean-Palaeoproterozoic contact zone of West Africa. *31st international geological congress.* Rio.

FEYBESSE, J.-L. & MILÉSI, J.-P. 1994. The Archaean/Proterozoic contact zone in West Africa: a mountain belt of décollement thrusting and folding on a continental margin related to 2.1 Ga convergence of Archaean cratons? *Precambrian Research,* 69**,** 199-227.

FLORES, A. 1946. El Sáhara Español. Ediciones de la Alta Comisaría de España en Marruecos. 167.

FLOYD, P. A. & WINCHESTER, J. A. 1977. Geochemical Discrimination of Different Magma Series and Their Differentiation Product Using Immobile Elements. *Chemical Geology,* 20**,** 325-343.

FRISCH, W., MESCHEDE, M. & BLAKEY, R. 2011. Subduction zones, island arcs and active continental margins. *Plate Tectonics: Continental Drift and Mountain Building.* Berlin, Heidelberg: Springer Berlin Heidelberg.

GÄRTNER, A., VILLENEUVE, M., LINNEMANN, U., EL ARCHI, A. & BELLON, H. 2013. An exotic terrane of Laurussian affinity in the Mauritanides and Souttoufides (Moroccan Sahara). *Gondwana Research,* 24**,** 687-699.

GASQUET, D., ENNIH, N., LIÉGEOIS, J. P., SOULAIMANI, A. & MICHARD, A. 2008. The Pan-African Belt. *In:* MICHARD, A., SADDIQI, O., CHALOUAN, A. & LAMOTTE, D. F. D. (eds.) *Continental Evolution: The Geology of Morocco.* Springer Berlin Heidelberg.

GAVALA, J. 1952. Nota sobre los criaderos de hierro del Sáhara Español. . *Notas y Comunicaciones IGME,* 27**,** 1-59.

GEBRE-MARIAM, M., HAGEMANN, S. G. & GROVES, D. I. 1995. A classification scheme for epigenetic Archaean lode-gold deposits. *Mineralium Deposita,* 30**,** 408-410.

GHOSH, B. & KONAR, R. 2011. Chromites from meta-anorthosites, Sittampundi layered igneous complex, Tamil Nadu, southern India. *Journal of Asian Earth Sciences,* 42**,** 1394-1402.

GOLDFARB, R. J., BAKER, T., DUBE, B., GROVES, D. I., HART, C. J. R. & GOSSELIN, P. 2005. Distribution, character, and genesis of gold deposits in metamorphic terranes. *Distribution, Character, and Genesis of Gold Deposits in Metamorphic Terranes***,** 407-450.

GOLDFARB, R. J. & GROVES, D. I. 2015. Orogenic gold: Common or evolving fluid and metal sources through time. *Lithos,* 233**,** 2-26.

GOLDFARB, R. J., GROVES, D. I. & GARDOLL, S. 2001. Orogenic gold and geologic time: a global synthesis. *Ore Geology Reviews,* 18**,** 1-75.

GOODENOUGH, K. M., LUSTY, P. A. J., ROBERTS, N. M. W., KEY, R. M. & GARBA, A. 2014. Post-collisional Pan-African granitoids and rare metal pegmatites in western Nigeria: Age, petrogenesis, and the 'pegmatite conundrum'. *Lithos,* 200-201**,** 22-34.

GRENHOLM, M. 2014. *The Birimian event in the Baoulé Mossi domain (West African Craton) : regional and global context.* Master's Thesis in Geology, Lund University.

GROSS, G. A. 1980. A Classification of Iron Formations Based on Depositional Environments. *Canadian Mineralogist,* 18**,** 215-222.

GROSS, J., TREIMAN, A. H. & MERCER, C. N. 2014. Lunar feldspathic meteorites: Constraints on the geology of the lunar highlands, and the origin of the lunar crust. *Earth and Planetary Science Letters,* 388**,** 318-328.

GROVES, D. I., GOLDFARB, R. J., GEBRE-MARIAM, M., HAGEMANN, S. G. & ROBERT, F. 1998. Orogenic gold deposits: A proposed classification in the context of their crustal distribution and relationship to other gold deposit types. *Ore Geology Reviews,* 13**,** 7-27.

HAMMOND, N. Q., ROBB, L., FOYA, S. & ISHIYAMA, D. 2011. Mineralogical, fluid inclusion and stable isotope characteristics of Birimian orogenic gold mineralization at the Morila Mine, Mali, West Africa. *Ore Geology Reviews,* 39**,** 218-229.

HART, S. R. & DAVIS, K. E. 1978. Nickel partitioning between olivine and silicate melt. *Earth and Planetary Science Letters,* 40**,** 203-219.

HAWKESWORTH, C. J., GALLAGHER, K., HERGT, J. M. & MCDERMOTT, F. 1993. Mantle and Slab Contributions in ARC Magmas. *Annual Review of Earth and Planetary Sciences,* 21**,** 175-204.

HAYES, B., ASHWAL, L. D., WEBB, S. J. & BYBEE, G. M. 2017. Large-scale magmatic layering in the Main Zone of the Bushveld Complex and episodic downward magma infiltration. *Contributions to Mineralogy and Petrology,* 172**,** 13.

HERNÁNDEZ-PACHECO, E., HERNÁNDEZPACHECO, F., ALÍA-MEDINA, M., VIDAL, C. & GUINEA, E. 1949. El Sáhara Español: estudio geológico, geográfico y botánico. *Instituto de Estudios Africanos CSIC***,** 808 p., 134 p. de lám.

HERON, K., JESSELL, M., BENN, K., HARRIS, E. & CROWLEY, Q. G. 2016. The Tasiast deposit, Mauritania. *Ore Geology Reviews,* 78**,** 564-572.

HIEBERT, R. S., BEKKER, A., WING, B. A. & ROUXEL, O. J. 2013. The Role of Paragneiss Assimilation in the Origin of the Voisey's Bay Ni-Cu Sulfide Deposit, Labrador: Multiple S and Fe Isotope Evidence. *Economic Geology,* 108**,** 1459-1469.

HIRDES, W. & DAVIS, D. W. 1998. First U/Pb zircon age of extrusive volcanism in the Birimian Supergroup of Ghana/West Africa. *Journal of African Earth Sciences,* 27**,** 291-294.

HIRDES, W. & DAVIS, D. W. 2002. U–Pb Geochronology of Palaeoproterozoic Rocks in the Southern Part of the Kedougou-Kéniéba Inlier, Senegal, West Africa: Evidence for

Diachronous Accretionary Development of the Eburnean Province. *Precambrian Research,* 118**,** 83-99.
HIRDES, W., DAVIS, D. W. & EISENLOHR, B. N. 1992. Reassessment of Proterozoic granitoid ages in Ghana on the basis of U/Pb zircon and monazite dating. *Precambrian Research,* 56**,** 89-96.
HIRDES, W., DAVIS, D. W., LÜDTKE, G. & KONAN, G. 1996. Two generations of Birimian (Palaeoproterozoic) volcanic belts in northeastern Côte d'Ivoire (West Africa): consequences for the 'Birimian controversy'. *Precambrian Research,* 80**,** 173-191.
HOLLAND, H. D., LAZAR, B. & MCCAFFREY, M. 1986. Evolution of the atmosphere and oceans. *Nature,* 320**,** 27.
HOLNESS, M. B. 2014. The effect of crystallization time on plagioclase grain shape in dolerites. *Contributions to Mineralogy and Petrology,* 168**,** 1076.
HOLNESS, M. B., STRIPP, G., HUMPHREYS, M. C. S., VEKSLER, I. V., NIELSEN, T. F. D. & TEGNER, C. 2011. Silicate Liquid Immiscibility within the Crystal Mush: Late-stage Magmatic Microstructures in the Skaergaard Intrusion, East Greenland. *Journal of Petrology,* 52**,** 175-222.
HOR, A. K., HUTT, D. K., SMITH, J. V., WAKEFIELD, J. & WINDLEY, B. F. 1975. Petrochemistry and mineralogy of early Precambrian anorthositic rocks of the Limpopo belt, southern Africa. *Lithos,* 8**,** 297-310.
IRVINE, T. N. 1977. Origin of chromitite layers in the Muskox intrusion and other stratiform intrusions: A new interpretation. *Geology,* 5**,** 273-277.
IRVINE, T. N. & BARAGAR, W. R. A. 1971. A Guide to the Chemical Classification of the Common Volcanic Rocks. *Canadian Journal of Earth Sciences,* 8**,** 523-548.
ISMAIL AHAMED, M. 1994. *Geología y recursos del subsuelo del Sáhara occidental.* Tesis doctoral inédita., ETSIM Madrid.
JESSELL, M. W., BEGG, G. C. & MILLER, M. S. 2016. The geophysical signatures of the West African Craton. *Precambrian Research,* 274**,** 3-24.
JESSELL, M. W. & LIÉGEOIS, J.-P. 2015. 100 years of research on the West African Craton. *Journal of African Earth Sciences,* 112, Part B**,** 377-381.
KAHOUI, M., KAMINSKY, F. V., GRIFFIN, W. L., BELOUSOVA, E., MAHDJOUB, Y. & CHABANE, M. 2012. Detrital pyrope garnets from the El Kseibat area, Algeria: A glimpse into the lithospheric mantle beneath the north-eastern edge of the West African Craton. *Journal of African Earth Sciences,* 63**,** 1-11.
KAHOUI, M. & MAHDJOUB, Y. 2004. An Eburnian alkaline–peralkaline magmatism in the Reguibat rise: the Djebel Drissa ring complex (Eglab Shield, Algeria). *Journal of African Earth Sciences,* 39**,** 115-122.
KAHOUI, M., MAHDJOUB, Y. & KAMINSKY, F. V. 2008. Possible primary sources of diamond in the North African diamondiferous province. *Geological Society, London, Special Publications,* 297**,** 77-109.
KEY, R., LOUGHLIN, S., GILLESPIE, M., DEL RIO, M. D. L. M., HORSTWOOD, M., CROWLEY, Q. G., DARBYSHIRE, F., PITFIELD, P. & HENNEY, P. 2008. Two Mesoarchaean terranes in the Reguibat shield of NW Mauritania. *In:* ENNIH, N. & LIEGEOIS, J. P. (eds.) *The boundaries of the West African craton.* London, UK: Geological Society of London.
KUNO, H. 1966. Lateral variation of basalt magma type across continental margins and Island Arcs. *Bulletin Volcanologique,* 29**,** 195-222.
KUNO, H. 1968. Differentiation of Basalt Magmas. *In:* HESS, H. H. & POLDERVAART, A. (eds.) *Basalts: The Poldervaart Treatise on Rocks of Basaltic Composition.* New York: Interscience Publishers.

LAGRAA, K., SALVI, S., BÉZIAT, D., DEBAT, P. & KOLLI, O. 2017. First insights on the molybdenum-copper Bled M'Dena complex (Eglab massif, Algeria). *Journal of African Earth Sciences,* 127**,** 159-174.

LAHONDÈRE, D., THIÉBLEMONT, D., GOUJOU, J. C., ROGER, J., MOUSSINE-POUCHKINE, A., LE MÉTOUR, J., COCHERIE, A. & GUERROT, C. 2003. *Notice explicative des cartes géologiques et gîtologiques à 1/200 000 et 1/500 000 du nord de la Mauritanie.* . Nouakchott: DMG, Ministère des Mines et de l'Industrie.

LAHONDÈRE, D., THIÉBLEMONT, D., TEGYEY, M., GUERROT, C. & DIABATE, B. 2002. First evidence of early Birimian (2.21 Ga) volcanic activity in Upper Guinea: the volcanics and associated rocks of the Niani suite. *Journal of African Earth Sciences,* 35**,** 417-431.

LAUNAY, N., QUESNEL, Y., ROCHETTE, P. & DEMORY, F. 2018. Iron Formations as the Source of the West African Magnetic Crustal Anomaly. *Frontiers in Earth Science,* 6.

LE BAS, M. J. 1962. The role of aluminum in igneous. clinopyroxenes with relation to their parentage. *American Journal of Science,* 260**,** 267-288.

LE BAS, M. J. & STRECKEISEN, A. L. 1991. The IUGS systematics of igneous rocks. *Journal of the Geological Society,* 148**,** 825-833.

LE MIGNOT, E., REISBERG, L., ANDRÉ-MAYER, A.-S., BOURASSA, Y., FONTAINE, A. & MILLER, J. 2017a. Re-Os Geochronological Evidence for Multiple Palaeoproterozoic Gold Events at the Scale of the West African Craton. *Economic Geology,* 112**,** 145-168.

LE MIGNOT, E., SIEBENALLER, L., BÉZIAT, D., ANDRÉ-MAYER, A.-S., REISBERG, L., SALVI, S., VELASQUEZ, G., ZIMMERMANN, C., NARÉ, A. & FRANCESCHI, G. 2017b. The Palaeoproterozoic Copper-Gold Deposits of the Gaoua District, Burkina Faso: Superposition of Orogenic Gold on a Porphyry Copper Occurrence? *Economic Geology,* 112**,** 99-122.

LE VAILLANT, M., FIORENTINI, M. L. & BARNES, S. J. 2016. Review of lithogeochemical exploration tools for komatiite-hosted Ni-Cu-(PGE) deposits. *Journal of Geochemical Exploration,* 168**,** 1-19.

LÉCORCHÉ, J.-P., BRONNER, G., DALLMEYER, R. D., ROCCI, G. & ROUSSEL, J. 1991. The Mauritanide Orogen and its northern extensions (Western Sahara and Zemmour), West Africa. *In:* DALLMEYER, R. D. & LÉCORCHÉ, J.-P. (eds.) *The West African Orogens and Circum-Atlantic Correlatives.* Berlin: SpringerVerlag.

LEDRU, P., JOHAN, V., MILÉSI, J. P. & TEGYEY, M. 1994. Markers of the last stages of the Palaeoproterozoic collision: evidence for a 2 Ga continent involving circum-South Atlantic provinces. *Precambrian Research,* 69**,** 169-191.

LEFORT, J.-P., AïFA, T. & BOURROUILH, R. 2004. Évidences paléomagnétiques et paléontologiques en faveur d'une position antipodale du craton Ouest-Africain et de la Chine du Nord : conséquences paléogéographiques. *Comptes Rendus Geoscience,* 336**,** 159-165.

LEHBIB NAYEM, S., MELGAREJO DRAPER, J. C., ARRIBAS MORENO, A., MARRIOTT, C., COMBS, J. & LYCHE, C. 2016a. An approach to the geology and metallogeny of the Precambrian of Western Sahara. *35th International Geological Congress.* Cape Town, South Africa.

LEHBIB NAYEM, S., MELGAREJO DRAPER, J. C., ARRIBAS MORENO, A., MARRIOTT, C., COMBS, J., LYCHE, C., BACH OLLER, N. & MERINO PÉREZ, I. 2016b. Precious metals in shear zones affecting ultrabasic rocks: examples from Western Sahara. *35th International Geological Congress.* Cape Town, South Africa.

LEHBIB, S. 2016. *Estudio Geológico y Metalogenético del Basamento Precámbrico del Sáhara Occidental.* Programa de Doctorado de Ciencias de la Tierra PhD Thesis, Universidad de Barcelona.

LEHBIB, S., ARRIBAS, A., MELGAREJO, J. C., PROENZA, J. A., ZACCARINI, F., THALHAMMER, O. & GARUTI, G. 2008. Chromite Deposits from Western Sahara: Textures, Composition and Platinum Group Minerals. *Revista de la Sociedad Española De Mineralogía,* 9**,** 143-144.

LETERRIER, J., MAURY, R. C., THONON, P., GIRARD, D. & M., M. 1982. Clinopyroxene composition as a method of identification of the magmatic affinities of paleo-volcanic series. *Earth and Planetary Science Letters,* 59**,** 139-154.

LEUBE, A., HIRDES, W., MAUER, R. & KESSE, G. O. 1990a. The early Proterozoic Birimian Supergroup of Ghana and some aspects of its associated gold mineralization. *Precambrian Research,* 46**,** 139-165.

LEUBE, A., HIRDES, W., MAUER, R. & KESSE, G. O. 1990b. The early Proterozoic Birimian Supergroup of Ghana and some aspects of its associated gold mineralization. *Precambrian Research,* 46**,** 139-165.

LIÉGEOIS, J.-P., ABDELSALAM, M. G., ENNIH, N. & OUABADI, A. 2013. Metacraton: Nature, genesis and behavior. *Gondwana Research,* 23**,** 220-237.

LIÉGEOIS, J. P., CLAESSENS, W., CAMARA, D. & KLERKX, J. 1991. Short-lived Eburnian orogeny in southern Mali. Geology, tectonics, U-Pb and Rb-Sr geochronology. *Precambrian Research,* 50**,** 111-136.

LOMPO, M. 2010. Palaeoproterozoic structural evolution of the Man-Leo Shield (West Africa). Key structures for vertical to transcurrent tectonics. *Journal of African Earth Sciences,* 58**,** 19-36.

LÜDTKE, G., HIRDES, W., KONAN, G., KONÉ, Y., N'DA, D., TRAORÉ, Y. & ZAMBLÉ, Z. 1999. Géologie de la région Haute Comoé Sud-feuilles Dabakala (2b, d et 4b, d). . *Direction de la Géologie Abidjan Bulletin,* 176.

LYCHE, C. 2012. *Lithology, Mineral Alteration and Mineralisation of Agarasras Labiad, Oum Abana Greenstone Belt, West African Craton, Western Sahara.* Bachelor of Science (Applied Geology) (Honours) Honours Thesis, Curtin University.

MAIER, W. D. 2005. Platinum-group element (PGE) deposits and occurrences: Mineralization styles, genetic concepts, and exploration criteria. *Journal of African Earth Sciences,* 41**,** 165-191.

MAIER, W. D., PRICHARD, H. M., BARNES, S. J. & FISHER, P. C. 1999. Compositional variation of laurite at Union Section in the Western Bushveld Complex. *South African Journal of Geology,* 102**,** 286-292.

MAIER, W. D., RASMUSSEN, B., FLETCHER, I. R., LI, C., BARNES, S.-J. & HUHMA, H. 2013. The Kunene Anorthosite Complex, Namibia, and Its Satellite Intrusions: Geochemistry, Geochronology, and Economic Potential. *Economic Geology,* 108**,** 953-986.

MARCHAND, J., BRONNER, G. & SOUGY, J. 1984. *Carte géologique provisoire du Maroc à l'échelle du 200 000.*, 1:200 000. Service Géologique du Maroc, Notes et Mémoires.

MARKWITZ, V., HEIN, K. A. A., JESSELL, M. W. & MILLER, J. 2016a. Metallogenic portfolio of the West Africa craton. *Ore Geology Reviews,* 78**,** 558-563.

MARKWITZ, V., HEIN, K. A. A. & MILLER, J. 2016b. Compilation of West African mineral deposits: Spatial distribution and mineral endowment. *Precambrian Research,* 274**,** 61-81.

MCDONOUGH, W. F. & SUN, S. S. 1995. The composition of the Earth. *Chemical Geology,* 120**,** 223-253.

MCFARLANE, C. R. M., MAVROGENES, J., LENTZ, D., KING, K., ALLIBONE, A. & HOLCOMBE, R. 2011. Geology and Intrusion-Related Affinity of the Morila Gold Mine, Southeast Mali. *Economic Geology,* 106**,** 727-750.

MERABET, N.-E., MAHDJOUB, Y., ABTOUT, A., HENRY, B., KAHOUI, M., MAOUCHE, S., LAMALI, A. & AYACHE, M. 2014. The Palaeoproterozoic Djebel Drissa ring complex (Eglab shield, Algeria): Post-collisional intrusions in a transtentional tectonic setting. *Tectonophysics,* 629**,** 197-210.

MERABET, N.-E., MAHDJOUB, Y., HENRY, B., ABTOUT, A., MAOUCHE, S., KAHOUI, M., LAMALI, A. & AYACHE, M. 2016. Palaeoproterozoic structural frame of the Yetti domain (Eglab shield, Algeria): Emplacement conditions of the Tinguicht late pluton from magnetic fabric study. *Journal of African Earth Sciences,* 114**,** 158-173.

MERNAGH, T. P. & BIERLEIN, F. P. 2008. Transport and Precipitation of Gold in Phanerozoic Metamorphic Terranes from Chemical Modeling of Fluid-Rock Interaction. *Economic Geology,* 103**,** 1613-1640.

MIDDLEMOST, E. A. K. 1989. Iron oxidation ratios, norms and the classification of volcanic rocks. *Chemical Geology,* 77**,** 19-26.

MILÉSI, J.-P., LEDRU, P., FEYBESSE, J.-L., DOMMANGET, A. & MARCOUX, E. 1992. Early proterozoic ore deposits and tectonics of the Birimian orogenic belt, West Africa. *Precambrian Research,* 58**,** 305-344.

MINGARRO, E. & ARRIBAS, A. 1956. Consideraciones sobre la edad absoluta del Precámbrico de Bulautad (Sáhara Meridional Español). . *Abstracts XX Int. Geol. Congress.* Mexico city, México.

MOHAMMED, T., JEAN-YVES, C., PETER, B. & CHRISTOPHE, R. Petrogenesis of the post-collisional Bled M'Dena volcanic ring complex in Reguibat Rise (western Eglab shield, Algeria). *Journal of African Earth Sciences*.

MOSES, B. V. C., RAM MOHAN, V. & MASARU, Y. 1999. Geochemical characteristics of mafic granulites and associated websterites from the Sittampundi complex, South India. *Journal of Geosciences***,** 215-225.

MURPHY, J. B. 2007. Igneous Rock Associations 8. Arc Magmatism II: Geochemical and Isotopic Characteristics. *2007*.

MYERS, J. S. 1978. Formation of banded gneisses by deformation of igneous rocks. *Precambrian Research,* 6**,** 43-64.

NALDRETT, A. J. 1989. *Magmatic sulfide deposits*, Clarendon Press.

NALDRETT, A. J. 1999. World-class Ni-Cu-PGE deposits: key factors in their genesis. *Mineralium Deposita,* 34**,** 227-240.

NALDRETT, A. J. 2010. Secular Variation of Magmatic Sulfide Deposits and Their Source Magmas. *Economic Geology,* 105**,** 669-688.

NALDRETT, A. J., KINNAIRD, J., WILSON, A., YUDOVSKAYA, M., MCQUADE, S., CHUNNETT, G. & STANLEY, C. 2009. Chromite composition and PGE content of Bushveld chromitites: Part 1 – the Lower and Middle Groups. *Applied Earth Science,* 118**,** 131-161.

NALDRETT, A. J., WILSON, A., KINNAIRD, J., YUDOVSKAYA, M. & CHUNNETT, G. 2012. The origin of chromitites and related PGE mineralization in the Bushveld Complex: new mineralogical and petrological constraints. *Mineralium Deposita,* 47**,** 209-232.

NISBET, E. G. & PEARCE, J. A. 1977. Clinopyroxene composition in mafic lavas from different tectonic settings. *Contributions to Mineralogy and Petrology,* 63**,** 149-160.

O'CONNOR, E. A., PITFIELD, P. E. J., SCHOFIELD, D. I., COATS, S., WATERS, C., POWELL, J., FORD, J., CLARKE, S. & GILLESPIE, M. 2005a. *Notice explicative des*

cartes géologiques et gîtologiques à 1/200 000 et 1/500 000 du Nord-Ouest de la Mauritanie. . Nouakchott: DMG, Ministère des Mines et de l'Industrie.

O'CONNOR, E. A., PITFIELD, P. E. J., SCHOFIELD, D. I., COATS, S., WATERS, C., POWELL, J., FORD, J., CLARKE, S. & GILLESPIE, M. 2005b. Notice explicative des cartes géologiques et gîtologiques à 1/200 000 et 1/500 000 du Nord-Ouest de la Mauritanie.: DMG, Ministère des Mines et de l'Industrie, Nouakchott.

OBERTHÜR, T., VETTER, U., DAVIS, D. W. & AMANOR, J. A. 1998. Age constraints on gold mineralization and Palaeoproterozoic crustal evolution in the Ashanti belt of southern Ghana. *Precambrian Research,* 89**,** 129-143.

ONSTOTT, T. C. & DORBOR, J. 1987. 40Ar/39Ar and paleomagnetic results from Liberia and the Precambrian APW data base for the West African Shield. *Journal of African Earth Sciences (1983),* 6**,** 537-552.

PARRA-AVILA, L. A. 2015. *4D evolution of felsic magmatic suites and lithospheric architecture of the Palaeoproterozoic Birimian terranes, West Africa.* PhD dissertation, University of Western Australia.

PARRA-AVILA, L. A., BELOUSOVA, E., FIORENTINI, M. L., BARATOUX, L., DAVIS, J., MILLER, J. & MCCUAIG, T. C. 2016. Crustal evolution of the Palaeoproterozoic Birimian terranes of the Baoulé-Mossi domain, southern West African Craton: U–Pb and Hf-isotope studies of detrital zircons. *Precambrian Research,* 274**,** 25-60.

PARRA-AVILA, L. A., KEMP ANTHONY, I. S., FIORENTINI, M. L., BELOUSOVA, E., BARATOUX, L., BLOCK, S., JESSELL, M., BRUGUIER, O., BEGG, G. C., MILLER, J., DAVIS, J. & MCCUAIG, T. C. 2017. The geochronological evolution of the Palaeoproterozoic Baoulé-Mossi domain of the southern West African Craton. *Precambrian Research*.

PATTEN, C., BARNES, S.-J., MATHEZ, E. A. & JENNER, F. E. 2013. Partition coefficients of chalcophile elements between sulfide and silicate melts and the early crystallization history of sulfide liquid: LA-ICP-MS analysis of MORB sulfide droplets. *Chemical Geology,* 358**,** 170-188.

PEARCE, J. A. 1996. A user's guide to basalt discrimination diagrams. *In:* D.A., W. (ed.) *Short Course Notes - Trace element geochemistry of volca-nic rocks: applications for massive sulphide exploration.*: Geological Association of Canada.

PEARCE, J. A. 2008. Geochemical fingerprinting of oceanic basalts with applications to ophiolite classification and the search for Archean oceanic crust. *Lithos,* 100**,** 14-48.

PEARCE, J. A. 2014. Immobile element fingerprinting of ophiolites. *Elements,* 10**,** 101-108.

PEARCE, J. A., HARRIS, N. B. W. & TINDLE, A. G. 1984. Trace element discrimination diagrams for the tectonic interpretation of granitic rocks. *Journal of Petrology,* 25**,** 956-983.

PESONEN, L. J., ELMING, S. Å., MERTANEN, S., PISAREVSKY, S., D'AGRELLA-FILHO, M. S., MEERT, J. G., SCHMIDT, P. W., ABRAHAMSEN, N. & BYLUND, G. 2003. Palaeomagnetic configuration of continents during the Proterozoic. *Tectonophysics,* 375**,** 289-324.

PEUCAT, J.-J., CAPDEVILA, R., DRARENI, A., MAHDJOUB, Y. & KAHOUI, M. 2005. The Eglab massif in the West African Craton (Algeria), an original segment of the Eburnean orogenic belt: petrology, geochemistry and geochronology. *Precambrian Research,* 136**,** 309-352.

PHILLIPS, G. N. 1986. Geology and alteration in the Golden Mile, Kalgoorlie. *Economic Geology,* 91**,** 779–808.

PIQUÉ, A.-. 2001. *Geology of Northwest Africa*. Berlin, Stuttgart: Gebrüder Borntraeger.

PITFIELD, P. E. J., KEY, R. M., WATERS, C. N., HAWKINS, M. P. H., SCHOFIELD, D. I., LOUGHLIN, S. & BARNES, R. P. 2005. Notice explicative des cartes géologiques et

gîtologiques à 1/200 000 et 1/500 000 du Sud de la Mauritanie, vol.1 - géologie. Nouakchott: DMG, Ministère des Mines et de l'Industrie.
POTREL, A., PEUCAT, J. J. & FANNING, C. M. 1998. Archean crustal evolution of the West African Craton: example of the Amsaga Area (Reguibat Rise). U□Pb and Sm□Nd evidence for crustal growth and recycling. *Precambrian Research,* 90**,** 107-117.
POTREL, A., PEUCAT, J. J., FANNING, C. M., AUVRAY, B., BURG, J. P. & CARUBA, C. 1996. 3.5 Ga old terranes in the West African Craton, Mauritania. *Journal of the Geological Society,* 153**,** 507-510.
QUIROGA, F. 1886a. Apuntes de un viaje por el Sáhara Occidental. . *Anales de la Sociedad Española de Historia Natural,* 15**,** 495-523.
QUIROGA, F. 1886b. Estudio de la Península de Río de Oro. *Revista Geografía Comercial Madrid* 2**,** 8-10.
QUIROGA, F. 1886c. Geología y Geografía del Sáhara Occidental. *Revista Geografía Comercial Madrid,* 2**,** 63-66.
QUIROGA, F. 1886d. La exploración al Sáhara occidental. *Bol. Institución Libre de Enseñanza. Madrid,* 10**,** 337-342.
QUIROGA, F. 1886e. Observaciones al mapa geológico del Sáhara, de M. Rolland. *Anales de la Sociedad Española de Historia Natural,* 21**,** 29-32.
QUIROGA, F. 1887a. El nivel del Sáhara occidental. *Revista de la Sociedad Española De Mineralogía,* 23**,** 242-246.
QUIROGA, F. 1887b. La estructura geológica del Occidente sahariano *Boletin de la Sociedad Geografica Madrid,* 22**,** 21-27.
QUIROGA, F. 1889. Observaciones geológicas hechas en el Sáhara Occidental. *Anales de la Sociedad española de Historia natural Madrid,* 18**,** 337-393.
ROBB, L. J. 2005. *Introduction to Ore-Forming Processes,* Oxford, UK, Blackwell Publishing.
ROBERTSON, M. & PETERS, L. 2016. West african goldfields. *Episodes,* 39**,** 155-176.
ROCCI, G., BRONNER, G. & DESCHAMPS, M. 1991. Crystalline Basement of the West African Craton. *In:* DALLMEYER, R. D. & LÉCORCHÉ, J. P. (eds.) *The West African Orogens and Circum-Atlantic Correlatives.* Berlin: Springer Verlag.
ROLLINSON, H. 1993. *Using Geochemical Data: Evolution, Presentation, Interpretation*.
ROLLINSON, H. 2016. Archaean crustal evolution in West Africa: A new synthesis of the Archaean geology in Sierra Leone, Liberia, Guinea and Ivory Coast. *Precambrian Research,* 281**,** 1-12.
ROLLINSON, H., REID, C. & WINDLEY, B. 2010. Chromitites from the Fiskenæsset anorthositic complex, West Greenland: clues to late Archaean mantle processes. *In:* KUSKY, T. M., ZHAI, M. G. & XIAO, W. (eds.) *The Evolving Continents: Understanding Processes of Continental Growth.* Geological Society of London.
SANTOSH, M. & LI, S.-S. 2018. Anorthosites from an Archean continental arc in the Dharwar Craton, southern India: Implications for terrane assembly and cratonization. *Precambrian Research,* 308**,** 126-147.
SCHOFIELD, D. I. & GILLESPIE, M. R. 2007. A tectonic interpretation of "Eburnean terrane" outliers in the Reguibat Shield, Mauritania. *Journal of African Earth Sciences,* 49**,** 179-186.
SCHOFIELD, D. I., HORSTWOOD, M. S. A., PITFIELD, P. E. J., CROWLEY, Q. G., WILKINSON, A. F. & SIDATY, H. C. O. 2006. Timing and kinematics of Eburnean tectonics in the central Reguibat Shield, Mauritania. *Journal of the Geological Society,* 163**,** 549-560.
SCHOFIELD, D. I., HORSTWOOD, M. S. A., PITFIELD, P. E. J., GILLESPIE, M., DARBYSHIRE, F., O'CONNOR, E. A. & ABDOULOYE, T. B. 2012. U–Pb dating

and Sm–Nd isotopic analysis of granitic rocks from the Tiris Complex: New constaints on key events in the evolution of the Reguibat Shield, Mauritania. *Precambrian Research,* 204–205**,** 1-11.
SCHWARTZ, M. O. & MELCHER, F. 2003. The Perkoa Zinc Deposit, Burkina Faso. *Economic Geology,* 98**,** 1463-1485.
SCOATES, J. S., LINDSLEY, D. H. & FROST, B. R. 2010. Magmatic and structural evolution of an anotherositic magma chamber: the Poe Mountain intrusion, Laramie anorthosite complex, Wyoming. *The Canadian Mineralogist,* 48**,** 851-885.
SERVICE GÉOLOGIQUE DU MAROC. 1999. *Carte géologique du Maroc*, 1:1,000,000. Service Géologique du Maroc.
SHERVAIS, J. W. 1982. Ti-V plots and the petrogenesis of modern and ophiolitic lavas. *Earth and Planetary Science Letters,* 59**,** 101-118.
SISSON, T. W. & GROVE, T. L. 1993. Experimental investigations of the role of H2O in calc-alkaline differentiation and subduction zone magmatism. *Contributions to Mineralogy and Petrology,* 113**,** 143-166.
SOUGY, J. 1962. Contribution à l'étude géologique des guelbs Bou-Leriah (région d'Aoucert, Sahara espagnol). . *Bulletin de la Societe Geologique de France,* 4.
SOUGY, J. 1969. Grandes lignes structurales de la chaîne des Mauritanides et de son avantpays (socle précambrien et sa couverture infracambrienne et paléozoïque),. *Afrique de l'Ouest. Bulletin de la Societe Geologique de France,* 11**,** 133-149.
STRECKEISEN, A. 1976. To each plutonic rock its proper name. *Earth-Science Reviews,* 12**,** 1-33.
SYLVESTER, P. J. & ATTOH, K. 1992. Lithostratigraphy and Composition of 2.1 Ga Greenstone Belts of the West African Craton and Their Bearing on Crustal Evolution and the Archean-Proterozoic Boundary. *The Journal of Geology,* 100**,** 377-393.
TAIT, J., STRAATHOF, G., SÖDERLUND, U., ERNST, R. E., KEY, R., JOWITT, S. M., LO, K., DAHMADA, M. E. M. & N'DIAYE, O. 2013. The Ahmeyim Great Dyke of Mauritania: A newly dated Archaean intrusion. *Lithos,* 174**,** 323-332.
TALUKDAR, M., SANYAL, S. & SENGUPTA, P. 2017. Metasomatic alteration of chromite from parts of the late Archaean Sittampundi Layered Magmatic Complex (SLC), Tamil Nadu, India. *Ore Geology Reviews,* 90**,** 148-165.
TAYLOR, C. D., FINN, C. A., ANDERSON, E. D., BRADLEY, D. C., JOUD, M. Y., TALEB MOHAMED, A. & HORTON, J. D. 2016. The F'derik-Zouérate Iron District: Mesoarchean and Palaeoproterozoic Iron Formation of the Tiris Complex, Islamic Republic of Mauritania. *In:* BOUABDELLAH, M. & SLACK, F. J. (eds.) *Mineral Deposits of North Africa.* Cham: Springer International Publishing.
TAYLOR, S. R. & MCLENNAN, S. M. 1985. *The Continental Crust: its Composition and Evolution. An Examination of the Geochemical Record Preserved in Sedimentary Rocks*.
THEURKAUF, E. & GROVER, B. 1974. Ein neues itabiritisches eisenerzvorkommen in Spanisch-Sahara. *Stahl u Eisen,* 94**,** 1094-1096.
TOKARSKI, A. K. 1991. Tectonics of Hank sequence (upper proterozoic) in the eastern part of Eglab massif, Reguibat Shield (West African craton). *Journal of African Earth Sciences (and the Middle East),* 12**,** 555-560.
TROMPETTE, R. 1994. Geology of Western Gondwana (2000- 500 Ma) - Pan-African-Brasiliano aggregation of South America and Africa. *A.A. Balkema, Rotterdam.***,** 350
VERMA, S. K. 2017. Precambrian plate tectonic setting of Africa from multidimensional discrimination diagrams. *Journal of African Earth Sciences,* 125**,** 137-150.
VERMA, S. K., PANDARINATH, K. & VERMA, S. P. 2012. Statistical evaluation of tectonomagmatic discrimination diagrams for granitic rocks and proposal of new

discriminant-function-based multi-dimensional diagrams for acid rocks. *International Geology Review,* 54**,** 325-347.
VERMA, S. K. & RIVERA-GÓMEZ, M. A. 2013a. Computer programs for the classification and nomenclature of igneous rocks. *Episodes,* 36**,** 115-124.
VERMA, S. K. & RIVERA-GÓMEZ, M. A. 2013b. New computer program TecD for tectonomagmatic discrimination from discriminant function diagrams for basic and ultrabasic magmas and its application to ancient rocks. *Journal of Iberian Geology,* 39**,** 167-179.
VERMA, S. P. 2010. Statistical evaluation of bivariate, ternary and discriminant function tectonomagmatic discrimination diagrams. *Turkish Journal of Earth Sciences,* 19**,** 185-238.
VERMA, S. P. & AGRAWAL, S. 2011. New tectonic discrimination diagrams for basic and ultrabasic volcanic rocks through log-transformed ratios of high field strength elements and implications for petrogenetic processes. *Revista Mexicana de Ciencias Geologicas,* 28**,** 24-44.
VERMA, S. P., CRUZ-HUICOCHEA, R., DIAZ-GONZALEZ, L. & VERMA, S. K. 2015. A new computer program TecDIA for multidimensional tectonic discrimination of intermediate and acid magmas and its application to the Bohemian Massif, Czech Republic. *Journal of Geosciences,* 60**,** 203-218.
VERMA, S. P., GUEVARA, M. & AGRAWAL, S. 2006. Discriminating four tectonic settings: Five new geochemical diagrams for basic and ultrabasic volcanic rocks based on log-ratio transformation of major-element data. *Journal of Earth System Science,* 115**,** 485-528.
VERMA, S. P., KAILASSA, P., VERMA, S. K., ARMSTRONG-ALTRIN, J. S., GONZALEZ, L. D., GÓMEZ, M. A. R., RIVERA, M. R., RUIZ, A. Q. & VALDEZ, A. A. 2018. *Geostatistical software* [Online]. Geoenergy group of the Institute of Renewable Energy (IER-UNAM). Available: http://tlaloc.ier.unam.mx/index.html [Accessed 30-05-2018 2018].
VERMA, S. P., PANDARINATH, K., VERMA, S. K. & AGRAWAL, S. 2013. Fifteen new discriminant-function-based multi-dimensional robust diagrams for acid rocks and their application to Precambrian rocks. *Lithos,* 168-169**,** 113-123.
VERMA, S. P., TORRES-ALVARADO, I. S. & SOTELO-RODRíGUEZ, Z. T. 2002. SINCLAS: standard igneous norm and volcanic rock classification system. *Computers & Geosciences,* 28**,** 711-715.
VERMA, S. P. & VERMA, S. K. 2013. First 15 probability-based multidimensional tectonic discrimination diagrams for intermediate magmas and their robustness against postemplacement compositional changes and petrogenetic processes. *Turkish Journal of Earth Sciences,* 22**,** 931-995.
VILLANOVA-DE-BENAVENT, C., TORRÓ, L., CASTILLO-OLIVER, M., CAMPENY, M., MELGAREJO, J. C., LLOVET, X., GALÍ, S. & GONÇALVES, A. O. 2017. Fe–Ti(–V) Oxide Deposits of the Kunene Anorthosite Complex (SW Angola): Mineralogy and Thermo-Oxybarometry. *Minerals,* 7**,** 246.
VILLENEUVE, M. 2005. Paleozoic basins in West Africa and the Mauritanide thrust belt. *Journal of African Earth Sciences,* 43**,** 166-195.
VILLENEUVE, M., BELLON, H., EL ARCHI, A., SAHABI, M., REHAULT, J.-P., OLIVET, J.-L. & AGHZER, A. M. 2006. Événements panafricains dans l'Adrar Souttouf (Sahara marocain). *Comptes Rendus Geoscience,* 338**,** 359-367.
VILLENEUVE, M. & CORNÉE, J. J. 1994. Structure, evolution and palaeogeography of the West African craton and bordering belts during the Neoproterozoic. *Precambrian Research,* 69**,** 307-326.

WANE, O., LIÉGEOIS, J.-P., THÉBAUD, N., MILLER, J., METELKA, V. & JESSELL, M. 2018. The onset of the Eburnean collision with the Kenema-Man craton evidenced by plutonic and volcanosedimentary rock record of the Masssigui region, southern Mali. *Precambrian Research,* 305**,** 444-478.

WILLIAMS, H. R. 1988. The Archaean Kasila Group of Western Sierra Leone: Geology and relations with adjacent granite-greenstone terrane. *Precambrian Research,* 38**,** 201-213.

WOOD, D. A. 1980. The application of a ThHfTa diagram to problems of tectonomagmatic classification and to establishing the nature of crustal contamination of basaltic lavas of the British Tertiary Volcanic Province. *Earth and Planetary Science Letters,* 50**,** 11-30.

XUE, S. & MORSE, S. A. 1993. Geochemistry of the nain massif anorthosite, labrador: Magma diversity in five intrusions. *Geochimica et Cosmochimica Acta,* 57**,** 3925-3948.

YAO, Y., MURPHY, P. J. & ROBB, L. J. 2001. Fluid Characteristics of Granitoid-Hosted Gold Deposits in the Birimian Terrane of Ghana: A Fluid Inclusion Microthermometric and Raman Spectroscopic Study. *Economic Geology,* 96**,** 1611-1643.

YAO, Y. & ROBB, L. J. 1999. Gold mineralization associated with the Birimian granitoids of Ghana. *final report to Gold Fields of South Africa Ltd.* Johannesburg: University of the Witwatersrand.

YAO, Y. & ROBB, L. J. 2000. Gold mineralization in Palaeoproterozoic granitoids at Obuasi, Ashanti region, Ghana: Ore geology, geochemistry and fluid characteristics. *South African Journal of Geology,* 103**,** 225-278.

YOUBI, N., KOUYATÉ, D., SÖDERLUND, U., ERNST, R. E., SOULAIMANI, A., HAFID, A., IKENNE, M., EL BAHAT, A., BERTRAND, H., RKHA CHAHAM, K., BEN ABBOU, M., MORTAJI, A., EL GHORFI, M., ZOUHAIR, M. & EL JANATI, M. H. 2013. The 1750Ma Magmatic Event of the West African Craton (Anti-Atlas, Morocco). *Precambrian Research,* 236**,** 106-123.

Appendices

Appendix A – Methodology

Work completed in this project required a combination of regional and detailed geological mapping, and a series of geochemical, petrological and geochronological studies on samples collected from the field.

The regional mapping in the project involved the use of Landsat, ASTER, Google Earth and QuickBird imagery, with ground traverses for rock distribution and structural data. During the course of the PhD, four field trips were undertaken, each ~1 month in duration. Carefully planned traverses undertaken with the use of 4WD vehicles to get maximum coverage. The traverses were planned based on a combination of previous work (both in the field and lab) and satellite imagery. Extensive field notes were taken in a field notebook, taking particular note of geological observations, structural data, sketches, with photos taken of representative or geologically interesting lithologies. Note that due to the main field camps being located at Agarasras Labiad and Elmalhat, there is an uneven distribution of observation points between the domains. As a result, mapping for much of the Leaareig Terrane relied more heavily on satellite interpretation.

The geological map was produced using a combination of these field notes, GPS data, previous work, with remote sensing imagery (Landsat, ASTER, Google Earth and QuickBird) used to help the interpretation of unit's in-between observation points.

Representative rock samples were collected from across the field area for U-Pb zircon geochronological work (Chapter 2; Appendix B), whole rock geochemistry (Sections 3.3.4, 3.5, 4.1.5, and 4.5; Appendix C), petrology, and mineral chemistry (Section 4.1.4; Appendix D)

Appendix B – Geochronology

Appendix B1 – U-Pb Zircon Data

Samples were analysed for zircon U-Pb through laser ablation inductively-coupled plasma mass spectrometry (LA-ICP-MS) at the John de Laeter Centre, Curtin University. Zircon grains were ablated using a Resonetics RESOlution M-50A-LR sampling system (incorporating a Compex 102 excimer laser) coupled to an Agilent 7700 ICP-MS. Following 15-20 seconds of background analysis, samples were ablated for 30 seconds at a 7 Hz repetition rate using a 33 μm beam spot, and laser energy of 1.5 J/cm^2. The sample cell was flushed by ultrahigh purity He (0.68 L min^{-1}) and N2 (2.8 mL min^{-1}). Isotopic intensities were measured using an Agilent 7700s quadrupole ICP-MS, with high purity Ar as the plasma gas. In each scan of the mass spectrum, the dwell time for most elements was 0.01 s, with the exception of ^{88}Sr (0.02 s), ^{139}La (0.04 s), ^{141}Pr (0.04 s), ^{204}Pb, ^{206}Pb, ^{207}Pb, ^{208}Pb (0.03 s), ^{232}Th (0.0125 s), and ^{238}U (0.0125 s). Standards OCG, Temora 2 and M257 were used. Standard blocks were typically run after 20 unknown analyses. During the time-resolved analysis, contamination resulting from inclusions and compositional zoning was monitored, and only the relevant part of the signal was integrated.

The results of this analysis presented in Table 1 below.

Table 5 - LA-ICP-MS U-Pb analyses of zircons extracted from granitoid, and metasedimentary samples from the Palaeoproterozoic Leaareig and Sfariat-Bu Daira Terranes of the Reguibat Shield, Western Sahara.

Sample ID	Concentration				Radiogenic Ratio				Calculated Ages				Discordance	
Spot	*U*	*Th*	*Pb*	f^{204}	$^{238}U/^{206}Pb^*$		$^{207}Pb^*/^{206}Pb^*$		$^{238}U/^{206}Pb^*$		$^{207}Pb^*/^{206}Pb^*$		*Disc*	Disc. %
no.	*ppm*			*(%)*	*±1s*		*±1s*		*date (Ma)*	*±1s*	*date (Ma)*	*±1s*	*(%)*	2s lim.
J247 - 1.d	178	245	1450	0.009	3.92157	0.27682	0.13516	0.00268	1464	1285	2166	34	32.40	23.777
J247 - 2.d	87	16.4	300	0.008	4.97512	0.47029	0.14477	0.00472	1181	2130	2285	55	48.33	36.148
J247 - 3.d	113	44.6	373		6.41026	0.30819	0.14834	0.00431	935	1524	2327	49	59.84	50.775
J247 - 4.d	59.8	22.9	301		2.72480	0.11137	0.13288	0.00337	2015	505	2136	44	5.67	
J247 - 5.d	153	176	880		4.14938	0.23243	0.12693	0.00293	1392	1107	2056	40	32.30	23.446
J247 - 6.d	36	16.2	244		2.22717	0.09425	0.12475	0.00353	2391	406	2025	49	-18.05	-4.781
J247 - 7.d	108	77	740	0.002	3.50877	0.24623	0.12753	0.00418	1616	1130	2064	57	21.69	6.878
J247 - 8.d	162	56	354	0.004	5.58659	0.29650	0.12515	0.00337	1062	1446	2031	47	47.73	38.385
J247 - 9.d	236	188	1060	0.001	4.03226	0.18698	0.13427	0.00258	1428	900	2155	33	33.71	27.422
J247 - 10.d	108	58	510	0.005	3.28947	0.23264	0.12406	0.00333	1711	1058	2015	47	15.10	0.650
J247 - 11.d	240	44.4	550	0.004	8.69565	0.64272	0.14239	0.00396	702	2934	2257	47	68.90	58.998
J247 - 12.d	678	505	1230	0.005	20.49180	0.60888	0.13952	0.00286	307	2951	2221	35	86.17	77.751
J247 - 13.d	194	132	527	0.003	8.69565	0.45369	0.14239	0.00374	702	2201	2257	45	68.90	59.983
J247 - 14.d	244	79.3	640	0.009	9.89120	0.37667	0.15418	0.00337	621	1897	2393	37	74.05	67.239
J247 - 15.d	527	161	860	0.004	20.96436	0.54938	0.16231	0.00370	300	2718	2480	38	87.89	78.827
J247 - 16.d	131	41.3	267	0.010	5.58659	0.17166	0.13744	0.00396	1062	876	2195	49	51.64	42.824
J247 - 17.d	294	102.2	574	0.016	13.60544	0.33319	0.15438	0.00317	457	1743	2395	34	80.91	73.854
J247 - 18.d	580	108.7	687	0.002	26.59574	0.88417	0.15686	0.00379	238	3973	2422	40	90.18	79.873
J247 - 19.d	266	188	980	0.000	7.86164	0.21014	0.13248	0.00337	772	1102	2131	44	63.78	55.463
J247 - 20.d	1008	513	1390		36.49635	0.86579	0.16657	0.00370	174	3940	2523	37	93.09	83.419
J247 - 21.d	104	33.6	340		4.52489	0.27641	0.13744	0.00379	1287	1315	2195	47	41.36	31.920
J247 - 22.d	161	52.4	510	0.004	4.27350	0.28307	0.13298	0.00329	1355	1331	2138	43	36.59	27.219
J247 - 23.d	35.2	8.6	103		5.31915	0.41025	0.13774	0.00872	1111	1912	2199	106	49.50	25.505

Sample ID	Concentration				Radiogenic Ratio				Calculated Ages				Discordance	
Spot	*U*	*Th*	*Pb*	f^{204}	$^{238}U/^{206}Pb^*$		$^{207}Pb^*/^{206}Pb^*$		$^{238}U/^{206}Pb^*$		$^{207}Pb^*/^{206}Pb^*$		*Disc*	Disc. %
no.	*ppm*			*(%)*	*±1s*		*±1s*		*date (Ma) ±1s*		*date (Ma) ±1s*		*(%)*	2s lim.
J247 - 24.d	295	105.2	680	0.003	9.96016	0.37698	0.13655	0.00329	617	1899	2184	41	71.76	63.412
J247 - 25.d	136	145	390	0.008	4.70146	0.09947	0.12931	0.00324	1243	508	2089	43	40.48	33.102
J247 - 26.d	269	369	870		7.36377	0.24401	0.12307	0.00329	821	1255	2001	47	58.98	49.740
J247 - 27.d	437	64.4	417		18.05054	0.70052	0.14467	0.00293	348	3282	2284	34	84.78	76.863
J247 - 28.d	86	26.6	275		4.46429	0.26905	0.12951	0.00366	1303	1281	2091	49	37.70	27.339
J247 - 29.d	191	204	1270		4.71698	0.27812	0.14219	0.00362	1239	1332	2254	43	45.01	36.896
J234 - 1.d	233	41.8	1100	0.011	9.79432	0.41249	0.19511	0.00431	627	2050	2786	36	77.50	71.269
J234 - 2.d	72	13.2	256	0.002	3.08642	0.16194	0.14398	0.00357	1809	744	2276	42	20.49	10.455
J234 - 3.d	272	43.2	1180	0.010	9.35454	0.32378	0.18778	0.00472	655	1654	2723	41	75.95	68.508
J234 - 4.d	399	59.8	2220	0.006	8.29187	0.20970	0.19630	0.00333	734	1106	2796	27	73.74	70.354
J234 - 5.d	399	126	2020	0.006	9.95025	0.25742	0.20294	0.00374	617	1355	2850	30	78.34	73.797
J234 - 6.d	329	48	1650	0.007	8.30565	0.28283	0.18946	0.00321	733	1451	2737	28	73.23	69.695
J234 - 7.d	362	59.7	1390	0.009	11.77856	0.31215	0.19214	0.00321	525	1630	2761	27	80.97	76.586
J234 - 8.d	72	35.1	429	0.014	4.60830	0.09450	0.14784	0.00522	1266	482	2321	59	45.46	34.859
J234 - 9.d	354	58	1510	0.011	11.77856	0.29134	0.20541	0.00427	525	1533	2870	33	81.69	75.653
J234 - 10.d	413	69.2	2850	0.013	10.75269	0.37577	0.27438	0.00431	573	1905	3331	24	82.79	79.585
J234 - 11.d	343	66.1	2550	0.014	8.96861	0.34587	0.25912	0.00454	681	1747	3241	27	78.98	75.507
J234 - 12.d	251	32.5	1090	0.005	10.34126	0.39568	0.18976	0.00422	595	1986	2740	36	78.28	71.767
J234 - 13.d	439	241	3400	0.013	10.31992	0.33548	0.26556	0.00409	596	1720	3280	24	81.82	78.841
J234 - 14.d	254	44.2	1790	0.011	9.39850	0.27824	0.27220	0.00499	652	1446	3319	28	80.36	76.510
J234 - 15.d	259	45.2	1720	0.013	8.67303	0.29336	0.23920	0.00413	703	1505	3115	27	77.41	74.049
J234 - 16.d	365	34.3	1660	0.009	10.64963	0.27787	0.20839	0.00353	579	1459	2893	27	80.00	75.945
J234 - 17.d	160	31.2	231	0.010	6.89655	0.30916	0.12931	0.00341	873	1541	2089	46	58.21	49.393
J234 - 18.d	98	16.6	211		4.44444	0.33580	0.13863	0.00486	1308	1562	2210	60	40.81	27.867
J234 - 19.d	208	35.5	900	0.008	9.39850	0.36658	0.19739	0.00454	652	1845	2805	37	76.76	70.328
J234 - 20.d	215	51.1	1850	0.011	7.29927	0.26640	0.25793	0.00518	828	1357	3234	31	74.41	70.597
J234 - 21.d	299	40.8	2320	0.013	9.88142	0.24899	0.30242	0.00383	621	1314	3483	19	82.16	80.597

Sample ID	Concentration				Radiogenic Ratio				Calculated Ages				Discordance	
Spot	*U*	*Th*	*Pb*	f^{204}	$^{238}U/^{206}Pb^*$		$^{207}Pb^*/^{206}Pb^*$		$^{238}U/^{206}Pb^*$		$^{207}Pb^*/^{206}Pb^*$		*Disc*	Disc. %
no.	*ppm*			*(%)*	*±1s*		*±1s*		*date (Ma) ±1s*		*date (Ma) ±1s*		*(%)*	2s lim.
J234 - 22.d	408	90.3	2850	0.011	9.68992	0.23474	0.24971	0.00353	633	1244	3183	22	80.11	77.802
J234 - 23.d	313	58.3	2980	0.016	8.84956	0.29760	0.29747	0.00418	690	1527	3457	22	80.04	78.212
J234 - 24.d	321	39.9	2120	0.009	10.06036	0.19736	0.25050	0.00458	611	1064	3188	29	80.84	76.701
J234 - 25.d	144	39.6	289	0.007	6.99301	0.36677	0.13318	0.00366	862	1794	2140	47	59.74	50.446
J234 - 26.d	193	54.6	310		6.36943	0.32456	0.12158	0.00309	940	1594	1980	45	52.51	43.618
J234 - 27.d	117	33	279		4.76191	0.22676	0.13139	0.00345	1229	1107	2117	45	41.95	33.344
J234 - 28.d	111	32.2	405	0.000	3.96825	0.22046	0.14021	0.00392	1449	1046	2230	48	35.03	25.434
J234 - 29.d	139	29.9	352	0.001	3.33333	0.11667	0.13397	0.00305	1691	554	2151	39	21.36	13.246
J234 - 30.d	247	76.6	630	0.000	3.50877	0.13543	0.13546	0.00265	1616	646	2170	34	25.50	18.847
J234 - 31.d	134	40.4	332	0.010	4.42478	0.20558	0.12426	0.00309	1314	999	2018	43	34.92	26.129
J234 - 32.d	194	44.4	450	0.000	3.25733	0.46154	0.12763	0.00366	1726	1950	2066	50	16.44	
J234 - 33.d	65.3	13.6	123	0.002	2.78552	0.15906	0.13655	0.00362	1977	714	2184	45	9.45	
J234 - 34.d	264	49.2	455	0.002	9.50570	0.23493	0.11940	0.00362	645	1242	1947	53	66.89	55.052
J234 - 35.d	208	29	700	0.003	4.52489	0.17403	0.15091	0.00286	1287	859	2356	32	45.37	41.018
J234 - 36.d	265	43.8	1250	0.003	4.48431	0.18098	0.16627	0.00301	1298	890	2520	30	48.51	44.993
J234 - 37.d	316	415	1560	0.007	6.25000	0.21484	0.13684	0.00282	957	1095	2188	35	56.26	50.668
J234 - 38.d	190	29.8	730		3.12500	0.13184	0.14001	0.00286	1790	614	2227	35	19.65	11.725
J234 - 39.d	132	32.8	381	0.003	6.17284	0.28578	0.13942	0.00396	968	1417	2220	48	56.40	47.363
J234 - 40.d	235	47	810	0.004	8.13008	0.42964	0.16578	0.00333	748	2088	2515	33	70.27	64.858
J234 - 41.d	122	35.9	490		4.18410	0.21883	0.13536	0.00349	1381	1048	2169	44	36.30	27.535
J234 - 42.d	149	43.4	1150	0.010	4.71698	0.25587	0.15458	0.00536	1239	1235	2397	58	48.30	37.495
J234 - 43.d	239	42.5	1050	0.006	10.23541	0.30381	0.19124	0.00472	601	1575	2753	40	78.17	70.696
J234 - 44.d	190	46.4	1020	0.005	6.60502	0.18105	0.18272	0.00392	909	941	2678	35	66.06	61.291
J234 - 45.d	209	47	1140	0.004	7.46269	0.33415	0.17846	0.00400	811	1665	2639	37	69.28	63.456
J234 - 46.d	281	65.2	960	0.004	10.24590	0.27819	0.14814	0.00392	600	1456	2325	45	74.17	65.064
J234 - 47.d	259	67.7	970	0.010	9.31966	0.33440	0.15319	0.00387	657	1701	2382	42	72.41	64.223
J234 - 48.d	430	80.2	1280	0.004	8.14332	0.25862	0.15488	0.00293	747	1336	2400	32	68.90	64.001

Sample ID	Concentration				Radiogenic Ratio				Calculated Ages				Discordance	
Spot	*U*	*Th*	*Pb*	f^{204}	$^{238}U/^{206}Pb^*$		$^{207}Pb^*/^{206}Pb^*$		$^{238}U/^{206}Pb^*$		$^{207}Pb^*/^{206}Pb^*$		*Disc*	Disc. %
no.	*ppm*			*(%)*	*±1s*		*±1s*		*date (Ma) ±1s*		*date (Ma) ±1s*		*(%)*	2s lim.
J234 - 49.d	269	52.3	756	0.003	9.62464	0.25474	0.14873	0.00392	637	1339	2331	44	72.67	63.832
J234 - 50.d	188	39.9	225		7.57576	0.31566	0.11881	0.00341	799	1586	1938	50	58.77	48.158
J227 - 3.d	80	54	540	0.011	2.97619	0.16830	0.12872	0.00286	1867	765	2081	39	10.24	
J227 - 4.d	92	61.9	650		2.99401	0.18376	0.13506	0.00337	1858	832	2165	43	14.18	1.608
J227 - 6.d	49.4	33.2	379		2.94985	0.11747	0.12991	0.00353	1882	542	2097	47	10.25	
J227 - 7.d	47.4	35.4	400		2.91545	0.15725	0.12515	0.00392	1901	714	2031	54	6.39	
J246 - 1.d	45.1	17.3	4710	0.018	1.38122	0.06105	0.53211	0.01960	3511	224	4333	53	18.97	10.522
J246 - 2.d	46	18.2	1290	0.010	2.09205	0.06127	0.25367	0.00921	2519	262	3208	56	21.49	12.077
J246 - 3.d	46.7	11.5	249	0.009	2.90698	0.12676	0.15399	0.00504	1906	581	2391	55	20.28	8.610
J246 - 4.d	92.3	49.1	531	0.005	4.76191	0.13605	0.18015	0.00454	1229	687	2654	41	53.70	48.172
J246 - 5.d	64.2	58.4	1190	0.007	3.43643	0.15942	0.24079	0.00726	1647	751	3125	47	47.31	41.172
J246 - 6.d	79.3	43	860	0.005	4.29185	0.17499	0.22682	0.00527	1350	856	3030	37	55.43	51.516
J246 - 7.d	82.9	92.2	1180	0.007	4.32900	0.21551	0.24277	0.00678	1340	1040	3138	44	57.31	51.706
J246 - 8.d	58.4	48.7	750		3.41297	0.18637	0.18579	0.00476	1657	868	2705	42	38.77	32.041
J246 - 9.d	53.3	43.4	760	0.010	3.55872	0.19630	0.22295	0.00678	1596	919	3002	48	46.82	39.869
J246 - 10.d	44.9	24.7	394	0.005	3.50877	0.22161	0.17737	0.00726	1616	1026	2628	67	38.50	25.776
J246 - 11.d	158	79.9	900	0.007	8.40336	0.38839	0.19085	0.00400	725	1921	2749	34	73.64	68.262
J246 - 12.d	65.6	38	330	0.010	5.00000	0.21250	0.16538	0.00522	1175	1051	2511	52	53.20	44.330
J246 - 13.d	53	20.3	251		3.90625	0.27466	0.13674	0.00458	1469	1275	2186	57	32.80	19.861
J246 - 14.d	35.1	13.4	156	0.000	2.46914	0.03353	0.13734	0.00405	2192	152	2194	50	0.09	
J246 - 15.d	42.1	13.5	191		2.50000	0.06875	0.14269	0.00449	2169	309	2260	53	4.03	
J246 - 16.d	39.1	10.7	113		2.71739	0.04061	0.13209	0.00522	2020	189	2126	68	4.98	
J246 - 17.d	56.2	5.57	101		3.14465	0.15328	0.13456	0.00431	1780	709	2158	55	17.53	4.467
J246 - 18.d	303	19.5	623	0.005	12.90323	0.29136	0.16013	0.00454	481	1543	2457	47	80.42	70.010
J246 - 19.d	323	53.3	680	0.010	17.21170	0.65173	0.16152	0.00472	364	3094	2472	48	85.27	73.629
J246 - 20.d	185	53.2	407	0.014	9.84252	0.28578	0.15944	0.00396	624	1487	2450	41	74.54	66.560
J246 - 21.d	449	916	2430	0.003	10.86957	0.33081	0.12505	0.00261	567	1706	2030	37	72.05	64.596

Sample ID	Concentration				Radiogenic Ratio				Calculated Ages				Discordance	
Spot	*U*	*Th*	*Pb*	f^{204}	$^{238}U/^{206}Pb^*$		$^{207}Pb^*/^{206}Pb^*$		$^{238}U/^{206}Pb^*$		$^{207}Pb^*/^{206}Pb^*$		*Disc*	Disc. %
no.	*ppm*			*(%)*	*±1s*		*±1s*		*date (Ma)*	*±1s*	*date (Ma)*	*±1s*	*(%)*	2s lim.
J246 - 22.d	69	18.5	287	0.011	3.62319	0.24942	0.14537	0.00409	1571	1151	2292	48	31.45	20.700
J246 - 23.d	143	71	920	0.005	5.40541	0.27757	0.16310	0.00396	1094	1357	2488	40	56.02	49.637
J246 - 24.d	47.5	14.2	166		3.03951	0.18477	0.13070	0.00481	1834	839	2107	63	13.00	
J246 - 25.d	19.8	5.2	74		3.03951	0.15706	0.11891	0.00775	1834	720	1940	112	5.48	
J246 - 26.d	20.4	7.2	88		2.47525	0.06127	0.13813	0.00532	2187	275	2204	65	0.75	
J246 - 27.d	297	118.2	930		9.69932	0.38101	0.15854	0.00631	633	1913	2440	66	74.08	59.413
J246 - 28.d	160	59.3	640	0.008	8.40336	0.52962	0.16786	0.00400	725	2498	2536	39	71.42	64.227
J246 - 29.d	50.9	21.7	338	0.010	3.28947	0.23264	0.16647	0.00678	1711	1058	2522	67	32.17	18.076
J246 - 30.d	141	142	1160	0.006	6.66667	0.24444	0.21106	0.00440	901	1242	2914	33	69.08	64.822
J246 - 31.d	57.6	32.2	580	0.011	3.69004	0.20425	0.19323	0.00631	1546	961	2770	53	44.19	35.569
J246 - 32.d	273	44.7	2060	0.009	10.26694	0.22663	0.29331	0.00678	599	1210	3435	35	82.56	76.582
J246 - 33.d	60.2	38.5	245	0.212	5.55556	0.29321	0.15557	0.00631	1067	1431	2408	67	55.69	42.426
J246 - 34.d	44.6	16.1	275		4.78469	0.26327	0.16548	0.00631	1223	1270	2512	63	51.30	39.639
J246 - 35.d	59.1	41.4	417	0.004	2.65675	0.03317	0.13100	0.00379	2059	154	2111	50	2.46	
J179 - 1.d	155	47.8	460		3.40136	0.19089	0.13268	0.00293	1661	887	2134	38	22.13	12.457
J179 - 2.d	72	32.3	410	0.000	2.73224	0.14930	0.12793	0.00337	2011	669	2070	46	2.86	
J179 - 3.d	26.9	10.6	140		2.32558	0.04327	0.12684	0.00536	2306	192	2055	73	-12.22	
J179 - 4.d	151	142.8	1000		4.25532	0.19919	0.13526	0.00329	1361	964	2167	42	37.22	29.388
J179 - 5.d	75	7.1	88	0.004	5.49451	0.28680	0.13922	0.00431	1078	1400	2218	53	51.39	41.274
J179 - 6.d	82	7.6	117	0.003	4.78469	0.30906	0.13744	0.00486	1223	1467	2195	60	44.26	31.827
J179 - 7.d	185	13.2	149	0.006	5.15464	0.14614	0.12892	0.00333	1143	744	2083	45	45.13	37.269
J179 - 8.d	18.4	7.54	60		2.74725	0.13585	0.12485	0.00678	2001	612	2027	93	1.26	
J179 - 9.d	30.8	17.5	201	0.003	2.68817	0.11562	0.13377	0.00583	2039	522	2148	74	5.09	
J179 - 10.d	134	41.1	219		3.69004	0.21105	0.13050	0.00297	1546	990	2105	39	26.55	17.167
J179 - 11.d	129	21.2	229		4.46429	0.13951	0.12862	0.00357	1303	696	2079	48	37.33	28.434
J179 - 12.d	188	140	755	0.352	8.69565	0.26087	0.12991	0.00321	702	1355	2097	43	66.53	58.124
J179 - 13.d	117	24.7	195		4.48431	0.22120	0.13169	0.00353	1298	1072	2121	46	38.81	29.779

Sample ID	Concentration				Radiogenic Ratio				Calculated Ages				Discordance	
Spot	*U*	*Th*	*Pb*	f^{204}	$^{238}U/^{206}Pb^*$		$^{207}Pb^*/^{206}Pb^*$		$^{238}U/^{206}Pb^*$		$^{207}Pb^*/^{206}Pb^*$		*Disc*	Disc. %
no.	*ppm*			*(%)*	*±1s*		*±1s*		*date (Ma)*	*±1s*	*date (Ma)*	*±1s*	*(%)*	2s lim.
J179 - 14.d	93	80	900		3.10559	0.17843	0.13298	0.00362	1799	816	2138	47	15.82	3.240
J179 - 15.d	71	47	510		2.96736	0.14529	0.12812	0.00392	1872	665	2072	53	9.66	
J179 - 16.d	31.7	16.5	133		4.58716	0.17886	0.14764	0.00726	1271	883	2319	82	45.17	28.640
J179 - 17.d	110	11.1	168		9.43396	0.66750	0.12971	0.00486	649	3044	2094	64	68.98	53.974
J179 - 18.d	51.4	28.7	360		2.49377	0.04664	0.13585	0.00396	2174	211	2175	50	0.06	
J179 - 19.d	19.8	6.56	89	0.008	2.80899	0.08285	0.13972	0.00678	1963	382	2224	82	11.72	
J179 - 20.d	61.2	11.4	169		3.48432	0.16390	0.13833	0.00392	1627	773	2206	48	26.28	16.108
J179 - 21.d	53.4	29.1	430	0.005	2.42718	0.08248	0.13754	0.00321	2224	366	2196	40	-1.26	
J179 - 22.d	26.5	6	101	0.015	2.80112	0.14123	0.13278	0.00583	1968	638	2135	75	7.83	
J179 - 23.d	82	42	294		4.31035	0.27869	0.13238	0.00362	1345	1315	2130	47	36.85	26.662
J179 - 24.d	19.6	7	81		2.73224	0.11198	0.14170	0.00583	2011	508	2248	69	10.57	
J179 - 25.d	44	7.8	135		2.68097	0.13297	0.13040	0.00427	2044	596	2103	56	2.85	
J179 - 26.d	37.8	15.5	186		2.59067	0.04363	0.13694	0.00449	2104	200	2189	56	3.87	
J179 - 27.d	23.5	8.8	124	0.007	2.33100	0.04075	0.13278	0.00631	2301	181	2135	81	-7.78	
J179 - 28.d	242	84.7	473	0.001	9.60615	0.33681	0.13456	0.00362	638	1716	2158	46	70.42	60.825
J179 - 29.d	47.2	17.3	186	0.002	4.31035	0.15792	0.13209	0.00387	1345	777	2126	50	36.73	27.208
J179 - 30.d	41	25.7	261	0.003	3.31126	0.17543	0.14269	0.00678	1701	815	2260	80	24.73	7.158
J179 - 31.d	31.5	13.1	166	0.013	2.36967	0.06738	0.12575	0.00413	2270	298	2039	57	-11.29	
J179 - 32.d	23.9	12.2	151	0.003	2.63852	0.08006	0.13179	0.00583	2072	364	2122	76	2.37	
J179 - 33.d	15.3	5.58	72	0.017	2.43902	0.05354	0.12684	0.00631	2215	240	2055	85	-7.80	
J179 - 34.d	139	17.3	186	0.009	10.61571	0.42823	0.12535	0.00463	580	2129	2034	64	71.46	56.298
J179 - 35.d	14.4	8.6	87.8	0.008	2.88184	0.06229	0.14368	0.00583	1920	291	2272	68	15.48	0.853
J179 - 36.d	297	215	710	0.000	16.47446	0.62424	0.11068	0.00387	380	2983	1811	62	79.02	62.275
J179 - 37.d	19.4	8.2	121		2.39234	0.06868	0.12783	0.00583	2251	305	2068	78	-8.85	
J179 - 38.d	97	59.7	580		3.67647	0.22302	0.13417	0.00413	1551	1041	2153	53	27.97	15.935
J179 - 39.d	25	10.6	161		2.68097	0.10781	0.13001	0.00522	2044	487	2098	69	2.60	
J179 - 40.d	34.1	9.7	132		2.55755	0.05233	0.13684	0.00413	2127	238	2188	52	2.75	

Sample ID	Concentration				Radiogenic Ratio				Calculated Ages				Discordance	
Spot	*U*	*Th*	*Pb*	f^{204}	$^{238}U/^{206}Pb^*$		$^{207}Pb^*/^{206}Pb^*$		$^{238}U/^{206}Pb^*$		$^{207}Pb^*/^{206}Pb^*$		*Disc*	Disc. %
no.	*ppm*			*(%)*	*±1s*		*±1s*		*date (Ma) ±1s*		*date (Ma) ±1s*		*(%)*	2s lim.
J179 - 41.d	38.8	22.1	257		2.50000	0.05938	0.13546	0.00440	2169	268	2170	56	0.04	
J179 - 42.d	27.1	6.3	104		3.86100	0.15653	0.12495	0.00486	1485	755	2028	67	26.79	12.180
J179 - 43.d	19.2	8.8	125		2.43902	0.09816	0.13774	0.00631	2215	434	2199	77	-0.73	
J179 - 44.d	47.3	20.1	250		2.91545	0.11475	0.13120	0.00467	1901	529	2114	61	10.07	
J179 - 45.d	18.4	8.4	123	0.007	2.42718	0.05891	0.13774	0.00678	2224	264	2199	83	-1.14	
J179 - 46.d	88	29	366	0.016	3.98406	0.25396	0.13595	0.00413	1444	1191	2176	52	33.66	22.313
J179 - 47.d	136	186	1220	0.001	4.34783	0.26465	0.13100	0.00305	1334	1256	2111	40	36.79	28.211
J179 - 48.d	149	164	1790	0.001	3.04878	0.17196	0.13219	0.00272	1829	785	2127	36	14.03	3.211
J179 - 49.d	47.3	37.4	426	0.000	3.15457	0.18410	0.13288	0.00383	1775	843	2136	50	16.91	3.918
J238 - 1.d	248	17.1	576	0.000	12.98701	0.46382	0.12802	0.00321	478	2309	2071	43	76.91	67.010
J238 - 2.d	28.5	28.5	410		2.66667	0.11733	0.13209	0.00476	2053	528	2126	62	3.43	
J238 - 3.d	207	17.1	484	0.007	7.92393	0.27627	0.12386	0.00333	766	1414	2013	47	61.93	52.447
J238 - 4.d	85	121	1670		2.88184	0.13703	0.13347	0.00413	1920	625	2144	53	10.44	
J238 - 5.d	105	107	1260	0.000	2.76243	0.14880	0.12981	0.00324	1992	668	2095	43	4.95	
J238 - 6.d	127	100	1420		2.95858	0.14880	0.12971	0.00341	1877	680	2094	45	10.36	
J238 - 7.d	146	96.4	800		5.34759	0.20018	0.12188	0.00301	1105	1005	1984	43	44.30	36.178
J238 - 8.d	134	90.6	410		4.65116	0.17307	0.12436	0.00366	1255	858	2020	51	37.84	27.790
J238 - 9.d	274	18.5	750	0.005	12.09190	0.51175	0.13575	0.00305	512	2495	2174	39	76.44	68.232
J238 - 10.d	142	11.3	300		5.23560	0.17817	0.12693	0.00333	1127	899	2056	46	45.19	36.880
J238 - 11.d	28.8	25	324		2.61780	0.07196	0.13684	0.00472	2086	327	2188	59	4.66	
J238 - 12.d	151	9.9	209		4.08163	0.14994	0.12535	0.00293	1413	733	2034	41	30.54	22.599
J238 - 13.d	129	11.4	287	0.001	6.41026	0.28764	0.12822	0.00362	935	1432	2074	49	54.94	45.380
J238 - 14.d	148	125	800	0.001	4.87805	0.21416	0.12129	0.00333	1202	1055	1975	48	39.14	29.474
J238 - 15.d	87.6	91.1	660		4.23729	0.12568	0.13734	0.00405	1366	624	2194	50	37.74	28.740
J238 - 16.d	44.7	26.2	292	0.003	2.73224	0.13064	0.12832	0.00387	2011	589	2075	52	3.11	
J238 - 17.d	67	44.9	480	0.000	2.84900	0.20698	0.12862	0.00400	1939	919	2079	54	6.72	
J238 - 18.d	105	123.9	750	0.001	5.88235	0.36332	0.13575	0.00396	1012	1743	2174	50	53.44	43.539

Sample ID	Concentration				Radiogenic Ratio				Calculated Ages				Discordance	
Spot	*U*	*Th*	*Pb*	f^{204}	$^{238}U/^{206}Pb^*$		$^{207}Pb^*/^{206}Pb^*$		$^{238}U/^{206}Pb^*$		$^{207}Pb^*/^{206}Pb^*$		*Disc*	Disc. %
no.	*ppm*			*(%)*	*±1s*		*±1s*		*date (Ma)*	*±1s*	*date (Ma)*	*±1s*	*(%)*	2s lim.
J238 - 19.d	54	46.4	670	0.002	2.85714	0.20000	0.12981	0.00583	1935	891	2095	77	7.67	
J238 - 20.d	17.3	25.9	356	0.012	2.57069	0.13547	0.14071	0.00872	2118	600	2236	103	5.27	
J238 - 21.d	18.9	16.5	271	0.007	2.67380	0.15728	0.13575	0.00536	2048	699	2174	67	5.77	
J238 - 22.d	122	7.3	377	0.004	9.43396	0.48950	0.13754	0.00329	649	2362	2196	41	70.43	62.210
J238 - 23.d	230	17.6	601	0.006	13.14060	0.48349	0.14021	0.00387	473	2392	2230	47	78.80	68.060
J238 - 24.d	50.9	47.2	750		2.63852	0.11835	0.12763	0.00387	2072	531	2066	53	-0.29	
J238 - 25.d	68	62	716		2.53165	0.03846	0.13001	0.00337	2146	175	2098	45	-2.28	
J238 - 26.d	84	19.1	278		3.16456	0.14020	0.13308	0.00436	1770	653	2139	56	17.24	4.145
J238 - 27.d	60	45	620		2.57069	0.07930	0.13447	0.00427	2118	358	2157	54	1.80	
J238 - 28.d	154	44.1	366		7.19425	0.36230	0.12584	0.00321	839	1780	2041	44	58.89	50.085
J238 - 29.d	180	271	920	0.006	7.46269	0.36200	0.13318	0.00333	811	1786	2140	43	62.12	53.867
J238 - 30.d	187	35.6	580		8.89680	0.29682	0.12475	0.00366	687	1525	2025	51	66.10	55.169
J238 - 31.d	56	30.4	363		2.63158	0.11427	0.13129	0.00374	2076	513	2115	49	1.85	
J238 - 32.d	188	20.4	432		6.13497	0.28228	0.13912	0.00329	973	1401	2216	40	56.08	49.059
J238 - 33.d	29.9	31.5	430	0.000	2.77778	0.15046	0.12684	0.00536	1982	676	2055	73	3.52	
J238 - 34.d	307	17.4	506	0.000	7.29927	0.31968	0.13575	0.00301	828	1597	2174	38	61.92	55.141
J238 - 35.d	44	29.9	370	0.001	2.83286	0.14846	0.12743	0.00392	1949	671	2063	53	5.52	
J238 - 36.d	173	14.8	430	0.001	7.24638	0.24680	0.13080	0.00301	833	1265	2109	40	60.48	53.310
J238 - 37.d	22.5	19.5	260	0.002	2.77008	0.14196	0.13179	0.00678	1987	640	2122	88	6.36	
J238 - 38.d	203	14.5	499	0.002	10.17294	0.36738	0.12396	0.00427	604	1860	2014	60	69.99	56.112
J238 - 39.d	26.8	17.6	235		2.42131	0.09380	0.13774	0.00518	2229	414	2199	64	-1.35	
J238 - 40.d	60	32.2	339	0.001	2.72480	0.12622	0.13080	0.00366	2015	569	2109	48	4.43	
J238 - 41.d	37.9	26.4	375	0.006	2.30947	0.02934	0.12822	0.00387	2319	131	2074	52	-11.84	-0.064
J238 - 42.d	304	17	676	0.000	13.28021	0.51146	0.12763	0.00400	468	2508	2066	54	77.34	64.235
J238 - 43.d	82	44.2	570	0.002	2.65957	0.14500	0.12832	0.00370	2058	646	2075	50	0.85	
J238 - 44.d	218	18	217	0.000	4.34783	0.17958	0.12466	0.00268	1334	879	2024	38	34.06	26.820
J238 - 45.d	25.4	17.2	219	0.004	2.63158	0.09349	0.14170	0.00631	2076	423	2248	75	7.64	

Sample ID	Concentration				Radiogenic Ratio				Calculated Ages				Discordance	
Spot	*U*	*Th*	*Pb*	f^{204}	$^{238}U/^{206}Pb^*$		$^{207}Pb^*/^{206}Pb^*$		$^{238}U/^{206}Pb^*$		$^{207}Pb^*/^{206}Pb^*$		*Disc*	Disc. %
no.	*ppm*			*(%)*	*±1s*		*±1s*		*date (Ma) ±1s*		*date (Ma) ±1s*		*(%)*	2s lim.
J238 - 46.d	212	16.6	530	0.002	9.66184	0.38274	0.11990	0.00345	635	1919	1955	50	67.52	56.284
J287 - 1.d	67	75	960		2.77778	0.10802	0.13149	0.00357	1982	493	2118	47	6.41	
J287 - 2.d	317	131.5	770	0.006	11.76471	0.56055	0.13813	0.00349	526	2685	2204	43	76.14	66.720
J287 - 3.d	456	54.5	2090	0.001	5.74713	0.18166	0.15131	0.00245	1034	927	2361	27	56.20	53.134
J287 - 4.d	50	31.5	405		2.56410	0.06575	0.14041	0.00405	2123	298	2232	49	4.90	
J287 - 5.d	326	37.5	1090	0.001	5.11247	0.12807	0.13338	0.00258	1152	656	2143	33	46.26	41.462
J287 - 6.d	347	128	1090	0.003	17.06485	0.56786	0.21899	0.00583	367	2768	2973	42	87.65	78.147
J287 - 7.d	51	28.4	460	0.007	4.16667	0.26042	0.15359	0.00583	1387	1229	2386	63	41.89	29.373
J287 - 8.d	58.8	56.2	700	0.002	2.47525	0.03676	0.13288	0.00329	2187	167	2136	43	-2.39	
J287 - 9.d	430	50	950	0.001	10.47120	0.41666	0.14824	0.00337	588	2078	2326	38	74.72	67.181
J287 - 10.d	108	58.5	680		4.71698	0.28925	0.13932	0.00392	1239	1380	2219	48	44.14	34.720
J287 - 11.d	109	67.5	610		3.49650	0.15282	0.12911	0.00329	1622	724	2086	44	22.27	12.420
J287 - 12.d	45.3	49	610	0.006	2.53807	0.05798	0.13595	0.00396	2141	263	2176	50	1.60	
J287 - 13.d	567	207	1200	0.001	10.79914	0.24490	0.13338	0.00282	571	1304	2143	37	73.36	66.133
J287 - 14.d	129	156	550		6.62252	0.35086	0.14596	0.00362	907	1715	2299	42	60.57	53.056
J287 - 15.d	98	94	2.60E+03	0.005	3.07692	0.28402	0.19917	0.00823	1814	1252	2819	66	35.66	21.615
J287 - 16.d	74	77	580		5.52486	0.45786	0.12584	0.00583	1072	2112	2041	80	47.45	29.081
J287 - 17.d	442	230	1380	0.005	20.96436	0.74716	0.22493	0.00536	300	3470	3016	38	90.04	81.339
J287 - 18.d	41.7	22.8	327	0.000	2.52525	0.08290	0.13288	0.00476	2151	372	2136	61	-0.67	
J287 - 19.d	599	587	2160	0.002	15.26718	0.51279	0.16816	0.00357	409	2533	2539	35	83.89	76.411
J287 - 20.d	729	547	2260	0.001	11.87648	0.38789	0.14715	0.00293	521	1972	2313	34	77.47	70.872
J287 - 21.d	67	55.3	600		3.31126	0.16995	0.13714	0.00374	1701	791	2191	47	22.37	11.644
J287 - 22.d	917	574	2910	0.004	21.18644	0.47131	0.23425	0.00313	297	2396	3081	21	90.35	86.336
J287 - 23.d	259	98.1	1010	0.000	5.12821	0.19724	0.14497	0.00261	1148	985	2287	31	49.79	45.625
J287 - 24.d	753	420	2920	0.001	5.78035	0.18377	0.13338	0.00252	1029	938	2143	33	52.00	47.167
J287 - 25.d	32.7	35.8	392		2.60417	0.05425	0.13120	0.00436	2095	248	2114	57	0.90	
J287 - 26.d	415	23.4	1130	0.001	7.47384	0.19830	0.14665	0.00290	810	1039	2307	34	64.91	59.756

Sample ID	Concentration				Radiogenic Ratio				Calculated Ages				Discordance	
Spot	*U*	*Th*	*Pb*	f^{204}	$^{238}U/^{206}Pb^*$		$^{207}Pb^*/^{206}Pb^*$		$^{238}U/^{206}Pb^*$		$^{207}Pb^*/^{206}Pb^*$		*Disc*	Disc. %
no.	*ppm*			*(%)*	*±1s*		*±1s*		*date (Ma)*	*±1s*	*date (Ma)*	*±1s*	*(%)*	2s lim.
J287 - 27.d	110	66.2	810		2.68817	0.14453	0.13030	0.00301	2039	646	2102	40	3.01	
J287 - 28.d	118	23.4	367	0.000	2.67380	0.12154	0.13129	0.00329	2048	546	2115	43	3.17	
J287 - 29.d	70.3	71	860	0.001	2.81690	0.10315	0.13040	0.00301	1958	473	2103	40	6.89	
J287 - 30.d	54.4	55.4	714	0.001	2.58398	0.03672	0.13575	0.00337	2109	168	2174	43	2.98	
J287 - 31.d	73.1	33	408		3.63636	0.13884	0.12604	0.00396	1566	666	2043	54	23.36	11.579
J287 - 32.d	57.9	14.8	175		2.63852	0.09398	0.13308	0.00422	2072	425	2139	54	3.15	
J287 - 33.d	79	45.1	570	0.002	2.73973	0.11259	0.13070	0.00309	2006	511	2107	41	4.82	
J287 - 34.d	56	56.3	800		2.80899	0.18148	0.14279	0.00413	1963	810	2261	49	13.18	
J287 - 35.d	80	33.7	462		4.08163	0.22491	0.13734	0.00445	1413	1071	2194	55	35.61	24.296
J287 - 36.d	542	186	1830	0.000	5.74713	0.16515	0.13853	0.00272	1034	848	2209	34	53.18	48.334
J287 - 37.d	584	119.1	1300	0.001	6.81199	0.18097	0.13318	0.00268	883	945	2140	35	58.74	53.209
J287 - 38.d	33.5	22	243		2.58398	0.04340	0.12921	0.00400	2109	199	2087	53	-1.04	
J287 - 39.d	108	73.2	830	0.000	4.27350	0.19176	0.14497	0.00324	1355	931	2287	38	40.74	34.383
J287 - 40.d	81.3	86.6	870		4.08163	0.21658	0.13783	0.00396	1413	1034	2200	49	35.79	25.995
J287 - 41.d	189	216	700	0.001	9.61539	0.50851	0.14130	0.00418	638	2442	2243	50	71.57	60.826
J287 - 42.d	26.5	9	126.9	0.002	3.71747	0.21420	0.13674	0.00678	1536	1005	2186	84	29.76	11.287
J287 - 43.d	215	173	750	0.002	8.80282	0.22472	0.14378	0.00305	694	1185	2273	36	69.49	63.142
J275 - 1.d	339	195	2200	0.006	20.57613	0.80442	0.40032	0.00726	306	3670	3910	27	92.18	86.692
J275 - 2.d	346	350	2520	0.007	20.44990	0.52275	0.43897	0.00726	308	2607	4048	24	92.40	87.649
J275 - 3.d	202	128.9	640	0.002	14.70588	0.41090	0.16072	0.00532	424	2098	2463	55	82.78	69.788
J275 - 4.d	312	386	3920	0.007	13.22751	0.46366	0.49248	0.00823	470	2311	4219	24	88.86	85.148
J275 - 5.d	334	243	4250	0.008	13.71742	0.55509	0.55292	0.00775	454	2688	4389	20	89.66	86.961
J275 - 6.d	326	249	4900	0.009	14.30615	0.47073	0.61535	0.00726	436	2351	4545	17	90.42	88.516
J275 - 7.d	285	42.7	1520	0.002	9.55110	0.34665	0.21146	0.00467	642	1759	2917	35	77.99	72.061
J275 - 8.d	414	98.4	2530	0.002	9.80392	0.27393	0.22067	0.00324	626	1431	2986	23	79.03	76.264
J275 - 9.d	339	85.3	1910	0.002	9.56938	0.25183	0.20531	0.00454	641	1324	2869	35	77.67	71.708
J292 - 1.d	366	36.8	2710	0.002	10.01001	0.32064	0.25664	0.00366	614	1649	3226	22	80.97	78.520

Sample ID	Concentration				Radiogenic Ratio				Calculated Ages				Discordance	
Spot	*U*	*Th*	*Pb*	f^{204}	$^{238}U/^{206}Pb^*$		$^{207}Pb^*/^{206}Pb^*$		$^{238}U/^{206}Pb^*$		$^{207}Pb^*/^{206}Pb^*$		*Disc*	Disc. %
no.	*ppm*			*(%)*	*±1s*		*±1s*		*date (Ma) ±1s*		*date (Ma) ±1s*		*(%)*	2s lim.
J292 - 2.d	274	103.9	2220	0.001	7.16846	0.24409	0.22791	0.00518	842	1251	3037	36	72.28	67.243
J292 - 3.d	387	57.7	2850	0.001	8.38223	0.19322	0.22523	0.00431	727	1027	3018	30	75.93	71.861
J292 - 4.d	272	56.2	1650	0.002	7.87402	0.31000	0.19947	0.00436	771	1566	2822	35	72.69	67.328
J292 - 5.d	377	116	3490	0.001	6.80272	0.27766	0.20878	0.00317	884	1397	2896	24	69.47	67.357
J292 - 6.d	257	51.9	1310	0.001	9.61539	0.43454	0.17945	0.00449	638	2140	2648	41	75.91	68.222
J292 - 7.d	441	537	3020	0.002	11.00110	0.35097	0.23742	0.00387	561	1798	3103	26	81.92	78.227
J292 - 8.d	181	21.3	450	0.001	6.25000	0.33203	0.14566	0.00362	957	1623	2296	42	58.32	50.864
J292 - 9.d	360	69	592	0.000	5.52486	0.16788	0.13040	0.00239	1072	857	2103	32	49.01	44.323
J292 - 10.d	126	33.2	342	0.000	2.83286	0.14846	0.12713	0.00279	1949	671	2059	38	5.33	
J292 - 11.d	346	60.1	2030	0.002	9.68054	0.27177	0.21522	0.00383	634	1419	2945	28	78.48	74.408
J292 - 12.d	223	52.7	1300	0.001	6.80272	0.34708	0.18143	0.00337	884	1704	2666	30	66.84	62.793
J292 - 13.d	355	43	3060	0.002	10.60445	0.28114	0.29707	0.00458	581	1474	3455	24	83.19	80.258
J292 - 14.d	91	20.5	350	0.001	3.93701	0.24800	0.14854	0.00396	1459	1163	2329	45	37.36	28.340
J292 - 15.d	244	42.2	1600	0.001	8.86525	0.31437	0.22513	0.00409	689	1604	3018	29	77.17	73.253
J292 - 16.d	359	62.3	1640	0.001	9.46074	0.32222	0.18371	0.00357	648	1649	2687	32	75.89	70.807
J292 - 17.d	462	81.4	2160	0.001	10.51525	0.33724	0.19887	0.00374	586	1731	2817	30	79.21	74.269
J292 - 18.d	121	69	610	0.001	4.95050	0.41663	0.14923	0.00427	1186	1918	2337	48	49.25	39.290
J292 - 19.d	405	48.9	2800	0.002	11.36364	0.27118	0.25228	0.00454	544	1435	3199	28	83.00	78.616
J292 - 20.d	491	102.2	2200	0.001	9.68054	0.21085	0.18926	0.00309	634	1127	2736	27	76.84	73.182
J292 - 21.d	265	70	2240	0.001	10.79914	0.36153	0.29132	0.00775	571	1843	3425	41	83.33	75.741
J292 - 22.d	214	52.5	1370	0.001	8.55432	0.27807	0.23098	0.00499	713	1433	3059	34	76.70	71.538
J292 - 23.d	380	61.3	3300	0.001	9.28505	0.23708	0.26170	0.00353	659	1250	3257	21	79.75	77.901
J292 - 24.d	399	85.5	3840	0.002	11.12347	0.29077	0.30976	0.00366	555	1524	3520	18	84.23	82.679
J292 - 25.d	165	19.3	430	0.001	7.17875	0.22417	0.15200	0.00409	841	1158	2369	45	64.51	56.422
J292 - 26.d	223	50	1060	0.000	6.84932	0.25802	0.16350	0.00349	879	1309	2492	36	64.75	59.404
J292 - 27.d	214	43.7	1350	0.002	6.13497	0.24465	0.18837	0.00392	973	1231	2728	34	64.32	59.948
J292 - 28.d	410	64.8	2390	0.001	9.50570	0.28011	0.20938	0.00362	645	1456	2901	28	77.77	73.917

Sample ID	Concentration				Radiogenic Ratio				Calculated Ages				Discordance	
Spot	*U*	*Th*	*Pb*	f^{204}	$^{238}U/^{206}Pb^*$		$^{207}Pb^*/^{206}Pb^*$		$^{238}U/^{206}Pb^*$		$^{207}Pb^*/^{206}Pb^*$		*Disc*	Disc. %
no.	*ppm*			*(%)*	*±1s*		*±1s*		*date (Ma) ±1s*		*date (Ma) ±1s*		*(%)*	2s lim.
J292 - 29.d	199	49.5	293		9.18274	0.18551	0.11772	0.00383	666	997	1922	57	65.33	52.444
J292 - 30.d	183	40.7	500	0.000	5.98802	0.32271	0.14120	0.00383	996	1574	2242	46	55.60	47.033
J292 - 31.d	506	169	2940	0.001	10.43841	0.41405	0.21780	0.00449	590	2066	2964	33	80.11	74.564
J292 - 32.d	281	63.9	950	0.000	8.94454	0.28402	0.16162	0.00313	683	1467	2473	32	72.37	67.168
J292 - 33.d	409	31.9	3710	0.001	10.82251	0.28110	0.33175	0.00518	570	1476	3625	24	84.28	81.326
J292 - 34.d	331	83.8	4390	0.001	7.22543	0.20622	0.32452	0.00418	836	1073	3591	20	76.73	76.174
J292 - 35.d	224	39.4	1280	0.000	8.14996	0.29558	0.20849	0.00427	746	1507	2894	33	74.22	69.453
J220 - 1.d	9.8	4.9	64		2.73973	0.12385	0.13972	0.00726	2006	560	2224	87	9.80	
J220 - 2.d	22.2	15.2	174		2.55102	0.07809	0.13754	0.00454	2132	352	2196	56	2.93	
J220 - 3.d	31.4	21	230		2.44499	0.06576	0.12981	0.00536	2210	294	2095	71	-5.49	
J220 - 4.d	65	42.6	490	0.001	2.82486	0.14364	0.12495	0.00400	1954	650	2028	56	3.67	
J220 - 5.d	23.1	11.9	110	0.001	2.49377	0.09017	0.12981	0.00583	2174	402	2095	77	-3.74	
J220 - 6.d	34.3	18.7	255	0.000	2.99401	0.15239	0.14566	0.00583	1858	697	2296	67	19.07	3.752
J220 - 7.d	45.5	40.7	490		2.50000	0.10000	0.13248	0.00490	2169	445	2131	63	-1.78	
J220 - 8.d	65.3	28.8	361		4.65116	0.22715	0.17638	0.00583	1255	1105	2619	54	52.07	42.945
J220 - 9.d	394	309	3050	0.001	13.07190	0.58097	0.35078	0.00631	475	2782	3710	27	87.19	82.730
J220 - 10.d	22.3	10	112		2.89017	0.18377	0.13972	0.00678	1915	825	2224	82	13.86	
J220 - 11.d	32.1	31	304		2.90698	0.17324	0.12575	0.00481	1906	782	2039	66	6.54	
J220 - 12.d	17	9.8	118		2.53807	0.12884	0.12287	0.00631	2141	570	1998	88	-7.16	
J220 - 13.d	100	110	1300	0.000	2.87356	0.16928	0.13377	0.00374	1925	763	2148	48	10.38	
J220 - 14.d	64	20.7	193		2.98508	0.15594	0.12832	0.00383	1863	712	2075	52	10.24	
J220 - 15.d	22.2	11.4	138	0.000	2.44499	0.07174	0.13972	0.00583	2210	320	2224	71	0.60	
J220 - 16.d	33.3	19.3	190	0.000	2.51889	0.05076	0.13080	0.00631	2155	230	2109	82	-2.20	
J220 - 17.d	530	753	3550		13.51351	0.31958	0.31332	0.00422	460	1679	3537	21	86.99	84.220
J220 - 18.d	24.8	12	200	0.000	2.36967	0.05896	0.13090	0.00413	2270	262	2110	54	-7.56	
J220 - 19.d	40.6	38.5	460	0.000	2.72480	0.13735	0.13764	0.00458	2015	617	2198	57	8.30	
J220 - 20.d	24.3	28.1	298	0.000	2.94118	0.19896	0.14071	0.00678	1887	892	2236	81	15.62	

Sample ID	Concentration				Radiogenic Ratio				Calculated Ages				Discordance	
Spot	*U*	*Th*	*Pb*	f^{204}	$^{238}U/^{206}Pb^*$		$^{207}Pb^*/^{206}Pb^*$		$^{238}U/^{206}Pb^*$		$^{207}Pb^*/^{206}Pb^*$		*Disc*	Disc. %
no.	*ppm*			*(%)*	*±1s*		*±1s*		*date (Ma)*	*±1s*	*date (Ma)*	*±1s*	*(%)*	2s lim.
J220 - 21.d	63	56.8	600		2.59067	0.06040	0.12584	0.00337	2104	275	2041	47	-3.11	
J220 - 22.d	60	52.5	514		3.35571	0.12950	0.13080	0.00387	1681	613	2109	51	20.27	9.057
J220 - 23.d	37.9	18.3	194		2.36407	0.04192	0.14368	0.00536	2274	187	2272	63	-0.09	
J220 - 24.d	154	149	617		7.40741	0.32922	0.15250	0.00486	816	1642	2374	53	65.62	55.170
J220 - 25.d	29.2	16.4	223		2.86533	0.08621	0.14477	0.00522	1930	399	2285	61	15.55	2.365
J220 - 26.d	159	75.3	295		4.95050	0.28184	0.14537	0.00337	1186	1358	2292	39	48.25	41.347
J220 - 27.d	78.6	63.3	366		3.98406	0.19841	0.13972	0.00405	1444	949	2224	49	35.08	25.415
J220 - 28.d	117	128	750	0.001	4.13223	0.23905	0.12783	0.00357	1397	1135	2068	48	32.45	21.794
J220 - 29.d	57	29.7	338	0.000	2.51889	0.07614	0.12277	0.00345	2155	342	1997	49	-7.93	
J220 - 30.d	440	257	1260		13.17523	0.49472	0.16429	0.00353	472	2439	2500	36	81.14	73.857
J220 - 31.d	159	164	730		7.35294	0.29736	0.15438	0.00374	822	1499	2395	41	65.68	58.640
J220 - 32.d	49	52.6	497		2.59067	0.03691	0.12793	0.00387	2104	169	2070	52	-1.67	
J220 - 33.d	102	130	1520		2.73224	0.17170	0.13278	0.00301	2011	763	2135	39	5.83	
J220 - 34.d	32.6	11.2	123	0.001	2.51889	0.03490	0.12882	0.00400	2155	159	2082	54	-3.52	
J220 - 35.d	32.6	29.4	293		2.40964	0.04064	0.12773	0.00337	2238	183	2067	46	-8.26	
J220 - 36.d	33.3	20.7	222	0.001	2.42131	0.03518	0.11871	0.00422	2229	159	1937	62	-15.06	-0.683
J220 - 37.d	60.8	66.3	592		2.65957	0.03537	0.12921	0.00374	2058	164	2087	50	1.42	
J220 - 38.d	29.2	27.5	261	0.074	2.43902	0.03867	0.13427	0.00481	2215	174	2155	61	-2.80	
J220 - 39.d	24.5	11.4	86		3.01205	0.11341	0.12783	0.00583	1848	527	2068	78	10.65	
J197 - 1.d	41.4	26.9	258	0.001	2.61780	0.05140	0.12456	0.00440	2086	235	2022	61	-3.12	
J197 - 2.d	28.7	15.4	179		2.53807	0.06120	0.12466	0.00490	2141	277	2024	68	-5.80	
J197 - 3.d	38.5	20.7	239		2.59067	0.09732	0.12664	0.00440	2104	437	2052	60	-2.56	
J197 - 4.d	30.3	20.8	217		2.60417	0.08816	0.13080	0.00583	2095	398	2109	76	0.65	
J197 - 5.d	37.7	23.3	238	0.001	2.53165	0.05448	0.12723	0.00431	2146	247	2060	59	-4.17	
J197 - 6.d	39.5	29.7	347		2.48756	0.06807	0.12713	0.00472	2178	306	2059	64	-5.81	
J197 - 7.d	36.8	24.7	264		2.63158	0.11080	0.12991	0.00481	2076	498	2097	64	0.97	
J197 - 8.d	20.7	13.8	152	0.005	2.57069	0.07930	0.13526	0.00476	2118	358	2167	60	2.27	

Sample ID	Concentration				Radiogenic Ratio				Calculated Ages				Discordance	
Spot	*U*	*Th*	*Pb*	f^{204}	$^{238}U/^{206}Pb^*$		$^{207}Pb^*/^{206}Pb^*$		$^{238}U/^{206}Pb^*$		$^{207}Pb^*/^{206}Pb^*$		*Disc*	Disc. %
no.	*ppm*			*(%)*	*±1s*		*±1s*		*date (Ma)*	*±1s*	*date (Ma)*	*±1s*	*(%)*	2s lim.
J197 - 9.d	28.7	18.7	211		2.80899	0.12625	0.12555	0.00522	1963	574	2037	72	3.60	
J197 - 10.d	21.4	11.2	97	0.004	2.87356	0.07844	0.14764	0.00583	1925	365	2319	66	16.98	2.961
J197 - 11.d	37	35.5	410	0.000	2.60417	0.11529	0.12713	0.00440	2095	516	2059	60	-1.76	
J197 - 12.d	54.1	32.6	264		2.79642	0.03597	0.12703	0.00383	1971	169	2057	52	4.21	
J197 - 13.d	35	23.1	232		2.49377	0.03731	0.14130	0.00418	2174	169	2243	50	3.10	
J197 - 14.d	26.5	11.4	148	0.006	2.53807	0.08374	0.12376	0.00440	2141	376	2011	62	-6.47	
J197 - 15.d	39.4	28.4	325	0.000	2.55102	0.06182	0.12971	0.00513	2132	280	2094	68	-1.82	
J197 - 16.d	46.2	29.8	322	0.000	2.55755	0.08830	0.12495	0.00353	2127	397	2028	49	-4.90	
J197 - 17.d	50.9	39.9	451		2.53165	0.07050	0.13060	0.00374	2146	318	2106	49	-1.90	
J197 - 18.d	35.1	22.2	320	0.001	2.94985	0.17838	0.13278	0.00536	1882	806	2135	69	11.86	
J197 - 19.d	27.6	15.9	160		2.46914	0.05182	0.12594	0.00409	2192	233	2042	56	-7.34	
J197 - 20.d	39.2	28	295	0.015	2.51256	0.05050	0.13169	0.00445	2160	229	2121	58	-1.85	
J197 - 21.d	49.3	32.2	348		2.43309	0.04440	0.13129	0.00413	2219	200	2115	54	-4.92	
J197 - 22.d	30.5	18.9	184	0.003	2.65252	0.09850	0.12575	0.00422	2062	445	2039	58	-1.12	
J197 - 23.d	26	16.6	165	0.003	2.53165	0.06089	0.12981	0.00536	2146	275	2095	71	-2.42	
J197 - 24.d	30.2	20.7	212	0.001	2.50000	0.05000	0.13526	0.00532	2169	226	2167	67	-0.08	
J197 - 25.d	38.1	24.1	234	0.005	2.68817	0.05781	0.13080	0.00431	2039	266	2109	57	3.32	
J197 - 26.d	18.4	8.2	130	0.008	2.70270	0.08766	0.16548	0.00631	2029	400	2512	63	19.23	6.545
J197 - 27.d	33.2	20.4	193	0.002	2.65252	0.05277	0.12684	0.00383	2062	242	2055	52	-0.37	
J197 - 28.d	34.9	19.1	219		2.59067	0.06040	0.12535	0.00387	2104	275	2034	54	-3.47	
J197 - 29.d	30.1	22.3	230	0.004	2.59067	0.06040	0.13674	0.00495	2104	275	2186	62	3.76	
J197 - 30.d	35	19	203		2.47525	0.04595	0.12059	0.00396	2187	208	1965	57	-11.32	
J197 - 31.d	27.1	14.9	176	0.001	2.54453	0.09712	0.12446	0.00486	2137	434	2021	68	-5.72	
J197 - 32.d	32.5	29	288		2.83286	0.14445	0.13674	0.00631	1949	654	2186	78	10.86	
J197 - 33.d	31.5	26.9	351	0.003	2.70270	0.15705	0.13575	0.00583	2029	700	2174	73	6.64	
J197 - 34.d	35.9	19.5	177		3.16456	0.21030	0.12723	0.00486	1770	956	2060	66	14.07	
J197 - 35.d	24.3	15.9	140		2.74725	0.13963	0.11891	0.00678	2001	628	1940	99	-3.16	

Sample ID	Concentration				Radiogenic Ratio				Calculated Ages				Discordance	
Spot	*U*	*Th*	*Pb*	f^{204}	$^{238}U/^{206}Pb^*$		$^{207}Pb^*/^{206}Pb^*$		$^{238}U/^{206}Pb^*$		$^{207}Pb^*/^{206}Pb^*$		*Disc*	Disc. %
no.	*ppm*			*(%)*	*±1s*		*±1s*		*date (Ma)*	*±1s*	*date (Ma)*	*±1s*	*(%)*	2s lim.
J197 - 36.d	37.7	11.5	147		3.53357	0.19353	0.12287	0.00583	1606	906	1998	82	19.61	
J197 - 37.d	35.8	29.5	316	0.005	3.10559	0.20254	0.13575	0.00583	1799	919	2174	73	17.22	
J197 - 38.d	48.4	28.7	325	0.002	2.52525	0.09565	0.12277	0.00418	2151	427	1997	59	-7.70	
J197 - 39.d	20.3	13.9	155	0.003	2.40964	0.07839	0.13674	0.00583	2238	348	2186	72	-2.35	
J197 - 40.d	33	22.5	272		2.40964	0.06968	0.13407	0.00374	2238	310	2152	48	-3.99	
J197 - 41.d	43.6	22	210	0.004	2.49377	0.03731	0.12535	0.00436	2174	169	2034	60	-6.88	
J197 - 42.d	18.8	12.5	162		2.49377	0.07463	0.12327	0.00513	2174	335	2004	72	-8.46	
J197 - 43.d	29.8	20.6	201	0.005	2.63158	0.11080	0.12485	0.00583	2076	498	2027	80	-2.45	
J197 - 44.d	35.4	21.1	256		2.39234	0.07154	0.12892	0.00513	2251	317	2083	68	-8.07	
J273 - 1.d	22.9	13.5	155		2.57069	0.09252	0.12485	0.00583	2118	416	2027	80	-4.51	
J273 - 2.d	35.5	31.7	365	0.005	2.50000	0.08438	0.13328	0.00436	2169	377	2142	56	-1.28	
J273 - 3.d	20.7	14.3	151		2.80112	0.16085	0.13080	0.00775	1968	722	2109	100	6.68	
J273 - 4.d	90.9	106	700		4.44444	0.20741	0.12475	0.00405	1308	1008	2025	56	35.41	23.659
J273 - 5.d	37	31.2	304	0.002	3.18471	0.17242	0.14071	0.00583	1760	795	2236	70	21.27	5.306
J273 - 6.d	30.7	19.2	224		2.73973	0.13511	0.13179	0.00583	2006	608	2122	76	5.47	
J273 - 7.d	36.3	39	490	0.002	2.62467	0.15500	0.13575	0.00583	2081	686	2174	73	4.27	
J273 - 8.d	36.4	33.8	412		2.57732	0.10296	0.12545	0.00518	2114	461	2035	71	-3.85	
J273 - 9.d	39.2	28.3	323	0.004	2.60417	0.10851	0.13011	0.00509	2095	487	2099	67	0.21	
J273 - 10.d	16.9	9.9	104	0.005	2.65252	0.10202	0.12783	0.00775	2062	461	2068	103	0.29	
J273 - 11.d	50.5	50.5	580	0.000	2.72480	0.13364	0.12515	0.00449	2015	601	2031	62	0.77	
J273 - 12.d	38.5	27.5	280	0.001	2.59067	0.04698	0.12545	0.00413	2104	215	2035	57	-3.40	
J273 - 13.d	48	36.2	385		2.53165	0.08332	0.12545	0.00324	2146	374	2035	45	-5.45	
J273 - 14.d	40.6	26.8	301		2.58398	0.11351	0.12911	0.00504	2109	507	2086	67	-1.10	
J273 - 15.d	37.5	35.6	412		2.57069	0.07930	0.13556	0.00449	2118	358	2171	57	2.44	
J273 - 16.d	59	50.8	670	0.005	2.72480	0.14478	0.13486	0.00374	2015	649	2162	48	6.80	
J273 - 17.d	68	78.7	530	0.004	3.66300	0.21468	0.13595	0.00467	1556	1005	2176	59	28.50	15.499
J273 - 18.d	33.2	24.8	335		2.55755	0.10466	0.12594	0.00486	2127	468	2042	67	-4.18	

Sample ID	Concentration				Radiogenic Ratio				Calculated Ages				Discordance	
Spot	*U*	*Th*	*Pb*	f^{204}	$^{238}U/^{206}Pb^*$		$^{207}Pb^*/^{206}Pb^*$		$^{238}U/^{206}Pb^*$		$^{207}Pb^*/^{206}Pb^*$		*Disc*	Disc. %
no.	*ppm*			*(%)*	*±1s*		*±1s*		*date (Ma)*	*±1s*	*date (Ma)*	*±1s*	*(%)*	2s lim.
J273 - 19.d	48.3	36.1	339	0.002	2.53807	0.04509	0.13298	0.00413	2141	205	2138	53	-0.17	
J273 - 20.d	33.8	29.4	320		2.68817	0.10478	0.13288	0.00532	2039	474	2136	68	4.57	
J273 - 21.d	51.5	41.4	458		2.40964	0.06387	0.12674	0.00413	2238	285	2053	56	-8.99	
J273 - 22.d	66.7	55.7	640	0.001	2.39234	0.05723	0.12723	0.00383	2251	255	2060	52	-9.29	
J273 - 23.d	49.4	37.2	460	0.003	2.52525	0.13391	0.12921	0.00509	2151	590	2087	68	-3.03	
J273 - 24.d	34.7	41.6	450	0.000	2.90698	0.16056	0.12872	0.00518	1906	727	2081	69	8.39	
J273 - 25.d	80	42	470		3.09598	0.15815	0.13308	0.00392	1804	728	2139	51	15.64	2.906
J273 - 26.d	47.7	34.3	405		2.63852	0.11835	0.13298	0.00383	2072	531	2138	50	3.09	
J273 - 27.d	39.1	36.5	364	0.000	2.87356	0.16515	0.13199	0.00476	1925	745	2125	62	9.39	
J273 - 28.d	31.1	34.2	350	0.001	2.93255	0.18920	0.13476	0.00678	1891	851	2161	85	12.47	
J273 - 29.d	50.6	38.7	390	0.000	3.08642	0.15718	0.11802	0.00418	1809	723	1926	62	6.08	
J273 - 30.d	21.1	13.4	154	0.002	2.63852	0.09050	0.13972	0.00631	2072	410	2224	76	6.84	
J273 - 31.d	61.9	45.6	422	0.004	3.30033	0.17427	0.12634	0.00400	1706	809	2048	55	16.68	2.849
J273 - 32.d	77.4	71	520	0.001	3.48432	0.17604	0.12723	0.00366	1627	826	2060	50	21.05	9.203
J273 - 33.d	97	126	690	0.003	4.18410	0.14005	0.12674	0.00341	1381	690	2053	47	32.71	23.777
J273 - 34.d	30.6	29.8	365	0.005	2.39234	0.07440	0.13357	0.00436	2251	330	2145	56	-4.94	
J273 - 35.d	40.1	31.6	305	0.008	2.63158	0.07618	0.13001	0.00383	2076	346	2098	51	1.04	
J273 - 36.d	36.3	36.2	430		2.51889	0.12055	0.12872	0.00467	2155	534	2081	63	-3.59	
J273 - 37.d	33.9	26.5	318		2.55102	0.09436	0.11683	0.00387	2132	423	1908	58	-11.73	
J273 - 38.d	42.7	31.9	426	0.002	2.22717	0.04464	0.11950	0.00392	2391	196	1949	57	-22.68	-10.406
J273 - 39.d	53.2	40.8	470	0.006	2.65252	0.11609	0.12307	0.00409	2062	522	2001	58	-3.05	
J273 - 40.d	41.2	29.9	263		2.78552	0.13578	0.12188	0.00495	1977	614	1984	71	0.33	
J273 - 41.d	45.8	51.1	382		3.21543	0.18093	0.13229	0.00440	1746	833	2129	57	17.99	3.832
J273 - 42.d	43.9	27.8	321	0.008	2.65957	0.11671	0.12485	0.00449	2058	525	2027	62	-1.52	
J273 - 43.d	97	159	1020	0.010	4.13223	0.21344	0.12753	0.00349	1397	1022	2064	47	32.32	22.247
J273 - 44.d	22.8	15.9	172		2.93255	0.18060	0.13674	0.00726	1891	814	2186	90	13.49	
J273 - 45.d	55	19.4	242	0.008	4.52489	0.25593	0.11851	0.00463	1287	1227	1934	68	33.44	17.948

Sample ID	Concentration				Radiogenic Ratio				Calculated Ages				Discordance	
Spot	*U*	*Th*	*Pb*	f^{204}	$^{238}U/^{206}Pb^*$		$^{207}Pb^*/^{206}Pb^*$		$^{238}U/^{206}Pb^*$		$^{207}Pb^*/^{206}Pb^*$		*Disc*	Disc. %
no.	*ppm*			*(%)*	*±1s*		*±1s*		*date (Ma)*	*±1s*	*date (Ma)*	*±1s*	*(%)*	2s lim.
J273 - 46.d	42	43	420	0.004	2.95858	0.18382	0.12485	0.00536	1877	830	2027	74	7.39	
J273 - 47.d	34.3	25.6	306		2.45098	0.07509	0.12634	0.00490	2206	335	2048	67	-7.72	
J273 - 48.d	50.8	47.3	397	0.002	2.92398	0.08977	0.13328	0.00454	1896	417	2142	58	11.45	
J273 - 49.d	30.4	27.8	335	0.005	2.61097	0.09203	0.13466	0.00440	2090	415	2160	56	3.21	
J273 - 50.d	57	41.4	420	0.003	2.69542	0.10535	0.12674	0.00409	2034	477	2053	56	0.93	
J253 - 1.d	263	45.1	690		7.00771	0.22835	0.14081	0.00313	860	1174	2237	38	61.56	55.232
J253 - 2.d	153	75.5	6.10E+03		2.28311	0.14074	0.31412	0.01265	2342	602	3541	61	33.87	24.231
J253 - 3.d	168	60.4	780		5.10204	0.20825	0.15428	0.00400	1154	1035	2394	43	51.80	44.790
J253 - 4.d	100	19.5	249		4.78469	0.32051	0.13813	0.00379	1223	1516	2204	47	44.49	35.001
J253 - 5.d	173	61.2	350	0.002	5.71429	0.26122	0.12178	0.00321	1040	1294	1982	46	47.56	38.481
J253 - 6.d	28.3	5.71	76	0.015	2.71739	0.17722	0.12446	0.00449	2020	785	2021	63	0.05	
J253 - 7.d	173	94.2	438		5.55556	0.18519	0.12773	0.00337	1067	940	2067	46	48.38	40.040
J253 - 8.d	218	32.2	463		11.24859	0.29735	0.16518	0.00445	549	1556	2509	45	78.12	68.904
J253 - 9.d	219	80.1	640		13.29787	0.45977	0.17668	0.00490	467	2295	2622	45	82.17	72.267
J253 - 10.d	318	21.9	780		15.77287	0.49757	0.18936	0.00532	396	2474	2737	45	85.52	75.195
J253 - 11.d	177	143.3	620	0.001	7.81250	0.36621	0.11792	0.00370	776	1812	1925	55	59.66	47.579
J253 - 12.d	134	70.1	465	0.001	8.84173	0.25798	0.15428	0.00513	691	1344	2394	56	71.15	59.634
J253 - 13.d	164	63.5	480		2.90698	0.11831	0.13486	0.00309	1906	544	2162	39	11.86	1.711
J253 - 14.d	82	22.1	248	0.000	3.09598	0.17253	0.13209	0.00362	1804	790	2126	47	15.12	2.488
J253 - 15.d	144	157	730		9.40734	0.27877	0.17608	0.00409	651	1449	2616	38	75.11	68.308
J253 - 16.d	99	53.7	668	0.003	2.41022	0.02817	0.12753	0.00309	2237	127	2064	42	-8.39	
J253 - 17.d	209	111	2140		3.35571	0.11261	0.19025	0.00405	1681	536	2744	35	38.73	34.730
J253 - 18.d	182	50.6	570		10.44932	0.36578	0.17985	0.00440	589	1857	2651	40	77.78	70.131
J253 - 19.d	147	40.3	440	0.003	10.86957	0.54939	0.19015	0.00509	567	2627	2743	43	79.32	70.646
J253 - 20.d	165	50.4	313		10.63830	0.62245	0.15121	0.00413	579	2904	2360	46	75.46	65.702
J253 - 21.d	162	26.8	301		9.09091	0.49587	0.13615	0.00427	673	2381	2179	54	69.12	57.521
J253 - 22.d	199	15.6	209	0.018	12.33046	0.43331	0.13437	0.00405	503	2173	2156	52	76.68	64.736

Sample ID	Concentration				Radiogenic Ratio				Calculated Ages				Discordance	
Spot	*U*	*Th*	*Pb*	f^{204}	$^{238}U/^{206}Pb^*$		$^{207}Pb^*/^{206}Pb^*$		$^{238}U/^{206}Pb^*$		$^{207}Pb^*/^{206}Pb^*$		*Disc*	Disc. %
no.	*ppm*			*(%)*	*±1s*		*±1s*		*date (Ma)*	*±1s*	*date (Ma)*	*±1s*	*(%)*	2s lim.
J253 - 23.d	202	50.8	560		12.04819	0.31935	0.17509	0.00509	514	1666	2607	48	80.28	70.090
J253 - 24.d	138	29.8	220		10.76426	0.48665	0.13476	0.00536	573	2374	2161	68	73.50	57.412
J253 - 25.d	303	80.6	680		11.57407	0.42197	0.14229	0.00345	534	2115	2255	41	76.31	67.627
J253 - 26.d	81	19.4	341		4.34783	0.22684	0.14586	0.00495	1334	1091	2298	57	41.93	30.958
J253 - 27.d	240	29.6	780		7.75194	0.39060	0.16598	0.00329	782	1915	2517	33	68.93	63.788
J253 - 28.d	98	30.6	430		5.74713	0.47893	0.14487	0.00454	1034	2206	2286	53	54.77	43.795
J253 - 29.d	102	26.5	550		5.81395	0.28732	0.14814	0.00431	1023	1413	2325	49	55.99	47.061
J253 - 30.d	168	126	950		6.71141	0.33782	0.18540	0.00413	895	1662	2702	36	66.86	61.426
J253 - 31.d	151	53.8	970		6.49351	0.27408	0.19917	0.00396	923	1374	2819	32	67.25	63.233
J253 - 32.d	31.7	7.2	135		2.66667	0.09600	0.13873	0.00527	2053	435	2211	64	7.17	
J253 - 33.d	314	79.7	1570		4.06504	0.15698	0.16191	0.00297	1418	765	2476	31	42.73	38.886
J253 - 34.d	137	44.1	308		8.20345	0.21198	0.14229	0.00463	741	1116	2255	55	67.12	55.822
J253 - 35.d	64	24	227		4.03226	0.25202	0.12644	0.00422	1428	1186	2049	58	30.30	17.021
J253 - 36.d	215	32.8	610		8.33333	0.45139	0.16171	0.00337	731	2183	2474	35	70.47	64.564
J253 - 37.d	192	600	2120		7.24638	0.39382	0.23484	0.00872	833	1916	3085	58	72.99	62.054
J253 - 38.d	152	39.1	480	0.000	6.99301	0.39122	0.14378	0.00357	862	1898	2273	42	62.10	54.305
J253 - 39.d	96	72.1	468		4.16667	0.16493	0.13229	0.00379	1387	805	2129	49	34.85	25.403
J253 - 40.d	158	101.8	530		5.02513	0.27777	0.12624	0.00357	1170	1343	2046	49	42.83	32.775
J240 - 1.d	66	33.6	400		3.12500	0.18555	0.13189	0.00396	1790	848	2123	52	15.71	1.937
J240 - 2.d	54	15.2	238		2.55102	0.10087	0.13833	0.00440	2132	451	2206	54	3.37	
J240 - 3.d	61	34.8	450	0.004	2.93255	0.18920	0.13843	0.00409	1891	851	2208	50	14.32	0.131
J240 - 4.d	65	36.9	390		3.28947	0.22723	0.13159	0.00454	1711	1036	2119	59	19.26	3.748
J240 - 5.d	35.5	15.4	178		3.73134	0.15315	0.13169	0.00527	1531	735	2121	68	27.82	13.292
J240 - 6.d	37.3	14.2	177		2.35294	0.05260	0.12624	0.00431	2283	234	2046	59	-11.58	
J240 - 7.d	89	36.2	456		2.50000	0.05938	0.12852	0.00324	2169	268	2078	44	-4.39	
J240 - 8.d	64	25.8	470		2.89855	0.12602	0.13754	0.00481	1911	577	2196	60	13.01	
J240 - 9.d	69	47.9	430		3.19489	0.23477	0.13070	0.00409	1755	1060	2107	54	16.70	1.208

Sample ID	Concentration				Radiogenic Ratio				Calculated Ages				Discordance	
Spot	*U*	*Th*	*Pb*	f^{204}	$^{238}U/^{206}Pb^*$		$^{207}Pb^*/^{206}Pb^*$		$^{238}U/^{206}Pb^*$		$^{207}Pb^*/^{206}Pb^*$		*Disc*	Disc. %
no.	*ppm*			*(%)*	*±1s*		*±1s*		*date (Ma)*	*±1s*	*date (Ma)*	*±1s*	*(%)*	2s lim.
J240 - 10.d	52.6	15.3	266		2.59740	0.10457	0.13030	0.00353	2100	469	2102	47	0.12	
J240 - 11.d	72	26.1	348		2.57069	0.08591	0.13258	0.00383	2118	387	2132	50	0.67	
J240 - 12.d	55.3	19.1	272	0.011	2.55102	0.12690	0.13050	0.00431	2132	562	2105	57	-1.30	
J240 - 13.d	66	26.3	420		2.65252	0.13016	0.12674	0.00436	2062	582	2053	59	-0.44	
J240 - 14.d	61	24.7	305		3.35571	0.23648	0.13892	0.00413	1681	1079	2214	51	24.05	11.183
J240 - 15.d	65	27.2	310		3.74532	0.25249	0.13813	0.00472	1526	1171	2204	58	30.78	17.654
J240 - 16.d	44.2	23.4	367	0.002	2.40385	0.09823	0.13625	0.00379	2242	432	2180	48	-2.85	
J240 - 17.d	5.24	1.92	64		2.09205	0.09848	0.13476	0.00970	2519	416	2161	120	-16.55	
J240 - 18.d	35.5	8.7	142		2.54453	0.14568	0.13080	0.00583	2137	641	2109	76	-1.33	
J240 - 19.d	46.4	15.5	214	0.010	2.48139	0.06773	0.12931	0.00400	2183	304	2089	53	-4.51	
J240 - 20.d	66	29.4	394		2.68097	0.13297	0.13258	0.00405	2044	596	2132	52	4.17	
J240 - 21.d	44.7	20.9	273	0.012	2.96736	0.19371	0.12773	0.00409	1872	872	2067	55	9.42	
J240 - 22.d	42.9	17.5	238	0.008	3.23625	0.20947	0.12872	0.00499	1736	957	2081	67	16.57	
J240 - 23.d	65	25.7	377		3.14465	0.15328	0.12366	0.00532	1780	709	2010	74	11.43	
J240 - 24.d	61	16.9	193	0.002	3.30033	0.09803	0.12684	0.00349	1706	468	2055	48	16.96	6.480
J240 - 25.d	60	28.1	380		2.93255	0.18060	0.13793	0.00454	1891	814	2201	56	14.08	
J240 - 26.d	47.4	15.4	261	0.008	3.50877	0.16005	0.13873	0.00583	1616	757	2211	71	26.90	11.759
J240 - 27.d	67	31	430	0.006	2.73973	0.14637	0.13447	0.00400	2006	657	2157	51	7.01	
J240 - 28.d	90	52.2	434	0.006	3.86100	0.26088	0.13040	0.00396	1485	1214	2103	52	29.41	17.000
J240 - 29.d	49.8	21.3	279	0.008	2.83286	0.12439	0.13387	0.00490	1949	567	2149	63	9.33	
J240 - 30.d	45.9	9.6	155		5.26316	0.38781	0.13179	0.00583	1121	1818	2122	76	47.15	30.476
J240 - 31.d	47	29.7	275		3.25733	0.13793	0.12753	0.00454	1726	647	2064	61	16.39	1.928
J205 - 1.d	50	18.3	271		3.75940	0.24733	0.13714	0.00486	1520	1150	2191	60	30.62	17.084
J205 - 2.d	71	86	1250		2.59740	0.09445	0.12763	0.00400	2100	425	2066	54	-1.65	
J205 - 3.d	115	32.4	830		4.83092	0.22171	0.17935	0.00678	1213	1087	2647	61	54.18	43.317
J205 - 4.d	38.1	30.3	380		3.08642	0.20005	0.12386	0.00536	1809	907	2013	75	10.10	
J205 - 5.d	114	126	980		5.29101	0.23796	0.13774	0.00383	1116	1176	2199	48	49.25	40.584

Sample ID	Concentration				Radiogenic Ratio				Calculated Ages				Discordance	
Spot	*U*	*Th*	*Pb*	f^{204}	$^{238}U/^{206}Pb^*$		$^{207}Pb^*/^{206}Pb^*$		$^{238}U/^{206}Pb^*$		$^{207}Pb^*/^{206}Pb^*$		*Disc*	Disc. %
no.	*ppm*			*(%)*	*±1s*		*±1s*		*date (Ma)*	*±1s*	*date (Ma)*	*±1s*	*(%)*	2s lim.
J205 - 6.d	89	71.9	630	0.007	5.07614	0.20614	0.15864	0.00387	1159	1024	2441	41	52.52	46.287
J205 - 7.d	78	70.7	338	0.004	6.36943	0.34484	0.13952	0.00527	940	1682	2221	64	57.68	44.435
J205 - 8.d	63	33	323	0.002	4.67290	0.31662	0.12634	0.00476	1250	1494	2048	65	38.95	24.434
J205 - 9.d	39.6	14.3	192	0.009	2.68097	0.12578	0.12931	0.00481	2044	565	2089	64	2.16	
J205 - 10.d	55.5	39.7	418	0.007	2.61097	0.04431	0.12555	0.00405	2090	203	2037	56	-2.64	
J205 - 11.d	85	78.2	490	0.002	6.94444	0.43403	0.15775	0.00472	867	2073	2432	50	64.34	54.803
J205 - 12.d	66	56.7	400	0.005	4.20168	0.28247	0.12921	0.00366	1376	1325	2087	49	34.06	22.888
J205 - 13.d	76.1	70.5	590	0.008	3.48432	0.15176	0.12515	0.00301	1627	719	2031	42	19.91	10.067
J205 - 14.d	73.2	70.1	680		3.54610	0.17605	0.13040	0.00366	1601	830	2103	48	23.86	12.901
J205 - 15.d	82	48.3	296		4.73934	0.22461	0.12555	0.00324	1234	1097	2037	45	39.40	30.508
J205 - 16.d	100	75.2	393	0.001	6.53595	0.38447	0.13883	0.00392	918	1855	2213	48	58.52	49.152
J205 - 17.d	88	81.2	488		7.19425	0.43994	0.15408	0.00481	839	2105	2392	52	64.92	54.652
J205 - 18.d	96	63.5	580	0.001	4.25532	0.22635	0.12584	0.00413	1361	1085	2041	57	33.32	21.038
J205 - 19.d	61.2	46.7	593	0.000	2.55102	0.03579	0.12951	0.00305	2132	164	2091	41	-1.95	
J205 - 20.d	57.9	58.8	690	0.001	3.73134	0.18100	0.13209	0.00463	1531	860	2126	60	28.00	15.084
J205 - 21.d	73	57	800	0.002	3.06749	0.14585	0.12941	0.00413	1819	673	2090	55	12.97	
J205 - 22.d	77	52.3	560	0.006	3.26797	0.15485	0.12475	0.00329	1721	722	2025	46	15.03	3.229
J205 - 23.d	50	44.7	580	0.006	2.65957	0.08488	0.12654	0.00396	2058	386	2050	54	-0.35	
J205 - 24.d	87	44.5	582	0.004	2.85714	0.04898	0.13040	0.00309	1935	230	2103	41	8.02	
J205 - 25.d	38.7	13.1	152		3.40136	0.21982	0.12466	0.00522	1661	1011	2024	72	17.91	
J205 - 26.d	90	80.3	406		5.71429	0.32653	0.12991	0.00317	1040	1581	2097	42	50.42	42.280
J205 - 27.d	87	45.2	460		4.62963	0.21433	0.14210	0.00409	1261	1047	2253	49	44.04	35.144
J205 - 28.d	42.8	32.4	431	0.015	2.76243	0.11447	0.12713	0.00476	1992	520	2059	65	3.26	
J205 - 29.d	33.9	33.6	418	0.004	2.69542	0.06539	0.12812	0.00392	2034	300	2072	53	1.85	
J205 - 30.d	96	50.3	430		6.99301	0.56237	0.15260	0.00631	862	2579	2375	69	63.73	48.911
J205 - 31.d	96	20	310	0.446	11.14827	0.47228	0.18233	0.00583	554	2321	2674	52	79.29	68.148
J205 - 32.d	73.3	53.4	640	0.005	2.71739	0.10707	0.13001	0.00349	2020	486	2098	46	3.72	

Sample ID	Concentration				Radiogenic Ratio				Calculated Ages				Discordance	
Spot	*U*	*Th*	*Pb*	f^{204}	$^{238}U/^{206}Pb^*$		$^{207}Pb^*/^{206}Pb^*$		$^{238}U/^{206}Pb^*$		$^{207}Pb^*/^{206}Pb^*$		*Disc*	Disc. %
no.	*ppm*			*(%)*	*±1s*		*±1s*		*date (Ma)*	*±1s*	*date (Ma)*	*±1s*	*(%)*	2s lim.
J205 - 33.d	38.1	37.8	536		2.40385	0.05778	0.14071	0.00583	2242	258	2236	70	-0.28	
J205 - 34.d	68	44.9	430		3.41297	0.19802	0.12624	0.00413	1657	919	2046	57	19.05	4.786
J205 - 35.d	63.7	12.1	130		6.99301	0.39122	0.12981	0.00536	862	1898	2095	71	58.88	43.253
J205 - 36.d	96	46.6	302		6.53595	0.44855	0.13377	0.00631	918	2118	2148	80	57.28	39.361
J205 - 37.d	65.2	32.9	441	0.007	2.57069	0.03635	0.14279	0.00313	2118	167	2261	37	6.33	
J205 - 38.d	30.7	12.7	164	0.488	2.39808	0.05176	0.12178	0.00476	2247	231	1982	68	-13.33	
J205 - 39.d	74	50.5	460	0.003	5.40541	0.27757	0.14190	0.00518	1094	1357	2250	62	51.38	39.180
J205 - 40.d	63	27.7	305		4.32900	0.34670	0.14309	0.00509	1340	1600	2265	60	40.85	27.737
J205 - 41.d	95	63.7	443	0.017	5.55556	0.40123	0.13318	0.00418	1067	1887	2140	54	50.15	38.819
J205 - 42.d	61	7.3	177	0.003	4.80769	0.28892	0.14219	0.00427	1218	1382	2254	51	45.96	36.089
J205 - 43.d	31.5	10.1	212	0.005	2.34192	0.06307	0.14368	0.00583	2292	279	2272	68	-0.89	
J205 - 44.d	115	58.2	820		4.34783	0.27410	0.13655	0.00301	1334	1297	2184	38	38.89	31.053
J205 - 45.d	29.8	29.9	430	0.000	3.17460	0.17637	0.13873	0.00583	1765	811	2211	71	20.17	3.624
J205 - 46.d	57.4	90	1100	0.000	2.58398	0.05675	0.12852	0.00362	2109	259	2078	49	-1.50	
J205 - 47.d	67	50.3	390	0.000	3.98406	0.26984	0.13456	0.00422	1444	1259	2158	54	33.11	21.018
J205 - 48.d	218	377	1.52E+04		2.76243	0.26327	0.50536	0.01612	1992	1139	4257	46	53.21	47.970
J205 - 49.d	116	74	520		5.12821	0.18409	0.12257	0.00387	1148	924	1994	55	42.41	31.427
J205 - 50.d	247	148	770		10.46025	0.41031	0.13506	0.00405	589	2051	2165	51	72.81	61.484
J205 - 51.d	105	47.5	402	0.001	7.29927	0.39960	0.16162	0.00476	828	1942	2473	49	66.53	57.287
J205 - 52.d	69	45.3	540	0.000	2.77778	0.11960	0.13288	0.00341	1982	543	2136	44	7.22	
J205 - 53.d	169	123.4	750		5.37634	0.23124	0.14428	0.00301	1100	1148	2279	35	51.75	46.268
J205 - 54.d	45.9	51	570		2.91545	0.11900	0.12703	0.00440	1901	547	2057	60	7.59	
J219 - 1.d	60	70	530		3.62319	0.13784	0.12674	0.00383	1571	661	2053	52	23.48	12.226
J219 - 2.d	17.4	7.3	120		2.43309	0.09176	0.12783	0.00631	2219	406	2068	84	-7.31	
J219 - 3.d	31.8	21.3	288		2.57732	0.06975	0.12822	0.00495	2114	316	2074	66	-1.92	
J219 - 4.d	34.2	28.7	362		2.63852	0.10791	0.12327	0.00495	2072	486	2004	70	-3.37	
J219 - 5.d	35	30.3	320	0.000	3.28947	0.22723	0.13179	0.00522	1711	1036	2122	68	19.36	2.110

Sample ID	Concentration				Radiogenic Ratio				Calculated Ages				Discordance	
Spot	*U*	*Th*	*Pb*	f^{204}	$^{238}U/^{206}Pb^*$		$^{207}Pb^*/^{206}Pb^*$		$^{238}U/^{206}Pb^*$		$^{207}Pb^*/^{206}Pb^*$		*Disc*	Disc. %
no.	*ppm*			*(%)*	*±1s*		*±1s*		*date (Ma) ±1s*		*date (Ma) ±1s*		*(%)*	2s lim.
J219 - 6.d	121	171	470	0.004	8.54701	0.76704	0.12327	0.00486	713	3370	2004	68	64.41	48.066
J219 - 7.d	41.5	60	400	0.003	4.18410	0.24509	0.13774	0.00583	1381	1164	2199	72	37.17	22.008
J219 - 8.d	30.2	18.6	239	0.002	2.55102	0.04881	0.12287	0.00495	2132	222	1998	70	-6.69	
J219 - 9.d	63	86	450	0.004	5.78035	0.30071	0.12485	0.00678	1029	1471	2027	93	49.25	28.182
J219 - 10.d	36.6	26.4	349		2.55102	0.10087	0.13883	0.00440	2132	451	2213	54	3.64	
J219 - 11.d	28.4	24.9	306	0.004	2.36407	0.04471	0.12287	0.00495	2274	199	1998	70	-13.80	
J219 - 12.d	41.6	41.8	620		2.95858	0.15318	0.12882	0.00486	1877	699	2082	65	9.84	
J219 - 13.d	40.2	31.2	440	0.504	2.71003	0.15056	0.13496	0.00490	2025	673	2164	62	6.42	
J219 - 14.d	26.9	16.5	226	0.020	2.82486	0.14364	0.13278	0.00631	1954	650	2135	81	8.50	
J219 - 15.d	208	287	2010	0.008	5.23560	0.24670	0.13080	0.00305	1127	1214	2109	40	46.57	39.246
J219 - 16.d	116	93.1	570	0.001	4.65116	0.24878	0.12832	0.00357	1255	1201	2075	48	39.50	29.703
J219 - 17.d	28.4	28.9	377	0.006	3.04878	0.18125	0.13575	0.00678	1829	825	2174	85	15.87	
J219 - 18.d	19.6	10	141		2.59067	0.07383	0.12882	0.00631	2104	335	2082	84	-1.07	
J219 - 19.d	60	61	660		2.95858	0.14005	0.12733	0.00396	1877	642	2061	54	8.95	
J219 - 20.d	21.8	13.9	162		2.50000	0.06875	0.12386	0.00583	2169	309	2013	81	-7.77	
J219 - 21.d	21.3	16.9	215		2.49377	0.07774	0.13575	0.00823	2174	348	2174	102	0.00	
J219 - 22.d	23.7	12.1	168	0.751	2.63852	0.12183	0.13020	0.00454	2072	546	2101	60	1.39	
J219 - 23.d	24.7	21.7	318		2.94985	0.21319	0.12287	0.00726	1882	952	1998	101	5.83	
J219 - 24.d	13.7	7.6	98	0.026	2.53165	0.06089	0.12386	0.00678	2146	275	2013	94	-6.63	
J219 - 25.d	23.8	15.4	225		2.54453	0.10036	0.12981	0.00583	2137	448	2095	77	-1.97	
J219 - 26.d	31.6	23.1	295		2.72480	0.13735	0.13774	0.00678	2015	617	2199	83	8.35	
J219 - 27.d	44.3	39.2	471	0.007	2.60417	0.04069	0.12208	0.00396	2095	187	1987	57	-5.44	
J219 - 28.d	28.7	13.9	173		2.74725	0.08302	0.14338	0.00405	2001	381	2268	48	11.79	0.900
J219 - 29.d	24.8	12.2	147		2.65252	0.05629	0.13001	0.00513	2062	258	2098	68	1.71	
J219 - 30.d	47.8	35.2	450		2.71739	0.13661	0.13427	0.00405	2020	614	2155	52	6.24	
J219 - 31.d	42.1	29.9	373	0.001	2.53807	0.08052	0.13139	0.00499	2141	362	2117	65	-1.17	
J219 - 32.d	31.7	17.8	245	0.006	2.61097	0.10567	0.13417	0.00458	2090	475	2153	58	2.92	

Sample ID	Concentration				Radiogenic Ratio				Calculated Ages				Discordance	
Spot	*U*	*Th*	*Pb*	f^{204}	$^{238}U/^{206}Pb^*$		$^{207}Pb^*/^{206}Pb^*$		$^{238}U/^{206}Pb^*$		$^{207}Pb^*/^{206}Pb^*$		*Disc*	Disc. %
no.	*ppm*			*(%)*	*±1s*		*±1s*		*date (Ma) ±1s*		*date (Ma) ±1s*		*(%)*	2s lim.
J219 - 33.d	36.7	26	315	0.004	2.71003	0.12852	0.13248	0.00463	2025	578	2131	60	4.99	
J219 - 34.d	55	52	690	0.003	2.99401	0.21514	0.12713	0.00427	1858	964	2059	58	9.76	
J219 - 35.d	41.4	29.1	490	0.002	2.47525	0.10109	0.13050	0.00353	2187	448	2105	47	-3.93	
J219 - 36.d	42.5	48.6	620	0.002	2.51889	0.06345	0.13080	0.00427	2155	286	2109	56	-2.20	
J204 - 1.d	230	16.9	1010	0.000	2.43902	0.10708	0.13823	0.00248	2215	472	2205	31	-0.44	
J204 - 2.d	181	174	2010		1.70940	0.05698	0.14655	0.00231	2969	228	2306	27	-28.75	-24.218
J204 - 3.d	710	133	4360		3.87597	0.11267	0.16231	0.00218	1480	553	2480	23	40.34	38.632
J204 - 4.d	113	35.3	480	0.009	2.48756	0.11757	0.13447	0.00286	2178	519	2157	37	-0.98	
J204 - 5.d	169	24.2	840		3.77359	0.22072	0.14824	0.00333	1515	1037	2326	38	34.84	27.275
J204 - 6.d	120	65	710		2.52525	0.18493	0.14051	0.00329	2151	802	2233	40	3.71	
J204 - 7.d	189	72	1430		3.47222	0.11454	0.15775	0.00333	1632	549	2432	35	32.91	27.637
J204 - 8.d	206	56.3	1270		3.18471	0.08621	0.15290	0.00309	1760	410	2379	34	25.99	20.582
J204 - 9.d	112	39.3	540	0.000	1.73611	0.08590	0.13833	0.00275	2932	342	2206	34	-32.90	-24.019
J204 - 10.d	242	117	1480		3.19489	0.10718	0.14814	0.00279	1755	506	2325	32	24.48	18.796
J204 - 11.d	157	81.5	460	0.004	7.87402	0.37200	0.12644	0.00392	771	1839	2049	54	62.39	50.991
J204 - 12.d	175	96.8	1040	0.003	8.38223	0.33374	0.17341	0.00467	727	1682	2591	44	71.96	63.809
J204 - 13.d	1159	136.6	3410		5.29942	0.11795	0.14487	0.00218	1114	610	2286	26	51.26	48.785
J204 - 14.d	91	27.1	400	0.000	2.80899	0.12625	0.13357	0.00329	1963	574	2145	42	8.50	
J204 - 15.d	950	44	1420		7.66284	0.21139	0.12158	0.00228	791	1105	1980	33	60.06	54.407
J204 - 16.d	180	56.5	490		8.19672	0.43671	0.12793	0.00370	742	2119	2070	50	64.15	53.564
J204 - 17.d	247	59.6	740		7.51880	0.48052	0.12773	0.00383	805	2279	2067	52	61.06	49.990
J204 - 18.d	862	225	2050		20.70393	0.70728	0.18302	0.00329	304	3324	2680	29	88.66	82.202
J204 - 19.d	252	61.1	630		7.38007	0.23692	0.13080	0.00293	819	1222	2109	39	61.15	54.230
J204 - 20.d	122	40.7	339	0.007	4.73934	0.24707	0.12020	0.00357	1234	1197	1959	52	37.01	25.840
J204 - 21.d	845	26.8	5500		10.71811	0.24124	0.24555	0.00333	575	1285	3156	21	81.78	79.405
J204 - 22.d	545	15.1	4730		5.55247	0.14336	0.20373	0.00293	1068	739	2856	23	62.63	61.517
J204 - 23.d	89	23.1	460		2.82486	0.18753	0.13704	0.00413	1954	836	2190	52	10.80	

Sample ID	Concentration				Radiogenic Ratio				Calculated Ages				Discordance	
Spot	*U*	*Th*	*Pb*	f^{204}	$^{238}U/^{206}Pb^*$		$^{207}Pb^*/^{206}Pb^*$		$^{238}U/^{206}Pb^*$		$^{207}Pb^*/^{206}Pb^*$		*Disc*	Disc. %
no.	*ppm*			*(%)*	*±1s*		*±1s*		*date (Ma)*	*±1s*	*date (Ma)*	*±1s*	*(%)*	2s lim.
J204 - 24.d	145	79.6	1160		3.75940	0.15546	0.15894	0.00313	1520	747	2444	33	37.80	32.961
J231 - 1.d	151	174	1470		4.69484	0.17633	0.12822	0.00333	1245	875	2074	45	39.97	31.661
J231 - 2.d	14.6	6.39	458		3.18471	0.21806	0.22692	0.01413	1760	990	3030	96	41.91	23.503
J231 - 3.d	14.5	15	385	0.018	3.89105	0.24224	0.17341	0.00726	1474	1136	2591	68	43.09	30.120
J231 - 4.d	751	395	4640		18.58736	0.60461	0.18530	0.00583	338	2923	2701	51	87.49	75.134
J231 - 5.d	46.7	79	1150		2.84900	0.09740	0.12624	0.00513	1939	449	2046	70	5.22	
J231 - 6.d	390	380	1.73E+04		2.57732	0.09300	0.13922	0.00265	2114	418	2218	33	4.69	
J231 - 7.d	696	280	1.91E+04		3.37838	0.09131	0.13645	0.00228	1671	439	2183	29	23.42	18.436
J231 - 8.d	874	378	2.95E+04		3.71747	0.11747	0.13595	0.00228	1536	571	2176	29	29.43	24.711
J213 - 3.d	39	17	360		2.028398	0.3250373	0.195	0.087	2580	190	2840	360		
J213 - 1.d	154.8	82.9	768		2.584647	0.03006181	0.1343	0.003	2108	14	2153	15		
J213 - 2.d	200	46.3	407		3.937008	0.2015004	0.1319	0.003	1452	65	2122	16		
J213 - 3.d	182	70.6	716		3.03859	0.04431854	0.1339	0.0031	1834	19	2151	21		
J213 - 5.d	55	11.2	1160		2.591345	0.05640657	0.282	0.019	2103	36	3340	100		
J213 - 6.d	215	153	1230		3.04878	0.1022457	0.1344	0.003	1826	52	2154	14		
J213 - 7.d	170	55	554		2.884338	0.06738719	0.1341	0.003	1918	36	2151	16		
J213 - 10.d	11.3	10.1	158.2		2.777778	0.09259259	0.1786	0.0083	1982	49	2625	65		
J213 - 11.d	336	408	1450		6.329114	0.3124499	0.1345	0.0031	944	43	2155	19		

Appendix B2 – U-Pb Zircon Processing

Following is a description of the processing done for each sample in order to interpret an age from the U-Pb data.

Sample J231

This sample consists of a representative orthogneiss in the west of the Leaareig Domain (23º49'11"N 12º 23' 05"W). Three zircon grains were recovered from the sample, one of which is acicular and the other two were broken grains (Figure 0-1.).

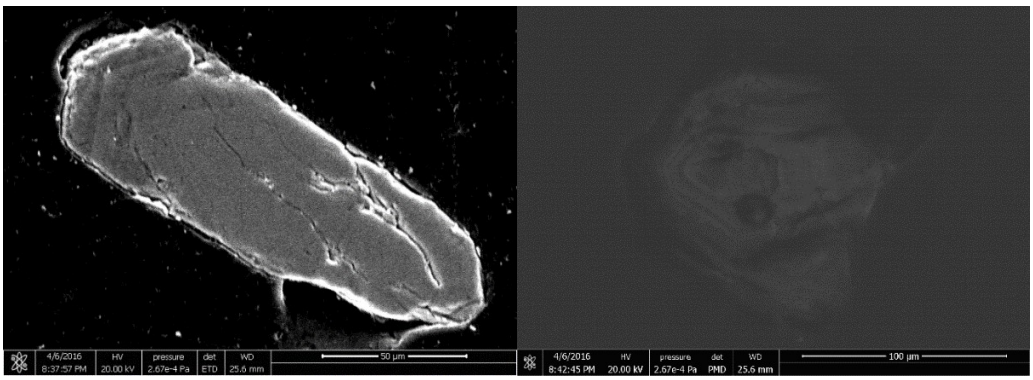

Figure 0-1 - Zircon grains from sample J231

Eight analyses were completed on the three zircon grains from the sample. The zircon grains have been affected by a significant degree of lead loss and common lead (Figure 0-2). Four of the points were excluded from the dataset as outliers. The trend of the four remaining points show the age of the zircon grains to be **2216 ± 60 Ma (MSWD 2.0),** with the lead loss event at 306 ± 210 Ma (Figure 0-3.).

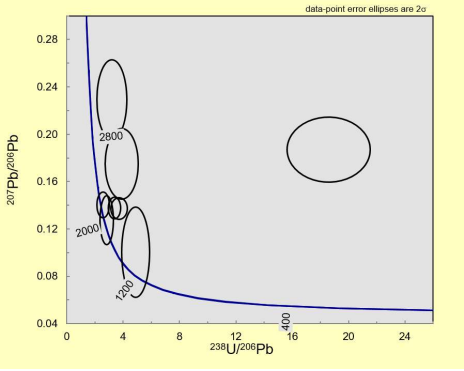

Figure 0-2 - All data from sample J231 illustrating a significant degree of lead loss and common lead

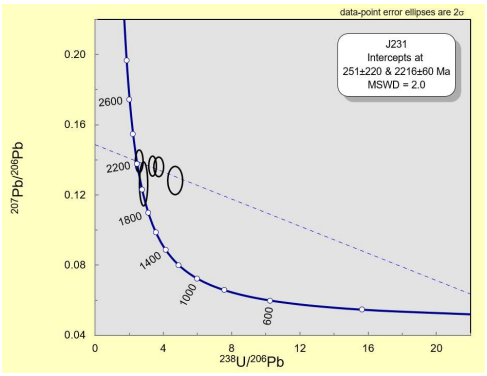

Figure 0-3 – The trend from a subset of data points from sample J231, giving an age of 2216 ± 60 Ma (MSWD 2.0), with the lead loss event at 251 ± 220 Ma

Sample J234

This sample is a representative granodioritic gneiss of the Leaareig Domain (23º53'06"N 12º 57' 59"W). A range of zircon morphologies were observed ranging from larger green zircon grains, through to more acicular transparent to translucent crystals (Figure 0-4). Inclusions were observed in most zircon grains independent of morphology.

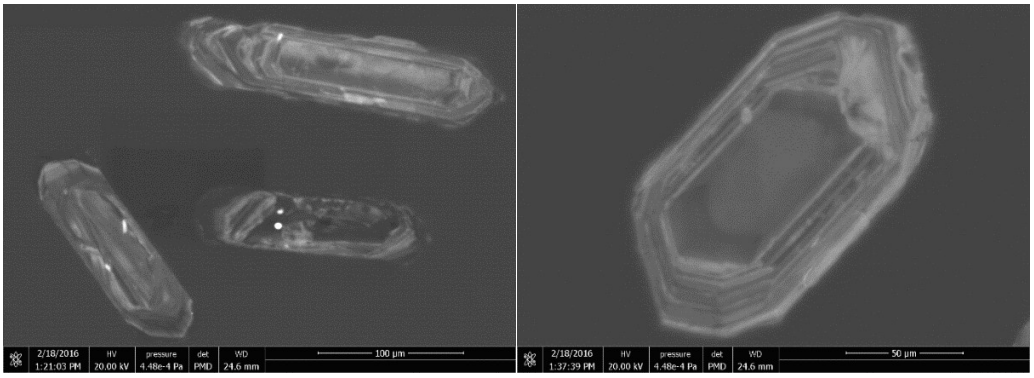

Figure 0-4 – Zircon grain morphologies observed in sample J234, including larger green zircon grains and more acicular transparent to translucent crystals

Fifty analyses were completed on 24 zircon grains from the sample. The zircon grains have been affected by a significant amount of lead loss and common lead (Figure 0-5). A subset of two concordant points gave an age of 2106 ± 60 Ma (MSWD 2.0) (Figure 0-6). With such a small subset, this age is unlikely to be very representative of the sample. The Anderson correction was applied to the data to remove the effect of common lead. With the correction applied, the data trend showed a strong lead loss event with the uncertainties of a large portion of the data points intersecting concordia at ~500 Ma. The trend of the most concordant of the corrected data gives an age of **2174 ± 69 Ma (MSWD 0.78)**, with the lead loss event pinned to 294 ± 86 Ma (Figure 0-7).

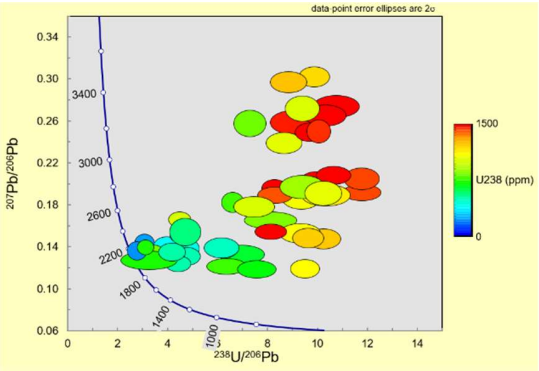

Figure 0-5 – Plot of the J234 analyses, coloured according to U238 concentration revealing a high degree of lead loss and common lead.

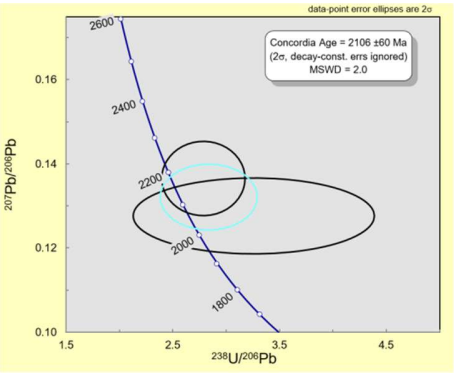

Figure 0-6 – Plot of a subset of two concordant analyses from J234

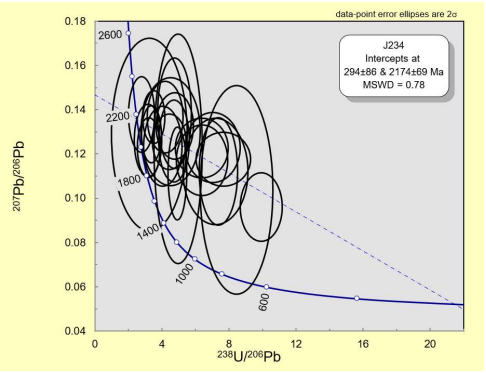

Figure 0-7 – Plot of the most concordant analyses from sample J234 after the Andersen (2002) correction was applied. Within uncertainty many of the data points intersect concordia at ~500-600Ma.

Sample J204

This sample is a paragneiss from the Agarasras Lakhadar Domain, bounded by a sole thrust bringing up the ophiolite complex (24º32’39”N 12º 33’ 48”W). The sample exhibits a moderate

degree of sericite alteration. Two zircon morphologies are observed in the sample including green coloured blocky grains; and smaller more transparent, acicular fractured grains (Figure 0-8). They both appear to have formed in the same event.

Twenty-four analyses were undertaken on 12 zircon grains. There was a high degree of discordance in most of the data points. The zircon grains have been affected to varying degrees of both lead loss and common lead in the system (Figure 0-9). The more discordant the data point, the more uranium the zircon has in it. This reflects the more metamict zircon grains, with more alpha damage to the crystal lattice allowing for a larger amount of common lead to be added. A subset of 5 concordant data points (discordance<11%) were used to calculate the concordant age of the sample at **2176 ± 32 Ma (MSWD 1.3;** Figure 0-10**)**. The Anderson (2002) spreadsheet was used to correct for common lead, with trend using all 24 corrected data points yielding an age of 2171 ± 49 Ma (MSWD 1.09) and a lead loss event at 374 ± 54 Ma (Figure 0-11). This is consistent with the age retrieved from the subset of concordant data. These have been interpreted as detrital zircons, representing an inherited age from the parent material.

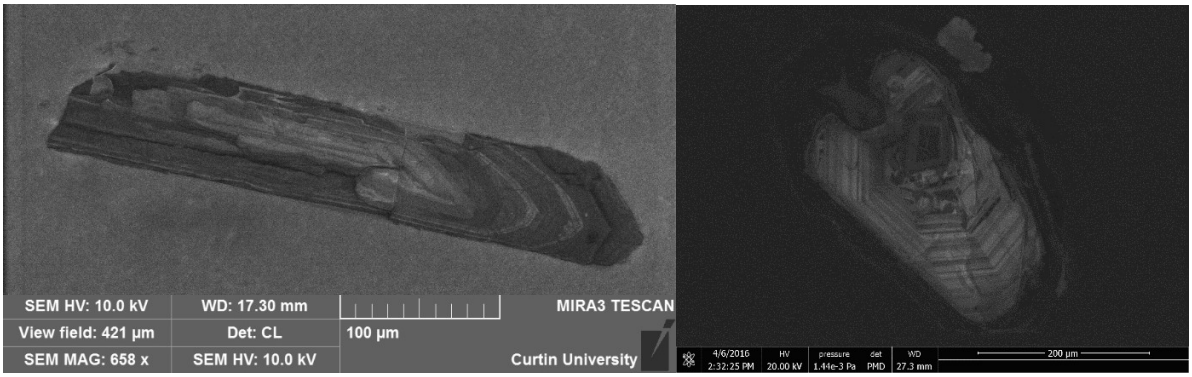

Figure 0-8 - - CL image of the two types of zircon morphologies in sample J204

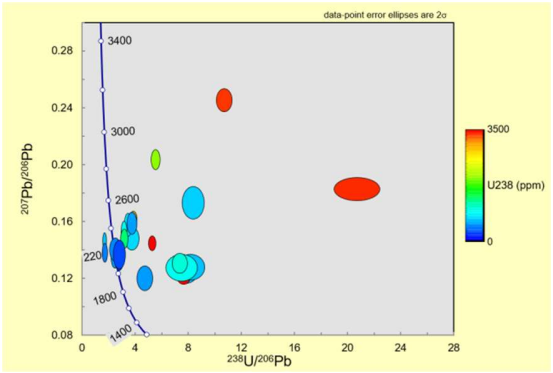

Figure 0-9 - Plot of the J204 analyses, coloured according to U238 concentration.

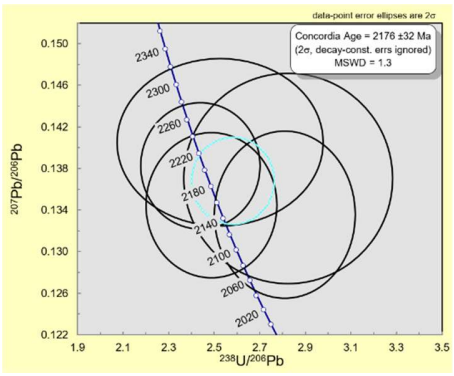

Figure 0-10 – Plot of 5 concordant points from sample J204

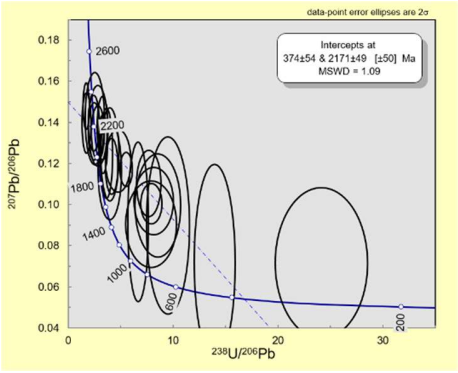

Figure 0-11 – Plot of the analyses from sample J204 after the Andersen (2002) correction was applied.

Sample J213

This sample is a weakly foliated granitic rock from the Taghsoumat-Aghsoumal Volcanic belt (24º20’00”N 12º 35’ 52”W). The sample has undergone a moderate to high degree of greenschist facies alteration with sericite alteration with chlorite and epidote present.

Due to sodium polytungstate precipitates forming during the heavy liquid stage of zircon separation no zircon grains were recovered from the separates. Zircon grains were identified, imaged and analysed in two polished thin sections. Zircon grains within the sample were relatively small ranging from very stubby to slightly acicular (Figure 0-12)

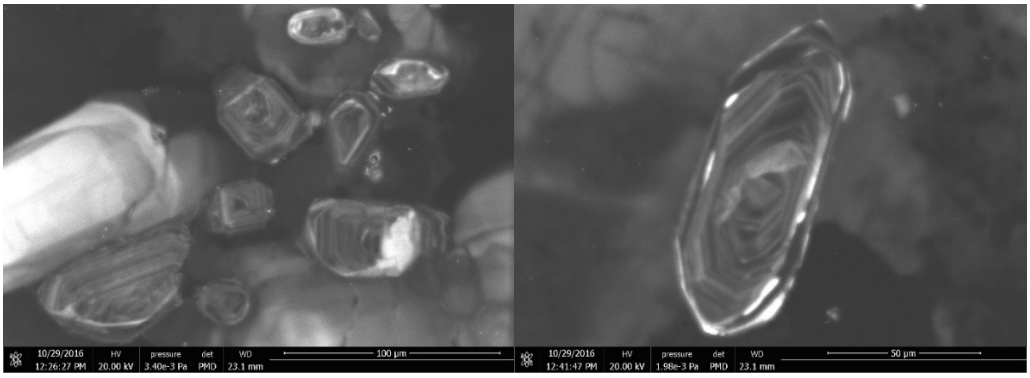

Figure 0-12 - CL images of zircon grains in-situ in a thin section of sample J213

Six analyses were undertaken on the sample. The sample had experienced a degree of lead loss with the regression providing an upper intercept at **2149 ± 21 Ma (MSWD 0.53;** Figure 0-13**)** A weighted average of the Pb207/Pb206 ages from five of the analyses were used to produce an age of 2152.9 ± 7.2 Ma (MSWD 0.041;Figure 0-14) which agrees with the regression age within uncertainty.

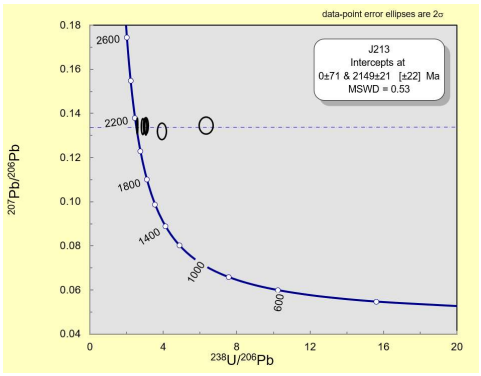

Figure 0-13 - Regression for the data from sample J213.

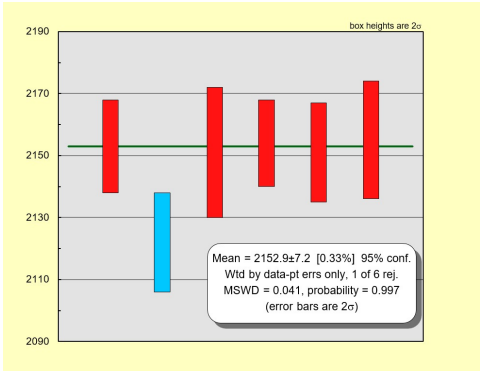

Figure 0-14 - Weighted average plot of the Pb207/Pb206 ages for J213

Sample J292

The sample is a red porphyry in the Taghsoumat-Aghsoumal Volcanic Belt metavolcanics belt (24º17'02"N 12º 30' 32"W), taken from a ~2m thick dyke. The sample is sericite altered and stained red in thin section. Variability in zircon morphology exists ranging from brightly cloudy medium sized block grains to clear acicular grains. Internal features shown in CL imagery is highly variable with some grains showing, mottled cores and inclusions and others showing more regular with small inclusions (Figure 0-15).

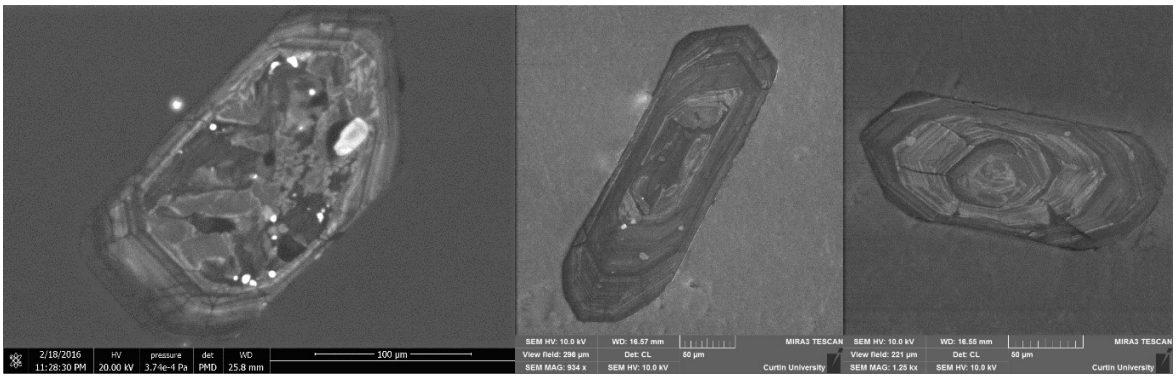

Figure 0-15 - CL images of zircons from sample J292 showing variations in form an, revealing complicated internal structures and inclusions

Thirty-five analyses were undertaken on sample J292. The data has been strongly affected by a major lead loss event and contained a large component of common lead (Figure 0-16). There is a greater amount of common lead in samples that have experienced more lead loss with the more discordant grains showing higher concentrations of U238. This strong trend reflects the more metamict zircon grains, with a greater degree of alpha damage to the crystal lattice, allowing larger amount of common lead to be added. Due to the large portion of common lead in the system, after the Andersen correction was applied, data points with the most lead loss and common lead had large uncertainties on them (Figure). A large portion of these points clustered around the 400-600Ma mark indicating that there was some sort of major lead loss event in this time period which removed almost all of the lead from this sample. A subset of 15 points revealed a concordant age of 561± 31 Ma (MSWD 1.4) interpreted as resenting a lead loss event. The trend of the most concordant corrected data reveals an intercept age of **2159 ± 140 Ma (MSWD 1.03;** Figure 0-17).

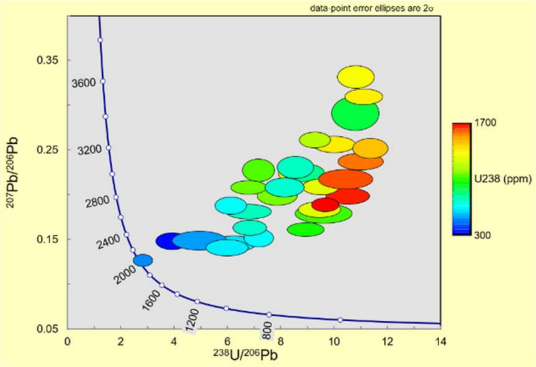

Figure 0-16 – Plot of the J292 analyses, coloured according to U238 concentration revealing the effect of lead loss and common lead.

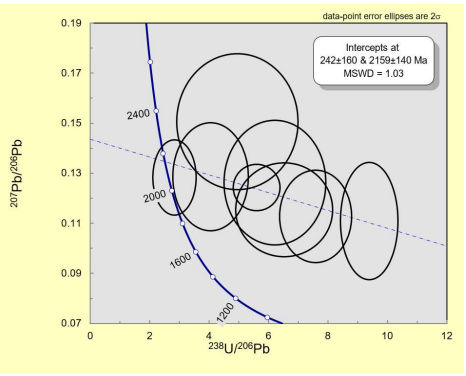

Figure 0-17 – Most concordant data plotted after the Andersen (2002) common lead correction has been applied to the data.

Sample J179

This sample comprises migmatitic gneiss outcropping to the south of the northen bulb of the Elmalhat Anorthosite Complex (23º52'51"N 12º 02' 34"W). The anorthosite complex is clearly observed intruding the gneiss on an outcrop scale with examples of it cross-cutting the gneissic fabric. Thus, this sample provides a maximum age constraint for the intrusion. The sample appears to have undergone very little alteration, having been metamorphosed to amphibolite facies. Two zircon morphologies were identified in the sample representing the same phase of crystallization. The larger blocky zircon grains were green in colour while the smaller, more acicular crystals were transparent to light pink with red staining along internal fractures (Figure 0-18).

Forty-nine analyses were undertaken on nineteen zircon grains. Two metamict data points, located on an internal feature within a zircon were excluded from the dataset as they had a very high concentration of uranium in the analysis (1258ppm, more than twice that of the rest of the points within the sample). These metamict analyses were not included.

The zircon grains had experienced a varying degree of lead loss. When plotted on the Tera-Wasserburg diagram, the trend of the 47 data points (with U<1000ppm) intersected concordia and

gave an age of **2142 ± 20Ma (MSWD 0.99;**Figure 0-19**)** having undergone very recent lead loss event (41± 50Ma). A subset of concordant points with a discordance of 5% or less within the data was then analysed. When plotted on a Tera-Wasserburg plot, these 13 points this produced an age of 2142 ± 21Ma with an MSWD of 1.2 (Figure 0-20), consistent with total dataset. The age interpreted for this sample, hence the maximum age constraint for the Elmalhat Anorthosite Complex is 2142 ± 20Ma.

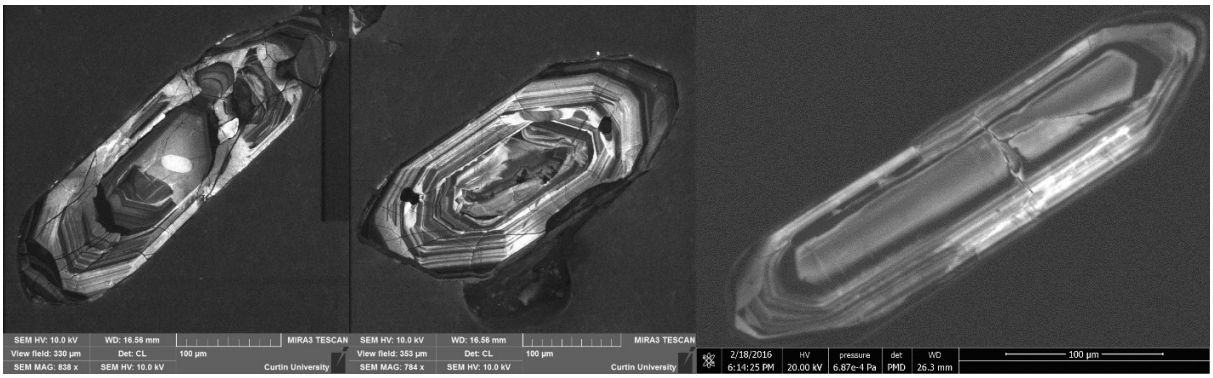

Figure 0-18 - Cathodoluminescence (CL) images of the two zircon morphologies in sample J179. a, b - blocky, green coloured zircon grains. c – acicular zircon grains colourless to pink sometimes with red staining along internal fractures.

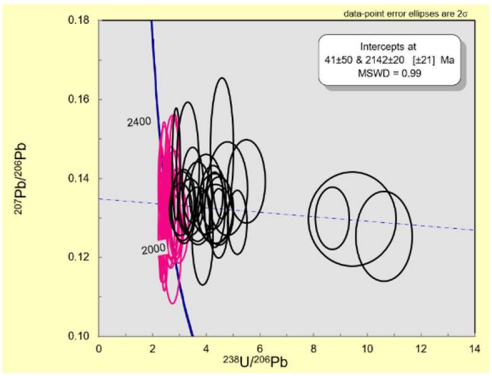

Figure 0-19 –Plot for J179 with 2 data points with U>1000ppm removed

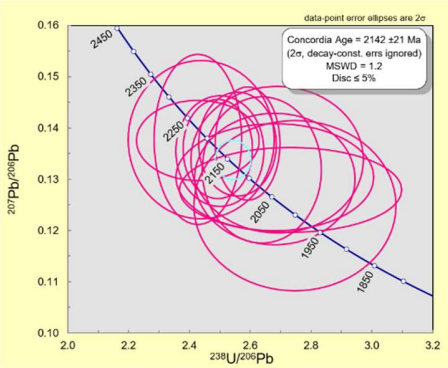

Figure 0-20 - Plot for J179 showing a subset of 13 concordant points with discordance of less than 5%

Sample J247

This sample is monzogranite from an intrusion in the Elmalhat Domain (23º59'16"N 12º 08' 07"W). It is observed in the field to be cross-cutting the anorthosite between the northern limb and the northern bulb. A range of zircon morphologies were observed with slightly smoky zircon grains with red staining in ranging from highly acicular to blocky (Figure 0-21).

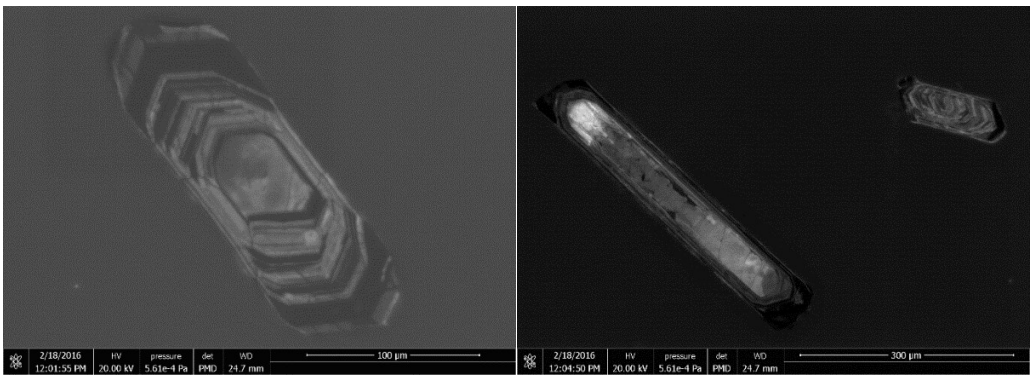

Figure 0-21 - Zircon grains from sample J247 ranging in form from blocky to acicular

Twenty-nine analyses were undertaken from 15 zircon grains. Plotted on a The sample has been affected both lead loss and the addition of common lead with the most discordant data points recording higher U238 content (Figure 0-22). The one concordant data point gives an indication of the age of the sample (Figure 0-23; 2103 ± 74 Ma), though the Andersen correction for common lead was applied to the data calculate a more robust age. With the exclusion of one metamict point with a ^{238}U concentration of over 4000ppm, the trend of the corrected data gave an intersect age of **2129 ± 46 Ma (MSWD 1.01)** with a lead loss event at 158 ± 34 Ma (Figure 0-24). The age calculated following the Andersen corrected data consistent with the single concordant data point within uncertainties.

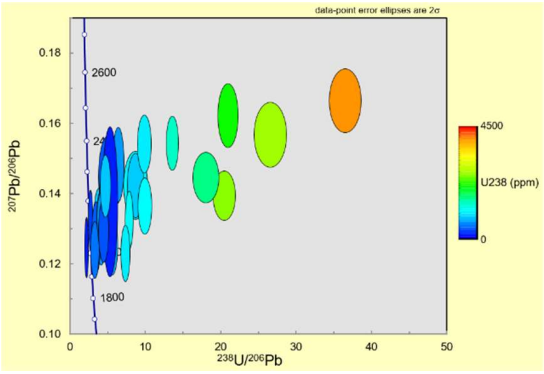

Figure 0-22 – Plot of the J247 analyses, coloured according to U238 concentration revealing a high degree of lead loss and common lead.

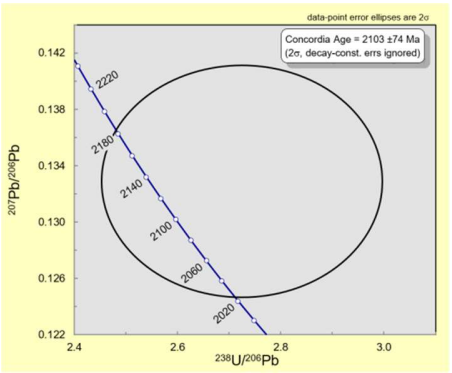

Figure 0-23 – Subset of one concordant point from J247

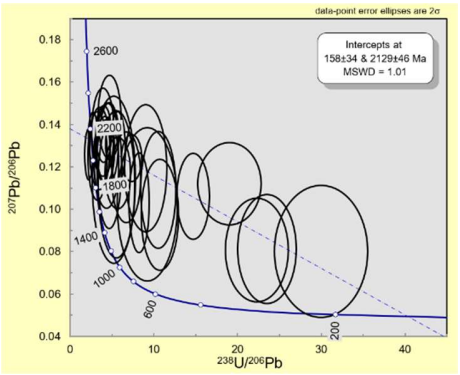

Figure 0-24 –Plot of the Andersen-corrected data from sample J247

Sample J240

This sample a weakly foliated muscovite-rich leucogranite in the Elmalhat domain to the south of Moug El Kaleb (23º47’27”N 12º 16’ 11”W). The zircon grains from the sample ranged from blocky to acicular grains some of which contained inclusions (Figure 0-25).

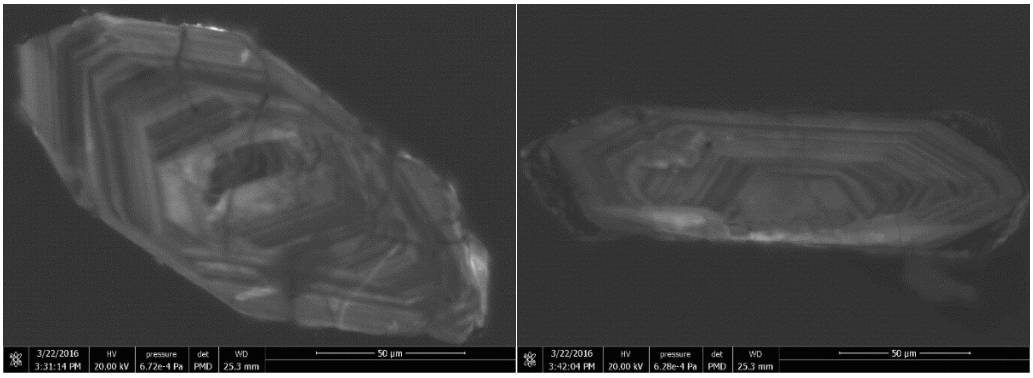

Figure 0-25 - Zircon morphologies from sample J240 showing blocky and acicular crystal form

Thirty-one analyses were undertaken on 14 zircon grains from the sample. The data has undergone some recent lead loss (Figure 0-26), and as such a weighted average of the $^{207}Pb/^{206}Pb$ ages was used for all 31 points to calculate the age for the sample as **2127 ± 20 Ma (MSWD 0.98;** Figure 0-27**)**. Subset of 13 concordant points (with a discordance less than 10%) was used to calculate a concordant age of 2121 ± 24 Ma (MSWD 1.06; Figure 0-28), consistent with the $^{207}Pb/^{206}Pb$ age within uncertainty.

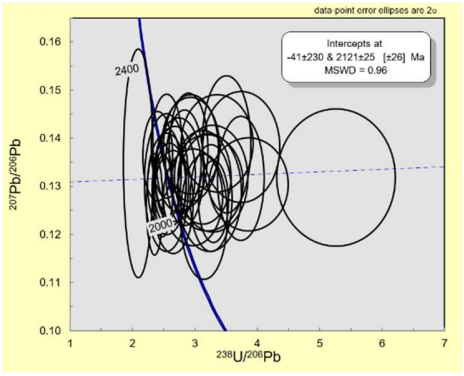

Figure 0-26 – Plot of the data form J240 indicating a recent lead loss event.

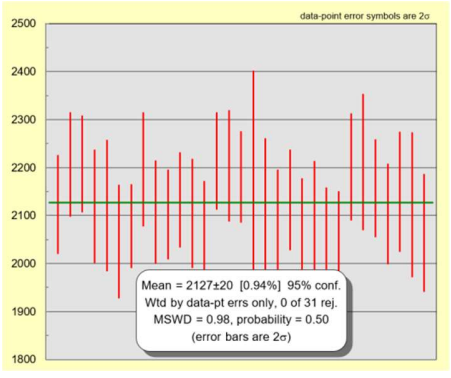

Figure 0-27 – Weighted average of $^{207}Pb/^{206}Pb$ ages for sample J240

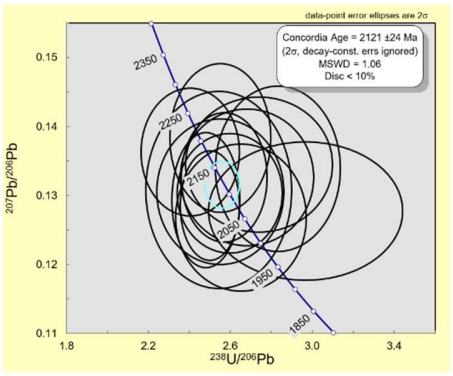

Figure 0-28 – Subset of 13 concordant points from sample J240.

Sample J246

This sample is a porphyry in the Elmalhat domain that cross-cuts the Elmalhat Anorthosite Complex and basement gneiss (23º52'31"N 12º 01' 17"W). The sample is taken from within the Anorthosite complex where the porphyry had cross-cut it.

Two types of zircon grains are observed from the sample. Blocky zircon grains with cores and rims observed using CL imaging and more acicular grains (Figure 0-29). These zircon grains represent two separate geochronological events with the cores of the blocky zircon grains representing xenocrysts while their rims and the acicular zircon grains represent later crystallisation, interpreted as the age of crystallisation following emplacement.

Thirty-five analyses were undertaken on 17 zircon grains. Two populations were identified in the data. The cores blocky zircon grains yielded an age of 2282 ± 54 Ma (MSWD 1.02) with a lower intercept of 108 ± 51 Ma (Figure 0-30). the acicular zircon grains as well as rims of the blocky zircon grains yielded an age of **2123 ± 69 Ma (MSWD 0.57)** with a lower intercept of 140 ± 120 Ma (Figure 0-31). The date from the cores is interpreted as being inherited from another rock while the rims while the acicular zircon grains and rims reflect the emplacement age.

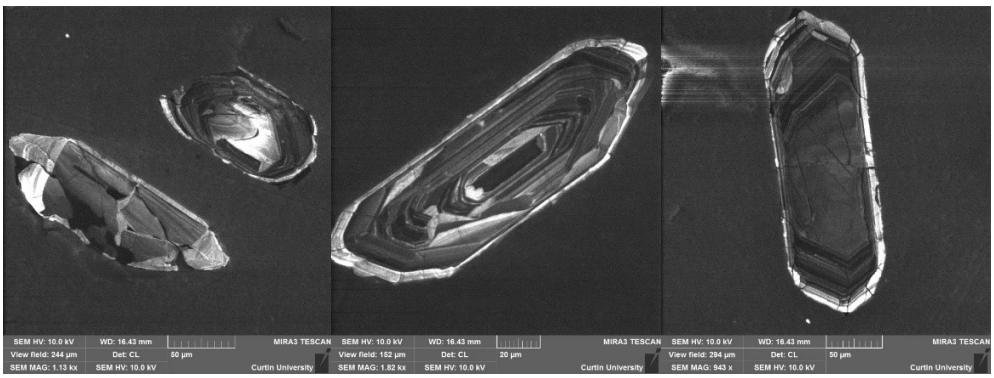

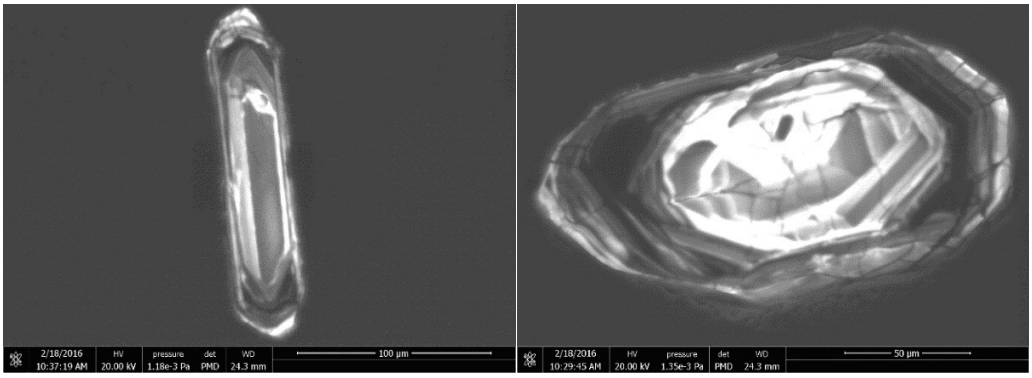

Figure 0-29 – Two types of zircon grains present in sample J246. Inherited blocky zircon grains with a younger rim and younger acicular grains formed during crystallisation of the porphyry.

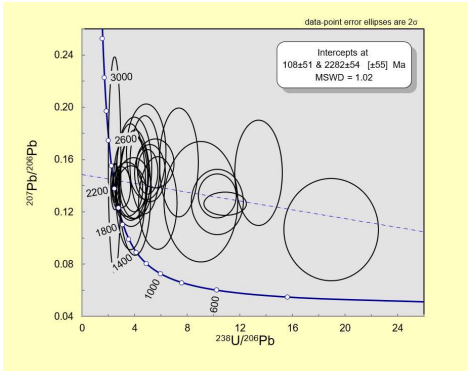

Figure 0-30 – Cores of blocky zircon grains reflecting an inherited age in sample J246

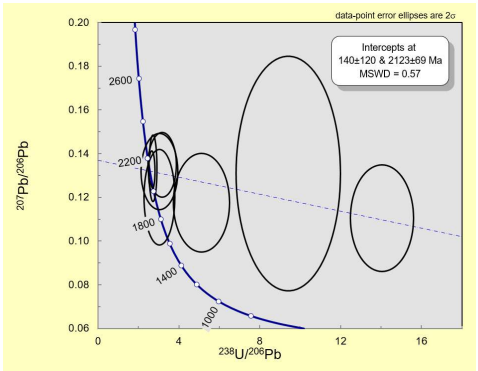

Figure 0-31 - Acicular zircon grains and rims reflecting the age of emplacement for J246

Sample J220

This sample is a monzogranite gneiss with minor sericite alteration, representative of the granite-gneiss belts of the Oum Abana belt (24º14’39”N 12º 25’ 50”W). Two zircon morphologies were

identified including larger, blocky smokey/green zircon grains and some smaller, fractured pink acicular grains (Figure 0-32), both of which appear to have formed at the same time.

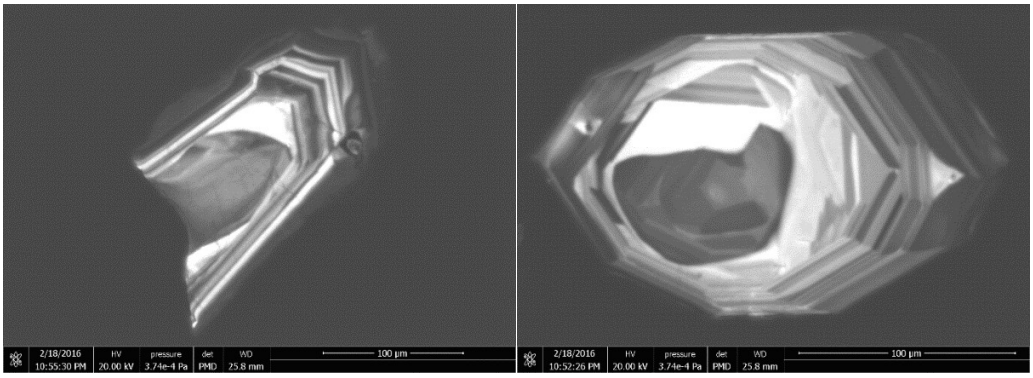

Figure 0-32 – morphologies of zircon grains from sample J220 including larger, blocky smokey/green zircon grains and smaller, fractured pink acicular grains.

Thirty-nine analyses were undertaken on 19 zircon grains. Some zircon grains appear to have been affected both by lead loss and common lead with more discordant grains have that the higher U (Figure 0-33). After applying the Andersen correction (discarding 6 metamict zircon points (24, 26, 30, 9, 17 and 30) with U concentrations above 400ppm and one point that could not be resolved by Andersen's algorithm (36)) a weighted average of the $^{207}Pb/^{206}Pb$ age was calculated as **2130 ± 25Ma** (MSWD 0.93; Figure 0-34). A subset of the 26 concordant data points following the Andersen (2002) correction was used to calculate the age of the sample as 2134 ± 22 Ma (MSWD 1.05; Figure 0-35), consistent with that of the $^{207}Pb/^{206}Pb$ weighted average .

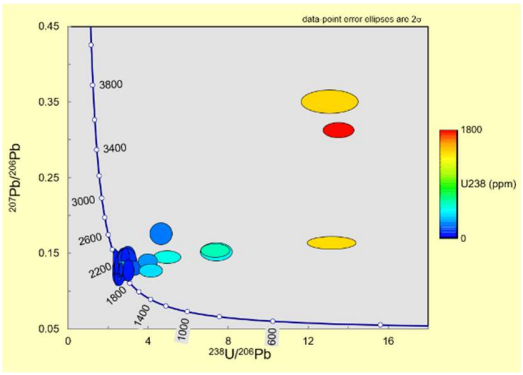

Figure 0-33 –Plot of the J220 analyses, coloured according to U238 concentration.

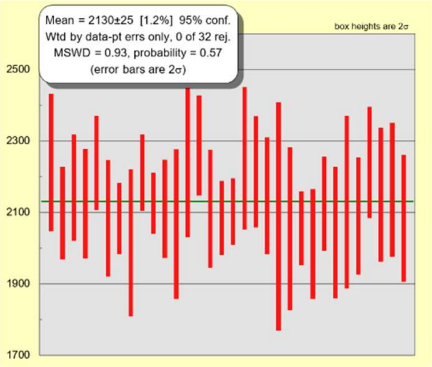

Figure 0-34 – Weighted average of the $^{207}Pb/^{206}Pb$ dates for J220 after the Andersen correction was applied

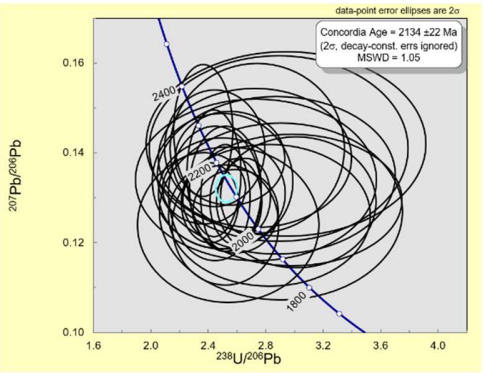

Figure 0-35 –Plot of 26 concordant data points after the Anderson Correction for sample J220

Sample J287

This sample consists of rhyolite from the Oum Abana belt to the south of Agarasras Labiad (24º26'03"N 12º 24' 33"W). The sample is slightly courser grained than other outcrops of rhyolite in the area. A variation was observed in the zircon grains from acicular and relatively transparent to dark and blocky (Figure 0-36), both reflecting the same ages.

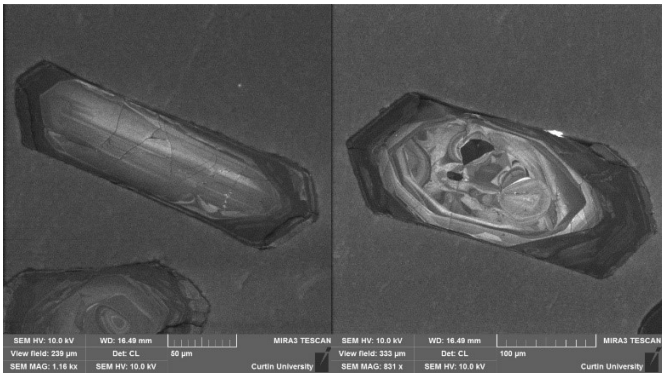

Figure 0-36 - CL images of zircons from sample J287 with blocky zircons showing more internal structure than acicular grains

Forty-three analyses were undertaken on 23 zircon grains from sample. The sample was strongly affected by both lead loss and common lead (Figure 0-37) as such a subset of 13 concordant points (Figure 0-38) with a discordance less than 7% were used to calculate a concordant age of **2122 ± 18 Ma (MSWD 1.2)**.

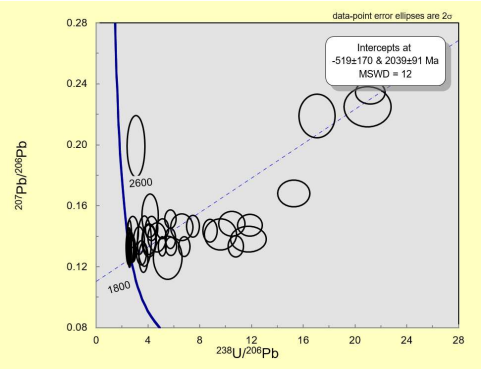

Figure 0-37 - All data from sample J287

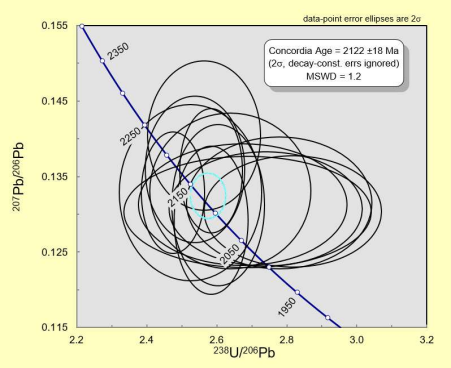

Figure 0-38 - Subset of 13 concordant points with a discordance <7% from sample J287 showing a concordant age of 2122 ± 18 Ma (MSWD 1.2).

Sample J205

This sample is biotite-muscovite-paragneiss from the Oum Abana belt, just south of the Agarasras Lakhadar thrust (24º31'54"N 12º 34' 25"W). It displays minor amount of sericite alteration. Two zircon morphologies were identified in this sample including pink, blocky grains and smaller, more acicular clearer grains (Figure 0-39), both of which appear to have formed in the same event.

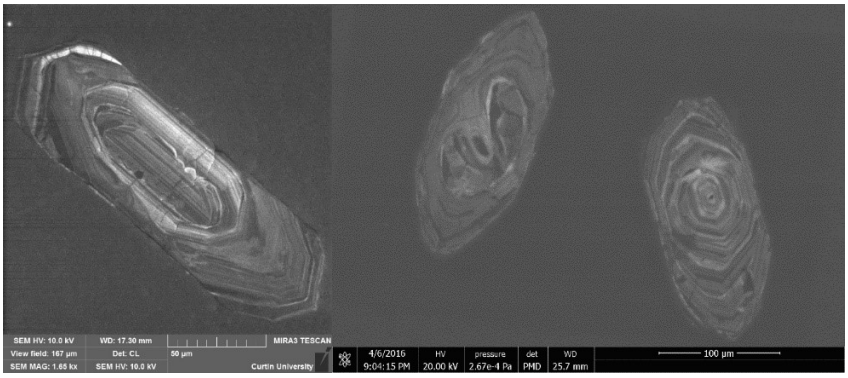

Figure 0-39 – CL image of the two types of zircon morphologies from sample J205 including a) – clear acicular grains and b) – more blocky, pink grains.

Fifty-four analyses were undertaken on 32 zircon grains. One metamict point was excluded from the dataset. The sample has been affected by a significant degree of lead loss as well as some common lead (Figure 0-40). There is a strong trend showing the more discordant grains have that the higher U, reflecting the more metamict zircon grains, with more alpha damage to the crystal lattice allowing for a larger amount of common lead to be added. It was not possible get a concordant age from a subset the data from this sample. The Andersen (2002) method was used to correct for common lead in the data. The trend of the 53 corrected data points gave an age of **2110 ± 25 Ma (MSWD 1.3;** Figure 0-41**)** with a recent lead loss event at 117 ± 82 Ma.

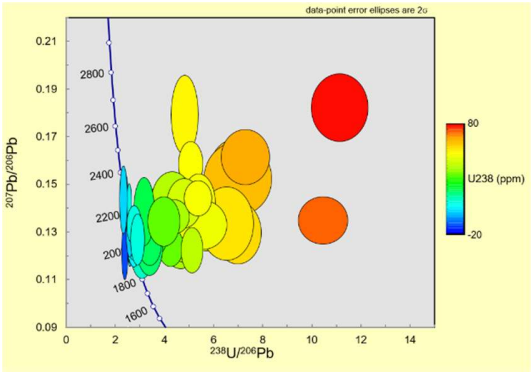

Figure 0-40 -Plot of the J205 analyses, coloured according to U238 concentration.

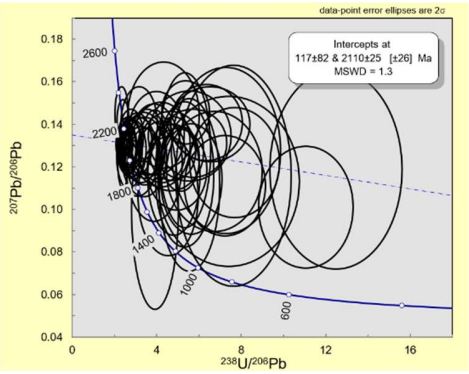

Figure 0-41 – Plot of the analyses from sample J205 after the Andersen (2002) correction was applied.

Sample J253

This sample is sericite altered monzogranite from a late intrusion in the Oum Abana belt to the north of Agarasras Labiad (24º37'45"N 12º 22' 32"W). The sample contains blocky zircon grains with internal features visible in CL imaging and inclusions present in some grains (Figure 0-42).

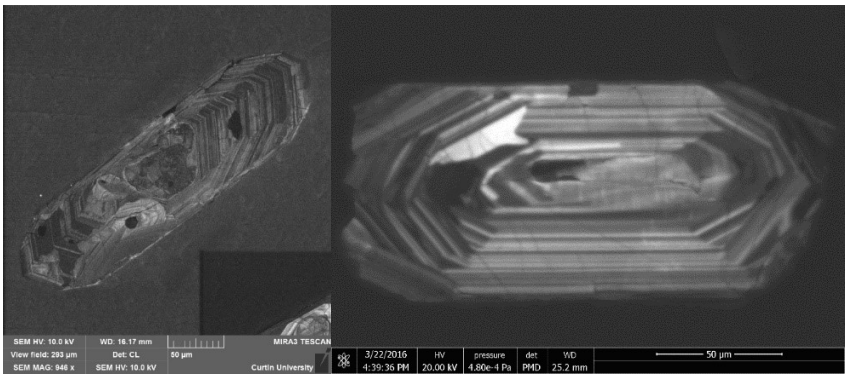

Figure 0-42 - CL images of zircons from sample J253 showing internal structure of the zircon grains ranging from acicular to blocky in form.

Forty analyses from 22 zircon grains were undertaken on the sample. The sample has been affected lead loss and had common lead, with two metamict data points having to be excluded for the analysis (Figure 0-43). A subset of two concordant data points gave an approximate age of 2080 ± 71 Ma with an MSWD of 2.2 (Figure 0-44). For a more statistically valid age, a trend of 38 points following the Anderson (2002) correction was used to calculate an age of **2109 ± 43 Ma (MSWD of 0.94)** and a lead loss event at 149 ± 47 Ma (Figure 0-45). This is constant with the concordant points within uncertainties.

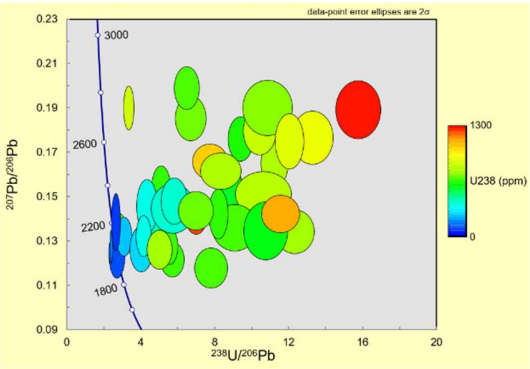

Figure 0-43 – Plot of the J253 analyses, coloured according to U238 concentration revealing the effect of lead loss and common lead.

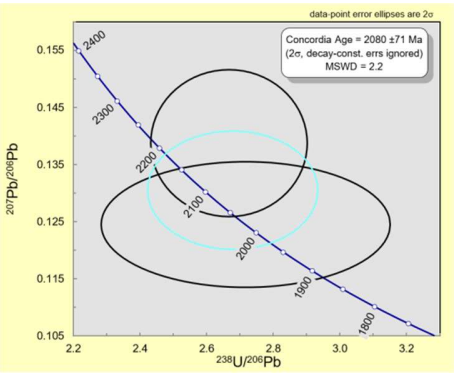

Figure 0-44 – Subset of two concordant point from J253

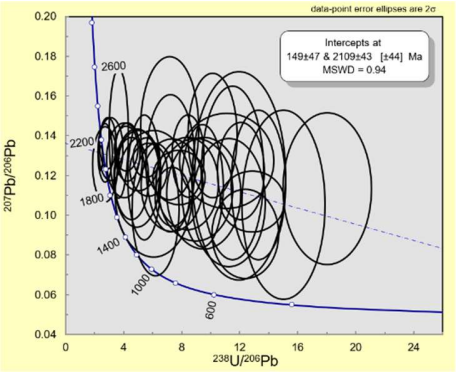

Figure 0-45 – Plot of the Andersen-corrected data from sample J253

Sample J219

This sample is a weakly sericite altered quartz monzodiorite gneiss, representative of the granite-gneiss belts of the Oum Abana belt (24º14’56”N 12º 25’ 47”W). Two zircon morphologies were identified in the sample including larger blocky grains with small inclusions and smaller, acicular grains (Figure 0-46) both of which appear to correspond to the same event.

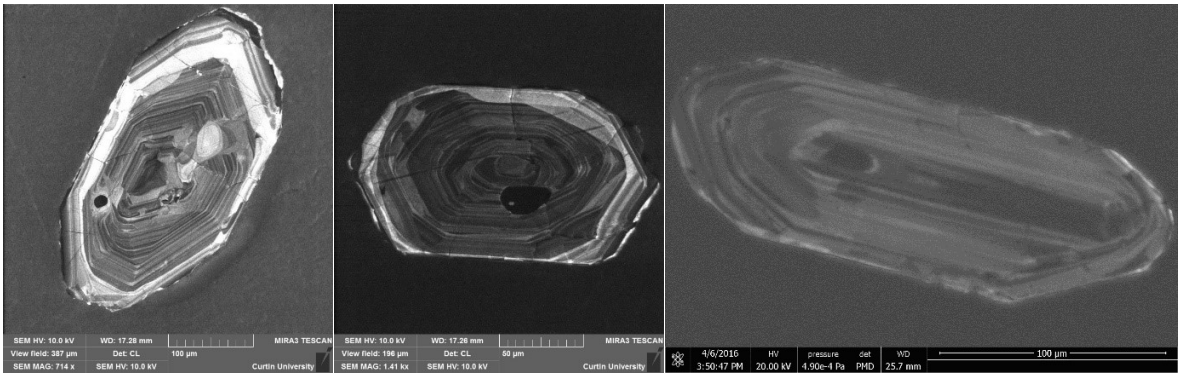

Figure 0-46 – Morphologies of zircon grains from sample J219 larger blocky grains with small inclusions and smaller, acicular grains.

Thirty-six analyses were undertaken on 21 zircon grains. The has been effected by having recent lead loss (Figure 0-47). The trend of the data on the plot indicates that the age of the sample is **2103 ± 24 Ma (MSWD 1.16)** with a recent lead loss event at 55 ± 94Ma. A subset of 26 concordant data points with a discordance of less than 10% was plotted, putting an age on the sample of 2101 ± 17 Ma (MSWD 1.19; Figure 0-48), a very similar age to the trend of all of the data points.

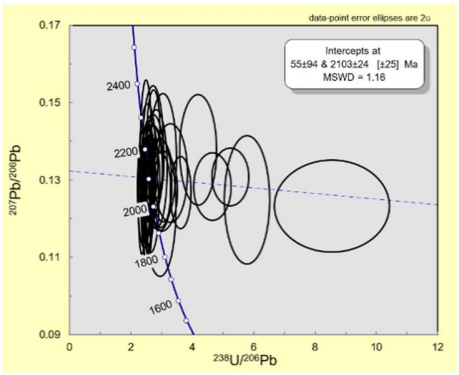

Figure 0-47 – Plot of all data from sample J219 with the trend showing an age of is 2103 ± 24 Ma (MSWD 1.16)

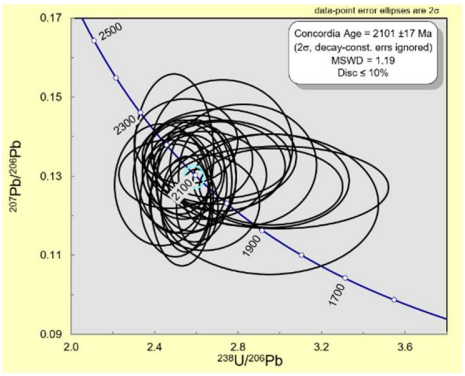

Figure 0-48 –Plot of a subset of 26 concordant points from sample J204 revealing an age of 2101 ± 17 Ma (MSWD 1.19)

Sample J197

This sample is a foliated tonalite from the Agarasras Labiad intrusion in the Oum Abana belt (24º30'34"N 12º 23' 11"W). Found in association with both copper and gold mineralisation, this intrusion is important from an economic point of view. The sample has undergone greenschist facies alteration, with extensive sericite alteration of the feldspars and the mafic components having been altered to chlorite. Only one zircon morphology was identified in the sample with pink blocky zircon grains (Figure 0-49), varying from larger darker pink zircon grains to smaller zircon grains that only have a tinge of pink.

Forty-four analyses were undertaken on 20 zircon grains. Two data points were excluded due to metamictisation (U238>500ppm). Although the sample has not been strongly affected by lead loss or common lead (36 analyses plotting concordantly with a discordance of less than 10% on a Tera-Wasserburg plot), a small degree of lead loss is evident, hence a weighted average of the $^{207}Pb/^{206}Pb$ dates were taken for the calculation of the age of this sample. This yielded an age of **2097 ± 21 Ma (MSWD 0.98;** Figure 0-50**)**. A Tera-Wasserburg plot of a subset of 22 points with a discordance of less than 4% indicated an age for the zircon grains of 2115 ± 16 Ma (MSWD 1.3; Figure 0-51). This is consistent with the Pb207/Pb206 weighted average within uncertainties.

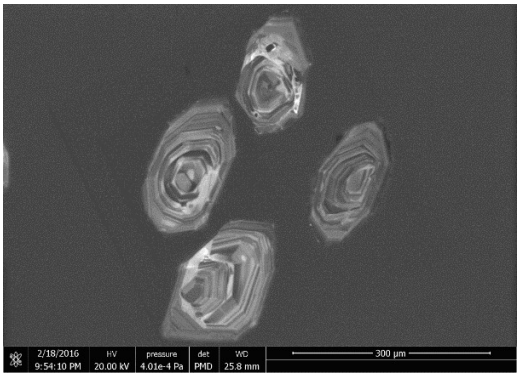

Figure 0-49 - CL image of pink, blocky zircon grains from sample J197.

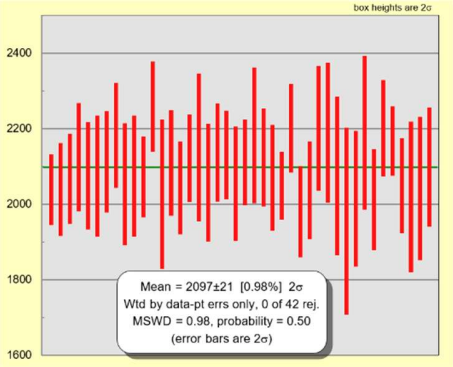

Figure 0-50 - Weighted average plot of the Pb207/Pb206 ages for J197

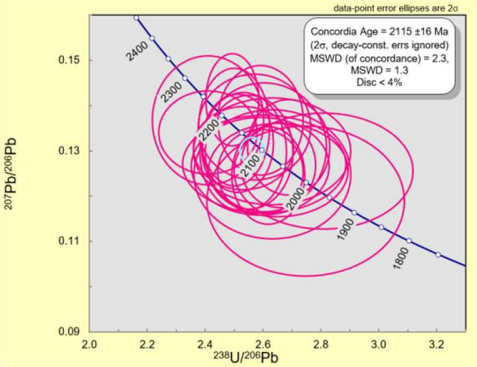

Figure 0-51 – Plot for J197 of a subset of 22 points with a discordance of less than 4%

Sample J273

This sample is granodioritic gneiss in the Oum Abana belt, to the east of the large mafic intrusion (24º26'59"N 12º 28' 34"W). It is moderately sericite, chlorite and epidote altered. Two zircon morphologies (Figure 0-52) were identified in the sample with clear, more acicular zircon grains and pink, blocky zircon grains ones ranging from darker pink when large and only a tinge of pink in the smaller grains. Some grains were also stained yellow.

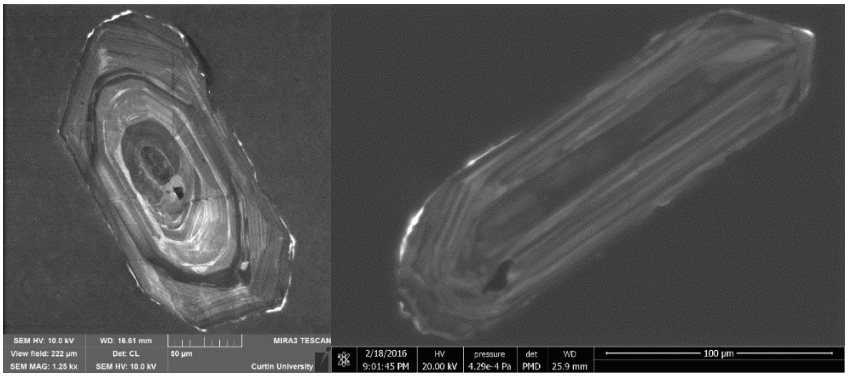

Figure 0-52 - CL images of zircon grains from sample J273 showing blocky and acicular grains.

Fifty analyses were undertaken on 23 zircon grains. One bad data point, located on an inclusion within the zircon was removed. The sample has been affected by lead loss with a minor component of common lead (Figure 0-53). A subset of 29 concordant points with a discordance of less than 7% gave an age of **2093 ± 17 Ma (MSDW 1.13;** Figure 0-54**)**. The trend of the entire data set gave an intercept age of 2079 ± 19 Ma (MSWD 1.3) with a lower intercept of 6 ± 180 Ma indicating recent lead loss, agreeing with the concordant point within uncertainty. As the concordant points have not been affected by lead loss and common lead and the number of analyses are statistically valid, the age of the sample has been interpreted as 2093 ± 17 Ma.

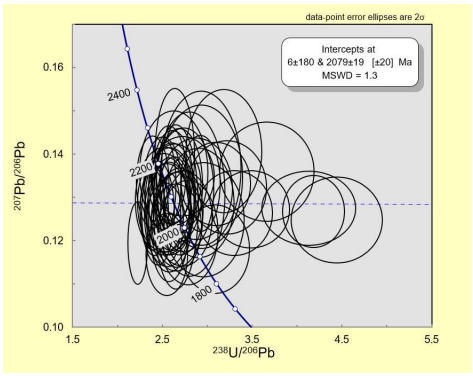

Figure 0-53 – Trend from all data points from sample J273

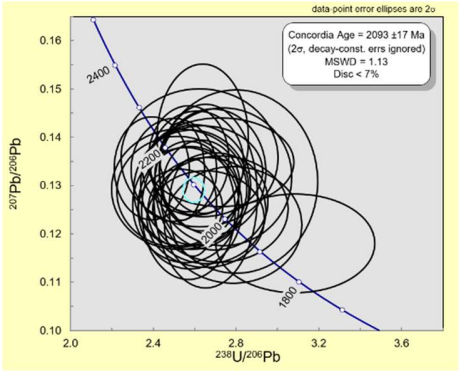

Figure 0-54 – Subset of 29 concordant points with a discordance of <7% from sample J273
Sample J275

This sample is sulphide-bearing granodiorite intruding the Oum Abana belt to the south of Agarasras Lakhadar (24º24'12"N 12º 32' 28"W). It has undergone a moderate-to-high degree of alteration (sericite, epidote and chlorite). Two of the zircon grains from the sample were corroded with internal features running through them. The other (incomplete) zircon was acicular with inclusions present (Figure 0-55)

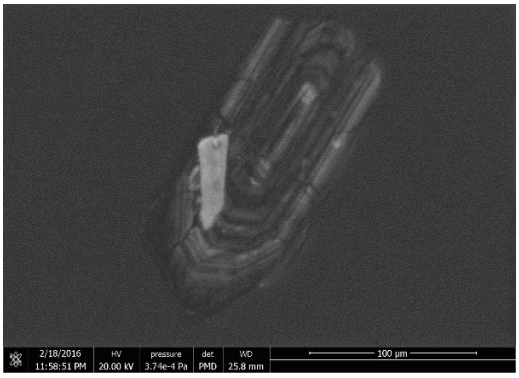

Figure 0-55 - CL image of an acicular zircon grain from sample J275 with inclusions

Nine analyses were undertaken on three zircon grains from the sample. Two of the zircon grains were metamict, strongly affected by lead loss and common lead with the data points scattered on a Tera-Wasserburg plot (Figure 0-56). The best interpretable data from this sample comes from three clustered points from one zircon. Using the assumption that this zircon was not affected by lead loss, the age was calculated by anchoring a common lead ratio of 0.83 and projecting back to the Concordia to get the age of the zircon. The age calculated is 513±17 Ma (MSWD 0.84) (Figure 0-57) is interpreted as reflecting a lead loss event at ca 500 Ma. A lead loss event also which is also observed in sample J292 (13.6km away in adjacent volcano-sedimentary belts) and sample J234 located close to a major shear zone.

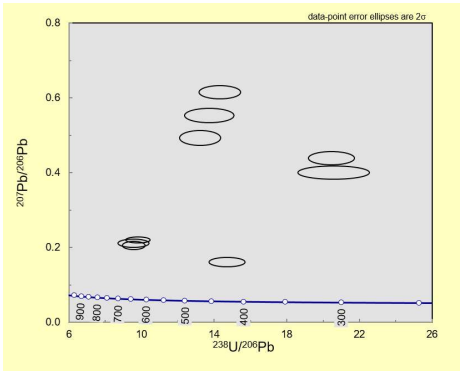

Figure 0-56 - Plot of all data from sample J275

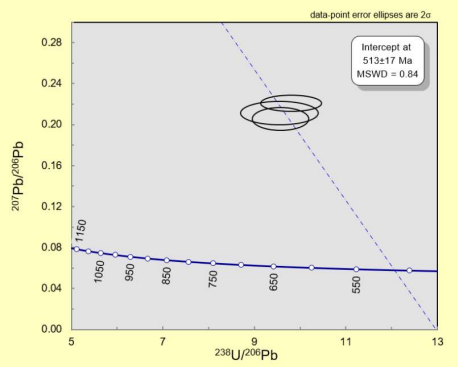

Figure 0-57 - Three clustered points from one zircon with a date interpreted by anchoring common lead (207/206) to a ratio of 0.83

Sample J238

This sample is an I-type migmatitic orthogneiss of the Saasaiat-Temmimchate-Tsabya Complex (23º37'21"N 12º 26' 12"W). The sample is relatively fresh having undergone a small degree of sericite alteration. Two main zircon morphologies were identified in the sample including larger stronger coloured (red and yellow) zircon grains and the smaller, more transparent zircon grains (transparent-pink tinge) both appearing to have formed at the same time. The zircon grains exhibit internal features with under CL imaging with inclusions present in some of the grains (Figure 0-58).

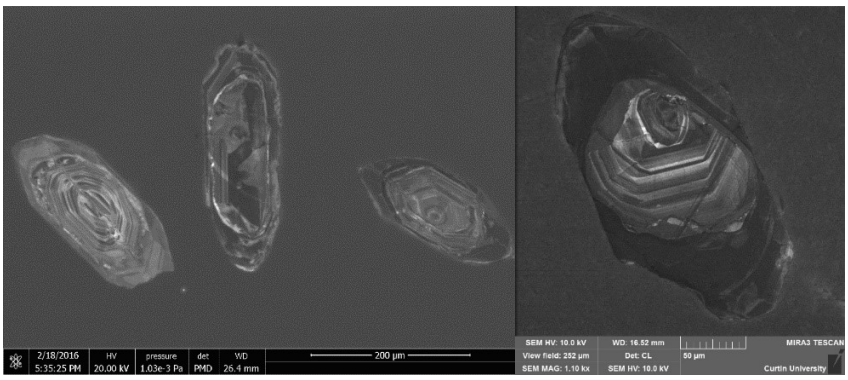

Figure 0-58 - CL images of zircon grains from sample J238

Forty-six analyses were undertaken on 22 zircon grains from the sample. As can be seen in Figure 22, the data has been strongly affected by lead loss (Figure 0-59). Eighteen metamict zircon points (U238>500ppm) were excluded from the examination of the data. A subset of the 21 concordant points were used to calculate a concordant age of **2100 ± 20 Ma (MSWD 1.05;** Figure 0-60**)**. The weighted average of the $^{207}Pb/^{206}Pb$ ages of 28 non-metamict points were used to calculate an age of 2119 ± 20 Ma (MSWD 1.00; Figure 0-61), consistent with the concordant sub-set. This is interpreted to represent the age of anataxis for the rock.

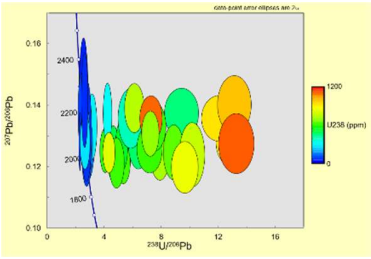

Figure 0-59 – Plot of the J238 analyses, coloured according to U238 concentration revealing a high degree of lead loss.

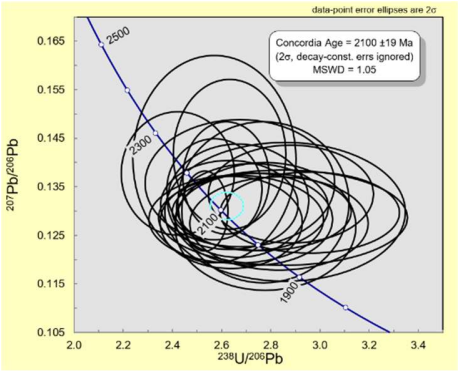

Figure 0-60 – Plot of a subset of 21 concordant points for sample J238 giving an age of 2100 ± 19 Ma.

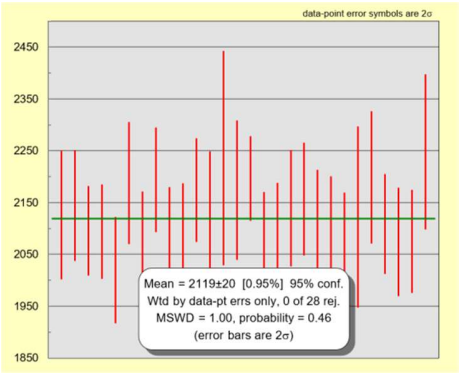

Figure 0-61 - Weighted average of the 207Pb/206Pb dates for J238

Sample J227

This sample is a biotite-muscovite-paragneiss of the Anajim Guebli Suite, north of the Elmalhat domain (23º58'17"N 11º 58' 46"W). Only two incomplete zircon grains were recovered from the sample, both very acicular (Figure 0-62)

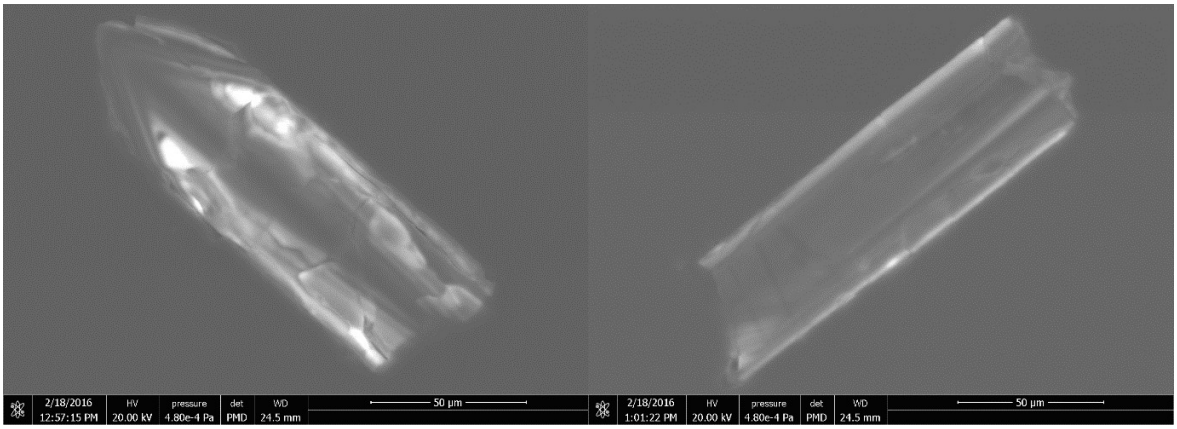

Figure 0-62 – Accicilar zircon grains from sample J227

Four analyses were completed on 2 zircon grains the sample. A subset of three concordant points was used to analyse the age of the sample with one metamict point being discarded (Figure 0-63). The weighted average of the $^{207}Pb/^{206}Pb$ ages for the three points produced an age of **2074 ± 51 Ma (MSWD 0.44;** Figure 0-64**)**. The same three concordant points were plotted on a Tera-Wasserburg diagram and gave an age of 2028 ± 98 Ma with an MSWD of 0.24 (Figure 0-65). These ages are consistent within the large uncertainties associated with such a small data set.

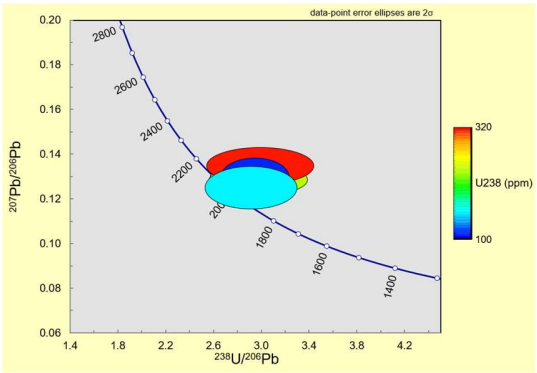

Figure 0-63 – Data points from sample J227 illustrating one uranium-rich metamict data point effected by the presence of common lead.

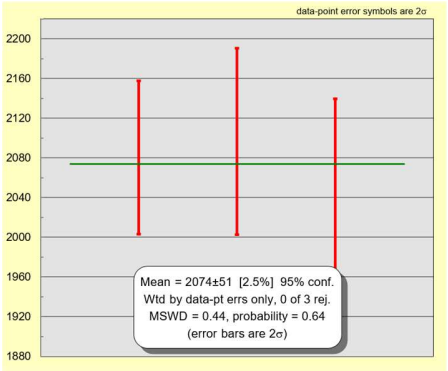

Figure 0-64 - Weighted average of the 207Pb/206Pb dates for J227

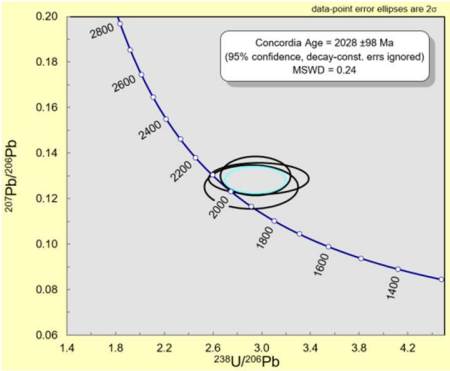

Figure 0-65 - Tera-Wasserburg plot of three concordant analyses from J227

Appendix B3 – Whole Rock Sm/Nd Geochronology

Six samples from the EAC were analysed for whole rock Sm-Nd geochronology Sm–Nd isotopic values were determined on whole-rock samples. The analyses were carried out at the Géosciences Rennes Laboratory using a 7 collectors Finnigan MAT-262 mass spectrometer. Samples were spiked with a 149Sm-150Nd mixed solution and dissolved in a HF-HNO3 mixture. They were then dried and taken up with concentrated HCl. In each analytical session, the unknowns were analysed together with the Ames Nd-1 Nd or the NBS-987 Sr standards, which during the course of this study yielded an average of 0.511956 (±5) and 0.710275 (±10) respectively. All the analyses of the unknowns have been adjusted to the long-term value of 143Nd/144Nd value of 0.511963 for Ames Nd-1. Mass fractionation was monitored and corrected using the value 146Nd/144Nd = 0.7219. Procedural blanks analyses yielded values of 50 pg for Nd and are therefore considered to be negligible.

The results of the analysis can be seen in

Table 6 – Whole rock Sm-Nd isotopic composition of samples from the EAC

Sample ID	J255	J256	J259	J262	J263	J270
Sm (ppm-prec.)	2.0	1.2	2.6	3.5	6.4	0.5
Nd (ppm-prec.)	8.9	5.9	11.4	12.9	32.2	1.9
Sm (ppm)	2.0	1.3	2.6	3.1	5.8	0.5
Nd (ppm)	8.2	6.1	11.8	12.4	31.1	1.9
147Sm /144Nd (± 0.4%)	0.146076	0.132402	0.133066	0.150487	0.112704	0.158337
143Nd / 144Nd (standard corrected)	0.512147	0.511933	0.511958	0.512192	0.511659	0.512338
Error (2se)	0.000005	0.000005	0.000005	0.000005	0.000005	0.000005
Epsilon (0)	-9.6	-13.7	-13.3	-8.7	-19.1	-2.2
Epsilon (t)	4.77	4.46	4.75	4.38	4.67	5.05
t (Ga)	2.2	2.2	2.2	2.2	2.2	2.2
T(DM2)	2142	2181	2153	2185	2169	2094
T(DM) de Paolo	2016	2080	2050	2051	2090	1935

Appendix C – Whole rock Geochemistry

Appendix C1 – Data

For whole rock geochemical analysis, 89 samples selected from across the study area were crushed, with an aliquot up to 250g then pulverised to 85% passing 75 microns. The sample was then analysed for 51 elements by Aqua Regia and ICP-AES/ICP-MS. The samples were analysed by ALS Geochemistry in laboratories in Dublin, Ireland.

The range of analysis for all major elements (SiO_2, Al_2O_3, Fe_2O_3, CaO, MgO, Na_2O, K_2O, Cr_2O_3, TiO_2, MnO, P_2O_5, SrO, BaO, LOI) is 0.01-100%. The range of analyses for the trace elements are listed in Table 7.

Table 7 – Analytical ranges for trace element analysis.

Ba	0.5-10,000	Hf	0.2-10,000	Sn	1-10,000	Y	0.5-10,000
Ce	0.5-10,000	Ho	0.01-1,000	Sr	0.1-10,000	Yb	0.03-1,000
Cr	10-10,000	La	0.5-10,000	Ta	0.1-2,500	Zr	2-10,000
Cs	0.01-10,000	Lu	0.01-1,000	Tb	0.01-1,000		
Dy	0.05-1,000	Nb	0.2-2,500	Th	0.05-1,000		
Er	0.03-1,000	Nd	0.1-10,000	Tm	0.01-1,000		
Eu	0.03-1,000	Pr	0.03-1,000	U	0.05-1,000		
Ga	0.1-1,000	Rb	0.2-10,000	V	5-10,000		
Gd	0.05-1,000	Sm	0.03-1,000	W	1-10,000		

Whole rock analyses from the Leaareig Terrane (Table 8), the Elmalhat Domain (Table 9), and the Oum Abana and Anajim Guebli Domains (Table 10) can be seen below.

Table 8 – Whole rock major and trace element geochemistry for the Leaareig Terrane. Data from ICP-MS analysis at ALS, Dublin.

Sample Number	*J174*	*J203*	*J204*	*J211*	*J212*	*J213*	*J231*	*J234*	*J238*
Domain	T-A belt	Agarasras Lakhadar	Agarasras Lakhadar	T-A Belt	T-A Belt	T-A Belt	Leaareig	Leaareig	Sassaiate
Name	Diorite	Gneiss	Para-gneiss	Rhyolite	Porphyry	Ortho-gneiss	Gneiss	Grano-dioritic gneiss	Migmatite
lat	23.970377	24.55205	24.544197	24.333802	24.324555	24.333309	23.819651	23.885054	23.622483
lon	-12.433128	-12.564392	-12.56327	-12.542169	-12.557362	-12.597654	-12.384619	-12.966311	-12.436566
SiO2	48.4	74.8	73.6	66	72.4	69.3	76.9	69.2	62.5
Al2O3	15	13.7	15.9	16.1	13.35	15.65	12.8	15.7	13.95
Fe2O3	7.54	1.57	1.11	3.14	2.55	3.02	1.48	3.72	8.08
CaO	12.4	1.28	2.24	3.92	1.21	3.03	1.07	3.23	5.13
MgO	9.33	0.35	0.08	1.25	0.84	0.9	0.11	1.05	2.77
Na2O	1.83	3.63	4.85	4.61	4.12	5.21	3.48	3.97	3.05
K2O	1.2	1.85	2.99	1.5	3.17	1.66	4.54	3.31	3.55
Cr2O3	0.02	0.01	0.01	0.01	0.01	0.01	0.01	0.01	0.02
TiO2	0.37	0.13	0.03	0.31	0.21	0.27	0.09	0.38	1.05
MnO	0.15	0.03	0.02	0.04	0.06	0.05	0.03	0.06	0.13
P2O5	0.12	0.01	0.02	0.05	0.07	0.07	0.01	0.1	0.36
SrO	0.05	0.02	0.03	0.06	0.01	0.06	0.01	0.02	0.03
BaO	0.06	0.05	0.11	0.1	0.17	0.05	0.11	0.07	0.13
LOI	2.31	1.67	0.5	2.78	1.33	1.41	0.47	0.6	0.97
Total	98.78	99.1	101.49	99.87	99.5	100.69	101.11	101.42	101.72
Ba	557	467	964	917	1480	443	913	594	1040
Ce	19	20.7	43.1	19	31.7	21.9	30.6	56.9	86.3
Cr	120	20	40	30	20	60	70	70	100
Cs	0.37	1.48	1.19	0.35	1.69	0.54	0.69	7.31	0.59
Dy	1.8	0.7	0.79	0.94	1.51	1.06	0.7	2.75	5.42
Er	0.96	0.36	0.33	0.54	0.91	0.63	0.35	1.43	3.01
Eu	0.84	0.45	0.78	0.48	0.48	0.59	0.44	0.9	1.67
Ga	14.1	18.8	16.6	18.3	18.6	20	18.3	20.3	16.8
Gd	2.05	1.17	1.88	1.41	2.15	1.43	1.1	3.08	6.24
Hf	0.9	2.8	3.2	2.5	2.4	2.5	2.1	4.4	6.7
Ho	0.34	0.12	0.12	0.15	0.3	0.19	0.15	0.6	1.2
La	8.5	10.9	25	9.4	16.2	10.6	16.9	31.7	42.7
Lu	0.14	0.01	0.01	0.03	0.08	0.06	0.03	0.23	0.43
Nb	1.5	8.7	1.3	3.6	7.4	2.5	3.8	6	14.8
Nd	11.3	8.3	18	8.2	12.7	10.8	10.7	25	43.2
Pr	2.41	2.25	4.55	2.29	3.63	2.69	3.13	6.34	10.15
Rb	27.2	68.5	74	33.8	100.5	36.2	137.5	151.5	106.5
Sm	2.33	1.6	2.9	1.6	2.49	2.37	1.91	4.28	8.49
Sn	1	4	3	1	1	1	3	3	3
Sr	485	224	318	579	185.5	627	167	301	388
Ta	0.1	1.2	0.2	0.3	0.6	0.2	0.2	0.6	0.9
Tb	0.24	0.13	0.16	0.16	0.27	0.16	0.13	0.36	0.92
Th	0.53	7.09	16.45	2.39	5.82	1.34	35.3	8.6	6.99
Tm	0.15	0.01	0.05	0.04	0.12	0.1	0.04	0.24	0.52
U	0.1	2.78	2.29	0.93	1.76	0.32	2.85	3.09	1.56
V	169	11	<5	48	27	38	<5	31	120
W	1	3	2	1	1	1	1	1	1
Y	8.8	4.1	3.5	5.1	9.7	6	3.9	15.8	30.9
Yb	0.9	0.36	0.24	0.37	0.73	0.53	0.32	1.61	2.94
Zr	34	82	112	85	67	100	50	160	287

Table 9 – Whole rock major and trace element geochemistry for the Elmalhat Domain. Data from ICP-MS analysis at ALS, Dublin.

Sample ID	*J159*	*J163*	*J169*	*J178*	*J179*	*J184*	*J190*	*J192*
Domain	Elmalhat	Elmalhat	Elmalhat	Elmalhat	Elmalhat	Elmalhat	Elmalhat	Elmalhat
Name	Metapyroxenite)	Massive Chromitite	Granite Gneiss	Granite	Migmatitic gneiss	Leuco-gabbro	Megacrystic Anorthosite	Garnet gneiss
lat	24.154923	24.047956	24.11850	23.88544	23.880726	23.87725	23.922225	24.06278
lon	-12.202961	-12.067477	-12.26046	-12.05139	-12.04286	-12.00169	-12.000427	-12.10082
wt%								
SiO2	44.3	13.85	65.9	73.2	65.1	51.4	44.4	76.2
Al2O3	5.89	21.7	17.15	15.25	17.45	25.4	30.8	14.4
Fe2O3	11.2	23.5	3.83	1.17	3.5	3.52	2.78	1.37
CaO	7.07	4.27	4.38	0.88	4.94	13	14.9	1.78
MgO	24.5	9.58	1.68	0.3	1.29	2.88	1.81	0.02
Na2O	0.5	0.04	5.18	4.82	4.54	3.02	1.9	6.13
K2O	0.15	0.06	0.82	2.18	0.88	0.6	0.49	0.54
Cr2O3	0.25	24.5	0.07	0.04	0.01	0.01	0.01	0.01
TiO2	0.46	0.63	0.33	0.03	0.28	0.18	0.07	0.01
MnO	0.15	0.25	0.06	0.04	0.07	0.05	0.03	0.28
P2O5	0.16	<0.01	0.1	0.02	0.1	0.25	0.01	0.01
SrO	0.01	<0.01	0.07	<0.01	0.04	0.02	0.02	<0.01
BaO	0.01	0.01	0.04	0.16	0.04	0.01	0.02	0.01
LOI	5.41	2.49	1.41	1.3	0.67	1.12	1.83	0.39
Total	100.06	98.9	101.02	99.39	98.91	101.46	99.07	101.15
(ppm)								
Ba	65.3	103.5	339	1425	395	111	185.5	116.5
Ce	29.1	1	24	17.2	12.3	16.1	7.5	17.9
Cr	1760	>10000	530	260	30	80	40	40
Cs	0.1	0.16	0.66	0.75	0.23	0.03	0.17	0.81
Dy	1.5	0.16	0.98	0.36	1.6	1.27	0.3	7.06
Er	0.75	0.08	0.57	0.39	0.9	0.7	0.18	4.08
Eu	0.94	0.08	0.64	0.17	0.55	0.6	0.29	0.28
Ga	8.8	46.5	19.7	21.2	19.4	21	15.9	25.9
Gd	2.44	0.16	1.42	0.45	1.53	1.75	0.41	4.43
Hf	1.7	<0.2	2.4	0.3	2.3	6.9	0.2	5.5
Ho	0.33	0.02	0.21	0.07	0.34	0.27	0.04	1.47
La	13.8	0.5	12	8.7	5.7	6.4	3.3	8.8
Lu	0.1	<0.01	0.05	0.04	0.11	0.12	<0.01	0.63
Nb	3.1	0.2	1.5	0.6	4.5	1	1.9	9.4
Nd	16.9	0.5	12	6.7	6.4	11	3.4	8.8
Pr	3.64	0.14	2.88	1.99	1.55	2.34	0.87	2.17
Rb	1.8	2.3	22	19.2	24	3	5.6	23.5
Sm	3.3	0.07	1.98	0.9	1.67	2.25	0.46	3.05
Sn	1	1	2	1	2	1	1	3
Sr	162	48.6	653	103.5	481	273	307	66.1
Ta	0.2	<0.1	0.1	<0.1	0.2	0.1	0.1	1.5
Tb	0.31	<0.01	0.14	0.02	0.26	0.19	0.05	1.07
Th	1.84	0.07	1.64	0.08	1.14	0.38	0.19	8.68
Tm	0.13	0.01	0.06	0.05	0.16	0.13	0.01	0.68
U	0.49	0.22	0.19	<0.05	0.13	0.14	0.17	4.77
V	68	1770	47	12	39	41	14	<5
W	2	1	1	2	1	1	1	1
Y	9.2	0.9	5.4	2.9	9.6	7.6	1.3	51.9
Yb	0.61	0.05	0.44	0.27	1.08	0.83	0.12	4.75
Zr	74	4	94	6	97	320	6	66

Table 9 – Continued

Sample ID	**J225**	**J229**	**J240**	**J241**	**J242**	**J243**	**J246**	**J247**	**J254**
Domain	Elmalhat domain	Elmalhat domain	Elmalhat domain	Elmalhat domain	Elmalhat domain	Elmalhat domain	Elmalhat domain	Elmalhat domain	Elmalhat domain
Name	Megacrystic	Metagreywacke	Leucogranite	Leuco-gabbro	Pegmatitic Leuco-gabbro	Orbitic Leuco-gabbro	Granite	Granite	Olivine Gabbro
lat	23.922235	23.824498	23.790883	23.741177	23.776768	23.802149	23.875368	23.987708	23.900018
lon	-12.005	-12.295214	-12.269589	-12.176479	-12.137448	-12.106119	-12.021498	-12.135325	-12.083901
wt%	(wt%)								
SiO2	46.6	70.8	77.9	47.7	49.6	49.5	67.9	69	48.2
Al2O3	30.2	15.75	13.25	9.59	22.8	24.1	16.2	15.55	10.3
Fe2O3	2.45	1.58	1.08	9.92	5.15	4.15	2.64	2.69	9.26
CaO	15.35	2.81	1.43	14.4	9.75	11.35	2.79	2.94	6.96
MgO	1.94	0.52	0.11	11.05	5.55	3.43	1.01	0.94	18.9
Na2O	1.91	5.32	3.63	1.75	2.97	3.41	5.88	4.89	2.3
K2O	0.12	0.85	2.73	0.45	0.21	0.3	0.86	1.61	1.03
Cr2O3	0.01	0.01	0.01	0.11	0.01	0.01	0.01	<0.01	0.21
TiO2	0.17	0.13	0.03	0.84	0.17	0.14	0.26	0.31	0.58
MnO	0.03	0.03	0.02	0.16	0.08	0.07	0.03	0.03	0.14
P2O5	<0.01	0.04	0.01	0.24	0.03	<0.01	0.09	0.12	0.2
SrO	0.01	0.06	<0.01	0.03	0.05	0.05	0.06	0.06	0.06
BaO	<0.01	0.08	0.14	0.06	0.02	0.01	0.08	0.08	0.04
LOI	1.8	1.36	0.74	1.94	2.53	1.81	2.07	0.46	0.52
Total	100.59	99.34	101.08	98.24	98.92	98.33	99.88	98.68	98.7
(ppm)	(ppm)								
Ba	41.2	675	1220	575	146.5	78.4	679	667	353
Ce	2	6.7	25.8	47.1	3.9	2.5	23.7	41.9	28.9
Cr	80	10	50	810	50	40	40	40	1520
Cs	16.3	0.67	0.12	0.12	0.08	0.23	0.15	2.71	0.67
Dy	0.71	0.34	0.44	3.77	0.47	0.53	0.41	0.65	1.99
Er	0.43	0.13	0.2	1.97	0.35	0.27	0.22	0.33	0.99
Eu	0.28	0.3	0.24	2.07	0.33	0.31	0.65	0.71	0.88
Ga	16.9	16	12.5	14.6	14.3	15.6	18.7	19.3	12.4
Gd	0.72	0.54	1.15	6.55	0.59	0.52	0.9	1.21	2.63
Hf	0.3	2.1	3	2.1	0.5	0.2	2.5	2.7	1.8
Ho	0.11	0.03	0.09	0.69	0.09	0.12	0.08	0.14	0.37
La	0.9	2.9	13.4	14.3	1.7	1.3	12.4	23	13
Lu	<0.01	<0.01	0.04	0.21	0.02	0.02	0.02	0.02	0.1
Nb	1	1	2.6	2.4	0.3	<0.2	1.7	4.3	3.8
Nd	1.5	3.5	9.6	36.1	2.4	1.9	9.8	17.2	16.8
Pr	0.3	0.81	2.7	7.65	0.48	0.37	2.7	4.45	3.82
Rb	10	32.9	29.9	9	2.1	6.7	22.3	62.7	27.3
Sm	0.32	0.62	1.52	8.03	0.49	0.41	1.78	2.88	3.43
Sn	1	1	4	1	1	3	1	2	1
Sr	174.5	586	110	330	497	539	571	588	575
Ta	<0.1	0.1	0.1	0.1	<0.1	<0.1	0.1	0.4	0.2
Tb	0.09	0.06	0.07	0.77	0.07	0.05	0.06	0.09	0.34
Th	0.08	0.53	8.13	0.32	0.1	0.09	0.83	4.72	1.56
Tm	0.06	<0.01	0.07	0.26	0.02	0.06	0.02	0.03	0.1
U	0.08	0.34	0.62	0.24	0.11	<0.05	0.1	1.66	0.39
V	46	14	<5	223	57	54	27	28	117
W	1	1	1	1	1	1	1	1	1
Y	3.9	1.6	2.4	20.7	3.2	3	2.3	3.6	10.7
Yb	0.26	0.12	0.26	1.63	0.28	0.29	0.17	0.25	0.94
Zr	9	68	65	57	14	6	98	118	62

Table 9 – Continued

Sample ID	**J255**	**J256**	**J257**	**J258**	**J259**	**J260**	**J261**	**J262**
Domain	Elmalhat domain	Elmalhat	Elmalhat domain	Elmalhat domain	Elmalhat domain	Elmalhat domain	Elmalhat domain	Elmalhat domain
Name	Olivine gabbro	Leuco-gabbro	Anorthosite	Pyroxenite	Leuco-gabbro	Anorthosite	Pyroxenite	Ultramafics
lat	23.895981	23.91502	23.912286	23.918026	23.918427	23.917873	23.91718	23.917182
lon	-12.117319	-12.103367	-12.059289	-12.052258	-12.049647	-12.045772	-12.040242	-12.023141
wt%	(wt%)							
SiO2	48.5	52.4	56.7	56.6	52.1	56.7	56.9	48.6
Al2O3	14.45	21.5	25	25.7	17.65	25.7	25.5	7.51
Fe2O3	8.95	4.5	1.27	1.12	8.46	1.24	1.34	9.96
CaO	8.71	10.9	8.08	8.44	9.26	8.61	8.23	13.7
MgO	13.45	4.58	0.27	0.11	5.07	0.16	0.15	18.05
Na2O	2.78	3.65	6.05	6.1	3.88	5.81	5.88	1.14
K2O	0.63	0.32	0.83	0.64	0.49	0.75	0.86	0.13
Cr2O3	0.17	0.02	0.01	0.01	0.01	0.01	0.01	0.3
TiO2	0.5	0.22	0.12	0.1	0.78	0.11	0.13	0.55
MnO	0.15	0.08	0.02	0.01	0.12	0.01	0.02	0.19
P2O5	0.04	0.03	0.05	0.04	0.05	0.01	0.03	0.02
SrO	0.07	0.09	0.14	0.14	0.09	0.14	0.14	0.02
BaO	0.02	0.11	0.08	0.07	0.05	0.06	0.08	0.01
LOI	1.07	1.46	0.45	0.58	0.16	0.61	0.69	1.04
Total	99.49	99.86	99.07	99.66	98.17	99.92	99.96	101.22
(ppm)	(ppm)							
Ba	200	912	664	641	392	511	701	50
Ce	12.6	10.7	14.1	15.2	19.4	14.3	18.8	14.6
Cr	1280	90	10	10	90	10	10	2060
Cs	0.06	0.1	0.06	0.02	0.06	<0.01	0.11	0.06
Dy	1.53	0.94	0.26	0.27	1.83	0.24	0.31	2.51
Er	0.98	0.63	0.09	0.06	1.02	0.07	0.12	1.36
Eu	0.81	0.71	1.51	1.29	1.24	1.3	1.36	0.88
Ga	14.8	17.2	22.7	22	18.2	20.6	21.5	8.3
Gd	1.91	1.41	0.51	0.29	2.42	0.32	0.55	2.95
Hf	0.7	0.5	0.2	0.2	0.9	<0.2	0.3	1.1
Ho	0.36	0.2	0.02	0.01	0.36	0.01	0.01	0.5
La	5.5	5.3	8.7	9.3	8.9	8.6	10.7	4.5
Lu	0.12	0.04	<0.01	<0.01	0.09	<0.01	<0.01	0.17
Nb	0.3	0.4	0.4	0.5	1.4	0.4	0.9	0.6
Nd	8.9	5.9	4.8	5.3	11.4	5.1	6.5	12.9
Pr	1.76	1.45	1.49	1.6	2.59	1.44	2.01	2.51
Rb	5.9	5.4	6.5	4.2	4.5	3.8	7.3	1
Sm	2.02	1.24	0.56	0.53	2.59	0.59	0.73	3.49
Sn	2	1	1	1	1	1	1	1
Sr	649	826	1180	1275	830	1230	1210	219
Ta	0.1	<0.1	<0.1	<0.1	0.1	<0.1	0.1	0.1
Tb	0.25	0.18	0.02	0.02	0.31	0.01	0.04	0.46
Th	0.12	0.34	0.16	0.16	0.23	0.11	0.31	0.15
Tm	0.17	0.04	<0.01	<0.01	0.07	<0.01	<0.01	0.18
U	<0.05	0.15	0.09	0.06	0.07	0.06	0.11	<0.05
V	148	77	13	5	207	6	11	196
W	1	1	1	1	1	1	1	1
Y	9.5	5.8	1	0.9	9.4	0.8	1.5	14.5
Yb	0.83	0.57	0.07	0.05	0.82	0.07	0.09	1.18
Zr	22	13	6	7	29	5	11	28

Table 9 – Continued

Sample ID	**J263**	**J264**	**J265**	**J266**	**J267**	**J268**	**J269**	**J270**
Domain	Elmalhat domain	Elmalhat domain	Elmalhat domain	Elmalhat domain	Elmalhat domain	Elmalhat domain	Elmalhat domain	Elmalhat domain
Name	Leuco-gabbro	Anorthosite	Orbicular Leuco-gabbro	Dark gabbro	Anorthosite	Anorthosite	Leuco-gabbro	Anorthosite
lat	23.918508	23.988859	23.988921	23.989588	23.990143	23.989817	23.99205	23.995014
lon	-12.010614	-12.013371	-12.013366	-12.012616	-12.011888	-12.010194	-12.010078	-12.007581
wt%								
SiO2	53.7	45.1	45.8	48.3	46.8	45.9	45.6	46.5
Al2O3	16.75	31.8	31.1	21.5	31.8	32.1	31	30.1
Fe2O3	9.04	1.18	1.83	4.62	1.35	1.45	2.14	2.25
CaO	7.77	16.35	16.3	14.25	16.3	17.1	15.7	15
MgO	5.24	0.61	1.65	7.44	0.31	0.56	1.41	0.69
Na2O	4.09	1.9	1.93	1.85	2.1	1.78	1.9	2.54
K2O	1	0.15	0.2	0.09	0.17	0.34	0.13	0.23
Cr2O3	0.01	0.01	0.01	0.07	0.01	0.01	0.01	<0.01
TiO2	0.85	0.04	0.03	0.07	0.13	0.09	0.08	0.18
MnO	0.16	0.02	0.03	0.09	0.02	0.02	0.03	0.04
P2O5	0.46	0.01	<0.01	<0.01	<0.01	<0.01	<0.01	0.04
SrO	0.08	0.01	0.01	<0.01	0.01	<0.01	0.01	0.02
BaO	0.05	<0.01	<0.01	<0.01	0.01	0.01	0.01	0.01
LOI	0.06	1.31	1.36	1.32	1.41	1.27	1.6	1.56
Total	99.26	98.49	100.25	99.6	100.42	100.63	99.62	99.16
(ppm)								
Ba	480	41	36.6	38.4	49.9	92.7	55.9	83.1
Ce	58.4	0.9	0.7	<0.5	1.2	1.2	0.9	3.6
Cr	80	30	70	480	20	20	50	<10
Cs	0.02	0.39	0.3	0.04	0.46	0.33	0.18	0.42
Dy	3.53	0.15	0.1	0.29	0.46	0.27	0.3	0.68
Er	2.05	0.06	0.05	0.13	0.24	0.18	0.22	0.42
Eu	2.19	0.21	0.22	0.2	0.28	0.26	0.24	0.35
Ga	18.5	16	19.8	14.1	19.3	17.4	17	18.3
Gd	5	0.13	0.14	0.14	0.38	0.33	0.27	0.65
Hf	1.4	<0.2	<0.2	<0.2	<0.2	<0.2	<0.2	0.4
Ho	0.66	<0.01	<0.01	0.04	0.06	0.04	0.02	0.11
La	26	<0.5	<0.5	<0.5	0.5	0.5	<0.5	1.9
Lu	0.18	<0.01	<0.01	<0.01	<0.01	<0.01	<0.01	0.07
Nb	5.2	0.3	0.2	<0.2	0.5	0.7	0.2	0.7
Nd	32.2	0.5	0.4	0.2	0.9	0.7	0.8	1.9
Pr	7.7	0.11	0.08	0.04	0.16	0.18	0.12	0.45
Rb	7.3	2.5	3.2	1.1	3.5	3	2.1	5.8
Sm	6.35	<0.03	0.03	0.03	0.23	0.26	0.16	0.51
Sn	1	1	1	1	1	1	1	1
Sr	764	176	189	139	212	169.5	175	226
Ta	0.3	<0.1	<0.1	0.1	0.1	0.1	<0.1	<0.1
Tb	0.62	<0.01	<0.01	0.01	0.03	0.02	0.01	0.08
Th	0.41	<0.05	<0.05	<0.05	<0.05	<0.05	<0.05	0.09
Tm	0.22	<0.01	<0.01	0.01	<0.01	0.01	<0.01	0.04
U	0.16	<0.05	<0.05	0.05	0.06	0.06	<0.05	0.07
V	152	14	9	69	19	22	37	32
W	1	<1	1	<1	1	1	1	<1
Y	18.1	0.7	0.5	1.5	2.5	1.7	1.5	4.4
Yb	1.4	0.03	<0.03	0.15	0.22	0.14	0.16	0.38
Zr	49	2	4	<2	5	5	3	16

Table 10– Whole rock major and trace element geochemistry for the Oum Abana and Anajim Guebli Domains. Data from ICP-MS analysis at ALS, Dublin.

Sample Number	*J148*	*J197*	*J198*	*J199*	*J200*	*J201*	*J205*
Domain	Oum Abana	Oum Abana	Oum Abana	Oum Abana	Oum Abana	Oum Abana	Oum Abana
Name	Gneiss	Gneiss	Marble	Microgranite dykes	Metamarl	Metabasalt - altered	Granite gneiss
lat	24.226405	24.509545	24.499823	24.497253	24.494095	24.492864	24.531652
lon	-12.22582	-12.386445	-12.394705	-12.392233	-12.388799	-12.38344	-12.573652
SiO2	72.9	66.1	1.34	72.7	33.2	44.1	72.4
Al2O3	13.85	16.85	0.24	14.15	8.53	6.42	15.05
Fe2O3	1.82	3.1	0.25	0.94	4.71	8.09	2.46
CaO	1.15	4.01	45.6	2.21	27.7	13.65	3.23
MgO	0.4	1.45	8.56	0.27	2.36	8.17	0.74
Na2O	5.29	5.09	0.03	5.89	2.13	0.06	4.34
K2O	1.02	1.02	0.14	0.83	0.19	0.44	1.75
Cr2O3	0.01	0.01	0.01	0.01	0.01	0.19	0.01
TiO2	0.1	0.28	<0.01	0.04	0.41	0.62	0.21
MnO	0.04	0.05	0.18	0.02	0.33	0.14	0.05
P2O5	0.03	0.09	<0.01	0.01	0.12	0.02	0.07
SrO	0.02	0.09	<0.01	0.04	0.03	0.02	0.07
BaO	0.11	0.04	0.03	0.07	0.16	0.14	0.07
LOI	1.67	2.09	44.7	1.2	18.6	16.5	1.14
Total	98.41	100.27	101.08	98.38	98.48	98.56	101.59
Ba	952	346	258	676	1475	1230	596
Ce	27	33.3	31.9	9.1	29.6	49.5	24.5
Cr	20	60	20	20	40	1320	50
Cs	1.52	0.21	0.02	0.17	0.17	0.78	2.06
Dy	1.15	0.73	1.28	0.19	2.26	2.89	0.64
Er	0.53	0.45	0.59	0.13	1.3	1.31	0.42
Eu	0.38	0.57	0.72	0.23	0.96	1.55	0.55
Ga	16	15.1	0.6	10.5	9.7	10.6	17.7
Gd	1.29	1.12	2.09	0.2	2.48	4.66	0.96
Hf	2.2	2.1	<0.2	1.4	2.2	1.9	2.2
Ho	0.23	0.17	0.22	0.01	0.47	0.49	0.17
La	14.3	17.3	19.8	5.1	13.1	14.2	13.3
Lu	0.11	0.08	0.03	<0.01	0.21	0.14	0.08
Nb	5.2	2.6	0.6	0.8	3.4	3.6	4.3
Nd	10.8	12.1	14.7	3.1	15.1	36	9.8
Pr	2.76	3.6	3.81	1.03	3.72	8.01	2.56
Rb	49.4	21.3	0.3	13.7	3.7	12.7	51.3
Sm	2.07	1.79	2.56	0.37	3.33	7.18	1.55
Sn	2	1	1	1	1	1	1
Sr	233	805	102.5	420	367	242	728
Ta	0.7	0.2	0.1	0.1	0.3	0.2	0.2
Tb	0.18	0.14	0.22	0.01	0.39	0.55	0.08
Th	3.98	1.54	0.07	0.25	2.01	0.42	2.56
Tm	0.09	0.04	0.04	<0.01	0.18	0.16	0.09
U	1.24	0.41	0.07	0.07	0.66	0.91	0.95
V	8	44	<5	6	117	148	24
W	1	1	1	1	1	7	2
Y	6	4.4	9.7	1.4	14.2	15	4
Yb	0.63	0.33	0.38	0.17	1.45	1.33	0.42
Zr	64	94	2	52	83	64	84

Table 10 – Continued

Sample Number	*J206*	*J207*	*J209*	*J217*	*J219*	*J220*	*J221*	*J222*
Domain	Oum Abana	Oum Abana	Oum Abana	Oum Abana	Oum Abana	Oum Abana	Oum Abana	Oum Abana
Name	Pyroxenite	Kunene pyroxenite	Rhyolite	Andesite	Sheared granodiorite	Granite gneiss	Fine-grained ultramafic	Anorthosite
lat	24.52516	24.525257	24.533175	24.587989	24.248837	24.244191	24.261303	24.265635
lon	-12.595342	-12.595385	-12.626319	-12.425035	-12.42981	-12.430501	-12.379316	-12.214503
SiO2	51.5	51.6	44.7	62.9	56.2	71.2	37.4	46.9
Al2O3	4.65	7.02	12.35	12.5	17.45	14.85	9.72	27
Fe2O3	8.92	9.53	11.8	8.01	6.83	1.72	12.1	2.52
CaO	12.4	12.1	10.35	9.88	6.24	2.51	9.91	13.7
MgO	17.75	15.3	6.03	2.25	4.21	0.42	11.1	3.03
Na2O	0.7	1.33	2.15	0.26	4.76	5.04	1.29	2.39
K2O	0.21	0.35	0.2	0.35	1.19	2.09	1.21	0.73
Cr2O3	0.16	0.11	0.03	0.01	0.02	0.01	0.09	0.01
TiO2	0.28	0.66	0.98	0.9	0.63	0.11	1.39	0.04
MnO	0.2	0.18	0.17	0.12	0.1	0.03	0.18	0.04
P2O5	0.07	0.01	0.06	0.19	0.29	0.03	0.3	<0.01
SrO	<0.01	<0.01	0.01	0.01	0.11	0.09	0.02	0.02
BaO	<0.01	0.01	0.01	0.06	0.07	0.12	0.02	0.01
LOI	1.83	1.66	12.4	2.44	1.8	1.23	15.3	1.93
Total	98.67	99.86	101.24	99.88	99.9	99.45	100.03	98.32
Ba	31.3	86.4	43.1	538	616	1000	187	95.5
Ce	13.3	17.1	7.9	37.9	51.4	27.8	59.9	2.6
Cr	1070	820	190	20	110	70	660	20
Cs	0.01	<0.01	0.13	0.03	0.41	0.42	18.85	1
Dy	1.3	2.77	3.39	4.23	2.4	0.7	6.47	0.21
Er	0.8	1.5	2.23	2.3	1.13	0.28	3.34	0.16
Eu	0.59	0.83	0.85	1.41	1.59	0.48	2.77	0.17
Ga	7.9	9.3	13.3	19.3	22.6	14.9	17.1	15.2
Gd	1.45	2.85	3.29	4.81	3.24	1.14	9.25	0.23
Hf	1.6	1.5	1.7	4.7	3.2	2	3	0.2
Ho	0.28	0.49	0.72	0.82	0.44	0.13	1.22	<0.01
La	4	6	2.8	16.6	22.1	15.8	17.7	1.1
Lu	0.16	0.17	0.29	0.32	0.16	0.04	0.41	<0.01
Nb	2.1	3.4	2.4	8.9	3.1	2	8.1	0.7
Nd	7.8	11.8	6.1	20.5	32.7	10.7	46.9	1
Pr	1.92	2.59	1.28	4.95	7.04	2.93	10.2	0.3
Rb	1.9	2.9	3	6.2	20.7	28	82	22.1
Sm	1.49	3.06	1.84	4.61	5.95	1.64	10.9	0.19
Sn	2	1	1	2	4	2	2	1
Sr	35.1	125.5	178.5	181.5	1020	810	267	239
Ta	0.2	0.2	0.2	0.7	0.2	0.1	0.3	0.1
Tb	0.2	0.44	0.48	0.7	0.45	0.08	1.24	0.01
Th	0.23	0.63	0.22	1.97	0.36	1.39	0.6	0.17
Tm	0.09	0.21	0.27	0.33	0.18	0.09	0.41	<0.01
U	0.25	0.49	0.15	0.61	0.14	0.2	0.4	0.16
V	74	158	292	138	144	10	312	17
W	1	1	1	1	1	1	3	1
Y	8.7	15	19.6	24.4	13.2	3.6	33.2	0.8
Yb	0.92	1.47	2	2.4	1.03	0.46	2.95	0.1
Zr	59	47	53	181	145	67	68	5

Table 10 – Continued

Sample Number	*J223*	*J224*	*J227*	*J253*	*J271*	*J272*	*J273*	*J275*
Domain	Oum Abana	Oum Abana	Anajim Guebli Suite	Oum Abana	Oum Abana	Oum Abana	Oum Abana	Oum Abana
Name	Granite (with pyrite)	Altered granite	Para-gneiss	Granite intrusion	Metasedimentary	Metagreywacke	Grano-diorite gneiss	Grano-diorite
lat	24.488213	24.488124	23.971316	24.629261	24.556945	24.465305	24.449812	24.403286
lon	-12.360858	-12.360959	-11.979466	-12.375615	-12.293255	-12.46506	-12.476072	-12.541036
SiO2	65.2	57.5	68.4	72.4	70.8	75.2	63	52.6
Al2O3	13.75	14.05	16.5	14.5	14.75	13.8	15.8	22.2
Fe2O3	3.99	6.75	3.41	1.88	1.76	1.06	5.25	4.06
CaO	3.58	5.68	3.19	2.36	2.39	1.56	5.11	6.75
MgO	1.96	3.09	0.65	0.42	0.49	0.18	3.16	1.5
Na2O	3.26	2.92	5.18	5.25	5.29	5.92	4.34	5.45
K2O	1.58	1.3	1.72	1.59	1.58	1.03	1.86	2.3
Cr2O3	0.01	0.02	0.01	0.01	0.01	<0.01	0.02	0.01
TiO2	0.42	0.77	0.31	0.12	0.16	0.05	0.51	0.49
MnO	0.05	0.1	0.1	0.04	0.04	0.02	0.08	0.06
P2O5	0.1	0.23	0.19	0.02	0.11	0.03	0.19	0.48
SrO	0.02	0.03	0.05	0.05	0.04	0.05	0.07	0.15
BaO	0.03	0.1	0.08	0.06	0.07	0.13	0.07	0.08
LOI	4.65	7.1	1.1	0.87	1.38	1.3	1.14	2.71
Total	98.6	99.64	100.89	99.57	98.87	100.33	100.6	98.84
Ba	293	876	633	509	548	1195	636	673
Ce	26.9	47.2	68.7	21	10	14.7	67.7	65.8
Cr	60	130	20	60	10	20	110	60
Cs	0.54	0.44	1.27	0.28	0.32	0.13	1.33	0.87
Dy	1.23	2.26	2.68	0.82	0.37	0.6	2.38	2.04
Er	0.67	1.14	1.58	0.48	0.21	0.39	1.28	1.02
Eu	0.68	1.14	1.27	0.44	0.29	0.4	1.18	1.92
Ga	14.8	17.6	18.4	18.2	16.5	12.4	18.5	22.2
Gd	1.64	3.08	3.22	1.17	0.65	0.67	2.99	2.95
Hf	2.8	3.4	4.9	2.5	2	1.5	3.9	3
Ho	0.21	0.38	0.49	0.14	0.04	0.13	0.5	0.42
La	13.5	22.5	32	10.3	5.1	7.5	34.8	34.5
Lu	0.07	0.12	0.23	0.07	0.03	0.1	0.19	0.13
Nb	4.1	5.9	7.4	3.9	3.6	3.8	5.6	8.4
Nd	11.8	21.8	30.2	9.9	5.2	5.5	29.3	28.4
Pr	3.28	5.81	7.71	2.36	1.32	1.58	7.68	7.5
Rb	44	40	41.4	38.9	39.9	17.1	51.9	82.9
Sm	1.95	4.16	5.15	1.78	0.91	0.89	4.85	4.67
Sn	1	1	2	1	1	<1	2	2
Sr	294	336	522	531	371	470	668	1310
Ta	0.3	0.4	0.6	0.3	0.2	0.5	0.4	0.5
Tb	0.19	0.37	0.4	0.12	0.04	0.12	0.4	0.35
Th	1.57	3.78	4.48	1.05	0.64	1.34	4.34	3.98
Tm	0.06	0.13	0.23	0.07	0.01	0.08	0.21	0.19
U	0.44	1.01	1.19	0.53	0.17	0.4	1.15	1.39
V	88	128	11	9	14	7	102	66
W	5	5	1	1	<1	1	1	1
Y	7	12.3	15.8	4.9	2.1	4.5	14.5	11.8
Yb	0.6	1.06	1.78	0.47	0.16	0.51	1.44	1.16
Zr	115	130	197	82	70	38	157	122

Table 10 – Continued

Sample Number	*J281*	*J282*	*J283*	*J284*	*J285*	*J286*	*J287*
Domain	Oum Abana	Oum Abana	Oum Abana	Oum Abana	Oum Abana	Oum Abana	Oum Abana
Name	Green Rhyolite	Green Rhyolite	Andesite	Andesite	White Rhyolite	White Rhyolite	White Rhyolite
lat	24.507334	24.501791	24.499248	24.498713	24.498652	24.476388	24.434041
lon	-12.371379	-12.371586	-12.371214	-12.37146	-12.371545	-12.375024	-12.40924
SiO2	71.4	60.4	60.8	55.9	75.9	76.4	75.1
Al2O3	14.35	16.9	15.2	16.85	12.9	13.85	13.5
Fe2O3	3.99	5.79	8.12	11.65	2	1.25	1.45
CaO	3.08	5.27	5.19	5.64	2.99	1.42	1.37
MgO	0.71	1.99	2.43	2.34	0.48	0.27	0.24
Na2O	4.43	3.89	3.58	4.59	2.46	6.09	4.51
K2O	0.84	1.46	1.32	0.19	2.33	0.83	3.2
Cr2O3	0.01	0.01	0.01	0.01	0.01	0.01	0.01
TiO2	0.34	0.55	0.85	1.02	0.3	0.09	0.08
MnO	0.02	0.09	0.11	0.17	0.05	0.02	0.04
P2O5	0.12	0.19	0.36	0.72	0.05	0.04	0.03
SrO	0.01	0.05	0.04	0.04	0.01	0.02	0.03
BaO	0.05	0.11	0.06	0.03	0.16	0.11	0.15
LOI	1.18	1.97	3.13	1.84	2.06	1.08	0.87
Total	100.53	98.67	101.2	100.99	101.7	101.48	100.58
Ba	425	1015	528	264	1405	974	1240
Ce	39.6	51	52.7	45.9	62.7	30.8	23.4
Cr	30	10	20	20	10	30	60
Cs	0.3	0.35	0.41	0.06	0.32	0.17	0.66
Dy	1.25	3.36	4.03	4.1	2.65	0.66	1.16
Er	0.63	2.14	2.46	2.14	1.69	0.48	0.79
Eu	0.8	1.2	1.81	1.82	0.77	0.27	0.31
Ga	18.5	18.8	18.9	20.6	16.6	11.6	14.9
Gd	1.72	3.67	5.1	5.21	2.83	1.08	1.19
Hf	4.4	4.5	4	2.8	5.4	2.1	1.9
Ho	0.18	0.69	0.95	0.77	0.56	0.14	0.24
La	19.2	21.9	23.1	20.5	29.2	15.8	11.6
Lu	0.09	0.36	0.35	0.31	0.33	0.08	0.13
Nb	7.4	8.6	5.8	4.2	8.3	5.1	8.6
Nd	14.9	23.3	28.6	26.5	23	10.3	9.8
Pr	4.33	6	6.86	6.2	6.75	3.19	2.49
Rb	13.6	33.5	29.8	5.6	58.9	18	76.9
Sm	2.55	4.53	5.8	5.64	4.31	1.48	1.79
Sn	1	2	1	1	2	<1	4
Sr	281	477	489	464	211	324	388
Ta	0.7	0.8	0.5	0.3	0.9	0.6	1.2
Tb	0.25	0.59	0.75	0.74	0.51	0.13	0.17
Th	1.53	3.28	3.59	2.66	8.12	2.09	4.15
Tm	0.08	0.35	0.4	0.34	0.29	0.07	0.12
U	0.28	1	0.96	0.57	2.19	0.61	1.51
V	39	95	129	206	21	9	8
W	1	1	2	13	2	1	1
Y	6.5	20.9	23.9	22.5	17	4.4	7.7
Yb	0.48	2.1	2.2	1.91	1.75	0.54	1.02
Zr	164	149	146	104	198	60	48

Appendix D – Microprobe Analyses

The mineral chemistry was analysed on the electron microprobe facilities at the University of Barcelona, Department of Materials. We used the JEOL JXA-8230 microprobe, with 5 wavelength dispersal spectrometers (WDS) and energy dispersal spectrometers (EDS-SDD) to analyse the silicate minerals under the following conditions. An electron beam acceleration voltage of 20 kV and a current of 15 nA. Counting times 10 s on peak and 5 s on each background position. We used the matrix correction effect with the method XPP (type phi-rho-z). Si and Al were analysed using the TAP crystal, Cr and Ti were analysed using the PETJ crystal, Mg and Na were analysed using the TAPH crystal, Fe, Mn and Ni were analysed using the LIFH crystal, and Ca, K and Sr were analysed using the PETL crystal. The following standards were used for silicates. Albite was used as the Na standard, periclase was used as the Mg standard, corundum was used for the Al standard, wollastonite was used for the Ca and Si standard, orthoclase was used for the K standard, rutile was used for the Ti standard, Cr2O3 was used for the Cr standard, rhodonite was used for the Mn standard, Fe2O3 was used for the Fe standard, Ni metal was used for the Ni standard, and celestite was used for the Sr standard.

The same conditions were used in the analysis of oxides although a higher current (20 nA) and V metal was used as the V standard. An interference correction for Ti Kβ--> V Kα was applied.

The tables below present the mineral chemistry of plagioclase (Table 11), orthopyroxene (Table 12), clinopyroxene (Table 13), olivine (Table 14) and amphibole (Table 15), analysed in samples from the EAC.

Table 11 – Plagioclase mineral chemistry from samples across the EAC

Sample	B104	B104	B104	B104	B104	B104	B104	B104	B104	B104	B104	B104	B104	B104	B104
Mineral	Pl	Pl	Pl	Pl	Pl	Pl	Pl	Pl	Pl	Pl	Pl	Pl	Pl	Pl	Pl
SiO2	58.3	58.3	57.9	57.8	57.7	58.0	58.0	58.2	58.1	57.2	57.9	58.1	57.7	57.9	58.4
TiO2	0.1	0.0	0.0	0.0	0.0	0.0	0.1	0.1	0.0	0.0	0.0	0.0	0.0	0.0	0.0
Al2O3	25.9	26.3	26.1	26.1	26.0	26.5	26.0	26.3	26.0	26.7	26.7	26.2	26.3	26.1	26.3
FeO	0.2	0.2	0.2	0.2	0.2	0.1	0.2	0.3	0.2	0.2	0.2	0.2	0.2	0.2	0.2
MnO	0.0	0.0	0.0	0.0	0.0	0.0	0.0	0.0	0.0	0.0	0.0	0.0	0.0	0.0	0.0
MgO	0.0	0.0	0.0	0.0	0.0	0.0	0.0	0.0	0.0	0.0	0.0	0.0	0.0	0.0	0.0
CaO	8.0	8.2	8.3	8.4	8.4	8.3	8.4	8.1	8.3	8.7	8.5	8.3	8.6	8.3	8.3
Na2O	6.9	6.9	6.7	6.8	7.0	6.9	6.7	6.9	6.8	6.5	6.8	6.8	6.5	6.8	6.8
K2O	0.4	0.4	0.4	0.5	0.4	0.4	0.4	0.5	0.4	0.4	0.4	0.4	0.4	0.4	0.5
Totals	99.8	100.2	99.6	99.7	99.7	100.2	99.7	100.4	99.8	99.6	100.4	100.1	99.7	99.8	100.4
Oxygens	8	8	8	8	8	8	8	8	8	8	8	8	8	8	8
Si	2.62	2.61	2.61	2.60	2.60	2.59	2.61	2.60	2.61	2.58	2.59	2.60	2.59	2.60	2.61
Ti	0.00	0.00	0.00	0.00	0.00	0.00	0.00	0.00	0.00	0.00	0.00	0.00	0.00	0.00	0.00
Al	1.37	1.38	1.38	1.39	1.38	1.40	1.38	1.39	1.38	1.42	1.41	1.38	1.40	1.38	1.38
Fe2+	0.01	0.01	0.01	0.01	0.01	0.00	0.01	0.01	0.01	0.01	0.01	0.01	0.01	0.01	0.01
Mn	0.00	0.00	0.00	0.00	0.00	0.00	0.00	0.00	0.00	0.00	0.00	0.00	0.00	0.00	0.00
Mg	0.00	0.00	0.00	0.00	0.00	0.00	0.00	0.00	0.00	0.00	0.00	0.00	0.00	0.00	0.00
Ca	0.39	0.39	0.40	0.40	0.40	0.40	0.40	0.39	0.40	0.42	0.41	0.40	0.41	0.40	0.40
Na	0.60	0.60	0.59	0.59	0.61	0.60	0.58	0.60	0.59	0.57	0.58	0.59	0.57	0.59	0.59
K	0.03	0.02	0.02	0.03	0.02	0.02	0.02	0.03	0.03	0.03	0.02	0.02	0.02	0.02	0.03
Sum	5.01	5.01	5.01	5.01	5.03	5.02	5.00	5.02	5.01	5.01	5.01	5.01	5.00	5.01	5.01

Sample	B104	B104	B104	B104	B104	B104	B133	B133	B133	B133	B133	B133	B133	B133	B133
Mineral	Pl	Pl	Pl	Pl	Pl	Pl	Pl	Pl	Pl	Pl	Pl	Pl	Pl	Pl	Pl
SiO2	57.9	57.7	57.7	57.7	57.7	58.0	60.0	56.9	57.0	58.5	58.2	58.9	58.4	59.0	60.4
TiO2	0.0	0.0	0.1	0.0	0.0	0.0	0.0	0.0	0.0	0.0	0.1	0.0	0.0	0.0	0.1
Al2O3	26.1	26.1	26.1	26.1	26.2	26.3	24.3	26.0	26.5	25.5	25.1	25.5	25.1	24.8	24.4
FeO	0.2	0.2	0.4	0.2	0.3	0.2	0.1	0.1	0.1	0.1	0.1	0.1	0.2	0.1	0.1
MnO	0.0	0.0	0.0	0.0	0.0	0.0	0.0	0.0	0.0	0.0	0.0	0.0	0.0	0.0	0.0
MgO	0.0	0.0	0.0	0.0	0.0	0.0	0.0	0.0	0.0	0.0	0.0	0.0	0.0	0.0	0.0
CaO	8.4	8.4	8.5	8.3	8.1	8.3	6.5	8.6	8.6	7.9	7.5	7.6	7.3	7.1	6.3
Na2O	6.7	6.5	6.7	6.6	6.9	6.8	7.6	6.5	6.5	6.9	7.0	7.0	7.4	7.6	8.0
K2O	0.4	0.7	0.4	0.5	0.4	0.4	0.3	0.4	0.4	0.5	0.5	0.4	0.5	0.5	0.6
Totals	99.7	99.7	99.8	99.4	99.7	100.0	98.9	98.5	99.0	99.3	98.5	99.5	98.9	99.1	99.9
Oxygens	8	8	8	8	8	8	8	8	8	8	8	8	8	8	8
Si	2.60	2.60	2.59	2.60	2.60	2.60	2.70	2.59	2.58	2.63	2.64	2.64	2.64	2.66	2.70
Ti	0.00	0.00	0.00	0.00	0.00	0.00	0.00	0.00	0.00	0.00	0.00	0.00	0.00	0.00	0.00
Al	1.39	1.39	1.38	1.39	1.39	1.39	1.29	1.40	1.41	1.36	1.35	1.35	1.34	1.32	1.29
Fe2+	0.01	0.01	0.02	0.01	0.01	0.01	0.00	0.00	0.00	0.00	0.01	0.00	0.01	0.00	0.01
Mn	0.00	0.00	0.00	0.00	0.00	0.00	0.00	0.00	0.00	0.00	0.00	0.00	0.00	0.00	0.00
Mg	0.00	0.00	0.00	0.00	0.00	0.00	0.00	0.00	0.00	0.00	0.00	0.00	0.00	0.00	0.00
Ca	0.41	0.40	0.41	0.40	0.39	0.40	0.31	0.42	0.42	0.38	0.36	0.37	0.36	0.34	0.30
Na	0.59	0.57	0.58	0.57	0.61	0.59	0.67	0.57	0.57	0.60	0.62	0.61	0.65	0.67	0.69
K	0.02	0.04	0.02	0.03	0.03	0.02	0.02	0.02	0.02	0.03	0.03	0.02	0.03	0.03	0.03
Sum	5.01	5.01	5.01	5.00	5.02	5.01	5.00	5.01	5.01	5.00	5.01	4.99	5.03	5.02	5.02

Table 11 - Continued

Sample	B133	B133	B133	B133	B133	B133	B133	B133	B45	B45	B45	B45	B83	B83	B83	B83
Mineral	Pl	Pl	Pl	Pl	Pl	Pl	Pl	Pl	Pl	Pl	Pl	Pl	Pl	Pl	Pl	Pl
SiO2	60.0	59.6	58.7	59.5	58.1	58.6	59.4	58.6	44.8	45.2	45.4	45.5	57.7	58.2	58.3	58.0
TiO2	0.0	0.0	0.0	0.0	0.0	0.0	0.0	0.0	0.0	0.0	0.0	0.0	0.0	0.0	0.0	0.1
Al2O3	24.4	24.6	25.3	25.1	25.2	25.2	24.9	25.2	34.8	34.7	34.7	34.6	26.4	25.8	25.8	26.0
FeO	0.1	0.1	0.2	0.1	0.1	0.1	0.1	0.1	0.1	0.1	0.0	0.0	0.2	0.2	0.2	0.2
MnO	0.0	0.0	0.0	0.0	0.0	0.0	0.0	0.0	0.0	0.0	0.0	0.0	0.0	0.0	0.0	0.0
MgO	0.0	0.0	0.0	0.0	0.0	0.0	0.0	0.0	0.0	0.0	0.0	0.0	0.0	0.0	0.0	0.0
CaO	6.3	6.5	7.4	7.0	7.8	7.4	6.9	7.2	18.7	18.5	18.3	18.4	8.3	7.8	7.4	7.8
Na2O	7.1	7.5	7.4	7.5	7.1	7.3	7.5	7.4	1.1	1.3	1.3	1.2	6.4	6.6	6.6	6.6
K2O	1.5	0.5	0.5	0.6	0.5	0.5	0.5	0.4	0.0	0.0	0.0	0.0	0.8	1.2	1.3	1.1
Totals	99.3	98.9	99.4	99.8	98.8	99.1	99.3	99.0	99.4	99.7	99.8	99.9	99.9	99.9	99.6	99.7
Oxygens	8	8	8	8	8	8	8	8	8	8	8	8	8	8	8	
Si	2.70	2.69	2.64	2.66	2.64	2.65	2.67	2.65	2.08	2.09	2.10	2.10	2.59	2.62	2.63	2.61
Ti	0.00	0.00	0.00	0.00	0.00	0.00	0.00	0.00	0.00	0.00	0.00	0.00	0.00	0.00	0.00	0.00
Al	1.30	1.31	1.34	1.33	1.35	1.34	1.32	1.34	1.90	1.89	1.89	1.89	1.40	1.37	1.37	1.38
Fe2+	0.00	0.00	0.01	0.00	0.00	0.00	0.00	0.00	0.00	0.00	0.00	0.00	0.01	0.01	0.01	0.01
Mn	0.00	0.00	0.00	0.00	0.00	0.00	0.00	0.00	0.00	0.00	0.00	0.00	0.00	0.00	0.00	0.00
Mg	0.00	0.00	0.00	0.00	0.00	0.00	0.00	0.00	0.00	0.00	0.00	0.00	0.00	0.00	0.00	0.00
Ca	0.30	0.31	0.36	0.34	0.38	0.36	0.33	0.35	0.93	0.92	0.91	0.91	0.40	0.38	0.36	0.38
Na	0.62	0.66	0.65	0.65	0.62	0.64	0.65	0.65	0.10	0.11	0.12	0.11	0.55	0.58	0.57	0.58
K	0.08	0.03	0.03	0.03	0.03	0.03	0.03	0.02	0.00	0.00	0.00	0.00	0.04	0.07	0.08	0.06
Sum	5.00	5.00	5.02	5.02	5.01	5.01	5.01	5.02	5.02	5.02	5.02	5.01	5.00	5.02	5.01	5.02

Sample	B85	B85	B85	B85	B85	B85	B87	B87	B87	B87	B87	B87	B87	B87	B87	B87
Mineral	Pl	Pl	Pl	Pl	Pl	Pl	Pl	Pl	Pl	Pl	Pl	Pl	Pl	Pl	Pl	Pl
SiO2	53.4	53.2	55.2	53.4	52.7	55.4	52.8	52.8	52.8	52.5	52.5	52.6	52.7	52.9	52.6	52.8
TiO2	0.0	0.0	0.1	0.1	0.0	0.0	0.0	0.0	0.0	0.0	0.1	0.0	0.0	0.0	0.0	0.1
Al2O3	29.1	28.7	28.0	29.3	29.4	27.7	30.1	29.7	29.8	29.9	29.9	29.9	29.4	29.7	29.7	30.1
FeO	0.3	0.3	0.3	0.4	0.3	0.4	0.2	0.2	0.1	0.1	0.1	0.1	0.1	0.1	0.1	0.1
MnO	0.0	0.0	0.0	0.0	0.0	0.0	0.0	0.0	0.0	0.0	0.0	0.0	0.0	0.0	0.0	0.0
MgO	0.0	0.0	0.0	0.0	0.1	0.0	0.0	0.1	0.0	0.0	0.0	0.0	0.0	0.0	0.0	0.0
CaO	11.8	11.7	10.3	11.9	12.0	10.1	12.5	12.2	12.4	12.6	12.6	12.3	12.0	12.6	12.2	12.4
Na2O	4.8	4.6	5.3	4.5	4.3	5.4	4.8	4.8	4.6	4.6	4.5	4.5	4.9	4.5	4.7	4.7
K2O	0.5	0.5	0.5	0.6	0.4	1.0	0.2	0.2	0.2	0.2	0.2	0.2	0.2	0.2	0.2	0.2
Totals	99.9	99.1	99.6	100.2	99.0	100.1	100.5	100.1	100.0	99.9	99.9	99.6	99.4	100.0	99.5	100.4
Oxygens	8	8	8	8	8	8	8	8	8	8	8	8	8	8	8	8
Si	2.42	2.44	2.50	2.42	2.41	2.50	2.39	2.40	2.39	2.39	2.39	2.39	2.41	2.40	2.39	2.39
Ti	0.00	0.00	0.00	0.00	0.00	0.00	0.00	0.00	0.00	0.00	0.00	0.00	0.00	0.00	0.00	0.00
Al	1.56	1.55	1.49	1.56	1.58	1.48	1.60	1.59	1.60	1.60	1.60	1.60	1.58	1.59	1.60	1.60
Fe2+	0.01	0.01	0.01	0.01	0.01	0.02	0.01	0.01	0.00	0.00	0.00	0.01	0.01	0.00	0.00	0.01
Mn	0.00	0.00	0.00	0.00	0.00	0.00	0.00	0.00	0.00	0.00	0.00	0.00	0.00	0.00	0.00	0.00
Mg	0.00	0.00	0.00	0.00	0.00	0.00	0.00	0.01	0.00	0.00	0.00	0.00	0.00	0.00	0.00	0.00
Ca	0.57	0.57	0.50	0.58	0.59	0.49	0.60	0.59	0.60	0.61	0.61	0.60	0.58	0.61	0.59	0.60
Na	0.42	0.41	0.46	0.39	0.38	0.47	0.42	0.42	0.40	0.40	0.39	0.40	0.43	0.39	0.42	0.41
K	0.03	0.03	0.03	0.04	0.02	0.06	0.01	0.01	0.01	0.01	0.01	0.01	0.01	0.01	0.01	0.01
Sum	5.02	5.01	5.00	5.01	5.00	5.02	5.03	5.03	5.02	5.02	5.01	5.01	5.03	5.01	5.02	5.02

Table 11 - Continued

Sample	B87	B87	B87	B87	B87	B87	B87	B87	B87	B87	B87	B87	B87	B87	B87	B87
Mineral	Pl	Pl	Pl	Pl	Pl	Pl	Pl	Pl	Pl	Pl	Pl	Pl	Pl	Pl	Pl	Pl
SiO2	52.3	52.6	52.8	52.1	52.5	52.8	52.4	52.4	52.5	53.3	52.9	52.8	53.4	53.4	53.6	53.3
TiO2	0.1	0.0	0.1	0.0	0.0	0.0	0.0	0.0	0.1	0.0	0.1	0.1	0.0	0.1	0.0	0.0
Al2O3	29.8	29.8	29.6	30.1	30.0	29.4	30.0	29.8	29.4	29.4	29.4	29.7	27.2	29.2	29.2	29.5
FeO	0.1	0.2	0.1	0.1	0.1	0.1	0.1	0.1	0.2	0.2	0.2	0.2	0.1	0.1	0.1	0.2
MnO	0.0	0.0	0.0	0.0	0.0	0.0	0.0	0.0	0.0	0.0	0.0	0.0	0.0	0.0	0.0	0.0
MgO	0.0	0.0	0.0	0.0	0.0	0.0	0.0	0.0	0.5	0.0	0.0	0.0	0.1	0.0	0.0	0.0
CaO	12.6	12.4	12.4	12.7	12.6	12.4	12.7	12.5	12.3	12.1	12.0	12.5	8.7	11.9	11.6	12.2
Na2O	4.6	4.6	4.6	4.5	4.4	4.7	4.7	4.6	4.6	4.8	4.9	4.8	4.4	4.9	5.2	4.7
K2O	0.2	0.2	0.2	0.2	0.2	0.2	0.2	0.2	0.2	0.2	0.2	0.2	0.3	0.2	0.2	0.2
Totals	99.8	99.9	99.8	99.7	100.0	99.6	100.1	99.7	99.7	100.0	99.6	100.2	94.2	99.8	100.1	100.0
Oxygens	8	8	8	8	8	8	8	8	8	8	8	8	8	8	8	8
Si	2.38	2.39	2.40	2.37	2.38	2.40	2.38	2.39	2.39	2.42	2.41	2.39	2.53	2.42	2.43	2.41
Ti	0.00	0.00	0.00	0.00	0.00	0.00	0.00	0.00	0.00	0.00	0.00	0.00	0.00	0.00	0.00	0.00
Al	1.60	1.60	1.59	1.62	1.61	1.58	1.60	1.60	1.58	1.57	1.58	1.59	1.52	1.56	1.56	1.58
Fe2+	0.01	0.01	0.00	0.00	0.00	0.00	0.00	0.01	0.01	0.01	0.01	0.01	0.00	0.00	0.00	0.01
Mn	0.00	0.00	0.00	0.00	0.00	0.00	0.00	0.00	0.00	0.00	0.00	0.00	0.00	0.00	0.00	0.00
Mg	0.00	0.00	0.00	0.00	0.00	0.00	0.00	0.00	0.04	0.00	0.00	0.00	0.00	0.00	0.00	0.00
Ca	0.61	0.61	0.60	0.62	0.61	0.60	0.62	0.61	0.60	0.59	0.58	0.60	0.44	0.58	0.56	0.59
Na	0.41	0.40	0.41	0.39	0.39	0.41	0.41	0.41	0.40	0.42	0.43	0.42	0.40	0.43	0.46	0.41
K	0.01	0.01	0.01	0.01	0.01	0.01	0.01	0.01	0.01	0.01	0.01	0.01	0.02	0.01	0.01	0.01
Sum	5.03	5.02	5.01	5.02	5.01	5.02	5.03	5.02	5.03	5.01	5.02	5.03	4.92	5.02	5.03	5.01

Sample	B87	B87	B87	J106	J106	J106	J106	J106	J106	J122	J122	J122	J122	J122	J122
Mineral	Pl	Pl	Pl	Pl	Pl	Pl	Pl	Pl	Pl	Pl	Pl	Pl	Pl	Pl	Pl
SiO2	53.0	53.4	53.2	46.8	46.5	45.7	46.9	46.5	45.1	58.1	58.4	58.6	58.0	58.1	58.1
TiO2	0.1	0.1	0.1	0.0	0.0	0.0	0.0	0.0	0.0	0.0	0.1	0.0	0.1	0.1	0.0
Al2O3	29.5	29.4	29.7	34.4	34.3	34.7	34.4	34.1	34.8	26.3	25.7	26.2	25.9	26.0	26.2
FeO	0.2	0.1	0.2	0.0	0.0	0.0	0.0	0.0	0.0	0.1	0.1	0.1	0.2	0.2	0.1
MnO	0.0	0.0	0.0	0.0	0.0	0.0	0.0	0.0	0.0	0.0	0.0	0.0	0.0	0.0	0.0
MgO	0.0	0.0	0.0	0.0	0.0	0.0	0.0	0.0	0.0	0.0	0.0	0.0	0.0	0.1	0.0
CaO	11.9	11.9	12.4	17.5	17.7	18.1	17.5	17.6	19.0	8.2	7.8	7.9	8.0	8.0	8.1
Na2O	5.0	4.9	4.8	1.8	1.7	1.4	1.9	1.8	1.2	7.1	7.0	7.1	7.1	6.4	7.4
K2O	0.2	0.3	0.2	0.0	0.0	0.0	0.0	0.0	0.0	0.3	0.4	0.4	0.5	0.4	0.4
Totals	99.8	100.0	100.5	100.4	100.3	99.9	100.8	100.1	100.2	100.3	99.5	100.4	99.7	99.1	100.3
Oxygens	8	8	8	8	8	8	8	8	8	8	8	8	8	8	8
Si	2.41	2.42	2.40	2.14	2.13	2.11	2.14	2.14	2.08	2.60	2.63	2.61	2.61	2.62	2.60
Ti	0.00	0.00	0.00	0.00	0.00	0.00	0.00	0.00	0.00	0.00	0.00	0.00	0.00	0.00	0.00
Al	1.58	1.57	1.58	1.85	1.86	1.88	1.85	1.85	1.89	1.39	1.36	1.38	1.38	1.38	1.38
Fe2+	0.01	0.00	0.01	0.00	0.00	0.00	0.00	0.00	0.00	0.01	0.01	0.00	0.01	0.01	0.01
Mn	0.00	0.00	0.00	0.00	0.00	0.00	0.00	0.00	0.00	0.00	0.00	0.00	0.00	0.00	0.00
Mg	0.00	0.00	0.00	0.00	0.00	0.00	0.00	0.00	0.00	0.00	0.00	0.00	0.00	0.00	0.00
Ca	0.58	0.58	0.60	0.86	0.87	0.89	0.85	0.87	0.94	0.39	0.38	0.38	0.38	0.39	0.39
Na	0.44	0.43	0.42	0.16	0.15	0.12	0.17	0.16	0.11	0.61	0.61	0.62	0.62	0.56	0.64
K	0.01	0.01	0.01	0.00	0.00	0.00	0.00	0.00	0.00	0.02	0.02	0.02	0.03	0.02	0.02
Sum	5.03	5.02	5.02	5.01	5.01	5.01	5.02	5.02	5.03	5.02	5.01	5.02	5.02	4.98	5.04

Table 11 - Continued

Sample	**J122**	**J122**	**J122**	**J122**	**J122**	**J122**	**J122**	**J122**	**J122**	**J122**	**J122**	**J122**	**J122**	**J122**	**J122**
Mineral	Pl	Pl	Pl	Pl	Pl	Pl	Pl	Pl	Pl	Pl	Pl	Pl	Pl	Pl	Pl
SiO2	57.8	58.1	59.0	58.5	58.9	59.1	58.8	58.7	59.2	57.7	57.1	57.6	58.1	58.2	58.4
TiO2	0.0	0.0	0.0	0.0	0.0	0.0	0.1	0.0	0.0	0.0	0.0	0.3	0.0	0.0	0.1
Al2O3	25.9	25.9	25.6	25.9	25.4	26.0	25.8	25.5	25.2	26.0	26.6	26.6	25.9	26.0	25.9
FeO	0.2	0.1	0.2	0.1	0.1	0.1	0.2	0.2	0.2	0.3	0.1	0.3	0.2	0.1	0.2
MnO	0.0	0.0	0.0	0.0	0.0	0.0	0.0	0.0	0.0	0.0	0.0	0.0	0.0	0.0	0.0
MgO	0.0	0.0	0.0	0.0	0.0	0.0	0.0	0.0	0.0	0.0	0.0	0.0	0.0	0.0	0.0
CaO	8.1	8.1	7.8	8.0	7.6	7.7	7.8	7.6	7.4	8.2	8.9	8.7	8.1	8.1	8.1
Na2O	7.2	7.0	7.0	7.1	7.1	7.2	7.3	7.3	7.5	7.2	6.6	6.5	7.0	7.2	7.1
K2O	0.4	0.3	0.4	0.4	1.0	0.4	0.4	0.5	0.4	0.4	0.4	0.4	0.4	0.4	0.4
Totals	99.6	99.6	100.0	100.0	100.1	100.5	100.4	99.7	99.9	99.7	99.8	100.4	99.7	100.0	100.2
Oxygens	8	8	8	8	8	8	8	8	8	8	8	8	8	8	8
Si	2.60	2.61	2.64	2.62	2.64	2.63	2.62	2.64	2.65	2.60	2.57	2.58	2.61	2.61	2.61
Ti	0.00	0.00	0.00	0.00	0.00	0.00	0.00	0.00	0.00	0.00	0.00	0.01	0.00	0.00	0.00
Al	1.38	1.37	1.35	1.37	1.34	1.37	1.36	1.35	1.33	1.38	1.41	1.40	1.37	1.37	1.37
Fe2+	0.01	0.00	0.01	0.00	0.00	0.00	0.01	0.01	0.01	0.01	0.01	0.01	0.01	0.01	0.01
Mn	0.00	0.00	0.00	0.00	0.00	0.00	0.00	0.00	0.00	0.00	0.00	0.00	0.00	0.00	0.00
Mg	0.00	0.00	0.00	0.00	0.00	0.00	0.00	0.00	0.00	0.00	0.00	0.00	0.00	0.00	0.00
Ca	0.39	0.39	0.37	0.38	0.36	0.37	0.37	0.36	0.36	0.40	0.43	0.42	0.39	0.39	0.39
Na	0.62	0.61	0.61	0.62	0.62	0.62	0.63	0.63	0.65	0.63	0.58	0.56	0.61	0.62	0.62
K	0.02	0.02	0.02	0.02	0.06	0.02	0.02	0.03	0.02	0.02	0.02	0.02	0.02	0.02	0.02
Sum	5.03	5.02	5.00	5.01	5.02	5.01	5.02	5.02	5.02	5.04	5.02	5.01	5.02	5.03	5.02

Sample	**J122**	**J122**	**B83**	**J122**	**J122**	**J262**	**J262**	**J262**	**J262**	**J263**	**J263**	**J263**	**J263**	**J263**	**J263**
Mineral	Pl	Pl	Pl?	Pl?	Pl?	Pl	Pl	Pl	Pl	Pl	Pl	Pl	Pl	Pl	Pl
SiO2	58.6	58.0	58.4	56.9	60.5	53.1	53.3	52.9	53.2	60.4	59.3	59.8	60.4	60.1	60.4
TiO2	0.0	0.0	0.0	0.0	0.0	0.1	0.0	0.0	0.0	0.0	0.0	0.0	0.0	0.0	0.1
Al2O3	25.7	26.5	25.5	25.7	21.4	30.4	30.2	30.7	30.9	25.4	25.9	25.5	25.5	25.1	25.5
FeO	0.2	0.3	0.1	0.1	0.1	0.1	0.2	0.2	0.1	0.2	0.3	0.1	0.2	0.2	0.2
MnO	0.0	0.0	0.0	0.0	0.0	0.0	0.0	0.0	0.0	0.0	0.0	0.0	0.0	0.0	0.0
MgO	0.0	0.0	0.0	0.0	0.0	0.0	0.0	0.2	0.0	0.0	0.0	0.0	0.0	0.0	0.0
CaO	7.8	8.4	7.4	7.8	2.9	12.6	12.7	12.6	12.7	7.0	7.5	7.0	7.0	6.6	7.0
Na2O	7.3	6.8	6.0	5.5	1.7	4.4	4.5	4.4	4.5	7.7	7.5	7.6	7.9	7.2	7.4
K2O	0.4	0.5	1.7	2.7	9.9	0.2	0.2	0.2	0.2	0.5	0.6	0.5	0.6	1.1	0.7
Totals	100.0	100.5	99.2	98.8	96.5	100.9	101.2	101.4	101.6	101.3	101.3	100.9	101.7	100.4	101.5
Oxygens	8	8	8	8	8	8	8	8	8	8	8	8	8	8	8
Si	2.63	2.59	2.64	2.60	2.85	2.39	2.39	2.37	2.38	2.67	2.63	2.66	2.66	2.68	2.67
Ti	0.00	0.00	0.00	0.00	0.00	0.00	0.00	0.00	0.00	0.00	0.00	0.00	0.00	0.00	0.00
Al	1.36	1.40	1.36	1.39	1.19	1.61	1.60	1.62	1.63	1.32	1.35	1.34	1.33	1.32	1.33
Fe2+	0.01	0.01	0.01	0.00	0.00	0.00	0.01	0.01	0.00	0.01	0.01	0.01	0.01	0.01	0.01
Mn	0.00	0.00	0.00	0.00	0.00	0.00	0.00	0.00	0.00	0.00	0.00	0.00	0.00	0.00	0.00
Mg	0.00	0.00	0.00	0.00	0.00	0.00	0.00	0.01	0.00	0.00	0.00	0.00	0.00	0.00	0.00
Ca	0.37	0.40	0.36	0.38	0.14	0.61	0.61	0.60	0.61	0.33	0.36	0.33	0.33	0.31	0.33
Na	0.63	0.59	0.52	0.49	0.15	0.39	0.39	0.38	0.39	0.66	0.64	0.65	0.67	0.62	0.63
K	0.02	0.03	0.10	0.16	0.60	0.01	0.01	0.01	0.01	0.03	0.03	0.03	0.03	0.06	0.04
Sum	5.02	5.02	4.99	5.03	4.93	5.01	5.01	5.01	5.01	5.01	5.03	5.02	5.03	5.00	5.01

Table 11 - Continued

Sample	**J263**	**J263**	**J263**	**J263**	**J403**	**J403**	**J403**	**J403**	**J403**	**J403**	**J403**	**J403**	**J413**	**J413**	**J413**
Mineral	Pl	Pl	Pl	Pl	Pl	Pl	Pl	Pl	Pl	Pl	Pl	Pl	Pl	Pl	Pl
SiO2	60.3	60.2	60.0	59.5	60.0	60.0	58.6	59.2	47.7	48.3	58.3	56.7	53.4	53.1	53.1
TiO2	0.0	0.0	0.0	0.0	0.0	0.0	0.0	0.0	0.0	0.0	0.0	0.0	0.1	0.0	0.1
Al2O3	25.1	25.6	25.8	25.6	26.0	25.9	26.6	26.4	33.8	33.5	26.8	28.2	30.1	30.2	30.3
FeO	0.2	0.1	0.2	0.1	0.1	0.0	0.1	0.2	0.3	0.2	0.1	0.2	0.3	0.2	0.2
MnO	0.0	0.0	0.0	0.0	0.0	0.0	0.0	0.0	0.0	0.0	0.0	0.0	0.0	0.0	0.0
MgO	0.1	0.0	0.0	0.0	0.0	0.0	0.0	0.0	0.0	0.0	0.0	0.0	0.0	0.0	0.0
CaO	6.9	6.9	7.2	7.2	7.1	7.0	8.1	7.9	16.7	16.1	8.4	9.9	12.3	12.4	12.5
Na2O	7.4	7.4	7.5	7.4	7.6	6.8	7.3	7.4	2.4	2.6	6.2	6.1	4.6	4.6	4.5
K2O	0.6	0.8	0.5	0.4	0.4	2.2	0.4	0.4	0.1	0.1	1.4	0.3	0.3	0.2	0.3
Totals	101.0	101.3	101.3	100.6	101.3	102.1	101.3	101.5	101.0	101.0	101.4	101.6	101.2	100.9	101.2
Oxygens	8	8	8	8	8	8	8	8	8	8	8	8	8	8	8
Si	2.68	2.66	2.65	2.65	2.65	2.65	2.60	2.61	2.17	2.20	2.59	2.52	2.40	2.39	2.39
Ti	0.00	0.00	0.00	0.00	0.00	0.00	0.00	0.00	0.00	0.00	0.00	0.00	0.00	0.00	0.00
Al	1.31	1.33	1.34	1.34	1.35	1.35	1.39	1.37	1.82	1.80	1.40	1.48	1.59	1.60	1.60
Fe2+	0.01	0.00	0.01	0.00	0.00	0.00	0.00	0.01	0.01	0.01	0.00	0.01	0.01	0.01	0.01
Mn	0.00	0.00	0.00	0.00	0.00	0.00	0.00	0.00	0.00	0.00	0.00	0.00	0.00	0.00	0.00
Mg	0.00	0.00	0.00	0.00	0.00	0.00	0.00	0.00	0.00	0.00	0.00	0.00	0.00	0.00	0.00
Ca	0.33	0.33	0.34	0.35	0.34	0.33	0.38	0.37	0.81	0.78	0.40	0.47	0.59	0.60	0.60
Na	0.63	0.63	0.64	0.64	0.65	0.58	0.63	0.63	0.21	0.23	0.53	0.52	0.40	0.40	0.39
K	0.04	0.04	0.03	0.03	0.02	0.13	0.02	0.02	0.01	0.00	0.08	0.02	0.02	0.01	0.02
Sum	5.00	5.01	5.01	5.01	5.01	5.04	5.03	5.02	5.03	5.02	5.01	5.01	5.01	5.02	5.01

Sample	**J413**	**J270**	**J270**	**J270**	**J270**	**J269**	**J269**	**J269**	**J269**	**J269**	**J269**	**J407**	**J407**	**J407**	**J407**
Mineral	Pl	Pl	Pl	Pl	Pl	Pl	Pl	Pl	Pl	Pl	Pl	Pl	Pl	Pl	Pl
SiO2	52.9	48.3	48.0	48.0	48.2	46.9	46.5	47.0	46.6	47.6	47.5	59.4	59.2	58.4	58.9
TiO2	0.0	0.0	0.0	0.0	0.0	0.0	0.0	0.0	0.0	0.0	0.0	0.0	0.1	0.0	0.0
Al2O3	30.4	33.3	33.4	33.9	33.7	33.3	33.5	33.6	33.4	34.3	34.3	26.7	26.5	27.1	26.7
FeO	0.2	0.1	0.1	0.0	0.1	0.1	0.1	0.0	0.0	0.0	0.1	0.2	0.2	0.2	0.2
MnO	0.0	0.0	0.0	0.0	0.0	0.0	0.0	0.0	0.0	0.0	0.0	0.0	0.0	0.0	0.0
MgO	0.0	0.0	0.0	0.0	0.0	0.0	0.0	0.0	0.0	0.0	0.0	0.0	0.0	0.0	0.0
CaO	12.5	15.9	16.1	16.6	16.4	16.6	16.8	16.8	16.8	17.2	16.9	8.2	8.2	8.6	8.2
Na2O	4.7	2.6	2.4	2.3	2.2	1.9	1.8	2.0	1.9	1.9	2.0	7.2	7.0	6.6	7.0
K2O	0.3	0.0	0.0	0.0	0.0	0.0	0.0	0.0	0.0	0.0	0.0	0.4	0.4	0.5	0.4
Totals	100.9	100.2	100.0	100.8	100.7	98.9	98.8	99.5	99.0	101.2	100.7	102.3	101.8	101.6	101.6
Oxygens	8	8	8	8	8	8	8	8	8	8	8	8	8	8	8
Si	2.38	2.21	2.20	2.18	2.19	2.18	2.16	2.17	2.17	2.16	2.16	2.61	2.61	2.58	2.60
Ti	0.00	0.00	0.00	0.00	0.00	0.00	0.00	0.00	0.00	0.00	0.00	0.00	0.00	0.00	0.00
Al	1.61	1.79	1.80	1.82	1.81	1.82	1.84	1.83	1.83	1.84	1.84	1.38	1.38	1.41	1.39
Fe2+	0.01	0.00	0.00	0.00	0.00	0.00	0.00	0.00	0.00	0.00	0.00	0.01	0.01	0.01	0.01
Mn	0.00	0.00	0.00	0.00	0.00	0.00	0.00	0.00	0.00	0.00	0.00	0.00	0.00	0.00	0.00
Mg	0.00	0.00	0.00	0.00	0.00	0.00	0.00	0.00	0.00	0.00	0.00	0.00	0.00	0.00	0.00
Ca	0.60	0.78	0.79	0.81	0.80	0.83	0.83	0.83	0.84	0.84	0.82	0.38	0.39	0.41	0.39
Na	0.41	0.23	0.21	0.20	0.20	0.17	0.16	0.17	0.17	0.17	0.17	0.61	0.60	0.57	0.60
K	0.02	0.00	0.00	0.00	0.00	0.00	0.00	0.00	0.00	0.00	0.00	0.02	0.02	0.03	0.02
Sum	5.02	5.01	5.01	5.01	5.00	5.00	5.00	5.00	5.00	5.01	5.00	5.02	5.01	5.01	5.01

Table 11 - Continued

Sample	J404	J404	J404	J404	J266	J266	J266	J266	J264	J264	J264	J264	J267	J267	J267
Mineral	Pl	Pl	Pl	Pl	Pl	Pl	Pl	Pl	Pl	Pl	Pl	Pl	Pl	Pl	Pl
SiO2	57.2	56.9	57.8	56.9	49.7	49.5	49.3	49.4	46.2	46.2	46.9	47.1	47.8	48.1	47.8
TiO2	0.0	0.0	0.0	0.0	0.0	0.0	0.0	0.0	0.0	0.0	0.0	0.0	0.0	0.0	0.0
Al2O3	24.7	24.5	26.6	27.4	31.7	32.1	32.3	32.3	33.9	34.3	33.7	33.8	33.4	32.7	33.3
FeO	0.1	0.1	0.1	0.1	0.0	0.1	0.0	0.0	0.0	0.1	0.1	0.1	0.3	0.2	0.1
MnO	0.0	0.0	0.0	0.0	0.0	0.0	0.0	0.0	0.0	0.0	0.0	0.0	0.0	0.0	0.0
MgO	0.0	0.0	0.0	0.0	0.0	0.0	0.0	0.0	0.0	0.0	0.0	0.0	0.0	0.0	0.0
CaO	7.3	7.1	8.3	9.3	15.1	15.3	15.6	15.6	17.7	17.8	17.2	17.4	16.6	16.0	16.4
Na2O	6.4	6.3	6.8	6.1	3.3	3.0	2.8	2.9	1.5	1.4	1.8	1.8	2.3	2.5	2.4
K2O	0.5	0.9	0.4	0.6	0.0	0.0	0.0	0.0	0.0	0.0	0.0	0.0	0.0	0.0	0.0
Totals	96.6	96.4	100.3	100.5	99.8	100.1	100.1	100.2	99.3	99.7	99.6	100.2	100.4	99.5	100.0
Oxygens	8	8	8	8	8	8	8	8	8	8	8	8	8	8	8
Si	2.65	2.65	2.59	2.55	2.27	2.26	2.25	2.25	2.14	2.13	2.16	2.16	2.19	2.21	2.19
Ti	0.00	0.00	0.00	0.00	0.00	0.00	0.00	0.00	0.00	0.00	0.00	0.00	0.00	0.00	0.00
Al	1.35	1.35	1.40	1.45	1.71	1.73	1.74	1.73	1.85	1.87	1.83	1.83	1.80	1.77	1.80
Fe2+	0.00	0.00	0.00	0.01	0.00	0.00	0.00	0.00	0.00	0.00	0.00	0.00	0.01	0.01	0.00
Mn	0.00	0.00	0.00	0.00	0.00	0.00	0.00	0.00	0.00	0.00	0.00	0.00	0.00	0.00	0.00
Mg	0.00	0.00	0.00	0.00	0.00	0.00	0.00	0.00	0.00	0.00	0.00	0.00	0.00	0.00	0.00
Ca	0.36	0.36	0.40	0.44	0.74	0.75	0.76	0.76	0.88	0.88	0.85	0.85	0.82	0.79	0.81
Na	0.58	0.57	0.59	0.53	0.29	0.27	0.25	0.25	0.14	0.12	0.16	0.16	0.20	0.22	0.21
K	0.03	0.06	0.03	0.03	0.00	0.00	0.00	0.00	0.00	0.00	0.00	0.00	0.00	0.00	0.00
Sum	4.97	4.98	5.02	5.01	5.02	5.01	5.00	5.01	5.00	5.00	5.00	5.01	5.02	5.01	5.02

Sample	J267	J259	J259	J259	J259	J259	J259	J259	J259	J259	J259	J259	J259	J411	J411
Mineral	Pl	Pl	Pl	Pl	Pl	Pl	Pl	Pl	Pl	Pl	Pl	Pl	Pl	Pl	Pl
SiO2	46.9	58.5	57.9	58.1	56.5	58.5	57.8	57.9	57.7	57.1	56.9	56.8	56.6	57.3	57.4
TiO2	0.0	0.2	0.0	0.1	0.0	0.0	0.0	0.0	0.0	0.0	0.0	0.0	0.1	0.0	0.0
Al2O3	33.6	25.9	26.0	26.3	27.3	26.0	26.1	26.4	26.3	27.0	26.8	27.3	27.1	26.9	26.2
FeO	0.1	0.2	0.1	0.1	0.2	0.1	0.1	0.1	0.1	0.1	0.1	0.2	0.2	0.2	0.1
MnO	0.0	0.0	0.0	0.0	0.0	0.0	0.0	0.0	0.0	0.0	0.0	0.0	0.0	0.0	0.0
MgO	0.0	0.0	0.0	0.0	0.1	0.0	0.0	0.0	0.0	0.0	0.0	0.0	0.0	0.0	0.0
CaO	17.1	7.9	8.3	8.8	9.6	8.4	8.5	8.7	8.6	9.4	9.5	9.6	9.6	9.5	8.4
Na2O	2.1	6.9	6.8	6.5	6.2	6.6	6.8	6.6	6.7	5.9	6.1	6.0	6.3	6.2	7.0
K2O	0.0	0.7	0.8	0.4	0.6	0.5	0.5	0.4	0.4	0.7	0.5	0.4	0.4	0.4	0.4
Totals	99.8	100.3	99.9	100.3	100.5	100.1	99.9	100.2	99.9	100.3	100.0	100.3	100.3	100.7	99.7
Oxygens	8	8	8	8	8	8	8	8	8	8	8	8	8	8	8
Si	2.16	2.62	2.60	2.60	2.54	2.62	2.60	2.59	2.59	2.56	2.56	2.55	2.54	2.56	2.59
Ti	0.00	0.01	0.00	0.00	0.00	0.00	0.00	0.00	0.00	0.00	0.00	0.00	0.00	0.00	0.00
Al	1.83	1.37	1.38	1.39	1.45	1.37	1.38	1.39	1.40	1.43	1.42	1.44	1.44	1.42	1.39
Fe2+	0.00	0.01	0.00	0.01	0.01	0.01	0.00	0.00	0.00	0.00	0.01	0.01	0.01	0.01	0.00
Mn	0.00	0.00	0.00	0.00	0.00	0.00	0.00	0.00	0.00	0.00	0.00	0.00	0.00	0.00	0.00
Mg	0.00	0.00	0.00	0.00	0.00	0.00	0.00	0.00	0.00	0.00	0.00	0.00	0.00	0.00	0.00
Ca	0.84	0.38	0.40	0.42	0.46	0.40	0.41	0.42	0.41	0.45	0.46	0.46	0.46	0.45	0.41
Na	0.19	0.59	0.59	0.56	0.54	0.57	0.60	0.58	0.58	0.51	0.53	0.53	0.55	0.54	0.61
K	0.00	0.04	0.04	0.02	0.03	0.03	0.03	0.02	0.02	0.04	0.03	0.02	0.02	0.03	0.02
Sum	5.02	5.01	5.02	5.00	5.02	5.00	5.02	5.01	5.01	5.00	5.01	5.01	5.02	5.01	5.03

Table 11 - Continued

Sample	J411	J411	J411	J429	J429	J429	J429	J429	J429	J428	J428	J428	J428	J428	J428
Mineral	Pl	Pl	Pl	Pl	Pl	Pl	Pl	Pl	Pl	Pl	Pl	Pl	Pl	Pl	Pl
SiO2	58.7	58.7	58.6	51.6	52.3	53.2	52.5	52.9	53.0	50.8	49.8	49.6	49.7	48.1	50.3
TiO2	0.0	0.1	0.0	0.0	0.1	0.0	0.0	0.0	0.1	0.0	0.0	0.0	0.0	0.0	0.0
Al2O3	26.2	26.2	26.0	31.0	30.6	29.6	30.3	30.3	30.2	31.5	32.3	31.9	32.1	33.6	31.5
FeO	0.1	0.2	0.2	0.1	0.1	0.1	0.1	0.1	0.1	0.3	0.1	0.1	0.1	0.1	0.1
MnO	0.0	0.0	0.0	0.0	0.0	0.0	0.0	0.0	0.0	0.0	0.0	0.0	0.0	0.0	0.0
MgO	0.0	0.0	0.0	0.0	0.0	0.0	0.0	0.0	0.0	0.0	0.0	0.0	0.0	0.0	0.0
CaO	8.3	8.4	8.3	13.9	13.5	11.9	12.6	12.6	12.4	14.6	15.3	14.8	14.9	16.7	14.7
Na2O	6.9	6.7	6.8	4.0	4.2	5.2	4.6	4.5	4.6	3.4	3.0	3.3	3.2	2.2	3.4
K2O	0.4	0.4	0.4	0.0	0.0	0.0	0.0	0.0	0.0	0.0	0.0	0.0	0.0	0.0	0.0
Totals	100.9	101.0	100.5	100.8	101.0	100.2	100.5	100.7	100.7	101.0	100.8	100.0	100.2	101.0	100.2
Oxygens	8	8	8	8	8	8	8	8	8	8	8	8	8	8	8
Si	2.61	2.61	2.62	2.33	2.36	2.41	2.38	2.39	2.39	2.30	2.26	2.27	2.27	2.19	2.29
Ti	0.00	0.00	0.00	0.00	0.00	0.00	0.00	0.00	0.00	0.00	0.00	0.00	0.00	0.00	0.00
Al	1.38	1.38	1.37	1.65	1.63	1.58	1.62	1.61	1.61	1.68	1.73	1.72	1.73	1.80	1.69
Fe2+	0.00	0.01	0.01	0.00	0.00	0.00	0.00	0.00	0.00	0.01	0.00	0.00	0.00	0.00	0.00
Mn	0.00	0.00	0.00	0.00	0.00	0.00	0.00	0.00	0.00	0.00	0.00	0.00	0.00	0.00	0.00
Mg	0.00	0.00	0.00	0.00	0.00	0.00	0.00	0.00	0.00	0.00	0.00	0.00	0.00	0.00	0.00
Ca	0.40	0.40	0.40	0.67	0.65	0.58	0.61	0.61	0.60	0.71	0.74	0.72	0.73	0.82	0.72
Na	0.60	0.58	0.59	0.35	0.36	0.45	0.40	0.39	0.40	0.30	0.27	0.29	0.28	0.19	0.30
K	0.02	0.02	0.02	0.00	0.00	0.00	0.00	0.00	0.00	0.00	0.00	0.00	0.00	0.00	0.00
Sum	5.01	5.00	5.00	5.02	5.01	5.03	5.01	5.01	5.01	5.01	5.01	5.02	5.01	5.01	5.01

Sample	J428	J428	J428	J428	J428	J428	J428	J428	J256	J256	C-95	C-95	C-95	C-95	C-95
Mineral	Pl	Pl	Pl	Pl	Pl	Pl	Pl	Pl	Pl	Pl	Pl	Pl	Pl	Pl	Pl
SiO2	51.4	51.3	50.5	49.9	50.5	50.6	50.5	51.4	55.1	55.1	45.6	47.5	45.9	46.1	46.3
TiO2	0.0	0.0	0.0	0.0	0.0	0.0	0.0	0.1	0.0	0.0	0.0	0.0	0.0	0.0	0.0
Al2O3	31.0	31.2	31.4	31.5	31.6	31.3	31.7	31.3	28.5	28.5	34.9	33.4	34.3	34.1	34.4
FeO	0.2	0.2	0.1	0.2	0.1	1.3	0.1	0.1	0.1	0.1	0.1	0.0	0.1	0.1	0.1
MnO	0.0	0.0	0.0	0.0	0.0	0.0	0.0	0.0	0.0	0.0	0.0	0.0	0.0	0.0	0.0
MgO	0.0	0.0	0.0	0.0	0.0	0.0	0.0	0.0	0.0	0.0	0.0	0.0	0.0	0.0	0.0
CaO	13.8	14.1	14.0	14.1	14.3	13.9	14.7	14.1	10.7	10.9	17.8	16.3	17.2	17.1	17.4
Na2O	3.8	3.8	3.5	3.4	3.5	3.7	3.4	3.7	5.8	5.7	1.6	2.4	1.9	2.0	1.8
K2O	0.2	0.1	0.1	0.0	0.0	0.0	0.1	0.1	0.1	0.1	0.0	0.0	0.0	0.0	0.0
Totals	100.6	100.9	99.8	99.4	100.4	101.1	100.6	100.9	100.4	100.5	99.9	99.7	99.5	99.5	99.9
Oxygens	8	8	8	8	8	8	8	8	8	8	8	8	8	8	8
Si	2.33	2.32	2.31	2.29	2.30	2.30	2.29	2.32	2.48	2.48	2.10	2.18	2.12	2.13	2.13
Ti	0.00	0.00	0.00	0.00	0.00	0.00	0.00	0.00	0.00	0.00	0.00	0.00	0.00	0.00	0.00
Al	1.66	1.67	1.69	1.71	1.69	1.68	1.70	1.67	1.51	1.51	1.90	1.81	1.87	1.86	1.87
Fe2+	0.01	0.01	0.00	0.01	0.00	0.05	0.00	0.00	0.00	0.00	0.00	0.00	0.00	0.00	0.00
Mn	0.00	0.00	0.00	0.00	0.00	0.00	0.00	0.00	0.00	0.00	0.00	0.00	0.00	0.00	0.00
Mg	0.00	0.00	0.00	0.00	0.00	0.00	0.00	0.00	0.00	0.00	0.00	0.00	0.00	0.00	0.00
Ca	0.67	0.68	0.69	0.69	0.70	0.68	0.72	0.68	0.51	0.52	0.88	0.80	0.85	0.85	0.86
Na	0.34	0.33	0.31	0.31	0.31	0.33	0.30	0.33	0.50	0.50	0.14	0.21	0.17	0.18	0.16
K	0.01	0.00	0.00	0.00	0.00	0.00	0.00	0.00	0.01	0.01	0.00	0.00	0.00	0.00	0.00
Sum	5.01	5.01	5.01	5.01	5.01	5.03	5.01	5.01	5.02	5.02	5.02	5.01	5.03	5.03	5.02

Table 11 - Continued

Sample	**C-95**	**C-95**	**C-95**	**C-95**	**C-95**	**C-95**	**C-95**	**C-95**	**C-95**	**C-95**	**C-95**	**C-95**	**J416**	**J416**	**J416**
Mineral	Pl	Pl	Pl	Pl	Pl	Pl	Pl	Pl	Pl	Pl	Pl	Pl	Pl	Pl	Pl
SiO2	46.5	48.6	45.6	44.9	45.2	45.1	44.1	44.0	44.8	44.4	43.9	43.5	56.7	56.7	56.2
TiO2	0.0	0.0	0.0	0.0	0.0	0.0	0.0	0.0	0.0	0.0	0.0	0.0	0.0	0.0	0.0
Al2O3	34.2	32.6	34.9	35.3	35.0	34.9	34.7	36.3	35.7	35.5	35.6	36.1	27.1	27.2	27.5
FeO	0.1	0.0	0.0	0.1	0.0	0.0	0.1	0.1	0.0	0.0	0.1	0.0	0.1	0.2	0.1
MnO	0.0	0.0	0.0	0.0	0.0	0.0	0.0	0.0	0.0	0.0	0.0	0.0	0.0	0.0	0.0
MgO	0.0	0.0	0.0	0.0	0.0	0.0	0.0	0.0	0.0	0.0	0.0	0.0	0.0	0.0	0.1
CaO	16.8	15.3	17.8	18.2	18.0	17.7	18.2	19.4	18.7	18.4	18.7	19.3	8.9	8.9	9.0
Na2O	2.1	3.2	1.5	1.3	1.4	1.5	1.0	0.6	1.1	1.1	0.9	0.7	6.4	6.3	6.4
K2O	0.0	0.0	0.0	0.0	0.0	0.0	0.0	0.0	0.0	0.0	0.0	0.0	0.6	0.9	0.5
Totals	99.9	99.7	100.0	99.8	99.7	99.2	98.2	100.5	100.3	99.5	99.3	99.8	100.2	100.4	100.1
Oxygens	8	8	8	8	8	8	8	8	8	8	8	8	8	8	8
Si	2.14	2.23	2.10	2.08	2.09	2.09	2.07	2.03	2.06	2.06	2.04	2.02	2.55	2.55	2.53
Ti	0.00	0.00	0.00	0.00	0.00	0.00	0.00	0.00	0.00	0.00	0.00	0.00	0.00	0.00	0.00
Al	1.86	1.76	1.90	1.93	1.91	1.91	1.93	1.97	1.94	1.94	1.95	1.97	1.44	1.44	1.46
Fe2+	0.00	0.00	0.00	0.00	0.00	0.00	0.00	0.00	0.00	0.00	0.00	0.00	0.01	0.01	0.00
Mn	0.00	0.00	0.00	0.00	0.00	0.00	0.00	0.00	0.00	0.00	0.00	0.00	0.00	0.00	0.00
Mg	0.00	0.00	0.00	0.00	0.00	0.00	0.00	0.00	0.00	0.00	0.00	0.00	0.00	0.00	0.00
Ca	0.83	0.75	0.88	0.90	0.89	0.88	0.91	0.96	0.92	0.92	0.93	0.96	0.43	0.43	0.44
Na	0.19	0.28	0.13	0.11	0.12	0.13	0.09	0.06	0.09	0.10	0.08	0.06	0.56	0.55	0.56
K	0.00	0.00	0.00	0.00	0.00	0.00	0.00	0.00	0.00	0.00	0.00	0.00	0.03	0.05	0.03
Sum	5.02	5.03	5.02	5.02	5.02	5.02	5.01	5.02	5.02	5.02	5.02	5.02	5.02	5.03	5.03

Sample	**J416**	**J416**	**J416**	**J414**	**J414**	**J414**	**J414**	**J414**	**J414**	**J414**	**J414**	**J414**	**J414**	**J414**	**J414**
Mineral	Pl	Pl	Pl	Pl	Pl	Pl	Pl	Pl	Pl	Pl	Pl	Pl	Pl	Pl	Pl
SiO2	56.2	56.9	56.6	58.2	58.3	57.8	57.5	57.5	57.9	57.6	57.0	57.1	56.9	55.3	57.8
TiO2	0.0	0.0	0.0	0.0	0.0	0.0	0.0	0.0	0.0	0.0	0.0	0.0	0.0	0.0	0.0
Al2O3	27.3	27.1	27.2	26.5	26.2	26.3	26.5	26.3	26.5	26.6	27.1	26.8	26.8	28.2	26.5
FeO	0.2	0.1	0.1	0.1	0.1	0.1	0.1	0.1	0.0	0.1	0.1	0.1	0.1	0.1	0.1
MnO	0.0	0.0	0.0	0.0	0.0	0.0	0.0	0.0	0.0	0.0	0.0	0.0	0.0	0.0	0.0
MgO	0.0	0.0	0.0	0.0	0.0	0.0	0.0	0.0	0.0	0.0	0.0	0.0	0.0	0.0	0.0
CaO	9.1	8.9	8.7	7.8	7.8	7.8	8.0	7.7	7.8	8.0	8.7	8.2	8.3	9.4	8.0
Na2O	6.3	6.7	6.3	7.3	7.4	7.5	7.4	7.3	7.6	7.5	6.9	7.3	7.2	6.1	7.6
K2O	0.8	0.5	0.9	0.3	0.3	0.3	0.3	0.3	0.3	0.3	0.3	0.3	0.3	0.3	0.3
Totals	100.0	100.5	99.9	100.4	100.3	99.9	100.1	99.3	100.3	100.2	100.2	99.9	99.8	99.4	100.4
Oxygens	8	8	8	8	8	8	8	8	8	8	8	8	8	8	8
Si	2.54	2.55	2.55	2.60	2.61	2.60	2.58	2.60	2.59	2.59	2.56	2.57	2.57	2.50	2.59
Ti	0.00	0.00	0.00	0.00	0.00	0.00	0.00	0.00	0.00	0.00	0.00	0.00	0.00	0.00	0.00
Al	1.45	1.43	1.44	1.39	1.38	1.39	1.41	1.40	1.40	1.41	1.43	1.42	1.43	1.51	1.40
Fe2+	0.01	0.00	0.00	0.00	0.00	0.00	0.00	0.00	0.00	0.00	0.00	0.00	0.00	0.00	0.00
Mn	0.00	0.00	0.00	0.00	0.00	0.00	0.00	0.00	0.00	0.00	0.00	0.00	0.00	0.00	0.00
Mg	0.00	0.00	0.00	0.00	0.00	0.00	0.00	0.00	0.00	0.00	0.00	0.00	0.00	0.00	0.00
Ca	0.44	0.43	0.42	0.37	0.38	0.38	0.38	0.37	0.37	0.38	0.42	0.40	0.40	0.45	0.38
Na	0.56	0.58	0.55	0.63	0.64	0.65	0.64	0.64	0.66	0.65	0.60	0.63	0.63	0.53	0.66
K	0.05	0.03	0.05	0.02	0.02	0.02	0.02	0.02	0.02	0.02	0.02	0.02	0.02	0.02	0.02
Sum	5.04	5.04	5.03	5.03	5.03	5.04	5.04	5.03	5.05	5.04	5.03	5.04	5.04	5.02	5.05

Table 11 - Continued

Sample	**J414**	**J414**	**J414**	**J414**	**J414**	**J414**	**J414**	**J414**	**J414**	**J418**	**J418**	**J418**	**J418**	**J418**	**J418**
Mineral	Pl	Pl	Pl	Pl	Pl	Pl	Pl	Pl	Pl	Pl	Pl	Pl	Pl	Pl	Pl
SiO2	58.0	57.4	57.7	58.2	58.5	58.0	57.8	58.1	58.0	61.1	61.3	61.2	60.2	62.2	61.8
TiO2	0.0	0.0	0.0	0.0	0.0	0.0	0.0	0.0	0.0	0.1	0.0	0.0	0.0	0.0	0.0
Al2O3	26.1	26.5	26.5	26.0	26.2	26.5	26.7	26.4	26.2	23.6	23.6	24.1	24.0	23.3	23.7
FeO	0.1	0.1	0.1	0.1	0.1	0.1	0.1	0.1	0.1	0.1	0.1	0.1	0.1	0.1	0.1
MnO	0.0	0.0	0.0	0.0	0.0	0.0	0.0	0.0	0.0	0.0	0.0	0.0	0.0	0.0	0.0
MgO	0.0	0.0	0.0	0.0	0.0	0.0	0.0	0.0	0.0	0.0	0.0	0.0	0.0	0.0	0.0
CaO	7.6	7.8	7.8	7.6	7.4	7.9	8.0	7.7	7.6	4.8	4.8	5.0	5.1	4.7	4.9
Na2O	7.5	7.6	7.6	7.6	7.6	7.5	7.4	7.6	7.6	8.4	9.2	8.9	8.9	9.1	9.0
K2O	0.3	0.3	0.3	0.3	0.4	0.3	0.3	0.3	0.3	1.8	0.5	0.6	0.6	0.6	0.6
Totals	99.7	99.9	100.4	100.0	100.4	100.5	100.4	100.4	100.0	99.9	99.7	100.0	99.1	100.1	100.1
Oxygens	8	8	8	8	8	8	8	8	8	8	8	8	8	8	8
Si	2.61	2.59	2.59	2.61	2.61	2.59	2.59	2.60	2.60	2.74	2.74	2.73	2.71	2.77	2.75
Ti	0.00	0.00	0.00	0.00	0.00	0.00	0.00	0.00	0.00	0.00	0.00	0.00	0.00	0.00	0.00
Al	1.38	1.40	1.40	1.38	1.38	1.40	1.41	1.39	1.39	1.25	1.25	1.27	1.27	1.22	1.24
Fe2+	0.00	0.00	0.01	0.00	0.00	0.00	0.00	0.00	0.00	0.00	0.00	0.00	0.00	0.00	0.00
Mn	0.00	0.00	0.00	0.00	0.00	0.00	0.00	0.00	0.00	0.00	0.00	0.00	0.00	0.00	0.00
Mg	0.00	0.00	0.00	0.00	0.00	0.00	0.00	0.00	0.00	0.00	0.00	0.00	0.00	0.00	0.00
Ca	0.37	0.38	0.38	0.36	0.36	0.38	0.38	0.37	0.37	0.23	0.23	0.24	0.25	0.22	0.23
Na	0.66	0.66	0.66	0.66	0.66	0.65	0.64	0.66	0.66	0.73	0.80	0.77	0.78	0.78	0.78
K	0.02	0.02	0.02	0.02	0.02	0.02	0.02	0.02	0.02	0.10	0.03	0.03	0.03	0.03	0.03
Sum	5.04	5.05	5.05	5.04	5.03	5.04	5.04	5.04	5.04	5.05	5.05	5.04	5.06	5.03	5.04

Sample	**J418**	**J418**	**J418**	**J418**	**J418**	**J418**	**J418**	**J418**	**J418**	**J418**	**J418**	**J418**	**J418**	**J418**	**J418**
Mineral	Pl	Pl	Pl	Pl	Pl	Pl	Pl	Pl	Pl	Pl	Pl	Pl	Pl	Pl	Pl
SiO2	56.5	58.5	59.7	61.1	60.3	61.5	61.1	60.5	59.9	58.2	60.1	60.4	61.3	61.0	61.5
TiO2	0.0	0.0	0.0	0.0	0.0	0.0	0.0	0.0	0.0	0.0	0.0	0.0	0.0	0.0	0.0
Al2O3	27.2	25.7	23.7	23.7	23.9	24.0	23.6	24.3	25.1	26.2	25.3	25.0	23.9	23.6	24.4
FeO	0.1	0.1	0.2	0.1	0.2	0.1	0.1	0.1	0.1	0.1	0.1	0.1	0.1	0.1	0.1
MnO	0.0	0.0	0.0	0.0	0.0	0.0	0.0	0.0	0.0	0.0	0.0	0.0	0.0	0.0	0.0
MgO	0.0	0.1	0.0	0.0	0.0	0.0	0.0	0.0	0.0	0.0	0.0	0.0	0.0	0.0	0.0
CaO	9.0	7.2	5.0	4.9	5.1	5.1	4.9	5.4	6.3	7.7	6.3	6.5	5.1	5.0	5.4
Na2O	6.8	7.6	8.1	9.0	9.0	7.6	8.6	8.8	8.1	7.5	8.2	8.3	8.9	7.8	8.8
K2O	0.4	0.5	0.6	0.6	0.5	0.5	0.6	0.5	0.5	0.3	0.5	0.4	0.9	1.8	0.5
Totals	100.0	99.8	97.4	99.7	99.1	99.1	99.2	99.6	100.1	100.2	100.5	100.8	100.1	99.3	100.8
Oxygens	8	8	8	8	8	8	8	8	8	8	8	8	8	8	8
Si	2.55	2.63	2.73	2.74	2.72	2.75	2.74	2.71	2.67	2.61	2.67	2.68	2.73	2.74	2.72
Ti	0.00	0.00	0.00	0.00	0.00	0.00	0.00	0.00	0.00	0.00	0.00	0.00	0.00	0.00	0.00
Al	1.44	1.36	1.28	1.25	1.27	1.27	1.25	1.28	1.32	1.38	1.32	1.31	1.25	1.25	1.27
Fe2+	0.00	0.00	0.01	0.00	0.01	0.00	0.00	0.00	0.00	0.00	0.00	0.00	0.00	0.00	0.00
Mn	0.00	0.00	0.00	0.00	0.00	0.00	0.00	0.00	0.00	0.00	0.00	0.00	0.00	0.00	0.00
Mg	0.00	0.00	0.00	0.00	0.00	0.00	0.00	0.00	0.00	0.00	0.00	0.00	0.00	0.00	0.00
Ca	0.43	0.35	0.25	0.24	0.25	0.24	0.24	0.26	0.30	0.37	0.30	0.31	0.24	0.24	0.26
Na	0.59	0.66	0.72	0.78	0.79	0.66	0.75	0.76	0.70	0.65	0.71	0.71	0.77	0.68	0.75
K	0.02	0.03	0.03	0.04	0.03	0.03	0.04	0.03	0.03	0.02	0.03	0.02	0.05	0.10	0.03
Sum	5.04	5.04	5.01	5.05	5.05	4.96	5.02	5.05	5.03	5.04	5.04	5.03	5.05	5.02	5.03

Table 11 - Continued

Sample	J418	J418	J418	J111	J111	J111	J111	J111	J111	J111	J111	J111	J111	J111	J111
Mineral	Pl	Pl	Pl	Pl	Pl	Pl	Pl	Pl	Pl	Pl	Pl	Pl	Pl	Pl	Pl
SiO2	61.8	62.1	61.3	46.7	46.4	47.1	46.8	46.5	45.8	45.3	45.9	45.4	46.0	46.1	46.2
TiO2	0.0	0.0	0.0	0.0	0.0	0.0	0.0	0.0	0.0	0.0	0.0	0.0	0.0	0.0	0.0
Al2O3	24.1	23.9	23.9	34.5	35.0	34.6	34.7	34.9	34.9	34.9	34.7	34.8	34.4	35.0	34.3
FeO	0.1	0.1	0.1	0.0	0.0	0.1	0.1	0.1	0.1	0.1	0.0	0.0	0.0	0.1	0.1
MnO	0.0	0.0	0.0	0.0	0.0	0.0	0.0	0.0	0.0	0.0	0.0	0.0	0.0	0.0	0.0
MgO	0.0	0.0	0.0	0.0	0.0	0.0	0.0	0.0	0.0	0.0	0.0	0.0	0.0	0.0	0.0
CaO	5.2	5.0	5.0	17.3	17.8	17.5	17.4	17.4	17.4	17.9	17.7	17.8	17.3	17.5	17.3
Na2O	8.8	8.8	8.7	1.9	1.7	1.8	1.9	1.6	1.7	1.6	1.6	1.6	1.8	1.8	2.0
K2O	0.5	0.5	0.6	0.0	0.0	0.0	0.0	0.0	0.0	0.0	0.0	0.0	0.0	0.0	0.0
Totals	100.6	100.5	99.6	100.4	101.0	101.1	100.9	100.5	100.0	99.8	100.0	99.7	99.6	100.5	99.9
Oxygens	8	8	8	8	8	8	8	8	8	8	8	8	8	8	8
Si	2.73	2.75	2.74	2.14	2.12	2.14	2.13	2.12	2.11	2.09	2.11	2.10	2.12	2.11	2.13
Ti	0.00	0.00	0.00	0.00	0.00	0.00	0.00	0.00	0.00	0.00	0.00	0.00	0.00	0.00	0.00
Al	1.26	1.24	1.26	1.86	1.88	1.86	1.86	1.88	1.89	1.90	1.88	1.90	1.87	1.89	1.86
Fe2+	0.00	0.00	0.00	0.00	0.00	0.00	0.00	0.00	0.00	0.00	0.00	0.00	0.00	0.00	0.00
Mn	0.00	0.00	0.00	0.00	0.00	0.00	0.00	0.00	0.00	0.00	0.00	0.00	0.00	0.00	0.00
Mg	0.00	0.00	0.00	0.00	0.00	0.00	0.00	0.00	0.00	0.00	0.00	0.00	0.00	0.00	0.00
Ca	0.25	0.23	0.24	0.85	0.87	0.85	0.85	0.85	0.86	0.88	0.87	0.88	0.86	0.86	0.85
Na	0.75	0.76	0.75	0.16	0.15	0.16	0.17	0.14	0.15	0.15	0.14	0.14	0.16	0.16	0.18
K	0.03	0.03	0.03	0.00	0.00	0.00	0.00	0.00	0.00	0.00	0.00	0.00	0.00	0.00	0.00
Sum	5.03	5.02	5.02	5.01	5.02	5.01	5.02	5.00	5.02	5.03	5.01	5.02	5.02	5.02	5.03

Sample	J111	J111	J419	J419	J419	J419	J419	J419	J419	J419	J419	J419	J419	J419	J419
Mineral	Pl	Pl	Pl	Pl	Pl	Pl	Pl	Pl	Pl	Pl	Pl	Pl	Pl	Pl	Pl
SiO2	46.2	46.3	47.7	47.6	47.5	47.6	48.0	48.8	48.5	48.4	47.5	47.4	47.4	48.3	47.8
TiO2	0.0	0.0	0.0	0.0	0.0	0.0	0.0	0.0	0.0	0.0	0.0	0.0	0.1	0.0	0.0
Al2O3	35.0	34.8	33.6	33.6	34.0	34.0	33.8	32.9	33.6	33.4	33.9	34.0	34.1	33.4	34.4
FeO	0.1	0.1	0.1	0.0	0.1	0.0	0.0	0.0	0.0	0.0	0.0	0.0	0.0	0.0	0.0
MnO	0.0	0.0	0.0	0.0	0.0	0.0	0.0	0.0	0.0	0.0	0.0	0.0	0.0	0.0	0.0
MgO	0.0	0.0	0.0	0.0	0.0	0.0	0.0	0.0	0.0	0.0	0.0	0.0	0.0	0.0	0.0
CaO	17.6	17.8	16.7	16.5	16.8	16.8	16.4	15.7	16.2	16.2	16.7	16.9	16.7	15.9	16.8
Na2O	1.5	1.7	2.4	2.4	2.3	2.3	2.6	3.0	2.6	2.6	2.4	2.2	2.2	2.5	2.1
K2O	0.0	0.0	0.0	0.0	0.0	0.0	0.0	0.0	0.0	0.0	0.0	0.0	0.0	0.0	0.0
Totals	100.5	100.7	100.5	100.2	100.8	100.7	100.9	100.4	101.0	100.6	100.5	100.5	100.5	100.3	101.1
Oxygens	8	8	8	8	8	8	8	8	8	8	8	8	8	8	8
Si	2.11	2.12	2.18	2.18	2.17	2.17	2.18	2.23	2.20	2.20	2.17	2.17	2.16	2.21	2.17
Ti	0.00	0.00	0.00	0.00	0.00	0.00	0.00	0.00	0.00	0.00	0.00	0.00	0.00	0.00	0.00
Al	1.89	1.88	1.81	1.82	1.83	1.83	1.81	1.77	1.80	1.79	1.82	1.83	1.83	1.80	1.84
Fe2+	0.00	0.00	0.00	0.00	0.00	0.00	0.00	0.00	0.00	0.00	0.00	0.00	0.00	0.00	0.00
Mn	0.00	0.00	0.00	0.00	0.00	0.00	0.00	0.00	0.00	0.00	0.00	0.00	0.00	0.00	0.00
Mg	0.00	0.00	0.00	0.00	0.00	0.00	0.00	0.00	0.00	0.00	0.00	0.00	0.00	0.00	0.00
Ca	0.87	0.87	0.82	0.81	0.82	0.82	0.80	0.76	0.79	0.79	0.82	0.83	0.82	0.78	0.82
Na	0.14	0.15	0.21	0.21	0.20	0.20	0.22	0.26	0.23	0.23	0.21	0.19	0.20	0.22	0.18
K	0.00	0.00	0.00	0.00	0.00	0.00	0.00	0.00	0.00	0.00	0.00	0.00	0.00	0.00	0.00
Sum	5.01	5.02	5.02	5.02	5.02	5.02	5.02	5.02	5.02	5.02	5.03	5.02	5.02	5.01	5.01

Table 11 - Continued

Sample	**J419**	**J419**	**J409**	**J409**	**J409**	**J409**	**J409**	**J409**	**J409**	**J409**	**J409**	**J409**	**J409**	**J409**	**J418**
Mineral	Pl	Pl	Pl	Pl	Pl	Pl	Pl	Pl	Pl	Pl	Pl	Pl	Pl	Pl	Pl
SiO2	48.5	47.2	56.0	57.1	57.3	57.5	56.7	56.8	56.4	57.0	56.8	57.3	56.7	57.1	62.7
TiO2	0.0	0.0	0.0	0.0	0.0	0.0	0.1	0.1	0.0	0.0	0.1	0.0	0.0	0.1	0.0
Al2O3	33.8	34.0	27.2	27.0	26.6	26.8	26.6	26.6	27.3	26.6	26.6	26.6	26.4	26.6	18.9
FeO	0.0	0.0	0.2	0.1	0.1	0.1	0.2	0.2	0.2	0.2	0.1	0.1	0.2	0.2	0.1
MnO	0.0	0.0	0.0	0.0	0.0	0.0	0.0	0.0	0.0	0.0	0.0	0.0	0.0	0.0	0.0
MgO	0.0	0.0	0.0	0.0	0.0	0.0	0.0	0.0	0.0	0.0	0.0	0.0	0.0	0.0	0.0
CaO	16.2	16.8	9.2	8.7	8.3	8.4	8.1	8.4	9.0	8.4	8.5	8.5	8.3	8.4	0.1
Na2O	2.7	2.2	6.3	6.6	7.0	7.0	6.5	6.7	6.5	6.8	7.0	6.6	6.6	6.9	0.7
K2O	0.0	0.0	0.4	0.4	0.6	0.4	1.4	0.3	0.4	0.4	0.4	0.4	0.4	0.4	15.5
Totals	101.2	100.2	99.6	100.1	100.0	100.4	99.8	99.2	100.1	99.6	99.7	99.8	98.7	100.0	98.0
Oxygens	8	8	8	8	8	8	8	8	8	8	8	8	8	8	8
Si	2.20	2.16	2.54	2.57	2.58	2.58	2.57	2.57	2.54	2.58	2.57	2.58	2.58	2.58	2.96
Ti	0.00	0.00	0.00	0.00	0.00	0.00	0.00	0.00	0.00	0.00	0.00	0.00	0.00	0.00	0.00
Al	1.80	1.83	1.45	1.43	1.41	1.42	1.42	1.42	1.45	1.42	1.42	1.41	1.42	1.41	1.05
Fe2+	0.00	0.00	0.01	0.01	0.00	0.00	0.01	0.01	0.01	0.01	0.01	0.01	0.01	0.01	0.00
Mn	0.00	0.00	0.00	0.00	0.00	0.00	0.00	0.00	0.00	0.00	0.00	0.00	0.00	0.00	0.00
Mg	0.00	0.00	0.00	0.00	0.00	0.00	0.00	0.00	0.00	0.00	0.00	0.00	0.00	0.00	0.00
Ca	0.79	0.82	0.45	0.42	0.40	0.40	0.39	0.41	0.44	0.41	0.41	0.41	0.40	0.41	0.00
Na	0.24	0.19	0.55	0.58	0.61	0.61	0.57	0.59	0.57	0.60	0.61	0.58	0.58	0.60	0.06
K	0.00	0.00	0.02	0.02	0.03	0.02	0.08	0.02	0.02	0.02	0.02	0.02	0.02	0.02	0.94
Sum	5.02	5.02	5.02	5.02	5.04	5.03	5.05	5.02	5.03	5.03	5.04	5.01	5.01	5.03	5.01

Sample	**J418**	**J414**	**J414**
Mineral	Pl	Pl	Pl
SiO2	62.1	61.6	62.1
TiO2	0.0	0.0	0.1
Al2O3	18.9	18.7	18.7
FeO	0.1	0.3	0.2
MnO	0.0	0.0	0.0
MgO	0.0	0.0	0.0
CaO	0.1	0.1	0.0
Na2O	0.8	0.4	0.5
K2O	15.3	15.3	15.4
Totals	97.6	96.6	97.2
Oxygens	8	8	8
Si	2.95	2.95	2.96
Ti	0.00	0.00	0.00
Al	1.06	1.06	1.05
Fe2+	0.00	0.01	0.01
Mn	0.00	0.00	0.00
Mg	0.00	0.00	0.00
Ca	0.00	0.00	0.00
Na	0.08	0.04	0.04
K	0.93	0.94	0.94
Sum	5.02	5.00	5.00

Table 12 - Orthopyroxene mineral chemistry from samples across the EAC

Sample	J259	J259	J259	J259	J259	J259	J259	J259	J259	J259	J262	J262	J262	J262
SiO2	51.8	51.4	51.6	51.7	52.1	51.8	51.6	51.6	52.0	51.3	52.7	53.1	53.9	53.6
TiO2	0.1	0.1	0.2	0.2	0.2	0.2	0.2	0.1	0.2	0.2	0.1	0.2	0.2	0.2
Al2O3	1.6	1.7	1.7	1.7	1.7	1.7	1.6	1.5	1.6	1.8	3.6	3.5	3.0	3.3
Fe2O3	0.0	0.0	0.0	0.0	0.0	0.0	0.0	0.0	0.0	0.0	0.0	0.0	0.0	0.0
Cr2O3	0.0	0.0	0.0	0.0	0.0	0.0	0.0	0.0	0.0	0.0	0.2	0.1	0.2	0.2
FeO	23.3	24.0	23.3	23.2	23.4	23.7	23.7	24.3	23.8	24.1	13.9	13.9	14.1	14.2
MnO	0.4	0.5	0.5	0.5	0.5	0.5	0.5	0.5	0.5	0.5	0.3	0.3	0.3	0.3
MgO	21.2	21.5	21.4	21.5	21.1	21.0	20.8	21.0	21.0	20.7	28.4	28.3	28.0	28.1
CaO	1.3	0.7	0.8	0.7	1.0	1.2	0.6	0.6	0.9	0.8	0.7	0.8	0.6	0.7
Na2O	0.0	0.0	0.0	0.1	0.1	0.0	0.1	0.1	0.0	0.0	0.0	0.0	0.0	0.0
K2O	0.0	0.0	0.0	0.0	0.0	0.0	0.0	0.0	0.0	0.0	0.0	0.0	0.0	0.0
Totals	99.8	100.0	99.5	99.5	100.1	100.1	99.1	99.7	100.0	99.4	100.0	100.1	100.3	100.7
Oxygens	6	6	6	6	6	6	6	6	6	6	6	6	6	6
Si	1.88	1.90	1.89	1.89	1.89	1.89	1.89	1.92	1.84	1.84	1.80	1.81	1.81	1.80
Ti	0.01	0.01	0.02	0.01	0.01	0.01	0.01	0.01	0.02	0.02	0.02	0.02	0.02	0.02
Al	0.13	0.13	0.13	0.13	0.12	0.12	0.13	0.06	0.24	0.22	0.27	0.31	0.27	0.26
Fe3+	0.11	0.09	0.11	0.10	0.11	0.12	0.13	0.11	0.11	0.13	0.13	0.10	0.13	0.15
Cr	0.00	0.00	0.00	0.00	0.00	0.00	0.00	0.00	0.00	0.00	0.00	0.00	0.00	0.00
Fe2+	0.23	0.22	0.23	0.30	0.32	0.23	0.19	0.28	0.13	0.10	0.11	0.12	0.13	0.10
Mn	0.01	0.01	0.01	0.01	0.01	0.01	0.01	0.01	0.01	0.01	0.01	0.01	0.01	0.01
Mg	0.74	0.70	0.72	0.75	0.77	0.78	0.72	0.75	0.79	0.83	0.77	0.74	0.80	0.80
Ca	0.83	0.91	0.86	0.77	0.72	0.80	0.88	0.83	0.78	0.79	0.82	0.83	0.78	0.80
Na	0.04	0.03	0.05	0.03	0.04	0.04	0.05	0.03	0.08	0.07	0.06	0.06	0.06	0.06
K	0.00	0.00	0.00	0.00	0.00	0.00	0.00	0.00	0.00	0.00	0.00	0.00	0.00	0.00
Sum	4.00	4.00	4.00	4.00	4.00	4.00	4.00	4.00	4.00	4.00	4.00	4.00	4.00	4.00

Sample	J263	J263	J263	J263	J263	J263	J263	J263	J263	J263	J403	J403	J403	J403	J404
SiO2	51.3	50.9	51.4	51.2	52.2	51.9	51.5	51.2	50.8	50.8	51.3	51.1	51.3	51.1	51.3
TiO2	0.2	0.2	0.3	0.3	0.2	0.2	0.2	0.2	0.2	0.1	0.1	0.1	0.1	0.1	0.2
Al2O3	1.2	1.2	1.2	1.2	1.1	1.1	1.2	1.2	1.2	1.2	1.1	1.2	1.0	1.1	1.3
Fe2O3	0.0	0.0	0.0	0.0	0.0	0.0	0.0	0.0	0.0	0.0	0.0	0.0	0.0	0.0	0.0
Cr2O3	0.0	0.0	0.0	0.0	0.0	0.0	0.0	0.0	0.0	0.0	0.0	0.0	0.0	0.0	0.0
FeO	26.2	26.3	26.0	26.1	26.5	26.5	26.8	26.8	26.5	26.8	26.8	27.4	28.0	28.3	26.0
MnO	0.6	0.6	0.6	0.6	0.6	0.6	0.6	0.6	0.6	0.6	0.7	0.6	0.7	0.7	0.6
MgO	19.5	18.9	19.2	19.2	19.6	19.7	18.9	18.8	18.9	19.0	17.8	17.9	17.8	18.1	19.3
CaO	1.0	1.6	1.0	1.1	0.7	0.7	1.2	1.2	1.4	0.8	2.4	1.8	1.0	1.0	0.8
Na2O	0.0	0.0	0.0	0.0	0.0	0.0	0.1	0.0	0.0	0.0	0.1	0.1	0.0	0.0	0.0
K2O	0.0	0.0	0.0	0.0	0.0	0.0	0.0	0.0	0.0	0.0	0.0	0.0	0.0	0.0	0.0
Totals	100.1	99.8	99.7	99.9	100.8	100.7	100.5	99.9	99.8	99.4	100.1	100.3	100.0	100.5	99.5
Oxygens	6	6	6	6	6	6	6	6	6	6	6	6	6	6	6
Si	1.82	1.81	1.82	1.80	1.82	1.80	1.82	1.80	1.81	1.82	1.89	1.86	1.83	1.82	1.84
Ti	0.02	0.02	0.02	0.02	0.02	0.02	0.02	0.02	0.02	0.02	0.01	0.01	0.02	0.02	0.02
Al	0.26	0.27	0.27	0.26	0.25	0.26	0.25	0.26	0.25	0.24	0.14	0.18	0.24	0.23	0.21
Fe3+	0.13	0.13	0.11	0.16	0.12	0.15	0.13	0.14	0.14	0.14	0.10	0.12	0.14	0.15	0.12
Cr	0.00	0.00	0.00	0.00	0.00	0.00	0.00	0.00	0.00	0.00	0.00	0.00	0.00	0.00	0.00
Fe2+	0.10	0.12	0.14	0.08	0.18	0.15	0.11	0.13	0.14	0.10	0.07	0.10	0.11	0.09	0.11
Mn	0.01	0.00	0.00	0.00	0.01	0.01	0.01	0.01	0.01	0.01	0.00	0.01	0.01	0.01	0.01
Mg	0.76	0.79	0.79	0.80	0.89	0.84	0.79	0.82	0.85	0.79	0.90	0.86	0.81	0.83	0.84
Ca	0.85	0.80	0.81	0.81	0.66	0.72	0.82	0.76	0.73	0.84	0.85	0.82	0.80	0.81	0.81
Na	0.06	0.06	0.05	0.06	0.05	0.05	0.06	0.05	0.05	0.05	0.03	0.04	0.06	0.05	0.05
K	0.00	0.00	0.00	0.00	0.00	0.00	0.00	0.00	0.00	0.00	0.00	0.00	0.00	0.00	0.00
Sum	4.00	4.00	4.00	4.00	4.00	4.00	4.00	4.00	4.00	4.00	4.00	4.00	4.00	4.00	4.00

Table 12 – Continued

Sample	J404	J404	J404	J404	J404	J407	J407	J407	J407	J407	J407	J409	J409	J409
SiO2	51.0	51.2	51.5	51.1	51.3	52.2	52.0	52.3	52.2	52.2	52.0	50.6	51.0	51.1
TiO2	0.2	0.3	0.1	0.1	0.1	0.1	0.1	0.1	0.1	0.2	0.2	0.2	0.2	0.1
Al2O3	1.3	1.4	1.6	1.4	1.4	1.7	1.6	1.6	1.6	1.6	1.6	1.7	1.8	1.8
Fe2O3	0.0	0.0	0.0	0.0	0.0	0.0	0.0	0.0	0.0	0.0	0.0	0.0	0.0	0.0
Cr2O3	0.0	0.0	0.0	0.0	0.0	0.0	0.0	0.0	0.0	0.0	0.0	0.0	0.0	0.1
FeO	26.1	24.4	24.0	24.6	25.3	22.7	21.7	23.1	20.6	23.4	23.8	24.1	24.3	23.8
MnO	0.6	0.6	0.5	0.6	0.6	0.5	0.5	0.5	0.5	0.5	0.5	0.5	0.5	0.6
MgO	19.3	19.1	18.9	18.8	19.3	21.8	21.1	21.8	20.6	21.4	21.5	20.8	20.7	21.4
CaO	0.7	2.5	3.4	2.8	1.7	1.4	2.8	1.2	4.3	1.0	0.8	0.9	0.7	0.7
Na2O	0.0	0.1	0.1	0.1	0.0	0.0	0.1	0.0	0.1	0.0	0.0	0.0	0.0	0.0
K2O	0.0	0.0	0.0	0.0	0.0	0.0	0.0	0.0	0.0	0.0	0.0	0.0	0.0	0.0
Totals	99.2	99.5	100.3	99.6	99.7	100.4	100.1	100.7	100.0	100.3	100.5	99.0	99.2	99.6
Oxygens	6	6	6	6	6	6	6	6	6	6	6	6	6	6
Si	1.87	1.87	1.89	1.85	1.80	1.81	1.82	1.81	1.81	1.81	1.82	1.90	1.90	1.90
Ti	0.01	0.01	0.01	0.01	0.02	0.02	0.02	0.02	0.02	0.02	0.02	0.01	0.01	0.01
Al	0.16	0.17	0.21	0.19	0.27	0.26	0.25	0.27	0.26	0.25	0.27	0.11	0.11	0.10
Fe3+	0.13	0.11	0.03	0.13	0.14	0.14	0.13	0.13	0.13	0.13	0.13	0.11	0.12	0.12
Cr	0.00	0.00	0.00	0.00	0.00	0.00	0.00	0.00	0.00	0.00	0.00	0.00	0.00	0.00
Fe2+	0.06	0.08	0.18	0.11	0.09	0.10	0.13	0.08	0.12	0.16	0.08	0.24	0.26	0.24
Mn	0.01	0.00	0.00	0.01	0.01	0.01	0.01	0.00	0.01	0.01	0.00	0.01	0.01	0.01
Mg	0.86	0.87	0.82	0.84	0.77	0.76	0.83	0.76	0.79	0.83	0.76	0.70	0.71	0.71
Ca	0.86	0.85	0.83	0.81	0.83	0.82	0.76	0.86	0.79	0.73	0.86	0.86	0.84	0.86
Na	0.04	0.03	0.03	0.05	0.06	0.07	0.06	0.06	0.06	0.05	0.07	0.05	0.04	0.05
K	0.00	0.00	0.00	0.00	0.00	0.00	0.00	0.00	0.00	0.00	0.00	0.00	0.00	0.00
Sum	4.00	4.00	4.00	4.00	4.00	4.00	4.00	4.00	4.00	4.00	4.00	4.00	4.00	4.00

Sample	J409	J409	J409	J409	J409	J411	J411	J411	J411	J411	J411	J411	J411	J413
SiO2	51.1	51.4	51.2	50.1	50.5	51.4	52.0	52.7	52.3	52.9	52.4	52.3	51.8	53.3
TiO2	0.2	0.1	0.2	0.2	0.2	0.2	0.2	0.1	0.1	0.1	0.2	0.1	0.1	0.2
Al2O3	1.8	1.7	1.6	1.8	1.7	1.7	1.7	1.4	1.5	1.6	1.7	1.6	1.5	2.7
Fe2O3	0.0	0.0	0.0	0.0	0.0	0.0	0.0	0.0	0.0	0.0	0.0	0.0	0.0	0.0
Cr2O3	0.0	0.0	0.0	0.0	0.0	0.0	0.0	0.0	0.0	0.0	0.0	0.0	0.0	0.1
FeO	24.0	23.2	22.9	23.7	23.3	24.4	23.9	22.5	22.5	22.4	20.0	22.7	22.9	16.6
MnO	0.5	0.5	0.5	0.5	0.5	0.5	0.5	0.4	0.4	0.4	0.4	0.4	0.4	0.4
MgO	21.5	21.8	21.6	20.9	21.2	20.8	21.1	22.6	22.6	21.9	21.0	22.2	22.5	25.9
CaO	0.8	0.8	0.7	1.1	1.1	0.8	0.8	0.6	0.8	1.4	4.3	0.5	0.6	0.6
Na2O	0.0	0.0	0.0	0.1	0.0	0.0	0.0	0.0	0.0	0.1	0.2	0.0	0.1	0.0
K2O	0.0	0.0	0.0	0.0	0.0	0.0	0.0	0.0	0.0	0.0	0.0	0.0	0.0	0.0
Totals	99.9	99.6	98.8	98.3	98.5	99.8	100.2	100.4	100.2	100.9	100.2	100.0	100.0	99.9
Oxygens	6	6	6	6	6	6	6	6	6	6	6	6	6	6
Si	1.90	1.92	1.92	1.90	1.92	1.99	1.88	1.89	1.88	1.87	1.87	1.88	1.88	1.88
Ti	0.01	0.01	0.01	0.01	0.01	0.00	0.01	0.01	0.02	0.02	0.02	0.02	0.02	0.01
Al	0.10	0.10	0.10	0.09	0.10	0.06	0.19	0.18	0.19	0.19	0.21	0.21	0.21	0.19
Fe3+	0.13	0.08	0.08	0.12	0.09	0.00	0.10	0.08	0.09	0.10	0.11	0.07	0.08	0.09
Cr	0.00	0.00	0.00	0.00	0.00	0.00	0.01	0.01	0.01	0.01	0.02	0.02	0.01	0.02
Fe2+	0.25	0.31	0.30	0.24	0.28	0.28	0.08	0.17	0.12	0.10	0.08	0.13	0.15	0.11
Mn	0.01	0.01	0.01	0.01	0.01	0.01	0.00	0.01	0.01	0.01	0.01	0.01	0.01	0.01
Mg	0.71	0.69	0.70	0.68	0.71	0.75	0.78	0.89	0.80	0.78	0.78	0.79	0.85	0.83
Ca	0.85	0.84	0.85	0.90	0.84	0.88	0.88	0.71	0.83	0.86	0.84	0.83	0.75	0.81
Na	0.04	0.04	0.04	0.04	0.04	0.03	0.05	0.05	0.06	0.06	0.06	0.05	0.05	0.05
K	0.00	0.00	0.00	0.00	0.00	0.00	0.00	0.00	0.00	0.00	0.00	0.00	0.00	0.00
Sum	4.00	4.00	4.00	4.00	4.00	3.99	4.00	4.00	4.00	4.00	4.00	4.00	4.00	4.00

Table 12 – Continued

Sample	J413	J416	J416	J416	J416	J416	J416	J416	J416	J416	J416	J416	J416	J418
SiO2	52.8	50.3	50.3	49.3	49.6	49.8	49.9	50.9	50.6	49.5	49.9	50.1	49.6	50.2
TiO2	0.3	0.2	0.1	0.3	0.1	0.2	0.2	0.2	0.2	0.2	0.3	0.1	0.1	0.0
Al2O3	3.0	1.6	1.4	1.4	1.2	1.3	1.5	1.2	1.2	1.5	1.5	1.4	1.4	0.6
Fe2O3	0.0	0.0	0.0	0.0	0.0	0.0	0.0	0.0	0.0	0.0	0.0	0.0	0.0	0.0
Cr2O3	0.0	0.0	0.0	0.0	0.0	0.0	0.0	0.0	0.0	0.0	0.0	0.0	0.0	0.0
FeO	16.7	24.8	25.8	26.7	27.9	27.1	27.0	26.1	26.8	27.4	27.0	26.4	27.8	28.8
MnO	0.4	0.6	0.6	0.7	0.7	0.7	0.7	0.6	0.7	0.7	0.7	0.6	0.7	1.4
MgO	26.1	18.9	19.5	17.6	17.5	18.5	18.2	19.2	19.3	18.3	18.6	18.2	18.1	17.0
CaO	0.8	2.4	1.2	1.7	1.0	1.0	0.9	1.0	0.9	1.0	1.2	1.7	0.8	1.0
Na2O	0.1	0.1	0.1	0.1	0.0	0.0	0.0	0.0	0.0	0.0	0.1	0.1	0.0	0.1
K2O	0.0	0.0	0.0	0.0	0.0	0.0	0.0	0.0	0.0	0.0	0.0	0.0	0.0	0.0
Totals	100.2	98.8	99.0	97.8	98.0	98.5	98.5	99.2	99.5	98.6	99.3	98.7	98.5	99.1
Oxygens	6	6	6	6	6	6	6	6	6	6	6	6	6	6
Si	1.22	1.93	1.91	1.90	1.94	1.95	1.93	1.94	1.86	1.86	1.87	1.87	1.85	1.86
Ti	0.01	0.01	0.01	0.01	0.01	0.01	0.01	0.01	0.02	0.03	0.02	0.02	0.03	0.02
Al	0.08	0.10	0.10	0.10	0.09	0.08	0.11	0.09	0.21	0.22	0.20	0.20	0.22	0.22
Fe3+	0.64	0.07	0.10	0.12	0.05	0.06	0.06	0.05	0.06	0.06	0.08	0.07	0.07	0.07
Cr	0.00	0.00	0.00	0.00	0.00	0.00	0.00	0.00	0.00	0.00	0.00	0.00	0.00	0.00
Fe2+	0.00	0.36	0.33	0.30	0.39	0.33	0.31	0.31	0.19	0.21	0.20	0.18	0.20	0.19
Mn	0.01	0.01	0.01	0.01	0.01	0.01	0.01	0.01	0.01	0.01	0.01	0.01	0.01	0.01
Mg	1.07	0.71	0.72	0.71	0.69	0.69	0.67	0.67	0.73	0.73	0.78	0.75	0.71	0.72
Ca	0.89	0.77	0.78	0.80	0.78	0.84	0.87	0.87	0.87	0.85	0.81	0.87	0.86	0.87
Na	0.07	0.04	0.04	0.04	0.04	0.04	0.04	0.04	0.04	0.04	0.04	0.04	0.05	0.05
K	0.00	0.00	0.00	0.00	0.00	0.00	0.00	0.00	0.00	0.00	0.00	0.00	0.00	0.00
Sum	4.00	4.00	4.00	4.00	4.00	4.00	4.00	4.00	4.00	4.00	4.00	4.00	4.00	4.00

Sample	J418	J418	J418	J418	J418	J418	J418	J418	J418	J428	J428	J428	J428	J429
SiO2	50.1	49.8	49.9	50.3	50.0	50.1	50.2	50.2	50.0	53.8	53.6	54.2	53.4	54.2
TiO2	0.1	0.1	0.1	0.1	0.1	0.1	0.1	0.1	0.1	0.1	0.1	0.0	0.0	0.2
Al2O3	0.6	0.6	0.6	0.6	0.6	0.6	0.6	0.7	0.7	3.3	3.3	3.2	3.5	2.5
Fe2O3	0.0	0.0	0.0	0.0	0.0	0.0	0.0	0.0	0.0	0.0	0.0	0.0	0.0	0.0
Cr2O3	0.0	0.0	0.0	0.0	0.0	0.0	0.0	0.0	0.0	0.1	0.1	0.0	0.0	0.2
FeO	29.2	29.3	29.2	29.3	28.2	28.9	29.2	28.9	28.8	14.9	15.3	14.8	14.8	13.0
MnO	1.4	1.4	1.4	1.3	1.4	1.3	1.4	1.2	1.2	0.3	0.3	0.3	0.3	0.3
MgO	16.8	16.9	17.1	16.9	16.5	16.9	16.7	16.9	17.0	27.8	27.8	28.1	27.7	28.5
CaO	0.8	0.8	0.8	0.9	1.5	1.0	0.9	1.0	0.8	0.8	0.3	0.3	0.4	1.4
Na2O	0.1	0.0	0.0	0.1	0.1	0.0	0.1	0.0	0.1	0.0	0.0	0.0	0.0	0.0
K2O	0.0	0.0	0.0	0.0	0.0	0.0	0.0	0.0	0.0	0.0	0.0	0.0	0.0	0.0
Totals	99.0	99.0	99.0	99.6	98.4	98.9	99.2	99.2	98.8	101.2	101.0	100.8	100.3	100.3
Oxygens	6	6	6	6	6	6	6	6	6	6	6	6	6	6
Si	1.88	1.88	1.86	1.85	1.92	1.91	1.93	1.93	1.91	1.90	1.92	1.92	1.91	1.91
Ti	0.02	0.02	0.03	0.03	0.01	0.01	0.01	0.01	0.01	0.01	0.02	0.01	0.01	0.02
Al	0.16	0.16	0.21	0.21	0.12	0.12	0.12	0.12	0.13	0.13	0.12	0.12	0.12	0.14
Fe3+	0.10	0.10	0.05	0.06	0.05	0.08	0.05	0.05	0.07	0.09	0.04	0.04	0.08	0.07
Cr	0.01	0.01	0.00	0.00	0.00	0.00	0.00	0.00	0.00	0.00	0.00	0.00	0.00	0.00
Fe2+	0.16	0.15	0.22	0.25	0.25	0.23	0.31	0.26	0.23	0.21	0.28	0.25	0.24	0.25
Mn	0.01	0.01	0.01	0.01	0.01	0.01	0.01	0.01	0.01	0.01	0.01	0.01	0.01	0.01
Mg	0.79	0.77	0.74	0.76	0.70	0.70	0.73	0.71	0.71	0.71	0.73	0.71	0.70	0.70
Ca	0.84	0.86	0.83	0.79	0.88	0.88	0.80	0.86	0.89	0.89	0.84	0.89	0.88	0.86
Na	0.04	0.04	0.05	0.04	0.05	0.05	0.04	0.05	0.04	0.05	0.04	0.04	0.04	0.04
K	0.00	0.00	0.00	0.00	0.00	0.00	0.00	0.00	0.00	0.00	0.00	0.00	0.00	0.00
Sum	4.00	4.00	4.00	4.00	4.00	4.00	4.00	4.00	4.00	4.00	4.00	4.00	4.00	4.00

Table 12 – Continued

Sample	J429	J429	J429
SiO2	54.6	54.3	54.2
TiO2	0.2	0.2	0.2
Al2O3	2.5	2.5	3.0
Fe2O3	0.0	0.0	0.0
Cr2O3	0.3	0.2	0.2
FeO	13.1	13.4	13.9
MnO	0.3	0.2	0.3
MgO	28.9	28.5	28.5
CaO	1.4	1.1	0.9
Na2O	0.0	0.0	0.0
K2O	0.0	0.0	0.0
Totals	101.3	100.5	101.2
Oxygens	6	6	6
Si	1.92	1.91	1.91
Ti	0.01	0.01	0.01
Al	0.12	0.12	0.13
Fe3+	0.07	0.07	0.06
Cr	0.00	0.00	0.00
Fe2+	0.21	0.21	0.24
Mn	0.01	0.01	0.01
Mg	0.74	0.74	0.71
Ca	0.89	0.88	0.88
Na	0.04	0.04	0.04
K	0.00	0.00	0.00
Sum	4.00	4.00	4.00

Table 13 - Clinopyroxene mineral chemistry from samples across the EAC

Sample	B104	B104	B104	B104	B104	B104	B104	B133	B83	B85	B87	B87	B87	B87	B87
Mineral	Cpx	Cpx	Cpx	Cpx	Cpx	Cpx	Cpx	Cpx	Cpx	Cpx	Cpx	Cpx	Cpx	Cpx	Cpx
SiO2	50.8	50.9	50.5	50.8	51.3	51.0	50.8	50.8	49.3	49.9	49.1	48.9	49.1	48.9	49.2
TiO2	0.5	0.4	0.5	0.5	0.4	0.4	0.4	0.2	0.8	0.8	0.8	0.8	0.7	0.8	0.8
Al2O3	3.0	2.9	3.0	3.0	2.7	2.8	2.9	1.4	5.5	5.0	6.3	7.0	6.3	5.9	6.0
Fe2O3	0.0	0.0	0.0	0.0	0.0	0.0	0.0	0.0	0.0	0.0	0.0	0.0	0.0	0.0	0.0
FeO	11.2	10.2	10.7	12.8	14.1	11.3	10.1	12.2	7.9	7.4	8.0	7.2	8.4	8.0	7.4
MnO	0.3	0.3	0.2	0.4	0.3	0.3	0.3	0.4	0.2	0.2	0.2	0.2	0.2	0.2	0.2
MgO	13.4	12.6	13.0	13.6	14.1	14.1	13.1	13.3	14.2	15.1	14.1	13.4	14.6	14.6	13.9
CaO	21.0	22.9	21.4	19.3	18.3	20.1	22.0	20.4	19.5	20.1	20.9	21.0	19.9	20.3	21.5
Na2O	0.6	0.5	0.6	0.5	0.5	0.6	0.7	0.4	1.1	1.0	0.8	0.9	0.8	0.8	0.8
K2O	0.0	0.0	0.0	0.0	0.0	0.0	0.0	0.1	0.0	0.0	0.0	0.0	0.0	0.0	0.0
Totals	100.8	100.5	99.9	100.8	101.8	100.7	100.3	99.0	98.4	99.4	100.2	99.4	99.8	99.6	99.6
Oxygens	6	6	6	6	6	6	6	6	6	6	6	6	6	6	6
Si	1.88	1.90	1.89	1.89	1.89	1.89	1.89	1.92	1.84	1.84	1.80	1.81	1.81	1.80	1.82
Ti	0.01	0.01	0.02	0.01	0.01	0.01	0.01	0.01	0.02	0.02	0.02	0.02	0.02	0.02	0.02
Al	0.13	0.13	0.13	0.13	0.12	0.12	0.13	0.06	0.24	0.22	0.27	0.31	0.27	0.26	0.26
Fe3+	0.11	0.09	0.11	0.10	0.11	0.12	0.13	0.11	0.11	0.13	0.13	0.10	0.13	0.15	0.13
Fe2+	0.23	0.22	0.23	0.30	0.32	0.23	0.19	0.28	0.13	0.10	0.11	0.12	0.13	0.10	0.10
Mn	0.01	0.01	0.01	0.01	0.01	0.01	0.01	0.01	0.01	0.01	0.01	0.01	0.01	0.01	0.01
Mg	0.74	0.70	0.72	0.75	0.77	0.78	0.72	0.75	0.79	0.83	0.77	0.74	0.80	0.80	0.76
Ca	0.83	0.91	0.86	0.77	0.72	0.80	0.88	0.83	0.78	0.79	0.82	0.83	0.78	0.80	0.85
Na	0.04	0.03	0.05	0.03	0.04	0.04	0.05	0.03	0.08	0.07	0.06	0.06	0.06	0.06	0.06
K	0.00	0.00	0.00	0.00	0.00	0.00	0.00	0.00	0.00	0.00	0.00	0.00	0.00	0.00	0.00
Sum	4.00	4.00	4.00	4.00	4.00	4.00	4.00	4.00	4.00	4.00	4.00	4.00	4.00	4.00	4.00

Table 13 – Continued

Sample	B87	B87	B87	B87	B87	B87	B87	B87	B87	B87	B87	B87	B87	B87	B87
Mineral	Cpx	Cpx	Cpx	Cpx	Cpx	Cpx	Cpx	Cpx	Cpx	Cpx	Cpx	Cpx	Cpx	Cpx	Cpx
SiO2	49.2	49.3	49.4	49.7	49.5	49.8	49.2	49.5	49.4	51.5	50.4	49.7	49.6	49.8	51.0
TiO2	0.7	0.8	0.8	0.7	0.8	0.7	0.8	0.8	0.7	0.3	0.4	0.6	0.7	0.6	0.4
Al2O3	6.2	6.2	6.0	5.9	6.1	5.9	6.1	5.9	5.4	3.3	4.0	5.4	5.2	4.7	3.8
Fe2O3	0.0	0.0	0.0	0.0	0.0	0.0	0.0	0.0	0.0	0.0	0.0	0.0	0.0	0.0	0.0
FeO	8.1	8.0	7.8	9.9	9.7	7.8	8.7	9.1	7.7	5.6	7.1	7.9	7.9	7.4	6.3
MnO	0.1	0.1	0.2	0.2	0.2	0.2	0.2	0.2	0.2	0.1	0.2	0.2	0.2	0.2	0.2
MgO	14.4	14.3	14.7	16.3	15.6	14.6	15.1	15.5	14.4	16.5	15.6	14.8	15.1	15.3	15.9
CaO	20.2	20.4	20.8	17.0	18.4	20.9	19.3	18.8	21.1	21.7	20.7	20.3	20.5	20.4	21.9
Na2O	0.8	0.7	0.9	0.7	0.7	0.8	0.7	0.7	0.7	0.5	0.6	0.9	0.7	0.6	0.6
K2O	0.0	0.0	0.0	0.0	0.0	0.0	0.0	0.0	0.0	0.0	0.0	0.0	0.0	0.0	0.0
Totals	99.7	99.8	100.4	100.4	100.9	100.7	100.2	100.5	99.6	99.4	98.9	99.8	100.0	99.1	100.0
Oxygens	6	6	6	6	6	6	6	6	6	6	6	6	6	6	6
Si	1.81	1.82	1.80	1.82	1.80	1.82	1.80	1.81	1.82	1.89	1.86	1.83	1.82	1.84	1.87
Ti	0.02	0.02	0.02	0.02	0.02	0.02	0.02	0.02	0.02	0.01	0.01	0.02	0.02	0.02	0.01
Al	0.27	0.27	0.26	0.25	0.26	0.25	0.26	0.25	0.24	0.14	0.18	0.24	0.23	0.21	0.16
Fe3+	0.13	0.11	0.16	0.12	0.15	0.13	0.14	0.14	0.14	0.10	0.12	0.14	0.15	0.12	0.13
Fe2+	0.12	0.14	0.08	0.18	0.15	0.11	0.13	0.14	0.10	0.07	0.10	0.11	0.09	0.11	0.06
Mn	0.00	0.00	0.00	0.01	0.01	0.01	0.01	0.01	0.01	0.00	0.01	0.01	0.01	0.01	0.01
Mg	0.79	0.79	0.80	0.89	0.84	0.79	0.82	0.85	0.79	0.90	0.86	0.81	0.83	0.84	0.86
Ca	0.80	0.81	0.81	0.66	0.72	0.82	0.76	0.73	0.84	0.85	0.82	0.80	0.81	0.81	0.86
Na	0.06	0.05	0.06	0.05	0.05	0.06	0.05	0.05	0.05	0.03	0.04	0.06	0.05	0.05	0.04
K	0.00	0.00	0.00	0.00	0.00	0.00	0.00	0.00	0.00	0.00	0.00	0.00	0.00	0.00	0.00
Sum	4.00	4.00	4.00	4.00	4.00	4.00	4.00	4.00	4.00	4.00	4.00	4.00	4.00	4.00	4.00

Sample	B87	B87	B87	B87	B87	B87	B87	B87	B87	B87	J122	J122	J122	J122	J122
Mineral	Cpx	Cpx	Cpx	Cpx	Cpx	Cpx	Cpx	Cpx	Cpx	Cpx	Cpx	Cpx	Cpx	Cpx	Cpx
SiO2	51.0	51.7	50.7	49.0	49.2	49.7	49.5	49.6	49.6	49.5	51.4	51.1	51.2	50.7	51.3
TiO2	0.4	0.4	0.4	0.7	0.8	0.7	0.8	0.8	0.8	0.8	0.4	0.3	0.3	0.3	0.4
Al2O3	4.0	4.9	4.5	6.2	6.0	5.8	6.1	6.1	5.8	6.2	2.6	2.4	2.3	2.4	2.4
Fe2O3	0.0	0.0	0.0	0.0	0.0	0.0	0.0	0.0	0.0	0.0	0.0	0.0	0.0	0.0	0.0
FeO	6.4	6.9	7.8	7.7	7.7	8.5	7.0	8.2	9.5	6.7	11.4	12.2	11.5	12.1	12.5
MnO	0.1	0.1	0.2	0.2	0.2	0.2	0.2	0.2	0.2	0.2	0.2	0.4	0.3	0.3	0.3
MgO	15.9	15.0	15.5	14.0	13.9	15.3	14.0	14.5	15.3	13.9	12.7	12.9	12.8	12.7	12.3
CaO	21.7	21.3	20.8	21.1	20.8	19.3	22.0	20.3	18.7	21.8	21.8	21.0	21.7	21.2	21.1
Na2O	0.5	0.5	0.7	0.8	1.0	0.8	0.8	0.8	0.7	0.9	0.7	0.6	0.7	0.6	0.5
K2O	0.0	0.0	0.0	0.0	0.0	0.0	0.0	0.0	0.0	0.0	0.0	0.0	0.0	0.0	0.0
Totals	100.0	100.7	100.5	99.8	99.7	100.3	100.3	100.4	100.5	100.0	101.1	100.8	100.7	100.3	100.8
Oxygens	6	6	6	6	6	6	6	6	6	6	6	6	6	6	6
Si	1.87	1.89	1.85	1.80	1.81	1.82	1.81	1.81	1.81	1.82	1.90	1.90	1.90	1.90	1.92
Ti	0.01	0.01	0.01	0.02	0.02	0.02	0.02	0.02	0.02	0.02	0.01	0.01	0.01	0.01	0.01
Al	0.17	0.21	0.19	0.27	0.26	0.25	0.27	0.26	0.25	0.27	0.11	0.11	0.10	0.10	0.10
Fe3+	0.11	0.03	0.13	0.14	0.14	0.13	0.13	0.13	0.13	0.13	0.11	0.12	0.12	0.13	0.08
Fe2+	0.08	0.18	0.11	0.09	0.10	0.13	0.08	0.12	0.16	0.08	0.24	0.26	0.24	0.25	0.31
Mn	0.00	0.00	0.01	0.01	0.01	0.01	0.00	0.01	0.01	0.00	0.01	0.01	0.01	0.01	0.01
Mg	0.87	0.82	0.84	0.77	0.76	0.83	0.76	0.79	0.83	0.76	0.70	0.71	0.71	0.71	0.69
Ca	0.85	0.83	0.81	0.83	0.82	0.76	0.86	0.79	0.73	0.86	0.86	0.84	0.86	0.85	0.84
Na	0.03	0.03	0.05	0.06	0.07	0.06	0.06	0.06	0.05	0.07	0.05	0.04	0.05	0.04	0.04
K	0.00	0.00	0.00	0.00	0.00	0.00	0.00	0.00	0.00	0.00	0.00	0.00	0.00	0.00	0.00
Sum	4.00	4.00	4.00	4.00	4.00	4.00	4.00	4.00	4.00	4.00	4.00	4.00	4.00	4.00	4.00

Table 13 – Continued

Sample	J122	J122	J122	J262	J262	J262	J262	J262	J262	J262	J262	J263	J263	J263
Mineral	Cpx	Cpx	Cpx	Cpx	Cpx	Cpx	Cpx	Cpx	Cpx	Cpx	Cpx	Cpx	Cpx	Cpx
SiO2	50.7	51.6	54.9	50.5	51.1	51.1	51.0	51.1	51.0	51.3	51.4	19.5	51.2	50.6
TiO2	0.3	0.4	0.1	0.5	0.5	0.7	0.8	0.6	0.7	0.5	0.5	0.2	0.3	0.3
Al2O3	2.1	2.3	1.5	4.3	4.2	4.4	4.4	4.8	4.7	4.9	4.4	1.1	2.4	2.2
Fe2O3	0.0	0.0	0.0	0.0	0.0	0.0	0.0	0.0	0.0	0.0	0.0	0.0	0.0	0.0
FeO	11.6	11.8	9.2	5.9	8.2	6.9	6.6	6.3	6.5	7.4	6.8	12.1	13.7	13.6
MnO	0.4	0.4	0.3	0.1	0.2	0.2	0.2	0.2	0.2	0.2	0.2	0.3	0.3	0.3
MgO	12.1	12.8	13.9	14.1	16.2	14.6	14.3	14.3	14.4	15.6	15.1	11.4	12.6	12.9
CaO	22.4	21.2	22.7	22.1	17.9	21.0	21.8	21.5	21.0	19.2	20.6	13.3	19.1	19.2
Na2O	0.5	0.6	0.4	0.8	0.7	0.8	0.8	0.8	0.6	0.7	0.7	0.6	0.6	0.5
K2O	0.0	0.0	0.0	0.0	0.0	0.0	0.0	0.0	0.0	0.0	0.0	0.0	0.0	0.0
Totals	100.2	100.9	103.0	98.7	99.4	100.2	100.3	100.6	99.8	100.4	100.2	58.4	100.4	99.8
Oxygens	6	6	6	6	6	6	6	6	6	6	6	6	6	6
Si	1.90	1.92	1.99	1.88	1.89	1.88	1.88	1.88	1.89	1.88	1.89	1.22	1.93	1.91
Ti	0.01	0.01	0.00	0.01	0.01	0.02	0.02	0.02	0.02	0.02	0.01	0.01	0.01	0.01
Al	0.09	0.10	0.06	0.19	0.18	0.19	0.19	0.21	0.21	0.21	0.19	0.08	0.10	0.10
Fe3+	0.12	0.09	0.00	0.06	0.05	0.06	0.07	0.05	0.02	0.04	0.05	0.64	0.07	0.10
Fe2+	0.24	0.28	0.28	0.12	0.20	0.15	0.13	0.15	0.18	0.19	0.16	0.00	0.36	0.33
Mn	0.01	0.01	0.01	0.00	0.01	0.01	0.01	0.01	0.01	0.01	0.01	0.01	0.01	0.01
Mg	0.68	0.71	0.75	0.78	0.89	0.80	0.78	0.79	0.79	0.85	0.83	1.07	0.71	0.72
Ca	0.90	0.84	0.88	0.88	0.71	0.83	0.86	0.85	0.84	0.75	0.81	0.89	0.77	0.78
Na	0.04	0.04	0.03	0.05	0.05	0.06	0.06	0.06	0.05	0.05	0.05	0.07	0.04	0.04
K	0.00	0.00	0.00	0.00	0.00	0.00	0.00	0.00	0.00	0.00	0.00	0.00	0.00	0.00
Sum	4.00	4.00	3.99	4.00	4.00	4.00	4.00	4.00	4.00	4.00	4.00	4.00	4.00	4.00

Sample	J263	J403	J403	J403	J403	J413	J413	J413	J413	J413	J413	J413	J413	J413
Mineral	Cpx	Cpx	Cpx	Cpx	Cpx	Cpx	Cpx	Cpx	Cpx	Cpx	Cpx	Cpx	Cpx	Cpx
SiO2	50.3	51.7	52.2	51.7	51.7	50.1	49.8	50.9	50.5	49.7	49.9	50.9	51.0	50.2	49.7
TiO2	0.4	0.3	0.2	0.3	0.3	0.9	0.9	0.7	0.6	1.0	0.9	0.6	0.6	1.2	1.0
Al2O3	2.1	1.9	1.9	2.4	2.1	4.9	4.9	4.6	4.7	5.0	4.9	3.7	3.6	4.8	4.9
Fe2O3	0.0	0.0	0.0	0.0	0.0	0.0	0.0	0.0	0.0	0.0	0.0	0.0	0.0	0.0	0.0
FeO	13.4	13.9	12.4	11.7	11.7	8.2	8.8	8.9	8.0	8.5	8.3	8.3	8.0	8.8	9.8
MnO	0.3	0.4	0.3	0.3	0.3	0.2	0.2	0.2	0.2	0.2	0.2	0.2	0.2	0.2	0.2
MgO	12.7	12.4	12.4	12.0	12.0	13.3	13.2	14.2	13.6	12.8	13.0	14.3	14.1	13.3	13.7
CaO	19.7	19.4	21.0	21.6	21.6	21.8	21.2	20.7	21.8	21.6	21.7	21.1	21.7	21.0	19.7
Na2O	0.6	0.5	0.5	0.6	0.6	0.6	0.5	0.6	0.5	0.7	0.6	0.6	0.6	0.7	0.5
K2O	0.0	0.0	0.0	0.0	0.0	0.0	0.0	0.0	0.0	0.0	0.0	0.0	0.0	0.0	0.0
Totals	99.5	100.6	100.9	100.6	100.4	100.0	99.6	101.0	100.1	99.6	99.6	99.8	100.1	100.1	99.7
Oxygens	6	6	6	6	6	6	6	6	6	6	6	6	6	6	6
Si	1.90	1.94	1.95	1.93	1.94	1.86	1.86	1.87	1.87	1.85	1.86	1.89	1.89	1.86	1.85
Ti	0.01	0.01	0.01	0.01	0.01	0.02	0.03	0.02	0.02	0.03	0.02	0.02	0.02	0.03	0.03
Al	0.10	0.09	0.08	0.11	0.09	0.21	0.22	0.20	0.20	0.22	0.22	0.16	0.16	0.21	0.21
Fe3+	0.12	0.05	0.05	0.06	0.05	0.06	0.06	0.07	0.06	0.06	0.06	0.07	0.08	0.05	0.06
Fe2+	0.31	0.39	0.33	0.31	0.31	0.20	0.22	0.21	0.19	0.20	0.19	0.18	0.17	0.22	0.25
Mn	0.01	0.01	0.01	0.01	0.01	0.01	0.01	0.01	0.01	0.01	0.01	0.01	0.01	0.01	0.01
Mg	0.72	0.69	0.69	0.67	0.67	0.73	0.74	0.78	0.75	0.71	0.72	0.79	0.78	0.74	0.76
Ca	0.80	0.78	0.84	0.87	0.87	0.87	0.85	0.81	0.87	0.86	0.87	0.84	0.86	0.83	0.79
Na	0.04	0.04	0.04	0.04	0.04	0.04	0.04	0.04	0.04	0.05	0.05	0.04	0.04	0.05	0.04
K	0.00	0.00	0.00	0.00	0.00	0.00	0.00	0.00	0.00	0.00	0.00	0.00	0.00	0.00	0.00
Sum	4.00	4.00	4.00	4.00	4.00	4.00	4.00	4.00	4.00	4.00	4.00	4.00	4.00	4.00	4.00

Table 13 – Continued

Sample	J407	J407	J407	J407	J259	J259	J259	J259	J259	J259	J411	J411	J411	J411	J411
Mineral	Cpx	Cpx	Cpx	Cpx	Cpx	Cpx	Cpx	Cpx	Cpx	Cpx	Cpx	Cpx	Cpx	Cpx	Cpx
SiO2	51.8	51.7	52.1	52.1	50.9	50.7	51.4	51.4	50.9	51.1	51.7	51.4	51.3	51.8	51.9
TiO2	0.5	0.5	0.4	0.4	0.5	0.5	0.5	0.5	0.5	0.5	0.5	0.5	0.5	0.5	0.4
Al2O3	2.8	2.8	2.6	2.7	2.9	2.8	2.8	2.8	2.8	3.1	2.7	2.7	2.9	2.9	2.6
Fe2O3	0.0	0.0	0.0	0.0	0.0	0.0	0.0	0.0	0.0	0.0	0.0	0.0	0.0	0.0	0.0
FeO	9.9	9.9	11.5	10.0	9.6	9.5	10.3	9.2	10.3	10.3	8.9	9.3	9.6	11.4	8.9
MnO	0.2	0.3	0.3	0.2	0.2	0.2	0.2	0.2	0.2	0.3	0.2	0.2	0.3	0.3	0.2
MgO	12.6	12.7	13.3	12.9	12.7	12.7	13.1	12.8	12.6	12.6	13.4	13.3	12.8	13.4	13.6
CaO	22.1	22.2	20.2	21.7	22.0	22.1	20.9	22.3	22.0	21.6	22.4	22.0	22.1	20.8	22.2
Na2O	0.7	0.7	0.6	0.6	0.6	0.6	0.6	0.5	0.6	0.6	0.6	0.6	0.5	0.5	0.5
K2O	0.0	0.0	0.0	0.0	0.0	0.0	0.0	0.0	0.0	0.0	0.0	0.0	0.0	0.0	0.0
Totals	100.7	100.9	101.0	100.7	99.4	99.3	99.8	99.8	99.8	100.2	100.3	100.0	100.1	101.6	100.4
Oxygens	6	6	6	6	6	6	6	6	6	6	6	6	6	6	6
Si	1.92	1.91	1.93	1.93	1.91	1.91	1.92	1.92	1.91	1.91	1.92	1.91	1.92	1.91	1.92
Ti	0.01	0.01	0.01	0.01	0.01	0.01	0.02	0.01	0.01	0.02	0.01	0.01	0.01	0.01	0.01
Al	0.12	0.12	0.12	0.12	0.13	0.13	0.12	0.12	0.12	0.14	0.12	0.12	0.13	0.13	0.11
Fe3+	0.05	0.07	0.04	0.04	0.07	0.08	0.04	0.04	0.08	0.06	0.07	0.07	0.05	0.07	0.06
Fe2+	0.25	0.23	0.31	0.27	0.23	0.22	0.28	0.25	0.25	0.27	0.21	0.22	0.25	0.28	0.22
Mn	0.01	0.01	0.01	0.01	0.01	0.01	0.01	0.01	0.01	0.01	0.01	0.01	0.01	0.01	0.01
Mg	0.70	0.70	0.73	0.72	0.71	0.71	0.73	0.71	0.70	0.70	0.74	0.74	0.71	0.74	0.75
Ca	0.88	0.88	0.80	0.86	0.89	0.89	0.84	0.89	0.88	0.87	0.89	0.88	0.89	0.82	0.88
Na	0.05	0.05	0.04	0.05	0.04	0.05	0.04	0.04	0.04	0.04	0.04	0.04	0.04	0.04	0.04
K	0.00	0.00	0.00	0.00	0.00	0.00	0.00	0.00	0.00	0.00	0.00	0.00	0.00	0.00	0.00
Sum	4.00	4.00	4.00	4.00	4.00	4.00	4.00	4.00	4.00	4.00	4.00	4.00	4.00	4.00	4.00

Sample	J411	J429	J429	J429	J429	J428	J428	J428	J428	J428	J428	J428	J428	J428	J428
Mineral	Cpx	Cpx	Cpx	Cpx	Cpx	Cpx	Cpx	Cpx	Cpx	Cpx	Cpx	Cpx	Cpx	Cpx	Cpx
SiO2	52.0	51.3	51.6	51.3	51.0	52.1	51.9	42.1	42.1	51.3	51.0	51.8	51.7	50.5	50.4
TiO2	0.4	0.6	0.5	0.7	0.7	0.5	0.6	1.1	1.0	0.6	0.5	0.5	0.6	0.5	0.4
Al2O3	2.7	4.3	4.3	4.2	4.0	3.8	3.7	15.0	15.2	4.2	3.8	3.9	4.1	4.5	4.6
Fe2O3	0.0	0.0	0.0	0.0	0.0	0.0	0.0	0.0	0.0	0.0	0.0	0.0	0.0	0.0	0.0
FeO	9.0	6.2	6.1	6.3	6.4	7.3	7.4	9.1	9.0	7.3	9.8	7.5	7.1	7.1	7.3
MnO	0.2	0.2	0.1	0.1	0.1	0.2	0.2	0.1	0.1	0.2	0.2	0.2	0.2	0.2	0.2
MgO	13.6	14.6	14.5	14.8	14.8	15.6	15.3	15.2	14.9	15.5	17.9	15.2	15.4	14.2	14.4
CaO	21.9	21.7	22.0	21.6	21.7	20.3	20.8	11.8	11.9	20.2	16.1	20.8	19.9	21.2	20.8
Na2O	0.4	0.7	0.7	0.8	0.7	0.5	0.5	2.4	2.4	0.5	0.4	0.6	0.5	0.6	0.6
K2O	0.0	0.0	0.0	0.0	0.0	0.0	0.0	0.8	0.8	0.0	0.0	0.0	0.0	0.0	0.0
Totals	100.3	100.2	100.4	100.4	99.9	100.5	100.6	97.7	97.6	100.1	99.9	100.7	99.8	99.1	99.0
Oxygens	6	6	6	6	6	6	6	6	6	6	6	6	6	6	6
Si	1.93	1.89	1.90	1.89	1.89	1.91	1.90	1.54	1.55	1.89	1.87	1.89	1.91	1.88	1.88
Ti	0.01	0.02	0.01	0.02	0.02	0.02	0.02	0.03	0.03	0.02	0.01	0.01	0.02	0.01	0.01
Al	0.12	0.19	0.19	0.18	0.17	0.16	0.16	0.65	0.66	0.18	0.17	0.17	0.18	0.20	0.20
Fe3+	0.03	0.04	0.04	0.06	0.07	0.02	0.04	0.28	0.27	0.05	0.09	0.05	0.01	0.06	0.06
Fe2+	0.25	0.15	0.15	0.13	0.13	0.20	0.19	0.00	0.00	0.17	0.21	0.18	0.21	0.16	0.17
Mn	0.01	0.00	0.00	0.00	0.00	0.01	0.01	0.00	0.00	0.01	0.01	0.01	0.01	0.01	0.01
Mg	0.75	0.80	0.79	0.81	0.82	0.85	0.84	0.83	0.82	0.85	0.98	0.83	0.85	0.79	0.80
Ca	0.87	0.86	0.87	0.85	0.86	0.80	0.82	0.46	0.47	0.79	0.63	0.82	0.79	0.84	0.83
Na	0.03	0.05	0.05	0.05	0.05	0.03	0.03	0.17	0.17	0.04	0.03	0.04	0.04	0.05	0.04
K	0.00	0.00	0.00	0.00	0.00	0.00	0.00	0.04	0.04	0.00	0.00	0.00	0.00	0.00	0.00
Sum	4.00	4.00	4.00	4.00	4.00	4.00	4.00	4.00	4.00	4.00	4.00	4.00	4.00	4.00	4.00

Table 13 – Continued

Sample	J428	J428	J256	J256	J256	J256	J416	J416	J416	J416	J416	J416	J416	J416	J414
Mineral	Cpx	Cpx	Cpx	Cpx	Cpx	Cpx	Cpx	Cpx	Cpx	Cpx	Cpx	Cpx	Cpx	Cpx	Cpx
SiO2	51.1	50.4	53.4	53.5	53.6	53.2	50.2	50.5	50.1	50.4	49.5	50.6	50.3	50.4	50.6
TiO2	0.5	0.7	0.1	0.2	0.1	0.2	0.3	0.3	0.4	0.4	0.6	0.4	0.4	0.3	0.3
Al2O3	3.9	4.6	1.1	1.3	1.1	1.5	2.2	2.2	2.8	2.6	2.5	2.8	2.5	2.4	2.2
Fe2O3	0.0	0.0	0.0	0.0	0.0	0.0	0.0	0.0	0.0	0.0	0.0	0.0	0.0	0.0	0.0
FeO	6.8	6.5	6.9	6.9	6.8	7.1	11.7	11.2	12.4	11.9	11.1	11.7	11.8	11.7	11.7
MnO	0.2	0.2	0.2	0.3	0.2	0.2	0.4	0.3	0.4	0.3	0.3	0.3	0.3	0.3	0.4
MgO	14.4	14.6	14.1	13.8	14.5	13.9	12.2	12.0	12.4	12.5	12.7	12.6	12.2	12.3	11.4
CaO	22.2	21.8	24.2	24.0	24.3	23.9	21.2	21.7	20.2	20.8	20.9	20.5	21.0	21.1	22.2
Na2O	0.5	0.6	0.4	0.4	0.3	0.4	0.5	0.5	0.5	0.5	0.5	0.5	0.5	0.5	0.6
K2O	0.0	0.0	0.0	0.0	0.0	0.0	0.0	0.0	0.0	0.0	0.0	0.0	0.0	0.0	0.0
Totals	100.0	99.6	100.4	100.4	101.1	100.4	98.7	98.7	99.2	99.3	98.1	99.5	99.1	98.9	99.3
Oxygens	6	6	6	6	6	6	6	6	6	6	6	6	6	6	6
Si	1.89	1.86	1.97	1.98	1.96	1.97	1.91	1.92	1.90	1.90	1.89	1.91	1.91	1.92	1.92
Ti	0.02	0.02	0.00	0.01	0.00	0.01	0.01	0.01	0.01	0.01	0.02	0.01	0.01	0.01	0.01
Al	0.17	0.20	0.05	0.06	0.05	0.06	0.10	0.10	0.12	0.11	0.11	0.12	0.11	0.11	0.10
Fe3+	0.06	0.08	0.03	0.00	0.04	0.02	0.10	0.07	0.09	0.09	0.12	0.07	0.08	0.08	0.09
Fe2+	0.15	0.12	0.18	0.21	0.17	0.20	0.27	0.28	0.30	0.28	0.24	0.30	0.29	0.29	0.28
Mn	0.01	0.01	0.01	0.01	0.01	0.01	0.01	0.01	0.01	0.01	0.01	0.01	0.01	0.01	0.01
Mg	0.79	0.80	0.78	0.76	0.79	0.76	0.69	0.68	0.70	0.70	0.72	0.71	0.69	0.70	0.64
Ca	0.88	0.86	0.96	0.95	0.95	0.95	0.87	0.89	0.82	0.84	0.85	0.83	0.86	0.86	0.90
Na	0.04	0.05	0.03	0.03	0.02	0.03	0.04	0.04	0.04	0.04	0.04	0.04	0.03	0.03	0.05
K	0.00	0.00	0.00	0.00	0.00	0.00	0.00	0.00	0.00	0.00	0.00	0.00	0.00	0.00	0.00
Sum	4.00	4.00	4.00	4.00	4.00	4.00	4.00	4.00	4.00	4.00	4.00	4.00	4.00	4.00	4.00

Sample	J414	J414	J414	J414	J414	J414	J414	J418	J418	J418	J418	J418	J418	J409	J409
Mineral	Cpx	Cpx	Cpx	Cpx	Cpx	Cpx	Cpx	Cpx	Cpx	Cpx	Cpx	Cpx	Cpx	Cpx	Cpx
SiO2	41.7	50.4	50.1	41.3	50.5	50.6	51.5	51.4	50.6	51.3	50.6	51.7	50.8	50.6	49.6
TiO2	1.5	0.3	0.4	0.9	0.3	0.2	0.2	0.1	0.1	0.1	0.2	0.2	0.2	0.5	0.5
Al2O3	10.9	2.3	2.4	12.0	2.1	2.3	1.8	1.1	1.3	1.2	1.2	1.3	1.2	3.0	3.1
Fe2O3	0.0	0.0	0.0	0.0	0.0	0.0	0.0	0.0	0.0	0.0	0.0	0.0	0.0	0.0	0.0
FeO	18.3	11.7	12.1	17.5	10.7	10.6	10.1	13.5	12.7	12.2	11.8	12.7	12.6	10.4	9.8
MnO	0.2	0.4	0.4	0.3	0.4	0.4	0.5	0.7	0.7	0.6	0.6	0.6	0.6	0.3	0.2
MgO	9.3	11.1	11.3	9.4	11.7	12.4	12.1	12.3	11.8	12.0	12.0	11.9	12.1	12.7	12.8
CaO	11.9	22.5	22.2	11.9	22.9	21.3	22.6	20.0	20.6	21.2	21.5	20.7	20.9	21.6	21.7
Na2O	1.1	0.6	0.7	1.1	0.6	0.5	0.5	0.6	0.6	0.6	0.6	0.6	0.6	0.6	0.7
K2O	1.6	0.0	0.0	1.5	0.0	0.0	0.0	0.0	0.0	0.0	0.0	0.0	0.0	0.0	0.0
Totals	96.6	99.5	99.5	95.7	99.3	98.4	99.4	99.7	98.5	99.2	98.6	99.7	98.9	99.5	98.6
Oxygens	6	6	6	6	6	6	6	6	6	6	6	6	6	6	6
Si	1.64	1.91	1.90	1.63	1.91	1.93	1.95	1.95	1.94	1.95	1.93	1.96	1.94	1.90	1.88
Ti	0.04	0.01	0.01	0.03	0.01	0.01	0.01	0.00	0.00	0.00	0.00	0.00	0.01	0.01	0.01
Al	0.50	0.10	0.11	0.56	0.09	0.10	0.08	0.05	0.06	0.05	0.05	0.06	0.05	0.13	0.14
Fe3+	0.30	0.10	0.12	0.29	0.11	0.07	0.05	0.09	0.10	0.09	0.12	0.07	0.10	0.08	0.13
Fe2+	0.30	0.27	0.26	0.28	0.22	0.27	0.27	0.34	0.31	0.30	0.26	0.33	0.30	0.24	0.18
Mn	0.01	0.01	0.01	0.01	0.01	0.01	0.01	0.02	0.02	0.02	0.02	0.02	0.02	0.01	0.01
Mg	0.54	0.63	0.64	0.55	0.66	0.70	0.68	0.69	0.67	0.68	0.68	0.67	0.69	0.71	0.72
Ca	0.50	0.92	0.90	0.50	0.93	0.87	0.92	0.81	0.85	0.86	0.88	0.84	0.86	0.87	0.88
Na	0.09	0.04	0.05	0.08	0.05	0.04	0.04	0.04	0.05	0.05	0.05	0.05	0.04	0.04	0.05
K	0.08	0.00	0.00	0.07	0.00	0.00	0.00	0.00	0.00	0.00	0.00	0.00	0.00	0.00	0.00
Sum	4.00	4.00	4.00	4.00	4.00	4.00	4.00	4.00	4.00	4.00	4.00	4.00	4.00	4.00	4.00

Table 13 – Continued

Sample	J409	J409
Mineral	Cpx	Cpx
SiO2	50.3	49.9
TiO2	0.5	0.5
Al2O3	3.0	3.1
Fe2O3	0.0	0.0
FeO	10.0	10.8
MnO	0.2	0.3
MgO	13.0	12.9
CaO	21.5	20.8
Na2O	0.6	0.6
K2O	0.0	0.0
Totals	99.1	99.1
Oxygens	6	6
Si	1.89	1.88
Ti	0.01	0.01
Al	0.13	0.14
Fe3+	0.10	0.11
Fe2+	0.21	0.23
Mn	0.01	0.01
Mg	0.73	0.72
Ca	0.87	0.84
Na	0.05	0.05
K	0.00	0.00
Sum	4.00	4.00

Table 14 – Olivine mineral chemistry from samples across the EAC

Sample	J429	J429	J429	J262	J429	J429	J429	J429	J429	J262	J262	J262	J429	J429
SiO2	39.7	39.8	39.8	38.9	38.8	40.0	39.6	39.6	39.7	38.7	38.8	38.8	38.5	40.0
TiO2	0.0	0.0	0.0	0.0	0.0	0.0	0.0	0.0	0.0	0.0	0.0	0.0	0.0	0.0
Al2O3	0.0	0.0	0.0	0.0	0.0	0.0	0.0	0.0	0.0	0.0	0.0	0.0	0.0	0.0
Cr2O3	0.0	0.0	0.0	0.0	0.0	0.0	0.0	0.0	0.0	0.0	0.0	0.0	0.0	0.0
FeO	16.4	15.9	15.9	21.8	20.9	17.2	16.8	16.8	16.4	21.8	21.8	21.8	21.0	17.2
MnO	0.4	0.3	0.3	0.3	0.3	0.3	0.3	0.3	0.4	0.3	0.3	0.3	0.3	0.3
MgO	44.6	44.6	44.6	39.7	40.4	43.8	43.8	43.8	44.6	39.1	39.2	39.0	40.3	43.8
CaO	0.0	0.0	0.0	0.0	0.0	0.0	0.0	0.0	0.0	0.0	0.0	0.0	0.0	0.0
Na2O	0.0	0.0	0.0	0.0	0.0	0.0	0.0	0.0	0.0	0.0	0.0	0.0	0.0	0.0
K2O	0.0	0.0	0.0	0.0	0.0	0.0	0.0	0.0	0.0	0.0	0.0	0.0	0.0	0.0
NiO	0.3	0.2	0.2	0.2	0.2	0.2	0.2	0.2	0.3	0.2	0.2	0.2	0.2	0.2
SrO	0.1	0.0	0.0	0.0	0.1	0.0	0.0	0.0	0.1	0.0	0.0	0.0	0.1	0.0
Totals	101.5	101.0	101.0	101.1	100.7	101.5	100.7	100.7	101.5	100.2	100.3	100.1	100.3	101.5
Oxygens	4	4	4	4	4	4	4	4	4	4	4	4	4	4
Si	1.07	1.07	1.07	1.05	1.04	1.08	1.06	1.06	1.07	1.04	1.04	1.04	1.03	1.08
Ti	0.00	0.00	0.00	0.00	0.00	0.00	0.00	0.00	0.00	0.00	0.00	0.00	0.00	0.00
Al	0.00	0.00	0.00	0.00	0.00	0.00	0.00	0.00	0.00	0.00	0.00	0.00	0.00	0.00
Cr	0.00	0.00	0.00	0.00	0.00	0.00	0.00	0.00	0.00	0.00	0.00	0.00	0.00	0.00
Fe+2	0.37	0.36	0.36	0.49	0.47	0.39	0.38	0.38	0.37	0.49	0.49	0.49	0.47	0.39
Mn	0.01	0.01	0.01	0.01	0.01	0.01	0.01	0.01	0.01	0.01	0.01	0.01	0.01	0.01
Mg	1.79	1.79	1.79	1.59	1.62	1.75	1.75	1.75	1.79	1.56	1.57	1.56	1.61	1.75
SUM	3.23	3.22	3.22	3.13	3.13	3.22	3.20	3.20	3.23	3.10	3.11	3.10	3.13	3.22

Table 14 – Continued

Sample	J262	J262	J411	J428	J429	J428	J428	J428	J413	J413	J428	J429	J428	J428
SiO2	38.7	38.6	38.8	39.1	38.8	38.9	38.9	38.9	37.4	37.9	38.7	38.5	38.5	39.1
TiO2	0.0	0.0	0.0	0.0	0.0	0.0	0.0	0.0	0.0	0.0	0.0	0.0	0.0	0.0
Al2O3	0.0	0.0	0.0	0.0	0.0	0.0	0.0	0.0	0.0	0.0	0.0	0.0	0.0	0.0
Cr2O3	0.0	0.0	0.0	0.0	0.0	0.0	0.0	0.0	0.0	0.0	0.0	0.0	0.0	0.0
FeO	21.8	21.9	21.6	20.4	20.9	20.8	21.7	21.7	27.4	26.2	21.6	21.0	22.2	20.4
MnO	0.3	0.3	0.3	0.3	0.3	0.2	0.3	0.3	0.4	0.4	0.3	0.3	0.3	0.3
MgO	39.4	39.3	39.8	40.9	40.4	40.8	39.8	39.8	34.9	36.3	40.2	40.3	39.5	40.9
CaO	0.0	0.0	0.0	0.0	0.0	0.0	0.0	0.0	0.0	0.0	0.0	0.0	0.0	0.0
Na2O	0.0	0.0	0.0	0.0	0.0	0.0	0.1	0.1	0.0	0.0	0.0	0.0	0.0	0.0
K2O	0.0	0.0	0.0	0.0	0.0	0.0	0.0	0.0	0.0	0.0	0.0	0.0	0.0	0.0
NiO	0.2	0.2	0.2	0.1	0.2	0.1	0.1	0.1	0.1	0.1	0.1	0.2	0.1	0.1
SrO	0.0	0.0	0.0	0.1	0.1	0.1	0.1	0.1	0.0	0.0	0.0	0.1	0.0	0.1
Totals	100.4	100.3	100.7	101.0	100.7	100.9	100.9	100.9	100.2	100.9	100.9	100.3	100.7	101.0
Oxygens	4	4	4	4	4	4	4	4	4	4	4	4	4	4
Si	1.04	1.04	1.04	1.05	1.04	1.04	1.04	1.04	1.00	1.02	1.04	1.03	1.03	1.05
Ti	0.00	0.00	0.00	0.00	0.00	0.00	0.00	0.00	0.00	0.00	0.00	0.00	0.00	0.00
Al	0.00	0.00	0.00	0.00	0.00	0.00	0.00	0.00	0.00	0.00	0.00	0.00	0.00	0.00
Cr	0.00	0.00	0.00	0.00	0.00	0.00	0.00	0.00	0.00	0.00	0.00	0.00	0.00	0.00
Fe+2	0.49	0.49	0.48	0.46	0.47	0.47	0.49	0.49	0.61	0.59	0.48	0.47	0.50	0.46
Mn	0.01	0.01	0.01	0.01	0.01	0.01	0.01	0.01	0.01	0.01	0.01	0.01	0.01	0.01
Mg	1.58	1.57	1.59	1.64	1.62	1.63	1.59	1.59	1.40	1.45	1.61	1.61	1.58	1.64
SUM	3.11	3.11	3.13	3.15	3.13	3.15	3.13	3.13	3.03	3.07	3.14	3.13	3.12	3.15

Sample	J413	J413	J428	J428	J413	J413	J411	J428	J428	J428
SiO2	37.7	37.1	39.0	38.7	37.7	33.6	38.8	38.9	39.0	38.5
TiO2	0.0	0.0	0.0	0.0	0.0	0.0	0.0	0.0	0.0	0.0
Al2O3	0.0	0.0	0.0	0.0	0.0	0.0	0.0	0.0	0.0	0.0
Cr2O3	0.0	0.0	0.0	0.0	0.0	0.0	0.0	0.0	0.0	0.0
FeO	27.5	27.3	22.1	21.6	27.5	26.8	21.6	20.8	22.1	22.2
MnO	0.4	0.4	0.3	0.3	0.4	0.4	0.3	0.2	0.3	0.3
MgO	35.3	35.0	39.4	40.2	34.8	36.2	39.8	40.8	39.4	39.5
CaO	0.0	0.0	0.0	0.0	0.0	0.0	0.0	0.0	0.0	0.0
Na2O	0.0	0.0	0.0	0.0	0.0	0.0	0.0	0.0	0.0	0.0
K2O	0.0	0.0	0.0	0.0	0.0	0.0	0.0	0.0	0.0	0.0
NiO	0.1	0.1	0.1	0.1	0.1	0.1	0.2	0.1	0.1	0.1
SrO	0.0	0.0	0.0	0.0	0.0	0.0	0.0	0.1	0.0	0.0
Totals	101.0	99.9	101.1	100.9	100.6	97.0	100.7	100.9	101.1	100.7
Oxygens	4	4	4	4	4	4	4	4	4	4
Si	1.01	1.00	1.05	1.04	1.01	0.90	1.04	1.04	1.05	1.03
Ti	0.00	0.00	0.00	0.00	0.00	0.00	0.00	0.00	0.00	0.00
Al	0.00	0.00	0.00	0.00	0.00	0.00	0.00	0.00	0.00	0.00
Cr	0.00	0.00	0.00	0.00	0.00	0.00	0.00	0.00	0.00	0.00
Fe+2	0.62	0.61	0.50	0.48	0.62	0.60	0.48	0.47	0.50	0.50
Mn	0.01	0.01	0.01	0.01	0.01	0.01	0.01	0.01	0.01	0.01
Mg	1.41	1.40	1.58	1.61	1.39	1.45	1.59	1.63	1.58	1.58
SUM	3.05	3.02	3.13	3.14	3.03	2.96	3.13	3.15	3.13	3.12

Table 15 – Amphibole mineral chemistry from samples across the EAC

Sample	B133	B133	B133	B133	B133	B133	B133	B133	B133	J122	J106	B45	B45	B45
SiO2	43.6	43.3	43.6	43.5	43.7	43.4	43.2	43.3	42.0	44.2	45.7	44.9	44.3	44.3
TiO2	1.6	1.9	2.2	2.2	2.4	2.1	1.8	1.9	1.9	1.8	0.3	0.3	0.3	0.3
Al2O3	10.5	10.2	9.4	9.7	9.8	9.7	9.9	9.9	11.4	10.4	12.1	14.4	14.8	14.7
Fe2O3	0.0	0.0	0.0	0.0	0.0	0.0	0.0	0.0	0.0	0.0	0.0	0.0	0.0	0.0
FeO	16.5	17.0	17.7	17.1	16.7	18.0	17.5	17.3	17.5	15.0	8.2	8.9	9.0	8.9
MnO	0.2	0.2	0.2	0.2	0.2	0.2	0.2	0.2	0.2	0.1	0.1	0.2	0.2	0.2
MgO	11.4	11.6	11.4	11.7	11.6	11.3	11.0	11.3	9.8	12.6	15.1	14.1	13.7	14.2
CaO	11.0	11.0	11.0	11.1	11.2	11.0	11.2	11.2	11.4	11.7	12.4	11.6	12.0	11.5
Na2O	1.5	1.6	1.6	1.8	1.6	1.5	1.5	1.4	1.2	1.4	1.4	1.7	1.8	1.8
K2O	1.5	1.4	1.5	1.5	1.4	1.5	1.4	1.4	1.8	1.6	0.2	0.2	0.2	0.2
NiO	-	-	-	-	-	-	-	-	-	-	-	-	-	-
Cr2O3	-	-	-	-	-	-	-	-	-	-	-	-	-	-
SrO	-	-	-	-	-	-	-	-	-	-	-	-	-	-
Total	97.7	98.1	98.5	98.6	98.5	98.6	97.8	98.0	97.3	98.7	95.7	96.1	96.3	96.1
Oxygens	23	23	23	23	23	23	23	23	23	23	23	23	23	23
Si	6.49	6.42	6.48	6.45	6.48	6.44	6.47	6.45	6.36	6.48	6.64	6.48	6.42	6.40
Ti	0.18	0.21	0.24	0.24	0.26	0.24	0.20	0.21	0.21	0.19	0.04	0.03	0.04	0.04
Al	1.84	1.78	1.65	1.69	1.72	1.69	1.75	1.75	2.03	1.80	2.07	2.45	2.53	2.50
Fe3	0.73	0.91	0.90	0.87	0.84	0.99	0.80	0.89	0.70	0.72	0.27	0.32	0.23	0.38
Fe2	1.32	1.21	1.30	1.26	1.22	1.24	1.38	1.27	1.52	1.11	0.73	0.75	0.86	0.69
Mn	0.03	0.03	0.03	0.02	0.02	0.02	0.02	0.02	0.03	0.01	0.01	0.02	0.02	0.02
Mg	2.53	2.56	2.51	2.58	2.57	2.50	2.45	2.51	2.22	2.76	3.27	3.04	2.96	3.06
Ca	1.76	1.75	1.75	1.76	1.77	1.74	1.80	1.79	1.85	1.83	1.93	1.79	1.87	1.79
Na	0.43	0.45	0.47	0.51	0.46	0.44	0.44	0.42	0.34	0.41	0.41	0.47	0.51	0.50
K	0.28	0.27	0.28	0.27	0.27	0.27	0.27	0.26	0.36	0.29	0.04	0.04	0.03	0.04
Sum	15.58	15.59	15.61	15.66	15.60	15.58	15.60	15.57	15.62	15.61	15.41	15.39	15.47	15.43

Sample	B45	J262	J262	J413	J413	J270	J270	J270	J270	J269	J269	C-95	C-95	C-95
SiO2	46.6	41.4	41.4	40.7	40.4	41.6	42.0	41.6	41.7	45.8	43.7	50.0	49.8	51.8
TiO2	0.5	4.0	3.9	3.4	3.4	0.4	0.3	0.4	0.4	0.3	0.3	0.2	0.2	0.1
Al2O3	12.2	13.1	13.2	14.3	13.8	16.2	16.2	15.8	15.6	12.3	14.3	6.7	7.3	5.5
Fe2O3	0.0	0.0	0.0	0.0	0.0	0.0	0.0	0.0	0.0	0.0	0.0	0.0	0.0	0.0
FeO	8.5	9.6	9.6	11.6	11.7	16.2	16.1	16.4	16.7	14.1	14.9	8.0	8.6	7.8
MnO	0.2	0.1	0.1	0.1	0.1	0.4	0.3	0.4	0.4	0.2	0.2	0.2	0.2	0.1
MgO	15.4	13.8	13.9	12.0	12.1	8.8	8.8	8.7	8.6	11.8	10.6	16.8	16.5	17.8
CaO	12.4	11.4	11.4	11.7	11.6	11.2	11.2	11.5	11.4	11.9	11.8	12.6	12.5	12.9
Na2O	1.4	2.8	2.7	2.1	2.0	1.5	1.5	1.5	1.3	1.0	1.4	0.8	1.0	0.7
K2O	0.2	1.1	1.1	1.7	1.7	0.3	0.3	0.4	0.4	0.2	0.4	0.1	0.1	0.1
NiO	-	-	-	-	-	-	-	-	-	-	-	0.1	0.1	0.1
Cr2O3	-	-	-	-	-	-	-	-	-	-	-	0.0	0.1	0.0
SrO	-	-	-	-	-	-	-	-	-	-	-	0.0	0.0	0.0
Total	97.3	97.9	97.8	97.8	96.7	96.5	96.7	96.8	96.6	97.8	97.6	95.5	96.3	96.9
Oxygens	23	23	23	23	23	23	23	23	23	23	23	23	23	23
Si	6.64	6.11	6.11	6.06	6.06	6.20	6.24	6.21	6.24	6.64	6.40	7.23	7.17	7.37
Ti	0.06	0.45	0.43	0.38	0.38	0.04	0.04	0.05	0.05	0.03	0.03	0.02	0.03	0.02
Al	2.05	2.29	2.30	2.51	2.44	2.85	2.84	2.77	2.75	2.10	2.46	1.15	1.24	0.92
Fe3	0.36	0.68	0.71	0.61	0.67	0.47	0.42	0.45	0.51	0.43	0.43	0.17	0.19	0.17
Fe2	0.65	0.51	0.48	0.83	0.80	1.55	1.58	1.60	1.57	1.28	1.40	0.79	0.84	0.75
Mn	0.02	0.01	0.01	0.01	0.02	0.05	0.04	0.04	0.05	0.03	0.03	0.02	0.02	0.02
Mg	3.27	3.03	3.06	2.66	2.70	1.94	1.95	1.94	1.92	2.55	2.31	3.63	3.53	3.77
Ca	1.90	1.80	1.80	1.87	1.87	1.79	1.78	1.84	1.82	1.85	1.85	1.96	1.93	1.96
Na	0.38	0.81	0.77	0.59	0.57	0.44	0.44	0.44	0.39	0.29	0.39	0.24	0.28	0.19
K	0.03	0.21	0.20	0.31	0.32	0.06	0.06	0.08	0.07	0.04	0.07	0.02	0.01	0.02
Sum	15.36	15.90	15.87	15.83	15.82	15.39	15.38	15.43	15.36	15.25	15.38	15.24	15.26	15.19

Table 15 – Continued

Sample	C-95	C-95	C-95	C-95	C-95	C-95	C-95	C-95	C-95	C-95	C-95	J111	J111	J256
SiO2	53.5	49.9	47.8	53.9	51.4	52.9	52.0	55.0	49.2	54.4	49.9	45.1	45.2	50.0
TiO2	0.1	0.2	0.2	0.1	0.2	0.1	0.1	0.0	0.1	0.0	0.1	0.5	0.5	0.5
Al2O3	3.6	6.7	12.1	3.7	6.4	3.7	4.6	2.4	8.5	3.5	7.7	11.2	9.6	6.2
Fe2O3	0.0	0.0	0.0	0.0	0.0	0.0	0.0	0.0	0.0	0.0	0.0	0.0	0.0	0.0
FeO	6.9	8.0	6.1	6.9	7.9	6.9	7.3	7.5	7.7	5.6	7.2	15.2	15.7	11.3
MnO	0.2	0.2	0.1	0.2	0.2	0.1	0.2	0.1	0.2	0.1	0.2	0.3	0.4	0.2
MgO	19.0	16.2	11.7	18.3	17.2	18.8	18.3	18.4	16.5	20.0	17.4	11.4	11.5	15.3
CaO	13.1	12.7	16.8	13.0	12.7	12.7	12.9	13.1	12.8	13.0	12.9	11.7	11.8	12.5
Na2O	0.4	0.8	0.6	0.5	0.8	0.4	0.5	0.2	1.1	0.4	1.0	1.1	1.0	0.5
K2O	0.1	0.1	0.1	0.1	0.1	0.1	0.1	0.0	0.2	0.0	0.1	0.4	0.3	0.2
NiO	0.0	0.0	0.0	0.1	0.0	0.0	0.0	0.1	0.1	0.1	0.1	0.0	0.0	0.0
Cr2O3	0.0	0.1	0.0	0.0	0.1	0.0	0.0	0.0	0.2	0.1	0.1	0.0	0.1	0.1
SrO	0.0	0.1	0.0	0.0	0.0	0.0	0.0	0.1	0.0	0.0	0.0	0.1	0.1	0.0
Total	96.8	95.0	95.6	96.7	97.1	95.6	96.0	96.9	96.7	97.4	96.7	96.9	96.3	96.8
Oxygens	23	23	23	23	23	23	23	23	23	23	23	23	23	23
Si	7.56	7.30	6.12	7.65	7.31	7.56	7.44	7.80	7.07	7.60	7.11	6.66	6.73	7.22
Ti	0.01	0.02	0.02	0.01	0.02	0.01	0.01	0.00	0.02	0.00	0.01	0.05	0.06	0.05
Al	0.60	1.15	1.82	0.62	1.07	0.63	0.77	0.40	1.44	0.57	1.30	1.95	1.69	1.06
Fe3	0.18	0.02	5.43	0.00	0.13	0.20	0.23	0.00	0.12	0.15	0.20	0.51	0.60	0.37
Fe2	0.63	0.95	-4.78	0.82	0.81	0.62	0.64	0.89	0.81	0.51	0.66	1.36	1.36	1.00
Mn	0.02	0.02	0.02	0.02	0.02	0.02	0.02	0.02	0.02	0.02	0.02	0.04	0.05	0.02
Mg	4.00	3.54	2.23	3.88	3.66	3.99	3.91	3.88	3.54	4.17	3.70	2.50	2.55	3.30
Ca	1.99	1.98	2.31	1.98	1.94	1.94	1.97	1.99	1.97	1.95	1.98	1.85	1.89	1.94
Na	0.10	0.22	0.15	0.12	0.22	0.10	0.15	0.04	0.30	0.12	0.27	0.32	0.29	0.15
K	0.01	0.02	0.02	0.01	0.02	0.01	0.01	0.01	0.04	0.00	0.02	0.07	0.06	0.04
Sum	15.11	15.23	13.33	15.11	15.20	15.09	15.14	15.03	15.31	15.10	15.28	15.31	15.30	15.15

Sample	J256	J256	J256	J256	J256	J256	J256	J256	J256	J256	J256	J256	J259	J262
SiO2	49.9	51.1	49.4	50.5	49.8	50.4	51.6	51.0	49.7	53.2	53.0	53.6	43.5	41.4
TiO2	0.4	0.5	0.4	0.4	0.6	0.4	0.3	0.4	0.5	0.3	0.2	0.2	1.7	4.0
Al2O3	5.7	5.8	6.5	6.1	6.4	6.7	5.4	5.8	6.6	4.1	4.3	3.9	11.3	13.1
Fe2O3	0.0	0.0	0.0	0.0	0.0	0.0	0.0	0.0	0.0	0.0	0.0	0.0	0.0	0.0
FeO	10.8	11.3	12.0	10.7	11.1	10.7	10.0	11.4	11.9	9.5	9.5	9.2	13.2	9.6
MnO	0.2	0.2	0.2	0.2	0.2	0.2	0.2	0.2	0.2	0.2	0.2	0.2	0.1	0.1
MgO	14.1	15.6	14.8	16.0	15.6	16.0	16.5	15.5	14.9	17.4	17.2	17.3	12.8	13.8
CaO	15.3	12.7	12.6	12.6	12.3	12.5	12.5	12.6	12.4	12.4	12.4	12.5	11.7	11.4
Na2O	0.5	0.5	0.5	0.5	0.6	0.6	0.5	0.5	0.5	0.4	0.4	0.5	1.3	2.8
K2O	0.2	0.2	0.2	0.2	0.3	0.2	0.2	0.2	0.3	0.1	0.2	0.1	1.5	1.1
NiO	0.0	0.0	0.1	0.1	0.0	0.0	0.0	0.0	0.0	0.0	0.1	0.0		0.0
Cr2O3	0.1	0.1	0.1	0.1	0.1	0.1	0.0	0.1	0.1	0.0	0.0	0.0	0.0	0.6
SrO	0.0	0.1	0.1	0.0	0.0	0.0	0.0	0.0	0.0	0.1	0.0	0.0		0.0
Total	97.2	98.0	96.9	97.3	96.9	97.7	97.2	97.7	97.0	97.7	97.4	97.6	97.1	97.9
Oxygens	23	23	23	23	23	23	23	23	23	23	23	23	23	23
Si	6.70	7.30	7.18	7.24	7.18	7.18	7.37	7.31	7.18	7.53	7.53	7.59	6.44	6.11
Ti	0.04	0.05	0.05	0.04	0.06	0.04	0.03	0.05	0.05	0.03	0.02	0.02	0.19	0.45
Al	0.89	0.98	1.12	1.03	1.09	1.12	0.90	0.98	1.13	0.68	0.71	0.65	1.96	2.29
Fe3	3.74	0.32	0.38	0.39	0.45	0.41	0.28	0.32	0.38	0.23	0.21	0.14	0.65	0.68
Fe2	-2.52	1.03	1.08	0.89	0.88	0.87	0.91	1.05	1.05	0.89	0.92	0.95	0.99	0.51
Mn	0.02	0.02	0.02	0.03	0.03	0.03	0.02	0.02	0.02	0.03	0.02	0.03	0.01	0.01
Mg	2.83	3.32	3.20	3.41	3.35	3.39	3.52	3.31	3.21	3.67	3.64	3.65	2.82	3.03
Ca	2.19	1.94	1.96	1.94	1.90	1.90	1.91	1.93	1.93	1.88	1.89	1.90	1.86	1.80
Na	0.13	0.13	0.15	0.13	0.16	0.16	0.13	0.13	0.15	0.12	0.12	0.13	0.37	0.81
K	0.04	0.03	0.04	0.04	0.05	0.04	0.03	0.04	0.05	0.03	0.03	0.03	0.28	0.21
Sum	14.07	15.13	15.17	15.14	15.16	15.15	15.12	15.13	15.16	15.09	15.09	15.09	15.58	15.90

Table 15 – Continued

Sample	J262	J264	J264	J266	J266	J266	J266	J269	J269	J270	J270	J270	J270	J413
SiO2	41.4	44.0	44.5	50.8	51.2	50.5	51.1	45.8	43.7	41.6	42.0	41.6	41.7	40.7
TiO2	3.9	0.4	0.4	0.1	0.1	0.2	0.2	0.3	0.3	0.4	0.3	0.4	0.4	3.4
Al2O3	13.2	13.5	13.4	6.8	7.1	7.6	7.1	12.3	14.3	16.2	16.2	15.8	15.6	14.3
Fe2O3	0.0	0.0	0.0	0.0	0.0	0.0	0.0	0.0	0.0	0.0	0.0	0.0	0.0	0.0
FeO	9.6	12.4	12.3	8.8	8.9	9.0	9.0	14.1	14.9	16.2	16.1	16.4	16.7	11.6
MnO	0.1	0.3	0.2	0.2	0.2	0.2	0.2	0.2	0.2	0.4	0.3	0.4	0.4	0.1
MgO	13.9	12.1	12.4	16.8	16.9	16.0	16.5	11.8	10.6	8.8	8.8	8.7	8.6	12.0
CaO	11.4	11.9	11.9	12.1	12.2	12.3	12.1	11.9	11.8	11.2	11.2	11.5	11.4	11.7
Na2O	2.7	1.4	1.4	0.8	0.9	0.8	0.8	1.0	1.4	1.5	1.5	1.5	1.3	2.1
K2O	1.1	0.2	0.3	0.1	0.1	0.1	0.1	0.2	0.4	0.3	0.3	0.4	0.4	1.7
NiO	0.1	-	-	-	-	-	-	0.0	0.0	0.0	0.0	0.0	0.0	0.1
Cr2O3	0.6	0.0	0.0	0.0	0.1	0.2	0.2	0.1	0.0	0.0	0.0	0.0	0.0	0.0
SrO	0.0	-	-	-	-	-	-	0.0	0.0	0.0	0.0	0.1	0.0	0.1
Total	97.8	96.2	96.8	96.5	97.5	96.9	97.2	97.8	97.6	96.5	96.7	96.8	96.6	97.8
Oxygens	23	23	23	23	23	23	23	23	23	23	23	23	23	23
Si	6.11	6.47	6.49	7.26	7.24	7.22	7.27	6.64	6.40	6.20	6.24	6.21	6.24	6.06
Ti	0.43	0.05	0.04	0.01	0.01	0.02	0.02	0.03	0.03	0.04	0.04	0.05	0.05	0.38
Al	2.30	2.35	2.30	1.14	1.18	1.29	1.18	2.10	2.46	2.85	2.84	2.77	2.75	2.51
Fe3	0.71	0.40	0.42	0.25	0.24	0.16	0.23	0.43	0.43	0.47	0.42	0.45	0.51	0.61
Fe2	0.48	1.12	1.08	0.80	0.81	0.92	0.84	1.28	1.40	1.55	1.58	1.60	1.57	0.83
Mn	0.01	0.03	0.03	0.02	0.03	0.02	0.02	0.03	0.03	0.05	0.04	0.04	0.05	0.01
Mg	3.06	2.64	2.70	3.57	3.56	3.42	3.50	2.55	2.31	1.94	1.95	1.94	1.92	2.66
Ca	1.80	1.87	1.86	1.85	1.85	1.88	1.85	1.85	1.85	1.79	1.78	1.84	1.82	1.87
Na	0.77	0.41	0.39	0.22	0.24	0.23	0.22	0.29	0.39	0.44	0.44	0.44	0.39	0.59
K	0.20	0.05	0.05	0.02	0.01	0.02	0.01	0.04	0.07	0.06	0.06	0.08	0.07	0.31
Sum	15.87	15.38	15.37	15.16	15.18	15.18	15.15	15.25	15.38	15.39	15.38	15.43	15.36	15.83

Sample	J413	J419	J419	J419	J419	J419	J419	J428	J428	J428	J428	J428	J428	J428
SiO2	40.4	44.0	44.2	42.7	42.8	45.0	43.7	57.4	58.0	42.3	42.0	42.3	42.5	42.7
TiO2	3.4	0.4	0.5	0.4	0.4	0.5	0.5	0.0	0.0	0.8	1.0	1.2	1.1	0.4
Al2O3	13.8	13.5	13.1	14.5	14.8	12.5	14.0	0.1	0.1	14.7	14.6	14.5	15.4	15.5
Fe2O3	0.0	0.0	0.0	0.0	0.0	0.0	0.0	0.0	0.0	0.0	0.0	0.0	0.0	0.0
FeO	11.7	13.9	13.8	14.5	14.2	13.7	14.0	12.5	12.0	8.7	9.0	9.9	9.8	8.3
MnO	0.1	0.2	0.3	0.2	0.2	0.2	0.2	0.4	0.4	0.1	0.1	0.1	0.1	0.1
MgO	12.1	11.1	11.7	10.9	11.0	12.3	11.2	26.6	26.7	15.6	15.5	14.4	13.8	15.4
CaO	11.6	11.5	11.6	11.9	11.7	11.2	11.7	0.5	0.5	11.7	11.7	11.7	11.8	12.0
Na2O	2.0	1.3	1.2	1.3	1.3	1.3	1.3	0.0	0.0	2.3	2.3	2.2	2.1	2.5
K2O	1.7	0.2	0.2	0.3	0.3	0.2	0.2	0.0	0.0	0.9	0.9	0.8	0.9	0.8
NiO	0.0	0.0	0.0	0.0	0.0	0.0	0.1	0.1	0.1	0.0	0.0	0.1	0.0	0.1
Cr2O3	0.0	0.0	0.0	0.0	0.1	0.0	0.0	0.0	0.0	0.0	0.1	0.1	0.0	0.0
SrO	0.0	0.1	0.0	0.0	0.0	0.0	0.0	0.0	0.0	0.0	0.0	0.0	0.0	0.1
Total	96.7	96.2	96.5	96.7	96.8	96.8	96.9	97.6	97.7	97.2	97.2	97.5	97.7	97.8
Oxygens	23	23	23	23	23	23	23	23	23	23	23	23	23	23
Si	6.06	6.50	6.48	6.30	6.29	6.55	6.41	7.94	7.99	6.10	6.06	6.14	6.15	6.12
Ti	0.38	0.05	0.05	0.05	0.04	0.05	0.05	0.00	0.00	0.09	0.11	0.13	0.12	0.04
Al	2.44	2.35	2.26	2.52	2.57	2.14	2.42	0.01	0.02	2.50	2.48	2.48	2.63	2.62
Fe3	0.67	0.43	0.59	0.60	0.60	0.62	0.52	0.06	0.00	0.69	0.80	0.65	0.49	0.49
Fe2	0.80	1.28	1.11	1.18	1.15	1.05	1.20	1.39	1.38	0.36	0.29	0.55	0.70	0.51
Mn	0.02	0.03	0.03	0.02	0.02	0.03	0.03	0.05	0.05	0.01	0.01	0.01	0.01	0.01
Mg	2.70	2.45	2.56	2.39	2.41	2.67	2.45	5.49	5.48	3.34	3.34	3.12	2.98	3.29
Ca	1.87	1.82	1.82	1.87	1.84	1.76	1.84	0.08	0.07	1.81	1.81	1.82	1.83	1.83
Na	0.57	0.37	0.34	0.36	0.37	0.36	0.37	0.00	0.00	0.65	0.64	0.63	0.60	0.69
K	0.32	0.04	0.04	0.06	0.05	0.03	0.05	0.00	0.00	0.16	0.16	0.15	0.16	0.15
Sum	15.82	15.32	15.28	15.35	15.34	15.26	15.33	15.02	15.00	15.71	15.70	15.69	15.67	15.75

Table 15 – Continued

Sample	J428	J428	J428	J429	J429	J429	J429	J429	J429	J429	J429	J429	J429	J429
SiO2	42.1	53.9	55.3	40.6	41.7	40.4	41.6	41.9	41.3	41.3	41.6	54.8	53.5	41.9
TiO2	0.4	0.4	0.2	1.6	1.7	0.0	0.1	2.1	2.0	1.9	1.9	0.2	0.2	1.5
Al2O3	16.0	4.9	3.4	13.9	14.0	17.5	15.9	14.0	13.7	14.3	14.3	3.4	4.4	13.8
Fe2O3	0.0	0.0	0.0	0.0	0.0	0.0	0.0	0.0	0.0	0.0	0.0	0.0	0.0	0.0
FeO	8.8	4.1	4.0	9.2	9.0	11.1	10.8	9.2	9.2	8.7	9.0	5.7	6.0	9.2
MnO	0.1	0.1	0.1	0.1	0.1	0.2	0.1	0.1	0.1	0.1	0.1	0.2	0.1	0.1
MgO	14.9	21.0	21.7	14.8	14.7	12.9	13.5	14.8	14.8	14.9	14.6	20.4	19.7	15.3
CaO	11.9	13.2	12.9	11.5	11.6	11.8	12.0	11.5	11.4	11.5	11.4	12.9	12.9	11.6
Na2O	2.4	0.8	0.5	2.7	2.6	2.7	2.6	2.5	2.5	2.4	2.4	0.6	0.7	2.5
K2O	0.9	0.0	0.0	1.0	1.0	0.2	0.2	1.0	1.0	0.9	0.9	0.0	0.0	0.7
NiO	0.0	0.0	0.0	0.0	0.1	0.0	0.0	0.1	0.1	0.0	0.0	0.0	0.1	0.1
Cr2O3	0.1	0.2	0.2	0.6	0.5	0.0	0.0	0.7	0.5	0.5	0.5	0.3	0.3	0.6
SrO	0.0	0.0	0.0	0.0	0.0	0.0	0.0	0.0	0.0	0.1	0.1	0.1	0.1	0.1
Total	97.6	98.6	98.3	96.2	96.9	96.9	96.8	97.7	96.6	96.6	96.9	98.5	98.0	97.5
Oxygens	23	23	23	23	23	23	23	23	23	23	23	23	23	23
Si	6.05	7.41	7.59	6.03	6.13	5.89	6.06	6.11	6.09	6.06	6.11	7.58	7.47	6.09
Ti	0.05	0.04	0.02	0.18	0.19	0.01	0.01	0.23	0.22	0.21	0.21	0.02	0.02	0.16
Al	2.71	0.80	0.55	2.44	2.42	3.01	2.73	2.41	2.39	2.48	2.47	0.56	0.72	2.37
Fe3	0.54	0.24	0.24	0.70	0.59	0.57	0.52	0.67	0.74	0.75	0.68	0.19	0.21	0.80
Fe2	0.52	0.23	0.22	0.44	0.52	0.78	0.79	0.45	0.40	0.32	0.43	0.46	0.48	0.32
Mn	0.01	0.01	0.01	0.01	0.01	0.02	0.02	0.01	0.01	0.01	0.01	0.02	0.01	0.01
Mg	3.20	4.31	4.43	3.27	3.22	2.79	2.93	3.21	3.26	3.25	3.18	4.20	4.10	3.33
Ca	1.84	1.94	1.89	1.83	1.82	1.84	1.87	1.80	1.80	1.81	1.80	1.91	1.94	1.81
Na	0.66	0.22	0.14	0.78	0.74	0.76	0.73	0.71	0.72	0.67	0.68	0.17	0.18	0.71
K	0.16	0.00	0.00	0.19	0.18	0.04	0.04	0.19	0.19	0.17	0.17	0.00	0.01	0.13
Sum	15.73	15.18	15.09	15.88	15.82	15.72	15.70	15.79	15.80	15.74	15.74	15.12	15.16	15.74

Sample	J429	J429	J429	J429	J429
SiO2	42.0	41.4	41.1	55.3	55.8
TiO2	1.8	0.0	0.0	0.2	0.2
Al2O3	13.8	17.6	17.7	3.4	2.8
Fe2O3	0.0	0.0	0.0	0.0	0.0
FeO	9.2	8.4	8.4	4.5	4.3
MnO	0.1	0.1	0.1	0.1	0.1
MgO	14.9	14.8	15.2	21.3	21.8
CaO	11.5	11.9	11.7	12.6	12.5
Na2O	2.5	2.9	3.3	0.6	0.5
K2O	0.9	0.2	0.3	0.0	0.0
NiO	0.1	0.0	0.1	0.0	0.0
Cr2O3	0.6	0.0	0.0	0.3	0.2
SrO	0.0	0.1	0.0	0.0	0.0
Total	97.3	97.4	97.9	98.3	98.4
Oxygens	23	23	23	23	23
Si	6.14	5.92	5.86	7.60	7.65
Ti	0.20	0.00	0.00	0.02	0.02
Al	2.38	2.97	2.98	0.55	0.46
Fe3	0.68	0.53	0.56	0.22	0.24
Fe2	0.45	0.47	0.45	0.29	0.26
Mn	0.01	0.02	0.02	0.01	0.02
Mg	3.24	3.16	3.22	4.36	4.46
Ca	1.80	1.82	1.80	1.86	1.84
Na	0.71	0.80	0.90	0.17	0.13
K	0.16	0.04	0.05	0.01	0.01
Sum	15.77	15.75	15.84	15.09	15.07

Appendix E – Assay Results from Hanno Resources Limited

The following tables present details of anomalous rock chip samples provided by Hanno Resources Limited. For all analyses Aqua Regia Digest was used and ICP-MS facilities, with the analyses carried out by ALS laboratories in Perth, Western Australia.

Table 16 - Details of rock chip samples >0.2 g/t Au, in the study area.

Area	Sample No.	UTM E	UTM N	Description	Au (g/t)
Agarasras G52	C00947	767917	2713422	White quartz with visible gold	13439
	C00949	767933	2713494	Hematite and sulphur stained quartz with pyrite and chalcopyrite and malachite	13.8
	C01177	767745	2711509	Chert with disseminated pyrite and voids	12.8
	C01178	767716	2711510	Chert with disseminated pyrite and voids	4.82
	C01159	767310	2711558	Sulphur stained quartz with pyrite	4.79
	C00950	767934	2713485	Hematite and sulphur stained quartz with pyrite and chalcopyrite and malachite	2.56
	C00941	766862	2710298	Carbonate altered granite with pyrite	1.33
	C00942	766861	2710290	Carbonate altered granite with pyrite	1.18
	C01157	766808	2710088	Carbonate altered granite with oxidised pyrite	0.67
	C00952	767695	2711886	Hematite and sulphur stained quartz with pyrite and chalcopyrite	0.53
	C00461	764486	2716836		0.51
	C00948	767935	2713481	Hematite and sulphur stained quartz with pyrite and chalcopyrite and malachite	0.51
	C01119	764069	2711671	Hematite stained quartz with malachite	0.45
	C01161	767392	2711069	Carbonate chlorite altered granite with oidised pyrite	0.37
	C00939	766912	2712251	White quartz with hematite stained blebs with chalcopyrite	0.32
	C01147	767845	2711028	Dark altered granite with oidised pyrite	0.25
	C00946	767928	2713456	Hematite and sulphur stained quartz with pyrite and chalcopyrite	0.22
Agarasras Labiad	C01002	764539	2716842	White quartz, high iron and sulphur staining, relic teture, black and fresh pyrite	20.8
	C01058	764309	2716723	Quartz boulder, significant iron and sulphur staining, bowork tecture, black pyrite	11.1
	C00453	764295	2716689		9.83
	C00512	764363	2716632		3.08
	C00516	764246	2716725		3.00
	C01056	764470	2716834	Granite in contact with quartz vein, yellow, relict pyrite, black mineral, iron rusting	2.48
	C01053	764511	2716845	White quartz, bowork teture, black surface pyrite and fresh pyrite	2.27
	C00434	765166	2715787		1.94
	C00455	764326	2716880		1.76
	C01059	764299	2716679	Alteration rim between quartz vein and granite, brown fine grained crystaline	0.66
	C01018	764809	2715967	Pink (potassic?) granite, iron staining, bowork and relic pyrite	0.54
	C00513	764341	2716648		0.50
	C01054	764383	2716938	White quartz, some iron staining and fresh pyrite	0.35
	C01012	765417	2717258	White quartz, tourmaline and chlorite veining, rusting bowork, small possible sulphide	0.26
	C01055	764320	2716927	White quartz, nodule of black mineral, some iron staining with possible fresh pyrite	0.25
	C00623	765177	2715890	Light pink potassic altered granite with goethite filled voids	0.22
Moug el Kaleb	C00983	775130	2636851	Quartz carbonate viein with possible disseminated pyrite	9.97
	C01201	775412	2635538	Plagioclase gabbro with pyrite and small malachite	0.84
	C00884	774135	2636651	Iron with chalcopyrite	0.59
	C00886	774116	2636679	Iron with malachite veining	0.42
	C00883	774137	2636653	Iron with malachite veining	0.33
	C00885	774108	2636700	Iron quartzite with bowork voids	0.24
	C00917	772080	2639272	Hematite and sulphur stained quartz with pyrite and chalcopyrite	0.22
	C00918	772044	2639279	Hematite and sulphur stained quartz with pyrite and chalcopyrite	0.2
Guelb Koujil	C01253	774929	2718732	Iron and sulphur staining quartz with disseminated pyrite	2.47
	C01254	774912	2718744	Iron and sulphur staining quartz with disseminated pyrite	0.91
	C01256	774916	2718739	Iron and sulphur staining quartz with disseminated pyrite, possible "electrum"	0.33
	C01255	774902	2718748	Iron and sulphur staining quartz with disseminated pyrite	0.23
Taghsoumat	C02089	747530	2692452	Quartz vein, iron and sulphur staining, black pyrite cubes	1.7
	C00932	749274	2689405	Hematite and sulphur stained quartz with pyrite and chalcopyrite	0.22
Agarasras Lakhadar	C02009	758843	2710849	Quartz boulder, possible galena, fresh chalcopyrite and malachite or fuchsite	0.37
	C00933	759028	2713731	Altered pyroxenite with chalcopyrite	0.22
Elmalhat	C01093	794303	2665975	Listwanite with malachite and possible sulphides	0.23

Table 17 - Details of rock chip samples >500 ppm Cu in the study area

Area	Sample No.	UTM E	UTM N	Description	Cu (ppm)
Moug el Kalab	C00886	774116	2636879	Iron with malachite veining	13153
	C00883	774137	2636853	Iron with malachite veining	7829
	C00882	774147	2636649	Iron with malachite	7266
	C01201	775412	2635538	Plagioclase gabbro with pyrite and small malachite	4261
	C01102	774707	2636292	Epidote altered plagioclase gabbro	3997
	C00880	774044	2637049	Gossan like iron float/lag with pyrite	3482
	C00881	774109	2636897	Iron with surface malachite	2769
	C00885	774108	2636700	Iron quartzite with boxwork voids	1636
	C01200	775402	2636178	Altered ultramafics	1634
	C02117	774882	2636789	Anothosite with pyrite and chalcopyrite	1099
	C00884	774135	2636651	Iron with chalcopyrite	901
	C01204	775617	2635336	Listwanite	796
	C00871	775218	2637191	Altered gabbro with pyrite	769
	C01104	774662	2636108	Dark red hematite iron possbile gossan	695
	C00987	775092	2635800	Plagioclase gabbro with chalcopyrite and malachite	673
Elmalhat	C01093	794303	2665975	Liswanite with malachite and possible sulphides	7912
	C01091	794268	2665958	Liswanite with malachite and possible sulphides	5894
	C01090	794282	2665977	Liswanite with malachite and possible sulphides	3877
	C01228	791709	2632437	Plagioclase gabbro with disseminate pyrite and possbile malachite halo	1016
	C01097	803008	2645751	Dark red hematite iron possbile gossan	882
	C01092	794256	2665982	Liswanite with malachite and possible sulphides, white carbonate fill	877
	C01084	805302	2648853	Dark anorthosite gabbro with disseminated sulphides	689
	C01197	800113	2660830	Massive chromite	599
Agarasras G52	C00948	767935	2713481	Hematite and sulphur stained quartz with pyrite and chalcopyrite and malachite	2477
	C01119	764069	2711671	Hematite stained quartz with malachite	2304
	C00938	766913	2712264	Hematite stained quartz relic voids	1536
	C02045	765445	2711208	Quartz, some iron and sulphur staining, fresh chalcopyrite and malachite, bornite	1139
	C00488	764557	2715387		1079
	C01147	767845	2711028	Dark altered granite with oxidised pyrite	920
	C00937	766923	2712243	White quartz with malachite	695
	C01141	767199	2711629	Ferrugenous black chert with pyrite	681
	C02121	765439	2710932	Altered rhyolite with pyrite	673
	C02120	765634	2710880	Hematite and sulphur stained quartz with chalcopyrite	649
	C00939	766912	2712251	White quartz with hematite stained blebs with chalcopyrite	546
	C01158	770302	2712253	Altered rhyolite	531
Agarasras Labiad	C00620	764890	2716029	Sericitic altered granite, quartz vein with malachite and small fresh and weathered chalcopy	1598
	C00621	764855	2716053	Quartz vein with hematite staining and small malachite	1193
	C00486	764517	2715306		1178
	C01065	764809	2716114	Quartz vein, thin vertical, black pyrite, malachite, possible chalcopyrite	1131
	C01027	764901	2716030	Granite with small quartz vein, chalcopyrite and malachite found by Chris	957
	C00447	765385	2715925		553
Agarasras Lakhadar	C02022	758915	2713904	Possible dunite, pure olvine, magnetic	1349
	C02009	758843	2710849	Quartz boulder, possible galena, fresh chalcopyrite and malachite or fuchsite	1342
	C01244	755921	2713177	Black listwanite/gossan	1237
	C00933	759028	2713731	Altered pyroxenite with chalcopyrite	1094
	C02095	758939	2710915	Quartz vein, iron and sulphur staining, fresh chalcopyrite	1026
	C02133	753591	2714690	Altered gabbro with pyrite	884
	C02010	758949	2710869	Quartz vein, possible galena, fresh chalcopyrite, possible dendritic silver	753
	C02017	759039	2713716	Iron rich mafic/ultramafic with surface vesicles	724
	C00934	758857	2713956	Possible chromite	550
G79	C01115	803788	2673178	Hematite stained voidy quartz with blue mineral	1263
	C01114	803770	2673227	Hematite stained voidy quartz with pyrite and malachite	828
12 km SW of Lakhad	C01258	749407	2701077	Porphyry granite with pyrite, chalcopyrite and malachite	1987
	C01259	749412	2701072	Porphyry granite with pyrite, chalcopyrite and malachite	990
15 km S of Ag. G52	C00636	770557	2693532	Black/red hematite altered quartzite with disseminated fresh pyrite	1045
8 km N of Ag. Labiad	C02082	765563	2728470	Grey quartz vein, fresh pyrite	958

Table 18 - Details of rock chip samples >500 ppm Ni, in the study area

Area	Sample No.	UTM E	UTM N	Description	Ni (ppm)
Elmalhat	C00915	799392	2651761	Possible weathered dunite, smooth surface texture, brown (with blue weathered pyroxene?)	1312
	C00911	799534	2652724	Possible weathered dunite, smooth surface texture, brown (with blue weathered pyroxene?)	1239
	C00912	799662	2652446	Possible weathered dunite, or iron rich gabbro	1217
	C01221	786001	2628163	Listwanite with green quartz veining	1015
	C01226	784202	2627845	Listwanite	958
	C01193	794361	2630756	Magnetite-Chromitite	775
	C01223	794358	2630752	Chromite	730
	C00913	799717	2652388	Listwanite	725
	C00861	793317	2645940	Listwanite	704
	C01220	784719	2625886	Listwanite	693
	C01107	798447	2662532	Liswanite with possible fuchsite	672
	C01079	802727	2657772	Massive chromitite	617
	C01097	803008	2645751	Dark red hematite iron possbile gossan	593
	C00868	802165	2643676	Listwanite	581
	C00855	779629	2649670	Listwanite	576
	C00857	793328	2645396	Listwanite	568
Moug el Kaleb	C00984	775252	2636207	Listwanite	881
	C01200	775402	2636178	Altered ultramafics	789
	C01204	775617	2635336	Listwanite	654
	C01104	774662	2636108	Dark red hematite iron possbile gossan	587
	C01205	775852	2635043	Listwanite	586
	C01201	775412	2635538	Plagioclase gabbro with pyrite and small malachite	557
Agarasras Lakhadar	C02018	759033	2713716	Iron rich mafic/ultramafic with platy/fibrous grained surface texture	906
	C02017	759039	2713716	Iron rich mafic/ultramafic with surface vesicles	795
	C02016	759101	2713693	Iron rich mafic/ultramafic	632
	C00491	759911	2713776		577
	C01243	758732	2713670	Chlorite altered ultramafic	573

Table 19 - Chromitite from the Northern Limb of the Elmalhat Anorthosite Complex with Pt+Pd >10ppb

Sample No	UTM Zone	Easting	Northing	Description	Pd (ppb)	Pt (ppb)	Pt + Pd
C00834	29	194739	2655028	Chromite	82	156	238
C02101	28	798247	2662648	Massive chromitite	36	106	142
C01197	28	800113	2660830	Massive chromite	43	17	60
C01190	28	799755	2661391	Chromitite	31	20	51
C00829	29	194744	2655070	Chromite with large surface crystals	38	13	51
C02110	28	800115	2660831	Massive chromitite	35	14	49
C02103	28	798427	2662520	Massive chromitite	35	13	48
C02106	28	797853	2662818	Massive chromitite	19	14	33
C00828	29	194806	2655071	Chromite	18	15	33
C01108	28	798419	2662533	Massive chromitite	23	5	28
C02109	28	797506	2663148	Massive chromitite	12	9	21
C02105	28	798529	2662434	Massive chromitite	12	6	18
C00997	28	797478	2663169	Massive chromitite with carbonate veining	0	15	15
C01079	28	802727	2657772	Massive chromitite	13	0	13
C00994	28	797854	2662823	Massive chromitite	0	11	11